IPNS
Upgrade

A Feasibility Study

MASTER

IPNS Upgrade:
A Feasibility Study

ARGONNE NATIONAL LABORATORY
9700 South Cass Avenue
Argonne, Illinois 60439-4801

April 1995

MASTER

Many of Argonne National Laboratory's (ANL's) scientific staff members were very active in R&D work related to accelerator-based spallation sources in the 1970s and early 1980s. In 1984, the Seitz/Eastman Panel of the National Academy of Sciences reviewed U.S. materials science research facilities. One of the recommendations of this panel was that the United States build a reactor-based steady-state source, the Advanced Neutron Source (ANS), at Oak Ridge National Laboratory. Subsequently, R&D activities related to the design of an accelerator-based source assumed a lower priority.

The resumption of pulsed-source studies in this country started simultaneously with design activities in Europe aimed at the European Spallation Source (ESS). The European Community funded a workshop in September 1991 to define the parameters of the ESS. Participants in this workshop included both accelerator builders and neutron source users. A consortium of European countries has proposed to build a 5-MW pulsed source, and a feasibility study is currently under way. Soon after the birth of the ESS, a small group at ANL set about bringing themselves up to date on pulsed-source information since 1984 and studied the feasibility of upgrading ANL's Intense Pulsed Neutron Source (IPNS) to 1 MW by means of a rapidly cycling synchrotron that could be housed, along with its support facilities, in existing buildings.

Coincidentally, in 1992, the U.S. Department of Energy asked its Basic Energy Science Advisory Committee (BESAC) to review the nation's neutron science facility needs. A BESAC subpanel, chaired by Walter Kohn, was appointed to carry out the review. Preliminary results of ANL's IPNS upgrade study were presented at the subpanel meetings, along with Los Alamos National Laboratory's plan for a 1-MW facility based around the Los Alamos linac.

In early 1993, the Kohn panel recommended that (1) design and construction of the ANS should be completed according to the proposed project schedule and (2) development of competitive proposals for cost-effective design and construction of a 1-MW pulsed spallation source should be authorized immediately. The panel urged that evaluation of these proposals be done as soon as possible, leading to a construction timetable that would not interfere with rapid completion of the ANS.

In response to these encouraging Kohn-panel recommendations, the ANL study group carried out a complete feasibility study of a 1-MW pulsed source. This document, together with three separate supplements, contains the results of the feasibility study.

Personnel from several ANL divisions contributed to this study. Y. Cho provided the overall leadership and integration for the study. Work related to the accelerator systems was performed by Y.-C. Chae, Y. Cho, E. Crosbie, H. Friedsam, K. Harkay, D. Horan, S. Kim, R. Kustom, E. Lessner, W. McDowell, D. McGhee, F. Mills, H. Moe, R. Nielsen, A. Rauchas, K. Symon, K. Thompson, D. Warner, and M. White, all from the Advanced Photon Source Project (APS). The linear accelerator feasibility study was performed by AccSys Technology, Inc., of Pleasanton, California, under the guidance of the study group.

J. Carpenter (IPNS) led the target station design effort. A concept development group comprising J. Carpenter and R.K. Crawford (IPNS), R. Kleb (Materials Science Division), and A. Knox (Technology Development Division) worked out the basic target station design. Providing engineering, analytical, management, and documentation assistance were J. Bailey, P. Calahan, L. Carlson, T. Fornek, A. Knox, and R. Smith (TD); T. Kassner and J. Routbort (Energy Technology Division); R. Kleb (MSD); I. Bresof, D. Jerng, and W. Ruzicka (IPNS); and T. Broome of ISIS (U.K.).

R.K. Crawford led the compilation of neutron scattering instrument requirements and the documentation of instrument designs. Instrumentation requirements and designs for specific neutron scattering instruments and components, and instrument performance evaluations, were provided by R. Birtcher, J.E. Epperson, G. Felcher, J. Jorgensen, R. Kleb, R. Osborn, and D. Price (MSD); W. Dozier, C.-K. Loong, F. Rotella, A. Schultz, P. Thiyagarajan, F. Trouw, and T. Worlton (IPNS); J. Haumann (Electronics and Computing Technologies Division); and G. Kearley of the Institut Laue-Langevin (Grenoble, France).

Conventional facilities work was performed by engineers and architects from the Plant Facilities and Services Division. Coordination and interfacing between technical and conventional facilities personnel were performed by G. Norek (PFS) and K. Peterson (APS). Costs of the conventional facilities were estimated by Hanscomb and Associates of Chicago, Illinois.

The costs and schedules are a result of work performed by Y. Cho, with management information support from A. Rauchas.

The editorial tasks of integrating and assembling the document were performed by M. White, with support from M. Addison, D. Haid, and A. Owens (APS); F. Bennett and staff from the Technical Communication Services Department (Information and Publishing Division); and B. Salbego and staff from the Document Processing and Control Department (IPD).

The Kohn panel report also included the following statement: "If the ANS is not built, a 5-MW pulsed spallation source would be needed to basically cover its capacities in neutron scattering." A feasibility study is currently under way for a future upgrade from the 1-MW source described in this report to a 5-MW facility; the 1-MW accelerator would be used as the injector for the 5-MW accelerator.

CHAPTER VI CONVENTIONAL FACILITIES

FIGURES

FIGURES (Cont.)

FIGURES (Cont.)

FIGURES (Cont.)

FIGURES (Cont.)

FIGURES (Cont.)

FIGURES (Cont.)

FIGURES (Cont.)

FIGURES (Cont.)

FIGURES (Cont.)

FIGURES (Cont.)

FIGURES (Cont.)

FIGURES (Cont.)

FIGURES (Cont.)

FIGURES (Cont.)

FIGURES (Cont.)

FIGURES (Cont.)

FIGURES (Cont.)

FIGURES (Cont.)

TABLES

TABLES (Cont.)

TABLES (Cont.)

. . .

TABLES (Cont.)

TABLES (Cont.)

TABLES (Cont.)

I

Background and Overview

1.1 BACKGROUND

Over the past 40 years, research based on slow neutron beams has been crucial to advances in fundamental science, technology, and medicine. Achievements in neutron scattering research have attracted many awards in recent years, including the highest when, last year, two of the early workers, Clifford G. Shull and Bertram N. Brockhouse, shared the 1994 Nobel Prize in Physics for their pioneering work in developing neutron scattering methods. Discussions and summaries of advances in this field appear regularly.[1-4]

Neutrons provide critical information that is impossible to acquire by any other means. Furthermore, for many purposes, they provide a necessary complement to x-rays, so that the parallel development of both neutron sources and x-ray synchrotron facilities is essential.

In the past 10 years, neutron studies have provided information critical to the understanding of new materials that have emerged and have had a singular impact in materials science. One can cite the following specific examples of key contributions of neutrons in fundamental science:

- Structure and excitations of high-T_c superconductors,

- Polymer conformations and interactions,

- Structure and dynamics of new-generation catalysts,

- Interfacial structure of polymeric and magnetic layers,

- Spin dynamics in highly correlated metals,

- Structure and phase transformations of fullerenes ("buckyballs"), and

- Condensate fraction in superfluid helium.

Important contributions to technological advances have paralleled the major developments in fundamental sciences cited above:

- Residual stress in metals and ceramics,

- Radiography of aircraft and energy-production components,

- Near-surface impurities and deposits in semiconductors,

- Giant magneto-resistant multilayers,

- Cavitation and embrittlement of structural alloys,

- Adhesion of polymer laminates,

- Materials irradiation for fission and fusion power programs, and

- Sintering processes of ceramics.

Over the last 20 years, the United States has fallen alarmingly behind the European scientific community in the availability of up-to-date neutron sources and instrumentation. HFBR and HFIR, which are the major research reactors of the U.S. Department of Energy (DOE), were built more than 25 years ago, and their remaining lifetimes of a decade or so are uncertain; the status of HFIR appears especially precarious. In June 1992, Dr. W. Happer, Director of DOE's Office of Energy Research, requested the formation of a panel to report on key issues concerning possible new sources, emphasizing especially the comparison of reactors and pulsed spallation neutron sources. The Panel, chaired by Professor Walter Kohn (University of California, Santa Barbara), had substantial representation from universities, industry, and government laboratories, and it included both neutron specialists and other condensed matter scientists. In addition to visiting the sites of the four DOE laboratories with interests in constructing future sources, the Kohn Panel organized a broad Review of Neutron Sources and Applications, with the participation of 70 national and international experts, in Oak Brook, Illinois. Separate working groups were assembled to (1) review the status of advanced research reactors and spallation sources and (2) provide an update on scientific, technological, and medical applications, including neutron scattering research in a number of disciplines, isotope production, materials irradiation, and other important uses of neutrons. The Kohn Panel's report was published in January 1993[1] and findings and conclusions of the working groups involved in the Review were published in January 1994.[4]

After reviewing the capability and cost-effectiveness of different alternatives, the Kohn Panel concluded that as a technologically leading nation, the United States urgently needs to construct a complementary pair of neutron sources: a next-generation research reactor and a powerful pulsed spallation source (PSS). These facilities are essential to maintain or reestablish U.S. leadership in broad areas of physical, biological, and materials sciences, in radiomedicine, and in associated technologies. Although the required investment is substantial, the payoff — in terms of both directly associated jobs and enhancement of the nation's technological and economic power — will be much greater and will extend far into the next century.

Recommendation 1: Complete the design and construction of the Advanced Neutron Source (ANS) according to the schedule proposed by the project.

Recommendation 2: Immediately authorize the development of competitive proposals for the cost-effective design and construction of a 1-MW PSS. Evaluation of these proposals should be done as soon as possible, leading to a construction timetable that does not interfere with rapid completion of the ANS.

Subsequently, two workshops took place within the PSS community. One workshop further evaluated accelerator prospects (Santa Fe, February 1993)[5]; the other addressed technological and scientific applications of a 1-MW PSS (Argonne, May 1993).[6] The accelerator workshop addressed the different possible methods of supplying 1-MW proton beams to spallation targets, while the technology and science workshop documented the great variety of problems that could be solved with a 1-MW pulsed source, ranging from fundamental science to engineering materials and technology.

The President's budget for fiscal year (FY) 1996, which was announced on February 6, 1995, calls for cancellation of the ANS project. This situation puts even more emphasis on the development of PSSs for the nation's future. This feasibility study represents the response of Argonne National Laboratory (ANL) to the Kohn Panel's recommendation for a cost-effective design and construction of a dedicated 1-MW PSS.

Argonne comes to this proposal with 12 years of successful experience in operating the Intense Pulsed Neutron Source (IPNS). The hallmarks of the IPNS experience are its very high reliability, continuous sequence of source and instrumentation developments, strong user program, and the highest scientific productivity per unit cost of operation, by any measure, of all the DOE neutron scattering facilities. The reliable operation of the facility has its origin in ANL's tradition of excellence in accelerator science and technology.

The present IPNS synchrotron was originally designed and built in the mid-1970s as the booster for a high-energy physics proton accelerator, the 12-GeV Zero Gradient Synchrotron (ZGS). The ZGS was used for the nation's high-energy physics program during the 1960s and 1970s. Notable achievements in accelerator science by ZGS personnel include the first-ever acceleration of polarized protons to the multi-GeV energy range[7] and the first demonstration of negative-hydrogen-ion charge exchange injection into a circular accelerator.[8] Existing pulsed source facilities, as well as those planned for the future, all use charge exchange injection.

From 1982 to 1983, accelerator scientists who formerly worked at the ANL ZGS designed a synchrotron option for Germany's SNQ (Spallations Neutronenquelle).[9,10] Many of the design concepts employed in this report originated in the SNQ studies. This group also studied a pulsed-source option using the fixed field alternating gradient (FFAG)[11] synchrotron concept. The FFAG proposal was presented to the Seitz-Eastman Panel in 1984, and it was designated as the fourth priority for new materials research facilities.

These same ZGS accelerator scientists planned and designed the Advanced Photon Source (APS)[12] from 1984 to 1987 and obtained approval for its construction in 1988. The construction of the APS at ANL is nearly complete; in the process, ANL accelerator personnel have accumulated a tremendous wealth of current information on the construction and procurement of accelerator components.

The proposal put forward here uses all buildings and infrastructure of the former ZGS facility. The ZGS Ring Building can house a synchrotron about 200 meters in circumference and has enough radiation shielding to accommodate a 1-MW accelerator system. Two of the former

high-energy physics experimental buildings can house two neutron-generating target stations and associated neutron beamlines. It is estimated that the use of existing buildings saves about $175 million in construction costs.

The IPNS Upgrade will be the fourth in a series of pulsed spallation sources constructed at Argonne. The first was the ZGS Intense Neutron Generator Prototype (ZING-P). This facility was built in 1973 and was the world's first test of the spallation neutron source concept. It used the ZGS 200-MeV prototype booster synchrotron and achieved a beam power of 100 W. ZING-P', a second prototype that used the present IPNS accelerator, operated very productively from 1977 through 1980. It achieved 2 kW of beam power. The IPNS, operational since 1981, achieves a beam power of 7 kW and is a scientifically prolific and efficient research installation that has led in the development of pulsed source technology and of pulsed source, time-of-flight neutron scattering instrumentation. The IPNS has set the standard for PSS operational reliability, being available 95% of the scheduled time since it started operation in 1981. From the outset, the IPNS has hosted a productive and highly cost-effective user program, producing more than 250 scientific publications and serving more than 200 users each year.

Argonne is conveniently located near Chicago, providing ready access from around the country and the world. Argonne has established an international reputation for neutron source and instrumentation development. The community of neutron scattering specialists, both residents and long-term users from other institutions, has consistently produced high-quality results. One of Argonne's major activities is materials research, which will provide important support to the research program at the IPNS Upgrade. As has been found at several other installations (for example, Brookhaven, Grenoble, and KEK), the collocation of a neutron source with a synchrotron radiation facility provides significant scientific synergism. The accelerator design and construction groups come from a series of successful programs that lead conveniently into the IPNS Upgrade project. Close collaboration is maintained with other installations around the world through frequent visits and cooperation and through the International Collaboration on Advanced Neutron Sources (ICANS), scheduled to hold its 13th meeting in October 1995 at the Paul Scherrer Institut (PSI) in Villigen, Switzerland.

1.2 ACCELERATOR AND TARGET STATION PARAMETERS

The IPNS Upgrade is a dedicated source for slow neutron scattering that uses a proton accelerator delivering a time-average beam power of 1 MW.

The choice of proton beam energy is determined by several factors, including neutron yield, heat removal from the target, ease of machine construction and serviceability, and available space in the ZGS Ring Building. Efficient production of neutrons by spallation requires proton

energies above 500 MeV, so that protons interact principally with nuclei in the target. The neutron yield (number of neutrons per proton) for thick targets is given by

$$Y(E, A) = \begin{cases} 0.1(E_{GeV} \pm 0.120)(A + 20), & \text{except fissionable materials} \\ 50(E_{GeV} \pm 0.120), & {}^{238}U, \end{cases} \qquad (I.1.2\text{-}1)$$

where E_{GeV} is the proton beam energy in GeV and A is the atomic number of the target material. For energies above the apparent threshold of 0.12 GeV, the neutron yield is roughly proportional to energy. The neutron production rate is proportional to the beam power.

The design is also influenced by the distribution of the deposited heat and the distribution of produced neutrons. Most experience to date has been confined to energies below 1 GeV and confirms Equation I.1.2-1 above. Monte Carlo studies show that the power density distribution, neutron production distribution, and total yield of neutrons favor energies higher than 1 GeV, as shown in Figure I.1.2-1,[13] at least up to about 3 GeV, the code-imposed limit of the study. The calculations confirm that the neutron production rate for constant beam power is approximately constant and that the neutron production rate is approximately proportional to the proton beam power within the range of proton energies studied.

Figure I.1.2-2 shows the variation of the emerging neutron current as a function of axial position in a target (tallied at a radius of 6.2 cm), and Figure I.1.2-3 shows the variation of the thermal power density (averaged over radius). Higher energies are preferable due to the lower peak power density at the upstream end of the target for a given beam power. These calculations indicate that proton energies above 1.5 GeV are equivalent with respect to the thermal and neutronic design of the target and moderator systems.

The choice of 30 Hz as the source repetition frequency was based upon a survey of scientific requirements and an evaluation of preliminary designs for neutron scattering instruments for a 1-MW pulsed source. Two categories of instruments emerged from the study of scattering instruments, those for which 30 Hz is preferable, and those that require a lower frequency, for which 10 Hz is satisfactory. Few of the instruments we considered could effeciently use frequencies higher than 30 Hz. Two targets that operate at different frequencies provide the flexibility to serve both classes of instruments and double the available number of beamlines and instruments. The accelerator delivers one out of three pulses to the low-frequency station at 10 Hz, and the high-frequency station receives the remaining two pulses of the 30-Hz pulse train. The high-frequency target is capable of using the full 1 MW of beam power, or all pulses of the 30-Hz pulse train.

Our preference is to have the highest possible energy and lowest possible current. This preference does not affect the neutron production rate, since the rate is proportional to the proton beam power. High-energy protons can be obtained by acceleration through a linear accelerator or through a circular machine. A single-pass machine such as a linac tends to have high construction and operating costs; therefore, proton linacs tend to be lower-energy machines.

1-MW Proton Beam
on 10cm x 100cm target
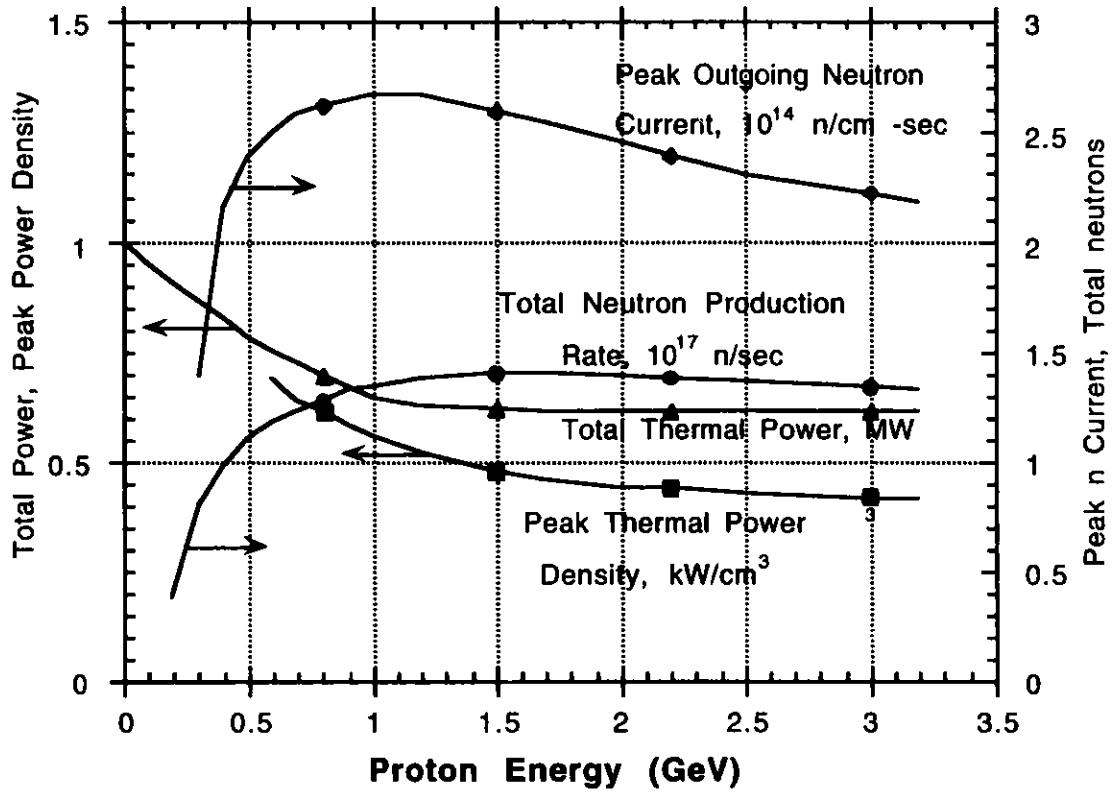
Figure I.1.2-1 Variation of the Thermal Power Density and Neutron Production Density as a Function of Axial Position in Targets Irradiated by Protons of Various Energies.
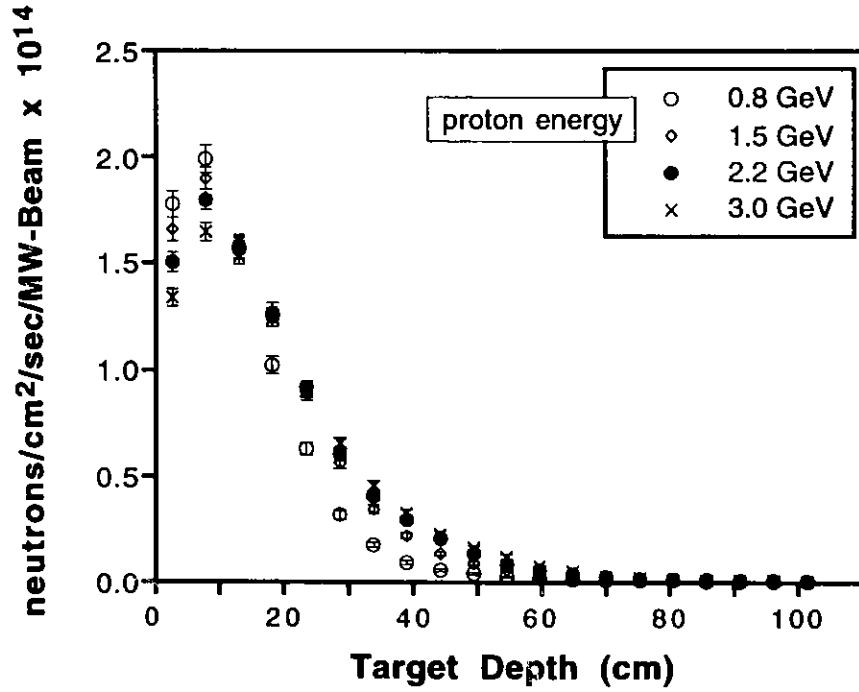
Figure I.1.2-2 Spatial Distribution of Neutrons Emerging from the Target as a
Function of Axial Position.
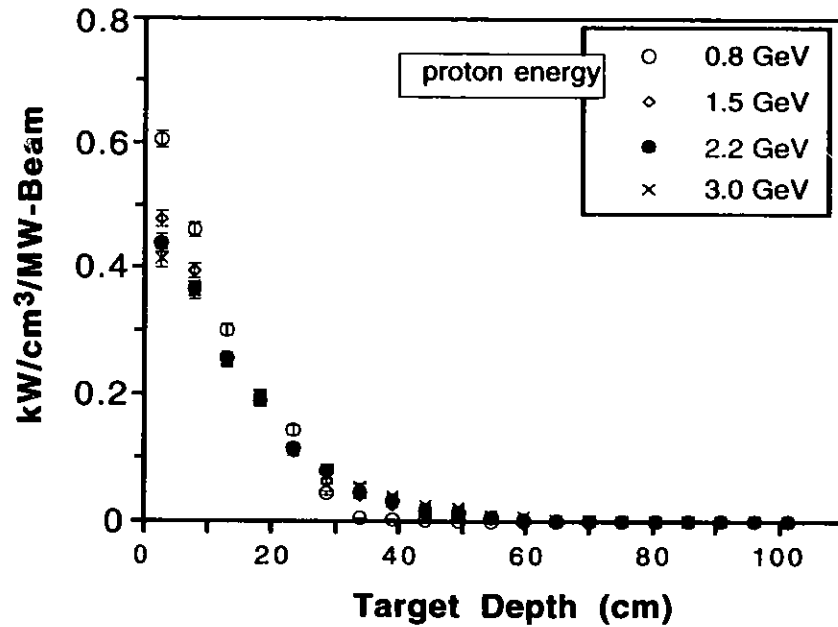
Figure I.1.2-3 Spatial Distribution of Thermal Power Density in the Target as
a Function of Axial Position.

For this reason, the highest-energy proton linac is the 800-MeV Los Alamos linac. Because a circular machine takes advantage of multiple traversals of the particles, the machine energy can be very high. Construction and operating costs for circular machines are substantially lower than those for linacs of similar energy. Circular machines can accelerate a time-averaged current of 0.5 mA to 1.0 mA to several GeV. We chose to use a linac to provide a 400-MeV H^- beam for injection into a rapid cycling synchrotron (RCS). The RCS is designed to accelerate an average proton beam current of 0.5 mA to 2 GeV.

2.1 ACCELERATOR SYSTEM

The accelerator system delivers a proton beam of 1-MW power at a repetition rate of 30 Hz. The required beam power is achieved by using a rapid cycling synchrotron (RCS). Its beam is extracted into two separate extraction lines. There are two targets, a low-frequency target and a high-frequency target operating at 10 Hz and 30 Hz, respectively. One target receives one pulse out of three from the accelerator; the other target receives the remaining two pulses.

The injector system consists of a negative hydrogen (H⁻) ion source similar to that of ISIS,[14] a beam chopper system, a low-energy beam transport, a 2-MeV radio-frequency (rf) quadrupole, a 70-MeV drift-tube linac, and a 330-MeV coupled-cavity linac. The linac design is similar to that of the Superconducting Super Collider linac and utilizes existing technology. The 400-MeV injector linac system delivers H⁻ ions to the synchrotron, where they are injected after stripping by a thin carbon foil. The RCS accelerates a time-averaged current of 0.5 mA of protons, corresponding to 1.04×10^{14} protons per pulse at a 30-Hz repetition rate, to 2 GeV.

The decision to design the RCS for the highest possible extraction energy and the lowest possible injection energy was driven by beam loss considerations. The injection energy of the RCS was determined on the basis of the space charge tune shift and the ring aperture. Experience with high-intensity proton accelerator operation shows that beam losses are usually associated with the injection and capture processes and that very few losses occur during the acceleration processes. Low-energy injection is preferable because of beam loss considerations, since there is less activation when beam is lost at low energy. Therefore, the design goal was to inject into the RCS at the lowest possible energy. A stacked-beam emittance of $375 \times 10^{-6} \pi$ m in both transverse planes and an injection energy of 400 MeV give a space charge limit of 1.04×10^{14} protons per pulse. The beam-stay-clear region for a $375 \times 10^{-6} \pi$ m emittance provides an RCS aperture similar to that of the ISIS. To reach the desired beam power, an appropriate amount of beam current is injected at 400 MeV and accelerated to the final energy of 2 GeV.

The synchrotron operates in the first harmonic mode with single-turn extraction. It delivers pulses of approximately 200-nsec duration and cycles at 30 Hz. The machine has four long sides, with four straight sections per side. Two of the straight sections are used to extract beam to the two target areas; one is used for the injection system, and the others are reserved for the rf system.

Design performance parameters of the accelerator system are summarized in Table I.2.1-1. Detailed descriptions are presented in Chapter II for the RCS and in Chapter III for the H⁻ injector linac.

There is about 55,000 m² of space available in the ZGS complex, and this space is used for the 1-MW source. The RCS must fit into the existing 200-m-circumference Ring Building. The locations of the two former experiment halls that house the two targets require construction of two separate extraction lines. These were the only geometrical constraints in designing this 1-MW source.

Table I.2.1-1 Accelerator Parameters

Parameters	Values	Units
Beam energy at extraction	2	GeV
Maximum beam energy attainable	2.2	GeV
Beam energy at injection	400	MeV
Beam average current	0.5	mA
Beam power	1.0	MW
Beam pulse length	< 1	μsec
Synchrotron repetition rate	30	Hz
Synchrotron circumference	~200	m
Number of external proton beams	2	-
Number of extraction lines	2	-
Linac beam energy	400	MeV
Linac energy spread (95%)	±2.5	MeV
Linac repetition rate	30	Hz
Linac pulse current	44	mA
Linac pulse length	0.5	msec
Linac emittance (rms normalized)[a]	$1.0 \times 10^{-6} \pi$	m

[a] rms = root mean square.

The existing Ring Building for the 12-GeV ZGS is adequate to house the 2-GeV RCS described in this report. The use of a 2-GeV beam reduces the maximum power density deposited in the target by about 25% from its value at 0.8 GeV, which is a significant advantage for target design.

2.2 NEUTRON SCATTERING CAPABILITIES

Shielded proton beam transport lines carry two extracted proton beams to two target stations, multiplexed so that the 30-Hz station receives two of the 30-Hz pulses while every third pulse goes to the 10-Hz target. Each station contains a neutron-producing target consisting of water-cooled tungsten plates in two sections. Moderators positioned close to each target slow down neutrons from the primary source energies (about 1 MeV) to useful energies (less than about 10 eV). Water, liquid methane, and liquid hydrogen moderators are used. Reflectors of beryllium metal or of beryllium and heavy metal surround the moderators to enhance the intensities of the neutron beams. Decouplers and heterogeneous poisons within the moderator-reflector system tailor the spectra and pulse characteristics of the neutron beams. Massive steel and concrete shields surround the targets and moderators and provide multiple levels of confinement of radioactive materials within. Because some components of the target have finite lifetimes and because changes need to be made over the years to accommodate changing demands of the instruments, each target station is equipped with a hot cell and remote handling equipment and is designed to facilitate moving and servicing the internal components.

Irradiation facilities for neutron activation and fast neutron materials irradiation applications are arranged close to the targets. These irradiation facilities do not interfere with the neutron scattering application. The irradiation facilities are accessible during operation.

The IPNS Upgrade provides 36 beam ports for neutron scattering instruments, 18 each at the 30-Hz and 10-Hz target stations. Neutron beams for more than one instrument are extracted from a single beam port in some cases, so more than 36 neutron scattering instruments can be supported at this facility. There are a total of 12 moderators, one for every three beam ports, so the moderator characteristics can be optimized to the requirements of the individual instruments. Table I.2.2-1 lists the IPNS Upgrade moderators, and Figure I.2.2-1 indicates the range of intensities and pulse widths available. The present IPNS moderators are also listed in the table for comparison.

The IPNS Upgrade provides 27 instruments for 24 of these 36 beam ports. The remaining 12 uninstrumented beam ports are available for later development and installation of new state-of-the-art instruments, as well as for the installation of specialized instruments developed by Participating Research Teams (PRTs). Chapter V of this document outlines a reference set of 27 instruments that provide a well-balanced initial instrumentation complement. Tables I.2.2-2 and I.2.2-3 briefly describe this reference set of instruments and indicate the wide range of neutron scattering science possible. This reference set of instruments has been used to

Table I.2.2-1 IPNS and IPNS Upgrade Moderators

Designation	Composition, Size	Temperature (K)
Present IPNS Moderators		
"H"	Solid CH_4, poisoned, 10×10 cm^2	25
"C"	Solid CH_4, grooved, 10×10 cm^2	25
"F"	Liquid CH_4, poisoned, 10×10 cm^2	100
IPNS Upgrade Moderators		
10-Hz Target (25 × IPNS)		
Upstream top, "F"	Liquid H_2, 10×10 cm^2	18
Upstream bottom, "A"	Liquid H_2, coupled, 10×10 cm^2	18
Flux trap right, "E"	Liquid H_2, coupled, 10×20 cm^2	18
Flux trap left, "B"	Undetermined	-
Downstream top, "D"	Undetermined	-
Downstream bottom, "C"	Liquid H_2, Poisoned, 10×10 cm^2	18
30-Hz Target (50 × IPNS)		
Upstream top, "F"	Liquid CH_4, poisoned, 10×10 cm^2	95
Upstream bottom, "A"	Liquid CH_4, poisoned, 10×10 cm^2	95
Flux trap right, "E"	Liquid H_2O, poisoned, 10×20 cm^2	320
Flux trap left, "B"	Liquid H_2O, poisoned, 10×20 cm^2	320
Downstream top, "D"	Liquid H_2, coupled, 10×10 cm^2	18
Downstream bottom, "C"	Liquid CH_4, poisoned, 10×10 cm^2	95
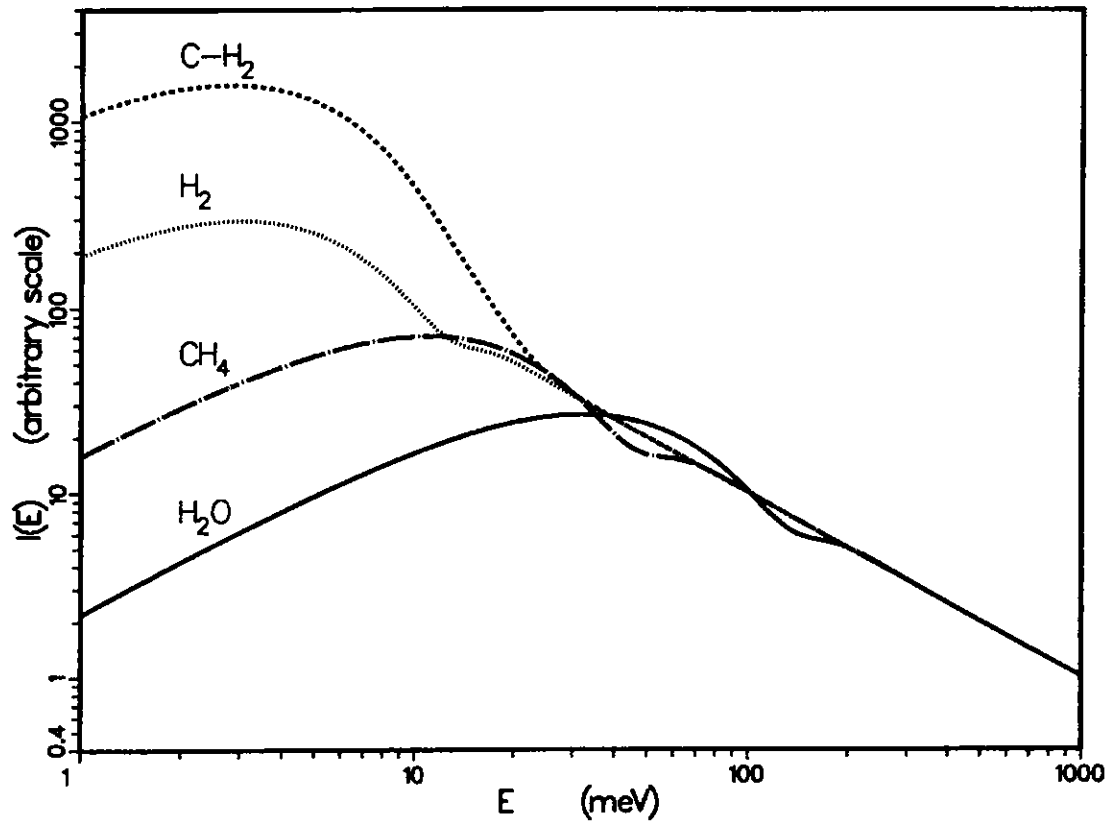
Figure I.2.2-1a Performance of the Different Moderators at IPNS Upgrade:
Intensities, Normalized to 1 at 1 eV.
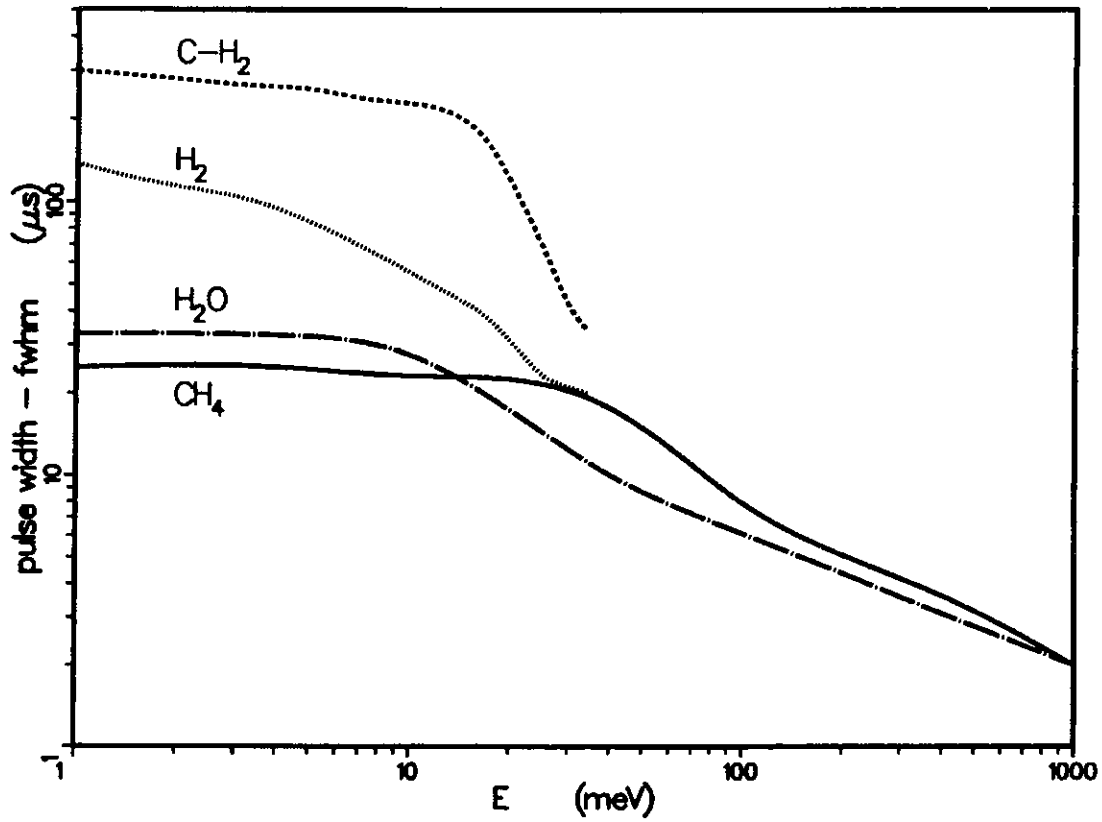
Figure I.2.2-1b Performance of the Different Moderators at IPNS Upgrade: Pulse Widths.
(Moderators are water at ~ 320K (H_2O), liquid methane at ~95 K [CH_4], decoupled
liquid hydrogen at ~18 K [H_2], and coupled liquid hydrogen at ~18K [C-H_2]).

Table I.2.2-2 Reference Set of Diffractometers and Reflectometers

Powder Diffractometers		Target	Moderator[a]	Range for d (Å)	Best $\Delta d / d$ (%)
VSPD	Very small samples (10-100 mg)	30-Hz	CH_4	0.2-17	0.35
SEPD[b]	High intensity	30-Hz	H_2O	0.2-17	0.35
GPPD[c]	Medium resolution (excellent at 90°)	30-Hz	H_2O	0.2-9	0.2
HRPD	High resolution	30-Hz	H_2O	0.2-5	0.08
RSD	Residual stress (12-m position)	30-Hz	H_2O	0.3-6	0.55
	(25-m position)	30-Hz	H_2O	0.2-3	0.30

Small-Angle Diffractometers		Target	Moderator[a]	Q_{min} (Å^{-1})	Q_{max} (Å^{-1})
SAND[b]	General purpose (wide Q range)	10-Hz	$C\text{-}H_2$	0.002	2
HRSAND	High resolution	10-Hz	$C\text{-}H_2$	0.0005	0.4
SPSAND	Reconfigurable for special purposes	10-Hz	$C\text{-}H_2$	Variable	Variable

Amorphous Materials Diffractometer		Target	Moderator[a]	Range for Q (Å^{-1})	$\Delta Q / Q$ (%)
GLAD[b]	Liquids and glasses	30-Hz	CH_4	0.07-120	1.2-10

Single-Crystal Diffractometers		Target	Moderator[a]	Range for Q (Å^{-1})	$\Delta Q / Q$ (%)
SCD[b]	General purpose	30-Hz	CH_4	0.9-17	0.6-0.9
HQSCD	High real-space resolution	30-Hz	H_2O	2-30	0.4

Reflectometers		Target	Moderator[a]	Sample	Minimum Reflectivity
POSY-I[c]	Polarized neutrons	10-Hz	H_2	Vertical	10^{-6}
POSY-II[c]	General purpose	10-Hz	H_2	Horizontal	10^{-7}
HIREF	High intensity	10-Hz	H_2	Horizontal	10^{-4}
GREF	Grazing incidence	10-Hz	H_2	Horizontal	10^{-7}

[a] Moderators are water at ~320 K (H_2O), liquid methane at ~95 K (CH_4), decoupled liquid hydrogen at ~18 K (H_2), and coupled liquid hydrogen at ~18 K ($C\text{-}H_2$). Moderator performance is shown in Figure I.2.2-1.

[b] Transferred from IPNS with little change.

[c] Transferred from IPNS with some modification.

Table I.2.2-3 Reference Set of Inelastic Scattering Instruments and Component Development Instruments

Chopper Spectrometers		Target	Moderator[a]	Range for E_{inc} (meV)	$\Delta E/E_i$ (%)
HRMECS[b]	High-resolution general purpose	30-Hz	CH_4	4-2000	2-4
LRMECS[c]	Low-resolution general purpose	30-Hz	CH_4	3-2000	4-7
CNCS	High-resolution low energy	10-Hz	H_2	0.3-20	<1
SCCS	Excitations in single crystals	30-Hz	H_2O	50-2000	~1

Crystal-Analyzer Spectrometers		Target	Moderator[a]	Range for E (meV)	ΔE (meV)
TFCA	General purpose	30-Hz	CH_4	0-1000	0.5-30
QENS[c]	Quasielastic, medium resolution	30-Hz	CH_4	0-150	0.05-3
HRBS	Microvolt resolution	10-Hz	H_2	0-10	0.005-0.06
MICAS	Survey of single-crystal excitations	30-Hz	CH_4	0-20	variable
QSTAXC	Cold-neutron triple axis (QSS)[d]	30-Hz	$C-H_2$	variable	variable

Spin-Echo Spectrometer		Target	Moderator[a]	Resolution (meV)	$\Delta Q/Q$ (%)
TOFNSE	TOF spin-echo, cylindrical geometry	10-Hz	$C-H_2$	10^{-6} to 10^{-1}	1.5

Component Development Instruments		Target	Moderator[a]		
REFD	Reflectometer development	10-Hz	H_2		
DEVEL	General purpose development	10-Hz	H_2		

[a] Moderators are water at ~320 K (H_2O), liquid methane at ~95 K (CH_4), decoupled liquid hydrogen at ~18 K (H_2), and coupled liquid hydrogen at ~18 K ($C-H_2$). Moderator performance is shown in Figure I.2.2-1.

[b] Transferred from IPNS with some modification.

[c] Transferred from IPNS with little change.

[d] Quasi-steady-state.

select the target station parameters, lay out the locations of the target stations within the experiment halls, and provide the cost estimates. Up to 10 of the instruments that are presently operating at the IPNS would be refurbished and transferred to the IPNS Upgrade as part of this initial instrument complement. This approach provides a core of proven instruments ready for operation at startup. The neutron scattering instruments are located in existing experiment halls that provide internal space for beamlines up to 50 m long, as shown in Figure I.2.2-2. Longer beamlines can be extended outside the buildings if necessary.

Most of the neutron scattering instruments use the neutron time-of-flight (TOF) principle for determination of neutron wavelengths. Of these instruments, the majority require good wavelength resolution. For such instruments, the IPNS Upgrade target stations provide 25-50 times the intensity available at the IPNS. However, for those instruments that do not require good wavelength resolution (for example, small-angle-scattering instruments), the coupled liquid hydrogen moderators shown in Figure I.2.2-1 are used to provide 100-200 times the intensity available at the IPNS.

These high fluxes open up a number of new and exciting scientific possibilities. These include:

- Rapid measurements of structure or dynamics, which make it possible to follow the evolution of sample properties or chemical processes in real time on a scale of minutes or even seconds.

- Structural or dynamic measurements on very small samples, opening up neutron scattering to entire classes of materials that have previously been inaccessible.

- Measurements to much higher resolution than previously available.

The upgraded source is sufficiently intense that it is no longer necessary that all instruments be based on TOF techniques. With moderators optimized for total neutron output rather than for sharp neutron pulse structure, time-averaged thermal or cold neutron fluxes are equivalent to those at a medium flux reactor. The reactor-equivalent cold neutron flux has been calculated to be $\sim 5 \times 10^{13}$ n/cm^2-sec for one of the liquid hydrogen moderators at the upgraded source. Thus, any instrument that works at a medium-flux reactor can be made to work at least as well at the IPNS Upgrade. Furthermore, even a moderator optimized for high time-averaged flux has a pulse width of less than one millisecond, and so has a duty factor of 1:30 or less at the IPNS Upgrade. This time structure can be used to significant advantage even on nominally steady-state instruments; for example, it can be used to reduce background and eliminate unwanted orders from crystal monochromators. A cold-neutron triple-axis spectrometer operating in this "quasi-steady-state" (QSS) mode is proposed as one instrument for the initial complement of IPNS Upgrade instruments.
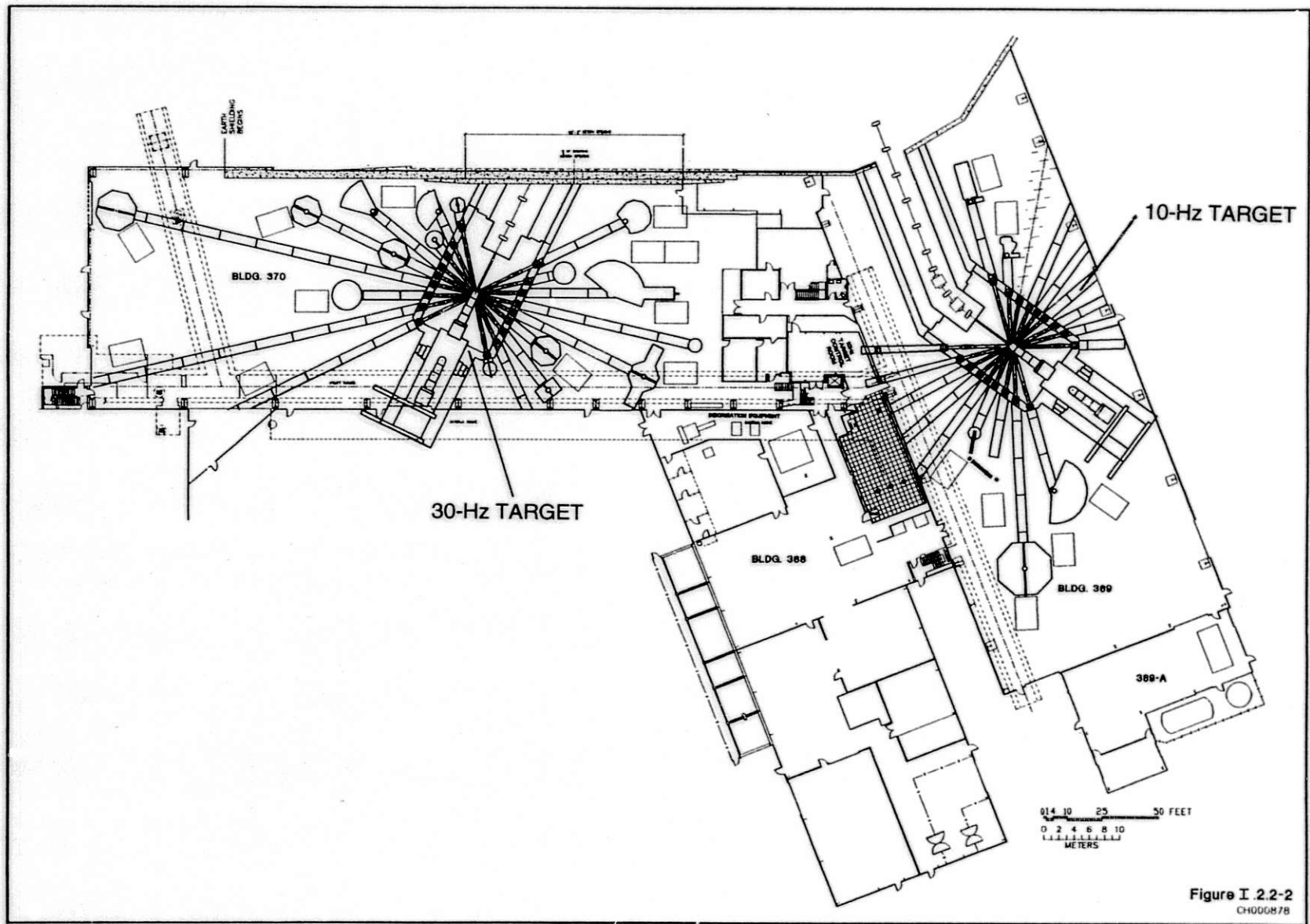
Figure I.2.2-2 Layout of the Experiment Halls, Showing the Locations of the Target Stations and Neutron Scattering Instruments.

2.3 OTHER EXPERIMENT FACILITIES

The IPNS Upgrade facilities can be expanded to allow for a number of other research opportunities — including radiation damage studies, isotope production, neutron activation analysis, neutron radiography and tomography, muon spin rotation studies for materials science research, and the study of some aspects of neutrino physics — with minimum interference to operation as a dedicated neutron scattering source. These possibilities are discussed briefly in Chapter V and in Appendix C. Facilities for radiation damage studies, isotope production, and neutron activation analysis are included within the present scope of the IPNS Upgrade project.

The major components of the IPNS Upgrade facility described here are an accelerator system, two target stations, and neutron scattering instruments. The accelerator system consists of a new, 400-MeV H^- linac and a new, 2-GeV rapid-cycling proton synchrotron (RCS). The RCS has a circumference of about 200 m and delivers a time-averaged proton current of 0.5 mA, for a total time-averaged power of 1.0 MW. Figure I.3-1 shows a general view of the installation.

The 400-MeV injector linac, along with its associated technical equipment, is housed in a new building and tunnel. The 400-MeV linac beam is transported by a low-energy transport (LET) line to the RCS. The linac tunnel and klystron gallery are the only new buildings to be built for the IPNS Upgrade project. An extensive study was undertaken to choose a location for the new injector that would avoid interruption of present IPNS operation. There will be an interruption of IPNS operation to move the instruments to the IPNS Upgrade facility.

All other technical components are housed in approximately 55,000 m^2 of the former ZGS-complex space and use existing infrastructure. The synchrotron is located in the existing ZGS Ring Building. The power supplies for the RCS magnets, rf system, and beam transport systems are housed in the Center Building and other adjacent buildings. The target stations and instruments are located in existing large buildings that previously housed high-energy experiments at the ZGS, a use very similar to the new use. System control rooms, maintenance facilities, and a considerable amount of laboratory and office space for resident personnel and visitors are provided in existing buildings. The project uses water systems, cooling towers, main power and transformer systems, roads, sewers, and general infrastructure items that already exist. There is little need for constructing new conventional facilities. The cost estimate includes an allowance for refurbishing these existing buildings and facilities. Use of these existing buildings results in a very large savings in cost and construction time.

We expect that there is no need for land-use studies, such as wetlands accommodation and archaeological investigations, because construction takes place within existing buildings or in areas such as parking lots that are already graded. Altogether, these factors effect considerable cost and time savings.

If the project is initiated in FY 1997, the total estimated cost (TEC) is $559 million. The facility commissioning is to start at the beginning of FY 2001. Construction of new components and refurbishment of existing facilities will not interfere with the present IPNS operations, except for reworking and relocation of the scattering instruments. An interval as short as a few months will be required to rework the scattering instruments and install them in their new locations. The accelerator commissioning period will be followed by commissioning of the target stations and instruments.

A detailed discussion of the cost and schedule is presented in Chapter VII.

GENERAL VIEW
OF THE
IPNS-UPGRADE

Figure I.3-1
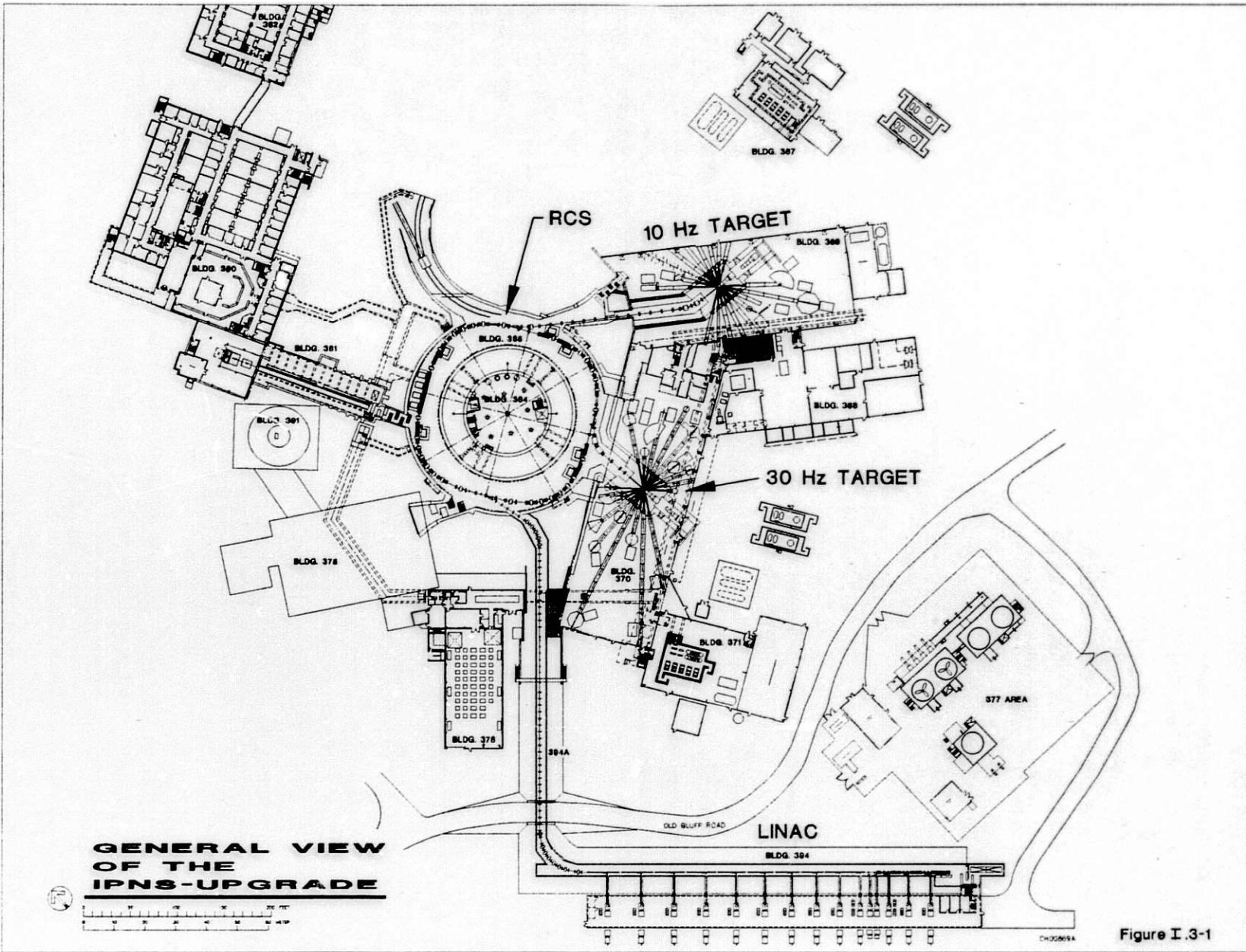
1. *Neutron Sources for America's Future*, Report of the DOE Basic Energy Sciences Advisory Committee Panel on Neutron Sources, chaired by W. Kohn, U.S. Department of Energy Report ER-0576P (Jan. 1993).

2. *Major Facilities for Materials Research and Related Disciplines*, F. Seitz and D. Eastman, Panel of the National Research Council, NTIS Report PB85-108850 (1985).

3. G.H. Lander and V.J. Emery, editors, *Scientific Opportunities with Advanced Facilities for Neutron Scattering*, Report of a Workshop held at Shelter Island, N.Y., Oct. 23-26, 1984, NTIS Report CONF-8410256 (1985).

4. J.J. Rush and D.L. Price, editors, *Neutron Sources and Applications*, Report of a review held at Oak Brook, Ill., Sept. 8-10, 1992, U.S. Department of Energy Report ER-0607P (Jan. 1994).

5. R.J. Macek and H.A. Thiessen, editors, *Proceedings of the Workshop on Accelerators for Future Spallation Neutron Sources* (Santa Fe, N.M., Feb. 16-20, 1993), Los Alamos National Laboratory Report LA-UR-93-1356 (1993).

6. G. Aeppli and B.S. Brown, editors, *Technology and Science at a High Power Spallation Source*, Proceedings of a Workshop held at Argonne National Laboratory, May 13-16, 1993, Argonne National Laboratory Internal Report (Feb. 1994).

7. Y. Cho, R.L. Martin, E.F. Parker, C.W. Potts, L. Ratner, J. Gareyte, C. Johnson, P. LeFevre, D. Mohl, and A.D. Krisch, "Phenomena Associated with the Acceleration of Polarized Protons in Circular Accelerators, " *AIP Proceedings of the High Energy Physics with Polarized Beams and Targets, No. 35*, Particles and Fields Subseries No. 12, p. 396 (1976).

8. E. Crosbie, A. Gorka, E. Parker, C. Potts, and L. Ratner, "Injection and acceleration of protons in the ZGS by stripping H$^-$ ions," IEEE Trans. Nucl. Sci. **NS-22**, 1056 (1975).

9. *Conceptual Design of a Rapid Cycling Synchrotron for the KFA - Jülich Spallation Neutron Source*, Argonne National Laboratory Report ANL-83-13 (Jan. 1983).

10. *Working Papers on the Conceptual Design of a Rapid Cycling Synchrotron for the KFA - Jülich Spallation Neutron Source*, Argonne National Laboratory Report ANL-83-13-Addendum (Jan. 1983).

11. T.K. Khoe and R.L. Kustom, "ASPUN, design for an Argonne super intense pulsed neutron source," IEEE Trans. Nucl. Sci. **NS-30**, 2086 (1983).

12. *7-GeV Advanced Photon Source Conceptual Design Report*, Argonne National Laboratory Report ANL-87-15 (Apr. 1987).

13. D.W. Jerng and J.M. Carpenter, "Heat generation and neutron beam characteristics in a high power pulsed spallation neutron source," submitted to IEEE Trans. Nucl. Sci. (1994).

14. L. Schroeder, K.N. Leung, and J. Alonso (editors), *Proceedings of the Workshop on Ion Source Issues Relevant to a Pulsed Neutron Source* (Lawrence Berkeley Laboratory, Berkeley, California, Oct. 24-26, 1994), Lawrence Berkeley Laboratory Report No. LBL-36347 (1994).

II

Synchrotron

1.1 CHOICE OF MACHINE TYPE

The accelerator for a pulsed spallation neutron source is required to produce a high-power (1-MW) proton beam with a short (<1-μsec) pulse length and a reasonable pulse repetition rate. Two commonly used accelerator configurations produce beams of the desired quality. One of these is a full-energy linac, which usually has a pulse length on the order of milliseconds, coupled with a pulse-compressor ring, which accepts the millisecond pulse and compresses it to the order of 1 μsec. In this scheme, the linac provides full power to the protons. The other configuration employs a linac of substantially lower energy that injects into a Rapid Cycling Synchrotron (RCS), and the RCS provides the major portion of beam power.

The present Intense Pulsed Neutron Source (IPNS) accelerator system consists of a 30-Hz, 500-MeV RCS coupled with a 50-MeV proton injector linac, and it provides 8 kW of beam power. The proposed IPNS Upgrade accelerator system provides 1 MW of beam power by using a 400-MeV injector linac, followed by a 2-GeV RCS. The RCS described here is, therefore, the centerpiece of the accelerator facility. The decision to use the RCS configuration to provide the beam power rather than to use other accelerator configurations, such as a linac pulse-compressor ring, was made after extensive comparisons between the two schemes.

Since the full-energy linac is a single-pass device, costs associated with its construction and operation are higher than those associated with a synchrotron, which is a multiple-pass device. Therefore, for a given beam power (1 MW), a pulsed spallation source using an RCS concept can have higher beam energy (2 GeV) and less beam current (0.5 mA) than a pulsed source based on the linac/pulse-compressor scheme, which necessarily has to have lower energy (0.8 GeV) and higher beam current (1.25 mA). Here, the numbers in parentheses are used to compare a 2-GeV RCS concept to an 800-MeV accumulator concept for a 1-MW pulsed source.

An important consideration with respect to the beam energy and current is that beam losses must be minimized or eliminated during the injection, acceleration, and extraction processes. Past experience shows that the beam loss, if any, usually occurs during injection and capture, not during acceleration and extraction. It is preferable to have beam losses occur at the lowest possible beam energy and least amount of beam current, another advantage that is offered by the RCS. Lower particle energy implies lower production of residual radioactivity, and lower beam current implies lower losses for the same fractional losses.

This concept of lower-energy injection at lower beam current has additional advantages with respect to the construction and operation of the facility. One advantage of having a lower current is that the existing ion source technology is capable of providing the required current without extensive development.[1] Another advantage is that injecting a lower-energy beam is easier than injecting a high-energy beam.

Present-day proton machines of this type are equipped with H⁻ injection systems, which enable the transverse phase space distributions of the injected beam to be controlled. This controlled populating of phase space uses the irreversible-charge-exchange injection process

known as phase space painting. The charge-exchange from H⁻ ions to protons is achieved by passing the H⁻ beam through a thin foil that strips the electrons.

State-of-the-art H⁻ ion sources provide the required 0.5-mA time-averaged current without further research and development (R&D) effort. The ion source required for the IPNS Upgrade can be a copy of the ISIS ion source, which has a proven record of reliability. Substantial R&D work is required to improve the peak beam current and pulse length performance and reliability for any source that produces more than a 0.5-mA average current.

The decision to use an RCS scheme for the IPNS Upgrade is made on the basis of the considerations described above. It is preferable to have the lowest possible beam current and highest possible beam energy at extraction. Fifty years of experience have shown that achieving higher energy by using a synchrotron is much easier than achieving high intensity. This implies that a higher-energy, lower-current machine can readily achieve the design goal.

An additional item that influenced the choice of machine parameters was the availability of existing buildings and infrastructure. Several buildings and accelerator enclosures that were formerly used by the high-energy physics program have been available for accelerator use since 1979. This underutilized area is the former Zero Gradient Synchrotron (ZGS) complex. The existing structures match the design requirements closely enough that very little compromise is needed in the design of the facility.

Moreover, Argonne National Laboratory (ANL) personnel have more than 20 years of experience in the development and operation of several rapid cycling synchrotrons, and in particular in neutron scattering.

The proposed plan utilizes the existing ZGS complex to house a 1-MW pulsed source.

1.2 CHOICE OF BEAM ENERGY

It has been shown that the neutron yield is roughly proportional to proton beam energy from several hundred MeV to about 10 GeV. There are no firm experimental data on the neutron yield from an operational, optimally coupled, heavy-metal target and moderator, in which practical necessities such as cooling have been incorporated into the target construction. At present, designers of neutron-generating targets are comfortable with a beam energy of 1 to 3 GeV.

The proposed RCS operates with a beam energy of 2 GeV. This energy was chosen because the ZGS Ring Building can accommodate a circular machine with a circumference of about 200 meters. A detailed optimization has shown that the ZGS Ring Building can house a 30-Hz separated-function RCS with a peak dipole field of 1.5 T. This configuration corresponds to a beam energy of 2.2 GeV. All proposed items of accelerator hardware are designed to be able to operate at up to 2.2 GeV. The accelerator operates at a nominal energy of 2 GeV, thus

providing built-in reliability from the beginning. The time-averaged beam current must be 0.5 mA for a 2-GeV beam.

1.3 CHOICE OF REPETITION RATE OF THE RCS

The choice of synchrotron repetition rate dictates several machine parameters, such as the number of protons per pulse to be accelerated to achieve the time-averaged current, and also the peak radio-frequency (rf) voltage. The repetition rate also influences the data-taking process of the scientific research program.

Scientific users prefer a lower repetition rate to avoid data pile-up and accidental counting of events from two consecutive machine pulses. Consultation with IPNS users indicates that a 30-Hz repetition rate is a desirable goal.

1.4 NEGATIVE HYDROGEN ION INJECTION

During the past decades, almost all proton synchrotrons have been converted from H^+ to H^- ion injection, because H^- charge exchange injection can be used to manipulate the transverse phase space during the injection process. The use of this process is essential to achieve a high-intensity beam with very little beam loss. An H^- linac is used as the injector for the IPNS Upgrade RCS.

1.5 CHOICE OF INJECTION ENERGY

The injection energy is determined by the space charge tune shift, RCS repetition rate, and time-averaged current. A machine operating at 30 Hz with a 0.5-mA average current requires an acceleration of 1.04×10^{14} protons per pulse.

As described in detail in Section II.2.1.3, the space charge tune shift due to the self-field of particles is proportional to the number of protons in a pulse and inversely proportional to the acceptance of the machine and to $\beta^2\gamma^3$ of the protons, where β and γ are the standard relativistic parameters.

The complete discussion of space charge and injection energy is given in Section II.2.1.3; after this discussion, the acceptance of the machine is discussed. A 400-MeV injection would provide a tune shift of 0.15, which is quite comfortable for reliable operation.

The high-level design goal parameters are summarized in Table II.1.5-1. The magnetic lattice for the RCS is designed to meet those performance requirements.

Table II.1.5-1 Design Goal Parameters

Parameter	Value	Units
Beam energy at extraction	2	GeV
Beam maximum attainable energy	2.2	GeV
Beam energy at injection	400	MeV
Beam repetition rate	30	Hz
Beam average current	0.5	mA
Beam power	1.0	MW
Linac beam energy	400	MeV
Linac energy spread (95%)	±2.5	MeV
Linac repetition rate	30	Hz
Linac pulse current	44	mA
Linac pulse length	0.5	msec
Linac emittance (rms normalized)[a]	1.0×10^{-6}	π m

[a] rms = root mean square.

1.6 REFERENCE

1. L. Schroeder, K.N. Leung, and J. Alonso (editors), *Proceedings of the Workshop on Ion Source Issues Relevant to a Pulsed Neutron Source* (Lawrence Berkeley Laboratory, Berkeley, California, Oct. 24-26, 1994), Lawrence Berkeley Laboratory Report No. LBL-36347 (1994).

2.1 SYNCHROTRON OPTICS

2.1.1 Magnet Lattice

The requirements and desirable features for a high-intensity proton machine lattice include:

1. Sufficient straight sections for radio-frequency (rf) cavities and injection/ extraction hardware,

2. Dispersion-free straight sections for injection,

3. Dispersion-free straight sections for rf cavities,

4. Largest possible transition energy of the machine, and

5. Peak field of the dipole magnet less than 1.5 T to avoid saturation effects.

A large transition energy, γ_t, has two implications. One has to do with the ease of manipulating synchrotron motions of the particles, and the other with beam instability thresholds due to high-intensity phenomena. The instability threshold current is proportional to the parameter $\eta = 1/\gamma_t^2 - 1/\gamma^2$. In order to make $|\eta|$ large for a machine below transition energy, γ_t should be large. This means the lattice should have a large horizontal tune, ν_x.

To implement all these features in the lattice, a FODO cell of ~ 90° phase advance in each transverse phase space was chosen for the normal cells that make up the arc of the ring. The desired dispersion suppression was achieved by removing one of the dipoles from a normal cell. The dispersion-free straight sections are formed by adding empty cells (normal cell with both dipoles removed) to the lattice after the dispersion-suppressor cell. A super-period is constructed by arranging normal cells, dispersion-suppressor cells, and empty cells followed by their mirror images.

The super-periodicity can be made to equal 3 or 4. This accelerator requires a substantial number of rf cavities, thus necessitating a large number of straight sections. A super-periodicity of 4 was chosen in order to take optimal advantage of space in the circular Zero Gradient Synchrotron (ZGS) tunnel.

Figure II.2.1-1 shows lattice functions of the normal cell, and Table II.2.1-1 lists cell parameters of each element in the normal cell. Figure II.2.1-2 shows the lattice functions through the dispersion-suppressor and dispersion-free cells. The S1 sextupole shown in Figure II.2.1-2 is for harmonic correction and is discussed in Section II.2.1.5. This segment of the lattice constitutes the straight section area. Figure II.2.1-3 shows the lattice functions for one-half of a super-period.
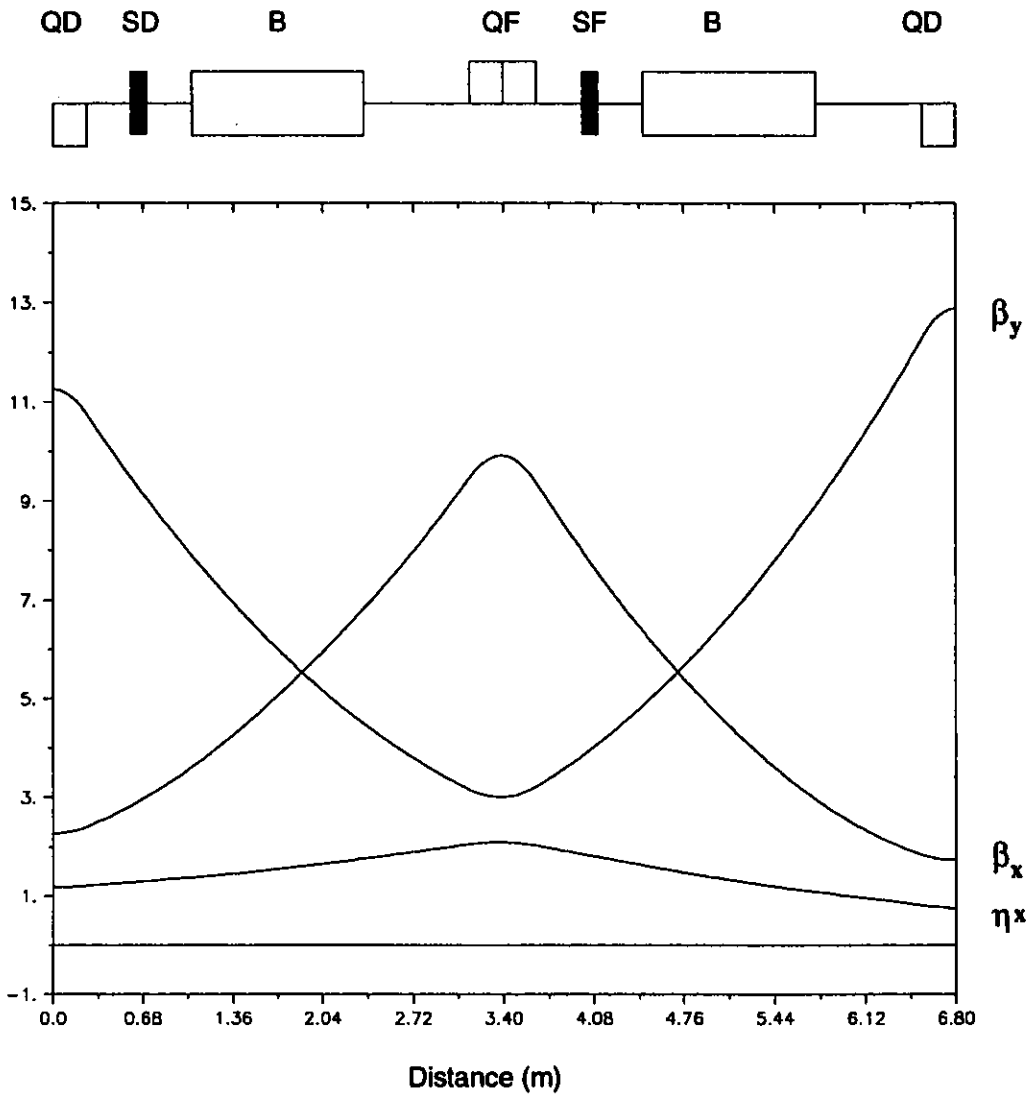
Figure II.2.1-1 Lattice Functions of the Normal Cell.

Table II.2.1-1 Normal Cell Parameters
(2.2 GeV, Bρ = 9.989 T·m)

Elements	Length (m)[a]	Strength	Units
QD	0.25	-7.276	T/m
D1	0.3		
SD	0.2	-0.843	m^{-2}
D1	0.3		
B	1.3	1.5088	T
D2	0.8		
QF	0.5	8.267	T/m
D1	0.3		
SF	0.2	0.612	m^{-2}
D1	0.3		
B	1.3	1.5088	T
D2	0.8		
QD	0.25	-7.276	T/m

[a] Total cell length = 6.8 m.
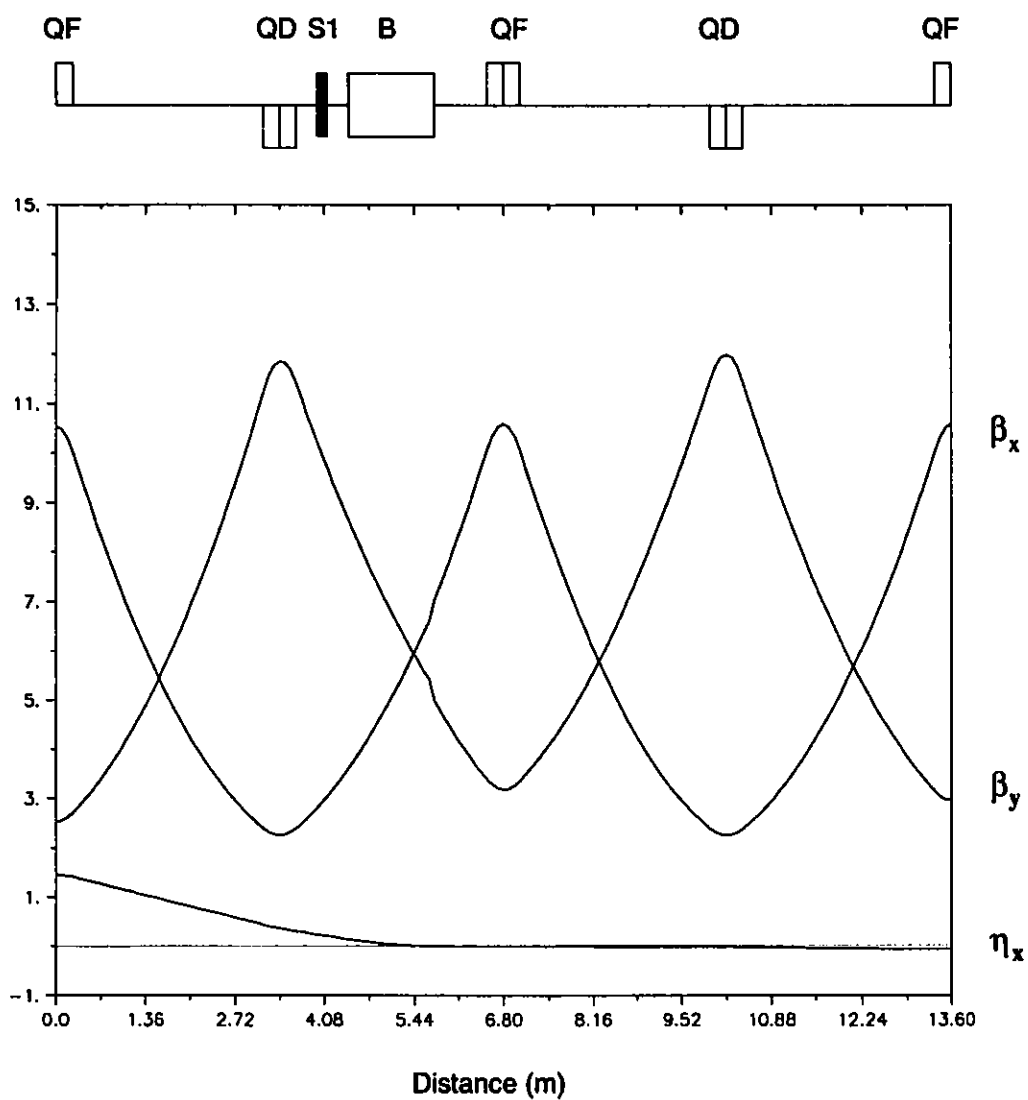
Figure II.2.1-2 Lattice Functions through the Dispersion-Suppressor and Dispersion-Free Cells.
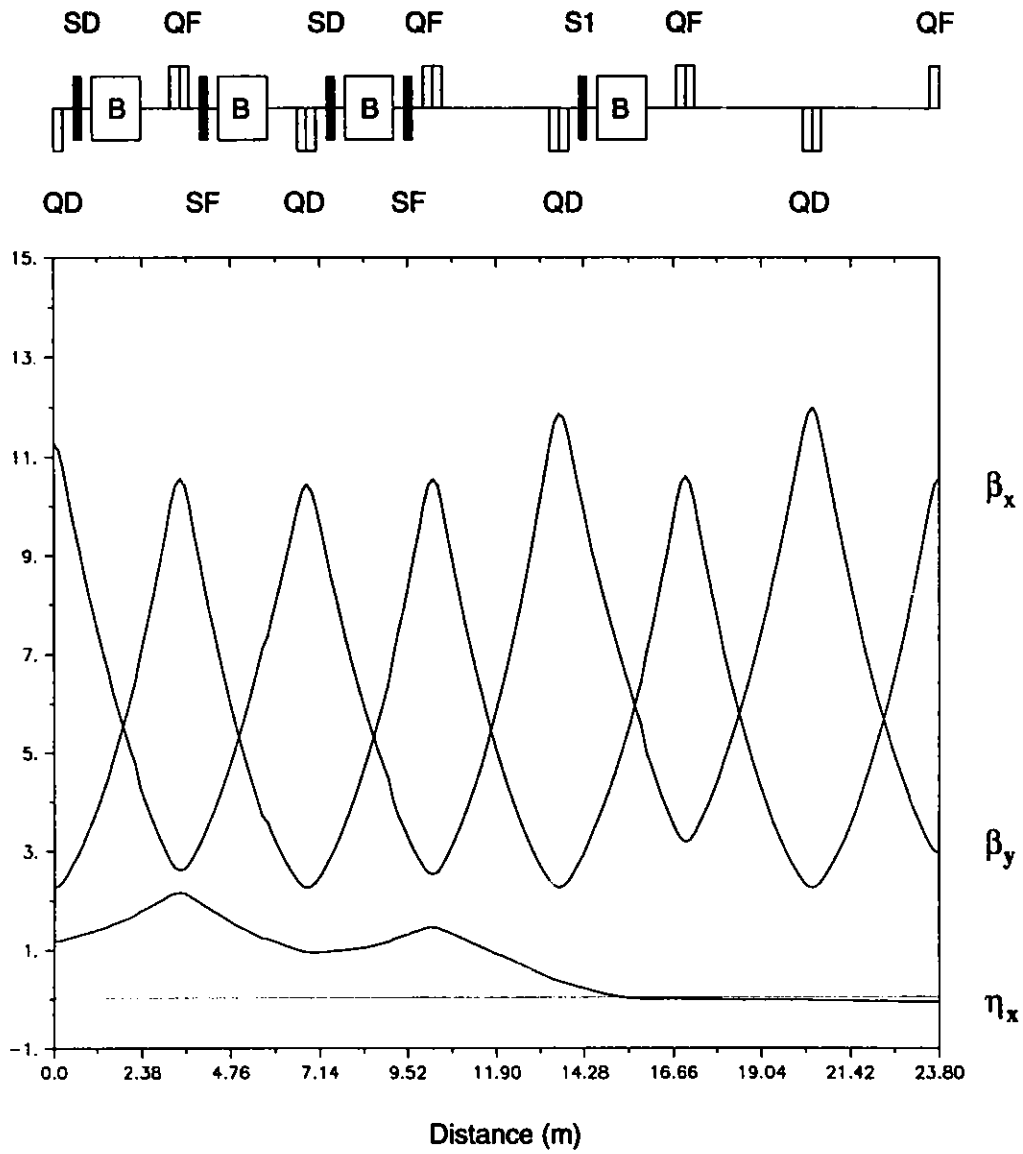
Figure II.2.1-3 Lattice Functions for One-Half of a Super-Period.

Table II.2.1-2 Synchrotron Parameters

Parameters	Values	Units
Circumference	190.4	m
Super-periodicity	4	-
Total number of cells	28	-
Number of normal cells	12	-
Number of dispersion suppressor cells	8	-
Number of straight section cells	8	-
Nominal length of straight section	2.9	m
Injection energy	400	MeV
Injection field	0.48	T
Nominal extraction energy	2.0	GeV
Maximum design energy	2.2	GeV
Dipole field at 2.2 GeV	1.5088	T
Bending radius	6.6207	m
Dipole length	1.3	m
Dipole good field region	0.45	m
Dipole gap height	0.182	m
Number of dipoles	32	-
Number of quadrupoles	56	-
Quadrupole length	0.5	m
Quadrupole aperture radius	0.1185	m
Maximum quadrupole gradient	8.8	T / m
Number of sextupoles (F)	16	-
Number of sextupoles (D)	16	-
Number of harmonic sextupoles	8	-
Maximum sextupole strength	1.2	m^{-2}
Sextupole length	0.2	m
Sextupole aperture radius	0.13	m
Horizontal tune, v_x	6.821	-
Vertical tune, v_y	5.7'	-
Normalized transition energy, γ_t	5.4	-
Natural chromaticity, $\xi_x = (\Delta v/v)_x/(\Delta p/p)$	-1.06	-
Natural chromaticity, $\xi_y = (\Delta v/v)_y/(\Delta p/p)$	-1.20	-
Maximum β function	12	m
Minimum β function	2.2	m
Maximum η function	2.2	m
Minimum η function	-0.06	m
Revolution time at injection	890.1	nsec
Revolution time at extraction	665.1	nsec
$\dot{B}_{max}$	64.5	T/sec
Maximum energy gain/turn	81.4	keV

The lattice is symmetrical about either end; the entire RCS is shown in Figure II.2.1-3b. Some parameters, such as the machine acceptance and chromaticity corrections, are discussed in Section II.2.1.6, while Table II.2.1-2 summarizes the pertinent synchrotron parameters.

2.1.2 Synchrotron Magnet Excitation and Repetition Rate

As noted in Section II.1.3, the synchrotron operates at a repetition rate of 30 Hz. It is customary that this kind of rapidly cycling synchrotron magnet system be energized by a resonant circuit power supply generating a sinusoidal wave form. This results in a time-varying field of the ring magnet, B(t), described by

$$B(t) = B_0 - B_1 \cos(2\pi\, f\, t)\,,$$

where B_0 and B_1 are the dc and ac components of the synchrotron magnetic field, respectively, and f is the repetition rate.

Particle energy gain is proportional to dB/dt, and dB/dt sets the first-order rf voltage required to accelerate the beam. From the above equation, dB/dt is $2\pi f B_1 \sin(2\pi f\, t)$. This means that the required rf voltage can be lowered by energizing the magnets at a lower frequency and de-energizing them at a higher frequency, keeping the overall repetition rate constant.

The synchrotron magnet system is energized with a dual resonant power supply system, which uses a 20-Hz magnet excitation rate and a 60-Hz magnet reset rate while keeping the overall 30-Hz rate. This reduces the required rf voltage by 1/3.

2.1.3 Beam Emittance and Synchrotron Acceptance

2.1.3.1 Space Charge Limit and Choice of Linac Energy

It is customary to use the Laslett tune shift due to space charge to calculate the number of protons that can be accelerated by a synchrotron. Knowledge of the longitudinal and transverse beam distributions is required to make these calculations. These distributions come either from assumptions based on previous experience or from tracking studies. The initial estimate of the space charge limit is obtained by using the elliptic beam distributions and a bunching factor obtained from assumptions. A refined study of the space charge limit was performed after a longitudinal tracking study from injection to full-energy acceleration was made.

We now discuss the initial estimate of the space charge limit and choice of the injection energy. The discussion presented here closely follows that described in *Report of the ISIS Project Group*.[1] It is reasonable to assume the local elliptic energy distribution of Hofmann and Pederson[2] for longitudinal motion of protons in the bunch. For this distribution, self-forces

MOVABLE SHIELDING SYSTEM
ON TRAIN RAILS

BLDG.
365

BLDG.
364

BLDG.
361

BLDG.
375

BLDG.
369

BLDG.
370

0   10   25   50 FEET

0   10 METERS

OVERVIEW OF THE RCS

Figure II.2.1-3b

CH00858A
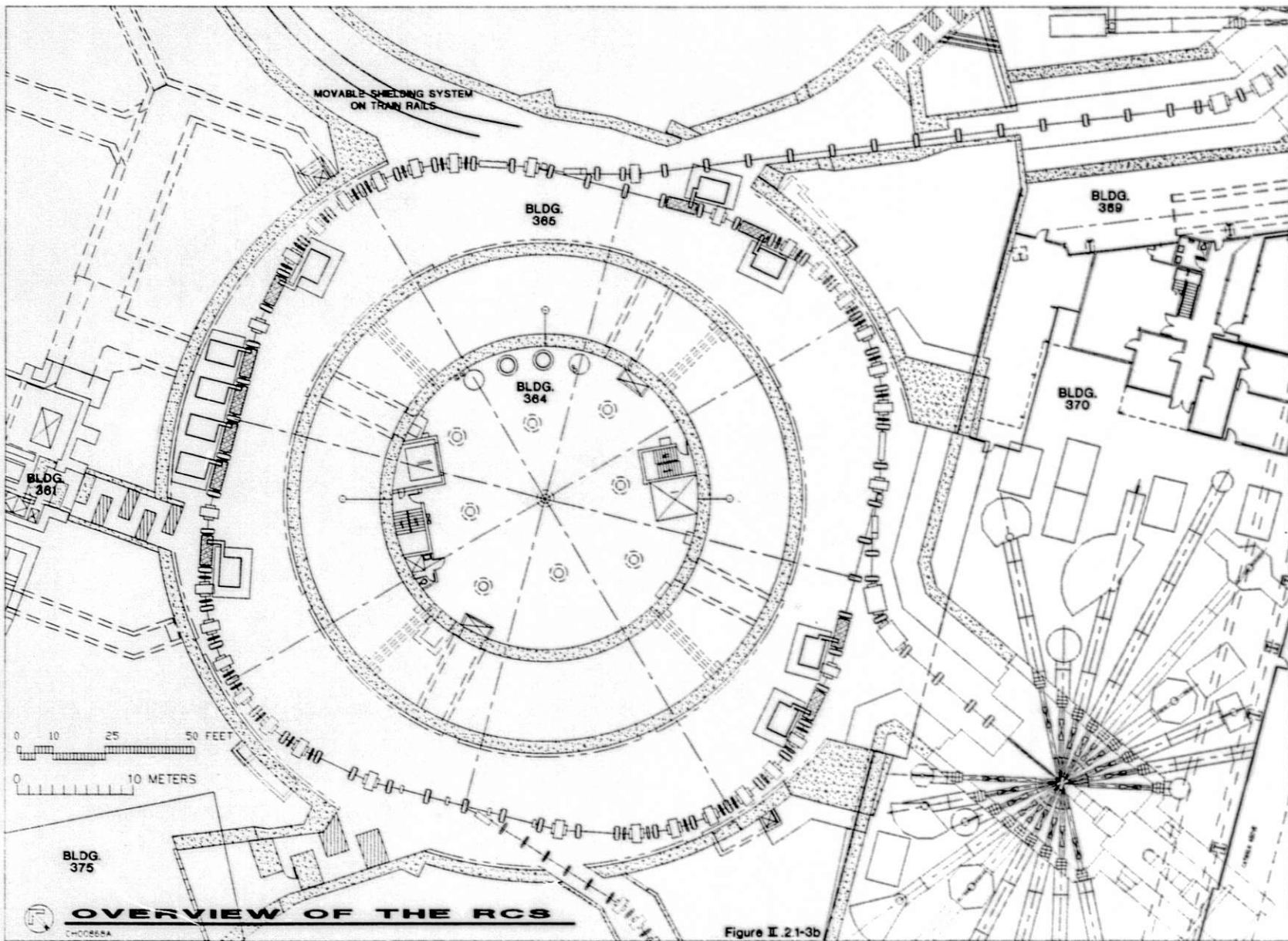
caused by longitudinal space charges are directly proportional to the external focusing forces. This allows bunching factors and rf bucket area reductions to be calculated analytically. The bunching factor, B_f, is defined to be the ratio of mean to peak number of particles per unit length, given by

$$B_f = \frac{1}{2\pi} \cdot \frac{\sin\phi_2 - \sin\phi_1 - (\phi_2-\phi_1)\cos\phi_2 - 0.5(\phi_2-\phi_1)^2\sin\phi_s}{\cos\phi_s - \cos\phi_2 + (\phi_s-\phi_2)\sin\phi_s} , \qquad (II.2.1-1)$$

where ϕ_2 is the maximum angle, ϕ_1 is the minimum angle, and ϕ_s is the synchronous angle.

If we assume a small synchronous phase angle of $5°$ for early acceleration, the bunching factor from Equation II.2.1-1 is about 0.4. For the transverse charge distribution, it is reasonable to assume that the protons are distributed in an elliptical geometry of semi-axes a (horizontal) and b (vertical) with the normalized two-dimensional elliptic density distribution, $\rho(x,y)$:

$$\rho(x,y) = \frac{3}{2\pi ab}\left[1-\left(\frac{x}{a}\right)^2-\left(\frac{y}{b}\right)^2\right]^{1/2} .$$

The density at the center of such a distribution is 1.5 times that of a beam with a uniform-filled, elliptical cross section. It is believed that the density at the core of the beam soon after the injection process will not exceed the assumed elliptic distribution. The Laslett transverse space charge limit, N, in a circular machine is directly proportional to the transverse emittance and inversely proportional to the central density. Therefore, the space charge limit for an elliptic distribution is 1.5 times less than that of a uniformly distributed beam of similar geometry.

The Laslett incoherent transverse space charge limit can be written

$$N = -\Delta v_y \varepsilon_y \left(1+\frac{a}{b}\right)\beta^2\gamma^3 \frac{B_f}{(r_p G_v F_v)} ,$$

where   (II.2.1-2)

$$F_v = 1 + \left(1+\frac{a}{b}\right)\left(\varepsilon_1\frac{b^2}{h^2}+\beta^2\gamma^2 B_f\left[\varepsilon_1\frac{b^2}{h^2}+\varepsilon_2\frac{b^2}{g^2}\frac{\rho_m}{R}\right]\right)\Big/G_v ,$$

h   =   vacuum chamber half-height;

g   =   bending magnet gap half-height;

ε_1 =   electrostatic image coefficient = 0.1;

ε_2 =   magnetostatic image coefficient = 0.411;

ρ_m =   bending radius of the machine;

R =   average radius of the machine;

r_p =   classical radius of proton = 1.5347×10^{-18} m;

Δv_y =   allowed vertical tune shift due to the space charge;

G_v =   form factor = 1.2 for elliptic distributions and 1.0 for uniform distributions; and

ε_y =   vertical emittance of injected beam, or acceptance of the machine not taking "beam-stay-clear" into account.

As noted above, the space charge limit is proportional to the phase space area of the stacked beam. Therefore, the phase space area must be decided while taking into account its implications for such machine parameters as magnet apertures and vacuum chamber dimensions. It is prudent to iterate the values of the choices of vertical and horizontal emittances, ε_y and ε_x, with consideration given to other parameters.

The study led to the following conclusions:

1. Although it is customary to have ε_y smaller than ε_x, so that the ring dipole magnet gap height can be made smaller, a very high-intensity machine like the one being described may not benefit from having $\varepsilon_y < \varepsilon_x$. The important point is to minimize the beam losses and to control them. There are some advantages to having the two emittances equal, because coupling resonances can be used to stack the beam in a Kapchinskij-Vladimirskij (K-V)-like distribution.[3] Having equal acceptances in both planes alleviates concerns over the coupling resonances.

2. Using Equation II.2.1-2 and assuming stacked beam emittances of $375 \pi \times 10^{-6}$ m rad in each plane, the space charge limit of the machine under these conditions gives the number of particles per pulse as a function of the injection energy. This number can be converted to the time-averaged beam current at a repetition rate of 30 Hz. The allowed tune shift, Δv_y, is 0.15. Figure II.2.1-4 shows the average current versus the injection energy.

From this figure, one can conclude that an injector linac of 400 MeV allows 0.5-mA operation of the synchrotron. The current of 0.5 mA at a 30-Hz repetition rate implies that the number of protons per pulse is 1.04×10^{14}.
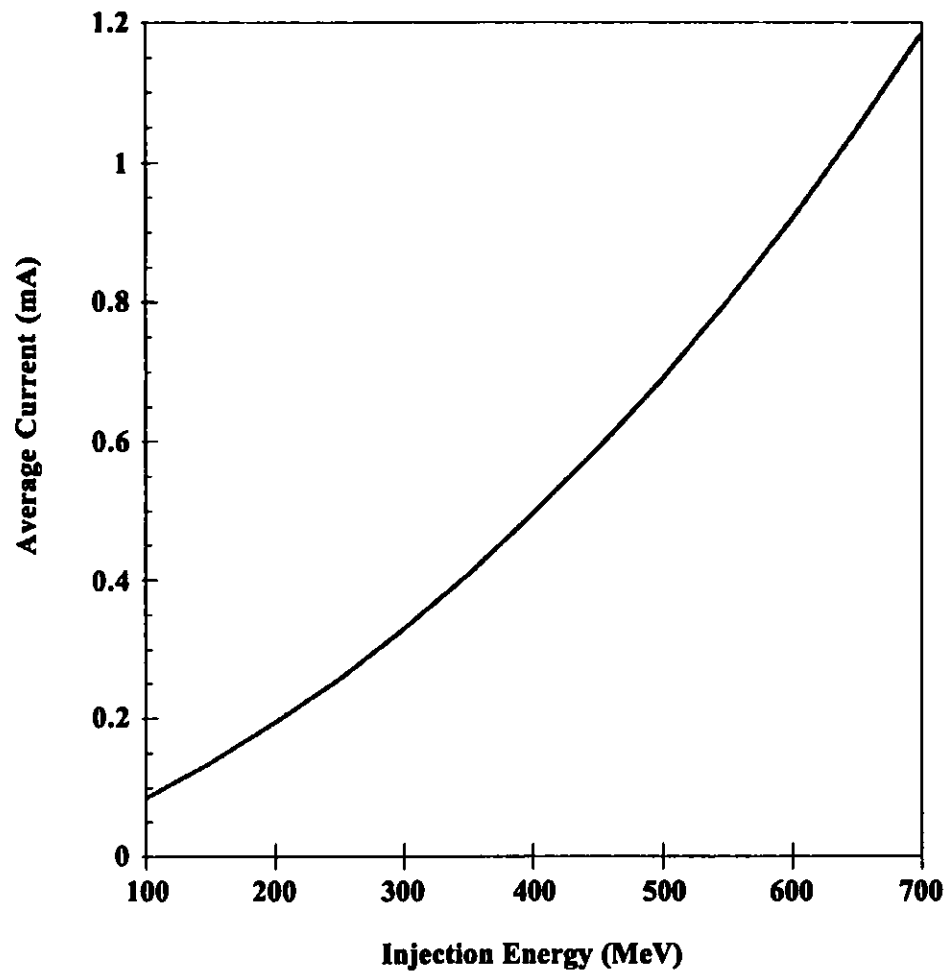
Figure II.2.1-4 Average Current from Space Charge Limit
$$\Delta v_y = 0.15, \ \varepsilon_y = \varepsilon_x = 375 \, \pi \times 10^{-6} \ \text{m}.$$

The beam emittance of $\varepsilon = 375\,\pi \times 10^{-6}$ m can be compared with the emittances of other machines. LANCSE-II uses $420\,\pi \times 10^{-6}$ m, the ESS uses $525\,\pi \times 10^{-6}$ m, and the BNL proposal uses $320\,\pi \times 10^{-6}$ m. Here, it is implied that the beam emittance contains 100% of the beam. Unlike electron beams, proton beams do not have Gaussian density distributions; instead, they tend to have cosine-squared distributions. For this reason, usage of rms quantities is avoided. The other often-used convention is to define the 100% emittance as six times the rms emittance.

In this preliminary estimate of the space charge limit, the use of $\Delta v = 0.15$ is quite conservative, and there is a safety margin associated with the assumption. However, the calculation was based on the assumption of an elliptic charge distribution. In order to obtain refined information on the particle distribution, an extensive tracking study was performed to simulate both the capture and acceleration processes and to minimize beam loss during these processes. A detailed discussion of the tracking is given in Section II.4.1. The longitudinal charge distribution as a function of time from injection to extraction is obtained from the tracking study. This gives the time-varying bunching factor.

Because the goal is to accelerate 1.04×10^{14} protons per pulse, we use the time-varying bunching factor, the emittance of $375\,\pi \times 10^{-6}$ m, and Equation II.2.1-2 to obtain a time-varying, incoherent, space charge tune shift. Figure II.2.1-5 shows both the time-varying bunching factor and the space charge tune shift during the first 6 msec of the acceleration cycle.

Note that the space charge tune shift is maximal around 1 to 2 msec after injection, and the maximum tune shift is about 0.19.

2.1.3.2 Beam Emittance and Machine Acceptance

On the basis of these studies, it was decided to use a beam emittance after injection of $375\,\pi \times 10^{-6}$ m in both planes and an injection energy of 400 MeV. Since the maximum and minimum β-functions in the transverse planes are 12 m and 2 m, respectively, the largest and smallest beam sizes due to the betatron motions are 6.7 cm and 2.7 cm, respectively.

For the synchrotron aperture, it is customary to add the maximum beam size due to betatron motion and synchrotron motion, plus some alignment tolerances, in order to obtain the dipole, quadrupole, and sextupole apertures. One of the design features is to have the smallest beam loss possible, so the aperture was chosen based on the following arguments. Clearly, the larger the aperture, the easier it is to prevent beam loss and to implement a lost beam catcher system. On the other hand, larger aperture results in higher construction and operating costs. The decision was made to define the beam-stay-clear (BSC) region as that calculated from the lattice β-functions and an acceptance of $750\,\pi \times 10^{-6}$ m. The acceptance is twice as large as the
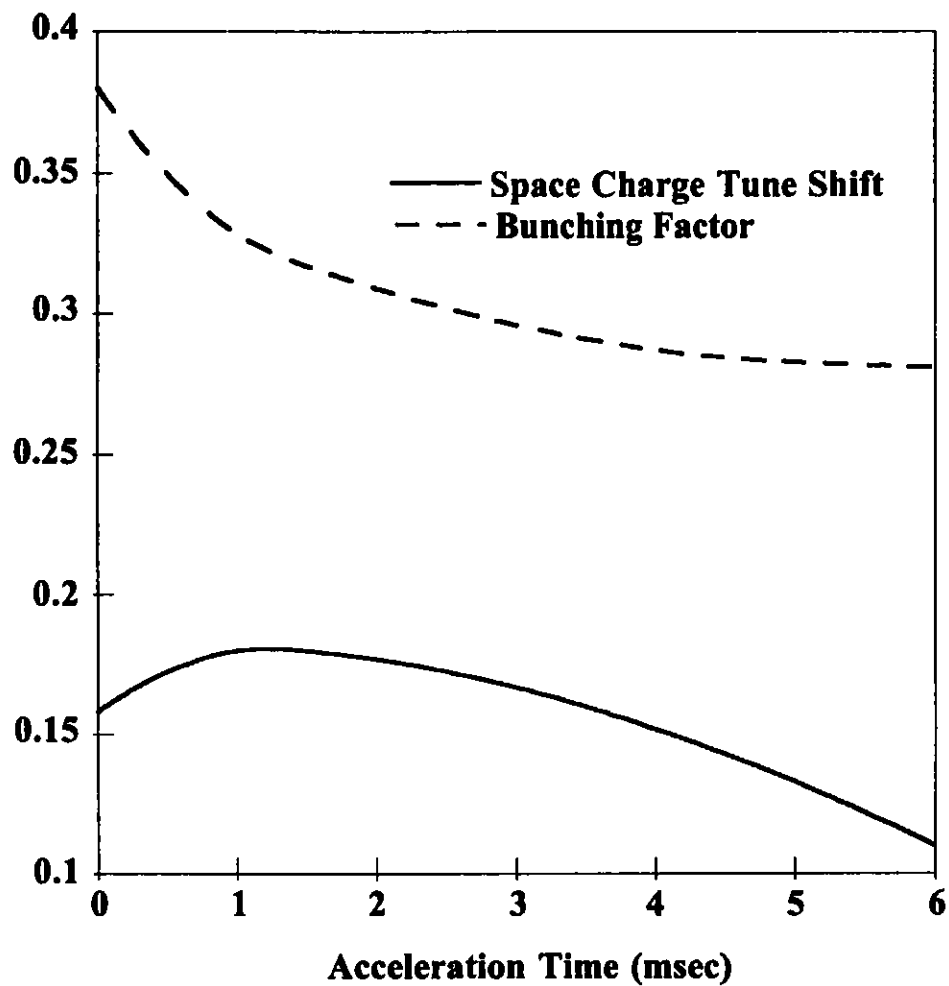
Figure II.2.1-5 Time Variation of the Bunching Factor (top curve) and
Time Variation of the Space Charge Tune Shift (bottom curve)
for the First 6 msec.

stacked beam emittance. In other words, the half-width of the BSC region, A_h is derived from the following formula:

$$A_h = \sqrt{\frac{2\beta\epsilon}{\pi}} + \left|\eta_{max}(\Delta p/p)_{max}\right| + COD$$

where COD, the expected closed-orbit distortion after the corrections are performed, is expected to be on the order of 0.1 cm. The horizontal and vertical emittances are six times the rms emittance, $\epsilon_x = \epsilon_y = 6\epsilon_{rms}$, and are $375\,\pi \times 10^{-6}$ m. The maximum values of the dispersion function and relative momentum spread are given by η_{max} and $(\Delta p/p)_{max}$, respectively. The maximum $\Delta p/p$ used for this case is 1%, which is about twice as large as the stacked beam momentum bite. This implies that

1. The acceptance is 12 times the rms emittance and

2. The vacuum chamber opening is 1.4 times larger than the beam size.

The design of the vacuum chamber system uses $750\,\pi \times 10^{-6}$ m acceptances in both planes and the beam size due to the momentum spread. The resulting chamber cross-sectional dimensions are quite similar to those of the ISIS synchrotron. Figure II.2.1-6 shows the chamber cross section in the quadrupole region, and the details of the chamber are discussed in Section II.6.

2.1.4 Single-Particle Instabilities

Single-particle instabilities arise through resonances between the natural oscillations of the particles and components of the magnetic guiding and rf accelerating fields. These resonances can be intrinsic to the fields or can be driven by imperfections in the fields. They are controlled through the rf and magnet lattice designs and the setting of appropriate tolerances on the magnetic field quality.

Betatron instabilities can arise when there is a resonance between the transverse oscillations of the particles and the harmonic components of the lattice magnetic fields. This relation can be expressed as

$$k\nu_x \pm l\nu_y = p ,$$
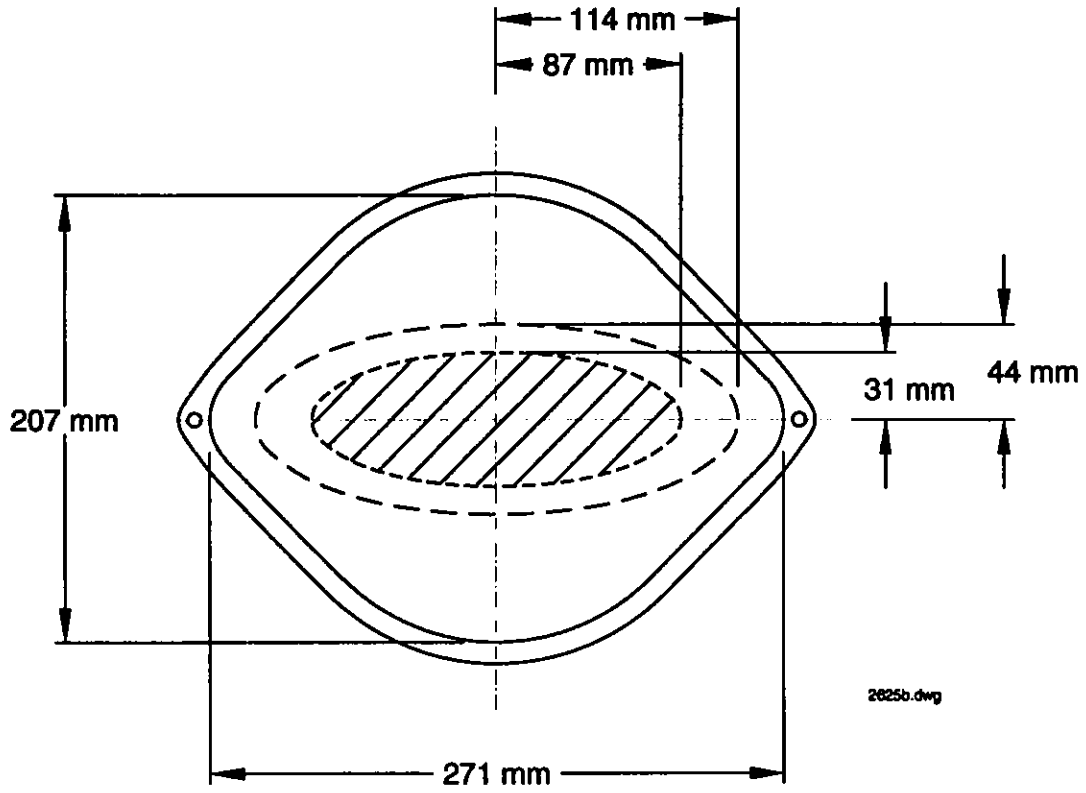
Figure II.2.1-6 Quadrupole Vacuum Chamber Cross Section Showing Beam-Stay-Clear (dashed line) and Beam Envelope (area containing diagonal lines).

where v_x and v_y are the horizontal and vertical betatron tunes, and k, l, and p are positive integers. The integer p refers to the driving harmonic of the magnetic structure originating from imperfections in the construction. In general, these imperfection resonances are weak and have no detrimental effects on the beam except when p is an integer multiple of some lattice structural numbers, such as the super-periodicity, and the total number of cells. In this latter case, the beam is subject to a potentially dangerous structural resonance. Because the resonance excitation force depends on the $(k + l - 1)$th derivative of the magnetic field, resonances of order $(k + l)$ must be considered. Since higher-order resonances are less harmful, lower-order multipole components are considered. The effects of the multipoles are discussed in Sections II.2.1.5 and II.2.1.6.

The other single-particle resonances that need to be considered are the synchro-betatron resonances, which couple the longitudinal and transverse oscillations through the relation:

$$kv_x \pm l v_y \pm m v_s = p,$$

where m is another integer and v_s is the synchrotron tune. In proton machines, the synchrotron tune is much smaller than the betatron tunes, and for the RCS machine, v_s is at least three orders of magnitude smaller than v_x or v_y. In such a case, synchro-betatron resonances $(m \geq 1)$ manifest as satellites of the $m = 0$ betatron resonances. The resonance condition is

$$v_{x,y} \pm m v_s = p. \qquad \text{(II.2.1-3)}$$

Here, the $\pm$ signs refer to the sum and difference resonances, respectively. These are driven by the position-dependent energy gains from the accelerating fields. A primary cause is the dispersion at rf cavity locations.

The RCS has 16 dispersion-free straight sections and eight straight sections with a dispersion of approximately 1 m. Six of ten rf cavities are located in the dispersion-free area, and the remainder are in the non-dispersion-free area. The decision to use the latter area for the rf cavities is made on the basis of following argument:

According to T. Suzuki,[4] when rf cavities are placed in non-dispersion-free straight sections, the maximum growth of the energy spread per revolution, $\delta(\Delta E/E)$, and the maximum betatron amplitude change per revolution, δx_{max}, are given by:

$$\delta\left(\frac{\Delta E}{E}\right) = \frac{1}{2^m(m-1)!}\frac{\beta^3|\alpha_m|\phi_{max}^m x}{cpR\beta_x}\frac{v_s A_\eta}{|\eta|(\Delta E/E)} \quad \text{and}$$

$$\delta x_{max} = \frac{1}{2^m m!}\frac{|\alpha_m|\phi_{max}^m}{cp\beta}A_\eta,$$

where

β = relativistic factor,

β_x = β-function at the cavities,

c = velocity of light,

p = momentum of the particle,

R = average radius of the ring,

η = slip factor,

ϕ_{max} = maximum synchrotron oscillation phase,

α_m = Taylor series expansion coefficient, less than or equal to 1, and

A_η = parameter that depends on the rf voltage and dispersion function.

The parameter A_η, calculated using the Suzuki formulation, is ~50 keV m for the RCS.[5] The largest v_s is 0.003, which occurs 4 msec into the acceleration period. From Equation II.2.1-3 together with v_s, v_x, and v_y, the minimum values of m are about 60 for a sum resonance and about 250 for a difference resonance. The estimated growth rates for these m values are vanishingly small for the synchro-betatron coupling resonance.[5] Therefore, the decision to place rf cavities in the non-dispersion-free straight area is acceptable.

2.1.5 Choice of Working Point

In addition to the single-particle instabilities discussed in the previous section and the Laslett space charge tune shift described in Section II.2.1.3, the considerations discussed below are taken into account in choosing the working point.

For a very-high-intensity machine, high tune values have several advantages, as discussed in Section II.2.1.1. One advantage is a relatively small space charge tune shift, and another is larger γ_t. The latter has implications for the collective instability threshold and the rf capability. Higher tunes are achieved by using a 90° phase advance cell as the base of the lattice. In addition, the phase advances in the horizontal and vertical planes are chosen to achieve the dispersion suppression with the removal of a single dipole from a normal cell. This is accomplished by choosing the vertical phase advance to be slightly less than 90°. The standard 90° cell dispersion-suppressor requires placement of a half-dipole in place of a full dipole.

This small difference in the phase advances between the two planes results in a ν_x that is larger than ν_y by one unit when the complete lattice is formed from the cells. The tune can be raised or lowered by 0.5 unit while keeping a difference of one unit between ν_x and ν_y and keeping the dispersion function through straight-section cells small (~10 cm). Therefore, the working point is not located in the vicinity of the traditional $\nu_x - \nu_y = 0$ line.

The next consideration for choosing the working point is placing it on the tune diagram. Figure II.2.1-7 shows the tune diagram in the region $6 \le \nu_x \le 8$ and $5 \le \nu_y \le 7$, with the sum resonances (solid lines) and the difference resonances (dashed lines) up to fourth order. The line thickness indicates the relative strength of the sum resonances. The working point of the bare machine (i.e., the machine without space charge), is indicated in the figure. It should be noted that it is not necessary to avoid all resonances for rapidly cycling machines, because the beam spends a relatively short time at the resonance lines. Thus, it is rarely necessary to consider resonances above fourth order.

The next item to be investigated is the spread in the working point due to space charge. The working point becomes diamond-shaped, as shown in Figure II.2.1-8. As discussed in Section II.2.1.3, this tune shift depends on the charge distribution in the machine and can differ by a factor of 1.5 between a uniform and an elliptic charge distribution. In the figure, the point P is the tune point of the bare machine. The point Q in the figure is the working point for a K-V distribution at 2 msec after injection, when the space charge tune shift is maximal. The diamond-shaped pattern is for the case in which the charge distribution is elliptic. The injection mechanism to achieve a K-V-like distribution is described in detail in Section II.2.2.

Figure II.2.1-8 also shows that the tune spread around the working point can cross the nonlinear structural resonances of $3\nu_x = 20$ and $\nu_x + 3\nu_y = 24$. These are important because 20 and 24 are divisible by 4, the super-periodicity.

The $\nu_x + 3\nu_y = 24$ resonance can be driven by skew-octupole fields. Such terms arise only from multipole errors and have little effect on the dynamic aperture, as discussed in Section II.2.1.6.

The $3\nu_x = 20$ resonance near the full space charge tune can be driven by the chromaticity-correcting sextupoles and can have a deleterious effect on the circulating beam. However, the 20th harmonic of the sextupole component is suppressed by placing harmonic-correcting sextupoles in the dispersion-free sections. Sextupoles with integrated strengths of 0.4 m^{-2} placed in each of the eight dispersion-suppressor cells eliminate the 20th harmonic. Figure II.2.1-9 shows the phase space motion with and without the harmonic correction for the particles oscillating with a tune of $\nu_x = 6\,^2/_3$. This is a standard technique used for a Chasman-Green lattice in third-generation synchrotron light sources.
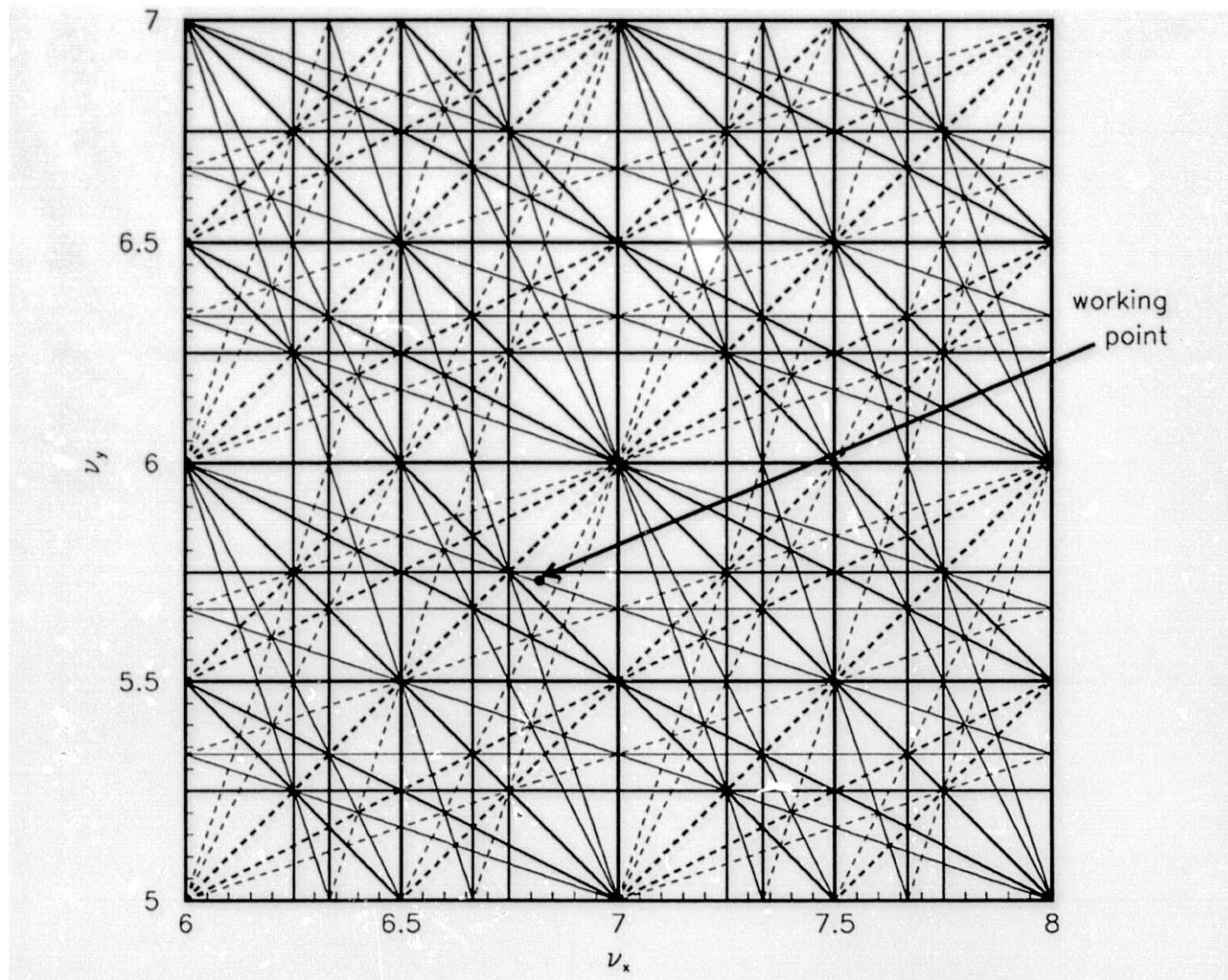
Figure II.2.1-7 Sum (solid lines) and Difference (dashed lines) Resonances Shown up to Fourth Order in the Region Bounded by $6 \le \nu_x \le 8$ and $5 \le \nu_y \le 7$. (Working point for the bare machine is indicated.)
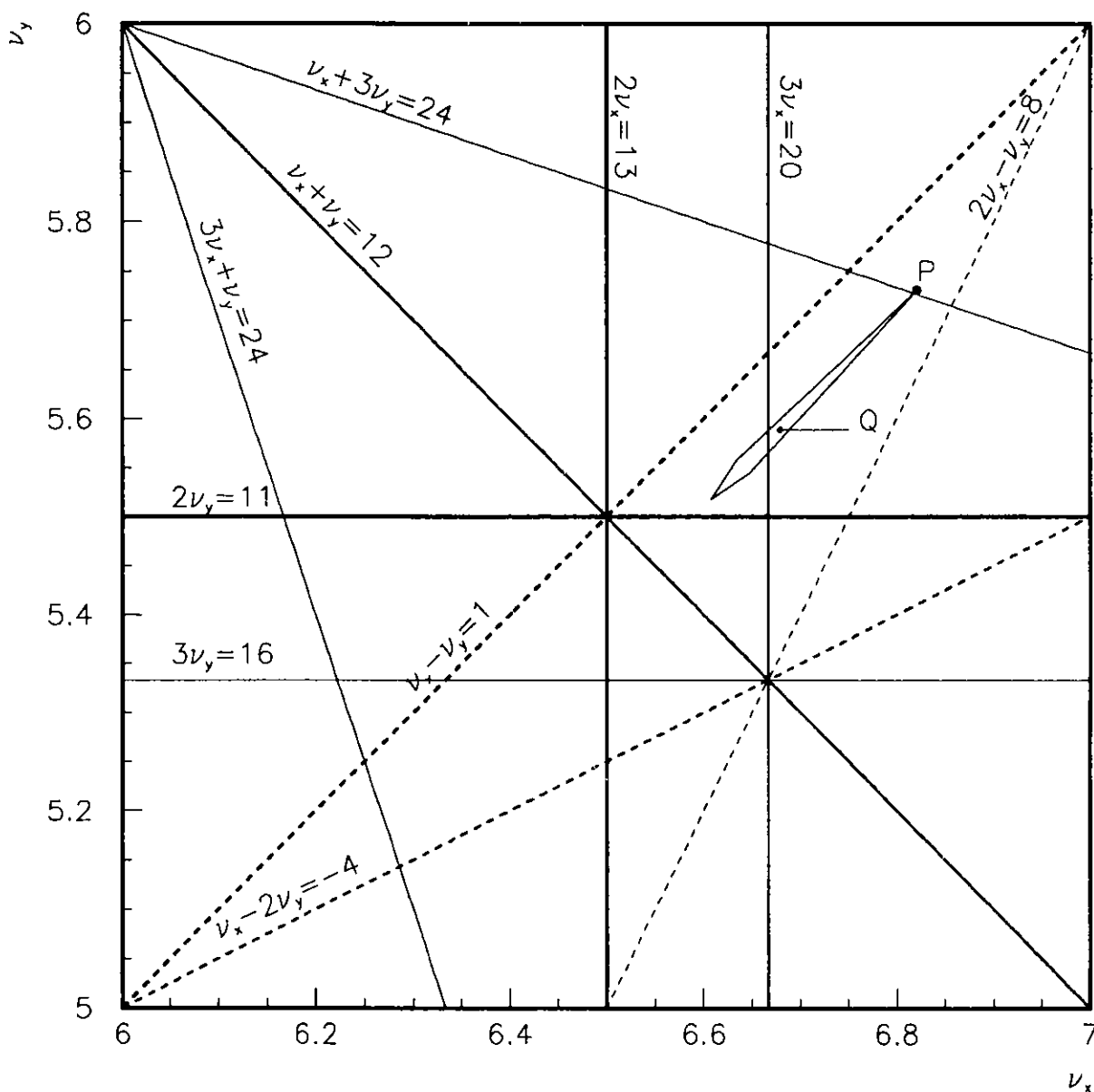
Figure II.2.1-8 Structure Resonances up to Fourth Order Shown for the Region Bounded by $6 < v_x < 7$ and $5 < v_y < 6$. The working point for the bare RCS machine is labeled P. The maximum space charge tune shift for a uniform, K-V distribution is labeled Q. The diamond-shaped area bounds the space charge tune shifts of individual particles in an elliptic distribution.

Horizontal Phase Space

(a)

Horizontal Phase Space
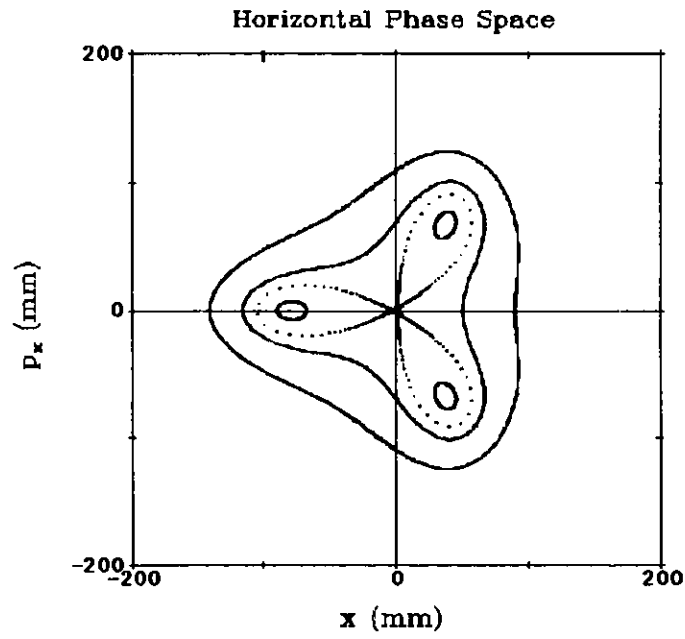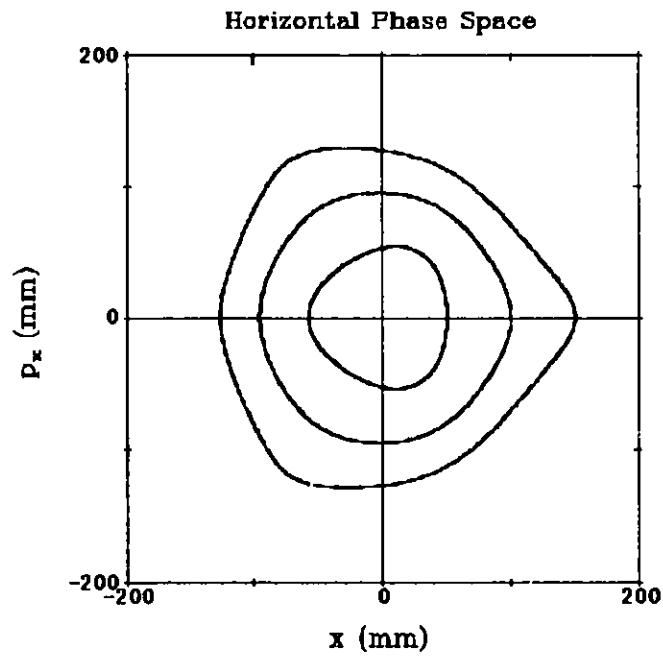
(b)

Figure II.2.1-9 Phase Space Motion with $v_x = 6\frac{2}{3}$ without (a) and

with (b) Harmonic Correction Sextupoles. (The variable p_x is defined to be [$p_x = \beta_x x' + \alpha_x x$].)

2.1.6 Transverse Tracking Studies

The key design feature of the RCS is the prevention of beam loss during the injection, capture, and acceleration processes. Beam loss prevention in the transverse phase space is achieved by providing large dynamic apertures in both transverse planes. We have performed tracking studies to ensure that the RCS has a dynamic aperture larger than the physical aperture of the ring vacuum chamber, taking into account magnetic field imperfections due to fabrication tolerances and misalignments caused by surveying tolerances.

The results of tracking studies of closed-orbit distortions and dynamic aperture reduction in the RCS are discussed below.

Closed-orbit distortions are caused by:

- Deviations of the vertical field value of dipole magnets, which introduce horizontal orbit distortions;

- Roll-angle misalignments of dipole magnets, which cause vertical orbit distortions; and

- Misalignments of quadrupole magnets, which produce extraneous dipole fields that distort the orbit.

Design specifications for the dipole corrector magnets are obtained from tracking studies.

The natural normalized chromaticities of the lattice described in Section II.2.1.1 are $\xi_x = -1.06$ and $\xi_y = -1.20$. Chromaticity is corrected by adding two families of sextupoles in the normal cells of the lattice.

The dynamic aperture is limited primarily by these chromaticity-correcting sextupoles. With the sextupoles energized to the values required to adjust the chromaticities to zero, we studied further reductions of the dynamic aperture caused by field deviations and misalignments, as cited above, and multipole components arising from magnet fabrication imperfections.

Dynamic aperture reduction caused by closed-orbit distortion is recovered by orbit corrections. The dynamic aperture is insensitive to reasonable levels of multipole components, up to four times the levels achieved in the APS Synchrotron magnets.

2.1.6.1 Closed-Orbit Correction

Closed-orbit distortions due to quadrupole misalignments and dipole field deviations can be estimated by using the following formula:

$$\frac{\Delta z}{\sqrt{\beta}} = \frac{1}{\sqrt{8}\,|\sin \pi \nu|}\left[\sum_Q \beta_Q k_Q{}^2 l_Q^2 (\delta z)_Q^2 + \sum_B \beta_B \theta_B^2 \left(\frac{\delta B}{B}\right)_B^2\right]^{1/2},$$

where the subscripts Q and B denote the quadrupole and dipole magnets, respectively, and

Δz = rms value of the COD in either the x- or y-plane,

β = amplitude function,

ν = tune of the lattice,

k_Q = quadrupole strength,

l_Q = quadrupole length,

$(\delta z)_Q$ = rms quadrupole misalignment,

θ_B = bending angle, and

$(\delta B / B)_B$ = rms field deviation in dipole magnet.

For the RCS, we find that

$$\frac{\Delta x}{\sqrt{\beta_x}} = \left[5.05^2 (\delta x)_Q^2 + 1.73^2 (\delta B/B)_B^2\right]^{1/2} \quad \text{and}$$

$$\frac{\Delta y}{\sqrt{\beta_y}} = \left[3.49^2 (\delta y)_Q^2 + 1.32^2 (\delta B/B)_B^2\right]^{1/2},$$

where $(\delta B / B)_B$ in the y-plane represents the dipole roll angle, and all lengths are in meters.

Thus, the amplification factors for quadrupole misalignments, $A_{x,y}$, defined as the ratio of the maximum COD in the ring and the rms quadrupole misalignments, are

$$A_x = 32.88 \text{ at } \beta_x = 10.60 \text{ m and } A_y = 24.12 \text{ at } \beta_y = 11.94 \text{ m},$$

where we used $(\Delta z)_{max} = 2(\Delta z)$, corresponding to 95% probability. These analytical values are compared with MAD[6] simulations. The results are shown in Figure II.2.1-10, where the horizontal axis represents 30 different machine simulations.

The APS Booster Synchrotron quadrupoles were aligned to an rms accuracy of $(\delta z)_Q = 0.2$ mm.[7] The RCS dynamic aperture is fairly insensitive to misalignment. For computational purposes, an alignment accuracy of 0.4 mm was used to estimate the maximum COD. Similarly, a value of $(\delta B / B)_B = 0.001$, corresponding to a dipole roll angle of 1.0 mrad, was used in the computations. This is a factor of three larger than the field deviations achieved at APS. These levels are expected to produce maximum orbit distortions of 18 mm in the horizontal plane and 14 mm in the vertical plane before correction.

The MICADO algorithm[8] included in the MAD program was used to simulate orbit corrections. Horizontal and vertical BPMs are located in the focusing and defocusing quadrupoles, respectively. Similarly, horizontal and vertical correctors are located near the focusing and defocusing quadrupoles. There are a total of 28 BPMs and 28 correctors in each plane. Horizontal and vertical corrector strengths of up to 85 and 71 G m, respectively, permit correction of the orbit to within the rms BPM accuracy of 0.1 mm. The maximum dipole corrector strength is specified as 110 G m. Typical CODs before and after correction are shown in Figure II.2.1-11. The corresponding corrector strengths are shown in Figure II.2.1-12.

2.1.6.2 Chromaticity Correction

The natural chromaticities of the lattice described in Section II.2.1.1 are $\xi_x = -1.06$ and $\xi_y = -1.20$, where $\xi = (\Delta v / v) / (\Delta p / p)$. Chromaticity is corrected by the addition of sextupoles in the normal cells of the lattice. The sextupole strengths, $B''l / B\rho$, required to make the chromaticities zero are $0.627 / m^2$ for each horizontal focusing sextupole (SF) and $0.863 / m^2$ for each horizontal defocusing sextupole (SD). There are 16 SF and 16 SD magnets.

The effects of chromaticity on the beam are discussed in Section II.5.4 in connection with transverse beam stability. We expect this lattice to operate with a chromaticity between zero and its natural chromaticity.

2.1.6.3 Dynamic Aperture

The dynamic aperture is reduced by the presence of chromaticity-correcting sextupoles as well as misalignments and magnet fabrication imperfections. Dynamic aperture limitations were simulated by using the tracking program RACETRACK.[9] The sextupoles were energized to the values required to adjust the chromaticities to zero.
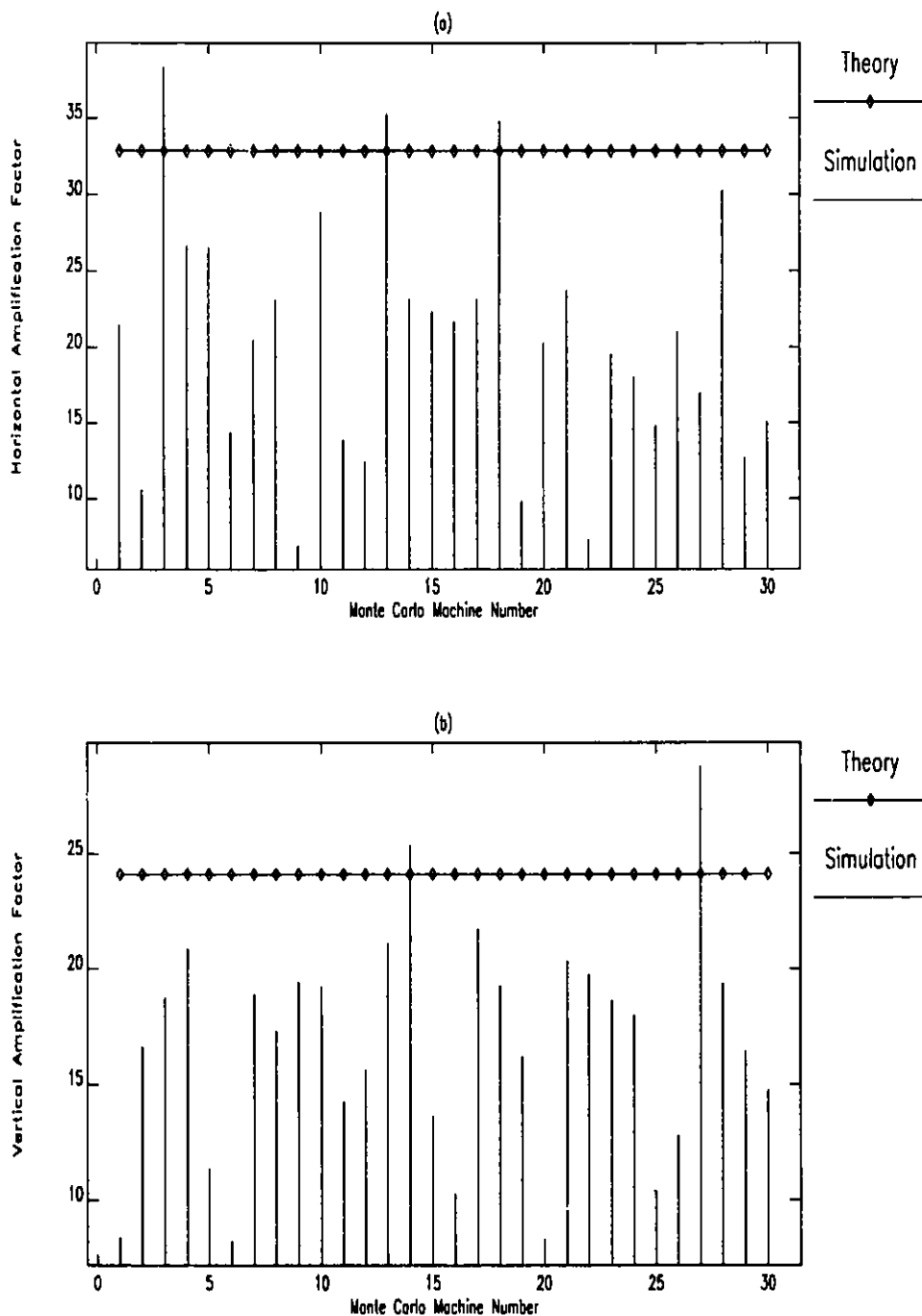
Figure II.2.1-10 Amplification Factors of the RCS. (Thirty different machines are simulated and compared with the theoretical estimation.)
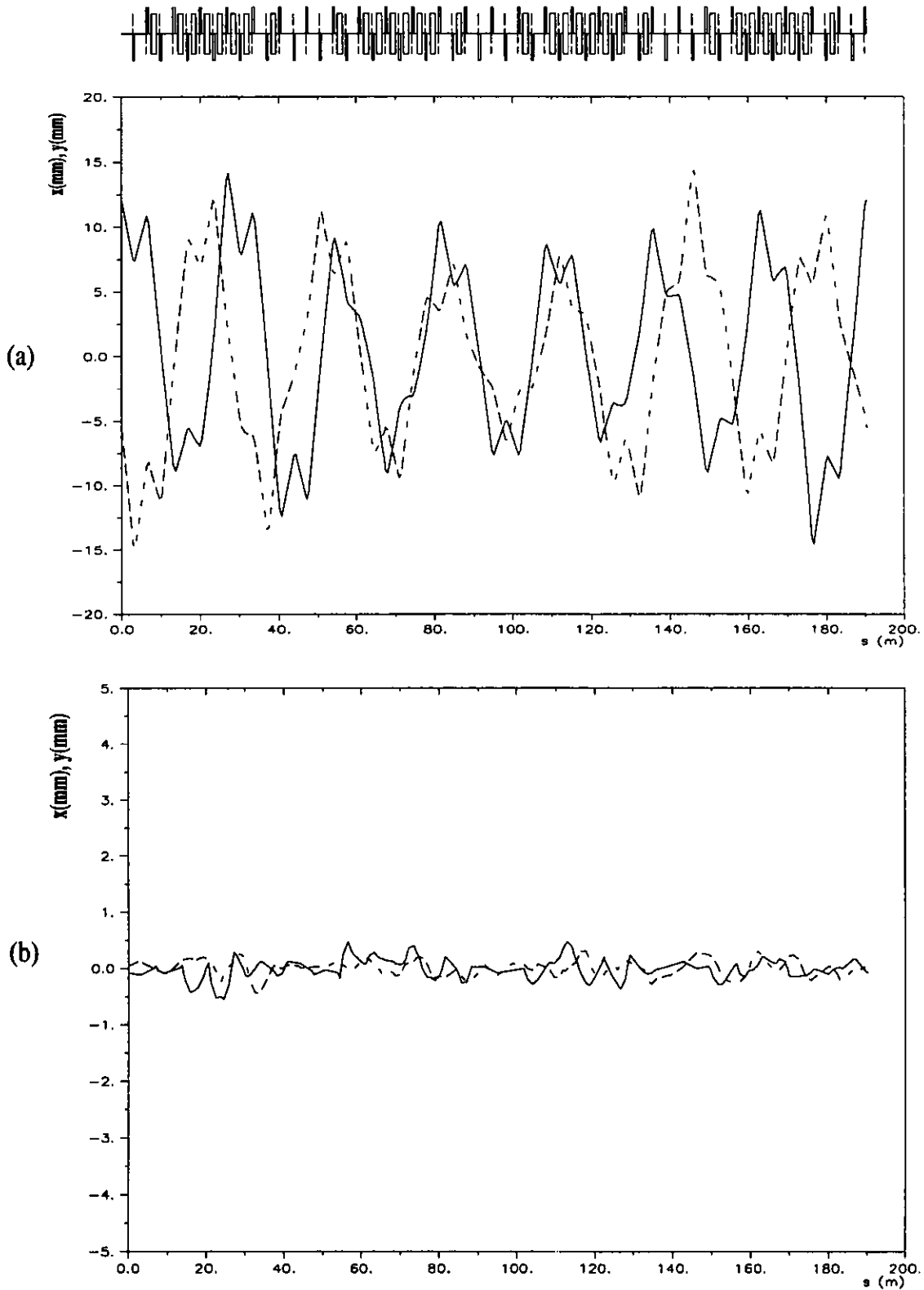
Figure II.2.1-11 Closed-Orbit Distortions before (a) and after (b) Correction for Quadrupole Misalignments $(\delta z)_Q = 0.4$ mm, Dipole Field Deviations $(\Delta B/B)_B = 0.001$, and Dipole Roll Angles $(\delta\theta)_B = 1.0$ mrad. (Solid/dashed lines represent the horizontal/vertical orbit distortions, respectively.)
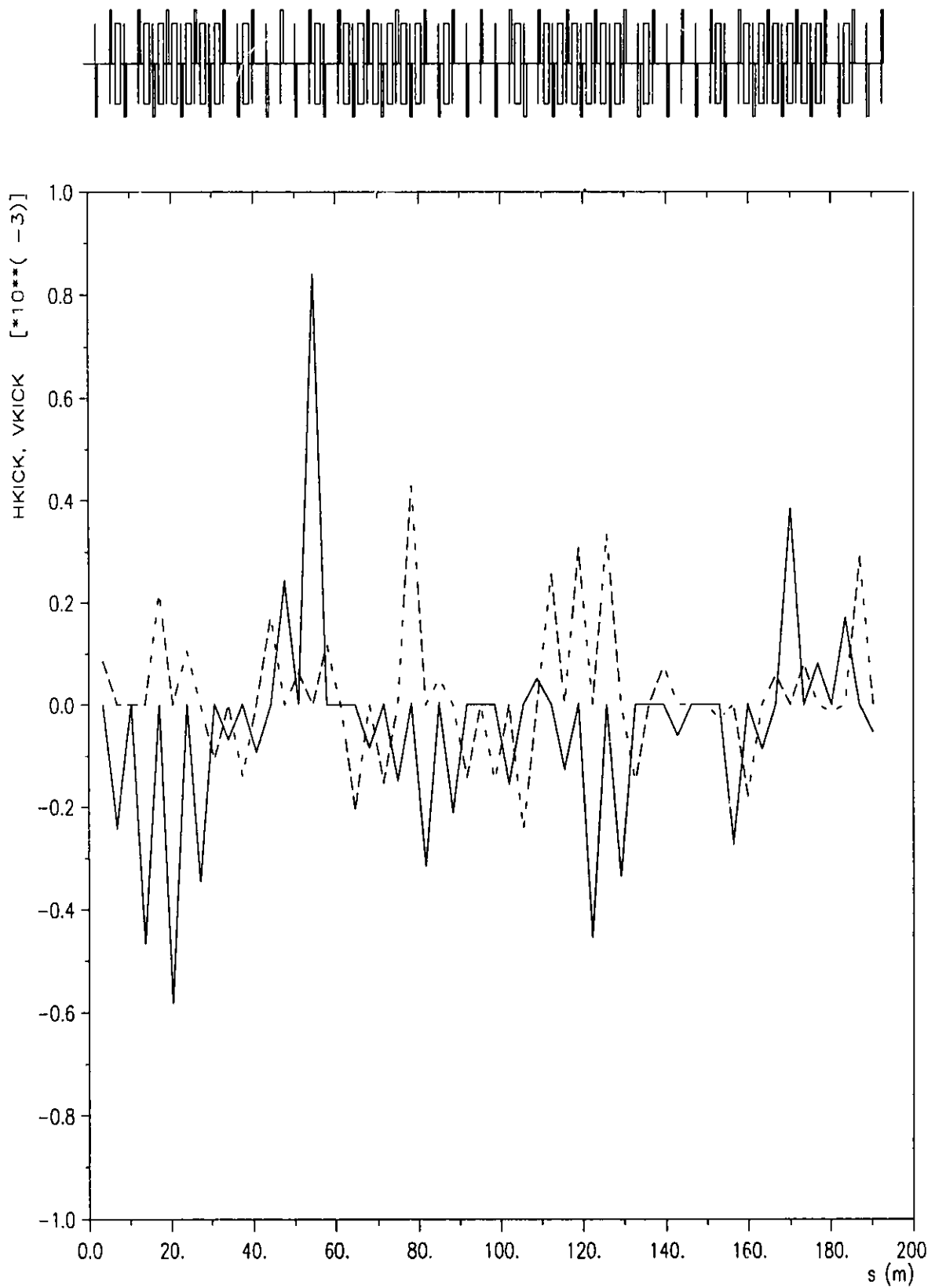
Figure II.2.1-12   Required Corrector Strengths to Correct the Closed-Orbit Distortion Shown in Figure II.2.1-11. (Solid/dashed lines represent the horizontal/vertical corrector strengths, respectively.)

The dynamic aperture was searched along five directions of the x-y plane. First the positive and negative horizontal directions along the y = 0 axis and the positive vertical direction along the x = 0 axis were searched. Then the diagonal directions y = ±x were searched. The dynamic aperture was defined as the limiting stable betatron oscillation amplitude of a particle that survived 2,000 turns in a static field.

The following discussion is limited to reductions caused by random misalignments and random multipole components arising from magnet imperfections. The distribution of errors was assumed to be Gaussian, with a cutoff of ±5σ. The simulations were performed for 10 different machines. The effects resulting from systematic errors were found to be smaller than those resulting from random errors and are not discussed.

First the dynamic aperture reductions caused by closed-orbit distortions arising from the alignment tolerances discussed in Section II.2.1.6.1 were investigated. Recovery of the dynamic aperture after orbit correction was also verified. Second, reductions caused by higher-order multipoles were investigated. Finally, dynamic aperture reduction due to alignment tolerances and higher-order multipoles was calculated. These calculations were performed with and without closed-orbit correction. It is particularly important to verify that the dynamic aperture is adequate to permit beam injection prior to initial startup of the machine.

Dynamic aperture reductions resulting from alignment tolerances, with and without closed-orbit corrections, are shown in Figure II.2.1-13. The lines in the figure are the averages and the error bars are the standard deviations for the 10 machines. The dynamic apertures are displayed at the focusing quadrupole. The dynamic aperture of the perfect machine and BSC are also shown in the figure. The closed orbit was corrected to 0.1 mm rms, as described in Section II.2.1.6.1. Before orbit correction, the dynamic aperture is sufficient to permit beam injection, as seen in Figure II.2.1-13. Correction of the orbit restores the dynamic aperture to that of the perfect machine.

Dynamic aperture reductions due to magnetic field imperfections were studied by using the multipole coefficients, a_n and b_n, shown in Table II.2.1-3. The coefficient values were obtained by scaling the measured data of the APS Booster Synchrotron magnets to the RCS magnets. The magnetic field expressed in terms of these coefficients is

$$B = B_0 \sum_{n=0}^{\infty} \left(b_n + ia_n \right)\left(x + iy \right)^n ,$$

where b_n and a_n are the normal and skew coefficients in units of cm^{-n}.

There were no appreciable effects on the dynamic aperture for multipoles up to twice the values depicted in Table II.2.1-3. Some reduction was observed for multipoles at four times those values, as shown in Figure II.2.1-14.
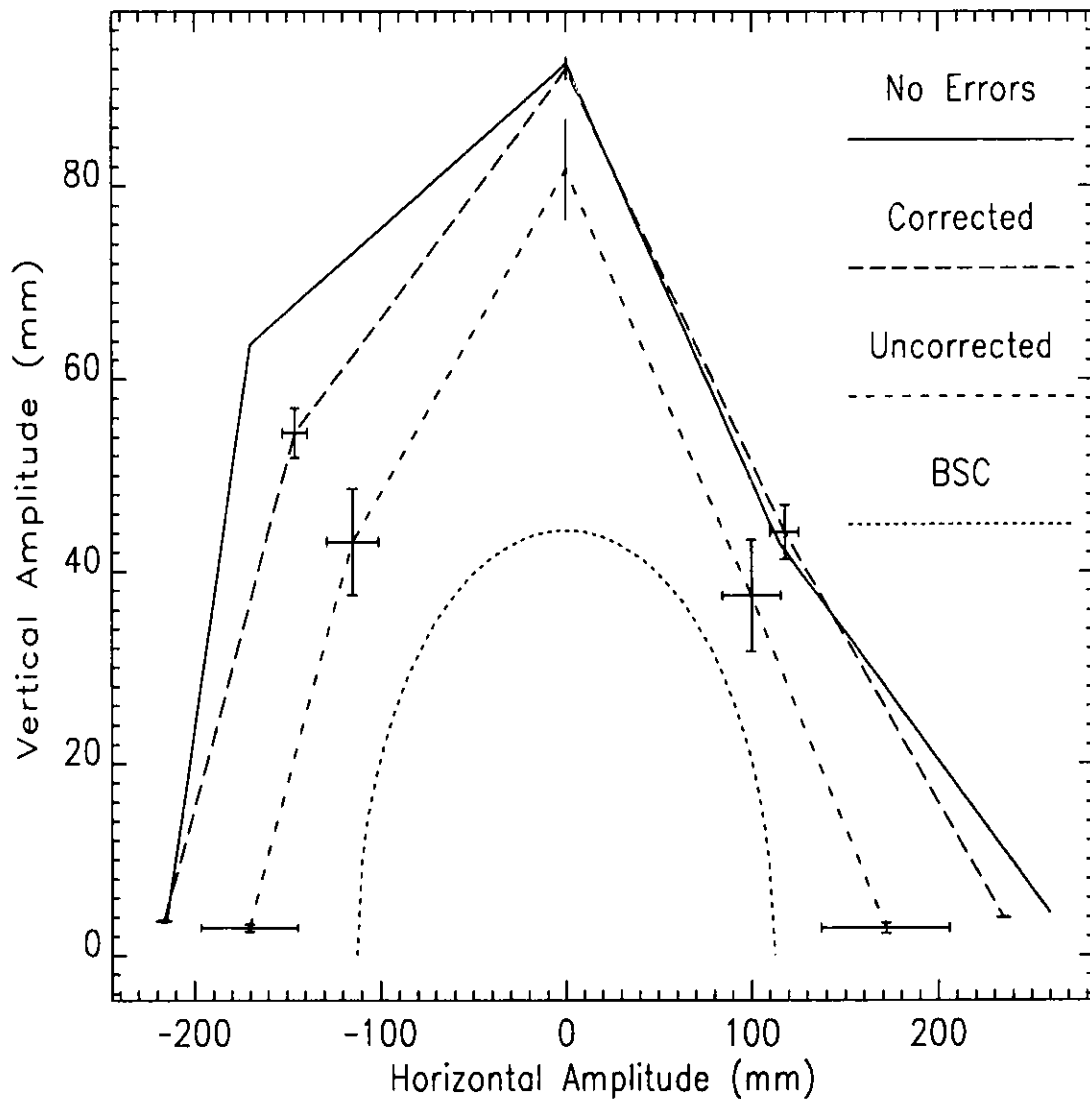
Figure II.2.1-13 Dynamic Apertures in the Presence of Quadrupole Misalignments of 0.4 mm, Dipole Field Deviations of 0.001, and Dipole Roll Angle Misalignments of 1.0 mrad Plotted before and after Corrections of the Closed Orbit to 0.1-mm Root Mean Square (rms). (Dynamic aperture for the perfect machine is shown for comparison. The ellipse represents the BSC region at the focusing quadrupole.)

Table II.2.1-3 Multipole Coefficients of Synchrotron Magnets

Multipole[a]	Random (cm^{-n})	Systematic (cm^{-n})
b_{1D}	2.60×10^{-6}	-7.10×10^{-6}
b_{2D}	3.90×10^{-8}	-0.70×10^{-6}
b_{1Q}	4.90×10^{-4}	2.50×10^{-4}
a_{1Q}	1.70×10^{-4}	-0.40×10^{-4}
b_{2Q}	4.80×10^{-6}	-1.20×10^{-6}
a_{2Q}	0.13×10^{-4}	0.28×10^{-6}
b_{3Q}	1.20×10^{-6}	-5.50×10^{-6}
a_{3Q}	0.62×10^{-6}	0.22×10^{-6}
b_{4Q}	3.60×10^{-8}	0.30×10^{-8}
a_{4Q}	4.50×10^{-8}	-0.80×10^{-8}
b_{5Q}	0.24×10^{-8}	1.95×10^{-8}
b_{2S}	1.36×10^{-3}	5.00×10^{-4}
a_{2S}	3.30×10^{-4}	-4.90×10^{-4}
b_{3S}	0.17×10^{-4}	-2.40×10^{-6}
a_{3S}	0.61×10^{-4}	3.20×10^{-6}

[a] D = dipole; Q = quadrupole; S = sextupole.
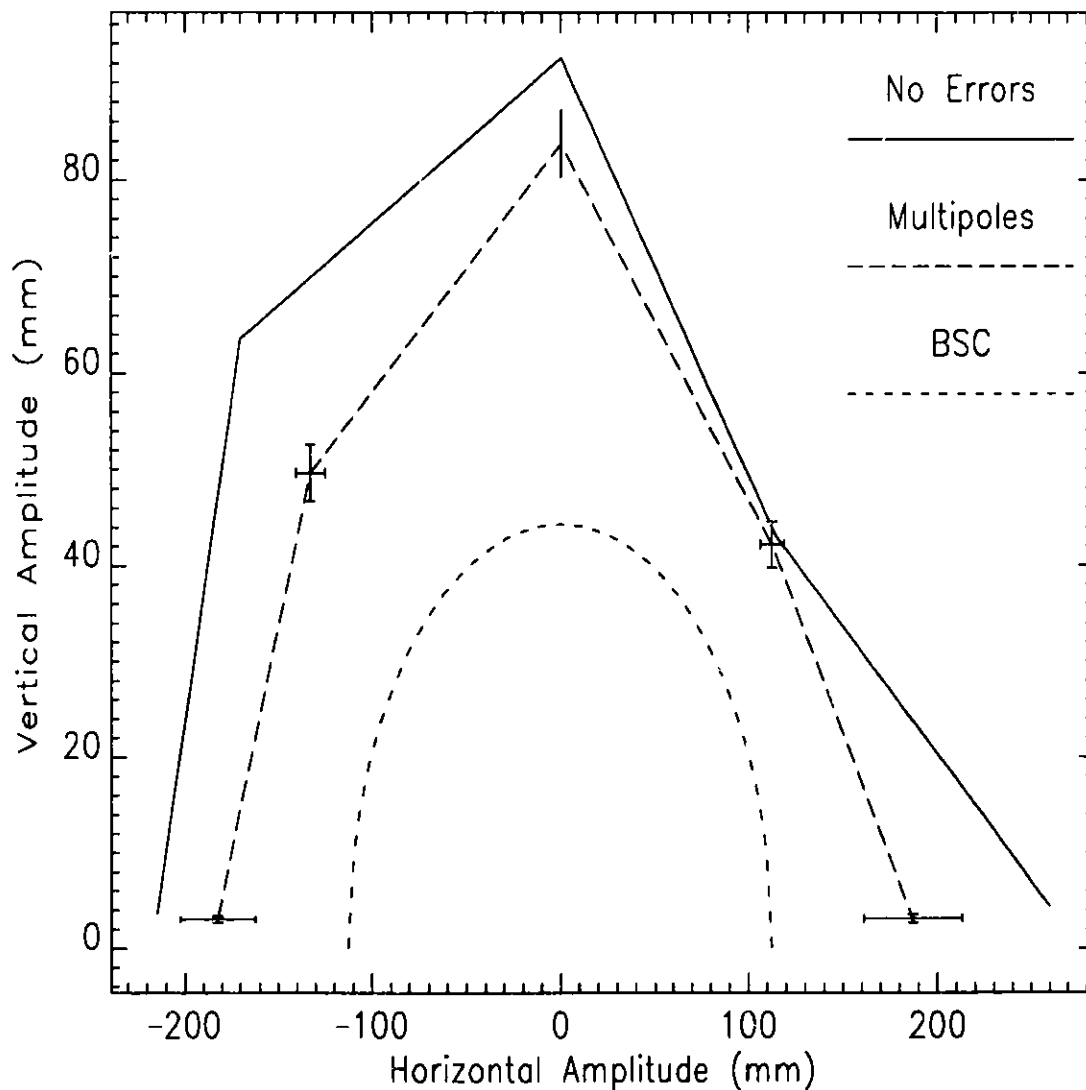
Figure II.2.1-14 Dynamic Aperture Reductions Caused by Multipoles at Four Times
the Values Listed in Table II.2.1-3.

Finally, alignment tolerances were included along with multipole components. Reductions, both before and after closed-orbit correction, were studied. The results are shown in Figure II.2.1-15. The dynamic aperture before COD is still as large as the BSC, thus permitting the establishment of a closed-orbit solution at injection. The dynamic aperture after correction of the closed orbit is very close to that shown in Figure II.2.1-14, which only included multipole components.
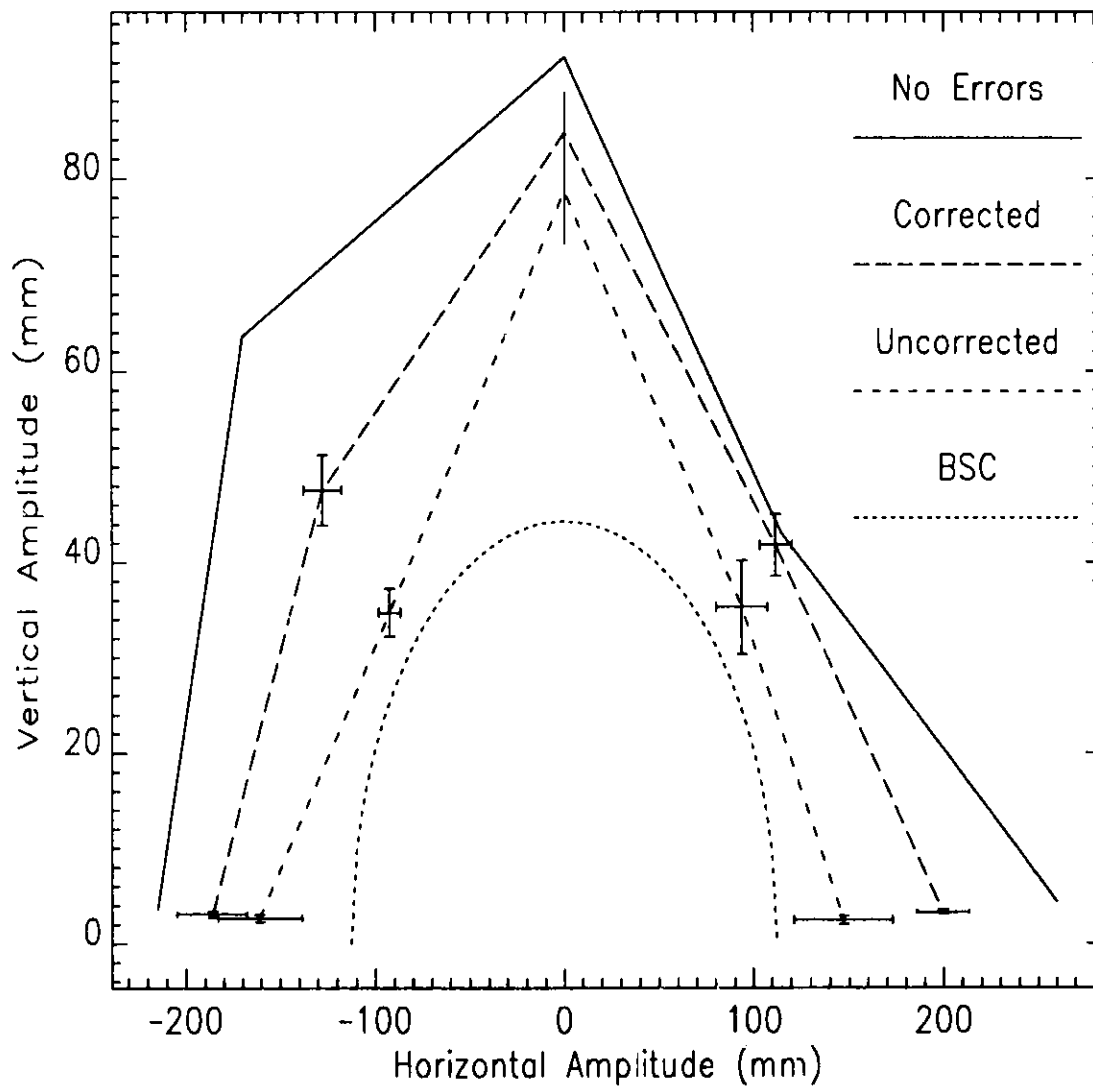
Figure II.2.1-15 Dynamic Aperture Reductions Caused by Misalignment and Multipoles, Plotted before and after Corrections of the Closed Orbit.

2.2 INJECTION OPTICS

2.2.1 H⁻ Injection

A total of 1.04×10^{14} protons are injected into the synchrotron in ~500 turns by stripping negative hydrogen ions. The stripping foil is located 10 cm downstream of the central horizontal focusing quadrupole in one of the four dispersion-free straight sections, as shown in Figure II.2.2-1. The betatron functions at the injection point are $\beta_x = 9.6279$ m, $\alpha_x = 2.0491$, $\beta_y = 3.2871$ m, and $\alpha_y = -0.7735$.

The separation of the H⁻ injected ions and the circulating protons is achieved in the quadrupole magnet upstream of the stripping foil. To prevent partially stripped H^0 neutral particles from entering the downstream bending magnet, the injection angle at the stripper is chosen so that these particles can be collected at an inside aperture stop upstream of the magnet. Stripping of the H^0 in the bending magnet would lead to an undesirable halo of the circulating proton beam. Additional details are discussed in Section II.2.2.2.

The horizontal betatron oscillation amplitude of the injected protons is controlled by a local bump of the orbit, as shown in Figure II.2.2-1. Two magnets, B_1 and B_2, placed upstream of the injection point are used to adjust the position, X_b, and angle, X_b', of the orbit at the stripper, which is located 10 cm from the central orbit. Two more magnets, B_3 and B_4, placed downstream of the injection point are required to restore the closed orbit.

Let

$$\Delta x = X_0 - X_b$$

and

$$\Delta x' = X_0' - X_b',$$

where X_0 and X_0' are the position and angle of H⁻ ions at the stripper. The horizontal oscillation amplitude is

$$A_x = \sqrt{\Delta x^2 + (\beta_x \Delta x' + \alpha_x \Delta x)^2}.$$
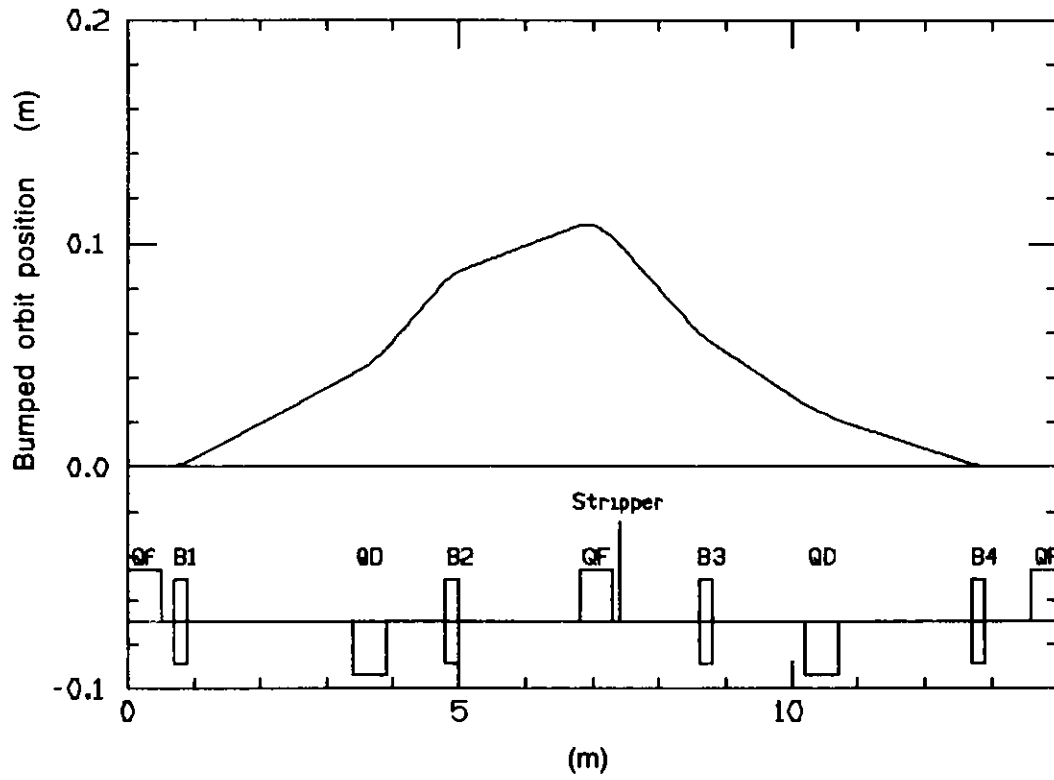
Figure II.2.2-1 Bumped Orbit in the Injection Straight Section.

To minimize the number of passes through the stripping foil by the circulating protons, one injects them at the maximum of the oscillation amplitude:

$$\beta_x \Delta x' + \alpha_x \Delta x = 0$$

and

$$A_x = \Delta x \ .$$

This condition is usually achieved by adjusting the injection angle, X_0', such that

$$\beta_x X_0' + \alpha_x X_0 = 0$$

and by controlling the bumped orbit to give

$$\beta_x X_b' + \alpha_x X_b = 0.$$

Under this condition, the bends required at all four bumper magnets are proportional to X_b.

With the injection point at 10 cm, these conditions result in an injection angle of –21.3 mrad. This injection angle, however, is too shallow to prevent the neutral particles from entering the downstream bending magnets. The required angle is –33.0 mrad. Injection at the maximum of the betatron oscillation amplitude now gives the condition:

$$X_b' = X_0' + \alpha_x (X_0 - X_b)/\beta_x \ .$$

The bends at the four bumper magnets have a constant term in addition to the normal X_b dependence.

Figure II.2.2-2 shows the injection details. The H^- ion beam enters at 84.0 cm and has an angle of –333 mrad with respect to the central orbit. Two injection septum magnets, 1.2-m long and 0.3-m long, produce outward bends of 228 mrad and 24 mrad, respectively. The quadrupole upstream of the stripper produces an additional outward bend and separates the H^- ions from the circulating protons. The upstream 1.2-m septum magnet has a field index of –20 to compensate for the defocusing effect of the quadrupole on negative ions. The phase-space distribution of the H^- beam is approximated by a Gaussian distribution with standard deviation σ. The emittance is defined as $\varepsilon = 6\pi\sigma^2/\beta$, which contains 99% of the beam. According to this definition, the emittance of the H^- beam is 6π mm mrad. The horizontal size of the injected beam shown in Figure II.2.2-2 is $\sqrt{6}\sigma$.
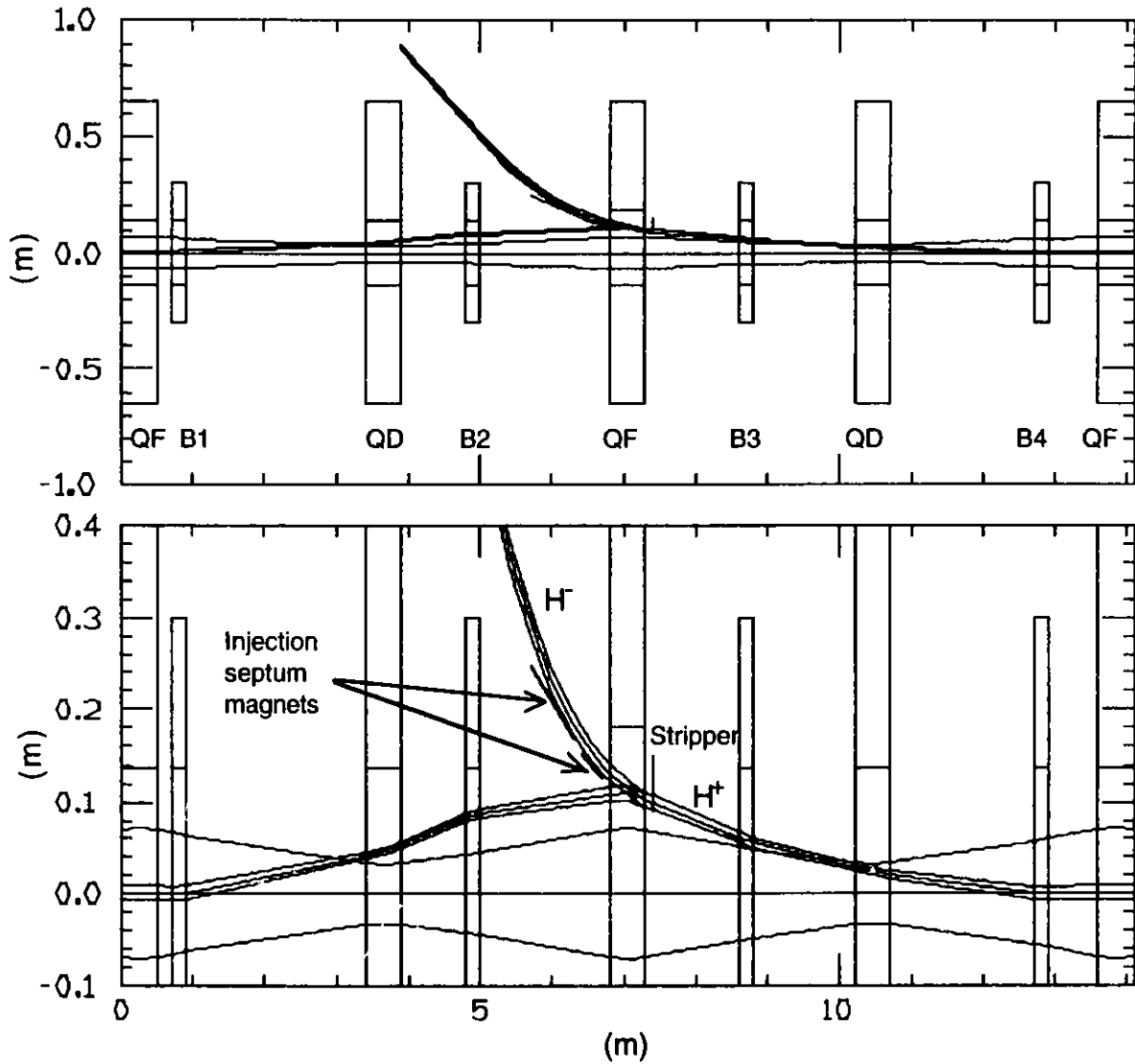
Figure II.2.2-2 Injection Details in Two Scales. (The horizontal size of the circulating beam after filling is also shown.)

The total phase space area occupied by the protons after injection is 375 π mm mrad in each plane. Thus the horizontal and vertical sizes of the proton beam at the stripper location are 12.0 cm and 7.0 cm, respectively. Figure II 2.2-2 also shows the horizontal circulating beam size in the injection straight section. Figure II 2.2-3 shows the time dependence of the bends required at the four bumper magnets.

To produce amplitude-independent tune shifts, the protons are injected in such a manner as to satisfy the K-V distribution function.[3] This requires that the horizontal and vertical amplitudes, A_x and A_y, lie on an ellipse, i.e.,

$$\frac{A^2_x}{A^2_x(max)} + \frac{A^2_y}{A^2_y(max)} = 1 .$$

At the stripper locations, A_x (max) and A_y(max) are 60 mm and 35 mm, respectively.

One way to satisfy the K-V distribution is to inject the protons so as to satisfy the following time relations:

$$A_x(t) = A_x(max)\sqrt{\frac{t}{t_f}}$$

and

$$A_y(t) = A_y(max)\sqrt{\frac{t_f - t}{t_f}} ,$$

where $t_f = 500 \times 0.89 = 445$ msec.

In the horizontal plane, the bumper magnets are timed to cause the bumped orbit to pull away from the injection position according to the relation

$$X_b(t) = X_0 - A_x(t).$$

This timing sequence produces the horizontal phase space and density distributions shown in Figure II.2.2-4. The figure shows the locations of each of the 500 turns at the end of injection. The circles are 1-sigma contours of the incoming linac beam.
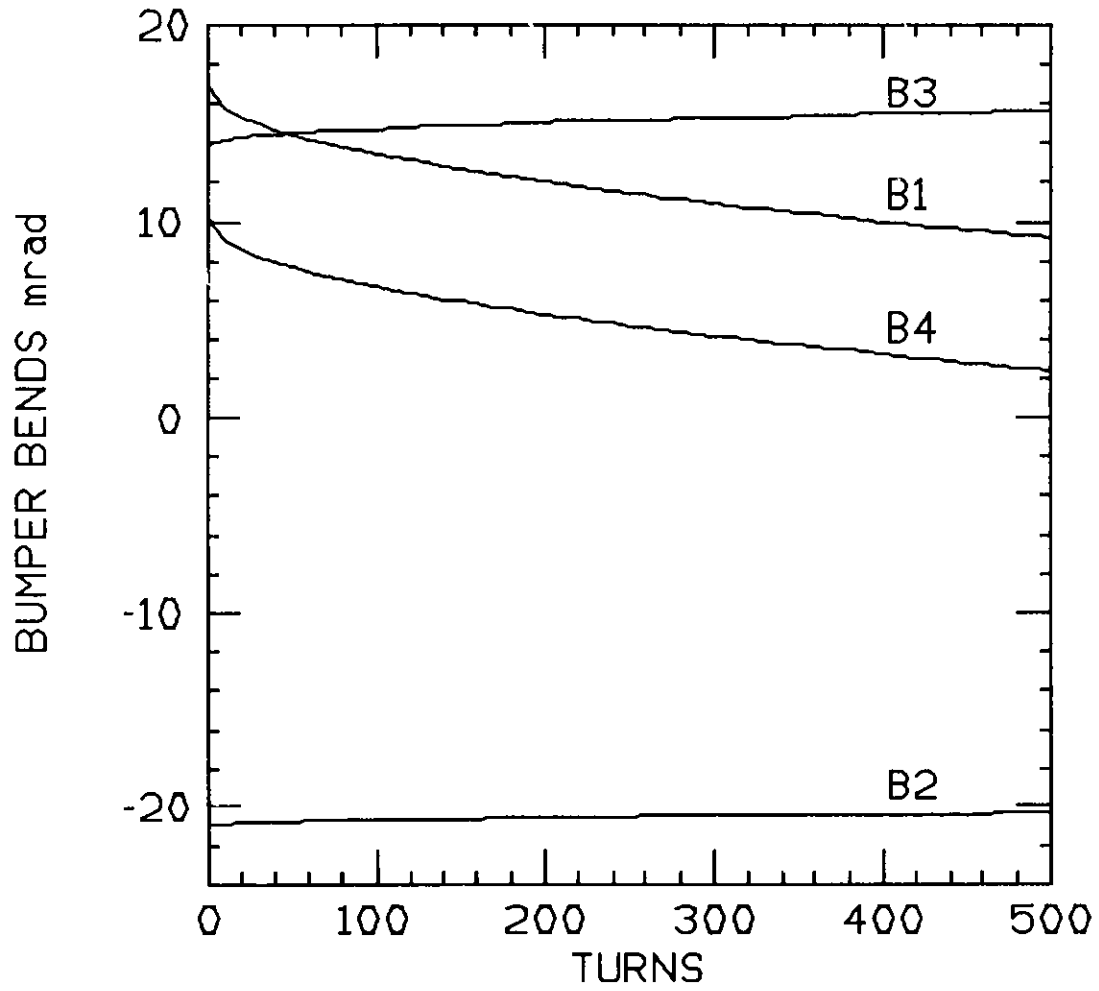
Figure II.2.2-3 Bending Angle of the Four Bumper Magnets as a Function
of Injected Turn Number.
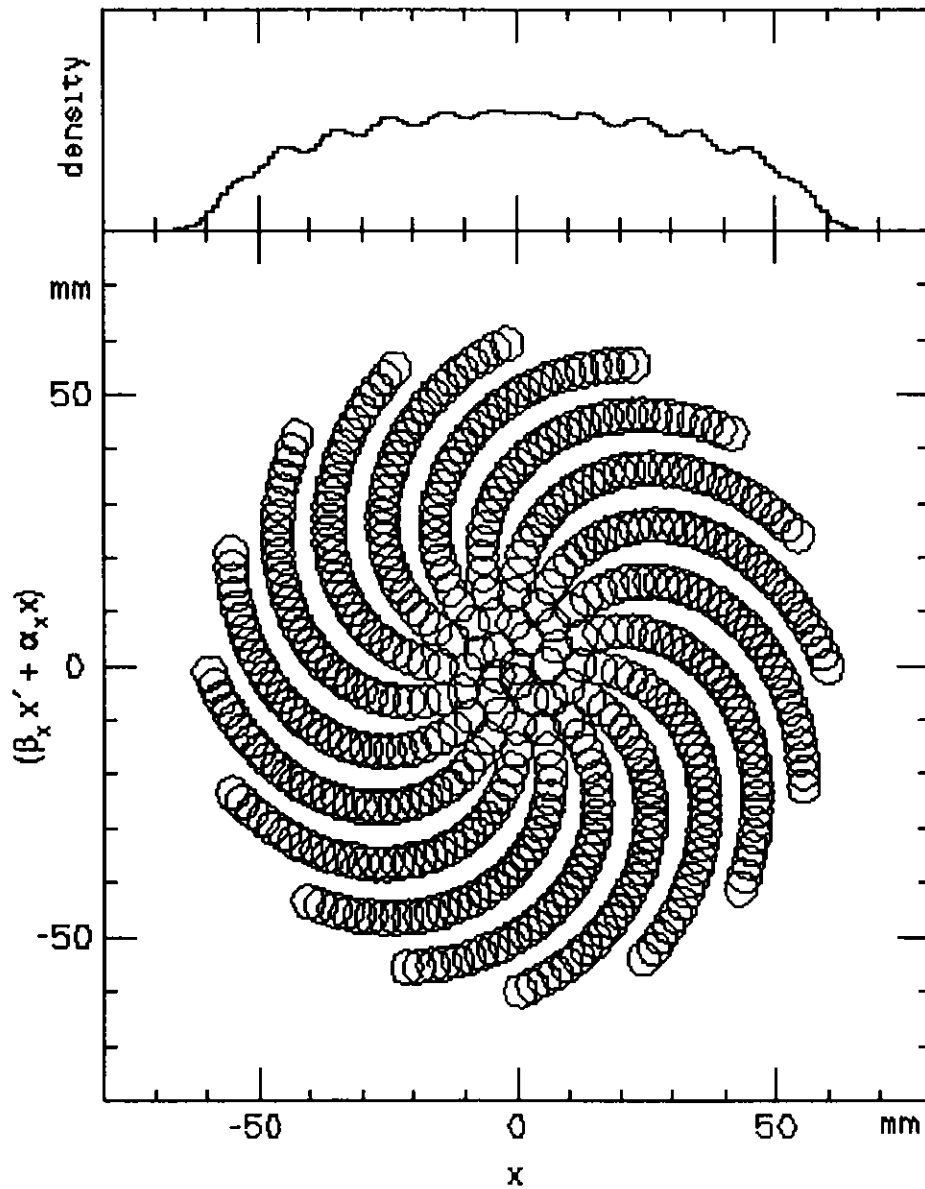
Figure II.2.2-4 Location of the 500 Turns, at the End of Injection, in the
Normalized (x, $\beta_x x' + \alpha_x x$) Horizontal Phase Space at the Stripper
Location. (Circles are 1-sigma contours of the incoming
linac beam. The horizontal density distribution
is shown at the top.)

Vertical phase space painting is achieved by using a vertical steering magnet placed 4.7 m upstream of the stripper in the H^- injection line. Taking into account the intervening focusing elements, a kick of θ produces the following results at the stripper:

$$y = 4.48\ \theta,$$

$$y' = -0.188\ \theta,$$

$$\beta_y y' + \alpha_y y = -3.92\ \theta,$$

and

$$A_y\ (t) = 5.95\ \theta\ (t)\ ,$$

where dimensions are in meters.

The timing sequence described above produces the ɩɩnal vertical phase space distribution and space density shown in Figure II.2.2-5. Figure II.2.2-6 shows the time dependence of A_x and A_y.

The final spatial distribution of the 500 turns, after a minor adjustment of the horizontal and vertical tunes to eliminate undesirable Lissajous patterns that arise from integer tune ratios, is shown in Figure. II.2.2-7.

Assuming a stripping foil with full vertical aperture, the average number of passes per injected proton through the stripping foil is 16. Actually, a foil with only a little more than half a vertical aperture is needed for the injection process described above. The rms scattering angle for passage through a 250-μg/cm^2 foil is 0.026 mrad. The horizontal and vertical divergences for the injected beam are $\sigma_{x'} = 0.32$ mrad and $\sigma_{y'} = 0.55$ mrad, respectively. The 16 foil passes for each turn produce only a 10% increase in the horizontal emittance and a 3% increase in the vertical emittance. Therefore, there is no need to use a half-aperture stripping foil.

Figure II.2.2-8 shows the equilibrium heating contours on the stripping foil caused by injection of the H^- and multiple passes of the circulating protons.   The temperatures are calculated assuming 500 injected turns, 2×10^{11} protons per turn, a foil thickness of 250 μg/cm^2, and a 30-Hz repetition rate. The vertical movement of the injected H^- beam and average of 16 foil passes for each injected proton produce a maximum equilibrium temperature of 700 K.
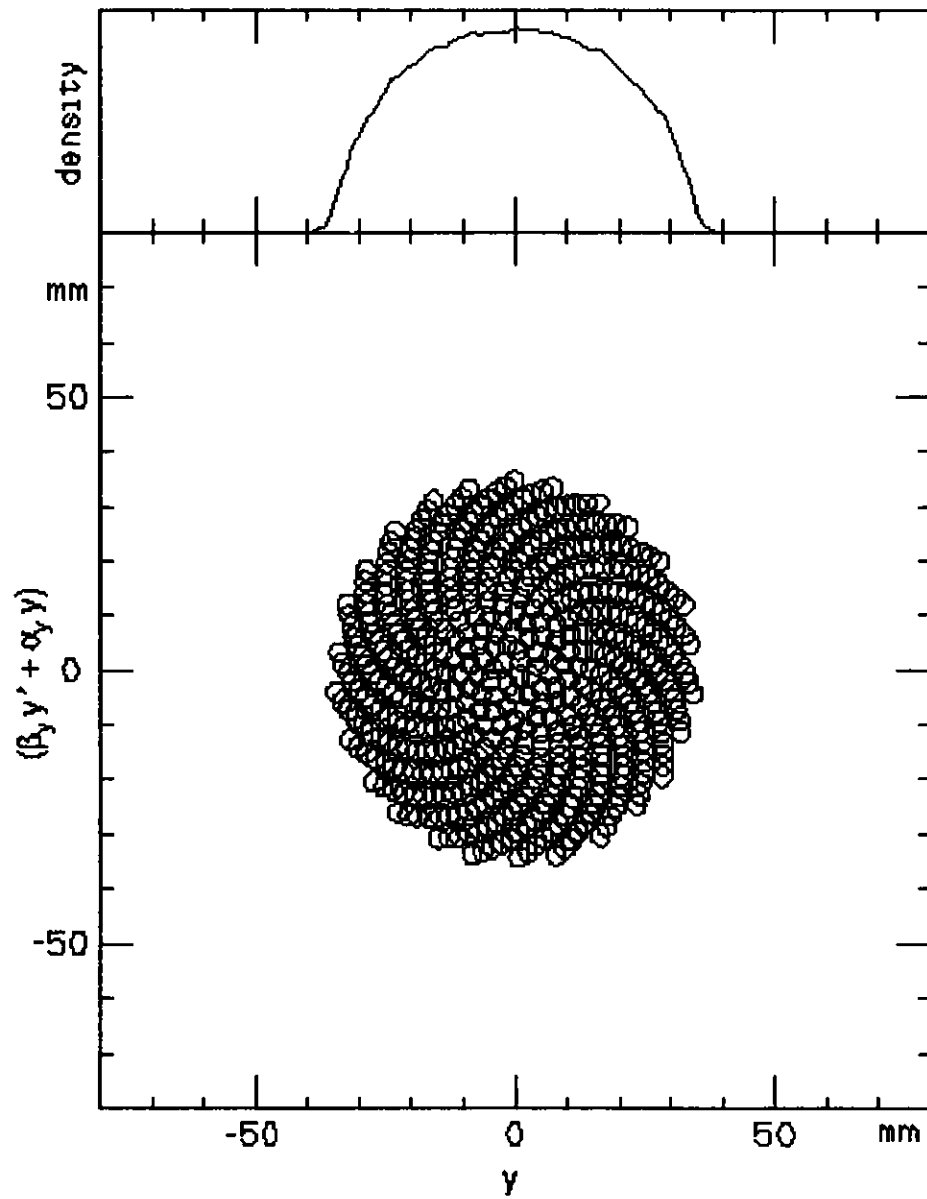
Figure II.2.2-5 Location of the 500 Turns, at the End of Injection, in the Normalized (y, $\beta_y y' + \alpha_y y$)
Vertical Phase Space at the Stripper Location. (Circles are 1-sigma contours of the
incoming linac beam. The vertical density distribution is shown at the top.)
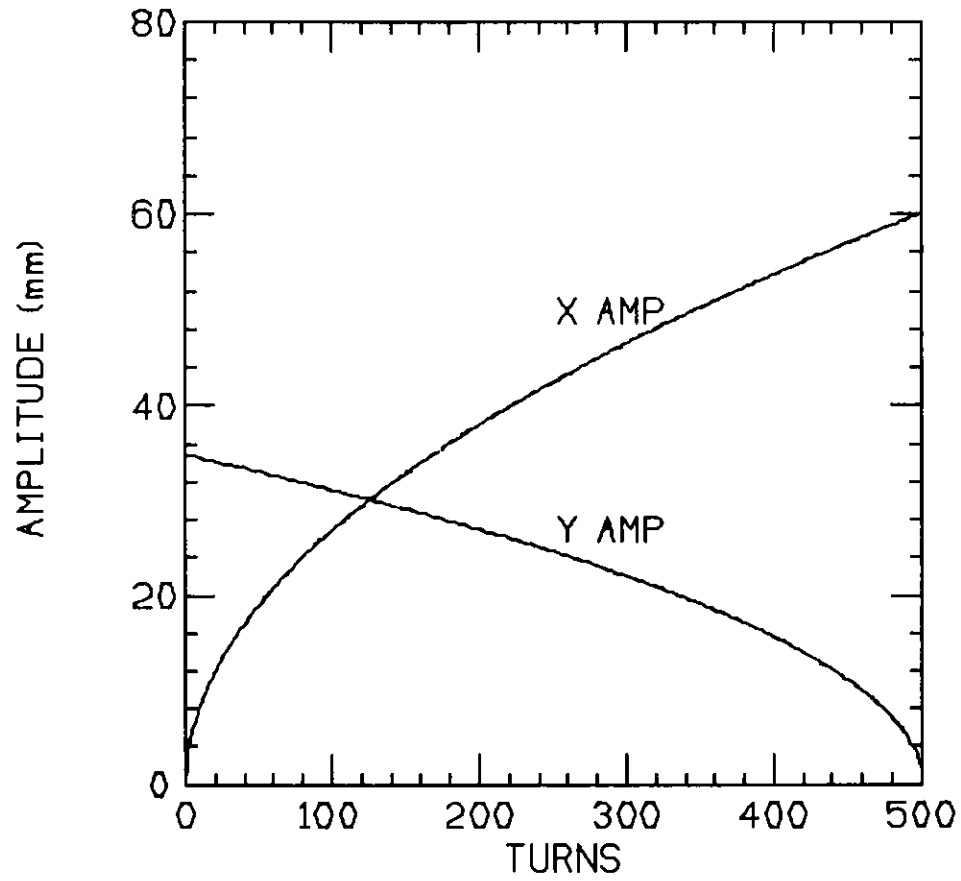
Figure II.2.2-6 Time Dependence of the Injected Horizontal and Vertical Amplitudes.
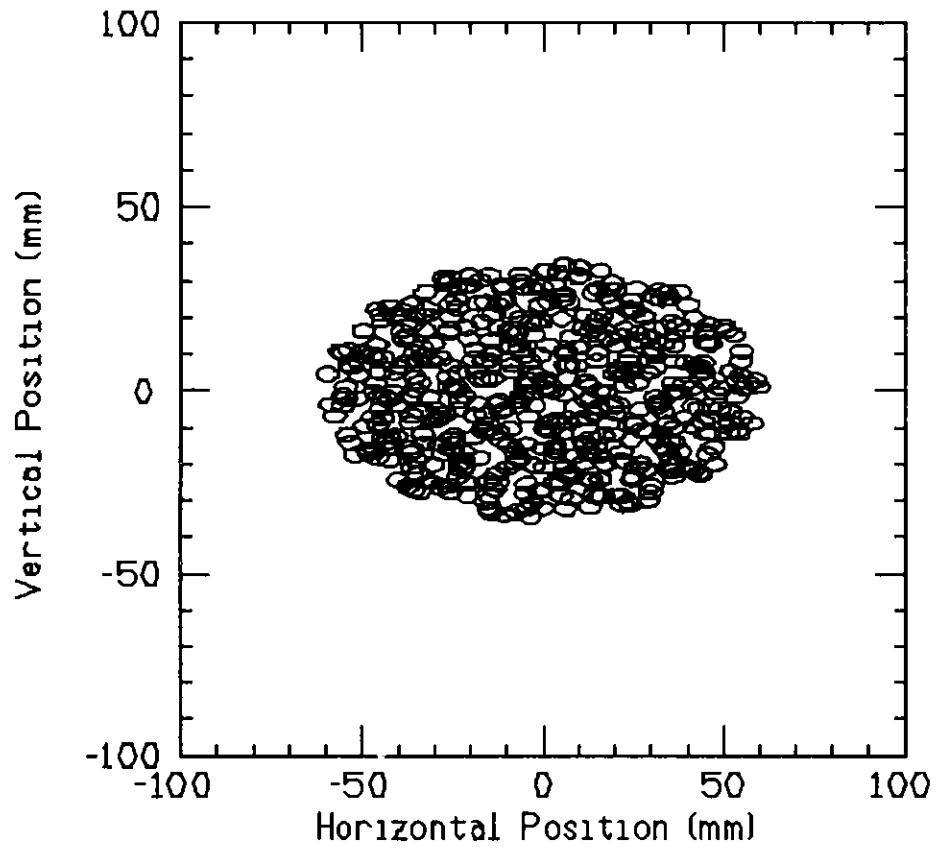
Figure II.2.2-7 Spatial Distribution of the 500 Turns at the End of Injection.

FOIL HEATING K deg
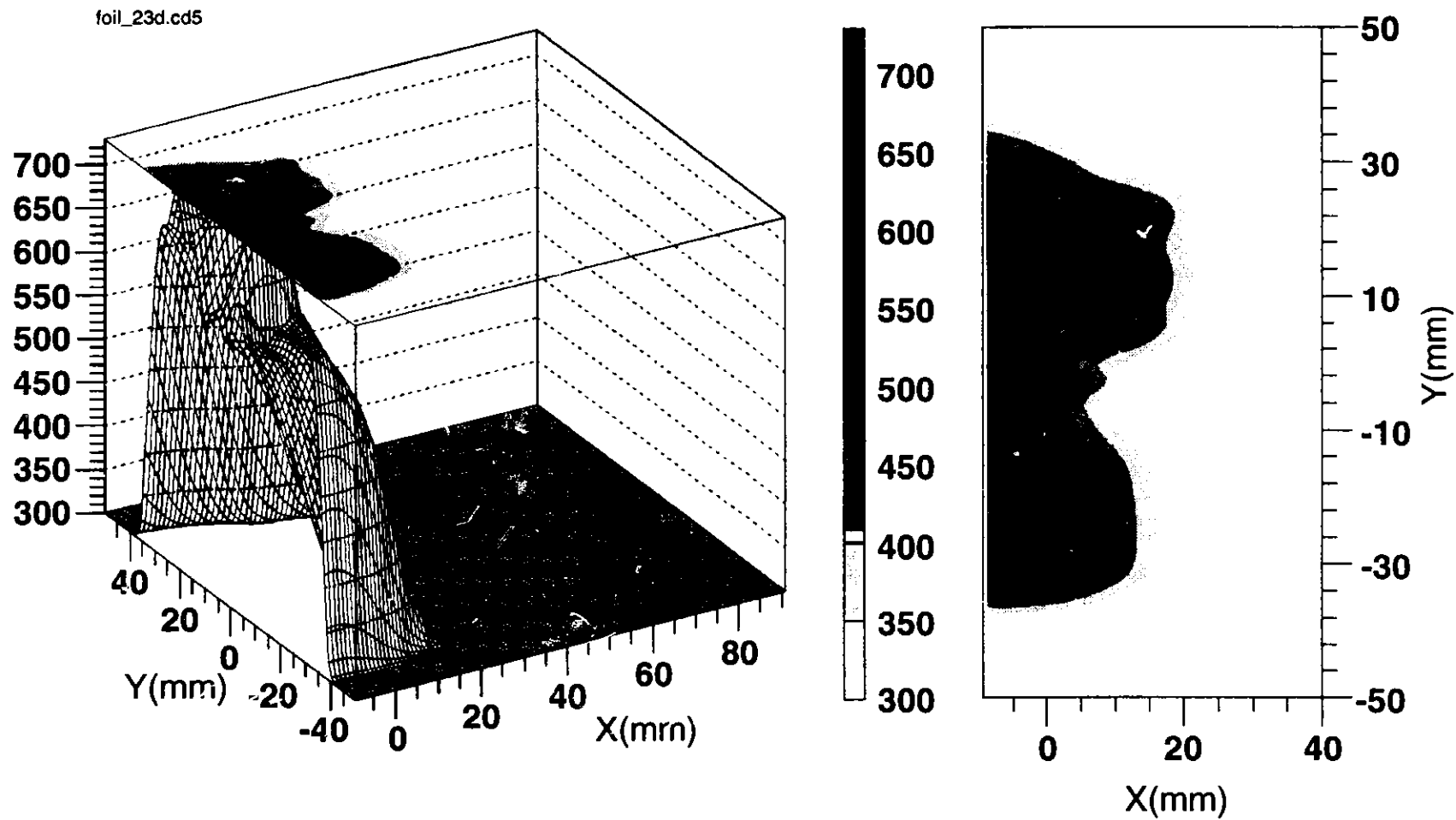
foil_23d.cd5

Figure II.2.2-8 Calculated Equilibrium Temperature Distribution on the Stripping Foil.

2.2.2 H^0 Catcher

With a 250-μg/cm^2 stripper foil, about 0.54% of the 500-μA H$^-$ beam emerges from the foil as partially stripped neutral hydrogen atoms, some of which are in the ground state and some of which are in an excited state. If these particles are allowed to enter a normal bending magnet field, they will become completely stripped and either hit the vacuum chamber wall or, if not lost, form a halo of large betatron oscillations around the normal proton beam. When the injection process and angle are as described in Section II.2.2.1, these neutrals can be collected before they enter strong magnetic fields.

Figure II.2.2-9 shows that the neutrals pass through the center of one quadrupole and enter the next quadrupole at −11 cm, where the field is 0.3 T. This field over a length of 0.5 m is enough to strip all electrons with n ≥5, or about 20% of the H^0 beam.[10] The catcher, therefore, is placed upstream of this quadrupole.
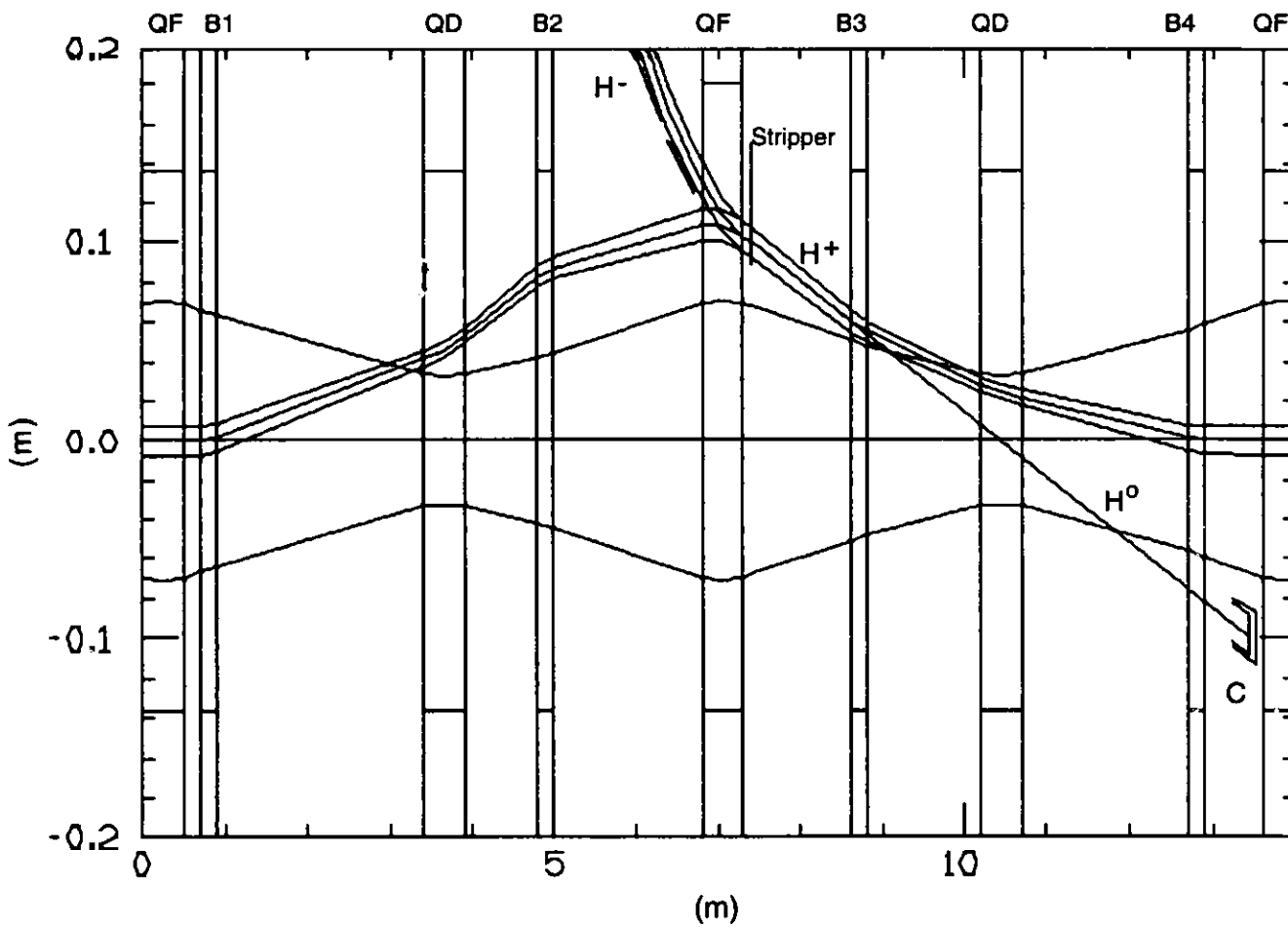
Figure II.2.2-9 Direction of Neutral Particles Created in the Stripper. (Location of the catcher, used to prevent the H^0 from passing through the last quadrupole, is indicated by a C.)

2.3 LOW-ENERGY TRANSFER LINE (LET)

The LET transports the 400-MeV beam from the linac to the RCS and matches the optics between the two accelerators. Figure II.2.3-1 shows the IPNS Upgrade accelerator layout, including the linac and LET line.

It is essential to match the beam optics between the linac and the RCS to obtain the best possible performance. Matching is performed from the downstream end of the RCS focusing quadrupole (F-quad), which combines the trajectories of the H^- and H^+ beams. This RCS F-quad functions as a defocusing quadrupole (D-quad) for the incoming H^- ions because of their opposite polarity.

An advantage of this defocusing action by the RCS quadrupole is that the incoming beam receives an extra kick; therefore, the LET has a large angular separation from the RCS in the interface region between the RCS and the LET. A drawback of having an effective D-quad is that the horizontal β-function is large. The β-function can be reduced by introducing a magnetic field gradient in the injection septum magnet.

The 157.36-m-long LET has three important regions: (1) Region-A is a 72° horizontal bend near the RCS, (2) Region-B is a 3.05 m vertical translation from the linac elevation to the RCS elevation, and (3) Region-C is a 90° horizontal bend near the linac. The β-function matching is performed for each of above three regions sequentially, and the dispersion function is suppressed at the ends of each horizontal bend and the vertical displacement. Figure II.2.3-2 shows the layout of the LET; the three regions are indicated. As the figure shows, the three regions are connected by a string of FODO cells.

The lattice functions of the 72° bend section are shown in Figure II.2.3-3. The first element, QD, shown in the figure is the F-quad of the RCS, which defocuses the H^- beam. The S1 septum has a field gradient of n = –20 to compensate for the defocusing effect of the QD. The maximum value of the dispersion function along this segment of the line is 5 m, and the effect is shown in the envelope functions in Figure II.2.3-4. A momentum-tail scraper and a wire-septum halo catcher can be placed in this region to take advantage of the large dispersion function.

The set of Twiss parameters from Region-A is back-tracked to Region-B by using the FODO cell optics.

Figure II.2.3-5 shows the beam optics in Region-B. The beam elevation change of 3.05 m is accomplished by two bending magnets. The phase advance between two bending magnets is required to be 360° to suppress the dispersion introduced by the dipoles. Also note in the figure that there are five matching quadrupoles preceding Dipole B.
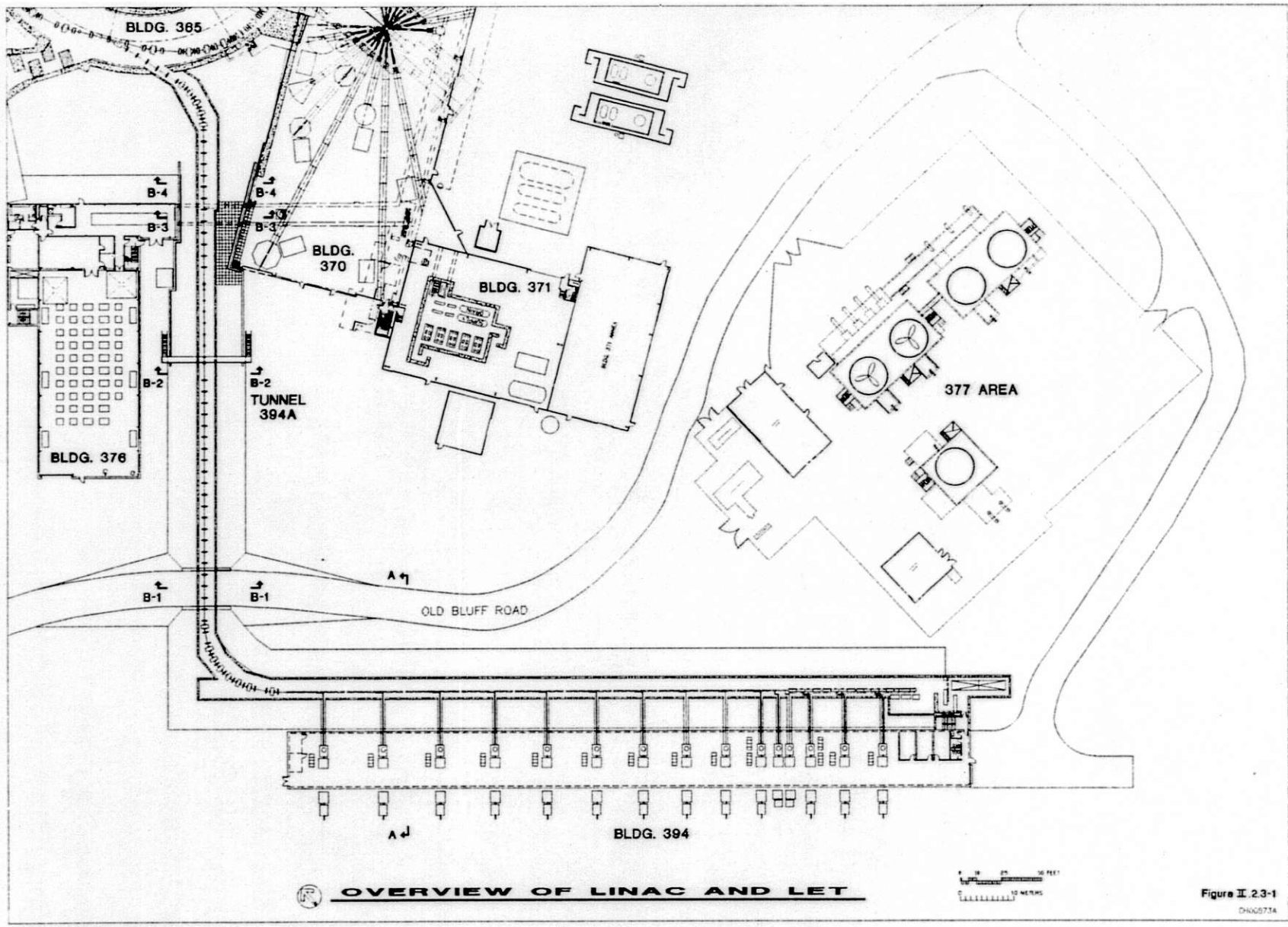
OVERVIEW OF LINAC AND LET

Figure II.2.3-1

BLDG. 365

REGION
A

BLDG. 375

BLDG.
370

BLDG. 371

ELEVATION
CHANGE

REGION
B

BLDG. 376

OLD BLUFF ROAD

REGION
C

LINAC   BLDG. 394

0 10   25   50 FEET

0   10 METERS

**INJECTION
SYSTEM
LINAC AND LET**

CH000894
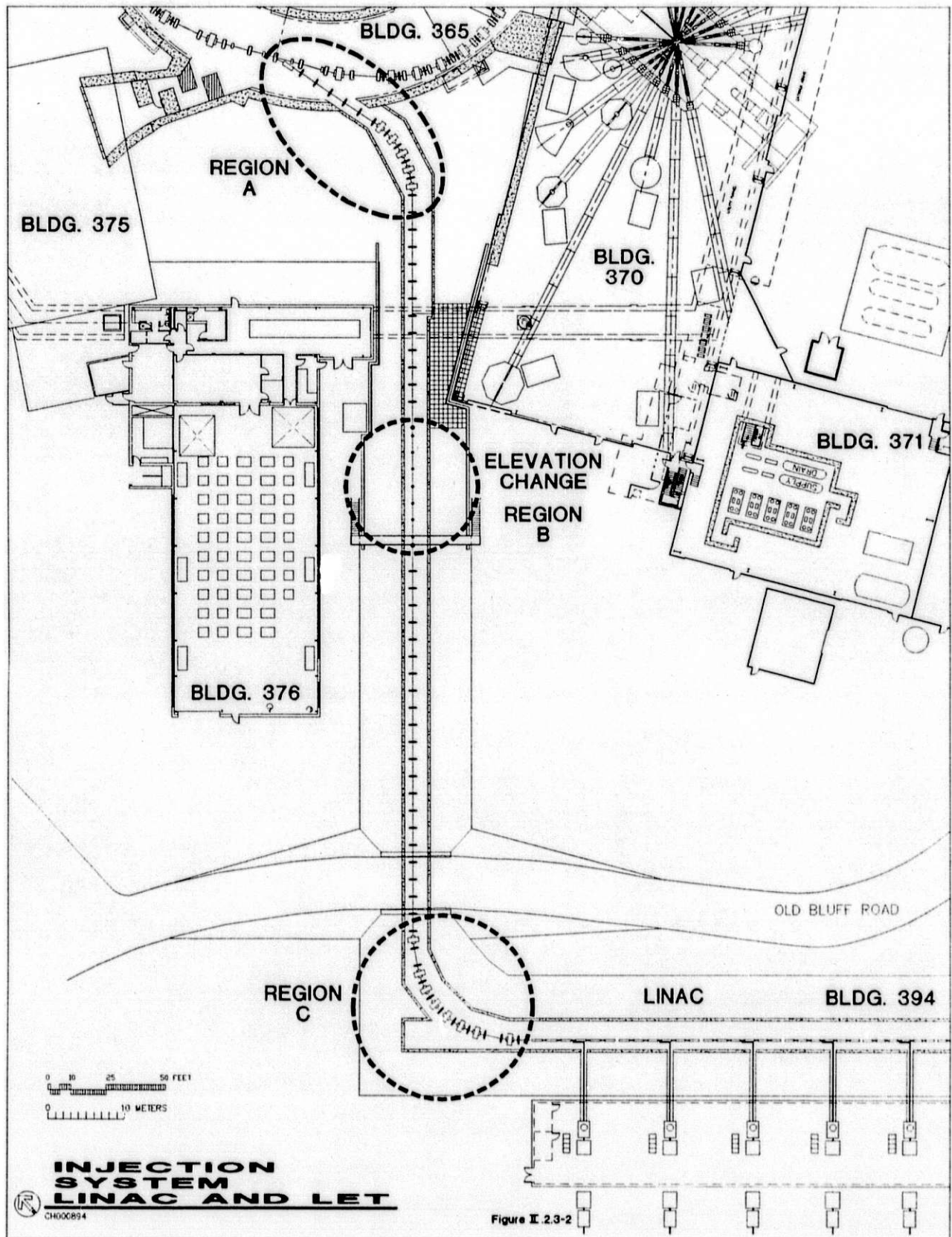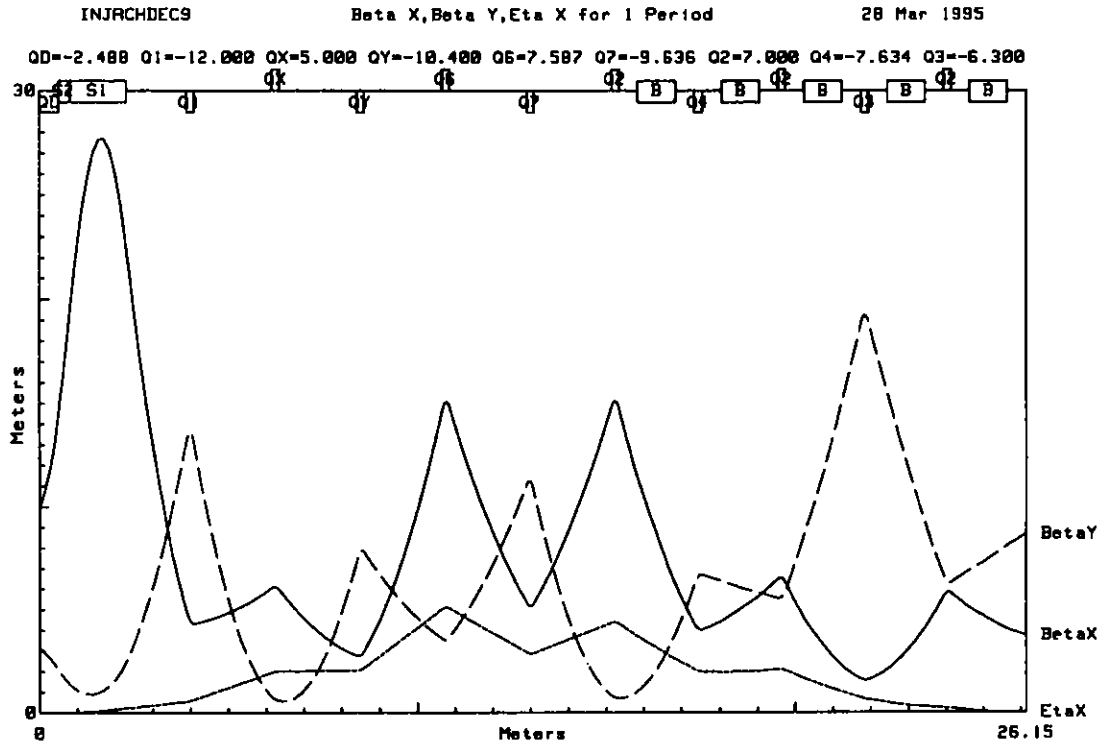
Figure II.2.3-2

Figure II.2.3-3 Lattice Functions for the 72° Bend Section of the LET (Region-A).
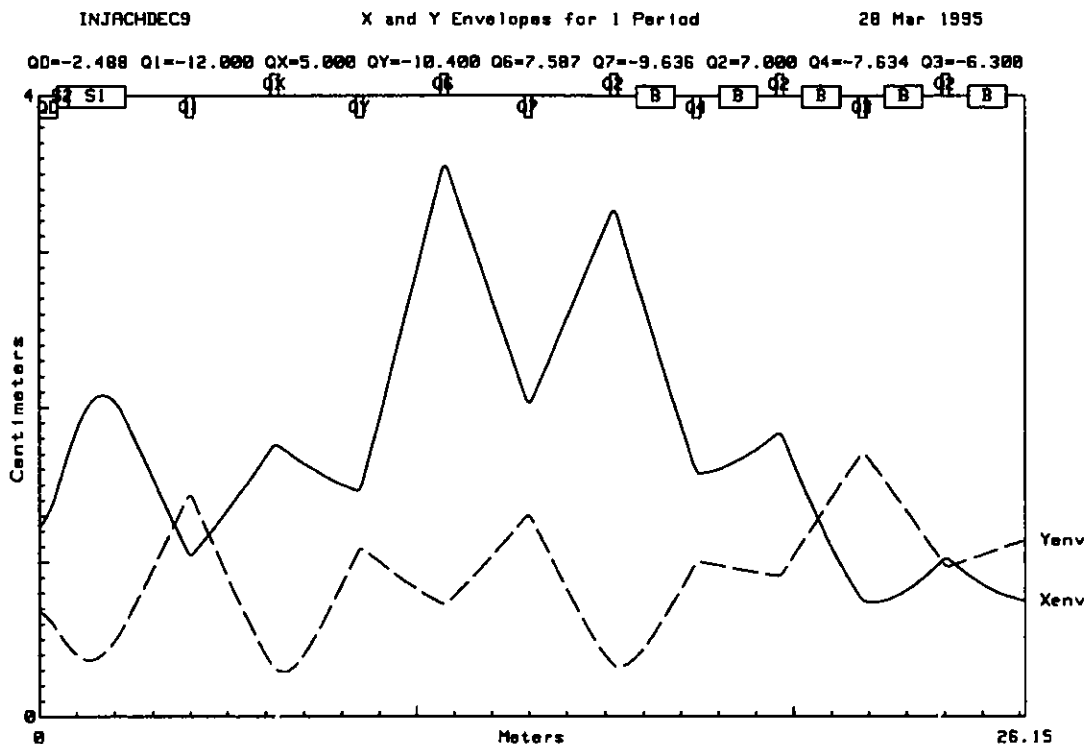
Figure II.2.3–4 Envelope Functions for the 72° Bend Section of the LET (Region-A). (The solid line is the horizontal envelope, and the dashed line is the vertical envelope.)
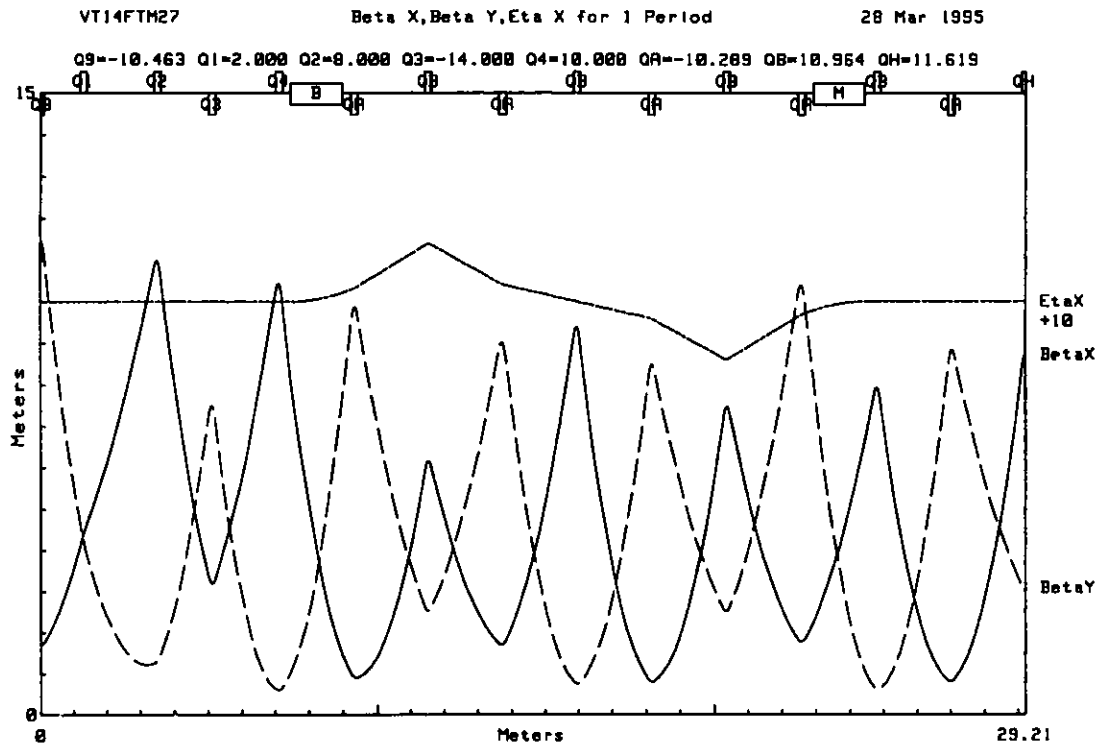
Figure II.2.3-5 Lattice Functions for Region-B. (The η-function is displaced by 10 m for clarity. Note that in this figure, x refers to the vertical direction, and y refers to the horizontal direction.)

A long string of FODO cells between regions B and C facilitates matching between those two regions.

The 90° bend of the linac beam in Region-C is accomplished using five FBDB cells. Each cell has a phase advance of 90°. An achromatic bend is obtained by removing a dipole from the next to the last half-cell at each end, as shown in Figure II.2.3-6. The figure also shows the lattice functions of the bend.

In this section, we have described the optics matching through the LET, particularly the dispersion matching. Matching between the linac and the LET has not yet been performed, but we do not expect any difficulty in the matching.

Figure II.2.3-6 Lattice Functions for Region-C. (The η-function is displaced by 10 m for clarity.)

2.4 BEAM EXTRACTION

Extraction kickers are placed in the dispersion suppressor cell where a dipole is missing, and the extraction septum magnets are placed at 90° phase advance relative to the kickers. The physical layout of the two extraction channels and their HETs is shown in Figure II.2.4-1.

The extraction trajectory, the associated horizontal envelope of the damped beam, and the BSC envelope of the injected beam are shown in Figure II.2.4-2. Since the extracted beam has to pass through an F-quad as shown in the figure, a short septum magnet S1 is placed just upstream of the F-quad magnet to compensate for the inward bending by the quadrupole.

The extraction process starts by moving the 2-GeV beam outward against the edge of the acceptance area inside the F-quad just upstream of the extraction kicker. This is done with a closed orbit bump around each extraction point. The horizontal displacement of this bump from the central orbit is 43.8 mm. This closed-orbit bump was introduced to reduce the required kicker strength. The kicker produces an integrated bend of 14 mrad. This places the beam at a radial position of 134 mm from the central orbit at the first septum. The beam then passes through an F-quad in the RCS lattice and enters the last two septa. The three septum magnets produce an integrated bend of 22.4°. This bend places the inside edge of the beam at a radial distance of 690 mm from the central orbit adjacent to the leading edge of the downstream quadrupole in the RCS lattice. This allows the beam to clear the quadrupole magnet that has a half-width of 664 mm.

The extraction kicker system is segmented into 3 independently powered kicker sections assembled around a shared ceramic vacuum chamber. This segmentation is used to reduce the impedance of each kicker to a manageable level. The aperture of each section is designed to accommodate the BSC of the injected beam and allows space for passage of the extracted beam. The field strength, effective length, and aperture dimensions were derived for each section through an iterative process while taking into account peak-current and voltage limits.

The required parameters for the three kicker sections and septum magnets are listed in Table II.2.4-1. A detailed description of the kicker magnets is given in Section II.3.4, and the septum magnets are described in Section II.3.5.

MOVABLE SHIELDING SYSTEM
ON TRAIN RAILS

Kicker

Septa

HET

Bldg 369

Building 365

Kicker

Septa

Bldg 370

BLDG. 361

HET

0 10 25 50 FEET

0 10 METERS

BLDG. 375

EXTRACTION SYSTEMS
AND HET LINES

Figure II.2.4-1

CH000884
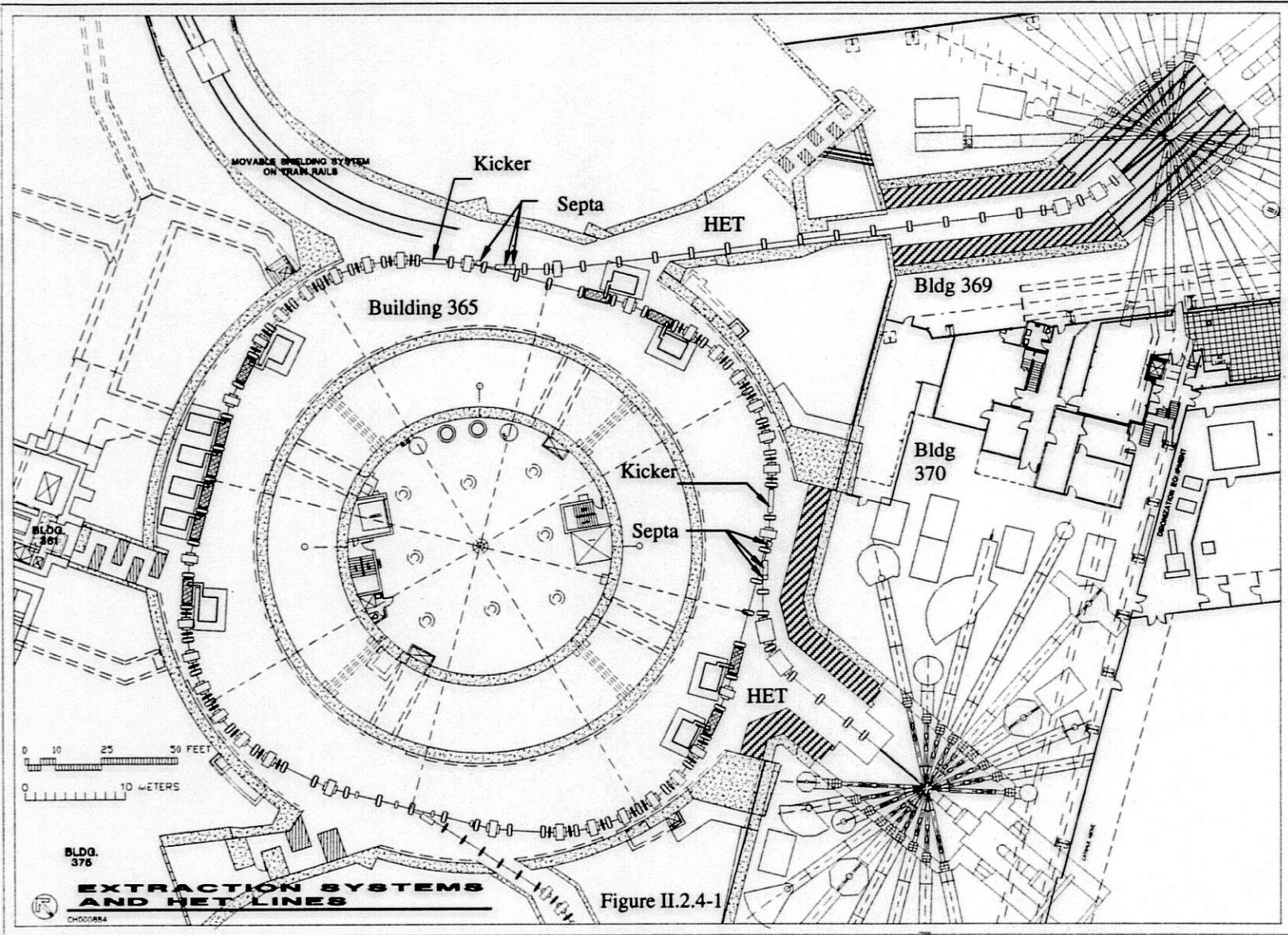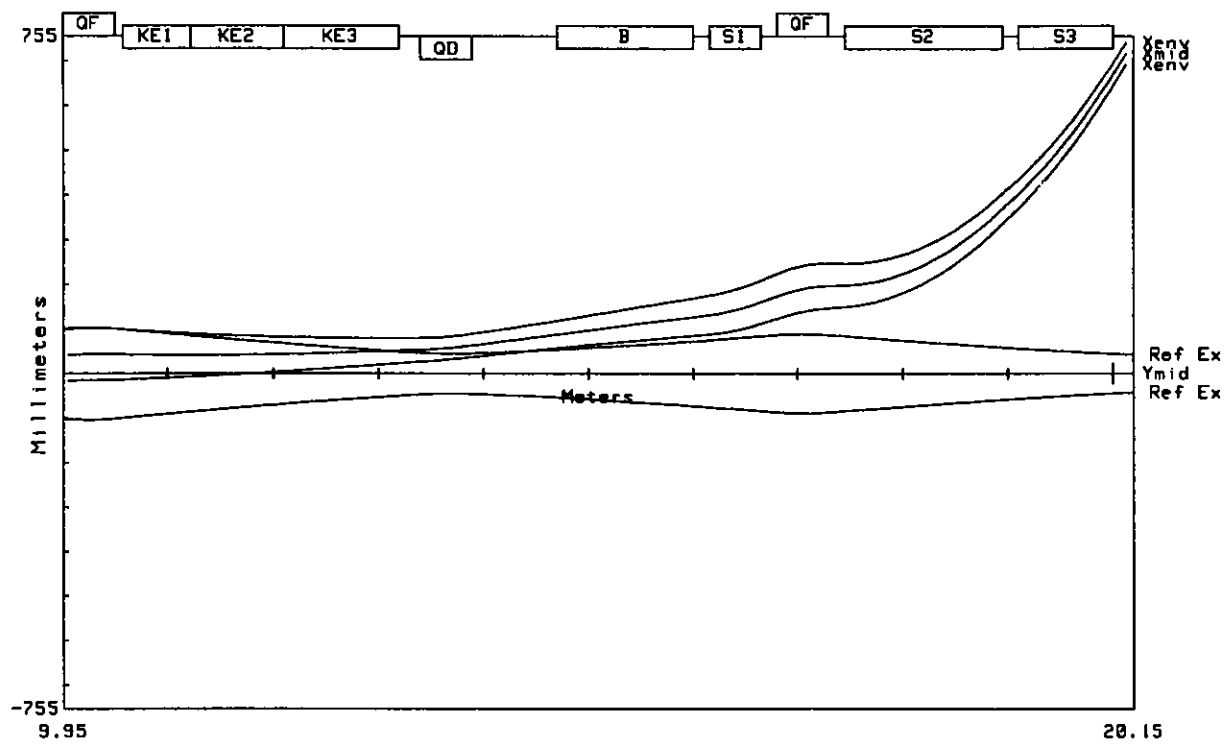
Figure II.2.4-2 Extraction Trajectory from the Kicker through the Septum Magnet.
(The horizontal envelopes of the injected and extracted beam are shown.)

Table II.2.4-1 Extraction Kicker and Septum Magnet Parameters

Magnet Type	Bend Angle (mrad)	Effective Length (m)	Strength @ 2-GeV (T)	Aperture Height (mm)	Aperture Width (mm)	Septum Thickness[a] (mm)
Kicker A	4.37	0.65	0.0618	107.4	195	-
Kicker B	4.79	0.87	0.0512	134.2	170	-
Kicker C	4.84	1.105	0.0408	175	145	-
Septum C	55.1	0.5	1.02	70	122	13
Septum D	210	1.5	1.3	84	97	66
Septum E	126	0.9	1.3	103	65	309

[a] Septum thickness in Table II.2.4-1 is the allowable minimum thickness of the septum.

2.5 HIGH-ENERGY TRANSFER LINE (HET)

Two HET lines transport the beam to the 10-Hz Target in Building 369 and to the 30-Hz Target in Building 370. These HET lines are shown in Figure II.2.4-1. Both HET lines have 45° bends near the targets in order to prevent backstreaming neutrons from irradiating the transport enclosures. Bending of the beam near the targets makes dispersion suppression difficult, and it is not planned.

The beam envelope functions for the both HET lines are shown in Figures II.2.5-1 and II.2.5-2. To achieve the required 5-cm-radius beam size at the target containing 100% of the beam, the quadrupoles near the targets must have large apertures and must be made of radiation-hard materials.
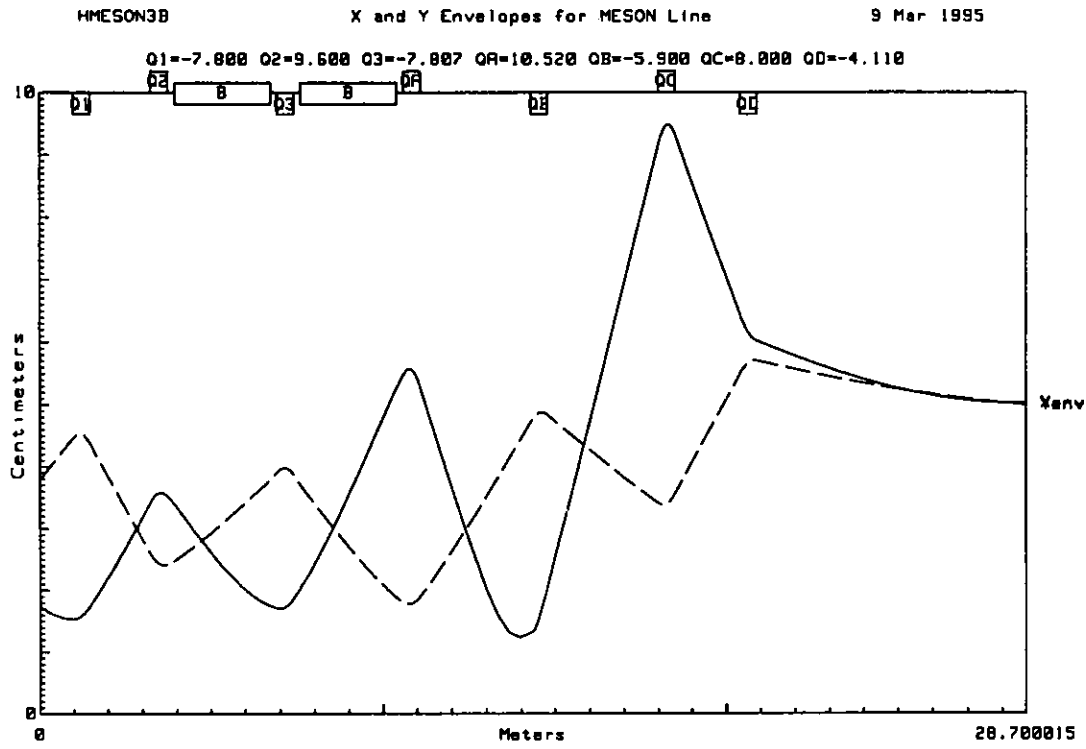
Figure II.2.5-1 Beam Envelope for the 30-Hz Target HET Line.

EPB1A   X and Y Envelopes for EPB1 Line   15 Mar 1995

Q1=-7.800 Q2=9.800 Q3=-7.500 QH=8.823 QD=-8.200 QF=7.623 Q4=-7.300 Q5=10.200 Q6=-5.820 Q7=4.000
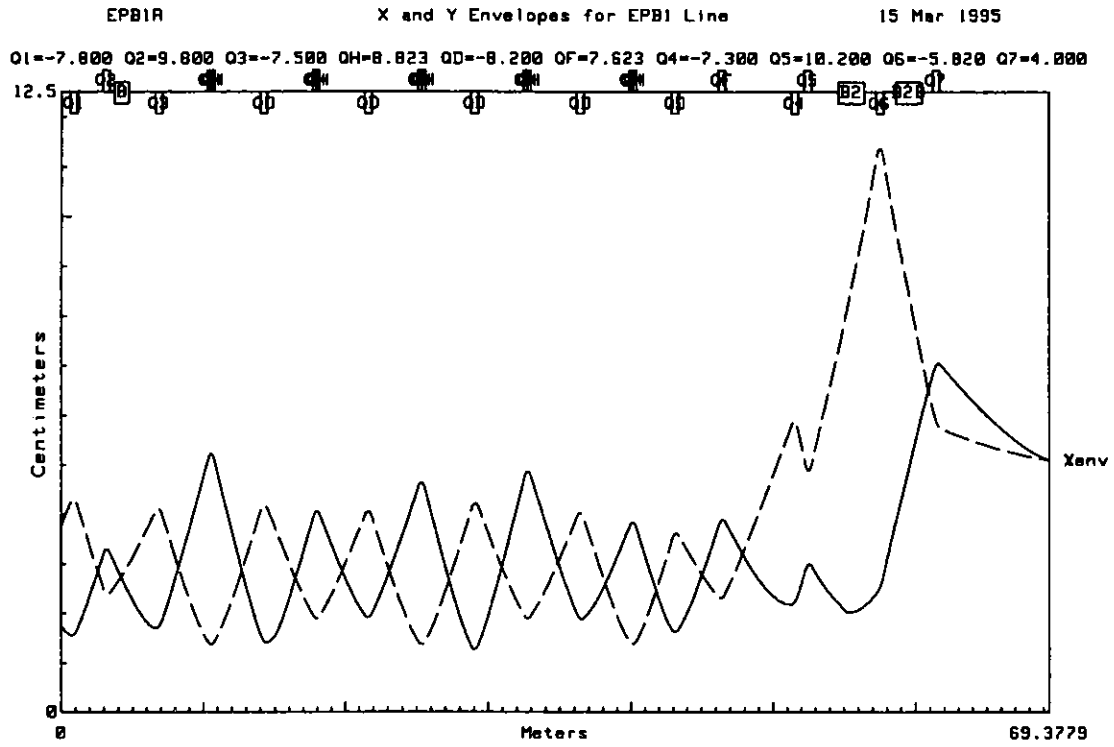
Figure II.2.5-2 Beam Envelope for the 10-Hz Target HET Line.

2.6 REFERENCES

1.   *Report of the ISIS Project Group*, Rutherford Laboratory (November 1986).

2.   A. Hofmann and F. Pederson, "Bunches with local elliptic energy distributions," IEEE Trans. Nucl. Sci. **NS-26** (3), 3526 (1979).

3.   I.M. Kapchinskij and V.V. Vladimirskij, "Limitations of Proton Beam Current in a Strong Focusing Linear Accelerator Associated with the Beam Space Charge, " in *Proceedings of the CERN Symposium on High Energy Accelerators* (1959).

4.   T. Suzuki, "Synchro-betatron resonances driven by dispersion in Rf cavities," in *Particle Accelerators* Vol. 18 (1985).

5.   K.C. Harkay, *Study of Synchro-betatron Coupling in the IPNS-II RCS*, Argonne National Laboratory Report No. NSA-95-3 (March 1995).

6.   H. Grote and F.C. Iselin, *The MAD Program, User's Reference Manual*, CERN Report No. CERN/SL/90-13 (AP), Rev. 4 (1994).

7.   H. Friedsam, "A New Accelerator Alignment Concept Using Laser Trackers," in *Proceedings of the European Particle Conference* 3, 2570-2572 (1994).

8.   B. Autin and Y. Marti, *Closed Orbit Correction of Alternating Gradient Machines Using a Small Number of Magnets*, CERN Report No. CERN/ISR-MA/73-17 (1973).

9.   A. Wrulich, *RACETRACK: A Computer Code for the Simulation of Nonlinear Particle Motion in Accelerators*, Report No. DESY 84-026 (1984).

10. Y.C. Chae, *Study of Field Ionization in H^- Charge Exchange Injection*, Argonne National Laboratory Report No. NSA-94-2 (April 1994).

3.1 SYNCHROTRON MAGNETS

The synchrotron ring lattice contains 128 main magnets consisting of 32 dipoles, 56 quadrupoles, and 40 sextupoles. An additional 56 correction magnets will serve to adjust the dipole field. The primary design features of the ring magnets are described in this section. The required field strengths and aperture dimensions for the ring magnets are listed in Table II.3.1-1.

All magnets are designed for a nominal beam energy of 2.0 GeV but are capable of handling a maximum value of 2.2 GeV. Two-dimensional static magnetic field calculations at 2.2 GeV were made with OPERA-2d[1] for the main magnets. Results of these calculations enable core saturation and the associated low magnetic efficiencies to be avoided. They also indicate that the higher harmonic coefficients of the fields can be reduced to appropriate levels. The design goal of the relative harmonic coefficients was 6.0×10^{-4} for points within the calculated beam envelopes previously defined in Section II.2.1.3. Detailed magnetic calculations were performed at 2.2 GeV, but magnetic field parameters were also studied as a function of magnetic field at lower values. The results satisfy design goals throughout the entire operating range of the machine. Eddy current effects are not expected to change the magnetic fields significantly.

Two-dimensional calculations do not take end-effects into account. Appropriate end-shapes and shims, similar to those successfully used at the Advanced Photon Source (APS),[2] are used here to reduce field imperfections introduced by the ends to acceptable levels.

The major engineering parameters for each of the synchrotron ring magnets were determined with the program MADEST[3] and are summarized in Table II.3.1-2. Dipoles, quadrupoles, sextupoles, and correction magnets are described in detail in the following sections, and design features common to all are described below.

The cores are parallel stacks of low-silicon steel laminations. The alloy, M45, is used because of its high saturation field values. The thickness of the laminations is 0.36 mm, which is commonly used in 60-Hz applications. This thickness is appropriate because the excitation frequency during the reset of the main fields is 60 Hz. The cores consist of two or three sections, depending on the magnet type, to allow assembly of the magnets around the ceramic vacuum chamber. Both ends of each section have bonded end-packs. These packs contain the special contouring required to control the field shapes at the ends. Each core section is held under compression by welded parts on the exterior surfaces and by insulated tie-rods that extend through the core. The pole taper-angles were selected to keep the calculated flux densities on the pole axes to less than 2.0 T at 2.2 GeV. Similarly, the yoke thicknesses result in average flux densities between 1.0 and 1.2 T. Keeping the flux density values low helps to control the core losses. Similar techniques were used in the cores of the storage ring magnets for the APS.[4]

The coils for the three main magnet types are made with hollow copper conductor. Estimates of the power losses due to the eddy currents in the coils were derived with the aid of OPERA-2d, and the results are included in the calculated power losses for each magnet. The insulation for each coil consists of polyimide film, fiberglass tape, mica tape, and

Table II.3.1-1 Synchrotron Ring Magnet Field Strengths and Aperture Requirements

Type of Magnet	Number Required	L_{eff} (m)	Strength at 2.0 GeV		Full Bore Dimension (mm)		
					Height	Width	Diameter
Dipole	32	1.3	1.40	T	182.0	450	-[a]
F-Quadrupole	28	0.5	7.73	T/m	-	-	237
D-Quadrupole	28	0.5	6.77	T/m	-	-	237
Sextupole	40	0.2	52	T/m^2	-	-	260
Corrector	56	0.15	0.070	T	300	300	-

[a] - = not applicable.

Table II.3.1-2 2.0-GeV Parameters for the Synchrotron Ring Magnets

Parameters	Dipoles	Quadrupoles	Sextupoles	Correctors	Units
Number required	32	56	40	56	-
Peak strength	1.40 T	7.73 T/m	52 T/m^2	0.070 T	-
Effective length	1.3	0.50	0.20	0.15	m
Gap height or diameter	182	237	260	300	mm
Bending radius	6.62				m
Magnet mass	21,200	3,607	550	460	kg
Coils per pole	1	1	1	1	-
Conductor					
Height	8.9	8.9	7.3	5.8	mm
Width	8.9	8.9	7.3	5.8	mm
Hole diameter	4.9	5.3	4.1	3.2	mm
Number of turns per pole	12	24	32	140	-
Number of parallel conductors	48	4	2	1	-
Inductance	2.8	10.0	16	3.6	mH
Resistance	0.66	12.4	28	243	mΩ
Time constant	4,242	806	571	15	msec
Supply current					
dc	5,733	1,267	498[a]	136[a]	A
ac peak	2,806	620	171[b]	0[b]	A
rms[c]	6,067	1,341	354	66	A
rms[c] current density in coil	1.0	3.0	2.5	1.4	A/mm^2
Peak voltage[d]	13,448	11,064	1,100	111	V
Power losses	47.9	24.7	3.8	1.1	kW
Cooling circuits/magnet	48	8	6	4	-
Total water flow	20.8	5.2	2.6	0.6	gal/min
Water pressure drop	100	100	100	100	psi
Water temperature rise	9	18	5	7	°C

[a] Maximum arbitrary function value.

[b] Minimum arbitrary function value.

[c] rms = root mean square.

[d] See Section II.3.2.

vacuum-impregnated, heat-cured epoxy. Although the insulating materials are radiation resistant, the potential of the coils to be exposed to radiation is further reduced by placing the coils well away from the midplanes. Parallel electrical paths are used for the coils in the dipoles, quadrupoles, and sextupoles. This procedure keeps the peak voltages across a series-connected group of magnets at manageable levels. The parallel circuits extend around pairs of poles to equalize the impedances of all paths for a given magnet.

The cooling water for the coils is provided by a deionized water system able to supply water at a temperature of 32°C and pressure drop or gradient of at least 100 psi across the magnets. The maximum temperature rise in the water is in the quadrupole magnets and is less than 18°C at 2.0 GeV. It is still less than 22°C at 2.2 GeV.

3.1.1 Synchrotron Dipole Magnets

An end view of the dipole, which is assembled from two halves, is shown in Figure II.3.1-1. The ceramic vacuum chamber is also shown for reference. There is at least a 3-mm clearance between the chamber and each of the poles.

The dipole magnet is curved with a radius of 6.62 m to minimize the inductance. The pole width is 1.5-gap-heights wider than the maximum beam envelope. The pole sides are tapered out by another 0.25 gap height on each side to reduce the saturation of the pole-root. The core has parallel ends, which results in a small edge-focusing effect but makes the magnet easy to construct. The curvature is formed by forcing the laminations against an appropriately curved surface in the stacking fixture. There are steel plates against the four long outside surfaces, which are welded to each other and to the laminations. These weldments stabilize the curvature and maintain the core compression. The coil on each pole consists of 24 layers, with 24 turns per layer.

The calculated deviation from uniformity of the static dipole field, $|\Delta B/B_0|$, is less than 5×10^{-4} within the calculated beam envelope at injection for energies between 400 MeV and 2.2 GeV. Contours of the field uniformity at injection, along with the calculated beam envelope, are shown in Figure II.3.1-2.

3.1.2 Synchrotron Quadrupole Magnets

All ring quadrupoles have the same design and are assembled from two halves. An end view of the quadrupole is shown in Figure II.3.1-3. The ceramic vacuum chamber is also shown for reference. There is a 5-mm clearance between the chamber and each of the poles. The taper-angle of the pole reduces saturation, resulting in a calculated magnetic efficiency of 95% at 2.2 GeV. The coils have a diamond cross section to allow the parallel connections and to enable installation of the coils onto the poles of a half-core. This shape also allows the coils to be
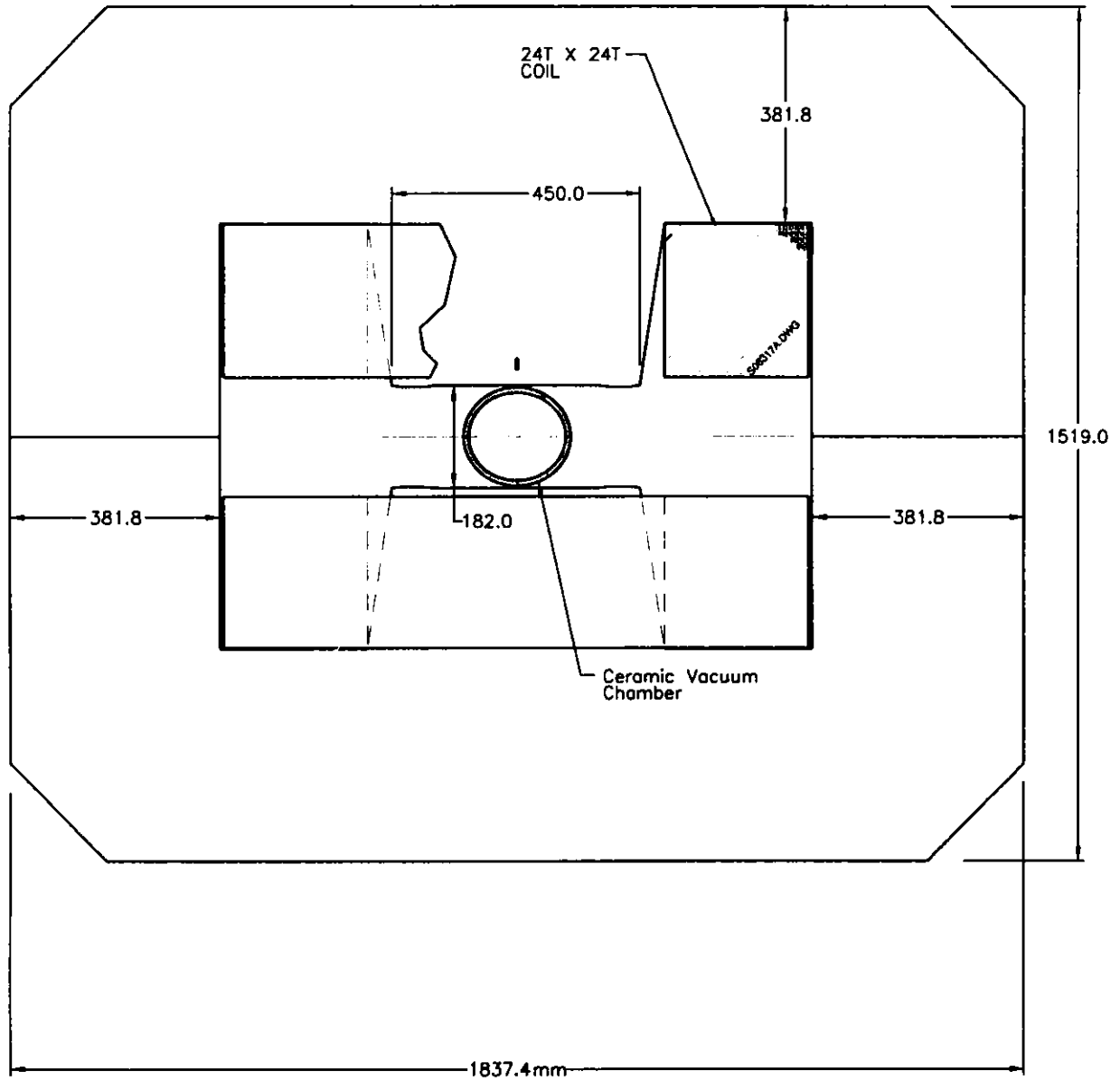
Figure II.3.1-1 End View of the Synchrotron Dipole Magnet.

UNITS

Length	: CM
Flux density	: TESL
Field strength	: OERS
Potential	: WBM
Conductivity	: SCM
Source density	: AMM2
Power	: WATT
Force	: NEWT
Energy	: JOUL
Mass	: KG

PROBLEM DATA
dip22ac.st
Quadratic elements
XY symmetry
Vector potential
Magnetic fields
Static solution
Scale factor = 0.31
  1758 elements
  3589 nodes
    12 regions

VF_DIPL3.dwg

7/Mar/95 12:49:37 Page 21

OPERA-2d
Pre and Post-Processor 1.4

Homogeneity of BY w.r.t. value 0.468689 at (0.0,0.0)
Minimum: -0.001, Maximum: 0.001, Interval: 0.0001

Figure II.3.1-2 Contours of Uniformity at Injection for Synchrotron Dipole along with the Calculated Beam Envelope. (Contour spacing is 0.01% and contour #11 is 0%.)
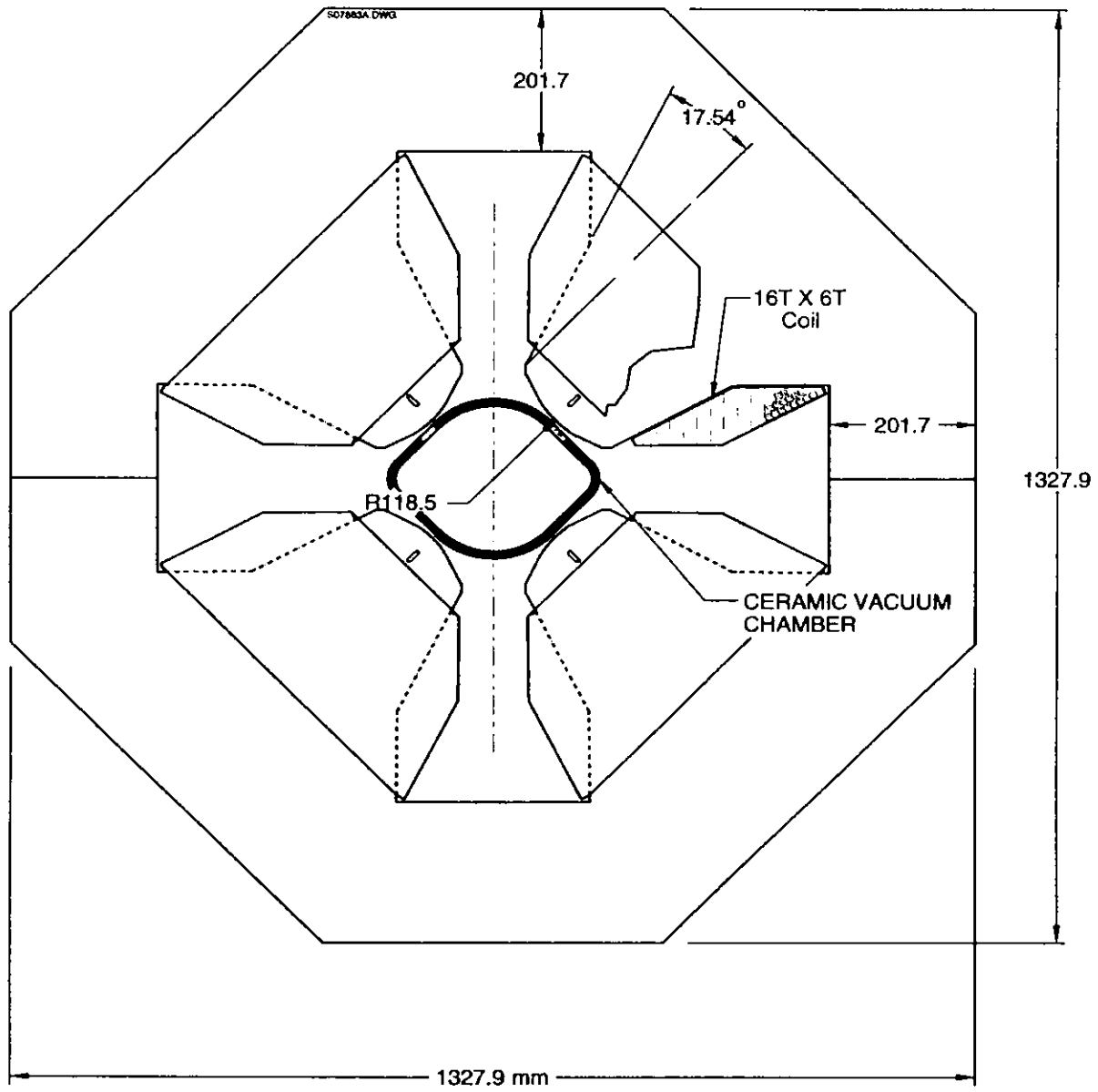
Figure II.3.1-3 End View of the Synchrotron Quadrupole Magnet.

mounted closely to the pole faces and to be well away from the midplanes. The coil on each pole consists of six layers, with 16 turns per layer.

The calculated deviation from uniformity of the quadrupole field gradient, $|\Delta B'/B_0'|$, is less than 3×10^{-4} within the calculated beam envelope for energies between 400 MeV and 2.2 GeV. Contours of the field uniformity at injection, along with the calculated beam envelope, are shown in Figure II.3.1-4.

3.1.3 Synchrotron Sextupole Magnets

All ring sextupoles have the same design and are assembled from three identical sections, each of which contains two poles. The magnetic field values are low enough to avoid core saturation. The sextupole bore diameter is slightly larger than that of the quadrupole. The same ceramic vacuum chamber is used in both magnets, and the extra space is required to accommodate the sloping sides of the chamber.

An end view of the sextupole is shown in Figure II.3.1-5. The ceramic vacuum chamber is also shown for reference. There is at least a 5-mm clearance between the chamber and each of the poles. The coil size shown allows the coils to be inserted between the two poles of each core section. The coil on each pole consists of four layers, with 16 turns per layer.

The calculated deviation from uniformity of the second derivative of the sextupole field, $|\Delta B''/B_0''|$, for the geometry shown is less than 7.0×10^{-3} within the calculated beam envelope for energies between 400 MeV and 2.2 GeV.

3.1.4 Synchrotron Correction Magnets

A horizontal correction dipole is located near each focusing quadrupole, and a vertical correction dipole is located near each defocusing quadrupole. These magnets have C-cores, which are manufactured from one-piece laminations of low-silicon electrical steel that are 0.36-mm thick. The core is bonded by a preapplied, B-staged epoxy coating on the laminations, which also serves as the electrical insulation between laminations. A single design provides both horizontal and vertical corrections, depending on the orientation of the magnet. These magnets can be installed over the vacuum chamber without being disassembled. The coils are made with hollow copper conductor and are insulated with the same materials as the main magnets. The coil on each pole consists of 10 layers, with 14 turns per layer. An end view of a vertical corrector and its vacuum chamber is shown in Figure II.3.1-6. The associated parameters are listed in Table II.3.1-2.
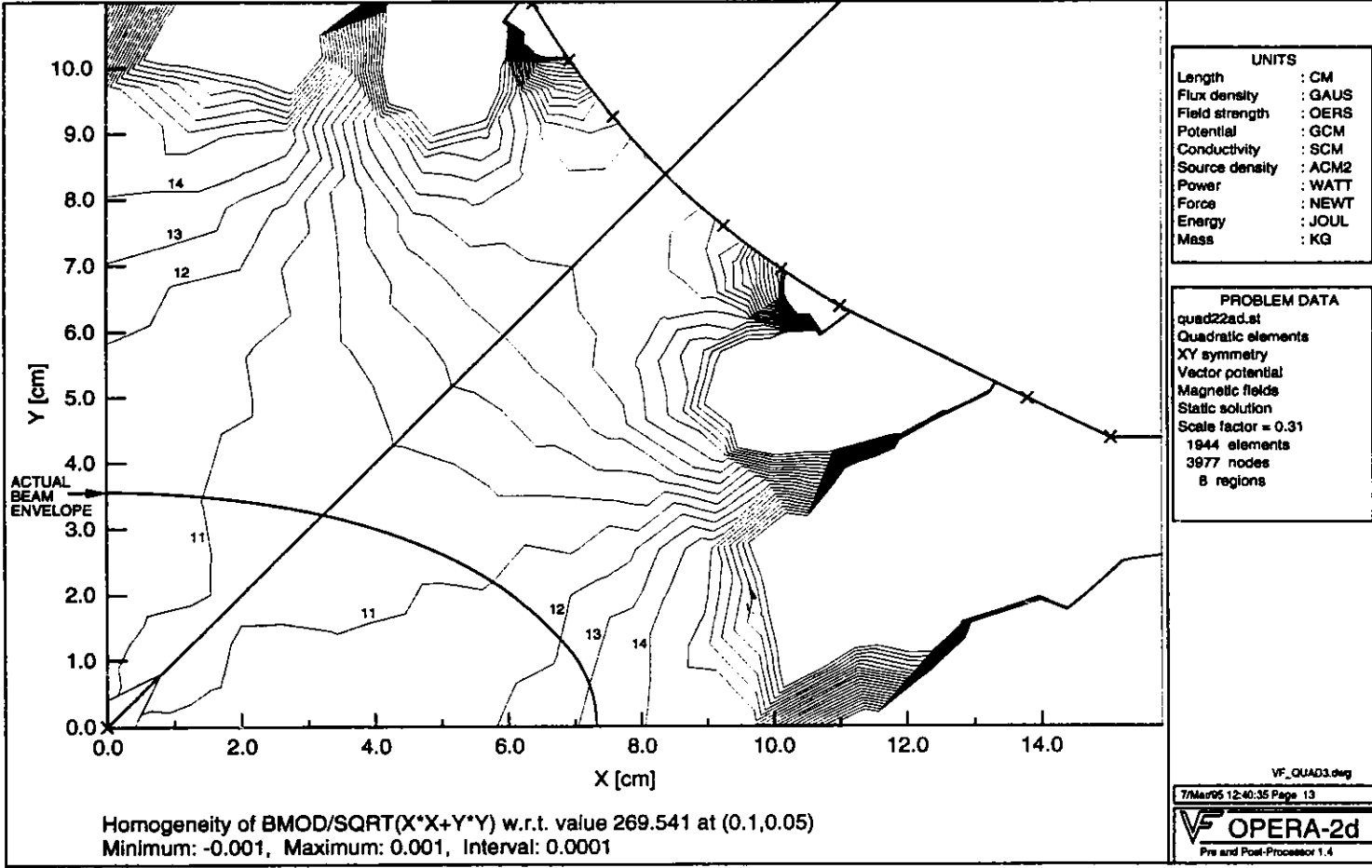
Figure II.3.1-4 Contours of Field Gradient Uniformity at Injection for an F-Quadrupole, along with the Calculated Beam Envelope. (Contour spacing is 0.01%, and contour #11 is 0%.)
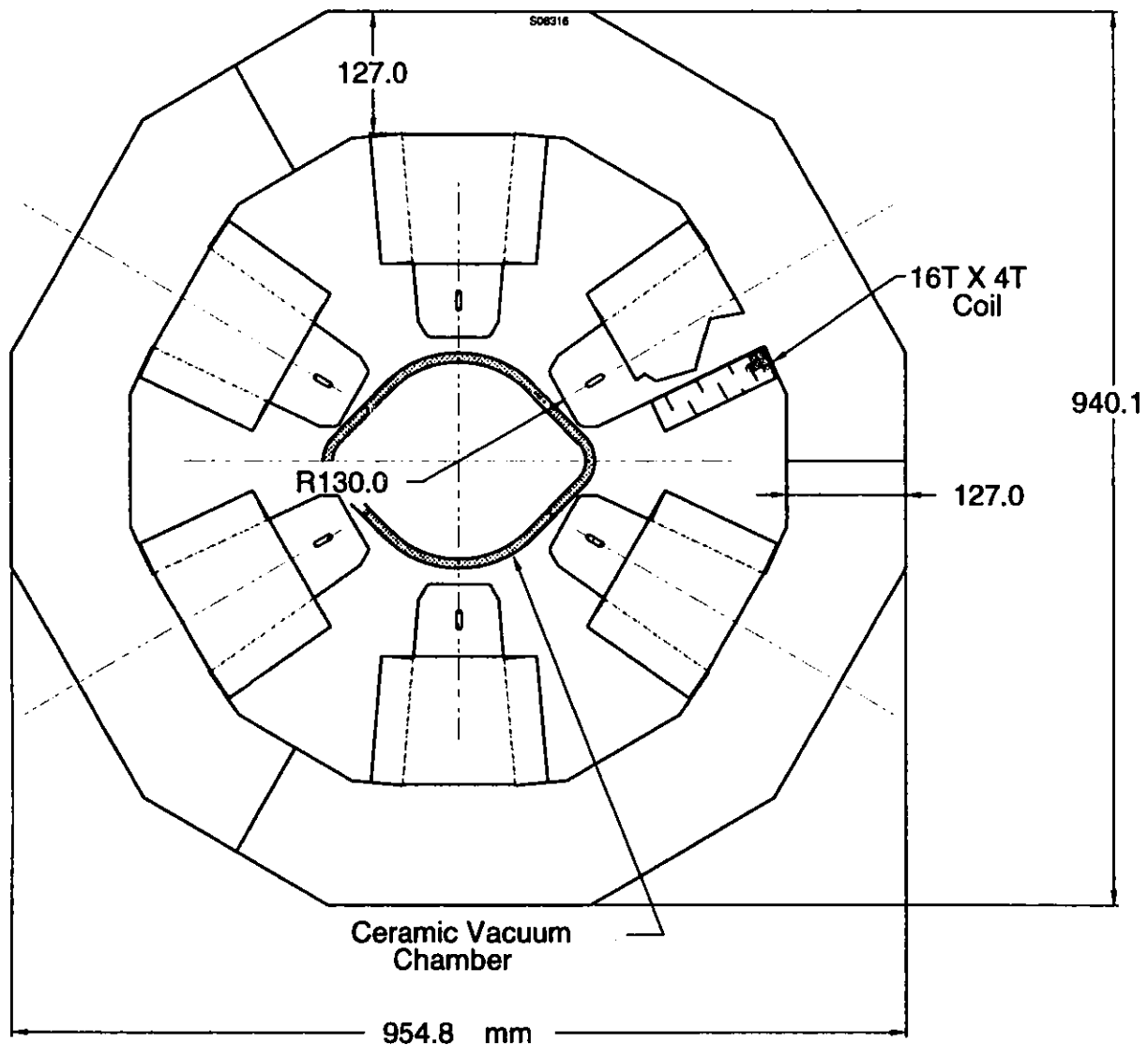
Figure II.3.1-5 End View of the Synchrotron Sextupole Magnet.
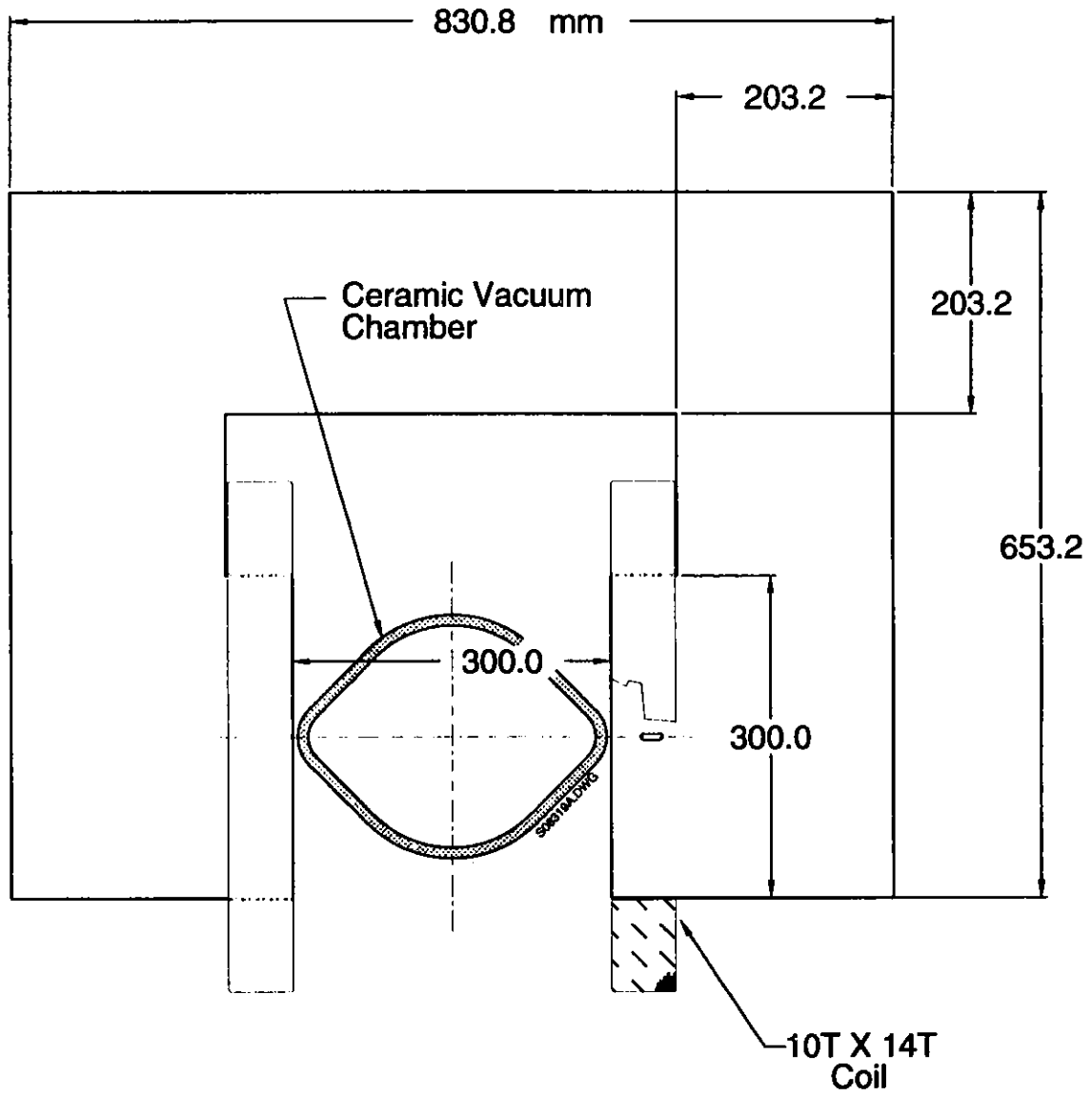
Figure II.3.1-6 End View of the Synchrotron Vertical Correction Dipole Magnet.

3.2 SYNCHROTRON MAGNET POWER SUPPLIES

3.2.1 Introduction

3.2.1.1 Power Supply Description

The synchrotron has a repetition rate of 30 Hz. A stability of ±100 ppm for the main bending and focusing magnet power supplies (dipoles and quadrupoles) is the design goal to achieve an overall magnetic stability of ±200 ppm. The requirements for the dipole corrector magnets are less stringent. These requirements range from ±300 ppm for sextupoles to ±400 ppm for dipole corrector magnets. The nominal operating values correspond to 2.0 GeV for all power supplies, and their maximum design values correspond to 2.2 GeV. The main dipole magnets are connected in series with eight parallel-resonant-cells and eight feed points, as shown in Figure II.3.2-1. The power circuits in this design are a resonant cyclo-converter/rectifier and are similar to those used in the 500-MeV RCS. The energy lost in the resonant circuit is resupplied by rectifier operation of the circuit. The combination of power supplies used for continuous excitation have a rectifier ripple frequency of 2,160 Hz (36-pulse) and a total power rating of 3.7 MW. The quadrupole magnets are divided into two families and are connected in the same manner as the dipoles, except that they have seven feed points per family, as shown in Figure II.3.2-2. The total power supply rating for the combination of the focusing and defocusing quadrupoles is 3.8 MW. The sextupole magnets are individually powered by 40 identical pulse-width-modulated (PWM) power supplies operating at a frequency of 15 to 20 kHz. They respond to an arbitrary function during the acceleration ramp, and the remaining stored energy after losses is returned to a capacitor bank for use during the next cycle. The peak sextupole power supply voltage rating is sufficiently high to provide twice the normalized rate of current change as that provided by the dipole power supply during acceleration. The regulator reference-voltage is supplied by a digital-to-analog converter (DAC) that is serially counted up and down, thereby creating the desired arbitrary current shape between zero and the maximum current in each cycle. Fifty-six independently controlled 6-kW bipolar power supplies are provided for the horizontal and vertical dipole corrector magnets. The need for smooth control of the dipole corrector magnet current through the zero point dictates the use of bipolar output stages.

3.2.1.2 Control System and Control Electronics

The power supplies require regulation and control to a resolution better than 100 ppm. The critical DAC and analog-to-digital conversion (ADC) devices, along with their regulator circuits, are located in a shielded enclosure near the analog signal source, generally in the power supply cabinet. One regulator is required for each group of ac-to-dc power converters for the resonant magnet circuits. Therefore, there are eight regulators for the dipole magnet system.
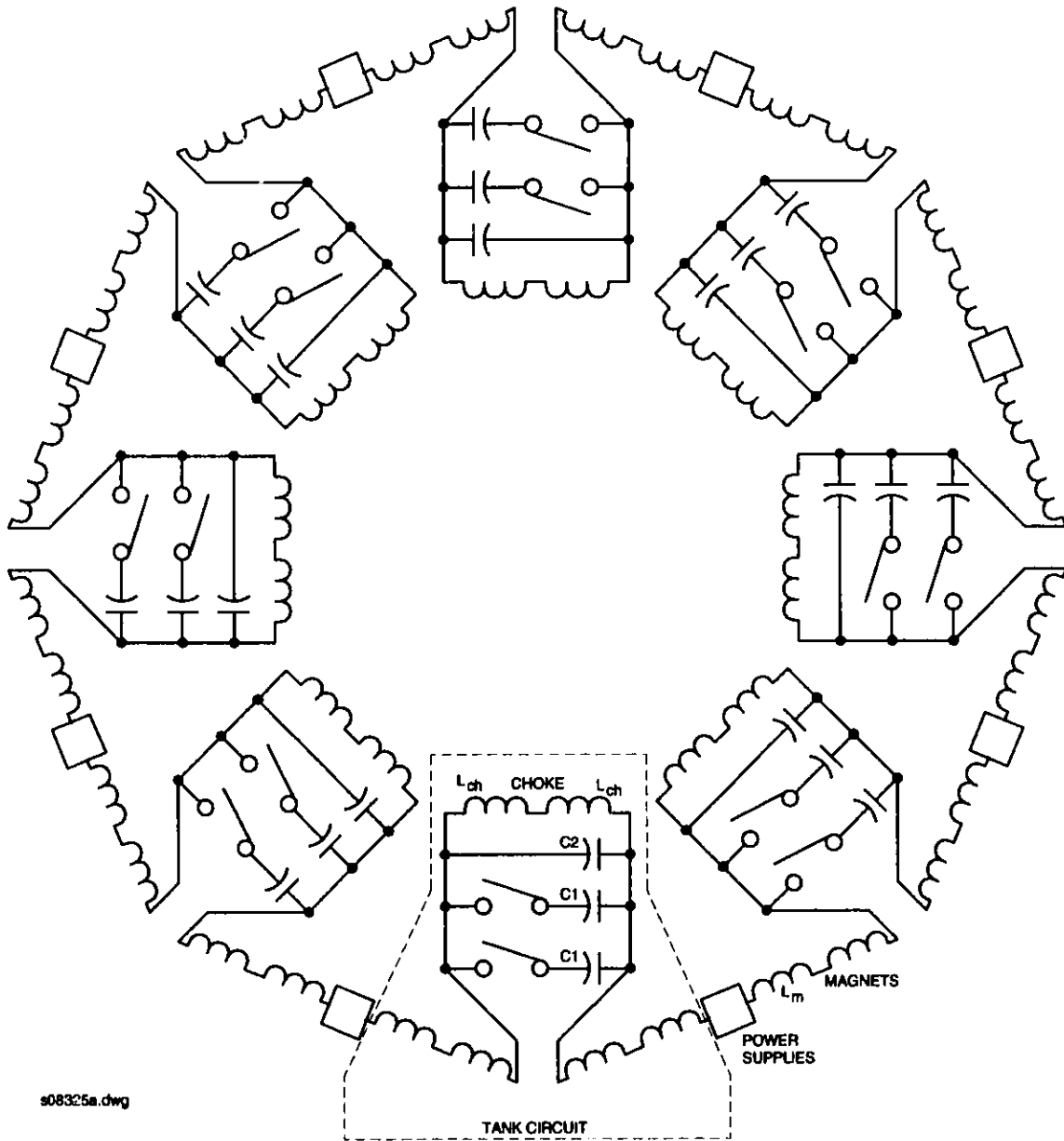
Figure II.3.2-1 Resonant Circuit Dipole Magnet Power Supply.
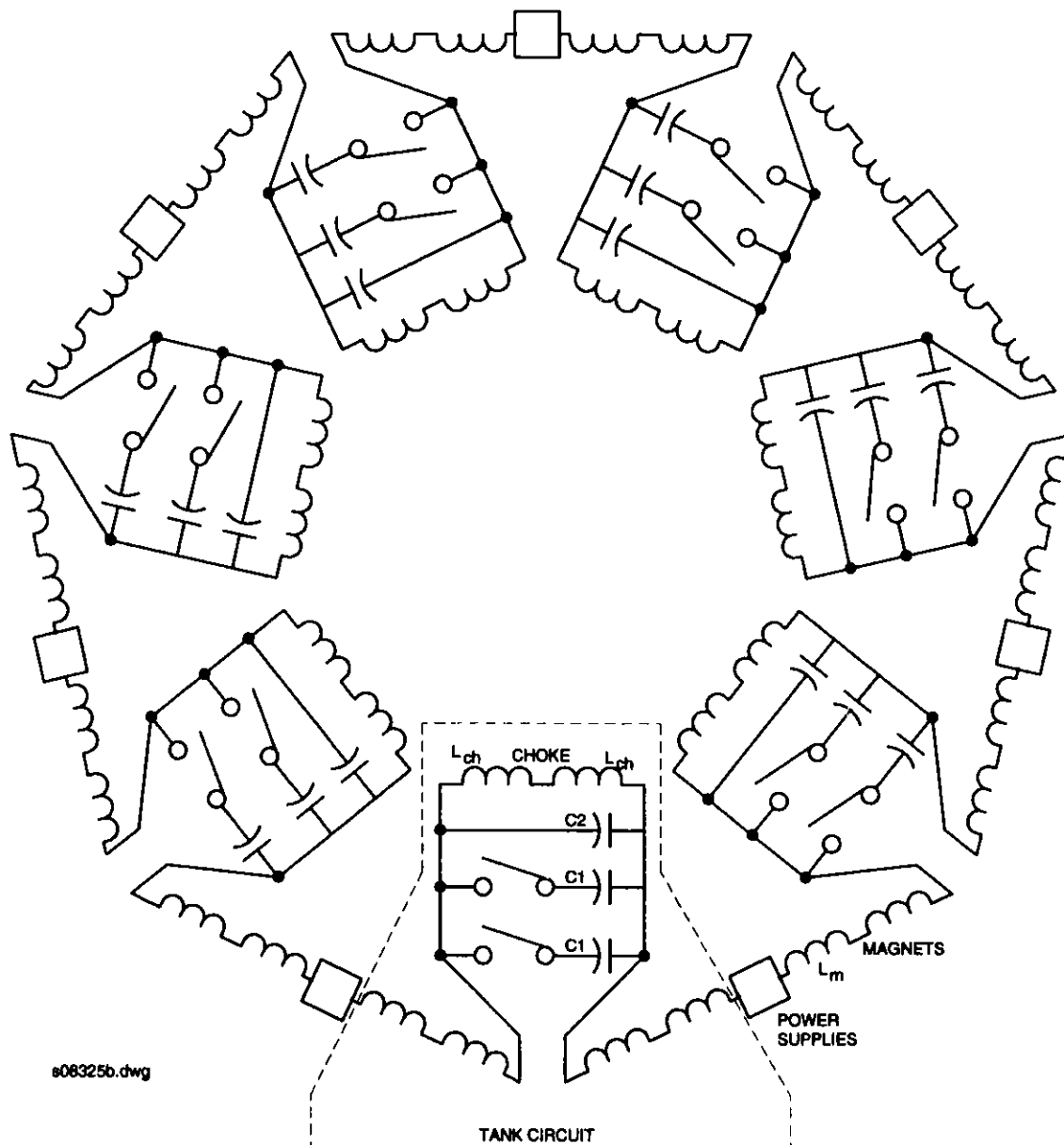
Figure II.3.2-2 Resonant Circuit Quadrupole Magnet Power Supply.

Communication with these regulator units is established by means of digital signals through optical cables, or at least optical couplers, to remove possible ground loops and reduce electrical noise. A multidrop-cable local network is used and is described in Section II.8.

A local microprocessor that uses digital signal processing techniques is used to keep the tank circuits tuned and balanced. It also controls, monitors, and balances the regulators.

Local control of the regulator group is by means of a local control console (a PC Notebook). This local console is able to emulate all local network actions while displaying regulator responses and status. This same system of local control and testing is used in the construction phase to bench-check the regulator systems; no other control system components are required.

3.2.1.3 Grounding

Most of the problems encountered in magnet power supply applications originate from inappropriate grounding practices, which can be explained by two different meanings attributed to the term "ground."

"Ground" is synonymous with "earth" in the context of an electrical utility or power grounding. Its function is to provide a low-impedance path for return of fault currents to the generator. This low-impedance path serves a safety role by limiting voltage differences during system faults and by allowing fault currents of sufficient magnitude to assure prompt opening of the source circuit breakers.

"Ground" is synonymous with "chassis" in electronics and data processing equipment. It can be a metal equipment enclosure or a single metal pad at the bottom of the cabinet, to which all connections to "ground" are routed. Data processing circuitry involves analog or pulse voltage signals that are generally less than 15 V and/or current loops of a few milliamperes. These signals can be transferred in a balanced, ungrounded circuit or a single-ended circuit with a common reference. Balanced circuits are isolated from ground, but the voltage with respect to ground (common mode) is still significant to the operation and potential susceptibility of the circuits. Single-ended circuits carry signals referred to a common potential, usually that of the equipment's internal chassis and generally called "reference." The concern in either case is that the referencing system might carry signal currents that can become polluted by spurious ground currents, either through common connection points with the "earthed" system or by common-mode noise coupling.

Because of the high frequencies associated with electronic and switching circuits, the inductance between the circuit and the reference should be kept to a minimum. Therefore, large existing copper cables, suitable for earthing, are not suitable for referencing. A ground reference grid providing a large number of different path-links for the various noise frequencies is incorporated into the system. For power supply applications, there is concern for personnel and equipment safety and for noise. Safe operation of the electrical or electronic system depends on

the integrity and low impedance of its "earth" system. Undisturbed operation of the same electrical or electronic system depends on the geometry and intrinsic low impedance of its reference grid, regardless of the impedance between the reference and the earth.

Electric and magnetic field coupling between circuits must be considered in addition to the noise voltages coupled to equipment by ground currents flowing through a common ground bus.

In summary, power supply monitoring and control circuits are designed to:

- Generate as little noise as practicable,

- Be affected by noise as little as practicable,

- Keep electromagnetic interference to a minimum,

- Keep conductive coupling to a minimum, and

- Keep common impedance coupling to a minimum.

Argonne National Laboratory (ANL) has a long and successful history of both conventional and digital computer-based control and monitoring of large, complex power systems. Solutions to problems associated with high and low signal levels in areas with high electromagnetic noise and in otherwise hostile environments have been found. These include both conventional and rapid cycling synchrotrons, bubble chamber magnets, large magnetohydrodynamic (MHD) magnets, and the fusion power devices APEX, FELIX, and ALEX.

3.2.1.4 Lockout/Tagout (LOTO) of Magnet Power Supplies

All magnet power supplies are powered from one 138-kV three-phase ac line through a 138-kV to 13.2-kV transformer. The 13.2-kV to 480-V distribution transformers used as the main source of power to the magnet power supplies have no other equipment connected to them. LOTO of the main power to the magnet power supplies is accomplished (see Figure II.3.2-3) in one of the following ways:

- One LOTO on the incoming 138-kV ac line breaker. This locks out all magnet power supplies.

- One LOTO on each of the 13.2-kV ac input line breakers for the 13.2-kV to 480-V distribution transformers used with the magnet power supplies. This can be used to lock out subsets of all major types of accelerator power supplies.
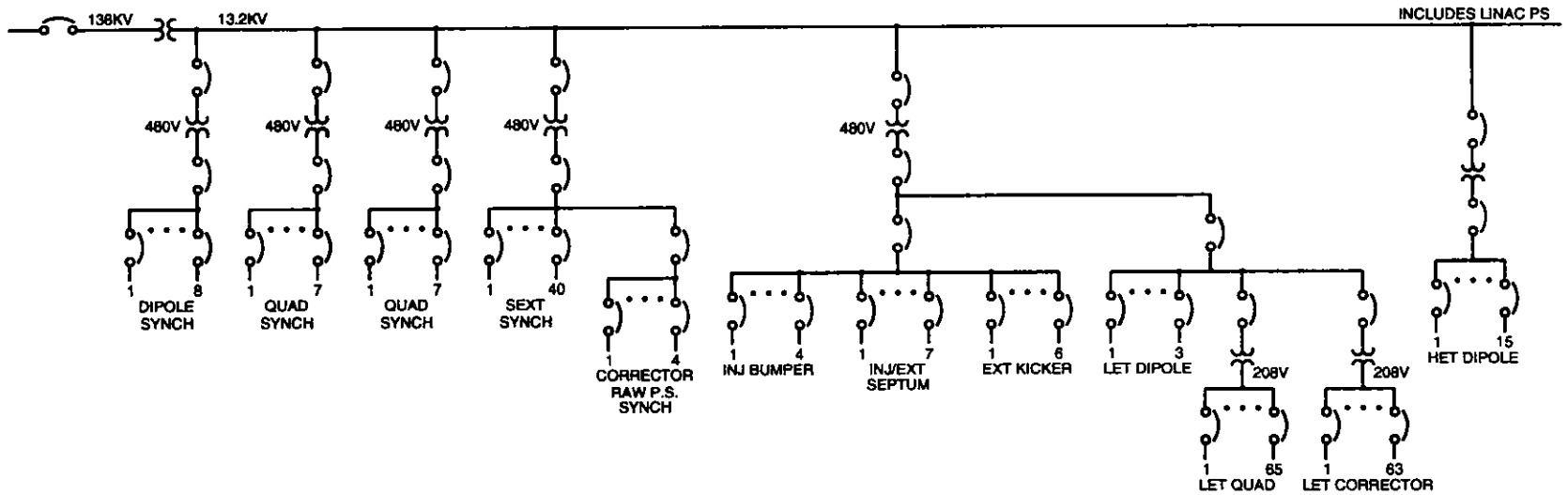
Figure II.3.2-3 Magnet Power Supply Input ac Distribution.

- One LOTO on each of the 480-V ac main transformer output breakers for the 13.2-kV to 480-V distribution transformers used with the magnet power supplies. This can be used to lock out individual major power supplies or groups of smaller power supplies.

- One LOTO on each of the 480-V distribution breakers used shown in Figure II.3.2-3. This can be used to lock out any individual power supply.

The 110-V ac control power for the power supplies is sometimes supplied from another source and must be locked out separately, if required.

3.2.2 Dipole Magnet Power Supplies

3.2.2.1 General Considerations

The RCS dipoles and quadrupoles are excited by dc-biased sinusoidal currents. Capacitors and chokes resonate with the magnets to save energy. A modulated multiphase dc power supply provides both dc and ac excitation from one source. The energy losses during each cycle are resupplied by the rectifier action of the supply. It operates at 20 Hz and 60 Hz and is readily phase-locked to the line or to a stable oscillator. Figure II.3.2-4 illustrates one of the ac-dc power sources, which uses three identical 12-pulse dc power supplies connected in series. Each has its three-phase ac inputs phase-shifted by 10 electrical degrees with respect to the others. The phase shifting is done by an autotransformer. This combination provides a 36-pulse, phase-controlled, dc power supply generating the desired wave shape. A slightly underdamped filter is connected to the power supply to attenuate ripple above the operating frequency. This configuration is repeated eight times around the ring to reduce the peak voltages. The capacitors are switched to achieve dual-frequency operation. The acceleration ramp is at 20 Hz, and the reset is at 60 Hz, which reduces the radio-frequency (rf) voltage required per turn compared with continuous 30-Hz.

3.2.2.2 Dual-Frequency Magnet Circuit

A dual-frequency resonant magnet circuit is used for the dipole magnets. The 30-Hz repetition rate is maintained for the RCS, while a 20-Hz magnet guide field is used during acceleration, and a 60-Hz reset field is used when no beam is present. The result is a longer accelerating-field rise time and shorter fall time; the duty factor is improved as a result of the longer acceleration time. The maximum $\dot{B}$ is reduced by 33%, reducing the maximum rf voltage by 33%. Figure II.3.2-5 shows current and voltage waveforms for dual-frequency operation.
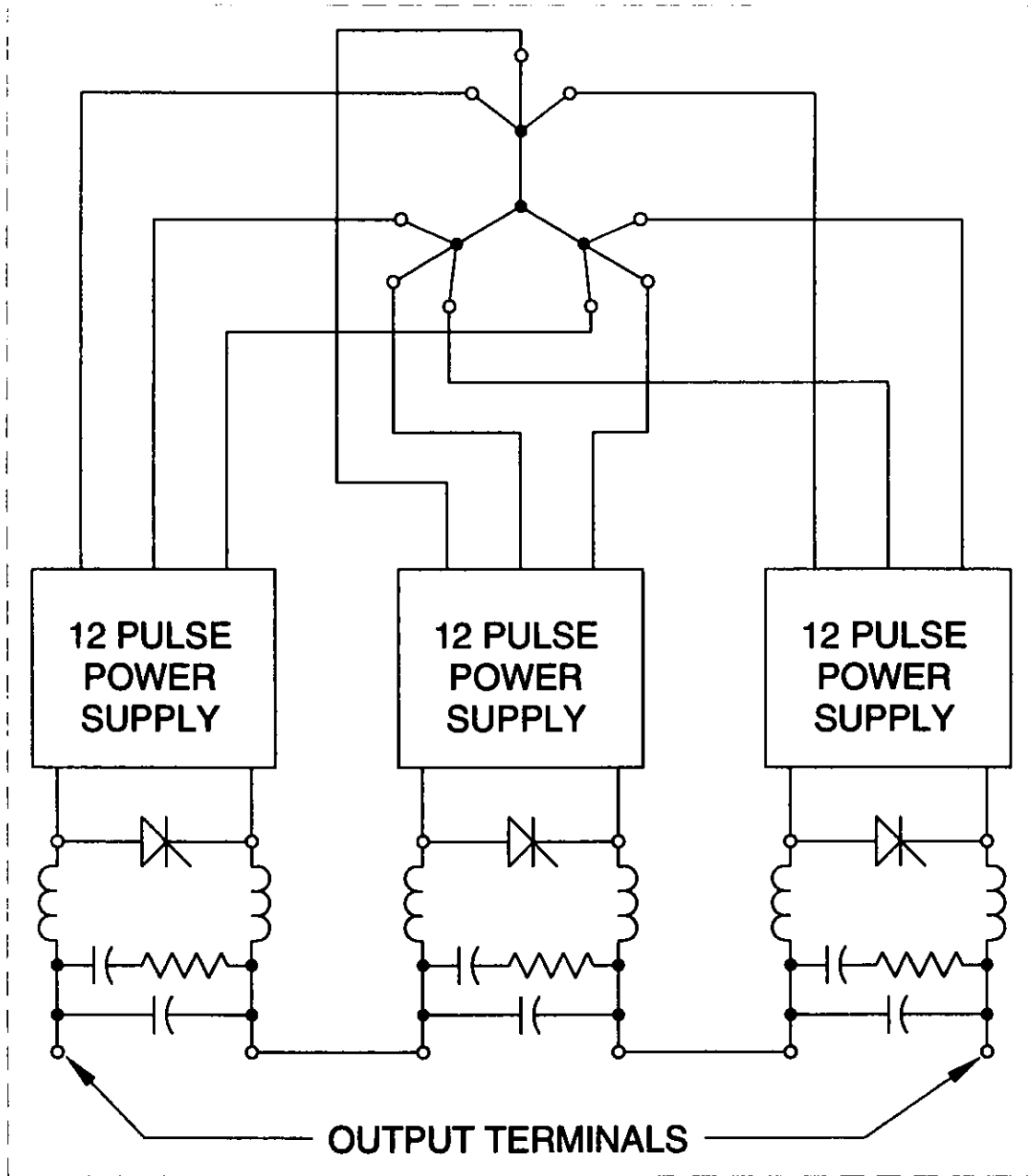
Figure II.3.2-4 Power Supply for One Feed Point.
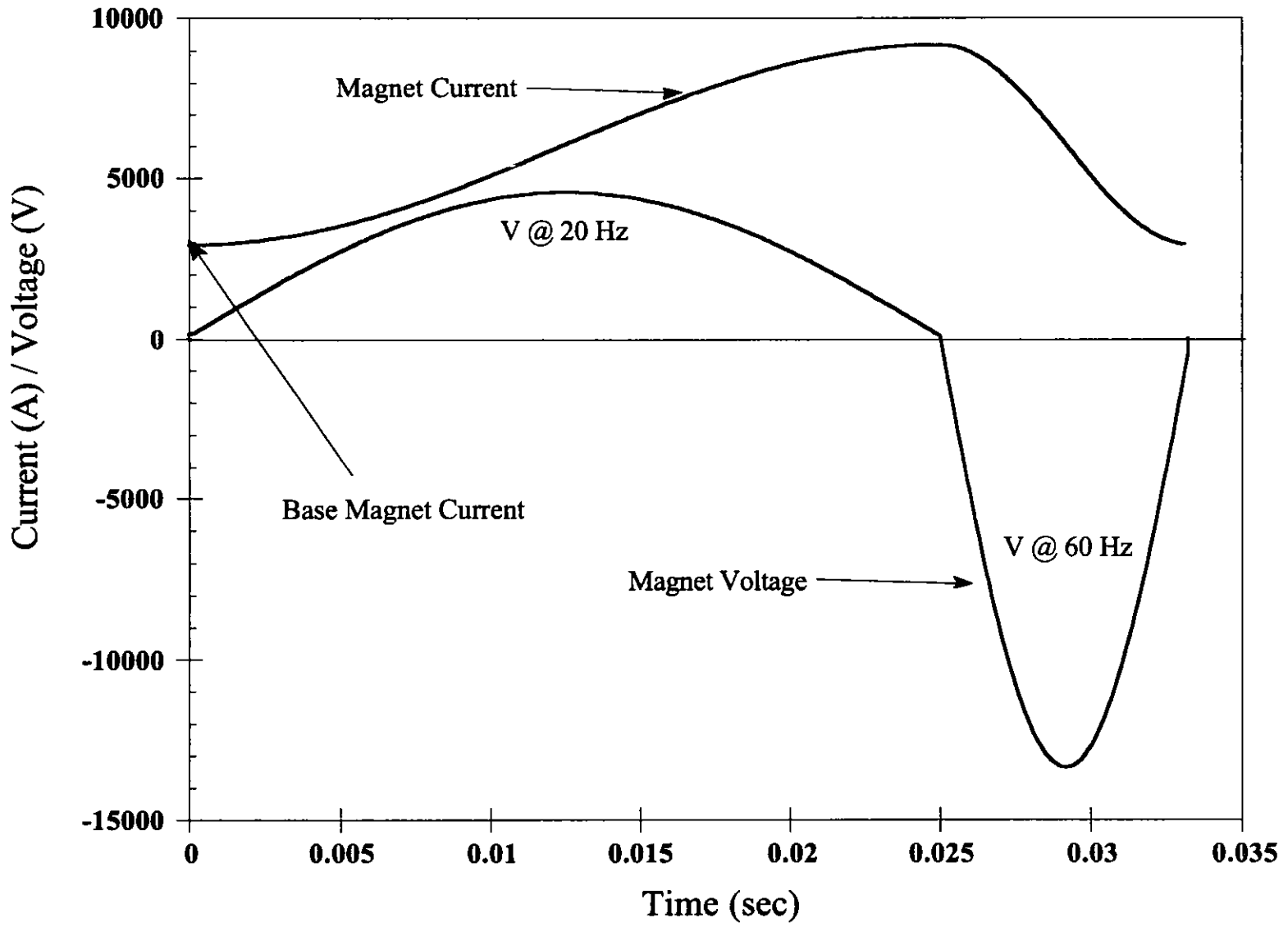
Figure II.3.2-5 Dipole Magnet Current and Voltage Waveforms for Dual-Frequency Operation.

When the frequency during acceleration is denoted by f_1 and the frequency during magnet reset is denoted by f_2, the effective RCS repetition rate, f_0, is given by:

$$f_0 = \frac{2 \times f_1 \times f_2}{f_1 + f_2} .$$

The peak magnet voltage during reset is proportional to f_2, provided $f_2 \geq f_1$. The capacitance of C_1 in Figure II.3.2-1 increases and the voltage across the C_1 capacitor decreases as the ratio f_0/f_1 increases. The capacitance of C_2 decreases and the voltage across the C_2 capacitor increases as the ratio f_0/f_1 increases.

For the baseline design, $f_1 = 20$ Hz, $f_2 = 60$ Hz, and $f_0 = 30$ Hz. These values can be changed in the future but are limited by the maximum tolerable voltage.

The magnet and choke currents are 180° out of phase. The stored energy is transferred back and forth between the choke and the magnet through the resonant capacitor C_1 during the acceleration ramp and through the C_2 capacitor during the resets. The choke inductance, L_{ch}, is selected to be equal to the magnet inductance, L_m, to optimize the voltage across the magnets. The resonant frequency, ω_0, of the circuit is given by

$$\omega_0 = \sqrt{\frac{L_m + L_{ch}}{L_m \times L_{ch} \times C}} ,$$

where

L_m = sum of the inductances of the magnets in one tank circuit,

L_{ch} = sum of the inductances of the choke in one tank circuit, and

C = capacitance value of one tank circuit at f_0.

When $L_{ch} = L_m$, then the capacitance of the circuit becomes

$$C = \frac{2}{L_m \times \omega_0^2} .$$

The time-variation of the magnet current during acceleration, i_{magnet}, when saturation effects are neglected, is given by

$$i_{magnet} = I_{dc} - I_{ac} \times \cos \omega_1 t .$$

The choke and capacitor currents, i_{choke} and $i_{capacitor}$, are given by

$$i_{choke} = I_{dc} + I_{ac} \times \cos \omega_1 t$$

and

$$i_{capacitor} = i_{magnet} - i_{choke} = -2I_{ac} \times \cos \omega_1 t .$$

The capacitor and magnet voltages, e_c and e_m, are given by

$$e_c = \frac{2I_{ac}}{\omega_1 C_1} \sin \omega_1 t$$

$$e_m = E_{dc} + e_c ,$$

where

I_{dc} = dc magnet or choke current,

I_{ac} = ac magnet or choke current peak,

E_{dc} = dc magnet voltage,

i_{magnet} = instantaneous magnet current,

i_{choke} = instantaneous choke current,

$i_{capacitor}$ = instantaneous capacitor bank current,

e_c = instantaneous capacitor bank voltage, and

e_m = instantaneous magnet voltage.

3.2.2.3 Dipole Circuit Loss Budget and Parameters

A loss budget for the dipole resonant circuit shown in Figure II.3.2-1 is given in Table II.3.2-1. Table II.3.2-2 lists the parameters for the dipole resonant circuit.

Table II.3.2-1 Loss Budget for the Dipole Dual-Frequency Resonant Circuit at 2.2 GeV[a]

Losses	Ring Dipole Magnets	Chokes	Capacitors	Inter-Connects	Filters	Power Supplies	Units
Percent of total	46	19	5	10	5	15	%
Per magnet	52.7	21.5	5.7	11.5	5.7	17.2	kW
Per tank circuit	210.6	86.0	22.9	45.8	22.9	68.7	kW
Full circuit	1,684.9	688.0	183.1	366.3	183.1	549.4	kW

[a] There are eight resonant tank circuits with eight feed points operating at 2.2 GeV. Each of the eight groups of three power supplies is required to make up 457 kW lost per feed point. Total system losses are 3,655 kW.

Table II.3.2-2 Parameters for the Dipole Dual-Frequency Resonant Circuit at 2.2 GeV

Parameters	Values	Units
Magnet inductance	2.85	mH
Magnet inductance of 1/8 of the total magnets	11.4	mH
Magnet dc current	6,056	A
Magnet peak ac current	3,129	A
Magnet rms current	6,448	A
Capacitor bank peak ac current	−6,258	A
Number of feed points	8	-
Total number of power supplies	24	-
Number of magnet families	1	-
Total number of magnets	32	-
ac loss per:		
Magnet	25.3	kW
Choke	8.2	kW
Capacitors (1/32 of the total)	3.9	kW
Interconnections (1/32 of the total)	3.9	kW
Filters (1/32 of the total)	2.0	kW
Power supplies (1/32 of the total)	5.9	kW
ac total loss	1,575.5	kW
dc loss per:		
Magnet	27.4	kW
Choke	13.3	kW
Capacitors (1/32 of the total)	0	kW
Interconnections (1/32 of the total)	7.9	kW
Filters (1/32 of the total)	3.9	kW
Power supplies (1/32 of the total)	11.8	kW
dc total loss	2,057.6	kW
Capacitance (1/8 of total) for 20-Hz operation	11.110	mF
Capacitance (1/8 of total) for 60-Hz operation	1.234	mF
One 185-kW power supply (kW value was selected to include 10% for low line and 10% for regulation)	184.7	kW
Voltage rms[a] of one power supply based on kW value selected	28.7	V
Voltage dc of one power supply based on kW value selected	17.5	V
Voltage ac peak of one power supply based on kW value selected	13.0	V
Voltage peak of one power supply based on power supply selected	30.6	V
ac voltage peak across the tank circuit for 20-Hz operation	−4,483	V
ac voltage peak across the tank circuit for 60-Hz operation	−13,448	V

[a] rms = root mean square.

3.2.3 Quadrupole Magnet Power Supplies

3.2.3.1 General Considerations

The quadrupole magnets are divided into two families, with seven feed points per family, as shown in Figure II.3.2-2. They have a total power rating of 3.8 MW and operate as a dual-frequency resonant circuit. Details are similar to those for the dipole circuit. The cells are repeated seven times per family. The design curves shown in Figure II.3.2-5 for the main dipole circuit also apply to the quadrupole circuits, but with different amplitudes.

3.2.3.2 Quadrupole Circuit Loss Budget and Parameters

A loss budget for the quadrupole resonant circuit shown in Figure II.3.2-2 is given in Table II.3.2-3. Table II.3.2-4 lists the parameters for the quadrupole resonant circuit.

3.2.4 Sextupole Magnet Power Supplies

The sextupole magnets are individually powered by 40 identical unipolar pulse-width-modulated (PWM) power supplies operating at a frequency of 15 to 20 kHz, as shown in Figure II.3.2-6. During the acceleration cycle, the power supply is operated by closing switch AA and pulse-width-modulating switch A. When switch A is closed, energy is transferred from the capacitor to the magnet. When switch A is open, the magnet freewheels through switch AA and diode D3, thereby losing energy. The regulator reference voltage is supplied by a DAC that is serially counted up and down, thus creating an arbitrary ramp. At the end of the acceleration ramp, the DAC is reset to zero, and switches A and AA are both opened. This procedure forces the remaining energy stored in the magnet to be returned to the capacitor bank through diodes D2 and D3 for use during the next cycle.

The peak sextupole power supply voltage rating is sufficiently high to provide twice the normalized rate of current change of the dipole magnet power supply during acceleration. The sextupole power supplies have a current stability of ±300 ppm.

3.2.5 Dipole Corrector Magnet Power Supplies

A total of 56 independently controlled bipolar power supplies are provided for the horizontal and vertical dipole corrector magnets. They are rated at 6 kW each. The bipolar power supplies provide smooth control of the current through zero. Figure II.3.2-7 shows a simplified circuit of a bipolar power supply. The topology is a PWM full-bridge converter operating at 20 kHz. The switches are insulated-gate bipolar-transistors (IGBTs), and the antiparallel diodes are included within them. L_c and C_c represent the inductance and capacitance

Table II.3.2-3 Loss Budget for the Quadrupole Dual-Frequency Resonant Circuit of One Family at 2.2 GeV[a]

Losses	Ring Quad Magnets	Chokes	Capacitors	Inter- Connects	Filters	Power Supplies	Units
Percent of total	44	22	5	10	5	15	%
Per magnet	30.0	15.0	3.3	6.5	3.3	9.8	kW
Per tank circuit	120.1	60.2	13.1	26.1	13.1	39.2	kW
Full circuit	840.7	421.1	91.4	182.8	91.4	274.2	kW

[a] There are seven resonant tank circuits with seven feed points operating at 2.2 GeV. Each of the seven groups of three power supplies is required to make up 271.7 kW lost per feed point. Total system losses are 1,901.6 kW.

Table II.3.2-4 Parameters for the Quadrupole Dual-Frequency Resonant Circuit of One Family at 2.2 GeV

Parameters	Values	Units
Magnet inductance	10	mH
Magnet inductance of 1/7 of the total magnets per family	40	mH
Magnet dc current	1,420	A
Magnet peak ac current	733.7	A
Magnet rms current	1,512	A
Capacitor bank peak ac current	−1,467.4	A
Number of feed points	7	-
Total number of power supplies	42	-
Number of magnet families	2	-
Total number of magnets	56	-
ac loss per:		
Magnet	2.6	kW
Choke	0.9	kW
Capacitors (1/28 of the total)	3.3	kW
Interconnections (1/28 of the total)	2.2	kW
Filters (1/28 of the total)	1.1	kW
Power supplies (1/28 of the total)	3.3	kW
ac total loss	53.4	kW
dc loss per:		
Magnet	27.4	kW
Choke	14.2	kW
Capacitors (1/28 of the total)	0	kW
Interconnections (1/28 of the total)	4.3	kW
Filters (1/28 of the total)	2.2	kW
Power supplies (1/28 of the total)	6.6	kW
dc total loss:	272.3	kW
Capacitance (1/7 of total) for 20-Hz operation	3.166	mF
Capacitance (1/7 of total) for 60-Hz operation	0.352	mF
One 110-kW power supply (kW value was selected to include 10% for low line and 10% for regulation)	108.9	kW
Voltage rms[a] of one power supply based on the kW value selected	72.8	V
Voltage dc of one power supply based on the kW value selected	62.3	V
Voltage ac peak of one power supply based on the kW value selected	15.2	V
Voltage peak of one power supply based on power supply selected	77.5	V
ac voltage peak across the tank circuit for 20-Hz operation	−3,688	V
ac voltage peak across the tank circuit for 60-Hz operation	−11,064	V

[a] rms = root mean square.
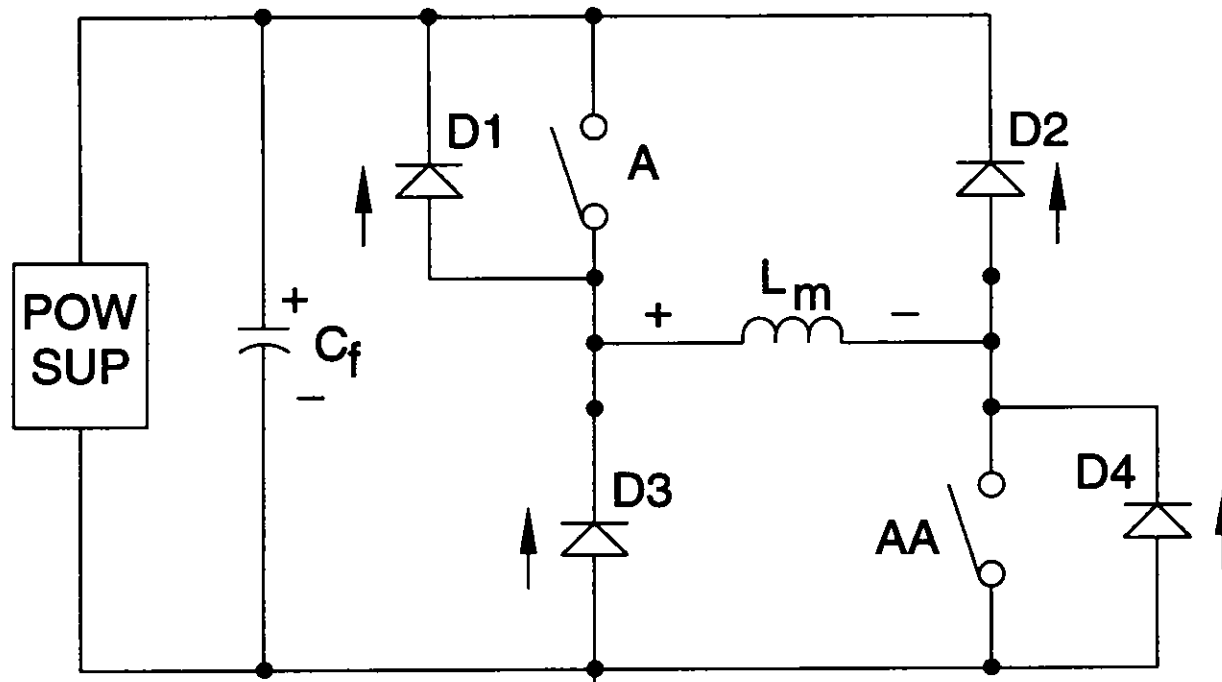
FILE: S08339C

Figure II.3.2-6 Sextupole Magnet Power Supply.
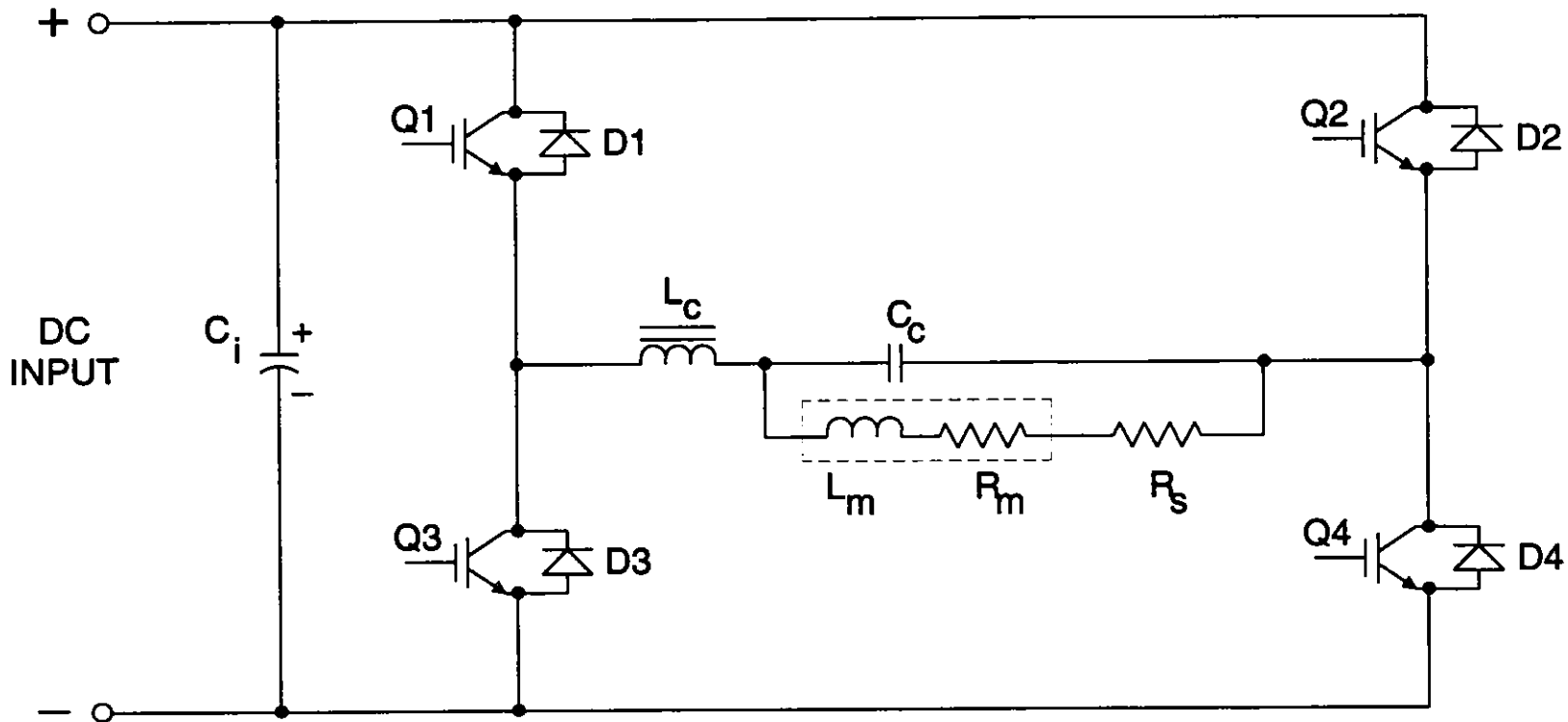
FILE: S08344.dwg

Figure II.3.2-7 Bipolar Power Supply that Powers the Dipole Corrector Magnets.

of the output filter; L_m and R_m are the inductance and resistance of the magnet; and R_s is the resistance of a current-sensing device. The peak output current and voltage are ± 149.2 A and ± 111 V, respectively, for 2.2 GeV. The current stability of the bipolar power supplies is ± 400 ppm.

3.3 BEAM TRANSFER LINE MAGNETS AND POWER SUPPLIES

3.3.1 Low-Energy Transport Line (LET)

3.3.1.1 Magnets

The LET has 15 dipole, 65 quadrupole, and 16 corrector magnets to transport the beam between the linac and the synchrotron injection septum magnets. All LET magnets are commercially supplied, and they have laminated cores constructed from 1.5-mm-thick low-carbon steel. The coils are made with copper conductors that are insulated with fiberglass and vacuum-impregnated, heat-cured epoxy. The parameters for the four LET magnet types are listed in Table II.3.3-1.

All LET dipoles are of the same design, using hollow water-cooled conductor. Each can be split into two halves for installation around the vacuum chamber.

There are 62 quadrupoles with 53-mm-diameter apertures (quad A) and three 72-mm-diameter-aperture quadrupoles (quad B) in the LET. Each quadrupole has coils made with hollow water-cooled conductor and is assembled from four quadrants. Each can be split into halves for installation around the vacuum chamber.

There are 16 small correction dipoles in the LET. The correctors are made with one-piece C-cores to facilitate assembly and installation around the vacuum chambers. Each has coils made with solid air-cooled conductor.

3.3.1.2 Power Supplies

The LET has 15 dipole, 65 quadrupole, and 16 dipole corrector magnets. All dipole corrector and quadrupole magnets are individually powered by air-cooled commercial dc power supplies. Current-regulator circuitry is added to the dipole corrector and quadrupole supplies. The dipoles are powered by three identical dc power supplies, which are water cooled and are built to a performance specification. Eight dipoles are powered by one supply, five dipoles are powered by the second supply, and two dipoles are powered by the third supply. All parameters are shown in Table II.3.3-2.

Table II.3.3-1 Parameters for LET Magnets

Parameters	Dipole A	Quad A	Quad B	LET Corrector	Units
Number required	15	62	3	16	-
Peak strength at 400 MeV	0.63 T	14.0 T/m	12.0 T/m	0.064 T	-
Effective length	1.0	0.20	0.20	0.10	m
Gap					
Height or diameter	40	53	72	53	mm
Width	140	-	-	135	mm
Magnet mass	2,000	110	210	55	kg
Conductor					
Height	8.3	4.2	5.8	1.6ϕ	mm
Width	8.3	4.2	5.8	-	mm
Hole diameter	4.6	2.4	3.2	Solid	mm
Number of turns per pole	96	26	26	720	-
Inductance	200	10	9	888	mH
Resistance	190	94	48	8684	mΩ
Time constant	1,052	106	188	102	ms
Maximum supply current	106	154	243	1.9	A
Maximum current density in coil	1.2	5.6	5.2	0.4	A/mm^2
Peak voltage	20	16	14	19	V
Power losses	2.1	2.2	2.8	0.03	kW
Cooling circuits/magnet	4	4	4	-	-
Total water flow	1.3	0.7	1.5	-	gal/min
Water pressure drop	100	100	100	-	psi
Water temperature rise	6	11	7	36[a]	°C

[a] Maximum estimated internal temperature for the coils.

Table II.3.3-2 LET Power-Supply Parameters at 10% over 400 MeV

| Parameters | Magnet Power Supply | | | | |
	Dipole A	Quad A	Quad B	Dipole Corrector	Units
Number of power supplies	3	62	3	16	-
Number of magnets	15	62	3	16	-
Inductance	200	10	9	888	mH
Resistance	190	94	48	8,684	mΩ
Maximum supply current	169.4	169.4	267.3	2.09	A
Peak voltage	31.9	15.4	13.2	18.7	V
Stability ($\pm$)	1×10^{-4}	2×10^{-4}	2×10^{-4}	3×10^{-4}	$\Delta i/Imax$
Current reproducibility ($\pm$)	2×10^{-4}	4×10^{-4}	4×10^{-4}	6×10^{-4}	$\Delta i/Imax$
Current ripple ($\pm$)	5×10^{-4}	6×10^{-4}	6×10^{-4}	1×10^{-3}	$\Delta i/Imax$
Tracking error ($\pm$)	5×10^{-4}	6×10^{-4}	6×10^{-4}	4×10^{-3}	$\Delta i/Imax$
Resolution bits	14	14	14	12	$\Delta i/Imax$

3.3.2 High-Energy Transport Line (HET)

3.3.2.1 Magnets

The two HET lines contain a total of 5 dipole, 25 quadrupole, and 16 corrector magnets to transport the beam from the synchrotron extraction septum magnets to the two external neutron targets. All HET magnets are commercially supplied, and they have laminated cores constructed from 1.5-mm-thick laminations of low-carbon steel. The coils are made with hollow copper conductors that are insulated with fiberglass and vacuum-impregnated, heat-cured epoxy. The parameters for the six HET magnet types are listed in Table II.3.3-3.

All dipole cores are made with the same lamination shape as that used for the synchrotron dipoles. Three different dipole lengths are required for the HET lines; these three are referred to as dipole B, dipole C, and dipole D in Table II.3.3-3.

There are 17 HET quadrupoles, quad C, which have a bore diameter of 170 mm, and 8 HET quad D magnets with a bore diameter of 264 mm. The four quadrupole magnets closest to the neutron target in each of the two HET lines are manufactured with radiation-hard insulation.

The 16 HET correction dipoles have cores identical to those used in the synchrotron correctors. The coils are also similar, but they use larger conductors.

3.3.2.2 Power Supplies

There are 5 dipole, 25 quadrupole, and 16 dipole corrector magnets in the HET lines to the 10-Hz and 30-Hz targets. All magnets are individually powered. The dipole dc power supplies are built to a performance specification and are water cooled. The quadrupoles are powered by air-cooled commercial dc power supplies to which current-regulator circuitry has been added. The dipole correctors are powered with bipolar pulse-width modulated (PWM) power supplies built to a performance specification. All parameters are shown in Table II.3.3-4.

Table II.3.3-3 Parameters for HET Magnets

Parameters	Dipole B	Dipole C	Dipole D	Quad C	Quad D	HET Corrector	Units
Number required	1	2	2	17	8	16	-
Peak strength at 2.0 GeV	1.20 T	1.43 T	1.36 T	9.1 T/m	7.3 T/m	0.127 T	-
Effective length	1.0	1.8	2.8	0.50	0.50	0.15	m
Gap							
Height or Diameter	182	182	182	170	264	300	mm
Width	450	450	450	-	-	300	mm
Magnet mass	19,000	36,600	58,200	5,100	6,900	410	kg
Conductor							
Height	12.7	12.7	12.7	12.7	15.2	5.8	mm
Width	12.7	12.7	12.7	12.7	15.2	5.8	mm
Hole diameter	7.0	7.0	7.0	7.0	8.4	3.2	mm
Number of turns per pole	306	306	306	113	129	140	-
Inductance	1,424	2,564	3,988	314	317	3.6	mH
Resistance	325	481	677	115	94	250	mΩ
Time constant	4,382	5,331	5,891	2,730	3,372	15	ms
Maximum supply current	266	318	303	219	371	252	A
Maximum current density in coil	1.3	1.5	1.5	1.2	1.4	5.9	A/mm^2
Peak voltage	100	178	236	29	40	70	V
Power losses	26.7	56.1	71.8	6.4	14.9	17.7	kW
Cooling circuits/magnet	18	18	18	4	4	10	-
Total water flow	18.2	14.9	12.5	3.1	4.7	2.7	gal/min
Water pressure drop	100	100	100	100	100	100	psi
Water temperature rise	6	14	22	8	12	25	°C

Table II.3.3-4 HET Power-Supply Parameters at 2.2 GeV

Parameters	Magnet Power Supply						Units
	Dipole B	Dipole C	Dipole D	Quad C	Quad D	Dipole Corrector	
Number of power supplies	1	2	2	17	8	16	-
Number of magnets	1	2	2	17	8	16	-
Inductance	1,424	2,564	3,988	314	317	3.6	mH
Resistance	325	481	677	115	94	240	$m\Omega$
Maximum supply current	286	342	326	236	399	±271	A
Peak voltage	112	197	264	32	44	±65	V
Stability ($\pm$)	1×10^{-4}	1×10^{-4}	1×10^{-4}	2×10^{-4}	2×10^{-4}	3×10^{-4}	$\Delta i/Imax$
Current reproducibility ($\pm$)	2×10^{-4}	2×10^{-4}	2×10^{-4}	4×10^{-4}	4×10^{-4}	6×10^{-4}	$\Delta i/Imax$
Current ripple ($\pm$)	5×10^{-4}	5×10^{-4}	5×10^{-4}	6×10^{-4}	6×10^{-4}	1×10^{-3}	$\Delta i/Imax$
Tracking error ($\pm$)	5×10^{-4}	5×10^{-4}	5×10^{-4}	6×10^{-4}	6×10^{-4}	4×10^{-3}	$\Delta i/Imax$
Resolution bits	14	14	14	14	14	12	$\Delta i/Imax$

3.4 BUMPER AND KICKER MAGNETS AND POWER SUPPLIES

3.4.1 Introduction

The synchrotron bumper and kicker magnets have large gaps to accommodate the beam-stay-clear (BSC) requirements. Four bumper magnets are used to move the circulating synchrotron beam close to the injection septum during injection of the beam from the linac to the synchrotron. The bumpers are of conventional design without stringent requirements, but the extraction kicker requirements are more demanding.

3.4.2 Injection Bumper Magnets

All four bumper magnets have the same apertures and coil configurations. The bumper magnet parameters for a maximum bend angle of 20 mrad are summarized in Table II.3.4-1. A cross section of an injection bumper magnet is shown in Figure II.3.4-1. The pole faces are machined in uncut cores to assure parallelism of the pole faces and dimensional stability of the air gaps. The coils are made with hollow copper conductor and are insulated with mica-glass tape and vacuum-impregnated heat-cured epoxy. After the coils are cured, the outer surfaces are coated with an electrically conducting paint to define the ground planes. This coating prevents corona formation at the sharp corners and edges of the grounded core laminations.

Tape-wound grain-oriented silicon steel cores that are 0.3 mm thick are used for all of the bumper magnets. A peak field of 0.212 T is generated in a pulse period of 1 msec. Detailed pulse requirements are described in Section II.2.2.

3.4.3 Injection-Bumper-Magnet Power Supplies

The four bumper magnets are individually powered. The circuit diagram is shown in Figure II.3.4-2. The four 0.3-m-long bumper magnets are energized to move the closed orbit closer to the injection septum when the incoming bunch and the bucket are synchronized. Switch S1 in Figure II.3.4-2 is closed, causing capacitor C to discharge in 500 μsec into the bumper magnets. The peak current is determined by the charge on C. All four bumper magnets are capable of peak fields of 0.212 T. The end of the pulse is shaped by closing switches S2 and S3, and by opening switch S1, which allows the current to decay through R1 to approximately two-thirds of its peak in 500 μsec. The final pulse shape is controlled by opening switch S3, putting R1 and R2 in series, and driving the current to zero in 50 μsec.

The transformer T1 is used to match the current and voltage ratings of the switching circuit components to the magnet. The regulation of the charging power supply and control of the switch timing keep the peak current repeatable to within ± 0.05%.

Table II.3.4-1 Parameters for Synchrotron Bumper Magnets

Parameters	Bumper	Units
Bend angle	20	mrad
Peak central field at 400 MeV	0.212	T
Effective length	0.3	m
Gap		
Height	241.5	mm
Width	300	mm
Conductor		
Height	7.3	mm
Width	7.3	mm
Hole diameter	4.1	mm
Number of turns	28	-
Number of parallel conductors	2	-
Inductance	0.13	mH
Resistance	10	mΩ
Supply current		
Maximum	2,427	A
rms[a]	475	A
Peak voltage	680	V
Power losses	2.3	kW
Cooling circuits/magnet	2	-
Total water flow	0.8	gal/min
Water pressure drop	100	psi
Water temperature rise	11	°C

[a] rms = root mean square.
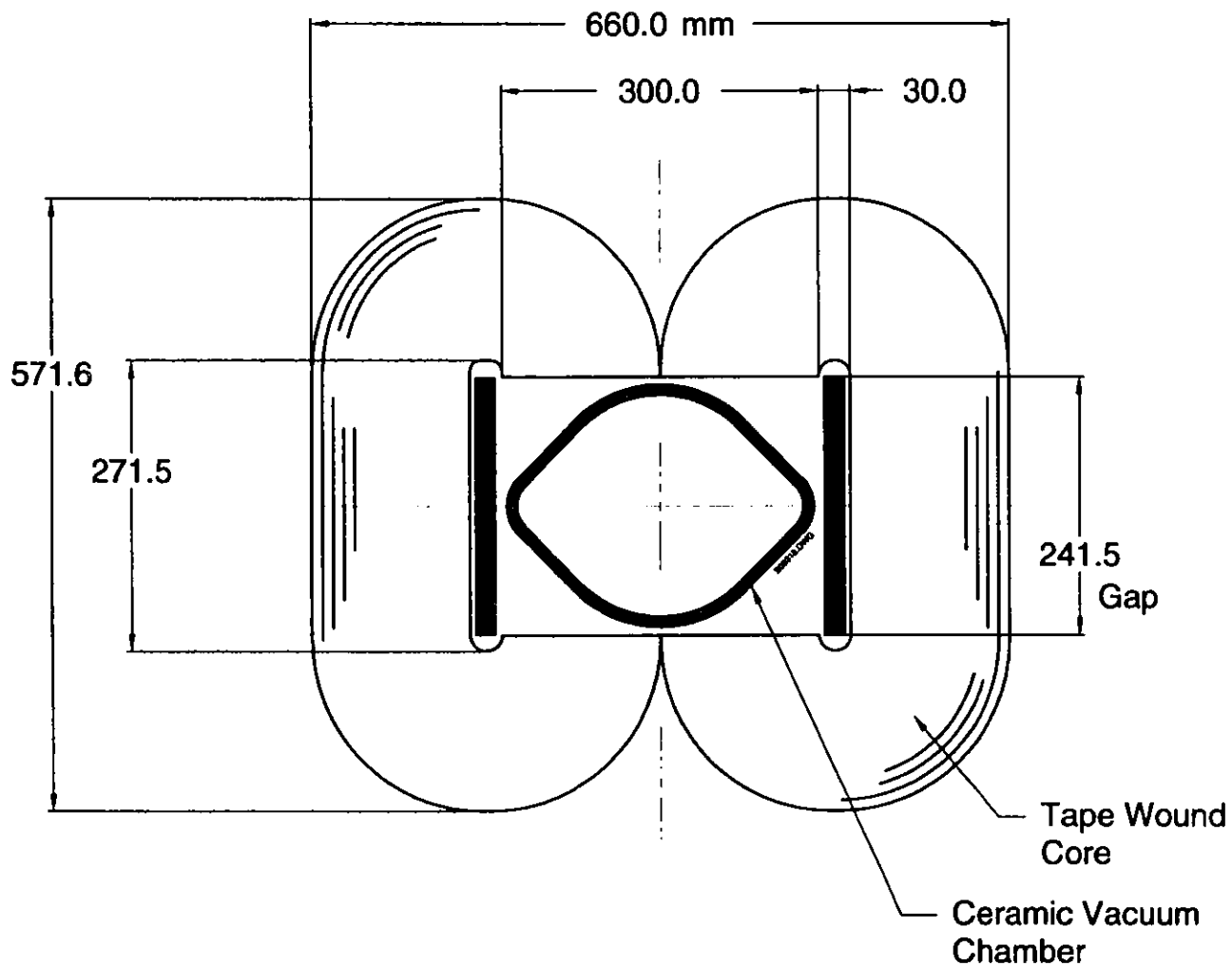
Figure II.3.4-1 Cross Section of an Injection Bumper Magnet.
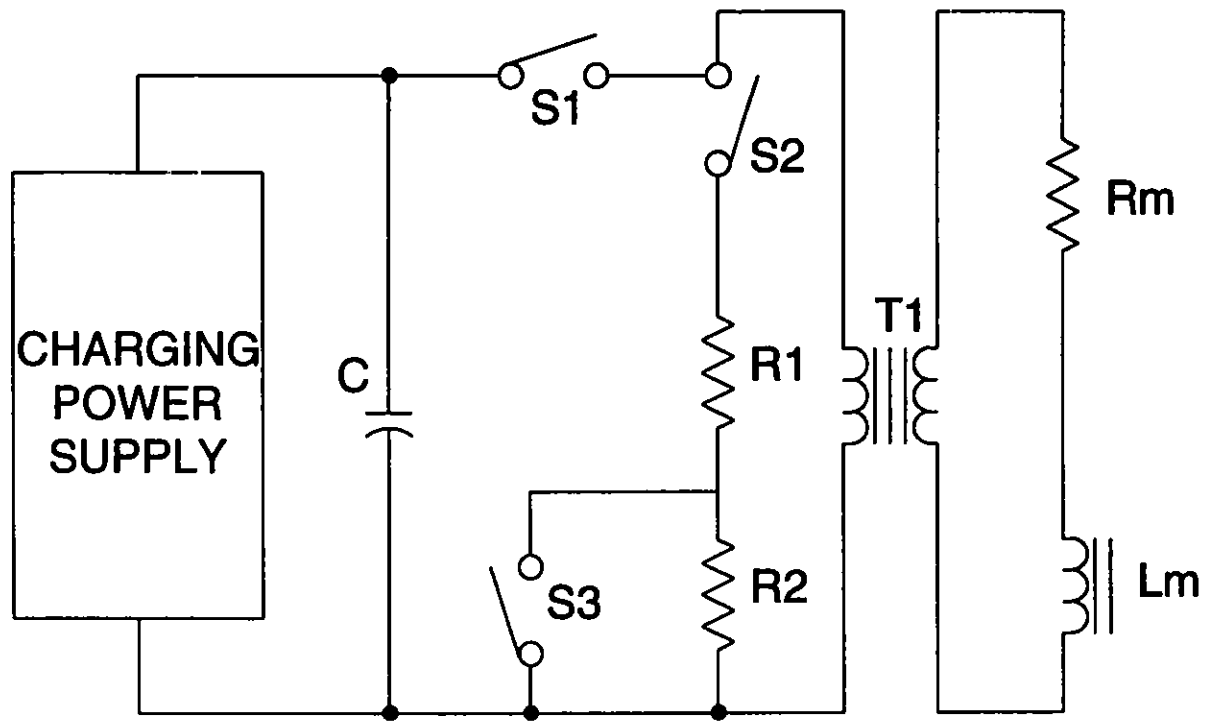
FILE: S06339F

Figure II.3.4-2 Circuit Diagram for the Bumper-Magnet Power Supply.

3.4.4 Extraction Kicker System

At extraction, the beam is kicked from the normal orbit into the aperture of the first septum magnet. Each of the two extraction kicker systems fits into a 2.9-m straight section. Each system is made up of three separate magnets, designated A, B, and C, to reduce the self-inductance. Thus, the required 350-nsec rise time is achieved with a commercially available 50-kV power supply. Each kicker magnet is individually powered. Extraction kicker parameters are listed in Table II.3.4-2. The aperture of each kicker magnet is large enough to match the BSC size in both height and width, to allow space for a ceramic vacuum chamber with 10-mm-thick walls and to provide 2.5-mm clearance on all sides. Each kicker magnet is also matched to the 15-kA peak current of the chosen thyratron and to the 50-kV peak power supply voltage.

The kicker cores are constructed of 102-mm-thick ferrite blocks of type CMD5005. Picture-frame ferrite cores are used in each kicker. Each kicker magnet is made of two half-turn distributed transmission lines powered in parallel and magnetically isolated from each other by a copper sheet. An equivalent impedance of $3.28\ \Omega$ is achieved by dividing the magnet core into longitudinal segments separated by matching capacitors and damping resistors. A cross section of kicker A and the vacuum chamber at the upstream end is shown in Figure II.3.4-3. This ceramic vacuum chamber tapers in height and in width as it extends through all three kickers. The inside surface of this chamber is metalized to minimize the impedance to the beam.

Each extraction-kicker power supply provides pulses with rise times of 350 nsec, flat-tops of 315 nsec, and fall times about the same as the rise times, as shown in Figure II.3.4-4. The fall time must be less than 4.1 msec, to allow the supply to charge for the next pulse. Each of these supplies has a high-voltage dc (HVDC) power supply, two pulse-forming networks (PFNs), and a thyratron switch. The HVDC power supply is a constant-current charging supply, which eliminates the need for a charging control circuit. Each PFN is made of five 52-m-long, 16.4-Ω coaxial cables connected in parallel to achieve an equivalent impedance of $3.28\ \Omega$. The total capacitance of two PFNs for one magnet is 0.2 μF. The stored energy in each PFN at 50 kV is 250 J. The power rating of the HVDC power supply at 30 Hz is 7.5 kW.

The fall time of the magnetic field for each of these kicker systems is about the same as the rise time. The current wave form has a trapezoidal shape, as shown in Figure II.3.4-4. The switching device is a commercially available thyratron that is rated for a maximum voltage of 70 kV, a peak current of 15 kA, and an average current of 5 A.

A schematic diagram of an extraction-kicker power supply and magnet section is shown in Figure II.3.4-5.

Table II.3.4-2 Parameters for Extraction Kicker Magnets

Parameters	Kicker A	Kicker B	Kicker C	Units
Bend angle	4.37	4.79	4.84	mrad
Peak central field at 2.0 GeV	0.0618	0.0512	0.0408	T
Effective length	650	870	1,105	mm
Gap				
Height	132.4	159.2	200.0	mm
Width	220.0	195.0	170.0	mm
Core				
Length	500	720	995	mm
Yoke thickness	102	102	102	mm
Inductance[a]	1.35	1.34	1.19	μH
Resistance[a]	0.10	0.10	0.09	mΩ
Supply current				
Maximum[a]	6,648	6,611	6,626	A
rms[a,b]	24	24	24	A
Average[a]	0.13	0.13	0.13	A
Peak voltage	50,000	50,000	50,000	V
Power losses	0.16	0.09	0.06	kW

[a] Parameter values are for series-connected coils.

[b] rms = root mean square.
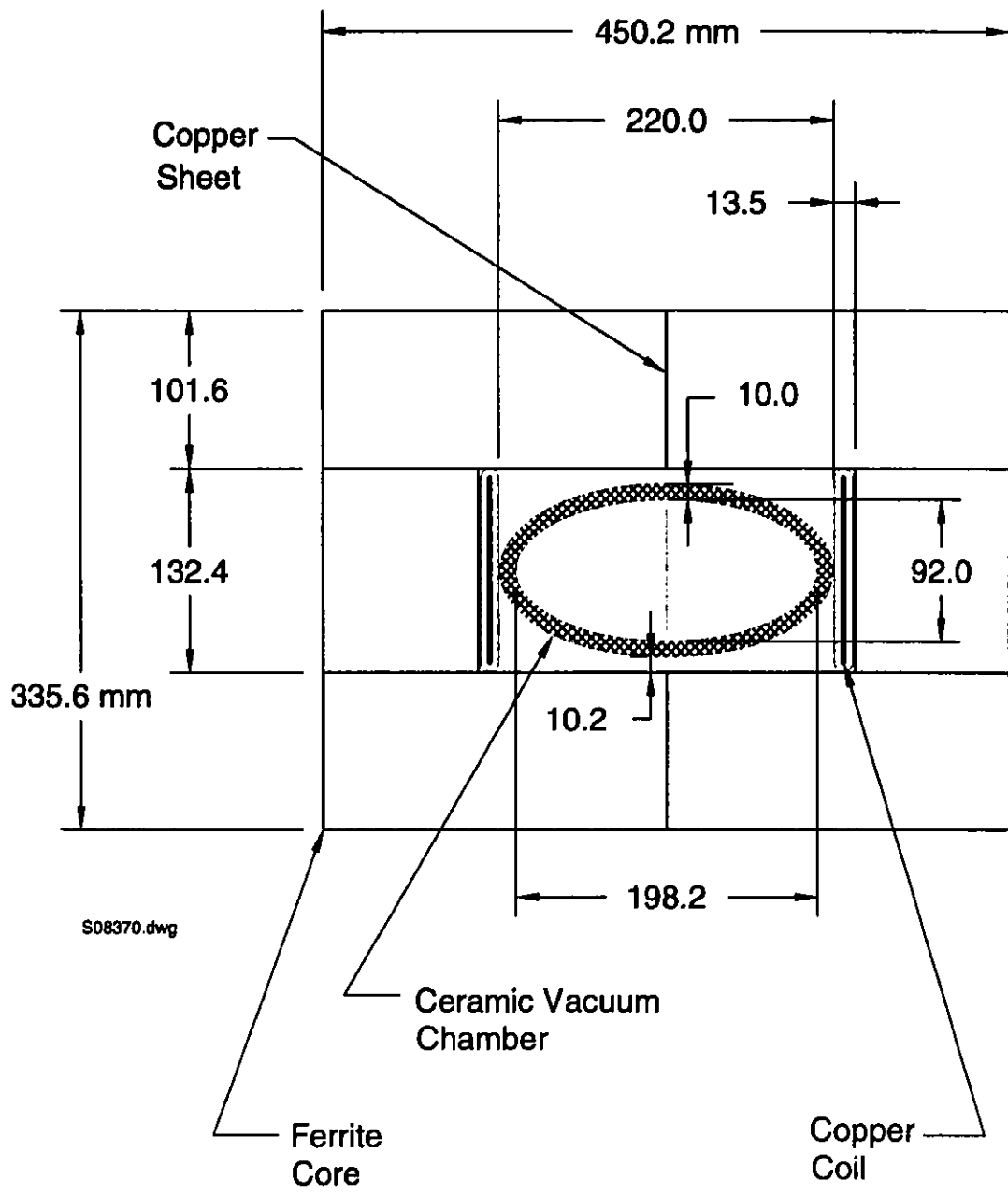
Figure II.3.4-3 Cross Section at Upstream End of Extraction Kicker A.
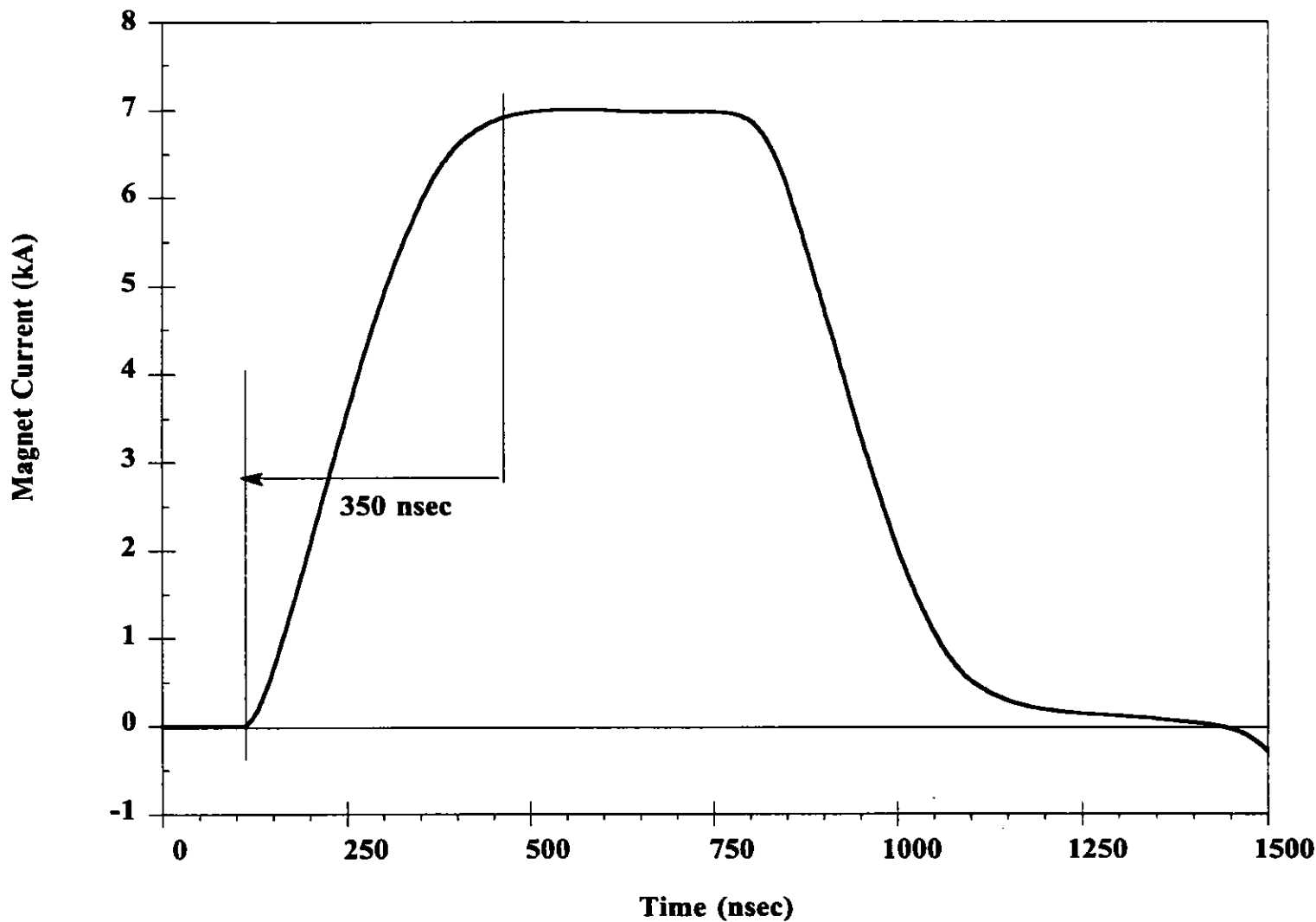
Figure II.3.4-4 Kicker Waveform.
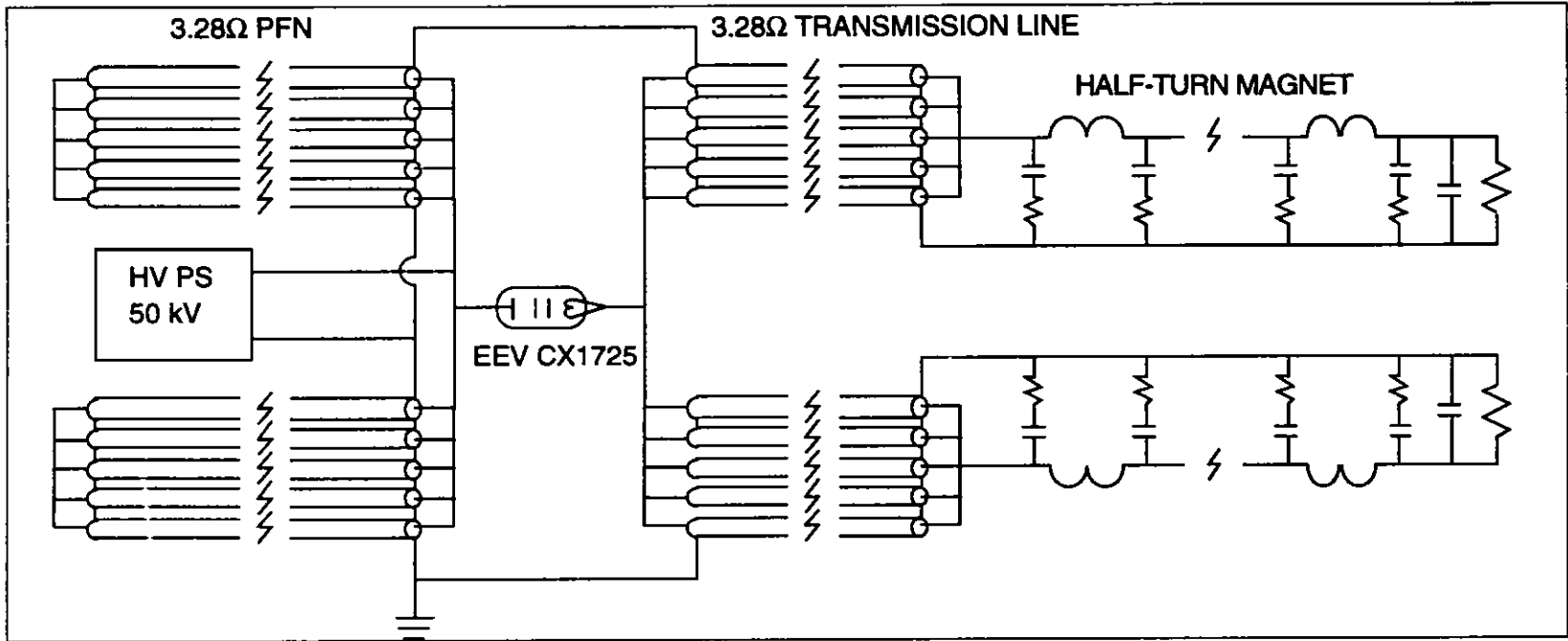
Figure II.3.4-5 Schematic of an Extraction Kicker Power Supply and Magnet.

3.5 SEPTUM MAGNETS AND POWER SUPPLIES

3.5.1 Introduction

Septum magnets are those dipole magnets that form the interfaces between the three beam transport lines and the RCS. Injection septa are required to place the incoming beam on orbit. Extraction septa accept the beam from the kicker system and bend it in order to clear the adjacent quadrupole, which requires a displacement of 0.664 m. The last injection septum element and the first extraction septum element are thin-pulsed septa. All septa are pulsed to reduce electrical power losses and to case the associated cooling requirements. The required magnet apertures for injection and extraction are defined in Sections II.2.3 and II.2.4, respectively. The thin-septum magnets are located inside the straight-section vacuum chambers. There are thin Inconel vacuum chambers inside the apertures of the other magnets.

3.5.2 Injection System

The magnets septum A and septum B are used for injection into the synchrotron. Septum A is 1.2-m long, has a field index $n = -20$, and has a curved axis to keep the beam trajectory centered in the gap. Septum B is 0.3-m long, has no field index, and is straight. Septum A and septum B are both excited with a single half-sine-wave pulse of 60 Hz. Septum B has a reset pulse of similar shape. The parameters for these two magnets are listed in Table II.3.5-1. The cross sections of septum magnets A and B are shown in Figures II.3.5-1 and II.3.5-2, respectively.

Septum A is a gradient dipole and is made with 0.36-mm-thick silicon steel laminations. The coil is made with a single size of hollow copper conductor that is insulated with mica-glass tape and vacuum-impregnated, heat-cured, radiation-resistant epoxy.

Septum B is a transformer type, with a single-turn secondary and a four-turn primary winding. The minimum total thickness of the septum is 3 mm, but the septum gradually thickens along its length to improve the magnetic, mechanical, and thermal characteristics. The design of this magnet is similar to that of the pulsed septum magnet[5] used to extract beam from the existing IPNS synchrotron. This design has proven performance and durability, >2 billion pulses at 30 Hz, and peak central fields of 1 T. The core is made with 0.36-mm-thick silicon steel laminations. The primary coil is made of hollow copper conductor that is insulated with mica-glass tape and vacuum-impregnated, heat-cured, radiation-resistant epoxy.

3.5.3 Extraction System

The septum magnets used for extraction from the synchrotron consist of a fast-pulsed septum magnet, septum C, followed by two slower-pulsed magnets, septum D and septum E.

Table II.3.5-1 Parameters for Synchrotron Injection Septum Magnets

Parameters	Septum A	Septum B	Units
Peak strength at 400 MeV	0.56	0.52	T
Field index	-20	0.0	-
Effective length	1.2	0.3	m
Gap			
Height	20	24	mm
Width	51	40	mm
Minimum septum thickness	33.4	3.0	mm
Conductor			
Height	4.2	5.0	mm
Width	4.2	5.0	mm
Hole diameter	2.4	4.9	mm
Number of turns per magnet	16	4	-
Inductance	1.1	0.023	mH
Resistance	74	3.4	mΩ
Pulse width (half-sine-wave shape)	8.3	8.3	msec
Repetition rate	30	30	Hz
Reset pulse width	-	8.3	msec
Supply current			
Maximum	568	2,533	A
rms[a]	201	1,264	A
rms current density in coil	6.2	38	A/mm^2
Peak voltage	240	306	V
Power losses	2.6	5.5	kW
Cooling circuits/magnet	4	2	-
Total water flow	1.0	1.8	gal/min
Water pressure drop	100	100	psi
Water temperature rise	11	12	°C

[a] rms = root mean square.
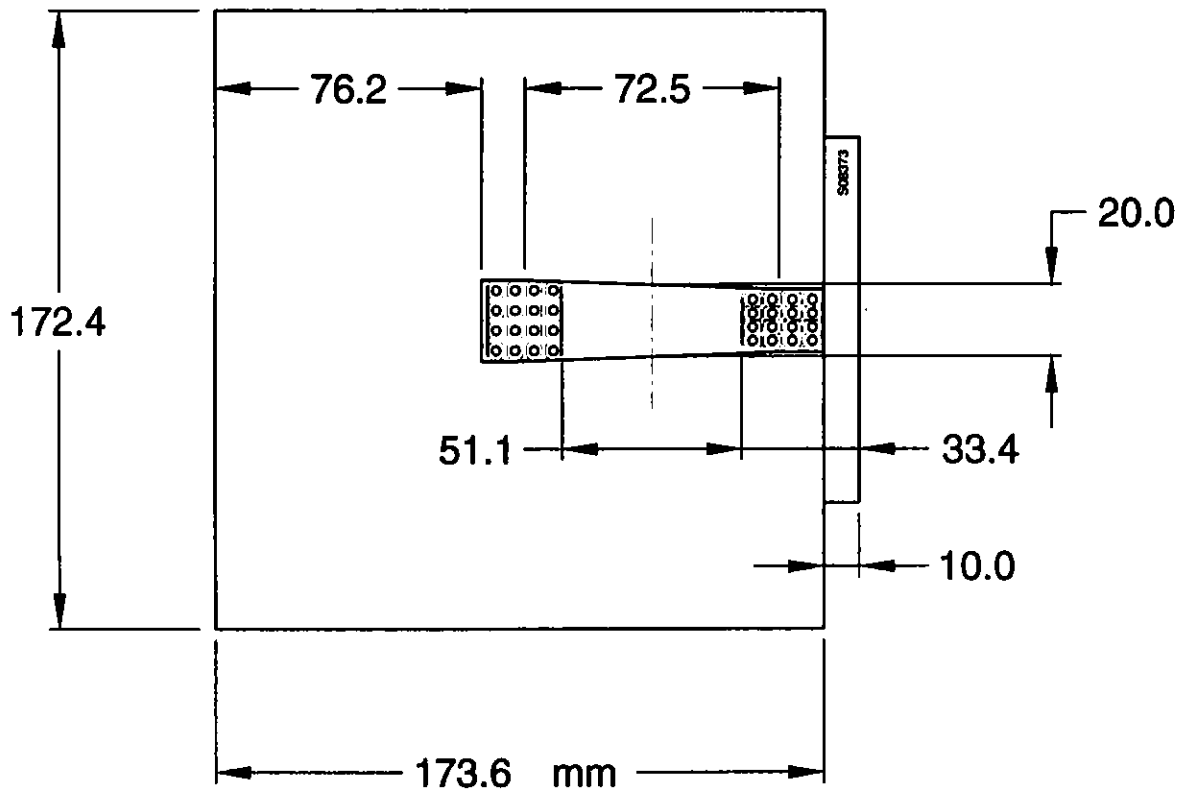
Figure II.3.5-1 Cross Section of Injection Septum A.
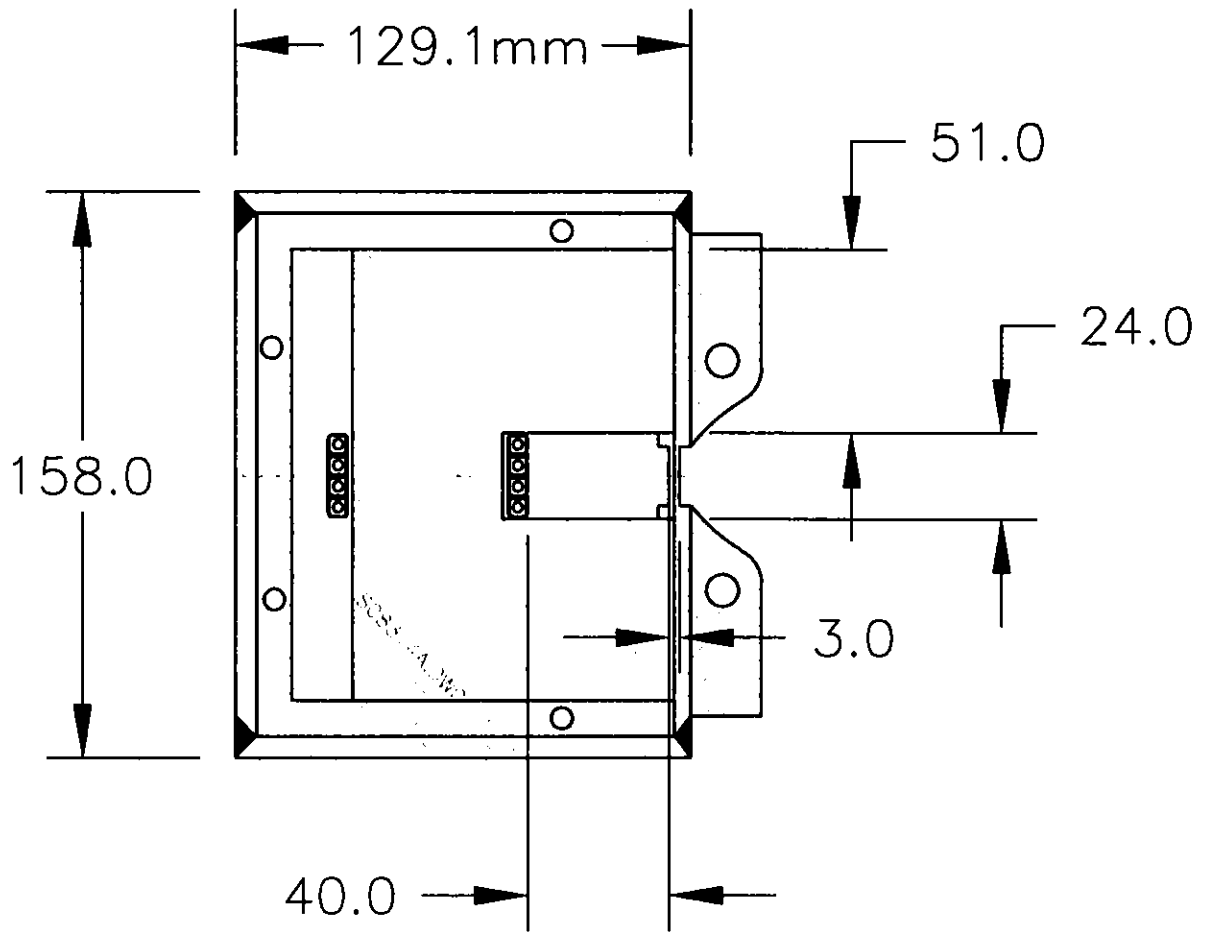
Figure II.3.5-2 Cross Section of Injection Septum B.

The axis of septum C is straight. The axes of septum D and septum E are curved to keep the magnet apertures as small as possible and to allow for thicker septa. The parameters for these three magnets are listed in Table II.3.5-2. The cross sections of septum C, septum D, and septum E are shown in Figures II.3.5-3, II.3.5-4, and II.3.5-5, respectively.

3.5.4 Septum-Magnet Power Supplies

There are eight septum magnets, as listed in Table II.3.5-3. Septum A and septum B are used for injection from the LET into the RCS; septum C, septum D, and septum E are used for extraction into the HET lines. All eight septum power supplies are designed for 30-Hz operation. They have the same components except for the charging-power supplies, the output capacitor banks, the chokes used for energy recovery from the five thick septa, and the impedance-matching transformers that are used with the three thin septa. Using the same components minimizes the spare parts count. The basic capacitor discharge power supply is shown in Figure II.3.5-6.

All magnets have a half-sine-wave discharge pulse width of 8.3 msec, except for septum C, which has a 1-msec discharge pulse. All septum power supplies use energy recovery. The thin septa get the correct polarity back on the discharge capacitor bank by means of a reset pulse through the magnets. The thick septa get the correct polarity back on the discharge capacitor bank by means of a reset pulse using a choke in place of the magnet. The peak current in all septa is repeatable within ±0.05%. The magnet and power supply parameters are given in Table II.3.5-3.

Table II.3.5-2 Parameters for Synchrotron Extraction Septum Magnets

Parameters	Septum C	Septum D	Septum E	Units
Peak strength at 2.0 GeV	1.02	1.30	1.30	T
Effective length	0.5	1.5	0.9	m
Gap				
Height	70	90	110	mm
Width	122	102	70	mm
Minimum septum thickness	6.0	57.1	227.7	mm
Conductor				
Height	7.3	7.9/12.0	12.3	mm
Width	7.3	7.9/12.0	12.3	mm
Hole diameter	4.1	4.4/6.6	6.8	mm
Number of turns per magnet	8	48	64	-
Number of parallel conductors	1	1	2	-
Inductance	0.072	9.2	6.4	mH
Resistance	6.1	47	15	mΩ
Pulse width (half-sine-wave shape)	1	8.33	8.33	msec
Repetition rate	30	30	30	Hz
Reset pulse width	1	-	-	msec
Supply current				
Maximum	7,268	1,982	1,817	A
rms	1,259	699	641	A
rms current density in coil	18	8.7/3.6	1.8	A/mm^2
Peak voltage	1,688	3,679	5,083	V
Power losses	12.2	35.8	12.6	kW
Cooling circuits/magnet	4	8	4	-
Total water flow	7.0	9.0	4.3	gal/min
Water pressure drop	100	100	100	psi
Water temperature rise	7	15	11	°C

[a] rms = root mean square.
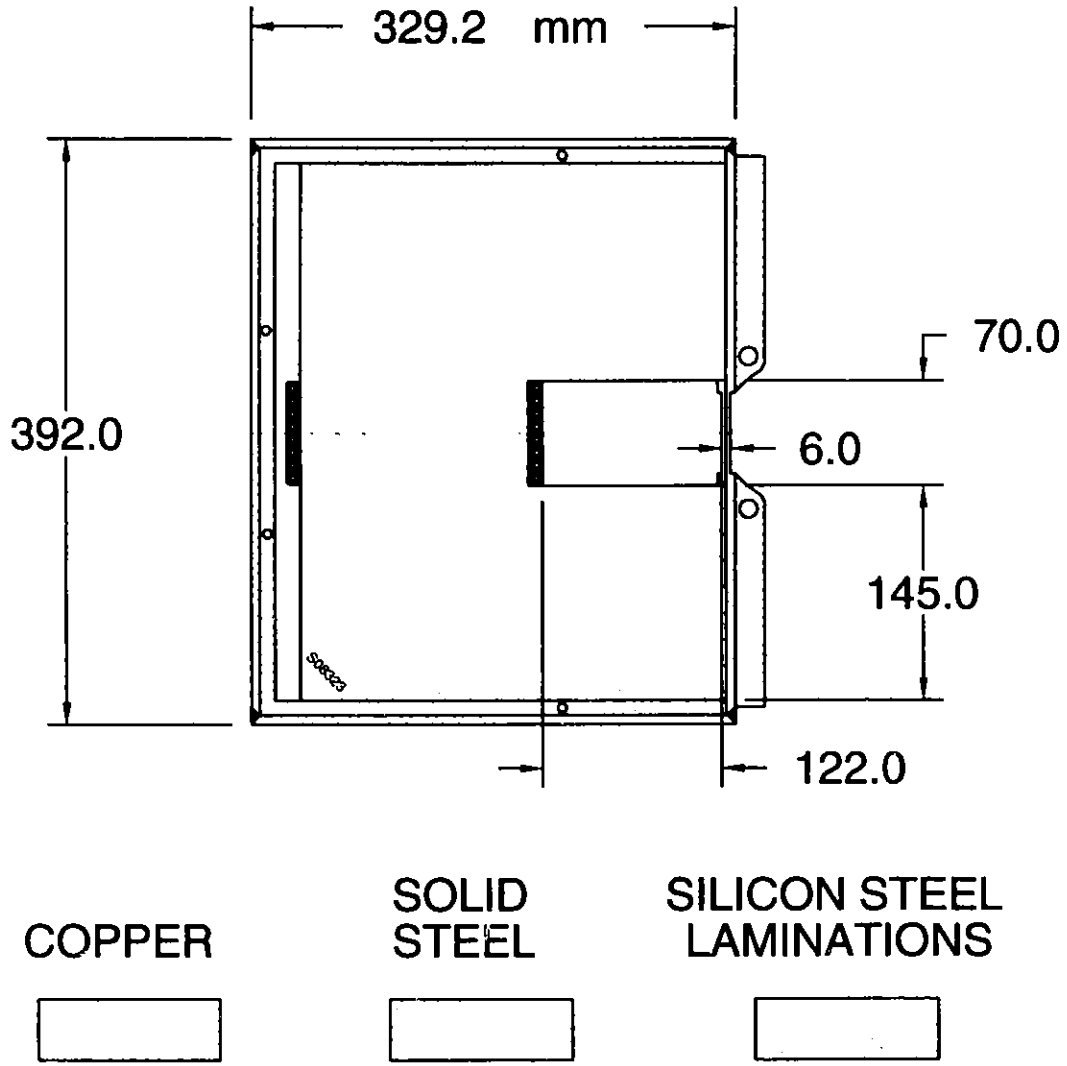
Figure II.3.5-3 Cross Section of Extraction Septum C.
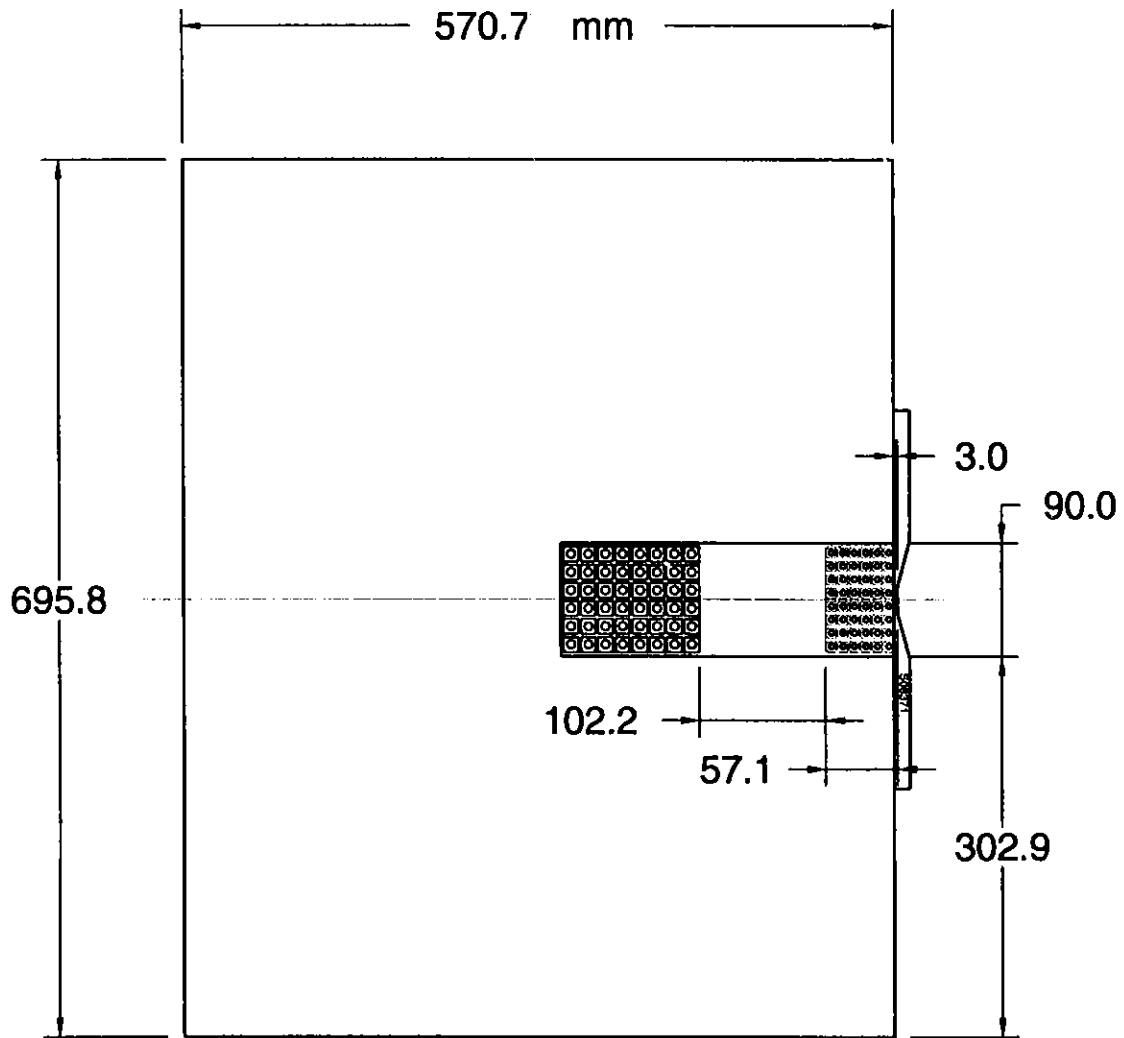
Figure II.3.5-4 Cross Section of Extraction Septum D.
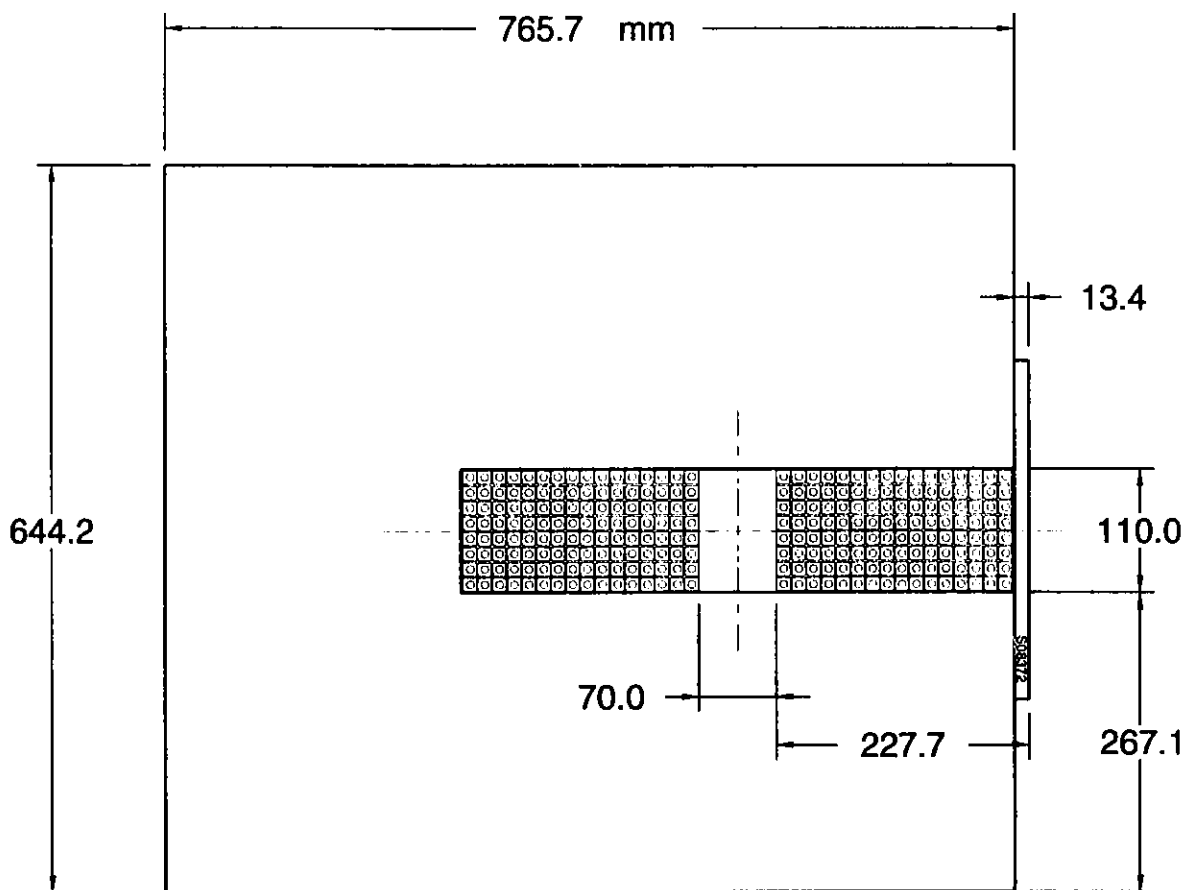
Figure II.3.5-5 Cross Section of Extraction Septum E.

Table II.3.5-3 Septum Magnet Power Supply Parameters for 2.2-GeV Operation

Location	LET	LET	HET	HET	HET	Units
Septum	A	B	C	D	E	-
Type	Thick	Thin	Thin	Thick	Thick	-
Number of magnets	1	1	2	2	2	-
Pulse width (half-sine wave)	8.3	8.3	1.0	8.3	8.3	msec
Repetition rate	30	30	30	30	30	Hz
PS[a] peak current	625	2,786	8,484	1,958	1,579	A
PS rms current	258	267	1,470	691	557	A
PS peak voltage	240	306	1,688	3,679	5,083	V
Magnet resistance	74	3.4	6.1	47	15	$m\Omega$
Magnet inductance	1.1	0.023	0.072	9.2	6.4	mH

[a] PS = power supply.
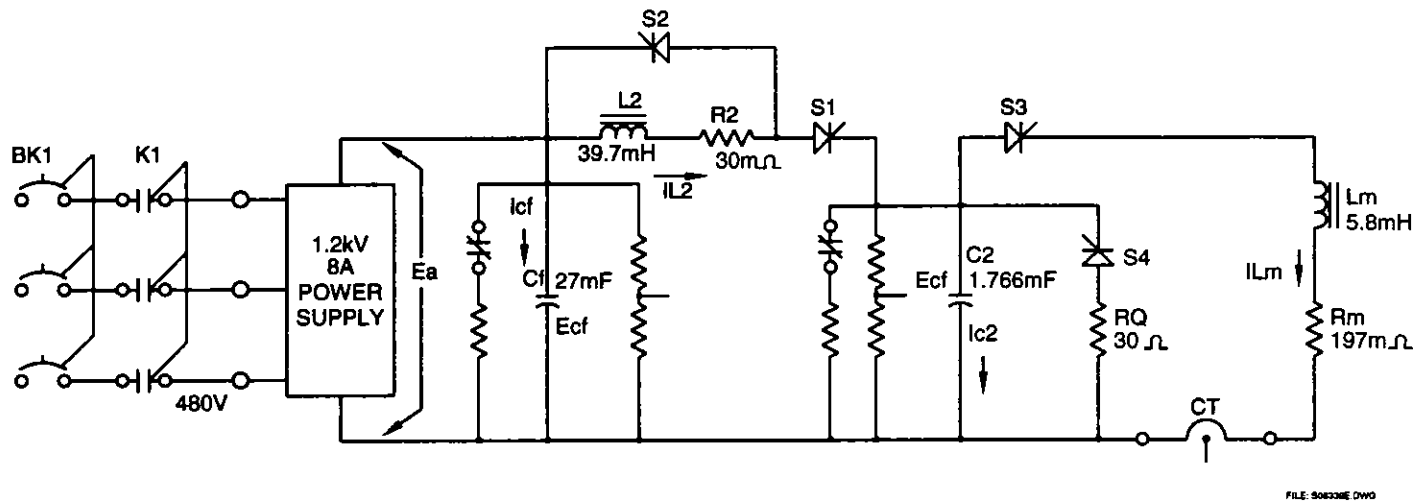
Figure II.3.5-6 Basic Septum Magnet Power Supply.

3.6 MAGNET SUPPORTS

3.6.1 Synchrotron

The synchrotron beam height is located 1.4 m above the floor. A structure that allows for both linear adjustments of ±25 mm in all three directions and angular adjustments of more than 50 mrad around all three axes is located between the bottom of the dipole and the floor. The dipole support shown in Figure II.3.6-1 includes an X-Y adjustor that is secured to the floor and a Z adjustor that is attached to the movable member. The Z adjustor incorporates a three-point support using fine-thread screws with spherical heads at each point, each of which can be adjusted and locked.

The quadrupole is held in place by a support structure similar to that for the dipole, but there is an additional weldment extending between the X-Y-Z adjustor on the floor and the bottom of the magnet. This support is shown in Figure II.3.6-1. There are outline representations of a sextupole and a horizontal correction dipole to show relative sizes and real estate usage. These smaller magnets have support hardware extending down to the quadrupole weldment, allowing them to be adjusted relative to the quadrupole.

3.6.2 Transport Lines

All of the transport-line dipoles have separate support stands and X-Y-Z adjustors. Quadrupoles and nearby correction dipoles are supported by a single stand and adjustor. The correctors are mounted to the associated quadrupole.

Dipole   Sextupole Quadrupole   Dipole

|← —— 1.3 ——— →|← 0.8 →|← 0.5 →|← 0.8 ——— →|← —— 1.3 —— →|

Horizontal
Dipole
Corrector

1.4M

0   1   2

s08315.dwg

METERS
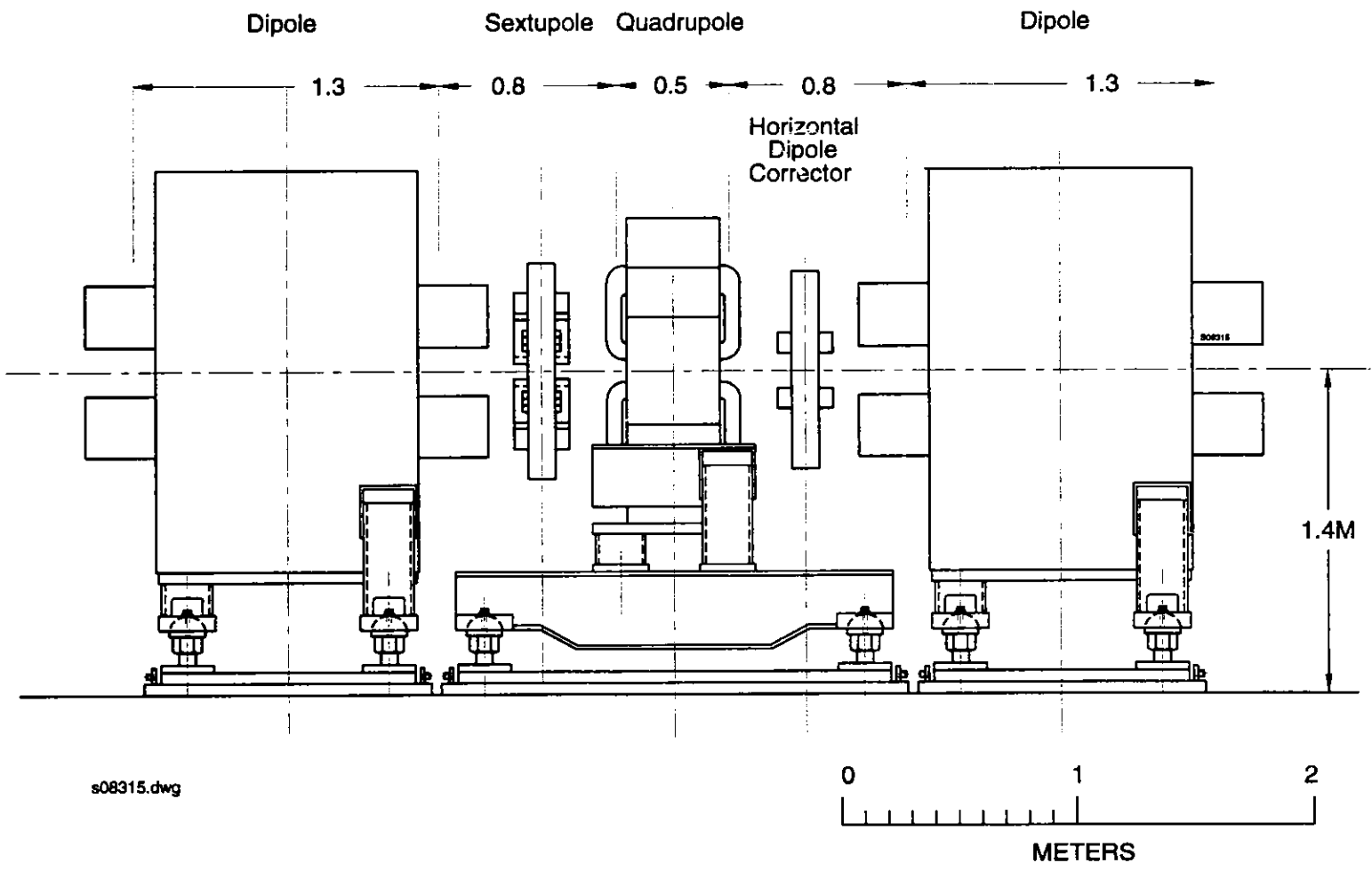
Figure II.3.6-1 Supports for the RCS Ring Magnets. (Dimensions are effective lengths.)

3.7 REFERENCES

1. Code OPERA-2d (formerly referred to as PE2D) is available from Vector Fields, Inc., Aurora, Illinois.

2. K. Kim et al., "Design and tests of the injector synchrotron magnets for the 7-GeV Advanced Photon Source," in *Proceedings of the 1993 IEEE Particle Accelerator Conference*, p. 2808 (1993).

3. K.M. Thompson, "An interactive computer program for the design and costing of magnets," in *Proceedings of the 8th International Conference on Magnet Technology* (Grenoble, France, 1983).

4. *7-GeV Advanced Photon Source: Conceptual Design Report*, Argonne National Laboratory Report No. ANL-87-15 (Apr. 1987).

5. M. Foss, K. Thompson, and W. Praeg, "A transformer septum magnet," IEEE Trans. Nucl. Sci. **NS-26**, 4024 (1979).

4.1 RF VOLTAGE PROGRAM

4.1.1 Introduction

The key design feature of the RCS is the prevention of beam loss during the injection, capture, and acceleration processes. Beam loss is prevented by providing large dynamic apertures in both transverse planes and by tailoring the injected beam bunch and the rf bucket areas to facilitate longitudinal motion without losses. In this section, we describe the rf voltage programming for beam capture and acceleration.

The rf system of the RCS has a harmonic number equal to one, which provides a time gap in the accelerated beam that facilitates fast kicker operation for clean extraction. The rf system has a modest frequency swing of 1.12-1.50 MHz, as shown in Figure II.4.1-1a. The maximum energy gain per turn is 81.4 keV, occurring at $\dot{B}_{max}$, where B is the sinusoidal ring magnet dipole field discussed in Section II.2.1.2. The energy gain per turn is shown in Figure II.4.1-1b. The $\dot{B}_{max}$ occurs at 12.5 msec into the acceleration cycle. The peak voltage requirement is estimated on the basis of $\dot{B}_{max}$ and the bucket acceptance.

The incoming linac beam energy spread[1] is expected to be about ±2.5 MeV. The circumference of the RCS is equivalent to 890 nsec of revolution time at injection. Therefore, a circulating dc beam has a bunch area of about 4.5 eV sec. This number is the starting point for bucket area considerations, which also take into account a dilution factor from bunch to bucket and chopped beam injection from the linac to tailor the bunch.

Simulation studies have shown that implementation of adiabatic capture,[2] which captures the entire linac macro-pulse, is impractical, due to the lack of a long "flat-bottom field" in the RCS. Another way to achieve 100% capture is to inject chopped linac macro-pulses into a waiting bucket. Our studies show that the best capture efficiency is achieved with 25% chopping. The disadvantage is that 25% of the linac beam is discarded, so better ion source performance is required.

Under the best circumstances, the adiabatic capture process provides a phase space dilution factor of $\pi/2$. Using that as a guide, we decided to allow a factor of about two in phase space dilution during the capture process, which makes the bucket area of the RCS equal to 9 eV sec soon after injection. This bucket area is sufficient to contain the beam during the initial stages of acceleration, when the space charge forces are largest. The space charge self-fields in the longitudinal direction vary as the inverse of the energy squared. In the later stages of the acceleration period, the bucket area is adjusted to increase the momentum spread of the bunch, to prevent instabilities.

In the following sections, we discuss the rf voltage programming that was obtained from tracking simulation studies. These studies take into account space charge effects and have been used to achieve low loss conditions during injection, capture, and acceleration, while maintaining a
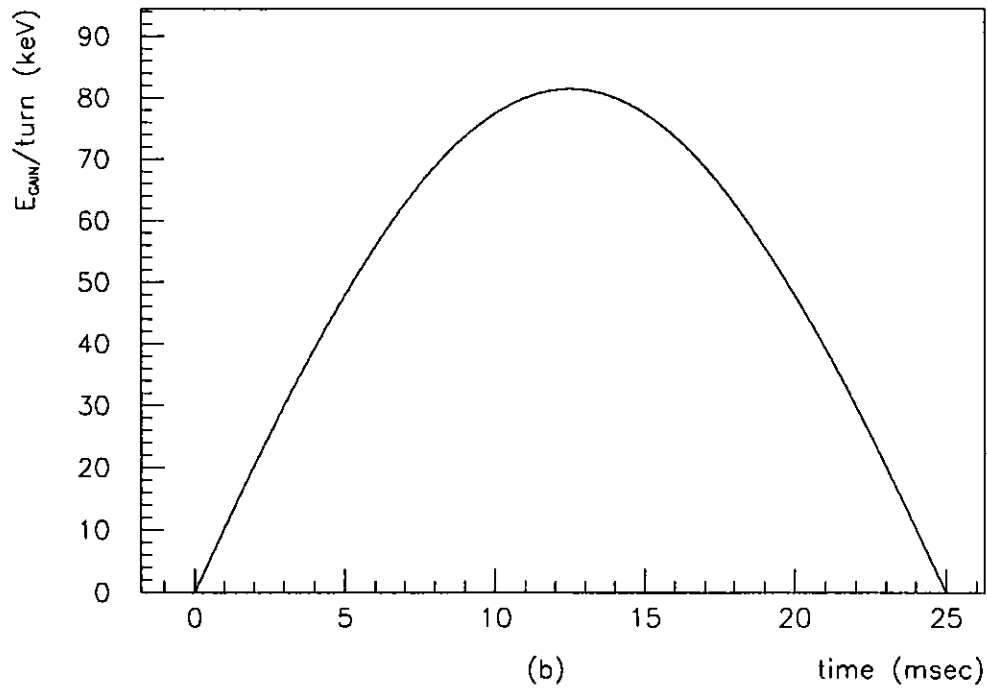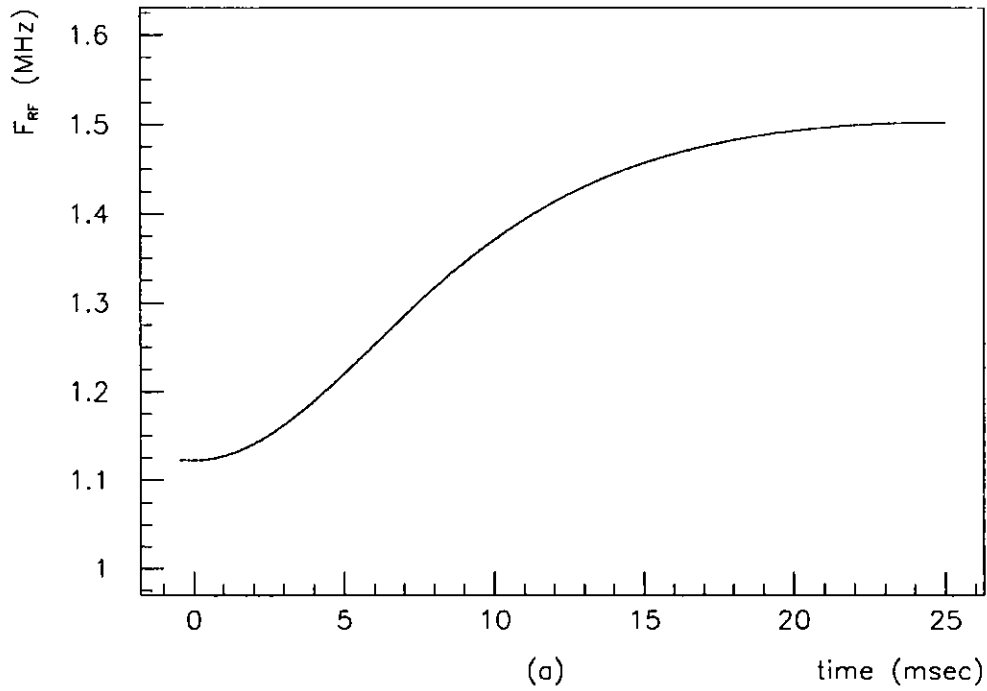
Figure II.4.1-1 (a) The rf Frequency of the RCS from Injection to Extraction and (b) Energy Increase per Revolution of the Synchronous Particle. (Beginning of the accelerator clock is at t = 0.)

large momentum spread to avoid the microwave instability. We discuss the algorithm used in the tracking studies and then present the rf voltage programming for the capture and acceleration processes that best meets the requirements.

4.1.2 Longitudinal Tracking Studies

The tracking studies are carried out using a Monte Carlo method according to the following algorithm:

- The incoming linac beam particle is represented by its energy deviation from the central energy, ΔE, and its phase coordinate, ϕ. The value of ϕ can range from -180° to 180° for unchopped beam injection or from -135° to 135° for 25% chopped beam injection.

- The accumulation of 561 turns during the 0.5-msec injection period is simulated turn-by-turn in order to understand the dynamics during accumulation with the rf voltage on.

- Macro-particle representation is used to describe the total charge in the bunch.

- The initial coordinates of each macro-particle, ΔE and ϕ, and the injection-turn number are retained throughout the calculation. Knowledge of the injection conditions of lost particles is used to minimize beam loss. This information is useful in designing a chopping system.

- At any point in time, the energy deviation and phase of all particles can be projected to the energy and phase coordinate axes to show the distributions of these quantities. The ΔE and ϕ projections give the momentum spread and length of the bunch, respectively.

- A set of finite-difference recurrence equations suitable for numerical calculations is used to track the particles.

- The recurrence relations follow a time-stepping leapfrog method. When the particle motion is slowly varying, a large time-step is used to expedite the calculation. The recurrence relations are recalculated with this larger step size.

We assume that there is a synchronous particle that remains on the equilibrium orbit whose energy is denoted by E_s. The Hamiltonian, H, for longitudinal motion in a synchrotron,[3] including space charge forces, for a particle of energy E and phase ϕ is

$$H = \frac{h\eta_s}{\beta_s^2}\frac{\omega_s^2}{E_s}W^2 + \frac{d\phi_s}{dt}W + \frac{eV}{2\pi}\left(\cos\phi + \phi\sin\phi_s - \cos\phi_s - \phi_s\sin\phi_s\right) - \frac{e^2 g_0 h^2}{4\pi\varepsilon_0\gamma_s^2 R}\lambda(\phi), \qquad \text{(II.4.1-1)}$$

where the subscript s refers to the synchronous particle and

h = harmonic number,

η_s = $1/\gamma_t^2 - 1/\gamma_s^2$,

ω_s = angular revolution frequency,

β_s, γ_s = relativistic factors,

γ_t = transition energy

ϕ_s = rf phase of the synchronous particle,

e = electric charge,

t = time,

V = peak rf voltage,

ε_0 = vacuum permittivity,

R = average ring radius,

λ = linear particle density, and

g_0 = capacitive geometrical factor = $1 + 2\ln(b/a)$, where a is the beam radius and b is the vacuum chamber radius.

We define $W = (E - E_s)/\omega_s$, such that $dW \cdot d\phi$ is conserved. The last term in Equation II.4.1-1 represents the space charge potential. The sign of the space charge term is opposite to that of the rf potential; thus, the space charge reduces the restoring force and changes the bucket shape.

The differential equations of motion derived from this Hamiltonian describe the time-evolution of a particle subject to an accelerating force that depends on the rf phase and to the space charge forces that act on the particle. These differential equations of motion are solved numerically by using leapfrog difference equations.[3] The leapfrog algorithm advances the coordinates of each particle, W and ϕ, by a specified time-step, τ, according to

$$\phi_{n+1} = \phi_n + h\tau\left(\frac{\eta_s\omega_s^2}{\beta_s^2 E_s}W\right)_{n+\frac{1}{2}} + \phi_{s,n+\frac{1}{2}} - \phi_{s,n-\frac{1}{2}} \qquad (II.4.1\text{-}2)$$

and

$$W_{n+\frac{1}{2}} = W_{n-\frac{1}{2}} + \frac{eV\tau}{2\pi}\left(\sin\phi_n - \sin\phi_{s,n}\right) + \frac{e^2 g_0 h^2 \tau}{4\pi\varepsilon_0 R\gamma_s^2}\left(\frac{d\lambda(\phi)}{d\phi}\right)_n , \qquad \text{(II.4.1-3)}$$

where the subscript n indicates that a quantity is to be calculated at a time $t = n\tau$. The values of the ϕ coordinates are calculated at integer time-steps, and the values of W are calculated at half-integer time-steps. The last two terms in Equation II.4.1-2 account for the changes in ϕ_s.

The numerical simulation of the injection, capture, and acceleration processes follows an ensemble of macro-particles, whose initial coordinates in phase and energy are chosen according to a specified distribution. A total of 10^4 macro-particles is used to represent the 10^{14} protons in the bunch.

The turn-by-turn injection process is simulated by randomly placing N_p/N_t macro-particles into the machine. Here, N_p is the total number of macro-particles, and N_t is the total number of injection turns. The particles are distributed uniformly in phase within the maximum and minimum values of the chopped beam. The energy distribution follows a cosine function from $-\pi/2$ to $\pi/2$, where the base is equal to ± 2.5 MeV. The particle distribution rapidly becomes governed by the synchrotron oscillations and is fairly insensitive to the initial energy distribution chosen.

During injection, the time-step size is equal to the revolution period. At each turn, the W coordinates of the N_p/N_t injected particles are advanced by a half-step. In the first half-step of each injection turn, the space charge forces due to the incoming particles are small and are neglected. In the iteration process, all the particles, including the most recently injected, are advanced in ϕ by a time-step according to Equation II.4.1-2. The space charge forces due to all particles present in the ring are then calculated, and their contribution is used in Equation II.4.1-3 to advance the W coordinates by a time-step.

During the acceleration process, the time-step size can be increased to reduce computer time, but it must be kept smaller than the synchrotron oscillation period, τ_s. In the simulations, the time-step size is kept smaller than $\tau_s/30$.

The initial phase space coordinates for each particle are saved. The analysis of lost particles using these parameters permits the design of a more efficient injection scheme by depopulating the undesirable phase space. The vacuum chamber wall is represented by a momentum cutoff of $\Delta p/p = 0.05$. A particle outside the separatrix at a given time, but with momentum $\Delta p/p < 0.05$, contributes to the space charge self-field and may be recaptured later in the cycle. The particle can also hit the vacuum chamber wall. In that case, the particle is removed from the calculations, so it cannot contribute to the space charge forces. In our tests, an average delay of 2 msec is observed between the time a particle leaves the separatrix and the time it hits the vacuum chamber wall.

To reduce the statistical fluctuations due to the relatively coarse ensemble of macro-particles used in the simulations, the projected phase distribution is binned by using the cloud-in-cell method. For each particle, a weighted contribution is assigned to the two closest grid points, according to how far the particle is from these points. The cell grid is chosen fine enough to describe the structure of the particle distribution in a bunch, yet coarse enough to attenuate the short wavelength noise due to the statistical fluctuations in a cell. The data are then fast-Fourier-transformed and filtered to reduce the Gibbs phenomenon. Our studies show that for the bunch lengths considered, cutoff frequencies ranging from the 9th to 11th harmonics reduce noise. The underestimation of the peak and overestimation of the bunch ends, introduced by the filtering process, are acceptable. As the bunch length shortens during the cycle, higher cutoff frequencies are used.

The simulation code was tested extensively. The code was checked for the correct stationary and moving buckets in the absence of space charge forces. The program was run above the transition energy by reversing the sign of the slip factor, η_s, to produce the negative mass instability. The rf voltage was turned off and space charge forces were included to verify that the negative mass instability appears with the correct threshold and correct growth rate. The simulation result for the negative mass instability threshold energy spread is 1.15 MeV, compared to the analytical prediction of 1.12 MeV. The growth rates for several perturbed density distributions were also in good agreement with the analytical values. For a beam with an initial energy spread of ± 1 MeV, perturbed by a density modulation of harmonic 2 and amplitude 0.1 MeV, a growth rate of 0.042 msec was obtained, compared to the analytical value of 0.040 msec.

The capture efficiency was studied for several scenarios of rf programming, initial phase space distribution of the injected particles, and chopping of the linac beam.[4] For each case, the momentum spread of the beam was tested against the theoretical microwave instability threshold at different times in the cycle. These studies led to the establishment of the rf programming and injected beam parameters that best meet the requirements of low loss and high microwave instability threshold. The rf programming is presented in the next section.

4.1.3 RF Voltage Program for Capture and Acceleration

The rf voltage program for the injection and acceleration cycles is depicted in Figure II.4.1-2. The time variation of the bucket and bunch areas is shown in Figure II.4.1-3. Details of the rf program and the bucket and bunch area variations during the injection period are shown in the inserts in these figures. The beginning of the acceleration clock is indicated by $t = 0$.

A beam with ± 2.5 MeV energy spread ($\Delta p/p = 3.7 \times 10^{-3}$), occupying 75% of the ring, is injected in 561 turns, which corresponds to an injection time of 0.5 msec. Since the variation of the magnetic field is negligible during that period, ϕ_s is assumed to be zero during injection. The bunch area of the injected beam is 3.3 eV sec.
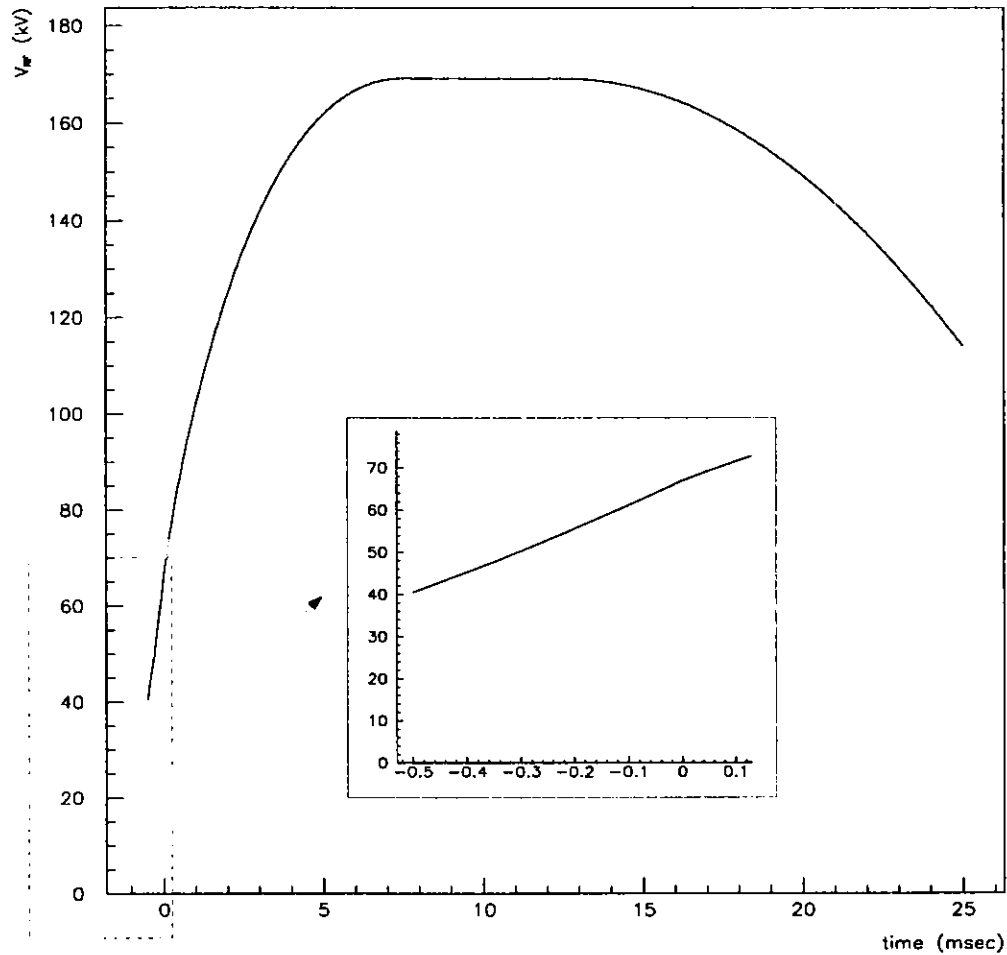
Figure II.4.1-2 Radio-Frequency Voltage Program for the Injection and Acceleration Cycles.
(The beginning of the acceleration clock is at t = 0. The insert shows the details of the
voltage program during injection. The voltage is chosen to maintain a constant
bucket area from the end of injection to 7.5 msec. The voltage for the
remainder of the cycle is adjusted to keep the beam below the
longitudinal microwave instability threshold.)
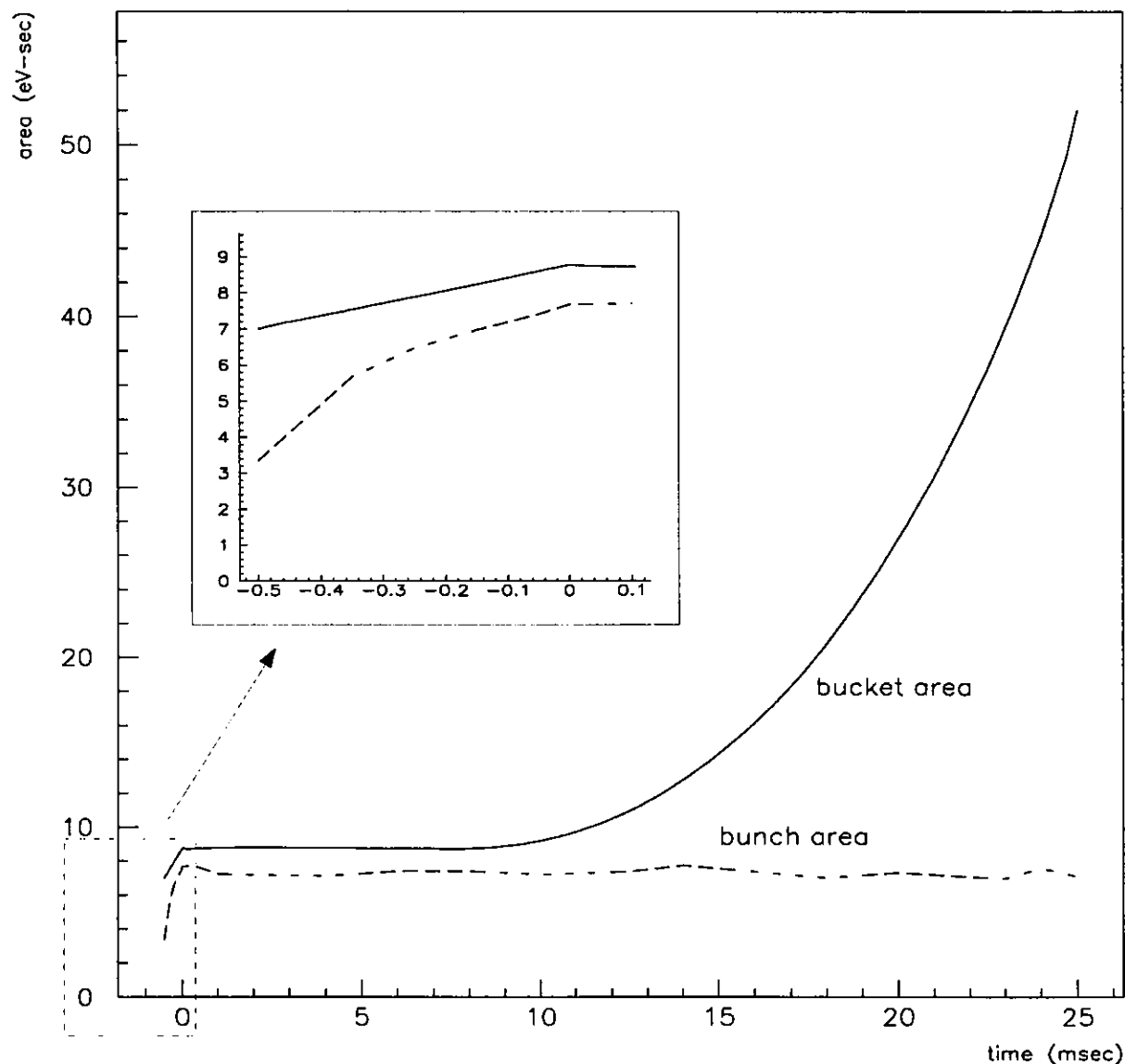
Figure II.4.1-3 Bucket and Bunch Areas, Obtained from the Simulation under the rf Voltage Program, Plotted as a Function of Time. (The injected beam has a ±2.5 MeV energy spread and occupies 75% of the ring. Details of the variations during injection are shown in the insert. The small variations in the bunch area are due to the Monte Carlo statistics.)

To prevent unnecessary dilution of the beam and thus avoid large voltages at later stages, the initial voltage was set as low as possible. The minimum voltage required to contain the beam during the initial injection is 40.5 kV. Figure II.4.1-4 depicts the bucket area formed by this voltage and the particle distribution of the first injected turn. The figure shows that 40.5 kV provides the necessary bucket height at the edges of the ± 2.5 MeV beam chopped by 25%. The corresponding bucket area of 7 eV sec allows an initial phase space dilution factor of two. During injection, the voltage must be increased from 40.5 kV to 66.9 kV to prevent beam loss. This rapid voltage rise is crucial to overcome space charge forces. The space charge forces increase with increasing particle density, which can lead to a reduction of as much as 50% in the bucket area. The bucket area changes from 7 to 9 eV sec during the injection period, as can be seen in Figure II.4.1-3. The bunch area grows from its initial value of 3.3 eV sec to 7.3 eV sec over the injection cycle, giving a dilution factor of 2.2. The bunch has undergone about 1.4 synchrotron oscillations during this period. The bunch area stays at 7.3 eV sec for the remainder of the cycle.

The 9 eV sec bucket area is maintained constant during the first 7.5 msec of the acceleration period. The voltage reaches a maximum of 169.2 kV at the end of this period. It should be noted that the maximum voltage does not occur at 12.5 msec, when $\dot{B}$ is at a maximum, but occurs at 7.5 msec, because η_s varies during acceleration.

In the remaining part of the cycle, the energy spread of the beam is controlled by manipulating the bucket area. As detailed in Section II.5.3, the $\Delta p/p$ requirement for longitudinal stability is met by making the bucket area large. Figure II.4.1-5a shows the $\Delta p/p$ variation from injection to extraction. The value of $\Delta p/p$ varies rapidly during injection, from 0.4% to 1.0% in 0.5 msec. It reaches a maximum of 1.2% at 2 msec of acceleration and decreases to a value of 0.8% at the end of the cycle. The bucket and bunch heights are shown in Figure II.4.1-5b.

From 7.5 msec to 12.5 msec, the bucket area increases from 9.0 to 11.3 eV sec while the voltage is maintained at 169.2 kV. The voltage is then decreased from 169.2 kV to 113.9 kV at extraction. The rf voltage for the latter part of the cycle is kept high, which causes the bucket area to increase, as shown in Figure II.4.1-3. The need to keep the voltage high is a consequence of the following phenomena: The value of $\dot{B}$ decreases rapidly and becomes zero at the peak field. Therefore, the synchronous phase angle also rapidly approaches 0° at the same time, as shown in Figure II.4.1-6a. In order for the particles in the bunch to follow this rapidly changing ϕ_s, they must have a synchrotron motion fast enough to follow the change in stable phase angle. A synchrotron frequency of about 1 kHz is required. Figure II.4.1-6b shows the synchrotron frequency through the acceleration cycle.

The phase space distributions from this simulation study are shown in Figures II.4.1-7 and II.4.1-8. The plots in Figure II.4.1-7 show the distributions at the earlier stages of injection and acceleration, while those in Figure II.4.1-8 show the distributions at later stages.
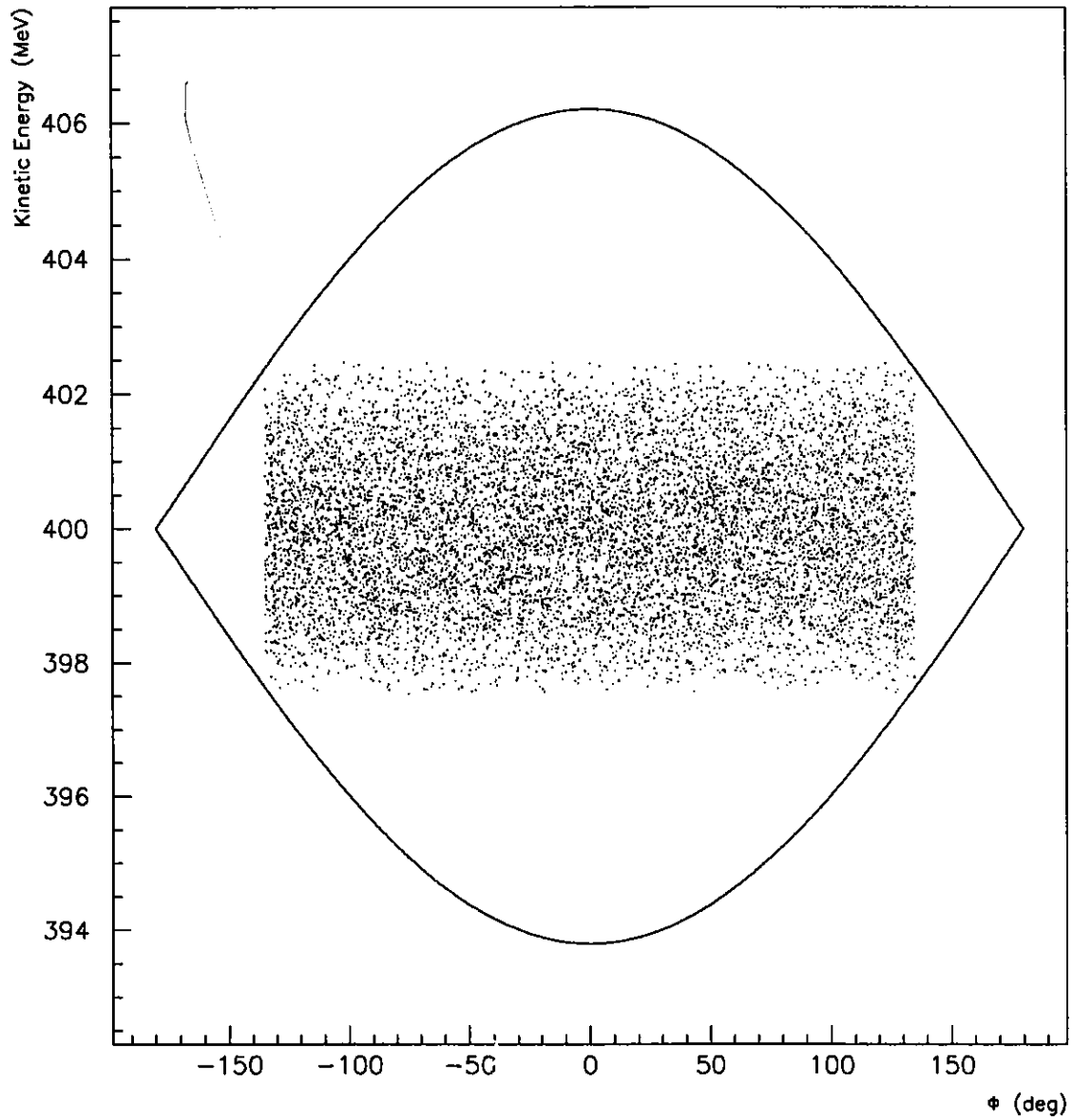
Figure II.4.1-4 Particle Distribution of the First Injected Turn. (The rf voltage of 40.5 kV provides the necessary bucket height to contain the ±2.5 MeV beam chopped at 25%. The bucket area is 7 eV sec and the bunch area is 3.3 eV sec.)
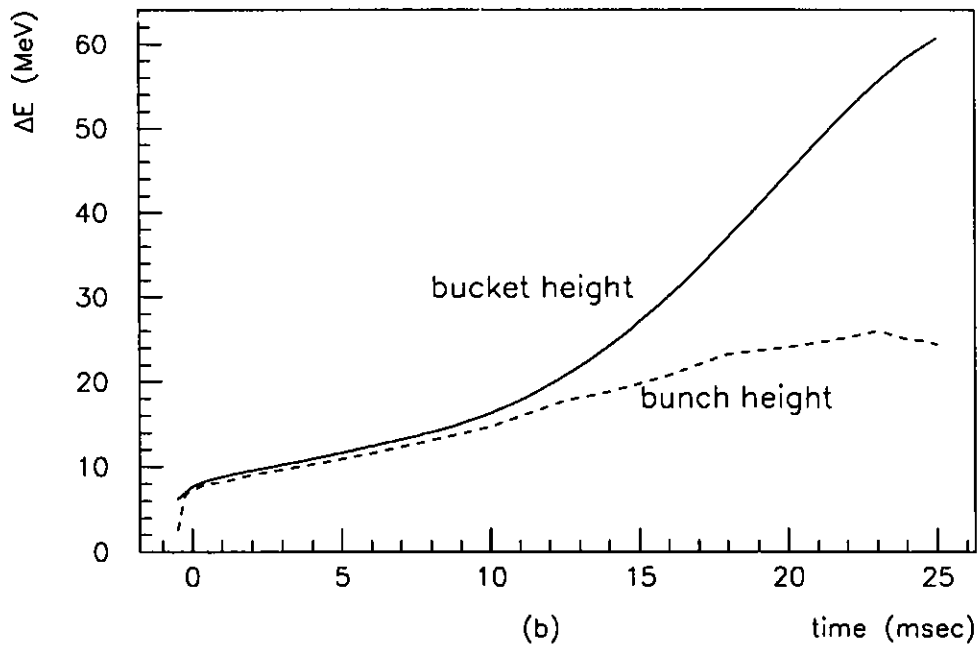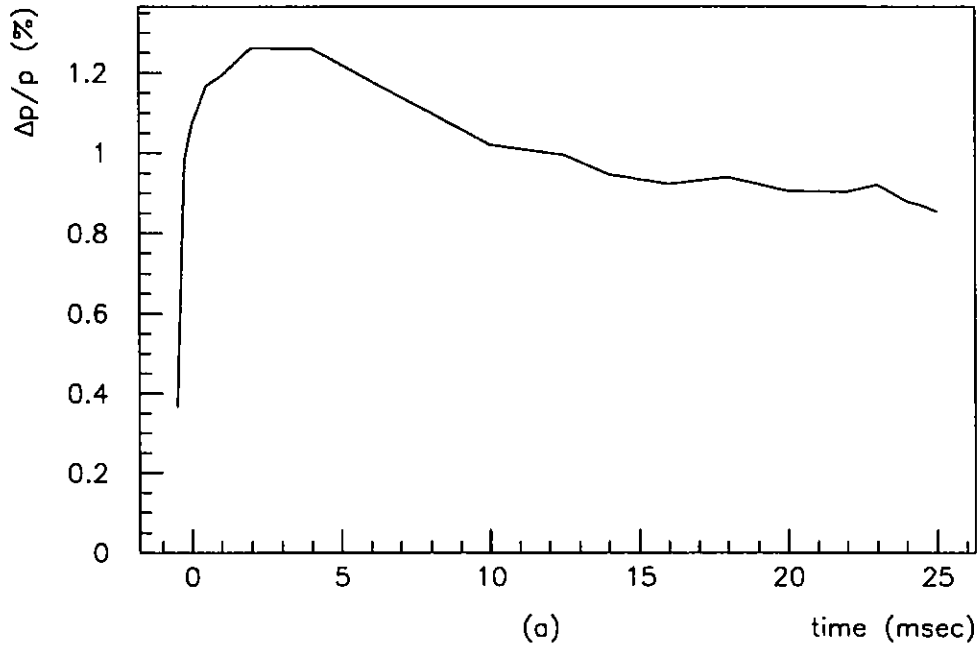
Figure II.4.1-5 (a) Half-Width of the Full Momentum Spread of the Bunch Obtained from the Simulation as a Function of Time; (b) Bucket and Bunch Height Growth from Injection to Extraction.
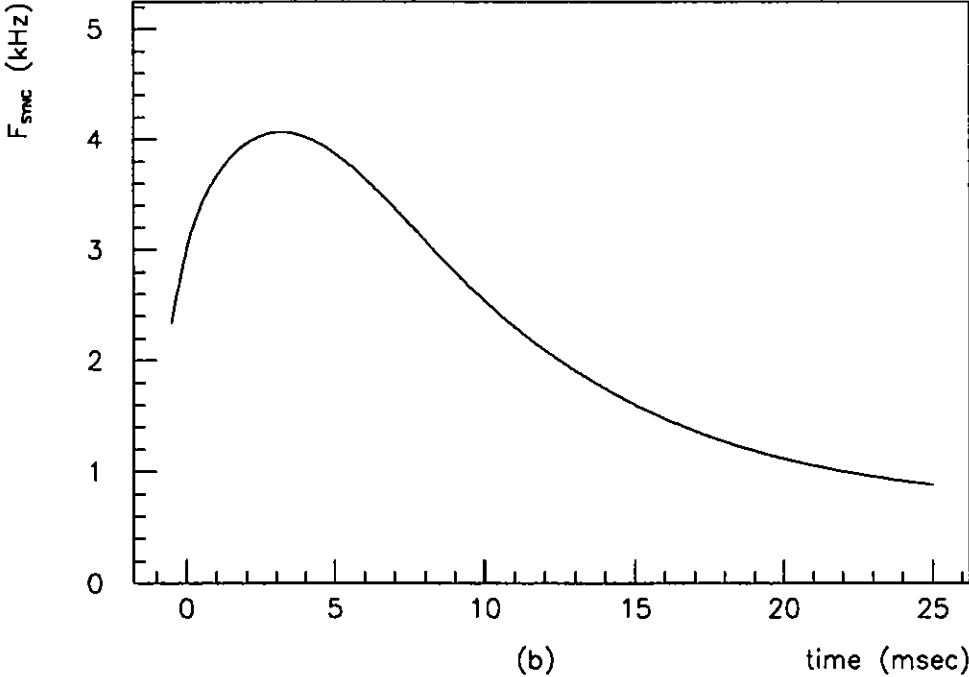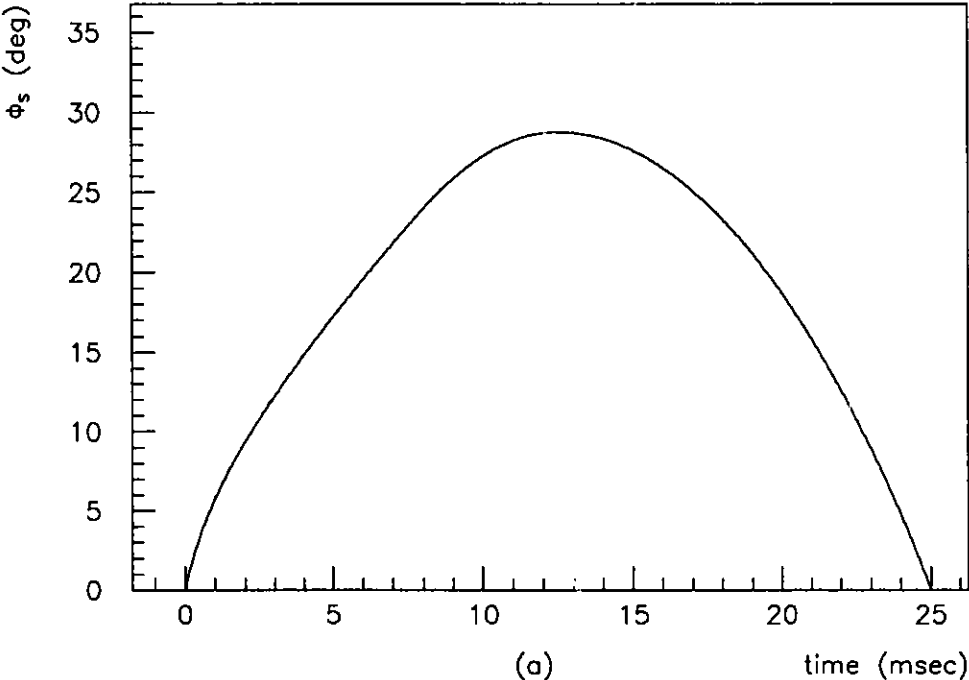
Figure II.4.1-6 Synchronous Phase (a) and Synchrotron Frequency (b) Variations from
Injection to Extraction
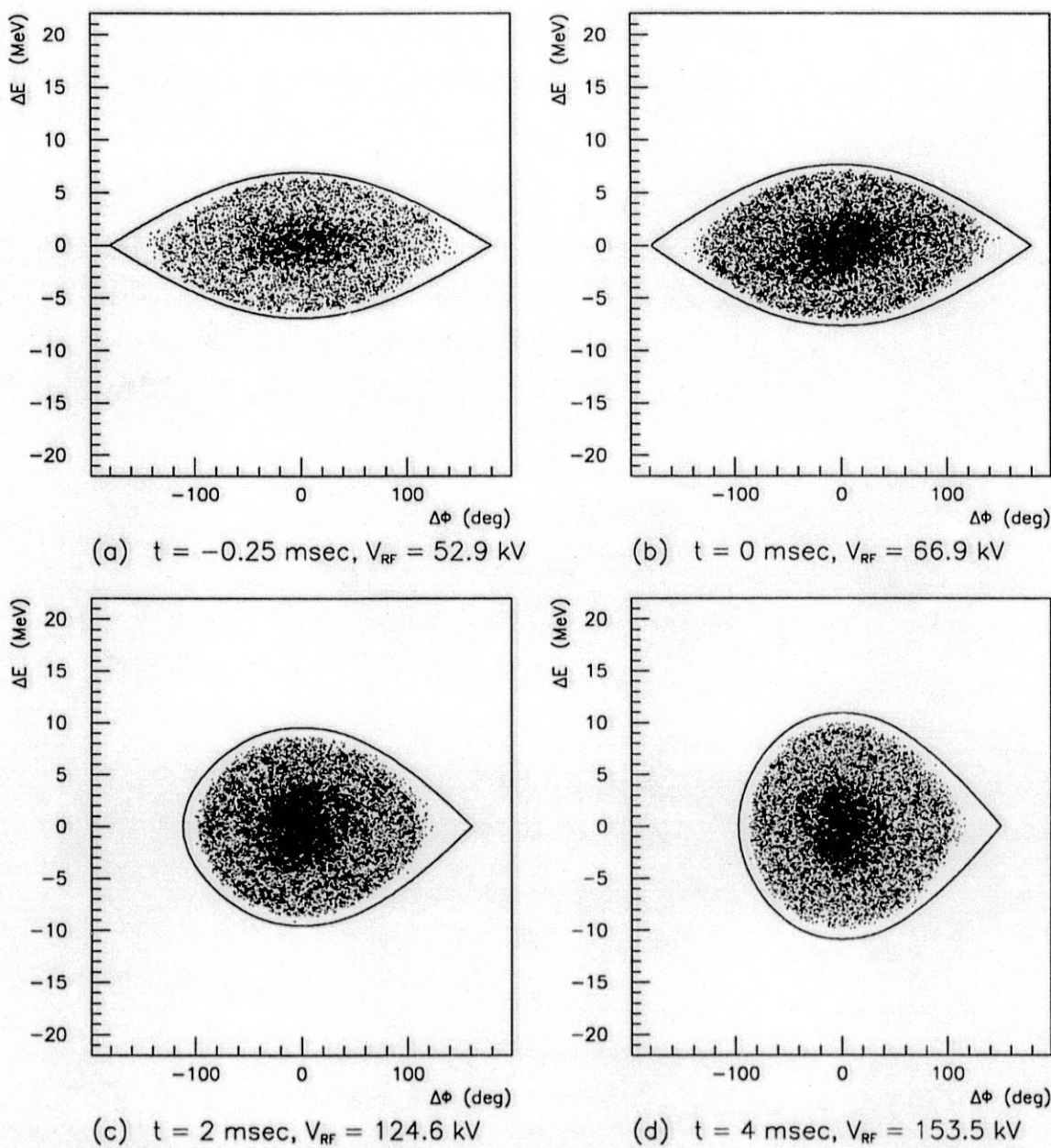
Figure II.4.1-7 Phase Space Distributions from the Simulation, from the Middle of Injection to 4 msec in the Acceleration Cycle.
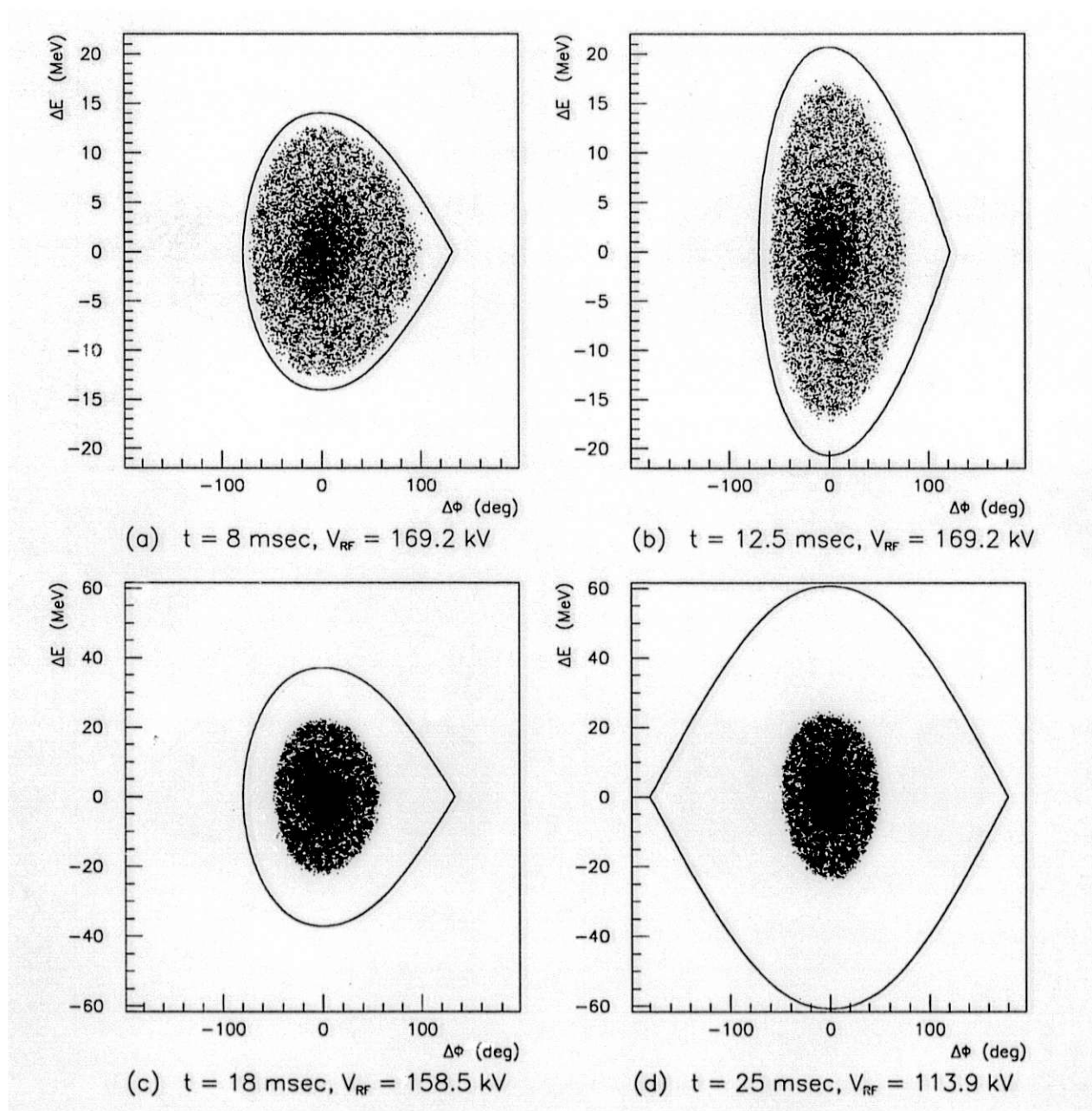
Figure II.4.1-8 Phase Space Distributions from the Simulation, from 8 msec in the Acceleration Cycle to Extraction.

Figure II.4.1-7a depicts the distribution at t = − 0.25 msec. At this time, half of the beam, or 281 turns, has been injected. The voltage is 52.9 kV, and the bucket area is 8 eV sec. The distribution at the end of injection is plotted in Figure II.4.1-7b. The voltage is 66.9 kV, producing a bucket area of 9 eV sec. The bunch has an area of 7.3 eV sec and fills 80% of the bucket. Figures II.4.1-7c and II.4.1-7d are plotted at t = 2 msec and 4 msec, respectively. At these times, the bucket area remains at 9 eV sec and the bunch area remains at 7.3 eV sec. The bunch is well-matched to the bucket.

The plots in Figure II.4.1-8 show the distributions at t = 8, 12.5, 18, and 25 msec. In Figures II.4.1-8a and II.4.1-8b, the voltage is constant at 169.2 kV. During the interval from 8 to 12.5 msec, the bucket area grows from 9 to 11 eV sec. The distribution at t = 18 msec is plotted in Figure II.4.1-8c, when the voltage is 158.5 kV and the bucket area is 21 eV sec. Figure II.4.1-8d depicts the distribution at the end of the cycle, when the voltage is 113.9 kV. The bucket area grows from 21 to 51 eV sec during the last 7 msec of acceleration. The rf program ensures that the synchrotron frequency is adequate to keep the bunch centered in the bucket.

We have shown that the rf voltage program described in this section is able to capture and accelerate 10^{14} protons per pulse with no loss of particles during the injection, capture, and acceleration processes. The engineering design of the rf system provides 180 kV peak voltage to satisfy the required voltage program.

4.2 BEAM LOADING

4.2.1 Introduction

The rf systems are able to handle the heavy beam loading that occurs in the RCS. Injection is the most demanding period for amplifier stability. The average circulating current at injection is about 18 A for 1.04×10^{14} protons. The total voltage per turn during injection varies from 40.5 to 66.9 kV. Since there are 10 cavities in the RCS, the gap voltage on each cavity varies between 4 and 6.69 kV. The voltage on each cavity needed at injection is about 4 kV. The effective shunt impedance of the cavities varies from 5 to 8 kΩ, which means that the beam can induce more than 20 times the accelerating voltage at injection. Although the beam current increases by as much as 40% during the acceleration cycle, the net beam loading effect decreases, because the demand for voltage increases to a peak value of 16.9 kV per cavity and remains relatively high, even up to extraction. Several techniques are used to handle the heavy beam loading: closed-loop feedback, which effectively lowers the impedance seen by the beam;[5] swamping resistors to lower the effective shunt impedance of the cavity;[6] and feed-forward techniques to compensate for the voltage and phase changes induced by the beam.[5] Another approach to heavy beam loading that has been proposed, but not yet used for acceleration, is to connect the power tube in a cathode-follower topology.[7,8,9]

The IPNS Upgrade baseline design uses a tetrode in a grounded-cathode topology, with feedback and feed-forward techniques to handle beam loading. The cathode follower is an option, dependent on the success of continuing research and development.

4.2.2 Stability of the Beam-Cavity Interaction

The analysis of the beam loading interaction presented in this section follows the conceptual development used by the TRIUMF-Kaon project team.[10] The tetrode amplifier acts like a current source, i_g; the cavity acts like an inductance-capacitance-resistance (LCR) parallel network; and the beam acts like a second current source, i_b, connected across the cavity gap. This circuit model is shown in Figure II.4.2-1. When the rf frequency is denoted by f_r, the resonant frequency of the cavity is denoted by f_0, and the difference between the rf frequency and the resonant frequency is denoted by Δf, the currents and voltages are as follows:

$$i_g = I_g e^{j\left(\phi_g + \omega_r t\right)} \; ,$$

$$i_b = -jI_b e^{-j\left(\phi_b - \omega_r t\right)} \; ,$$

$$i_t = I_t e^{-j\left(\phi_t - \omega_r t\right)} = i_g + i_b \; ,$$

and

$$V = V_m e^{j\left(\phi_v + \omega_r t\right)} \; ,$$

(II.4.2-1)

where $j = \sqrt{-1}$; $\omega_r = 2\pi f_r$; I_g, I_b, I_t, and V_m are constants denoting peak magnitudes; and ϕ_g, ϕ_b, ϕ_t, and ϕ_v are constants denoting relative phase.

The sum of the generator current and beam current is equal to the total cavity current:

$$I_t e^{-j\left(\phi_t - \omega_r t\right)} = C\frac{dV}{dt} + \frac{1}{L}\int V dt + \frac{V}{R} \; ,$$

$$I_t e^{-j\phi_t} = \left(j\omega_r C + \frac{1}{j\omega_r L} + \frac{1}{R} \right) V_m \; ,$$
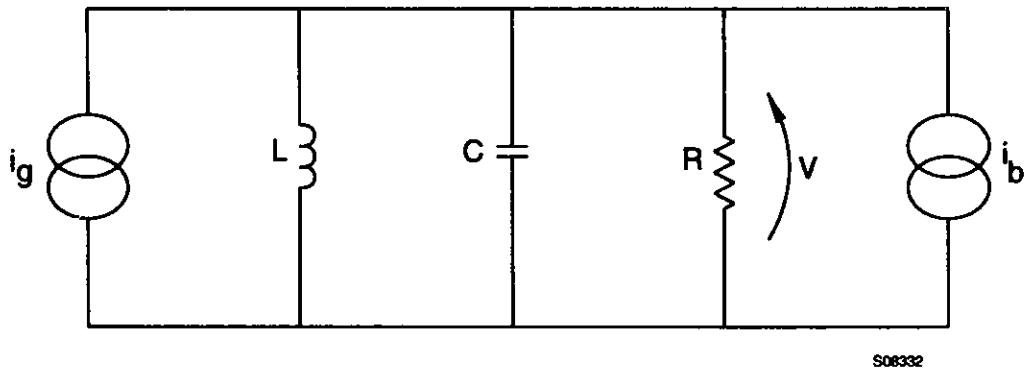
Figure II.4.2-1 Circuit Representation of Amplifier, Cavity and Beam Loading Current.

where C is the capacitance; L is the inductance; R is the resistance; and the voltage, V, is selected to be the reference value for all phasors (i.e., $\phi_V = 0$):

$$I_t e^{-j\phi t} = \left(j(\omega_o + \Delta\omega)C + \frac{1}{j(\omega_o + \Delta\omega)L} + \frac{1}{R} \right) V_m \quad , \tag{II.4.2-2}$$

and because $\omega_o^2 = 1/LC$,

$$I_t e^{-j\phi t} \approx \left[j\Delta\omega C + j\frac{\Delta\omega}{\omega_o}\left(\frac{1}{\omega_o L}\right) + \frac{1}{R} \right] V_m \quad . \tag{II.4.2-3}$$

For a parallel resonant circuit, the quality factor, Q, is equal to $R/\omega_o L$ and is also equal to $R\omega_o C$. Then, Equation II.4.2-3 becomes

$$I_t e^{-j\phi t} \approx \frac{V_m}{R}\left(1 + j2Q\frac{\Delta\omega}{\omega_o} \right) \quad . \tag{II.4.2-4}$$

The term $(1 + j2Q\Delta\omega/\omega_o)$ converted to exponential form is

$$1 + j2Q\frac{\Delta\omega}{\omega_o} = \sqrt{1 + \left(2Q\frac{\Delta\omega}{\omega_o} \right)^2} \; e^{j\Psi} \quad , \tag{II.4.2-5}$$

where $\tan\Psi = 2Q\Delta\omega/\omega_o$. The square root term of Equation II.4.2-5 reduces to $1/\cos\Psi$. Thus, the cavity voltage is

$$V_m = R\cos\Psi e^{-j\Psi} I_t e^{-j\phi t} \quad . \tag{II.4.2-6}$$

Normally the cavity resonance is adjusted to compensate for the reactive term of the beam current. The condition is met by the phase angles $\phi_g = \phi_V = 0$ and $\phi_b = \Psi$. The phasor diagram is shown in Figure II.4.2-2. The following expressions result:

$$-jI_r e^{-j\phi b} = -jI_b\left(\cos\phi_b - j\sin\phi_b\right) \quad , \tag{II.4.2-7}$$

$$-jI_b e^{-j\phi b} = -jI_b \cos\phi_b - I_b \sin\phi_b \quad , \tag{II.4.2-8}$$

and $I_g = V_m/R + I_b\sin\phi_b$.

The magnitude of the reactive part of the beam current equals the reactive part of the total current:

$$Im(i_t) = \frac{V_m}{R}\left(2Q\frac{\Delta\omega}{\omega_o}\right)$$

$$= I_o\left(2Q\frac{\Delta\omega}{\omega_o}\right) \quad , \tag{II.4.2-9}$$

where $I_o = V_m/R$. From Equation II.4.2-8,

$$I_b\cos\phi_b = I_o\left(2Q\frac{\Delta\omega}{\omega_o}\right) \quad . \tag{II.4.2-10}$$

As shown by Robinson[11] and developed by the TRIUMF-Kaon staff, stability below the transition energy requires

$$\frac{I_b}{I_o} < \frac{2\cos\phi_b}{\sin2\Psi} \quad . \tag{II.4.2-11}$$

Since from Equation II.4.2-10,

$$\cos\phi_b = \frac{I_o}{I_b}\left(2Q\frac{\Delta\omega}{\omega_o}\right) \quad ,$$

$$\cos\phi_b = \frac{I_o}{I_b}\tan\Psi \quad ,$$

Equation II.4.2-11 for stability becomes

$$\left(\frac{I_b}{I_o}\right)^2 < \frac{2\tan\Psi}{\sin2\Psi} \quad . \tag{II.4.2-12}$$

The parameter Ψ, called the detuning angle, is the angle by which the cavity phase is changed from no load to the beam loaded condition.
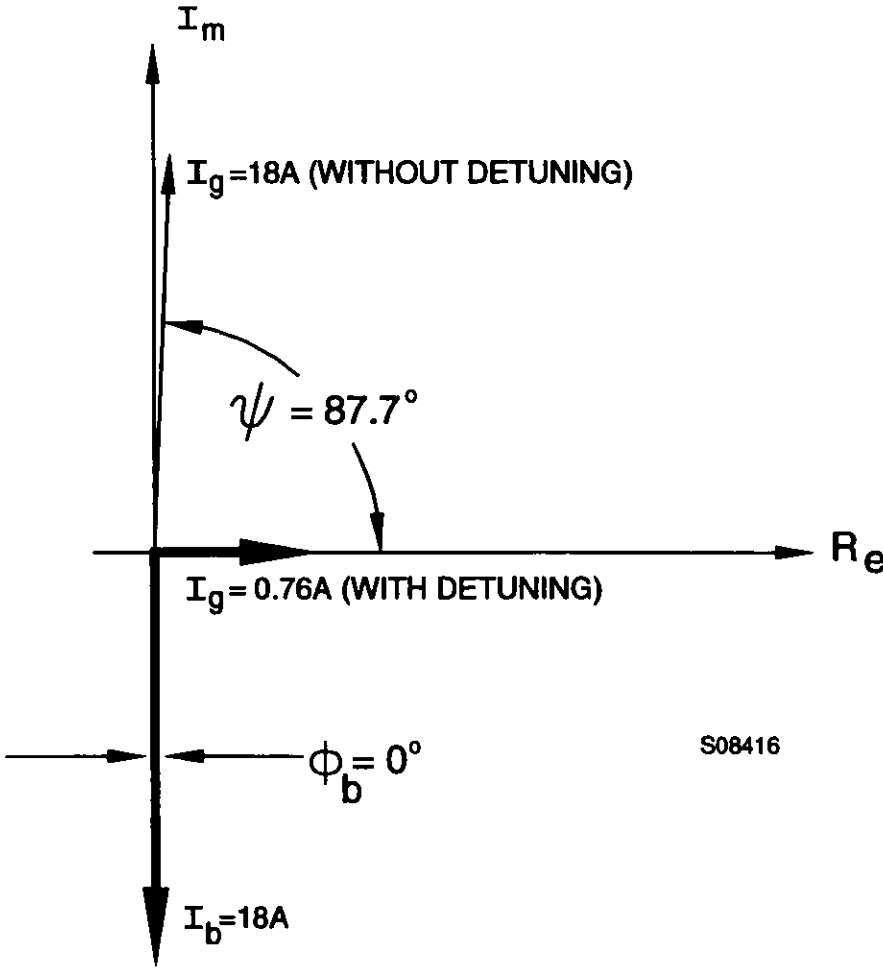
Figure II.4.2-2 RF Phasor Diagram at Injection Currents Referenced to Gap Voltage. (Not to scale.)

For the cavity parameters described in Section II.4.3, the value of Q at injection is 33.2, the value of I_0 is only 0.76 A, and the circulating beam current is about 18 A for 1.04×10^{14} protons. The ratio of I_b/I_0 is about 23.6, and tan Ψ is 24.9, to compensate for the reactive beam current. At extraction, the Q of the cavity is 63.3, the shunt impedance is 8,108 Ω, the value of I_0 is 1.406 A, and the beam current is 24.6 A. The ratio of I_b/I_0 is 17.5, and tan Ψ is 17.4, to compensate for the reactive beam current.

Because these values of tan Ψ are large, it is proposed to place a resistance across the cavity gap to lower the cavity Q, thus reducing this term, as discussed in Section 4.2.3.

4.2.3 Transient Beam Loading

The most severe beam loading conditions exist at injection, when the cavity phase in the absence of detuning is changed by 87.7°, as seen in Figure II.4.2-2. The feedback loop that maintains the generator phase at 0° detunes the cavity by 38% over the injection period. It is unlikely that the magnetic field in the ferrite can be changed this rapidly. In order to overcome this problem, a resistance is connected across the accelerating gap to lower the cavity Q and fast feedback is used. Copper sulfate resistors were successfully used at ISIS[6] to lower the Q. Resistors with values between 8 and 9 kΩ can decrease the detuning range by almost a factor of two. In addition, fast feedback, as proposed by Boussard,[5] further reduces the beam loading effect. A signal proportional to the gap voltage is fed back into the reference signal for the amplifier chain. The effective resistance of the cavity seen by the beam is reduced by a factor of (1 + H), where H is the loop gain. The limitation on achievable loop gain is the loop delay. According to Boussard,[5]

$$H \leq \frac{Q}{2\pi f_r T} ,$$
(II.4.2-13)

where T is the delay in the feedback chain. This requirement forces the amplifiers to be located inside the ring tunnel close to the cavities. Therefore, the amplifiers are located within 6 m of the cavities, so that the cable lengths only impose about 40 nsec of delay in the feedback loop. It should be possible to achieve a total loop delay of no more than about 50 to 75 nsec, in which case, H $\leq$ 66. The value of H must be greater than $\sqrt{2}$ tan Ψ for stability, i.e., at least 35.2 at injection, giving a factor of two in the safety margin. This, coupled with the use of copper sulfate resistors, should be sufficient to achieve amplifier stability at the fundamental frequency.

The harmonic content of the circulating beam current can also be a problem, especially the second harmonic, which is as large as 37% to 40% of the peak value of the fundamental current. The cavity impedance is capacitive and has a value of 116 Ω at the second harmonic frequency. This value results in a second harmonic voltage of as much as 2,500 volts being induced on the

cavity. The loop gain at the second harmonic frequency is down to only about 10 or 20, but it should be large enough to reduce the second harmonic voltage to an acceptable level. Moreover, to ensure that the longitudinal beam loading is kept sufficiently low, fast feed-forward is planned with tuned filters and digital delay lines for some of the other harmonics.

These compensation techniques are used throughout the entire acceleration cycle. Stability is easier to achieve during the acceleration cycle than at injection.

4.2.4 Summary and Conclusions

Despite the heavy loading on the RCS cavities and the heavy demand put on the amplifier system, longitudinal stability is achievable. The use of swamping resistors is needed to complement the fast-feedback loops, especially at injection. Fast feedback is needed throughout the acceleration cycle. Feed-forward at the fundamental frequency and at some of the higher harmonics is used throughout the acceleration cycle.

The compensation schemes appear to provide a factor of three or more safety margin in amplifier stability for a beam of 1.04×10^{14} protons per pulse. Care is to be taken to ensure that the beam bunching factor and the delays in the feedback networks do not become too large, so as to avoid amplifier instability.

4.3 RADIO-FREQUENCY SYSTEM

4.3.1 Introduction

The RCS rf system has 10 single-ended, ferrite-loaded cavities to generate the required 180 kV. There is one cavity per straight section, and a total of ten straight sections dedicated for the installation of the cavities. A change in resonant frequency from 1.1235 MHz at injection to 1.5035 MHz at extraction is accomplished by changing the dc current in the bias windings that are wound around the ferrite. The design choice for the ferrite type is Philips 8C12, which is the same as that used in the GSI Heavy Ion Synchrotron[12] and for which extensive performance data are available.

Each cavity is driven by a Class-B tetrode in grounded-cathode configuration. The entire amplifier chain is located in the Ring Building (Building 365), close to the cavities. This close proximity keeps the loop delay down, in order to achieve high gain in the fast-feedback loops. The final amplifier is driven by a grounded-grid triode Class-C amplifier. The amplifier circuit is discussed in detail in Section II.4.3.3.

4.3.2 Synchrotron Cavities

Each cavity delivers 18 kV across a single accelerating gap. The physical length of a cavity is 2.59 m from flange face to flange face, with the accelerating gap at one end. There are 15 ferrite rings per subassembly and 4 ferrite subassemblies in each cavity. Four bias windings are wound in the typical figure-eight configuration[13] around each pair of ferrite subassemblies, so that the rf induction cancels at the input terminals of the bias supply. The cavity layout is shown in Figure II.4.3-1, and the physical parameters are listed in Table II.4.3-1.

The ferrite rings are made of 0.0254-cm-thick Philips 8C12 material, or equivalent. The inner radius of each ring is 0.125 m, and the outer radius is 0.25 m. Copper cooling plates, each 3 mm thick, separate the ferrite rings. A cooling-water tube is brazed along the outer circumference of the exposed copper fins of the cooling plates. This arrangement is shown in Figure II.4.3-2.

A ferrite subassembly consists of 15 ferrite rings, 16 cooling plates, and aluminum oxide clamping plates at the end of each ferrite stack. The cooling plate surfaces are coated with a heat-conducting compound to make good thermal contact with the ferrite rings. The entire assembly is put into compression by means of threaded copper rods extending from one end of the stack to the other. These rods are also part of the bias windings.

The cavity fabrication plan is to assemble each stack of 15 ferrite rings, cooling plates, and bias windings separately. Each assembly is slid over the vacuum pipe and locked into position. The final bias and water connections are completed from access panels on the top of the cavity, after all the ferrite assemblies are in place on the vacuum pipe.

The relative rf permeability of the ferrite, μ_r, at the injection and extraction operating points, with and without beam loading, is shown in Figure II.4.3-3. With four bias windings, the dc current varies from 80 A at injection to 115 A at extraction, when the cavity is unloaded, which results in a change in relative rf permeability from 116 to 68. In order to cancel the inductive portion of the beam current, the cavity resonant frequency is operated above the rf frequency by the amount given by Equation II.4.2-5; i.e., the resonant frequency needs to be 1.137 times the rf frequency at extraction. Resonant operation at this frequency requires a higher bias current, 142 A, to lower the relative rf permeability to 52. An 8-kW (50 V at 160 A) programmable dc bias supply is required to drive the four-turn winding over 0.5 T in 8.33 msec.

The maximum rf field during acceleration reaches 0.0106 T, which is less than the field at which the Q-loss effect was observed by the GSI team. The Q-loss effect occurred at GSI when the product of field and frequency was equal to 18 mT MHz. For our design, the threshold for Q-loss is about 1.5 times higher than the maximum rf field. The operating characteristics for the cavities under nominal conditions are listed in Table II.4.3-2.
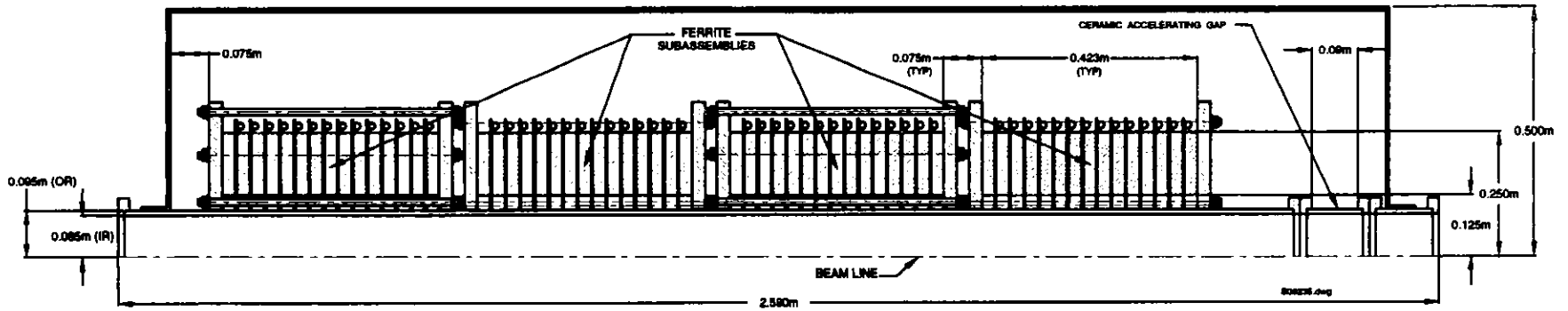
Figure II.4.3-1 Quarter Sector of Single-Ended RF Cavity with Four Ferrite Subassemblies.

Table II.4.3-1 Physical Parameters of Cavity

Parameters	Values	Units
Physical length of cavity, flange-to-flange	2.59	m
Inside length of cavity	2.39	m
Length of accelerating gap	0.09	m
Outer radius of cavity (inside dimension)	0.50	m
Inner/outer radii of beam tube	0.085/0.095	m
Type of ferrite	Philips 8C12	-
$\mu_r Q$ of ferrite	6,000	-
Ferrite ring dimensions:		
Inner radius	0.125	m
Outer radius	0.250	m
Thickness	0.0254	m
Single-ended single-gap cavity:		
Number of ferrite rings/cavity	60	-
Volume of ferrite/cavity	0.224	m^3
Thickness of copper cooling plates	0.003	m
Number of turns on bias winding	4	-
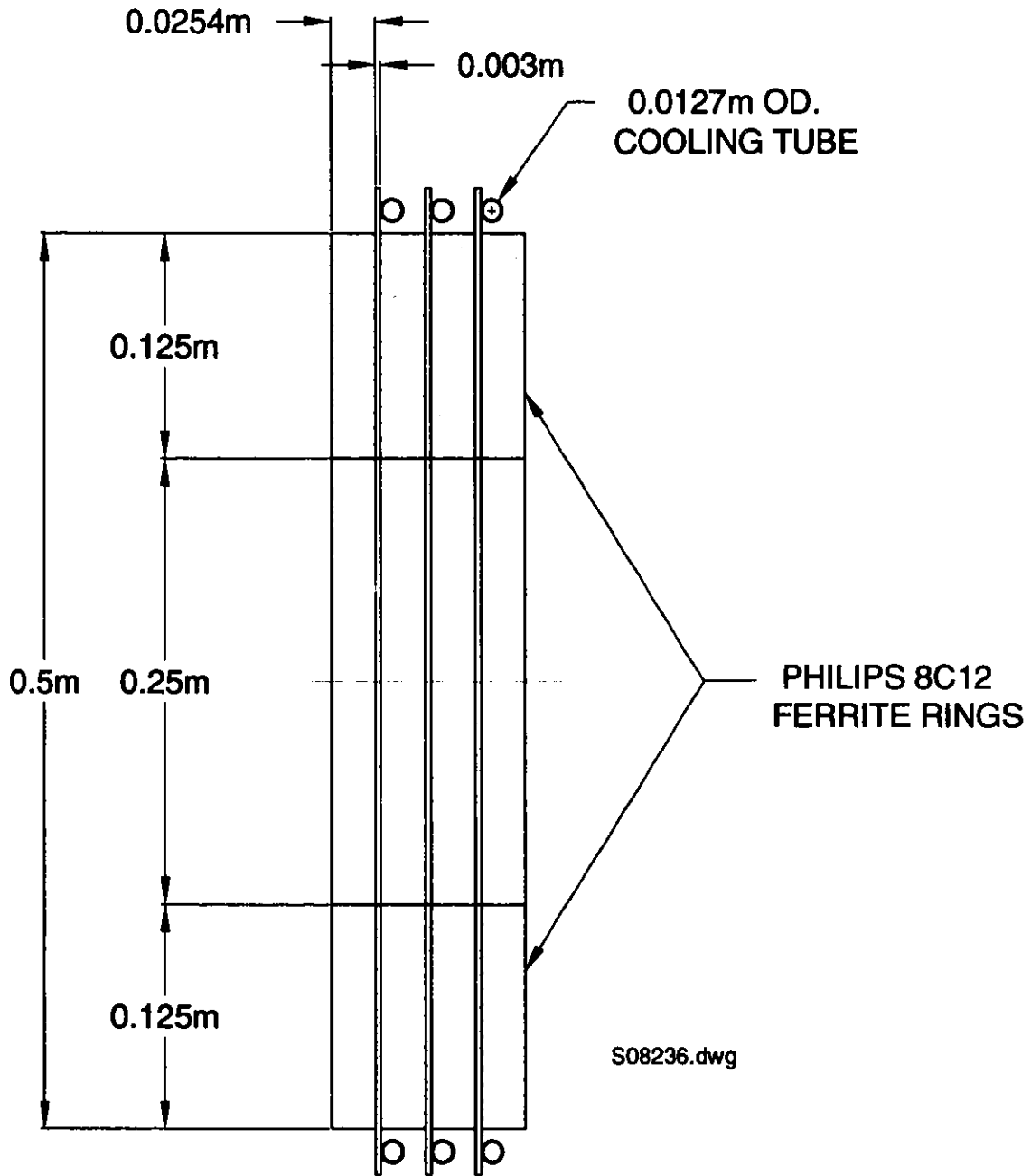
Figure II.4.3-2 Ferrite Ring Assembly Details.

P00344.dwg
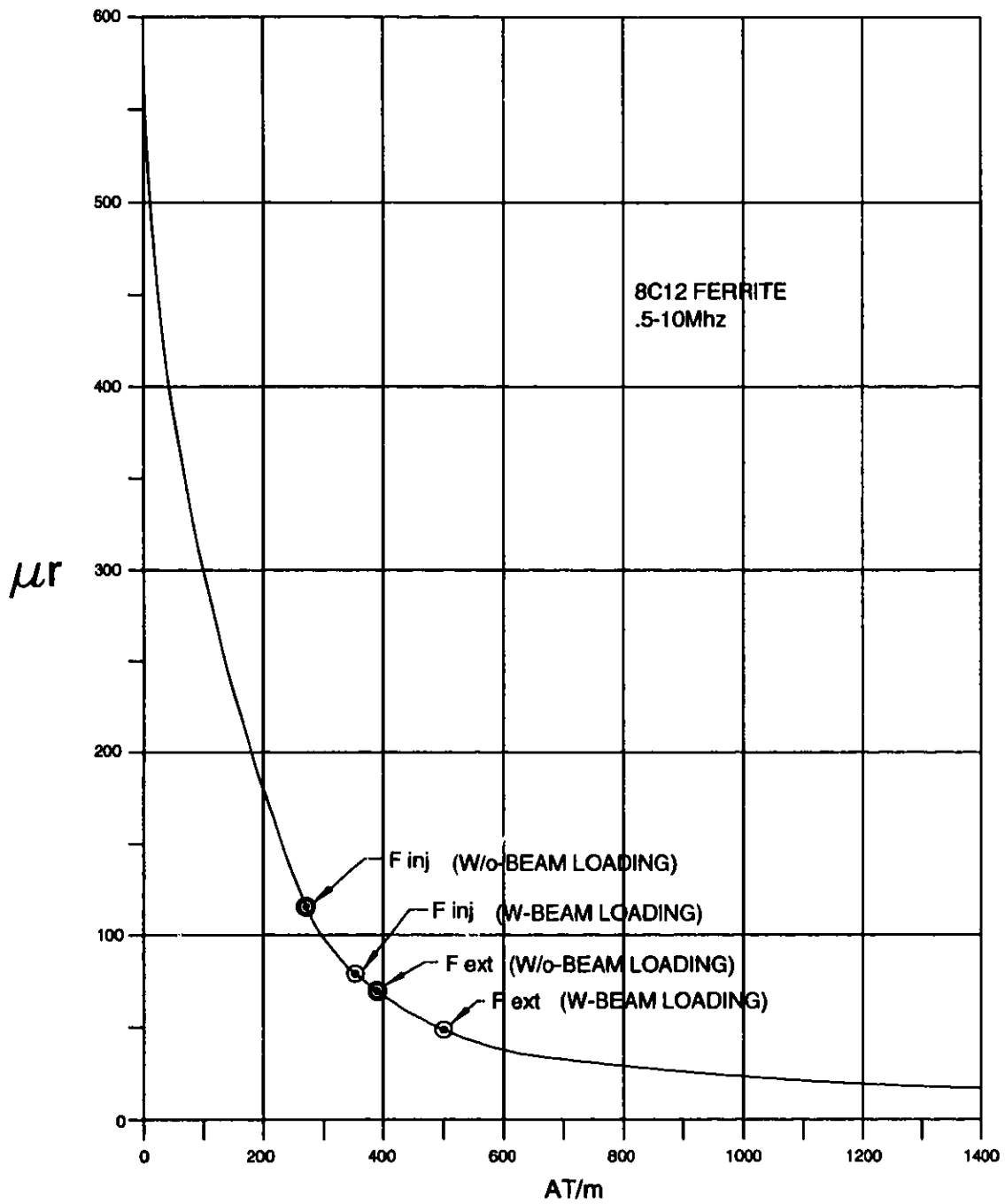
Figure II.4.3-3 Rf Relative Permeability versus dc Bias. (Bias
is expressed in ampere-turns per meter.)

Table II.4.3-2 Operating Characteristics of Cavity for Nominal Operation

Parameters	Values	Units
Maximum flux density	0.0106	T
Maximum voltage per cavity	18.0	kV
Peak power in ferrite	75.4	kW/m^3
Average power in ferrite	28.2	kW/m^3
Average power in ferrite per cavity	6.3	kW
Peak power to copper	7.2	kW
Average power to copper	2.7	kW
dc coercive force at injection, without beam loading	271	AT/m
dc current at injection, without beam loading	80	A
Relative permeability at injection, without beam loading	116	-
dc coercive force at injection with beam loading	360	AT/m
dc current at injection with beam loading	106	A
Relative permeability at injection with beam loading	80	-
dc coercive force at extraction, without beam loading	390	AT/m
dc current at extraction, without beam loading	115	A
Relative permeability at extraction, without beam loading	68	-
dc coercive force at extraction, with beam loading	484	AT/m
dc current at extraction, with beam loading	142	A
Relative rf permeability at extraction, with beam loading	52	-

4.3.3 RF Amplifiers

The final amplifier is a Class-B, grounded-cathode type, using a single Eimac 8973 tetrode, or equivalent. The tube characteristics are given in Table II.4.3-3, and the tube outline is shown in Figure II.4.3-4.

The amplifier provides 18 kV to the gap and is able to deliver at least 90 A to compensate for the instantaneous beam current, deliver enough current to excite the resonant cavity, and deliver the necessary power to the beam. The Eimac 8973 is capable of delivering considerably more current than is required.

The basic circuit diagram of the amplifier, with the predriver, driver, and the final stage, is shown in Figure II.4.3-5. The plate supply voltage is 22 kV, and the screen voltage is +1500 V. The dc bias on the control grid is −700 V. The final amplifier characteristics are listed in Table II.4.3-4. The grid of the Eimac 8973 is driven by a Class-B grounded-grid amplifier using an Eimac 3CW20000A7, or equivalent. The 3CW20000A7 is driven by a 1-kW Eimac 4-400 tetrode, operating in Class-AB$_1$ common-cathode configuration.

The low-level rf system consists of four major elements: (1) a dc bias control system to keep the cavity on resonance and synchronous with the changing magnetic field, (2) an automatic gain control to maintain amplitude at the prescribed reference level for voltage on the accelerating gap, (3) a phase-control system that measures the beam position relative to the cavity phase and makes incremental changes in frequency to keep the beam at the phase-stable angle, and (4) an adaptive feed-forward system that uses the difference between the instantaneous beam current and the difference signal between the instantaneous amplifier current and the circulating current in the cavity to generate a change in the AGC reference to further correct for beam loading.

All amplifiers are located in the Ring Building (Building 365), close to the rf cavities to keep the loop delays to a minimum. A plan view is shown in Figure II.4.3-6 and a view looking down the beam axis is shown in Figure II.4.3-7. The amplifier cabinets are surrounded by a walkway on the platform for servicing. The main transformers and dc power supplies are located outdoors, on the roof of Building 364. A single dc supply provides high-voltage dc power for two complete amplifier systems. The plan view of the power supply layout is shown in Figure II.4.3-8. Much of the control equipment, bias supplies, etc., are located on the third floor of Building 364, as shown in Figure II.4.3-9.

Table II.4.3-3 Eimac 8973 Tetrode, Class-B Operation

Parameters	Values	Units
Plate voltage (maximum)	22.5	kV
Plate current (maximum)	110	A
Plate dissipation (maximum)	1,000	kW
Grid #1 dissipation (maximum)	2	kW
$\mu(G_1-G_2)$	4.5	-
Plate resistance	~90	Ω
Plate rf power output (maximum)	~750	kW
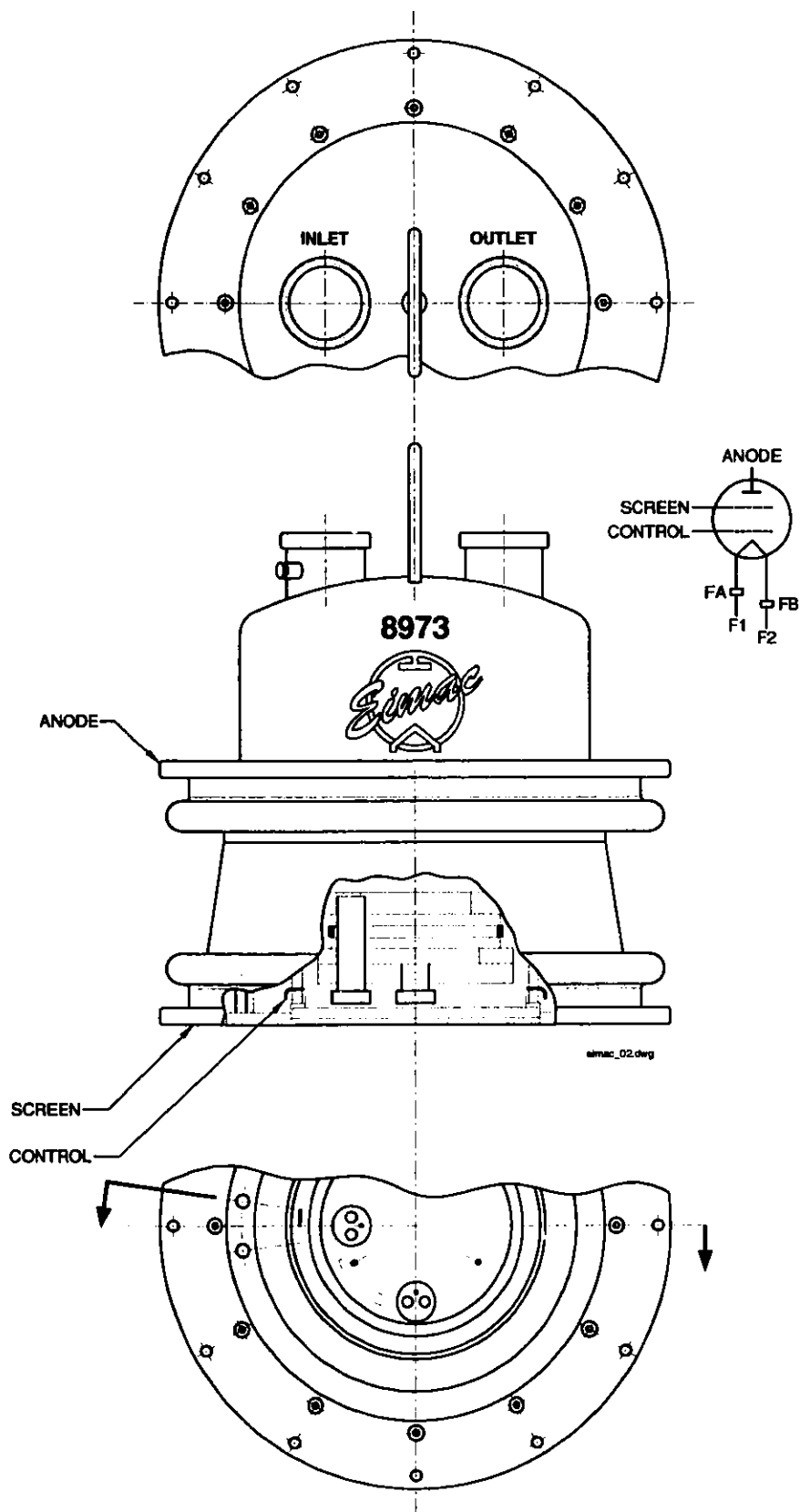
Figure II.4.3–4 8973 Tetrode Outline.
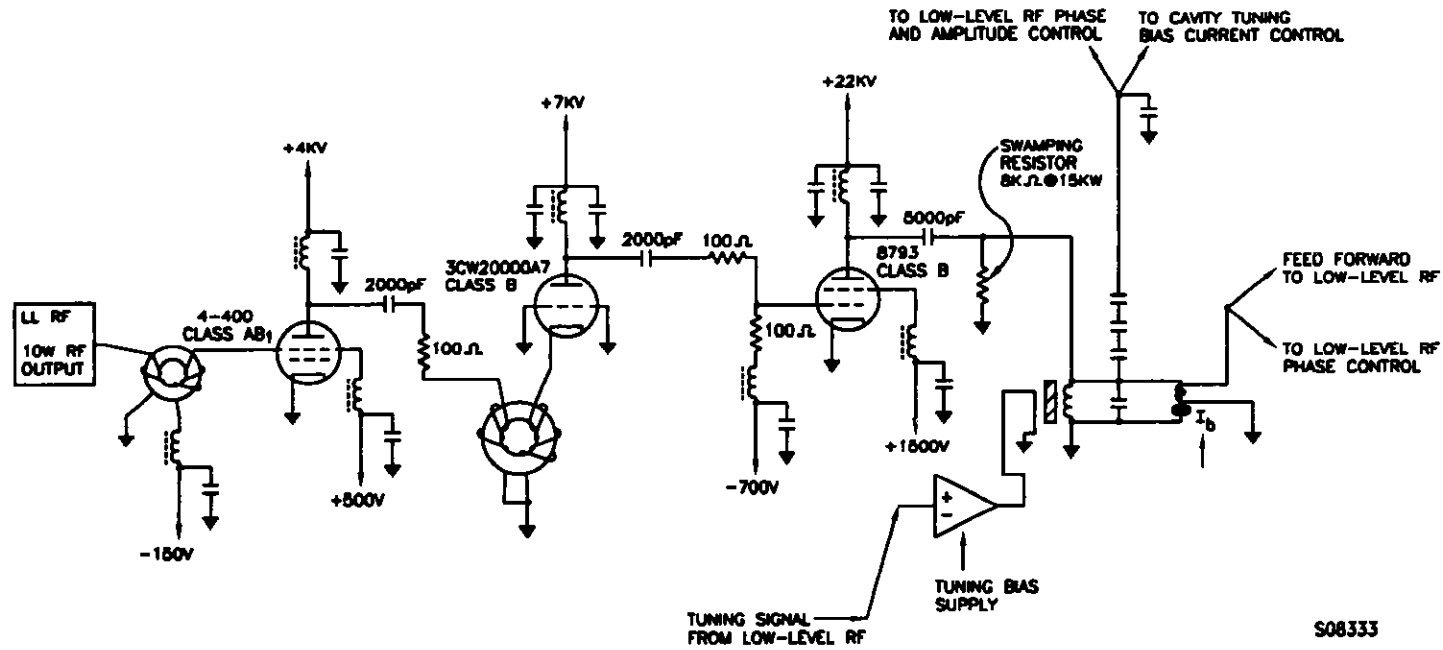
Figure II.4.3-5 RF Amplifier Circuit Diagram.

Table II.4.3-4 Final Amplifier Characteristics for Single-Ended
Grounding Cathode

Parameters	Values	Units
Tube type	Eimac 8973	-
Plate voltage	22.0	kV
Maximum gap voltage	18.0	kV
Peak plate current to beam	61.0	A
Peak plate current from amplifier	~80.0	A
Peak power to beam per amplifier	237.9	kW
Peak power to ferrite per cavity	16.9	kW
Peak power to copper per cavity	7.2	kW
Average rf power from amplifier	99.0	kW
Approximate dc power to amplifier	141.0	kW
Approximate ac power to amplifier	176.0	kW
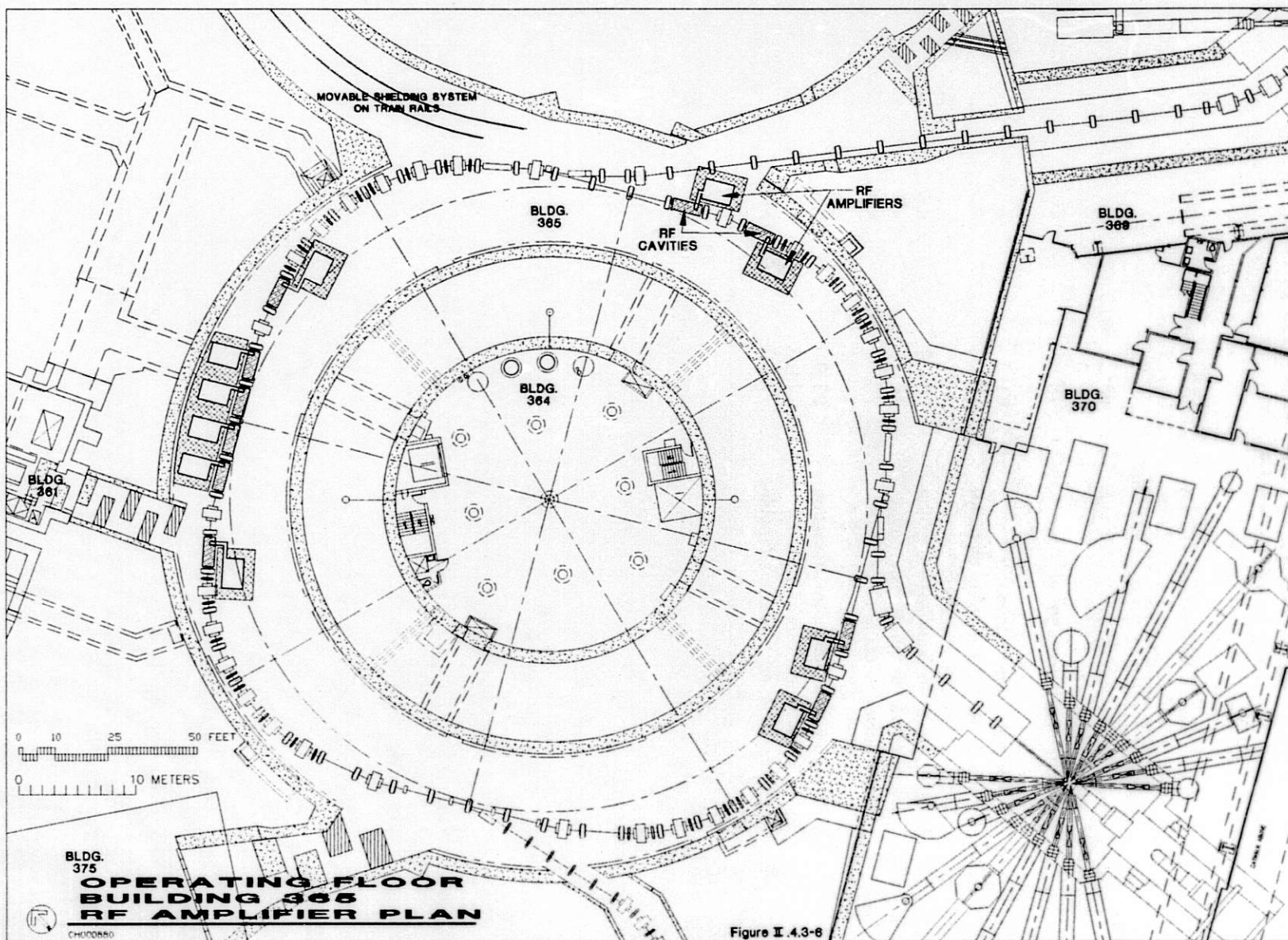
Figure II.4.3-6 Building 365, Operating Floor, RF Amplifier Plan, Showing 10 Amplifiers and Cavities.

TOP OF TUNNEL
ELEV. 745.5'

AIR
SUPPLY

TOP OF CRANE
RAIL BRACKET
ELEV. 735.50'

20 TON CRANE

TOP OF SHIELDING
SUPPORT BRACKET
ELEV. 721.58'

RF AMPLIFIER
SYSTEM

RF
CAVITY

TOP OF
OPERATING FLOOR
ELEV. 711.00'

1.4 Meter

TOP OF
SERVICE FLOOR
ELEV. 700.5'

ELEV. 697.00'

CH00858A

FEET

METERS
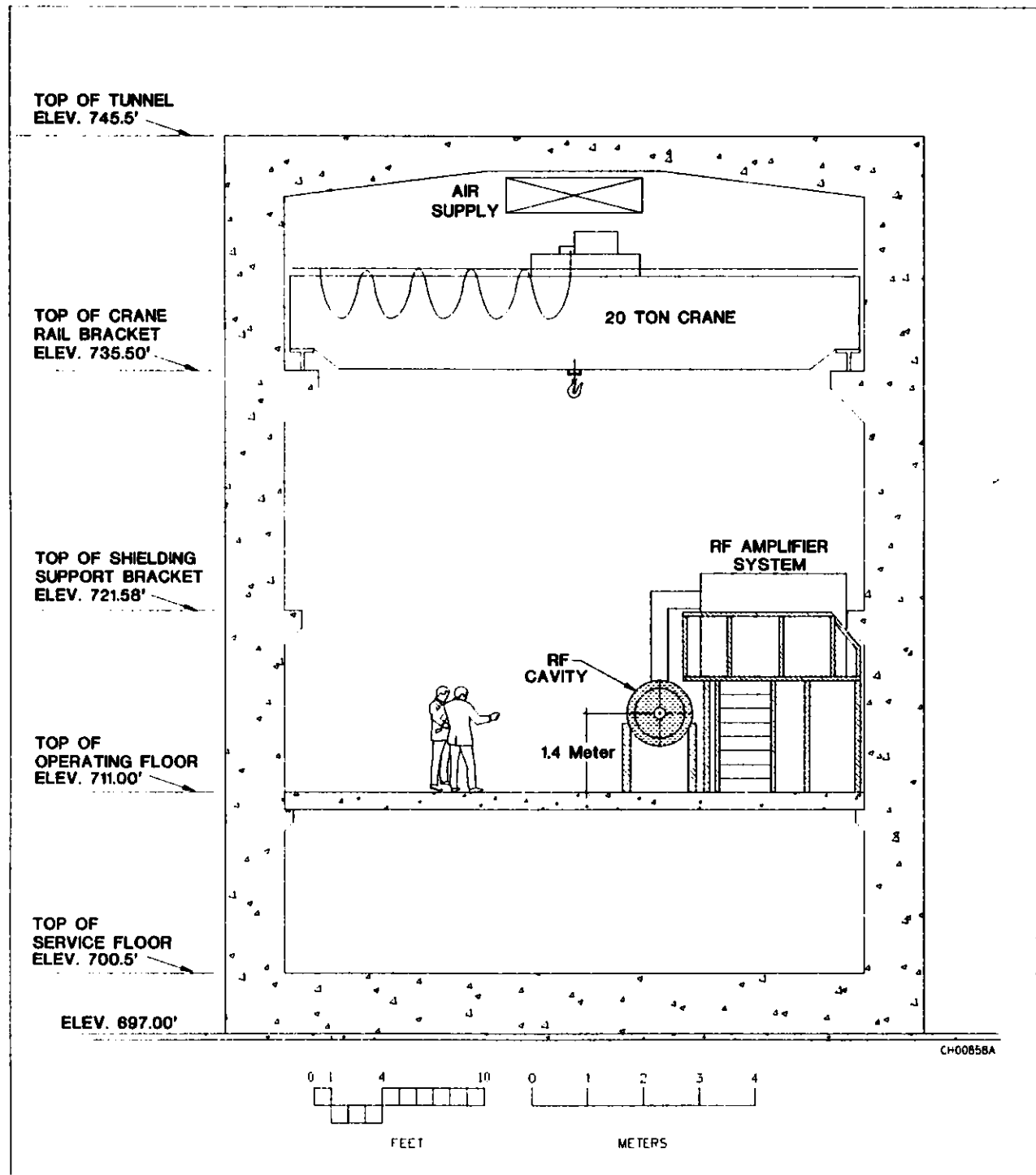
Figure II.4.3-7 RF Amplifier System Layout.

BUILDING 364 ROOF
RF POWER SUPPLY LAYOUT

Figure II.4.3-8

CENTER BUILDING 364
THIRD FLOOR
RF CONTROL LAYOUT
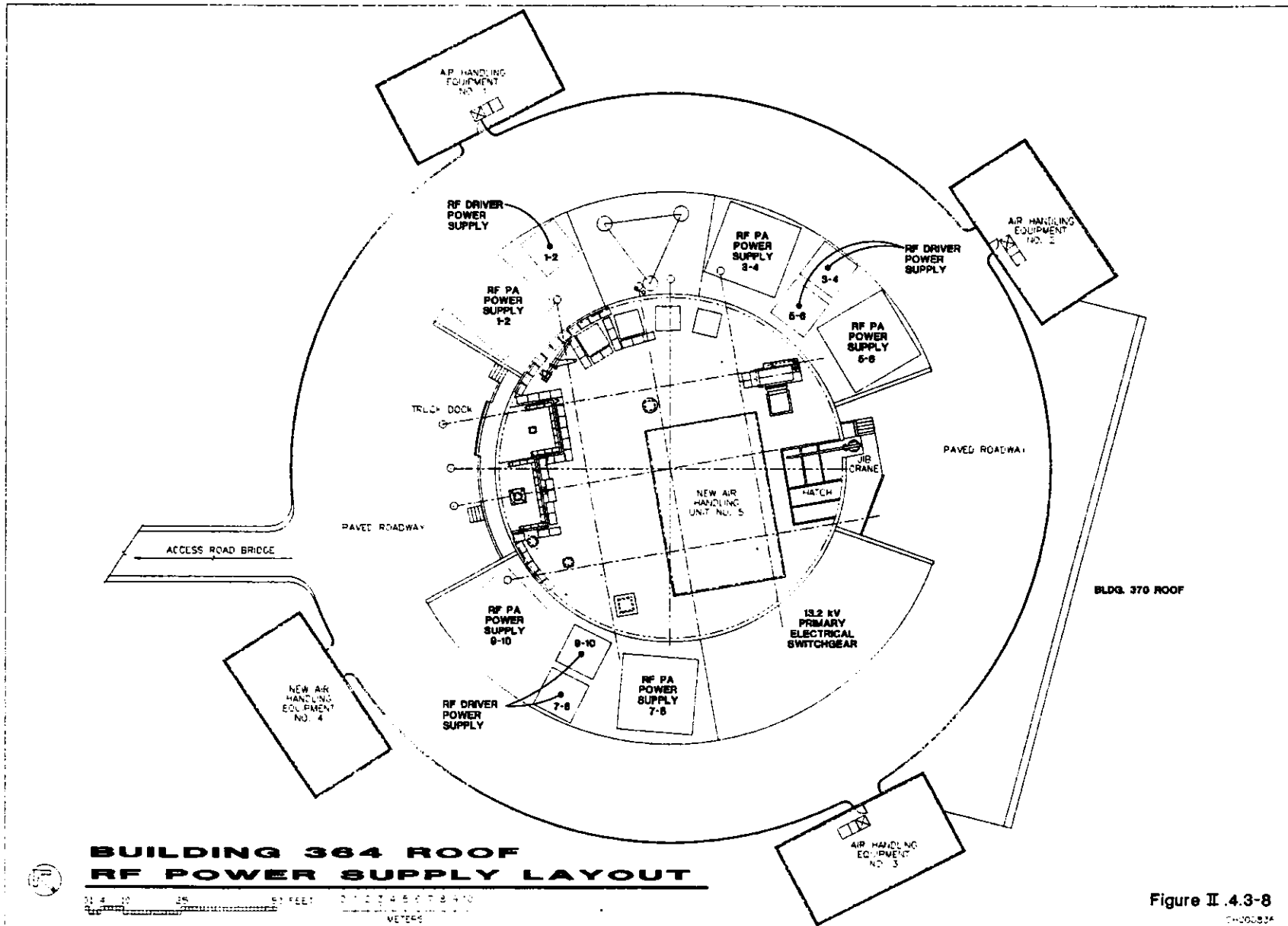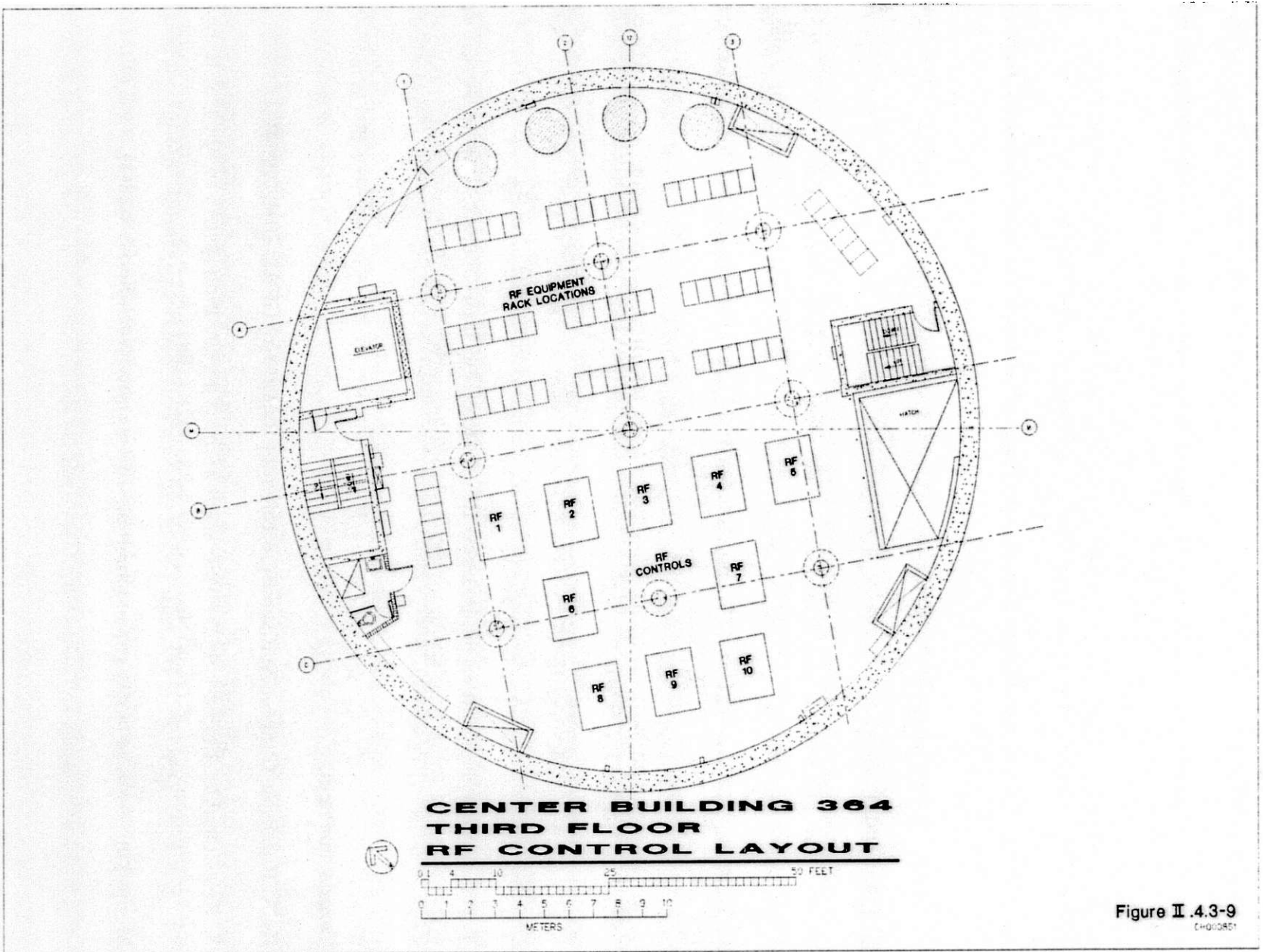
Figure II.4.3-9

4.4 REFERENCES

1. G. Hemmie (compiler), *Catalogue of High Energy Accelerators*, XVth International Conference on High Energy Accelerators (Hamburg, Germany, Nov. 1992).

2. E. S. Lessner and Y. Cho, "RF capture studies for injection into a synchrotron," in *Proceedings of the 1993 Particle Accelerator Conference*, p. 399 (1993).

3. K. Symon, *Synchrotron Motion with Space Charge*, Argonne National Laboratory Report No. NSA-94-3 (1994).

4. Y. Cho, E. Lessner, and K. Symon, "Injection and capture simulations for a high intensity proton synchrotron," in *Proceedings of the European Particle Accelerator Conference*, p. 1228 (1994).

5. D. Boussard, "Control of cavities with high beam loading," IEEE Trans. Nucl. Sci. NS-32(5) (1985).

6. G. H. Rees, "Status report on ISIS," presented at 1987 IEEE Particle Accelerator Conference (March 16-19, 1987), IEEE Catalog No. 87CH2387-9 (1987).

7. T. W. Hardek and W. E. Chyna, "Common anode amplifier development," IEEE Trans. Nucl. Sci. NS-26(3) (1979).

8. S. Giordano and M. Puglisi, "A cathode follower power amplifier," IEEE Trans. Nucl. Sci. NS-30(4) (1983).

9. Y. Irie, "Very low output impedance RF system for high intensity accelerators," in *Proceedings of the 12th Meeting of the International Collaboration on Advanced Neutron Sources*, p. A131 (May 1993).

10. *Kaon Factory Study, Accelerator Design Report* (TRIUMF, Vancouver, British Columbia, Canada, undated).

11. K. W. Robinson, Cambridge Electron Accelerator Report No. CEAL-1010 (1964).

12. K. Kasper and M. Emmerling, "Development of the rf accelerating system for the GSI heavy ion synchrotron," IEEE Trans. Nucl. Sci. NS-28, 3028 (1981).

13. M. Plotkin, "Isabelle cavity gap assemblies," IEEE Trans. Nucl. Sci. NS-28(3), 2752 (1981).

5.1 INTRODUCTION

Collective instabilities are an important consideration in the RCS. These instabilities are intensity-dependent effects that arise as a result of the electromagnetic wake fields generated by the beam as it interacts with its surroundings. The interactions are characterized by the coupling impedance. In the circulating current, small density fluctuations driven by wake fields of sufficient magnitude and the proper phase can grow, leading to emittance growth and/or beam loss.

The machine coupling impedance is described first, followed by discussion of collective instabilities, which must be controlled in a high-intensity machine of this type. Longitudinal, transverse, and electron-proton instabilities are discussed separately. Passive control is included as an integral part of the discussion because it is preferred, where possible, in mitigating collective instabilities. This passive control includes minimizing the coupling impedance and making use of Landau damping by introducing a tune spread. It is expected that active control of instabilities through beam feedback can be avoided.

5.2 COUPLING IMPEDANCE

The coupling impedance is estimated by using the standard, approximate models.[1-5] The results for the longitudinal impedance, $Z_{\parallel}$, and the transverse impedance, $Z_{\perp}$, are summarized in Table II.5.2-1, and detailed calculations follow in the next two sections. The longitudinal impedance is normalized by the mode numbers, $n = \omega/\omega_0$, where ω_0 is the revolution frequency. For the longitudinal case, the coupling impedance of interest corresponds to the mode numbers $n \leq 500$, using the cutoff frequency $\omega_c = c/b$, where b is the average rf shield radius, and c is the velocity of light. For the transverse case, $\omega = (p + v)\omega_0$, where p is a negative integer near v, the horizontal or vertical tune.

The impedance is dominated by the space charge self-field. The beam position monitors (BPMs), extraction kickers, rf cavities, and the rf shield also contribute to the impedance. The impedance due to other components, such as vacuum ports and bellows, is expected to be negligible, because these are isolated from the beam by the rf shield. The components of the coupling impedance depend on time-varying machine parameters. The results in the table correspond to injection, unless otherwise noted. The time-dependence of the other components is discussed in Section II.5.2.2. The space charge impedance is capacitive, while the others are inductive at the frequencies of interest and include a resistive term.

Table II.5.2-1 RCS Impedance Estimation

	$Re(Z_{\parallel}/n)$ (Ω)	$Im(Z_{\parallel}/n)$ (Ω)	$Re(Z_{\perp})$ ($k\Omega/m$)	$Im(Z_{\perp})$ ($k\Omega/m$)
Space charge (injection)	- [a]	−220	-	−2,800
Space charge (extraction)	-	−50	-	−1,500
r f shield	$0.2/\sqrt{n}$	$0.2/\sqrt{n}$	$11/\sqrt{\omega}$ [b]	$11/\sqrt{\omega}$ [b]
Extraction kickers	-	-	30 [c]	50
r f cavities	14 [d]	[e]	-	-
BPMs [f]	$10^{-3}\,n$	0.06	$10^{-2}\,\omega$ [b]	110

[a] - = negligible or not applicable.

[b] ω has units of 10^6 rad/sec.

[c] Maximum value, at 1 MHz, decreasing thereafter as ω^{-1}.

[d] Maximum value, at ω_c, decreasing to zero at $\omega \ll \omega_c$ and $\omega \gg \omega_c$.

[e] Zero at ω_c, inductive for $\omega < \omega_c$, capacitive for $\omega > \omega_c$.

[f] Valid up to 125 MHz.

5.2.1 Space Charge Impedance

The impedance due to the self-field of a charged beam in a vacuum chamber, commonly called the space charge impedance, is given by[1,3]

$$\frac{Z_\parallel}{n} = -j\frac{Z_0}{2\beta\gamma^2}g_0 \qquad\qquad Z_\perp = -j\frac{RZ_0}{\beta^2\gamma^2}g_\perp, \qquad (II.5.2\text{-}1)$$

where $Z_0 = \mu_0 c = 377\,\Omega$, R is the average radius of the synchrotron, and β and γ are the standard relativistic factors, which are time-varying because of the acceleration. The beam has an elliptical cross section, its major axis alternating between the horizontal and vertical planes. However, for the calculations, a uniform, round, unbunched beam of radius a in a vacuum chamber of radius b is assumed in evaluating the geometrical factors g_0 and $g_\perp$:

$$g_0 = 1 + 2\ln\left(\frac{b}{a}\right), \qquad\qquad g_\perp = \frac{1}{a^2} - \frac{1}{b^2}. \qquad (II.5.2\text{-}2)$$

The transverse beam radius, a, decreases during the acceleration cycle.

The vacuum chamber is constructed with a special rf shield, shown in Figure II.5.2-1, to minimize the impedance due to space charge. The shield follows the beam envelope at an aperture equal to the BSC, as discussed in Section II.2.1.3. Details of the design are discussed in Sections II.5.2.2 and II.6.2.

The impedance is estimated by using the average beam and rf shield radii, which are 5 cm and 7 cm, respectively, at injection. The results for the space charge impedance during the acceleration cycle are shown in Figure II.5.2-2 for both the longitudinal and transverse planes. The difference between calculating $Z_\parallel$ by using the average values of a and b, and calculating the average value of $Z_\parallel$ directly, is no more than 1% for the longitudinal plane and 10% for the transverse plane. Compared with a fixed-radius rf shield, this contour-following scheme reduces the longitudinal space charge impedance by 30% at injection and 20% at extraction. The transverse impedance is reduced by 35% at injection and 10% at extraction.

A number of corrections to the geometrical factors have been proposed to account for the wires and the more realistic elliptical beam cross section. The electrostatic fields produced by a uniform beam propagating inside a round, rf-screening wire cage have been derived by T. Wang.[6] A second correction, derived by H. Okamoto, takes into account the varying elliptical shape of the beam in a smooth, metallized vacuum chamber without wires and with a fixed radius.[7] These

DIA.1.5mm

120 PLACES

W/3mm SPACING

BSC APERTURE

CERAMIC VACUUM
CHAMBER

207.0mm

88.0mm

CERAMIC
RIB

228.0mm

271.2mm

S08324.dwg

Figure II.5.2-1 Ceramic Vacuum Chamber Cross Section in the Focusing Quadrupole Magnet, Showing Placement of the rf Shield Wires at the BSC Aperture.
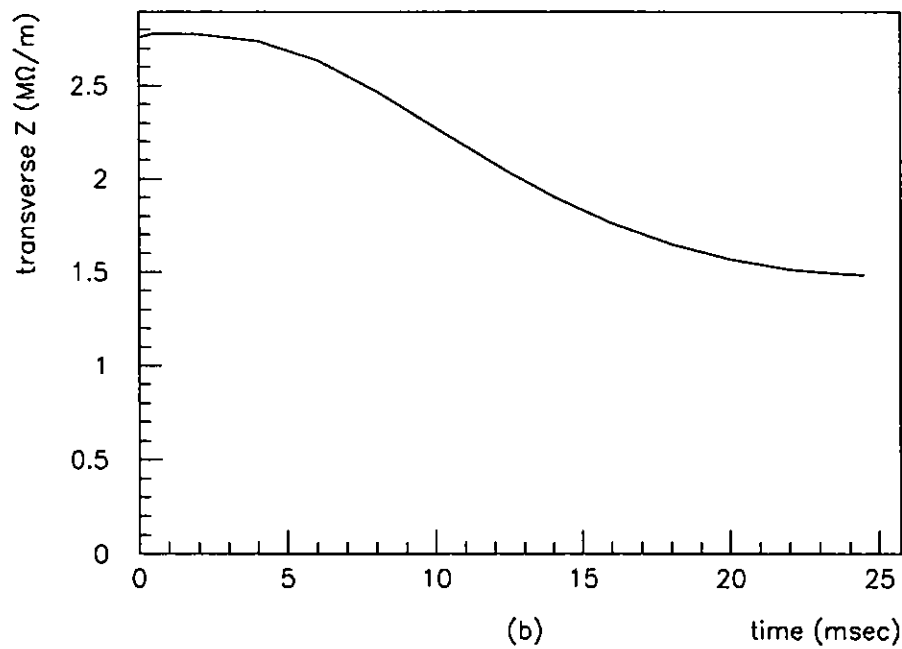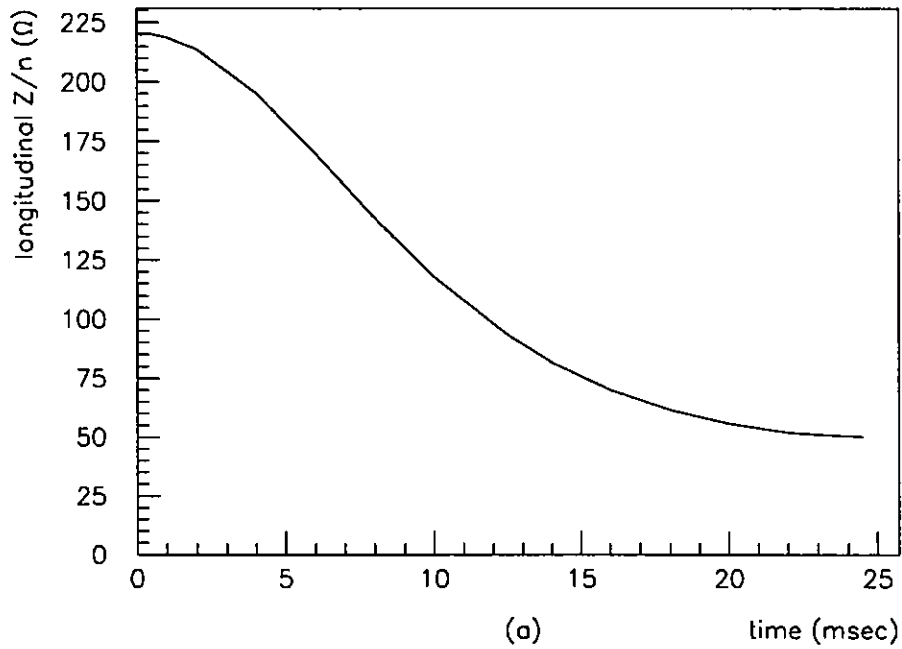
Figure II.5.2-2 Impedance due to Space Charge Plotted as a Function of Time. (Longitudinal impedance is shown in the top plot, a; transverse impedance is shown in the bottom plot, b.)

corrections result in a difference of less than 2% in the longitudinal impedance. Wang's method results in a +15% correction in the transverse impedance, and Okamoto's method results in a −20% correction.[8] Until a rigorous derivation is performed for a contour-following wire rf shield, we retain the averaged result and treat the above corrections as an uncertainty.

5.2.2 Other Contributions

Contributions to the coupling impedance from the rf shield, kickers, rf cavities, and BPMs are evaluated in this section. Unless otherwise noted, the formulae are derived in Reference 4.

The RCS has a ceramic vacuum chamber to avoid eddy current losses and distortions of the magnetic field. The rf shield is designed to make good contact between neighboring chambers to reduce the resistive impedance and to provide a return path for the image current. It shields the beam current and allows penetration of the slowly varying magnetic fields. About 120 equally spaced beryllium-copper wires, with an electrical conductivity of $\sigma = 1.4 \times 10^7 \ \Omega^{-1} m^{-1}$,[9] are mounted axially inside the chamber, as shown in Figure II.5.2-1. Formulae for a smooth, cylindrical, conducting beam pipe are used to estimate the impedance due to the rf shield at frequency ω:

$$\left(\frac{Z_\parallel}{n}\right)_{wall} = (1+j)\frac{R}{\sigma\delta b}\frac{\alpha}{n} \qquad\qquad \left(Z_\perp\right)_{wall} = \frac{2c}{\omega b^2}\left(Z_\parallel\right)_{wall} ,$$

where $\delta = \sqrt{2/\mu\sigma\omega}$ is the skin depth, $\alpha = (1+e^{-2(1-j)d/\delta})/(1-e^{-2(1-j)d/\delta})$ is a multiplier, and d is the thickness of the conducting surface. The multiplier becomes unity when the thickness of the conducting surface is greater than the skin depth, or $d \gg \delta$. The lowest possible frequencies occur at the values $n = 1$ in the longitudinal case and $|p + v| \approx 0.2$ in the transverse case. The skin depth is 0.28 mm for the lower frequency, 200 kHz, compared with a wire diameter of 1.5 mm. Therefore, the thick-wall approximation is used. $Z_\parallel/n$ scales in time with $\sqrt{\omega_0}$ and is 16% higher at extraction than at injection for a given n. $Z_\perp$ scales with $1/\sqrt{\omega_0}$ and is 16% lower at extraction for a given p.

The coupling impedance due to the six extraction kicker magnets is estimated by following the approach of Nassibian and Sacherer.[5] For no eddy current losses and infinite permeability in the ferrite core, the impedance due to a window-frame magnet is given by

$$\left(\frac{Z_\parallel}{n}\right) = \frac{\omega^2 \mu_0^2 x_0^2 l^2}{4w^2 Z_k} \frac{1}{n} \qquad \left(Z_\perp\right) = \frac{c\omega\mu_0^2 l^2}{4w^2 Z_k} ,$$

where l and w are the length and half-width of the magnet, respectively. The maximum horizontal displacement, x_0, of the corrected beam centroid is 1.0 mm. The kickers are traveling-wave structures terminated into a matched load; therefore, the magnet circuit impedance is $Z_k = 2Z_s$, where Z_s is the characteristic impedance of the cables that feed the magnet. When transit-time effects are included, the impedance due to the kickers becomes[4]

$$\text{Re}\left(\frac{Z_\parallel}{n}\right) = \frac{Z_s}{2} \frac{x_0^2}{ng^2} \sin^2\left(\frac{kl}{2}\right), \qquad \text{Im}\left(\frac{Z_\parallel}{n}\right) = \frac{Z_s}{4} \frac{x_0^2}{ng^2}\left(kl - \sin kl\right),$$

$$\text{Re}Z_\perp = \frac{Z_0 l}{4wg} \frac{1}{kl}\left(1 - \cos kl\right), \qquad \text{Im}Z_\perp = \frac{Z_0 l}{4wg} \frac{1}{kl}\left(kl - \sin kl\right),$$

where g is the gap half-height and $kl = \frac{\omega Z_0 g}{c Z_s w} l$ is the electrical length of the kicker winding. The magnet parameters are given in Table II.3.4-2. The longitudinal impedance is negligible. The real part of the transverse impedance is peaked around 1 MHz.

The aggregate effect of all the rf cavity higher-order modes (HOMs) on the bunch is described by an rf-equivalent broadband impedance. This is represented by a single, $Q = 1$ resonator centered at the cutoff frequency ω_c and is calculated by using[10]

$$\left(\frac{Z_\parallel}{n}\right)_{\text{HOM}} = N_{rf} \sum_{q=2}^{M} \left(\frac{R_{sh}}{Q}\right)_q \frac{\omega_0}{\omega_{res,q}}, \qquad (\text{II.5.2-3})$$

where R_{sh} is the shunt resistance of cavity mode q, ω_{res} is the resonant frequency, Q is the quality factor, and $N_{rf} = 10$ is the total number of cavities. The fundamental mode is excluded from the sum. Modal analysis of the rf cavities described in Section II.4.3 was performed by using URMEL-T,[11] and the resulting mode frequencies and ratio R_{sh}/Q are summarized in Table II.5.2-2. These solutions correspond to a cavity tuned to the fundamental frequency of 1.3 MHz about midway through the acceleration cycle and for which R_{sh}/Q is equal to 105. The

mode at 5.6 MHz is the first quarter-wave resonance. At the fundamental frequency, the gap capacitance and ferrite inductance appear as lumped elements.

Modes where q is greater than 4 do not contribute significantly. The impedance in Table II.5.2-1 is obtained by using the values from Table II.5.2-2 and Equation II.5.2-3. The deflecting modes, corresponding to transverse impedance, lie considerably above the fundamental frequency and do not couple well to the beam. The lowest transverse mode occurs at 34 MHz, with an $R_\perp/Q$ of 0.03 Ω/m, and is negligible, as indicated in Table II.5.2-1.

There are a total of 56 two-electrode, stripline BPMs, one in each quadrupole. Half of these are horizontal pickups, and half are vertical. The impedance of each BPM is calculated by using

$$\left(\frac{Z_\parallel}{n}\right)_{BPM} = \left(\frac{\omega l}{c} + j\right)\left(\frac{\varphi}{2\pi}\right)^2 \frac{\omega_0 l}{c} Z_s \qquad \left(Z_\perp\right)_{BPM} = \frac{c}{\omega b^2}\left(\frac{4}{\varphi}\right)^2 \sin^2\left(\frac{\varphi}{2}\right)\left(Z_\parallel\right)_{BPM},$$

where it is assumed that $Z_s = 50\ \Omega$ is the characteristic impedance, $l = 0.6$ m is the length, and $\varphi = 0.25$ rad is the angle subtended by one 2.5-cm-wide stripline. The longitudinal impedance is evaluated at $\omega = n\omega_0$. These expressions are valid up to the frequency $\omega = \pi c/(2l)$, or 125 MHz. $\mathrm{Re}\left(Z_\parallel/n\right)$ increases by 80% at extraction, and $\mathrm{Im}\left(Z_\parallel/n\right)$ increases by 34%. $\mathrm{Re}\left(Z_\perp\right)$ increases by 15% at extraction, and $\mathrm{Im}\left(Z_\perp\right)$ is constant.

The impedance due to other components, such as vacuum ports and bellows, is expected to be negligible, because these components are isolated from the beam by the rf shield.

The impedances obtained from these calculations are summarized in Table II.5.2-1.

Table II.5.2-2 Ratio of Shunt Impedance and
Q of First Few HOMs for an rf Cavity

$\omega_{res}/2\pi$ (MHz)	R_{sh}/Q (Ω)
5.6	5.5
10.5	0.8
14.8[a]	0.2

[a] Extrapolation of ferrite properties beyond normal operating range of 0.5 to 10 MHz.

5.3 LONGITUDINAL INSTABILITIES

Of the several known longitudinal instabilities, only the microwave instability due to the coupling impedance between the beam and its surroundings needs to be considered for the RCS. This instability should not occur in a machine operating below transition energy if the coupling impedance for the ring is purely capacitive. In the RCS, the impedance is largely capacitive, and the instability is not expected to occur; however, the instability could occur when there are resistive components. The instability growth rate then depends on the momentum distribution of the beam, particularly the shape of the distribution tails. A rigorous analysis of this instability requires knowledge not only of the coupling impedance seen by the beam, but also of the peak current and energy spread of the beam. At this stage, this beam information was obtained through Monte Carlo simulations.

The following steps are taken to design a conservative system to prevent the onset of instability:

- The impedance contributions from the various RCS components are estimated.

- The Keil-Schnell criterion, derived for a coasting beam, is applied to bunched beams; this is a commonly accepted practice.

- Although the Keil-Schnell criterion overestimates the severity of the instability below transition, this criterion is used to obtain the required $\Delta p/p$ to raise the threshold current.

- By using the peak current and energy spread of the circulating beam obtained from the longitudinal tracking studies described in Section II.4.1.3, a detailed analysis of the stability diagram is made.

A simplified criterion for the longitudinal stability threshold, independent of the details of the particle phase space distribution and applicable to bunched beams, is written as[1,2]

$$\left|\frac{Z_{\parallel}}{n}\right| \le F \frac{|\eta|\beta^2 E/e}{I_{pk}} \left(\frac{\Delta p_{fwhm}}{p}\right)^2, \qquad (II.5.3-1)$$

where local values of the current and momentum are used. Equation II.5.3-1 is commonly referred to as the Keil-Schnell (K-S) criterion. Here, $F \approx 1$ is a form factor, I_{pk} is the peak current, and $\eta = 1/\gamma_t^2 - 1/\gamma^2$, where γ_t is the transition energy.

The K-S criterion imposes a lower bound on the ratio $(\Delta p)^2/I_{pk}$. This requirement drives the peak rf voltage, because the momentum spread and peak current both depend on the rf voltage. Since the K-S criterion depends quadratically on the momentum spread and is inversely proportional to the peak current, increasing the momentum spread is more effective in achieving stability than is lowering the peak current. The optimal rf voltage profile over the cycle is obtained through simulation studies, as discussed in Section II.4.1.3. The peak current is obtained from the simulation by searching for the maximum of the particle distribution projected on the phase axis. The time-varying rf voltage and peak current are shown in Figure II.5.3-1a, and the bunching factor, $B_f = I/I_{pk}$, is shown in Figure II.5.3-1b. The energy spread is obtained from the projection of the particle distribution on the energy axis.

The momentum spread corresponding to the threshold for the microwave instability is computed by substituting the impedance listed in Table II.5.2-1 and the peak current from Figure II.5.3-1a into Equation II.5.3-1. The time variation in the longitudinal instability threshold is plotted together with the momentum spread obtained from tracking in Figure II.5.3-2. The beam remains in the stable region throughout the cycle, within the assumptions of the theory and the impedance estimate.

Below transition energy, it is possible to operate the machine with a large capacitive impedance outside the K-S boundary and preserve stability. The stable region is dependent on both the resistive component of the impedance and the shape of the distribution tails. The stable region can be seen in Figures II.5.3-3a and II.5.3-4a for two different momentum distributions; the details are discussed below.

The response of a beam to a periodic perturbation, $\exp(j(\Omega t - n\varphi))$, is given by the Vlasov equation, where φ is the azimuthal phase coordinate and Ω is the driving frequency of the perturbation. The solution to the small-amplitude Vlasov equation leads to a dispersion relation, which, for a coasting beam, is given by [12]

$$1 = -\frac{2}{\pi} \frac{I}{(E/e)\beta^2 |\eta|(\Delta p/p)^2} \frac{Z_\parallel}{n} I'_D .$$
(II.5.3-2)

I'_D is the normalized dispersion integral, given by

$$I'_D = j \int \frac{\partial f/\partial x}{x - x_1} dx ,$$
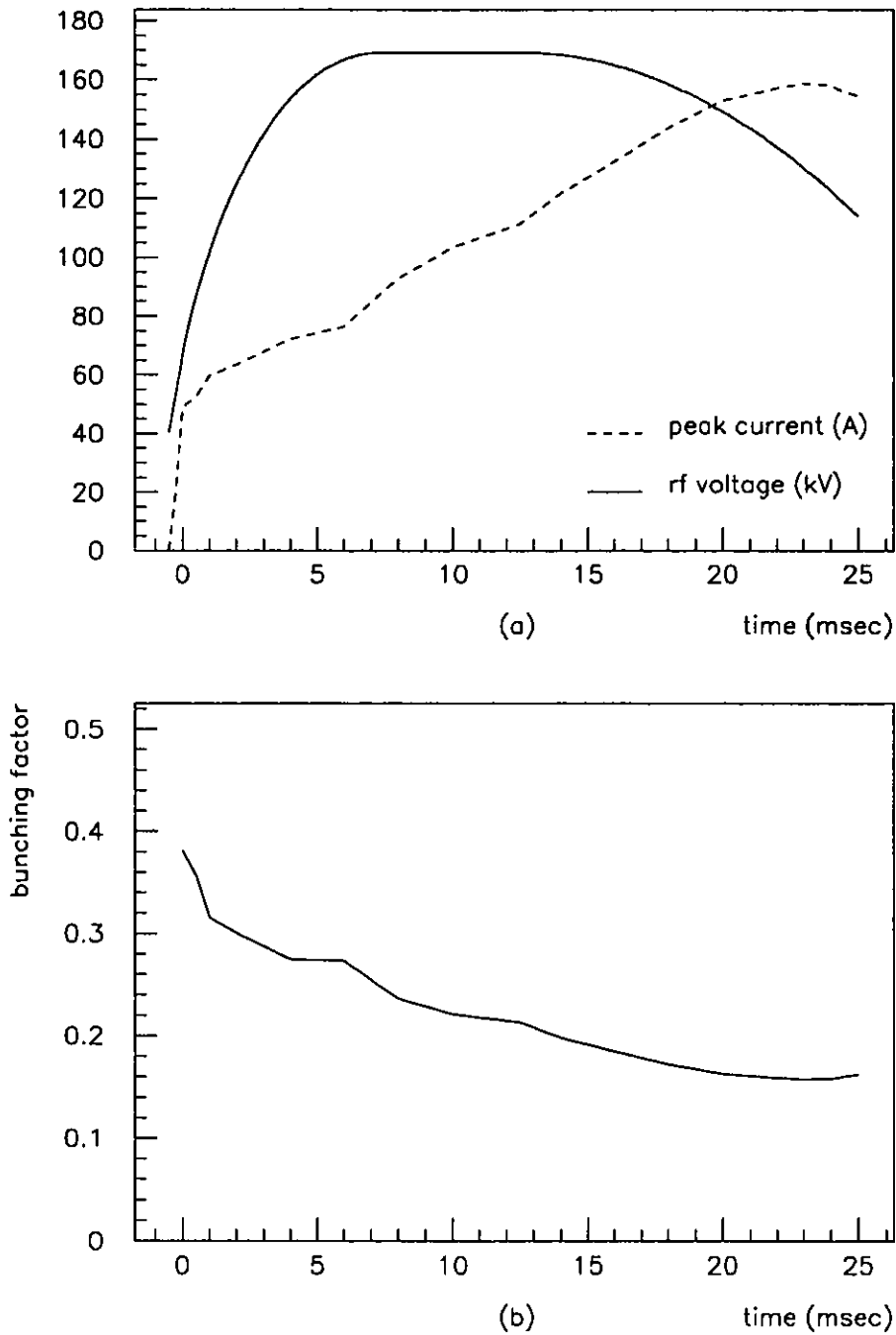
Figure II.5.3-1 Variation of the (a) Peak Current and (b) Bunching Factor, $B_f = I/I_{pk}$. (The rf voltage program is superimposed in the top graph, a. The peak current is obtained from the longitudinal tracking, and the small fluctuations are due to Monte Carlo statistics.)
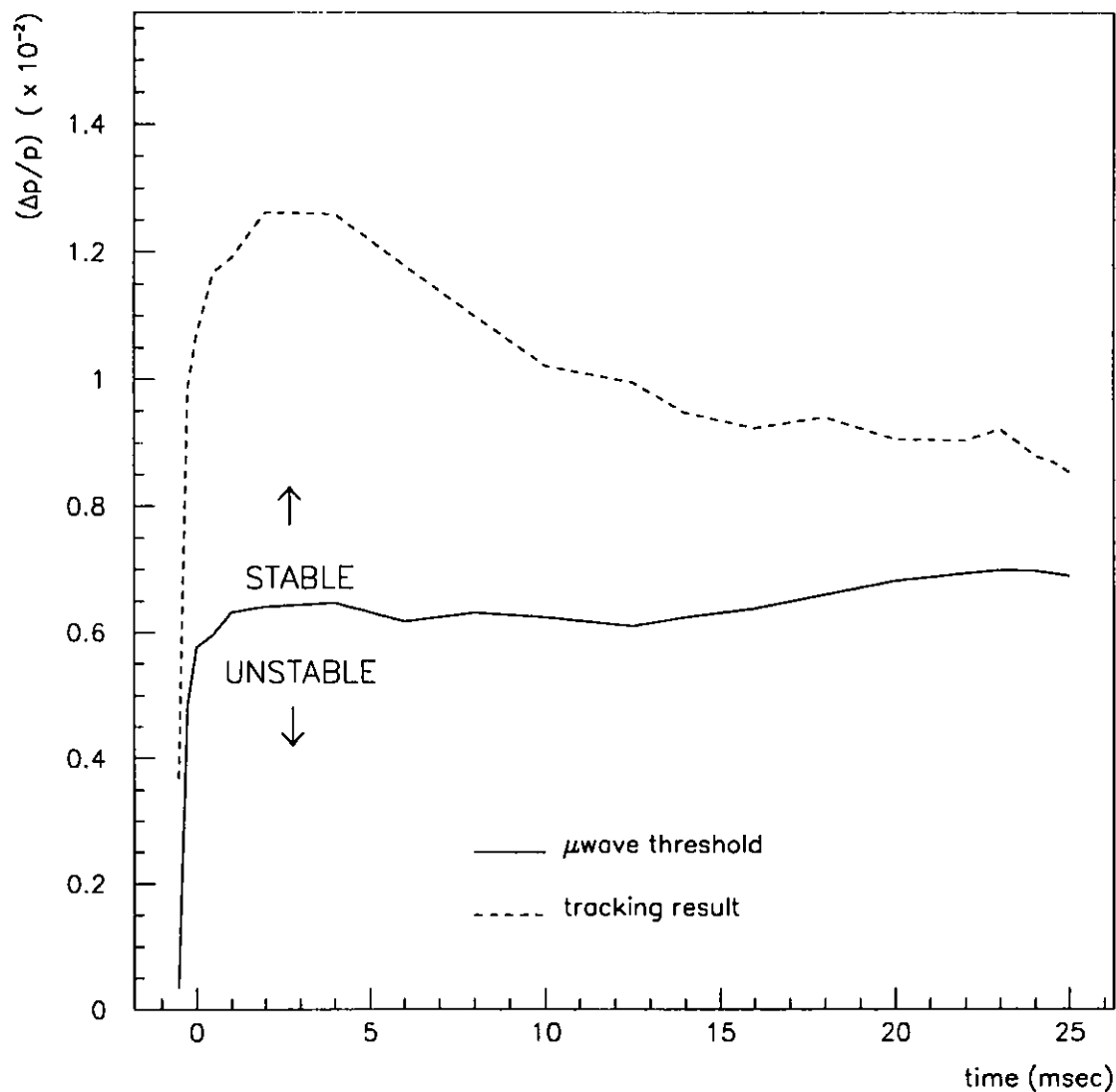
Figure II.5.3-2 Longitudinal Instability Threshold According to the K-S Criterion (lower curve) Plotted Together with the Momentum Spread Obtained from Tracking. (The small fluctuations are due to the Monte Carlo statistics. The beam remains in the stable region throughout the cycle.)

(a) quartic fit

(b) distrib ΔE (MeV): quartic fit $p2*(p1^2-x^2)^2$
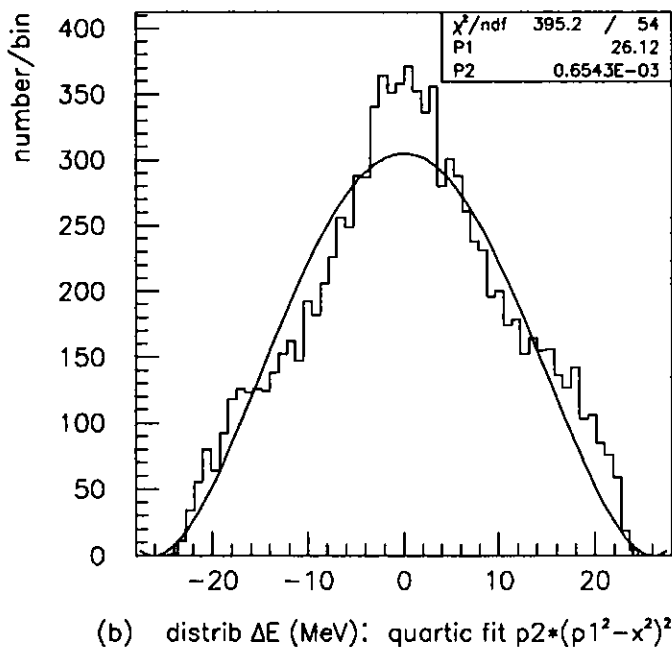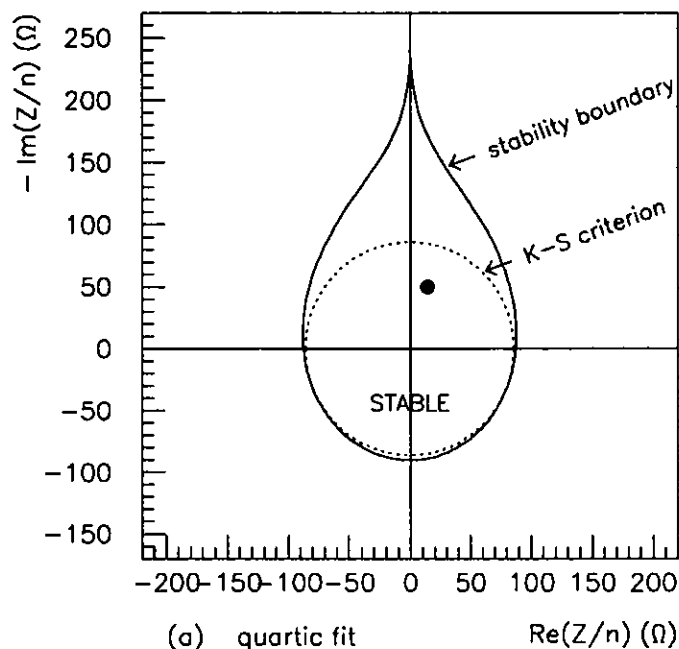
Figure II.5.3-3 Longitudinal Stability Boundary (a) for a Quartic Momentum Distribution (b). (The particle distribution is obtained from the tracking. The region in the top plot, a, that includes the origin is stable. Plot a also shows the stable region that satisfies the K-S criterion. The value of the longitudinal coupling impedance from Table II.5.2-1 is indicated by a dot near the vertical axis.)
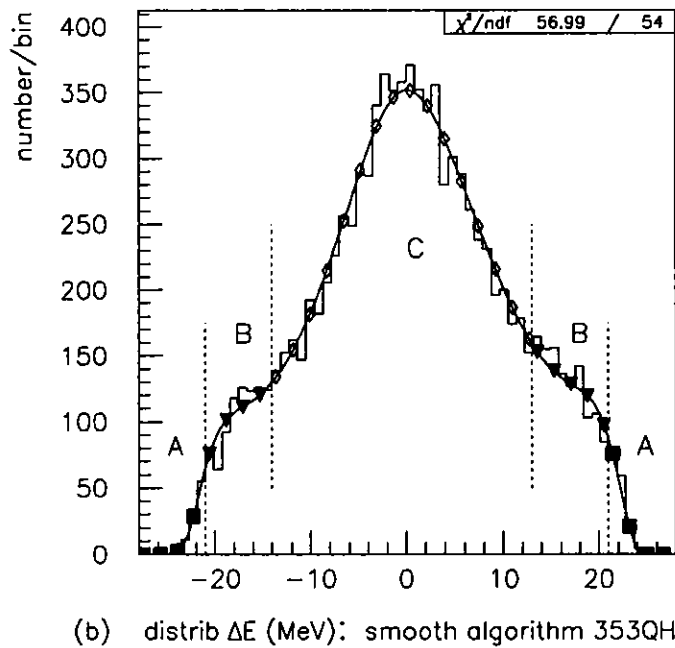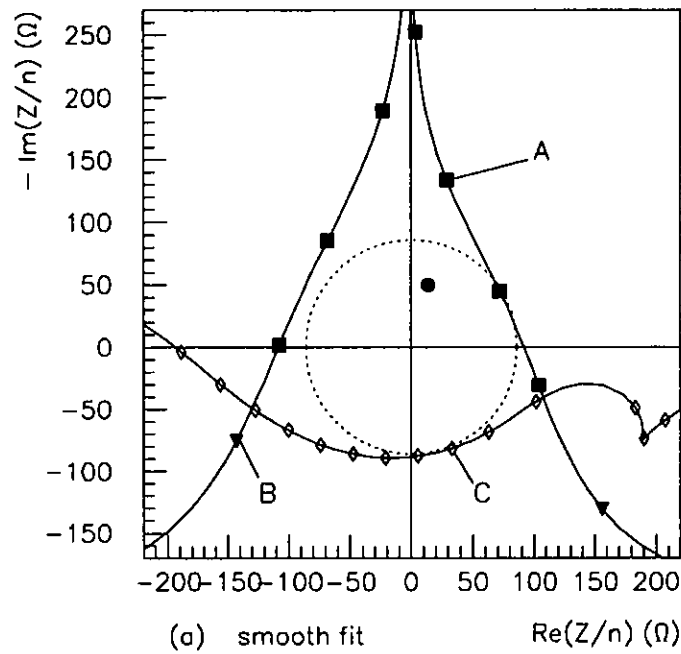
Figure II.5.3-4 Dependence of the Longitudinal Stability Boundary (a) on Momentum Distribution, Using the Distribution in (b). (The particle distribution in the lower plot, b, is a smooth fit of the results from the tracking. Sections of the stability diagram are labeled with the corresponding sections of the distribution. The upper portion of the stable region is entirely determined by the tails of the distribution.)

where

$x = (n\omega - n\omega_0)/(nS)$ describes the frequencies of the particles in the beam,

$x_1 = (\Omega - n\omega_0)/(nS)$ is related to the driving frequency of the perturbation,

$2S = -\eta\omega_0(\Delta p/p)$ is the full spread at half maximum of the revolution frequency distribution, and

$f(x)$ = normalized beam density distribution in frequency space.

The real part of the driving frequency, Ω, is related to an energy shift, while the imaginary part leads to growth of the perturbation.

   A finite spread in the revolution frequency or, equivalently, in momentum, gives rise to Landau damping through I'_D. The factor in Equation II.5.3-2 in front of I'_D is defined as

$$(V' + jU') = -\frac{2}{\pi} \frac{I}{(E/e)\beta^2 |\eta|(\Delta p/p)^2} \frac{\left(ReZ_\parallel + jImZ_\parallel\right)}{n}. \qquad (II.5.3-3)$$

Therefore, the dispersion relation can be rewritten as

$$1 = (V' + jU')\, I'_D.$$

This leads to the (U'-V') stability diagram, where the stability boundary is obtained when the dispersion integral is evaluated with $Im\,\Omega = 0$. The stability diagram can be plotted in the $Z_\parallel/n$ impedance plane by using Equations II.5.3-3 and II.5.3-2.

   The stability diagram for the RCS at 2 GeV is plotted in the impedance plane in Figure II.5.3-3a for the quartic momentum spread shown in Figure II.5.3-3b. Also shown in Figure II.5.3-3a is the stability region that satisfies the K-S criterion. The positive vertical axis denotes capacitive impedance, and the longitudinal coupling impedance listed in Table II.5.2-1 is plotted as a large dot. The particle momentum distribution in Figure II.5.3-3b is obtained from the simulation results.

   The stability boundary, which depends specifically on the momentum distribution, can give a higher limit than the K-S criterion. However, the upper portion of the stability boundary, which corresponds to the tails of the distribution, is highly sensitive to the beam distribution. This can be seen in Figure II.5.3-4a, which shows the stability boundary obtained by using a

different distribution, shown in Figure II.5.3-4b. The latter is obtained by using the 353QH smoothing algorithm.[13] Sections of the stability diagram are marked according to the corresponding section of the momentum distribution. Experience shows that in measured data, the tails in the line density can be rather unpredictable.

The machine is dominated by the capacitive space charge impedance, which then determines the resistive $\text{Re}(Z_\parallel/n)$ limit for stability. The stable boundary satisfying the K-S criterion in Figure II.5.3-3a suggests that the beam is stable to a threshold $\text{Re}(Z_\parallel/n)$ of 70 Ω. This can readily be achieved in the RCS. A similar analysis at 400 MeV gives a resistive limit of 550 Ω. The stability criterion is most critical near extraction because the peak current increases by a factor of five, while the momentum spread decreases by 30%. The result is that the right-hand side of Equation II.5.3-1 decreases by a factor of ten, while the impedance decreases by a factor of four.

5.4 TRANSVERSE INSTABILITIES

A transversely displaced beam generates an imbalance in the image current, which in turn perturbs the circulating beam. A non-zero resistivity in the coupling impedance causes a phase delay in the wake field, which can amplify the perturbations and cause them to grow. The head-tail instability is discussed first using Sacherer's bunched beam formalism.[14] Further discussion of damping transverse instabilities considers the coasting beam stability criterion.

The head-tail effect has been observed at the 500-MeV IPNS,[15] the KEK Booster,[16] and ISIS.[17] Therefore, it is analyzed in some detail for the RCS. In the absence of a tune spread, the growth rate of the head-tail instability, assuming a time dependence of $\exp(j\Omega_m t)$, is given by the imaginary part of [14]

$$\Omega_m = \frac{j}{(1+m)} \frac{cI Z_\perp(\omega_p)}{4\pi v(E/e)} F'_m,$$

where

$$F'_m = \frac{1}{B} \frac{h_m(\omega_p - \omega_\xi)}{\sum\limits_p h_m(\omega_p - \omega_\xi)}.$$

In this expression, it is assumed that the instability is dominated by the contribution from the impedance evaluated at a single frequency, $\omega_p = (p + v)\omega_0$. The total growth rate involves a convolution of this impedance with the bunch spectra, which are given by the functions h_m. The

lowest mode numbers, m, which denote the number of nodes along the bunch, give the highest growth rates. The chromatic frequency is $\omega_\xi = (\xi/\eta)v\omega_0$, where $\xi = (\Delta v/v)/(\Delta p/p)$ is the normalized chromaticity. The head-to-tail phase difference in the bunch is given by $\chi = \omega_\xi \tau_L$, where τ_L is the bunch length in seconds. The ratio of bunch length to ring circumference is given by B. When $\mathrm{Re}\,Z_\perp(\omega_p) < 0$, the instability grows; when $\mathrm{Re}\,Z_\perp(\omega_p) > 0$, the instability is damped.

For the RCS at 400 MeV, the form factor, F'_m, for m = 0 has a half-width of about 2 MHz, and the form factor for m = 1 peaks around 1 MHz. The chromaticity is generally corrected to zero to avoid a large betatron tune spread in the large-momentum particles, as discussed in Section II.2.1.6. When the chromaticity is zero, $\chi = 0$ and the bunch spectra are centered at zero frequency, where the rf shield and kicker impedances are important. In the vertical plane, the largest growth due to the rf shield impedance occurs when p = –6, and the largest growth due to the kicker impedance occurs when p = –7. The BPM impedance does not contribute significantly to the instability growth. The growth rates of the first few head-tail modes are given in Table II.5.4-1 for the corrected and uncorrected chromaticities at the end of injection. Similar results are found for the horizontal plane. The impedance and the frequency giving the largest growth are also listed; note that $\mathrm{Re}\,Z_\perp(\omega_p) = -\mathrm{Re}\,Z_\perp(-\omega_p)$. The lowest modes are stabilized at the natural chromaticity, $\xi = -1.2$. With the value of $\Delta p/p = 1.2\%$ obtained from the longitudinal tracking, however, the corresponding betatron tune spread at the natural chromaticity is 0.1. Therefore, the chromaticity is adjusted to be between 0 and –1.2 to shift the bunch spectrum to higher-order head-tail modes that have lower growth rates, while at the same time ensuring that the tune spread remains inside a resonance-free working region. The available region can be seen in the tune diagram, Figure II.2.1-8. The stability of modes m ≤ 2 is assured with $\xi \le -0.35$. This gives a betatron tune spread of 0.024.

Discussed next is the transverse stabilization of the beam, achieved by using a betatron tune spread or shift. An amplitude-dependent tune spread is introduced by octupoles and second-order effects in the sextupoles, leading to Landau damping. A momentum-dependent tune shift results from a finite chromaticity. The stability criterion derived for coasting beams is extended heuristically to bunched beams. According to Chao,[18] there are two stability criteria that can apply to bunched beams, depending on whether the instability growth rate is much larger or much smaller than the synchrotron frequency, ω_s. As shown in Table II.5.4-1, the expected

Table II.5.4-1 Head-Tail Instability Growth Rate vs. Chromaticity in the
Vertical Plane at the End of Injection

Mode number, m	$Re(Z_\perp)$ (kΩ/m)	Frequency (MHz)	Source of Impedance	Growth Rate (sec)$^{-1}$	
				$\xi = 0$	$\xi = -1.2$
0	8	0.3	rf shield	350	0
0	14	0.3	kickers	620	0
1	28	1.4	kickers	730	0
2	28	1.4	kickers	590	0

growth rates are of the order of the synchrotron frequency. Therefore, to be conservative, the peak current is used. The transverse stability criterion for the RCS is given by

$$|Z_\perp| < \frac{4\pi v \omega_0 (E/e)}{c I_{pk}} \Delta v.$$

The stability criterion is evaluated to determine the threshold tune spread, $(\Delta v)_{thresh}$, by equating the left- and right-hand sides of the above equation:

$$(\Delta v)_{thresh} = \frac{c I_{pk} |Z_\perp|}{4\pi v \omega_0 (E/e)}$$

Because the impedance is dominated by space charge effects, this expression is equivalent to the coherent Laslett tune shift (due to image charges only.) The results are presented in Table II.5.4-2 for the vertical plane at 400 MeV and 2 GeV. The impedance is taken from Table II.5.2-1.

The threshold tune spread determined from the stability criterion can be met by using the momentum-dependent chromatic contribution, $\Delta v_\xi = |(p - v)\eta + v\xi|(\Delta p/p)$, and/or the amplitude-dependent octupolar contribution, $\Delta v_{oct} = \frac{\beta_y a_y^2}{32\pi} k_{oct}$,[19] where $k_{oct} = \left(\frac{B'''l}{B\rho}\right)$ is the octupole strength. The standard strategy requires that each term satisfy the stability criterion independently, if possible.

Considered first is a solution using the condition $\Delta v_\xi \geq \Delta v_{thresh}$, and using the chromatic term only. In the vertical plane, the value of p is 6. If the momentum spread is left as a variable and the natural chromaticity is used, simple manipulations give

$$\frac{\Delta p}{p} \geq \frac{(\Delta v)_{thresh}}{|(p - v)\eta + v\xi|} = \begin{cases} 0.8\% & 400 \text{ MeV} \\ 0.6\% & 2 \text{ GeV} \end{cases}.$$

This is to be compared with a momentum spread of about 1% obtained in the longitudinal tracking study. Conversely, using the momentum spread from the tracking, one obtains the required chromaticity:

$$\xi \leq \frac{(\Delta v)_{thresh}}{v(\Delta p/p)} - \frac{(p - v)\eta}{v} = \begin{cases} -0.97 & 400 \text{ MeV} \\ -0.66 & 2 \text{ GeV} \end{cases}.$$

Table II.5.4-2 Threshold Tune Spread According
to the Coasting Beam Stability Criterion

Time in Cycle (msec)	$\text{Im}\,Z_{\perp}$ (MΩ/m)	$(\Delta\nu)_{thresh}$
0	2.7	0.06
25	1.4	0.03

Considered next is a solution using octupoles only and chromaticity fully corrected to zero. The required octupole tune spread is

$$\Delta v_{oct} \geq \Delta v_{thresh}.$$

With a beta function, β_y, of 12 m and beam size, a_y, of 0.07 m at 400 MeV and 0.04 m at 2 GeV, the integrated octupole strength per super-period required for stability is given by

$$k_{oct} \geq \frac{1}{4} \frac{32\pi}{\beta_y} \frac{(\Delta v)_{thresh}}{a_y^2} = \begin{cases} 24 \text{ m}^{-3} & 400 \text{ MeV} \\ 44 \text{ m}^{-3} & 2 \text{ GeV} \end{cases}.$$

It is assumed that the octupoles are located in each of the four super-periods, at the location of each defocusing quadrupole. The required octupole strength does not degrade the dynamic aperture. It has long been observed in other low-energy accelerators that the current required in the correction octupoles is found to be less than that predicted by the theory.[16,20]

Active beam feedback is an option to suppress or damp undesired beam oscillations for the head-tail instability. A typical feedback system consists of a beam position detector, processing electronics and a delay unit, a power amplifier, and a deflection kicker. The characteristics of the feedback system include specifications of the bandwidth, gain, and kicker strength. Other considerations for the system, not discussed here, include reducing noise sensitivity and maintaining synchronicity with the rapidly varying revolution frequency. The bandwidth is about $\omega_0/2$, or 500 kHz. The angular deflection given by an electrostatic kicker is given by

$$\Delta\theta = \frac{\Delta x}{l} = \frac{eE_k l}{2\beta^2 (E_{beam})},$$

where E_{beam} is the beam energy, E_k is the electric field, and l is the length of the kicker. If an instability rise time of 1 msec and a revolution period of 1 μsec are assumed, the instability amplitude growth is

$$\frac{\Delta x}{x_0} = \frac{\tau_{rev}}{\tau_{growth}} = 10^{-3},$$

where x_0 is the minimum detected beam deviation, assumed to be 0.5 mm. This ratio is the gain

divided by two. Since $x' = \dfrac{x}{\beta_x}\bigg|_{max}$, the kicker deflection angle can be written as $\Delta\theta = \dfrac{\Delta x}{x_0}\dfrac{x_0}{\beta_x}$,

and the electric field for the kicker becomes

$$E_k \geq 10^{-3}\, \frac{x_0}{\beta_x}\, \frac{2\beta^2\left(E_{beam}\right)}{e l}\ .$$

This becomes 230 V/m for a 0.5-m kicker length at 400 MeV, and 950 V/m at 2 GeV, using the average value $\beta_x = 6$ m. It is customary, in practice, to design in an extra factor of 5 to 10 in the electric field.

5.5 ELECTRON-PROTON INSTABILITY

The residual gas in the vacuum chamber is ionized by the beam due to collisional processes. The electrons liberated from the gas molecules can be trapped in the proton beam's potential well. Because the trapped electrons oscillate in the potential well, the transverse motions of electrons and protons are coupled, which can result in amplitude growth. This instability, first observed in the coasting beam at the CERN Intersecting Storage Ring (ISR), is called the electron-proton ("e-p") instability. This instability is characterized by a growth time that is comparable with the fastest coherent instabilities caused by coupling impedances. This instability should not be a concern in the RCS because the circulating beam is bunched, and it has also not been observed in similar rapid cycling machines, such as ISIS[21] at Rutherford, IPNS at Argonne, and the KEK Neutron Source (KENS).

However, a fast instability known as "PSR instability," which is similar to the e-p instability, was recently observed at the Proton Storage Ring (PSR) at Los Alamos during chopped beam accumulation.[22] Whether or not this is a true e-p instability is unknown; however, prior to the onset of the instability, the gap between the bunch passages is filled by bunch leakage. The RCS rf voltage is high enough to avoid bunch leakage during the acceleration period (see Section II.4.1).

The longitudinal beam distribution in the waiting bucket during injection is sensitive both to chopper efficiency and to injection mismatch from the linac. The possibility of e-p instability during injection was investigated, assuming a coasting beam, which is the worst case. The analytical results show that the required neutralizations (electrons/protons) are between 5% and

10%, depending on the tune and the beam size.[23] Neutralization from the residual gas satisfies the following formula:[24]

$$\eta = 0.85 \, P(nTorr) \, t(sec).$$

The vacuum pressure must be less than 10^{-7} Torr for $t = 0.5$ msec injection time. The design value is 10^{-8} Torr.

    The stripping foil is also a source of electrons, because each H^- ion produces two electrons after stripping. This is potentially dangerous, because the circulating bunch could interact with the electron cloud during the injection period of every turn. Clearing electrodes are installed around the foil to circumvent this potentially dangerous situation.

5.6 REFERENCES

1. V.K. Neil and A.M. Sessler, "Longitudinal resistive instabilities of intense coasting beams in particle accelerators," Rev. Sci. Instrum. **36**(4), 429 (1965).

2. E. Keil and W. Schnell, *Concerning Longitudinal Stability in the ISR*, CERN Report No. TH-RF/69-48 (1969).

3. L.J. Laslett, V.K. Neil, and A.M. Sessler, "Transverse resistive instabilities of intense coasting beams in particle accelerators," Rev. Sci. Instrum. **36**(4), 436 (1965).

4. K.-Y. Ng, "Fields, impedances, and structures," in *The Physics of Particle Accelerators*, AIP Conference Proceedings 184, p. 515f (1989).

5. G. Nassibian and F. Sacherer, "Methods for measuring transverse coupling impedances in circular accelerators," Nucl. Instrum. Methods **159**, 21 (1979).

6. T-S. F. Wang, *Electrostatic Field of a Perturbed Beam with RF-Screening Wires*, CERN Report No. PS 94-08 (DI) (1994).

7. AUSTRON Accelerator Feasibility Study, Chapter 4, p. 145 (Oct. 26, 1994).

8. K.C. Harkay, *Study of Corrections to the Geometrical Factor in the Space Charge Impedance for the IPNS-II*, Argonne National Laboratory Report No. NS-95-4 (Mar. 1995).

9. *CRC Handbook of Physics and Chemistry*, 74th edition.

10. J.L. Laclare, "Bunched beam coherent instabilities," in *Proceedings of 1985 CERN Accelerator School*, CERN Report No. 87-03 (1987).

11. U. Lauströer, U. van Rienen, and T. Weiland, *URMEL and URMEL-T User Guide*, DESY Report No. M-87-03 (Feb. 1987).

12. A. Hoffman, "Single-beam collective phenomenon – longitudinal," in *Proceedings of Theoretical Aspects of the Behavior of Beams in Accelerators and Storage Rings*, CERN Report No. 77-13 (Erice, Nov. 1976).

13. J.H. Friedman, "Data analysis techniques for high energy particle physics," in *Proceedings of the 1974 CERN School of Computing*, CERN Report No. 74-23, p. 295 (Godoysund, Norway, Aug. 1974).

14. B. Zotter and F. Sacherer, *Transverse Instabilities of Relativistic Particle Beams in Accelerators and Storage Rings*, CERN Report No. 77-13 (1977).

15. Y. Cho and A.V. Rauchas, "Observations and cure of the head-tail effect in the Argonne Rapid Cycling Synchrotron," IEEE Trans. Nucl. Sci. **NS-28**(3), 2585 (June 1981).

16. Y. Kimura et al., "Transverse coherent instability in the KEK Booster," in *Proceedings of the Xth International Conference on High Energy Accelerators*, Vol. 2, p. 30 (Serpukhov, July 1977).

17. G.H. Rees, "Interpretation of the higher-order mode, head-tail motion observed on ISIS," Particle Accelerators **39**, 159 (1992).

18. A. Chao, *Physics of Collective Beam Instabilities in High Energy Accelerators* (John Wiley and Sons, Inc., 1993).

19. E. Wilson, *Nonlinearities and Resonances*, CERN Report No. 85-19 (Nov. 1985).

20. D. Möhl and H. Schonauer, "Landau damping by non-linear space-charge forces and octupoles," in *Proceedings of the 9th International Conference on High Energy Accelerators*, p. 380 (1974).

21. C.W. Planner, "Reaching 200 μA on ISIS," in *Proceedings of the 12th ICANS Workshop* (Abingdon, U.K., May 1993).

22. D. Neuffer, "Transverse instability in the PSR," in *Proceedings of the Workshop on Accelerators for Future Spallation Neutron Sources*, LA-UR-93-1356, Vol. II B (Feb. 1993).

23. Y.C. Chae, *Electron-Proton Instability in the IPNS-Upgrade RCS: Part I,* Argonne National Laboratory Report No. NSA-95-2 (Feb. 1995).

24. Y.C. Chae, *Calculation of Beam Neutralization in the IPNS-Upgrade RCS,* Argonne National Laboratory Report No. NSA-95-1 (Jan. 1995).

6.1 INTRODUCTION

An operating pressure on the order of 10^{-8} Torr is achieved by using ion pumps distributed evenly around the RCS ring. The vacuum chamber is made of high-purity ceramic to avoid eddy current effects from the ramping fields. It has a wire liner, which acts as a radio-frequency (rf) shield to minimize coupling impedances, in a manner similar to that previously accomplished at ISIS.[1,2]

6.2 VACUUM CHAMBER DESIGN

The vacuum chamber is constructed in sections made of 99.7%-pure alumina ceramic. These sections span several magnets and are independently supported. Clearance is sufficient to avoid thermal and mechanical stresses. The nominal cross sections for a dipole chamber and a quadrupole/sextupole chamber are shown in Figure II.6.2-1. Vacuum chamber dimensions are listed in Table II.6.1-1.

Ceramic chambers with these cross sections are produced in standard lengths of up to 60 cm by means of the isostatic forming process. This process provides the most accurate dimensional control of both interior and exterior ceramic surface geometry, and it allows modest curvatures to be imparted without sacrificing dimensional accuracy. Both cross sections have been analyzed for mechanical strength at the aforementioned operating pressure with the ANSYS 5.0 finite-element-analysis software. Maximum tensile loading for both sections was calculated to be less than 4,000 pounds per square inch (psi). High-purity alumina ceramics have an ultimate tensile strength ranging from 38 to 40 ksi for material with the normal amount of inclusions and flaws.

A typical vacuum chamber cell is longer than 60 cm; therefore, several of the isostatically formed 60-cm-long sections must be fused together. The doweling system shown in Figure II.6.2-2 is used to maintain chamber-to-chamber alignment during glass fusion.

At the end of each section are glass-fused ceramic flanges that mate with the metallic sections of adjoining components. A metallic O-ring forms the vacuum seal between the ceramic and metal flanges. A clamping system uniformly compresses the seal circumferentially while keeping the ceramic flange in compression, as shown in Figure II.6.2-3. A typical cell is shown in Figure II.6.2-4. Vacuum integrity is maintained at pressures on the order of 10^{-8} Torr.

A semiconducting ceramic glaze consisting of conductive materials within a lead-quartz glass matrix is applied to the interior of the ceramic chamber. The coating is bonded to the ceramic at high temperature, resulting in a surface resistance of 100 KΩ per square. Outgassing rates are typically between 10^{-8} and 10^{-14} Torr-L/sec-cm^2 for such coatings.[4,5] The design value for this machine is 10^{-10} Torr-L/sec-cm^2. The coating provides static charge dissipation, and some rf shielding.

Table II.6.1-1 Vacuum Chamber Dimensions

Parameters	Values	Units
Dipole chamber height	15.6	cm
Dipole chamber width	17.6	cm
Quadrupole chamber height	20.7	cm
Quadrupole chamber width	27.1	cm
Total RCS chamber length	19,040	cm
Total RCS chamber volume	6,390	L
Total RCS chamber surface area	1.29×10^6	cm^2

6.1 INTRODUCTION

An operating pressure on the order of 10^{-8} Torr is achieved by using ion pumps distributed evenly around the RCS ring. The vacuum chamber is made of high-purity ceramic to avoid eddy current effects from the ramping fields. It has a wire liner, which acts as a radio-frequency (rf) shield to minimize coupling impedances, in a manner similar to that previously accomplished at ISIS.[1,2]

6.2 VACUUM CHAMBER DESIGN

The vacuum chamber is constructed in sections made of 99.7%-pure alumina ceramic. These sections span several magnets and are independently supported. Clearance is sufficient to avoid thermal and mechanical stresses. The nominal cross sections for a dipole chamber and a quadrupole/sextupole chamber are shown in Figure II.6.2-1. Vacuum chamber dimensions are listed in Table II.6.1-1.

Ceramic chambers with these cross sections are produced in standard lengths of up to 60 cm by means of the isostatic forming process. This process provides the most accurate dimensional control of both interior and exterior ceramic surface geometry, and it allows modest curvatures to be imparted without sacrificing dimensional accuracy. Both cross sections have been analyzed for mechanical strength at the aforementioned operating pressure with the ANSYS 5.0 finite-element-analysis software. Maximum tensile loading for both sections was calculated to be less than 4,000 pounds per square inch (psi). High-purity alumina ceramics have an ultimate tensile strength ranging from 38 to 40 ksi for material with the normal amount of inclusions and flaws.

A typical vacuum chamber cell is longer than 60 cm; therefore, several of the isostatically formed 60-cm-long sections must be fused together. The doweling system shown in Figure II.6.2-2 is used to maintain chamber-to-chamber alignment during glass fusion.

At the end of each section are glass-fused ceramic flanges that mate with the metallic sections of adjoining components. A metallic O-ring forms the vacuum seal between the ceramic and metal flanges. A clamping system uniformly compresses the seal circumferentially while keeping the ceramic flange in compression, as shown in Figure II.6.2-3. A typical cell is shown in Figure II.6.2-4. Vacuum integrity is maintained at pressures on the order of 10^{-8} Torr.

A semiconducting ceramic glaze consisting of conductive materials within a lead-quartz glass matrix is applied to the interior of the ceramic chamber. The coating is bonded to the ceramic at high temperature, resulting in a surface resistance of 100 KΩ per square. Outgassing rates are typically between 10^{-8} and 10^{-14} Torr-L/sec-cm^2 for such coatings.[4,5] The design value for this machine is 10^{-10} Torr-L/sec-cm^2. The coating provides static charge dissipation, and some rf shielding.

Table II.6.1-1 Vacuum Chamber Dimensions

Parameters	Values	Units
Dipole chamber height	15.6	cm
Dipole chamber width	17.6	cm
Quadrupole chamber height	20.7	cm
Quadrupole chamber width	27.1	cm
Total RCS chamber length	19,040	cm
Total RCS chamber volume	6,390	L
Total RCS chamber surface area	1.29×10^6	cm^2

Figure II.6.2-1 Dipole Chamber Cross Section (upper) and Quadrupole/Sextupole Chamber Cross Section (lower).
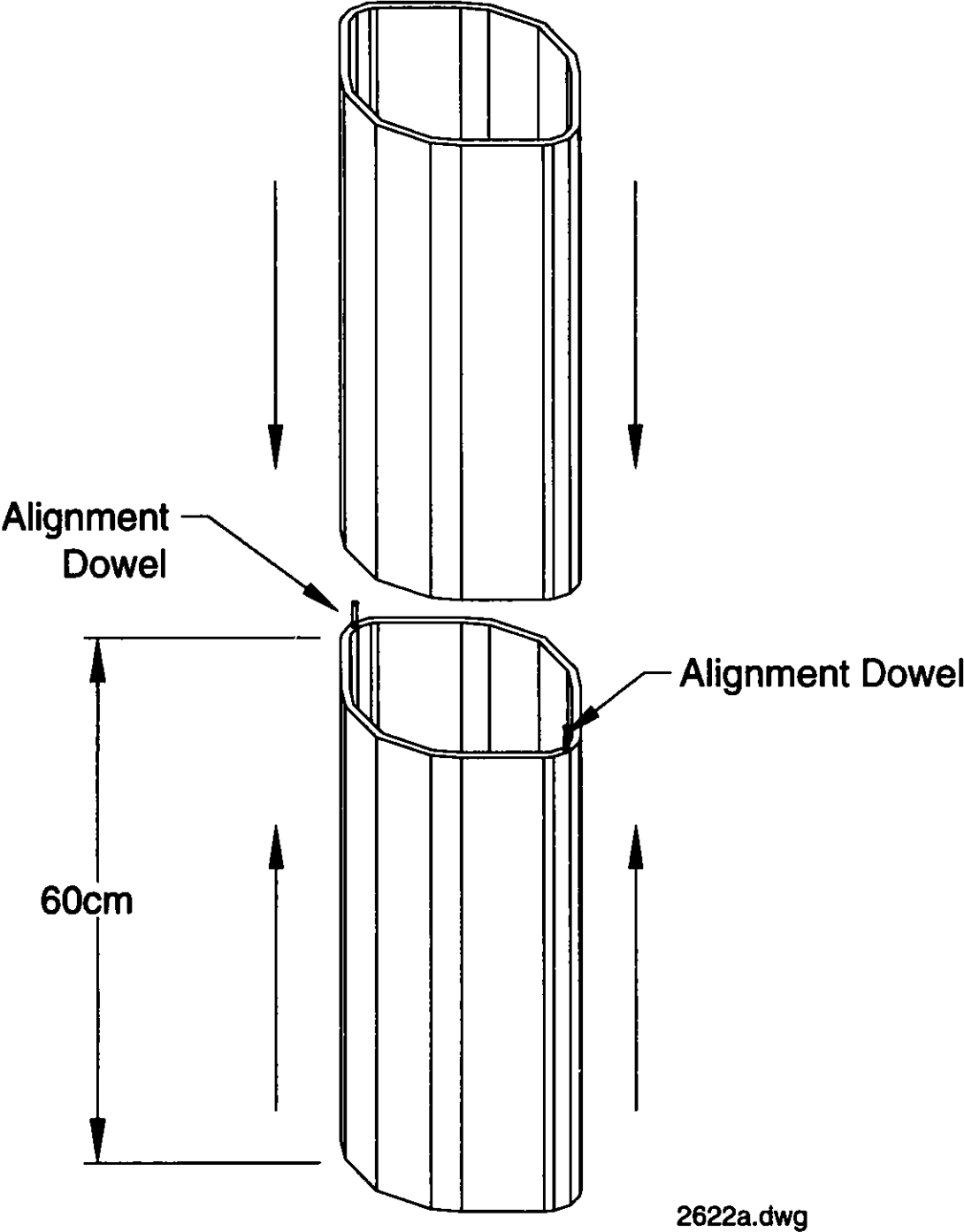
Figure II.6.2-2 Alignment System for Glass Fusion Bonding of Alumina Sections.
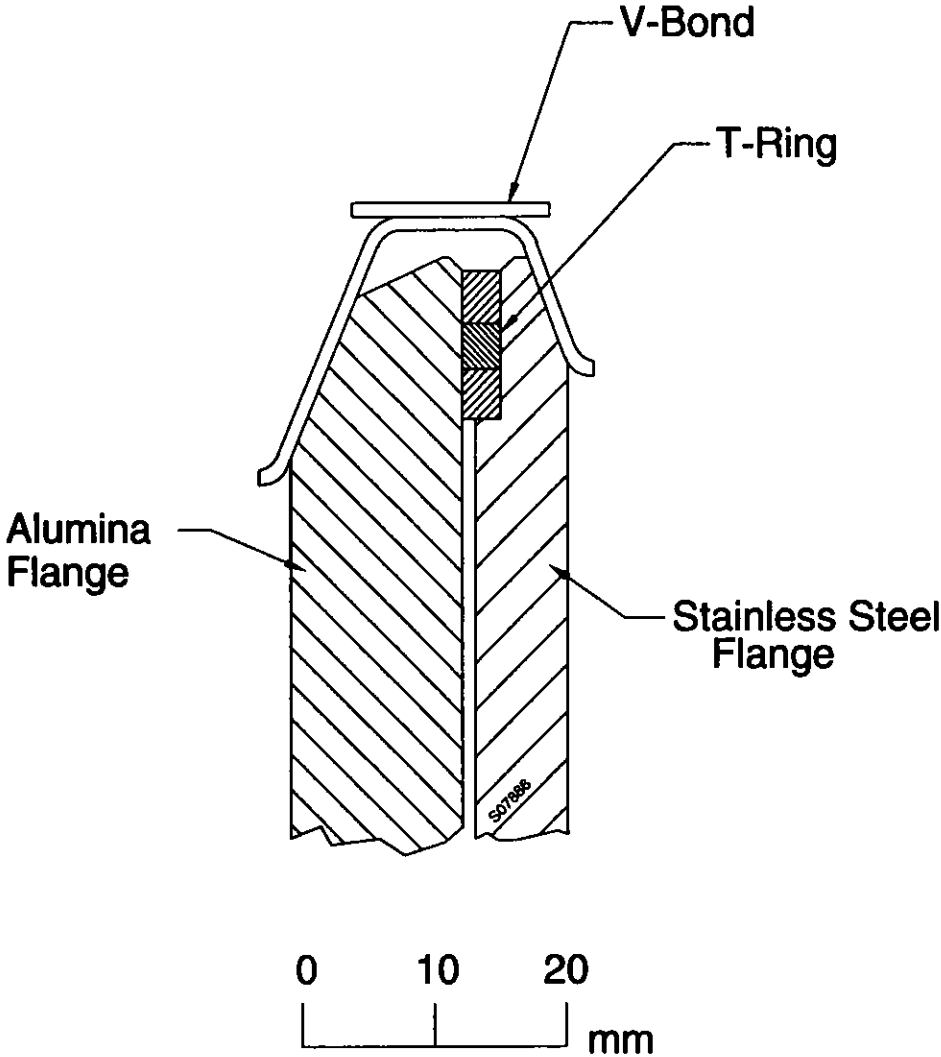
Figure II.6.2-3 Ceramic Vacuum Chamber Joint Detail.

S.Steel Bellows

Ceramic End Flange

Glass-Fusion Interfaces

S.Steel
End Flange

2.5m

2624a.dwg

S.Steel Flange Mates to
Ceramic End Flange
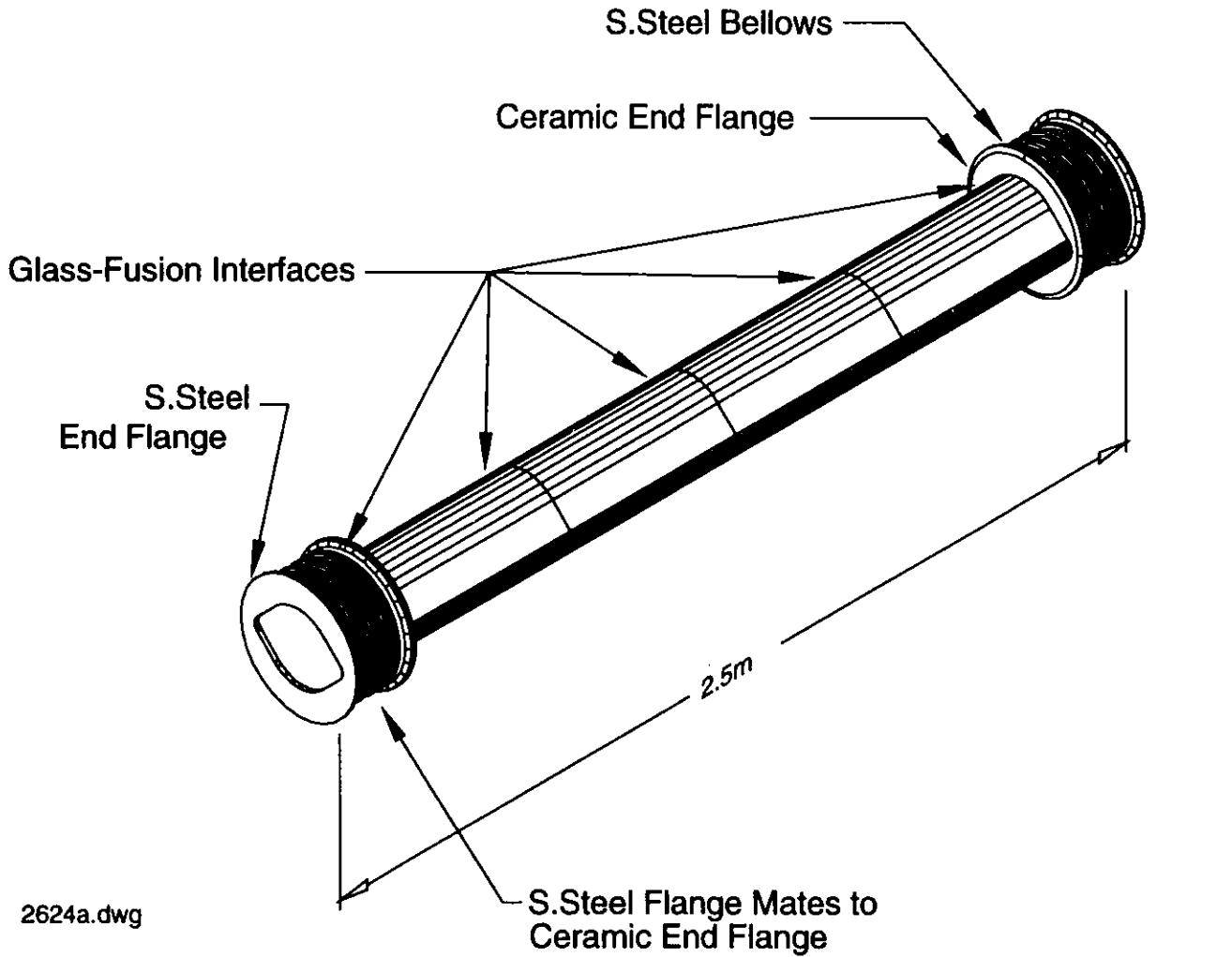
Figure II.6.2-4 Typical Quadrupole/Sextupole Ceramic Chamber Cell.

DIA.1.5mm

120 PLACES

W/3mm SPACING

BSC APERTURE

CERAMIC VACUUM
CHAMBER

207.0mm

88.0mm

228.0mm

271.2mm

S08324.dwg

CERAMIC

RIB
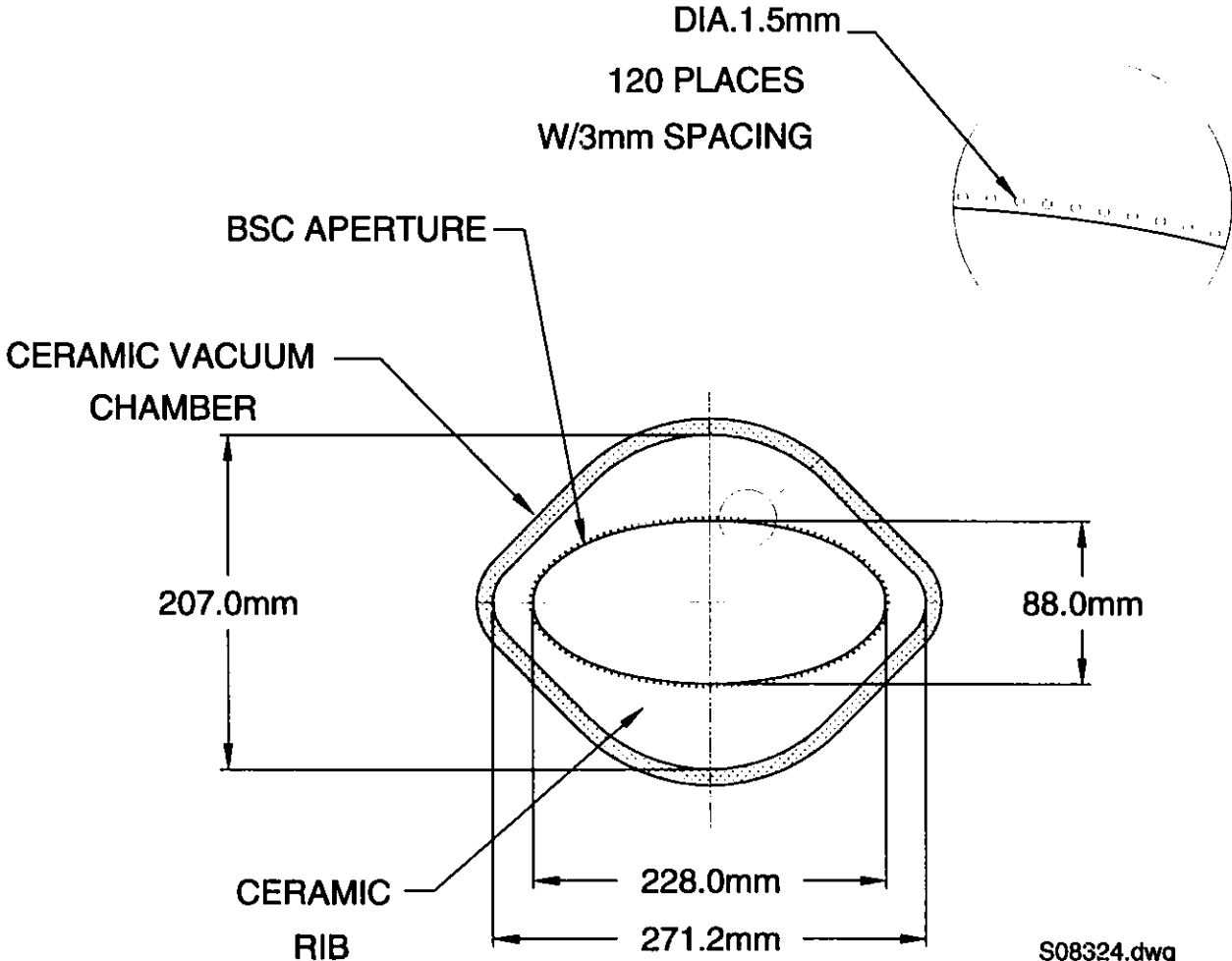
Figure II.6.2-5 Wire Liner, Which Acts as a Radio-Frequency Shield
and Is Supported on Ceramic Ribs.

The rf shield is actually a wire liner that runs the entire length of the vacuum chamber. Its cross section follows the beam envelope along the lattice, as shown in Figure II.6.2-5. It shields accelerator components from rf energy induced by the beam, and it also provides a low-impedance return path for beam image currents.

The wires are made of 1.5-mm-thick Be-Cu and have a center-to-center spacing of 4.5 mm around the perimeter of the chamber. They are periodically supported on ceramic ribs. One of the ceramic ribs in a quadrupole chamber is shown in Figure II.6.2-5.

Each wire is terminated in discrete capacitors at the flanged ends, as shown in Figure II.6.2-6. The capacitors inhibit current flow around the loop formed by the rf shield wires and ground.[2,3]

Intracell compliance, and also alignment between cells and individual special components such as kicker magnets, is achieved by the use of flanged bellows, such as those shown in Figure II.6.2-4.

Metallic finger assemblies provide electrical continuity for rf shielding and maintain the vacuum chamber geometry in the bellows region, as shown in Figure II.6.2-7.

This vacuum chamber system uses existing technologies and designs and can be produced by commercial vendors. Coating materials and manufacturing techniques exist.

6.3 VACUUM PUMPING SYSTEM

Eight 300-L/min mechanical pumps and eight 400-L/sec turbo-molecular pumps are used for the roughing system. Rough pumping from atmospheric pressure to 10^{-3} Torr takes about one hour. The turbo-molecular pumps reduce the pressure to the order of 10^{-6} Torr in six hours.

Thirty-six 220-L/sec ion pumps plus four 60-L/sec ion pumps are used to pump the RCS down to less than 10^{-7} Torr.

Ion pump locations around one quarter of the ring (or one super-period) are shown in Figure II.6.3-1. The total pumpdown time from atmospheric pressure to 10^{-7} Torr is about 10 hours.

A vacuum finite-element-analysis computer program developed at Argonne National Laboratory has successfully modeled other vacuum systems.[6] This program was used to help design the RCS vacuum system.
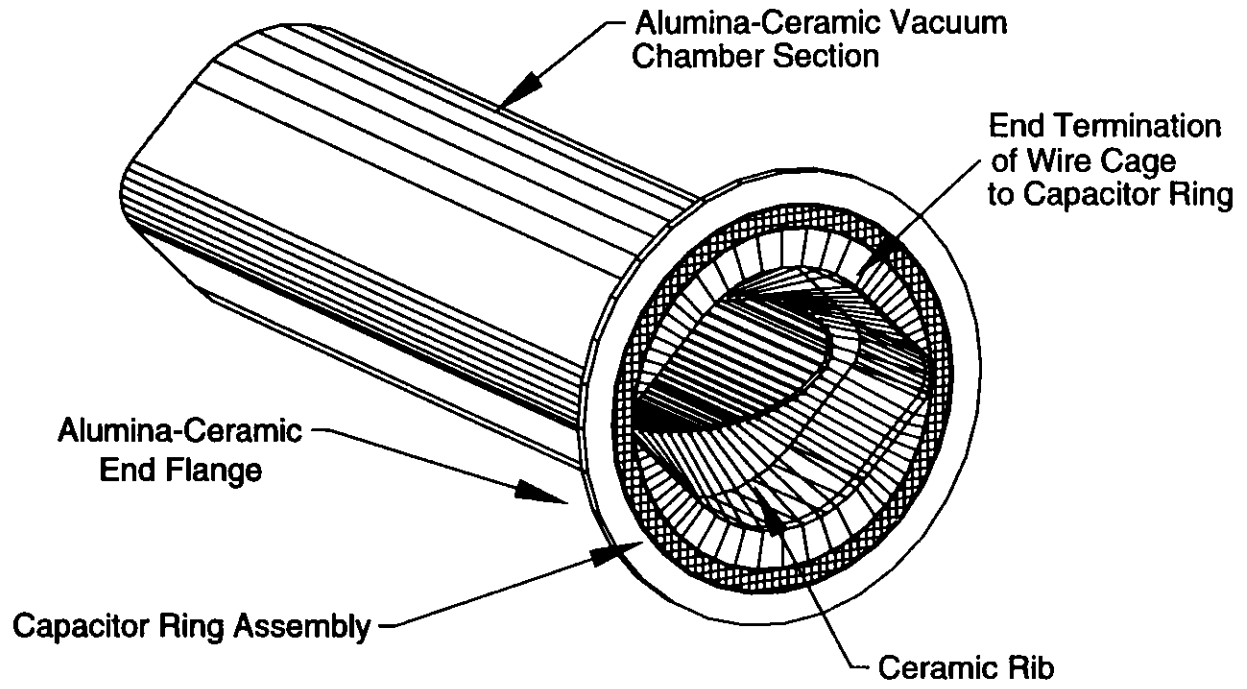
Figure II.6.2-6 Vacuum Chamber Cell-to-Cell Capacitive Coupling Layout.
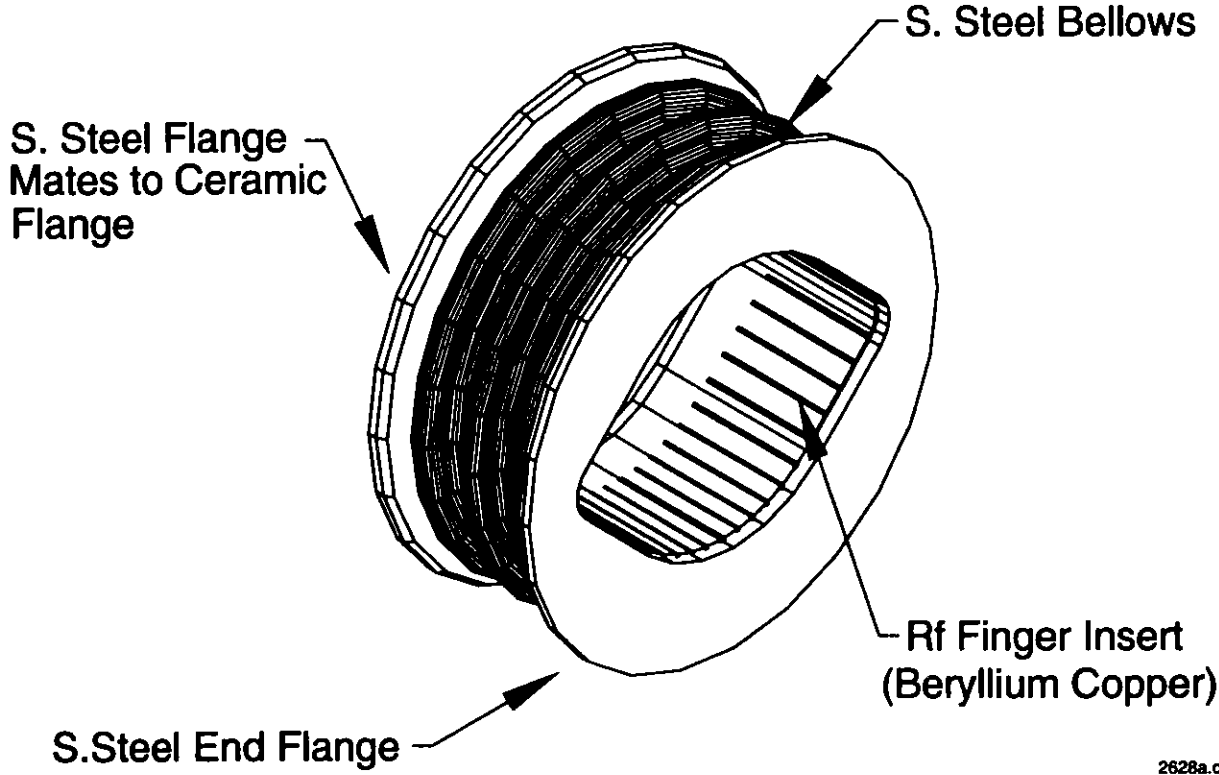
Figure II.6.2-7 Radio-Frequency Finger Layout.

SM = SEXTUPOLE MAGNET

QM = QUADRUPOLE MAGNET

BM = BENDING MAGNET

= ION PUMPS

FILE: 808388C.DWG

Figure II.6.3-1 Ion Pump Locations Around One Quarter of the Ring.

A super-period is divided into 20 elements. Data on the volume, surface area, outgassing rate, pumping speed, and conductance for each element are input for the program. Table II.6.3-1 lists the input data for the program. Figure II.6.3-2 shows the calculated vacuum profile in one sector. The highest pressure is less than 3×10^{-8} Torr.

Table II.6.3-1 Input Data for Vacuum Finite-Element-Analysis Computer Program

Element Number	Volume (L)	Conductance (L/sec)	Pumping Speed (L/sec)	Thermal Desorption (Torr L/sec)
1	3.99E+01	1.24E+03	0	7.50E-07
2	2.67E+01	4.00E+02	0	6.61E-07
3	9.54E+01	6.20E+02	2.00E+02	1.92E-06
4	2.67E+01	4.00E+02	0	6.61E-07
5	9.54E+01	6.20E+02	2.00E+02	1.92E-06
6	2.67E+01	4.00E+02	0	6.61E-07
7	2.25E+02	3.31E+02	2.00E+02	4.36E-06
8	2.67E+01	4.00E+02	0	6.61E-07
9	1.60E+02	3.31E+02	2.00E+02	3.43E-06
10	1.64E+02	3.34E+02	2.00E+02	3.21E-06
11	1.60E+02	3.21E+02	2.00E+02	3.43E-06
12	1.60E+02	3.21E+02	2.00E+02	3.43E-06
13	2.67E+01	4.00E+02	0	6.61E-07
14	2.25E+02	2.31E+02	2.00E+02	4.36E-06
15	2.67E+01	4.00E+02	0	6.61E-07
16	8.88E+01	6.20E+02	0	1.76E-06
17	2.67E+01	4.00E+02	2.00E+02	6.61E-07
18	8.88E+01	6.20E+02	0	1.76E-06
19	2.67E+01	4.00E+02	0	6.61E-07
20	4.89E+01	1.24E+03	6.00E+01	1.00E-06
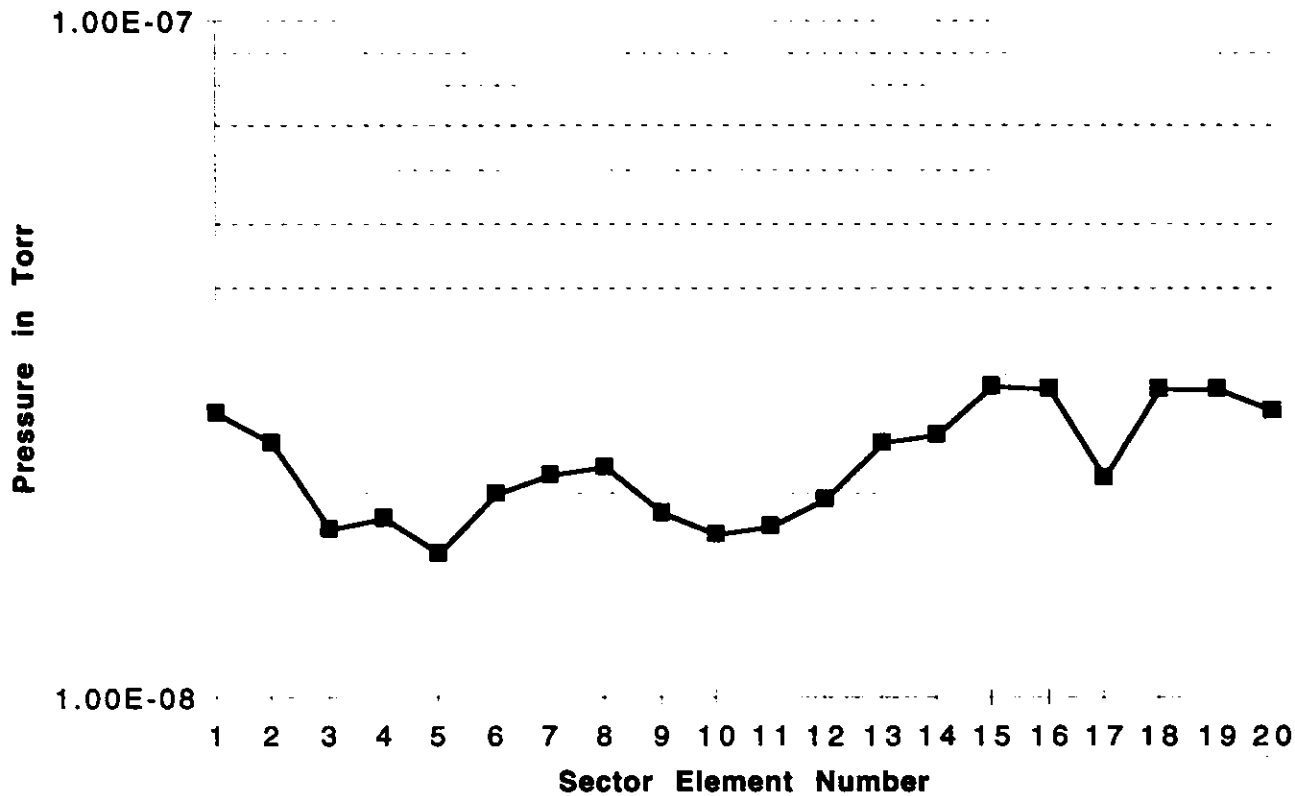
Figure II.6.3-2 RCS Sector Vacuum Profile.

6.4 REFERENCES

1. G.H. Rees, "Status report on ISIS," in *Proceedings of the IEEE Particle Accelerator Conference* (March 16-19, 1987), IEEE Catalog No. 87CH2387-9 (1987).

2. *Kaon Factory Study, Accelerator Design Report* (TRIUMF, British Columbia, Canada, undated).

3. R. Cappi, "RF bypass on the proton synchrotron vacuum chamber flanges," in *Proceedings of the IEEE Particle Accelerator Conference*, pp. 2012-2014 (March 1989).

4. J.W. Ackley et al., 1962 Vacuum Symp. Trans., p. 380 (1963).

5. D. Alpert and R.S. Buritz, J. Appl. Phys. **25**, 200 (1954).

6. *7-GeV Advanced Photon Source: Conceptual Design Report*, Argonne National Laboratory Report No. ANL-87-15, pp. II.6-16 (1987).

7.1 INTRODUCTION

The RCS has diagnostic instrumentation to monitor the beam position, profile, current, and losses. In addition, the high-energy transport (HET) lines and low-energy transport (LET) line leading to and from the RCS have beam diagnostics. Table II.7.1-1 lists the types and quantities of beam diagnostics provided for the RCS and transport lines. Diagnostic instrumentation provided for the linac is covered in Chapter III.

7.2 RCS DIAGNOSTICS

7.2.1 RCS Beam Position Monitors

The synchrotron's beam position monitors consist of pairs of traveling-wave (stripline) electrodes located within each of the quadrupole magnets. The angles of the pairs alternate by 90°, so they provide horizontal position information in horizontally focusing quadrupoles and vertical position information in vertically focusing quadrupoles. Each plane has 28 electrodes. The rf shield inside the vacuum chamber is modified near the electrodes to provide the proper characteristic matching impedance. Constant impedance and matching feedthroughs are provided at each end of the electrode.

The signals from each electrode of the pair are processed by a hybrid junction that provides the sum and difference information. This information is then heterodyned to an intermediate frequency for synchronous detection. The detected signals are digitized by 14-bit analog-to-digital converters (ADCs). Local processors normalize the beam position, and the information is provided to circuitry for orbit control feedback and to the control console for operator monitoring. The measurement accuracy of the system is better than 500 μm.

7.2.2 RCS Current Transformers

Two current transformers are installed in the RCS. A slow current transformer is used to accurately measure the intensity of the accelerated beam and to detect and quantify gross beam losses. The other current transformer has high-frequency response and is used to monitor bunch structure.

7.2.3 RCS Beam Loss Monitors

Beam losses in the synchrotron are detected by a gas-filled, coaxial-cable ion chamber. The ion chamber is composed of four segments that overlap, a configuration that ensures that losses can be localized to any octant of the synchrotron. The signals can be switched to a high-resolution timing chassis to precisely detect the position of persistent, highly localized losses.

Table II.7.1-1 Beam Diagnostic Instrumentation

Location	Monitor	Quantity
RCS	Beam position monitor electrodes	56 (28 H, 28 V)[a]
	Current transformers	2
	Beam loss monitors	4 segments
	Pingers	2 (1 H, 1 V)
	Segmented injection-orbit Faraday cups	6 (3 H, 3 V)
	Solid first-turn Faraday cup	1
LET line	Current transformers	3
	Beam position monitor electrodes	8
	Profile detectors	16
	Beam loss monitors	1 segment
HET line (30 Hz)	Current transformers	3
	Beam position monitor electrodes	4
	Profile detectors	4
	Beam loss monitors	1 segment
	Target protection monitors	1
HET line (10 Hz)	Current transformers	3
	Beam position monitor electrodes	6
	Profile detectors	4
	Beam loss monitors	1 segment
	Target protection monitors	1

[a] H = horizontal; V = vertical.

7.2.4 Special Beam Studies Instrumentation

The RCS includes a set of vertical and horizontal pinger magnet systems that allow excitation of the beam to measure the betatron frequencies. The resulting betatron motion is measured by pickup electrodes. High-frequency instrumentation and high-speed digitizing circuitry are provided to allow complete analysis of the resulting signals.

7.2.5 Injection Diagnostics

Three segmented-Faraday-cup assemblies and one solid Faraday cup are located in the RCS. A horizontal and vertical Faraday cup are mounted on one actuator. The actuators are motorized and designed so either cup can be inserted into the beam path. Three of the cups are designed to allow half of the beam to be intercepted on the segments. The other half continues around the synchrotron. The segmented cups allow several injection orbits to be viewed. The solid Faraday cup is located just upstream of the injection region and is used to measure the first-turn beam intensity. The charge from all Faraday cup segments is digitized, and the resulting profiles are analyzed by the control system to provide operators with injection orbit information.

7.3 TRANSPORT LINE DIAGNOSTIC INSTRUMENTATION

7.3.1 General Instrumentation

Each of the two HET lines and the single LET line has three current transformers distributed along its length. The current pulse from each transformer is integrated by precision integrators and digitized by the control system to calculate transport efficiency.

Beam position in the transport lines is monitored by arrays of four traveling-wave stripline electrodes similar to the ones used in the RCS. Such monitoring allows both horizontal and vertical information to be gathered from each array. The detection system for the LET line is optimized to detect the 1,275-MHz component of the beam. In the HET lines, the peak of the single, high-current beam pulse is detected from each of the electrodes. It is then digitized, and its position is calculated.

Moving-wire scanners are used in the LET line to measure the H⁻ ion beam profile. Segmented-wire ion chambers, mounted in vacuum valve assemblies, are used to measure the profile in each of the HET lines. The beam profile measurement devices are not designed to be operated at full beam power. They are operated at either low currents or low repetition rates.

Beam losses in all of the transport lines are measured by gas-filled, coaxial-cable ion chambers, identical to the system used in the RCS.

7.3.2 Target Protection Monitors

Maintaining a predetermined minimum beam profile and beam position at the neutron generating target is essential to the operation of the facility, because severe target damage can occur if the beam size becomes smaller than the predetermined size or if the beam drifts out of position. Target protection instrumentation that shuts off the beam in the event of changing spot size or position is necessary, but the standard beam-intercepting profile monitors cannot survive very long under full beam power. The target is instrumented with the nonintercepting target protection monitors (TPMs) described below, which provide adequate protection against fast changes or long-term drifts in beam size and position.

A TPM consists of four secondary emission monitors (SEMs), arranged as shown in Figure II.7.3-1 and positioned upstream of the target. SEM-A and SEM-B are placed at the upper and lower sides of the target, while SEM-C and SEM-D are at the left and the right sides of the target. The SEM support stands have position adjustment mechanisms, so that the position of each SEM can be precisely adjusted. The SEMs are modular, and individual units can be replaced by new ones without requiring realignment. The SEMs are placed at the positions shown in the figure and do not intercept any portion of the beam. They provide a null signal unless the beam shape or position changes. Heartbeat signals ensure that all monitor channels are functioning.

The TPM provides a signal when the beam position changes or when the beam size increases in either of the transverse planes. Since the HET lines are constructed with quadrupole focusing magnets, a decrease in the horizontal beam size would most likely occur with a corresponding increase in the vertical beam size, and vice versa. Therefore, signals from a pair of SEMs indicate a change in beam size. Any individual SEM would be able to indicate a change in beam position.

At initial start-up, the HET lines are tuned at very low beam power by using signals from beam-intercepting profile monitors. The SEMs are then brought into position and adjusted to bring them close to the beam. The beam-intercepting profile monitors are removed, and full beam power is directed onto the target. From this time on, the TPM monitors changes in the beam position and changes in the beam profile. Information from the TPM is processed together with monitored HET magnet setpoints and readback values and provides the desired beam shutdown signal.

Some research and development are required to ensure the long-term reliability and optimize the functionality of these devices.
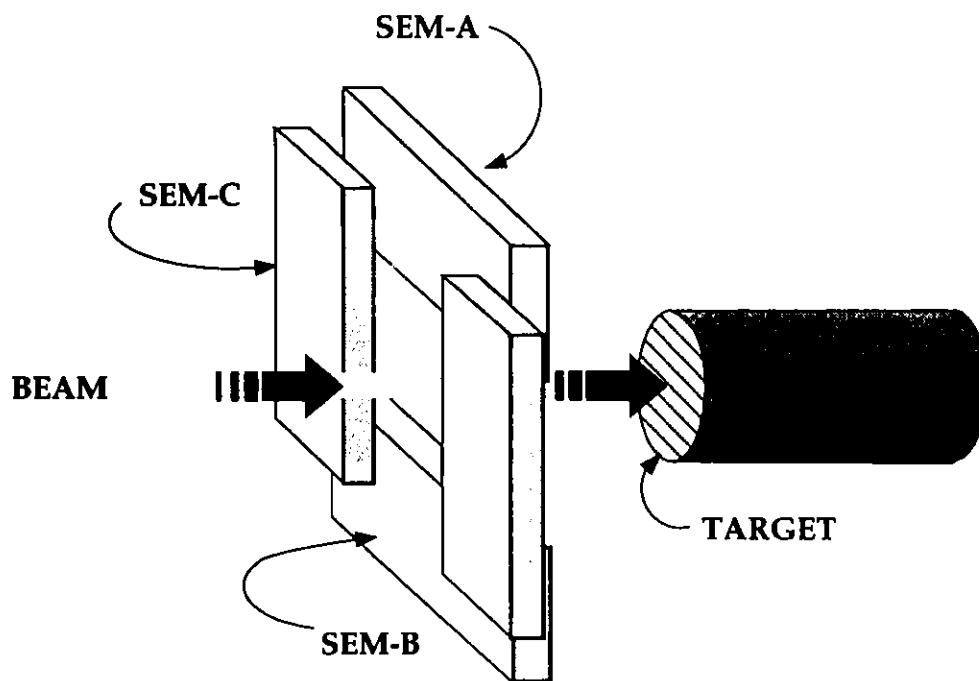
(a) Side View
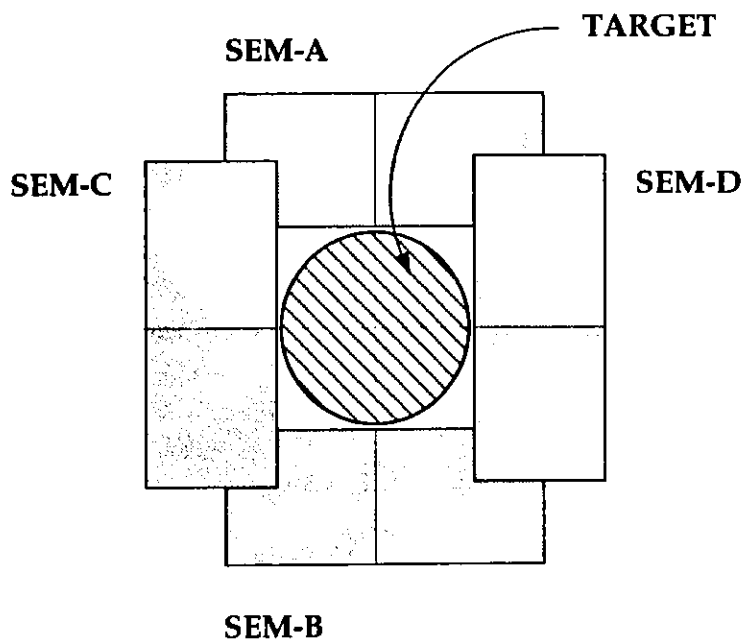
(b) Beam View

Figure II.7.3-1 Target Protection Monitor That Uses Secondary Emission Monitors as Detectors, Shown from the Side (a) and from the Beam's Perspective (b).

8.1 INTRODUCTION AND PHILOSOPHY

The IPNS Upgrade control system design is based on using high-performance workstations to act as the operator consoles, distributed microprocessors to control equipment interfacing and preprocess data, and an interconnecting network. Figure II.8.1-1 shows in schematic form all major components and their relationships. The IPNS Upgrade design includes 58 distributed microprocessors and 10 workstation console systems. Some of the workstations have at least two physical screens.

The IPNS Upgrade control system is a direct application of the Experimental Physics and Industrial Control System (EPICS),[1-4] created by a collaboration between the Controls and Computing group at the Argonne Advanced Photon Source (APS) and the ATO-8 group at Los Alamos National Laboratory. Other laboratories and universities, including Lawrence Berkeley Laboratory (LBL), the Continuous Electron Beam Accelerator Facility (CEBAF), the Stanford Linear Accelerator Center (SLAC), the Deutsches Elektronen Synchrotron (DESY), MIT-Bates, the Duke Free Electron Laser (FEL), and the KECK II and Gemini telescopes, are developing control systems using EPICS software tools. They are also developing additional tools that will be shared with all EPICS users. EPICS has been successfully installed on the existing IPNS, replacing its outdated computer system. Three commercial vendors now supply EPICS.

Accelerator control system designers face the following challenges:

1. Obtain system requirements and specifications from the machine and subsystem designers,

2. Protect the investment in hardware and software from rapid obsolescence, and

3. Find methods to quickly incorporate new generations of equipment and replace obsolete equipment without disrupting the existing system.

To help solve these and related problems, the control system designers are committed to the use of standards in system design and to collaboration with other laboratories when possible. This approach allows the IPNS Upgrade controls team to build a control system by using the software techniques and hardware developed at Argonne and other laboratories. This philosophy has been demonstrated to save development time and expense associated with inventing a system from first principles. EPICS and its implementation in the IPNS Upgrade control system are described in this section.

8.2 EPICS OVERVIEW

EPICS-based control systems include operator interfaces (OPIs) consisting of Unix workstations that use a graphical user interface (GUI) based on the X Window Motif model. The selection of a workstation implementation based on X Window for the operator interface

UNIX Workstations
Operator Interface
(OPI)

Controls network - Ethernet, FDDI, ATM ...

Controlled
Equipment

Subnetworks
Allen Bradley
BitBUS, GPIB,...

IOC (VME/VXI)
M68060 CPU
Interface Functions
Alarm Checking
Closed Loops
18 in Linac
4 in Beamline
16 in RF
20 in RCS
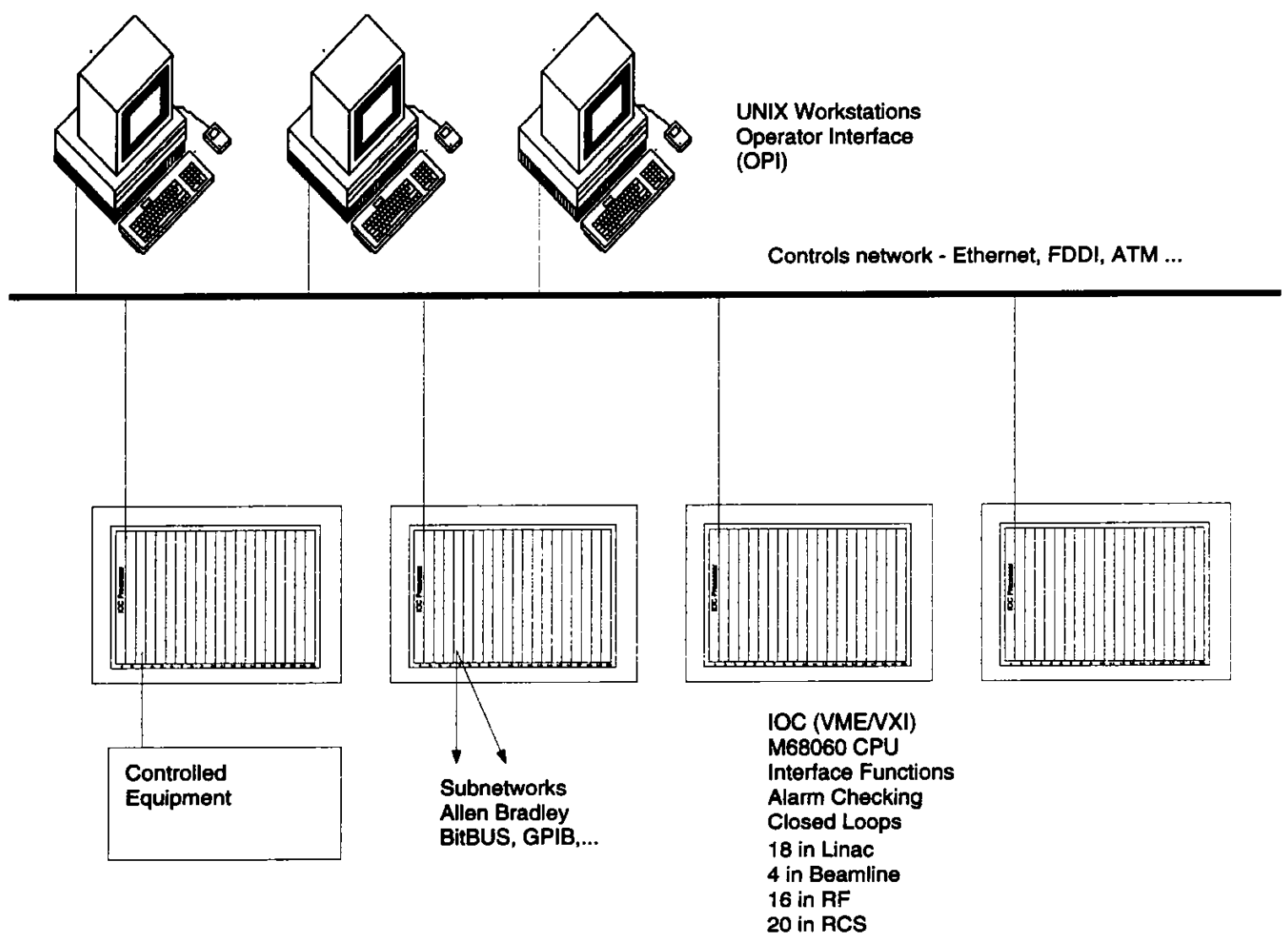
Figure II.8.1-1 IPNS Upgrade Control System.

allows the software development effort to take place in the same environment as the field instruments, video tools, and the interfaces for controls and data acquisition. Consoles can be located in offices, labs, seminars, and wherever they are required in the field. The OPI includes menu-selection lists, diagrams, flow charts, and maps, as well as the more standard text-based selection menus. The workstation supports external software interfaces, including spreadsheets and commercial applications (such as IDL/PvWave and Mathematica) and application software (such as accelerator modeling codes written in Fortran, C, or other languages). Auxiliary displays using X Window terminals, as well as projection and large-screen displays in the main control room and seminar rooms, are easily implemented by means of commercial equipment. EPICS OPI runs on SUN Sparc, Hewlett-Packard PA, and Digital Equipment Alpha architecture workstations.

8.2.1 Specific EPICS Features

EPICS provides a number of tools for control system implementation. This minimizes the need for custom coding and helps ensure uniform operator displays. As long as the network is not saturated, an arbitrary number of input/output controllers (IOCs) and OPIs can be supported. If a single IOC becomes CPU-bound, its functions can be spread over several IOCs, or additional CPUs can be added to a single IOC. Rather than having all applications run on a single host, the applications can be spread over many OPIs.

8.2.2 EPICS Core Software

EPICS consists of a set of core software components and a set of optional components. The core software consists of a channel-access client and server, database scanners-monitors, and the database configuration tool (DCT). All other software components are optional.

8.2.3 Channel Access

Channel access is based on a client-server model and provides network-transparent access to IOC databases. Each IOC provides a channel-access server that is capable of establishing communication with an arbitrary number of clients. Channel-access client services are available on both OPIs and IOCs. A client can communicate with a number of servers, within the limits of available memory.

The central feature of both the OPI and IOC software designs is the protocol for connections between software modules for the purpose of exchanging information. This protocol is called channel access and is built on the transmission control protocol/Internet protocol (TCP/IP) standard. TCP/IP is an integral part of every Unix-based workstation and is also built into VxWorks, the real-time operating system. When an OPI application program needs to connect to a process variable located in an IOC, it issues a broadcast over the network, and the

IOC in whose database the requested process variable resides provides a response. A socket-to-socket connection is established, and efficient two-way communication takes place. IOC-to-IOC channel access can take place to exchange inter-IOC information. The location of the desired process variable is transparent to the OPI, and only its name must be unique within a subnet.

The database that defines all IOC channel connections and properties is distributed over the IOCs and downloaded at IOC boot-time along with the IOC operating system, VxWorks, and the particular device driver software modules required by that IOC. The entire database is centrally maintained and configured.

8.2.4 Database

The heart of an IOC is a memory-resident database, together with various memory-resident structures describing the contents of that database. These structures are manipulated by the application designer through the use of database records. EPICS supports a large and extensible set of record types, such as ai (analog input) and ao (analog output). Each record type has a fixed set of fields. Some fields are common to all record types; others are specific to particular record types. Every record has a record name and every field has a field name. The first field of every database record holds the record name, which must be unique across all IOCs attached to the same TCP/IP subnet. A number of data structures are provided so that the database can be accessed efficiently. These structures are transparent to most software components because they access the database via database access routines.

8.2.5 Database Scanning

With the exception of record and device support, all access to the database is through the channel or database access routines. Database scanning is the mechanism for deciding when to process a record. Four types of scanning are possible: periodic, event, input/output (I/O) event, and passive. Periodic scanning supports a number of time intervals. Event scanning is based on the posting of an event by any IOC software component. The I/O event scanning system processes records on the basis of external hardware interrupts. Passive record processing is triggered by processing of linked records.

8.2.6 EPICS Tools

The EPICS tools are used by application developers to build a control system. The Motif-based editor display/manager tool (MEDM) allows designers to easily create, configure, and modify displays and then activate and connect displays to actual hardware. The display editor portion of MEDM (Figure II.8.2-1) provides process connections via an interactive display editor/control. Editing/drawing commands are used to build displays with little or no
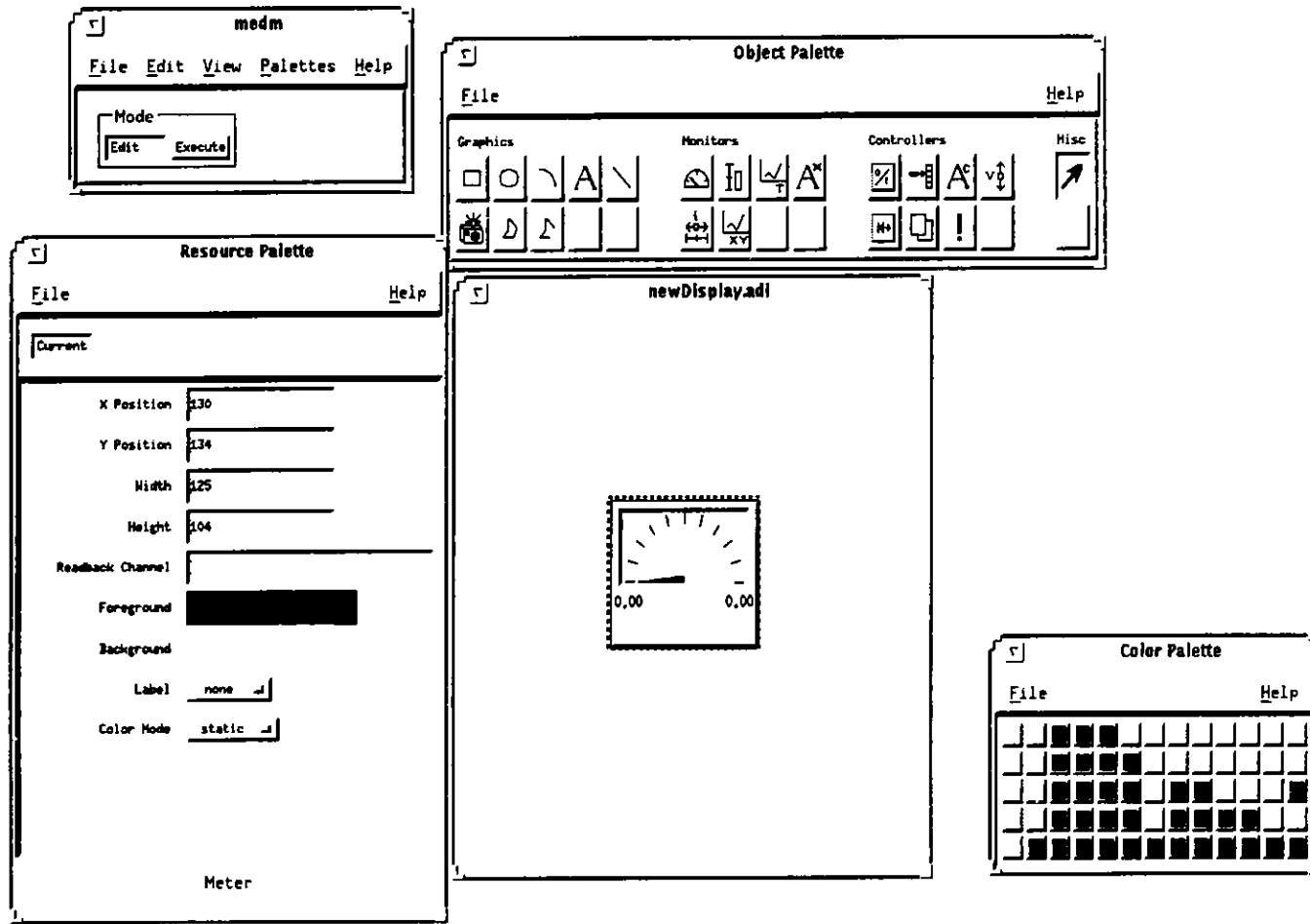
Figure II.8.2-1 MOTIF Editor and Display Manager (MEDM) in Edit Mode.

custom programming required. Process connections to the data are entered as process variable and field names. MEDM allows the designer to modify any aspect of the display element, as well as to copy, align, and group the display elements. Standard drawing tools can be used to create backgrounds, which can then be imported into MEDM by means of graphic interface format (GIF) files.

The alarm handler (Figure II.8.2-2) displays alarm messages in a hierarchical manner. The backup and restore tool (BURT) stores and retrieves data from selected channels. A graphical database configuration tool (GDCT), shown in Figure II.8.2-3, allows the application designer to configure the run-time database. The knob manager (KM) (Figure II.8.2-4) allows the operator to attach physical knobs to process variables.

8.3 CONTROL SYSTEM HARDWARE

The IPNS Upgrade system hardware is depicted in Figure II.8.1-1. The front-end computers or IOCs are based on Motorola M68060 processors with direct upgrade paths to the new Motorola Power PC processors as they become available. The hardware is based upon the VME/VXI family, and the choice of crate is dictated by the particular application. The OPIs run Unix software and have an X Window GUI. The workstations are connected to the network by using a single-attach fiber-distributed data interface (FDDI) for high-speed access to all data. Standard network monitoring tools, such as remote network monitoring and out-of-band hub management, are provided.

8.3.1 Console Computers

A computer workstation is the primary operator interface. It has a high-resolution color display and is capable of supporting several separate graphic windows simultaneously. Each OPI has access to all process variables in the IPNS Upgrade complex and, depending on system permissions, can control any of the various systems. Depending on machine mode (commissioning, operations, or system maintenance), each console is used alone or in conjunction with adjacent console systems.

In the X Window client-server paradigm, an application program is divided into the "client," which provides the computation and logic of the program, and the "server," which provides the interaction facilities for the human operator or user. Both client and server are implemented in processors at the OPI level in the IPNS Upgrade control system. The client and server need not reside in the same processor. For example, a specialized parallel processor can be running an application and that application can be accessed by a common workstation or X Window terminal. In this way, each OPI is able to have windows open to clients operating both locally and on other processors on the network.

File Action View Setup   Help

PAR-LET-IOCSTATUS ▶ <—->   parOliocstatus <—->
RM-B107 <—->   par02iocstatus <—->
                                            par03iocstatus <—->
                                            partuneiocstatus <—->
                                            parbpmiocstatus <—->
                                            let2iocstatus <—->

Mask <CDATL>: (Cancel,Disable,noAck,noackT,noLog)   ⌐ SilenceForever
Group Alarm Counts: (INVALID,MAJOR,MINOR,NOALARM)   ⌐ SilenceCurrent
Channel Alarm Data: Current(Status,Severity),Highest Unack(Status,Severity)
Filename: /home/helios1/injsys/par/iocstatus

Figure II.8.2-2 Alarm Handler Console Readout.

Figure II.8.2-3 Graphical Database Configuration Tool.

File   Edit   Format   Misc   **Help**

Channel 2 selected

❶   ▲ ▼ Ⓜ ◔ ◯

vong:ai00

NO ALARM   NORMAL

530.000 kV

0.000   1000.000

☿ 349.900

Min   Max

0.000   530.000

❺   ▲ ▼   ◔ ◯

vong:ao00

NO ALARM   NORMAL

2.1810e+02 kV

0.0000e+00   1.0000e+03

Min   Max

0.0000e+00   2.1810e+02

❷   ▲ ▼   ◔ ◯

vong:ao01

HIHI   MAJOR

7000.000 rpm

0.000   7000.000

Min   Max

0.000   7000.000

❻   ▲ ▼   ◔ ◯

vong:ao02

HIGH   MINOR

0.000078 torr

0.000000   0.001000

Min   Max

0.000000   0.000512

❸   ▲ ▼   ◔ ◯

vong:ao03

UDF   INVALID

0.000000 g

-3.000000   9.000000

Min Max

0.000000   0.000000

❼   ◯

vong:bi00

UDF   INVALID

off

❹   ◯

vong:si00

UDF   INVALID

❽   ▲ ▼   ◔ ◯

vong:sineWave

LOLO   MAJOR

-10.88 volt

-15.00   5.00

Min   Max

-15.00   5.00

Figure II.8.2-4 Knob Manager.

8.3.2 Front End Systems

The IOC is based on the VME/VXI standard and uses a Motorola 68060 microprocessor for control. A fast, real-time kernel, VxWorks, is the operating system. No local disk drive is required in this system. The software image can be downloaded from a file server or from on-board programmable read-only memory (PROM). The IOC also supports task priorities and interrupts as well as custom code. The IPNS Upgrade control system uses 58 IOC crates. More than 20 VME input-output modules, including analog input/output, motor control, and binary input/output, are currently supported. Others will be supported as required.

Most information preprocessing is performed at the IOC level, including sequential and control-loop operations. In this way, maximum benefit is gained from the many IOC processors operating in parallel.

Hardware I/O can be generalized into several types: analog and binary I/O, stepper motor, and subnetwork connections. Hardware records contain information for run-time processing, including scaling, engineering units, hardware address, and scanning. The IOC database contains such parameters as scan requirements, I/O address, engineering unit conversions, alarm limits, control parameters, and current values for each defined process variable. Database records can be linked together to implement complex algorithms.

The database scanner processes database records and updates the dynamic fields in the database, such as value, alarm status, and severity. Data conversions are supported. Alarm checking for limit violations, state violations, hardware communication errors, and alarm severity is supported. Binary and analog I/O are provided through the database. Analog input can be smoothed; analog output can be either incremental or positional and the output rate of change can be specified. Multi-bit (16 states) and single binary I/Os are supported.

All I/O fields can be connected to a hardware device or another database element, such as a calculator record or proportional integral derivative (PID) record, or can fan out to several devices. Timing signals, motion control, and transient digitizers are supported through the database.

Stepper motor records receive position/velocity input from user or other data, provide positional or velocity mode operation, provide position feedback through an encoder or another database record, and allow simple closed-loop position. Limit switches are supported.

General purpose calculations, a PID algorithm, and a signal selector are supported to provide closed-loop control and data filtering. The calculation record supports up to six sets of input, C language expressions, algebraic operations, relational operations, Boolean operations, and trigonometric functions. The PID algorithm allows user control of setpoint, proportional, integral, and derivative gains; incremental or positional outputs; and anti-windup and reset on the integral term.

8.3.3 Subnets

The IPNS Upgrade control system provides for VME-based IOCs to be distributed throughout the facility and interconnected via Ethernet to one another and also to Unix-based operator interface consoles. Although this distributed architecture allows for intelligent processors near the major subsystems, I/O subnets are frequently required to interface directly to the equipment and to communicate I/O information to the nearest IOC. The concept of a subnet is an important element in control systems in general and EPICS in particular. EPICS supports several types of subnets: Allen-Bradley, general-purpose interface bus (GPIB), and BITBUS. The Allen-Bradley I/O subnet uses AB1771 series I/O modules to provide basic binary and analog I/O support for the control system. Allen-Bradley is an inexpensive and rugged standard for industrial control systems. Copper and fiber-optic-based multidrop subnets are available for this equipment.

Laboratory test and measurement equipment often uses the IEEE-488 (GPIB) standard as an interface to an external control system. IEEE-488 subnets present some serious challenges and potential problems to the system designer. IEEE-488 has a distance limitation of 20 m, which requires the instruments connected to the bus to be in close proximity to the IOC. In addition, the signals within the GPIB cable are not balanced and thus are susceptible to EMI/RFI noise and ground spikes. Signal transfer and isolation techniques are not part of the GPIB standard, and although commercial equipment is available to extend the distance of a GPIB interface, it is prohibitively expensive. To overcome these limitations, a BITBUS has been developed for use with EPICS to provide a method of high speed transfer of short control messages over a multidrop network. The BITBUS subnet can be used as a method for remote, single point I/O as well as for a gateway for remote IEEE-488 and RS232 signals. A differential, opto-isolated, wired subnet is the BITBUS standard; however, a BITBUS multidrop fiber-optic network has been developed for use with EPICS.

8.3.4 Networks and Protocols

Argonne uses FDDI as the intralaboratory network (Figure II.8.3-1). Backbone cables are in place in individual buildings, and communication between buildings is presently done via FDDI and high-speed asynchronous transfer mode (ATM) networks. The IPNS Upgrade facility uses FDDI and ATM to connect network hubs, as shown in Figure II.8.3-2. The network hubs connect to OPIs. The IOCs will use ATM, FDDI, or fiber-optic-connected Ethernet branches as performance needs dictate.

8.4 APPLICATION SOFTWARE

Application software is available to provide features or services not provided by the control system. For example, the software required to provide a local orbit bump is application software. These application programs can be of two general forms. The first is a control panel

IPNS Area Network

The World

Argonne
FDDI

IPNSII Firewall
Router

Router with FDDI

Master Hub

File
Servers &
Storage

Experiment FDDI

To IOCs
&
Servers

Hub 1

Hub 2

Home
Run FDDI
or ATM

Hub 8

Controls
FDDI

Router

Router

Ex 1
Hub 1

Ex n
Hub n

To Desktop and
Beamlines

To Desktop and
Beamlines
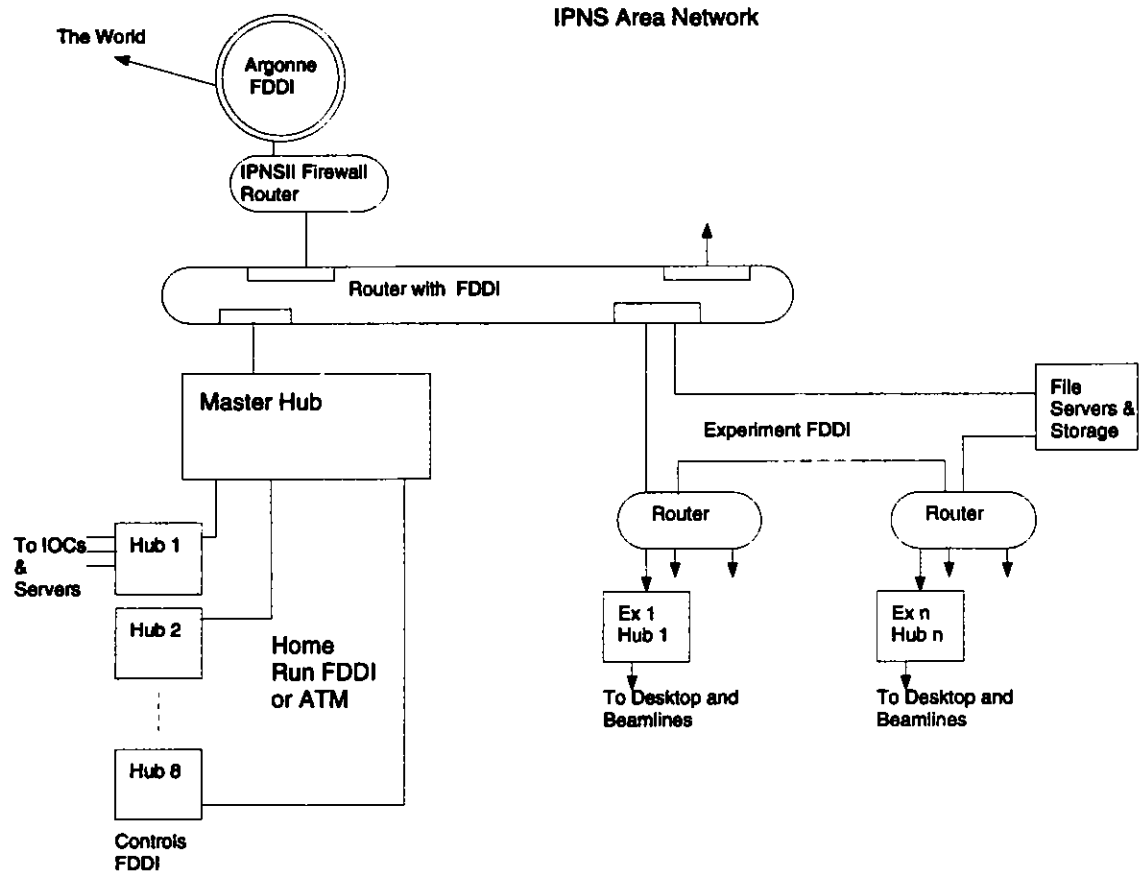
Figure II.8.3-1 IPNS Facility Network.
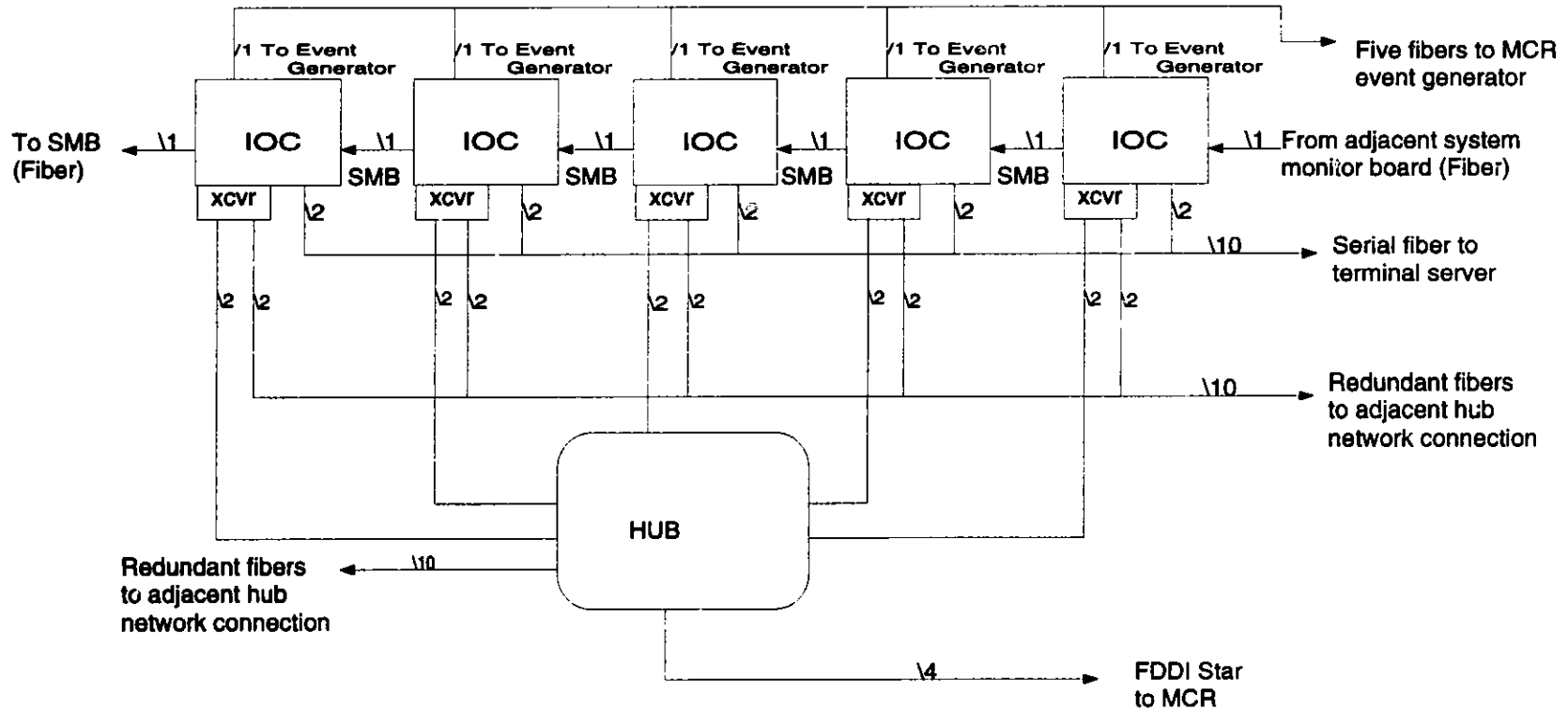
Figure II.8.3-2 IPNS Upgrade Local Control Network.

created with MEDM, in which graphic tools such as buttons, sliders, indicator lights and meters, and graph paper are selected, attached to process variable (pv) names, and located on the panel (Figure II.8.4-1). Static entities are used to depict the physical system, such as piping diagrams, and are added where appropriate. When complete, the panel is called up for execution, and channel-access calls are made. No actual code is written, and no compilation is made.

The second form of application program generates classic in-line code. In this case, standard entry points are provided in the same manner as for the graphic and channel-access tools. When this approach is used, existing code can be adapted to EPICS by calling the channel-access routines and displaying the results as either traditional line-by-line or graphical output.

All software is developed under Unix, including that for the IOCs. Multiple windows can be opened for software development, actual run-time applications, database configuration, and electronic mail. This capability streamlines software development, database servicing, and system troubleshooting.

8.5 EPICS APPLIED TO IPNS UPGRADE

Figure II.8.1-1 schematically depicts the IPNS Upgrade controls network. The IOCs are located as close as possible to the equipment to be controlled. All network connections to the IOCs are through fiber-optic cables to eliminate most sources of electrical noise.

8.6 OTHER SERVICES

8.6.1 Timing System

Two classes of timing coordination are necessary. Beam transfer events and signal sampling between the Linac and the RCS are controlled. The second class is associated with the need to control sampling of beam position in the RCS. Both systems use essentially the same method, but with different clock rates and sources. Depending on the mode of operation, various delay counts are downloaded to the microprocessor clusters and set into clock-delay modules in the VME crates. A systemwide start pulse based on the magnetic field is generated, and the delay modules count a clock source and produce a pulse output after their programmed delay. For event sequencing in the RCS, a crystal-derived clock is used; it produces real-time triggers for sampling beam parameters.

Accelerator control and monitoring tasks are performed by using the timing configuration that is generated by a magnetic-field-triggered crystal clock.
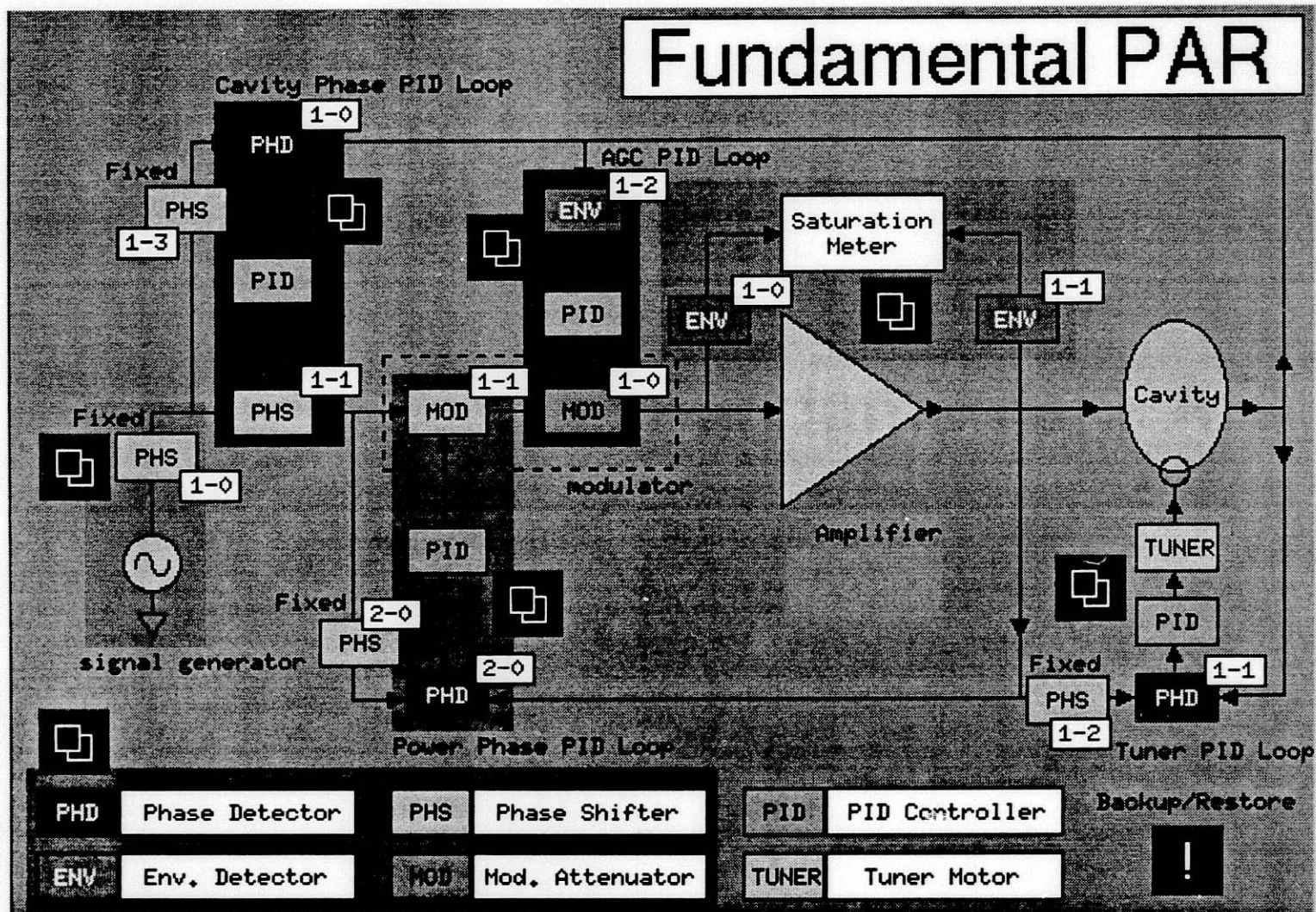
Figure II.8.4-1 MEDM Control Panel.

8.6.2 Event System

The event system provides the ability to generate signals on the basis of timing and software events. This system has been designed to work hand-in-hand with EPICS. It consists of two types of interfaces, an event generator and an event receiver. An event receiver is located at each IOC.

8.6.3 Analog Signal System

To convey the required number of high-bandwidth analog signals to the main control room, a signal distribution system is used. Commercial, VME-based, coaxial relay modules and commercial, high-bandwidth fiber-optic systems are used and controlled by the IOCs. At the console end, the analog signals are switched to the desired display or instrument. The choice of signal and output destination are selected by the operator from standard EPICS screens.

8.6.4 Computer-Controlled Video Signal System

The same method used for the analog system is used for video signals. Again, the computer system provides the control. The video sources are also delivered to frame grabbers for on-line, dynamic beam analysis. All of these techniques are in use at the APS.

8.6.4 Network Access from Offices and Laboratories and User Housing Facility

The distributed nature of the IPNS Upgrade control system allows the system to be monitored from the office and laboratory areas by the operational staff. This feature facilitates equipment checkout, status inquiries, and software development, which can take place on a noninterfering basis. Actual control of the various systems is highly restricted and controlled by the EPICS software on each IOC.

8.7 CONCLUSION

The IPNS Upgrade control system allows monitoring and control of the accelerator and experiments from offices, laboratories, and the user residence facility.

8.8 REFERENCES

1. M. Knott et al., "EPICS: A control system software co-development success story," Nucl. Instrum. Methods **A 352**, 486 (1994).

2. L. Dalesio et al., "The experimental physics and industrial control system architecture: Past, present and future," Nucl. Instrum. Methods **A 352**, 179 (1994).

3. McDowell et al., "Status of the Advanced Photon Source and its accelerator control system," Nucl. Instrum. Methods **A 352**, 13 (1994).

4. L. Dalesio et al., "EPICS architecture," in *Proceedings of the International Conference on Accelerator and Large Experimental Physics Control Systems* (KEK, Tsukuba, Japan, November 11-15, 1991), pp. 278-281 (1991).

9.1 INTRODUCTION

Shielding provides protection for workers and for the general public during operation of the IPNS Upgrade accelerators. The shielding limits the radiation dose for both on-site and off-site exposure to less than that allowed by the U.S. Department of Energy (DOE) guidelines.

The shielding design utilizes semi-empirical formulae with experimental dose data and measured attenuation characteristics as input parameters, when these data are available. The calculations with the semi-empirical formulae are in reasonable agreement with the results of computer simulations. The accelerator design has been carried out with the objective of limiting beam losses to less than 1×10^{-3}. Low beam losses help ensure that radiation levels in the vicinity of the equipment are not excessive during shutdown periods and that the level of activation is sufficiently low to allow hands-on maintenance.

9.2 SHIELDING DESIGN OBJECTIVES

The design standard[1] for new facilities and major modifications to existing facilities, Article 128 of DOE/EH 0256T Revision 1 requires that individual worker dose be less than 5 mSv/yr (500 mrem/yr) and as low as reasonably achievable (ALARA). The neutron quality factor has been doubled for design purposes; thus, the design dose rate is 1.25 µSv/h for occupational exposure (40 hours per week, 50 weeks per year) for those situations in which neutrons dominate the dose rate. The shielding is designed to meet a more conservative value than this criterion to ensure that occupational radiation doses are ALARA. DOE Order 5400.5 limits the annual dose to members of the public[2] to 1 mSv/yr. A further requirement of this Order is that actual or potential doses in excess of 100 µSv in a year to any member of the public require notification of DOE Headquarters. These dose-limiting objectives and guidances are used as the basis for establishing the adequacy of the bulk shielding design and other dose-mitigation systems for normal operations of the facility.

The bulk shielding provided for the Rapid Cycling Synchrotron (RCS), high-energy transport (HET) line, and target biological shields limits the dose rate to <1.25 µSv/h at 30 cm from the outside of the shielding walls under normal loss conditions. This dose rate assumes a current of 500 µA of protons at 2.2 GeV. The computations are based upon semi-empirical formulae and attenuation data presented in the literature.[3-10]

The calculations for the low-energy transport (LET) line and linac are based on 500 µA of protons at 400 MeV. The calculations are based on semi-empirical formulae and attenuation data presented by Tesch.[11]

The methodology of Stevenson and Thomas[12] was used to estimate the skyshine contribution at the nearest site boundary, which is 350 m away. The results of the calculations for both direct and skyshine radiation indicate that the total off-site contribution is less than 80 µSv/yr for 8,000 hours of operation.

A continuing accidental loss of the entire proton beam at one point is considered an unlikely event. However, sufficient shielding is provided to ensure that the potential dose to an individual on the outside of the shield in the vicinity of the loss is mitigated. The objective is to provide enough shielding to limit the dose, from the onset of the occurrence to its termination, to less than 1 mSv.

An assumed occupancy factor of 0.1 has been applied in order to estimate the radiation dose outside of the shield in the vicinity of the linac, injection or extraction areas, or a high-energy transport line. This factor is a conservative estimate of the time an individual may be required to be in these regions.

The dominating radiation, which determines the necessary shielding thickness for a high-energy proton beam, is the high-energy neutron component formed in nuclear cascades.[13] The amount of shielding necessary is determined by the attenuation of the high-energy component in equilibrium with the slowing-down spectrum of lower energy neutrons. This high-energy component is composed of neutrons with E > 150 MeV, for which the attenuation length is independent of energy; for low-energy neutrons (<100 MeV), attenuation lengths decrease rapidly with neutron energy. Typically, in concrete, the low-energy neutron attenuation length is a factor of three less than for high-energy neutrons. Therefore, designing the shields to attenuate the high-energy neutron component automatically takes care of the low-energy neutrons because of their shorter attenuation lengths. The gamma dose outside thick shields has been estimated to be 10-16% of the neutron dose;[14,15] therefore, no additional calculations for gamma radiation are necessary.

9.2.1 Radiation Attenuation Lengths

Information on the attenuation of high-energy and evaporation neutrons in several shield media was obtained from the literature.[3,4,8,9] For each material, the quoted values for attenuation length vary, depending upon the angle at which the radiation was measured and on assumptions made about the neutron spectrum. Much of the measured data deals only with "transverse attenuation." Transverse attenuation as used here means the attenuation of secondary particles produced when the beam hits a target. These particles are measured after passing through a shield wall, generally at 90°, as shown in Figure II.9.2-1. Data on longitudinal attenuation are scarce and limited mainly to published computer simulations.[7,9,10,16] Table II.9.2-1 lists representative values for high-energy neutron attenuation lengths in typical shield materials, measured at 90°.

The attenuation length at 90° in other materials can be scaled from

$$\lambda/\lambda_E = (A/A_E)^{1/3} \, , \tag{II.9.2-1}$$
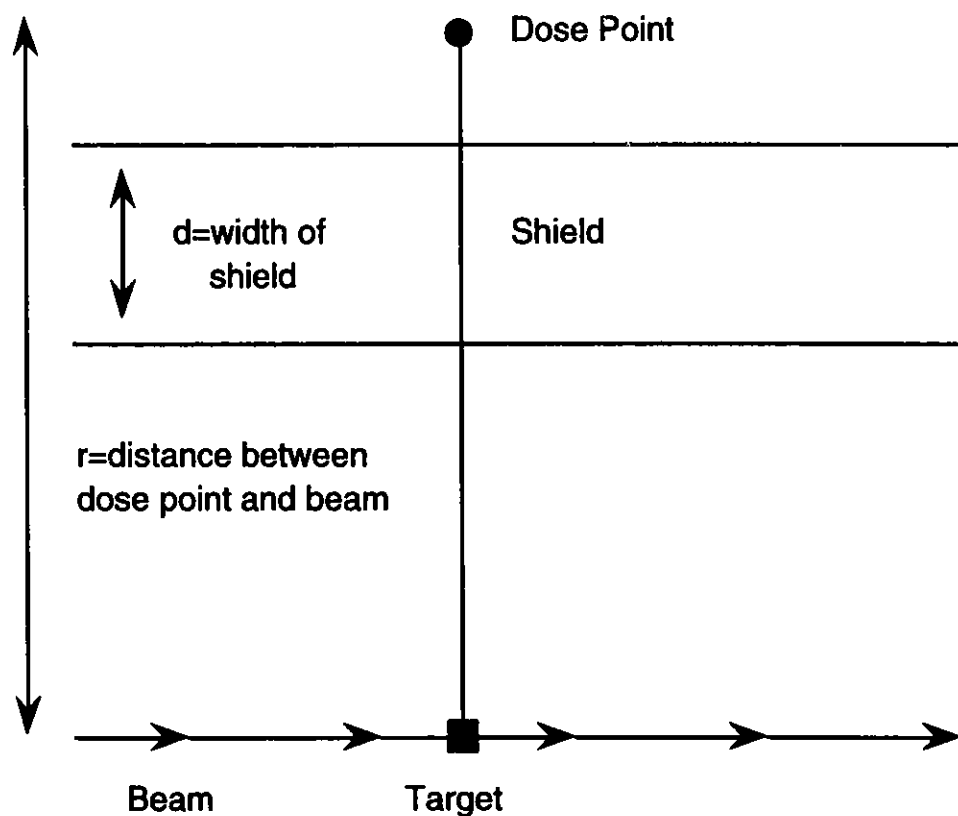
Figure II.9.2-1 Geometry for Calculating the Transverse Dose Due to Secondary Particles Attenuated by a Shield.

Table II.9.2-1 Transverse Attenuation Lengths
for High-Energy Neutrons

Shielding Material	Density (g/cm^3)	Attenuation Length λ (g/cm^2)
Ordinary Concrete	2.35	99-117
High Density Concrete	3.7	116-134
Iron	7.8	140-180
Earth	1.6	117

where λ and A are the attenuation length and atomic number of the shield material, normalized to λ_E and A_E of earth ($\lambda_E = 117$ g/cm^2 and $A_E = 20.4$).[4] Tesch and Zazula[3] give $\lambda = 240$ g/cm^2 for the attenuation length in iron at 5° in the forward direction, and Dinter et al.[10] give $\lambda = 150$ g/cm^2 at 40° for forward-directed radiation in ordinary concrete.

9.2.2 Bulk Shielding Calculations

The linac features an ion source, a 2-MeV radio-frequency quadrupole (RFQ), a 25-m long, 70-MeV drift-tube linac, and a 92-m-long, 330-MeV coupled-cavity linac. H⁻ ions are accelerated in pulses of 1.04×10^{14} protons/pulse to 400 MeV at a repetition rate of 30 Hz. The resultant average current of 500 µA is transported by the LET line and is injected into the RCS. The entire linac is housed in a tunnel with inner dimensions 3.65 m wide by 2.74 m high, which is located 3.04 m below grade. Beam height is 1.4 m above the tunnel floor. The linac shielding is adequate for limited access to the Klystron Gallery during operation at the design parameters.

The RCS is housed in the existing Zero Gradient Synchrotron (ZGS) Ring Building, which is shown in Figure II.9.2-2. The ZGS was a 12.5-GeV proton synchrotron, which accelerated more than 7×10^{12} protons per pulse at 0.5 Hz. The Ring Building (Building 365) is an annular-shaped building approximately 83 m^2 in cross section and 61 m in diameter. Located in the center region of the annulus is the Center Building (Building 364). This building is approximately 26.8 m in diameter and 24 m high. The Ring Building is covered with a mound of earth of minimum thickness 6.1 m on the side.

The RCS roof shielding amounts to about 4.9 m of earth on top of 0.61 m of reinforced concrete. The walls of the Ring Building are made of 1.07 m of reinforced concrete. The earth shielding thickness between the Ring Building and the Center Building is about 7 m, and at beam height, the earth shielding thickness outward from the Ring Building is about 21.3 m. When the ZGS was in use, beams of protons were sent to Building 369 (EPB1) and Building 370 (Meson Building). For the IPNS Upgrade, the 30-Hz target station is housed in Building 370 and the 10-Hz target station is housed in Building 369. The existing Ring Building shielding is sufficient for the IPNS Upgrade, as is demonstrated in the following sections.

The RCS accelerates protons from 400 MeV to 2.0 GeV. High-energy transport lines deliver 2.0-GeV protons to either of two neutron-generating target areas. The design goals are an average current of 500 µA at 2.0 GeV for a maximum power level of 1.0 MW. Shielding requirements for the target biological shields are discussed in Chapter IV.

The shielding achieves the design goal of <1.25 µSv/h at all normally occupied points on the outside of the shield. Access to all accelerator areas is administratively controlled. The shielding requirements are satisfied by using sufficient iron and/or concrete as a bulk shield to ensure adequate attenuation of the high-energy and evaporation neutrons. The concrete is supplemented by earth berms in some regions, including the linac, a portion of the LET, and the
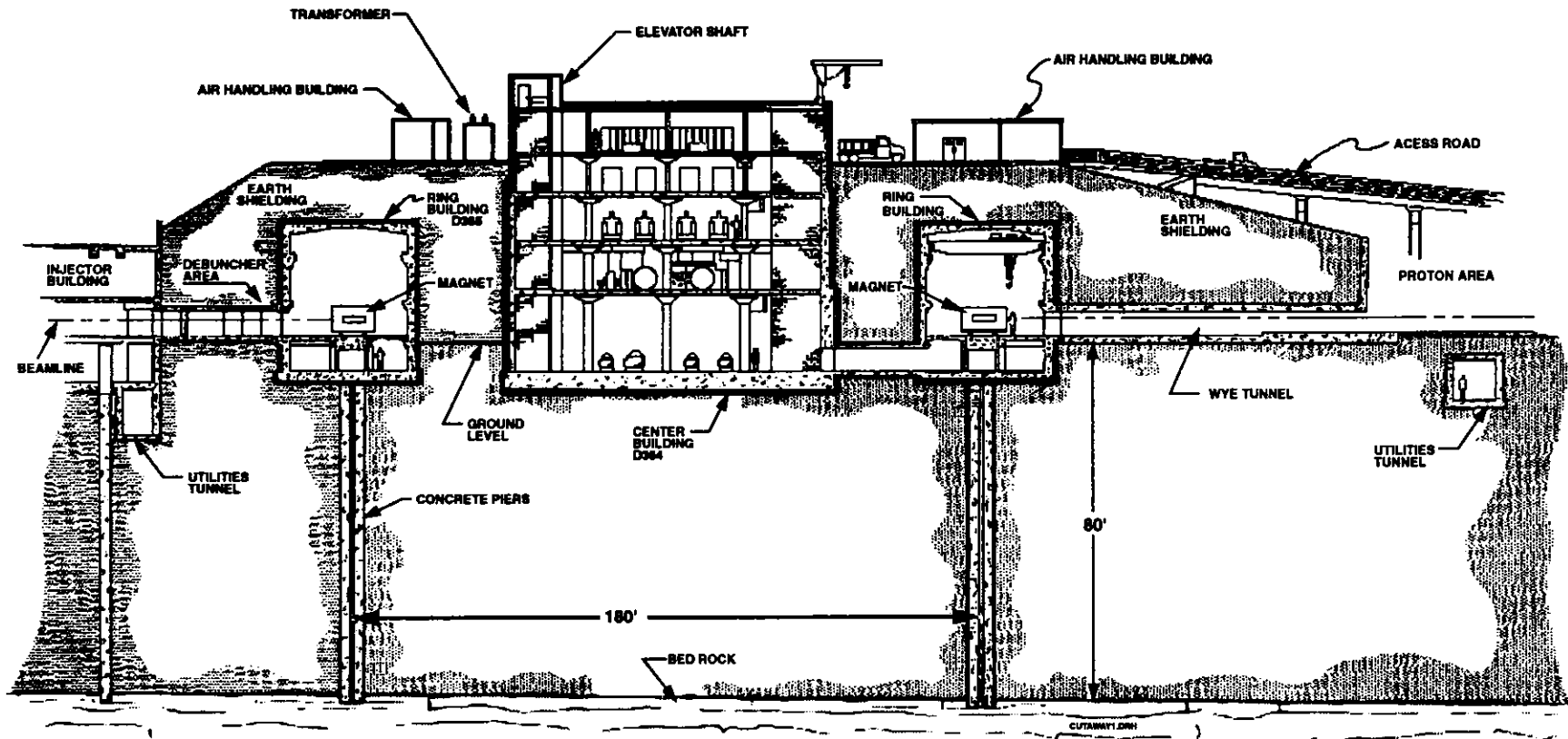
Figure II.9.2-2 Cross Section of the Zero Gradient Synchrotron Ring and Center Buildings.

perimeter shielding of the RCS. Lead, steel, dense polyethylene, and castable-composite shielding are used to improve the localized shielding, as required. Localized losses can occur at septum magnets and at other bending and focusing magnets during injection and extraction.

9.2.3 Radiation Dose Equivalent Factors

The dose equivalent in Sv per incident proton, H, based on the Moyer model,[17] is given by McCaslin,[4] when E_p is the incident proton energy (GeV), d is the shield thickness (g/cm^2), and r is the transverse distance to the beam (m):

$$H = \frac{H_o E_p^{0.8}}{r^2} e^{-d/\lambda} , \qquad (II.9.2\text{-}2)$$

H_o has units of Sv m^2/GeV$^{0.8}$ per proton and is the unshielded dose at 1 m. The value of H_o is dependent on the target material. Attenuation length, λ, for the relevant shield materials is found in Table II.9.2-1. For angles other than 90°, data in the literature were used.[3,5,11]

We use the concept of a line source to estimate dose from beam losses over an extended distance. For an assumed uniform beam loss over an extended region, the Moyer model can be numerically integrated to find the line source contribution.

The attenuation properties of iron shields backed up by concrete have been calculated by Tesch and Zazula.[3] Parameters for a modified Moyer model representation are provided, including attenuation by the concrete. They suggest values of $H_o = 4 \times 10^{-14}$ and $\lambda = 180$ g/cm^2 for an iron target and an iron shield, respectively. A problem in using only iron is that neutrons of approximately 25 keV and 125 keV tend to build up and stream through the iron after deep penetration. This effect can be handled by including 1 m of concrete to back up the iron. Tesch and Zazula quote an attenuation length of 30 g/cm^2 for low-energy neutrons and 107 g/cm^2 for high-energy neutrons in concrete. The 1 m of concrete represents about eight attenuation lengths for the low-energy neutrons and effectively removes them. The final expression for the dose equivalent rate, $\dot{H}_{tot}$ for an iron shield backed up by 1 m of concrete is then

$$\dot{H}_{tot} = \dot{H}_{Fe} \, e^{-235/107} , \qquad (II.9.2\text{-}3)$$

in which $\dot{H}_{Fe}$ is the dose equivalent rate through the iron shield. The dose equivalent through the iron shield is obtained from Equation II.9.2-2 and converted to dose equivalent rate by multiplying by the proton loss rate.

The dose equivalent factor can be calculated using the Moyer model, or the values can be taken from Tesch and Zazula.[3] At 2 GeV, the Moyer model gives a dose per proton of 1.3×10^{-14} Sv at 1 m, and Tesch and Zazula give a dose per proton of 4×10^{-14} Sv at 1 m, based on their recent computer studies. The values from Tesch and Zazula are a factor of three more conservative and are used in our calculations of the dose rates from the RCS, HET, and through the target biological shields. The calculations for 400 MeV protons are based on Tesch,[11] since his formalism is based on measured data over the energy range from 50 to 1000 MeV.

9.2.4 Beam Loss Assumptions and Shielding Requirements

To estimate bulk shielding needs, a distributed loss of 10^{-3} is assumed for each subsystem of the accelerator under normal operating conditions. This loss is distributed over the length of the subsystem for analysis as a line source. The loss rate along the linac and the LET under normal operating conditions is assumed to be a uniform 5 nA/m, but the unshielded dose contribution is not uniform because of the increase in energy as the protons are accelerated. The line source contribution from the linac system was numerically integrated to determine the total dose equivalent rate at the relevant dose point. The bulk shielding requirements for the various parts of the accelerator system are summarized in Table II.9.2-2. This shielding ensures that the dose rate is less than 1.25 μSv/h. For point losses, the assumption was made that shutdown would occur within a few pulses of the onset of an abnormal condition. The shielding described in Table II.9.2-2 is adequate under these conditions.

9.2.5 H⁰ Beam Catcher, Beam Stop, and Collimators

The beam catcher is needed to stop the H^0 atoms formed during the stripping reaction of the injected beam by the carbon stripping foil. An analysis by Chae[18] showed that the stripping efficiency to protons of a 250-μg/cm² foil is 99.46%. The fraction of H^0 emerging is 5.4×10^{-3}. These atoms are caught in a beam catcher before they enter the second quadrupole after the carbon stripping foil. This is discussed in Section II.2.2.2. Since the 30-Hz injected beam contains 1×10^{14} p/pulse, the number of hydrogen atoms is significant. Sullivan[19] gives an expression for the angular distribution of the fluence of secondary particles from a thick target for interacting protons of energy in the range 50 to 1000 MeV. This formulation takes into account the ionization losses as well as the interaction probability to predict the fluence per proton at 1 m at a given angle θ:

$$\phi(\theta) = 0.5\left(1 - e^{-m}\right)\big/\left(\theta + 40/\sqrt{E}\right)^2 \text{ neutrons/cm}^2, \qquad \text{(II.9.2-4)}$$

Table II.9.2-2 Shielding Requirements for the IPNS Upgrade

Subsystem	Shielding Requirements (m)		
	Earth	Concrete	Iron
Drift-Tube Linac	1.5	0.3	
Coupled-Cavity Linac	3.2	0.3	
LET	2.0	2.4	
RCS	8.0	1.07	
HET (10 Hz)		1.0	2.0
HET (30 Hz)		1.0	2.3

in which the proton energy E is in GeV and m = $3.6 \times 10^{1.6}$. The $1 - e^{-m}$ term corrects for the fractional energy lost due to ionization by the lower energy protons. Using attenuation lengths given in the same reference[19] for relevant materials, the necessary shielding in the lateral and forward directions can be calculated. Assuming a shield made of iron and concrete, the inner iron core is used to completely stop the protons, whereas the outer concrete shield is used to absorb low-energy neutrons that can cause activation. The beam catcher consists of an iron core, 15.2 cm in diameter and 20.32 cm in length, surrounded by concrete 1 m thick on the sides and 1.3 m thick in the forward direction. The concrete shield overlaps the iron core on the front face by 15.2 cm to protect against backscattered radiation. This shield reduces the neutron fluence at 2 m by a factor of 100 in the longitudinal direction.

The 30-Hz target is used to tune up the synchrotron. The tune-up is performed at 1-Hz operation. Since the target biological shield is designed for 30-Hz operation, this shield is also adequate for 1-Hz operation, and resultant dose rates are less than 0.06 μSv/h.

Collimators are used to remove halo particles that would otherwise be lost in the RCS. Off-momentum protons are removed by collimators in the high-dispersion areas, and betatron collimation is done by collimators in the high-beta areas. There are eight collimators total, or one of each type in each of the four sectors of the RCS. These collimators cause losses to occur at specific, highly shielded regions. This shielding reduces uncontrolled losses around the ring and reduces activation of the accelerator components. The power dissipated in each of the collimators is expected to be of the order of 0.5 kW. This amount of power dissipation necessitates collimator dimensions on the order of 1.4 m in diameter and 2 m long.

9.3 ACTIVATION

Activation of accelerator components by high-energy protons occurs because of spallation reactions in the accelerator materials, which generally leave the struck nucleus in an excited or radioactive state. Further radioactivation can be produced by the secondary particles released in the spallation reaction and by the evaporation neutrons that are emitted as the excited nucleus rids itself of excess energy. Finally, slowing down of evaporation neutrons and high-energy neutrons leads to activation by capture of low-energy neutrons. The overall amount of activity formed depends on the primary beam losses. The production of radionuclides in a given material depends upon the spallation cross section for high-energy hadrons and the mean free path in the target material.[19] The formation of a particular radionuclide depends upon the composition of the struck material, the energy spectrum of the secondaries, and the production cross section for that radionuclide. Among the radionuclides produced in shielding and accelerator components by spallation reactions are ^{22}Na and ^{24}Na in concrete and ^{54}Mn, ^{56}Mn, and ^{60}Co in steel. Thermal neutron capture produces ^{64}Cu and ^{65}Zn in copper, radioactive sodium in concrete, and radioactive manganese and cobalt in iron and steel. Other products, such as ^{7}Be, ^{11}C, ^{51}Cr, ^{46}Sc, and ^{56}Co, are also formed.

Since a number of products are formed in the various interactions, each with a different half-life, the time variation of the radionuclide population depends upon the beam irradiation time

and the time of decay following shutdown. Because of the different types of radiation emitted by the radionuclides, the dose rate is time-dependent. Of critical importance for the maintenance of the accelerator and the minimization of down time is the dose rate from activated accelerator components within a day or two following an accelerator run of reasonable duration. After short irradiation times, the induced activity in the system is proportional to the number of interacting protons, and the activity level decreases inversely with time.[19] "Hands-on" maintenance of the machine requires careful design attention to minimize the loss rate of protons in the various machine components.

Sullivan[19] gives an expression for estimating the order of magnitude of dose rates produced by induced activity along a beam line or accelerator component. The majority of the activity remains inside the machine and is shielded by the iron in the magnets. Sullivan assumes around 10% of the activity actually contributes to the dose rate. On this basis, the dose rate (in units of μSv/h) at 50 cm from the accelerator components, for protons of energy E_0 GeV, t days after the beam is switched off, following beam loss of 1 W/m for a period of T days, is approximately

$$\dot{H} = 30E_0^{-0.08} \ln\left[\frac{T+t}{t}\right] \qquad \mu\text{Sv/h} . \qquad \text{(II.9.2-5)}$$

The above expression was used to estimate dose rates from accelerator components, using the assumed loss rates in the various IPNS Upgrade accelerator systems and taking T = 30 days and t = 1 day. These dose rates are from 140-220 μSv/h in the linac and LET, and 290 μSv/h in the RCS. The dose rates are in the range that allows hands-on maintenance by workers without excessive down-time delays and without high radiation doses.

9.4 REFERENCES

1. U. S. Department of Energy, *Radiological Control Manual*, DOE/EH 0256T Revision 1 (April 1994).

2. U. S. Department of Energy, "Radiation Protection of the Public and the Environment," DOE Order 5400.5 (Feb. 8, 1990).

3. K. Tesch and J. M. Zazula, "Shielding properties of iron at high energy proton accelerators studied by a Monte Carlo code," Nucl. Inst. Meth. **A300**, 179-187 (1991).

4. J. B. McCaslin et al., "Moyer model approximations for point and extended beam losses," Nucl. Inst. Meth. **A256**, 418-426 (1987).

5. A. H. Sullivan, "The intensity distribution of secondary particles produced in high energy proton interactions," Rad. Prot. Dos. **27**(3), 189-192 (1989).

6. R. H. Thomas and G. R. Stevenson, *Radiological Safety Aspects of the Operation of Proton Accelerators*, IAEA Technical Report Series No. 283, IAEA, Vienna, Austria (1988).

7. K. Tesch and J. M. Zazula, "Study of the neutron field from a hadronic cascade in iron: verification of a Monte Carlo calculational model by comparison with measured data," Nucl. Inst. Meth. **A300**, 164-178 (1991).

8. G. Stevenson et al., "Determination of transverse shielding for proton accelerators using the Moyer model," Health Phys. **43**(1), 13-29 (1982).

9. K. Tesch and H. Dinter, "Estimation of radiation fields at high energy proton accelerators," Rad. Prot. Dos. **15**(2), 89-107 (1986).

10. H. Dinter et al., "Shielding of proton accelerators: a comparison between the Moyer model and Monte Carlo calculations," Nucl. Inst. Meth. **A276**, 1-7 (1989).

11. K. Tesch, "A simple estimation of the lateral shielding for proton accelerators in the energy range 50 to 1000 MeV," Rad. Prot. Dos. **11**(3), 165-172 (1985).

12. G. R. Stevenson and R. H. Thomas, "A simple procedure for the estimation of neutron skyshine from proton accelerators," Health Phys. **46**(1), 115-122 (1984).

13. J. T. Routti and M. H. Van de Voorde, "Dose estimates outside the shielding of the CERN intersecting storage rings by the Moyer method," Nucl. Eng. & Des. **21**, 421-434 (1972).

14. J. M. Zazula and K. Tesch, "Analysis of the transverse shielding problem at proton accelerators using a hadronic cascade code with low energy particle modules," Nucl. Inst. Meth. **A286**, 279-294 (1990).

15. H. Dinter and K. Tesch, "Determination of neutron spectra behind lateral shielding of high energy proton accelerators," Rad. Prot. Dos. **42**(1), 5-10 (1992).

16. J.M. Zazula et al., "Sky- and groundshine phenomena and related radiological quantities evaluated for the environment of a high-current spallation facility," *Part. Accel.* **21**, 28-42 (1987).

17. B. J. Moyer, "Method of calculation of the shielding enclosure for the Berkeley bevatron", presented at 1st International Conference on Shielding around High Energy Accelerators, Presses Universitaires de France, Paris 65 (1962).

18. Y. Chae, "Study of field ionization in H$^-$ charge exchange injection for the proposed neutron spallation source at Argonne," internal Neutron Source note, NSA-94-2, Argonne National Laboratory (1994).

19. A. H. Sullivan, *A Guide to Radiation and Radioactivity Levels Near High Energy Particle Accelerators*, Nuclear Technology Publishing, Ashford, Kent, England (1992).

10.1 INTRODUCTION

The IPNS Upgrade is a 2-GeV proton accelerator with two neutron-generating targets for condensed-matter research. The accelerator system consists of a linear accelerator section, a linac-to-RCS transfer line, the RCS, and two extraction lines to the target stations. The RCS is housed in the already existing ZGS Ring Building. Approximately 350 to 400 beam components require positioning to critical alignment tolerances. To accomplish this task efficiently and economically, state-of-the-art survey equipment and techniques are employed. For the most part, existing APS alignment equipment is utilized, resulting in significant cost savings for this project.

10.2 GEODETIC REFERENCE SYSTEM

The absolute positioning of the IPNS Upgrade components largely depends on the accuracy with which the position of the control network can be determined. Four preexisting, intervisible, and very stable alignment monuments, P1-P4, are used to establish the primary reference within the ZGS Ring Building, shown in Figure II.10.2-1. When electronic distance measurement (EDM) systems and electronic theodolites are used, an accuracy of better than ±0.5 mm can be achieved for these control points.[1] To ensure the proper location of the linac and the beam transfer line from the linac to the RCS, a gyro-theodolite is used to establish a homogeneous coordinate system for all accelerator subsystems, eliminating the need for the installation of a costly surface control network.

10.3 ALIGNMENT TOLERANCES

To obtain a smooth particle beam path, the vertical and radial deviations from the ideal position of one beam component to the next must be minimized. The relative alignment accuracy required to position the RCS quadrupoles and sextupoles is ±0.2 mm in the vertical and radial positions. In the longitudinal direction, components have to be placed to within ±0.5 mm. The dipoles have to be set to ±1 mrad of roll. On a global scale, the position of each RCS beam element should not deviate from the ideal location by more than ±2 mm. The deviation of the circumference of the RCS is expected to be less than ±12.6 mm. Similar positioning tolerances have been specified and actually achieved for the alignment of the APS booster beam components.

10.4 ALIGNMENT CONCEPT

The alignment concept is based on the definition of a common coordinate system. The task is to determine the coordinates of the control network points and magnet fiducials by using redundant measurements and statistical analysis tools for blunder detection.[2] To guarantee repeatability of the control points, the centering system used is the same as that used for the
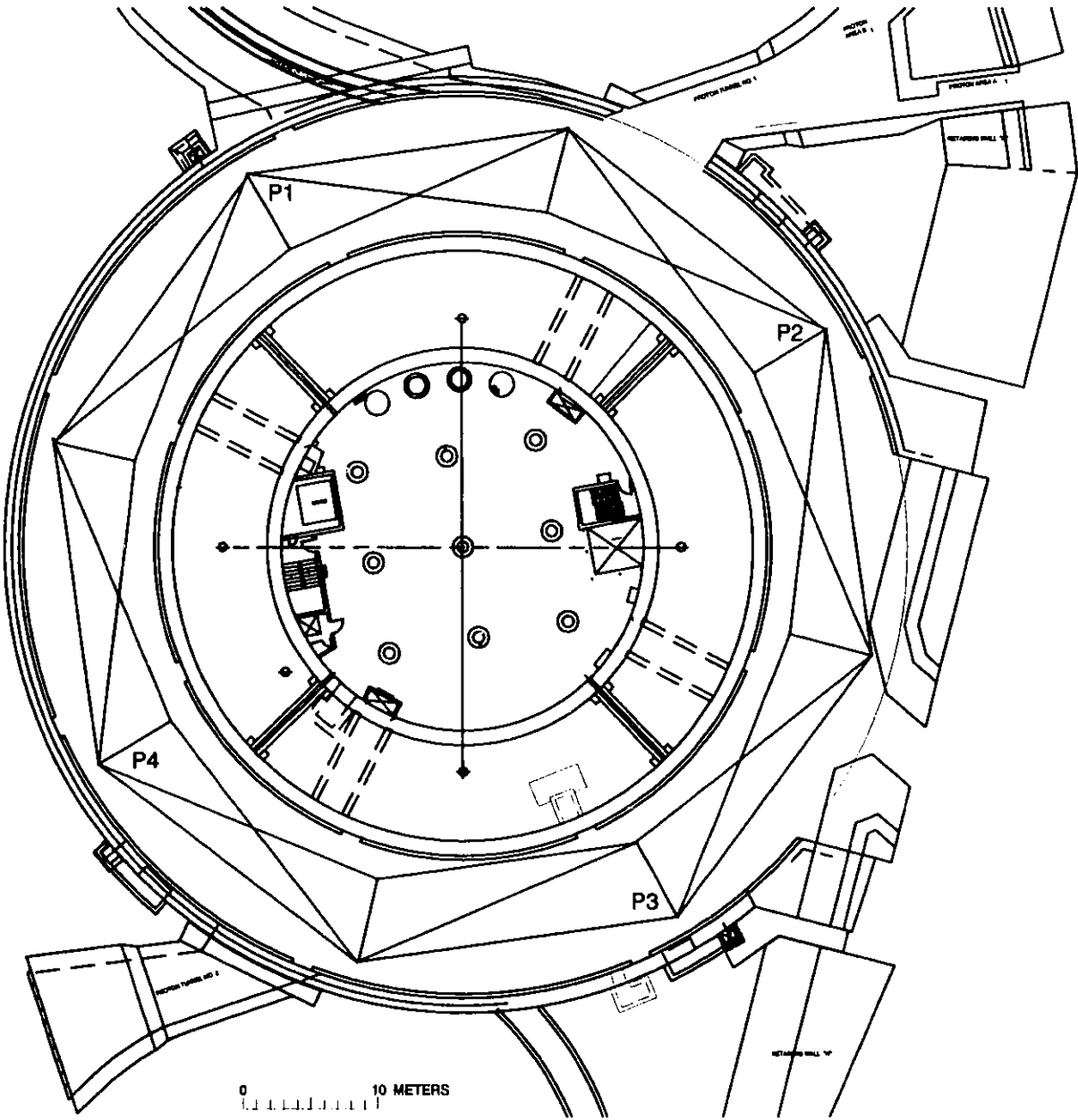
Figure II.10.2-1 Example of an RCS Survey and Alignment Control Network Design.

alignment of the APS. This system is based on a nearly perfect fit between a conical surface and a sphere, as shown in Figure II.10.4-1. It provides the means for determining the three-dimensional coordinates of each control point. Appropriate adapters to use this system have been designed and used for the APS project, as depicted in Figures II.10.4-2 and II.10.4-3.

Secondary control points are connected to the primary control network and are used to position the magnet support system and all beam components. The symmetrical lattice structure of the RCS ring lends itself to the use of templates for the purpose of laying out the beam component supports. The coordinates of the secondary control points are determined by means of a laser tracking system.

The ideal position of each beam component in the global coordinate system is calculated by using the information on each magnet fiducial cup location that was gathered during the magnet mapping process. With the use of this information and the laser tracking system, which provides data on the actual measured position of each beam component with respect to the control network, all beam elements are positioned.[3] The magnet location resulting from this step is only as good as the accuracy of the control network. Considering the possible accumulation of instrumental[4] and procedural errors, the accuracy of the control network for positioning beam components can only be viewed as an upper limit that, in reality, can never be reached. Therefore, a final alignment step is required.[5]

The final alignment step abandons the control network information for determining the position of beam elements. It serves two purposes. The first purpose is to check for blunders that may have been introduced during the previous positioning phase. The second is to ensure the quality of the alignment efforts. As a result, the radial and vertical deviations of each beam component from a smooth curve are calculated,[6] thus providing a quantitative assessment of the achieved tolerances.[3]

The initial alignment of all RCS beam components and support structures is closely tied to the component installation schedule. The time frame for the installation of all technical RCS components is six months. The survey and alignment tasks to support this rapid installation schedule can easily be accomplished by using state-of-the-art equipment and procedures.

It is estimated that the realignment of all RCS beam elements, when necessary, can be done in three to five weeks.

10.5 CONTROL NETWORK SIMULATIONS AND DATA HANDLING

Before the installation of the control network takes place, simulations are performed to find the optimal network design that meets the constraints given by the ZGS Ring Building while obtaining the required control network accuracy with the least number of measurements.[7] The results of such a simulation are shown in Figure II.10.5-1. It shows the estimated accuracy in the form of error ellipses around the control points for a given network geometry and observation plan. The major axes of the largest error ellipses depicted are on the order of 0.3 mm.

⌀3.5 TAYLOR HOBSON TARGET BALL

TARGET BALL
RECEPTOR

CONCRETE

EPOXY GROUT
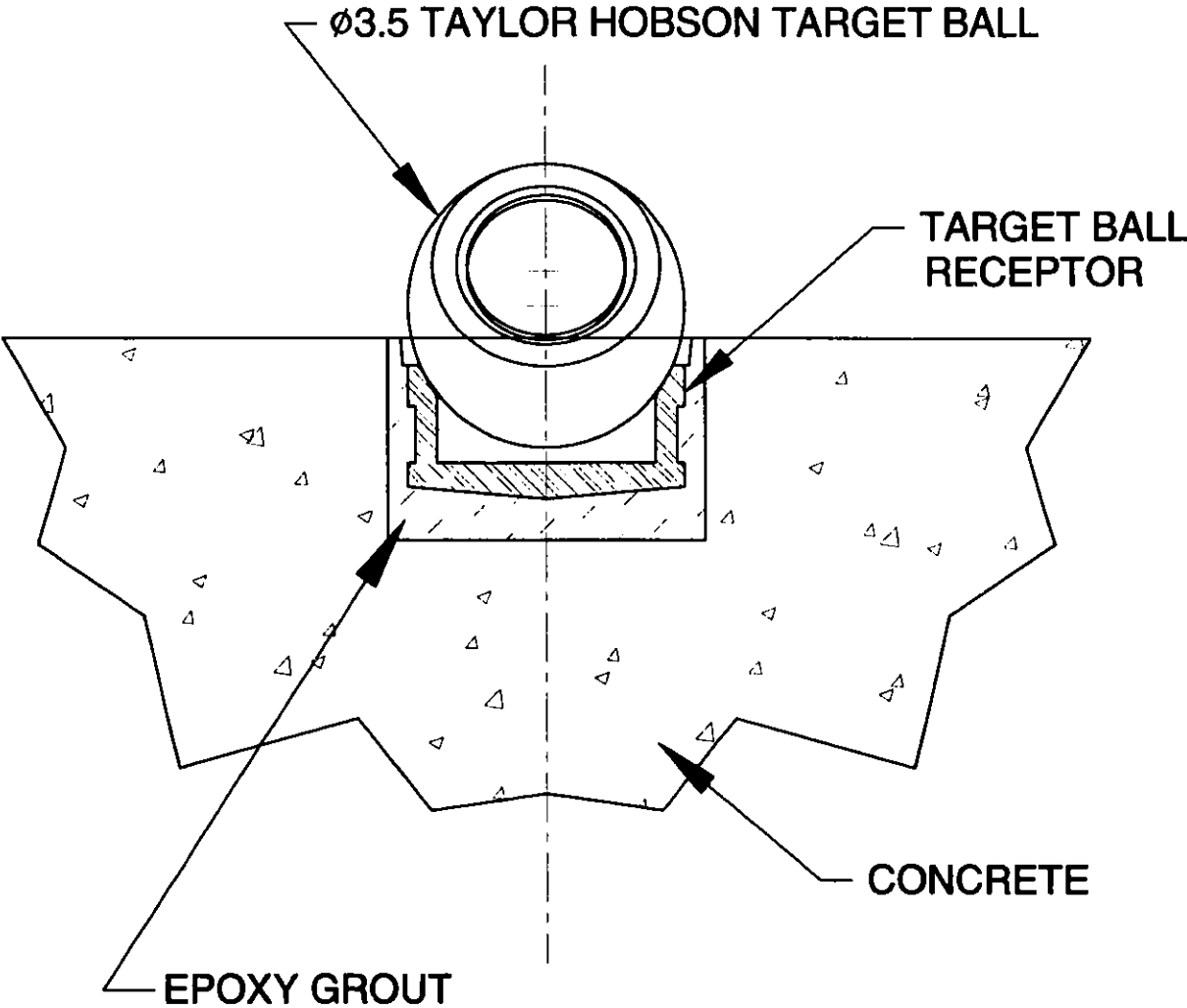
Figure II.10.4-1 Target Ball Receptor at the Control Point.

TOP VIEW   TOP VIEW
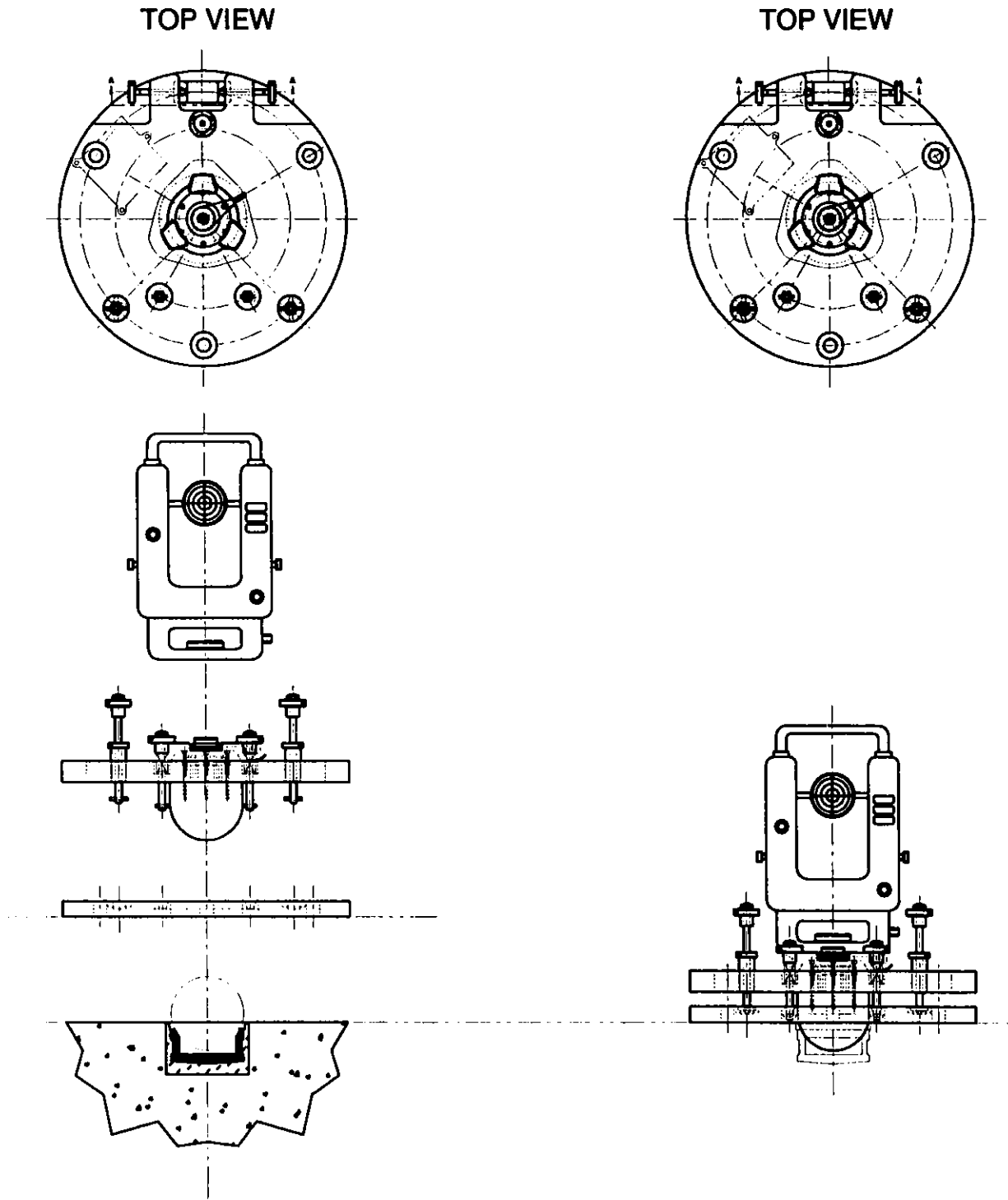
Figure II.10.4-2 Explosion (left) and Assembly (right) Views of Floor Mounting Instrument Adapter.
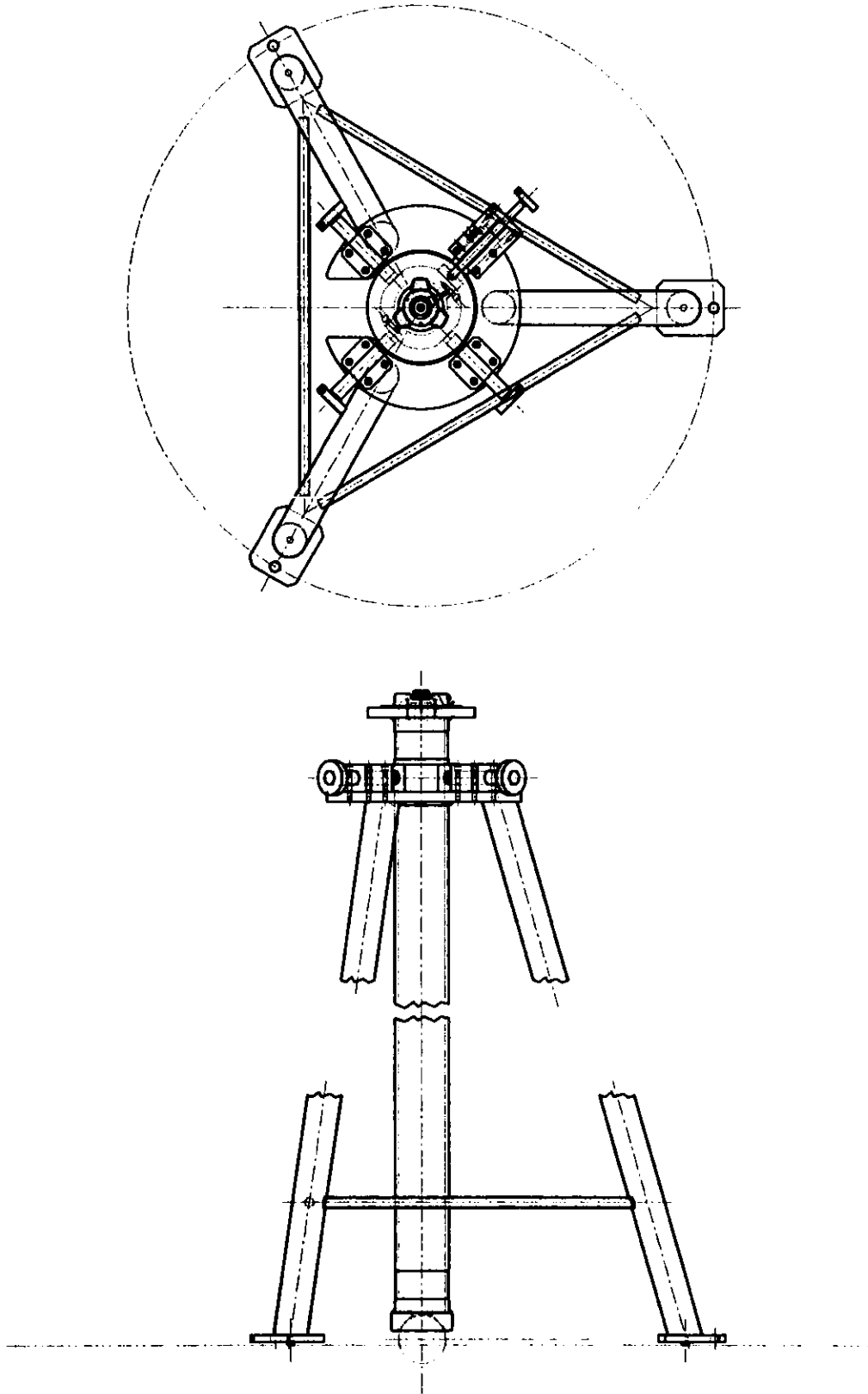
Figure II.10.4-3 Monopod Instrument Adapter, Extending the Floor Reference Point to a Height of 1.4 m.
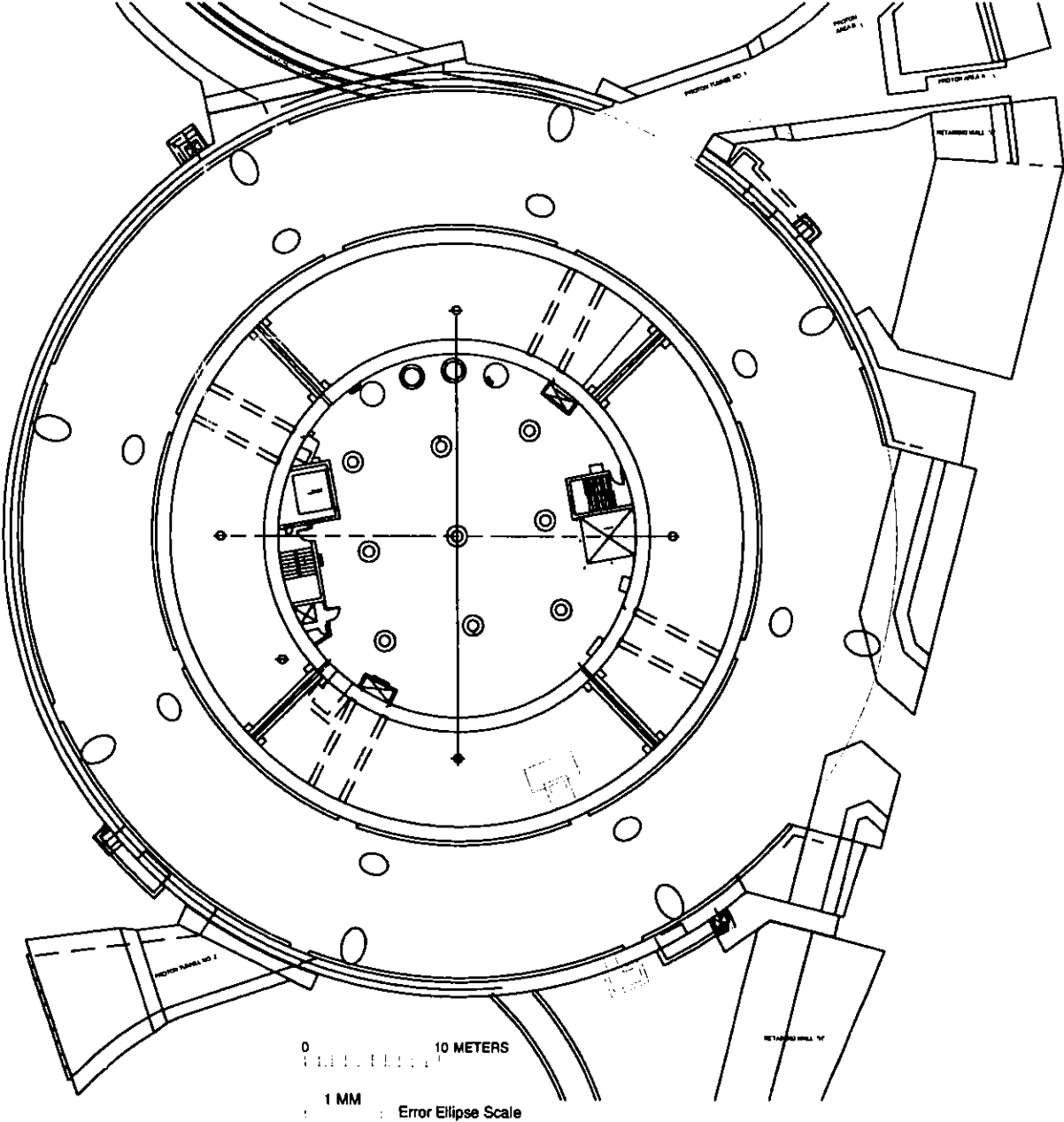
Figure II.10.5-1 Error Ellipses of an RCS Survey Network Design Simulation. (Ellipses are shown at a different magnification than the rest of the drawing.)

Throughout all the alignment efforts, automated data flow is used. This not only improves the alignment productivity in terms of output, but also results in fewer errors when measurement data are recorded. Laptop computers are connected to electronic theodolites, electronic distance measuring systems, and automatic levels.[8] The data are analyzed on a personal computer connected to the local area network. The resulting coordinates from this process are then used to supply the laser tracker system with information for beam element positioning.

10.6 INJECTOR ALIGNMENT

Both the linear accelerator section and the low-energy transfer line between the linac and the RCS are long straight layouts. Such layouts are ideally suited for common optical tooling techniques in conjunction with an established secondary control network. To extend the RCS control network into the linac, a 250-m-long traverse is required. To ensure the proper direction of the linac with respect to the transfer line and the proper location of the transfer line to the RCS, observations with a gyro-theodolite are necessary to support such a long open-ended traverse.

10.7 REFERENCES

1. H. Friedsam, J. Penicka, and S. Zhao, *Survey and Alignment Report on the Primary Control Network for the APS*, Light Source Note LS-220 (1993).

2. H. Friedsam, "The alignment of the Advanced Photon Source at Argonne National Laboratory," in *Proceedings of the Third International Workshop on Accelerator Alignment* (Annecy, France, 1993).

3. H. Friedsam, "A new accelerator alignment concept using laser trackers," in *Proceedings of the Fourth European Particle Accelerator Conference* (London, England, 1994).

4. H. Friedsam and J. Penicka, "A new method to position the APS dipoles with the use of a laser tracker," in *Proceedings of the Fourth European Particle Accelerator Conference* (London, England, 1994).

5. H. Friedsam and W. Oren, *The Application of the Principal Curve Analysis Technique to Smooth Beamlines* (Stanford Linear Accelerator Center, Stanford, California, 1991).

6. T. Hastie, *Principal Curves and Surfaces*, SLAC Report No. 276 (Stanford Linear Accelerator Center, Stanford, California, 1984).

7. I. Burstedde, *Adjustments of Geodetic Networks at SLAC* (1983).

8. H. Friedsam, *Survey and Alignment Workshop on Data Processing Using GEONET for Accelerator Alignment* (Stanford Linear Accelerator Center, Stanford, California, 1992).

III

Injector System

A 400-MeV H⁻ linac capable of delivering a time-averaged current of 0.5 mA is required for the IPNS Upgrade injector. The linac system was designed by AccSys Technology, Inc. The design relies heavily on those of previous linac systems, including the injector linac for the Superconducting Super Collider (SSC), to obtain the most practical system with proven technology. Existing, available linac structure designs were used.

This linac design is shown schematically in Figure III.1-1. The linac is 120 m long and can accelerate an H⁻ beam of 50-mA peak current at a duty factor up to 1.5%. The total peak radio-frequency (rf) power required for operation is 104 MW; average input power is less than 4.85 MW. The design is optimized to achieve the lowest capital cost available, consistent with routinely achievable accelerating gradients and the lowest attainable operating costs.

The H⁻ linac has the following accelerator components:

- H⁻ ion injector — A cesium-enhanced volume ion source produces a 50-mA H⁻ beam at an energy of 35 keV. Alternatively, the ISIS H⁻ source can be used without further development.[1] An electrostatic deflector driven by a field effect transistor (FET) and located at the output of the ion injector electrode stack permits beam chopping at duty factors up to 75%.

- Low-energy beam transport (LEBT) — The 35-keV H⁻ beam from the ion injector is matched into the RFQ linac by using two large-bore solenoid lenses.

- Radio-frequency quadrupole (RFQ) — A conventional 4-vane RFQ, operating at 425 MHz, bunches and accelerates the 35-keV H⁻ ion beam up to 2.0 MeV, while focusing the 50-mA pulsed current.

- Ramped-gradient drift tube linac (RGDTL) — A short section of a conventional DTL, also operating at 425 MHz, is close-coupled to the RFQ. The fields in it are ramped to match the beam from the RFQ into the DTL. The RGDTL accelerates the bunched 2-MeV beam from the RFQ up to 4.2 MeV for injection into the DTL.

- Drift tube linac (DTL) — A standard drift tube linac, also operating at 425 MHz, accelerates the H⁻ beam up to 70 MeV. This 20-m-long DTL consists of three tank sections, each driven by a 4-MW klystron rf system.

- Matching section (MS) — The 70-MeV H⁻ beam from the DTL is matched into the coupled cavity linac by using a 3.2-m-long beam transport system containing two buncher tanks and ten quadrupole magnets.
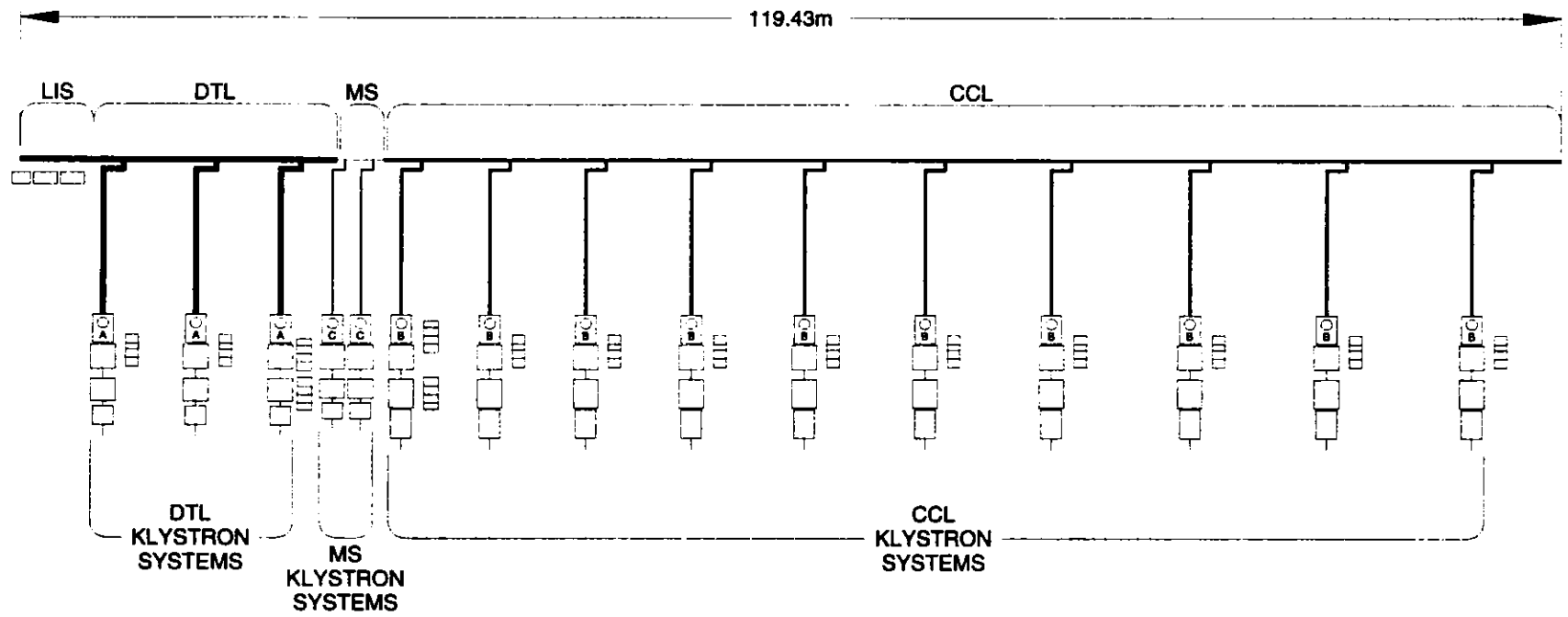
Figure III.1-1 IPNS Upgrade Injector Linac Layout.

- Coupled cavity linac (CCL) — The final stage of the system is a conventional side-coupled linac (SCL) operating at 1,275 MHz. This 92-m-long structure contains 10 accelerating modules, each consisting of six short tanks connected by conventional bridge couplers, and each driven at the middle bridge coupler by a 9-MW klystron rf system.

This chapter describes the background and scope of the physics design and provides a technical description of the subsystems listed above.

The IPNS Upgrade requires a 400-MeV H⁻ ion linac that is capable of delivering a 35-mA, unchopped peak beam current or a 44-mA, 25% chopped beam current in a 500-μsec pulse at a 30-Hz repetition rate.[1] The IPNS Upgrade injector linac performance requirements are shown in Table III.2-1.

The linac design is based on existing subsystems and designs from Los Alamos National Laboratory (LANL), Fermilab, and the SSC. Where possible, existing, proven components are used. The entire H⁻ injector linac can be commercially procured.

Table III.2-1 IPNS Upgrade Injector Linac Performance Requirements

Parameters	Values	Units
Accelerated ion	H⁻	-
Output kinetic energy	400	MeV
Pulsed beam current[a]	35	mA
Beam pulse length	500	μsec
Beam repetition rate	30	Hz
Time-averaged current	500	μA
Radio-frequency duty factor	3	%
Normalized rms transverse emittance[b]	0.1	π cm-mrad
Output energy spread (fwhm)[c]	2.5	MeV

[a] Unchopped; the requirement for 25% chopped beam is 44 mA.

[b] rms = root mean square.

[c] fwhm = full width at half maximum.

The IPNS Upgrade injector linac delivers a 400-MeV H⁻ beam with pulse lengths up to 500 μsec at a nominal peak current of 35 mA for injection into the Rapid Cycling Synchrotron (RCS). The required energy spread is less than 2.5 MeV fwhm and the transverse normalized rms emittance is less than 0.1 π cm-mrad. As shown in Figure III.3-1, the linac consists of an H⁻ ion source, which includes a beam chopper, LEBT system, 2.0-MeV RFQ, 70-MeV DTL, and 400-MeV CCL. The beam from the RFQ goes directly into the DTL. Matching is achieved in a short ramped-gradient tank section, while a separate matching section is used between the DTL and CCL. The dimensions of these subsystems are indicated in Figure III.3-1. Calculated rf power for each subsystem is also noted in the figure.

The physics design of the IPNS Upgrade injector linac was based on several existing designs, including those of the SSC injector linac and the high-current proton linac designed by AccSys for commercial radioisotope production. The H⁻ ion injector design is based on the Lawrence Berkeley Laboratory (LBL) rf-driven H⁻ volume ion source, with its output energy optimized at 35 keV for injection into the RFQ. The RFQ and DTL physics designs are based on the AccSys high-current proton linac and are very similar to the SSC design. This RFQ is designed for up to 50-mA output current to ensure an adequate safety margin for the IPNS Upgrade injector. The 70-MeV DTL provides maximum shunt impedance while maintaining a low beam loss during acceleration. This DTL is shorter than the SSC 70-MeV DTL, primarily because of the much shorter ramped-gradient tank.

The designs of the DTL/CCL matching section and CCL configuration are similar to those of the SSC, but are optimized at a lower accelerating gradient to accommodate the much longer beam pulse and higher duty factor. This was done to minimize capital cost and lower input power consumption. The SSC design was based on rf klystrons capable of 20-MW peak power each. The IPNS Upgrade design is based on 9-MW peak power klystrons, the maximum available at a 3% duty factor.

A summary table of the final physics design parameters for the linac sections is given in Table III.3-1.

End-to-end beam dynamics were calculated for output currents of 38 and 50 mA. The ion source extraction system was designed by using the code SNOW,[2] which includes space charge effects due to H⁻ ions and the extracted electrons. The output from the ion injector was characterized in two-dimensional phase space, because it is a dc beam. The code TRACE2D[3] was then used to obtain the LEBT design and to match the beam into the RFQ, as seen in Figure III.3-2. The matched beam was then put into the RFQ, and the code PARMULT[4] was used to simulate the RFQ. Figure III.3⁻3 shows the beam size, phase, and energy profiles as the 45-mA input beam traverses the RFQ. The output beam particles from the RFQ are shown in Figure III.3.3-4. A total of 720 input particles was used. The output was used as input to the code PARMILA[5] to simulate the beam dynamics in the DTL. Figure III.3-5 shows the beam size, phase and energy profiles calculated through the DTL, and Figure III.3-6 gives the output phase space projection at 70 MeV.

Table III.3-1 Summary of IPNS Upgrade Injector Linac Physics Design Parameters

Parameters	RFQ	DTL	MS	CCL	Units
Input energy	0.035	2.0	70.0	70.0	MeV
Output energy	2.0	70.0	70.0	400.0	MeV
Output current[a]	35.0	35.0	35.0	35.0	mA
Output norm rms transverse emittance[b]	0.0120	0.0135	0.0151	0.0194	π cm-mrad
Operating frequency	425	425	1,275	1,275	MHz
Peak surface field	36 $(1.8 \times E_{kp})$	28 $(1.4 \times E_{kp})$	24 $(0.8 \times E_{kp})$	28 $(0.9 \times E_{kp})$	MV/m
Accelerating gradient, $E_o T$	-	2.4 - 4.6	-	5.9 - 5.5	MV/m
Bore radius	2.4 - 3.0	5.0 - 9.0	10.0	10.0 - 12.0	mm
Synchronous phase	-30	-30		-30 to -25	deg
Structure power	0.22	6.28	1.2	52.8	MW
Number of tanks/modules	1	4	2	6/10	-
Structure length	2.16	20.54	3.2	92.1	m
Beam power at 40 mA	0.08	2.72	-	13.2	MW

[a] Unchopped; 25% chopped beam requirement is 44 mA.

[b] rms = root mean square.

Structure	Volume	Sol	4 Vane	RG+CG (PMQ)	Quad	Side-Coupled
Field	35 kV DC		$1.8\ E_{KP}$	$1.4\ E_{KP}$		$0.9\ E_{KP}$
RF Systems	.07MW		0.3 MW	$1 \times 0.3 + 3 \times 4$ MW	2×1 MW	10×9 MW
Length	0.5m	0.6m	2.2m	20.5m	3.2m	92.36m

Ion Source — LEBT — RFQ 425.0 MHz — DTL 425.0 MHz — MS — CCL 1275.0 MHz

Energy   35 keV   2.0 MeV   70.0 MeV   400 MeV
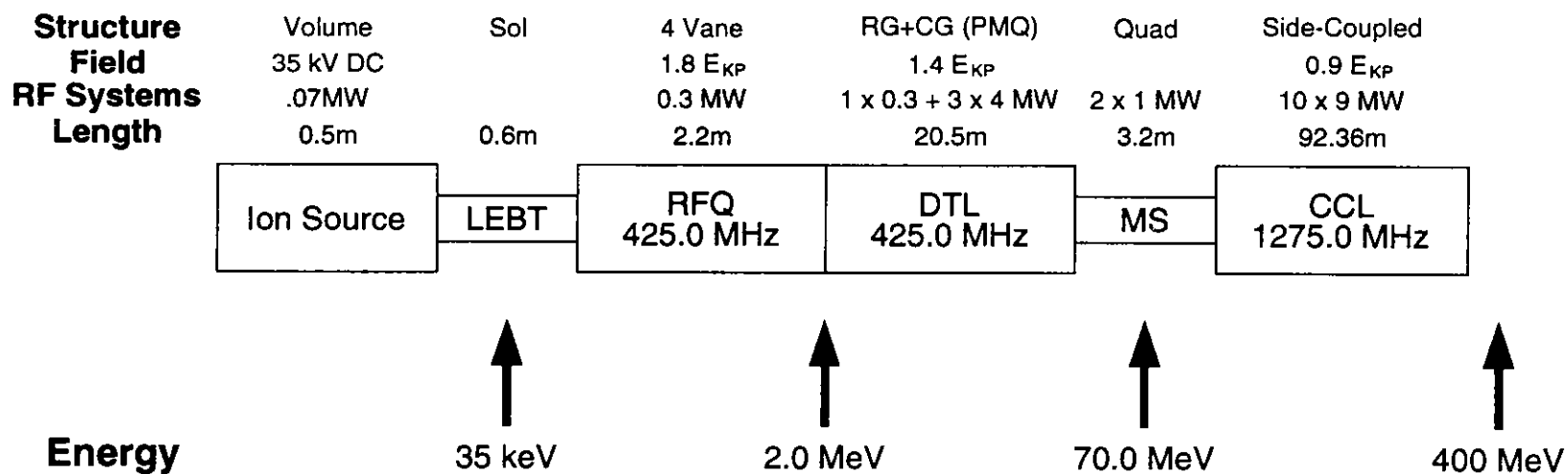
Fiii43-1.dwg

Figure III.3-1 Block Diagram of the IPNS Upgrade Injector Linac.
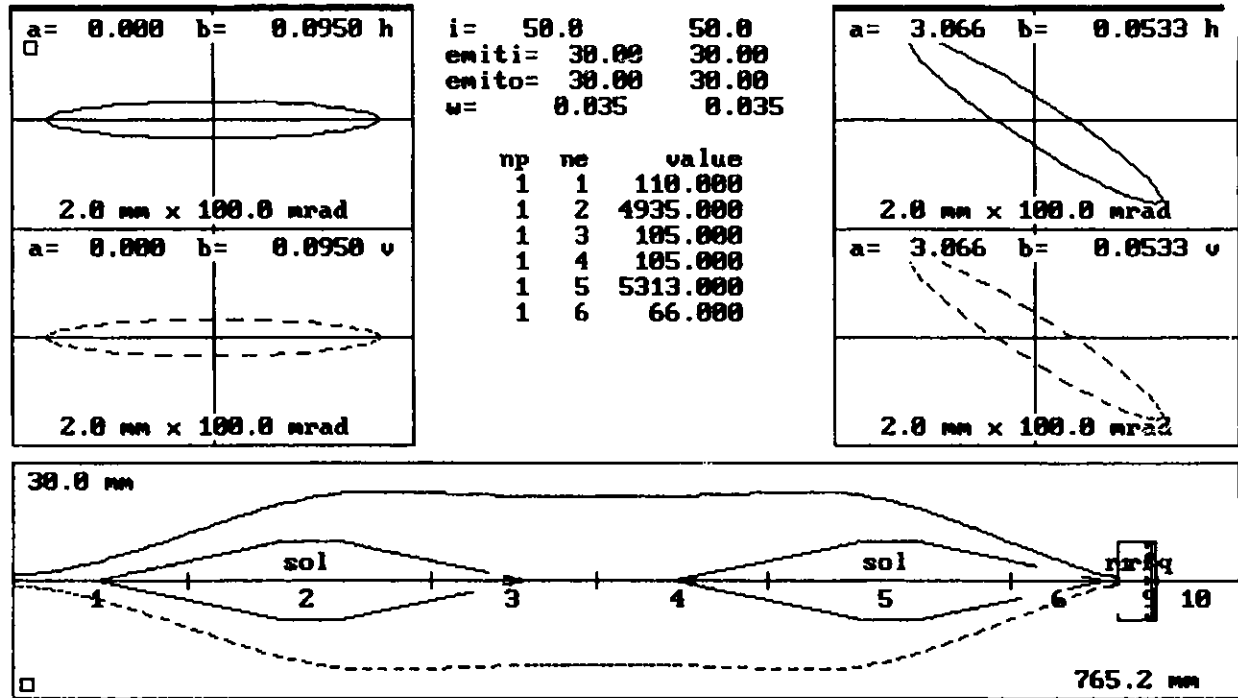
Figure III.3-2 LEBT Optics.
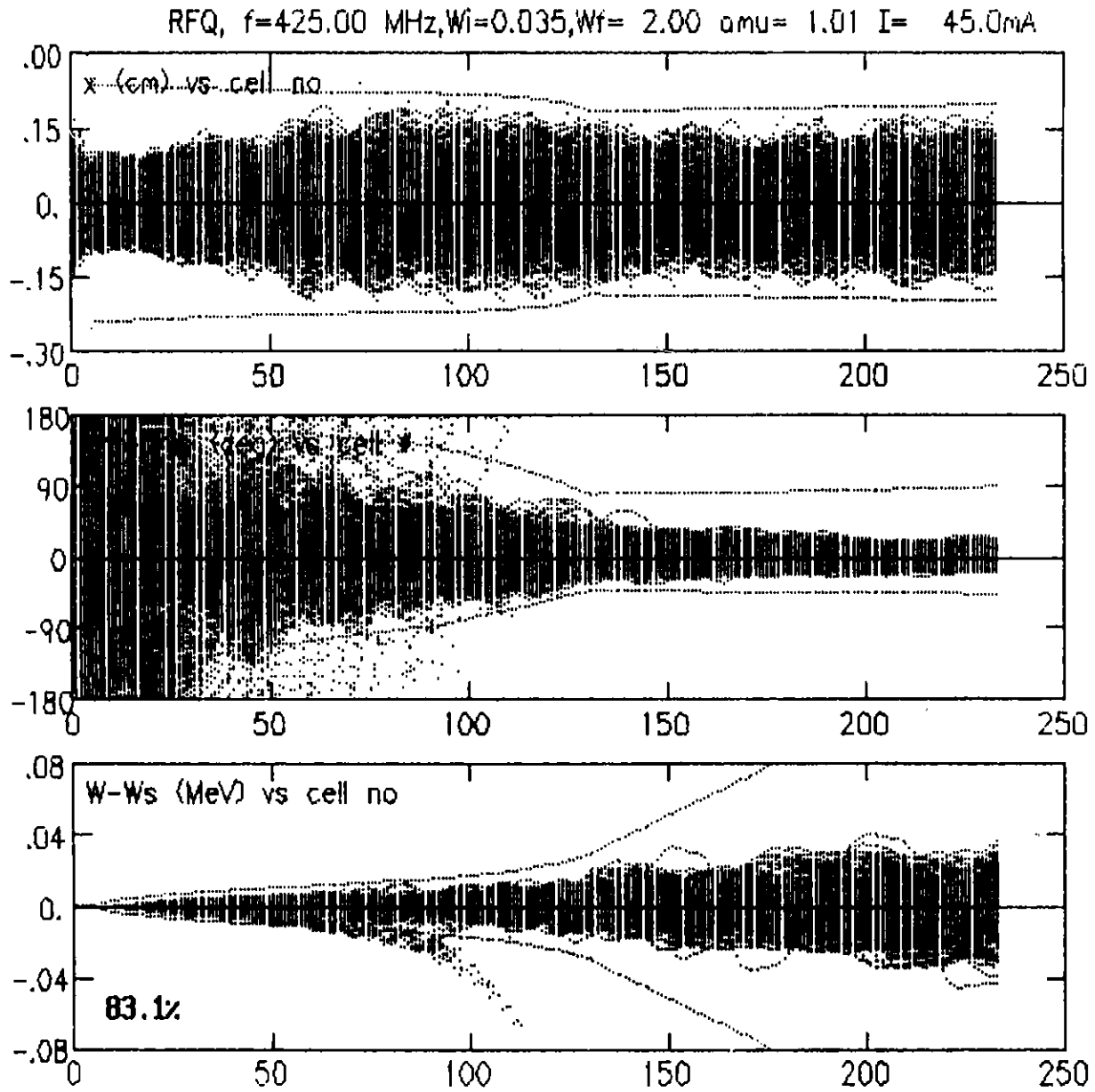
Figure III.3-3 Calculated Beam Dynamics through the RFQ. (Beam size [top], phase [center], and energy profile [bottom] are plotted as the 45-mA beam traverses the RFQ.)
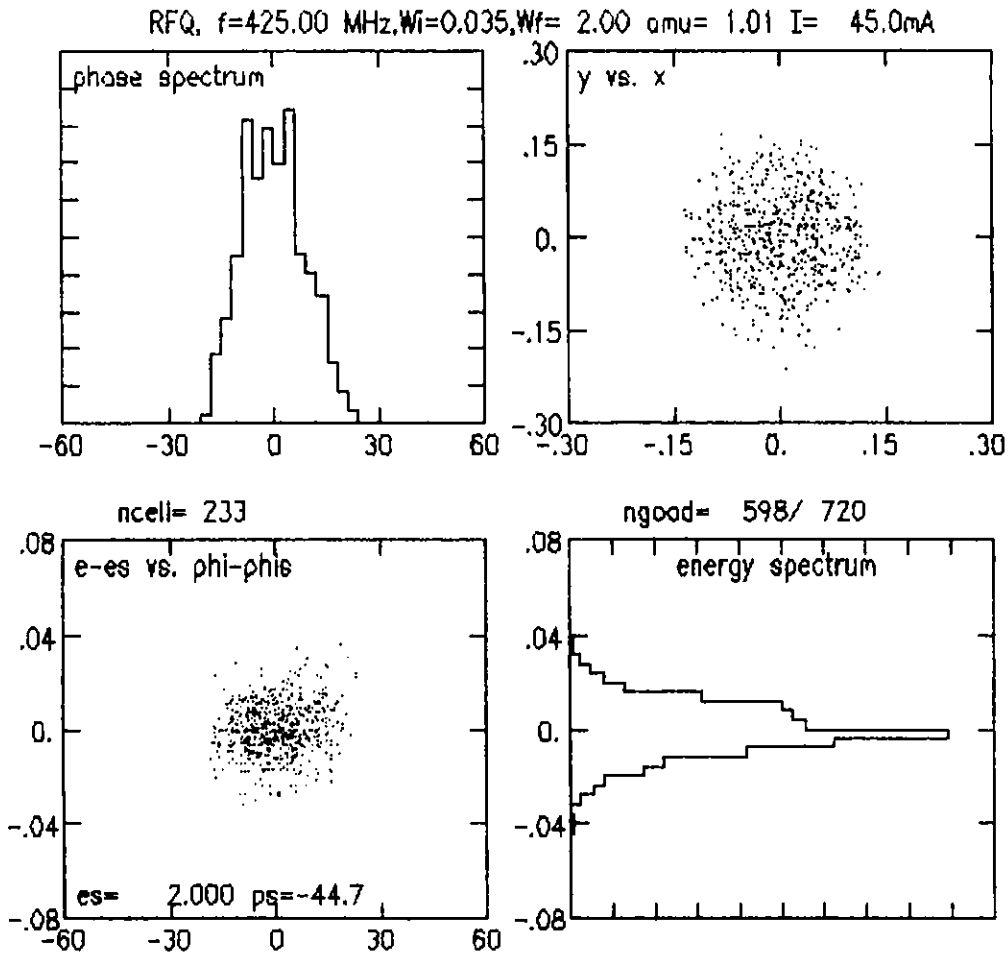
Figure III.3-4 Output Beam Phase Space Projections from the RFQ.
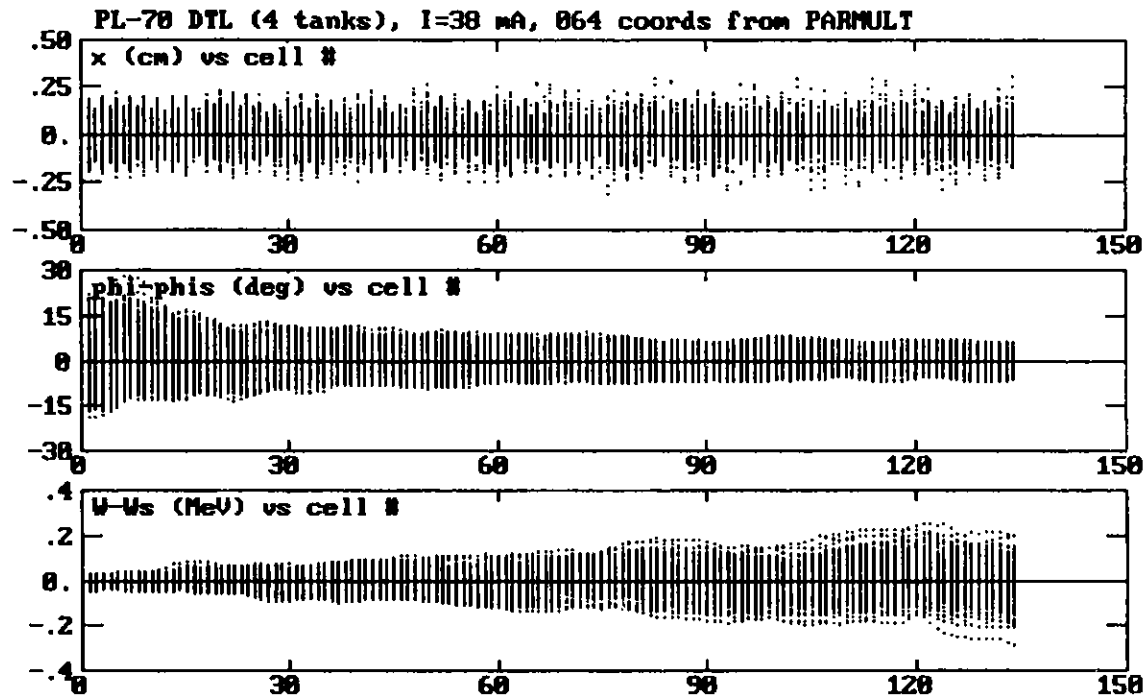
Figure III.3-5 Calculated Beam Dynamics through the DTL. (Calculated size [top], phase [center], and energy profile [bottom] are shown in the DTL.)
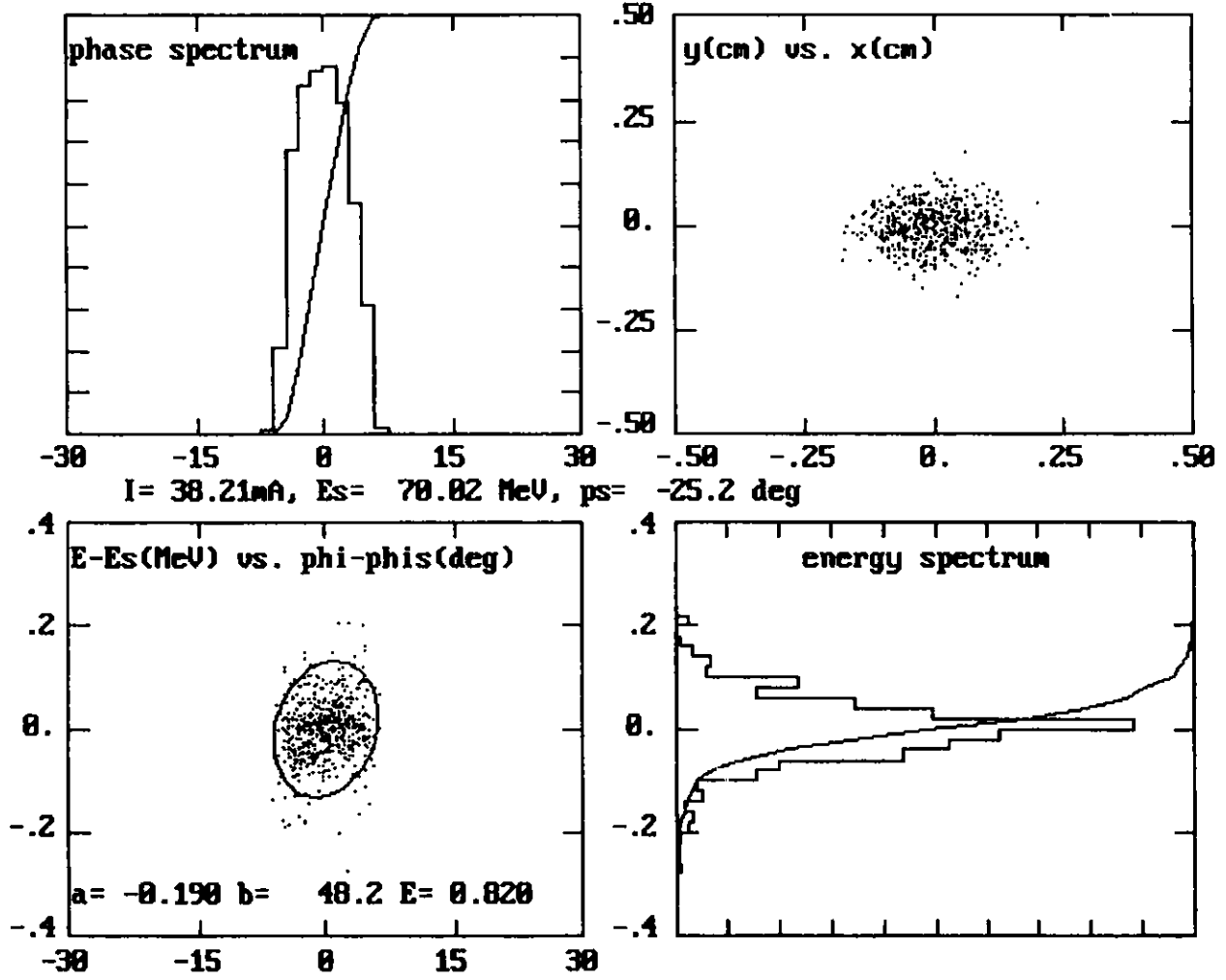
Figure III.3-6 Output Beam Phase Space Projections from the DTL.

The code TRACE-3D[6] was used with the output beam rms phase space parameters to design the DTL/CCL matching section and to determine the quadrupole magnet strengths and buncher cavity voltages. Figure III.3-7 shows the TRACE-3D beam optics through this matching section. Elements of the transport region downstream from the DTL were input to the code PARMILA to obtain the particle coordinates at the input to the CCL.

The longitudinal coordinates of the original particles that had been injected in the RFQ and followed through the RFQ, DTL, and matching section were redefined with respect to the CCL frequency. Then the particles were followed through the CCL by using CCLDYN.[7] Figure III.3-8 shows the beam dynamics through the CCL. Figure III.3-9 shows the projected six-dimensional output phase space, from which the final transverse emittance in each plane and the final energy spread can be estimated.

The baseline design of the 400-MeV IPNS Upgrade injector linac provides the 33-mA H⁻ output current required for injection into the RCS. The calculated rms transverse emittance is approximately 0.02 π cm-mrad, which is sufficiently below the required value of 0.1 π cm-mrad to leave adequate margin for realistic fabrication tolerances. The energy spread provides for a factor-of-two dilution and is not as sensitive to mechanical tolerances.
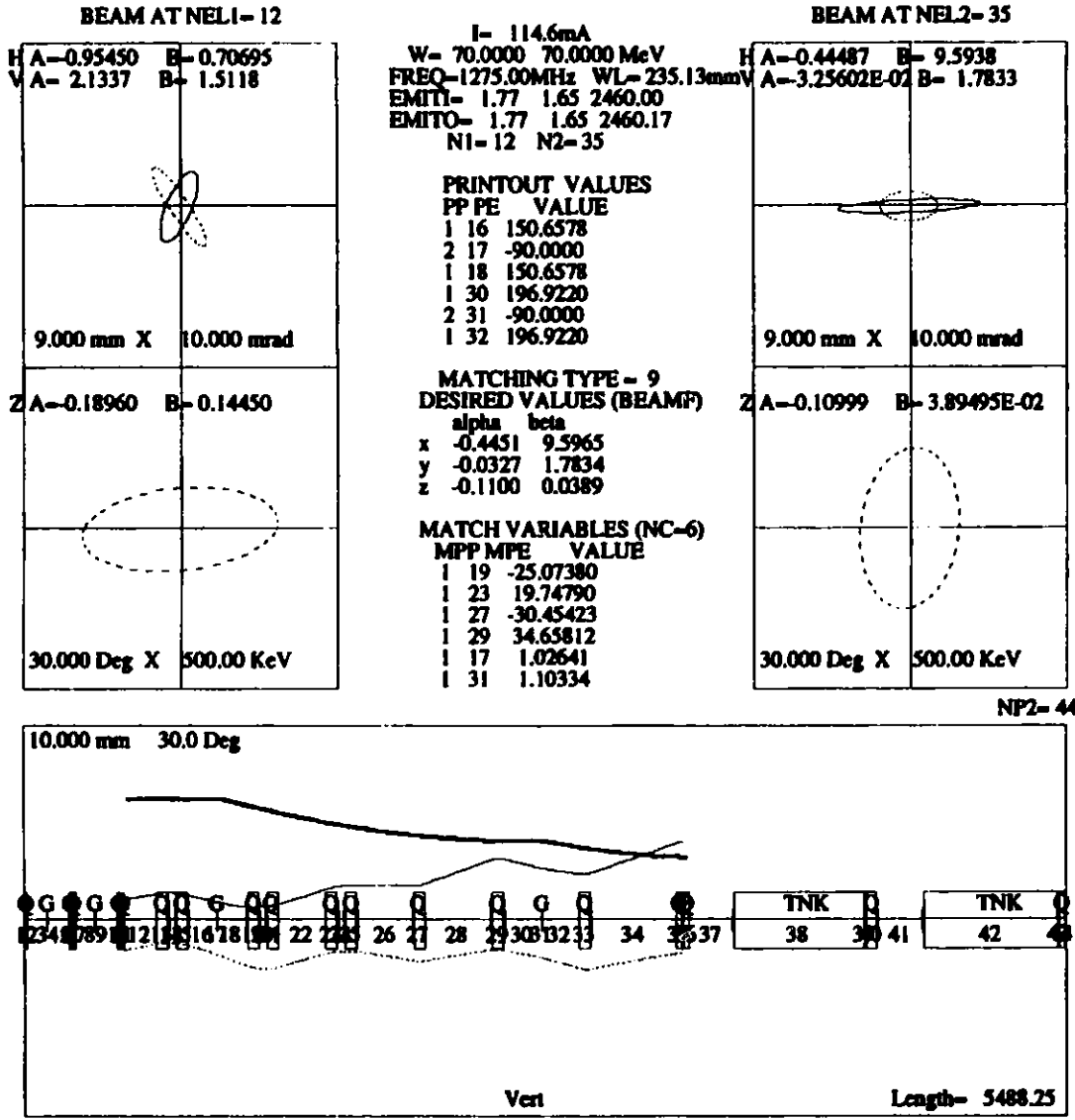
Figure III.3-7 Calculated Beam Optics through the DTL/CCL Matching Section.
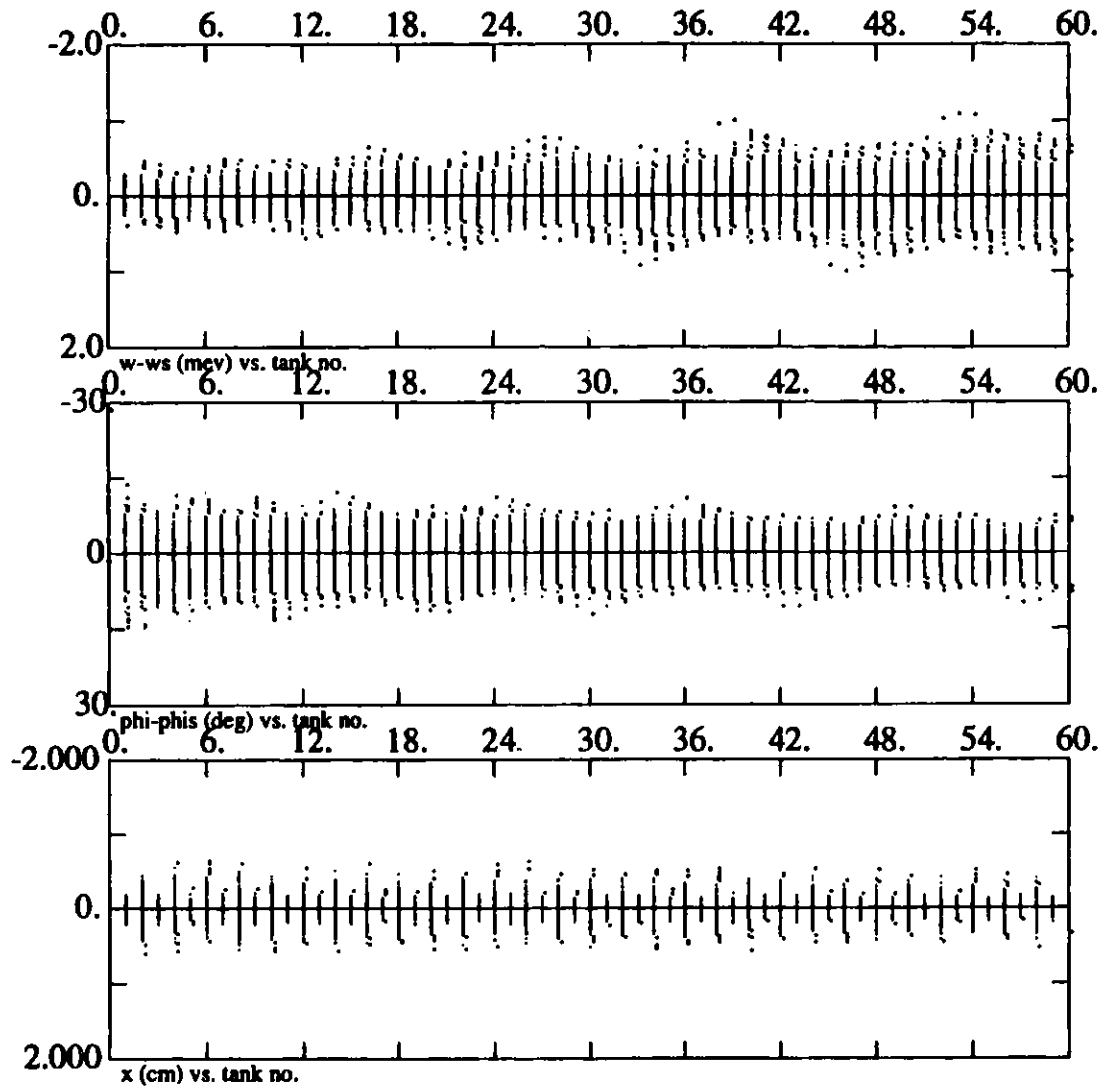
Figure III.3-8 Calculated Beam Dynamics through the CCL.
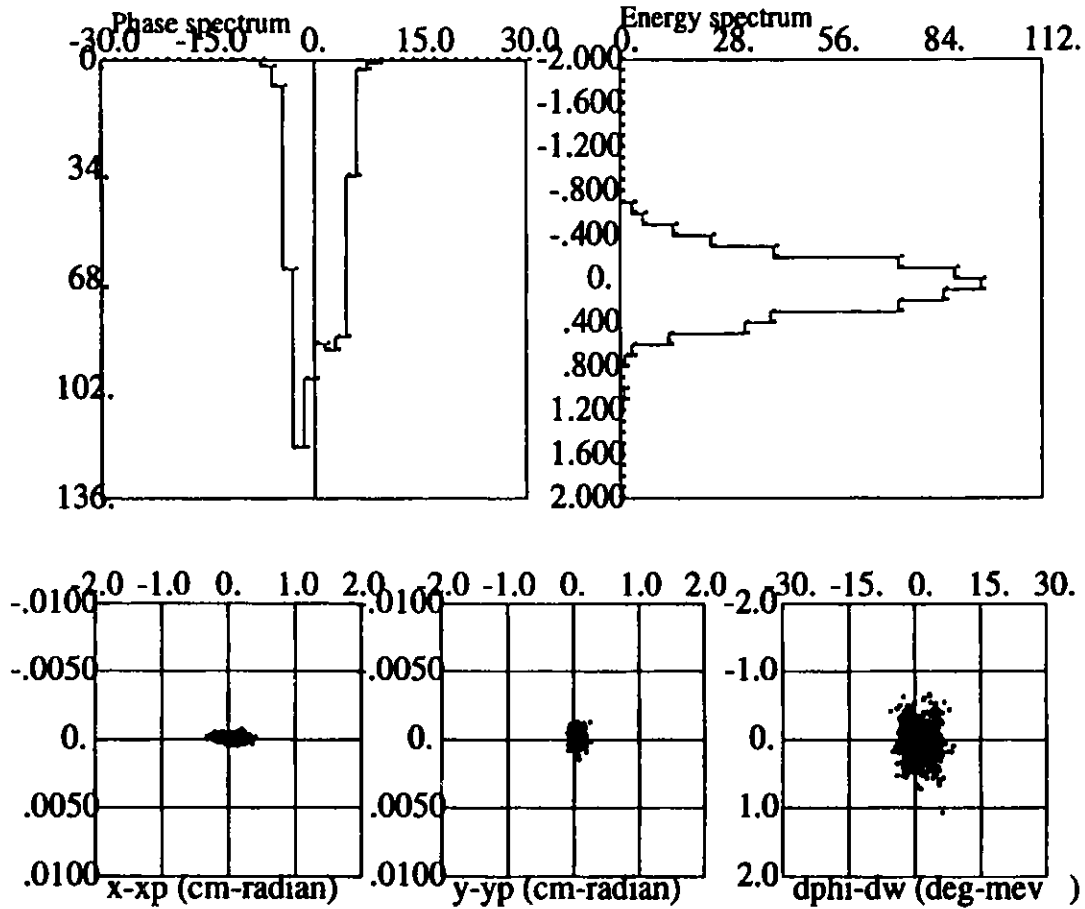
output phase-space projections at tank 60 ngood = 598

Figure III.3-9 Output Phase Space Projections at 400 MeV.

4.1 INTRODUCTION

This section describes the various subsystems of the linac. The actual designs presented are those most familiar to AccSys and ones that have been used successfully in several programs at the national laboratories. The first 70 MeV of the linac is based on the AccSys standard design for a high-duty-factor DTL, with the exceptions of the chopper and the higher current required from the H$^-$ ion source. The matching section and CCL are based on designs from LANL, Fermilab, and the SSC. Whenever possible, commercially available components have been used. When that has not been possible, components already developed at one of the national laboratories or other research centers have been used. For enhanced reliability, all components are designed for operation at a 3% system duty factor, although the linac operation is planned at a 1.6% system duty factor and a 1.5% beam duty factor.

4.2 LINAC SUBSYSTEMS

The linac consists of the following main subsystems:

- Linac injector subsystem (LIS) — The LIS includes the ion source, chopper, LEBT, RFQ, RGDTL, and also associated amplifiers, power supplies, and vacuum and cooling systems.

- Drift tube linac (DTL) — The DTL includes three accelerating tanks, with a total of 118 drift tubes. Each tank is made of several sections. Rf power is fed to each tank through a waveguide window mounted on the tank.

- Matching section (MS) — The MS includes two buncher tanks and 10 quadrupole focusing magnets.

- Coupled-cavity linac (CCL) — The CCL consists of 10 side-coupled-linac (SCL) modules, each with six tanks connected by bridge couplers. Each tank has 16 identical accelerating cavities. Rf power is fed to each module through a waveguide window into the center bridge coupler.

- Klystron/modulator systems — Three different klystron amplifier systems are used to power the linac. Three 4-MW (peak), 425-MHz klystrons are used to power the constant gradient DTL tanks. Two 1.0-MW (peak), 1,275-MHz klystrons are used for the buncher tanks in the matching section, and ten 9-MW (peak), 1,275-MHz klystrons power the CCL tanks. These klystrons and their modulators are located in the klystron gallery and are connected to the linac by transmission waveguide.

- Control system — The Experimental Physics and Industrial Control System (EPICS)[8] is used as the tool kit to design the front end control software. The hardware interface to the linac is done in VME and VXI.

4.3 LINAC INJECTOR SUBSYSTEM

The LIS is shown in Figure III.4.3-1. Its main components are described in this section.

4.3.1 H⁻ Ion Source

A cesium-enhanced volume ion source produces a 50-mA H⁻ beam at an energy of 35 keV. Alternatively, the ISIS H⁻ source can be used without further development.[1] Only the volume source is described.

The plasma in an rf-driven volume ion source is confined by a multicusp magnetic field produced by samarium cobalt magnets. The plasma chamber is 10 cm in diameter. Hydrogen plasma is produced by exciting an antenna coil inside the source. The coil is driven by a 70-kW peak rf power amplifier at a frequency of about 2 MHz. The hydrogen gas pressure in the ion source is controlled by a pulse-width-modulated gas control system synchronized to the linac repetition rate. The antenna coil is made of water-cooled copper tubing coated with a thin layer of porcelain to insulate the antenna from the plasma and to protect the copper tubing from plasma bombardment. A small heated tungsten filament, the igniter, provides electrons that allow plasma to ignite at lower pressures than would be possible with only the rf drive. This source has two of these igniters for redundancy.

NdFe permanent magnets in water-cooled tubes form a magnetic filter that divides the H⁻ ion source into two regions. A stainless steel insert defines the extraction aperture; it is mounted on the plasma electrode, along with a stainless steel collar. The collar projects back into the source to reduce the extracted electron current. Small cesium dispensers installed on the collar provide a thin cesium layer that enhances H⁻ production. The plasma electrode is isolated from the source so that it can be biased up to 10 V with respect to the source body. A cross section of the H⁻ ion source is shown in Figure III.4.3-2. The operating parameters are listed in Table III.4.3-1.

Three electrodes — the plasma electrode, extractor, and ground electrode — extract the beam from the ion source and accelerate it to 35 keV. These electrodes are as open as possible to minimize H⁻ stripping in the background gas. Injection energy and extraction voltage can be independently adjusted to optimize beam optics. A potential difference of 20 kV is applied between the plasma electrode and the extractor electrode to extract the beam from the source. Four permanent magnets in the electron dump create a double dipole field that bends extracted electrons into a graphite-lined cavity while deflecting the ions only slightly. A current transformer is mounted at the exit of the injector to measure current leaving the accelerating column.

POWER
SUPPLIES

TEMPERATURE
CONTROL UNIT

ROUGHING
PUMP
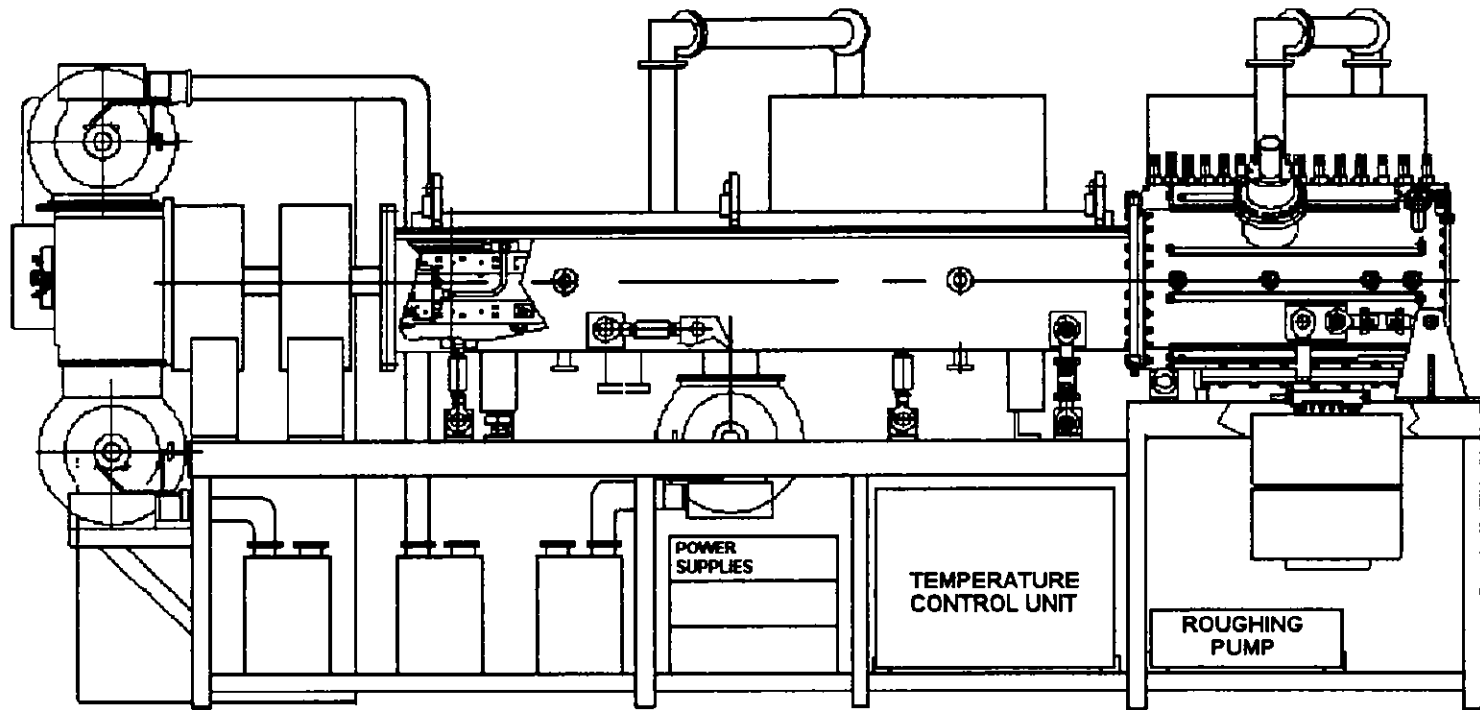
Figure III.4.3-1 Linac Injector Subsystem (LIS).
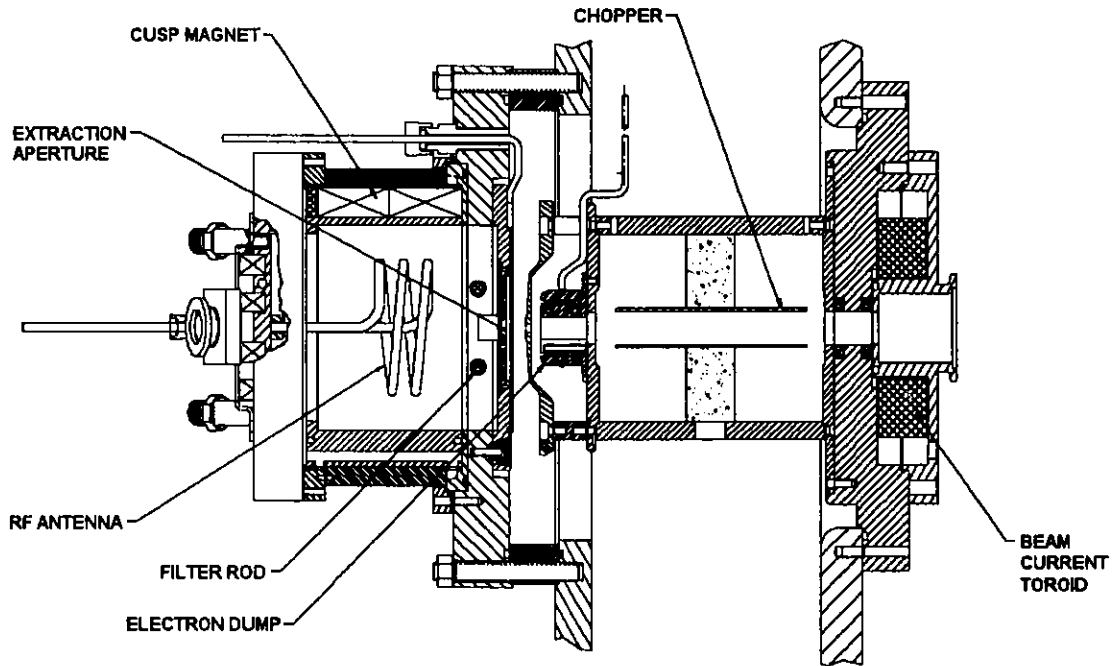
Figure III.4.3-2 H⁻ Ion Source.

Table III.4.3-1 Ion Source Operating Parameters

Parameters	Values	Units
Extraction voltage	35	kV
Extracted beam current	60	mA
Hydrogen gas flow	5 - 7	atm cm^3/min
Norm rms beam emittance[a]	0.01	π cm-mrad
Peak pulsed radio-frequency power	70	kW
ac input power	5	kW

[a] rms = root mean square.

4.3.2 Chopper

Injection into the RCS requires that the beam be chopped at about 1 MHz and that it be on 75% of the time. An electrostatic chopper located at the exit of the ion source is used to modulate the beam intensity in response to a timing signal from the synchrotron control system. An FET pulser drives the chopper.[9] A schematic diagram of the ion source electrical connections is shown in Figure III.4.3-3.

Chopping the beam has a deleterious effect on space charge compensation needed to transport a high-current H⁻ ion beam with minimal emittance growth.[10] A second magnetic double dipole, located at the exit of the injector just after the chopper, limits the extent of the perturbation. Effects still occur downstream, as the neutralization channel is displaced toward the direction of the beam deflection.

The chopper subsystem requires additional development.

4.3.3 Low-Energy Beam Transport (LEBT)

The beam transported from the injector is focused into the RFQ by using two large-bore solenoid lenses. There is space between these lenses for beam diagnostics.

4.3.4 Ion Source, Chopper, and LEBT Electronics

This electronics system includes the rf driver for the source, high- and low-voltage supplies for the ion source and associated systems, power supplies for the LEBT solenoids, and monitoring, control, and interlock circuits. A schematic of the rf and high-voltage circuits is shown in Figure III.4.3-3.

The electronics are housed in a standard cabinet that is grounded and interlocked. The cabinet contains a commercial 2-MHz rf driver and its power supplies. The driver provides up to 70 kW of pulsed power at 2 MHz. All components in this system are conservatively rated for long life and high reliability. The cabinet also contains power supplies and control and interface circuits. The ion source igniter and plasma electrode power supplies, valve driver, and instrumentation are isolated at 35 kV in the injector electronics rack. Power that is fed to the ion source is shielded to reduce transient coupling to other parts of the system. The injector electronics rack contains the 35-kV high-voltage power supply; the high-voltage isolation transformer; pulsing and timing controls; LEBT power supplies; and vacuum control and monitoring. The injector's electronics feature extensive transient protection.

The timing, monitoring, and control signals are transmitted through fiber-optic links.
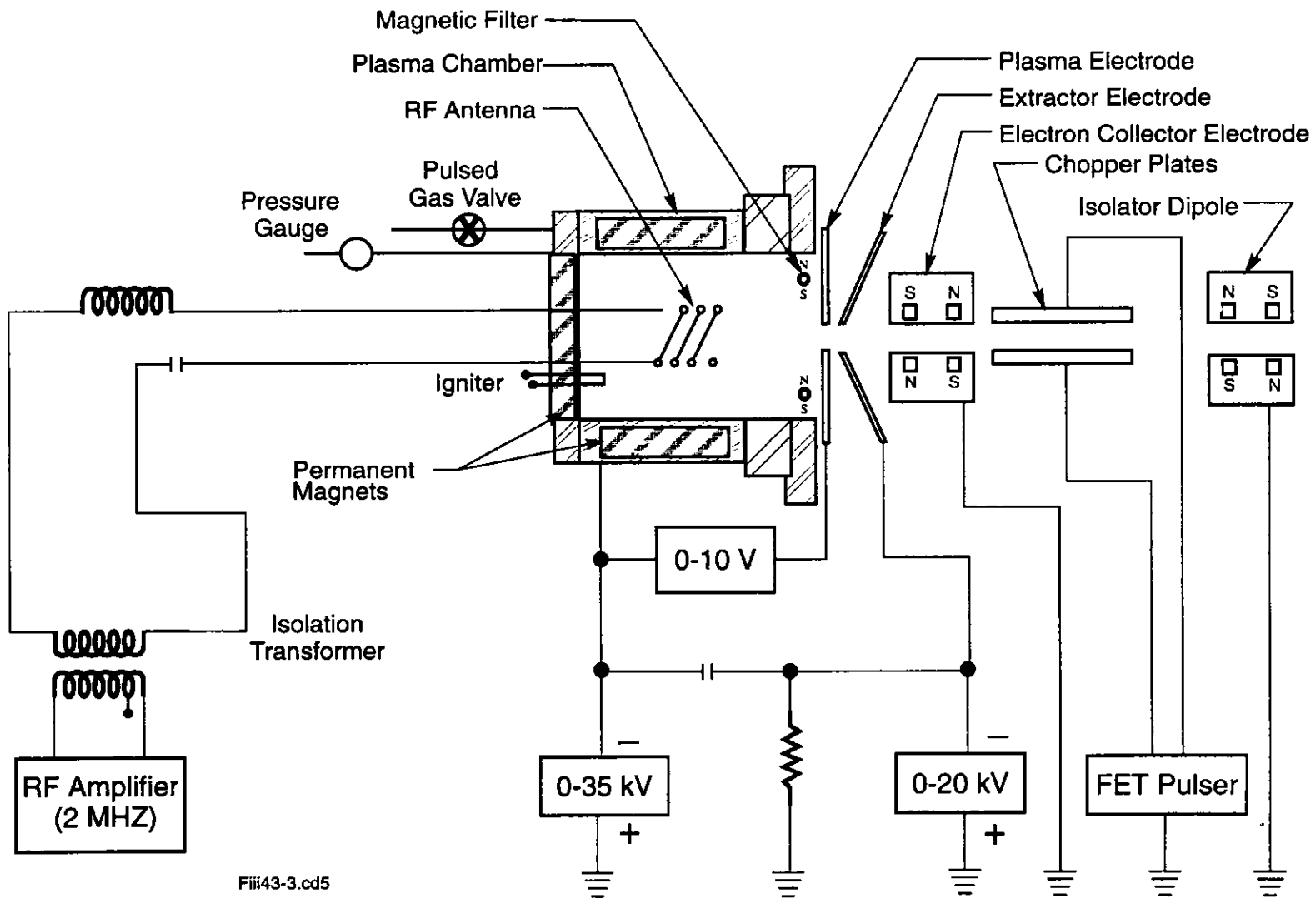
Fiii43-3.cd5

Figure III.4.3-3 Schematic of Ion Source Electrical Connections.

4.3.5   Radio-Frequency Quadrupole (RFQ)

The RFQ resonator has four identical vane sections, machined from aluminum extrusions and bolted to the resonator wall. The rf joint is independent of the vane mounting. This geometry minimizes the number of parts required and is rugged, easy to machine, and simple to assemble and tune. A continuous water cooling passage is provided along the vane at several locations, including one that is very near the narrow vane tip. These cooling channels allow the structure's temperature to be regulated to stabilize the resonant frequency, thereby eliminating the problem of differential expansion that results from the thermal isolation of two parts. A cross-sectional view of the RFQ is shown in Figure III.4.3-4.

The open geometry allows precise machining of the vane tips. Machining accuracy is readily checked before assembly by means of a coordinate measuring machine. Surfaces are precision-mated to ensure that the structure is accurately and reproducibly assembled without requiring critical adjustments. The mating surfaces are rigidly bolted together, thus minimizing the chance of relative movement of the pieces from vibration or thermal cycling. Because the RFQ is bolted together, it can be easily disassembled and reassembled to facilitate surface cleaning if it accidentally becomes contaminated during vacuum system servicing. The four vane tips can be initially located with enough accuracy to reduce the dipole fields to a level that they do not interfere with the main quadrupole accelerating field. Small tuners placed in openings along each quadrant and four rod tuners in each end wall are used to fine-tune the field components and resonant frequency. The thermal and mechanical stability of this RFQ has been demonstrated on a system at LANL. The RFQ operated at the design field for several months at a high duty factor.[11] The parameters of the RFQ are given in Table III.4.3-2, and a photograph is shown in Figure III.4.3-5.

The entire RFQ is placed in a vacuum chamber with vacuum feedthroughs for the rf drive loop, water cooling, and rf pick-up loops. This configuration decouples the rf and vacuum seals. The rigid vacuum system preserves internal alignment of the RFQ. A simple cylindrical vacuum chamber with a hinged cover provides easy access to the RFQ for alignment of the structure. This strategy, which provides more effective pumping than traditional designs in which the RFQ serves as the vacuum enclosure, speeds up conditioning and minimizes beam loss.

Resonant frequency control during operation is achieved by use of servo-driven tuning slugs with a range of ± 100 kHz. A single 3-1/8-in. coaxial drive loop couples the rf power into the RFQ at an operating frequency of 425 MHz.

4.3.6 Ramped-Gradient Drift Tube Linac (RGDTL)

The first tank immediately following the RFQ is the RGDTL, which is a short matching drift tube linac tank. The field in the RGDTL gaps is ramped to match the focal properties of the RFQ to the focal properties of the DTL. Closely coupling the RGDTL to the RFQ eliminates
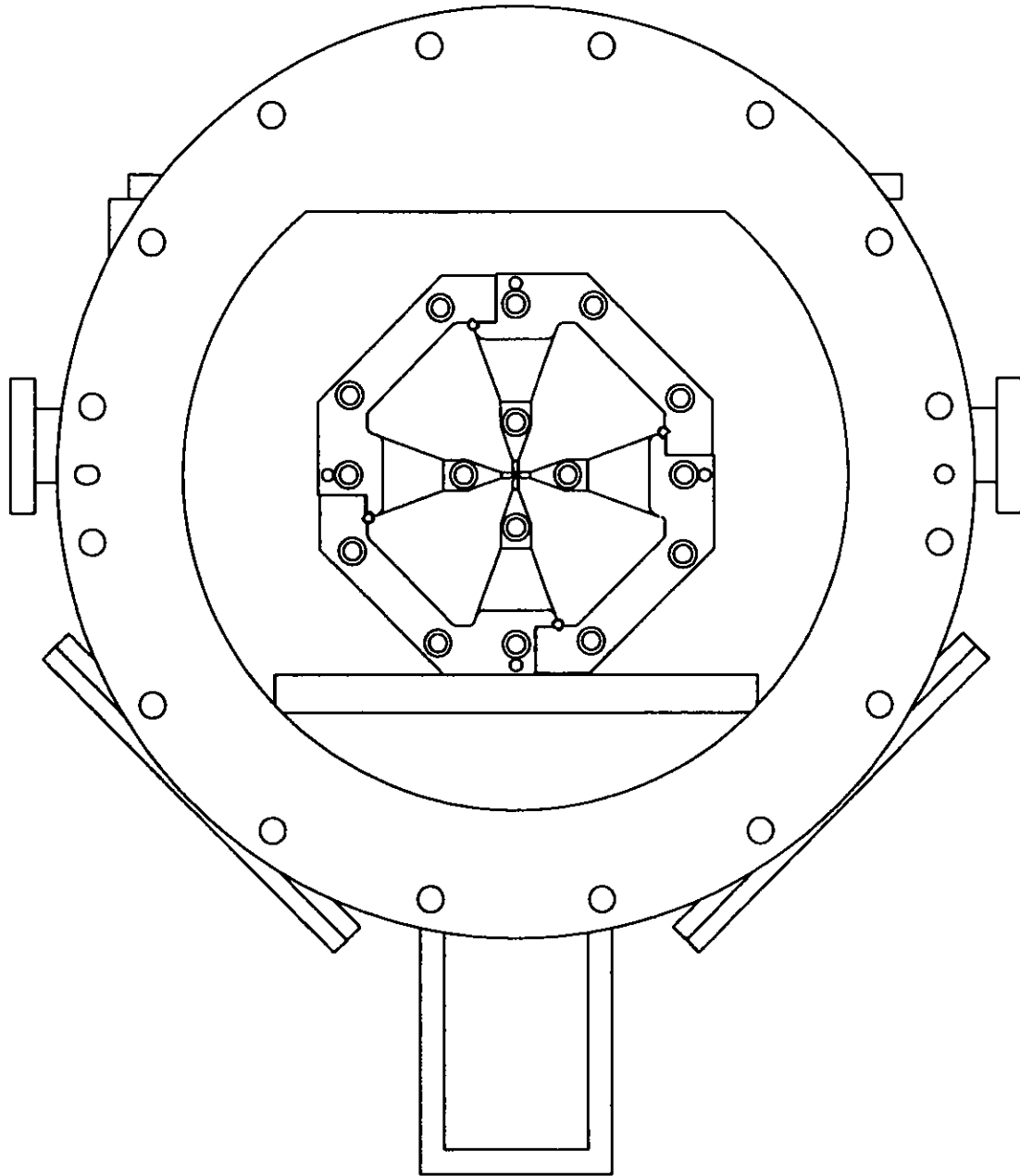
Figure III.4.3-4 Cross-Sectional View of the RFQ.

Table III.4.3-2 Main RFQ Parameters

Parameters	Values	Units
Operating frequency	425	MHz
Injection energy	35	keV
Final energy	2	MeV
Design input current	50	mA
Current limit	100	mA
Transmission	87	%
Input transverse emittance (normalized, rms)[a]	0.010	π cm-mrad
Output transverse emittance (normalized, rms)	0.012	π cm-mrad
Vane tip radius (ρ)	1.8 - 2.7	mm
Bore radius (r_o)	2.4 - 3.0	mm
Peak radio-frequency field	36 MV/m	$(1.8 \times E_{kp})$
Structure length	2.16	m
Peak structure power	220	kW
Peak beam power	80	kW
Peak radio-frequency input power	300	kW
Average structure power	6.8	kW
Coolant flow	25	gal/min

[a] rms = root mean square.
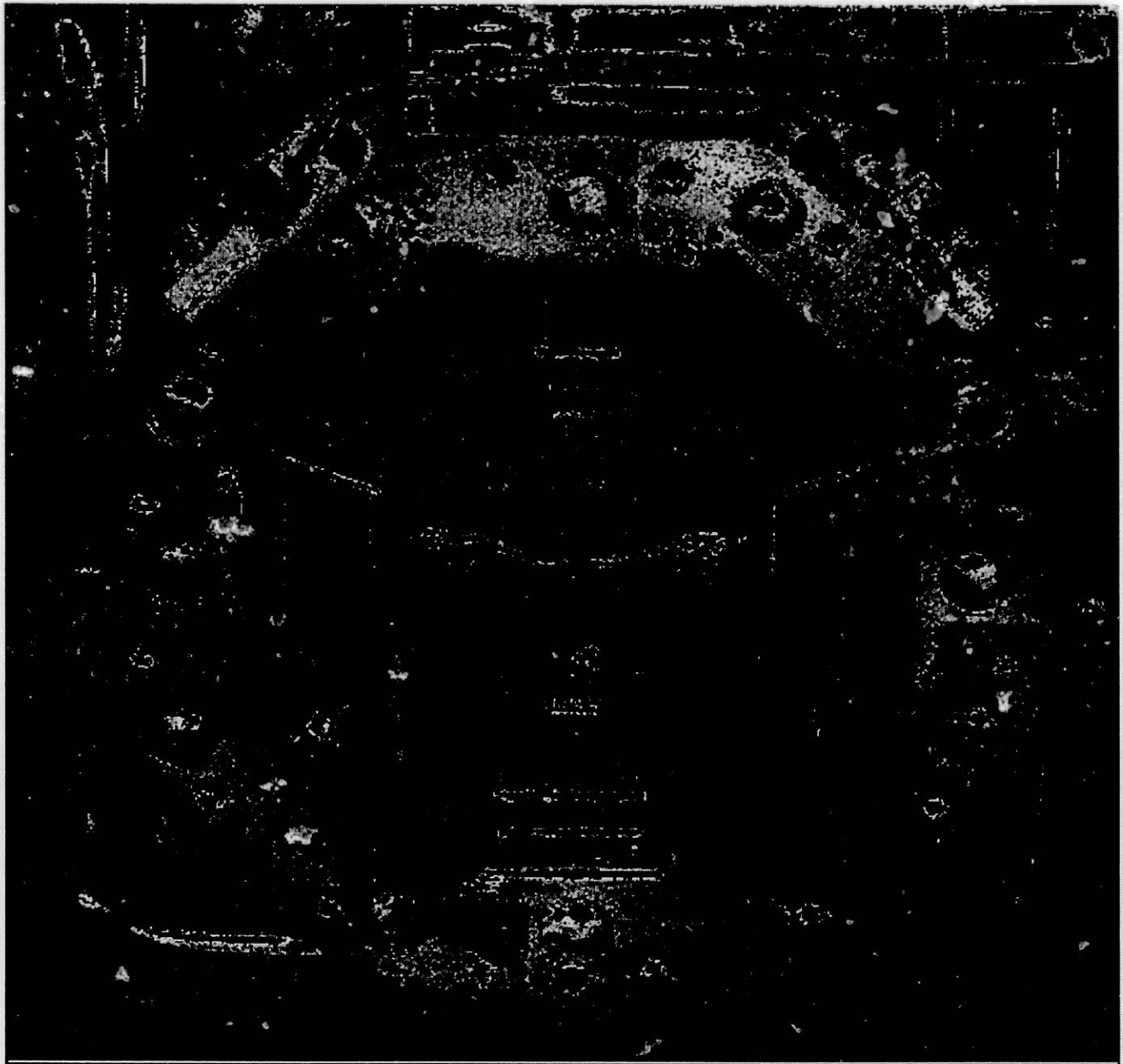
Figure III.4.3-5 Photograph of the RFQ.

the need for a complex beam-matching section. Parameters of this tank are listed in Table III.4.3-3. The mechanical design of the RGDTL tank is described in Section III.4.4, along with the rest of the DTL.

4.3.7 Radio-Frequency System for the RFQ and RGDTL

The RFQ and the RGDTL tanks are driven by commercial, modular rf power systems with wide-bandwidth amplitude and phase control. These amplifiers use 12 YU-176 planar-triode tubes in a parallel self-balancing array as the final power stage. Special circuits eliminate the need to match tube characteristics to ensure equal power contributions.[11] The YU-176 has large-area oxide-coated cathodes for efficient and reliable pulse operation. The peak power output is more than 1 kW per watt of heater power. Standard design features include load fault protection and dynamic amplitude and phase control to within $\pm 0.5\%$ and $\pm 0.5°$, respectively, with less than 3.0-μsec response time. The RFQ and RGDTL amplifiers operate at 425 MHz, with a peak power output of 360 kW.

Figure III.4.3-6 is a block diagram of the rf power amplifier system. Amplitude and frequency feedback control systems are provided. The driver amplifier is a solid-state unit capable of supplying 150 W at a 100% duty factor with an input drive power of 10 mW. The intermediate power amplifier stages are tuned amplifiers. The first stage (IPA1) uses a single YU-176 tube and provides a 3.0-kW drive to the second stage. The second stage (IPA2) has two YU-176 triodes in parallel and provides 30-kW output. Both stages are conservatively designed so they are not stressed in high-duty-factor operation. All of the control and tube protection circuits have been successfully implemented, and the tube output and cooling have been demonstrated at a 3% duty factor.[12]

The amplifier stages are operated Class-C for stability at high gain with a pulsed rf drive. The tubes are protected by electronic crowbar circuits that limit the fault energy dissipated in a tube to a safe value. These systems are specifically designed for operation with a high-Q resonant-cavity load, such as an rf linear accelerator. The amplifier, transmission line, and resonant cavity load are tuned together for maximum performance. The tuned output circuit handles the high turn-on and turn-off VSWR without requiring expensive rf power isolators. Each system can handle the large dynamic change in load impedance that occurs in an accelerator when the beam is turned on and off.

The built-in amplitude, phase, and frequency control loops respond rapidly to changes in the load cavity fields. The output stage bandwidth is greater than 20 MHz. The amplitude control loop uses high-level cathode modulation of the power amplifier stage for fast response. The systems are high gain, requiring only 150-mW CW drive power, simplifying the distribution of the rf source power in multiple unit systems. The units are fully interlocked for personnel and equipment protection and fully shielded from electromagnetic interference (EMI).

Table III.4.3-3 RGDTL Parameters

Parameters	Values	Units
Operating frequency	425	MHz
Input beam energy	2	MeV
Output beam energy	4.2	MeV
Length	0.9	m
Number of drift tubes	16	-
Aperture radius	0.5	cm
Electric field gradient	2.4 - 4.2	MV/m
PMQ[a] gradient	180	T/m
Peak structure power	165	kW
Peak beam power at 40 mA	89	kW
Total peak radio-frequency power	254	kW
Average structure dissipation	5	kW
Cooling water flow	20	gal/min

[a] PMQ = permanent magnet quadrupole.

AC In

Ctrl In — Control & Interlock Chassis

Driver Power Supply

IPA1 Power Supply

IPA2 Power Supply

FPA Power Supply

Energy Storage Chassis

RF In — 0.01 W — Buffer Amplifier — 0.15 W — Driver Amplifier — 150 W — IPA1 — 30 kW — IPA2 — Final Power Amplifier — 360 kW — **RF Out**

Solid State

YU-176

2 x YU-176

12 x YU-176

Modulator (Bias & Heater Supply)

Amplitude Control
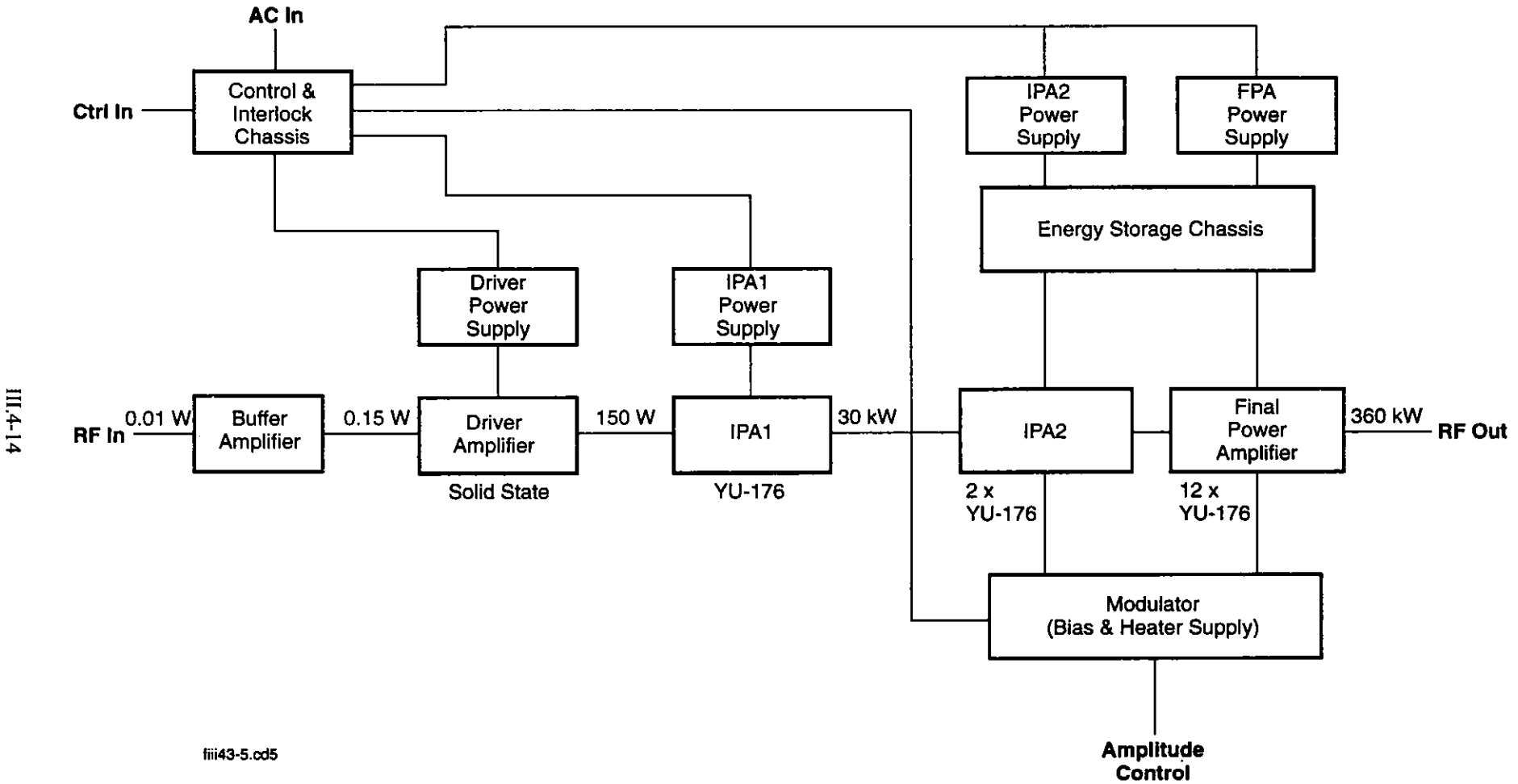
fiii43-5.cd5

Figure III.4.3-6 Planar Triode rf Amplifier Schematic.

4.3.8 Vacuum and Auxiliary Systems

The ion injector has its own vacuum system, with an isolation valve for routine source maintenance. This system uses two 2,200-L/sec turbomolecular pumps to handle the high hydrogen gas load from the H⁻ source. The vacuum is sufficient to prevent any sparking in the extraction gap and to reduce stripping losses. A vacuum gauge unit that uses two ion gauges and two thermocouple gauges monitors the pressure in the injector, beamline, and roughing lines. This unit provides local indication of pressure readings on its front panel, and it sends this information to the control system. The pressure in the injector vacuum chamber is typically 2 to 3×10^{-5} Torr during operation.

A 2,200-L/sec turbomolecular pump mounted on the RFQ vacuum chamber maintains a 3×10^{-7} Torr in the RFQ resonator. The restricted openings at the exit of the ion source mounting chamber and the entrance to the RFQ limit the gas flow between the ion source and the RFQ. The RGDTL uses a 500-L/sec ion pump to maintain a pressure of less than 1×10^{-7} Torr. Some differential pumping of the RFQ is provided through the small bore of the half-drift-tube end of the RGDTL. Ion gauges are used to monitor the vacuum in both tanks.

A single commercial, packaged temperature controller with ±1°C stability is used to maintain stable temperature for both the RFQ and the RGDTL. It is installed on the LIS support frame.

4.4 DRIFT TUBE LINAC

4.4.1 Overview

Three DTL tanks are used to accelerate the beam to 70 MeV. They are constant gradient tanks with one ßλ spacing. Permanent-magnet quadrupoles (PMQs) installed in each drift tube focus the beam through the structure and maintain beam emittance. The size of the beam aperture in the drift tubes is gradually increased along the DTL to minimize beam loss. Each gradient tank is powered by a 4-MW-peak, 425-MHz klystron. Major parameters of the DTL tanks are shown in Table III.4.4-1.

The final operating frequency is achieved by using a hierarchy of tuning mechanisms. Tuning bars with a range of ±2 MHz are used for coarse-tuning of frequency during initial setup. Servo-driven tuning slugs with a range of ±200 kHz are used for fine-tuning during operation. In addition, the tank operating temperature can be varied to control the frequency over a range of ±15 kHz.

A side view of a typical DTL tank is shown in Figure III.4.4-1, a cross-sectional view is shown in Figure III.4.4-2, and a photograph is shown in Figure III.4.4-3. The main components are the (1) rf and vacuum vessel, (2) drift tubes and post-stabilizer assemblies, (3) integral vacuum and cooling systems, and (4) support stand. Each of these components is described in the following subsections.

Table III.4.4-1 DTL Parameters

Parameters	Tank 1	Tank 2	Tank 3	Units
Operating frequency	425	425	425	MHz
Input beam energy	4.2	28.7	50.1	MeV
Output beam energy	28.7	50.1	70	MeV
Length	7.14	6.27	6.23	m
Number of drift tubes	60	32	26	-
Aperture radius	5 - 7	8	9	mm
Accelerating field gradient	4.39	4.63	4.60	MV/m
PMQ[a] gradient	173 - 105	100	95	T/m
Peak structure power	2.1	2.02	2.0	MW
Peak beam power at 40 mA	0.98	0.86	0.8	MW
Total peak radio-frequency power	3.1	2.9	2.8	MW
Average structure dissipation	63	61	60	kW
Cavity fill time	35	35	35	μsec

[a] PMQ = permanent magnet quadrupole.
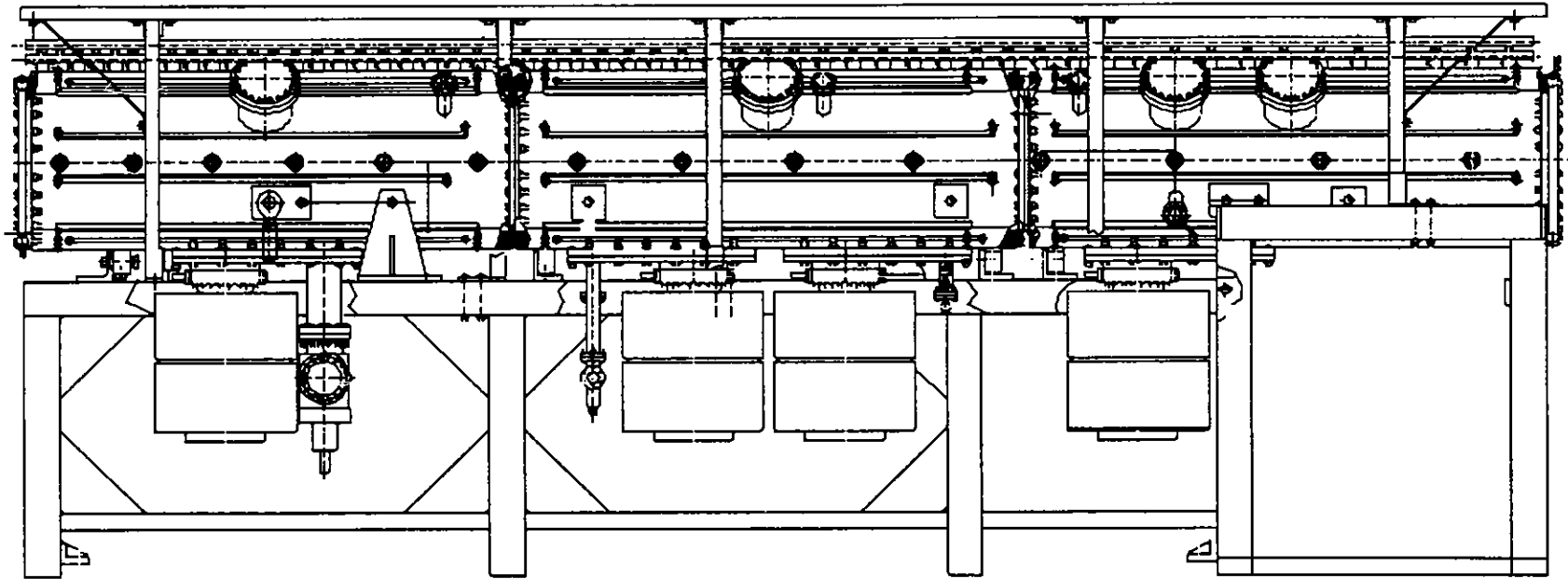
Figure III.4.4-1 Side View of a Typical DTL Tank.
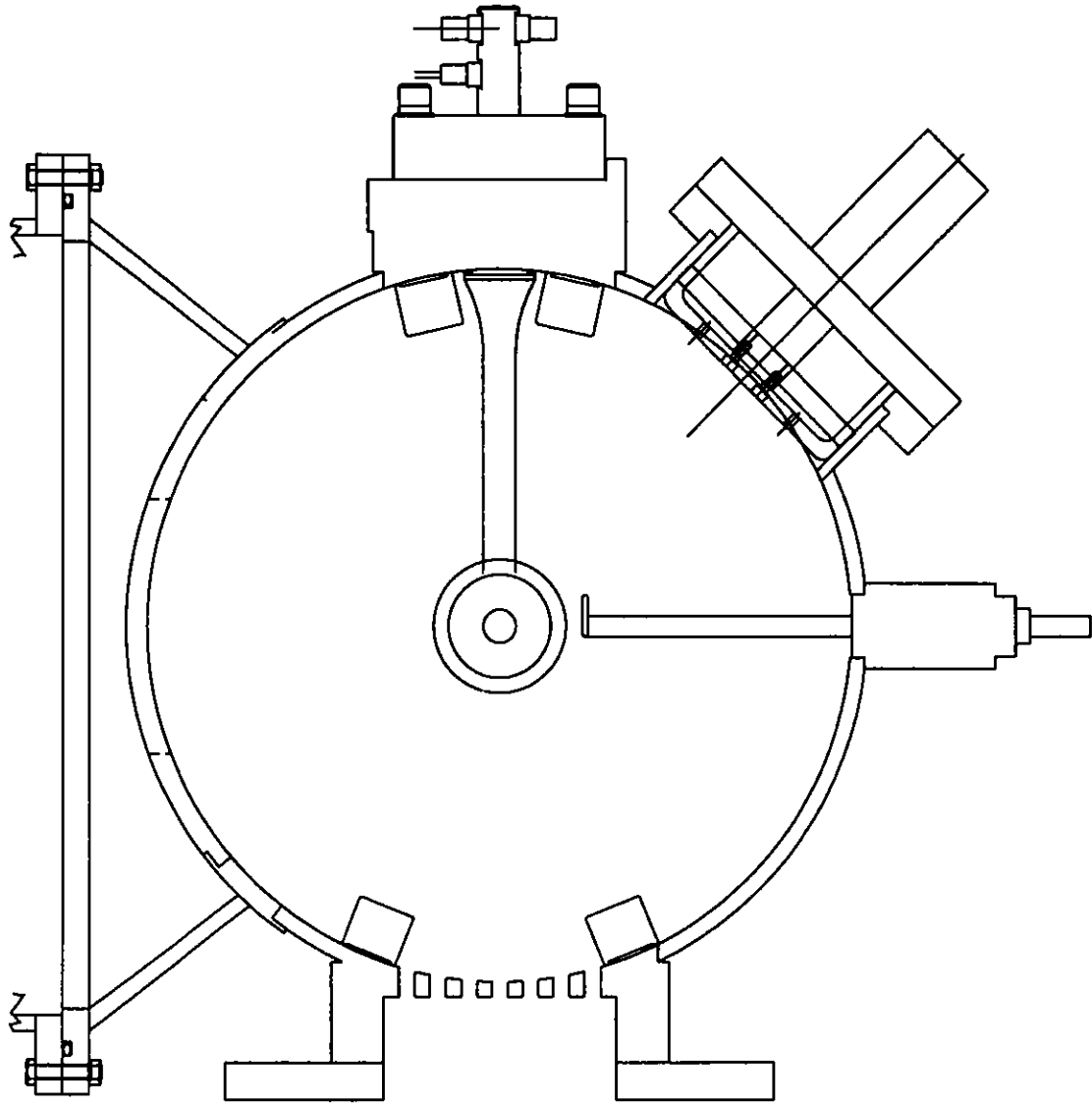
Figure III.4.4-2 Cross Section of a Typical DTL Tank.
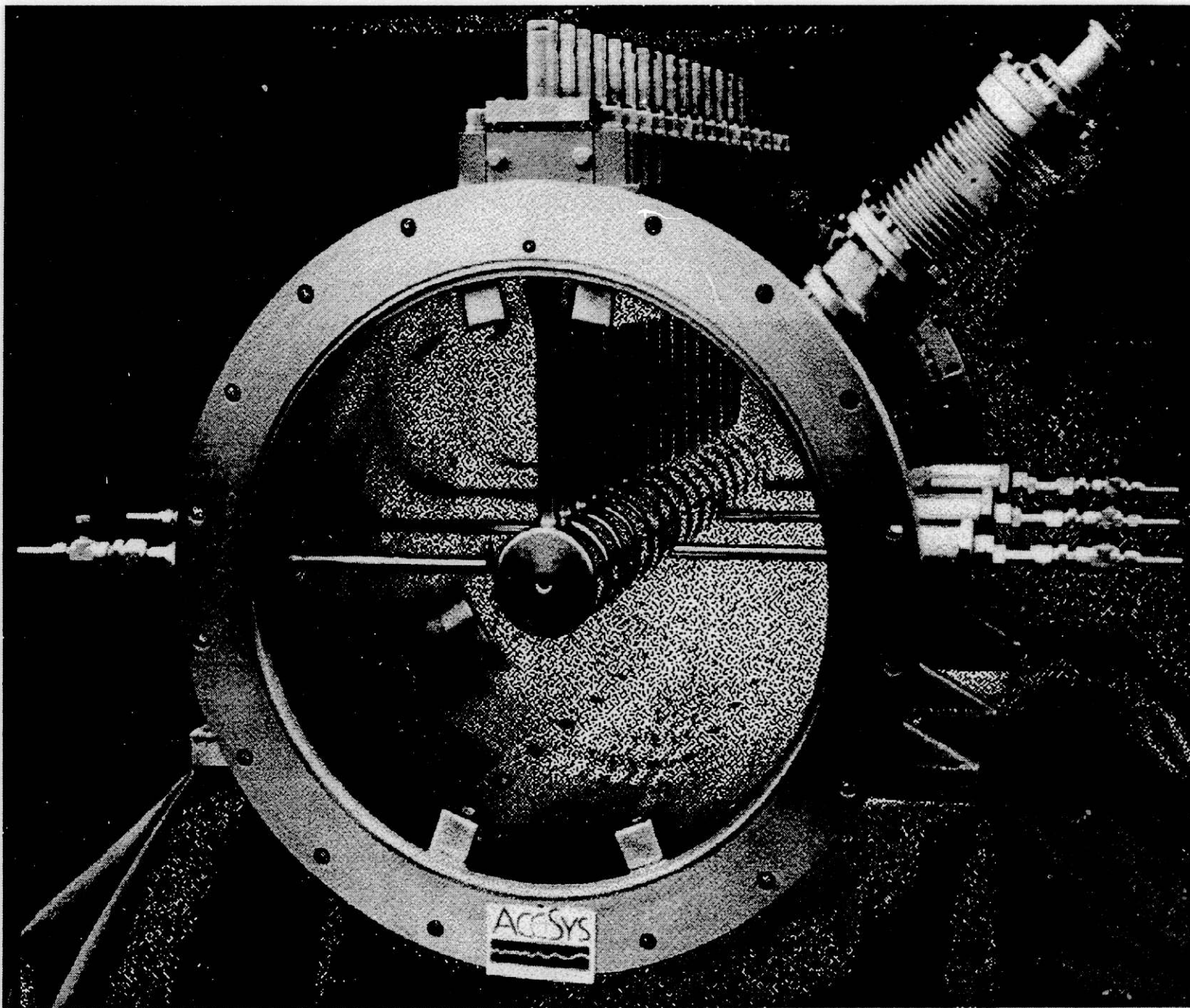
Figure III.4.4-3 Photograph of the Cross Section of a Typical DTL Tank.

4.4.2 Radio-Frequency and Vacuum Vessel

Each tank is made in several sections for ease of handling and fabrication. The number of sections depends on the total length. These sections are made of steel for easy fabrication and are copper-plated for high conductivity. Each section is designed for maximum mechanical stability and consists of two rails, an upper and a lower, joined together by welding two circular wall sections between them. The upper rail supports the drift tubes as well as two tuning bars used for coarse frequency adjustments. Supporting the drift tubes on a rail that is integral to the main vessel eliminates the need for a large and difficult rf and vacuum joint. The bottom rail increases structural stability while providing a mounting surface for additional tuning bars and vacuum pumps. The post-stabilizer mounts, slug tuner ports, and other vacuum penetrations are welded directly to the walls of the tank. Cooling channels brazed to the outer wall remove energy dissipated in the tank by the rf fields.

The twin-rail design provides exceptional long-term dimensional stability. The tank is stress-relieved before plating and final machining to ensure that the drift tubes remain accurately aligned after installation. This design also simplifies fabrication by eliminating the need to accurately roll up a cylinder to the required inside diameter. The DTL tanks are separated by a short drift space to allow insertion of beam diagnostic instruments and magnetic optics correction magnets.

4.4.3 Drift Tubes and Post-Stabilizer Assemblies

The drift tube stems are made of stainless steel for strength and rigidity. They are copper-plated and brazed into the drift tube bodies. Compact permanent-magnet quadrupoles in the drift tubes maintain transverse beam focusing. Each copper drift tube is sealed to make it a vacuum-tight enclosure. The drift tube rf surfaces are made from two copper shells that fit closely over the drift tube body and are electron-beam-welded to a copper ring. The drift tube bodies have internal cooling channels that are fed through the stem. The cooling channels are also sealed separately within the drift tubes.

The drift tubes are mounted to adjustable sockets on the upper rail and are rigidly aligned with little residual stress. Accurate positioning of the drift tubes is accomplished by using shims between reference surfaces on the drift tube stem and the support rail. This procedure provides precise incremental adjustment with long-term stability, eliminates expensive adjusting apparatus that is used only once in the life of the DTL, and allows the drift tubes to be removed and accurately reinstalled. It has been demonstrated that drift tube assemblies can be removed and reinstalled to less than ±0.013 mm of their initial position.[13]

Resonant post-stabilizers are used to stabilize and fine-tune the on-axis electric field distribution of the DTL. The post-stabilizers greatly relax the tolerances on the drift tube dimensions and alignment. They also eliminate the need for continuous critical adjustment of rf tuners to maintain the field distribution during operation. The post-stabilizers are in an adjustable mount that allows precise movement of the posts during tuning. The post-stabilizer

mounting scheme allows accurate adjustment with a removable, reusable adjuster apparatus. The post-stabilizers are permanently locked into position after adjustment. The adjustment is made by using the tilt-sensitivity method developed at LANL for tuning the 100-MeV DTL tanks of its Meson Physics Facility accelerator.[14] These adjustments are independent of the rf and vacuum seals, thereby allowing the required electric field distribution to be easily achieved. A coaxial cooling channel removes heat generated by rf fields.

This approach to designing and positioning drift tubes and post-stabilizers meets the key performance objectives of high beam transmission and optimal electric field distribution. It results in an operation that is accurate and stable for many years.

4.4.4 Vacuum and Cooling

The DTL tanks are maintained at a vacuum of 1×10^{-7} Torr by 500-L/sec ion pumps connected to a port at the bottom of each section. Metal vacuum seals provide long-term reliability and radiation resistance.

A closed-cycle cooling system maintains the DTL's operating temperature. Temperature is stabilized in the tank by supplying temperature-controlled water through channels on the outside of the tank walls as well as through the drift tube assemblies and post-stabilizers. Individual commercial units are used for each tank.

4.4.5 Support Stand

The stand that supports the DTL is a weldment of square steel box beams. The weight of each tank rests on four adjustable supports. The DTL tank is supported on six adjustable struts for precise alignment.

Room underneath the tanks is sufficient to allow easy removal of the vacuum pumps. The frame also supports the cooling water manifold.

4.5 MATCHING SECTION

4.5.1 Introduction

The beam from the DTL is bunched at 425 MHz and is matched into the CCL that operates at 1,275 MHz. The matching section transforms the beam from the DTL into the phase space volume required by the CCL. Two buncher cavities — short sections of side-coupled cavities that operate at 1,275 MHz — and 10 quadrupole magnets are used to achieve this match. Matching section parameters are listed in Table III.4.5-1.

Table III.4.5-1 Matching Section Parameters

Parameters	Values	Units
Length	3.2	m
Buncher type	SCL cavities	-
Number of bunchers	2	-
Buncher frequency	1,275	MHz
Number of cells per buncher	5 and 7	-
Power required	500 and 700	kW
Number of quadrupole doublets	3	-
Number of quadrupole singlets	4	-
Quadrupole gradient	40	T/m
Quadrupole bore	23	mm
Quadrupole length	40	mm
Cavity fill time	10	μsec

4.6 COUPLED-CAVITY LINAC

4.6.1 Overview

The CCL consists of 60 side-coupled-cavity tanks with 16 accelerating cavities per tank. There are 10 modules, each of which consists of six tanks and five bridge couplers. The tanks increase in length as beam energy increases. There are no bridge couplers between modules. Rf power is fed to each module by a WR650 waveguide connected to the center bridge coupler. The main parameters of the CCL are listed in Table III.4.6-1. A side view of three tanks and two bridge couplers is shown in Figure III.4.6-1.

4.6.2 Radio-Frequency Structure Fabrication

Half-cavities of the 1,275-MHz rf structures are machined from bar stock. The half cavities and cavity subassemblies are made with steps and matching counterbores to maintain alignment during brazing. The coupling cavities are also machined from solid stock and brazed together to form a subassembly. The post-stabilized bridge couplers consist of a cylinder with discs and end-cells brazed in place. They are equipped with lifting eyes at each end. The bridge couplers are connected to the tanks by means of rectangular brazed flanges. These flanges and their associated seals provide both an rf and a vacuum joint. The same type of flange and rectangular vacuum seal are used for all of the CCL tanks and bridge couplers.

Integral cooling water passages, machined into the half-cavities before brazing, allow effective frequency stabilization of the rf structure. Integral water passages are used in order to achieve superior thermal performance, simpler construction, and lower cost.

Slots are milled into the side walls of the tank and bridge coupler cavities to permit fine-tuning by dimpling the copper at the bottom of the slot. A vacuum nipple is brazed into each tank coupling cavity to allow access to the internal coupling cavity posts for tank tuning. The upper vacuum ports are capped; the lower ports are connected to the vacuum manifold by a bellows. A standard Conflat vacuum flange is brazed into the end of each tank for the inlet and outlet beamline.

The braze joint designs are important factors in the CCL tank fabrication process. The cavities are brazed by using washers of braze alloy to ensure complete joint wetting. The different alloys used for step-brazing the cavity components are selected because of their melting temperature, conductivity, braze reliability, and cost. Allowance is made for the braze alloy thickness remaining after brazing. Oxygen-free, high-conductivity (OFHC) copper is used for the accelerating and coupling cavities because of its high electrical conductivity and compatibility with brazing processes. The time-temperature profile of the brazing process is controlled and monitored to ensure good dimensional control and leak-tight joints.

Table III.4.6-1 CCL Parameters

Parameters	Values	Units
Frequency	1,275	MHz
Input energy	70	MeV
Output energy	400	MeV
Number of modules	10	-
Number of tanks per module	6	-
Number of cavities per tank	16	-
Peak surface field	28	MV/m
Field gradient (E_oT)	5.9 - 5.5	MV/m
Synchronous phase	−30 to −25	deg
Peak structure power	52.8	MW
Peak beam power at 40 mA	13.2	MW
Total peak radio-frequency power	66.0	MW
Magnet lattice	FODO	-
Length	92.1	m
Bore radius	≥10	mm
First-neighbor coupling constant	5	%
Intertank and intermodule spacing	3.5	$\beta\lambda$
Number of bridge couplers	50	
Bridge coupler coupling constant	10	%
Cavity fill time	10	μsec
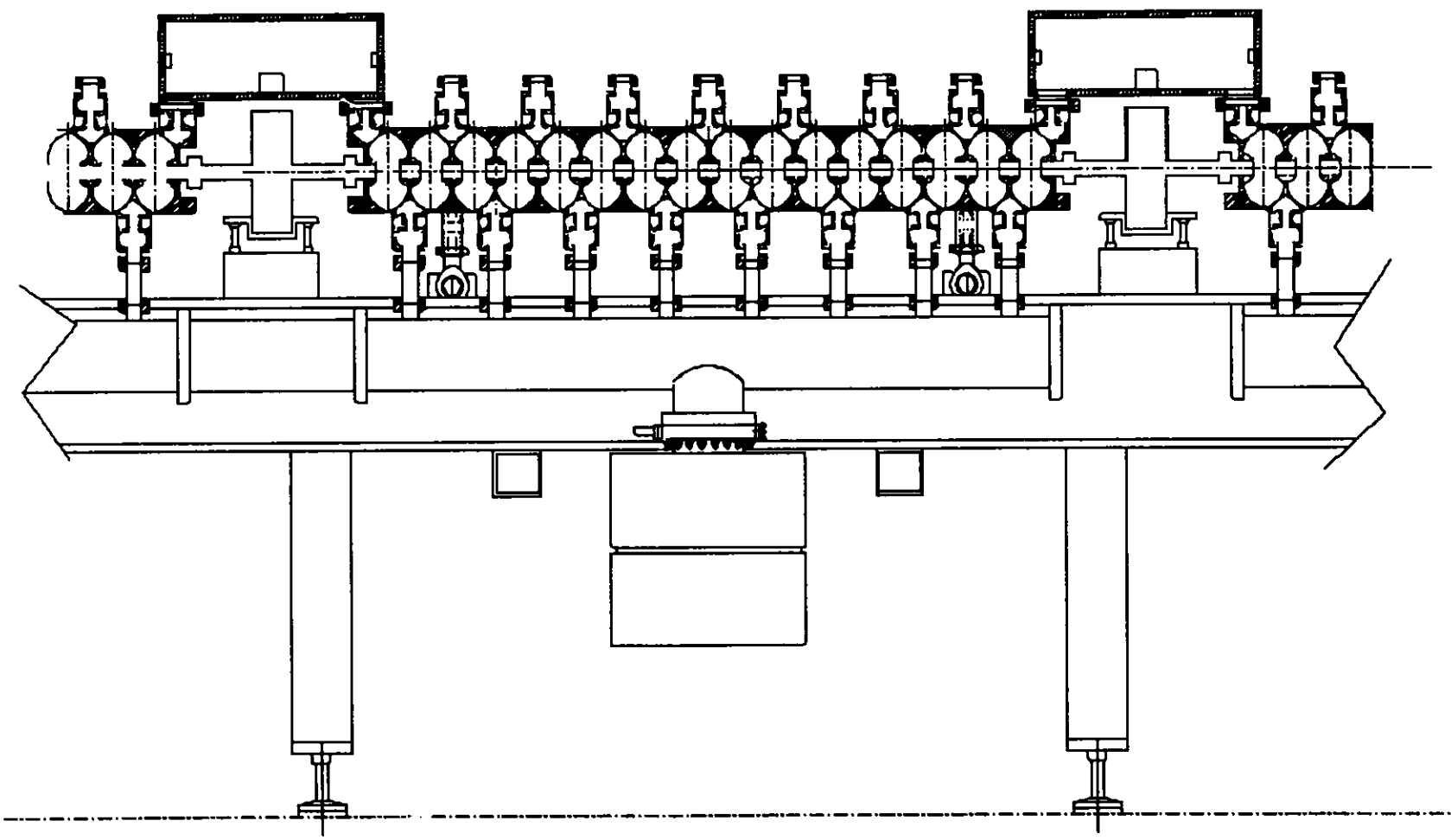
Figure III.4 1 Side View of CCL with Vacuum Manifold and Bridge Couplers.

Four alignment target holders are mounted on the access aisle side of each tank. Steel-ball alignment targets are used to align the linac beam line to the required tolerance. There is a clear line of sight from the CCL alignment monuments to the floor monuments.

4.6.3 Support Systems and Mechanical Design Features

The rf structure is supported by a series of six-strut support systems mounted on steel support stands. Each stand supports six tanks, five bridge couplers, a vacuum manifold, and associated water manifolding, as shown in Figure III.4.6-2. The intertank quadrupole magnet and diagnostics are also mounted on the support stand. Temporary legs and casters are mounted to the support stand to facilitate handling in the tuning area and linac tunnel. The stand — with its tanks, bridge couplers, and associated equipment — is lowered into the tunnel, wheeled into place, and installed. Then the temporary supports and casters are removed, and the stand is bolted to the tunnel floor. Adjustable legs allow rough alignment to the beamline, and fine adjustments are made with the six-strut support system.

The six-strut support system includes three vertical, one axial, and two horizontal struts. These six struts form an optimally constrained system. Each strut consists of a threaded body and two differentially threaded spherical rod ends. One full turn of the body changes the length of the strut by 1.06 mm. The spherical strut joints allow the structure to expand and contract without binding or warping.

Individual tanks are supported on ledges machined into the tank support brackets. The brackets are bolted to threaded inserts in the tank walls. After a tank is bolted to a bracket, the bracket and tank are match-drilled for dowel pins. The tank support brackets, which are the attachment points for the six-strut support system, are fitted with lifting eyes. The longitudinal struts are located in the center of each module. A bellows is included with the intermodule diagnostics and beam steering to allow for longitudinal expansion and contraction.

The CCL tanks and bridge couplers are frequency-stabilized by pumping temperature-contolled water through the cavity water passages. A temperature sensor located at each end of a tank senses the rf structure temperature and sends a signal to the temperature control unit (TCU). Stainless steel water manifolds distribute the cooling water to the rf structure. One TCU is used per CCL module to control the cavity temperature within ±0.1°C.

4.6.4 Vacuum System

Attached to each CCL tank assembly are a vacuum manifold section and a 500-L/sec ion pump. The vacuum manifolds are bolted together during assembly to form a common vacuum manifold. The manifold is connected to the CCL tanks by demountable joints and bellows. The bellows allow for some misalignment between the manifold and the tanks and accommodate
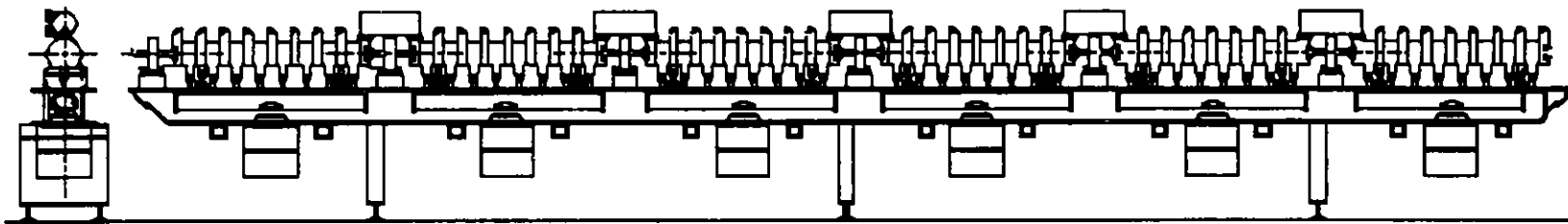
Figure III.4.6-2 Assembly View of CCL with Support Stand.

differential expansion and contraction. A gate valve between modules allows a module to be serviced without loss of vacuum in the rest of the linac beamline. Typical vacuum pressure is less than 1×10^{-7} Torr.

4.7 KLYSTRON POWER SYSTEMS

4.7.1 Overview

The three large DTL tanks, matching section bunchers, and CCL are powered by klystrons driven by modulator systems containing the dc power supply, power switching tubes, and energy storage components. Table III.4.7-1 lists the operating parameters common to all these systems, and Table III.4.7-2 lists specific parameters for the different linac sections. The pulse width can be varied to allow for easier conditioning of the accelerator cavities.

The nominal VSWR is 1.6 with the CCL filled but no beam current. The klystron window is located at a point in the waveguide that is near the null position of the standing wave under these conditions. The VSWR decreases to a value of 1.1 at full beam current because of beam loading. The rf drive level is controlled to maintain a constant field level in the load cavity regardless of beam current.

4.7.2 Klystrons

Three different klystrons manufactured by Varian are used as the basis for estimating cost of the linac. A sixth cavity in the Varian tubes increases the rf conversion efficiency from less than 50% to an estimated 63%. This ensures that a high rf efficiency is achieved. Table III.4.7-3 lists the operating parameters of the selected klystrons.

Circulators are installed on all of the klystrons to protect them from high reflected power during cavity arcs and conditioning. Three-port circulators with a single load are used to protect the 425-MHz klystrons. Four-port circulators with two loads are used to protect the 1,275-MHz klystrons.

The circulators and loads handle reflected power under four conditions: normal operating mode, cavity filling, conditioning, and cavity arcs. During cavity filling, there is a triangular spike of reflected power with an amplitude that is about half of the amplitude of the forward power. The total pulse duration is about a quarter of the cavity fill time. The fill time is 35 μsec for the DTL and 10 μsec for the matching section and CCL. The cavity coupling is adjusted so that with full beam current, the VSWR is < 1.1. During conditioning, the nominal VSWR with the load cavity filled and no beam current is 1.6. The full power from the klystron is reflected during an arc. This condition persists until the klystron is crowbarred within 10 μsec.

Table III.4.7-1 Klystron Operating Parameters Common to the Entire Injector

Parameters	Maximum	Minimum	Nominal	Units
Radio-frequency duty factor	3	0.1	1.5	%
Pulse width - DTL	550	100	535	μsec
Pulse width - CCL	550	100	510	μsec
Pulse rate	60	1	30	Hz
Pulse-to-pulse amp. variation	±0.2	±0.2	±0.2	%
Pulse-to-pulse time jitter	±10	±6	±8	nsec
Pulse ripple, total	0.5	0.5	0.5	%
Pulse droop	3	1	3	%
Supply voltages	-	-	480 V, 3 ø, 60 Hz	-

Table III.4.7-2 Klystron Operating Parameters for Linac Subsystems

Parameters	DTL	MS	CCL	Units
Operating frequency	425	1,275	1,275	MHz
Peak output power	4	1	9	MW
Radio-frequency output power, average	120	30	270	kW
Radio-frequency output waveguide	WR1800	WR650	WR650	-
Number of amplifiers	3	2	10	-
Peak power, VSWR < 1.1 (full beam)	4	0.8	9	MW
Peak power, VSWR = 1.25	3.6	0.72	8.1	MW
Peak power, VSWR = 1.6 (no beam)	2.8	0.56	6.3	MW

Table III.4.7-3 Varian Klystron System Parameters

Parameters	DTL	MS	CCL	Units
Tube type	VKP-8812	TBD by Varian[a]	VKL-7796(M)	-
Frequency	425	1,275	1,275	MHz
Peak power output	4	1	9	MW
Average power output	120	30	270	kW
Efficiency	57	50	53	%
Beam voltage (maximum)	130	70	140	kV
Beam current (maximum)	57	32	121	A
Beam power (maximum)	7.0	2.0	16.9	MW
Modulation type	mod-anode	mod-anode	mod-anode	
Mod-anode voltage, full beam	130	TBD	140	kV
Mod-anode voltage, cut-off	- 4	TBD	- 3	kV
Peak inverse voltage rating	26	TBD	30	kV
Heater voltage	24	25	25	V
Heater current	75	12	30	A
Magnet voltage (maximum)	200	200	200	V
Number of magnet coils	6	TBD	9	-
Magnet power (maximum)	6	2.5	10	kW
Tube weight	1,700	TBD	700	lb
Solenoid magnet weight	2,400	TBD	1,400	lb
High-voltage seal insulation	Oil	Oil	Oil	-
Cooling water inlet temperature	25±15	25±15	25±15	°C
Collector water flow (minimum)	120	20	200	gal/min
Collector pressure drop	60	55	55	psi[c]
Body water flow (minimum)	26	TBD	13	gal/min
Body pressure drop	60	TBD	70	psi
Output window coolant (medium)	N_2	TBD	TBD	-
Output window coolant, flow	200	TBD	TBD	ft^3/min
Solenoid water flow	5	5	5	gal/min
Tube lifetime (mtbf)[b]	100,000	100,000	100,000	h
Mounting position	Vertical, cathode down	Vertical, cathode down	Vertical, cathode down	-

[a] TBD = to be determined.

[b] mtbf = mean time before failure.

[c] psi = pounds per square inch.

4.7.3 Modulators

The modulator system supplies the operating voltages for the klystron gun, solenoids and filament, and mod-anode. Each modulator consists of the following:

- Regulator unit — SCR-controlled, 480 V, 3 φ input; 240-528 V, 3 φ ac output; air cooled and insulated.

- Transformer-rectifier unit — high-voltage transformer (140 kV), solid-state rectifier stack and filter choke; oil insulated, convectively cooled via finned tank structure.

- Crowbar and capacitor unit — energy storage capacitors and compensation circuits to minimize voltage droop during the pulse; high-voltage crowbar to dissipate stored energy and protect klystron in the event of a fault.

- Klystron tank — supports klystron, magnet, and associated equipment; contains isolation transformer, klystron heater supplies, modulator switch tubes, and related supplies; is oil filled.

- Controls — low-level controls and instrumentation, interlock logic, magnet power supplies, VME crate.

The first two components are located outside, adjacent to the klystron gallery. The other items are located inside. The modulators are energized from a 480 V, 3 φ, 60-Hz input. All cooling for the klystron is routed through the modulator. Table II.4.7-4 lists the specifications for the modulators for the different accelerator sections.

4.8 BEAM DIAGNOSTICS

4.8.1 Overview

Diagnostics are an important part of any accelerator, especially one with high average current. Typical parameters of interest are beam size, position in the beam tube, energy, phase, bunch length, and beam loss. Beam loss is particularly important. Excessive beam loss causes so much activation that hands-on maintenance is impossible. The microstrip beam diagnostics and the beam loss monitors are described below.

Table III.4.7-4 Klystron Modulator Specifications by Subsystem

Parameters	DTL	MS	CCL	Units
Power, maximum load	350	100	750	kVA
Power, no load	75	20	100	kVA
Current per phase, maximum load	425	125	900	A
Cooling required, maximum load	275	75	600	kW
Cooling required, no load	25	8	30	kW
Coolant flow	160	80	220	gal/min
Coolant inlet temperature	35	35	35	°C
Coolant pressure	60	60	60	psi[a]

[a] psi = pounds per square inch.

4.8.2 Microstrip Beam Diagnostics

Microstrip beam diagnostics measure the centroids of the transverse beam positions, angles, synchronous phase, and energy.[15] Beam positions are measured by comparing the relative signal amplitudes from opposite sides of the microstrip probes. The beam centroid angle is calculated from the centroid position at two different probes that are some distance apart. Energy is derived from the time-of-flight measurement between two separated probes. Synchronous phase is determined by comparing the probe signal from the beam bunch centroid with the cavity field phase from a monitor loop in the cavity. The cavity field phase is corrected for the drift time to the probe derived from the energy measurement.

The probe is very compact and consists of four microstrip transmission lines that are connected to multilayer stripline transmission lines upstream and downstream. These striplines transport the signals through a vacuum flange to processing electronics. Image currents from the beam bunch induce electromagnetic signals onto the upstream and downstream striplines as the beam passes through the probe. The upstream signal is proportional to the beam intensity. Differences in the signal from opposite lobes of the probe are proportional to the centroid offset.

This diagnostic system has been extensively tested and characterized.[16] Processing electronics that interface with the VME standard and processing software that is compatible with the software chosen for this linac are available.

4.8.3 Beam Loss Monitors

Although the microstrip probes give information on the gross characteristics of the beam, they give no information on the beam halo. It is this halo that leads to beam loss and activation of the structure and equipment in the linac tunnel. Beam loss monitors measure the radiation induced when the beam halo strikes the beam tube. Beam loss measurement permits fine-tuning and optimization of the accelerator to minimize activation. Beam loss monitors provide prompt warning of catastrophic beam loss. This signal is used to provide fast shut-down to minimize damage to the structure and activation.

The beam-loss-monitor system consists of fast-ionization detectors and processing electronics that monitor the radiation level.[17] The ionization detectors are mounted close to the beamline to monitor the radiation from (p,γ) reactions. The system provides two trip points. The higher-level trip point is used to shut the accelerator down in 10 μsec and protect against burnthrough from a major beam loss.

4.8.4 Other Diagnostics

Additional linac diagnostics include beam current toroids, segmented apertures, wire scanners, and Faraday cups. A slit and collector emittance unit is used for initial commissioning.

4.9 CONTROL SYSTEM

4.9.1 Overview

This section includes the control system, data acquisition system, and the distribution systems for the rf master oscillator signals and accelerator timing.

4.9.2 Data Acquisition and Control

The linac data acquisition and control system is a distributed network consisting of operator, network, and hardware interfaces, as shown schematically in Figure III.4.9-1. EPICS is used to develop the front-end control software.[8] Commercial and custom VXI modules are used to interface the control system to the linac hardware. These VXI modules are located in the racks of the systems to which they interface.

The operator interface is a Unix-based workstation with an X-Window graphical user interface (GUI). The workstation can be located at any point on the network and still maintain full functionality. The user can generate and alter control displays and can access interactive control programs, the archiver, the alarm handler, custom code, and various tools. Five operator workstations are associated with the linac; however, the linac can be controlled by any workstation on the network.

The network provides the communication path between the operator workstations, input and output crates, other hardware in the linac control system, and the controls for the rest of the facility. Transmission control protocol/Internet protocol (TCP/IP) is the underlying protocol for the network. A fiber-based Ethernet network is used for noise immunity.

The input/output controller (IOC) provides an input/output interface between the accelerator hardware and the rest of the control system. The standard crate uses the VXI standard and contains a network interface and various interfaces to the accelerator hardware. The crate controller is a Motorola 68040-based processor. The VxWorks operating system provides the basis for real-time control, allowing the 68040 processor to run its software autonomously with respect to all other devices in the system.

Table III.4.9-1 lists the number of each type of data channel for each of the major subsystems, and Table III.4.9-2 lists the numbers of the various VXI components required for each subsystem.

The EPICS and the IPNS Upgrade accelerator control systems are described in Section II.8. The same control system is used to control the linac.
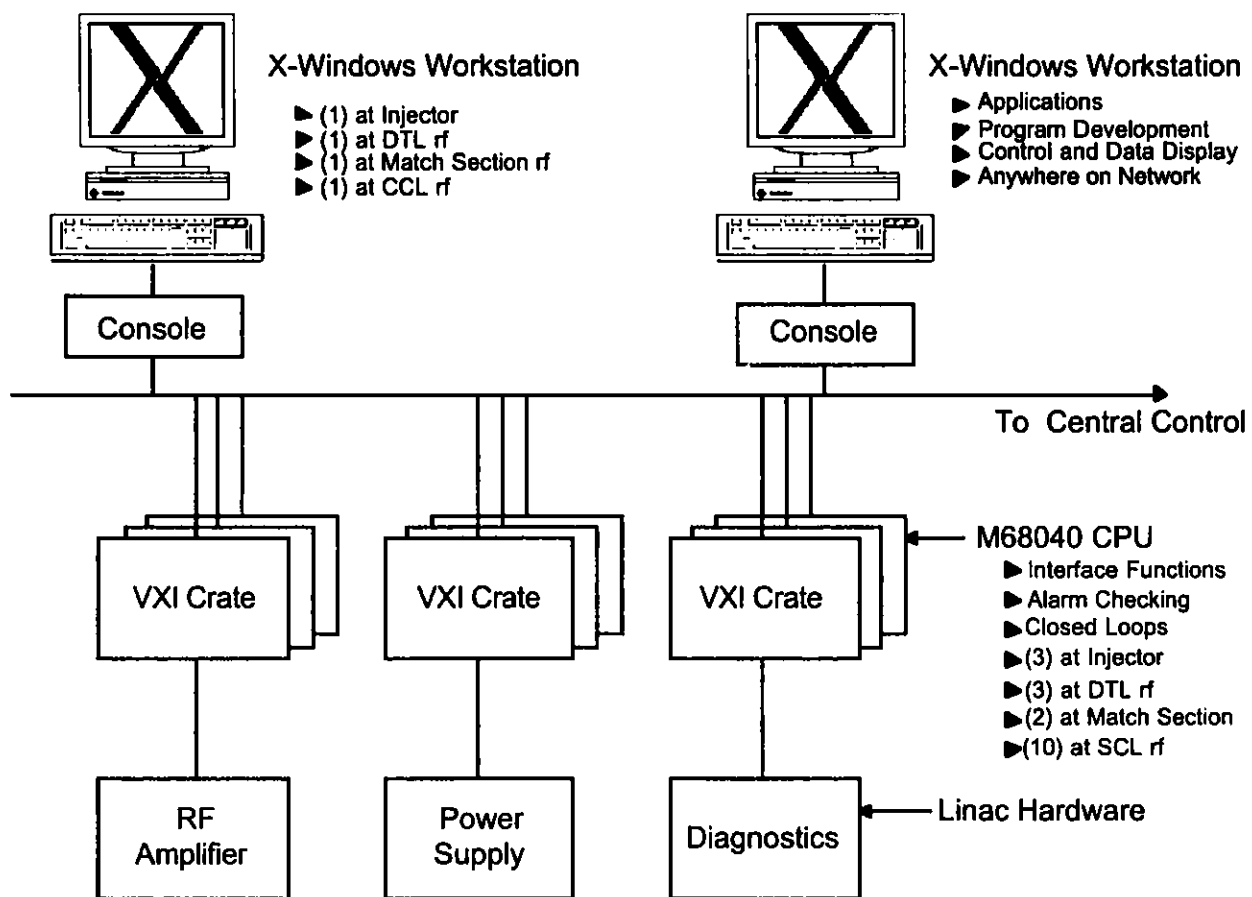
Figure III.4.9-1 Control System Diagram

Table III.4.9-1 Number of Data Channels Required by Linac Subsystems

Channel Type	LIS	DTL	MS	CCL	Total
Digital input	144	288	192	1,040	1,664
Digital output	104	156	120	600	980
Slow analog input	226	312	232	1,160	1,930
Slow analog output	72	84	72	360	588
Counter/timer outputs	13	36	24	120	193
Waveform inputs	24	36	36	120	216
Total					5,571

Table III.4.9-2 Number of VXI Components Required
by Linac Subsystems

Component	LIS	DTL	MS	CCL	Total
VXI crate	3	3	2	10	18
Crate controller	3	3	2	10	18
Network interface	3	3	2	10	18
32-bit digital in	6	9	6	40	61
32-bit digital out	6	6	4	20	36
64-channel analog input	4	6	4	20	34
16-channel analog output	6	6	6	30	48
Counter/timer outputs	4	9	6	30	49
4-channel waveform digitizer	7	9	9	30	55
Low-level radio-frequency	2	3	2	10	17

4.9.3 Radio-Frequency Reference Signal Distribution and Low-Level System

The RFQ and DTL operate at 425 MHz, and the matching section and CCL operate at 1,275 Mhz. These two frequencies are harmonically related. There are 17 amplifiers that power the linac, and precise frequency and phasing are maintained. The rf reference generation system for the linac is based on one developed for the GTA at LANL.[18]

The rf reference generation system is configured as a star distribution network and provides coherent, phase-stable signals to the low-level rf subsystems for each amplifier and any other systems requiring these signals. The transport network maintains the phase error to ± 0.036° over 50 meters of phase-stable cable.

The low-level rf provides the necessary amplitude and phase feedback control for the amplifiers. The VXI-based modules used in this linac are derived from ones developed at Fermilab.[19] Phase and amplitude can be electronically adjusted. In addition, feed-forward control is available. In normal operation, the reference frequency signal comes from the reference signal distribution system. However, for cavity warm-up and conditioning, an internal VCO tracks the cavity frequency during warm-up.

4.9.4 Timing Signal Distribution

A dedicated timing system is required because of the asynchronous nature of TCP/IP Ethernet. This linac uses a system developed for the GTA at LANL.[20] A central master timing device generates the timing signals and distributes them to the various subsystems via optical fibers. The network is configured as a star with dedicated fibers for each subsystem IOC.

Four types of timing signal are provided: the system clock, system trigger, time tag clock, and time tag reset. The 5-MHz system clock is the reference for all timing events in the system. The system trigger synchronizes control and data acquisition. The time tag and time tag reset provide a unique event number and date/time stamp for recorded events.

This timing is implemented in VME modules, with EPICS used for programming. Ten channels with 200-nsec resolution are provided in each module. More channels per IOC can be provided by multiple modules.

5.1 DIMENSIONED FACILITY LAYOUT

A cross-sectional view through the DTL is shown in Figure III.5.1-1. Figure III.5.1-2 is a plan view of the linac showing the linac tunnel and the klystron gallery. The locations of major utility requirements including electricity, cooling water, and gas cooling for the DTL rf windows are shown on the drawing.

5.2 UTILITY REQUIREMENTS

Table III.5.2-1 lists the electricity and cooling water requirements for the 400-MeV linac. The values are the installed capacities and not the amounts actually consumed. All cooling for the klystrons is included in the numbers listed for the modulators. The water flow values given for the DTL load cooling system are for the water provided from the facility to the load heat exchangers. The 425-MHz loads use a 50:50 mixture of ethylene glycol and water from a closed-loop system for cooling. The 1,275-MHz loads are cooled by plain water because the rf absorption is adequate at that frequency.
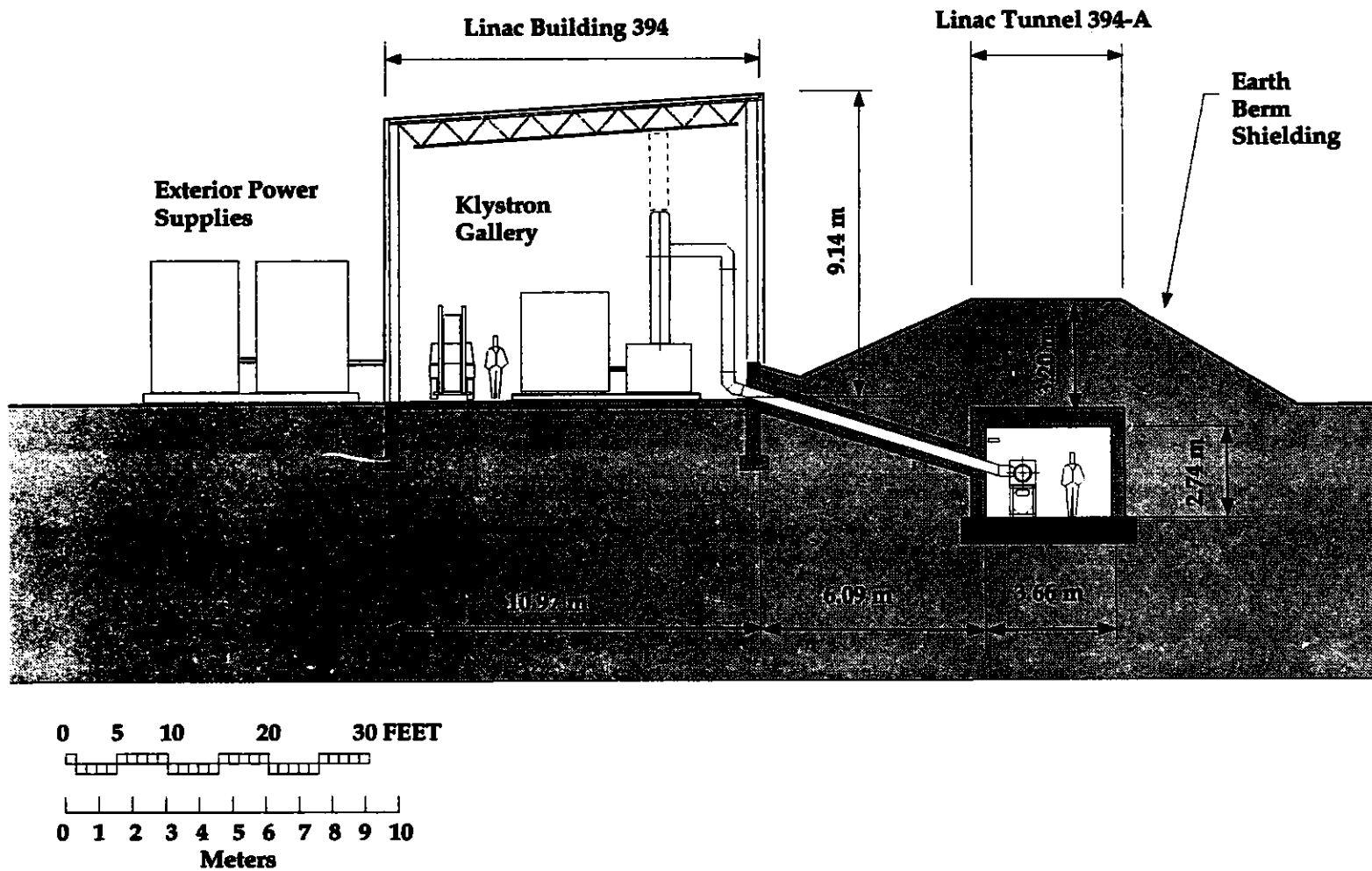
Figure III.5.1-1 Section through Linac Facility Showing Building and Tunnel Configuration.
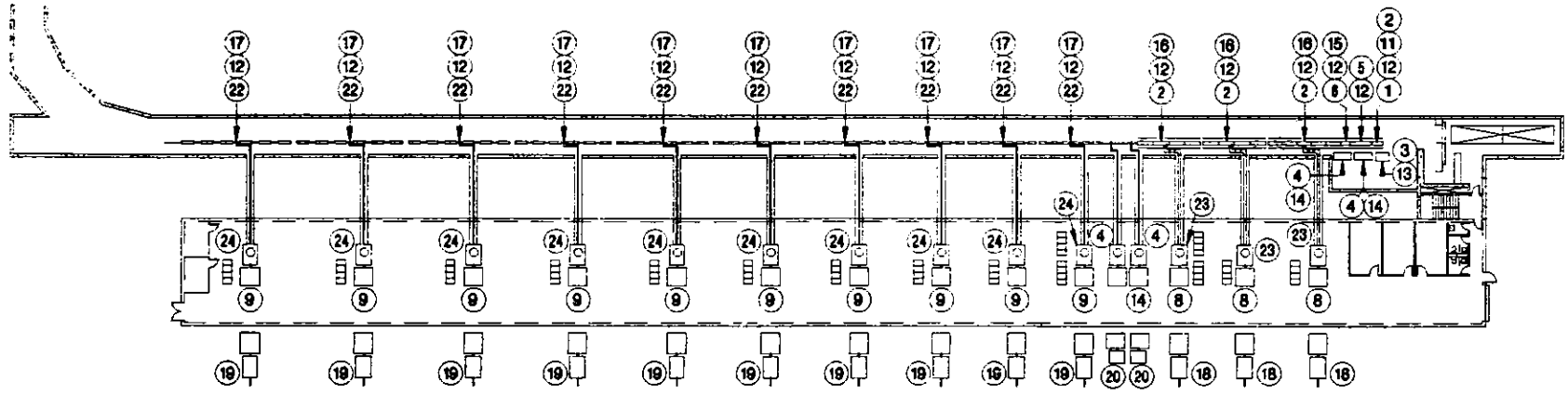
DI WATER, 20 deg. C max.
60 psi min./120 psi max.

(1) 1.3 gpm
(2) 6 gpm
(3) DIW 7 gpm
(4) 12 gpm
(5) 3 gpm
(6) 5 gpm
(7) 60 gpm
(8) 160 gpm
(9) 220 gpm
(10) 100 gpm
(22) 150 gpm
(23) 35 gpm 50/50 ETHYLENE GLYCOL AND WATER
(24) 50 gpm

POWER

(11) 208V AC/3 ph AT 23A
(12) 110V AC AT 3A
(13) 208V AC/3 ph AT 100A
(14) 208V AC/3 ph AT 80A
(15) 220V AC/1 ph AT 15A
(16) 220V AC/1 ph AT 30A
(17) 220V AC/1 ph AT 45A
(18) 480V AC/3 ph AT 160A
(19) 480V AC/3 ph AT 900A
(20) 480V AC/3 ph AT 125A
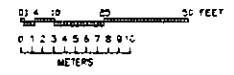
PLAN VIEW OF THE LINAC SHOWING LOCATIONS OF UTILITY REQUIREMENTS

Figure III .5.1-2

Table III.5.2-1 Power and Water Cooling Requirements for the Injector Linac System

Description	Maximum Water		Installed Total A/Phase				
	Q_{min} (gal/min)	q (kW)	1 φ/ 110 V	1 φ/ 220 V	3 φ/ 208 V	3 φ/ 480 V	N_2 at 25 psig (ft^3/min)
LIS							
Ion source/beamline	7 (DI)	13	-	-	-	-	-
Ion source electronics	-	-	-	-	100	-	-
2,200-L/sec turbopump (3)	1	6	-	30	-	-	-
Roughing pumps (3)	-	-	-	30	-	-	-
LEBT solenoids (2)	6	13.2	-	-	-	-	-
RFQ amplifier	12 (DI)	6	-	-	40	-	-
RGDTL amplifier	12 (DI)	5	-	-	40	-	-
Cooling system	7	7	-	9	-	-	-
DTL Tanks							
Waveguide window	-	-	-	-	-	-	600
Cooling system	125	100	-	45	-	-	-
DTL RF System							
Klystrons	incl. in modulator		-	-	-	-	600
Load cooling system [a]	25	15	-	30	-	-	-
Modulator/HVPS [b]	480	400	-	-	-	700	-
DTL Vacuum System							
Ion pump controllers	-	-	-	210	-	-	-
Matching Section							
Klystrons	incl. in modulator		-	-	-	-	-
Modulator/HVPS	100	75	-	-	-	140	-
Circulator and load	30	2	-	-	-	-	-
Cavity cooling system	30	25	-	15	-	-	-
Quadrupoles	18	50	-	-	-	-	-
Quadrupole PS [c]	-	-	-	-	225	-	-
Ion pump controller	-	-	-	30	-	-	-
CCL Module							
Cooling systems	1,000	900	-	-	60	-	-
Quadrupoles	120	215	-	-	-	-	-
Quadrupole PS	-	-	-	-	1,000	-	-
CCL Vacuum System							
Ion gauge and controller	-	-	30	-	-	-	-
Ion pump controller	-	-	-	900	-	-	-
CCL RF System							
Klystrons	incl. in modulator		-	-	-	-	-
Modulator/HVPS	2,200	2,500	-	-	-	4,500	-
Circulator and load	300	60	-	-	-	-	-

[a] Closed, recirculating loop of 50/50 ethylene glycol/water with heat exchange to facility water.

[b] HVPS = high-voltage power supply.

[c] PS = power supply.

5.3 REFERENCES

1. L. Schroeder, K.N. Leung, and J. Alonso (editors), *Proceedings of the Workshop on Ion Source Issues Relevant to a Pulsed Neutron Source*, Lawrence Berkeley Laboratory Report No. LBL-36347 (Oct. 24-26, 1994).

2. J. DeBoers, *SNOW — A Digital Computer Program for the Simulation of Ion Beam Devices*, Sandia International Report No. SAND 79-1027 (1980).

3. *Documentation for TRACE: An Interactive Beam Transport Code*, Los Alamos National Laboratory Report No. LA-10235-MS (1985).

4. PARMULT, Los Alamos Accelerator Code Group (Los Alamos National Laboratory, Los Alamos, N.M.).

5. G. Boicourt and J. Merson, *PARMILA Users and Reference Manual* (Los Alamos National Laboratory, Los Alamos, N.M., Jan. 10, 1990).

6. K.R. Crandall, *TRACE 3-D Documentation*, Los Alamos National Laboratory Report No. LA-11054-MS (Aug. 1987).

7. K.R. Crandall, private communication, as cited in F.W. Guy, in *Proceedings of the 1993 Particle Accelerator Conference*, p. 122 (1993).

8. L. Dalesio et al., "EPICS architecture," in *Proceedings of the International Conference on Accelerator and Large Experimental Physics Control Systems*, pp. 278-281 (KEK, Tsukaba, Japan, Nov. 11-15, 1991).

9. M.J. Barnes et al., "A variable duty factor beam chopper for a 300 keV injection beamline," in *EPAC Proceedings* (1994).

10. J.G. Alessi, J.M. Brennan, and A. Kponou, "H⁻ source and low energy transport for the BNL RFQ preinjector," in *Proceedings of the Fifth International Symposium on Production and Neutralization of Negative Ions and Beams*.

11. J.M. Potter, "A parallel planar triode array high power rf system for accelerator applications," in *EPAC 90 Proceedings, Editors Frontiers*, p. 991 (1990).

12. R.E. Morgado et al., "The effects of proton beam quality on the production of gamma rays for nuclear resonance absorption in nitrogen," in *SPIE Proceedings on Substance Detection Systems*, Vol. 2092, p. 503 (1994).

13. U.S. Patent No. 5,179,350.

14. J.H. Billen and A.H. Shapiro, "Post-coupler stabilization and tuning of a ramped gradient drift tube linac," presented at 1988 Linear Accelerator Conference, CEBAF Report No. 89-001, p. 128 (1989).

15. J.D. Gilpatrick et. al., *Overview of the microstrip beam diagnostics*, Los Alamos National Laboratory Report No. LA-CP-89-460 (1989).

16. S.P. Jachim et al., in *Proceedings of the 1993 IEEE Particle Accelerator Conference*, IEEE 93 CH 3279-7, p. 1154 (1993).

17. C.R. Rose, C.M. Fortgang, and J.P. Power, "GTA beamloss monitor system," in *1992 LAC Conference Proceedings*, AECL-10728, p. 365 (1992).

18. A.H. Regan and P.M. Denney, "RF Reference Generation for the Ground Test Accelerator," in *Proceedings of the 1991 Particle Accelerator Conference*, p. 2946 (1991).

19. B.E. Chase and R.J. Pasquinelli, "VXI based low level RF system for Fermilab linac upgrade," in *Proceedings of the 1993 Particle Accelerator Conference*, p. 2355 (1993).

20. M. Stettler et al., "A distributed timing system for synchronizing control and data acquisition," in *1992 LAC Conference Proceedings*, AECL-10728, p. 820 (1992).

IV

Target Stations

1.1 GENERAL

This chapter describes the target stations that produce the neutrons utilized by the neutron scattering instruments at IPNS Upgrade. A target station consists of the biological shield and hot cell and all the components they contain, including target and moderators, together with the necessary external cooling and ventilation systems. The pulses of protons from the accelerator impinge on the target, and the resulting spallation interactions produce large quantities of fast neutrons. The moderators slow these neutrons down to energies suitable for use by the neutron scattering instruments, and a portion of the neutrons pass through ports in the target station shielding into beam lines, which lead to the instruments.

The design for the target stations for IPNS Upgrade is based on a careful assessment of the requirements of the neutron scattering instruments. The IPNS Upgrade design is site-specific in that it uses existing buildings at Argonne. The target stations accept horizontal proton beams from the accelerator and provide neutron beams that make optimal use of the existing experiment halls. Vertical injection of the proton beam into the target, which is another option, was rejected because it appeared to be more expensive than horizontal injection and offered too few advantages in view of the cost. This site-specific design results in significant cost savings while introducing few, if any, compromises in the performance of the facility.

Section IV.1.2 gives a brief overview of the target station components. These components are described and analyzed in detail in the remaining sections of this chapter.

Section IV.2 provides a detailed analysis of the power deposited in the target and of the cooling system required to extract this power. This includes a thermal-hydraulic analysis of the heat transfer from the target material to the coolant and calculations of thermally induced stresses in the target. This section also contains a discussion of metallurgy and corrosion questions that relate to the choice of machinable tungsten alloy as the target material.

Section IV.3 describes the moderators and reflectors and the associated cooling systems. Monte Carlo calculations of the power deposition in the different moderators are used to size the various water and cryogenic-liquid cooling systems. The neutron beam currents produced by the moderators are also calculated.

Section IV.4 provides details of the biological shield. The effectiveness of the shielding in reducing the radiation dose rate is also analyzed. Section IV.5 describes the remote handling facilities used to manipulate the activated target and moderator components in order to make repairs or to replace damaged components. Section IV.6 covers the various levels of containment designed to prevent accidental release of activity.

The controls and instrumentation required for safe and reliable operation of the target stations are discussed in Section IV.7.

Section IV.8 discusses the neutron beam ports and their interfaces to the portions of the neutron beam lines that are external to, and extend radially from, the target stations. These

external beam lines are considered to be parts of the neutron scattering instruments and are discussed in Chapter V.

1.2 OVERVIEW OF THE DESIGN

IPNS Upgrade has two target stations, one operating at 10 Hz and one operating at 30 Hz. The purpose of the target stations is to house and shield the primary-neutron-producing targets and the moderators that slow down the primary neutrons to useful energies. Neutron beam ports penetrate the shield to allow neutrons from the moderators to reach instruments outside the shield. The target stations also contain internal facilities for neutron activation and radiation-effects experiments. A switching system alternately directs pulses of 2-GeV protons delivered at 30 Hz from the accelerator system to the two target stations. The 10-Hz target station receives one pulse out of three. The 30-Hz target station receives two pulses out of three in an iambic pattern, with an average frequency of 20 Hz under normal operating conditions, but it can efficiently utilize the full 1 MW at 30 Hz if desired.

The target stations are housed in existing buildings to which slight modifications are made. Chapter VI describes the conventional facilities for IPNS Upgrade. The target stations are new construction. The two target stations are identical except for details of the moderators, which are differently optimized for the 10-Hz and 30-Hz instruments. This chapter describes the components of one of these target stations and, unless otherwise noted, all these components are duplicated for the second target station. Both targets and associated cooling systems are able to accept the full 1-MW beam power. The 30-Hz scattering instruments are designed to tolerate the 1/30-s inter pulse interval, so when the 10-Hz target is not operating, the 30-Hz target can usefully accept the full-power 30-Hz beam.

Figure IV.1.2-1 shows the two target stations located in Buildings 369 and 370. Each station provides neutron beams through 18 beam ports, derived from six individually tailored moderators optimized for the intended scattering instruments. This figure also shows a representative set of neutron scattering instruments located in appropriate positions on the neutron beam lines, as discussed in Chapter V. The inner portions of the target stations, consisting of the targets, moderators, and innermost reflectors, can move into the adjacent hot cells, equipped with shielding windows and manipulators, for modification and repair. The figure shows these components withdrawn into the servicing cells. Space is available within the experiment halls for other types of experimental capabilities, such as a pulsed-muon spin-rotation facility. Appendix C describes this and other possible facilities that are not within the scope of this project. The outlying Buildings 367 and 371 and the vaults shown in Figure IV.1.2-1 house components of the cooling and containment systems.

Figure IV.1.2-2 schematically illustrates the target and moderator layout. The target is of the split-target or flux-trap design. This geometry allows the installation of four moderators in the tangentially viewed wing configuration and two flux-trap moderators. Each of the moderators provides three neutron beams from one viewed surface. The flux-trap moderators provide good

30 Hz TARGET STATION

10 Hz TARGET STATION

360 AREA TUNNEL SYSTEM

GAS HOLDING TANKS
TARGET PUMPS
COOLING SKIDS
HEAT EXCH.

370

GAS
HOLDING TANKS
(2)

WATER
HOLDING
TANK

VAULT

GAS HOLDING TANKS
TARGET PUMPS
COOLING SKIDS
HEAT EXCH.
FOR BLDG. 369

371

GAS
HOLDING TANKS
(2)

WATER
HOLDING
TANK

VAULT

SHIELDED
OVERHEAD
PIPEWAY
(4.4m
CLEARANCE)

368

369

367

SHIELDED
OVERHEAD
PIPEWAY
(4.4m
CLEARANCE)

371
ANNEX.

CRYO. AREA
FOR BLDG. 370

CRYO. AREA
FOR BLDG. 369

N

0   50 FEET

0   10 METERS

Figure IV.1.2-1 Floor Plans for the 30-Hz Target Building (370), 10-Hz Target Building (369),
Sample Preparation Laboratories (368), and Cooling System Buildings (367, 371).
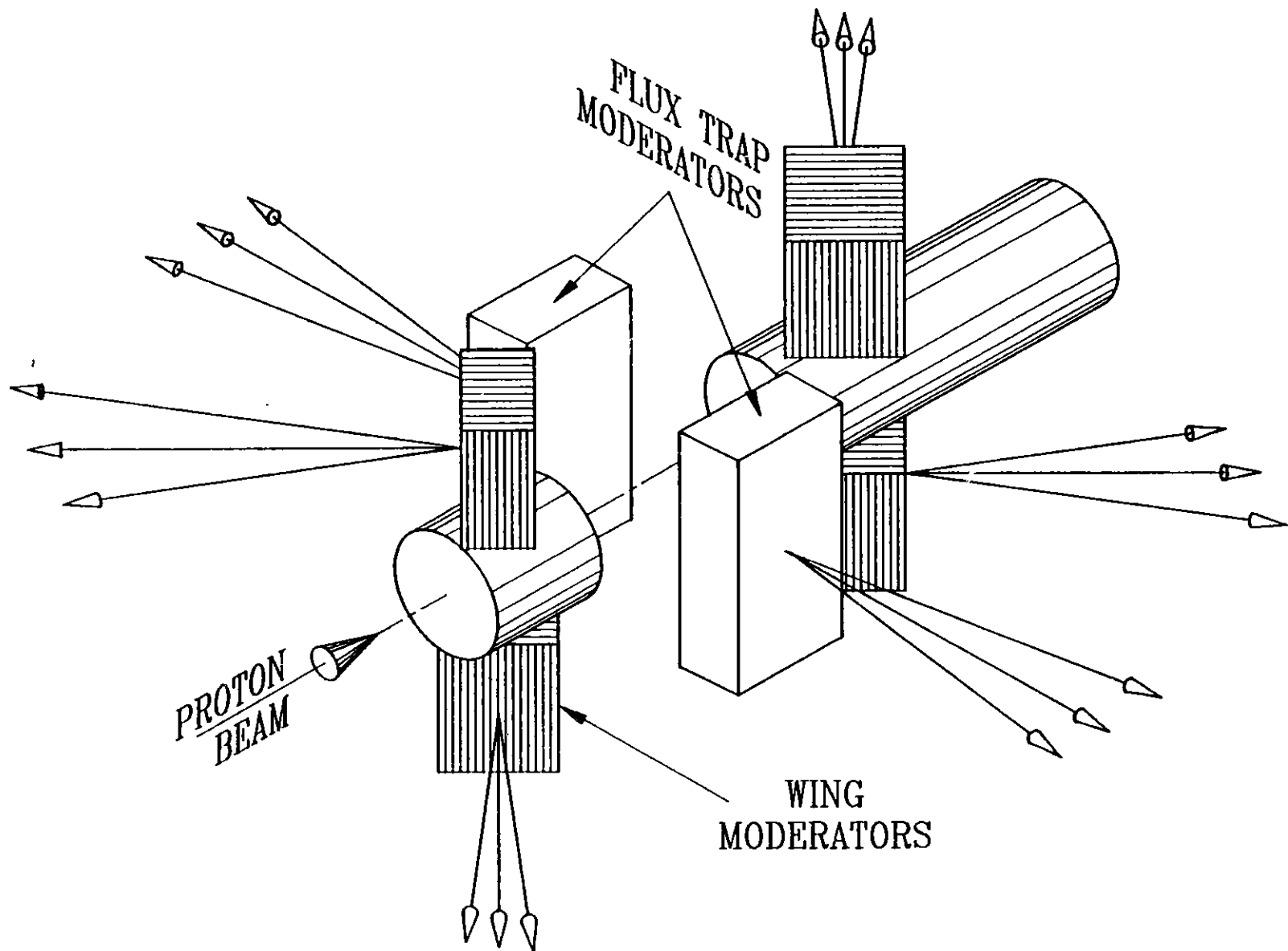
Figure IV.1.2-2 Schematic View of the Target and Moderator System. (Arrows indicate the directions of extracted neutron beams.).

coupling to the primary neutron source. They are viewed at near 90° to the proton beam direction, so the neutron beams do not view target material struck by the proton beam and there is little high-energy neutron contamination in the beams. In addition, because the flux-trap moderators are centered about the axis of the target, they are taller than the canonical wing moderator. This feature is advantageous for a number of scattering instruments and is easily accommodated with the horizontal proton beam geometry.

Figure IV.1.2-3 shows the design for the split target. This design is analyzed in detail in Section IV.2. The split is arranged so that neutrons are evenly shared between moderators in the upstream and downstream positions, while the gap is chosen in order to minimize losses in neutron production, maximize coupling to the flux-trap moderators, and avoid a direct view of the target by the neutron beam lines, thus reducing fast neutron backgrounds. The diameter of the target is selected to maximize neutron production and coupling to the moderators while minimizing proton leakage to the surroundings. The total target length exhausts the nuclear cascade and leaves little power in the downstream shielding. The proton beam profile used for target design is Gaussian with 5-cm full width at half maximum, which is roughly the maximum size feasible from the point of view of proton beam transport. The two sections of the target share one common coolant flow. The local power densities in the target are low enough that the heat generated can be easily handled by conventional water cooling. The neutronic and thermal consequences of tighter focusing or more uniform spreading of the proton beam, to provide performance improvements or extend target lifetimes, are part of the preconstruction R&D program.

The target material is a machinable tungsten alloy. A thin, plasma-sprayed titanium coating is applied for improved corrosion resistance. This target provides high atomic number and mass density for high neutron yield, high strength, and good properties at high temperature. Cooling is by light water that passes across the face of the target disks, guided by channels machined in the disk surfaces. Disk thicknesses in the upstream section are chosen to maintain single-phase (no boiling) convective heat transfer at the surface, while disk-center temperatures govern disk thickness in the back section. Disks are spring-loaded to take up dimensional changes due to thermal and radiation-induced growth. The front part of the target consists of circular disks with guide notches, clamped with four compression springs. The back part of the target consists of circular disks similar to those in the front, compressed by nested coil springs.

The target vessel is of welded stainless-steel construction, contains both front and back sections of the target, and provides water-flow plena that distribute cooling water to the disks and all parts of the vessel, including all springs. Cooling water is carried in and out from the downstream side of the target. The cooling plena located above and below the target disks allow the target cooling water in the plena to act as premoderator for the wing moderators. The cooling pipes clear the moderators and irradiation facilities and exit downstream of the biological shield, where they connect to the cooling system. The vessel and its attached piping constitute a single unit to facilitate handling and increase integrity.

PROTON
BEAM

A

A

SEC. A- A

|ı||||||||||ı|||||||||||ı||||||||||ı|||||||||
0   10   20   30   40
CM
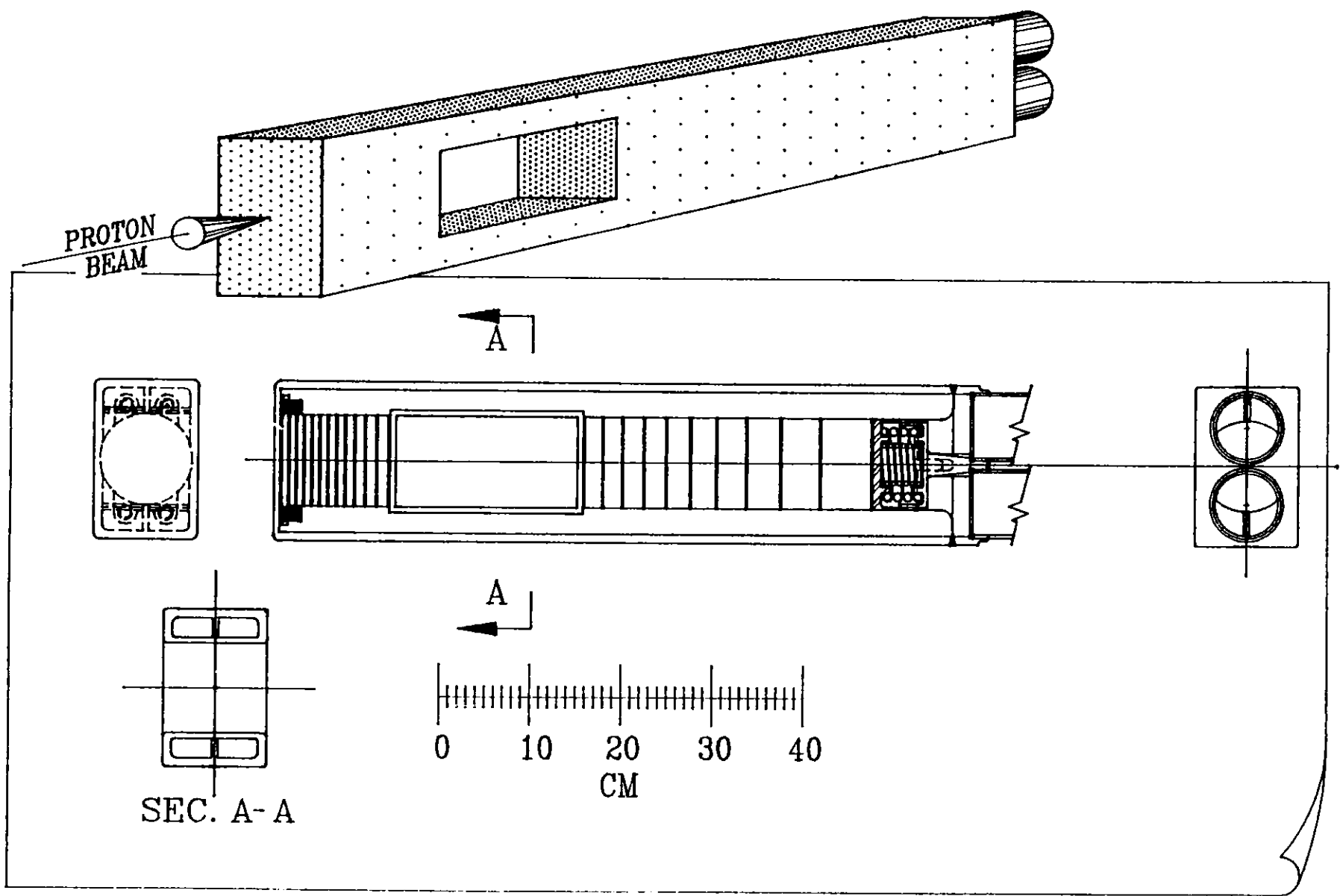
Figure IV.1.2-3 View of the IPNS Upgrade Integral Split Target.

Moderators are of several types, optimized according to the intended applications for scattering instruments and arranged according to the requirements dictated by the surrounding scattering instruments. Three beams are extracted from each of the six viewed surfaces to provide a total of eighteen beams, nine beams on each of the two sides of each target station. The beams are separated by angles of 13° and are about 1.4 m apart at the shield face, 6 m from the center. The moderators selected and placed as described in this design satisfy the requirements of the neutron scattering instruments as described in Chapter V.

Wing moderators are nominally $10 \times 10 \times 5$ cm^3, and flux-trap moderators are nominally $20 \times 10 \times 5$ cm^3. Moderating materials are light water, liquid methane, and liquid hydrogen. Premoderators significantly reduce the power that is removed at cryogenic temperatures and reduce the rate of radiation damage in the cryogenic media. Moderator vessels and housings are constructed of aluminum alloy. Figure IV.1.2-4 shows the six moderators in greater detail. Moderator and premoderator fluids flow in the attached piping, which consists of vacuum-insulated tubing. The exterior tubing is actively cooled. Each moderator and its associated piping constitute a single integrated unit to facilitate replacement and repair. Moderator piping emerges downstream of the biological shield where it connects to the cooling systems. Section IV.3 describes the moderators in more detail.

The cryogenic moderators of IPNS Upgrade rely heavily on the use of premoderators placed between the target and the portion of the moderator viewed by the neutron beams. This is a well-known concept,[1] but one that has not yet been incorporated into any existing pulsed spallation neutron sources. Useful and informative neutronic tests have been performed at the Hokkaido Linac moderator testing facility.[2] A solid methane moderator with a water premoderator is being installed in the 2-MW Russian IBR-2 pulsed reactor.[3] Both of these will contribute important experience to the development of the premoderator concept. The function of premoderators is to slow down neutrons from high energies, so that most of the resulting heat is removed at ambient temperature. The ambient medium performs most of the thermalization, while the cryogenic material produces cold neutrons. Both water, and metal hydrides with higher proton densities than water, are possible premoderator materials. In the IPNS Upgrade cryogenic moderators, the face viewed by the neutron scattering instruments is cryogenic material, but the medium surrounding it on the other five faces is ambient-temperature water. This geometry is described in detail in Section IV.3.1. Only a few neutron mean-free-paths are required to thermalize the neutrons to the lower temperature in the cryogenic region.

Reflectors of beryllium, or of beryllium and heavy metal, are placed around the moderators to reflect neutrons back into the moderators. Considerable heat is generated in the reflectors due to the slowing down of neutrons and the absorption of gamma radiation. Active cooling removes this heat. The complete target-moderator-reflector assembly provides spaces for all the beam ports and coolant piping. Figure IV.1.2-5 shows the arrangement of the spaces in the bottom half of the reflector.
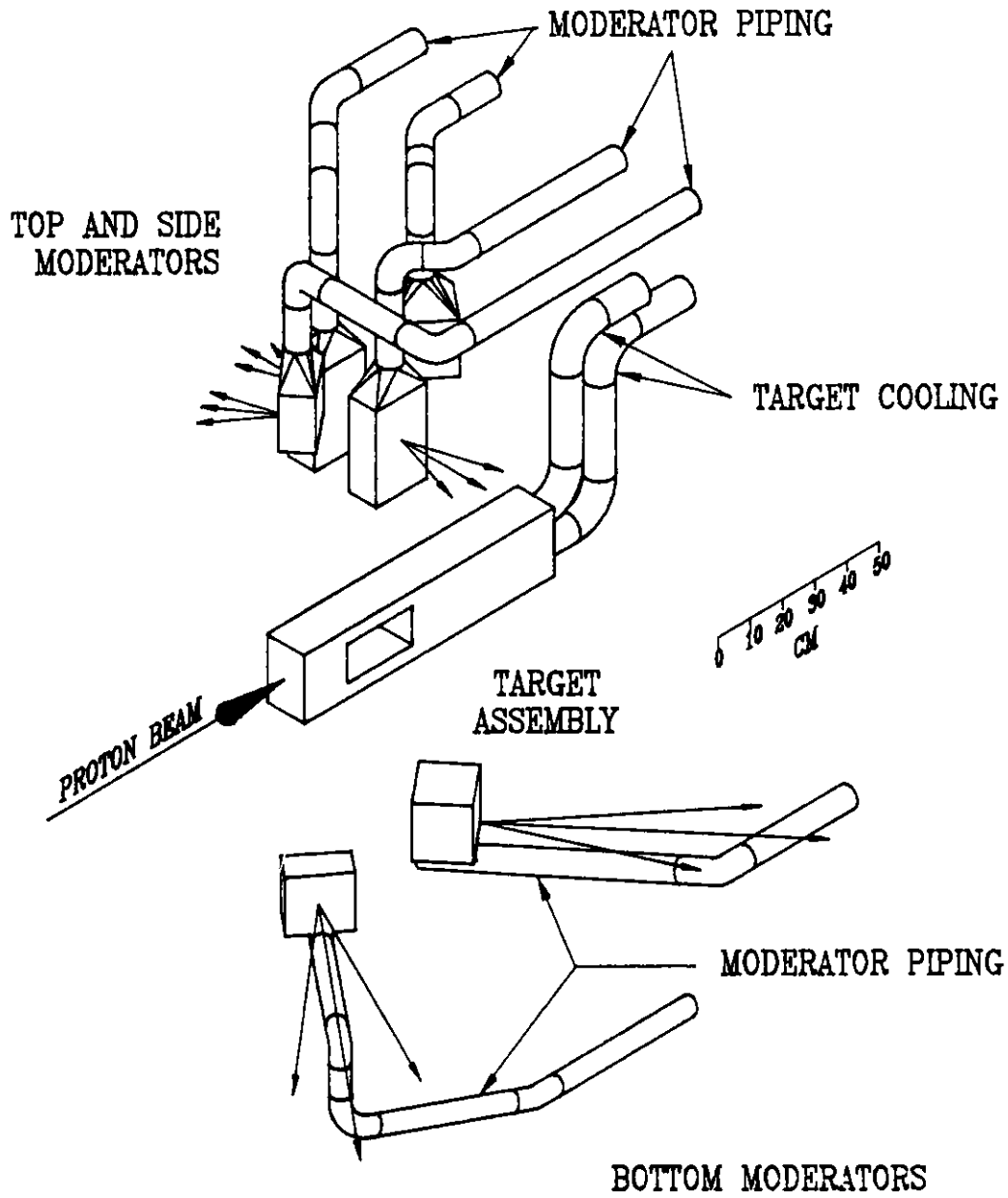
Figure IV.1.2-4 Six Moderators Arranged around the Target. (Exploded view; arrows emerging from the moderator faces represent the 18 neutron beams.)

FLUX TRAP MODERATOR AND
BEAM PORT CAVITIES

CHANNELS FOR
IRRADIATION TUBES

TARGET CAVITY

PROTON
BEAM

BOTTOM WING MODERATOR
AND BEAM PORT CAVITY

50
40
30
20
10
CM
0
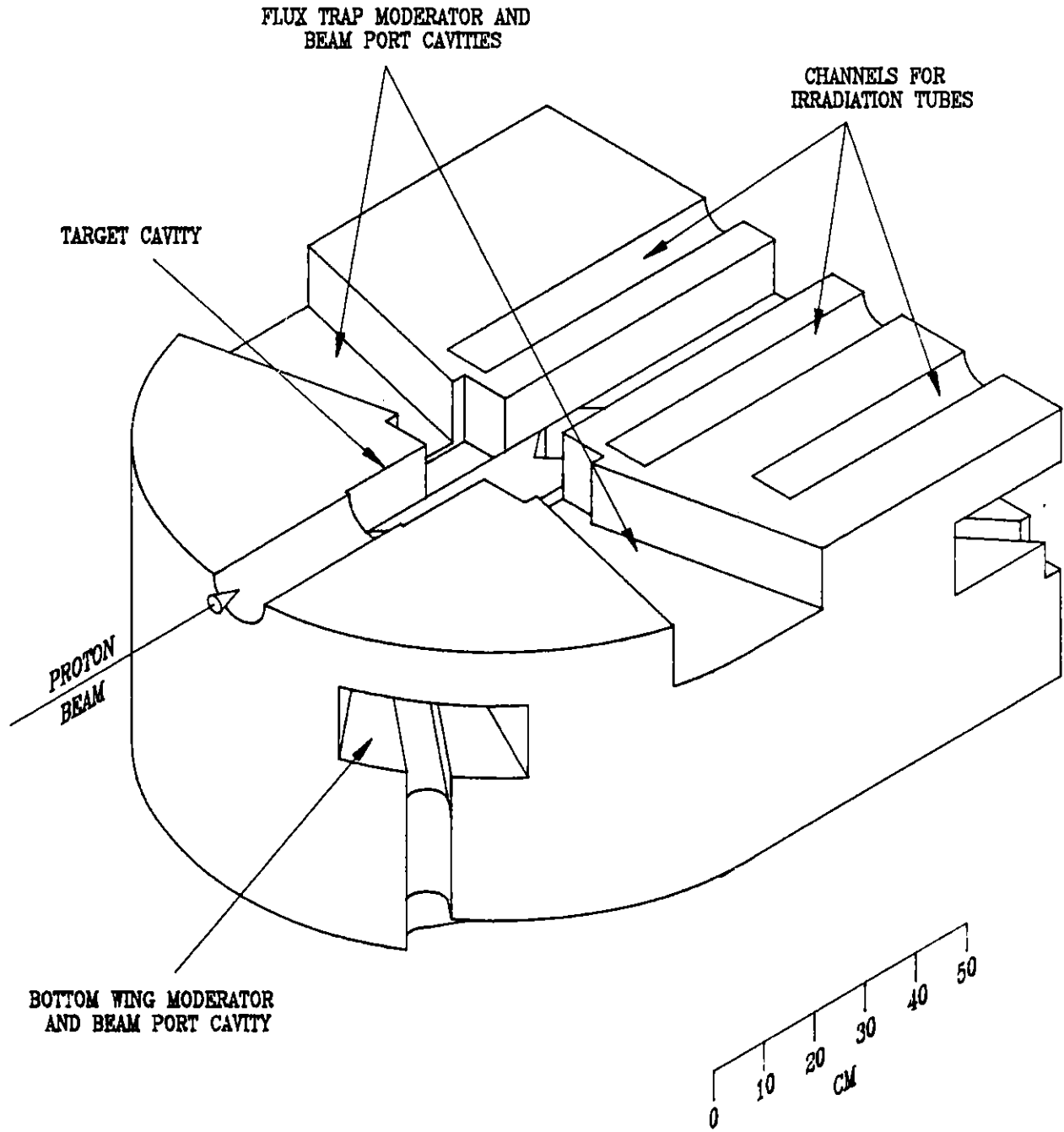
Figure IV.1.2-5 Bottom Reflector, Showing Neutron Beam Ports, Coolant Passages,
Proton Duct, and Target and Moderator Cavities.

Layers of neutron-absorbing material, or decouplers, are placed between the reflector and the moderators to preserve short pulses, because neutrons dwell longer in the reflector than in the moderators. These decouplers are transparent to neutrons with high energies, but opaque to neutrons at the lower energies of interest. The neutron beam ports require neutron-absorbing void liners, because the ports represent voids across which neutrons can fly back into the moderators after considerable delays. The reflector, decouplers, and void liners require active cooling because they are heated by scattered and absorbed neutrons and gamma rays. Water-cooling systems remove this heat.

Three irradiation tubes provide close access to the target for neutron activation and neutron radiation-effects experiments. Samples can be inserted and withdrawn through the curved tubes from remote locations within and outside the remote-handling facility even while the target is in operation. These irradiation facilities are described in Section V.4. The irradiation tubes are gas-cooled to remove heat from irradiated samples and from the walls of the tubes.

The target-moderator-reflector assembly, portions of the piping for their respective cooling systems, portions of the irradiation tubes, and the massive steel shield blocks downstream from the target comprise an assembly called the target train. Figure IV.1.2-6 shows the target train, including the reflector system and the neutron beam ports. The target-moderator-reflector assembly arrangement allows the target and any of the moderators to be individually removed from the system without disturbing the other parts, which simplifies servicing and allows easy replacement of components.

During operation, the target train rests inside a sealed, helium-filled volume defined by a stationary liner inside the shield. This target tank is shown in Figure IV.1.2-7. The sealed volume provides containment of radioactive gases and solid residue produced in the target-moderator-reflector assembly. The containment systems are described in Section IV.6. Neutron beams emerge from windows, which are thinned sections in the aluminum target tank. The downstream end of the target train carries a metal sheet that forms a seal with the target tank during operation, which can be disengaged to enable retraction of the target train. The upstream end of the target tank has a cavity for proton beam diagnostics. Figures IV.1.2-8a and IV.1.2-8b show the target-train assembly inserted into the target tank, and Section IV.5 details the steps involved in withdrawing the target-train assembly and servicing it in the hot cell. The target tank can also be removed into the hot cell and replaced.

The biological shield, illustrated in Figure IV.1.2-9, consists of an inner core of iron and an outer layer of concrete extending to a distance of about 6 m from the target in the shortest dimension that is 90° from the proton beam direction. The shield is designed so that all parts of the hall housing the scattering instruments can be occupied during operation. The innermost portion of the shield receives active cooling to remove the heat. This shield is described in greater detail in Section IV.4.
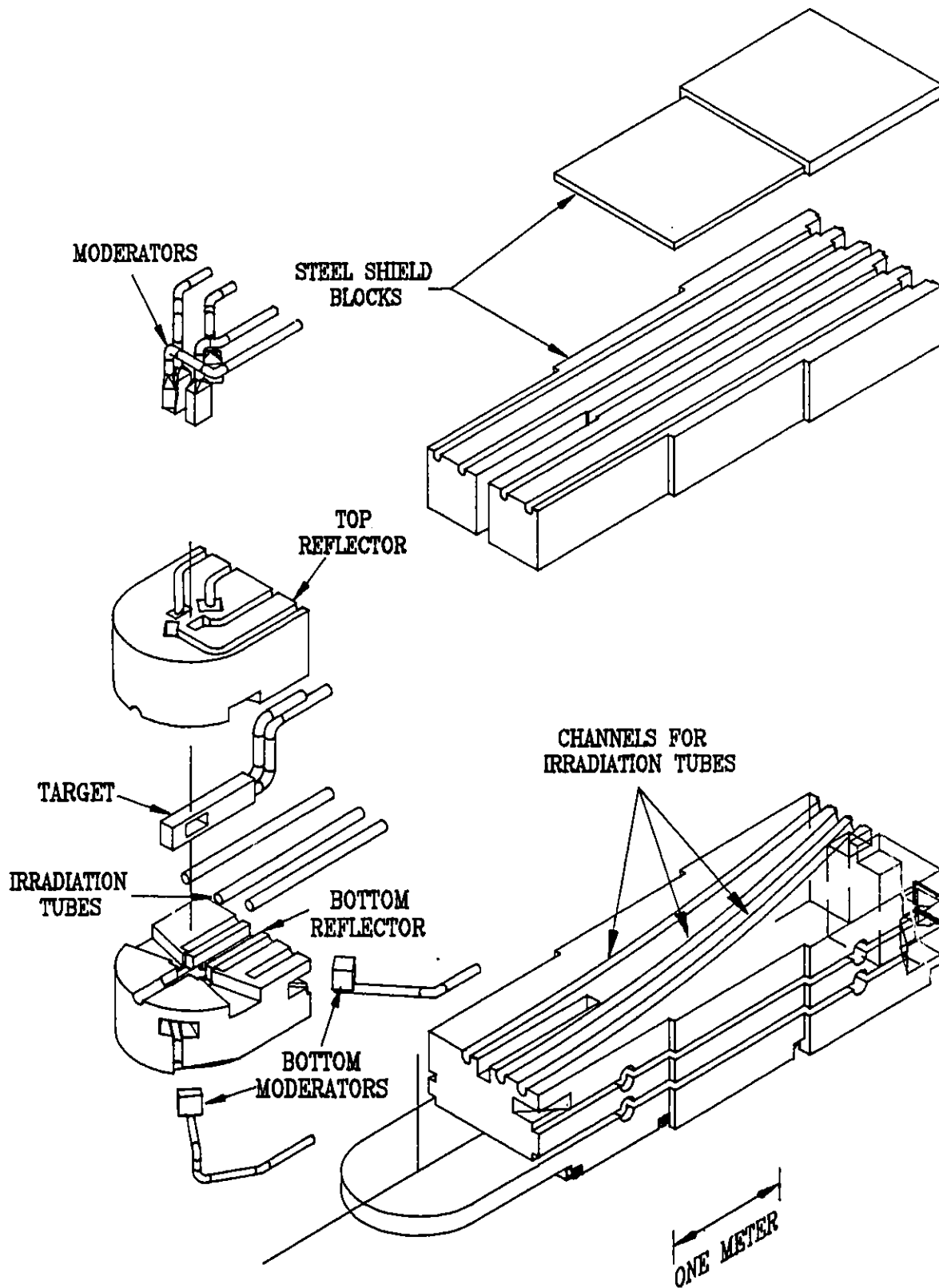
Figure IV.1.2-6 Exploded View of the Target-Train Assembly.
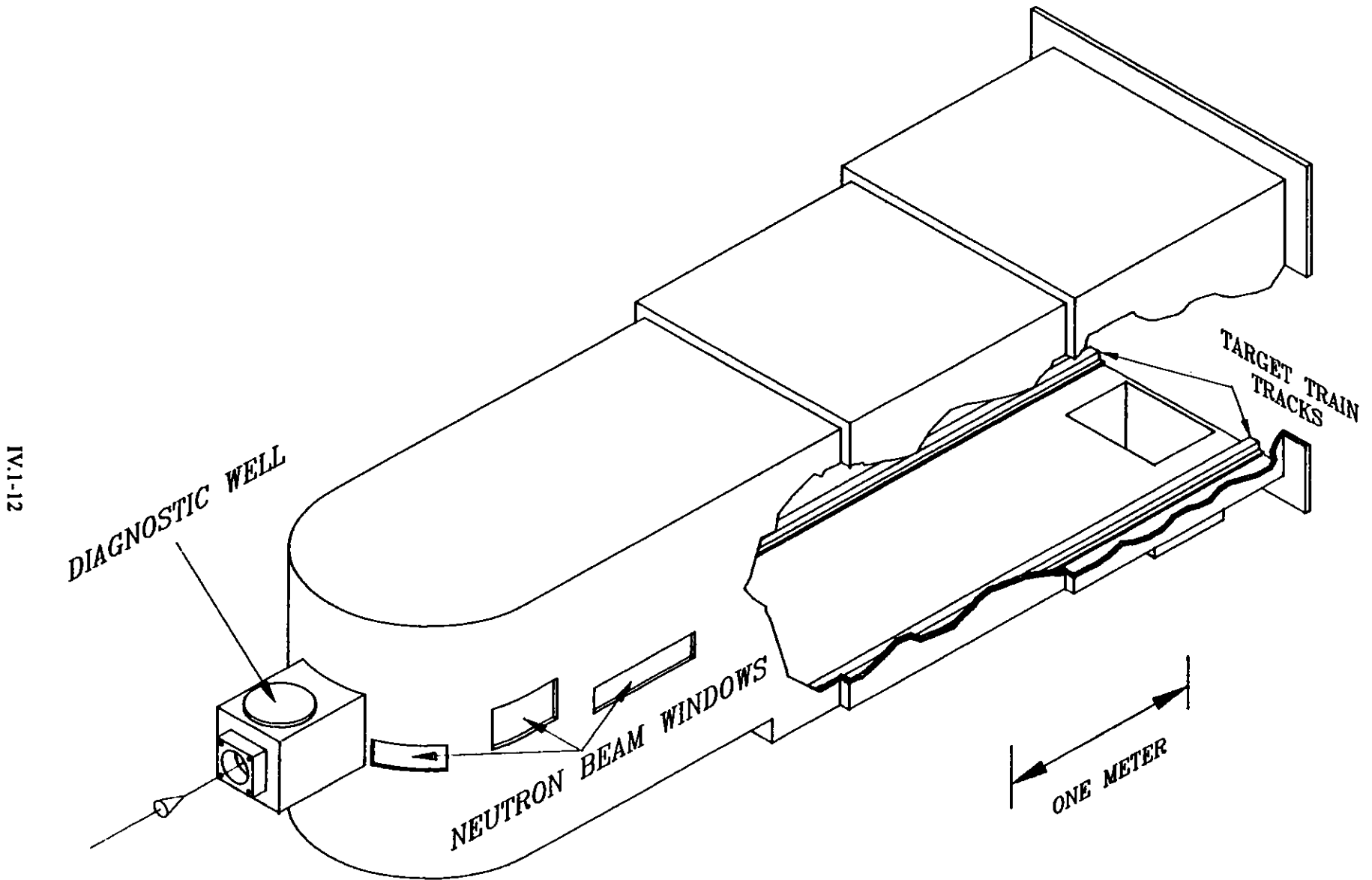
Figure IV.1.2-7 Sealed Target Tank into Which the Target Train Is Inserted for Operation. (Window sections are thinned to improve neutron beam transmission.).

BIOLOGICAL SHIELD

BASE TRACK

PLAN VIEW

0   1   2   3
METERS

TARGET, MODERATOR,
REFLECTOR ASSEMBLY

SEAL SHEET

PLUMBING
CAVITY

MOTORIZED SHIELD
BLOCK

TIE RODS

CARRIAGE

BASE TRACK

SIDE ELEVATION
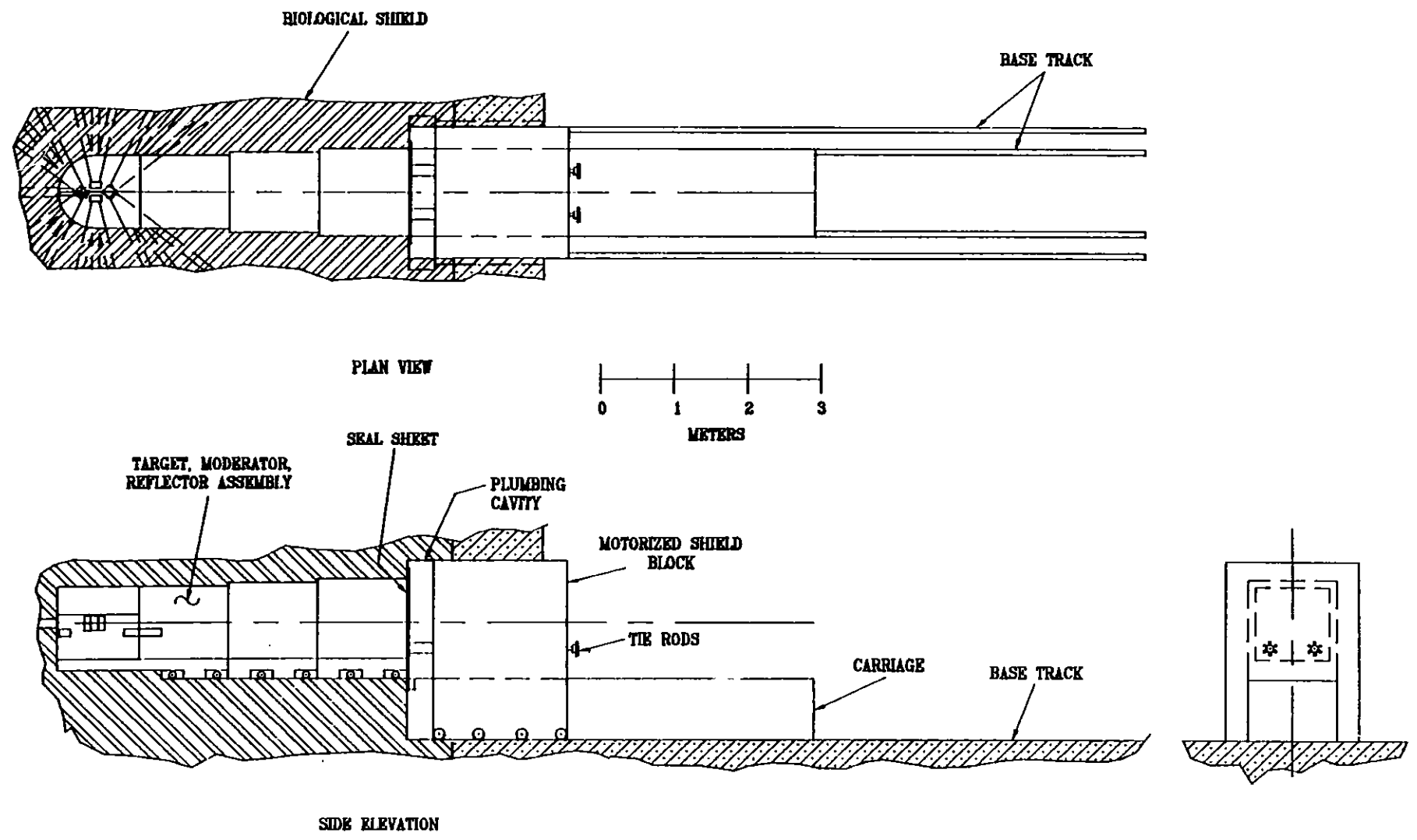
Figure IV.1.2-8a Target-Train Assembly Inserted into the Target Tank. (The rolling mechanism for extracting the target train is also shown.)

DIAGNOSTIC
WELL

TOP VIEW

PROTON
BEAM

ONE METER

VERTICAL SECTION
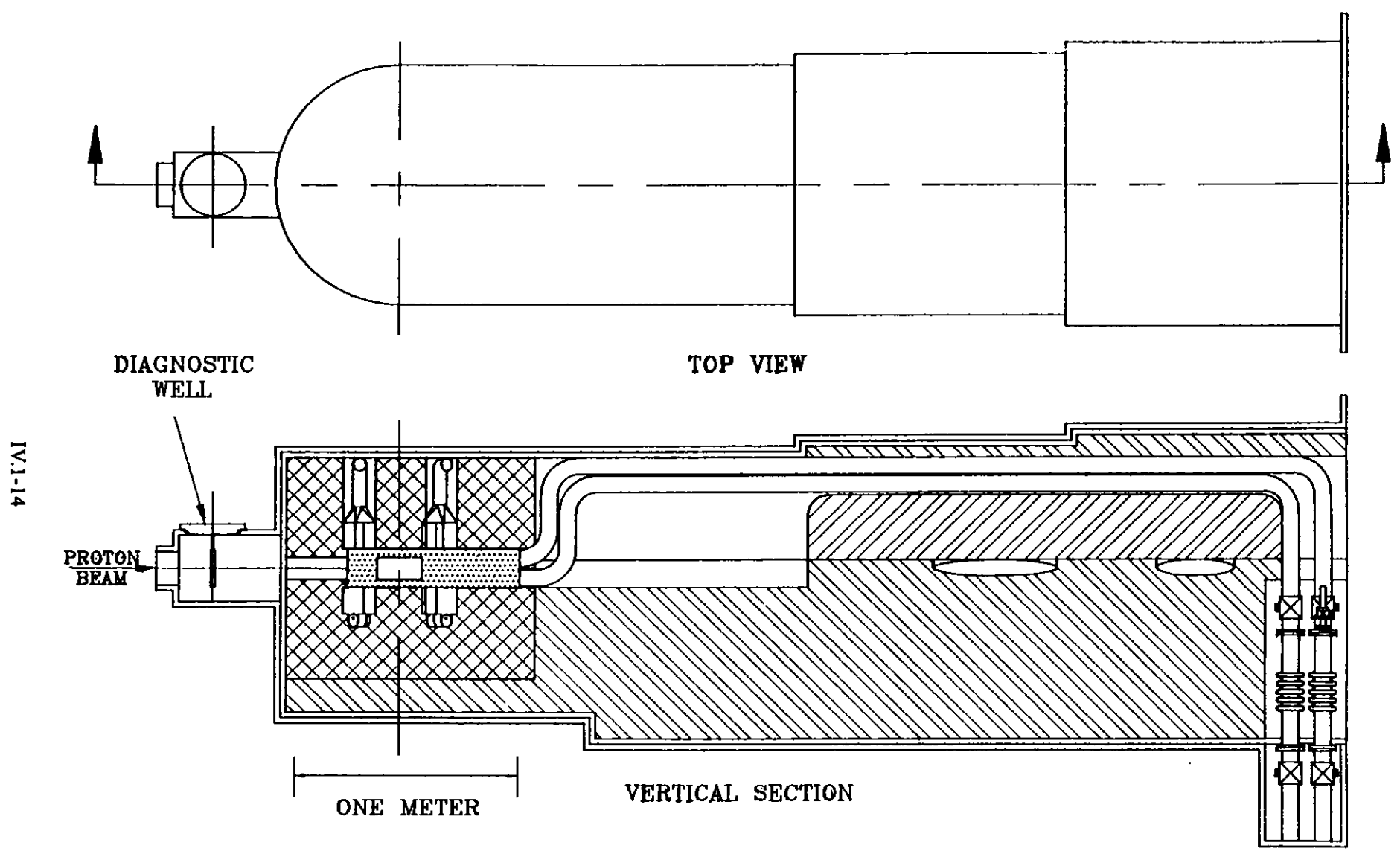
Figure IV.1.2-8b Target-Train Assembly Inserted into the Target Tank, Showing Internal Details.

SCALE

0   5   10   15

METERS

HOT CELL

BIOLOGICAL SHIELD
AND HOT CELL

BOTTOM OF BUILDING
TRUSS
10.9 m ABOVE FLOOR

BOTTOM OF 10-TON
CRANE HOOK
9.0 m

TOP OF SHIELDING
7.47 m

BOTTOM OF 35-TON
CRANE HOOK
7.65 m

A

A

FLOOR
LEVEL
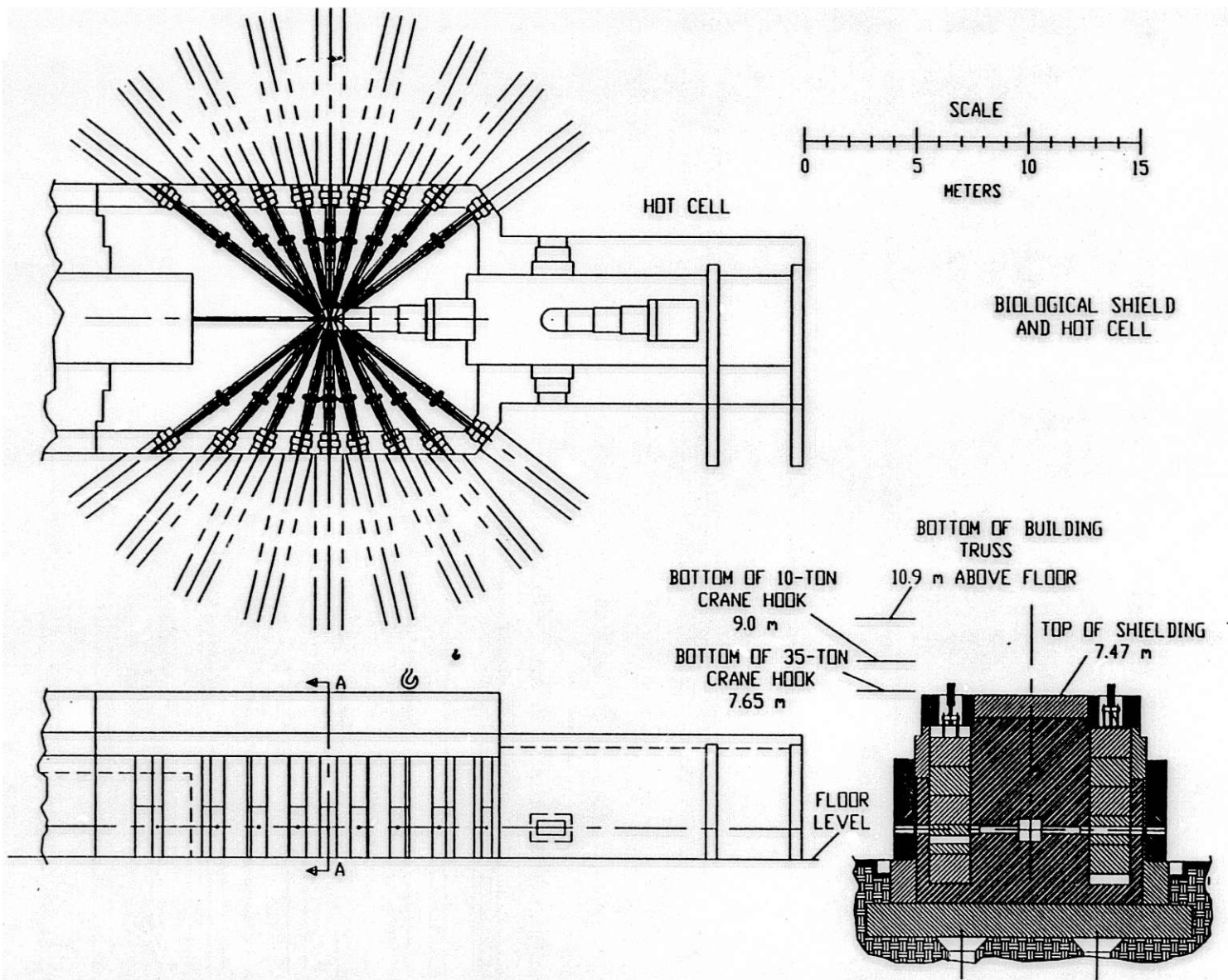
Figure IV.1.2-9 Plan, Elevation, and Cross-Sectional Views of the Biological Shield and Hot Cell.

The biological shield rests on a newly-constructed reinforced-concrete pad. The entire structure weighs about 14,000 metric tons and is supported by columns extending to bedrock 24 m below. This provides long-term stability. A service trench surrounds the biological shield.

Neutrons stream to the instruments through beam ports containing collimating elements or neutron guide tubes. Hydraulically operated gates that can be raised and lowered in guided channels can be closed to attenuate the neutron beams to such a level as to permit hands-on changing of samples in the instruments. The beam ports and beam gates are described in Section IV.8.

Protons from the accelerator system enter the biological shield from the HET line through a water-cooled, double-walled, vacuum-tight window, which is shown in Figure IV.1.2-10. This window provides the interface between the vacuum of the proton beamline and the helium atmosphere of the target tank. Coolant water circulates through the annulus between the tube walls, cooling both the beam pipe and the window. Helical guides separate the inlet and outlet flows. The window has a lifetime of several years,[4] so its design permits access and replacement. This proton beam port assembly also seals the helium atmospheres in the target tank and the shielding tank.

The proton beam port assembly passes through the shielding tank and extends to the target tank. A stainless-steel proton beam port tube, which has a circular cross section, is inserted in the opening and fastened by four threaded tie rods to the target tank. The insert tube has a series of square guides along its length to ensure alignment. The proton beam port tube is protected from the weight of the stacked steel shield by surrounding it with a steel tube with a square cross section. This steel tube is constructed of at least 1.25-cm-thick steel plate and is welded to the target tank housing and to a reinforced area on the shielding tank.

The proton beam port tube is sealed to the target tank with metal O-rings, making it part of the target tank containment barrier. O-rings and a flanged bellows mechanism seal the other end of this tube to the shielding tank, as shown in Figure IV.1.2-10. This provides a seal for the shielding tank atmosphere. The vacuum window insert is also sealed to the proton HET line vacuum chamber external to the shielding tank.

PROTON BEAM PORT TUBE

BIOLOGICAL SHIELD

TIE RODS

O-RING SEAL

TARGET TANK

GUIDES

PROTON BEAM PORT TUBE ASSEMBLY

5.93 m

WATER FLOW GUIDES

VACUUM WINDOW

PROTON HET LINE VACUUM WINDOW INSERT

VACUUM TUBE

ONE METER
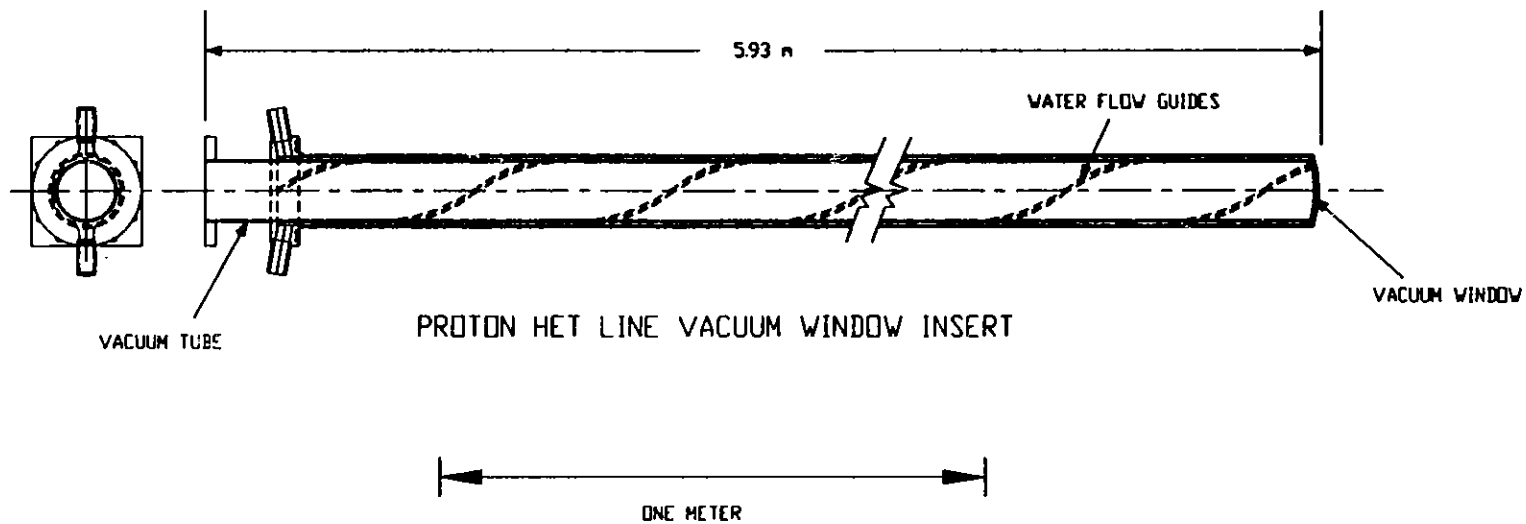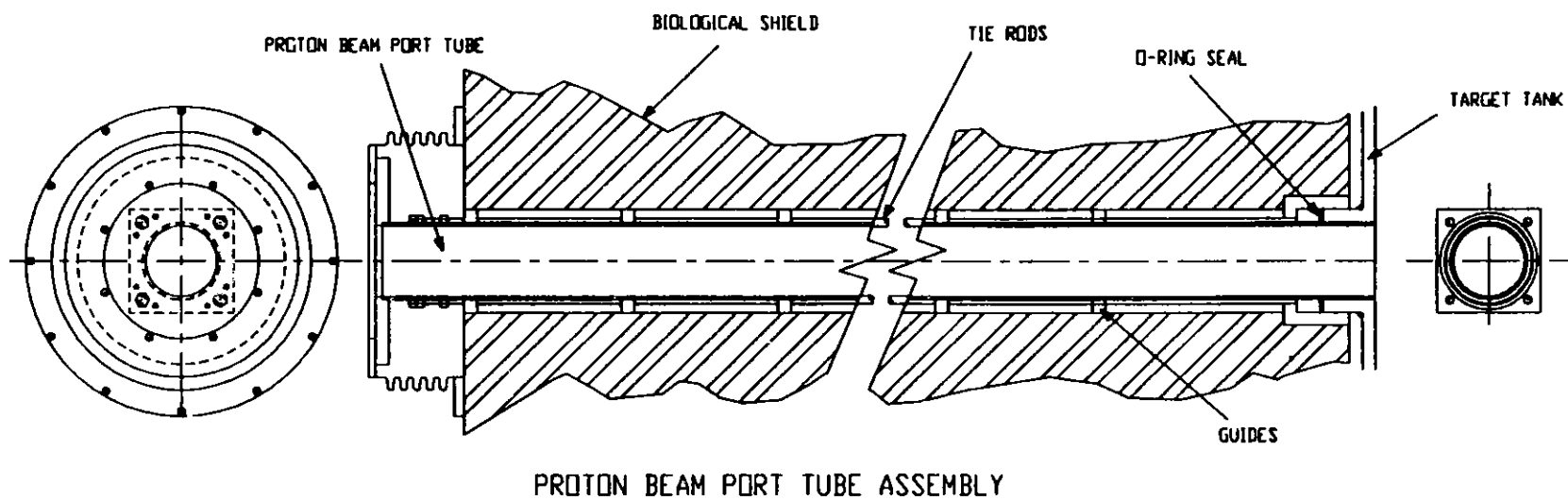
Figure IV.1.2-10 Proton Beam Port and Window Insert Assembly, Which Transports the Proton Beam through the Biological Shield to the Target.

1.3 REFERENCES

1. N. Watanabe, Y. Kiyanagi, K. Inoue, M. Furusaka, S. Ikeda, M. Arai, and H. Iwasa, "Preliminary optimization experiments of coupled liquid hydrogen moderator for KENS-II," in *Advanced Neutron Sources 1988,* Proceedings of the 10th Meeting of the International Collaboration on Advanced Neutron Sources (ICANS X*)* (Los Alamos, N.M., Oct. 3-7, 1988); IOP Conference Series, No. 97 (Institute of Physics, New York, 1989), pp. 787-797 (1989).

2. Y. Kiyanagi, N. Watanabe, and H. Iwasa, "Experimental studies on neutronic performance of coupled liquid-hydrogen moderator for pulsed spallation neutron sources," Nucl. Instrum. Methods **A312**:561-570 (1992).

3. A.A. Beljakov, V.G. Ermilov, V.L. Lomidze, V.V. Melichov, and E.P. Shabalin, "First experience of cold moderator operation and solid methane irradiation at the IBR-2 pulsed reactor," in *Proceedings of the 12th Meeting of the International Collaboration on Advanced Neutron Sources (ICANS XII)* (Abingdon, U.K., May 24-28, 1993), Rutherford Appleton Laboratory Report No. 94-025, pp. T144-T155 (1994).

4. G.S. Bauer, presented at the Workshop on Materials for Spallation Neutron Sources, Los Alamos, N.M., Feb. 6-10, 1995 (unpublished).

This section describes the target design and provides a detailed analysis of target performance and requirements. Section IV.2.1 gives an overview of the target geometry and of the selection of target material. Target geometry is determined by balancing the neutronic performance (Section IV.2.2) against the need to extract the deposited heat from the target. The relevant thermal-hydraulic analyses are presented in Section IV.2.3. The choice of target material depends on neutronic performance (Section IV.2.2), mechanical strength of the target relative to the induced stresses (Section IV.2.4), and the corrosion resistance and other nuclear and thermophysical properties of the material (Section IV.2.5).

Section IV.2.2 describes the Monte Carlo model used to calculate the detailed power deposition in the target and surroundings and to determine the neutronic output. The calculated power density distribution serves as input to the thermal-hydraulic calculations in Section IV.2.3. However, most of the discussion of neutronic performance is deferred until the moderators are discussed in Section IV.3.

Section IV.2.3 describes the thermal-hydraulic analyses related to the extraction of heat from the target. These analyses are used to refine the target geometry and to determine the target cooling capacity required. The target cooling system is discussed in Section IV.2.6. Section IV.2.4 presents analyses of the stresses induced in the target disks due to the temperature gradients calculated in Section IV.2.3.

The relevant materials properties data for candidate target materials are presented in Section IV.2.5. These data play an important role in the choice of target material, as discussed in Section IV.2.1.

Finally, Section IV.2.7 presents a brief discussion of potentially hazardous incidents. The preliminary assessments made here indicate no difficult safety-related problems. A detailed safety assessment will be performed once the project is underway.

2.1 TARGET GEOMETRY AND MATERIAL

Spallation neutron targets must be of a dense material with a high mass number in order to produce the greatest number of neutrons per proton in the spallation process. In addition, the material must have good thermal and corrosion properties, and it must be mechanically robust, easy to fabricate, and resistant to radiation damage. Targets made of tungsten,[1] tantalum,[2] depleted uranium,[3-5] and enriched uranium[6] have all seen extensive operation in pulsed neutron sources, and such other materials as lead, gold, and platinum are also candidates. The numbers of spallation neutrons produced per proton differ by only a small amount among all these materials. However, in the case of depleted uranium, additional neutrons are produced by fast-neutron-induced fissions, leading to an overall gain of a factor of ~1.7 over the nonfissioning target materials. Enriched-uranium targets operated as subcritical "boosters" can provide a considerably greater fission gain.

A large fraction of the proton beam energy is deposited in the target via the spallation process in nonfissioning targets. This spallation energy deposition is also present in fissioning targets, but in these targets a large amount of energy is deposited by the fission process as well. Fission is a much less efficient process for the production of neutrons than is spallation, so the energy deposition per neutron produced is much greater in the fissioning targets than in the spallation-only targets. In the case of an enriched-uranium target, most of the neutrons are produced by fission, and heat removal becomes a major problem.

Because of heat-removal and materials-property problems, the use of an enriched-uranium target does not appear practical at the beam power levels of IPNS Upgrade. Depleted uranium is probably practical, but it must be clad in order to contain the fission products and to prevent corrosion. Fabrication difficulties, lifetime problems due to radiation damage, and problems in heat removal make this a very difficult material for use at the power levels being considered here.[2] However, the gain of 1.7 is attractive, making it worthwhile to continue to investigate the possibility of using depleted-uranium targets at IPNS Upgrade. Experience at IPNS and ISIS with both depleted and enriched uranium targets, α-phase Springfield alloy clad with zircaloy, indicates that these fail as a result of anisotropic growth due to irradiation and thermal cycling. Efforts are under way at both facilities to improve uranium target metallurgical design, but experience so far indicates that uranium targets cannot yet be counted upon to serve in 1-MW facilities.

Both tantalum-based and tungsten-based alloys were considered for the IPNS Upgrade targets. Assessment of the consequences of a Loss of Coolant Accident (LOCA) discussed in Section IV.2.7.1 indicated that the tantalum target temperature rose to very high values, short of melting but still potentially damaging to the surroundings. We also found that the afterheat in tungsten is much smaller than in tantalum (Section IV.2.2.4), so that LOCA temperatures are much lower. Moreover, we learned of recent Russian work[7] in which plasma-sprayed titanium coatings on tungsten have been tested for corrosion resistance in an irradiated water environment and found to have very low corrosion rates. The combination of low afterheat and prospects for low corrosion rates led us to choose tungsten rather than tantalum. The neutronic calculations for tantalum apply with sufficient accuracy to tungsten as well, because densities and mass numbers of tantalum and tungsten are nearly identical. Therefore we have not repeated the calculations of neutron or power density distributions for tungsten.

A major problem in target design is the removal of heat from the target. Most pulsed spallation neutron source targets operated to date have utilized a "plate" design, with plates of target material oriented perpendicular to the beam and separated by thin coolant channels. Water (heavy water at ISIS) is used as the coolant in all such systems operated so far. This technology is well developed and understood. The analyses in the following sections indicate that this technology can be readily extended to the power levels at IPNS Upgrade, so this is the selected target geometry.

Russell[1] developed the innovative idea of using a split target to provide a "flux-trap" gap along the proton beam axis between the two portions of the target. This creates a neutronically favorable position for the location of the flux trap moderators, avoiding a direct view of the

target. It also extends the effective length of the target providing good positions for additional wing-geometry moderators. For these reasons, a split-target design is selected for the IPNS Upgrade targets.

The IPNS Upgrade target design consists of an upstream target section, the first struck by the proton beam, ~10 cm in length and a downstream target section ~30 cm in length mounted in the same housing (see Figure IV.1.2-3). Each of these target sections consists of stacks of disks of machinable tungsten. The disk shape provides for mechanical support of the disks and good target-moderator neutronic coupling. Figures IV.2.1-1 and IV.2.1-2 show details of the upstream and downstream sections of the target. Disk thicknesses increase from the upstream to the downstream end of each target section. The thicknesses are determined by cooling requirements and stress limitations (Sections IV.2.3 and IV.2.4). Cooling water flows through the 0.159-cm-thick gaps between the disks and between the end disks and the target housing windows. Plena above and below the disks direct the cooling water to these gaps. In both target sections, the disk assemblies are spring-loaded in order to maintain this spacing and to compensate for expansion and contraction.

The two target sections are cooled by water in the common plena, reducing the external plumbing requirements and simplifying target replacement. Figure IV.1.2-4 shows the relative locations of the target, moderators, and their associated coolant pipes. Six different moderators are located in neutronically favorable positions, as shown in Figure IV.1.2-2, providing great flexibility in the selection of moderators to meet the requirements of the individual neutron scattering instruments. This arrangement also provides several locations for irradiation tubes close to the target, as shown in Figure IV.1.2-6. The two target stations are identical, although the choices of moderator materials will be different in the two cases.

2.2 NEUTRONICS AND HEAT GENERATION

2.2.1 Calculational Model

A Monte Carlo computing model was set up for the calculation of neutron beam characteristics and thermal power generation in the target system and its surroundings. The Los Alamos High Energy Transport (LAHET) code system[8] was chosen for the calculations after an extensive search. The LAHET code system consists of a LANL version of the High Energy Transport Code (HETC) and the Monte Carlo code for Neutron and Photon transport (MCNP), with a few other associated codes. HETC calculates and transports high-energy particle cascades, including neutrons with energies above 20 MeV. The Bertini model was used for the intranuclear cascade calculation in HETC, as it is generally recognized to be acceptable up to a particle energy of 3.5 GeV. MCNP is used to calculate the transport of neutrons below 20 MeV and of photons. For the photon cascade calculation, a hybrid model between the Troubetzkoy (E1) model and the spin-dependent model were used to provide the photon source distribution for MCNP.

TYPICAL DISK

CM
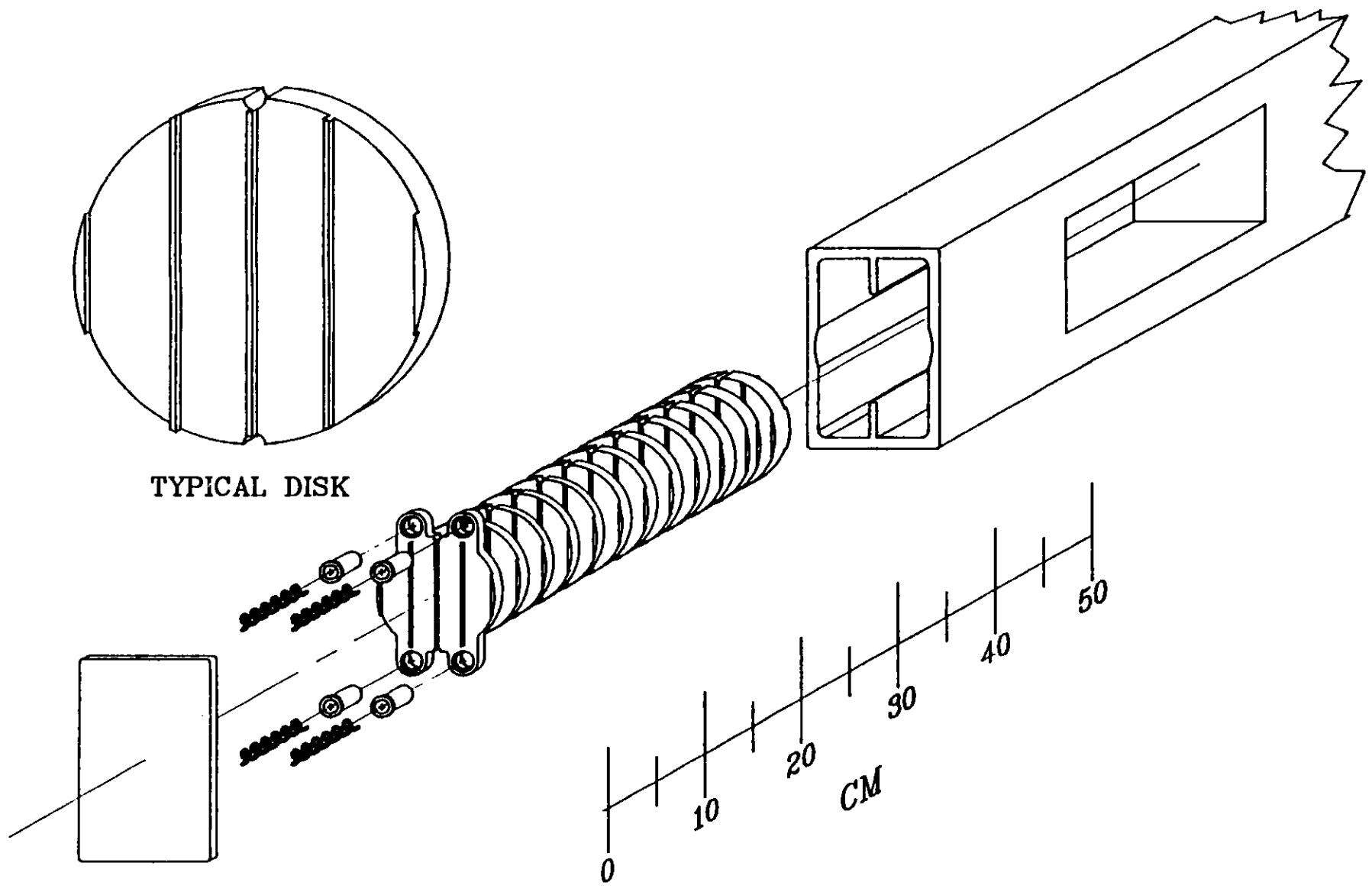
Figure IV.2.1-1 Exploded View of the Upstream Target Section. (The disk thicknesses shown are schematic. Actual disk thicknesses are discussed in Section IV.2.3.)
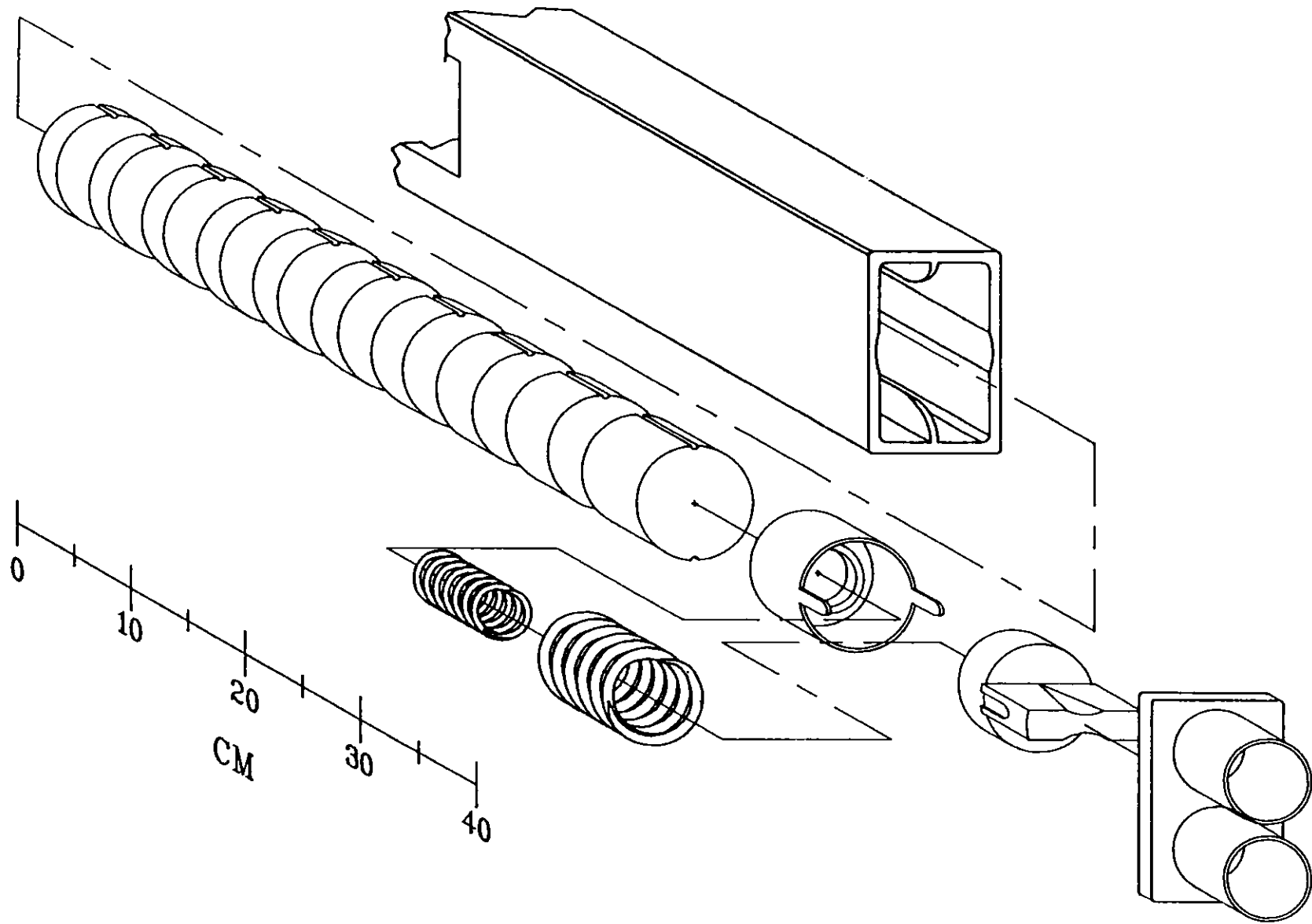
Figure IV.2.1-2 Exploded View of the Downstream Target Section. (The disk thicknesses shown are schematic. Actual disk thicknesses are discussed in Section IV.2.3.)

A validation of the LAHET code system and physical model was performed upon the installation of the code system. For this validation, a simple model consisting of a cylindrical target surrounded by a beryllium reflector was used. Figure IV.2.2-1 shows the calculated ratio of energy deposition in the target to the proton beam energy. The calculation was performed with tantalum and compared to other published results.[9] Figure IV.2.2-1 confirms the validity of the LAHET code system and physical models used in the calculation. Figure IV.2.2-2 shows that the neutron production rate in the tantalum target is a little higher than that in a lead target.[10]

The LAHET code system uses a combinatorial surface geometry in which a system configuration is represented in terms of combinations of quadratic surfaces. The IPNS Upgrade target system model includes targets, moderators, neutron beamlines, and associated reflector and shield. Geometrical and material features of key components are listed in Table IV.2.2-1. In order to simplify the computational model, the shield has been truncated at a radius of 1 m from the target. This has no significant effect on the results for the target, moderator, and reflector regions. An isometric view of the modeled target station is shown in Figure IV.2.2-3, and in Figure IV.2.2-4 a plan view of the system is shown to illustrate the neutron beamlines. There are three neutron beamlines from each moderator, for a total of 18 beamlines in the target station. Figure IV.2.2-5 provides a detailed view of the target and moderator model and indicates the labels used to designate the six moderators. Figures IV.2.2-6 through IV.2.2-8 show the dimensions of the major components: Figure IV.2.2-6, the shield and reflector; Figure IV.2.2-7, the details of targets; and Figure IV.2.2-8, the details of moderators and the arrangement of neutron beamlines. As seen in Figure IV.2.2-8, the boron decoupler covers each neutron beamline in the reflector region and surrounds each moderator, except on the viewed surface. For most of the calculations, the model illustrated in Figures IV.2.2-3 through IV.2.2-8 was used. In some cases, slight modifications were made to this model; these modifications are described with the corresponding calculations.

The modeled system is somewhat simpler than the actual design of the target station. For instance, irradiation facilities and coolant pipes for moderators are not included in the model. However, the model is sufficiently accurate to provide the necessary parameters for the engineering design, such as heat deposition in the system and neutron beam characteristics from the moderators.

All calculations are based on a 2.2-GeV proton beam with a Gaussian distribution of 5 cm full width at half maximum (fwhm) diameter and truncated at 10 cm diameter. The calculated results presented in subsequent sections are normalized results based on a 1-MW proton beam, unless otherwise noted.

2.2.2 Heat Deposition in the Target and Surroundings

The power deposited in the target and surroundings is summarized in Table IV.2.2-2. About 90% of the proton beam power is deposited in the modeled system. The remaining 10%
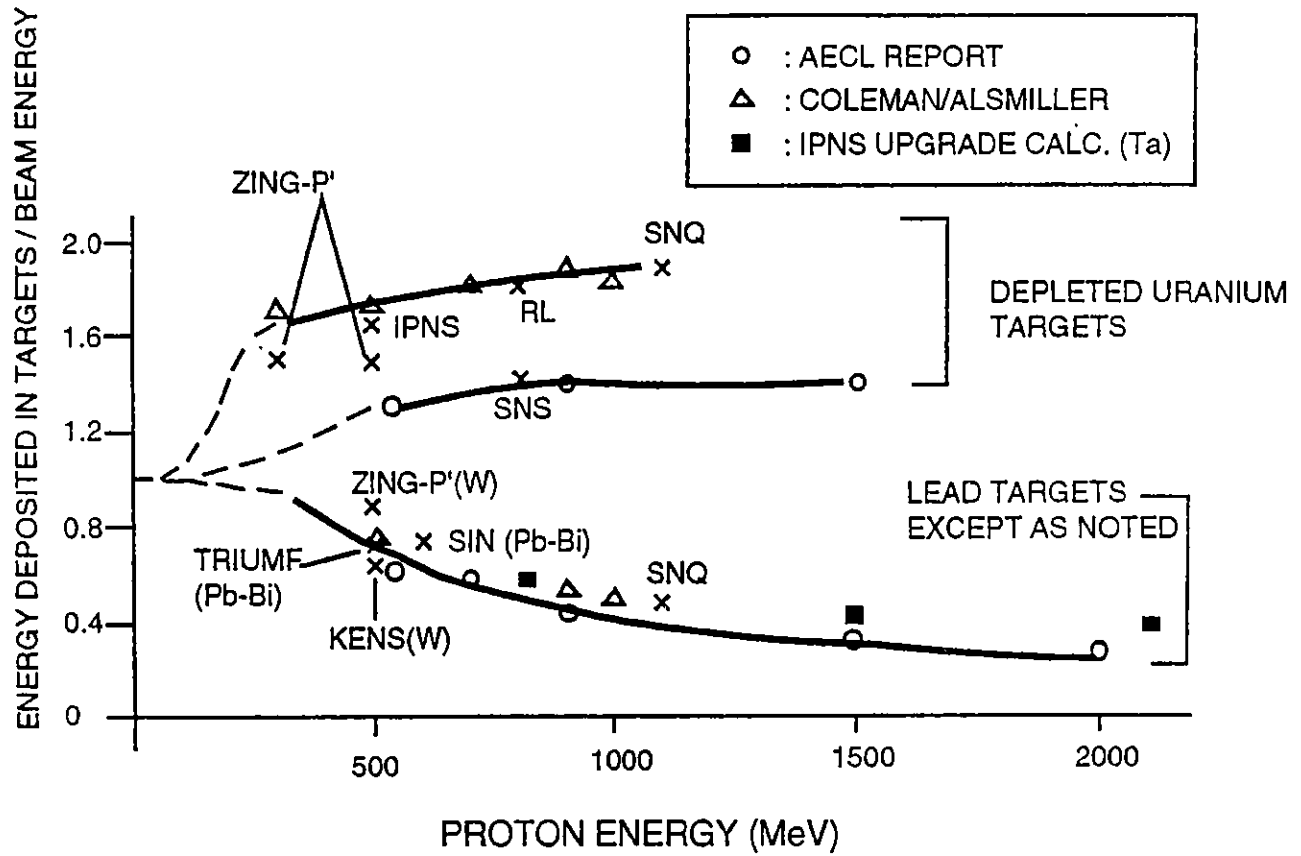
Figure IV.2.2-1 Validation of IPNS Upgrade Calculational Model for Heat Deposition in Targets. (Present calculations are compared with previous computed and experimental results. Legend: X, measured values for sources and targets indicated; O, AECL report; Δ, Coleman/Alsmiller; ■, present IPNS Upgrade calculations for Ta.) (Source: Reference 9).
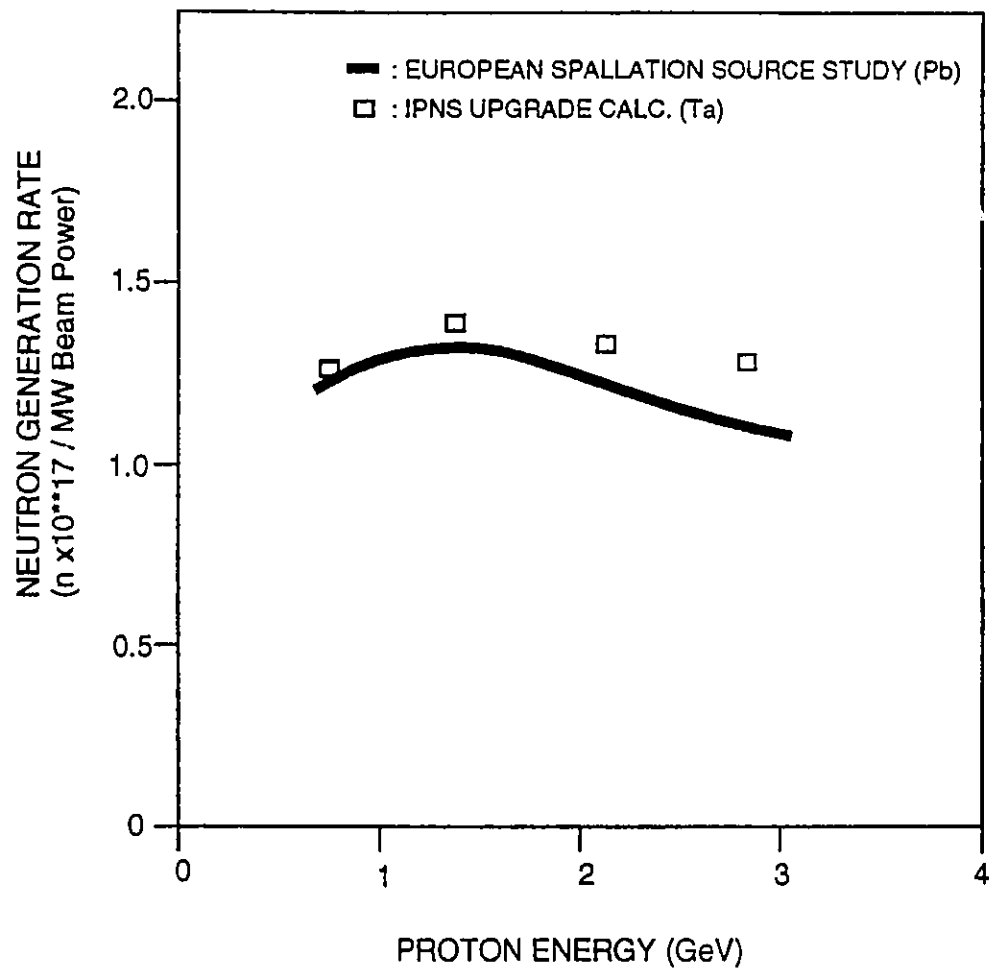
Figure IV.2.2-2 Validation of IPNS Upgrade Calculational Model for Neutron Generation Rate. (Present calculations are compared with previous computed results. Legend: —, European Spallation Source study [Pb]; □, IPNS Upgrade calculations for Ta.) (Source: Reference 10).

Table IV.2.2-1 Geometrical and Material Features of the Target Station Model

Component	Geometry and Dimensions[a]	Material
Target	Two split targets with a flux-trap region in-between	Tantalum
Upstream section	four elliptical disks with semiaxes of 5.5 and 7.5 cm, thickness 2.5 cm	
Downstream section	nine elliptical disks with semiaxes of 5.5 and 7.5 cm, thickness 3.5 cm	
Housing	Rectangle with rounded side surfaces	0.5-cm-thick stainless steel
Upstream section	18 cm wide, 12 cm high, 12 cm long	
Downstream section	18 cm wide, 12 cm high, 40 cm long	
Flux Trap	The 18-cm-long section between the housings	Vacuum
Coolant	Coolant channel gap size between target disks: 0.2 cm	Water
Moderator		Water
Upstream moderators (top and bottom)	5 cm thick, 10 cm wide, 10 cm high	
Flux-trap moderators (left and right)	5 cm thick, 10 cm wide, 20 cm high	
Downstream moderators (top and bottom)	10 cm thick, 10 cm wide, 10 cm high	
Boron Decoupler	2-cm-thick cladding surrounding moderators and neutron beamlines, except the beamline face	20% ^{10}B and 80% ^{11}B with 3.3% of natural boron density[b]
Reflector	Cylinder of 54 cm radius, 100 cm height	Beryllium
Shield	Annulus of 54 cm inner radius, 100 cm outer radius, 100 cm height	Iron

[a] See Figures IV.2.2-3 through IV.2.2-7.

[b] This boron density is based on the neutron decoupling energy of 1.0 eV for 1/e reduction of neutron flux across the decoupler.
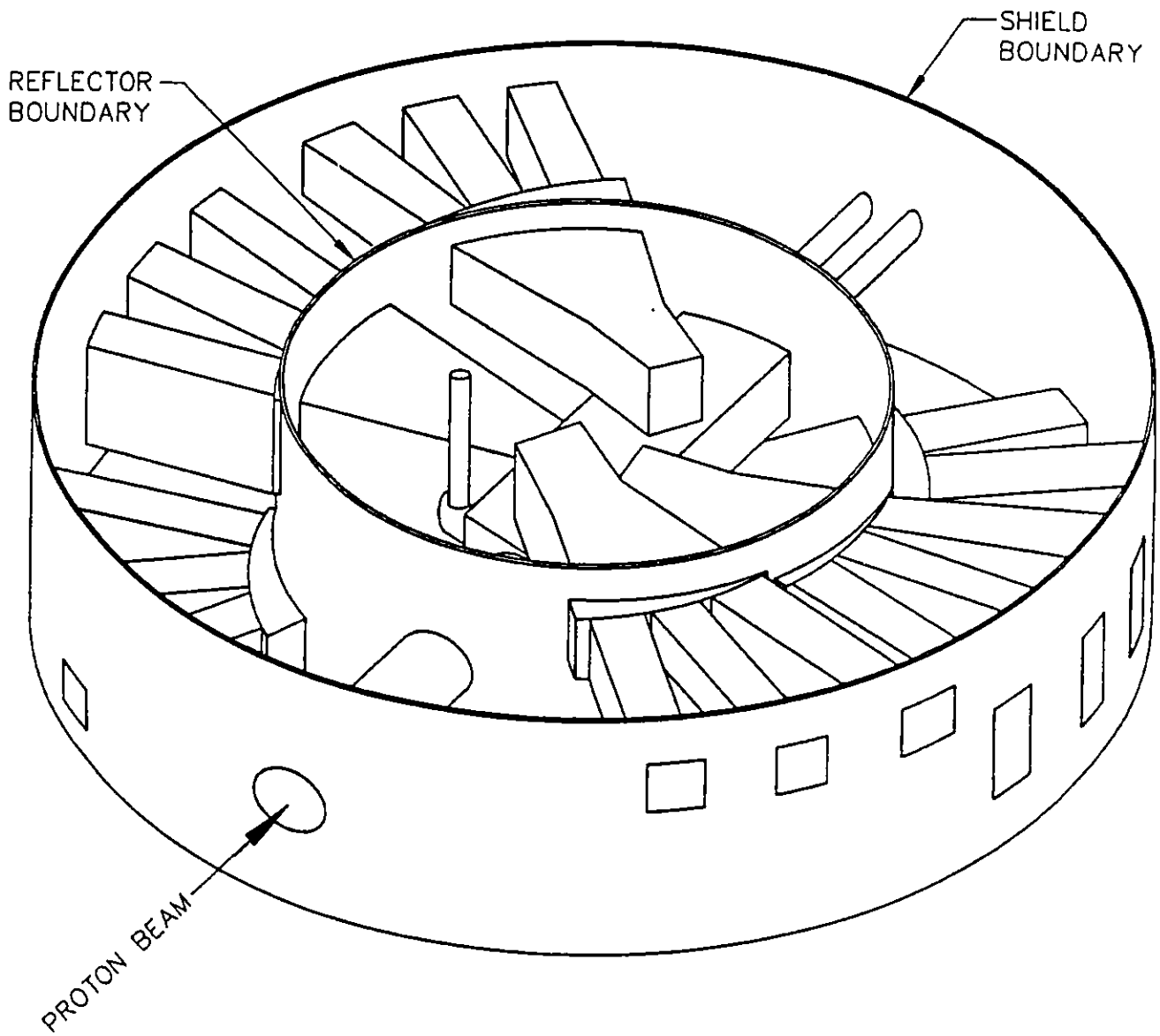
Figure IV.2.2-3 Isometric View of the Target Station Model.
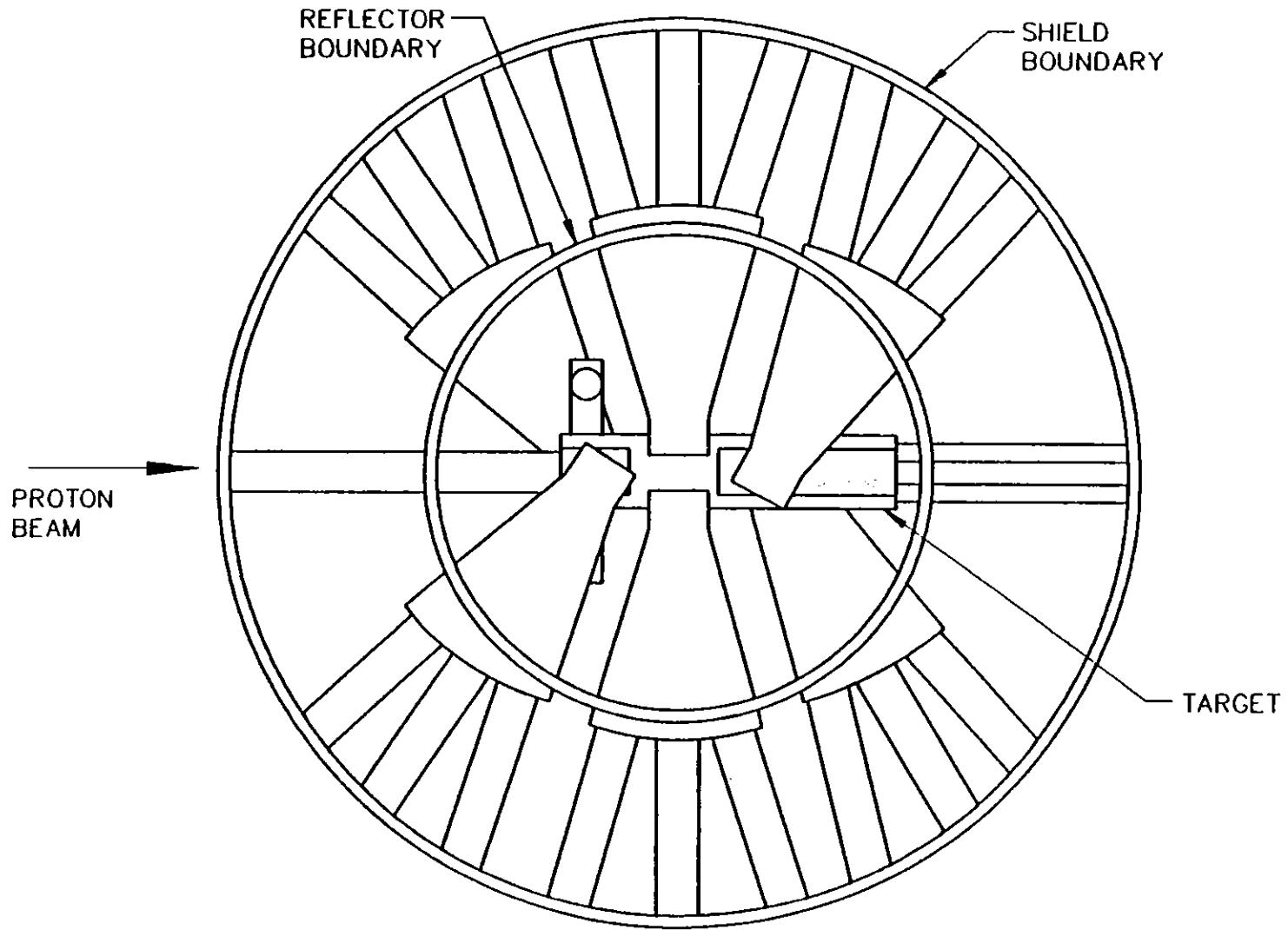
Figure IV.2.2-4 Plan View of the Modeled Target Station.
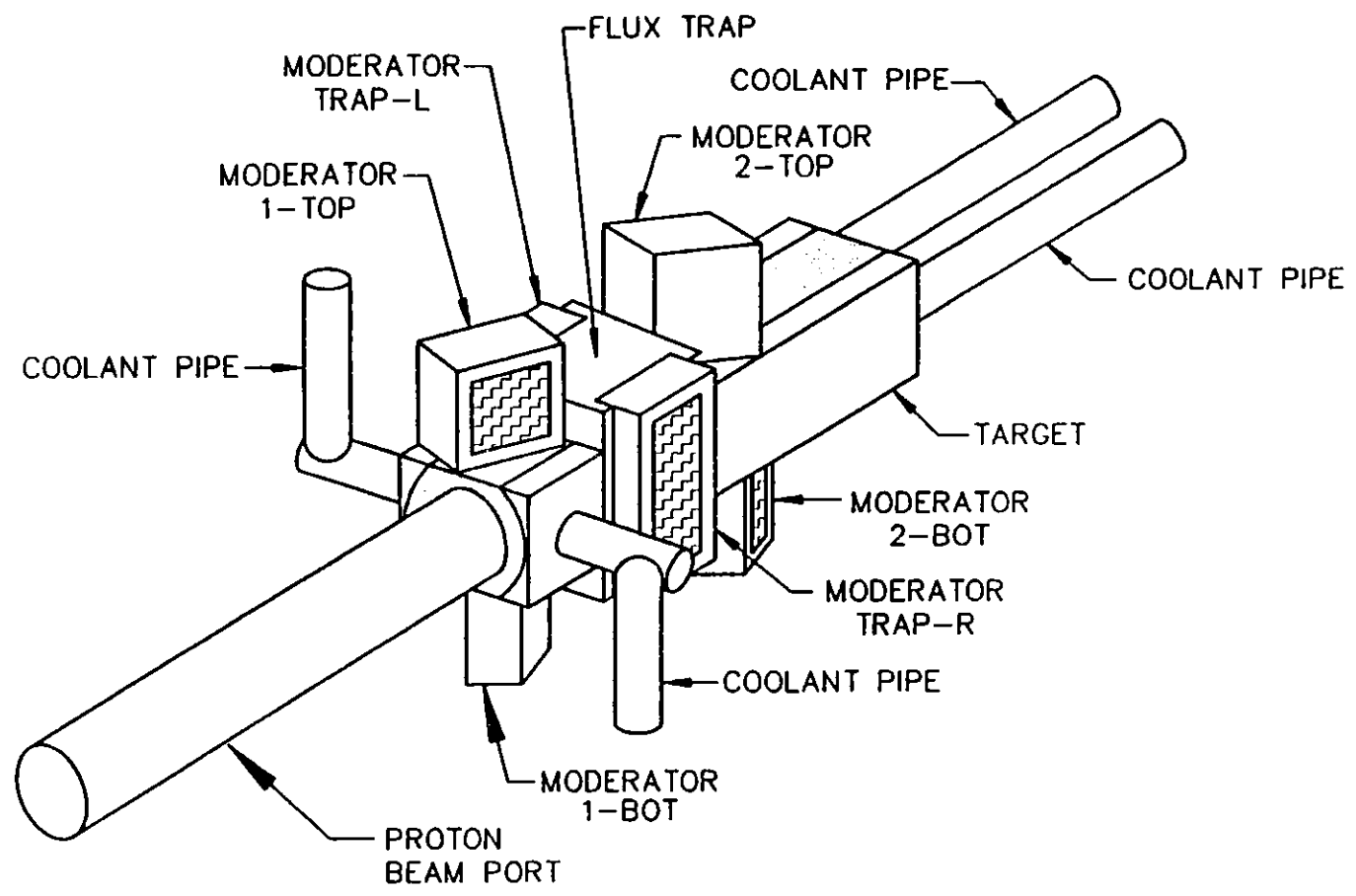
Figure IV.2.2-5 Isometric View of the Modeled Target and Moderator Arrangement.
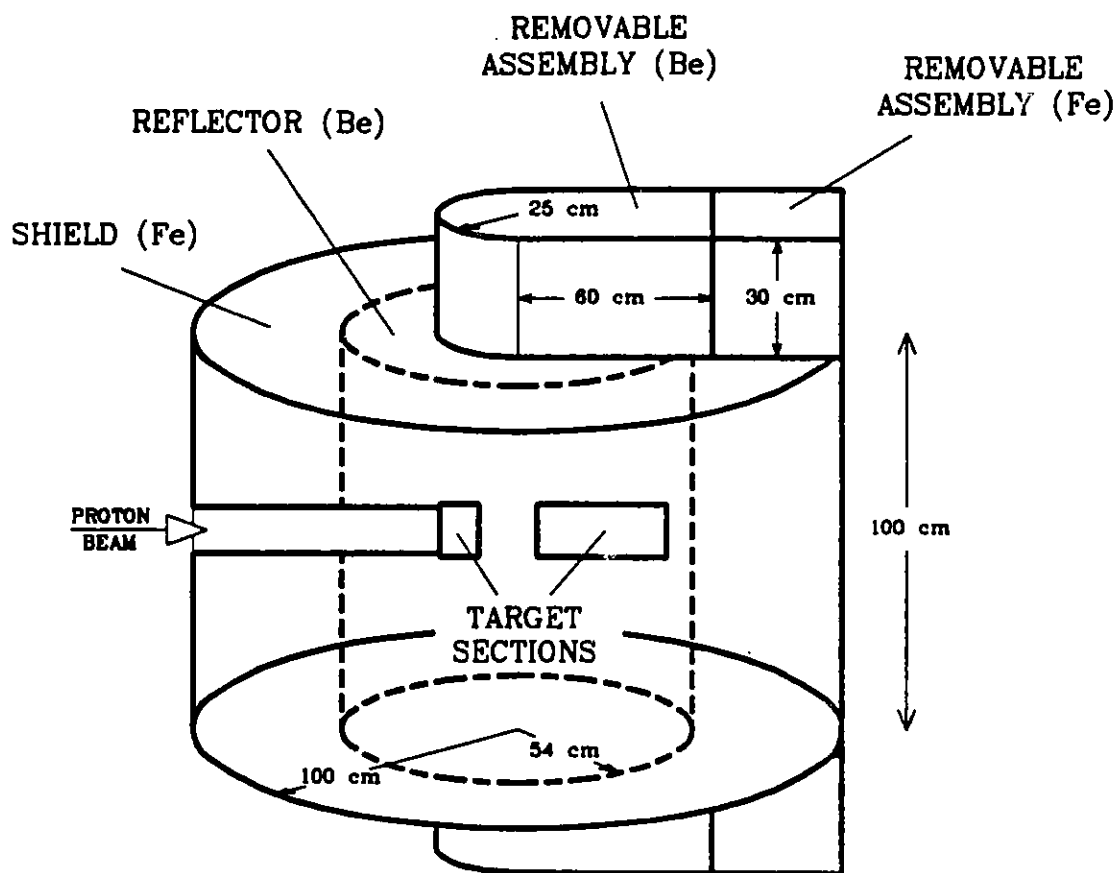
Figure IV.2.2-6 Modeled Configurations of the Reflector and Shield.
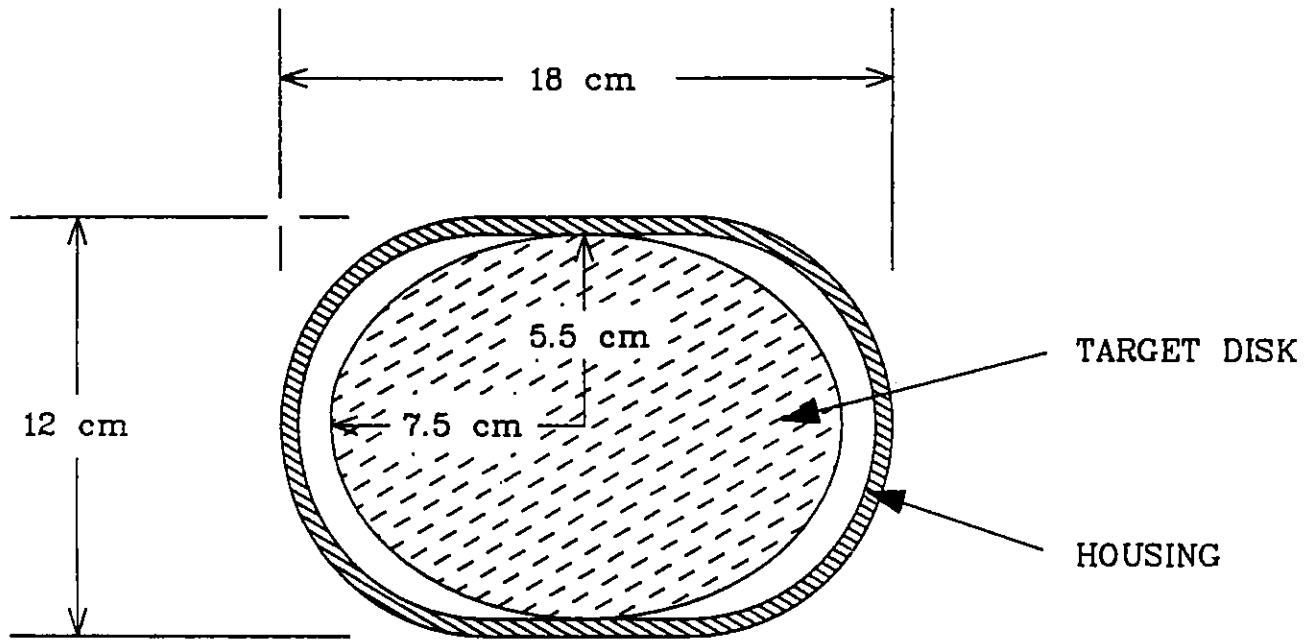
Figure IV.2.2-7 Cross Section of the Modeled Target Sections. (The target sections are modeled as a smaller number of thicker disks than is the actual case, in order to reduce computational time.)
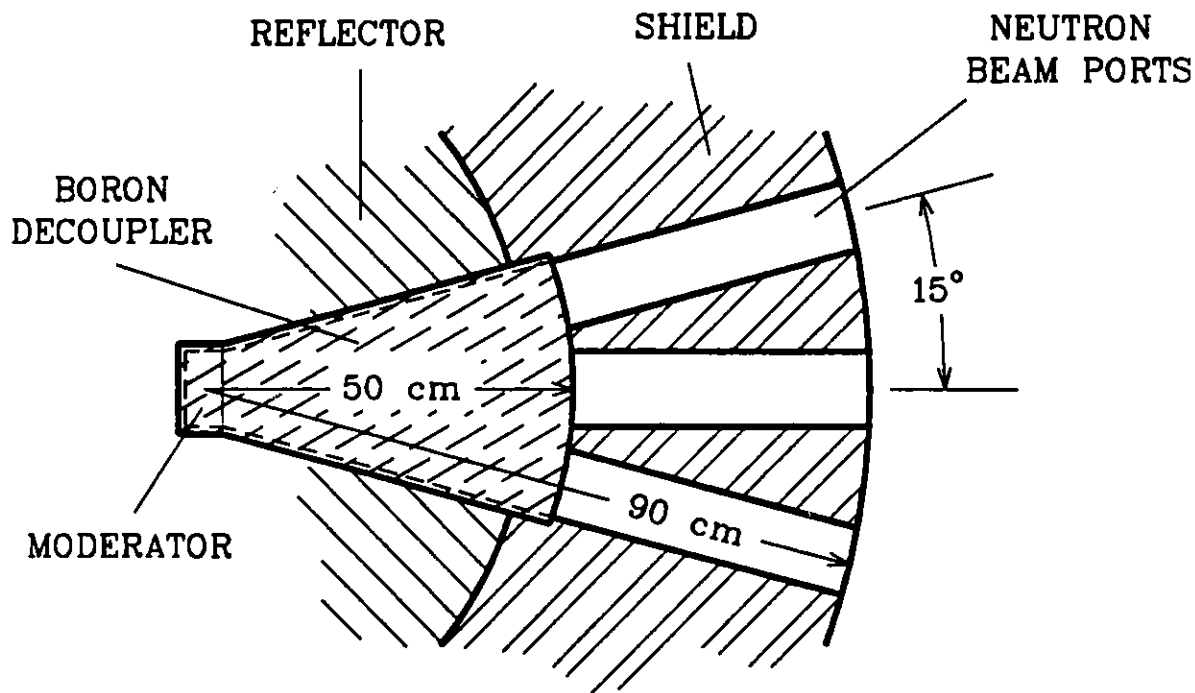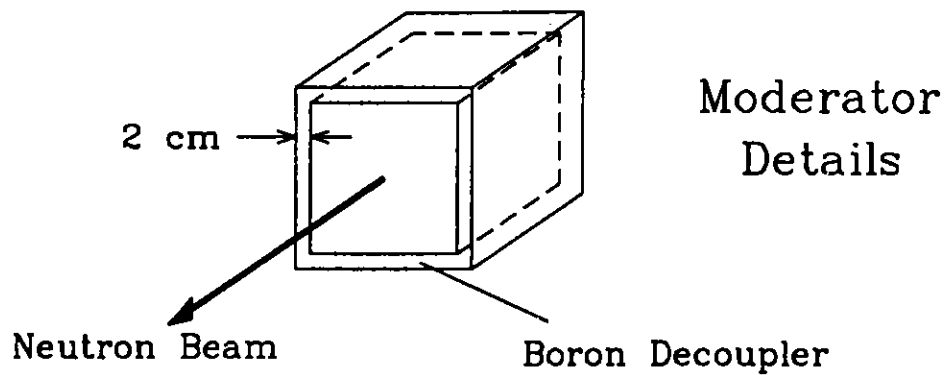
Figure IV.2.2-8 Modeled Configurations of Moderators and Neutron Beamlines. (Moderators are all 10 cm wide. Flux-trap moderators are 20 cm tall; others are 10 cm tall. Downstream moderators are 10 cm deep; others are 5 cm deep.)

Table IV.2.2-2 Power Deposition in the Target Station for Proton Beam
Power of 1 MW

| | Power Deposition (kW) | |
Component	Subcomponent	Total
Target	-	550.8
Coolant	-	21.0
Structure Total	-	34.2
Window	9.40	
Upstream housing downstream plug	6.62	
Downstream housing upstream plug	4.49	
Downstream housing downstream plug	0.45	
Upstream housing	1.91	
Downstream housing	6.69	
Spring	4.66	
Moderator Total		7.6
Upstream top moderator	0.78	
Upstream bottom moderator	0.77	
Flux-trap moderator - 1	1.52	
Flux-trap moderator - 2	1.50	
Downstream top moderator	1.58	
Downstream bottom moderator	1.48	
Boron Decoupler		26.7
Reflector Total		126.6
Upstream	29.75	
Middle	28.12	
Downstream	68.75	
Shield Total		128.0
Upstream	17.02	
Middle	10.28	
Downstream	100.72	
Removable Assembly		7.0
Target Station Total		902.0

either is in the form of binding energy resulting from the change of isotope composition during the cascade process or escapes through neutron and photon leakage. For instance, the number of neutrons escaping from the system in the model is about 9.7 neutrons per proton. If 8 MeV is assumed for the neutron separation energy, this leakage constitutes about 35 kW per MW of beam power. The overall energy balance is satisfied in the calculation.

About 55% of the proton beam power is deposited in the target, as is indicated in Table IV.2.2-2. Table IV.2.2-3 and Figure IV.2.2-9 show the distribution of heat deposition, both in terms of total power and of power density, in each target disk along the proton beam direction. Table IV.2.2-4 indicates the radial distribution of power density and provides a fitted function that represents the radial power density in each of the four modeled disks in the upstream target section. Figure IV.2.2-10 illustrates the change in radial power density along the target axis. As expected, with increasing depth the profile flattens as a result of the spreading of the particle cascades and the widening of the proton beam due to collisions.

Figure IV.2.2-11 illustrates the spatial distribution of heat deposited in the shield and reflector, showing the total power in each modeled segment. The volumes of the upstream and downstream segments of the reflector are the same, while the middle segments are much smaller. The segmentation of the shield is similar to that of the reflector. Figure IV.2.2-11 indicates that the power deposited in the downstream segments of both shield and reflector is much greater than in the upstream segments. This difference arises because protons are still energetic even at the downstream end of the target (see Table IV.2.2-3) and the neutron distribution is forward-directed. Negligible differences exist in power depositions in symmetrically-located moderator pairs (e.g., top and bottom upstream moderators), or in symmetric segments of the reflector or shield. These internal consistencies also confirm the soundness of the geometrical model used in the calculation.

2.2.3 High-Energy Neutron Distribution around the Target

To provide a basis for the shield design and to aid in understanding the power distribution in the reflector and shield shown in Figure IV.2.2-11, a simple calculation for the distribution of high-energy (> 20 MeV) neutrons around the target was performed. The much-simplified model used for this calculation includes a cylinder of tantalum having approximately the same dimensions as the actual target and a 3-m-radius evacuated sphere for tallying the neutrons. This model is sufficient for the calculation of the angular distribution of high-energy neutrons around the target, because these high-energy neutrons penetrate the reflector and shield and dominate the shielding requirements. The angular distribution of the high-energy neutrons is depicted in Figure IV.2.2-12, along with a schematic of the model. The neutron spectra are shown in Figure IV.2.2-13. Figure IV.2.2-12 shows that the total angular yield is forward-directed. The neutron spectrum is much harder (shifted to higher energies) in the forward direction, as shown in Figure IV.2.2-13. This anisotropic, forward-directed distribution of high-energy neutrons is due to the relatively high proton beam energy of 2.2 GeV.

Table IV.2.2-3 Power Distribution in the Target Sections for Proton
Beam Power of 1 MW

Modeled Target Disk[a]	Total Power (kW)	Power Density (kW/cm^3)
Upstream Target Section[b]		
Disk 1	88.5	0.273
Disk 2	83.9	0.259
Disk 3	72.0	0.222
Disk 4	62.2	0.192
Downstream Target Section[c]		
Disk 1	53.8	0.119
Disk 2	47.4	0.105
Disk 3	38.7	0.085
Disk 4	29.9	0.066
Disk 5	23.7	0.052
Disk 6	18.5	0.041
Disk 7	13.9	0.031
Disk 8	10.5	0.023
Disk 9	7.9	0.017

[a] Disk 1 is at the upstream end.

[b] The modeled upstream target disks are each 2.5 cm thick.

[c] The modeled downstream target disks are each 3.5 cm thick.
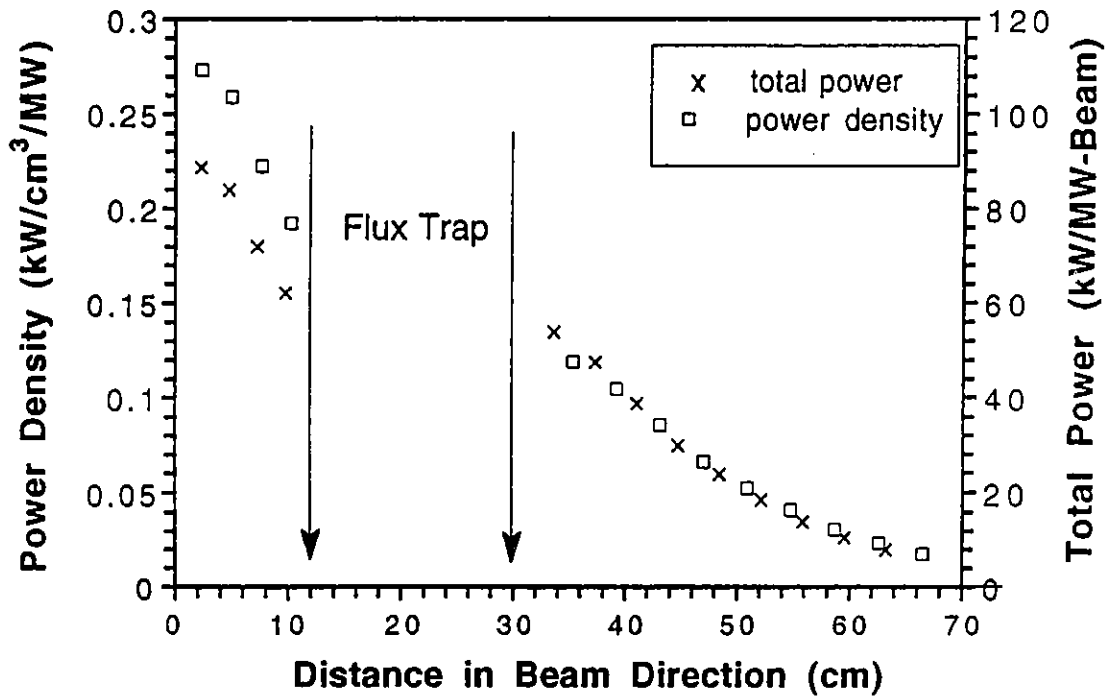
Figure IV.2.2-9 Power Density Distribution in the Target along the Proton Beam Direction.

Table IV.2.2-4 Radial Power Distribution in the Disks of the Upstream
Target Section for Proton Beam Power of 1 MW

Region[a,b]	Mean Power Density (kW/cm^3)	Standard Error σ (kW/cm^3)	Radial Functional Form (kW/cm^3)
Disk 1			1.767 exp(-0.1433 r^2)
zone 1	1.650	0.073	
zone 2	0.988	0.022	
zone 3	0.339	0.010	
zone 4	0.090	0.005	
zone 5	0.019	0.001	
Disk 2			1.587 exp(-0.1384 r^2)
zone 1	1.444	0.065	
zone 2	0.944	0.022	
zone 3	0.314	0.009	
zone 4	0.091	0.004	
zone 5	0.025	0.001	
Disk 3			1.285 exp(-0.1312 r^2)
zone 1	1.199	0.055	
zone 2	0.748	0.018	
zone 3	0.286	0.008	
zone 4	0.084	0.004	
zone 5	0.030	0.002	
Disk 4			1.040 exp(-0.1232 r^2)
zone 1	0.954	0.047	
zone 2	0.646	0.017	
zone 3	0.245	0.007	
zone 4	0.082	0.003	
zone 5	0.028	0.001	

[a] zone 1: r ≤ 1.0 cm
   zone 2: 1.0 cm < r ≤ 2.5 cm
   zone 3: 2.5 cm < r ≤ 4.0 cm
   zone 4: 4.0 cm < r ≤ 5.0 cm
   zone 5: 5.0 cm < r ≤ ellipse of minor and major radii 5.5 cm
   and 7.5 cm

[b] All zones are 2.5 cm thick.
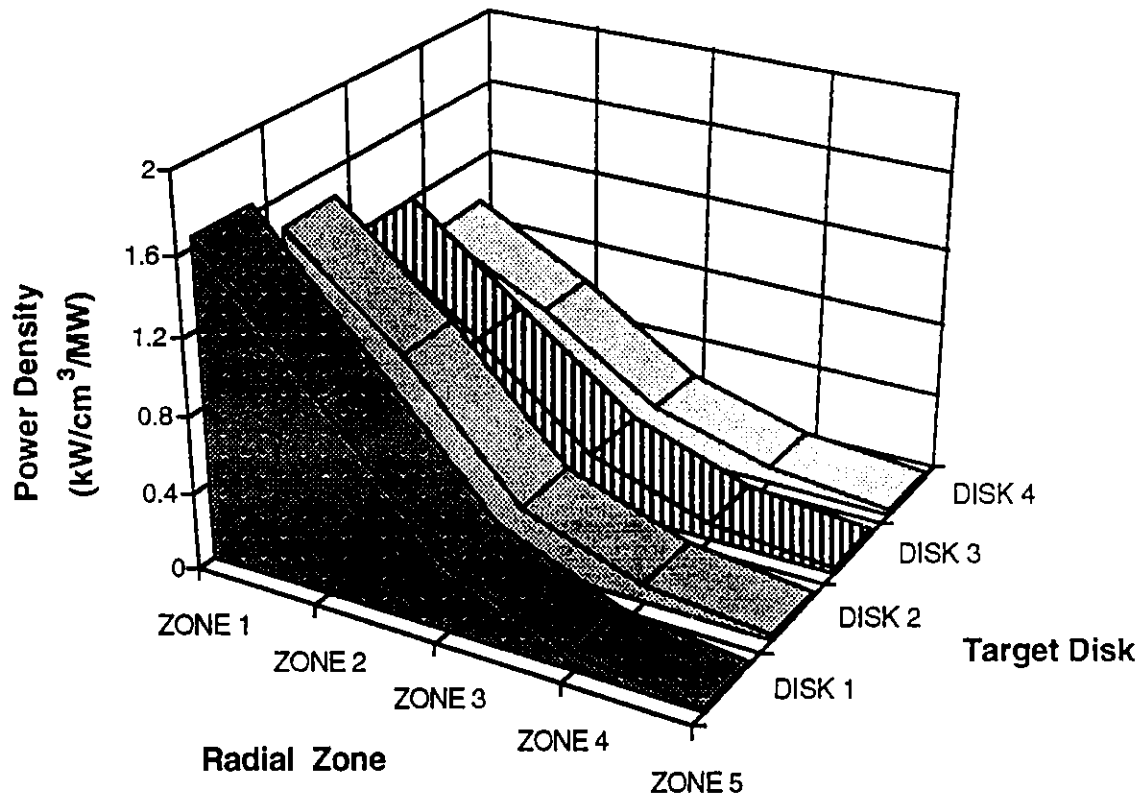
Figure IV.2.2-10 Radial Power Distribution in the Disks in the Upstream Target Section. (See Table IV.2.2-4 for zone definitions.)
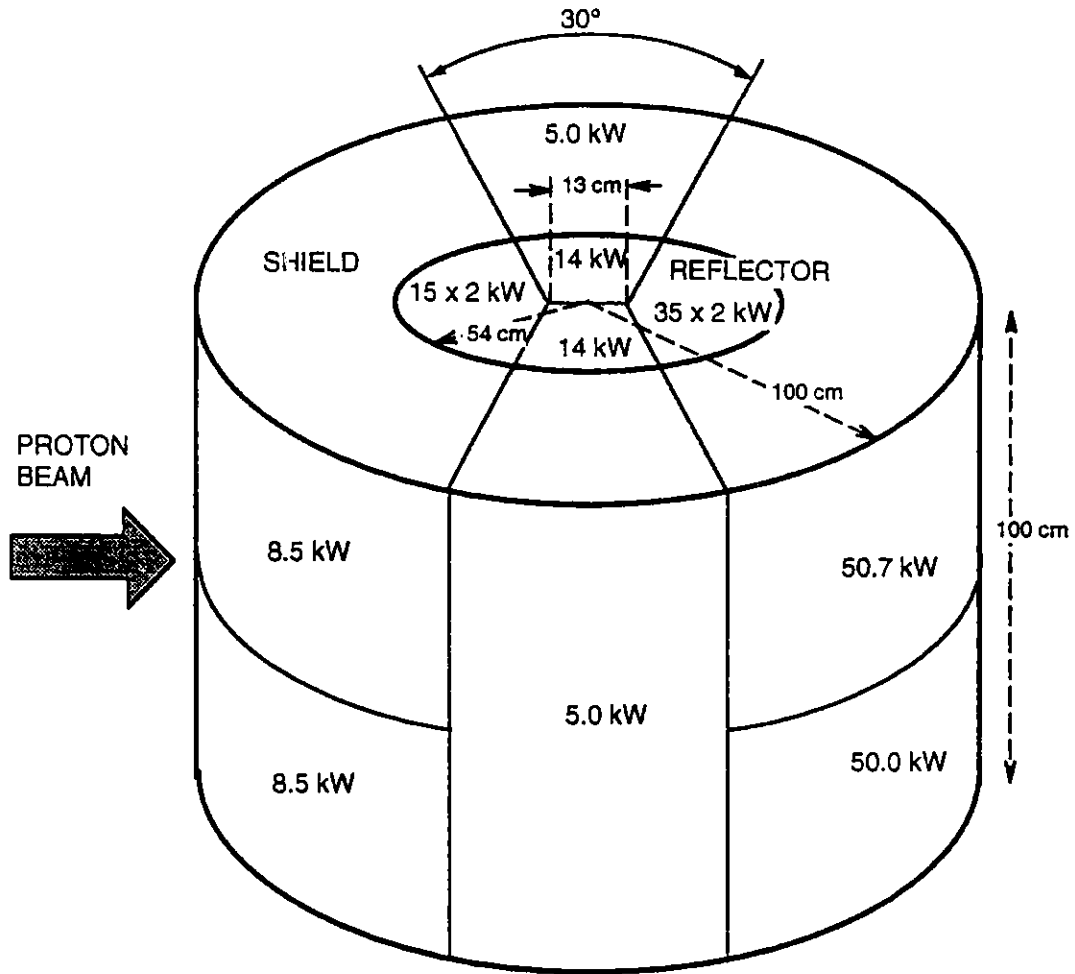
Figure IV.2.2-11 Power Distribution in the Reflector and Shield.

2.2.4 Activation Analyses

Activation analyses[11] were performed for a simplified, conservative model of IPNS Upgrade that provides upper-bound estimates of radioactivity and the buildup and decay of afterheat from decay of the induced activity in tantalum and tungsten targets. Tables IV.2.2-5 through IV.2.2-7 summarize the results. The detailed output for the activation calculations is available[11] but is not presented here.

The calculations were performed using HETC, O5R, and ORIGEN, with a somewhat different geometrical model than that described above. The geometry for the HETC and O5R calculations was as follows:

- The target modeled was of elliptical cross section, with axes of 15 cm and 11 cm.

- The upstream section of the target was 10 cm long and downstream section of the target was 30 cm long, the two sections being separated by 18 cm. No coolant was included in the model.

- The target was enclosed in a solid beryllium reflector 20 cm thick, having a hole with the same cross section as the target to represent the proton beam pipe.

- The proton energy was 2.2 GeV and the current was 500 μA. The proton beam distribution was Gaussian, with a full width at half maximum diameter of 2.5 cm.

The low-energy-neutron transport in O5R has a cutoff at 1 eV, because it was judged that thermal neutron transport with no coolant present would be misleading. The results of these activation calculations thus include no contribution from interactions below 1 eV, but this should be a minor effect.

The production rates were used as input to a buildup and decay code, ORIGEN, used to calculate activity and afterheat. The calculation was performed for irradiation times of 1 d, 7 d, 30 d, and 1 yr; for each of these periods, the decay was calculated for the following cooling times: 0 min, 5 min, 10 min, 30 min, 1 h, 8 h, 1 d, 30 d, and 1 yr.

Table IV.2.2-5 shows the buildup of activity and afterheat, which for continuous operation builds up most of the way in one year and saturates after about six years. Tables IV.2.2-6 and IV.2.2-7 show that for typical irradiation times of several weeks (or longer), the activity and afterheat decay rather slowly during cooldown periods.
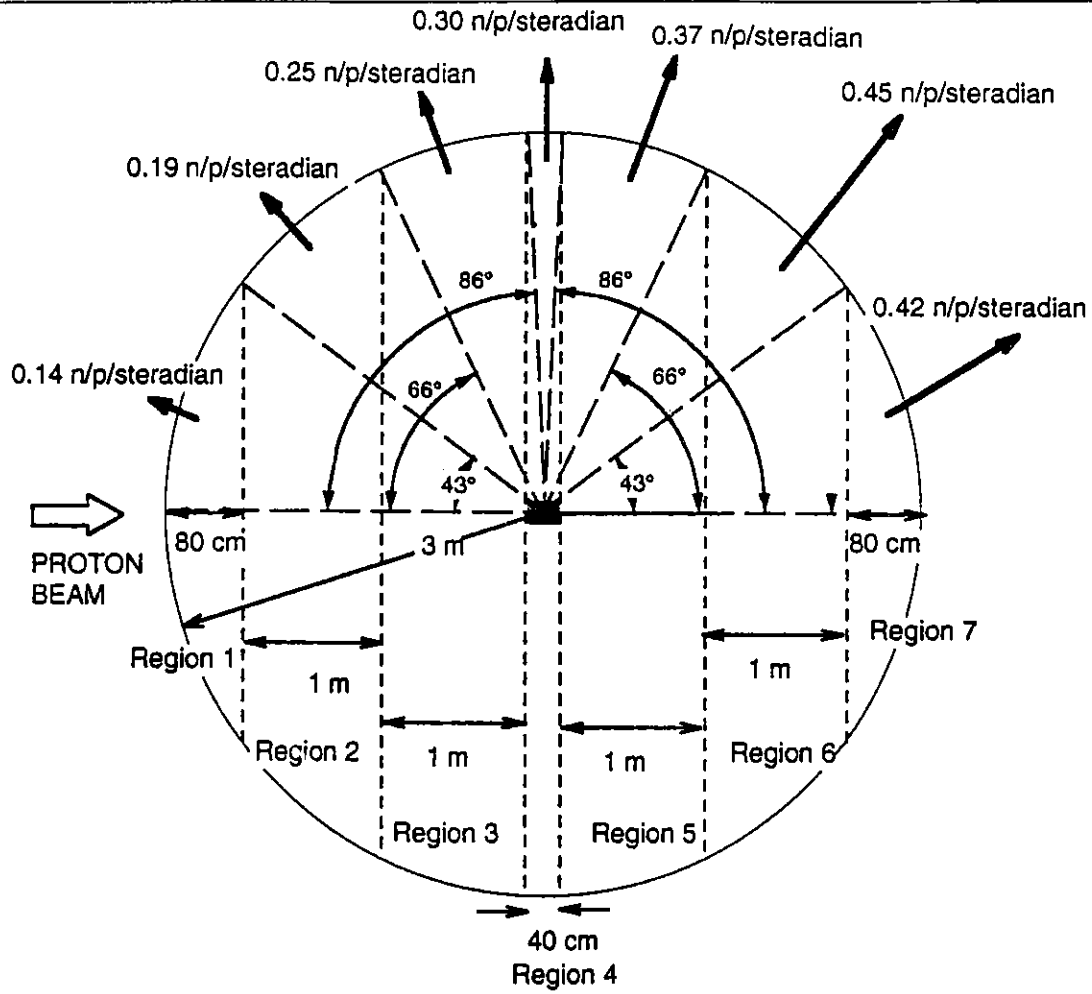
■ : TARGET (41.5 cm long 6.4 cm radius cylinder of tantalum)

Figure IV.2.2-12 High-Energy Neutron Yield around the Target.
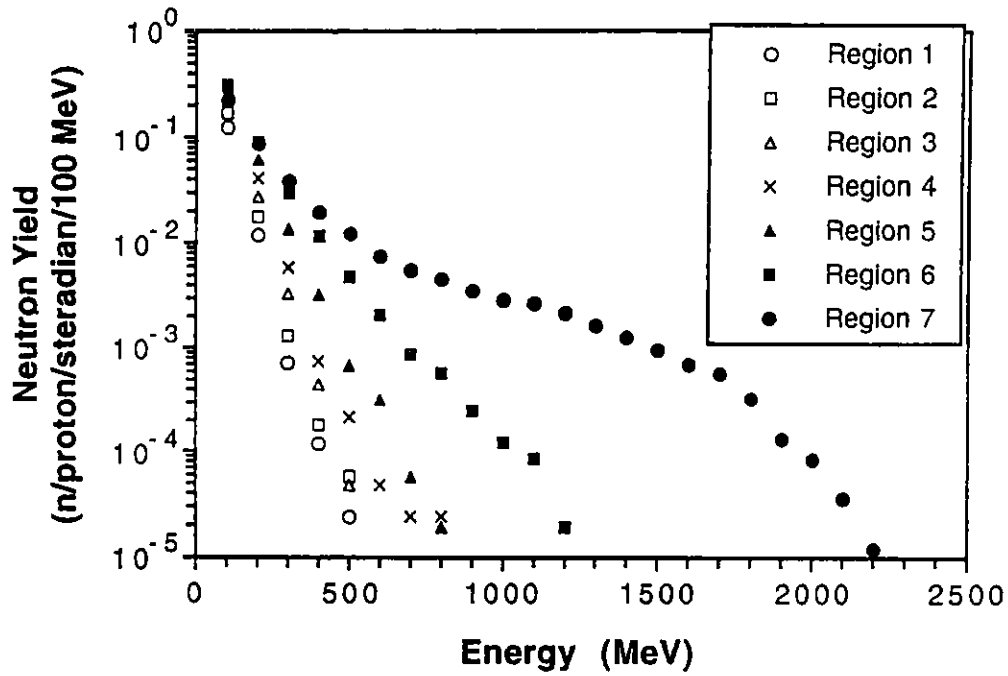
Figure IV.2.2-13 High-Energy Neutron Spectra around the Target.

Table IV.2.2-5 Buildup of Activity and Afterheat for the IPNS Upgrade Target

Irradiation Time (weeks)	Tantalum		Tungsten	
	Activity (TBq)	Afterheat (W)	Activity (TBq)	Afterheat (W)
1	21,800	3,290	24,700	3,230
2	24,700	3,820	26,300	3,320
3	26,900	4,280	27,300	3,360
4	29,100	4,730	28,100	3,380
6	32,900	5,530	29,000	3,410
8	36,400	6,280	29,600	3,440
10	39,500	6,760	30,700	3,460
20	51,600	9,610	31,800	3,490
30	59,500	11,400	35,100	3,600
40	64,800	12,500	37,800	3,690
60	70,700	13,700	39,000	3,750
80	73,400	14,300	39,400	3,780
100	74,700	14,500	39,800	3,800
200	76,400	14,700	40,500	3,870
300	77,000	14,800	40,800	3,900
400	77,200	14,800	40,900	3,930
500	77,400	14,800	41,000	3,940
600	77,500	14,800	41,100	3,950

Table IV.2.2-6 Decay of Afterheat Power for the IPNS Upgrade Target (Watts)

Cooling Time	Tantalum, Irradiation Time (days) at 1 MW				Tungsten, Irradiation Time (days) at 1 MW			
	1	7	30	365	1	7	30	365
0	2,410	3,280	4,840	13,300	2,410	3,230	3,380	3,720
5 min	858	1,390	3,030	11,500	1,880	2,710	2,860	3,200
10 min	822	1,350	3,000	11,500	1,750	2,560	2,720	3,070
30 min	738	1,290	2,910	11,300	1,500	2,310	2,460	2,800
1 h	671	1,240	2,830	11,300	1,310	2,120	2,260	2,610
8 h	387	966	2,500	11,000	750	1,410	1,550	1,900
1 d	196	732	2,240	10,600	390	850	982	1,320
7 d	77	494	1,910	10,000	21	84	175	500
30 d	59	405	1,620	8,700	3	22	81	353
1 yr	8	54	218	1,200	<1	2	9	76

Table IV.2.2-7 Decay of Activity for the IPNS Upgrade Target (TBq)

Cooling Time	Tantalum, Irradiation Time (days) at 1 MW				Tungsten, Irradiation Time (days) at 1 MW			
	1	7	30	365	1	7	30	365
0	16,500	21,800	29,700	68,900	17,780	24,730	28,270	38,690
5 min	7,210	11,200	18,400	57,100	15,410	22,350	25,900	36,210
10 min	6,410	10,400	17,500	56,200	14,310	21,260	24,800	35,120
30 min	4,850	8,810	16,000	54,600	11,970	18,880	22,420	32,740
1 h	4,100	8,030	15,200	53,800	10,230	17,070	20,620	30,930
8 h	2,270	5,890	13,000	51,700	6,260	11,220	14,690	25,000
1 d	1,240	4,380	11,400	49,800	3,050	7,290	10,650	20,890
7 d	394	2,490	9,050	46,100	2,390	1,480	4,280	13,960
30 d	272	1,870	7,410	39,700	109	730	2,670	10,530
1 yr	37	255	1,020	5,920	7	47	190	1,170

2.3 THERMAL-HYDRAULIC ANALYSES

A thermal-hydraulic analysis of the IPNS Upgrade target was undertaken to determine maximum temperatures and to supply temperature distributions for use in the stress analyses. Two models that were developed using the THTB computer code[12] formed the basis for the thermal analysis. One has three-dimensional rectangular geometry with continuous power input. The second is a two-dimensional version for transient studies.

The geometry for the first model is shown in Figure IV.2.3-1. Because of symmetry, only half of the width and half of the thickness for both the target and the coolant channel are modeled. Variations in the power input in the axial (y) direction (see Figure IV.2.3-1) are small and are neglected at this stage of analysis. Because of temperature rise in the coolant, the longitudinal (z) direction (direction of coolant flow, normal to the target axis) is modeled in its entirety. The radial and axial power distributions were obtained from the neutronics analysis described in Section IV.2.2. Each succeeding target disk has a lower power according to the calculated axial distribution. Heat-transfer coefficients were calculated using the Dittus-Boelter formulation with entrance length correction. A roughened surface was assumed, as discussed in Section IV.2.6. A continuous power input equivalent to an average over the actual pulsed operation was assumed, giving a steady-state temperature solution. The target disks are represented as being rectangular, which is not the case for the actual disks (Figures IV.2.1-1 and IV.2.1-2). However, because power levels are low at the edges of the disks, heat transfer there is minimal. Therefore, this geometrical simplification has negligible impact on the calculations.

A separate two-dimensional THTB model was developed to study the transient operation in more detail. This model, shown in Figure IV.2.3-2, used results from the first model to set coolant-temperature boundary conditions. Because the energy is deposited more or less uniformly through the thickness of the disks and then flows axially to the coolant, this model yields accurate results. This model includes a more detailed nodal structure in the radial and axial directions and a coordinate system compatible with the power input, which the first model does not have. A machinable tungsten material coated with a 10-μm thickness of titanium was assumed for both models. The temperature-dependent conductivity for machinable tungsten was approximated by that for pure tungsten, decreased by the ratio of conductivities at room temperature (0.745).[13]

Results of the thermal-hydraulic analyses based on the first model are shown in Figures IV.2.3-3 through IV.2.3-12, and the transient studies with the second model are shown in Figures IV.2.3-13 through IV.2.3-16. Figure IV.2.3-3 shows the radial power distribution used for the upstream target section. Four axial positions are shown, corresponding to the calculations in the neutronics model. Parametric studies were performed for various disk thicknesses, coolant flow velocities, and disk materials, using the power distributions at these positions as input. The effect of coolant velocity on the centerline, surface, and outlet coolant temperatures for a 1-cm-thick tungsten target disk is shown in Figure IV.2.3-4. Figure IV.2.3-5 shows the effect of disk
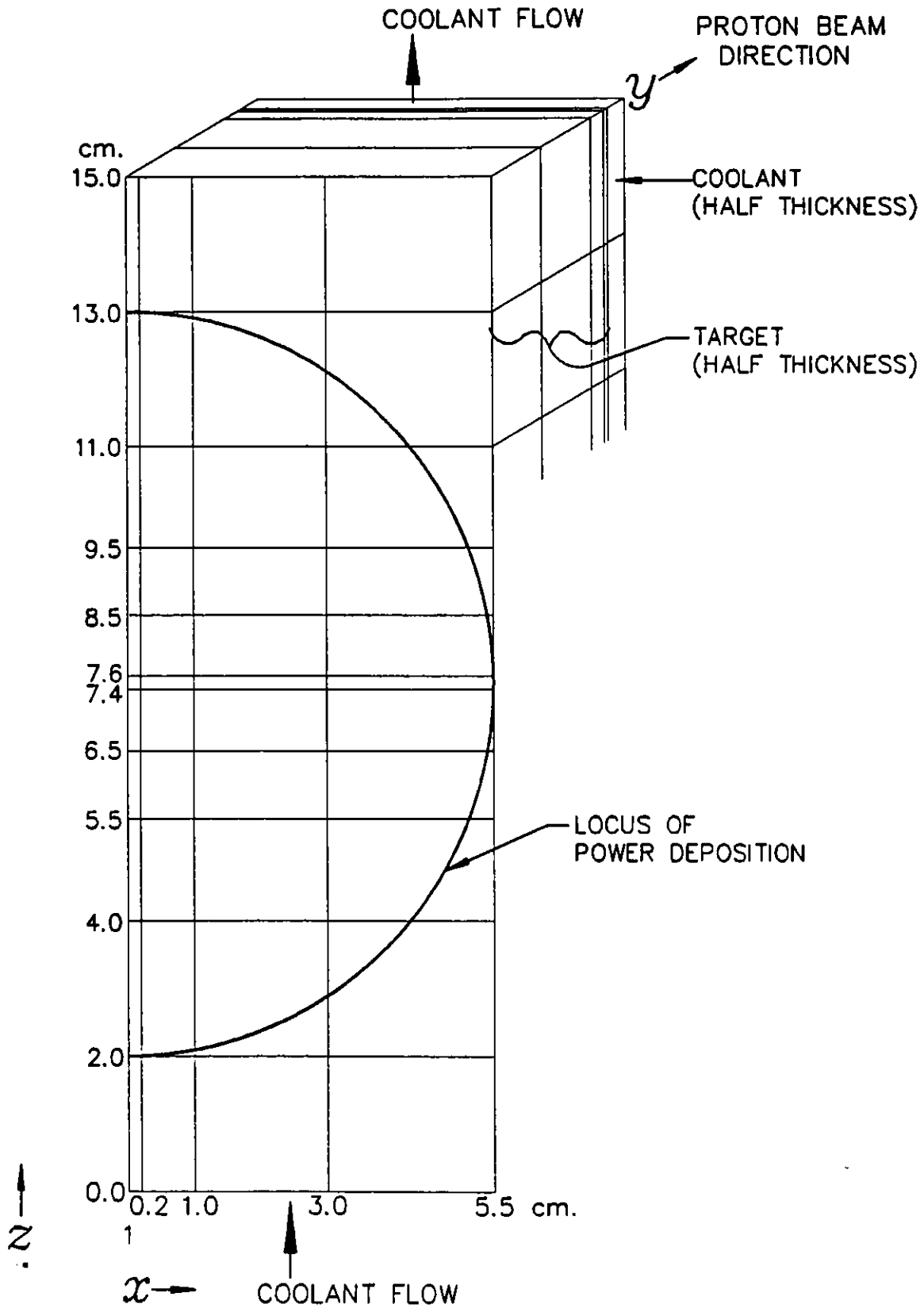
Figure IV.2.3-1 Geometry for Three-Dimensional Thermal-Hydraulic Model of IPNS Upgrade Target Disk.
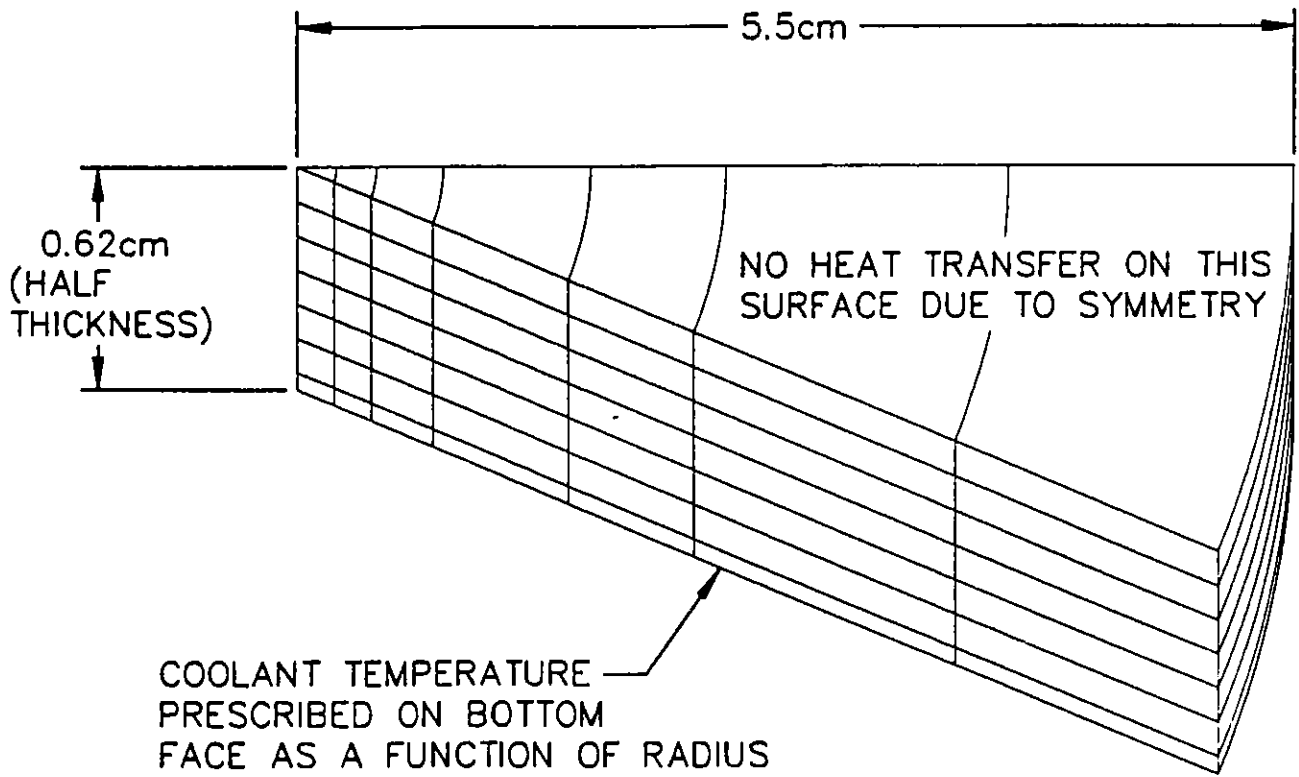
Figure IV.2.3-2 Geometry for Two-Dimensional Thermal-Hydraulic Model. (Note that axial and radial scales differ by a factor of 2.)
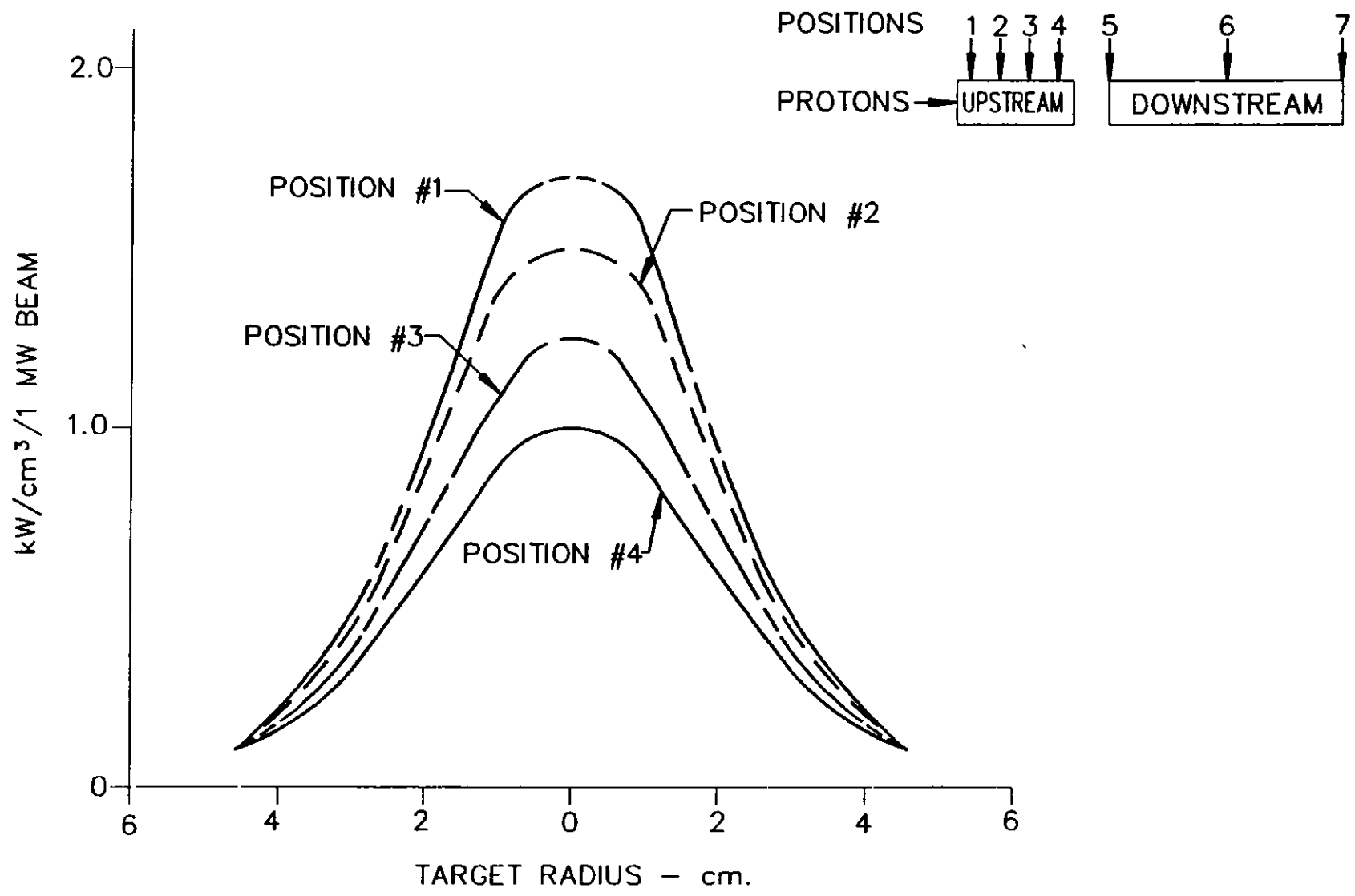
Figure IV.2.3-3 Power Density Distribution vs. Radius for Four Axial Positions in the Upstream Target Section.

THICKNESS – DISK – 1cm.
                    CHANNEL – 1.59 mm
MATERIAL – TUNGSTEN

POWER LEVEL AND DISTRIBUTION
AS AT POSITION 3
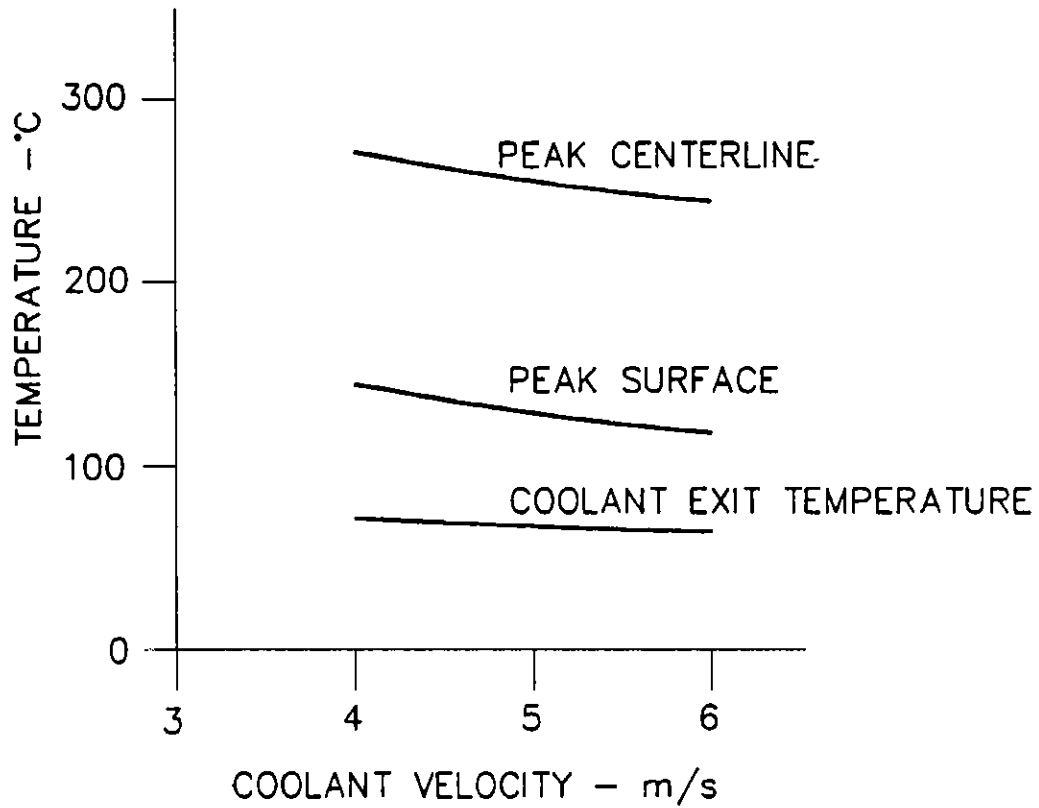
Figure IV.2.3-4 Centerline, Surface, and Coolant Exit Temperature vs. Coolant Velocity for Disk at Position 3.
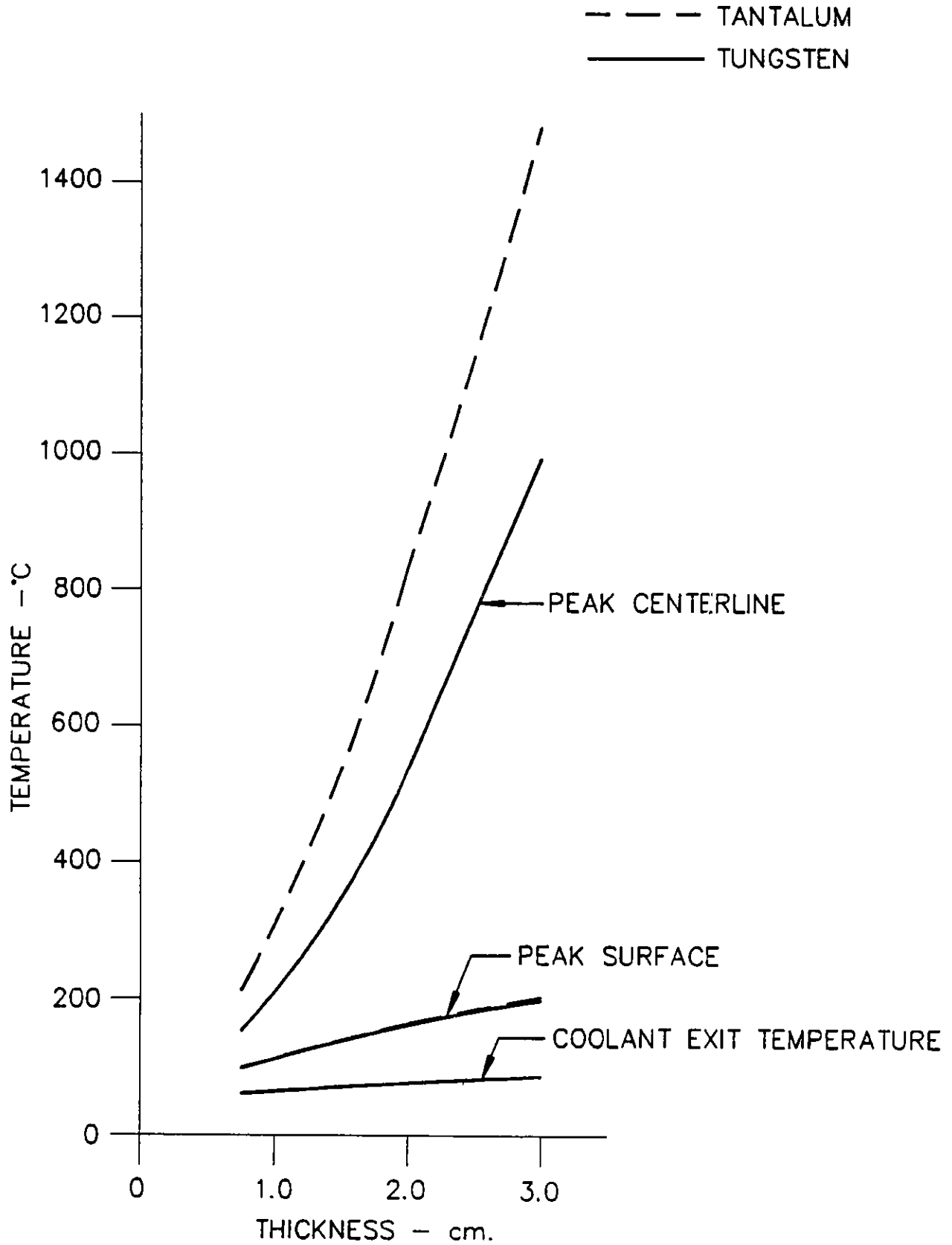
Figure IV.2.3-5 Centerline, Surface, and Coolant Exit Temperature vs. Disk Thickness for Disk at Position 1.

THICKNESS TO MAINTAIN 127°C SURFACE

POS'N #1 .715cm.   POS'N #2 .80cm.
POS'N #3 .97cm.   POS'N #4 1.27cm.
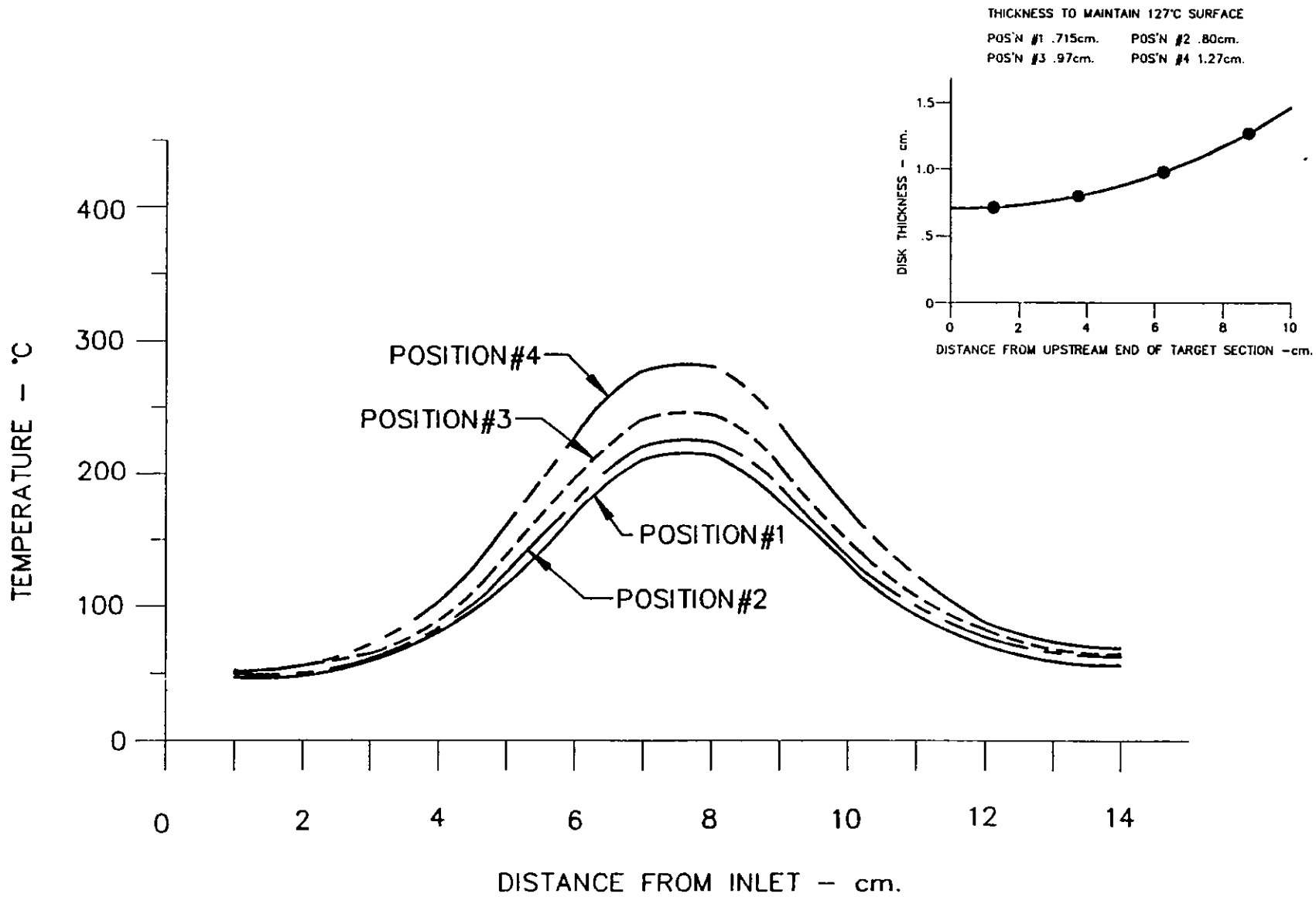
Figure IV.2.3-6 Mid-Thickness Temperature Distribution in Flow Direction for Four Axial Positions in the Upstream Target Section.
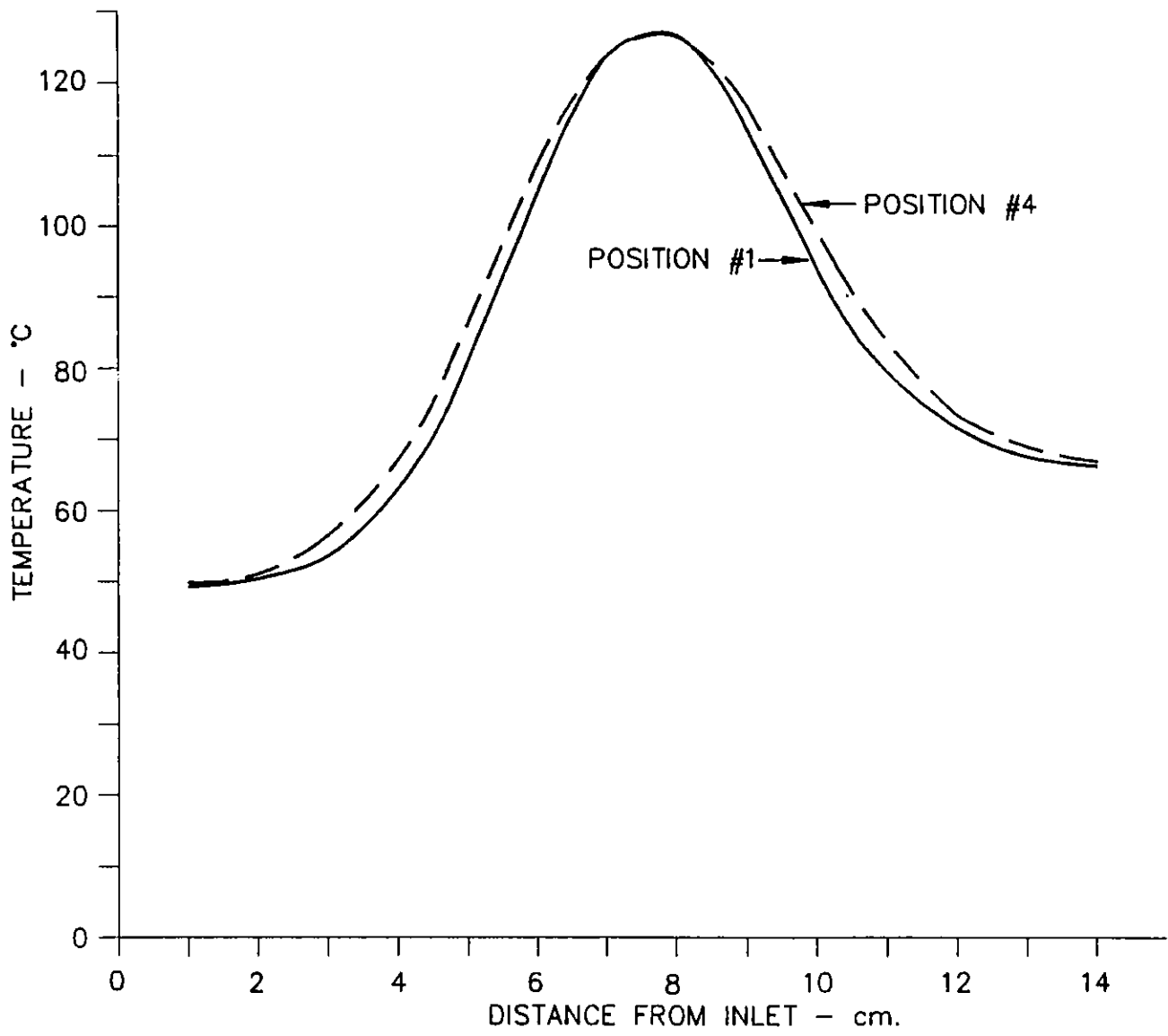
Figure IV.2.3-7 Surface-Temperature Distribution in Flow Direction for Two Axial Positions in the Upstream Target Section.

ACTUAL—THICKNESS DISKS WITH
1.59—mm COOLING CHANNELS (12.06 cm TOTAL)

	DISK THICKNESS	
	MAX.	ACTUAL
	(cm.)	
1	.70	.65
2	.71	.70
3	.72	.70
4	.74	.70
5	.76	.75
6	.79	.75
7	.82	.80
8	.87	.85
9	.94	.90
10	1.02	1.0
11	1.14	1.1
12	1.30	1.1
	10.51	10.0
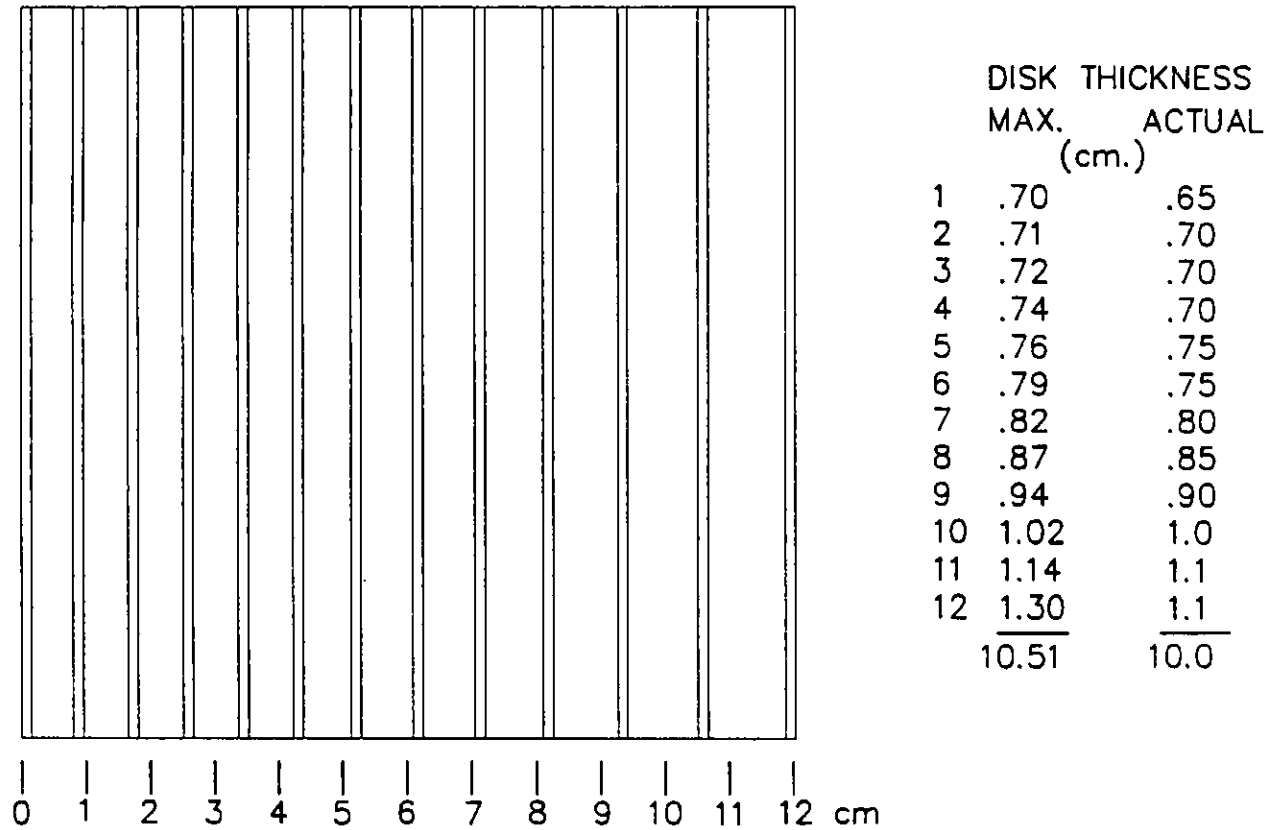
Figure IV.2.3-8 Upstream Target Section Configuration.
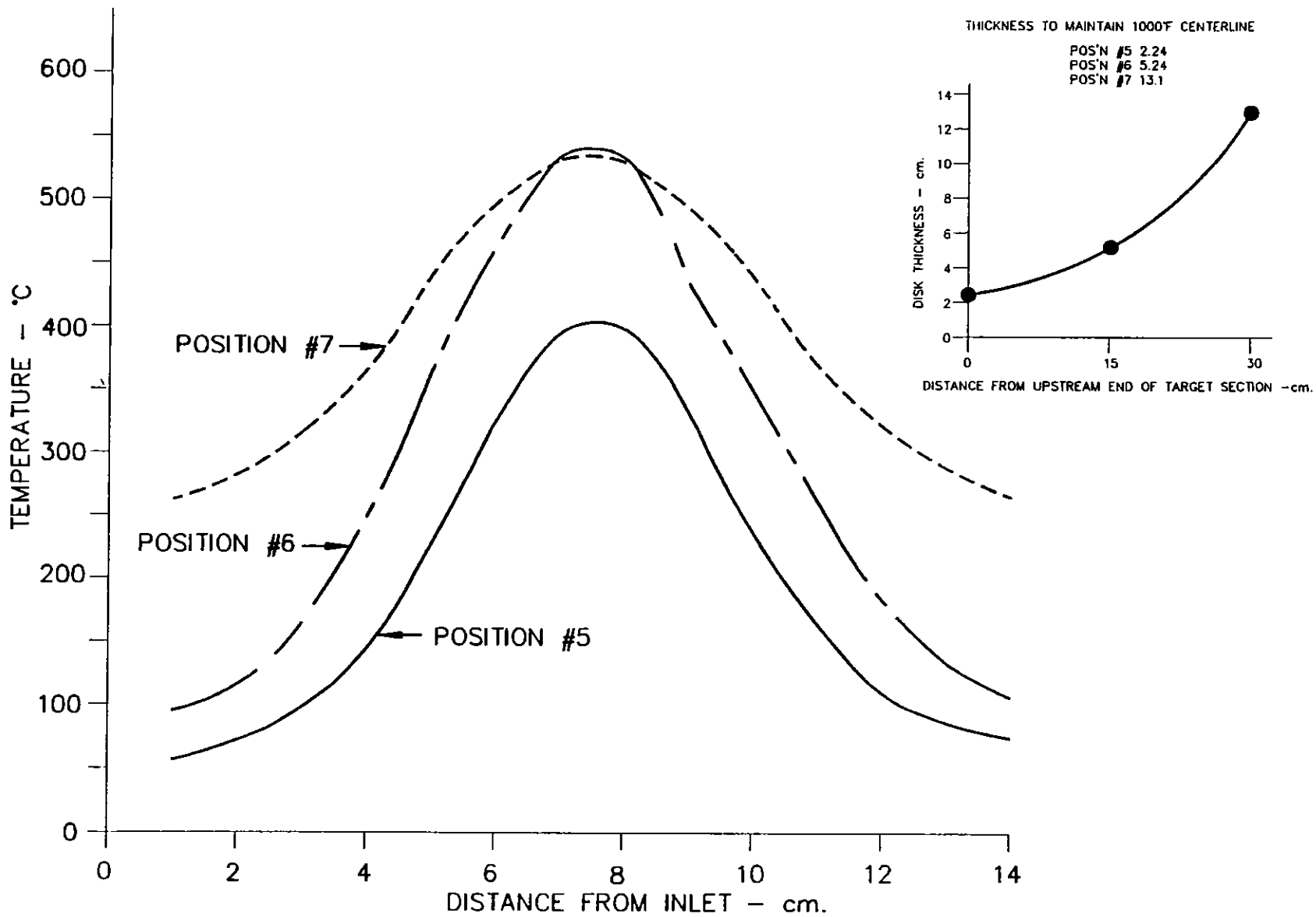
Figure IV.2.3-9 Mid-Thickness Temperature Distribution in Flow Direction for Three Axial Positions in the Downstream Target Section. (Positions are identified in Figure IV.2.3-3.)
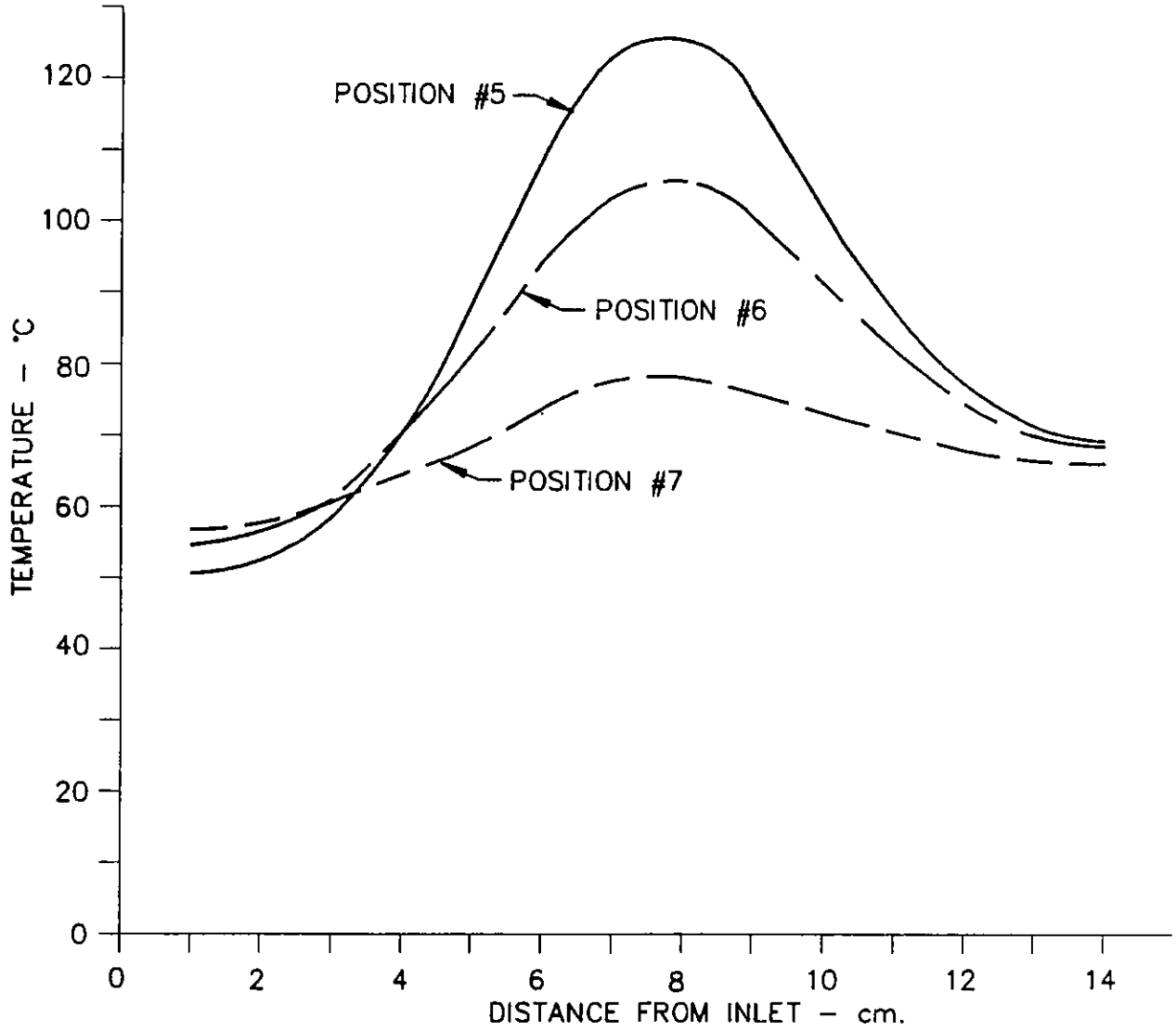
Figure IV.2.3-10 Surface Temperature Distribution in the Flow Direction for Three Axial Positions in the Downstream Target Section.

ACTUAL–THICKNESS DISKS WITH
1.59–mm COOLING CHANNELS (31.59 cm TOTAL)
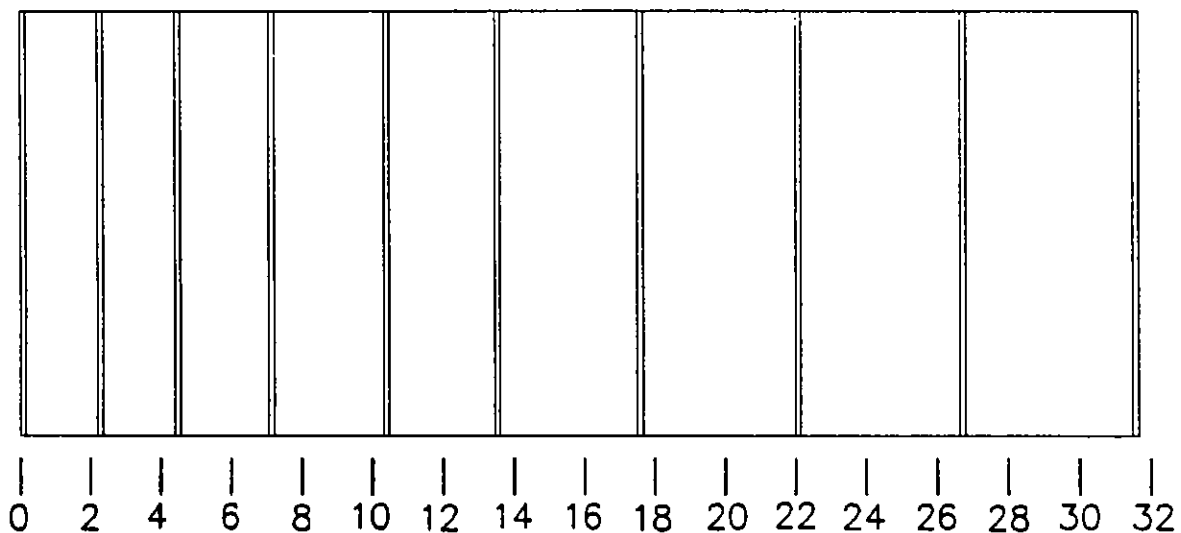
DISK THICKNESS

	MAX.	ACTUAL
		(cm.)
1	2.2	2.0
2	2.4	2.0
3	2.7	2.5
4	3.2	3.0
5	3.7	3.0
6	4.4	4.0
7	5.8	4.5
8	7.7	4.5
9	10.3	4.5
	42.4	30.0

Figure IV.2.3-11 Downstream Target Section Configuration.
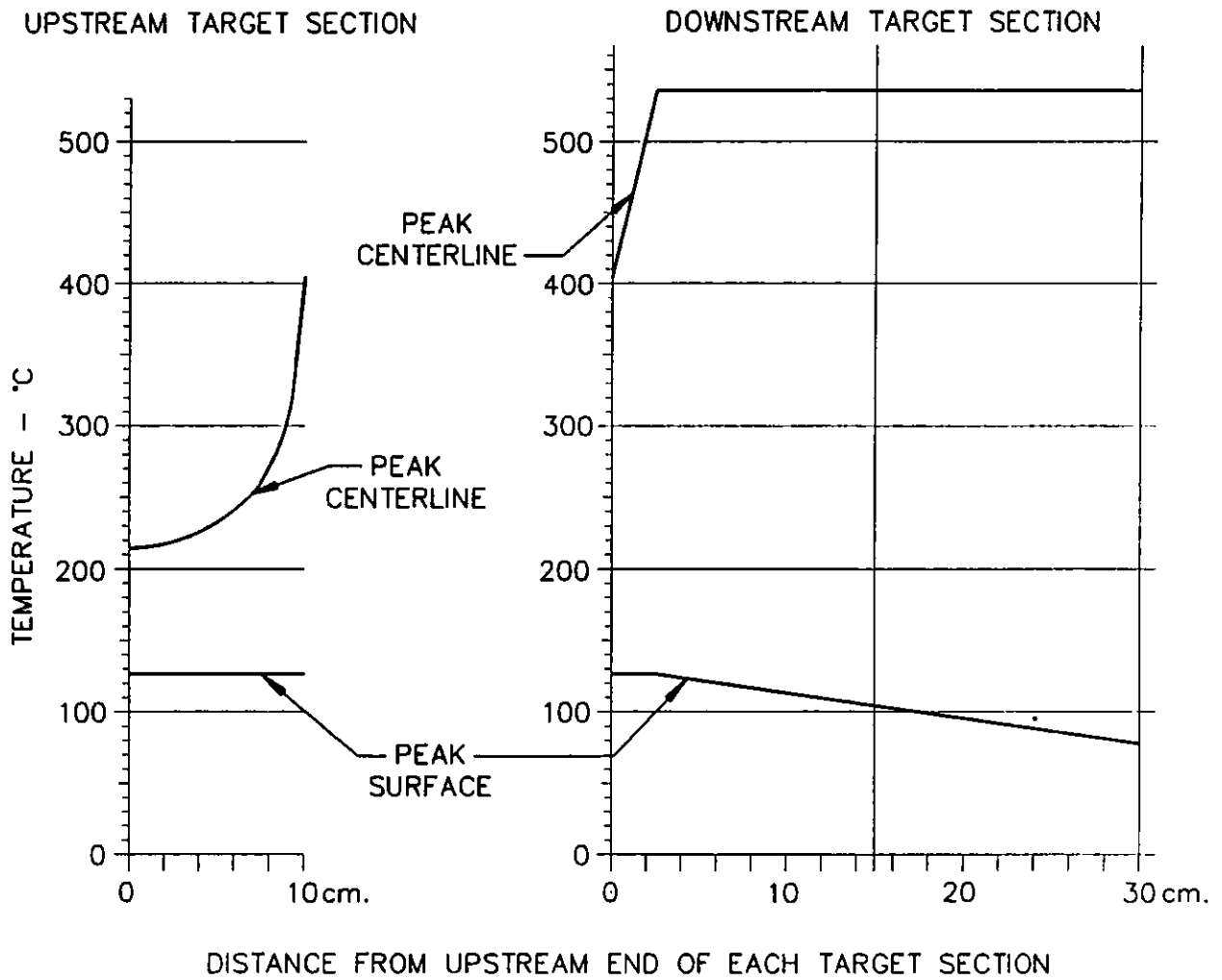
Figure IV.2.3-12 Peak Centerline and Surface Temperature vs. Axial Position, Upstream and Downstream Target Sections.
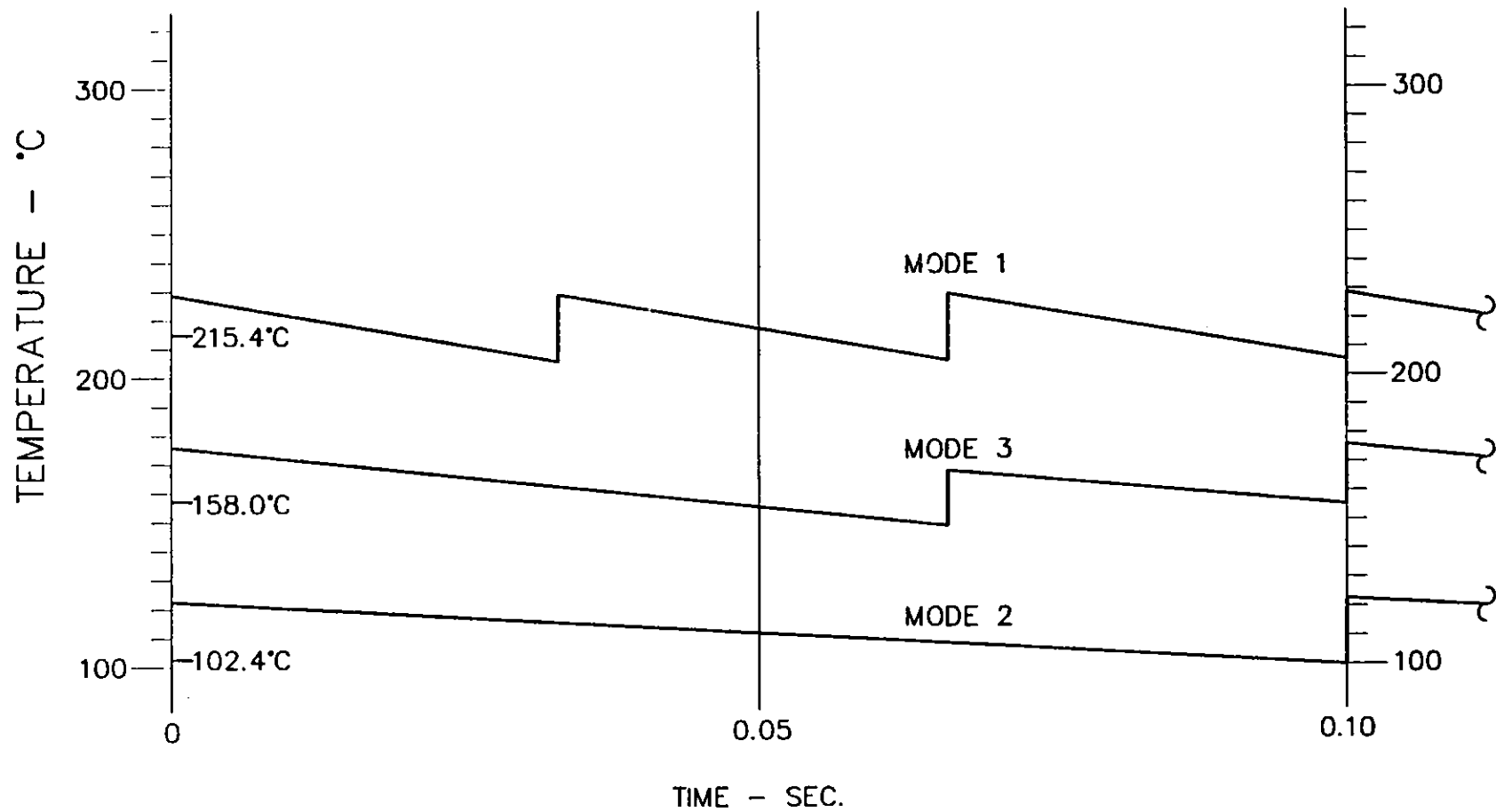
Figure IV.2.3-13 Variation of the Peak Temperature in the First Disk in the Upstream Target Section for Three Modes of Operation. (See text for definition of modes. Fixed temperatures shown were obtained from the steady-state analyses.)
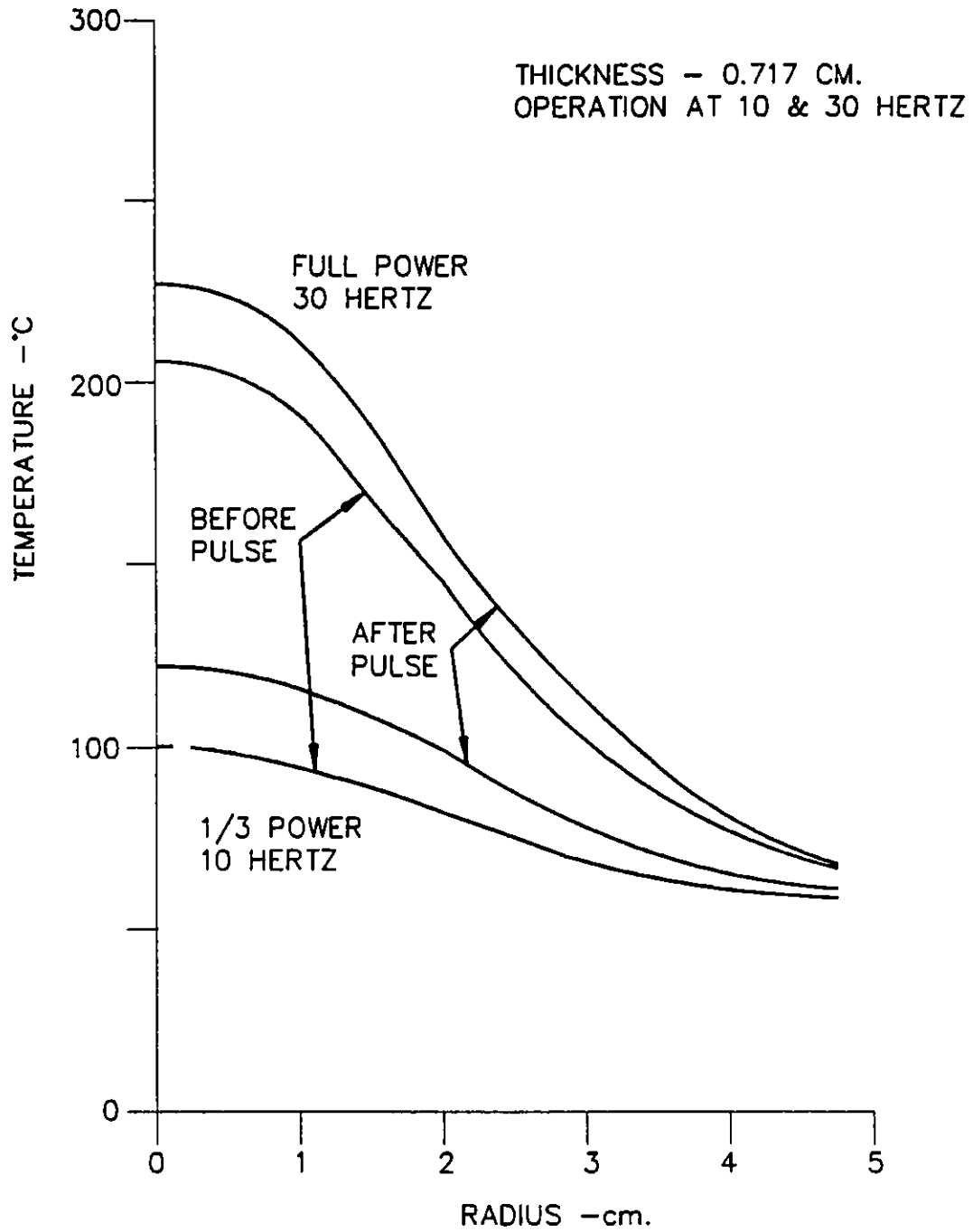
Figure IV.2.3-14 Radial Temperature-Time Variation in a Disk at Position 1 in the Upstream
Target Section, Operated in Mode 1 or 2.

THICKNESS — 0.717cm.
OPERATION — 2 PULSES ON, 1 OFF
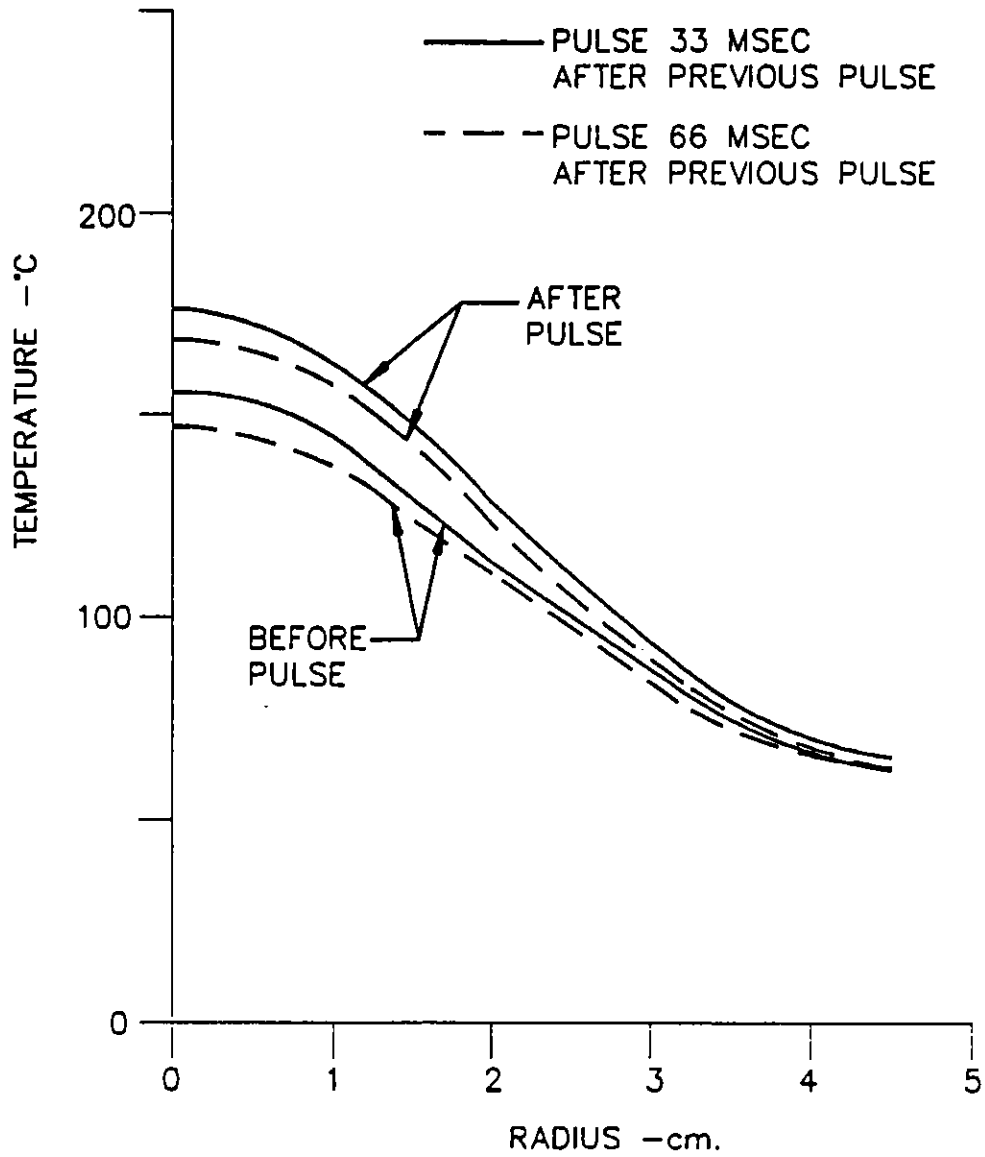
Figure IV.2.3-15 Radial Temperature-Time Variation in a Disk at Position 1 in the Upstream Target Section, Operated in Mode 3.

THICKNESS _ 1.24 cm.
OPERATION — FULL POWER AT 30 Hz.
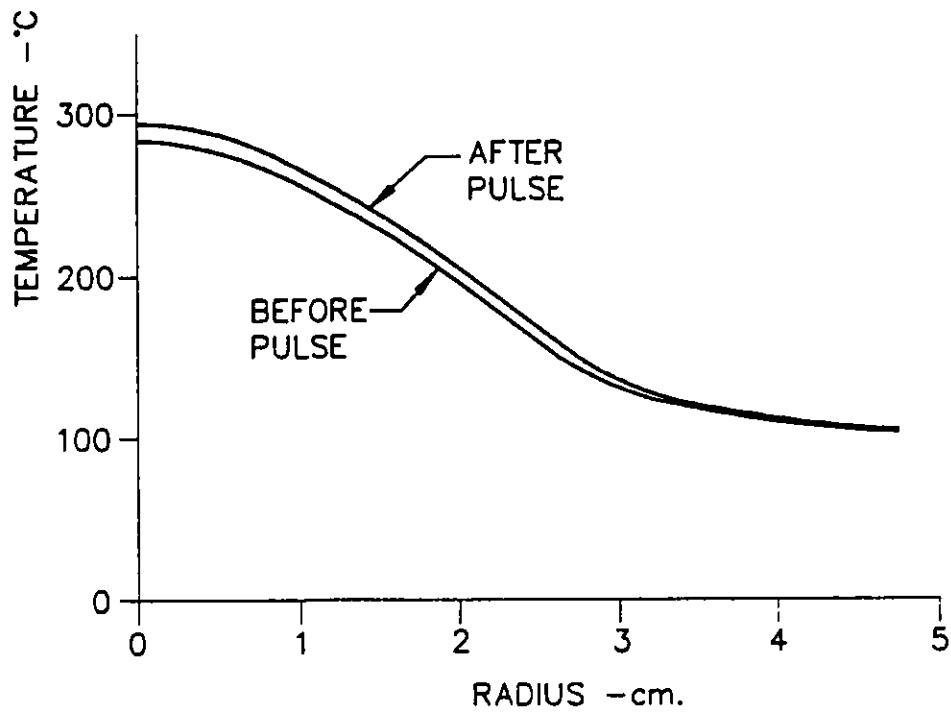
Figure IV.2.3-16 Radial Temperature-Time Variation in a Disk at Position 4 in the Upstream Target Section, Operated in Mode 1.

thickness on disk and coolant temperatures for a coolant velocity of 5 m/s for target disks fabricated from machinable tungsten and also from tantalum.

The peak disk temperature for these four power distributions is at the center of the disk, as shown in Figure IV.2.3-6. The maximum thickness of each disk was adjusted to limit the surface temperature to 127°C. This maximum temperature occurs over a very local area at the peak of the energy input (center of the target disk), as seen in Figure IV.2.3-7. This surface temperature was chosen avoid local boiling at the design system pressure of 830 kPa. The maximum disk thicknesses at each of these four positions are plotted as a function of axial position in the small graph of Figure IV.2.3-6. Interpolations on this curve were used to determine the maximum thicknesses of all the disks in the upstream target section, under the requirement that the maximum surface temperature be ≤127°C. Actual disk thicknesses were adjusted down from these maximum values to achieve the desired overall length of the target section. The resulting upstream target section consists of 12 disks, which vary in thickness from 0.65 to 1.1 cm as shown in Figure IV.2.3-8. This target section contains a total of 10-cm thickness of target material, with 0.159-cm coolant gaps between adjacent target disks and at the ends. Because the actual disk thicknesses are less than the maximum thicknesses, the peak surface temperatures are lower than 127°C.

A similar analysis was carried out to determine the disk thicknesses in the downstream target section (Figures IV.2.3-9 to IV.2.3-11), which consists of nine elements and has a total of 30-cm thickness of target material. The radial power distribution in the downstream target section was extrapolated from the upstream target section, scaled to the calculated axial power distribution in the downstream target section. The resulting power distributions were used to determine the thicknesses of the disks in the downstream target section. This assumption is conservative because the actual power distributions are flatter. Beginning at a depth of 2.5 cm, the disk thicknesses in the downstream target section are limited by centerline temperature rather than by surface temperature. The maximum disk thicknesses were chosen to keep the centerline temperature below 538°C. Figure IV.2.3-11 shows the actual disk thicknesses, which were chosen to be less than the calculated maximum values. Figure IV.2.3-12 shows both the centerline and surface temperatures used to determine the thicknesses in both target sections.

The power input to the target is not constant with time, as was assumed in the first model. The time-power history is coordinated with the proton pulses, which occur at a 30-Hz rate in the accelerator but are multiplexed between the two target stations. Thus, one target may receive a pulse every 1/30th of a second (Mode 1), every 1/10th of a second (Mode 2), or alternating between 1/30th and 1/15th of a second (Mode 3). These three modes of operation were analyzed with the second thermal model. Figure IV.2.3-13 shows the peak target-temperature response in a 0.717-cm-thick disk at position 1 of the front target, along with the corresponding results for steady-state operation. It can be seen that the steady-state (continuous power input) temperatures accurately represent the average of the time-varying values. The radial temperature distributions before and after the pulse are shown in Figures IV.2.3-14 and IV.2.3-15 for the three modes of operation. Figure IV.2.3-16 shows these

radial temperatures for position 4 in the upstream target section, calculated for the 30-Hz operation.

Protons enter the target vessel through a stainless-steel window, which heats in a similar fashion to the target but is cooled on only one surface. Figure IV.2.3-17 shows the temperature distribution across the face of the window on both the cooled and uncooled window surfaces, calculated with the first model for a 0.5-cm-thick window.

A high-density target can be easily fabricated using the parameters derived in this analysis. Maximum temperatures are within tolerable limits to prevent local boiling, so the flow is stable. Further refinement of the design may show some advantages in narrower flow channel widths and superior target materials.

2.4 STRESS ANALYSIS

A stress analysis performed on the target disks showed that all stresses are within acceptable limits. A thermal stress analysis of the target disks was performed by means of an analytical formulation[14] that uses a one-dimensional approximation to the temperature distribution. The analytical relations used are:

$$\sigma_r = \alpha E \left[1/R^2 \int^R T(r')r'dr' - 1/r^2 \int^r T(r')r'dr' \right], \qquad \text{(IV.2.4-1)}$$

$$\sigma_t = \alpha E \left[-T(r) + 1/R^2 \int^R T(r')r'dr' + 1/r^2 \int^r T(r')r'dr' \right], \qquad \text{(IV.2.4-2)}$$

$$\sigma_a = 0 , \qquad \text{(IV.2.4-3)}$$

and
$$SI = MAX\{|\sigma_r - \sigma_t|, |\sigma_r - \sigma_a|, |\sigma_t - \sigma_a|\} \qquad \text{(IV.2.4-4)}$$

where

σ_r, σ_t, and σ_a are radial, tangential, and axial stresses;

SI is the stress intensity;

α is the coefficient of thermal expansion;

E is the modulus of elasticity;
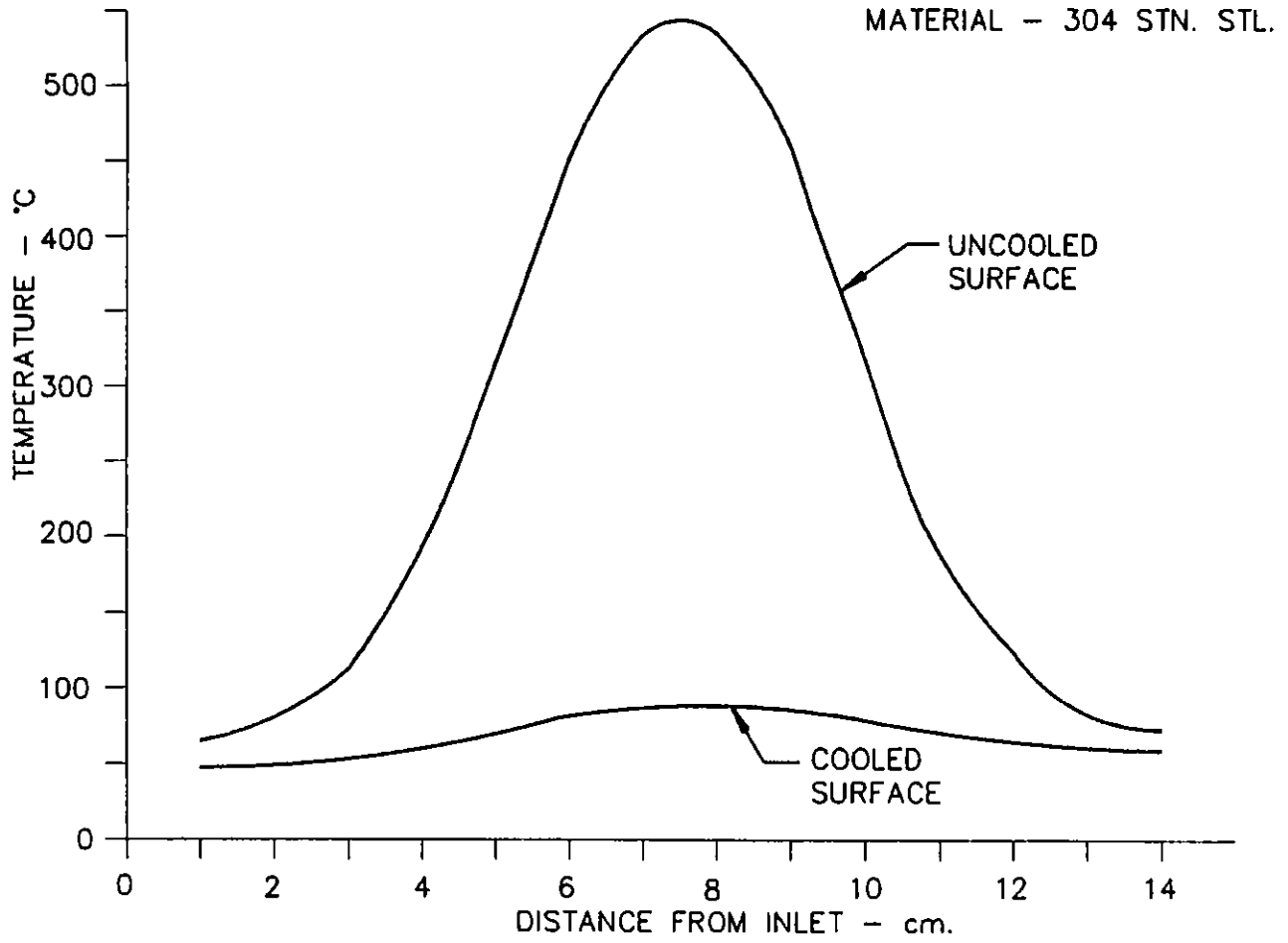
Figure IV.2.3-17 Surface Temperature of Target Vessel Window.

T(r) is the temperature at r minus that at R; and

R and r are the full and local radii of the disk, respectively.

Equations IV.2.4-1 through IV.2.4-4 give the stress in a circular disk heated symmetrically about its center and uniformly through its thickness. The temperature is assumed to be a function of radius only.

Additionally, an ANSYS code[15] model was used to obtain stresses from a two-dimensional (radial and axial) temperature distribution for one disk. Figure IV.2.4-1 shows this model.

Figure IV.2.4-2 shows the ultimate strength for pure tungsten as a function of temperature. Also shown are room temperature values for yield and ultimate strength for machinable tungsten alloys (K1700 and K1850).[13] The curve for pure tungsten shows the general trend for variation of ultimate strength for the machinable tungsten materials. For most materials yield strength follows ultimate strength at a somewhat lower value. The maximum calculated stresses at positions 1-4 in the upstream target section and positions 5-7 in the downstream section are also plotted in this figure. These stresses all fall well below the ultimate strength curve for pure tungsten, and this can be expected for the machinable tungsten alloys as well.

The distribution of stress intensity over the radius of the disks, on the basis of Equations IV.2.4-1-IV.2.4-4, is plotted in Figure IV.2.4-3 for positions 1 and 4 in the upstream target section and in Figure IV.2.4-4 for positions 5, 6, and 7 in the downstream target section. The stress intensities in the upstream target section are higher in the thicker disks located toward the downstream end of that section. However, these stresses are less than the ultimate stress, so major deformations or cracking should not result. The highest stress in either target section occurs in the middle of the downstream target section (Figure IV.2.4-4), with a maximum value of 265 MPa at the center. This is still sufficiently below the alloy's yield stress to present no difficulty.

Table IV.2.4-1 lists the stresses for cyclic operation, which could cause fatigue damage to the disks. Stresses in the steady-power cases are also tabulated. We have not yet assessed the effect of fatigue on the life of the target.

A two-dimensional ANSYS model was used to assess the combined influence of axial and radial temperature gradients on the stress level. A temperature distribution corresponding to radial variation only (uniform axial) was input to the 2-D model for comparison to the analytical results. The radial and tangential stresses over the radius agreed with the 1-D model within about 5% for a 1.27 cm thick disk at position 4 of the upstream target section. This agreement supports the validity of the results obtained with 2-D temperature variation. Figure IV.2.4-5 shows the results of this computation. In this 2-D calculation, the radius of the

Figure IV.2.4-1 ANSYS Model for 2-D Thermal Stress.
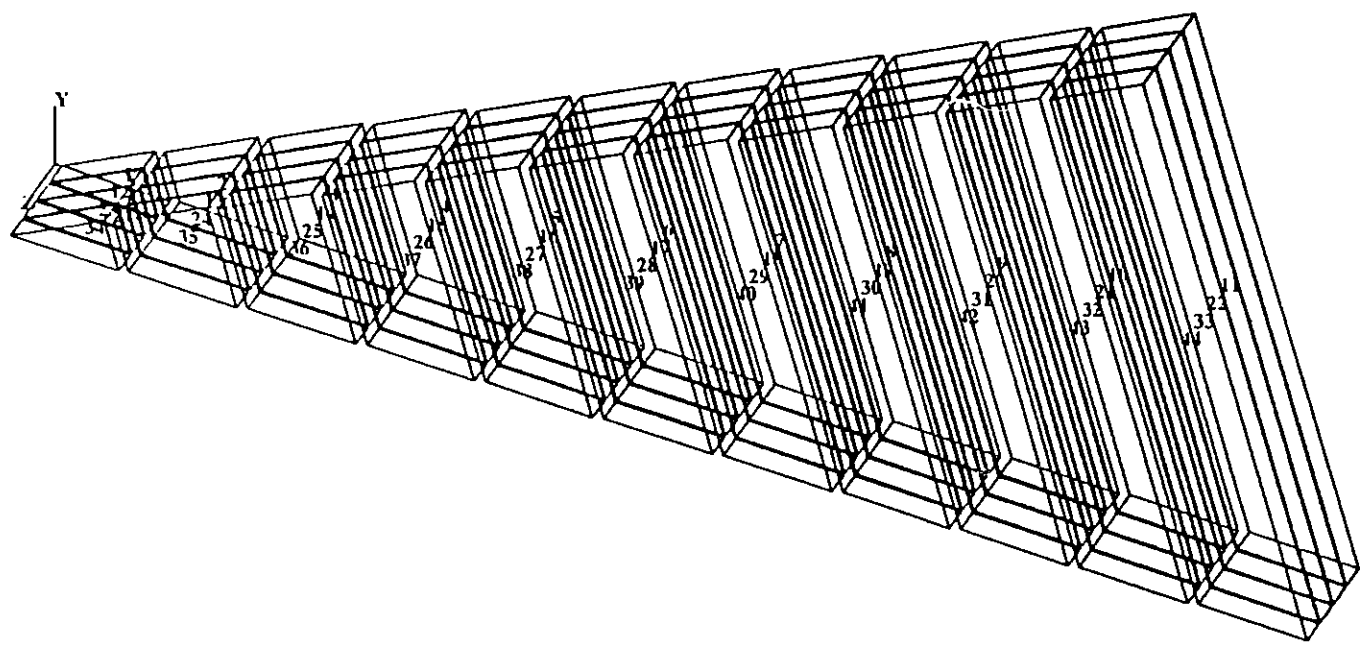
ANSYS 4.4A

MAR 19 1993

15:20:13

PLOT NO. 2

PREP7 ELEMENTS

ELEM NUM

XV =0.5

YV =1

ZV =1

DIST=3.94

XF =3.85

YF =1.925

ZF =0.31
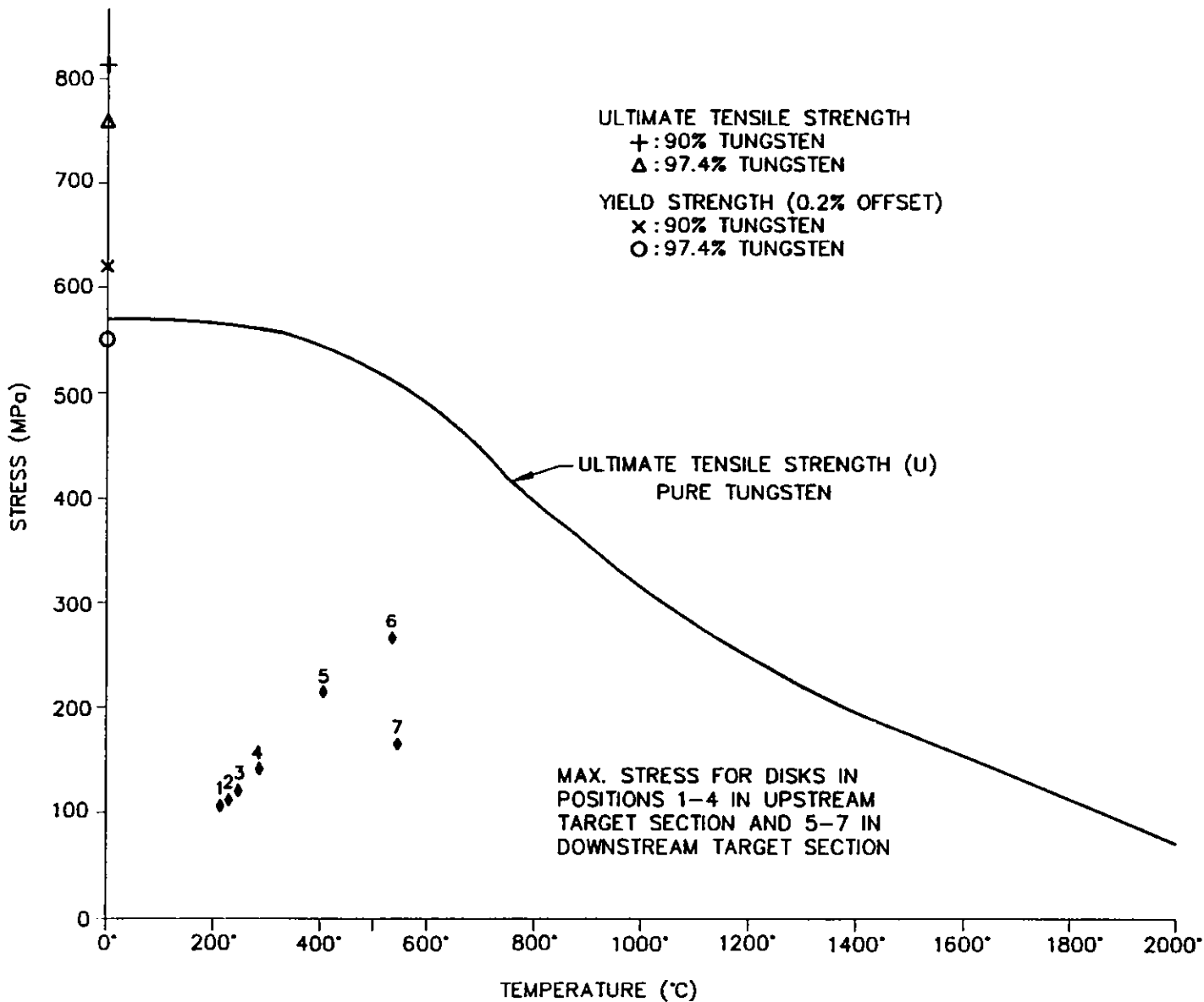
Figure IV.2.4-2 Mechanical Properties of Tungsten.
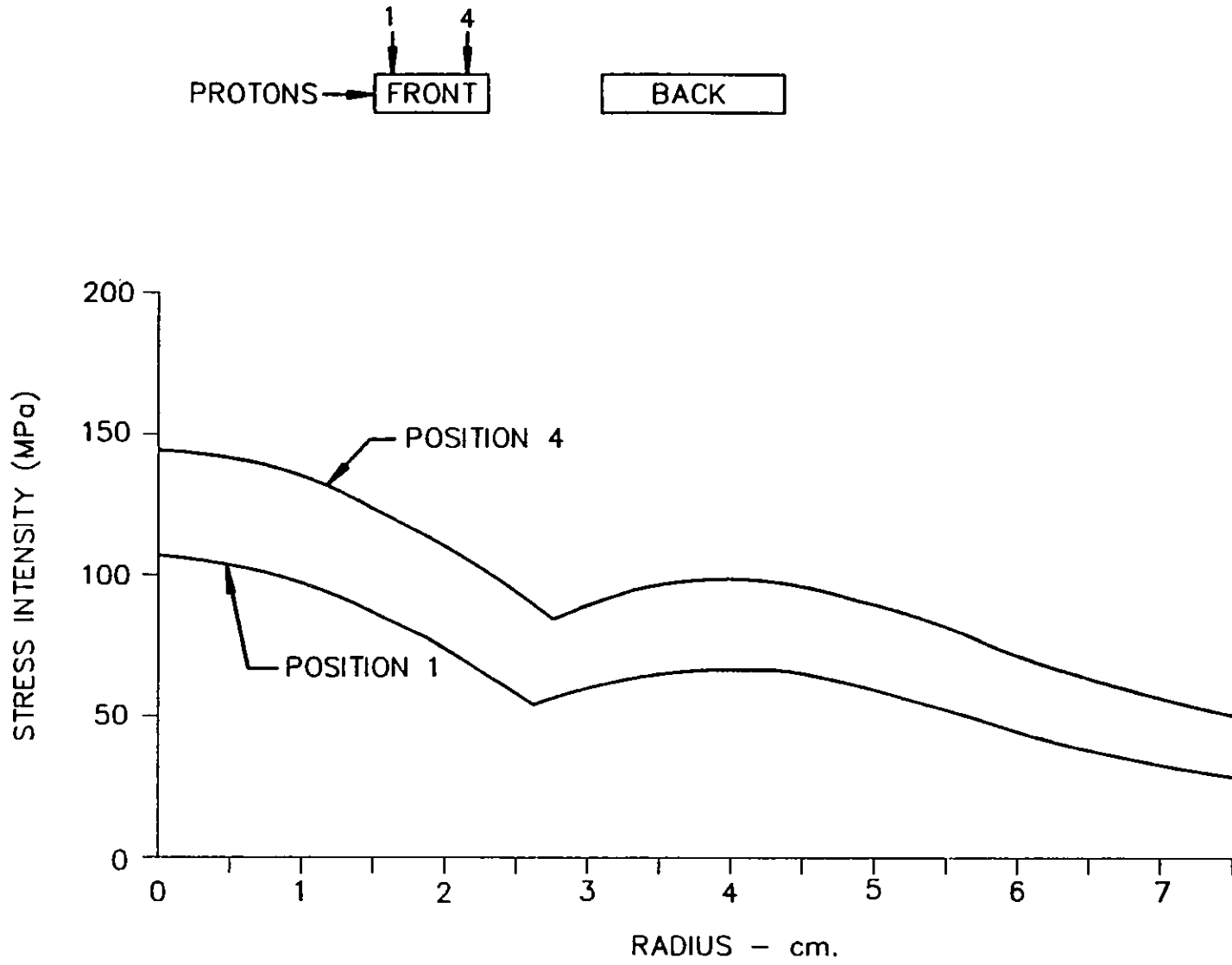
Figure IV.2.4-3 Stress Intensity in Disks at Two Positions in the Upstream Target Section Due to Radial Gradient Only.
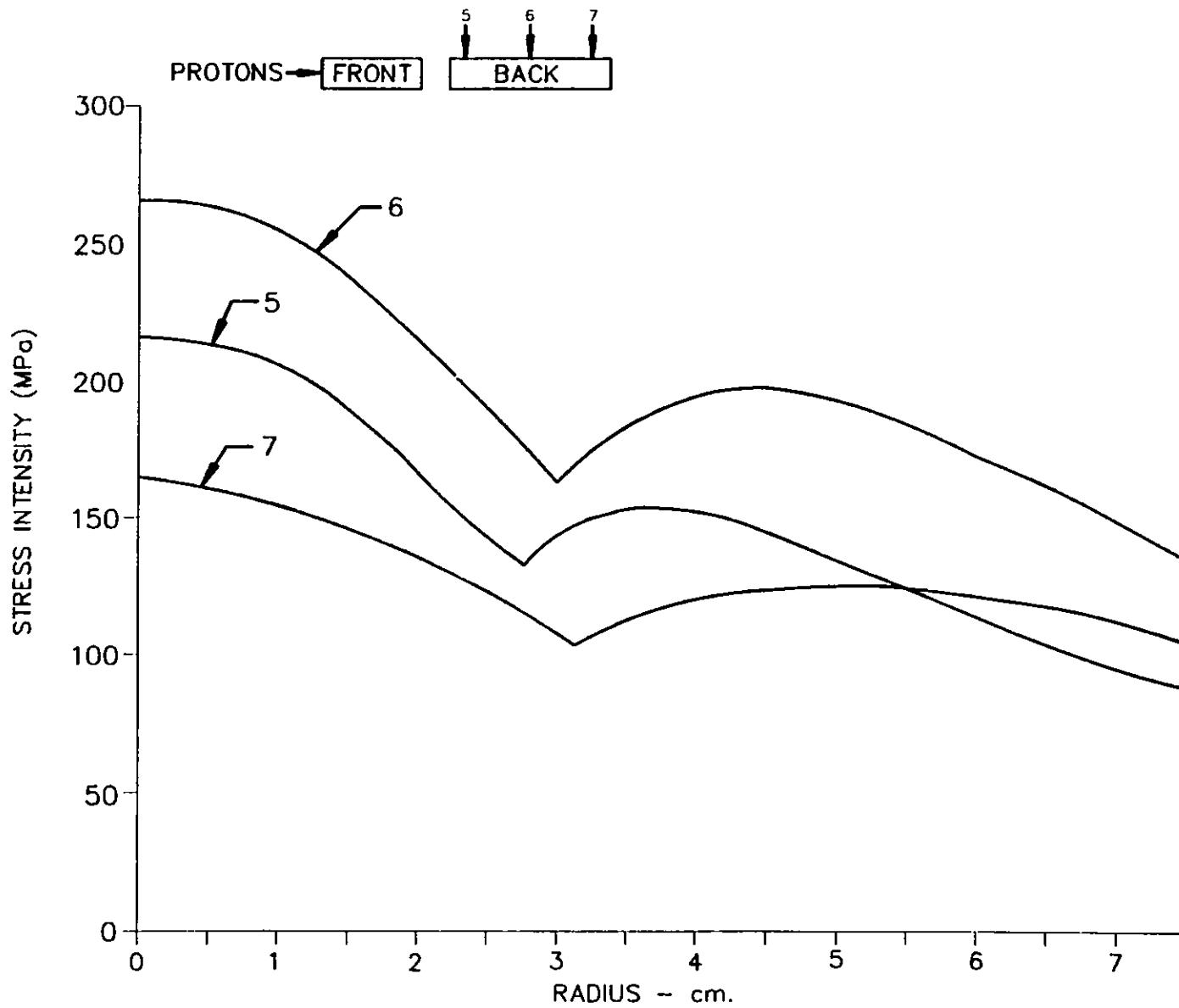
Figure IV.2.4-4 Stress Intensity in Disks at Three Positions in the Downstream
Target Section Due to Radial Temperature Gradient Only.

Table IV.2.4-1 Summary of Stresses

Target Section	Position	Mode of Operation	Power Level	Maximum Temperature,[a] °C	Maximum Stress Intensity (MPa)
Upstream	# 1	Steady power	Full	214.	96.4
Upstream	# 2	"	Full	223.	100.4
Upstream	# 3	"	Full	243.	111.5
Upstream	# 4	"	Full	280.	130.0
Downstream	# 5	"	Full	403.	215.9
Downstream	# 6	"	Full	540.	265.5
Downstream	# 7	"	Full	540.	165.0
Upstream	# 1	Mode 1, pre-pulse	Full	206.	83.1
Upstream	# 1	Mode 1, post-pulse	Full	228.	96.4
Upstream	# 1	Mode 2, pre-pulse	1 / 3	100.	24.6
Upstream	# 1	Mode 2, post-pulse	1 / 3	122.	36.7
Upstream	# 1	Mode 3, pre-pulse after 33 ms off	2 / 3	156.	55.3
Upstream	# 1	Mode 3, post-pulse after 33 ms off	2 / 3	177.	67.4
Upstream	# 1	Mode 3, pre-pulse after 66 ms off	2 / 3	148.	50.8
Upstream	# 1	Mode 3, post-pulse after 66 ms off	2 / 3	169.	63.1
Upstream	# 4	Mode 1, pre-pulse	Full	281.	108.0
Upstream	# 4	Mode 1, post-pulse	Full	294.	114.6

[a] Temperatures for the steady-power cases were calculated from a different model and hence are not directly comparable with those in Modes 1, 2, and 3.

heated disk increases 26 µm, while both flat surfaces have maximum outward deformations of 8 µm at their centers (at r = 0.0 cm).

This 2-D calculation gives peak tangential and radial stresses at r = 0.0 cm that are about double those obtained above using the 1-D model. Other disks are expected to show similar increases in stress when a 2-D calculation is carried out. ANSYS calculations for a more representative geometrical model should not significantly change these stresses. The yield strength of tungsten alloy is substantially higher than stresses from the 2-D calculation. On the basis of the 1-D calculations, we expect that the stresses in all other disks will also be found to be below the yield strength. Because thermal stresses are secondary stresses, the ASME code limit is twice the yield strength giving an even greater margin of safety. Thus, all stresses appear to be within tolerable limits.

2.5 TARGET METALLURGY AND CORROSION

2.5.1 Introduction

The selection of feasible materials for the target for the 1-MW neutron spallation source was based on the criteria and the priorities listed in Table IV.2.5-1. These have been discussed in further detail in two engineering notes.[16,17] The highest priority is that the target have a high mass number and density in order to produce the greatest number of neutrons per proton in the spallation process. The amount of afterheat produced by the target should be minimized to mitigate consequences of a loss of coolant accident (LOCA). The target material must have good mechanical, thermal, and corrosion properties, be resistant to radiation damage, resist surface damage due to cavitation, and not be subject to hydride formation. The target yield stress should be higher than the thermoelastic stress. High cycle fatigue could occur due to thermomechanical shock stresses because the beam is pulsed in times that are short compared to sound wave transit times. Table IV.2.5-1 summarizes the prioritization of material properties desired for a spallation target.

This prioritization of properties is a simplification because, for example, a candidate material could satisfy all of the priority 1-3 items but suffer severe cavitation damage under the water flow. The oxidation behavior of the candidate materials should be known. Formation of a protective oxide layer could be a positive factor, but on the negative side, incorporation of oxygen, especially as interstitials, could cause loss of ductility.

2.5.2 Mechanical Properties

Properties considered were strength, ductile-to-brittle transition temperature, fatigue resistance, ductility, and swelling. The mechanical properties of tungsten and tantalum and their
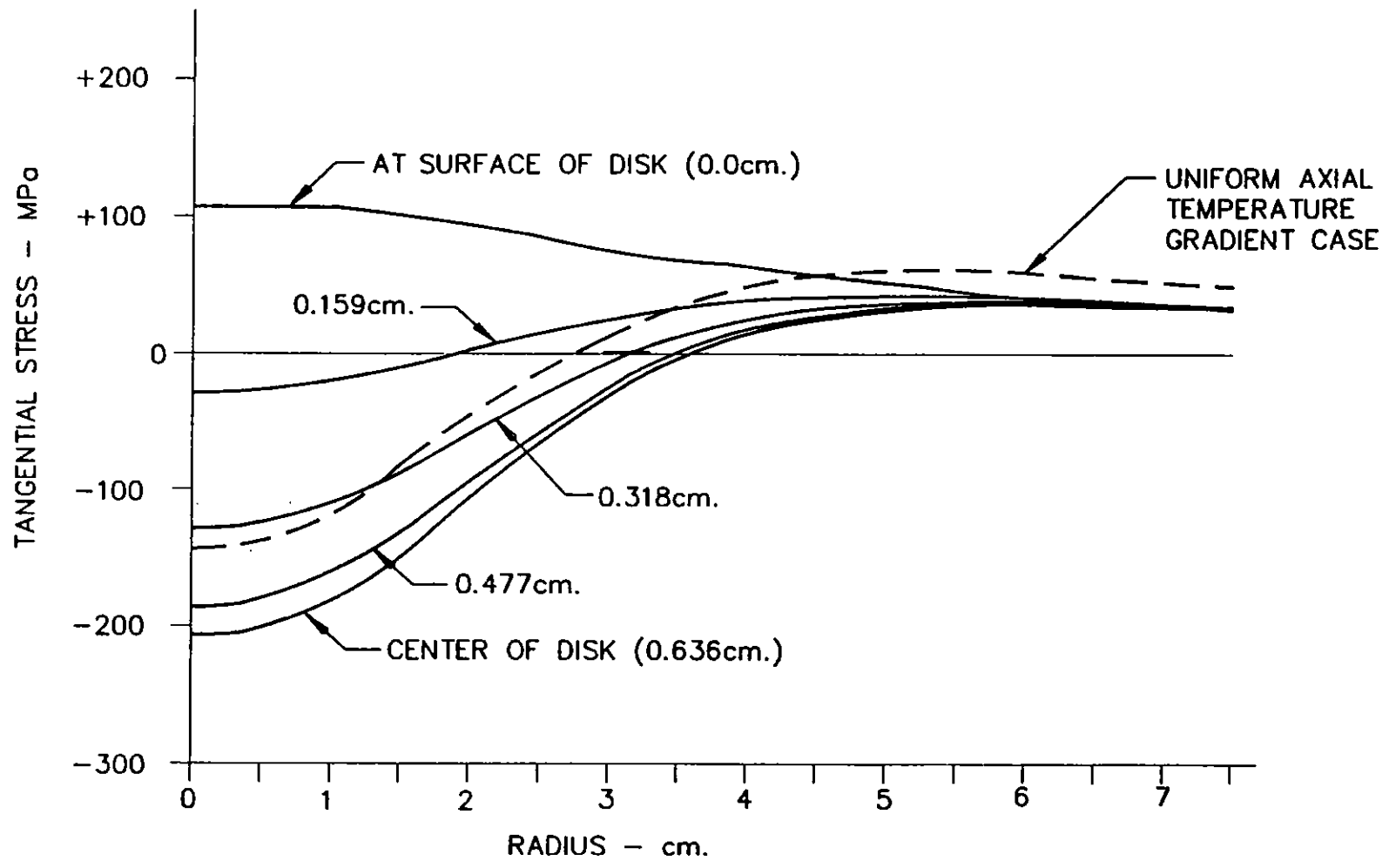
Figure IV.2.4-5 Tangential Stress Distribution in Last Disk of the Upstream Target Section Using 2-D Temperature Distribution.

Table IV.2.5-1 Properties to Consider in Selection of Target Material

Property	Priority
High atomic number	1
High density	1
Afterheat (LOCA consideration)	1
Corrosion resistance	2
Fatigue resistance	2
Hydrogen embrittlement and hydride formation	2
Strength	2
Swelling and radiation resistance	3
Machinability and cost	4
Cavitation	4
Oxidation resistance	4

alloys are favorable. It is generally true that the alloys, such as W-25% Re or Ta-10%W, are stronger than the elements alone, as shown in Figure IV.2.5-1.[18-20] Additionally, alloying increases the ductile-to-brittle transition temperature and the fatigue resistance. Irradiation increases the yield stress, but it decreases the ductility, as is demonstrated for tungsten in Figure IV.2.5-2.[21] Brittle fracture is not a problem as long as the thermoelastic stresses are less than the yield stress. Swelling of the tantalum-based alloys is quite low,[22] lower than pure tantalum.[20] Swelling of tungsten or its alloys has evidently not been measured.

2.5.3 Corrosion

The most extensive corrosion studies of high-density sintered tungsten and tungsten alloys showed that tungsten and all of the alloys tested undergo corrosion and that pure tungsten has the lowest corrosion rate of ≈ 0.5 μm/yr in a salt solution and ≈ 20 μm/yr in distilled water.[23] The LANSCE target, a tungsten cermet with a 3% Ni-Fe binder phase, has been running at 60 kW with 800 MeV protons for approximately 4 years. Fine particulate matter has been detected in the cooling water,[24] and the results of preliminary analysis indicate that the particles contain tungsten. Recent investigations of the corrosion of titanium and tungsten in distilled water indicate that titanium corrodes at least a factor of ten less than tungsten at 200°C.[7] The corrosion rate at 200°C for titanium is < 0.2 μm/year. This is negligible, so titanium is used as a corrosion-resistant coating.

2.5.4 Hydrogen Embrittlement

Hydrogen enters the target material during corrosion or by the accumulation of spallation-produced protons. The resulting formation of hydrides can cause significant embrittlement of the target material and is expected to be a major factor in determining target lifetime. Figure IV.2.5-3 shows the pronounced increased in brittleness with increasing hydrogen concentration in tantalum and a number of tantalum alloys. Embrittlement is expected to be important for tungsten as well, but comparable data are not yet available. Helium may also cause embrittlement, so it requires consideration.

2.5.5 Afterheat

Estimates of afterheat (radioactive decay heat) and activation have been obtained from numerical simulations for tantalum and tungsten (Section IV.2.2.4). The afterheat in tantalum results in very high temperatures under LOCA conditions (Section IV.2.7.1). Tungsten or its alloys, under similar conditions, have less than one-third of the afterheat power of tantalum or its alloys, and tungsten is therefore preferred.
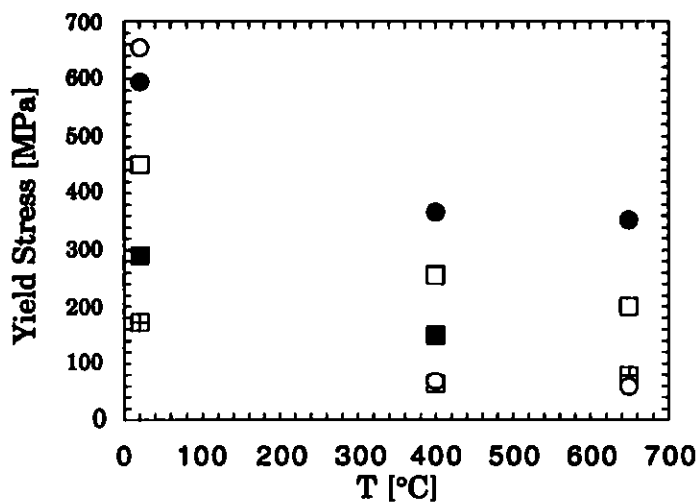
Figure IV.2.5-1 Yield Stress Measured at a Strain Rate, $\dot{\varepsilon} \approx 1 \times$
10^{-4} s^{-1} (about the $\dot{\varepsilon}$ achieved during cool down) for Pure Ta
(squares with cross from Ref. 18, filled squares from Ref. 19,
and open squares from Ref. 20), Pure W (open circles
from Ref. 19), and T-111 (filled circles from Ref. 18).
(T-111 is the designation for a commercial alloy,
Ta with 7.9%W and 2.3% Hf.).
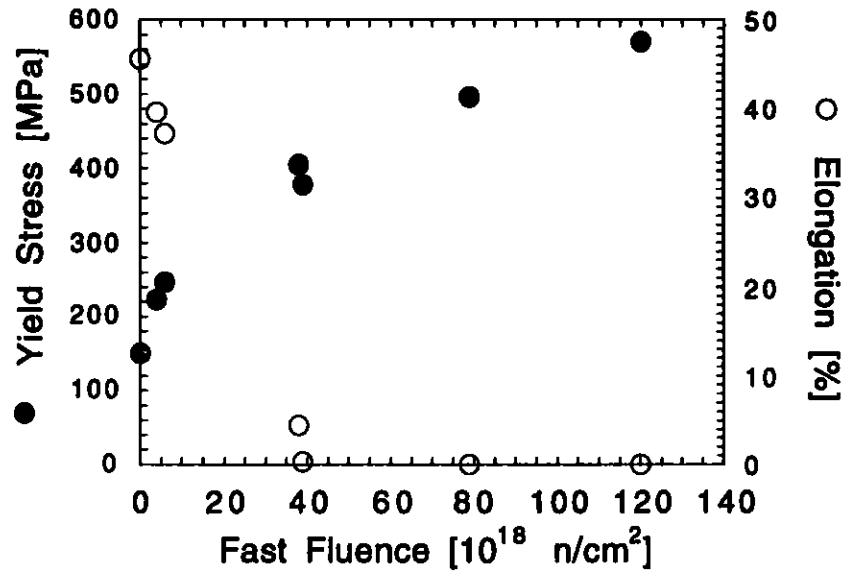
Figure IV.2.5-2 Variation of the Yield Stress and Percent Elongation at 400°C for Tungsten (Reference 21).
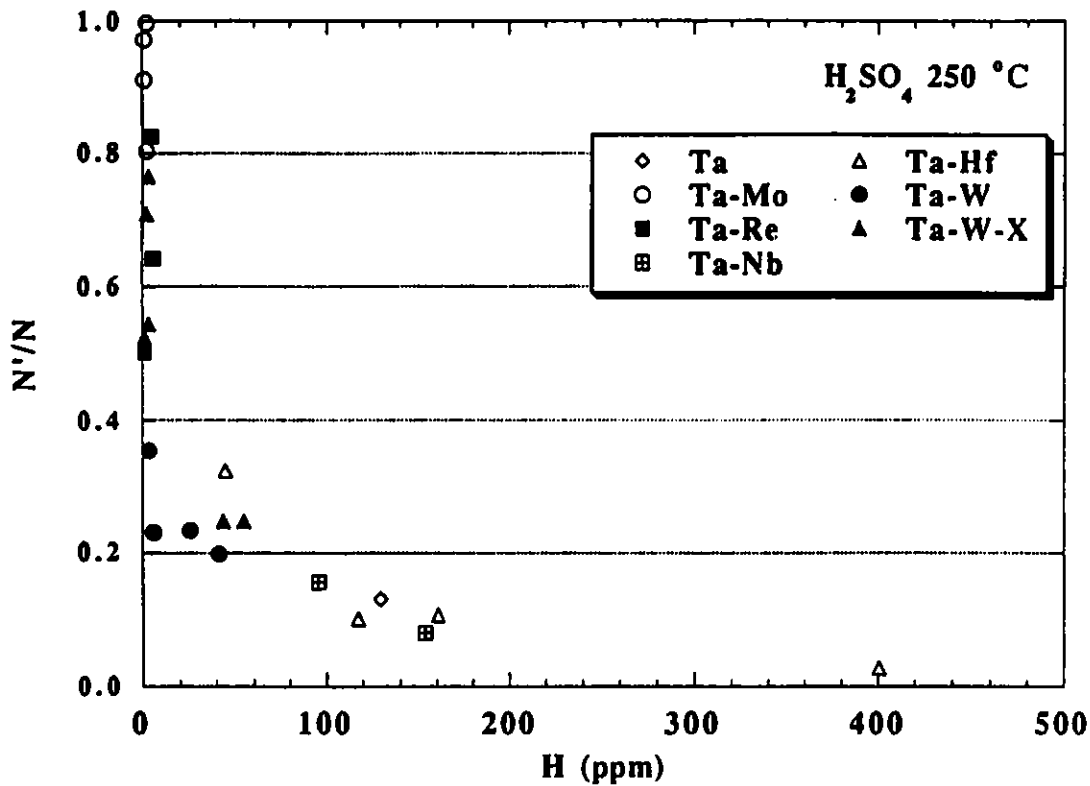
Figure IV.2.5-3 Variation of Brittleness with Hydrogen Concentration for Various Tantalum Alloys. (Brittleness is measured as the ratio of number of bends to fracture specimens with and without hydrogen [N'/N]. Source: Reference 25.)

2.5.6 Other Properties

Investigations of cavitation are usually performed at flow velocities about an order of magnitude higher than those expected in the IPNS Upgrade target, and under conditions of pulsating flow, to ensure that cavitation occurs.[26] Therefore, it is anticipated that cavitation will not be a problem for the IPNS Upgrade target.

2.5.7 Target Material Selection

The available property data for the candidate target materials are compared to the prioritized properties listed in Table IV.2.5-1. Uranium and liquid metal targets have not been discussed, but they remain as options after further development. Table IV.2.5-2 presents a list of acceptable materials, presented in the order of preference for a particular property. On the basis of this assessment, tungsten, or a tungsten alloy, is the chosen target material.

2.6 TARGET COOLING SYSTEM

With proton beam power of 1 MW, a total heat load of approximately 610 kW is deposited in the two target sections, as described in Section IV.2.2.2 and Table IV.2.2-2. The upstream target section consists of 12 thin tungsten alloy disks with 13 coolant passages. The downstream target section has 9 thicker tungsten alloy disks and 10 cooling passages. The water velocity must be controlled through each of the cooling passages between disks.

A number of process-related assumptions are made that underlie the design of the water flow system for each target. The heat load corresponds to the full beam power of 1 MW, which is the maximum power that the 30-Hz target receives. Both targets and their cooling systems are identical. This leads to savings in terms of design effort, procurement, maintenance, and the provision of spares.

The bulk water temperature adjacent to the convective film at the target surface in the direct path of the beam is approximately 60°C, and the maximum target disk surface temperature is 127°C (Section IV.2.3.) The saturation temperature of water is 172°C at the minimum design water pressure of 830 kPa. Thus, there is a minimum margin to boiling of at least 45°C. Some additional suppression of boiling due to convective flow occurs, so the temperature margin is even higher. The values calculated for the maximum surface heat flux from the first and last titanium-coated tungsten disks are 580 W/cm^2 and 530 W/cm^2, respectively. These flux values, and the design surface-to-bulk temperature difference of 67°C, are used to calculate the necessary convective film coefficients for smooth surfaced target disks.

Smooth surfaces provide the least effective convective film heat transfer. Mechanical roughening of the surfaces is known to increase convective film coefficients by almost a factor of

Table IV.2.5-2 Acceptable Candidate Materials in Order of Preference, Compared
to the Desired Prioritized Properties of a Target Material

Property	Acceptable Materials	Unacceptable or Borderline Materials
High atomic number	Pt, Ir, Os, Re, W, Ta, Hf, Au	Mo, Nb, V, Zr
Afterheat	W	Ta
Strength	Re, T-111, ASTAR-811C, W-(10-25%)Re, Ir, W,[a] Ta[a]	Pt, Au
Corrosion resistance	Pt, noble metals, Ti, Ta-10%W, Ta, W	
Fatigue resistance	Au, Ta, W, Ta-10%W	
Hydrogen embrittlement, hydride formation	W, Ta-(2-10%)W, Ta	
Swelling and radiation resistance	T-111, Ta-10%W	Ta, Mo
Machinability and cost	Ta, T-111, ASTAR-811C, W-Re, W	
Cavitation	No data available	
Oxidation behavior	Pt, W, Ta	

[a] After some radiation hardening.

two, albeit at the price of pressure loss. In order to assure a conservative cooling system design, these enhancements are not assumed. In the calculation of the required flow rates in the thermal-hydraulic analysis reported in Section IV.2.3, such heat-transfer enhancements were considered. Therefore, the required flow rate indicated in Section IV.2.3 is substantially less than the one used in this section to size the cooling system. The reduced flow rate is used in the thermal-hydraulic analysis because the lower flow rate causes a higher average bulk coolant temperature, and this introduces some conservatism in the thermal analysis of the target disks.

The respective required Reynolds numbers are calculated using the Dittus-Boelter convective film coefficient correlation and thermophysical properties of water evaluated at the assumed bulk temperature. These Reynolds numbers determine the required water velocities. Cooling the first disk requires a water velocity of 15.4 m/s, while cooling the last disk requires 13.4 m/s. The flow circuit provides for a uniform water velocity of 15.4 m/s to give an extra cooling margin and to simplify the design. The rectangular flow passages between target disks are 0.159 cm thick, and the height is 9.0 cm, so the required water flow rate for each target section is 28 L/s.

Pressure drops throughout various portions of the flow circuit are calculated by using standard Moody friction factors. The flow circuit is shown in Figure IV.2.6-1. Two 75 kW pumps (28 L/s each) supply the water to the target cooling circuit for normal operation. This arrangement allows flow reduction for the 10-Hz target and provides some reduced cooling capability during a single pump failure. Two 0.75-kW pumps are adequate for decay heat removal.

The design decay heat load of 5 kW (Section IV.2.2.4) is removed by means of a cooling-water flow rate of 0.2 L/s with a bulk temperature rise of 20°C. Pressure drop within the target cooling system is negligible for this small flow rate. A mobile cart having a small water pump, a small supply tank (20 L), and independent pressurization, level control, and gas safety relief systems provides cooling when targets are removed from the biological shield for servicing.

Each cooling circuit also has a control valve, flowmeter, heat exchanger, filter, and remote temperature and pressure transducers. The heat exchangers are located downstream of the pumps to remove power input by the pumps. The major portion of the piping for each flow circuit is nominally 8.9 cm diameter (3 in. Sch 40), while that portion of piping within the shielding is space-limited to 6.0 cm diameter (2 in. Sch 10). A single demineralizer is located in a side stream to the larger piping. The water supply tank has a capacity of 4,500 L to provide adequate water-storage volume and gas ullage space, and it includes a H_2/O_2 recombiner. A liquid-level gauge is used to maintain the water level in the tank at three-quarters full. A helium gas supply pressurizes the system initially to 690 kPa. It provides a gas bleed flow rate of 0.016 L/s through a back-pressure control valve for purging the ullage of oxygen, hydrogen, and any activation products and for stabilizing the tank pressure level. A pressure relief valve and burst diaphragm and a large vent valve are included for rapid tank depressurization. Bleed and

Figure IV.2.6-1 Target Coolant Flow Circuit.

vent gases are routed to an 11,000-L holdup tank, which allows adequate time for radioactive species to decay. More details on the purge and vent gas holdup tank and exhaust system are given in Section IV.6.2.1.

The calculated total pressure drops through each target cooling-flow circuit are 1.7 MPa. The required pumping power in each circuit is 150 kW, which allow 20% of the pressure drop for control and an assumed pump efficiency of 0.7. The heat exchanger is sized to remove slightly more than 750 kW.

Figure IV.2.6-2 shows the arrangement of the cooling-system components for the 30-Hz target. Figure IV.2.6-2a is a sectional view through A-A of Figure IV.2.6-2. Those components associated with the target cooling system are highlighted in these figures. The supply and drain water tanks, target pumps, target decay-heat pumps, heat exchanger, and demineralizer are located in a concrete-shielded enclosure in Building 371. Piping from the shielded enclosure in 371 runs to the target biological shield in Building 370.

Figure IV.2.6-3 shows the general arrangement of the cooling system components for the 10-Hz target, with supply and drain water tanks, target pumps, target decay-heat pumps, heat exchanger and demineralizer located in a concrete shielded enclosure in Building 367. These components are highlighted in the figure. Figure IV.2.6-3a shows a sectional view of the same area. Piping from Building 367 runs to the target biological shield in Building 369.

The supply water tank and water drain tank are approximately 1.4 m in diameter and 4 m long, constructed of 304SS. The tanks are mounted horizontally. The drain tank is located above the target pump suction to allow reuse of the drained water. The supply tank has two 16.8 cm (6 in. Sch. 40) connections for the target pump supply and cooling system return piping. The 16.8-cm supply line also connects to the water drain tank so that water from the drain tank can be pumped back into the system.

The target cooling pumps are constructed of corrosion resistant materials. The installed motor power is 94 kW each. The pump outlet flow passes through a flowmeter and then through a water-cooled heat exchanger. The 304SS shell-and-tube heat exchanger is 3 m long with a 0.25-m nominal diameter. It is mounted horizontally with 24-mm flanged connections on both the shell and channel sides. Raw cooling water at 1,600 L/min passes through the shell side of the heat exchanger. A de-ionized water supply is provided for initial system fill and make-up.

Insulation covering all cooling water lines limits heat transferred to the shielding enclosures.

2.7 POTENTIALLY HAZARDOUS INCIDENTS

Credible incidents have been examined for the IPNS Upgrade target stations. These incidents generally fall into the category of low-probability, low-consequence events.
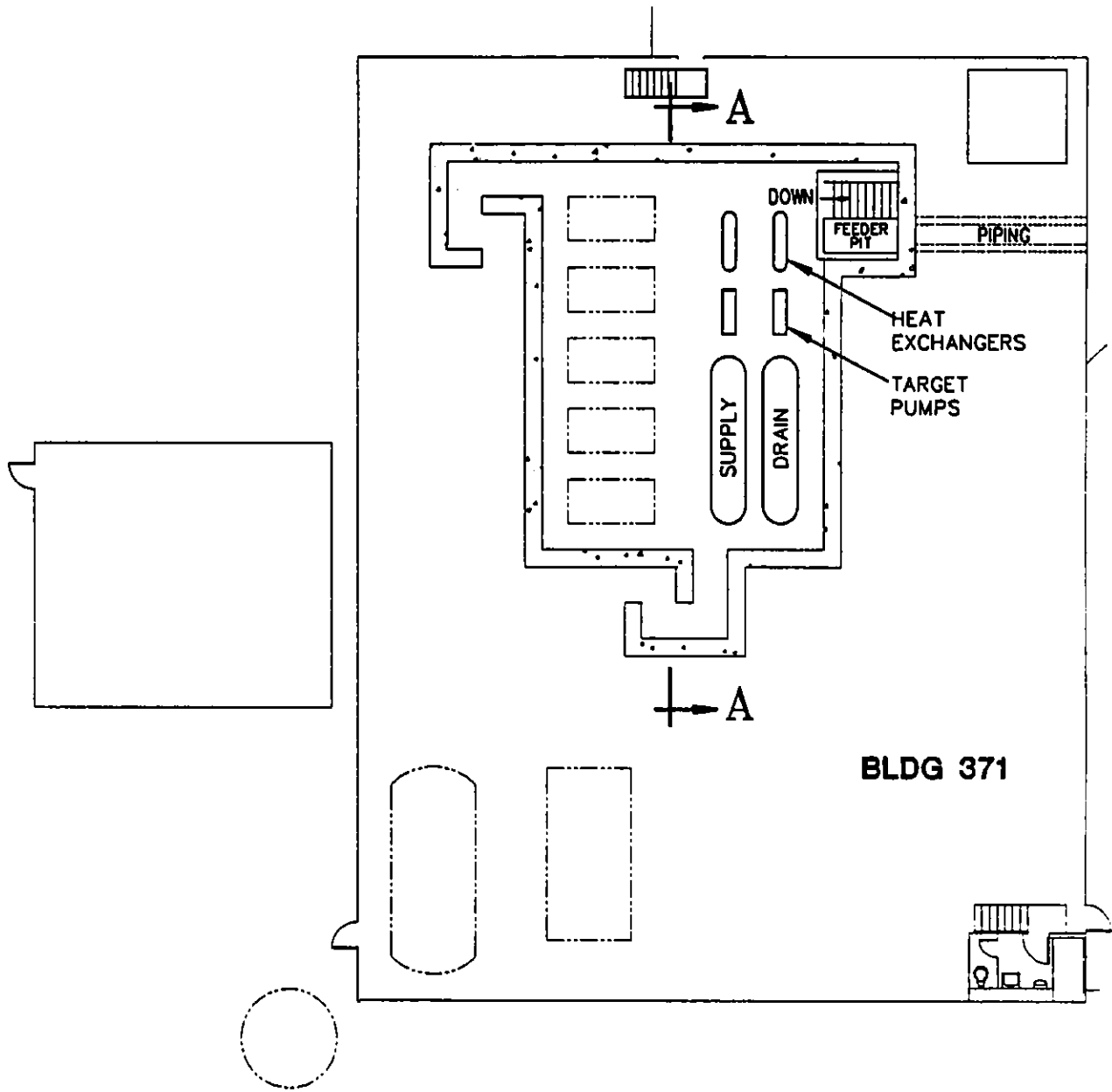
Figure IV.2.6-2 Arrangement of the 30-Hz Target Cooling System in Building 371.
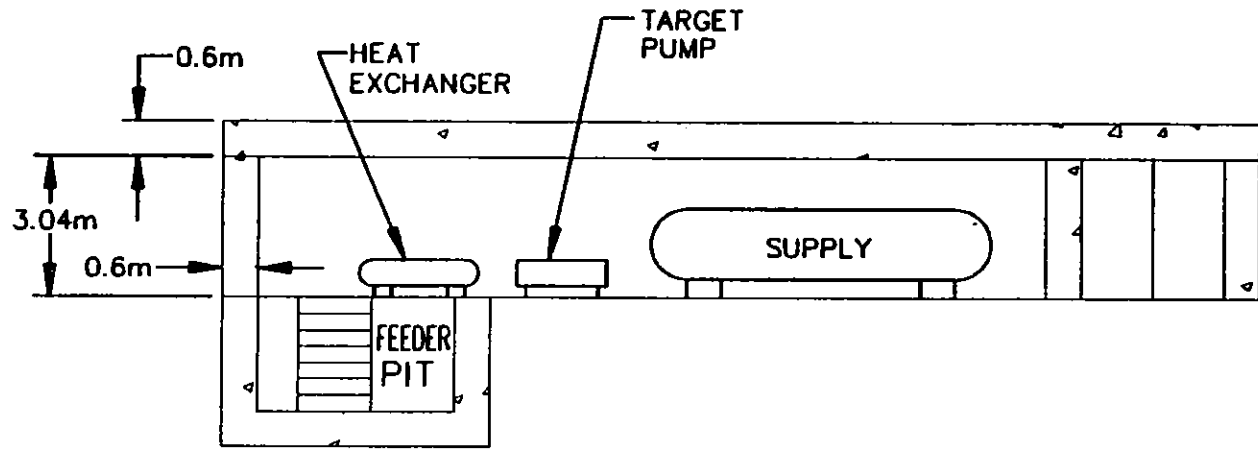
SECTION A-A

Figure IV.2.6-2a Sectional View of the 30-Hz Target Cooling System in Building 371.

HEAT EXCHANGERS

TARGET
PUMPS

A

A

DRAIN

SUPPLY

DOWN

FEEDER
PIT

BLDG 367
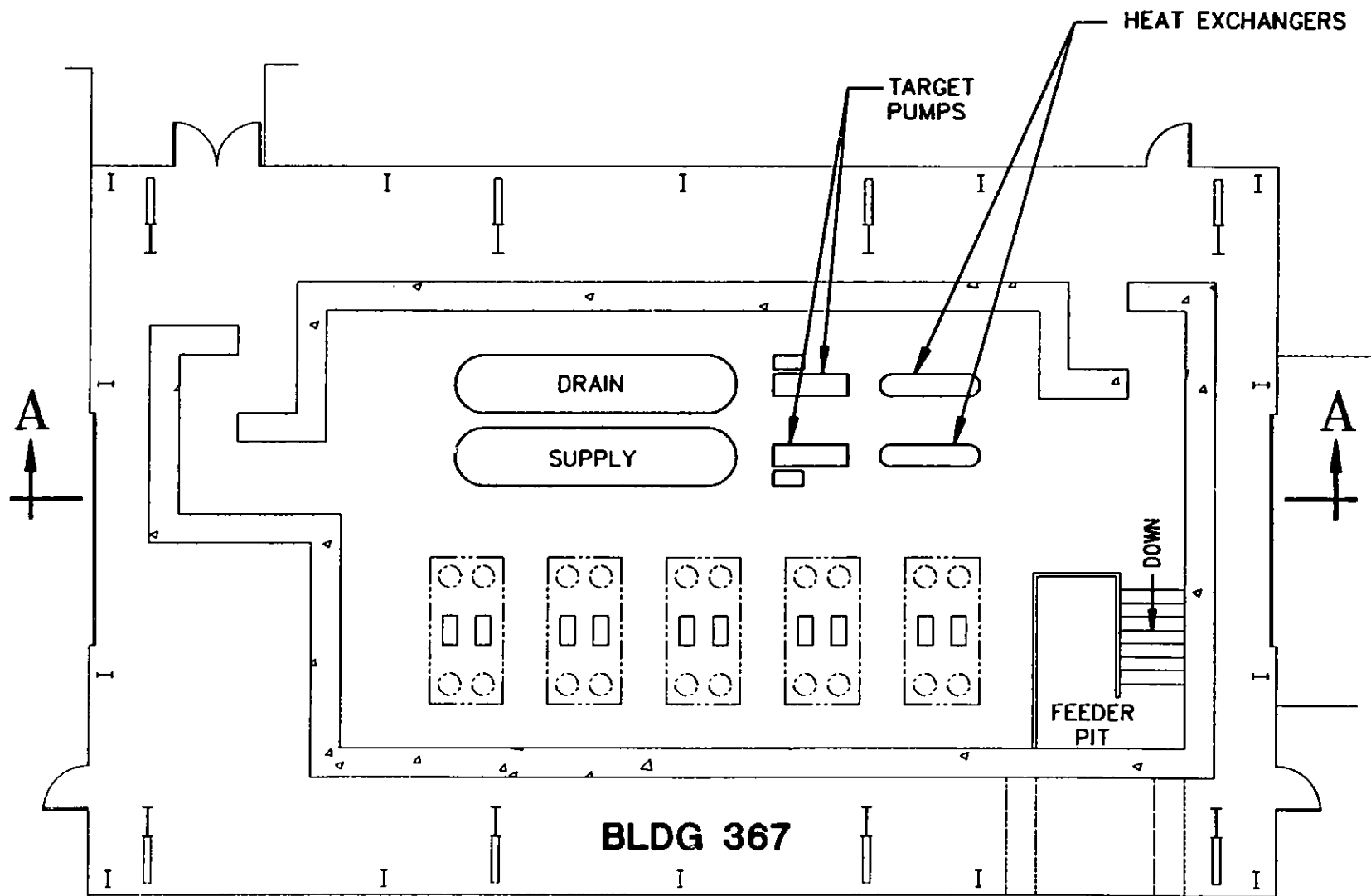
Figure IV.2.6-3 Arrangement of the 10-Hz Target Cooling System in Building 367.
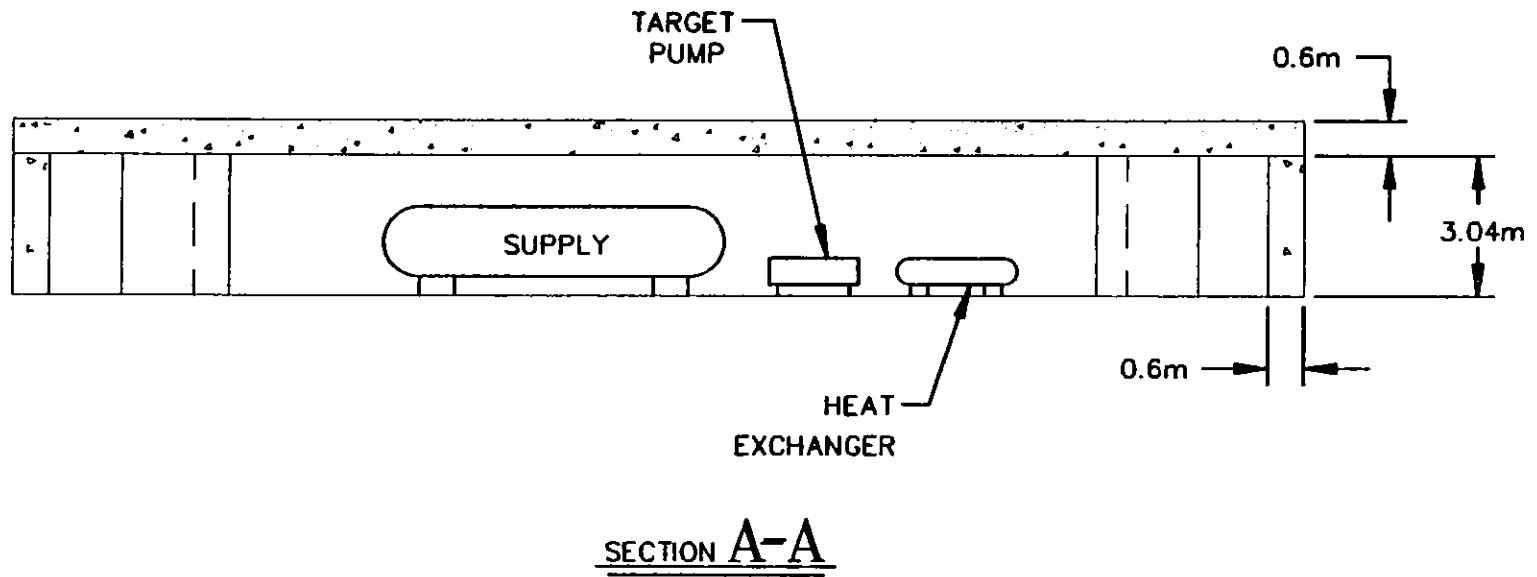
Figure IV.2.6-3a Sectional View of the 10-Hz Target Cooling System in Building 367.

The IPNS Upgrade follows the standard practice of designing for defense in depth. This practice incorporates several barriers to the release of radioactive substances. The vast majority of the radioactive products are contained within the target. The target is enclosed in the primary water cooling system, which is a welded, pressure-rated, stainless-steel system. Next, a sealed helium-purged aluminum tank encloses the water system. The exhaust from this volume goes into a holdup tank and then through high-efficiency particulate air (HEPA) filters. Finally, the biological shield, a welded steel barrier, is also a helium-purged vented volume. The exhaust from the biological shield is also passed through HEPA filters. These numerous barriers provide in-depth containment and confinement of radioactive substances. In addition to these passive barriers to prevent activity release, the IPNS Upgrade also provides uninterruptible battery and diesel power supplies to provide electricity for coolant and ventilation systems.

Preliminary conceptual examination of credible incidents has been done. These will be studied in detail in the IPNS Upgrade Title II Design Safety Assessment Documents. The minimum list is:

1. Loss of target primary coolant flow;

2. Loss of target primary coolant;

3. Loss of vacuum surrounding the moderator cans;

4. Explosion of cryogenic fluids in moderator systems;

5. Loss of secondary coolant supply;

6. Tornado;

7. Earthquake; and

8. Facility fire.

DOE Order 6430.1A, titled "General Design Criteria," gives radiological siting guidelines for DOE nonreactor facilities. The postulated credible incidents listed above will have consequences less than the limits specified in DOE 6430.1A.

The IPNS Upgrade target is made of nonfissionable material. The reactor concerns involving prompt criticality and rapid power increases are not possible in spallation sources. Although reactors can be designed to safely control these processes, accelerator-driven spallation sources need not address them.

2.7.1 Loss of Coolant Analyses

Consequences of a Loss of Coolant Accident (LOCA) were assessed by calculating the transient temperatures under LOCA conditions using a simple one-dimensional (radial) model. The target was represented as a cylinder of 5.5-cm radius surrounded by a 0.5-cm-thick stainless-steel vessel, separated from an annular 47.3-cm thick beryllium reflector by a 3.5-cm helium-filled gap. Cases included helium conduction; without helium conduction, to represent totally evacuated conditions; and without helium conduction but with the steel vessel maintained at 49°C, as if by active cooling. In the ranges of temperature encountered, emissivities range from 0.2 to 0.5 for steel, 0.01 to 0.36 for tantalum, and 0.05 to 0.24 for tungsten. The emissivity for beryllium is 0.2. The heat transfer is nonlinear because of radiative (T^4) heat transfer and the variation of the emissivities and the helium thermal conductivity with temperature. Therefore, the time to reach peak temperature varies with power input, reaching a maximum in about 30 minutes for tantalum and about one hour for tungsten at the higher powers. It always reaches maximum within less than five hours for the lower-power values studied. The calculations account for the decay of afterheat during the transient.

Afterheat powers of tantalum and tungsten are described in Section IV.2.2.4. Two scenarios were studied: first, for afterheat immediately following continuous irradiation for one year at 1 MW; second, for continuous irradiation at 2/3 MW for one year, followed by continuous irradiation at 1 MW for one month up to the beginning of the transient. Table IV.2.7-1 shows the resulting peak temperatures of the target and the vessel and the temperature of the reflector after 48 hours.

Tantalum, tungsten, and their practical alloys remain solid at the highest of these temperatures. Stainless steels melt at around 1425°C, so the vessel would melt in either case if the target were of tantalum and the vessel were not actively cooled. The vessel retains its integrity without active cooling if the target is tungsten. Internal steel parts weaken or melt, however, even for tungsten-target material. Beryllium approaches its melting temperature (1275°C) with tantalum, but not with tungsten in any of these cases. With a tungsten target, a LOCA would have no impact on the facility as a whole, but the target would have to be replaced. This is a tolerable consequence of a hypothetical loss of coolant accident. Tungsten is acceptable without any backup decay heat removal system, unlike the case for tantalum. Therefore, we choose tungsten or a practical tungsten alloy as the design basis target material and plan no decay heat removal systems for LOCA incidents.

Table IV.2.7-1 Peak LOCA Transient Temperatures in the Target, Target Vessel, and Reflector[a]

Material/ Scenario	Power (W)	Temperatures (°C)							
		Case 1[b]			Case 2[c]			Case 3[d]	
		Target	Vessel	Reflector	Target	Vessel	Reflector	Target	Vessel
Tantalum									
Scenario 1	13300	2624	1700	1135	2737	1750	1135	2486	49
Scenario 2	9695	2118	1468	877	2232	1517	876	2049	49
Tungsten									
Scenario 1	3720	1394	1067	372	1533	1129	371	1421	49
Scenario 2	3615	1371	1050	355	1513	1114	344	1403	49

[a] Reflector temperatures are those after 48 hours, at which time they are still rising.

[b] With conduction in helium.

[c] No conduction in helium.

[d] No conduction in helium, cooled vessel.

2.8 REFERENCES

1. G.J. Russell et al., "The LANSCE target system," in *Proceedings of the 9th Meeting of the International Collaboration on Advanced Neutron Sources (ICANS IX)* (Villigen, Switzerland, Sept. 22-26, 1986), Swiss Institute for Nuclear Research, ISBN 3-907998-01-4, pp. 177-244 (1987).

2. M. Holding and T.A. Broome, "The status of the ISIS targets," in *Proceedings of the 11th Meeting of the International Collaboration on Advanced Neutron Sources (ICANS XI)* (Tsukuba, Japan, Oct. 22-26, 1990), National Laboratory for High Energy Physics (KEK) Report No. 90-25, pp. 478-487 (1991).

3. J.M. Carpenter, "Status of Argonne's Intense Pulsed Neutron Source IPNS-I," in *Proceedings of the 5th Meeting of the International Collaboration on Advanced Neutron Sources (ICANS V)* (Jülich, Germany, June 22-26, 1981), Kernforschungsanlage Jülich Report No. Jül-Conf-45, pp. 33-52 (1981).

4. A. Carne et al., "The ISIS target," in *Advanced Neutron Sources 1988*, Proceedings of the 10th Meeting of the International Collaboration on Advanced Neutron Sources (ICANS X) (Los Alamos, N.M., Oct. 3-7, 1988), IOP Conference Series, No. 97 (Institute of Physics, New York, 1989), pp. 79-90 (1989).

5. Y. Ishikawa, "Present status and future project of KENS facility," in *Proceedings of the 8th Meeting of the International Collaboration on Advanced Neutron Sources (ICANS VIII)* (Oxford, U.K., July 8-12, 1985), Rutherford Appleton Laboratory Report No. RAL-85-110, pp. 17-43 (Chilton, U.K., 1985).

6. A.E. Knox et al., "Progress on the IPNS enriched uranium booster target," in *Proceedings of the 9th Meeting of the International Collaboration on Advanced Neutron Sources (ICANS IX)* (Villigen, Switzerland, Sept. 22-26, 1986), Swiss Institute for Nuclear Research, ISBN 3-907998-01-4, pp. 557-589 (1987).

7. A.V. Dementyev, S.F. Sidorkin, N.M. Sobolevsky, Y.Y. Stavissky, V.G. Miroschnichenko, I.I. Konovalov, A.A. Maslov, I.T. Tretakov, V.I. Trushkin, and A.D. Pogov, "The Moscow Meson Factory pulsed neutron source based on a uranium target," in *Proceedings of the Second International Conference on Pulsed Advanced Neutron Sources (PANS II)* (Dubna, Russia, June 1994).

8. R.E. Prael and H. Lichtenstein, *User Guide to LCS: The LAHET Code System*, Los Alamos National Laboratory Report No. LA-UR-89-3014 (Sept. 1989).

9. T.W. Armstrong et al., "Theoretical target physics studies for the SNQ spallation neutron source," Jul-Spez-120 (KfK Karlsruhe, Germany, July 1981).

10. N. Watanabe et al., "Report of the moderator working group," presented at International Workshop on the Technology of Targets and Moderators for Medium to High Power Spallation Neutron Sources (Paul Scherrer Institute, Switzerland, Feb. 1992).

11. T.A. Broome, *Calculations of Activity and Afterheat for the IPNS-II Tantalum and Tungsten Targets*, Rutherford Appleton Laboratory Report No. ISIS/TS/N1/95 (Jan. 1995).

12. J. Kaganove, *THTB at ANL*, TM 281 (Sept. 1982).

13. Cabot Performance Materials, P.O. Box 1607, Boyertown, Pennsylvania.

14. R.J. Roark, *Formulas for Stress and Strain* (McGraw-Hill, New York, 1954).

15. *ANSYS User Manual*, DN-R144:44, Rev. 4.4, Swanson Analysis Systems, Inc. (May 1989).

16. J.L. Routbort, IPNS Upgrade NST Note 2 (1994).

17. J.M. Carpenter et al., IPNS Upgrade NST Note 3 (1993).

18. J.H. Bechtold, Acta Metall. **3**:249 (1955).

19. *Metals Handbook*, Vol. 10 (ASM, Metals Park, Ohio, 1990).

20. F.W. Wiffen, "Defects and defect clusters in BCC metals and their alloys," in Nuclear Metallurgy **18**, edited by R.J. Arsenault, p. 176 (NBS, Gaithersburg, Md., 1973).

21. R.C. Rau, J. Moteff, and R.L. Ladd, J. Nucl. Mater. **24**:164 (1967).

22. M.L. Grossbeck and F.W. Wiffen, *Space Nuclear Power Systems, 1985, Vol. 3*, edited by M.S. El-Genk and M.D. Hoover, p. 85 (Orbit Book Co., Malabar, Fla., 1986).

23. J.J. Batten, I.G. McDonald, B.T.Y. Moore, and V.M. Silva, *Corrosion of High-Density Sintered Tungsten Alloys, Part I: Immersion Testing*, Department of Defense Materials Research Laboratory Report No. MRL-R-1139 (Maribyrnong, Australia, 1988).

24. T. Brun, 1994 (private communication).

25. L.A. Gypen, M. Brabers, and A. Deruyttere, Werkstoffe und Korrosion **35**:37 (1984).

25. F.G. Hammitt and M.K. De, Wear **52**:243 (1979).

This section discusses the moderators and the reflectors. Neutrons produced in the target have energies up to hundreds of MeV, while the neutron scattering instruments require neutrons with energies less than a few tens of eV. It is the function of the moderators and the reflector to slow down the neutrons produced in the target to the energies required by the instruments and to direct as many as possible of these moderated neutrons down the beamlines to the instruments. In this process, the moderators and the reflector must not degrade the time-structure of the neutron pulses beyond limits imposed by the instruments, because this time structure is essential to the time-of-flight (TOF) energy analyses performed by the instruments.

Section IV.3.1 discusses the moderator geometry and materials and the importance of premoderators, decoupling, and poisoning. The neutronic requirements of the instruments, as discussed in Chapter V, determine the optimal moderator characteristics, but these must be tempered by such practical considerations as radiolysis of the moderator materials and moderator cooling requirements.

Section IV.3.2 discusses the Monte Carlo calculations of the moderator heat loads and the neutron beam currents from the moderators. The basic model for the Monte Carlo calculations is discussed in Section IV.2.2. Section IV.3.2 also makes use of known moderator performances at neutron energies of use to the instruments to estimate the energy spectra and pulse shapes for neutron beams from the various moderator types and positions.

Section IV.3.3 discusses the problems associated with radiolysis of the moderator materials.

Finally, Section IV.3.4 describes cooling systems sized to handle the cooling needs of the various room-temperature and cryogenic moderators. Other water cooling systems are also included in this section.

3.1 MODERATOR AND REFLECTOR GEOMETRY AND MATERIALS

As shown in Figure IV.1.2-2, each target station contains six moderators, four in wing geometry and two in flux-trap geometry, and each of these moderators provides neutrons to three beam ports. Each moderator is independently tuned to optimize the trade-offs among neutron pulse-width, spectral temperature, and overall flux, as appropriate for the instruments to which it supplies neutrons. One possible set of instrument locations and the resulting roughly optimized selection of moderators is described in Section V.2.9.

We considered ambient-temperature water (H_2O), liquid methane (CH_4) at ~95 K, and liquid hydrogen (H_2) at ~20 K as moderator materials. These materials span a wide range of spectral temperatures for the moderated neutrons, which allows good matching to the very different requirements of the various instruments. All three of these materials have high hydrogen densities, making them very efficient moderators. Also, the heat deposition and radiolysis that occur in the high radiation field (at the moderator) are relatively well-understood, or at least empirically determined, for these materials.

The liquid methane and liquid hydrogen moderators require cryogenic cooling systems for liquefying these gases and for extracting the heat deposited in the liquids during operation. The required cryogenic cooling capacity and also the problems associated with radiolysis can be significantly reduced by making the cryogenic moderator thin and surrounding it with a much larger ambient-temperature liquid water premoderator, except on the face through which the neutrons exit to the neutron beamlines. Such a premoderator-moderator combination can be optimized to provide essentially the same neutronic response as would be given by a much larger cryogenic moderator alone. All of the cryogenic moderators at IPNS Upgrade use such liquid water premoderators. A typical configuration is shown schematically in Figure IV.3.1-1. The liquid methane and liquid hydrogen moderators use continuous recirculation of the cooled moderator material to provide the necessary heat extraction. Each of the liquid water moderators and each of the liquid water premoderators also have a system to continuously recirculate and cool the water to extract the large amounts of heat deposited in these systems. The recirculating water and cryogenic-liquid systems require the attachment of several pipes to each of the moderators. These pipes are brought out from the tops or bottoms of the moderators through channels in the reflector, as shown in Figure IV.1.2-6. The associated cooling systems are described in Section IV.3.4.

An important part of any pulsed neutron source is the reflector, which directs fast neutrons back into the moderators. This can increase the moderated beam currents by as much as an order of magnitude relative to that from the same moderators with no reflector.[1] At each of the IPNS Upgrade target stations, the targets and moderators are surrounded by a beryllium reflector, which provides at least 30 cm of reflector material in most directions. This reflector is made in two sections, as shown in Figure IV.1.2-6, to simplify remote servicing of the targets and moderators.

Other components of the moderator system are also varied to optimize the trade-off between pulse-width and intensity. These include the choice and location of the decoupler material and the poisoning material. The decoupler is a layer of material that absorbs low-energy neutrons but is transparent to higher-energy neutrons. This material is placed between the reflector and the moderator to prevent neutrons that undergo significant moderation in the reflector from leaking back into the moderator and, subsequently, out into the neutron beam. Because moderating times in the reflector are much longer than those in the moderator, such neutrons add a significant long-time tail onto the neutron pulse if they are not stopped. For most instruments, such a tail spoils the overall quality of the data; consequently, such instruments must view moderators that are decoupled. The decoupling material is cadmium in most cases, but a boron-loaded laminate can be used if higher decoupling energies are desired.[2] The decoupler is located in intimate contact with the recirculating water of the moderator, in the case of liquid water moderators, or premoderator, in the case of cryogenic moderators, in order to remove the deposited heat. This geometry is indicated schematically in Figure IV.3.1-1.
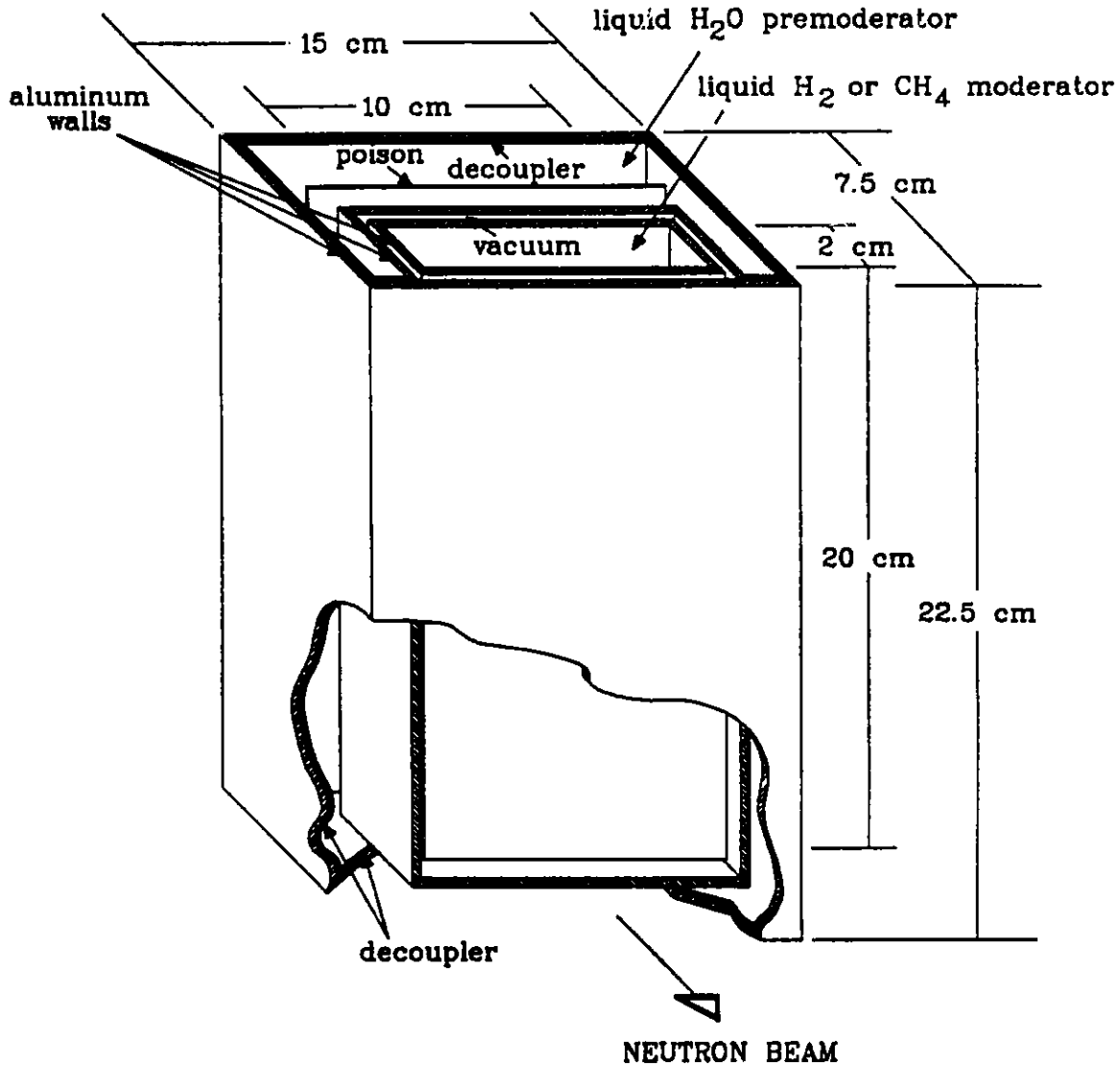
Figure IV.3.1-1 Schematic Representation of a Typical Cryogenic Moderator Assembly for IPNS Upgrade. (The moderator assembly is shown with the top and connecting plumbing removed. Dimensions are approximate and refer to one of the flux-trap moderator assemblies. For wing moderators, the moderator height is reduced from the 20 cm shown to 10 cm with all other dimensions remaining the same.)

The moderator poisoning is accomplished by placing within the moderator assembly a layer of material that absorbs low-energy neutrons but is transparent to high-energy neutrons. This absorber is usually gadolinium, either in foil or in other convenient form. This makes the moderator effectively thin, and hence provides a narrow neutron pulse-width, for low neutron energies, while providing much more intensity than would be possible if the moderator assembly were actually this thin. The location of the poison within the moderator assembly can be adjusted to provide the desired relationship between intensity and pulse-width. Because significant heat is deposited in the poisoning material, this material is located in the recirculating water of the moderator or premoderator, as shown in Figure IV.3.1-1.

Decoupling and poisoning can be applied to any of the moderators to achieve the desired performance. Both of these processes reduce the total neutron beam current emerging from the moderator and, consequently, are not applied unless necessary. For most of the intended scattering instruments, decoupling is necessary, but for many of these, poisoning may not be necessary. The highest neutron intensity is achieved when the decoupling material is omitted. The poisoning material is usually omitted in this case as well. Such a coupled moderator is used when there is little concern about the pulse-width, and in such cases the intensity can be increased even further by using a larger volume of moderating material, i.e., the moderator car be much thicker. Figure IV.3.1-2 shows typical dimensions of a coupled liquid hydrogen moderator in wing geometry at IPNS Upgrade. Such coupled moderators can provide up to about six times greater time-averaged neutron beam current than does a typical decoupled moderator.[3]

The performance of moderators is known for a few different types of poisoning and decoupling and for a few different geometries. Considerable development is required in order to provide the final optimization for the IPNS Upgrade moderators. Changes in the moderator systems will be made with some frequency, so the target-moderator-reflector assembly design allows easy replacement of moderators. This means that moderator parameters can be further optimized even after IPNS Upgrade is operational. Most of the basic principles underlying such optimization have been known for some time and have been reviewed in several places.[1,4] Premoderators have not yet been used in conjunction with cryogenic moderators at any pulsed-neutron source. A solid methane moderator with a liquid water premoderator is currently under construction for installation at the pulsed reactor at Dubna,[5] and premoderated liquid hydrogen moderators have been proposed for use at KENS-II in Japan.[6]

3.2 MODERATOR NEUTRONICS

3.2.1 Monte Carlo Calculations for Room-Temperature Water Moderators

Some of the neutron beam characteristics were calculated with the model illustrated in Figures IV.2.2-3 through IV.2.2-8 in Section IV.2.2. Figure IV.3.2-1 shows the neutron beam spectra from the room-temperature water moderators. The data shown in this figure are neutron
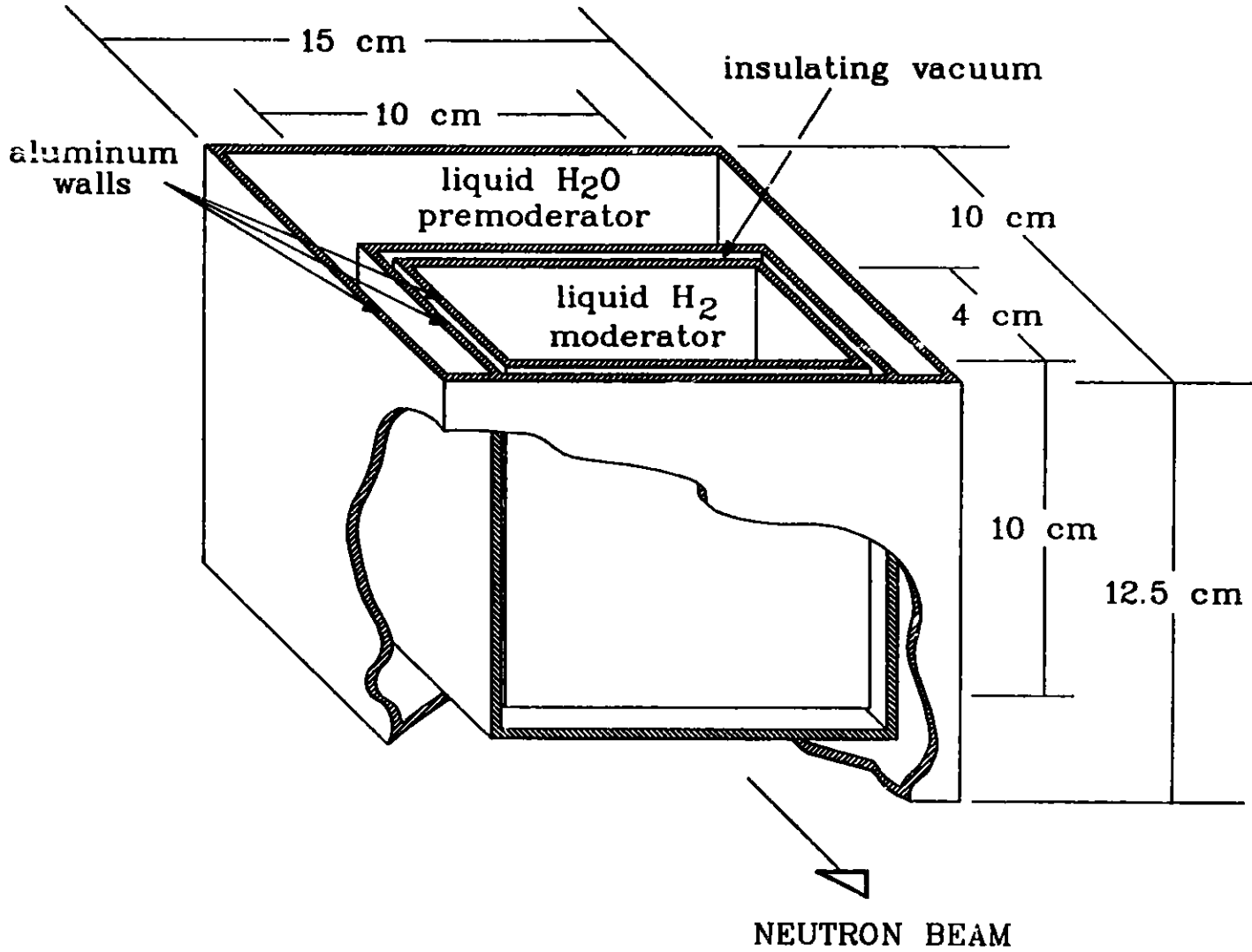
Figure IV.3.1-2 Typical Dimensions of a Coupled Liquid Hydrogen Moderator Assembly in Wing Geometry at IPNS Upgrade.
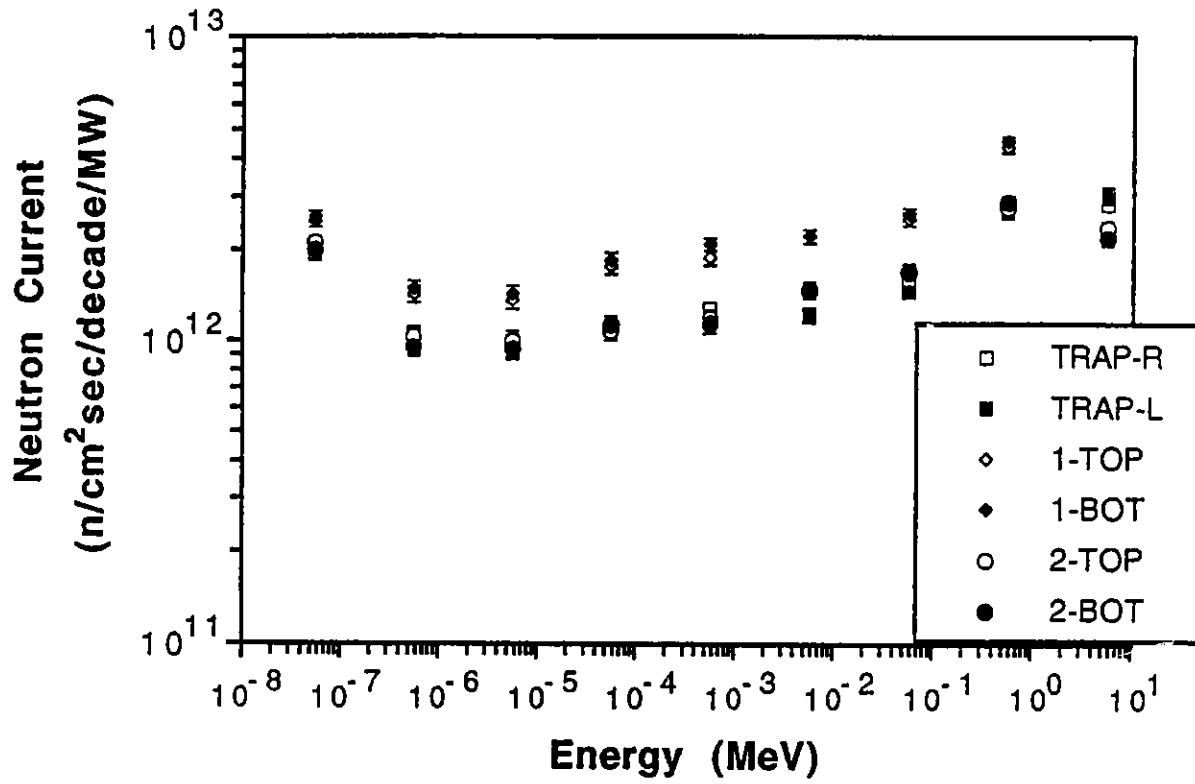
Figure IV.3.2-1 Neutron Beam Spectra at the Ambient Water Moderator Surfaces.
(Moderator locations are defined in Figure IV.2.2-5.)

currents weighted by the cosine of the angle to the normal direction of the moderator surface and are tallied in decade bins (i.e., 0.1 to 1 MeV, 1 to 10 MeV, etc.). The labels of moderators shown in Figure IV.3.2-1 are defined in Figure IV.2.2-5. Figure IV.3.2-1 shows that in the range of epithermal energies, the shape of the neutron spectrum is almost the same for all six moderators and that the upstream moderators (1-TOP and 1-BOT; see Figure IV.2.2-5 for notation) yield the highest neutron current in all energy bins. The total number of neutrons produced in the target is 49 neutrons per proton, for 2.2 GeV protons.

The moderator material has been modeled as ambient-temperature water. Small changes in the details of the moderator and poisoning materials produce significant differences in the details of the low-energy spectra, but the epithermal spectra, that is, those above about 1 eV, are insensitive to these differences. Thus the spectra calculated are valid at this energy and above.

3.2.2 The Effects of Premoderators

The full premoderator geometry indicated in Figures IV.3.1-1 and IV.3.1-2 was not modeled. However, a premoderator layer between the target and the cryogenic moderator was modeled, and the power distributions in slices within the moderators were calculated. For these calculations the shield region was omitted, and a premoderator region was attached to each moderator. Also, liquid hydrogen was used for the downstream-top (2-TOP) and one of the flux-trap (TRAP-R) moderators. The downstream moderators were modeled without a boron decoupler.

The calculated power depositions for a 1 MW proton beam are shown in Figure IV.3.2-2, along with a detailed illustration of the modeled moderator configuration. It is seen in Figure IV.3.2-2 that the power deposition in the directions parallel to the target is almost uniform, while the power deposition decreases rapidly with increasing distance from the target. The amount of heat eliminated by the premoderator depends on its dimensions. One conclusion drawn from Figure IV.3.2-2 is that much of the heat that would have been deposited in the cryogenic moderator can be eliminated by using a premoderator of a few centimeters thickness. For instance, 37% of the heat deposition occurs in the 2-cm-thick premoderator, as seen in the upstream top moderator (1-TOP) of Figure IV.3.2-2, and almost 86% of the heat can be eliminated by the 3-cm thick premoderator, as seen in the flux-trap-right moderator (TRAP-R). Also, more than half of the heat is deposited in the premoderator region used with the liquid hydrogen moderator in the downstream top moderator position (2-TOP) in Figure IV.3.2-2.

The power deposition in liquid methane is assumed to be the same as that in liquid water because of the similarity in hydrogen densities. The total power deposition in a $2 \times 10 \times 10$ cm^3 moderator in the upstream moderator position is estimated to be ~200 W. For this case, ~600 W is deposited in the premoderator (Figure IV.3.1-1). The power deposition in a $2 \times 10 \times 20$ cm^3 moderator in the flux-trap position is estimated to be ~470 W, while that in the corresponding premoderator is ~1050 W.

1—TOP (10x12x5)		
1	H_2O	299
2	H_2O	188
3	H_2O	132
4	H_2O	86
5	H_2O	56
6	H_2O	45

TRAP—L (10x20x5)		
1	H_2O	425
2	H_2O	338
3	H_2O	284
4	H_2O	268
5	H_2O	198

2—TOP (10x12x10 — coupled)		
1	H_2O	702
2	H_2	193
3	H_2	121
4	H_2	94
5	H_2	81
6	H_2	65

1—BOT (10x12x5)		
1	H_2O	153
2	H_2O	161
3	H_2O	152
4	H_2O	153
5	H_2O	149

TRAP—R (10x20x5)		
1	H_2O	444
2	H_2O	317
3	H_2O	253
4	H_2	91
5	H_2	79

2—BOT (10x12x10 — coupled)		
1	H_2O	395
2	H_2O	388
3	H_2O	432
4	H_2O	370
5	H_2O	378

Figure IV.3.2-2 Calculated Power Distribution in Moderators and Premoderators. (The table indicates the composition in each slice and the power (W) deposited in that slice. Shaded slices are treated as premoderators. Moderator dimensions (cm) are width × height × depth in direction of neutron beams. Moderators are decoupled unless indicated as coupled.)

The power deposition in a $2 \times 10 \times 20$ cm^3 liquid hydrogen moderator in the flux-trap position is estimated to be ~170 W with 1010 W in the premoderator. For a $4 \times 10 \times 10$ cm^3 liquid hydrogen moderator in the downstream position (Figure IV.3.1-2) the power deposition is estimated to be ~220 W, with 1460 W in the premoderator.

The power deposition density in the aluminum walls of the moderator containers is conservatively estimated to be the same as that calculated for water in similar locations: ~1.01 W/cm^3 in the upstream position, ~1.17 W/cm^3 in the flux-trap location, and ~1.26 W/cm^3 in the downstream location.

The effects of the premoderator on the neutron current spectra from the moderator surfaces were also calculated. Neutron spectra with and without premoderators and decouplers are compared in Figures IV.3.2-3 through IV.3.2-7. Some of these calculations involved a model with no shield, but this difference in modeling is insignificant for the comparison of neutron spectra in moderators, as demonstrated in Figure IV.3.2-3. The comparison in Figure IV.3.2-3 is for a flux-trap moderator that has the same configuration and material in both models. Figure IV.3.2-4 shows that the thermal neutron spectrum is essentially unchanged by the presence of a premoderator. The fast-neutron spectrum decreases because the addition of a premoderator layer increases the water volume. In the comparison shown in Figure IV.3.2-4, water was used for both premoderator and moderator. If cryogenic material is used for the moderator and water is used for the premoderator, however, the neutron spectrum will be affected by the presence of a premoderator and by its dimensions. Further studies should be done for optimization of the premoderator geometry. Nevertheless, it is thought that the neutron spectrum from the cryogenic moderator will not be strongly affected by the water premoderator as long as the cryogenic moderator thickness represents several mean-free-paths of neutron scattering. Tests are under way at the moderator development facility at Hokkaido University to obtain more precise information.

The effects of the boron decoupler on the neutron spectrum are shown in Figure IV.3.2-5. The thermal spectrum is much higher in the moderator without the boron decoupler, as expected. A slight decrease of the fast-neutron spectrum in the moderator with no decoupler is due to the presence of the premoderator.

3.2.3 Monte Carlo Calculations for Liquid Hydrogen Moderators

As shown in Figure IV.3.2-2, two of the six moderators (TRAP-R and 2-TOP) were modeled as liquid hydrogen moderators with water premoderators. The premoderator in the model covers only one side of the moderator, rather than five sides as in Figures IV.3.1-1 and IV.3.1-2. The cross-section data of the hydrogen atom at room temperature (300 K) were used, but with the density set to a nominal liquid hydrogen density.
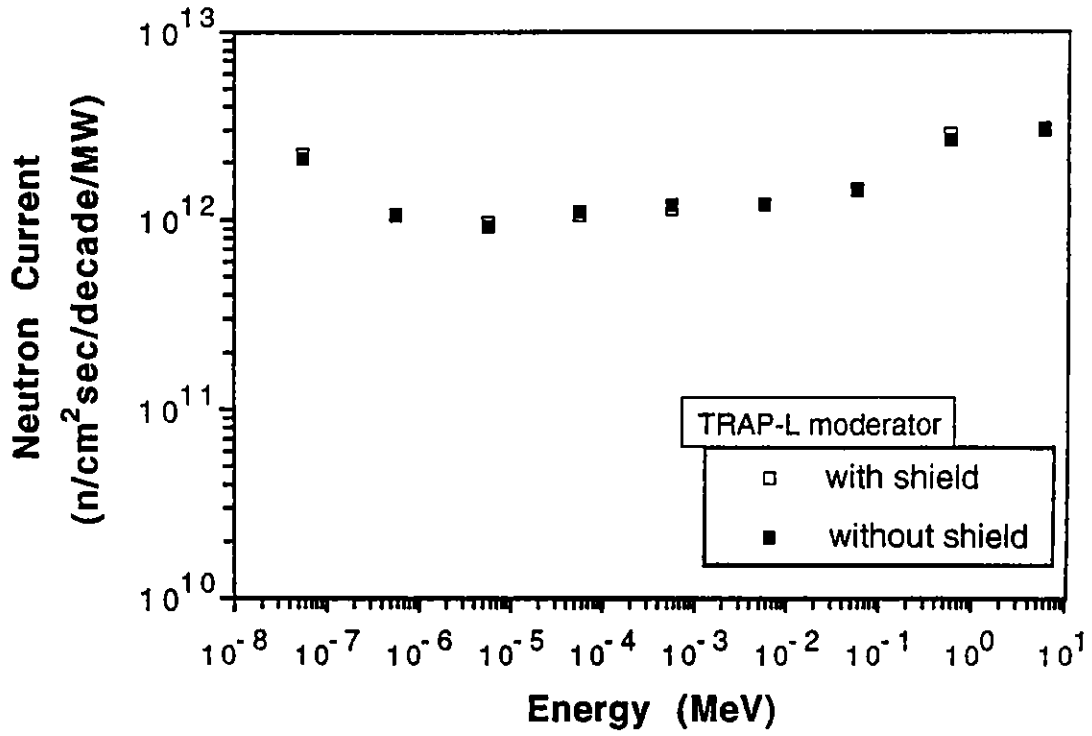
Figure IV.3.2-3 Comparison of Neutron Spectra from the Models with and without Shield.
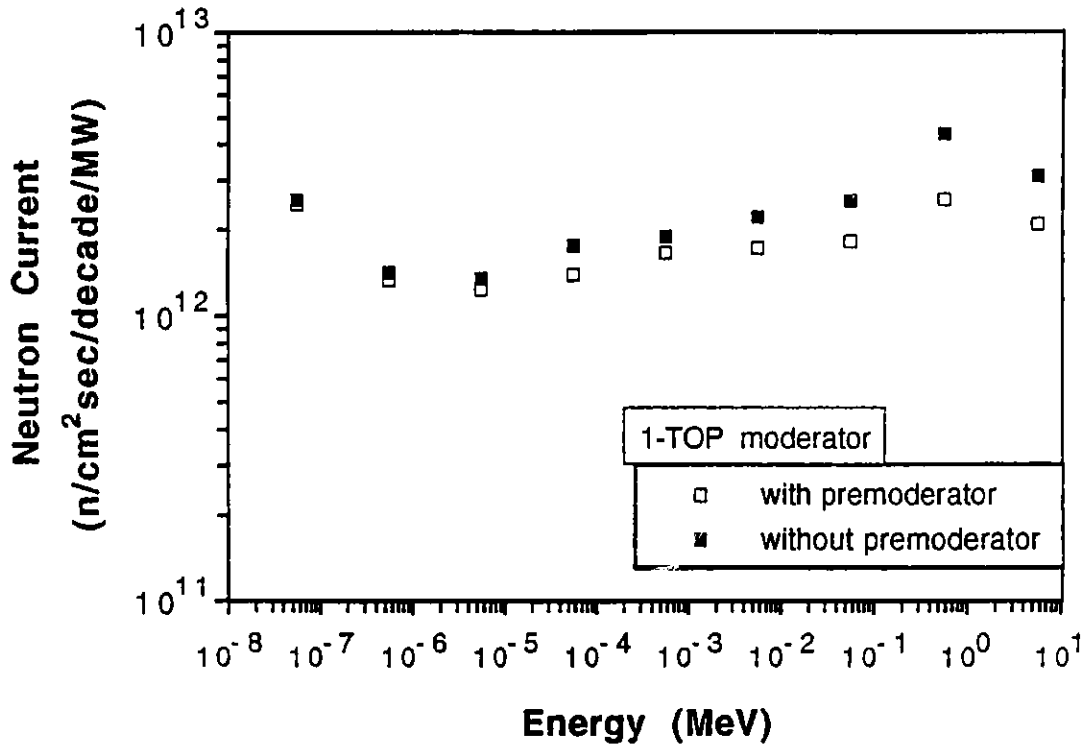
Figure IV.3.2-4 Effects of the Premoderator on the Neutron Beam Spectrum.
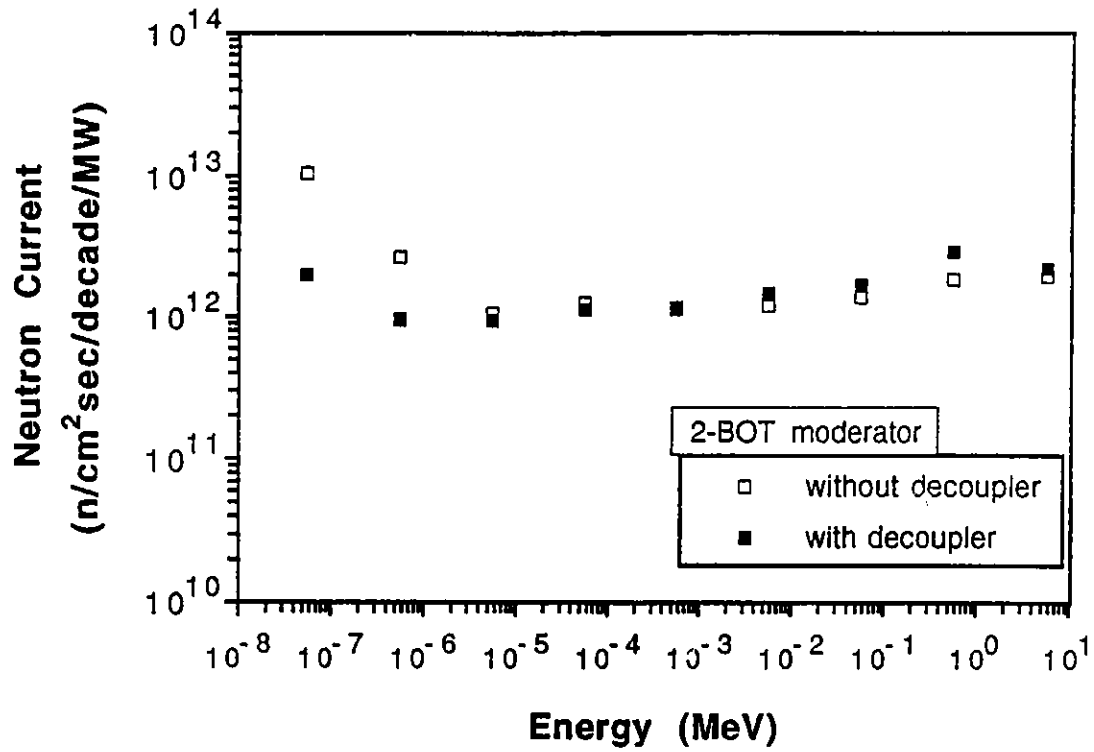
Figure IV.3.2-5 Effects of the Decoupler on the Neutron Beam Spectrum.
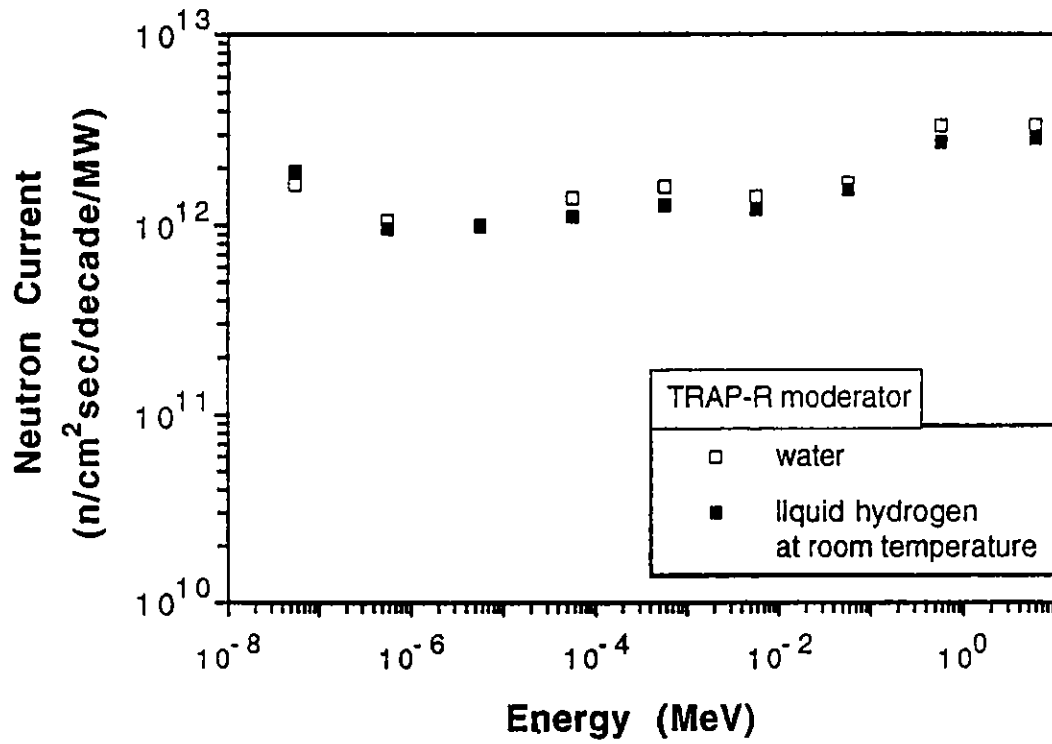
Figure IV.3.2-6 Comparison of Neutron Beam Spectra for Water and
Liquid Hydrogen Moderators at Room Temperature.
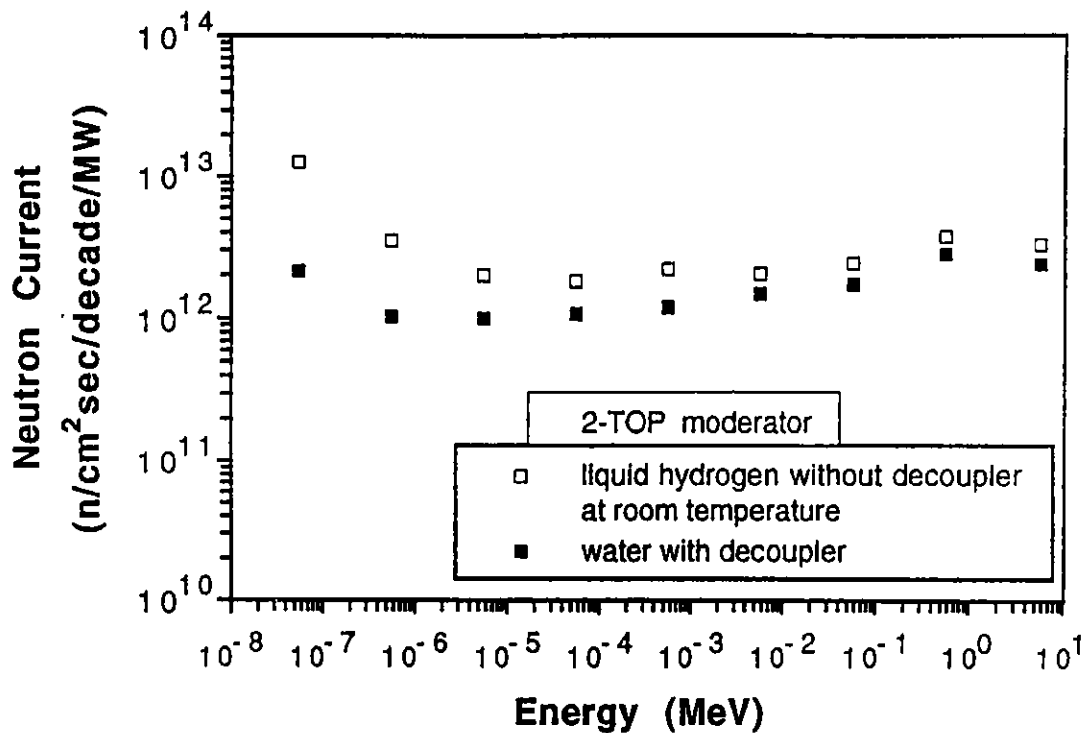
Figure IV.3.2-7 Effects of the Decoupler.

Figure IV.3.2-6 shows that the neutron spectra for water and hydrogen moderators are almost identical. Figure IV.3.2-7 shows the effects of the neutron decoupler on the neutron-beam spectrum. The case without a decoupler was obtained with the hydrogen moderator, and the case with a decoupler was calculated with the water moderator. Considering that the calculated neutron spectra from hydrogen and water moderators are almost identical, as shown in Figure IV.3.2-6, the effect of the decoupler is thought to be the same for the hydrogen moderator as for the water moderator. Removing the decoupler causes the thermal spectrum to increase significantly, while only changing the fast-neutron spectrum slightly.

3.2.4 Neutron Beam Currents at 1 eV

The quantities calculated in the previous section are the total outgoing neutron currents J emerging from the moderator faces, integrated over the moderator face and over 2π solid angle of emergence. The quantity relevant to the neutron beam instrumentation is the neutron beam current $I = dJ/d\Omega$, which is the total current per unit solid angle emerging in a fixed direction near normal to the moderator face.[1] The relationship between J and I for the planar geometry used here is the Milne problem, common in many applications of transport theory.[7] The exact solution to the Milne problem, for I normal to the moderator surface is[7]

$$I = 0.41 \ J. \tag{IV.3.2-1}$$

The Monte Carlo results in the preceding section are tabulated as neutrons per decade of energy E. The quantity EI(E) can be obtained by multiplying these tabulated results by $0.41/\ln_e 10 = 0.18$. Using this conversion factor, the Monte Carlo calculations of Figures IV.3.2-3 through IV.3.2-7 give the results shown in Table IV.3.2-1. Beam currents at 1 eV for the liquid methane moderator are assumed to be the same as for the liquid water moderator because hydrogen densities are roughly the same in both materials.

For the present IPNS with a depleted uranium target, the corresponding value[8] for EI(E) at 1 eV is 4.2×10^{11} n/sr-sec. The values in Table IV.3.2-1 range from ~40 to ~110 times the IPNS value. A representative estimate is that the time-averaged neutron beam currents at IPNS Upgrade, with the full 1-MW beam power on a single target, are ~75 times the present IPNS values. In normal operation, time-averaged beam currents at the 30-Hz target station are two-thirds this value, or ~50 times those at IPNS, while at the 10-Hz target station they are ~25 times those at IPNS. The actual beam currents will vary significantly from moderator to moderator, depending on the location of the moderator, choice of moderator material, decoupling and poisoning used, etc. However, these ratios of 50 × IPNS and 25 × IPNS should be realistic when comparing similar moderators at IPNS and IPNS Upgrade. It is likely that these ratios can be increased somewhat by further optimization of the IPNS Upgrade target-moderator-reflector geometries and materials.

Table IV.3.2-1 Neutron Beam Current at 1 eV from Moderator[a]

Moderator Material	Premoderator	Decoupler	Neutron Beam Current, EI(E), at 1 eV from Moderator (10^{13} n/sr-sec)		
			Upstream	Flux-Trap	Downstream
Water	No	Yes	2.4	3.5	1.7
Water	Yes	Yes	2.3	3.5	-[b]
Hydrogen	Yes	Yes	-	3.5	-
Water	Yes	No	-	-	3.1
Hydrogen	Yes	No	-	-	4.7

[a] Calculated for full 1-MW proton-beam power.

[b] - = No calculations for this configuration.

3.2.5 Neutron Spectra and Pulse-Widths below 1 eV

3.2.5.1 Neutron Spectra

The time-averaged neutron beam current I(E) from a moderator at a pulsed source, the number of neutrons per steradian per unit energy per unit time, is usually well-represented by a Maxwellian thermal spectrum joined to a nearly 1/E epithermal spectrum as

$$I(E) = I_{th}\left[\frac{E}{E_t^2} e^{-E/E_t}\right] + I_{epi}\left[\frac{\Delta(E)}{E}\right]\left[\frac{E}{E_{ref}}\right]^\alpha \qquad (IV.3.2-2)$$

In this equation, E_t is a characteristic energy of the Maxwellian portion of the spectrum; $\Delta(E)$ is a joining function, which goes smoothly from 0 (for E below about 5 E_t) to 1 (for E above about 5 E_t); E_{ref} is a reference energy, typically taken to be 1 eV; and α is between 0 and 0.1. I_{th} and I_{epi} are scaling constants for the thermal and epithermal portions of the spectrum, respectively. We take a value of 1 eV for E_{ref} so that the values of EI(E) at 1 eV from Table IV.3.2-1 directly give I_{epi} for some of the different moderators at IPNS Upgrade.

Because of the limited availability of scattering kernels for low-energy neutrons in real moderator materials, it is usual to estimate the thermal portion of the spectrum by empirical methods, rather than from Monte Carlo calculations. This is done by matching measured spectra with the calculated neutron beam currents at 1 eV, or by using empirical values of E_t and I_{th}/I_{epi} in Equation IV.3.2-2. Several empirical values are given in Table IV.3.2-2. The values in Table IV.3.2-2 should be taken as representative values only, because the decoupling energy, poisoning material and location, and moderator geometry can have significant effects on the performance of these moderators in the thermal energy range. Detailed calculations, tests, and interpolation among the empirical data in the literature will be required to provide the combinations of these parameters that optimize the moderator performance for the various sets of neutron scattering instruments.

The effective, time-averaged total thermal flux (reactor equivalent) ϕ_{eff} is given by

$$\phi_{eff} = 4\pi I_{th}/A , \qquad (IV.3.2-3)$$

where A is the area of the face of the moderator. For the coupled liquid hydrogen moderator in the downstream position,

$$\phi_{eff} = 4\pi \left[EI(E)_{1 \text{ eV}}\right] \times \left[I_{th}/I_{epi}\right]/A$$

$$\approx 4\pi \times 4.7 \times 10^{13} \times 12/100 = 7.1 \times 10^{13} \text{ n/cm}^2\text{-s}, \qquad (IV.3.2-4)$$

Table IV.3.2-2 Maxwellian Parameters for Several Moderators

Moderator Type	E_t (MeV)	I_{th}/I_{epi}
Poisoned, decoupled, 320 K liquid water	32[a]	2.3[a]
Poisoned, decoupled, 95 K liquid methane	11[a]	2.1[a]
Decoupled, 18 K liquid hydrogen	3.0[b]	2.4[b]
Coupled, 320 K liquid water	~32[c]	~22[c]
Coupled, 18 K liquid hydrogen	2.8[b]	12[b]

[a] ISIS moderator data; Source: Ref. 9.

[b] Based on the data of Kiyanagi et al. (Ref. 3); values are only approximate because liquid hydrogen spectra are not fit well by a Maxwellian function.

[c] Rough factor of 9.8 intensity increase over poisoned, decoupled water moderator is based on SNQ mock-up measurements (Ref. 10).

and a similar calculation for the coupled liquid water moderator in the downstream position gives

$$\phi_{eff} \approx 8.6 \times 10^{13} \ n/cm^2\text{-s}. \tag{IV.3.2-5}$$

In normal operation, such moderators at the 30-Hz target station produce two-thirds these equivalent flux values, while at the 10-Hz station, they produce one-third these fluxes. It should be noted that ϕ_{eff} represents actual equivalent 4π "perturbed" fluxes for the beams emerging from the moderators. In order to obtain a flux of this magnitude from a liquid hydrogen or deuterium cold moderator at a reactor, the nominal reactor flux would have to be significantly greater than $10^{14} \ n/cm^2$-s. For example, the high-flux reactor at ILL has a peak calculated unperturbed flux of $\sim1.5 \times 10^{15} \ n/cm^2$-s in the ambient D_2O moderator vessel. The calculated unperturbed flux[11] at the location of the liquid deuterium cold moderator within this vessel is only $\sim5 \times 10^{14} \ n/cm^2$-s, and the actual perturbed flux at this location is even lower.

The Monte Carlo calculations indicate that these reactor-equivalent time-averaged fluxes can be increased significantly by placing the coupled moderators near the upstream target, rather than near the downstream target. It is likely that using larger moderators or premoderators in the coupled case will produce appreciable gains. Additional Monte Carlo studies are required to optimize such moderators in order to obtain the maximum possible neutron beam current for instruments that operate in the quasi-steady-state (QSS) mode.

3.2.5.2 Neutron Pulse-Widths

The neutron pulse shapes emerging from a moderator are highly energy dependent. The overall widths of these pulses can be changed dramatically by varying the poisoning and decoupling parameters, as well as by varying the moderator material. The premoderator geometry may also have an effect. Thus, there are a large number of degrees of freedom that can be varied in designing moderators optimized for the requirements of specific sets of instruments. Figure IV.3.2-8 shows the energy-dependent pulse-widths (fwhm) for the moderators specified in Table IV.3.2-2. These are representative values only, as small changes in the poisoning and/or decoupling give rise to variations of a factor of 2 in I_{th} and to correspondingly large variations in the pulse-width. Because of this great degree of tunability in moderator performance, moderator optimization must be studied in much greater detail before the final selections are made.

3.3 RADIOLYSIS

3.3.1 Production of Hydrogen

Irradiation of liquid water, methane, or hydrogen with fast neutrons causes the molecules to be radiolytically decomposed into lighter constituents, which can then recombine into new
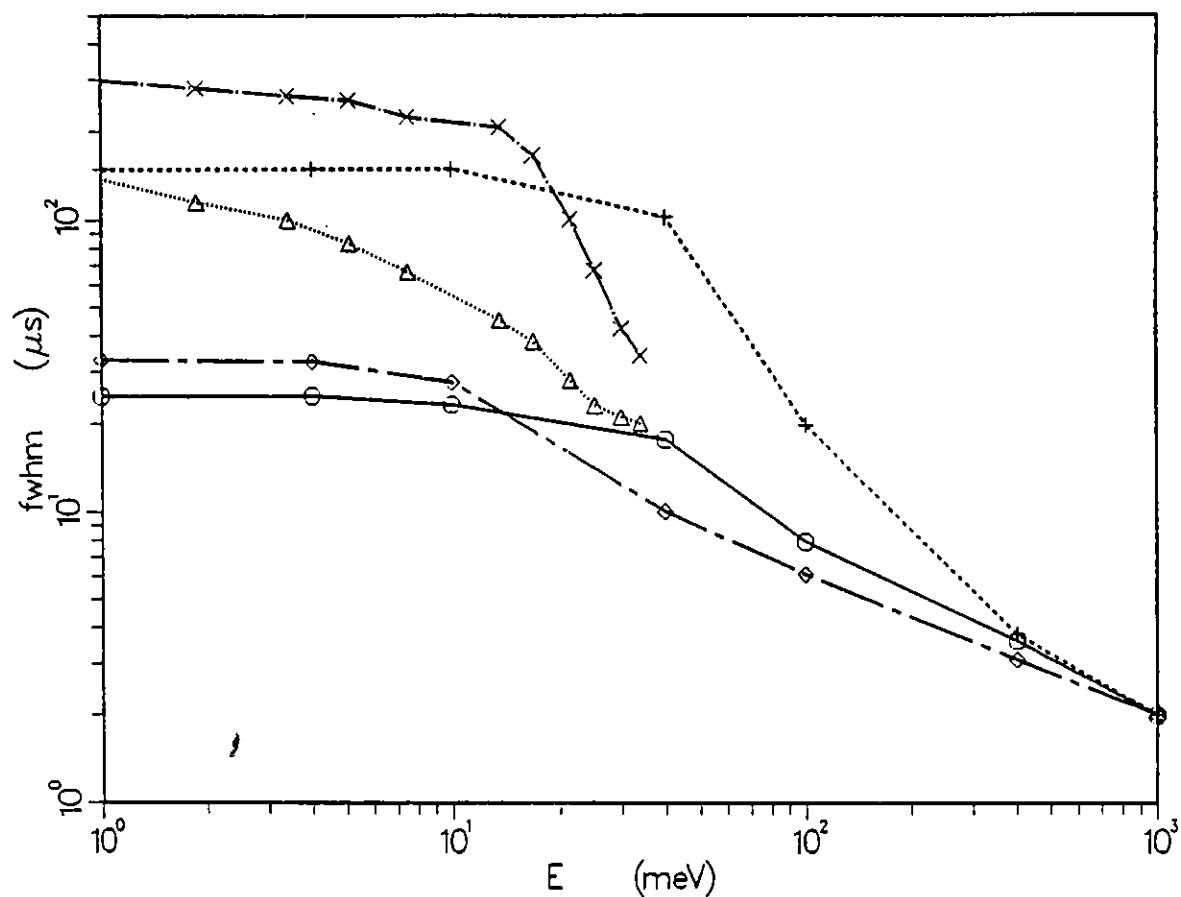
Figure IV.3.2-8 Pulse-Widths (fwhm) for the Moderators Listed in Table IV.3.2-2. (Circle = decoupled, poisoned liquid water; diamond = decoupled, poisoned liquid methane; triangle = decoupled liquid hydrogen; plus = coupled liquid water; cross = coupled liquid hydrogen. The lines are a guide to the eye only.).

forms. Hydrogen moderator systems must be free of reactive contaminants to avoid reaction of the radiolytically formed hydrogen radicals to produce species that cause problems. Hydrogen at low temperatures gradually and spontaneously tends to the lowest-energy para state, which has significantly different total and differential inelastic scattering properties from the higher energy ortho state. Recombination of radiolytically decomposed hydrogen is into the statistically determined 3:1 ortho:para mixture, so that under irradiation the result is a mixture of ortho and para hydrogen that depends on the rate of radiolysis and on the time. The spectrum and emission time distributions may depend on the composition of the ortho:para mixture. Although this is not likely to have a major effect on moderator performance, the effect needs to be investigated.

The possible undesirable radiolytic products of water are hydrogen, oxygen, ozone, and hydrogen peroxide. Because several of these are gases under the conditions of operation of the water moderators and premoderators, they must be removed or recombined before they either displace a significant portion of the liquid water from the moderator container or reach potentially explosive concentrations. The moderators and premoderators are designed so that the resulting water flow patterns do not allow significant accumulation of gases in the moderator and premoderator regions. The recirculating systems for the IPNS Upgrade water moderators and premoderators contain provisions for recombining or purging the hydrogen and oxygen gases. Production rates for hydrogen and oxygen in the IPNS Upgrade liquid water moderators and premoderators are difficult to estimate, and some research and development effort is required in this area.

Possible undesirable radiolytic products of methane include hydrogen and virtually all higher hydrocarbons. The hydrogen is gaseous under the operating conditions of the liquid methane moderator and displaces methane from the moderator if it is allowed to accumulate. The methane flow pattern is designed to prevent accumulation of hydrogen gas in the moderators. The recirculating systems for the IPNS Upgrade liquid methane moderators contain provisions for removal of hydrogen gas produced. They also contain provisions for removal of some of the higher hydrocarbons from the recirculating mixture. However, not all of these higher hydrocarbons can be removed, which leads to an additional set of problems discussed in the following section.

3.3.2 Buildup of Higher Hydrocarbons in the Liquid Methane Moderator

No solid products result from radiolysis of water or hydrogen. The radiolysis of methane can form radicals that can recombine to form high-molecular weight hydrocarbons such as waxes or solids. These tend not to circulate with the liquid methane, but rather to deposit on the walls of the moderator container and associated piping, where they are subject to further radiation damage. Experience has shown that the resulting buildup, which cannot be flushed away with any practical solvents, eventually fills enough of the moderator container to degrade the moderator performance. This leads to a finite, predictable lifetime for liquid methane moderator assemblies.

Since its startup in 1985, the ISIS pulsed-neutron facility has been operating a liquid methane moderator. By the end of 1990, the performance of this moderator had deteriorated to the extent that it had to be replaced.[12] The moderator assembly that was removed was subsequently cut apart to assess the reasons for its failure. It was found that the moderator container was partially filled with a solid black residue, the result of the radiolytic decomposition of the methane and subsequent formation and deposition of higher hydrocarbons. This residue was determined by analysis to consist of highly cross-linked polymers.[13] Tests of similar material collected from IPNS liquid methane moderators show that it is insoluble in any common solvent and refractory against thermal decomposition at reasonable temperatures.[14]

ISIS has since tried three different liquid methane moderators, with frequent replacement of the methane and with different flow configurations.[13] However, during the same time the proton current at ISIS has been steadily increased up to the design goal of 200 μA at 800 MeV. The net result is that the lifetime of each of these moderators has been shorter than that of the previous one, even when measured in terms of the integrated proton current. These lifetimes are summarized in Table IV.3.3-1, which is based on data from Broome.[13] Also included in this table is an estimate of the lifetimes of liquid methane moderators at IPNS Upgrade, based on the assumptions that the flow conditions would be similar and that the correct scaling factor is the ratio (6.25) of the proton beam powers at IPNS Upgrade and ISIS.

Liquid methane moderator lifetimes can also be estimated in a somewhat different manner. At the design operating parameters of 200 μA and 800 MeV, the power deposition in the ISIS liquid methane moderator was calculated to be somewhere between 283 W and 625 W when the depleted uranium target was used.[15,16] For a tantalum or tungsten target, these estimates should be divided by ~2. The respective power deposition densities are ~0.21 W/cm^3 and ~0.48 W/cm^3. By comparison, the calculated power deposition density is ~1.0-1.2 W/cm^3 in the liquid-methane portion of a premoderated liquid methane moderator at IPNS Upgrade operating at full power (see Section IV.3.2.2). Assuming that the rate of radiation damage and deposition of solid hydrocarbons scales with the power deposition density, this leads to projected liquid methane moderator lifetimes at IPNS Upgrade ranging from ~340 h to ~1,570 h at full power before the same degree of deterioration in performance is experienced that was observed at ISIS.

Both approaches suggest that operating lifetimes for liquid methane moderators at IPNS Upgrade could range from two weeks to two months. A two-month lifetime is marginally acceptable, but two-week lifetimes certainly are not acceptable. Thus, it is important that a development program be undertaken to provide better understanding of this hydrocarbon buildup and to develop procedures for its reduction, with the goal of eventually providing longer lifetimes for liquid methane moderators. A development program along these lines has already begun at ISIS.[13] If liquid methane moderators with suitable lifetimes cannot be developed, it will still be possible to use either liquid hydrogen or water moderators in place of the liquid methane moderators. All of the instruments can still be operated, although in some cases there would be a reduction in performance if liquid methane were not available.

Table IV.3.3-1 Lifetimes of Liquid Methane Moderators

| | Effective Integrated Proton Current | | Estimated Lifetime | |
| | Depleted U Target (mA-h) | Ta or W Target[b] (mA-h) | ISIS[c] (h) | IPNS Upgrade[d] (h) |
Moderator[a]				
#1 single foil	747	1494	7470	1195
#2 single foil	575	1150	5750	920
#3 double foil, reverse flow	198	396	1980	317
#4 single foil, reverse flow	164	328	1640	262

[a] Single or double foil refers to the poisoning configuration within the moderator.

[b] Tantalum or tungsten produces roughly a factor of two fewer neutrons per proton than does depleted uranium, so a conversion factor of 2 has been used, as in Ref. 13.

[c] Lifetime with a tantalum or tungsten target.

[d] Projected lifetime, based on a tungsten target and scaled from ISIS by using the relative proton beam powers.

3.4 COOLING

3.4.1 Component Layouts for Water Cooling Systems

This section describes the water cooling systems for moderators, reflectors, the biological shield, the target tank, and the proton beam window. Components for these cooling systems are located on separate skids in shielded areas in Buildings 367 (10-Hz target) and 371 (30-Hz target). Figures IV.3.4-1a and IV.3.4-1b show the layout of shielding and skid-mounted components in Building 367 for the 10-Hz target. Figures IV.3.4-2a and IV.3.4-2b show the layout of components in Building 371 for the 30-Hz target.

The different water cooling systems are discussed in Sections IV.3.4.2, IV.3.4.5, IV.3.4.6, IV.3.4.7 and I.V.3.4.8.

3.4.2 Room-Temperature Water Moderators and Premoderators

Each target station has six moderators or premoderators, each of which contains water. The heat deposited in the water of a premoderator or moderator is within the range of one to several kilowatts. Also, the approximate 500-W nuclear heating that occurs in the vacuum jacket surrounding the cryogenic lines is absorbed by the same water cooling circuits. In all cases, a water flow rate of 0.021 L/sec cools any water moderator and its attached piping with a relatively low increase in bulk temperature (25 K). This rise in bulk temperature does not approach saturation temperature (445 K), so boiling does not occur.

Water for each of the six water moderator circuits is supplied from a common manifold supplied by one of two redundant pumps, as depicted in Figure IV.3.4.3. The pumps are constructed of corrosion-resistant materials, primarily 316SS. Installed motor power is 0.6 kW. The active pump draws from a 100-L water supply tank at a pressure of 690 kPa and discharges 0.13 L/sec total water flow rate at a pressure of 790 kPa. The supply tank has an H_2/O_2 recombiner. A 100-L drain tank provides for local hold-up of the cooling water inventory. Check valves preclude reverse flow through the nonoperating pump. The pressure loss in the water supply and return lines is very small, so most of the head developed by the pump is due to pressure drop across the six identical, parallel flow-control orifices, each of which are 1.9 mm in diameter.

The tanks, pumps, heat exchanger, and demineralizer for the 10-Hz target are located on a common skid in a shielded room in Building 367. A duplicate housed in Building 371 serves the 30-Hz target. This is shown in Figures IV.3.4-1a, IV.3.4-1b, IV.3.4-2a, and IV.3.4-2b. Supply and return piping between the cooling system components and the moderators and premoderators is shielded. All tanks and plumbing are insulated to reduce heat loads in the shielding and pump room.

BLDG 367

DRAIN

SUPPLY

DOWN

FEEDER
PIT

B

B

MODERATOR COOLING

REFLECTOR COOLING

TARGET TANK COOLING

BIOLOGICAL SHIELD COOLING

PROTON HET LINE
VACUUM WINDOW
INSERT COOLING
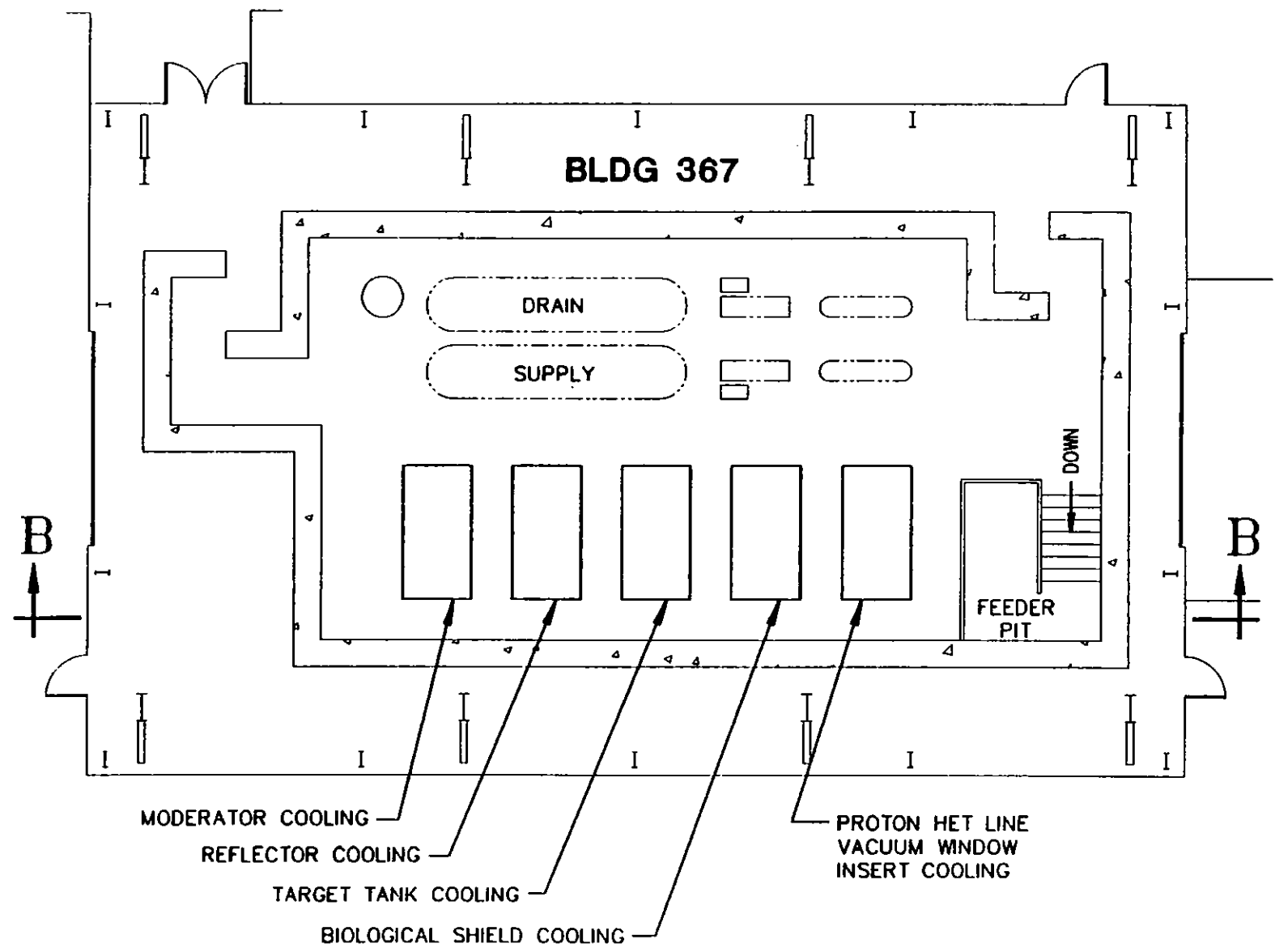
Figure IV.3.4-1a Layout of Skid-Mounted Cooling Systems in Building 367, for the 10-Hz Target.

BIOLOGICAL SHIELD COOLING

TARGET TANK COOLING

REFLECTOR COOLING

PROTON HET LINE
VACUUM WINDOW
INSERT COOLING

MODERATOR COOLING

0.6m

3.04m

0.6m

FEEDER
PIT
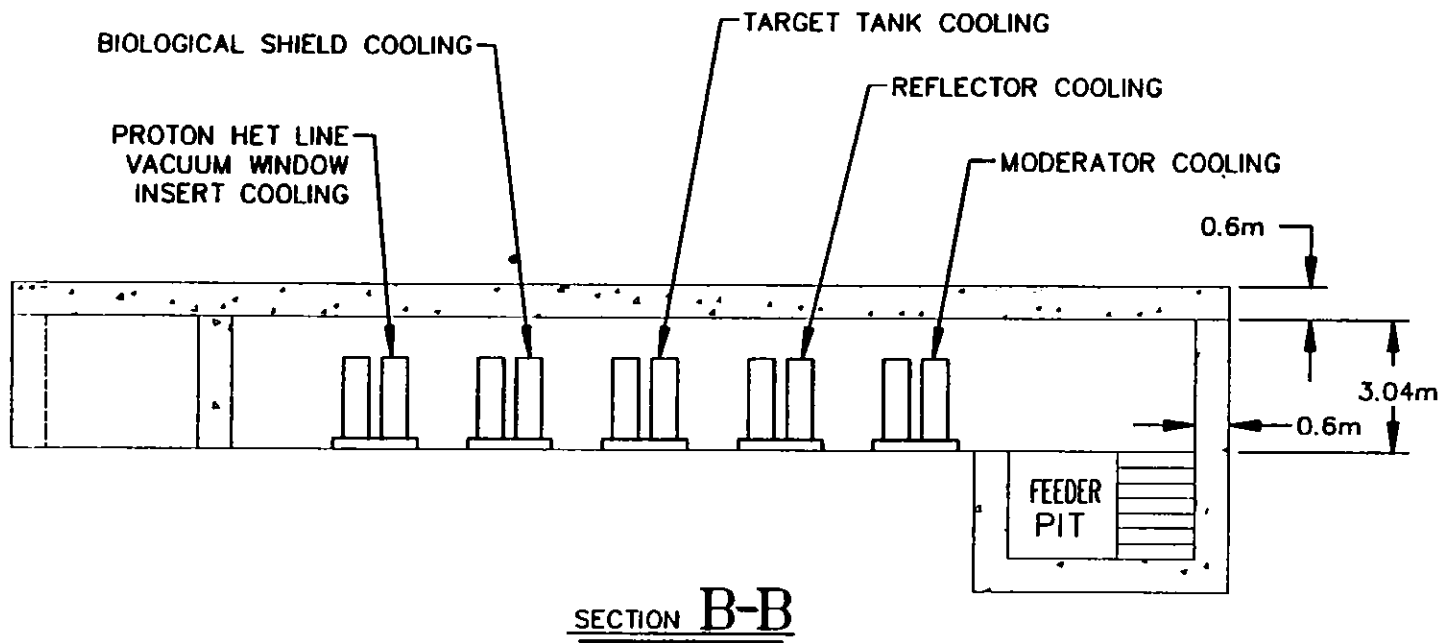
SECTION B-B

Figure IV.3.4-1b Sectional Elevation of Skid-Mounted Cooling Systems in Building 367, for the 10-Hz Target.
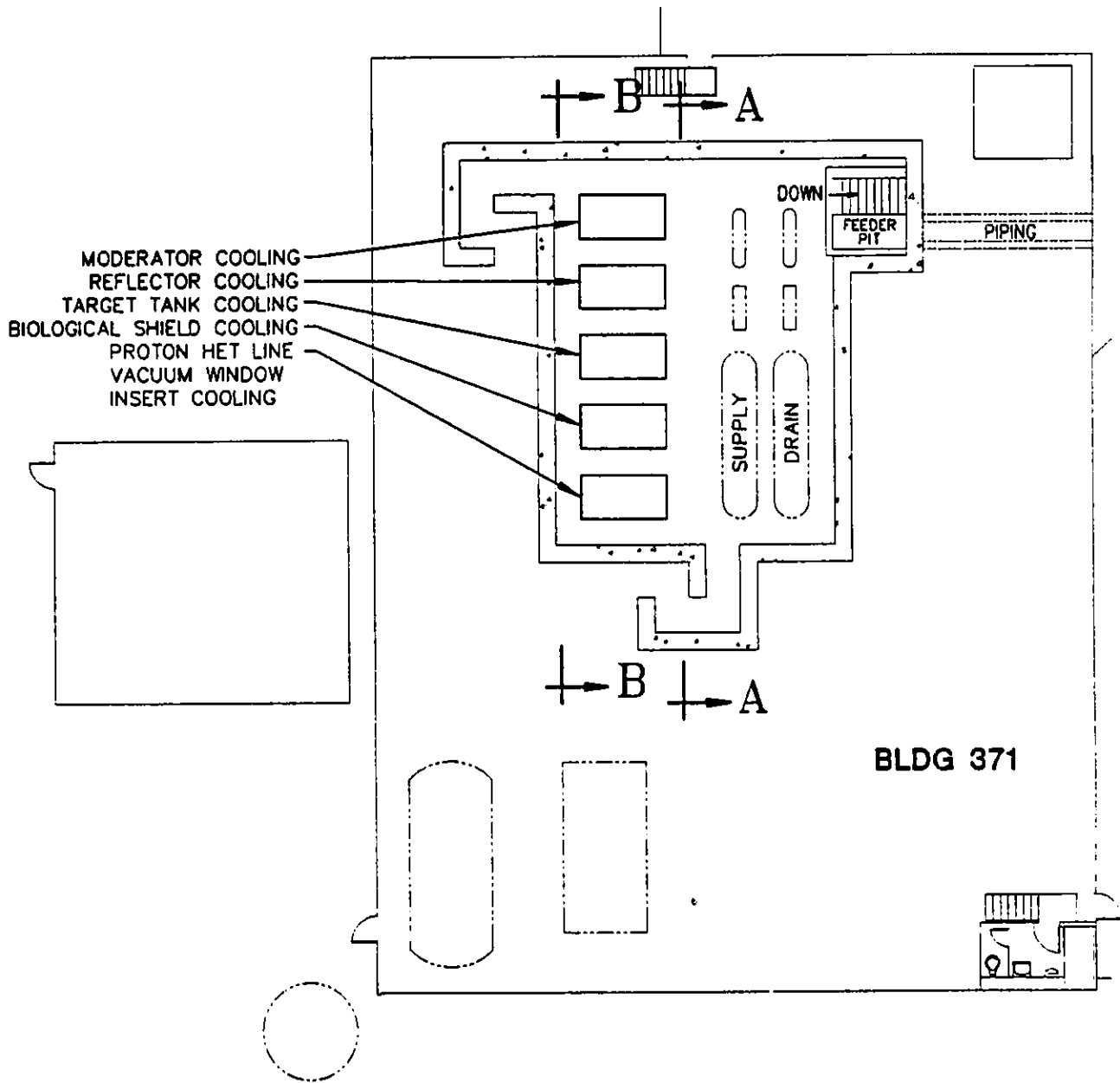
Figure IV.3.4-2a Layout of Skid-Mounted Cooling Systems in Building 371, for the 30-Hz Target.

TARGET TANK COOLING

BIOLOGICAL SHIELD COOLING

REFLECTOR COOLING

PROTON HET LINE
VACUUM WINDOW
INSERT COOLING

MODERATOR COOLING

0.6m

3.04m

0.6m

FEEDER
PIT
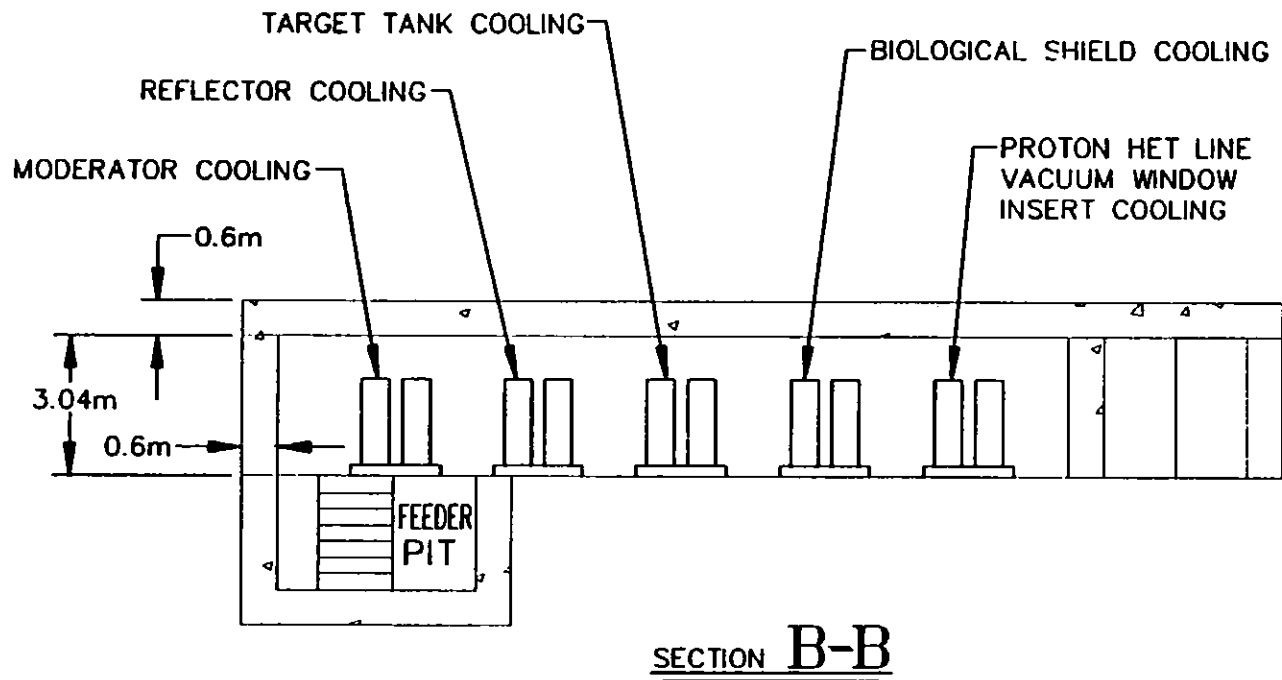
SECTION B-B

Figure IV.3.4-2b Sectional Elevation of Skid-Mounted Cooling Systems in Building 371, for the 30-Hz Target.
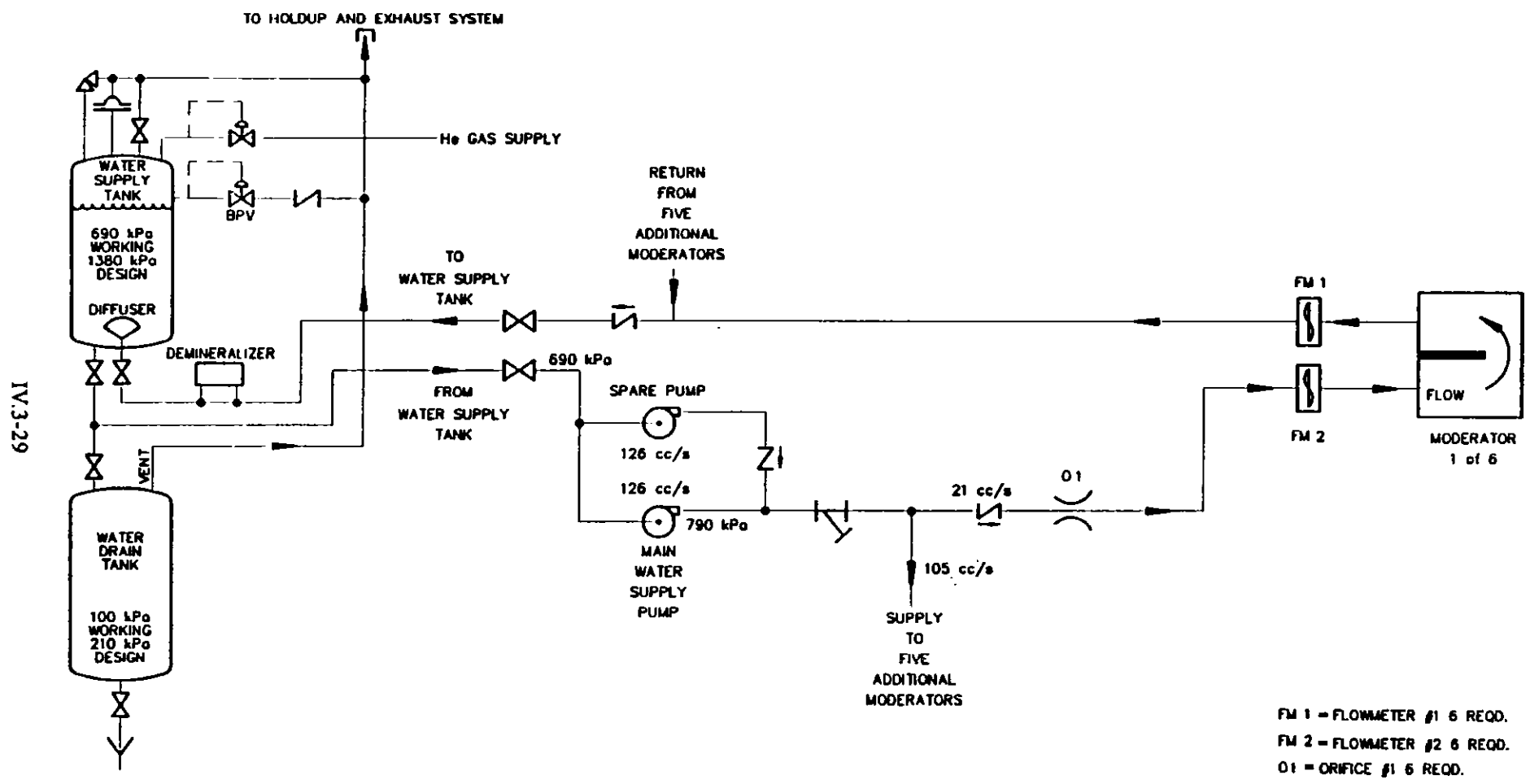
Figure IV.3.4-3 Cooling Circuit Schematic for Water Moderators and Premoderators.

3.4.3 Liquid Methane Moderators

Each target station can have several liquid methane moderators. The methane moderators operate at approximately 90 K, while the surrounding water premoderator is at a temperature near 300 K. The methane is contained within an aluminum box with wall thickness of 1.5 mm. This box is suspended by spring spacers within the vacuum space separating it from the aluminum premoderator box. This geometry is shown in Figures IV.3.1-1 and IV.3.1-2.

The heat loads estimated from the neutronics calculations of Sections IV.2.2 and IV.3.2 and the thermal analyses of preliminary moderator designs provide the basis for the analysis in this section. For simple spring spacer elements made of thin aluminum sheet, the thermal conduction loss is 11 W. Thermal radiation from the water to the methane is 13 W, assuming an emissivity of 0.8. Gamma and neutron heating in the walls of the methane container is 40 W. Gamma and neutron heating in the bulk methane is 200 W. All of these values are for a moderator in the upstream position and are twice as high for a liquid methane moderator in the flux-trap position. The heat loss in the vacuum-jacketed transfer line is 25 W. The vacuum jacket absorbs approximately 500 W of gamma and neutron heating over a 1-m length near the targets. This heat is absorbed and removed by the water moderator/premoderator cooling circuits. The moderator heat load of 300-600 W is removed by flowing methane. An allowable temperature rise of 5-10 K in the methane is maintained by a volumetric flow rate of 36 cm^3/sec. A pressure drop of 34 kPa is required to produce this flow in a tube with 13-mm OD by 0.9-mm wall by 80-m length. A pressure drop of 200 kPa is allowed to provide for flow control and metering and extra parasitic losses. Pump power of 260 W provides a total flow rate of 108 cm^3/sec at a pump efficiency of 0.1 (the efficiency of low-flow-rate cryogenic pumps is very low).

The long-chain hydrocarbons, oils, waxes, and tars that form from chemically active methane fragments (Section IV.3.3.2) must be removed from the flowing methane as they are formed to prevent plugging. Two pebble beds acting alternately are used to continuously clean the methane. One bed is regenerated while the other bed cleans the methane. The heavy hydrocarbons plate out on all surfaces, and since the pebble beds provide a much larger surface area the heavy hydrocarbons will tend to accumulate in the bed rather than on piping or the moderator-container surface.

The methane-moderator heat loads, transfer-line heat loads, pumping power, and other parasitic heat loads total approximately 500 W per moderator. All of this energy is deposited in a liquid nitrogen heat sink. This results in a liquid nitrogen boil-off rate of 4 cm^3/sec per moderator. Liquid nitrogen kept at an absolute pressure of 350 kPa boils above the freezing point of methane, so the system does not freeze and plug. Figure IV.3.4-4 shows the cooling circuit. All of the cryogenic hardware, with the exception of transfer-lines, is enclosed within a superinsulated vacuum cold box 1.5 m high and 2 m in diameter. A pressure vessel which is 1 m high × 1.2 m in diameter and is located off-axis inside the cold-box has a design pressure rating of 690 kPa and contains liquid nitrogen maintained at 350 kPa and a depth of 200 mm. A coil of stainless-steel tubing that is 13 mm OD × 20 m long and is immersed in the liquid nitrogen serves
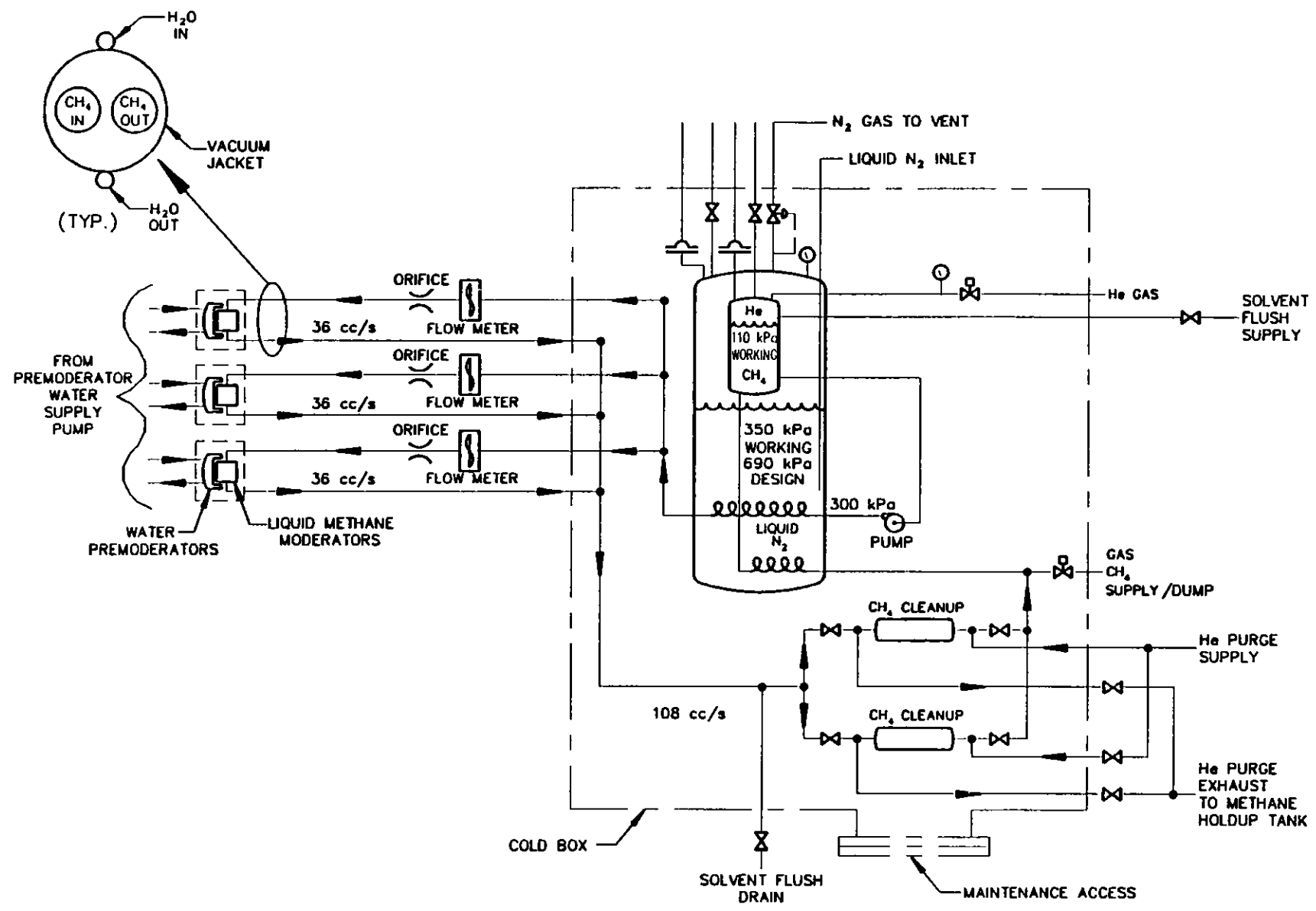
Figure IV.3.4-4 Liquid Methane Moderator Cooling Circuit Schematic, Shown for Three Moderators.

as the methane-to-nitrogen heat exchanger. Suspended inside the liquid nitrogen vessel is another pressure vessel that is 250 mm in diameter × 300 mm long and contains helium-pressurized liquid methane at 110 kPa, maintained at a liquid depth of 200 mm. A pump draws liquid methane from the suspended tank and pressurizes it to 300 kPa. The pressurized liquid methane travels through the heat exchanger to the outlet manifold, where control valves split it into equal flows for each of the liquid methane moderators. Each of the flows is continually monitored, and methane cleaners are regenerated when the pressure drop exceeds a certain level, yet to be determined.

The liquid methane moderator cooling-system components for the 30-Hz target station are mainly located in a shielded area between Building 370, Building 371, and Building 368. The liquid methane moderator cooling-system components for the 10-Hz target station are mainly in a shielded area about 25 m from the Building 369 annex. The locations of these shielded areas are shown in Figure IV.1.2-1. The structure of these shielded areas and the layout of components within them are shown in Figures IV.3.4-5a, IV.3.4-5b, and IV.3.4-5c. The shielded areas for the methane moderator cooling-system components are adjacent to but separate from similar areas for the hydrogen moderator cooling-system components, as shown in the figures. All components containing methane, exclusive of the transfer piping and the moderator, are located inside a 15-cm-thick by 1.9-m-high shield wall. The shield labyrinth has no doors, and this allows natural ventilation. A lightweight lean-to roof covers the equipment but is supported separately from the walls. A 0.6-m gap is provided between the shield and the roof for ventilation. Liquid methane flows to and from the moderators in vacuum-insulated piping in a shielded overhead pipeway, as shown in Figure IV.1.2-1.

All electrical equipment located in the methane moderator cooling-system meets the National Electrical Code, NFPA 70, requirements (or approved alternatives) for class I, division I, group B locations. The methane system design conforms to the applicable sections of the following:

- NFPA 54 National Fuel Gas Code; and

- NFPA 59A Standard for the Production, Storage, and Handling of Liquefied Natural Gas (LNG).

A 24,000-L liquid nitrogen tank outside Building 371 supplies liquid nitrogen to the methane cold box for the 30-Hz target station. Nitrogen for the 10-Hz target station is supplied from a 12,000-L nitrogen tank outside the Building 369 annex.

3.4.4 Liquid Hydrogen Moderators

Several of the moderators on each target station are of liquid hydrogen. Each includes a water premoderator to slow neutrons and reduce the neutron thermalization and gamma ray heating of the cryogenic parts. Construction of the hydrogen moderator and water premoderator

A ←

GAS. METHANE OR
GAS. HYDROGEN
HOLD-UP AND FILL TANKS

15cm THK x 1.9m HIGH
SHIELDING BLOCK WALL

METHANE OR
HYDROGEN
"K" BOTTLES

STACK

EXHAUST
BLOWER

METHANE COLD BOX OR
HYDROGEN COLD BOX

B

FREE STANDING
LIGHTWEIGHT ROOF

METHANE AREA

HYDROGEN AREA

B'

1.9m BETWEEN
WALLS

A ←

NOTE:
METHANE AREA SHOWN
HYDROGEN AREA MIRROR IMAGE
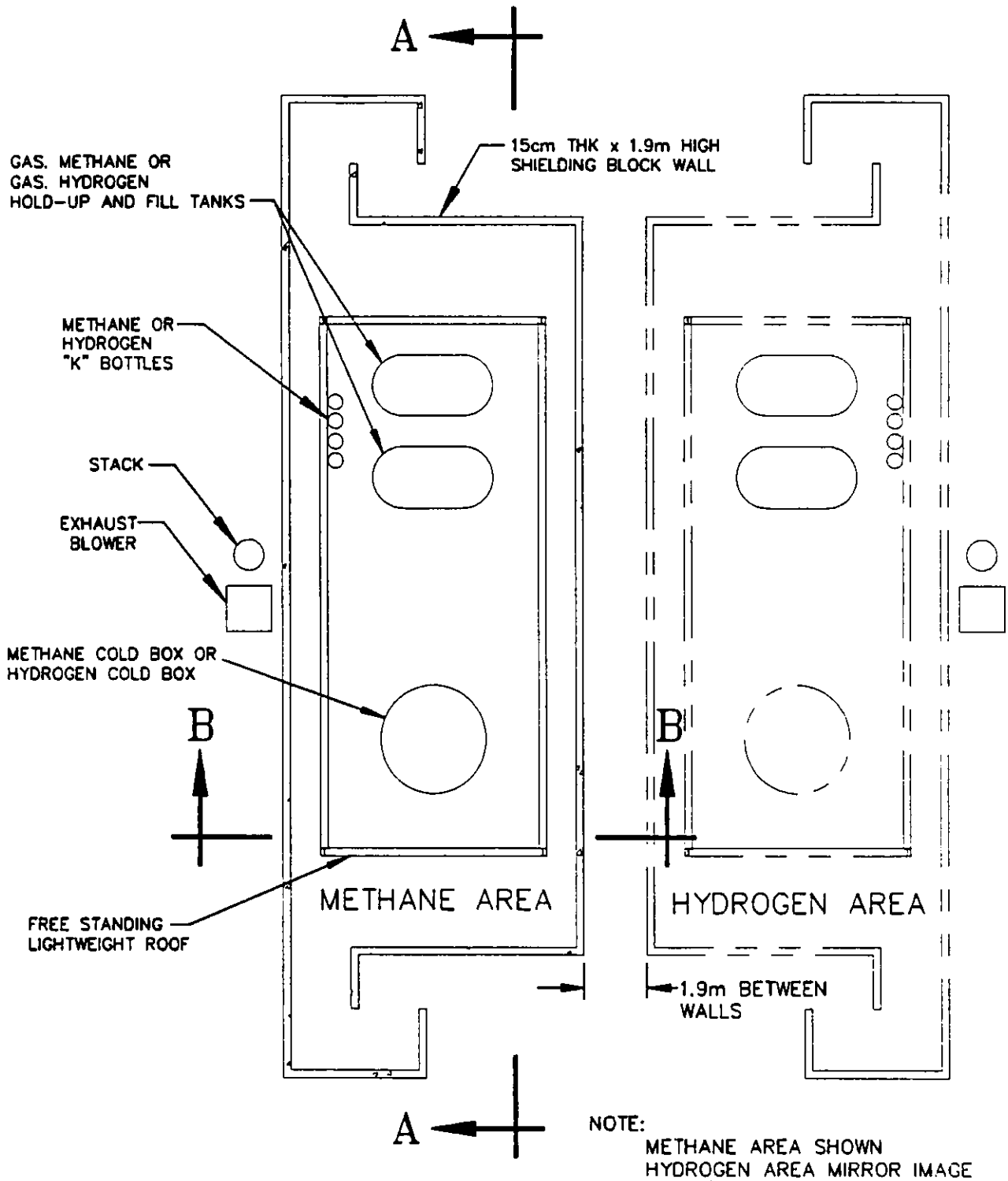
Figure IV.3.4-5a Plan View of One of the Shielded Areas Housing the
Liquid Methane and Liquid Hydrogen Cooling Systems.

STACK

FREE STANDING
LIGHTWEIGHT
ROOF

METHANE COLD BOX OR
HYDROGEN COLD BOX

METHANE OR
HYDROGEN
"K" BOTTLES

GAS. METHANE OR
GAS. HYDROGEN
HOLD-UP AND FILL TANKS

15cm THK. x 1.9m HIGH
SHIELDING CONCRETE WALL

60cm OPEN

60cm OPEN

GROUND
LEVEL
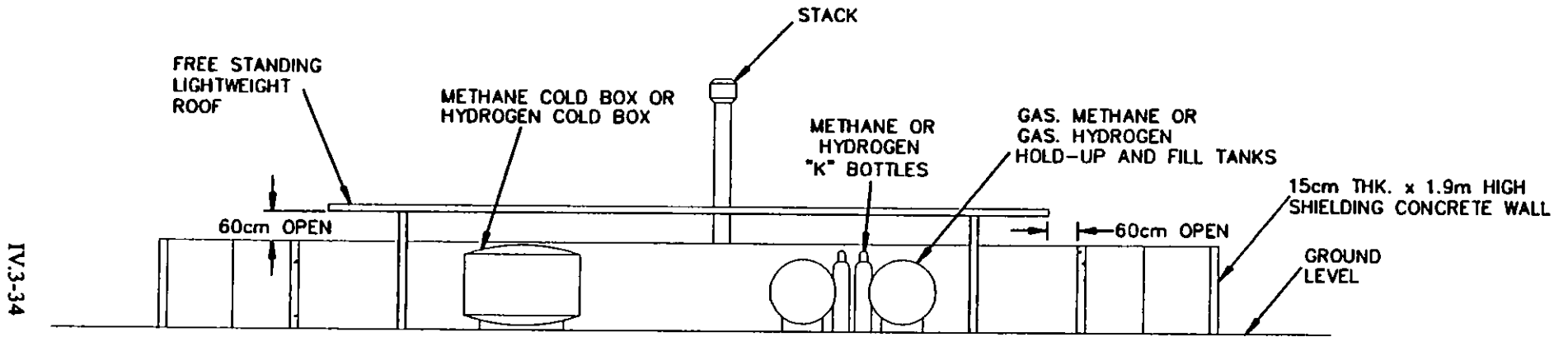
SECTION A-A

NOTE:
METHANE AREA SHOWN
HYDROGEN AREA MIRROR IMAGE

Figure IV.3.4-5b Sectional View A-A of One of the Shielded Areas Housing the Liquid Methane and Liquid Hydrogen Cooling Systems.

STACK

GAS. METHANE OR
GAS. HYDROGEN
HOLD-UP AND FILL TANKS

METHANE COLD BOX OR
HYDROGEN COLD BOX

METHANE OR
HYDROGEN
"K" BOTTLES

FREE STANDING
LIGHTWEIGHT
ROOF

60cm OPEN

60cm OPEN

EXHAUST BLOWER

15cm X 1.9m HIGH
SHIELDING CONCRETE WALL

GROUND LEVEL
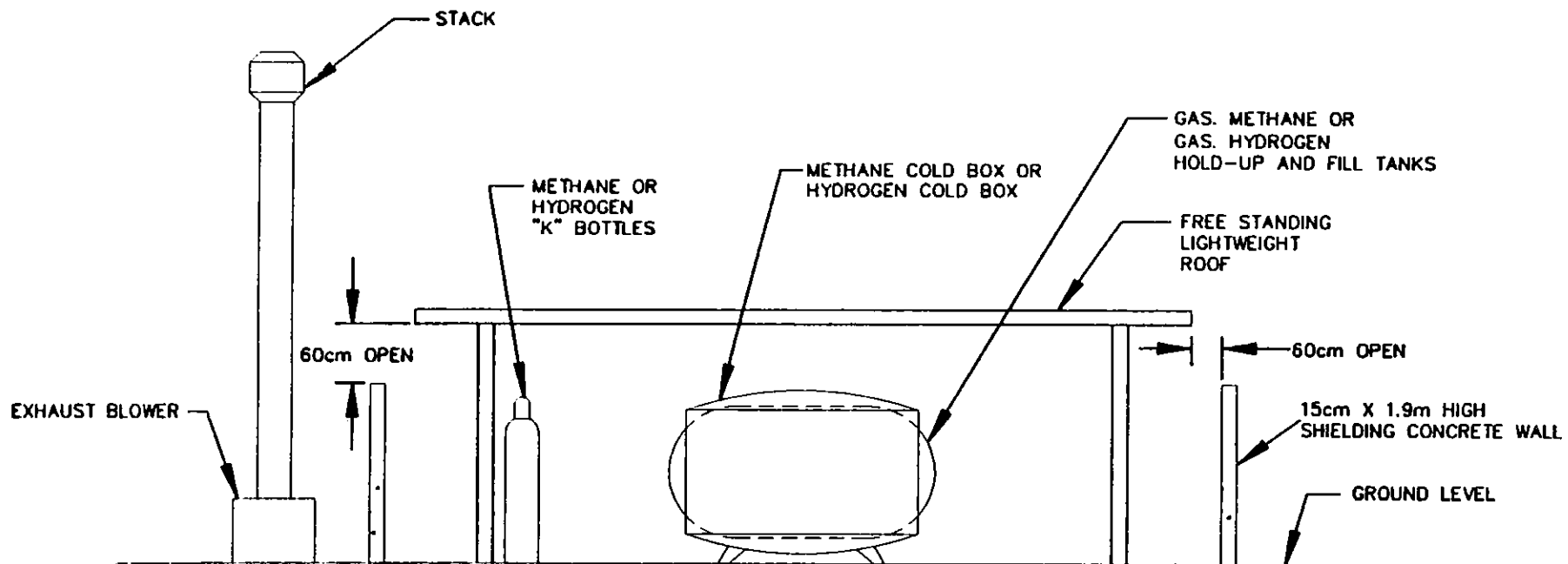
NOTE:
METHANE AREA SHOWN
HYDROGEN AREA MIRROR IMAGE

SECTION B-B

Figure IV.3.4-5c Sectional View B-B of One of the Shielded Areas Housing the Liquid Methane and Liquid Hydrogen Cooling Systems.

containers is similar to that described for the methane and water systems; however, the dimensions are different. One of the hydrogen containers is $2 \times 10 \times 20$ cm^3 and is constructed of 1.5-mm 6061 aluminum.

The various heat loads are estimated using the neutronics calculations of Sections IV.2.2 and IV.3.2 and thermal analyses of the designs. The total heat load in a liquid hydrogen flux-trap moderator is 300 W. Contributions are 19 W from thermal radiation, 21 W from conduction through the spacers, 170 W from gamma and neutron heating in the bulk hydrogen, and 90 W from gamma and neutron heating in the hydrogen container walls. The total heat load in a liquid hydrogen wing moderator is 314 W. Contributions are 18 W from thermal radiation, 7 W from conduction through the spacers, 221 W from gamma and neutron heating in the bulk hydrogen, and 68 W from gamma and neutron heating of the container.

Liquid hydrogen is supplied to each moderator through vacuum-jacketed and superinsulated tubing. The vacuum jacket is 60 mm OD and has approximately 1 W/m heat gain. Designing for a 5 K temperature rise in the hydrogen, from 18 to 23 K, gives a total liquid hydrogen flow rate of 200 cm^3/sec. A pumping power of 70 W forces the hydrogen through 13-mm OD lines. Allowing for an additional 50-W heat gain in an evacuated, superinsulated cold box sets the requirement for a helium refrigeration system for two moderators to have 800 W capacity at 13 K. Although heat loads in the hydrogen moderator system for the 10-Hz target station are less, an identical helium refrigeration unit is used to cool the hydrogen moderators in the 10-Hz target system as well.

The helium refrigerators, supplied as packaged units, use a liquid nitrogen heat sink for the cryogenic portion of the heat load. Figure IV.3.4-6 shows the process diagram for the hydrogen and helium cryogenics. A 250-kW oil-flooded screw helium compressor with an electric motor running a direct drive at 3,600 rpm is used. A water-cooled heat exchanger removes the compression energy from the helium. The helium travels through three stages of oil removal to reduce the oil contamination to less than 10 parts per billion (ppb). The helium is chilled to 80 K in a liquid-nitrogen-cooled heat exchanger and further cooled to approximately 25 K by counterflow exchange with helium returning from the hydrogen heat exchanger. Helium expanded in a multistage turbine to 13 K enters the hydrogen cooler at 14 K. The helium flow rate and refrigeration capability vary according to the process requirements over a 3-to-1 range. Variable compressor inlet pressure and compressor bypass recycle flow accommodate this variation. This turndown capability allows the use of identical helium refrigeration systems for both the 10-Hz and 30-Hz target stations.

The liquid hydrogen moderator cooling-system components for the 30-Hz target station are mainly located in a shielded area between Building 370 and Building 371. The liquid hydrogen moderator cooling-system components for the 10-Hz target station are mainly in a shielded area about 25 m from the Building 369 annex. The locations of these shielded areas are shown in Figure IV.1.2-1. The structure of these shielded areas and the layout of components within them are shown in Figures IV.3.4-5a, IV.3.4-5b, and IV.3.4-5c. The shielded areas for the hydrogen moderator cooling-system components are adjacent to but separate from similar areas for the
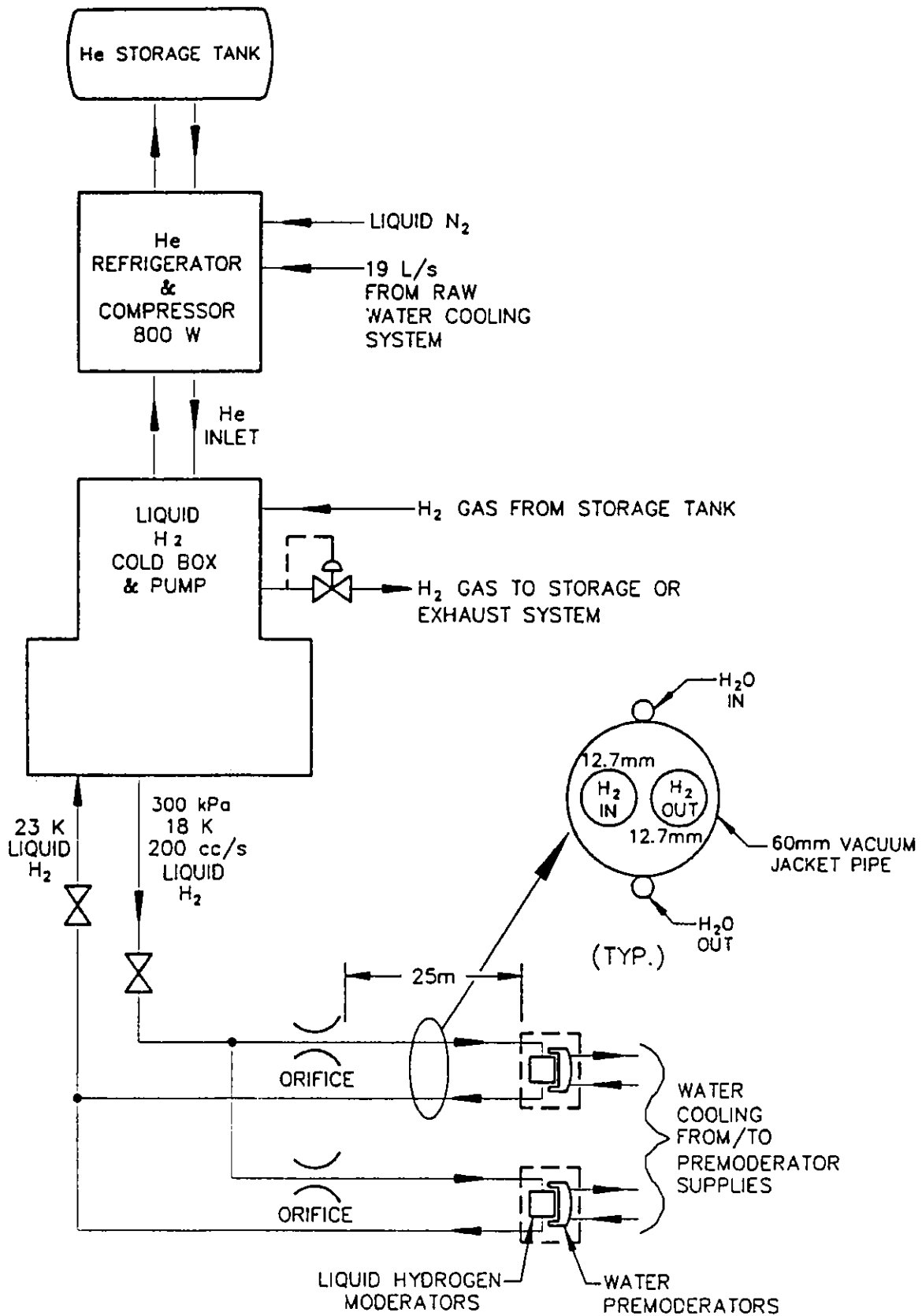
Figure IV.3.4-6 Schematic Diagram of the Liquid Hydrogen Moderator Cooling System, Shown for Two Hydrogen Moderators.

methane moderator cooling-system components, as shown in the figures. All components containing hydrogen, exclusive of the transfer piping and the moderator, are located inside a 15-cm-thick by 1.9-m-high shield wall. The shield labyrinth has no doors, and this allows natural ventilation. A lightweight lean-to roof covers the equipment but is supported separately from the walls. A 0.6-m gap is provided between the shield and the roof for ventilation. Liquid hydrogen flows to and from the moderators in vacuum-insulated piping in a shielded overhead pipeway, as shown in Figure IV.1.2-1. The vacuum jacket pressure relief-valve vents are monitored for hydrogen and are routed to the hydrogen vent stack. Figure IV.3.4-6 shows a typical sectional view of the vacuum-jacketed hydrogen piping.

All electrical equipment located in the hydrogen moderator cooling-system area meets the National Electrical Code, NFPA 70, requirements (or approved alternatives) for class I, division I, group B locations. The hydrogen system design conforms to the applicable sections of the following:

- 29 CFR Ch. XVII, Section No. 1910.103, "Hydrogen";

- NFPA 50A Standard for Gaseous Hydrogen Systems at Consumer Sites;

- NFPA 50B Standard for Liquefied Hydrogen Systems at Consumer Sites; and

- ANL ES&H Manual, Chapter 4-8, "Hydrogen Safety."

A 24,000-L liquid nitrogen tank rests on a pad outside Building 371 and supplies the 30-Hz target liquid methane and liquid hydrogen moderator cooling systems. The moderator cooling systems together require about 12,000-L storage capacity. The additional 12,000-L capacity provides general purpose liquid and gaseous nitrogen for both the 10-Hz and 30-Hz target areas.

The helium refrigerator and compressor system and the gaseous helium storage tank for the 30-Hz target station are located in Building 371. The gaseous helium storage tank has a capacity of 15,500 L and a maximum working pressure rating of 1725 kPa. Helium gas from the compressor travels to the liquid hydrogen cold box in the shielded area outside Building 371. A vacuum pump skid outside the shielding services the liquid hydrogen cold box.

The liquid nitrogen supply for the 10-Hz target systems is a 12,000-L liquid storage tank located on a pad outside the annex to Building 369. Vacuum-jacketed plumbing brings liquid from the nitrogen tank to the cold box in the shielded area outside the annex to Building 369. This liquid nitrogen system serves only as a heat sink for the liquid methane and liquid hydrogen moderator cooling systems.

The annex to Building 369 houses the helium refrigerator and compressor system for the 10-Hz target liquid hydrogen moderator cooling system. The 15,500-L gaseous helium storage tank is outside Building 369. Helium gas from the compressor is routed to the liquid hydrogen cold box in the shielded area outside the Building 369 annex. The liquid hydrogen cold box is in

the shielded area approximately 25 m from the Building 369 annex. Also located in this area are the hydrogen gas holdup tank and fill tank. Just outside the shielding are an exhaust fan, vent stack, and the vacuum pump skid to provide the cold box vacuum.

3.4.5 Reflector

Neutronic calculations described in Section IV.2.2 indicate that the heat load in the reflector is approximately 130 kW. Figure IV.3.4-7 shows the reflector water-cooling system, which includes a 230-L stainless-steel storage-surge tank and has a working pressure of 690 kPa. The system also includes two redundant identical water pumps connected in parallel, check valves to preclude reversed flows, flowmeter, filter, water-to-water counterflow heat exchanger, demineralizer, and interconnecting piping. This water-cooling system is entirely separate from the other water-cooling systems to preclude the possible spread of beryllium contamination.

The water-supply tank has a regulated helium supply for the initial pressurization and for providing a continuous bleed flow rate of 8 cm^3/sec to sweep radiolysis and activation products from the ullage space. The supply tank has an H_2/O_2 recombiner. The tank is vented through a remote valve. A pressure-relief valve and a backup burst diaphragm provide additional safety. The continuous helium bleed discharges through a back-pressure control valve. The vent gases are collected and held in the holdup tank described in Section IV.6.3. A 230-L drain tank allows local holdup of the system water inventory.

The water circuits for the top beryllium reflector and for the bottom beryllium reflector split downstream of the heat exchanger and rejoin ahead of the demineralizer. The major portion of each of these piping circuits consists of 2.54-cm-diameter stainless-steel tubing. Other piping is nominally 6.0-cm OD. Tubing sections are joined by using standard flared fittings. Larger piping is welded. An 8.9-cm (3-in., schedule 10) outer pipe sheath supports and protects the four tubing runs within the target-train assembly that slides into the biological shield as shown in the inset in Figure IV.3.4-7.

The total calculated pressure drop around the water-flow circuits is 435 kPa. However, a pump-head capacity of 650 kPa is used to permit flow control. Each of the redundant pumps requires a 3.75-kW motor.

The pumps, tanks, demineralizer, and heat exchanger for the 10-Hz target are located on a skid in the shielded room in Building 367. The shielded room in Building 371 contains an identical skid arrangement for the 30-Hz target. These layouts are shown in Figures IV.3.4-1a, IV.3.4-1b, IV.3.4-2a, and IV.3.4-2b.
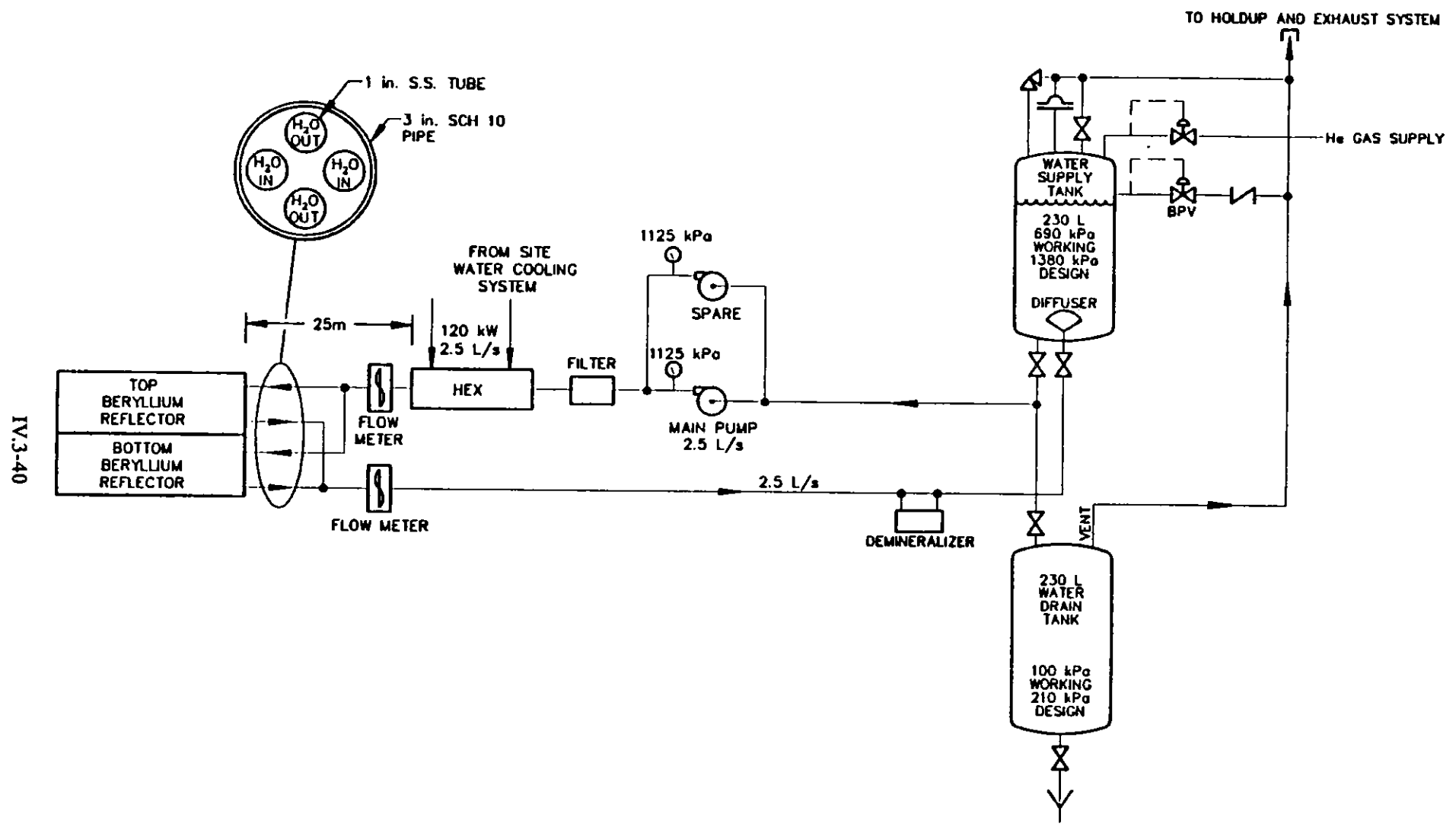
Figure IV.3.4-7 Schematic Diagram of the Reflector Cooling System.

3.4.6 Biological Shield

Neutronic calculations indicate that the gamma and neutron heat load in the shield region close to the reflector is approximately 130 kW. The water-cooling system for the biological shield is shown in Figure IV.3.4-8. It is identical in configuration and capacity to the beryllium-reflector cooling system, with the exception that a demineralizer is not required.

The shield adjacent to the reflector is iron. Cooling water flows in passages drilled into the iron blocks. The remainder of the water-cooling system also is constructed of iron to eliminate galvanic effects. As a further measure, buffered water is used to prevent corrosion. The 230-L water-supply tank has a helium pressurization, a 16 cm^3/sec bleed purge system, and an H_2/O_2 recombiner. A liquid-level gauge is provided. Nominal tank pressurization is 690 kPa. Redundant 3.75-kW motor pumps supply 2.5-L/sec water flow through 2-in. Schedule 40 pipe to the parallel water-cooling passages in the shield. Orifices apportion water at equal flow rates to each cooling channel. Each of the vertical-axis cooling channels has a bayonet tube that extends down near the bottom of the cooling channel. The bayonet tube supplies water for reverse-flow back through the annular flow space between the coaxial tube and the drilled cooling channel. The cooling water is filtered before it is returned to the biological shield. A flowmeter monitors the total coolant flow rate. A counterflow water-to-water heat exchanger removes the steady heat load of approximately 130 kW.

The tanks, pumps, filter, and heat exchanger for the 10-Hz target are mounted on a skid in the shielded area of Building 367. Building 371 houses an identical cooling system for the 30-Hz target. These layouts are shown in Figures IV.3.4-1a, IV.3.4-1b, IV.3.4-2a, and IV.3.4-2b. Piping is routed from the cooling skids to the targets. All piping is insulated to limit heat loads on the shielded room and piping tunnel ventilation systems.

3.4.7 Target Tank

The target train fits within the target tank, which is described in Section IV.1.2. The target tank has its own cooling system, which is shown schematically in Figure IV.3.4-9. The system incorporates 240-L supply and drain tanks of 304SS construction, pressurized to 690 kPa. The supply tank has a H_2/O_2 recombiner. The main water supply pump, constructed of corrosion-resistant materials, draws water from the supply tank. Pump power is 0.6 kW, which provides a differential pressure of 104 kPa. A spare pump is plumbed in parallel to the main pump.

The shielded room in Building 367 houses the target tank cooling system for the 10-Hz target tank. The tanks, pumps, heat exchanger, and demineralizer share a common skid. Plumbing from the cooling system skid runs from Building 367 to Building 369.

The target tank cooling system for the 30-Hz target tank is located in the shielded room in Building 371. The tanks, pumps, heat exchanger, and demineralizer share a common skid. Plumbing from the cooling system skid runs from Building 371 to Building 370.
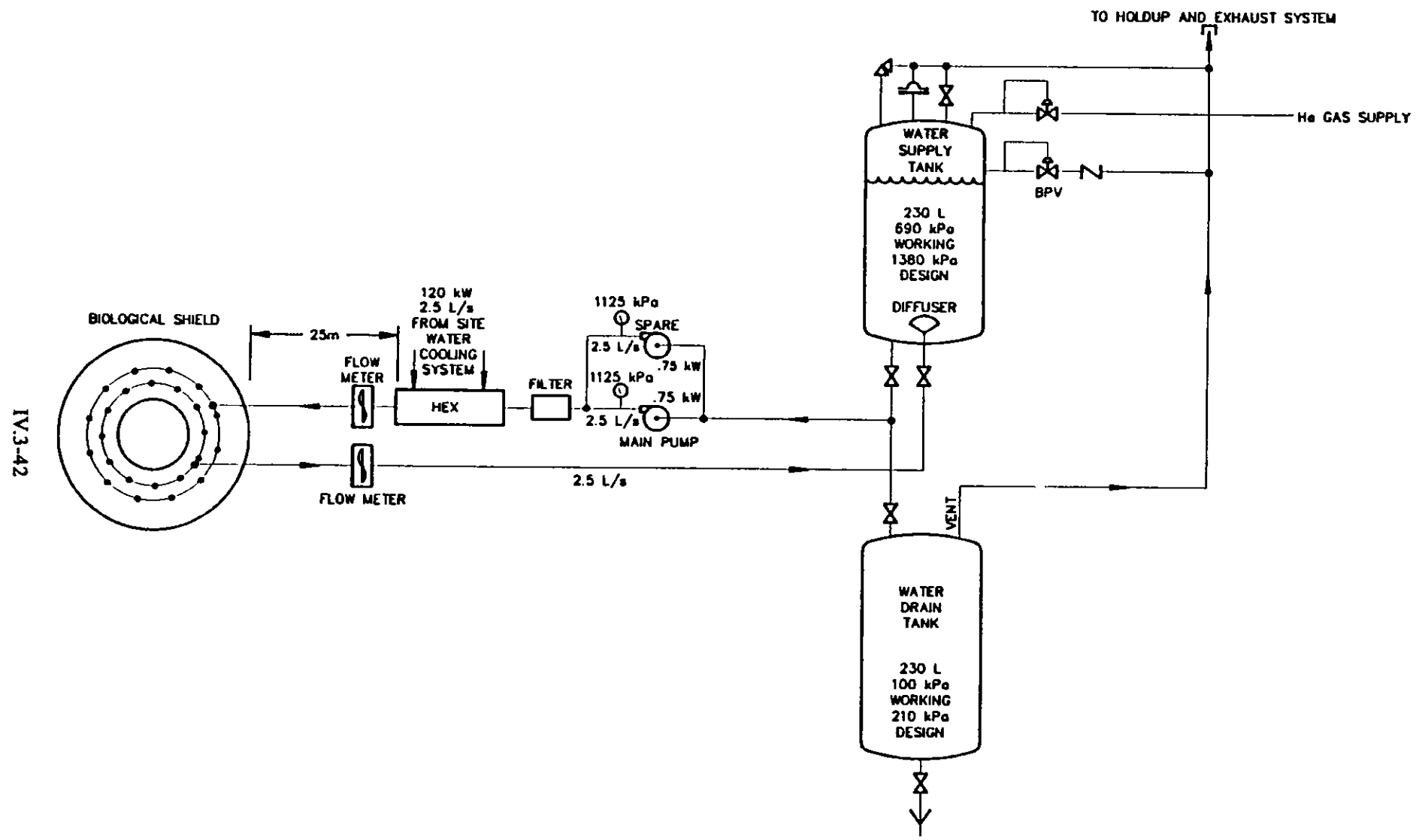
Figure IV.3.4-8 Schematic Diagram of the Biological Shield Cooling System.

TO HOLDUP AND EXHAUST SYSTEM

He GAS SUPPLY

WATER
SUPPLY
TANK

690 kPa
WORKING
1380 kPa
DESIGN

DIFFUSER

BPV

DEMINERALIZER

TO
SUPPLY
TANK

FROM
SUPPLY
TANK

690 kPa

SPARE PUMP

250 cc/s

250 cc/s

25mm

25mm

MAIN
WATER
SUPPLY
PUMP

FILTER

FROM SITE
WATER COOLING
SYSTEM

10 kW

HEX

25mm x 8mm

25mm x 8mm

TARGET TANK

WATER
DRAIN
TANK

100 kPa
WORKING
210 kPa
DESIGN
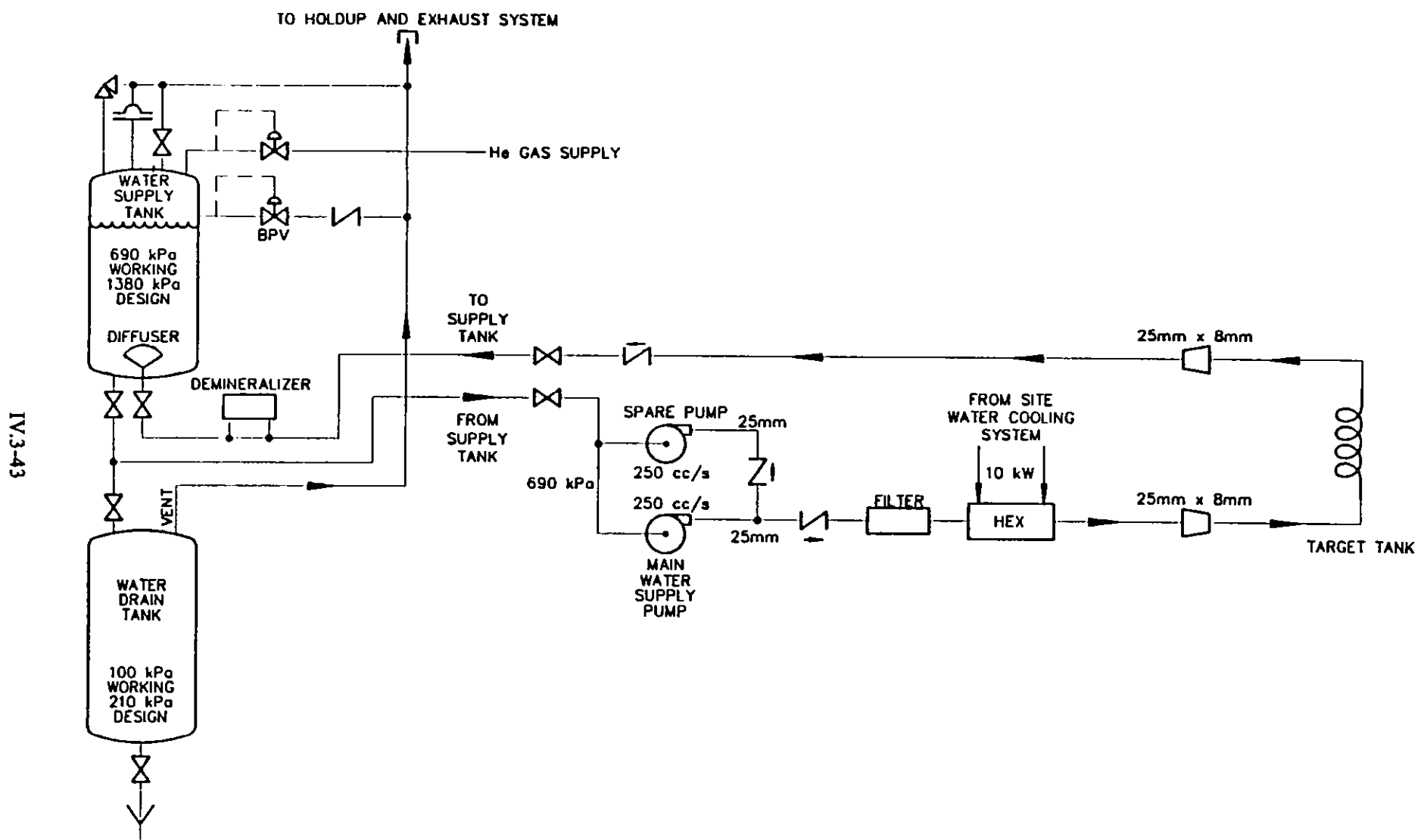
VENT

Figure IV.3.4-9 Schematic Diagram of the Target Tank Cooling System.

All piping has insulation to reduce the heat loads and ventilation requirements.

3.4.8 Proton HET Line Vacuum Window Insert

Water circulates between the two walls of the proton HET line insert tube and across the window at the end, with helical guides separating the inlet and outlet flows, as shown in Figure IV.1.2-10. Calculations described in Section IV.2.2.2 (see Table IV.2.2-2) indicate that the proton beam deposits about 9 kW of heat in the proton beam line vacuum window. Figure IV.3.4-10 shows the proton HET line vacuum window insert cooling system. The system consists of a 240-L 304SS surge and supply tank with an H_2/O_2 recombiner, a similar drain tank, a pump, and a 10-kW heat exchanger. The pressure in the supply tank is 690 kPa. The supply tank feeds the main water supply pump. A spare pump is plumbed in parallel to the main pump. The pump differential pressure is 104 kPa. All plumbing components are stainless steel or other suitable corrosion-resistant materials.

The proton beamline vacuum window insert cooling system for the 10-Hz target system is in the shielded room in Building 367. The tanks, pumps, heat exchanger, and demineralizer are located on a common skid. Plumbing from the cooling system skid runs from Building 367 to Building 369. The shielded room in Building 371 houses the proton HET line vacuum window insert cooling system for the 30-Hz target system. The tanks, pumps, heat exchanger, and demineralizer are located on a common skid. Plumbing from the cooling system skid runs from Building 371 to Building 370. Component layouts are shown in Figures IV.3.4-1, IV.3.4-1a, IV.3.4-2, and IV.3.4-2a.

All system components have insulation to reduce the heat load and ventilation requirements in the shielded rooms.

TO HOLDUP AND EXHAUST SYSTEM

He GAS SUPPLY

WATER
SUPPLY
TANK

690 kPa
WORKING
1380 kPa
DESIGN

DIFFUSER

BPV

DEMINERALIZER

TO
SUPPLY
TANK

FROM
SUPPLY
TANK

690 kPa

SPARE PUMP

25mm

250 cc/s

250 cc/s

25mm

MAIN
WATER
SUPPLY
PUMP

FILTER

FROM SITE
WATER COOLING
SYSTEM

10 kW

HEX

25mm x 8mm

25mm x 8mm

PROTON BEAM
WINDOW

WATER
DRAIN
TANK

VENT

100 kPa
WORKING
210 kPa
DESIGN
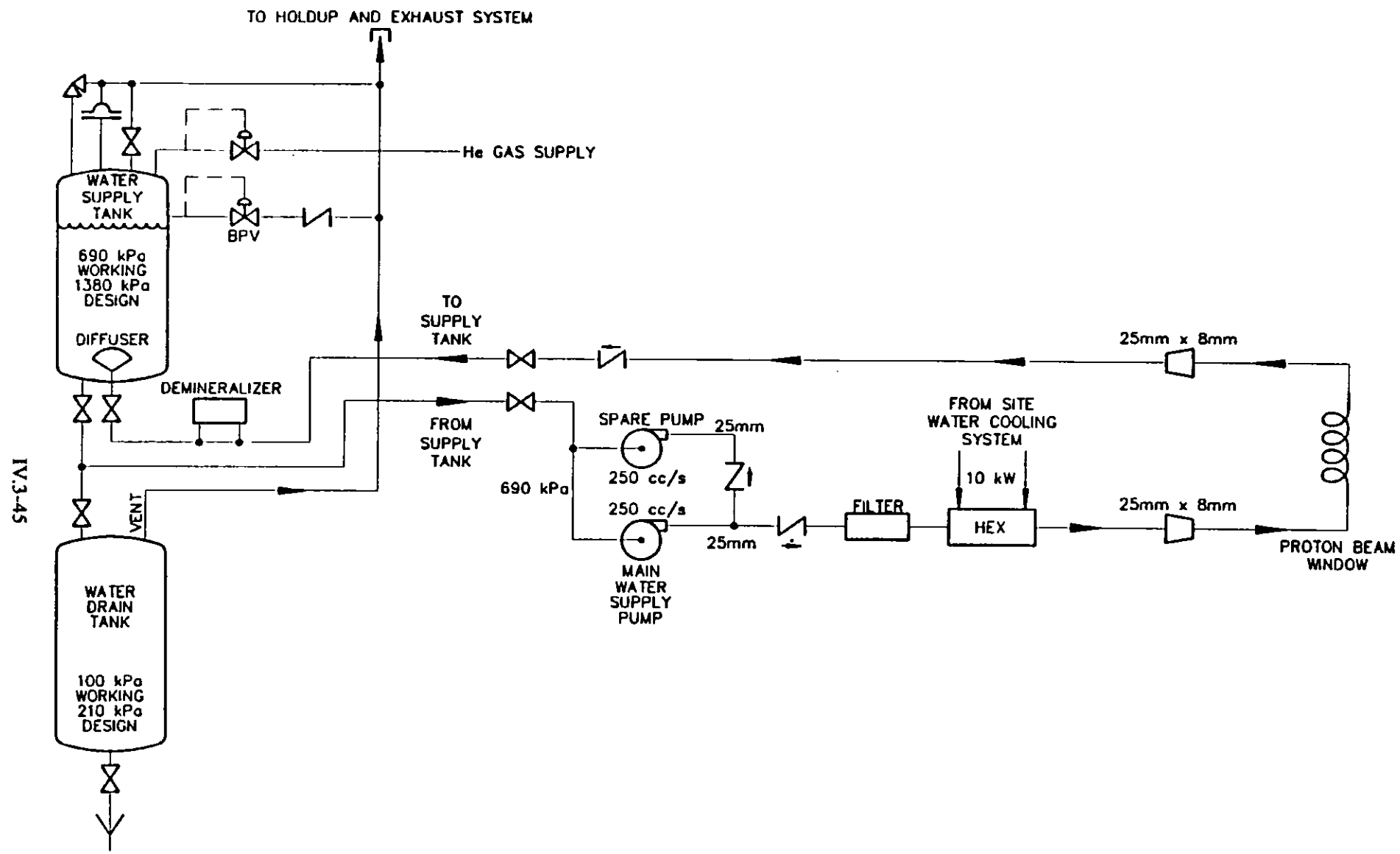
IV.3-45

Figure IV.3.4-10 Schematic Diagram of the Proton HET Line Vacuum Window Cooling System.

3.5 REFERENCES

1. J.M. Carpenter, "Pulsed spallation neutron sources for slow neutron scattering," Nucl. Instrum. Methods 145:91-113 (1977).

2. A. Carne, "Progress on the SNS target station," in *Proceedings of the 6th Meeting of the International Collaboration on Advanced Neutron Sources (ICANS VI)* (Argonne, Ill., June 28-July 2, 1982), Argonne National Laboratory Report No. ANL-82-80, pp. 315-326 (1982).

3. Y. Kiyanagi, N. Watanabe, and H. Iwasa, "Experimental studies on neutronic performance of coupled liquid-hydrogen moderator for pulsed spallation neutron sources," Nucl. Instrum. Methods A312:561-570 (1992).

4. J.M. Carpenter, and W.B. Yelon, "Neutron sources," in *Methods of Experimental Physics, Volume 23, Neutron Scattering, Part A*, edited by K. Sköld and D.L. Price, pp. 99-196 (Academic Press, New York, 1986).

5. E.P. Shabalin, "Pulsed neutron sources at DUBNA: Their past, present and future status," in *Proceedings of the 11th Meeting of the International Collaboration on Advanced Neutron Sources (ICANS XI)* (Tsukuba, Japan, Oct. 22-26, 1990), National Laboratory for High Energy Physics (KEK) Report No. 90-25, pp. 109-118 (1991).

6. N. Watanabe, "A design concept of target-moderator-reflector assemblies for KENS-II — A high-efficiency pulsed spallation neutron source," in *Proceedings of the 11th Meeting of the International Collaboration on Advanced Neutron Sources (ICANS XI)* (Tsukuba, Japan, Oct. 22-26, 1990), National Laboratory for High Energy Physics (KEK) Report No. 90-25, pp. 471-477 (1991).

7. A.M. Weinberg and E.P. Wigner, *The Physical Theory of Neutron Chain Reactors*, pp. 219-278 (The University of Chicago Press, Chicago, Ill., 1958).

8. J.M. Carpenter, C.W. Potts, and G.H. Lander, "Intense Pulsed Neutron Source (IPNS) at Argonne National Laboratory (ANL): A status report as of June, 1982," in *Proceedings of the 6th Meeting of the International Collaboration on Advanced Neutron Sources (ICANS VI)* (Argonne, Ill., June 28-July 2, 1982), Argonne National Laboratory Report No. ANL-82-80, pp. 77-101 (1983).

9. A.D. Taylor, "SNS moderator performance," in *Proceedings of the 8th Meeting of the International Collaboration on Advanced Neutron Sources (ICANS VIII)* (Oxford, U.K., July 8-12, 1985), Rutherford Appleton Laboratory Report No. RAL-85-110, pp. 319-328 (Chilton, U.K., 1985).

10. G.S. Bauer et al., "Relative intensities and time structure of thermal neutron leakage from various moderator-decoupler systems for a spallation neutron source," in *Proceedings of the 5th Meeting of the International Collaboration on Advanced Neutron Sources (ICANS V)* (Jülich, Germany, June 22-26, 1981), Kernforschungsanlage Jülich Report No. Jül-Conf-45, pp. 417-444 (1981).

11. P. Ageron, "Les possibilités expérimentales généralités," Bulletin d'Informations Scientifiques et Techniques du Commissariat a l'Energie Atomique, No. 166 (Jan. 5-16, 1972).

12. *ISIS Annual Report 1991, Vol. 1,* edited by C. Wilson, Rutherford Appleton Laboratory Report No. RAL-91-050, pp. 3-4 (Chilton, U.K).

13. T.A. Broome, "The ISIS liquid methane moderator," in *Proceedings of the Second International Seminar on Pulsed Advanced Neutron Sources, PANS-2* (Dubna, Russia, June 13-20, 1994) (in press).

14. J.M. Carpenter and T.L. Scott, Argonne National Laboratory, 1994 (unpublished information).

15. B. Boardman, *Spallation Neutron Source: Description of Accelerator and Target,* Rutherford Appleton Laboratory Report No. RL-82-006 (Chilton, U.K., 1982).

16. A.T. Lucas, "Cryogenic moderators for ISIS," Rutherford Appleton Laboratory Report No. ISIS/TS/N7/87, Issue 2 (Chilton, U.K., Jan. 16, 1992).

4.1 GEOMETRY AND COMPOSITION

4.1.1 Overview of Components

The IPNS Upgrade biological shields provide the primary protection for personnel from direct radiation emitted from the target regions during operation and shutdown. During the operation of the facility, high-energy protons are directed to either or both of two target stations, where the protons interact with the targets to release neutrons that are utilized in research. Interaction of neutrons and protons with the target and shield materials also results in beta and gamma radiation. During a shutdown of the facility, this radiation is emitted in various intensities due to radioactive decay. The biological shields also provide structural support for the neutron facilities. They enclose components of the target systems and protect against physical damage from external forces.

The biological shields for both target stations are shown in their respective experiment halls in Figure IV.4.1-1. Figures IV.4.1-2 and IV.4.1-3 show one of these biological shields in greater detail. The shields for both target stations are identical rectangular structures of steel and concrete weighing approximately 14,000 metric tons (15,400 tons) each. These structures effectively limit the radiation dose rate at any location in the experiment areas to acceptable levels during operation and shutdown, as is described in Section IV.4.3. Each structure contains an aluminum target tank, as described in Section IV.1.2. For structural reasons, the target tank is enclosed by a steel target tank housing, which in turn is surrounded by cut and stacked steel plate required for shielding. This assembly of steel shielding is enveloped within a steel and reinforced-concrete shielding tank. In addition, the shielding tank is covered with at least 1 m of poured-in-place concrete and concrete blocks. This steel and concrete assembly is the biological shield. The entire structure rests on a slab of reinforced concrete, which is supported by steel pilings that extend into Dolomite bedrock.

There are a total of 18 gated penetrations, 9 on each of two sides, extending radially from the target tank through the biological shield. These penetrations are the beam ports through which the neutrons travel to the neutron scattering instruments, and are described in detail in Section IV.8.

4.1.2 Steel Shielding

The purpose of the biological shielding, shown in Figures IV.4.1-2 and IV.4.1-3, is to attenuate high-energy and fast neutrons. It is a massive structure consisting of steel plate cut to fit into the shielding tank and around the target tank housing, beam port tubes, and other tubes and devices. Cracks and voids are filled with a dry grout consisting of steel shot or iron garnet. This grout is worked in by using a common vibration technique. Each biological shield requires 9,000 metric tons (9,900 tons) of steel for a geometry somewhat better optimized than that shown in the figures.

10 Hz TARGET STATION

30 Hz TARGET STATION

370

371

368

369

N

0   50 FEET

0   10 METERS
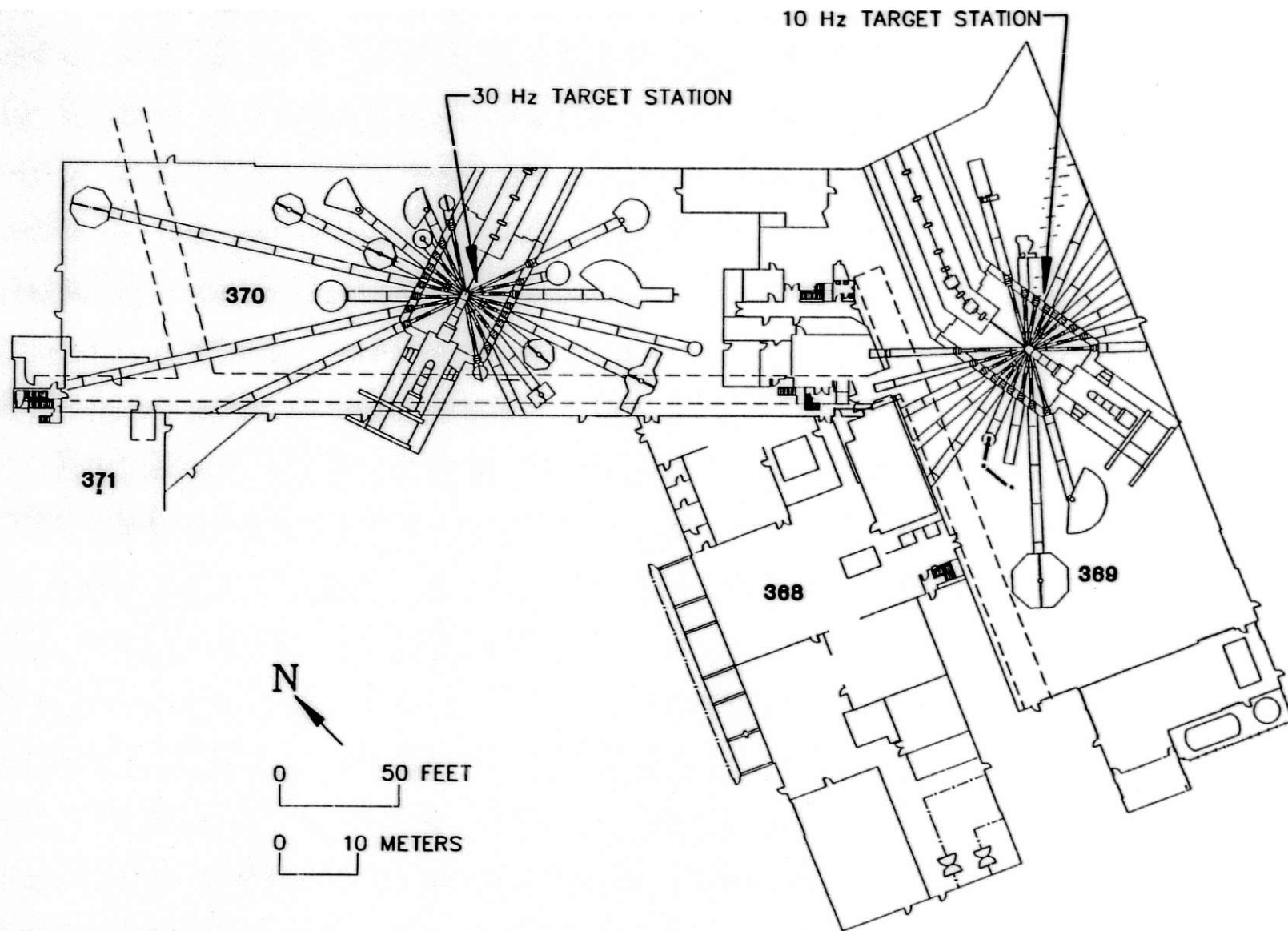
Figure IV.4.1-1 Locations of the Biological Shields for the 30-Hz and 10-Hz Target Stations.
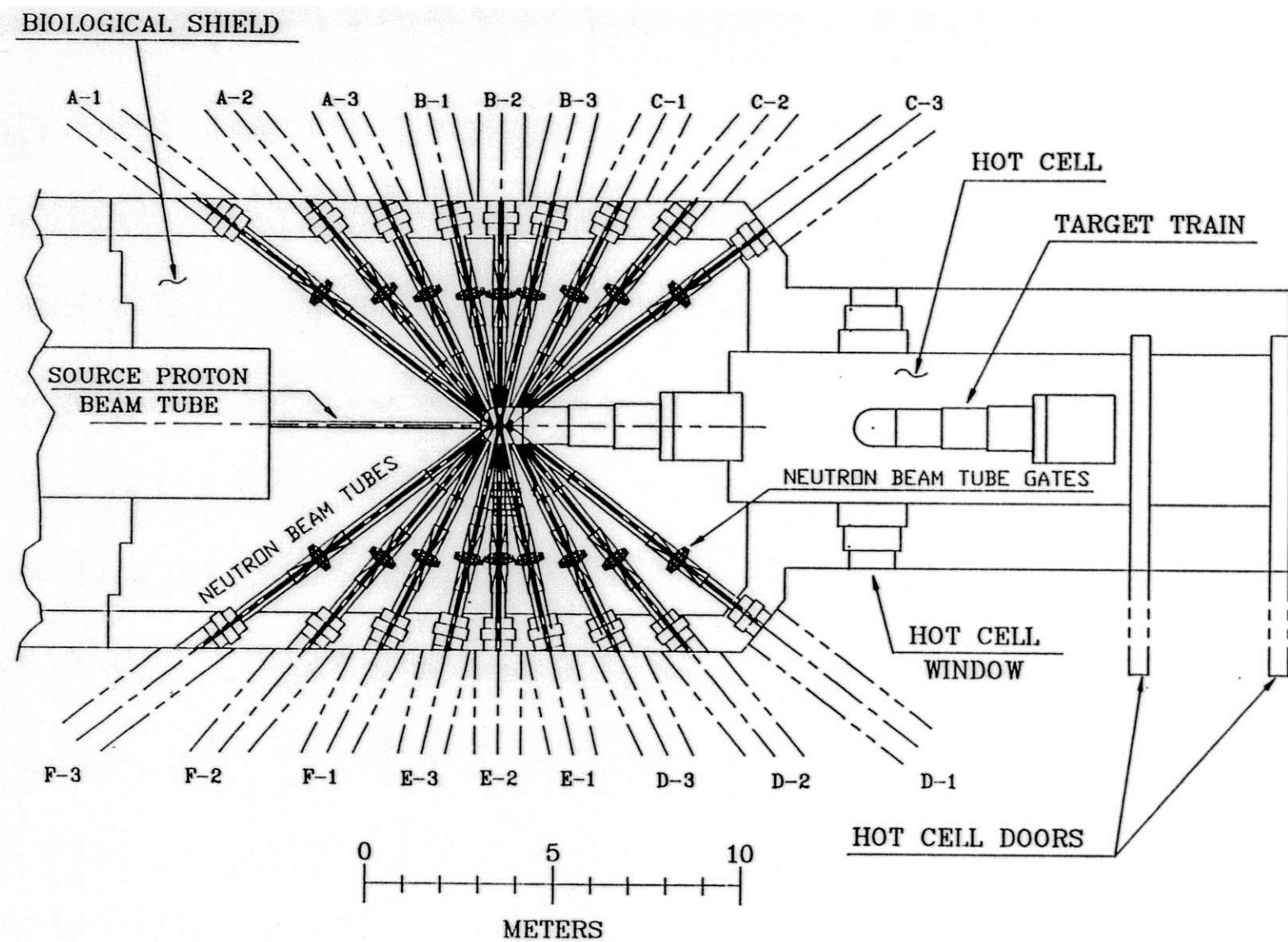
Figure IV.4.1-2 Layout of a Target Station, Showing the Biological Shield and the Remote-Handling Hot Cell.

GATE IN CLOSED
POSITION

GATE IN OPEN
POSITION

SHIELDING TANK

STEEL SHIELD

CONCRETE SHIELD

MOVEABLE CONCRETE
SHIELD

BEAM GATE

SHIELDING TANK

BEAM LINE

0
5
10

METERS
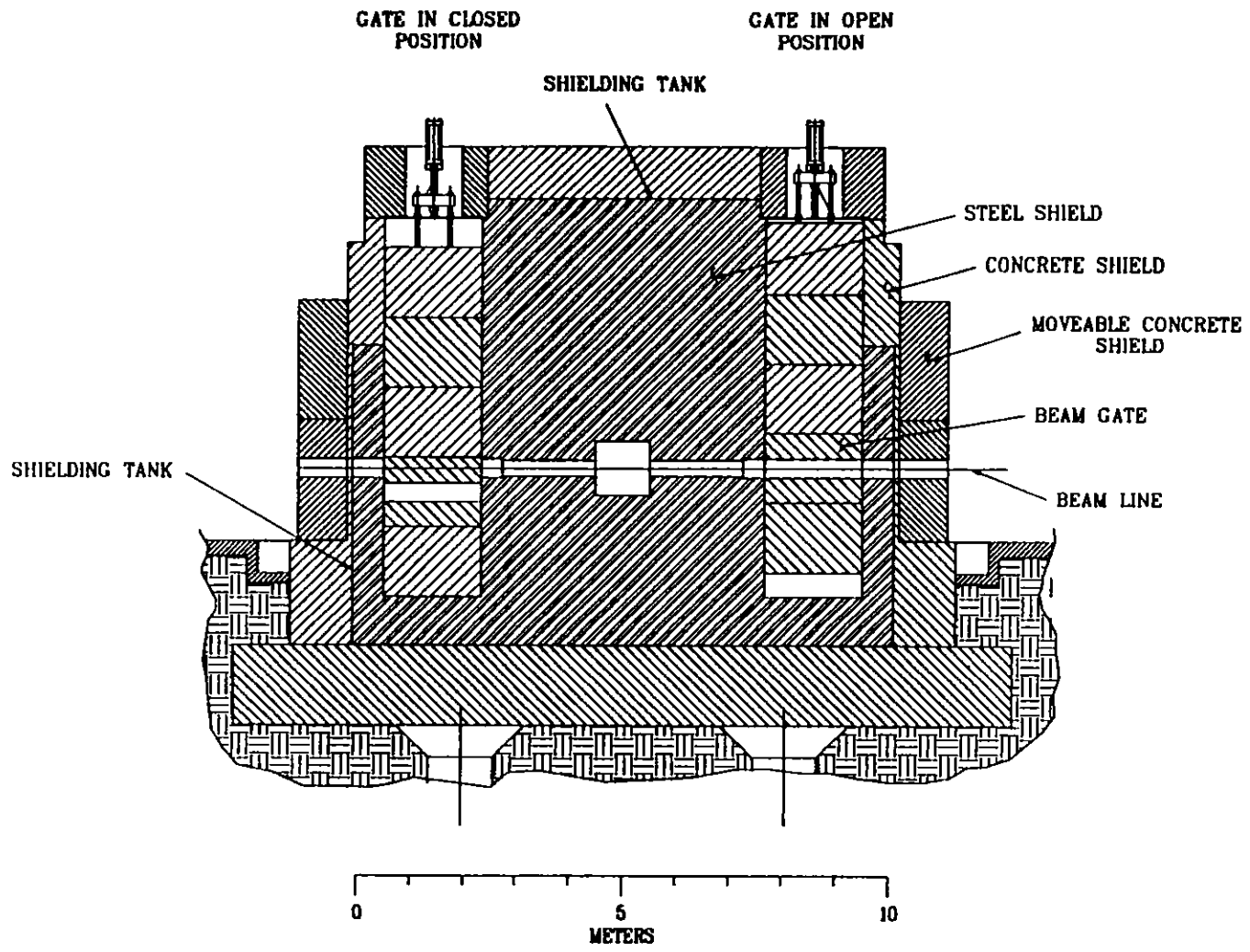
Figure IV.4.1-3 Cross Section through the Biological Shield, Centered on
Neutron Beam Ports B-2 and E-2 of Figure IV.4.1-2.

A target tank housing is located between the target tank and the stacked steel shielding in order to support the weight of the steel shield. This housing is water cooled and is made of 7.6-cm steel plate welded together to conform to the target tank shape within a tolerance of 6 mm. Openings are made in the target tank housing for the neutron beam tubes and for the proton beam tube.

4.1.3 Concrete Shielding

The shield material around the outside of the shielding tank is concrete. At least 1 m of concrete is poured on all sides of the structure, including the top. The slab that supports the structure is at least 2 m thick to provide adequate shielding. Custom-made removable concrete blocks are used in the areas on the shielding tank where the neutron beams exit the structure, as discussed in Section IV.8.

4.1.4 Hot Cell

The hot cell, shown in Figure IV.4.1-2, is a rectangular sealed enclosure having dimensions of approximately 6.1 m × 7.6 m × 10.7 m. It is located at the end of the biological shield and is composed of 2 m thick steel-reinforced concrete. The primary purpose of the hot cell is to provide for safe remote handling and maintenance of the target train. The operation of the hot cell and the assembly and disassembly of the target train are described in Section IV.5.

4.2 SUPPORT STRUCTURE

The large size of the IPNS Upgrade biological shields and their locations inside two existing buildings impose some limitations on the equipment and methods to be used for the installation of the foundation system. The requirements of the facility call for steel piles driven to bedrock some 30 to 33 m below existing grade.

The foundation system is illustrated in Figure IV.4.2-1. The existing concrete floor is saw-cut along the required perimeter and disposed of in an off-site landfill. The underlying material is excavated to the required depth and similarly disposed of. Any facility that is affected by the construction activities is rerouted in order to minimize disruption of those facilities to their users.

The foundation system under the biological shield structure consists of single steel piles on a square grid. The overhead clearance limitations inside the buildings dictate that each pile be driven in segments shorter than the standard mill lengths. Each segment is welded to the preceding one, and the assembly is driven into the ground. The process is repeated until the pile

FOUNDATION PLAN

LONGITUDINAL SECTION A-A THROUGH
BIO-SHIELD FOUNDATION

CROSS-SECTION B-B THROUGH
HOT CELL FOUNDATION
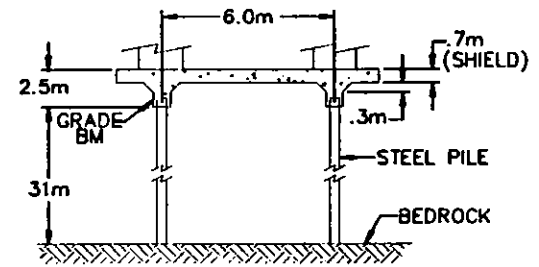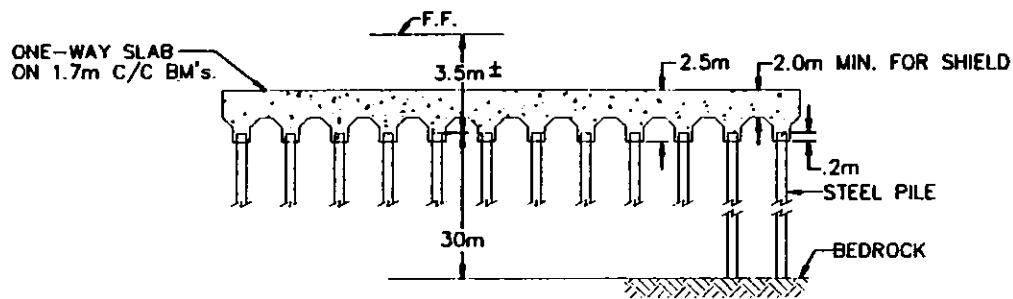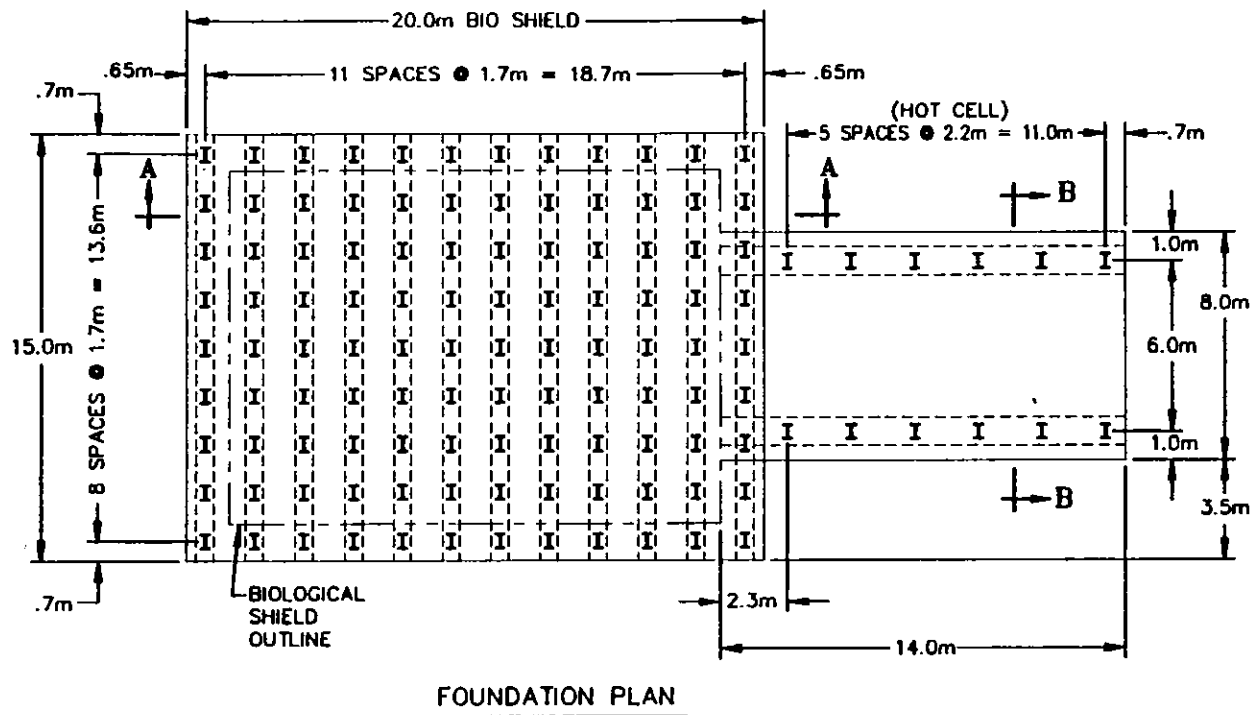
Figure IV.4.2-1 Foundation Plan and Section Views.

tip reaches bedrock, approximately 30 to 33 m below existing grade. The pile tops are then leveled and tied together in rows by cap beams, over which a structural slab is constructed. The slab thickness is 2 m to provide shielding. The load-bearing capacity of this structure is 64,000 kg/m^2, which is well above the loading from the biological shield.

The hot cell foundation is similarly constructed, except that two grids of piles are installed. The hot cell floor slab is tied to the biological shield floor slab structure with keys and shear-reinforcing steel to minimize any differential movement between the two structures. The slab thickness is at least 61 cm to provide shielding.

4.3 SHIELDING EFFECTIVENESS

4.3.1 Design Objectives

The biological shield complies with the design standards contained in Article 128 of DOE/EH-0256T.[1] The design criterion is that the dose for an individual worker is less than 500 mrem/yr (5 mSv/yr) and "As Low As Reasonably Achievable" (ALARA). The major contribution to the dose outside the main shield is expected to be due to neutrons, so the recommended neutron quality factor has been doubled for design purposes. The basis of the shielding design is a dose rate of 250 mrem/yr (2.5 mSv/yr), conservatively augmented to ensure that radiation doses are ALARA. This augmentation accounts for such factors as differences between calculated and measured attenuations, local radiation leakage due to shield penetrations, and potential skyshine contributions at other on-site facilities. Personnel radiation exposures are maintained well below regulatory dose limits and reflect additional conservatism in that workers' exposure represents at maximum about 2000 hours per year.

4.3.2 Shielding Parameters

The shielding achieves the design goal at most accessible points on the outside of the biological shield during normal operations. To achieve a dose rate of 2.5 mSv/yr (250 mrem/yr), the average dose rate is <1.25 μSv/h (<0.125 mrem/h), based on an occupational year of 2000 h. The calculations are based on a 500-μA, 2.2-GeV proton current. Iron shielding, backed up by concrete to attenuate the low-energy-neutron component, is the main shield material. At 90° to the target, the thickness is nominally 6 m, consisting of 5 m of iron and 1 m of concrete.

4.3.3 Shielding Methodology

The shield effectiveness is determined by using the modified Moyer model approximation of Tesch and Zazula.[2] The modified expression is

$$H = \frac{H_0 E_p^{0.8} e^{-d\rho/\lambda}}{r^2},$$ (IV.4.3-1)

where H is the maximum dose equivalent per incident proton of energy E_p (GeV), λ is the attenuation coefficient for neutrons, ρ is the shield density, d is the shield thickness, and r is the transverse distance to the beam. The suggested values for the other parameters for $E_p = 2.2$ GeV with an iron shield and an iron target are $H_0 E_p^{0.8} = 4 \times 10^{-14}$ Sv-m^2/proton (the dose per proton at 1 m) and $\lambda = 180$ g/cm^2. Taking the ratio of total neutron production in tungsten to that in iron as 2.8, the expected dose rate at r = 6.3 m through a lateral iron shield (5.0 m) is then

$$\dot{H}(Fe) = \frac{2.364 \times 10^{11} e^{-d\rho/180}}{r^2} = 19 \ \mu Sv/h \ (1.9 \ mrem/h).$$ (IV.4.3-2)

The iron is backed up by 1 m of concrete to attenuate neutrons of approximately 25 keV and 125 keV that stream through the iron. The 1 m of concrete represents about eight attenuation lengths for the low-energy neutrons and effectively removes this component. The high-energy neutron component is further reduced by the 1 m of concrete according to

$$\dot{H}_{Total} = \dot{H}(Fe) \ e^{-235/107} = 19 \times 0.111 = 2.1 \ \mu Sv/h \ (0.21 \ mrem/h).$$ (IV.4.3-3)

Here, the 107 g/cm^2 is the attenuation coefficient for the high-energy neutron component in concrete. The total dose rate exceeds the design goal of 1.25 μSv/h (0.125 mrem/h), allowing only about 24 hours of access per week at the face of the biological shield in the 90° direction from the beam. This is administratively regulated.

4.4 REFERENCES

1. *Radiological Control Manual*, U.S. Department of Energy Report No. DOE/EH-0256T, rev. 1 (Washington, D.C., April 1994).

2. K. Tesch and J.M. Zazula, "Shielding properties of iron at high energy proton accelerators studied by a Monte Carlo code," Nucl. Instrum. Methods **A300**:179-187 (1991).

5.1 HOT CELL

The target train can be withdrawn from its normal operating position in the target tank into a hot cell for servicing. To facilitate removal, the target train rests on a platform that also supports a stepped steel and concrete shield block. The entire train and shield block assembly moves on wheels between the operating position and the service position. Figure IV.5.1-1 indicates this arrangement, with the target train and shield shown in the operating position.

All of the components of the target-train assembly can be removed for exchange or servicing by means of remote-handling equipment in this hot cell, which is similar to the one in use for the ISIS target station.[1-3] The cell is attached to the downstream end of the biological shield, as shown in Figure IV.4.1-2. Two shielding doors provide an air-lock cavity in line behind the remote-handling cell. The air-lock cavity maintains the desired conditions within the remote-handling cell during transfer operations in and out of the cell. Two viewing ports are provided on opposite sides of the 1.7-m-thick shield walls. These 1-m-square, stepped windows are made of radiation attenuating lead glass, and are located in the same plane as the target-reflector sections. Panning television cameras are used to view all other sections of the remote-handling cell and the air-lock cell. Two remote manipulators, one located in the midplane of each window, have gripping capabilities as well as adapters for various tools such as cutoff saws for in-cell work. A third manipulator is located at the downstream end of the hot cell. This manipulator is used to install eyebolts for hoisting the shield blocks and to move piping sections attached to moderators or target sections into the air-lock or into shielded casks. A fourth manipulator is located in the air-lock cell for transfer of activated components into shielded casks. Two traveling bridge cranes ride on rails along each side of the remote-handling cell.

Access to the hot cell area is accomplished in two steps after appropriate environmental conditions are established. The first step is to open the outer, sliding main door between the hot cell air lock and the experimental area. The second step is to close the main door and open the door between the hot cell area and the air lock. This ensures that the hot cell atmosphere does not mix with the experimental-area atmosphere.

The hot cell is purged by a ventilation and exhaust system. The pressure of the cell is kept slightly below the local barometric pressure in order to assure confinement of the hot cell environment. The atmosphere of the cell is constantly monitored for radioactive contaminants prior to exhausting to the exhaust stack, as described in Section IV.6.

5.2 PLUMBING CONNECTIONS

Figure IV.5.2-1 shows the target train assembly with target, moderators, piping, and ducts through the shield plug. A seal sheet completes the containment enclosure when the target train is in its normal operating position. Just outside this sheet is the plumbing cavity, which allows hands-on servicing of the piping connections. All moderator fluid lines, three of the irradiation tubes, and the reflector water cooling lines pass through the seal sheet into this plumbing cavity.

BIOLOGICAL SHIELD

BASE TRACK

PLAN VIEW

0   1   2   3
METERS

SEAL SHEET

TARGET, MODERATOR,
REFLECTOR ASSEMBLY

PLUMBING
CAVITY

MOTORIZED SHIELD
BLOCK

TIE RODS

CARRIAGE

BASE TRACK

SIDE ELEVATION
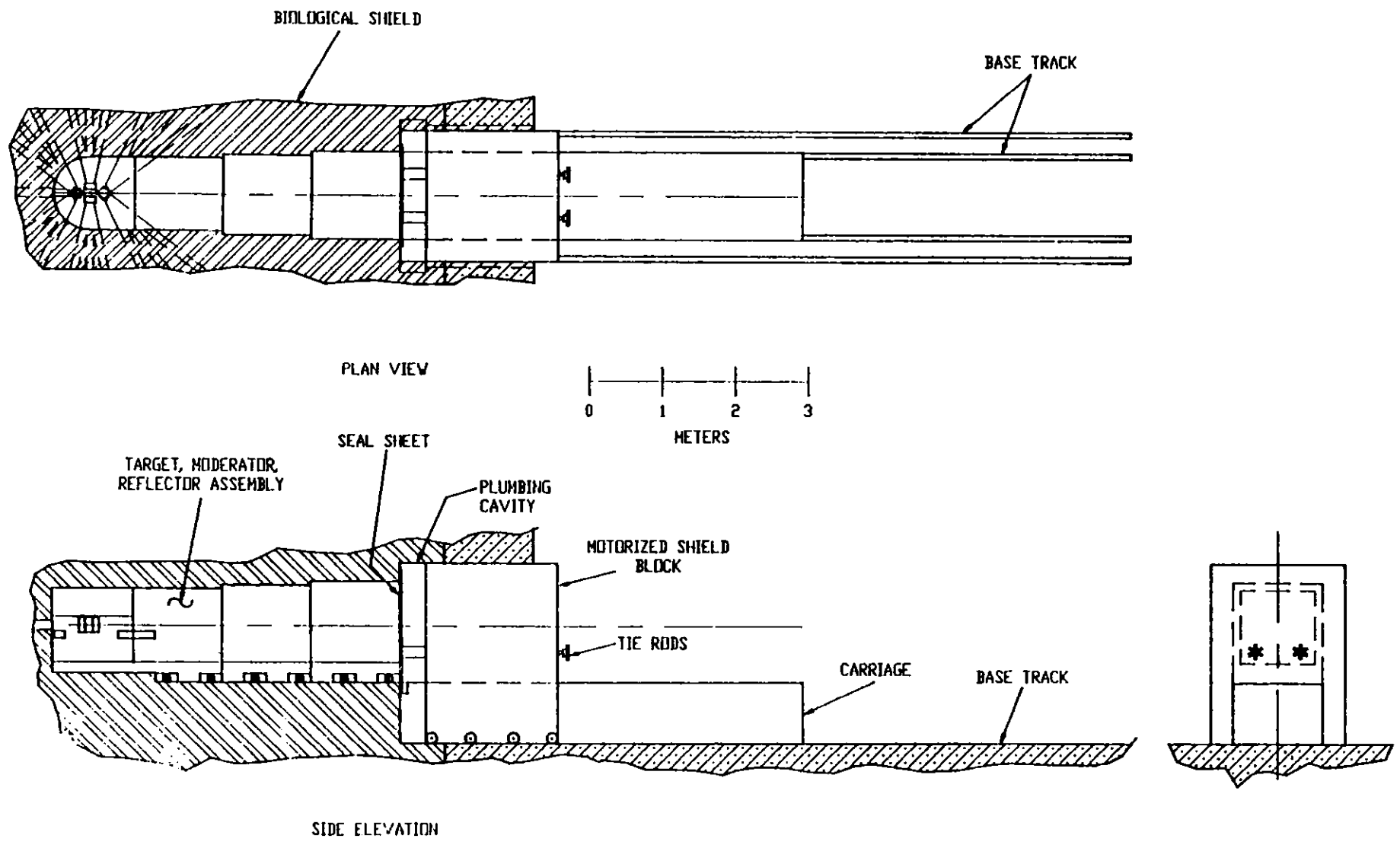
Figure IV.5.1-1 Target-Train Assembly Shown in the Operating Position.

PLUMBING CAVITY

SEAL SHEET

MOTORIZED
SHIELD BLOCK

PLAN VIEW

ELEVATION

ONE METER
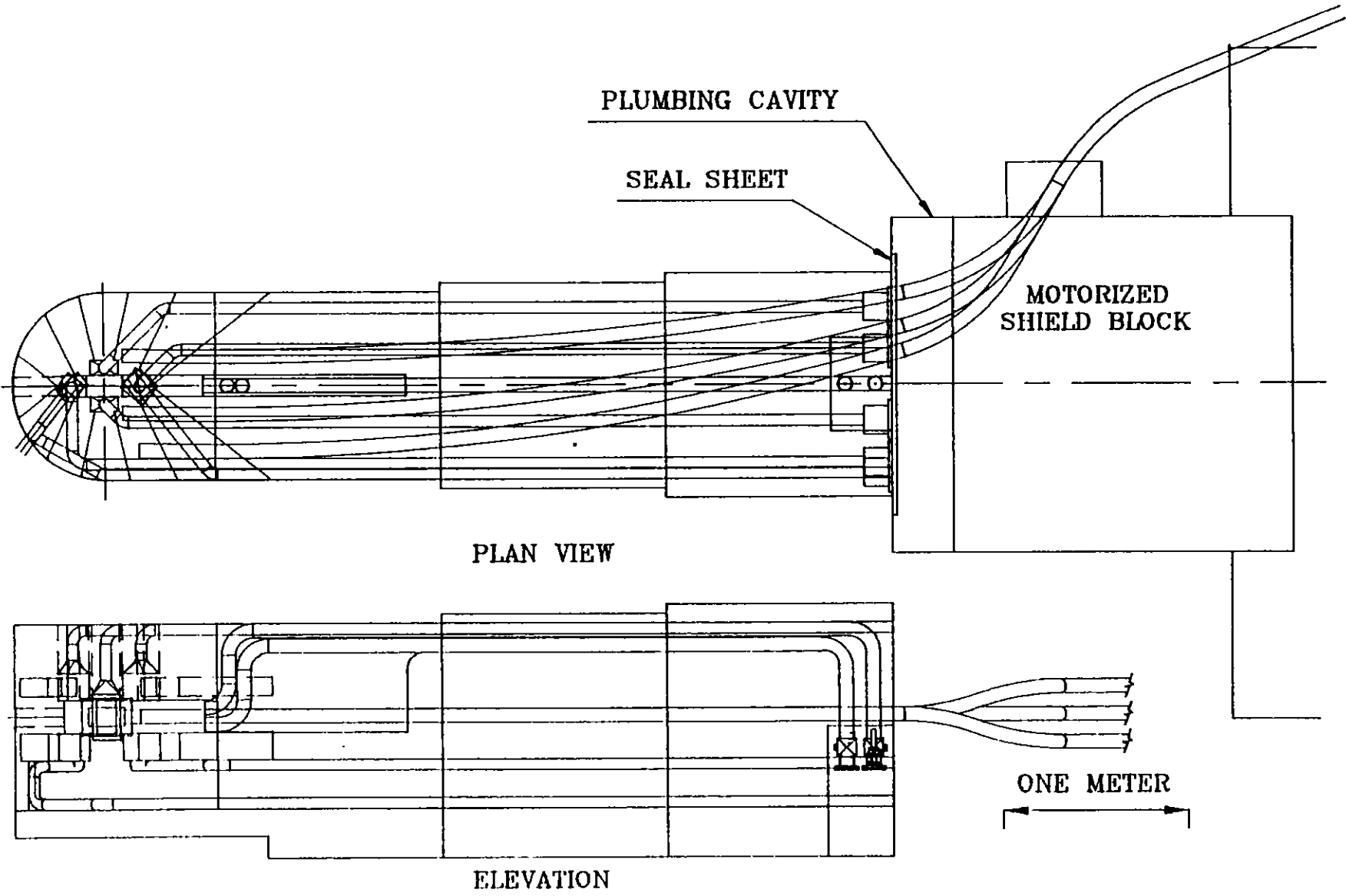
Figure IV.5.2-1 Details of the Target-Train Assembly.

Figure IV.5.2-2 shows the arrangement of the cooling and moderator fluid connections in the plumbing cavity, and Figure IV.5.2-3 shows the seal sheet. Figure IV.5.2-4 shows the arrangement of the target cooling water connections. Figure IV.5.2-5 illustrates a typical junction box, showing the arrangement of the water cooling lines and the bayonet connections for the cryogenic lines.

5.3 TARGET TRAIN REMOVAL AND DISASSEMBLY

The sequence of operations necessary to access the plumbing cavity and manually disconnect lines is shown in Figure IV.5.3-1. The target sections are continuously cooled with flowing water because each can generate up to 5 kW of afterheat power. The plumbing cavity provides the means to manually change over from the main cooling circuits to a small-flow cooling circuit. The latter is mounted on a movable cart and is connected through flexible lines to the target cooling circuits. Small valves are connected by tee-joints to each of the target water coolant lines on the target side of the shutoff valves, as shown in Figure IV.5.2-2. These small valves are connected to the mobile-cart water cooling supply before shutting off the main water coolant supplies and returns. After the main valves are shut, water is drained from the main lines at the field joints on the opposite sides of the shutoff valves before these joints are opened.

An exploded view of the targets, moderators, reflectors, and shield blocks is shown in Figure IV.1.2-6. Following withdrawal of the entire target-train assembly into the remote-handling cell, the target and any of the moderators can be removed individually after the top shield block is dismounted. The lower wing moderators can be withdrawn horizontally. Irradiation tubes can be withdrawn backwards into the hot cell. There is room on the hot cell floor for temporary storage of components alongside the target-train assembly.

5.4 HANDLING OF SPENT COMPONENTS

The target sections remain very radioactive for a long time after irradiation, as shown in Table IV.2.2-6. Irradiated targets are temporarily stored in the hot-cell storage wells, before removal for permanent storage or disposal. The targets will be contained within heavy mobile shielding during transfers out of the cell.

There are eight storage wells in the hot cell, each capable of storing a target before its removal from the cell. The storage wells are fitted with a separate cooling circuit to remove decay heat. The targets are cooled at all times.

Water lines are cut near the target and disposed of in shielded containers. Less shielding is required because the water lines will not be activated to the same high levels.

Moderator containers and associated piping are not highly activated, and can be transferred out of the remote-handling cell in a manner similar to the target water lines.

ONE METER
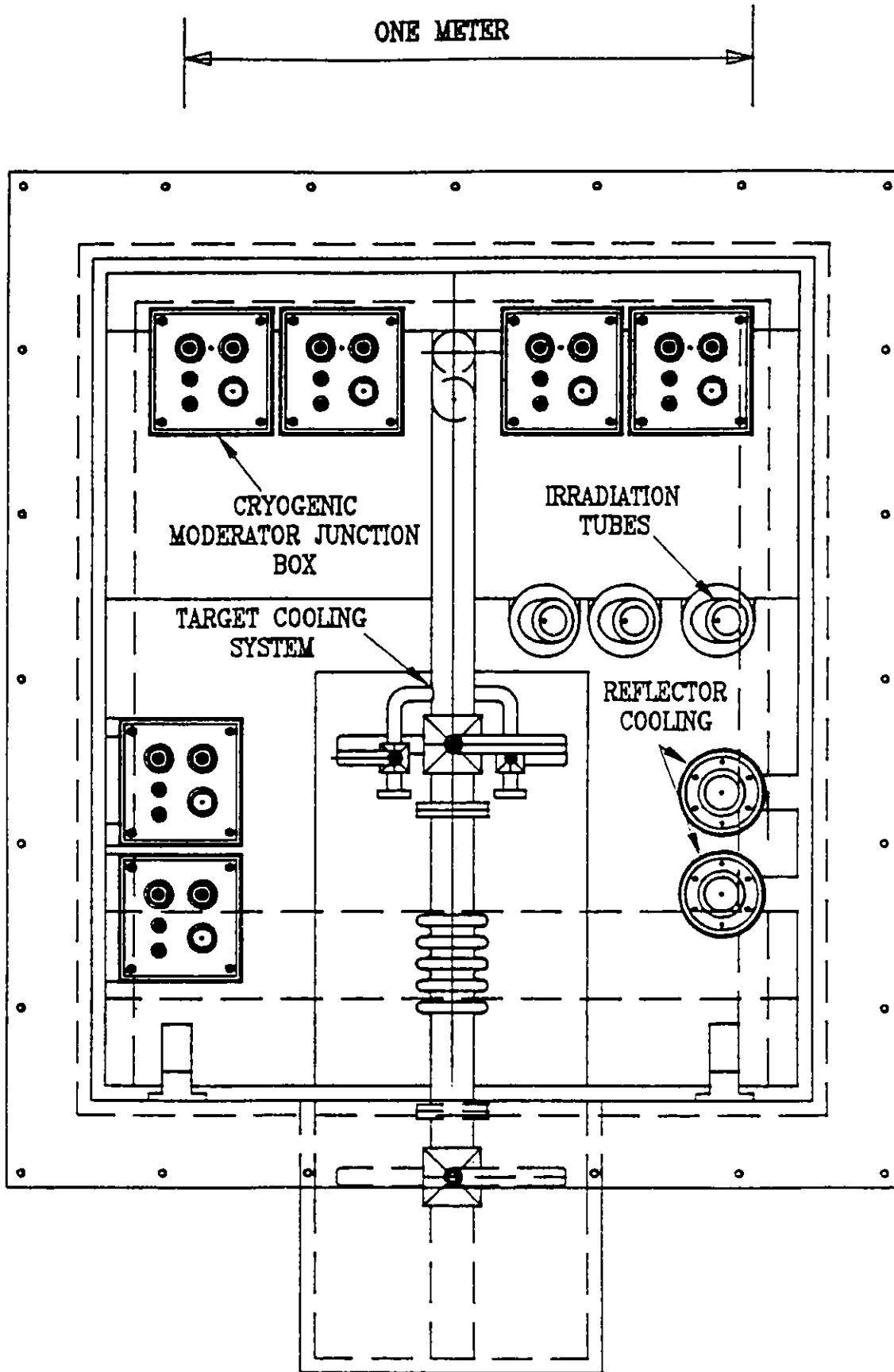
Figure IV.5.2-2 Arrangement of Target-Train Fluid Connections behind the Seal Sheet.
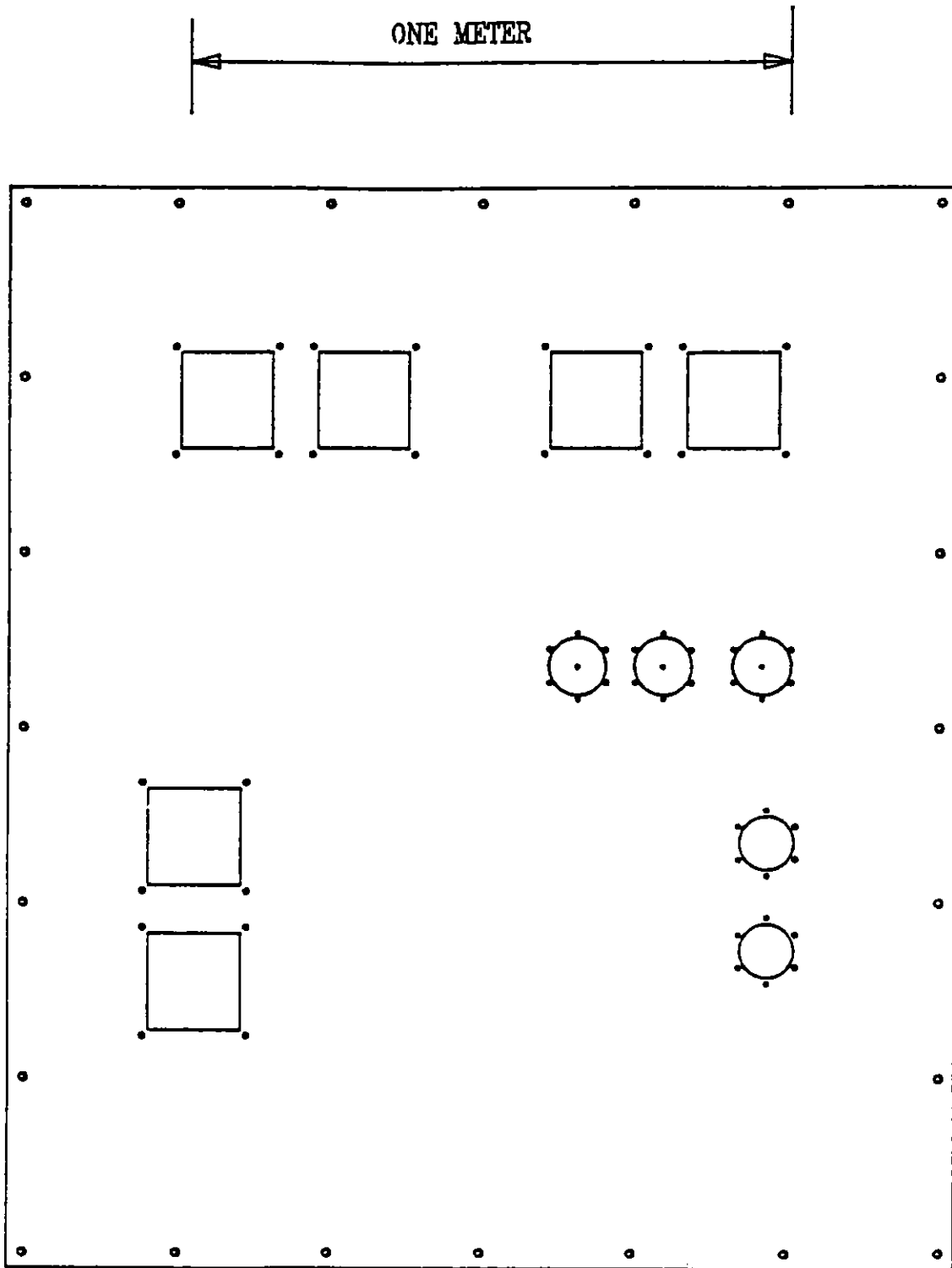
Figure IV.5.2-3 Outside View of the Target Seal Sheet. (Remove seals at each opening to release.)
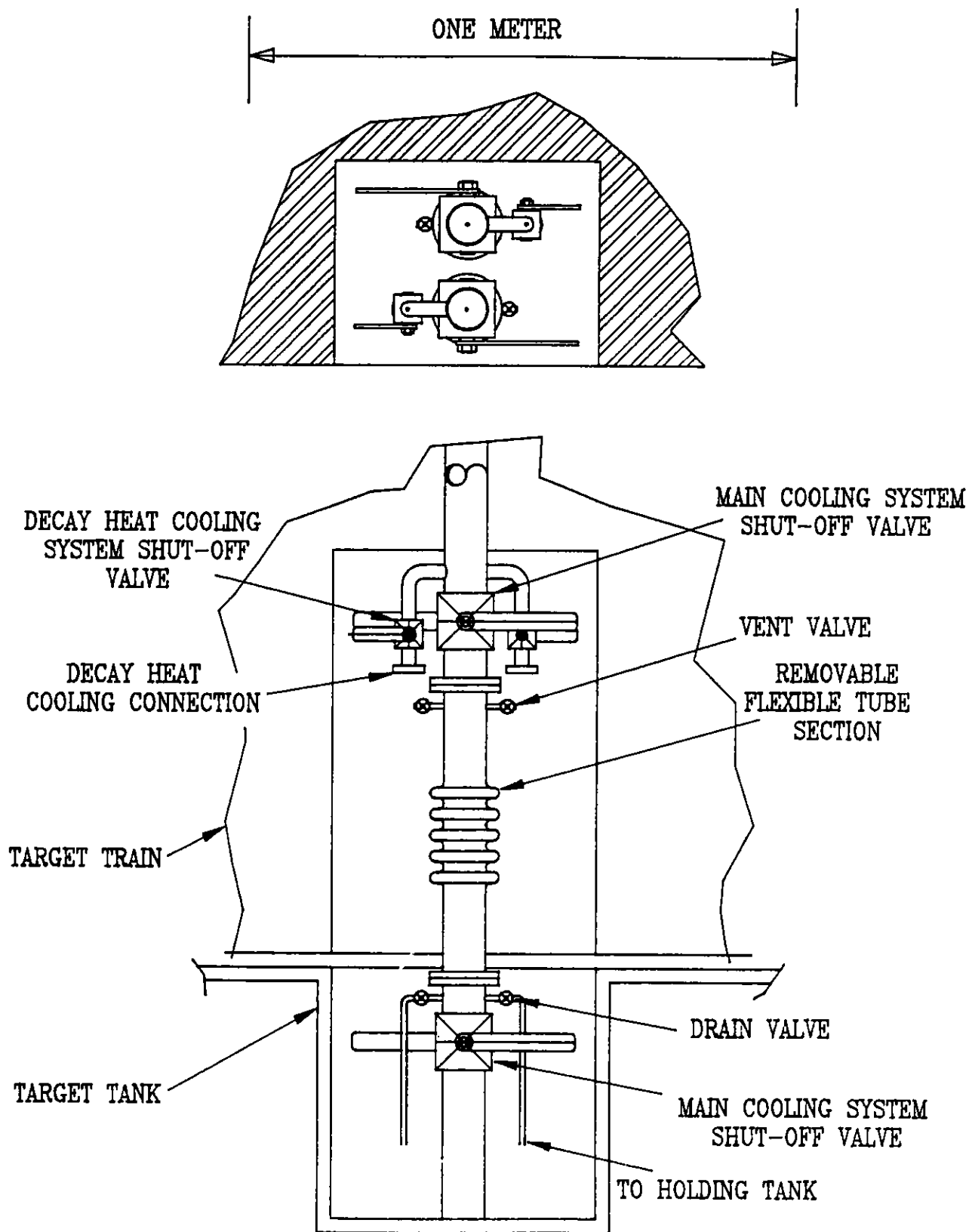
Figure IV.5.2-4 Arrangement of Target Cooling Water Connections behind the Seal Sheet.

TARGET CAVITY
SEAL SHEET

TRANSFER LINE
TO MODERATOR
(ONE PIECE)

CRYOGENIC BAYONETS
SUPPLY AND RETURN

VACUUM PORT

COOLING WATER
SUPPLY AND RETURN

O-RING SEAL

NOTE: NONE OF THE VEE-TYPE
CONNECTING CLAMPS ARE SHOWN
ON ANY OF THE PORTS.

0   10   20

CM
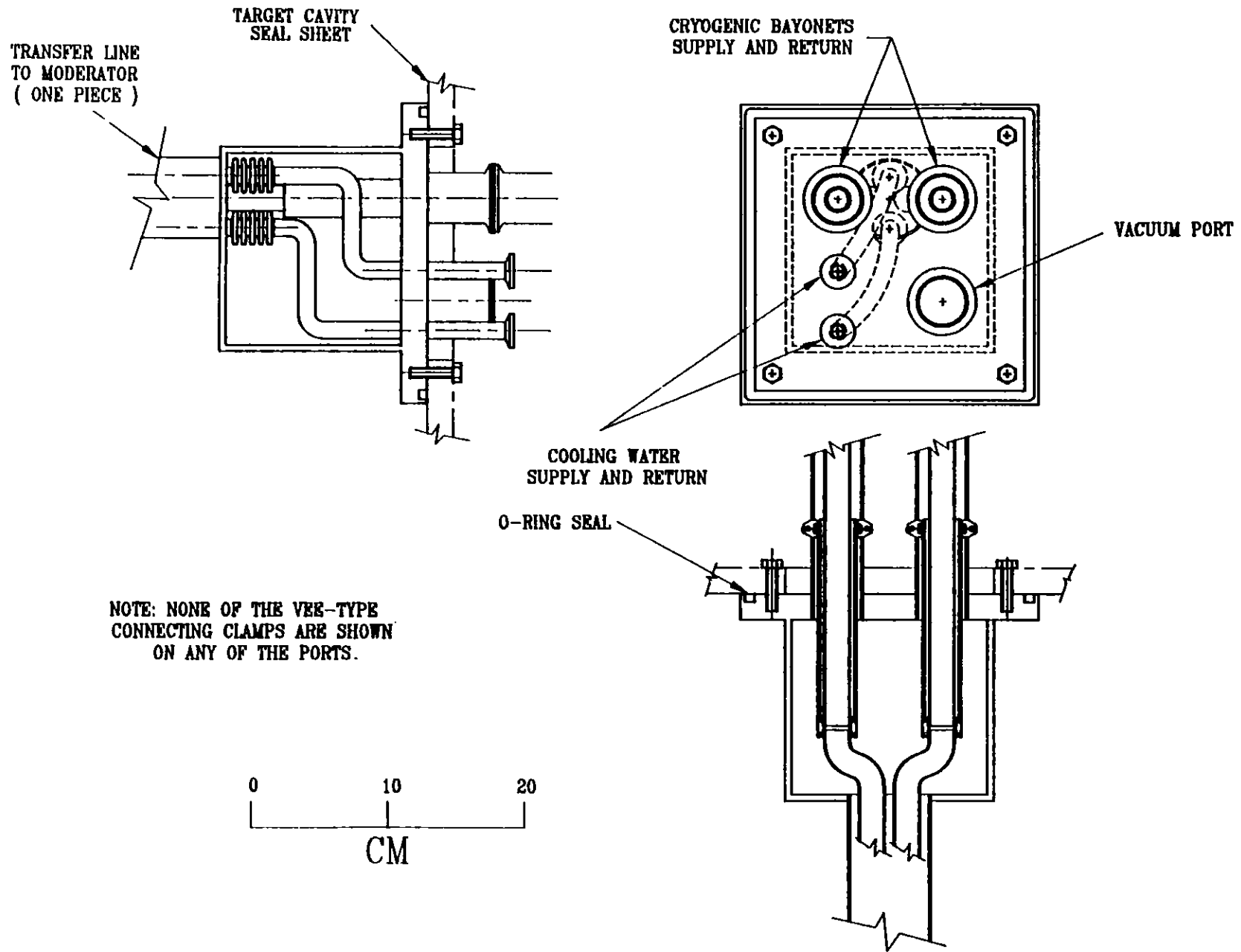
Figure IV.5.2-5 Typical Junction Box for Cryogenic Moderator Fluid Connections.
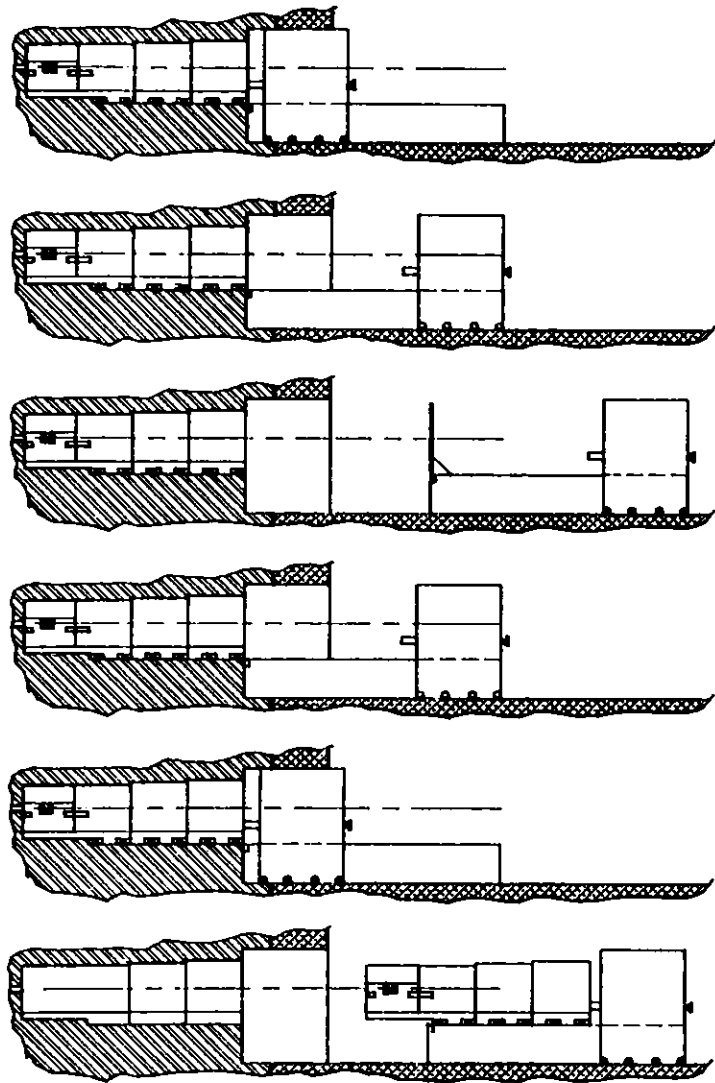
① In normal operation, the carriage is fully to the left and anchored to the base track. The motorized shield is to the left and against the seal sheet.

② The first step in the withdrawal of the system after beam shutdown is to drive the motorized shield block to the right end of the carriage. This allows access to the plumbing cavity and seal sheet. The plumbing jumpers between the seal sheet and the biological shield are removed (hands on). A stabilizing fixture is mounted to the carriage and the seal sheet. The seals between the plumbing and the seal sheet are unfastened. The seal sheet is disconnected from the target tank.

③ The carriage is unlocked from the base track and locked onto the motorized shield block. The motorized shield block is driven to the right with the seal sheet and the carriage attached. The seal sheet and the stabilizing fixture are removed from the carriage by overhead crane.

④ With the carriage still locked to the motorized shield block, the carriage and the shield block are driven to the left. The carriage is anchored to the base track and unlocked from the motorized shield block. The motorized shield block is driven to the right to clear the area. Flexible decay heat cooling lines are attached to the target assembly and flow established. The main target cooling lines are shut off and the removable flexible tube sections are drained and removed.

⑤ The motorized shield block is driven to the left until it contacts the target-moderator-reflector assembly. The tie rods are fastened to the target-moderator- reflector assembly. With the carriage still anchored to the base tracks, the motorized shield block is driven to the right end of the carriage, pulling the target-moderator-reflector assembly onto the carriage.

⑥ The carriage is locked to the motorized shield block and unlocked from the base track. The motorized shield block is driven to the right pulling the carriage and exposing the system.

✳ Left and right refer to the position in the drawing.

Figure IV.5.3-1 Sequence of Operations to Remove the Target-Train Assembly into the Remote-Handling Cell.

The beryllium reflector pieces need to be handled safely for both radioactivity and beryllium toxicity. Radiation levels are not as high as those for the target sections. However, toxicity considerations dictate special handling procedures.

The irradiation tubes are not activated any more than the other piping leading in and out of the target area, and receive the same treatment as the other piping.

ANL does not have provisions for permanent storage of radioactive waste at its Illinois site. However, such facilities are available at Hanford, Washington. Transport of similar radioactive materials between sites is done routinely.

5.5 REFERENCES

1. T.A. Broome and M. Holding, "ISIS target station experience," presented at Argonne National Laboratory (Argonne, Ill., Nov. 23, 1992).

2. B. Boardman, *Spallation Neutron Source: Description of Accelerator and Target*, Rutherford Appleton Laboratory Report No. RL-82-006 (Chilton, U.K., March 1982).

3. B.H. Poulten, "Remote handling equipment for SNS," in *Proceedings of the 6th Meeting of the International Collaboration on Advanced Neutron Sources (ICANS VI)* (Argonne, Ill., June 28-July 2, 1982), Argonne National Laboratory Report No. ANL-82-80, Argonne, Ill., pp. 339-355 (1982).

6.1 CONTAINMENT BARRIERS

Most of the radioactive products produced in the target are contained within the target material. The sealed target container and cooling system, described in Section IV.2, provide additional containment. Two secondary containment barriers, the target tank and the shielding tank are provided within the biological shield to prevent uncontrolled releases.

The moderator and premoderator boxes and associated piping are the primary containment for moderator and premoderator materials and their radioactive by-products. The vacuum jacketing required for insulation serves as an additional containment barrier in the cryogenic moderator systems. The target tank and the shielding tank are additional barriers against uncontrolled release of radioactive by-products.

Figure IV.1.2-7 shows the target tank, which encloses the target-reflector-moderator assembly. This tank is welded of 2.5 cm-thick aluminum sheet. Portions of the target tank are machined thinner to provide windows for the neutrons to exit to the beam ports. The target tank is designed to sustain at least 3.4 kPa of internal pressure and is able to withstand ordinary activities associated with moving heavy equipment. A seal sheet covers the open end of the target tank to complete the containment, as shown in Figure IV.5.2-1.

The target tank contains a helium atmosphere controlled at a positive pressure with respect to the local barometric pressure. This prevents air from entering the tank and avoids production of any of the air-associated activation products. A purge and exhaust ventilation system controls this atmosphere.

The shielding tank encloses the stacked steel portion of the biological shield, as shown in Figures IV.4.1-2 and IV.4.1-3. It is a welded helium-leak-tight container constructed of 2.5-cm-thick carbon steel plate. The shielding tank atmosphere is helium gas maintained at a slight positive pressure with respect to local barometric pressure. A purge and exhaust system controls this atmosphere. The shielding tank is designed to sustain an internal pressure of at least 3.4 kPa, and to withstand ordinary activities associated with moving heavy equipment.

The water cooling systems for the reflector and for the shield have low activity levels. Their plumbing is the primary containment for this activity. Secondary containment for the reflector system is provided by both the target tank and the shielding tank. The shield cooling water has much lower activity levels, and the shielding tank and shield cooling plumbing system provide adequate barriers against uncontrolled release of any of this activity.

All of these separate containment spaces, as well as the space inside the hot cell, have separate gas exhaust systems, discussed in Section IV.6.2. These feed into gas holdup tanks and a common HEPA filter and stack system, as discussed in Sections IV.6.3 and IV.6.4. Each of these spaces has a drain and retention system for containment of any liquids, as discussed in Section IV.6.5.

6.2 GAS EXHAUST SYSTEMS

6.2.1 Target Coolant Gases

Figure IV.6.2-1 shows the exhaust system that handles the radioactive gases from the target cooling system. This same system also handles all gas exhausts discussed below, except those from the cryogenic moderators. Two methods are used to remove the oxygen, hydrogen and other radiolysis products generated in the target cooling water. The first method employs a heated catalyst pack, which recombines most of the hydrogen and oxygen in the water supply tank ullage space to form water. The resulting water condenses and remains within the tank. A continuous helium-gas purge of the ullage space removes the remaining gaseous products. The continuous helium bleed replenishes the ullage volume with clean gas within a time period of several hours. The purge gas is stored in a holdup tank where radioactive gaseous products are allowed to decay to safe levels before they are released through an exhaust system, as discussed in Section IV.6.3. HEPA filters capture particulate matter in the exhaust system, and the effluent is exhausted to atmosphere through a monitored stack.

6.2.2 Moderator Gases

The water premoderator and moderator radiolysis products are contained within the closed-circuit cooling system. The radiolysis products are handled with the other coolant gases, as discussed in Section IV.6.2.3.

The liquid hydrogen and liquid methane moderators must be periodically emptied and disconnected from their flow systems. The highly-flammable liquids are vaporized and the resulting gases are warmed to near-ambient temperatures. These gases are routed to separate holdup tanks, as discussed in Section IV.6.3. After sufficient decay time the gases are mixed with air so that the effluent mixture is nonflammable. This diluted mixture is exhausted to the atmosphere through HEPA filters and through a monitored stack.

6.2.3 Shield, Reflector, and Other Coolant Gases

The beryllium reflector system is separate to preclude beryllium contamination in the other cooling systems. This also permits the use of heavy water (D_2O) for cooling, if desired. The shield cooling system is a buffered-water system, and is separate from the other water cooling systems. Radiolysis gases are produced at significantly lower rates in the reflector and shield than in the target cooling system. Consequently, a smaller helium purge into the ullage space of each supply tank sweeps the oxygen, hydrogen, and activation products away with the helium exhaust. The helium flow dilutes the oxygen and hydrogen gas mixture to a composition that is below combustion and detonation limits. These two gas streams are emptied into

TO HEPA FILTERS AND STACK

2-WAY TANK
SELECTOR EXHAUST
VALVE

GAS
HOLDUP
TANK 1

11000 L
100 kPa
WORKING
210 kPa
DESIGN
HOLDUP TIME
30 MIN

2-WAY TANK
SELECTOR EXHAUST
VALVE

GAS
HOLDUP
TANK 2

11000 L
100 kPa
WORKING
210 kPa
DESIGN
HOLDUP TIME
30 MIN

TARGET TRAIN CAVITY PURGE

SHIELDING PURGE

WATER SUPPLY TANK
ULLAGE PURGE, 6 SYSTEMS

SYSTEM VENTS
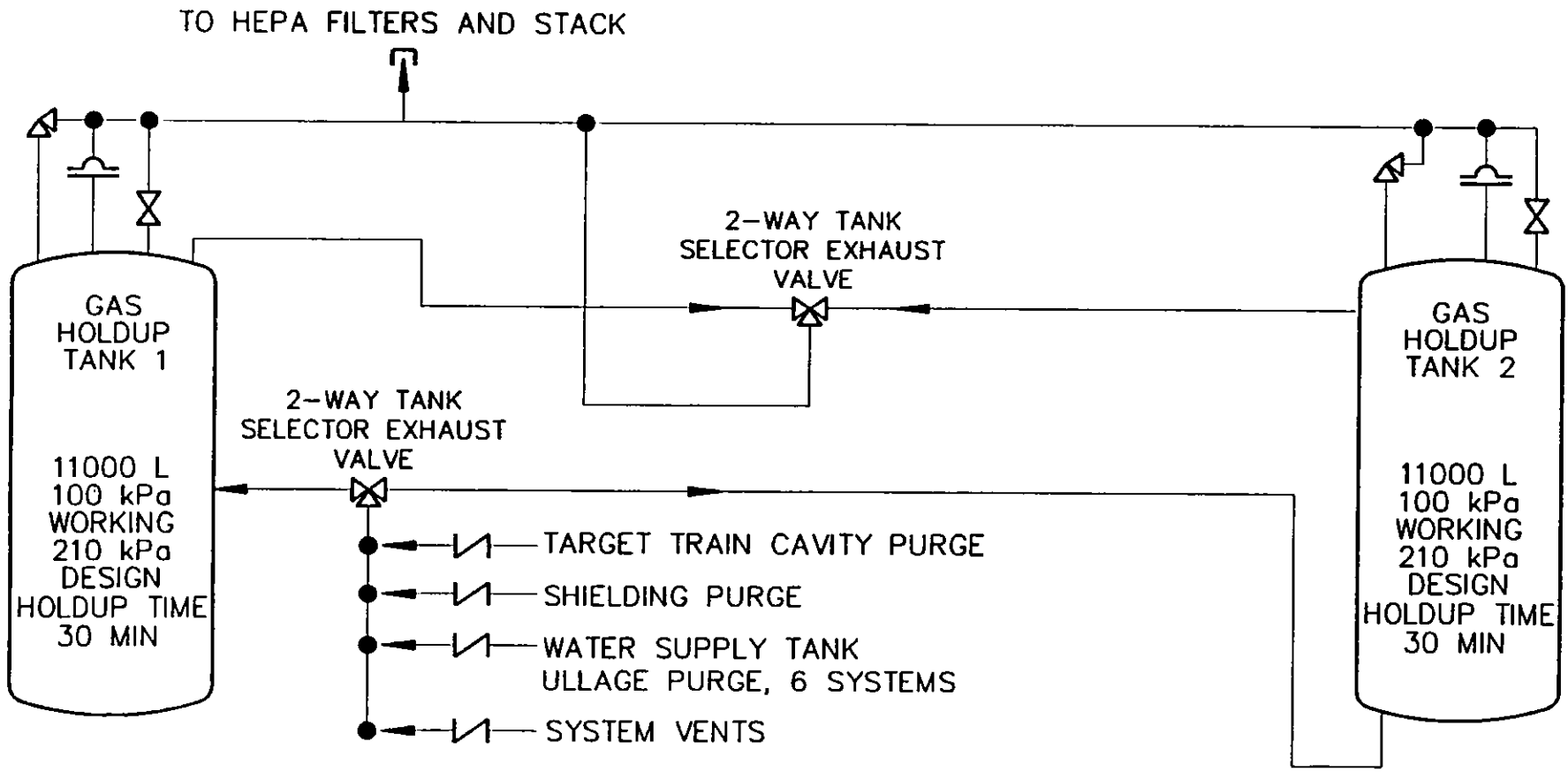
Figure IV.6.2-1 Common Holdup and Exhaust System Used for Most Gaseous Exhausts.

the holdup tank to allow sufficient decay time for activation products, before being exhausted to atmosphere through HEPA filters and a monitored stack. This same design is used for the exhausts from the target tank cooling system and the proton HET line window cooling system.

6.2.4 Neutron Beamline Exhaust

The neutron beamlines that are not evacuated contain helium gas. The flowing helium purge-gas streams and the exhaust gases from the vacuum pumping systems are held for a period of time so that any radioactivity decays to a safe level. The common holdup tank system is used for this purpose.

6.2.5 Irradiation Tube Exhaust

The three horizontal irradiation tubes within the reflector and the fourth, vertical, irradiation tube are gas-cooled. The gases contained within the irradiation tubes are recirculated to prevent the spread of radioactive species. During operation, a hermetically sealed blower located outside the biological shield circulates gas to the ends of each tube, past the irradiation capsule, and back through the piping to a heat exchanger. Gases are exhausted from the tubes only when irradiation capsules are removed from the system. At these times, the gases are exhausted through the common holdup tank, HEPA filters, and the monitored stack. Gases from vents and pressure-relief safety valves are also exhausted through the common holdup tank, HEPA filters, and monitored stack.

6.2.6 Purge and Exhaust Systems for Target Tank, Shielding Tank, and Hot Cell

The purging systems for the target tank and the shielding tank consist of ventilation and exhaust systems as shown in Figure IV.6.2-2. Each space is continuously purged with at least 16 standard cm^3/sec of helium gas, at a slight positive pressure. Each of these volumes has a separate supply and exhaust system. Two regulators operate in series to decrease the pressure to the level required. Appropriate pressure-relief devices prevent over-pressurization.

A volumetric pump employing differential pressure-control devices pressurizes the gases from the purged regions up to 100 kPa. The gases then flow to a common manifold and into the holdup tank which ensures an appropriate hold time prior to being exhausted to the atmosphere. These gases are continuously monitored for combustibles, such as hydrogen and methane.

The hot cell is maintained at a slight negative pressure to ensure that no leakage takes place from the cell into the target tank, shielding tank, or experiment area. Air through an inlet HEPA filter constantly purges the hot cell. Exiting gases from the hot cell purge system pass
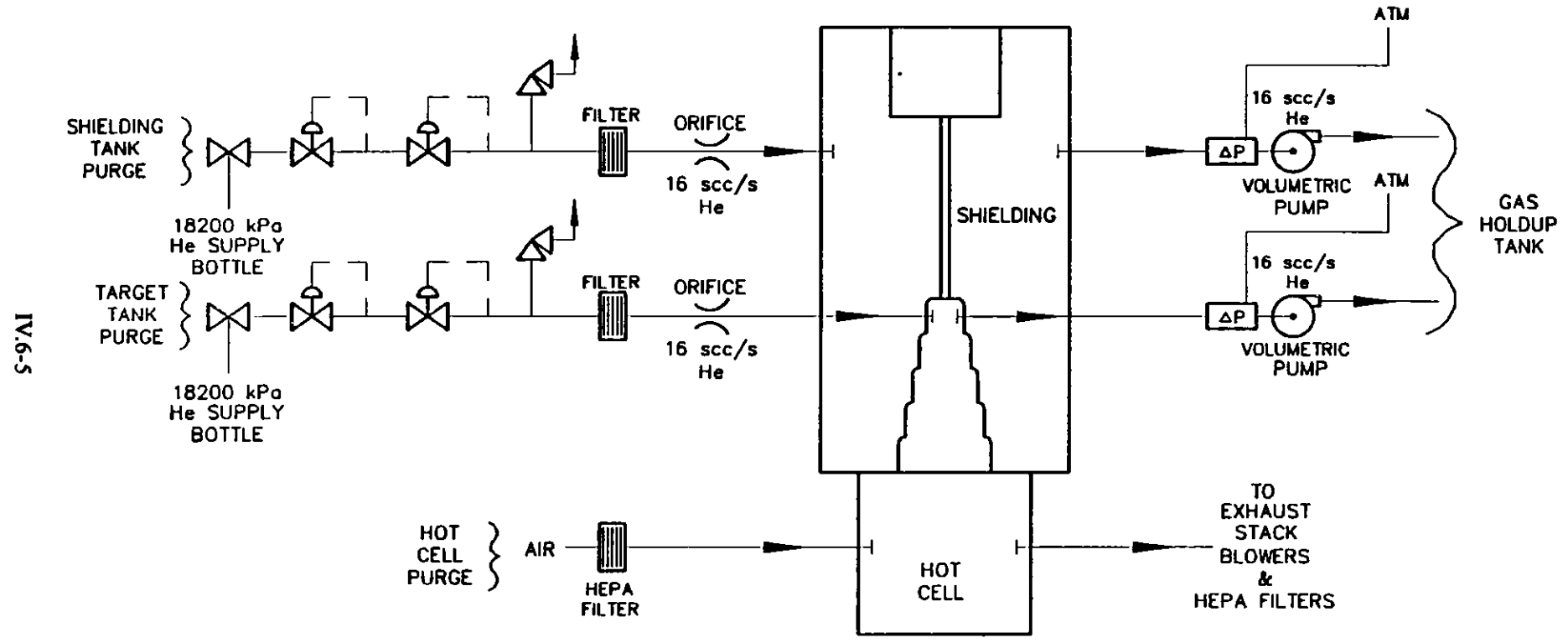
Figure IV.6.2-2 Purge System for Target Tank, Shielding Tank, and Hot Cell.

directly to the local building HEPA filter, exhaust blowers, and radiation-monitored exhaust stack system. The exhaust blower has 0.7 m³/sec capacity. The exhaust stack is a 46-cm-diameter stainless-steel single-wall stack, which is supported by the exterior building wall. The stack wall thickness is 1.22 mm. The stack exhausts about five meters above the highest point of the building roof. Lightning protection for the stack is tied into the existing building lightning protection system.

Exhaust stacks are located on the south wall of Building 370 and on the east wall of Building 369.

6.3 GAS HOLDUP TANKS

As shown in Figure IV.6.2-1, exhaust gases from the target cooling system, the water moderator and premoderator cooling systems, the reflector cooling system, the shield cooling system, the biological shield purge, the neutron irradiation facilities, and the target area purge are retained in one of two holdup tanks to allow decay of radioactivity. Two 11,000-L tanks are used. One tank accumulates suspect gases, while the other tank statically holds gas for radioactive decay to safe levels. Each holdup tank is sized to hold a fast dump of all ullage gas in the target water supply tank, in addition to all of the purge gases from the various sources, for a time interval sufficient for adequate decay in the other tank. The exhaust-gas sources are connected to manifolds on the two holdup tanks by means of three-way valves which operate in unison. Each gas source is always connected to one of the holdup tanks. Each holdup tank has appropriate pressure-relief valves and a burst diaphragm to protect against over-pressurization. The effluents from relief valves and the vents are ducted through HEPA filters to the monitored stack.

Two additional 2,000-L tanks hold the hydrogen and methane moderator gases to permit decay of any radioactive products. These tanks are located in the shielded moderator components areas and are not interconnected. Each is dedicated to one of the two gases. Each tank is rated for service from vacuum to 180 kPa pressure at ambient temperature. Safety relief and vent valves are provided. Vacuum pumps provide for initial evacuation.

The two 11,000-L gas holdup tanks for the 30-Hz target system are in an underground vault located between Building 371 and Building 370. An underground vault located between Building 367 and Building 369 houses the two 11,000-L gas holdup tanks for the 10-Hz target system.

6.4 HIGH-EFFICIENCY PARTICULATE AIR FILTERING

None of the IPNS Upgrade buildings is designed as a containment building. The target systems, the remote-handling facilities, and hoods for work with radioactive materials require ventilation. Exhaust from these systems passes through HEPA filters before release to the environment.

HEPA filtration assemblies precede all blowers that direct exhaust gases to the two target station stacks. All HEPA filtration assemblies include prefilters, testing provisions, and redundancy if required. They meet all required U.S. Department of Energy (DOE), federal, and state requirements.

The suspect exhaust ventilation systems in Buildings 369 and 370 consist of a series of ducts from the sources of possibly radioactive or chemically active gases described in this section to a single, airtight main exhaust duct header. Each system header carries the gases to a plenum manifold and from there, through a HEPA filter. A centrifugal vane blower exhausts this gas through a 45-cm-diameter exhaust stack, where the gases pass a stack radiation monitor before being exhausted to the outside atmosphere. Exhausts from pressurized areas have manual isolation valves. Two HEPA filter-blower combinations are installed in parallel on each main suspect exhaust system. One HEPA filter-blower combination operates and the other is in a standby condition. This standby unit starts automatically if the operating blower fails for any reason. Check dampers prevent back-flow through the standby blower. A pressure alarm sensor supplied from an independent power source reduces the likelihood of total system failure when power-source failures occur. Both blowers are connected to the area emergency power source. A tee in the blower suction line is equipped with a pressure control damper to mix outdoor air with the suspect exhaust stream to maintain a constant stack exit velocity. The stack terminates approximately 18 m above grade. A radiation monitor system installed in the stack provides a warning of any release of gaseous radioactive material to the ventilation system, as described in Section IV.7.1.1.

Each fan and filter in the ventilation system is designed to handle the gas flows independently under the worst credible emergency conditions.

Independent auxiliary ventilation exhaust systems, each with a separate HEPA filter and blower fan, are connected to the main exhaust stack to provide general ventilation and maintenance connections and serve hoods in Buildings 368, 369, and 370.

6.5 LIQUID DRAIN AND RETENTION-TANK SYSTEM

Each target station and associated remote-handling hot cell has its own drain system and retention tanks for suspect radioactive waste. This radioactive waste drain system collects liquid waste from points within the biological shield and remote-handling cell. It carries them by gravity to the main retention tank. Suspect wastes are characterized periodically and disposed of in a manner consistent with the hazard level, according to Laboratory procedures. The 16,000-L retention tank for the 10-Hz target system is located in the underground concrete vault between Building 367 and Building 369, as shown in Figure IV.6.5-1. The underground concrete vault near Building 370 houses the 16,000-L retention tank for the 30-Hz target system. The main retention tank, drainage headers, and the drainage system of the remote-handling cell are vented to the vault ventilation system and out each vault stack. The 16,000-L volume of the main retention tank represents approximately 125% of the total liquid inventory of a target station.

EXISTING CRANE

EXHAUST STACK

EXISTING BUILDING 367

REMOVABLE REINFORCED
CONCRETE PANELS

SHIELDED COOLING
SYSTEM AREA

U/G SHIELDED
VAULT

RETENTION TANK

UNDERGROUND TUNNEL

0 1 2 3 4 5 6 7 8 9 10 METERS

0 5 10 15 20 25 30 FEET
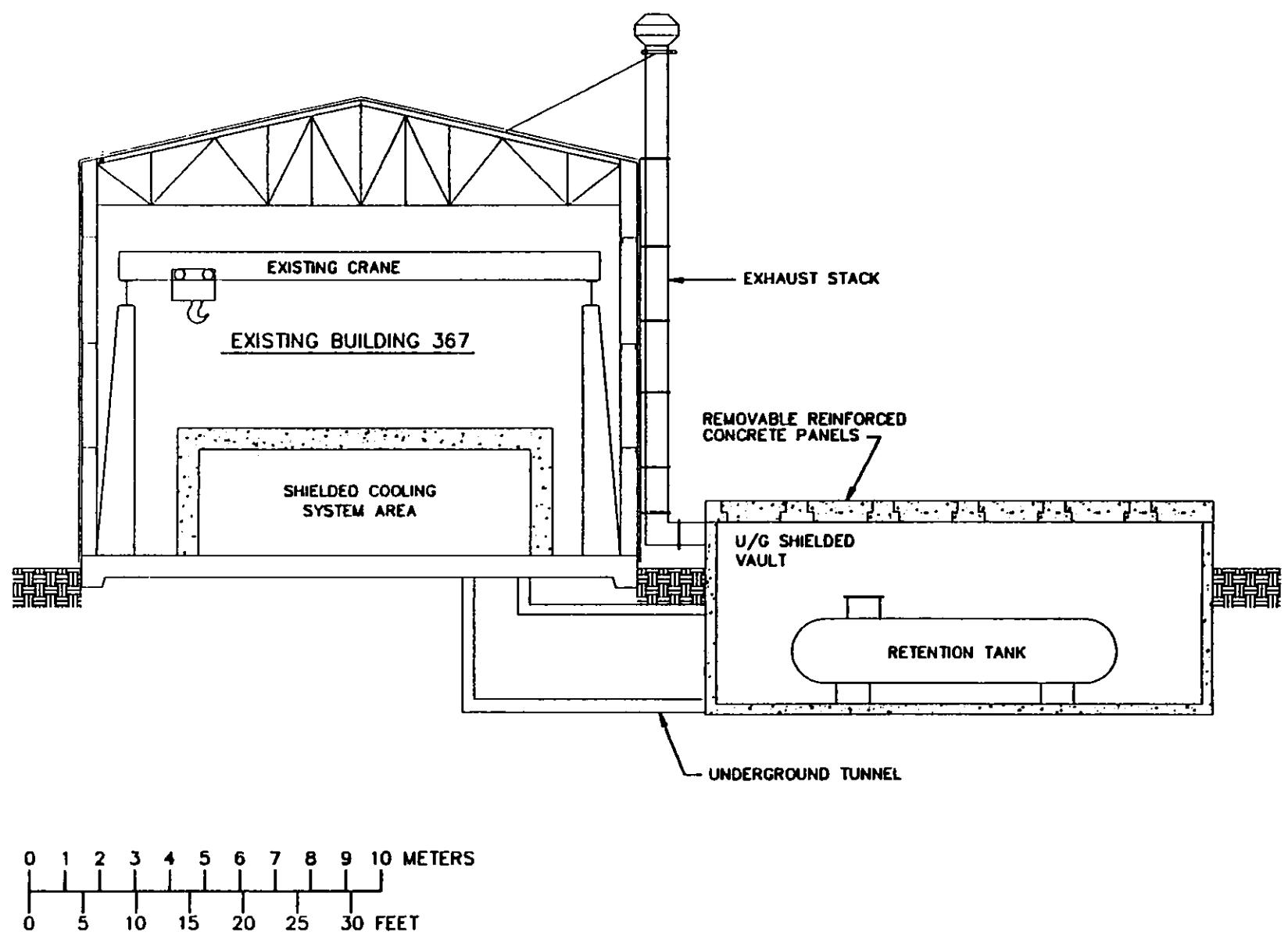
Figure IV.6.5-1 Radioactive Waste Retention Tank for the 10-Hz Target Station, Located in the Vault near Building 367.

A separate drainage system and 400-L retention tank, sealed from the main drainage system by a remotely operated valve, serves each target tank and biological shielding tank system. This isolates the various gas spaces in each target station. Administrative control governs the opening of these valves.

All drainage systems use double-walled piping, and the vault floors and walls are sealed. These features provide an additional containment barrier for the liquid waste systems.

All tanks for suspect waste have redundant level sensors. These sensors alarm and shut down appropriate systems on a high-level alarm and bring into operation administrative procedures to handle accumulated suspect liquid waste.

The suspect waste drainage and retention system is primarily constructed of stainless steel, but it also uses other components compatible with the target station liquids are also used. The systems are of welded construction and are periodically leak-tested.

6.6 RADIOACTIVE EFFLUENTS

6.6.1 Gaseous Effluents

All airborne activity ends up in the ventilation system, where the particulate matter is captured by HEPA filters. The effluents are monitored for radioactivity before release to the atmosphere.

Spallation of air within the target station is predicted not to be a significant source of radioactive gaseous effluents.

The water spallation products C^{10} (19-second half life), O^{14} (70-second half life), O^{15} (2-minute half life) and N^{16} (7-second half life) also do not contribute significantly to the radioactive gaseous effluent. These isotopes are short-lived and are minimized by the exhaust-line delay systems. The radioactive gaseous or airborne particulate products of significance are Ar^{41}, H^3, Be^7, and C^{11}. The Ar^{41} (1.8-hour half life) is produced via thermal neutron capture by Ar in any air in the controlled atmospheres of the target station . The H^3, Be^7, and C^{11} are water spallation products that are vented from the target cooling water system. The half lives of these isotopes are 12 years for H^3, 53 days for Be^7, and 20 minutes for C^{11}. The half lives of both H^3 and Be^7 are long enough that they will build up continually.

A simple model was used to estimate the radioactive gaseous effluents from the 1-MW IPNS Upgrade target. The present IPNS enriched target effluent isotope quantities were taken as a benchmark. Since the power of the 1-MW IPNS Upgrade is a factor of 25 higher than the IPNS enriched target, all significant effluent radionuclides were multiplied by 25 and compared with the regulatory limits. In the case of the IPNS enriched target, the conversion of released activity to doses at the nearest ANL site boundary was done by using the AIRDOS-EPA/RADRISK Model

and taking into account the annual probabilities of wind speed, wind direction, and wind stability class. Total doses for the effluent isotopes of H^3, Be^7, C^{11}, and Ar^{41} were calculated and are listed in Table IV.6.6-1 for the 1-MW target station. The continuous-year-operations quantities are multiplied by 0.66 to account for normal downtime.

Title 40 of the Code of Federal Regulations, Part 61, subpart H, establishes standards for radioactive emissions from DOE facilities. The regulation limits radionuclide emissions based on an effective dose equivalent to the maximally exposed individual to 0.1 mSv/yr (10 mrem/yr).

Table IV.6.6-1 shows that the predicted doses at IPNS Upgrade are less than the 10 mrem/yr radiation protection standards as given in DOE Order 5400.5, which follows the standards of 40 CFR 61, subpart H.

6.6.2 Target Cooling Water System Tritium Level

The present IPNS enriched target cooling water system H^3 concentration is estimated to be 0.056 μCi/cm^3 after five years of continuous operation.[1] The IPNS Upgrade target power will be 25 times greater than the IPNS enriched target. Multiplication by this factor of 25 results in a predicted target cooling water H^3 inventory of 1.4 μCi/cm^3 after five years.

The water H^3 level is of concern during cooling water system maintenance and when it exceeds the level that can be safely released as liquid to the environment. Personnel protective gear and procedures make these predicted H^3 water levels workable. The liquid to be disposed of is treated as radioactive liquid waste and handled according to Laboratory procedures.

6.6.3 Cooling Water System Piping Dose Rates

Operational data from the ISIS facility indicate that dose rates near pipework at ISIS reach levels as high as 0.5 mSv/h (50 mrem/h).[2] Much of this is due to Be^7, which plates out on the inside of the pipes. IPNS Upgrade operates at a power six times greater than ISIS. This scaling factor of six predicts a dose rate around some pipework as high as 3 mSv/h (300 mrem/h) for IPNS Upgrade. This dose rate causes problems for some maintenance and requires the use of extra shielding. This dose rate is greatly reduced by the addition of full flow filters and ion exchange columns and by carrying out periodic chemical pipe-flush operations.

Table IV.6.6-1 Annual Predicted Dose from 1-MW IPNS
Upgrade to an Individual at the Nearest ANL Site Boundary

Radionuclide	Immersion (mrem)	Inhalation (mrem)	Ingestion (mrem)
H^3	<0.025	<0.025	<0.025
Be^7	<0.025	<0.025	<0.025
C^{11}	10.95	0.975	<0.025
Ar^{41}	<0.75	<0.75	<0.75
Total	<11.75	<1.78	<0.825
	x 0.66	x 0.66	x 0.66
	7.75	1.17	0.54

6.7 REFERENCES

1. A.W. Schulke, Jr., A.V. Rauchas, A.E. Knox, J.L. Bailey, and T.R. Clayton, *Final Safety Analysis Report (FSAR-II) for the Intense Pulsed Neutron Source Facility for Operation with the Enriched Uranium Booster Target*, Argonne National Laboratory (March 1991).

2. T.A. Broome, Rutherford Appleton Laboratory, Chilton, U.K., May 1994 (private communication).

7.1 PERSONNEL AND FACILITY PROTECTION SYSTEMS

7.1.1 Overview

IPNS Upgrade has a personnel protection system and a facility protection system, both of which are separate from the control system and employ redundant logic channels that provide independent means of inhibiting proton beam generation. The facility protection system receives inputs from all areas of the accelerator and target stations and initiates a proton beam shutdown upon detection of any out-of-limit conditions, for the purpose of component protection. As the primary safety system that ensures radiation containment boundaries, the facility protection system is important to public safety.

The personnel protection system shares some of the same shutdown devices, but otherwise is not associated with the facility protection system. The personnel protection system ensures that facility personnel are not exposed to unacceptable levels of radiation, high voltages, temperature extremes, pressure extremes, etc. This is accomplished primarily by shutting down the proton beam and closing neutron beam gates if personnel attempt to enter dangerous areas or if dangerous conditions develop.

This section discusses the target station and experimental area components interfaced to the facility protection and personnel protection systems. Interfacing of the accelerator to these protection systems is discussed in Chapter II.

7.1.2 Facility Shutdown Interface

Selected target systems must be in the beam permissive condition for proton beam generation and acceleration to be allowed. Similarly, the personnel protection system associated with the target station and its scattering instruments collects signals from various systems important to personnel protection, such as access gate switches, ventilation systems that provide confinement, and excess radiation monitors. It is required that all these systems be in the proton beam permissive condition for operation. Additionally, many of the personnel protection trip signals command neutron beam gate closures. All sensing signals are carried by dedicated wires carrying a fixed current (current loops). Open and short circuit and random signal protection is provided for all of these wires. Fail-safe outputs are provided by the individual systems, such that the outputs have to be energized to permit proton beam operation or keep neutron gates open. The shutdown time delay depends on the initiating device and the reason for shutdown, but it is less than a second in all cases for the proton beam and less than 30 seconds for a neutron beam gate.

The shutdown conditions for any operating mode are predetermined, and the summations and interlocking equations for all of the input signals are implemented redundantly within digital logic circuits. Each redundant circuit is powered by individual power supplies. The redundant outputs of the target station proton beam shutdown system are summed into the redundant

facility protection system with other, accelerator-based shutdown summations through current loop interfaces. Any of the inputs into the personnel or facility protection systems are able to inhibit the generation of the proton beam. Due to the high power capability of the proton beam, the beam is inhibited at the point of lowest possible energy. Three independent devices are used. Two of these are physical devices, faraday cups, which have to be removed from the low-energy beam path for the beam to be accelerated. The other device is an electronic inhibitor that prevents beam generation in the ion source.

7.1.3 Radiation

The area radiation monitoring system uses microprocessor-based, multifunction ratemeters with dual channels and digital/analog dose rate display. Each unit supports both a neutron and a gamma probe and is capable of simultaneous detection. Separate, normally energized fail-safe contacts are provided. The ratemeter, which has a built-in diagnostic and failure alarm, utilizes a serial communication link for remote communications with a host computer. Lead acid batteries located within the unit provide a minimum of 8 h of operation. The gamma probe is an ion chamber with both steady-state 0.001-10 mGy/h (0.1-1000 mRad/h) and satisfactory pulsed-radiation response capability, 10 Gy/h (1000 Rad/h) for 10-μsec pulses at 100 Hz. The neutron counter is a BF_3 proportional counter, housed in an Anderson-Braun-type moderator, with a range of 0.001-10 mSv/h (0.1-1000 mrem/h) and featuring gamma rejection up to 2.5 Gy/h (250 Rad/h). The detector has a 1-μsec response time and performs satisfactorily in a pulsed field.

Gamma and neutron detectors are placed as necessary through the experiment areas. Radiation dose rates are displayed on the digital readout. The ratemeter is set for a warning-level alarm to indicate elevated radiation fields and a high-level alarm that initiates automatic shutdown of the proton beam. Additional detector units are placed along the neutron beamlines to measure radiation fields and to initiate proton beam shutdown and neutron beam gate closures.

7.1.4 Cooling Systems

An IPNS Upgrade target station has a number of individual cooling systems, each of which is important to the safety and operation of the facility. The consequences of a loss of cooling vary from system to system, but operation of the entire facility requires proper operation of all of the cooling systems.

The cooling systems and the sections in which they are discussed are listed here. The complement of instrumentation and control devices shown on the cooling system diagrams for these systems is the minimum needed to control the system and does not represent the entire complement needed for control, protection, and monitoring.

1. Target cooling (Section IV.2.6)

2. Moderator and premoderator water cooling (Section IV.3.4.2)

3. Reflector cooling (Section IV.3.4.5)

4. Biological shield cooling (Section IV. 3.4.6)

5. Target tank assembly cooling (Section IV.3.4.7)

6. Proton HET line vacuum window cooling (Section IV.3.4.8)

7. Liquid methane moderator cooling (Section IV.3.4.3)

8. Liquid hydrogen moderator cooling (Section IV.3.4.4)

9. Neutron irradiation facilities cooling (Sections IV.6.2.5 and V.4.3)

The facility protection system monitors all cooling systems and carries out the ultimate protective actions should the other systems fail to work. The protection system's high reliability generally requires fully redundant systems to monitor critical parameters and to provide a protective action. The reliability required for the individual protection systems is commensurate with consequences of the failure of the monitored system. For instance, the failure of a target cooling system on the IPNS Upgrade requires an immediate proton beam shutdown to prevent the most significant radiological and economic consequences. Such a system requires the highest reliability of monitoring instruments and shutdown logic connecting this cooling system and the proton beam shutdown devices.

The protection system primarily relies on monitoring parameters such as flows, pressures and liquid levels that directly indicate a loss of cooling function, rather than relying on temperature measurements.

7.1.5 Containment Systems

The IPNS Upgrade containment and confinement systems described in Section IV.6 control the releases of radioactive gases, explosive gases, and radioactive liquids. This includes collecting all potentially radioactive or explosive gases and directing them to the stacks, minimizing activity at the stacks by delaying releases or by keeping air out of the biological shield purge gases, and collecting and storing all liquid leakages in sealed collection systems.

Most of the facility or personnel protective actions associated with the containment and confinement systems require human intervention. Most systems allow sufficient time for operator reaction. Interlocks shut the facility down in the event of critical failures, such as failure of the main facility exhaust ventilation, overpressurization events, and coolant leakage events.

7.1.6 Mechanical Systems

A number of mechanical systems are critical to the safe operation of an IPNS Upgrade target station. These include neutron beam gates, hot-cell doors, personnel-entry safety interlocks, and irradiation facilities interlocks. These systems protect operating personnel, and must be in a permissive state to allow IPNS Upgrade operations.

Many systems associated with the neutron scattering beamlines also have interlocks that prevent their inadvertent operation or proton beam operation whenever their area is accessed. If a mechanical system ceases to be in a permissive state, there are a number of hard-wired shutdown and alarm systems that provide very reliable protective actions and alarms, as conditions warrant. For instance, if a person enters an interlock-protected area near a scattering instrument without prior required actions being taken, system logic shuts down the proton beam, closes appropriate neutron beam gates, and sounds local and control console alarms.

7.2 CONTROL AND MONITORING SYSTEMS

7.2.1 Overview

In addition to the protection system, there is also a control system, which provides the operator interface for normal facility operation. The IPNS Upgrade control system uses the Experimental Physics and Industrial Control System (EPICS), which has been developed by the Controls group at the Advanced Photon Source (APS) and the AT-8/GTA groups at Los Alamos National Laboratory. EPICS uses high-performance graphic workstations with an X-Window Graphical User Interface (GUI) at the operator level. It connects to VME/VXI-based microprocessors at the field level by means of high-performance networks. EPICS performs all of the control and monitoring of the accelerator systems and supervisory monitoring and control of the target stations. EPICS is described in more detail in Chapter II.

7.2.2 Control System Interface

Standardized interface modules are mounted in crates near the sources of the signals to be interfaced. The analog signals from target station devices are asynchronously converted to 12-bit binary form every 18 ms, providing an accuracy of 0.025% of full scale. The digital input signals are handled by optically coupled input circuits to provide isolation from the transducer signal and conditioning devices. These binary signals are transmitted to the local microprocessors, where

the raw data base is converted to appropriate engineering units and placed in a processed data base; in the latter, each signal is checked against preset levels. These levels, in descending algebraic order, are high out-of-transducer range, high transducer trip level, high transducer alarm level, low transducer alarm level, low transducer trip level, and low out-of-transducer range. Not all signals are checked for all of these conditions. The alarm level gives an opportunity for correcting the problem before shutdown occurs. The failure function calls attention to any type of channel malfunction, which causes the analog output of the channel to go to the limit opposite the alarm or shutdown level. The appropriate alarm/trip limits are predetermined for all operating modes and are preset into the microprocessor data base and regularly confirmed by the central control computer. All data from the field level microprocessor are transmitted to the GUI operator consoles for operator display. Trip conditions are also relayed to the personnel and facility protection systems as redundant control system inputs to these hard-wired shutdown systems.

7.2.3 Radiation Monitoring

7.2.3.1 Exhaust Monitoring

The stack sampling system is equipped with suitable detectors to quickly identify potentially serious incidents. Air emissions are surveyed for radioactivity with a microprocessor-controlled, continuous stack monitor located in a shielded enclosure downstream of the HEPA filters. The system includes the following components:

1. Particulate Monitor — A plastic scintillator counts beta emissions from particles collected on a cyclically moving, high-efficiency filter paper. A portion of the stack exhaust air is diverted through the filter, which is mounted close to the plastic scintillator. The system is used to document the adequacy of the HEPA filtering during normal operations and to detect increased levels of activity. Gamma spectrometry of exposed filter paper also identifies Be^7 and other contributors.

2. Radionuclide Monitors — The diverted exhaust stream flows through a charcoal cartridge or other suitable collection medium. Two NaI(Tl) crystals scan this medium. Different spectral regions, each corresponding to a specific photon energy (e.g., 1.3 MeV for Ar^{41} and 1.12 MeV for Ta^{182}), are set up and the counts from these photons recorded.

3. Residual Gas Monitor — Another plastic scintillator is located in a sample chamber to monitor any gaseous radioactivity that has passed the filter paper and other collection media. This monitor indicates the presence of beta-emitting radionuclides as the gas passes through a cylindrical chamber. These data are registered as a count rate and also are accumulated for use in estimating total stack releases. Grab samples obtained at IPNS with a

100-cm^3 sampler featuring a thin window indicated that the major activity is C^{11}.

The flow rate through the stack monitor system is dynamically controlled by the microprocessor to achieve isokinetic sampling of the stack environment. Stack flow rates are determined by periodic Pitot tube measurements. Remote readouts of the detector outputs and flow measurements are provided at the Control Room and in the Health Physics Office. The remote readouts are displayed, recorded, and alarmed for control and monitoring purposes only.

7.2.3.2 Personnel Monitoring

Argonne has an extensive radiation protection program, supported by the ESH Division. Details of the control requirements and procedures can be found in the ANL site-specific Radiological Control Manual.[1] The IPNS Upgrade complies with the requirements of the manual. ESH supplies personal monitoring devices, collects them for analysis, processes the devices and analyzes the readouts to provide dose results. ESH maintains its own calibration facility with both gamma and neutron capability.

Buildings 367, 369, 370 and 371 are radiologically controlled areas. Each building has hand and shoe monitors, each with a frisk detector, at the entrance and exit doors.

In addition to the personnel monitoring program, ESH provides monitoring and survey services and hazard analyses. These services include instrument surveys for alpha and beta-gamma contamination, as well as neutron and gamma fields, air samples of the ambient atmosphere, and surface and smear surveys for alpha and beta contamination.

7.2.4 Cooling Systems

Controllers monitor the cooling systems under the supervision of EPICS. EPICS provides setpoints and directly monitors critical cooling system parameters: usually flows, temperatures, pressures, and fluid levels. It also alarms or shuts down systems when out of normal operating range.

7.2.5 Mechanical Systems

Neutron beam choppers are located within a target station, but they are considered a part of the neutron scattering instrument they serve, as are most of their instrumentation and control systems. However, EPICS monitors their operation, and they are required to have interlocks that prevent their inadvertent operation or proton beam operation whenever their area is accessed.

Most of the mechanical systems, such as neutron beam gates and personnel entry safety interlocks, are locally controlled, but all are under the monitoring, alarming, and protective-action

features of the IPNS Upgrade EPICS. EPICS software protective actions include proton beam shutdown, neutron beam gate closure, chopper shutdown, and local area alarms.

7.3 CONTROL ROOM

An rf-shielded control room enclosure that currently exists in Buildings 368 and 370 serves as the control room for both the 10-Hz and 30-Hz target stations. The raised floor area of this control room exists and covers about $100 \, m^2$. An adjacent office area, which is also rf-shielded, covers an additional $100 \, m^2$. Modern fire protection systems exist in the control room.

7.4 REFERENCE

1. *Environmental Safety and Health Manual*, Argonne National Laboratory-East, Chapter 5 (April 1991).

8.1 BIOLOGICAL SHIELDING PENETRATIONS

Each of the target stations has a total of 18 penetrations through the biological shield, 9 on each of two sides. These are the neutron beam ports through which neutrons are allowed to pass to the neutron scattering instruments. One or more neutron beams can be brought out through each beam port. Figure IV.4.1-2 shows the locations of these beam ports in the biological shield. Each of the six moderators in the target station is viewed by three such beam ports, with ~13° separation between beam ports in the horizontal plane.

Figure IV.8.1-1 shows a section through the biological shielding along the length of a representative beam port. The innermost end of the beam port closest to the moderator consists of a cutout section in the beryllium reflector. Here the three beam ports viewing that moderator converge, resulting in a single cutout in the reflector adjacent to each moderator, as shown in Figure IV.8.1-2. The cutouts for the different moderators are at different levels in the reflector, as can be seen in Figure IV.1.2-5. Each of these cutouts is lined with an absorbing void liner to prevent broadening of the neutron pulses by neutrons thermalized in the reflector. These cutouts allow each beam port to view the full 10×10 cm^2 or 10×20 cm^2 moderator face. The sealed aluminum target tank isolates this inner portion of the beam port from the outer portion in the biological shield. Helium gas fills this target tank, and hence also the reflector cutout portion of the beam port.

A separate steel beam port tube defines each beam port from the target tank to the shielding tank. Each tube is constructed of at least 1.25-cm-thick steel plate and has a cross section of 35×35 cm^2 at the inner end. The cross-section is increased in several steps along the tube length to prevent neutron streaming. The tubes vary in length from 3.65 m to 4.9 m and are welded to the shielding tank and to the target tank housing. Each of these tubes is also welded to a beam gate housing to allow a gate to block the beam, as shown in Figure IV.8.1-1. The atmosphere of these tubes is the same as the shielding tank atmosphere, because they are isolated from the target tank by the beam windows on the target tank. An O-ring and flange arrangement seals an aluminum window at the outer end of the beam port tube.

Outside the shielding tank, each beam port enlarges to provide a well-shielded chopper cavity that can accommodate neutron choppers or filters. The beam port then terminates in an interlocking transition to the external neutron beamline shielding. This external beamline shielding is considered to be part of the neutron scattering instruments, and is discussed in Chapter V.

8.2 BEAM GATES

The neutron beam gates are each 2 m long in the direction of the beam and 40 cm wide, and extend from ~2.5 m below the beam ports to ~4 m above the beam ports. These gates are made either of steel or of steel-shot-loaded concrete, and are made in sections to facilitate

GATE
(SHOWN IN CLOSED POSITION)

REMOVABLE
SHIELD BLOCKS

CHOPPER CAVITY

ALUM. WINDOW
SEAL

FLOOR LEVEL

TARGET,
MODERATOR,
REFLECTOR CAVITY

3 METERS
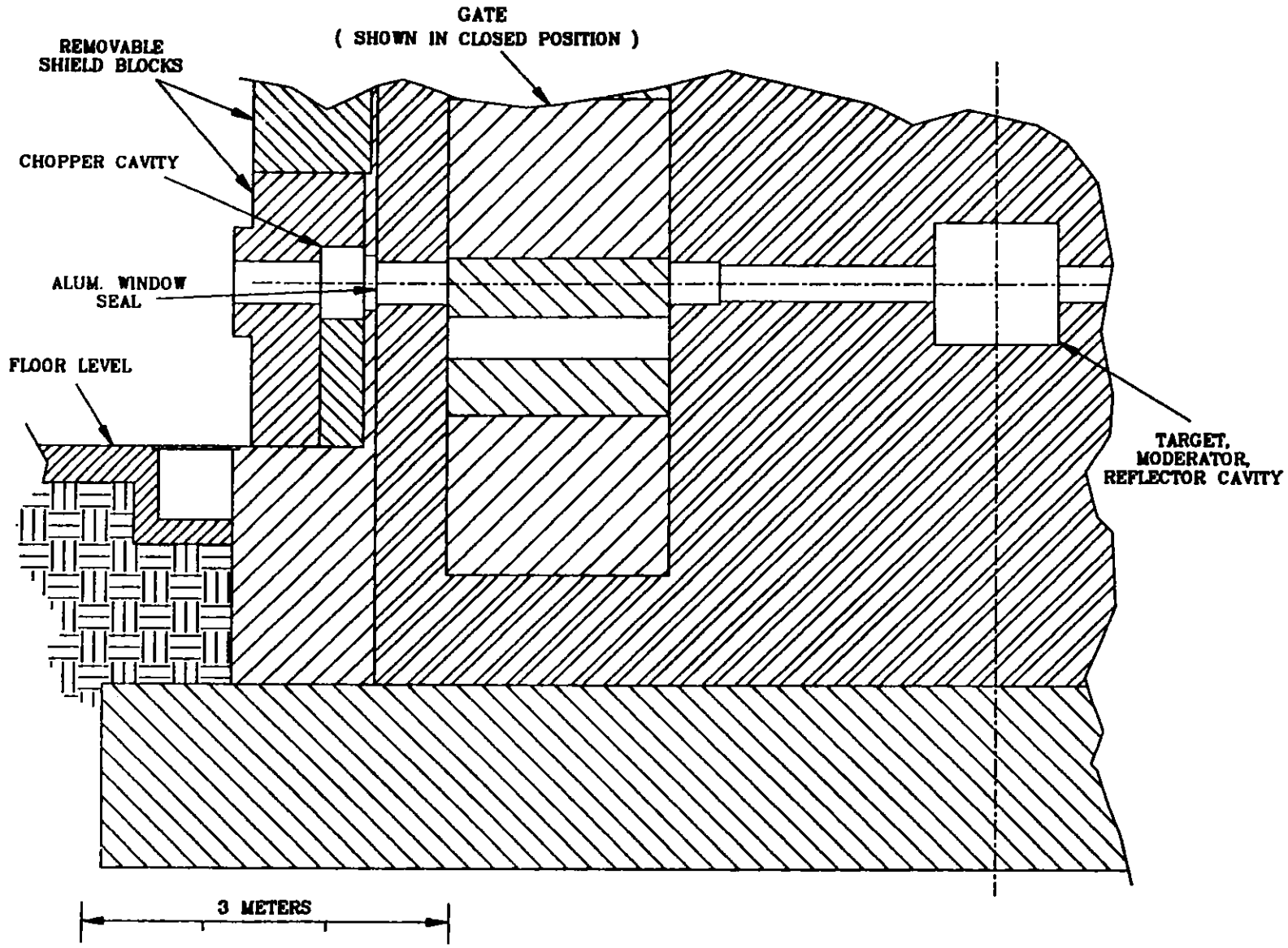
Figure IV.8.1-1 Longitudinal Section through a Typical Neutron Beam Port.

PROTON
BEAM

MODERATORS

BERYLLIUM
REFLECTOR

ONE METER
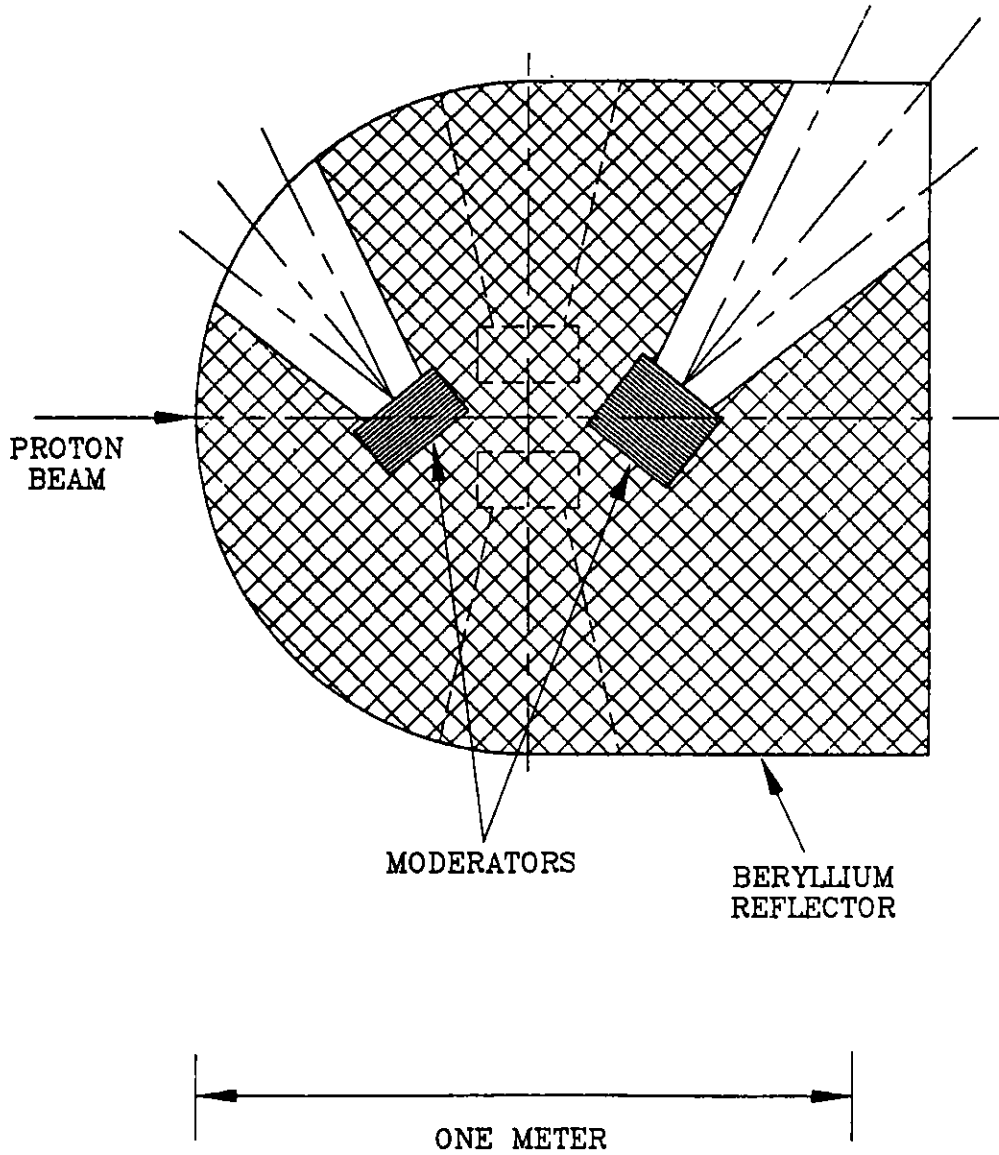
Figure IV.8.1-2 Horizontal Slice through the Reflector at the Midplane of the Upper
Moderators, Showing the Cutouts for the Neutron Beams.

installation. Hydraulic actuators move the gates vertically to either the gate-open or gate-closed positions. Each gate has an opening cut through it which is moved into alignment with the remainder of the beam port for the gate-open position. In the gate-closed position, this opening is moved some distance below the beam port, so the beam port is blocked by 2 m of gate material. The gate width is greater than the width of the beam port and is of stepped shape to prevent streaming of neutrons around the edges of the gate. The gate moves inside a steel housing which is welded to the beam port tube.

Figure IV.4.1-2 shows the locations of the gates in the biological shield and Figure IV.8.2-1 shows a cross-sectional view of two of the gates, one in the open position and one in the closed position. As indicated in Figure IV.4.1-2, all gates have their inner faces 2.5 m or more from the target, so heating of the gates is estimated to be less than 100 W per gate and no special cooling is required. This large separation from the target also minimizes activation of the gate materials and the beamline inserts.

The cutouts in the neutron beam gates contain neutron collimation elements or neutron guides to continue the definition and transport of the neutron beams appropriate for the specific neutron scattering instruments being served, whereas the remainder of the space in the gate is filled with neutron shielding. An individual hydraulic actuator at the top of each gate, shown in detail in Figures IV.8.2-1 and IV.8.2-2, drives that gate against adjustable stops to provide an aligned and reproducible open position. Adjustments on the actuator mount permit a small rotation of the gate about a vertical axis in order to optimize the angular alignment of the in-gate collimator or guide with the remainder of the beamline optical elements. A metal sheet seals the opening for the gate in the top of the shielding tank to complete the containment barrier.

The 2 m of shielding placed in a neutron beam when the gate is closed provides excellent biological shielding against any radiation resulting from residual activity inside the target station. This permits work in the external neutron beamline when the gate is closed and the accelerator is not running. However, when the accelerator is providing protons to this target station, this beam gate does not reduce the dose levels in the neutron beamline low enough to allow unrestricted access to the beamline. To make the gate sufficiently effective for this purpose requires a gate as thick as the remainder of the biological shielding, or approximately 6 m, which is not practical. The gate does reduce external radiation in the beamline sufficiently to allow limited access to such beamline components as choppers or filters and to permit changing samples in the neutron scattering instrument while the accelerator is running. The gate is closed when these activities occur.

8.3 NEUTRON BEAM GUIDES AND COLLIMATORS

Some of the neutron scattering instruments use neutron guides to provide efficient transport of neutrons to the instrument. Section V.3.2 indicates which of the instruments require guides and also specifies parameters for these guides. In some cases the guide is required to extend to within 1-2 m of the moderator. This region is easily accessible with the present beam

HYDRAULIC CYLINDER

LIFT ROD SEAL ON
SEAL COVER

REMOVABLE SHIELD
BLOCKS

GATE IN CLOSED
POSITION

GATE IN OPEN
POSITION

HELIUM
ATMOSPHERE

LIFT RODS

ONE METER

FIVE METERS
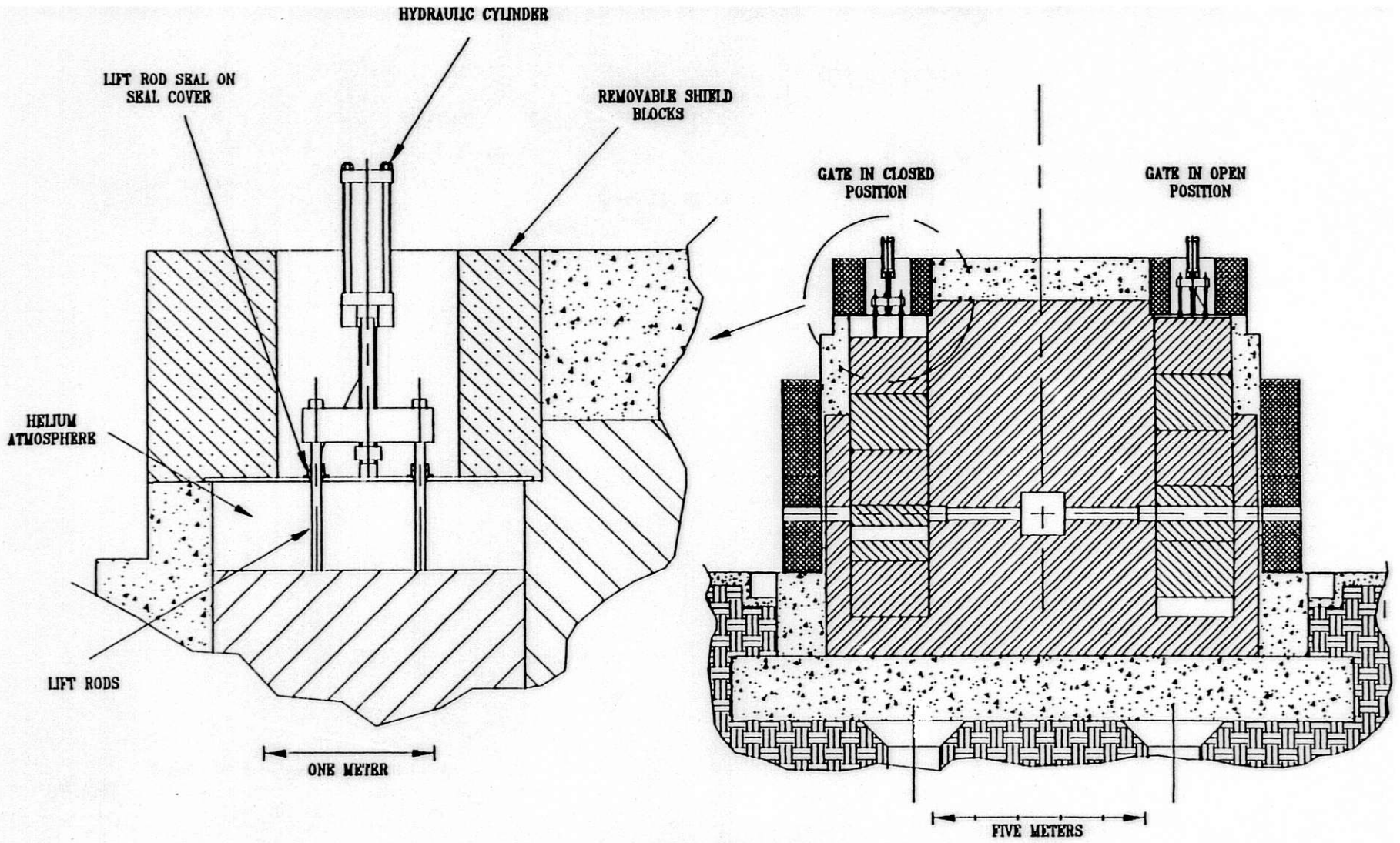
Figure IV.8.2-1 Cross-Sectional Views of the Biological Shield, Showing Details of the Neutron Beam Gates and Gate Actuators.
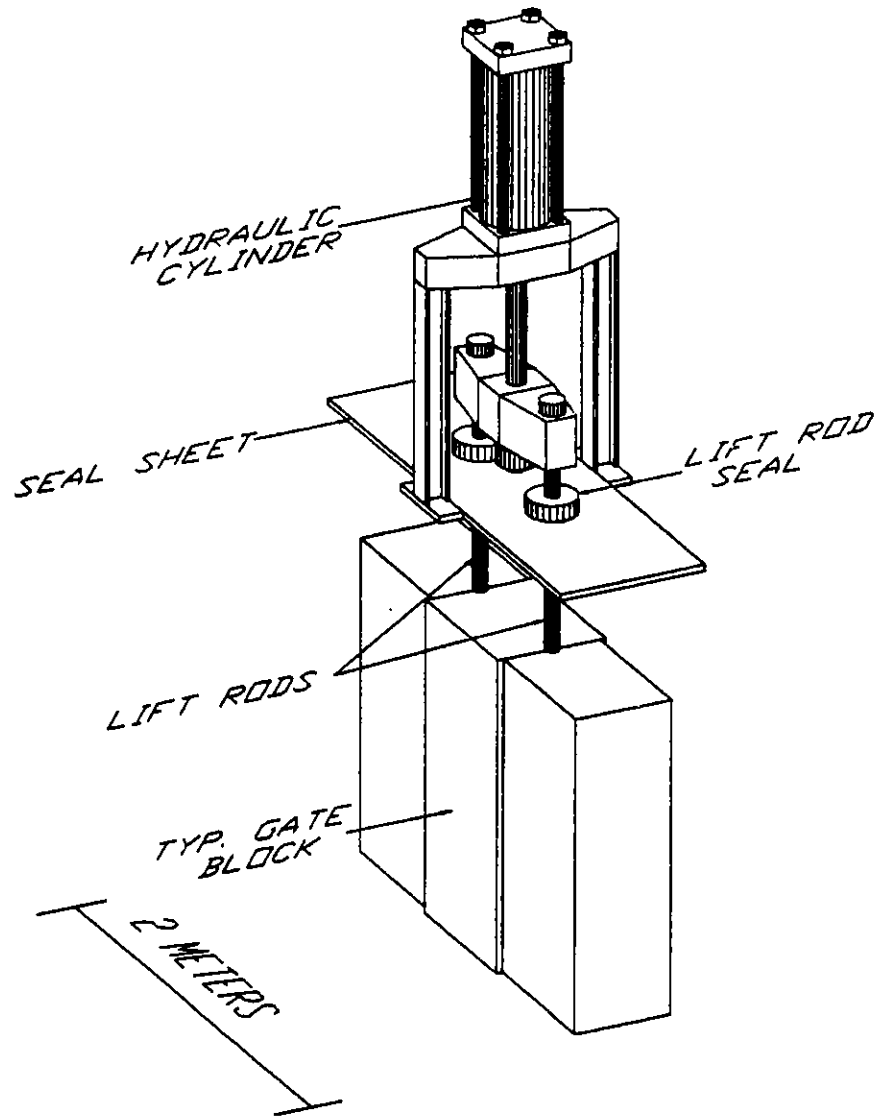
Figure IV.8.2-2 Details of a Neutron Beam Gate and Actuator.

port design, as shown in Figure IV.8.1-1. Neutron guides are usually made of glass, with a thin coating of nickel to provide the reflective surface. However, at 1-2 m from the target, these guide materials deteriorate relatively rapidly due to radiation damage. At ISIS, the portions of guides that are in high radiation fields are made of polished steel,[1] which has worked quite well with no deterioration yet observed. Those portions of the neutron guides that are in high radiation fields at IPNS Upgrade utilize similar construction. Construction of the remaining sections of the guides, including sections that must extend through the neutron gates, is also similar to that used at ISIS.[1,2] Any remaining space between the exterior of the guide and the walls of the beam port is filled with appropriate shielding material.

The interior of the remaining beam ports, including the portion that extends through the beam gate, is filled with shielding material arranged to leave a channel for the neutron beam. These beam port inserts are individually designed to the requirements of specific instruments. Neutron beam collimation is provided by a series of B4C irises, following standard practice.[3]

In some cases it is possible to bring out more than one neutron guide or collimated beamline within a single beam port. This is the case if there are two or more instruments that are very small and that require small beams from the same moderator, as is the case for the neutron reflectometers. Multiple guides from the same beamport can also be used for the QSS instruments, similar to the case at a neutron guide hall at a reactor. It is possible to bring out as many as three guides from a single beam port, where this is appropriate.

8.4 CHOPPER CAVITIES FOR CHOPPERS AND FILTERS

Many of the neutron scattering instruments require neutron choppers or filters in the beamline. Requirements for neutron choppers are discussed in detail in Section V.3.1. These devices scatter unwanted neutrons out of the beam before they reach the instrument, and hence introduce intense local radiation sources requiring massive shielding. Furthermore, it is desirable to locate most of these devices as close to the moderator as practical. For both of these reasons, each beam port includes a chopper cavity at the face of the biological shield, as shown in Figure IV.8.1-1, to accommodate choppers and filters. In this location, the biological shield provides most of the shielding required by the chopper or filter.

Removable shielding blocks above the cavity provide access. These extend to the top of the biological shielding, as shown in Figures IV.4.1-3 and IV.8.1-1. This design allows the chopper or filter to be serviced without disturbing the remainder of the instrument beamline or its shielding. Interlocks require that the beam gate be closed whenever these shielding pieces are removed.

8.5 INTERFACE TO NEUTRON BEAMLINE SHIELDING

The shielding at the face of the chopper cavity interlocks with the shielding for the external portion of the neutron beamline. This design, shown schematically in Figure IV.8.1-1, prevents any streaming through cracks between shielding pieces.

8.6 ATMOSPHERE CONTROL

A helium gas atmosphere is maintained inside the target tank surrounding the target-moderator-reflector region. A second, independent helium atmosphere is maintained throughout the portions of the biological shielding inside the shielding tank, including the beam port and beam gate regions. A thin aluminum window and O-ring flange assembly seals this atmosphere inside the beam port at the point where the beam port enters the chopper cavity (see Figure IV.8.1-1). Neutrons interact only minimally with gaseous helium, so this helium is satisfactory for most of the beamlines. When desired, an independently controlled helium atmosphere or a vacuum can be provided inside the neutron guide or collimator sections within the beam port. Channels in the biological shield at the beam gate and in the beam gate itself accommodate the necessary gas flow or vacuum lines for connection to such guide or collimator sections.

8.7 REFERENCES

1. J.C. Sutherland et al., "The performance of the IRIS and HRPD guides on the SNS," in *Proceedings of the 8th Meeting of the International Collaboration on Advanced Neutron Sources (ICANS VIII)* (Oxford, U.K., July 8-12, 1985), Rutherford Appleton Laboratory Report No. RAL-85-110, Chilton, U.K., pp. 771-776 (1985).

2. C.J. Carlile, M.W. Johnson, and W.G. Williams, *Neutron Guides on Pulsed Sources,* Rutherford Appleton Laboratory Report No. RL-79-084, Chilton, U.K. (1979).

3. A.D. Taylor, T.A. Broome, and D.J. Picton, "Neutron beam shielding at ISIS," in *Proceedings of the 9th Meeting of the International Collaboration on Advanced Neutron Sources (ICANS IX)* (Villigen, Switzerland, September 22-26, 1986), Swiss Institute for Nuclear Research, Villigen, Switzerland, ISBN 3-907998-01-4, pp. 519-528 (1987).

V

Experimental Facilities

1.1 OVERVIEW OF NEUTRON BEAM INSTRUMENTATION

In Sections V.2 and V.3, the experimental facilities that are located on neutron beamlines are discussed. Other types of experimental facilities that do not occupy one of the neutron beamlines are discussed in Section V.4.

1.1.1 Instrument Discussions and Reference Set of Instruments

A number of different neutron scattering instruments are discussed in sufficient detail in Section V.2 that their expected performances can be evaluated. A representative "reference set" is selected from among those instruments and is considered for the cost analysis in Chapter VII. The reference set of instruments is chosen to represent a plausible initial complement of instruments to be installed at IPNS Upgrade, under the assumption that 24 of the 36 available beam ports are to be instrumented initially. The set of instruments that will actually be selected for initial installation will be based on the requirements of the user community as assessed at the time of the construction project.

A number of very good neutron scattering instruments are currently operational at IPNS. IPNS Upgrade includes 10 of these instruments, in some cases with little change and in other cases with upgrading. The availability of these already-proven instruments makes it possible to have a large number of instruments fully operational at startup. Use of existing instruments also results in significant cost savings.

In most cases, the instrument data rates specified in this chapter for IPNS Upgrade are estimated by scaling from known rates for the same or similar instruments at IPNS, ISIS, or the Institut Laue-Langevin (ILL), taking into account differences such as path lengths, numbers of detectors, and types of moderators. This scaling is performed under the assumptions (1) that the proton beam is shared between the 30-Hz and 10-Hz targets in a 2:1 ratio and (2) that the time-averaged current of neutrons per beam with a decoupled moderator at the 30-Hz target station at IPNS Upgrade is ~50 times the corresponding current at IPNS with the depleted-uranium target, as described in Section IV.3.2.4. The time-averaged current per beam at the 10-Hz target station is one-half the amount at the 30-Hz station. Additional factors of 4-6 in intensity are gained by using coupled moderators, where appropriate.

Most of the instruments discussed in this chapter use neutron time-of-flight (TOF) techniques, as is the case for all of the instruments currently operational at pulsed neutron sources. IPNS Upgrade has sufficient time-averaged intensity to make it practical to operate some of the beamlines in a quasi-steady-state (QSS) mode. In this mode, only the time-averaged flux from the moderator is of importance, and in principle, any instrument that works at a steady-state source (reactor) can be made to work in this QSS mode at IPNS Upgrade as well. The time-averaged flux from a moderator optimized for this type of operation at IPNS Upgrade is roughly equivalent to that at a $\sim10^{14}$ n/cm^2-s reactor, as discussed in Section IV.3.2.5. With many of these instruments the time-structure of the source can be used to advantage to reduce background contributions because of the reduced duty factor of 1:30 to 1:60, and to eliminate

undesirable orders from monochromators and analyzers. Several instruments that work in this mode are discussed here. One of these, a cold-neutron triple-axis spectrometer, is included in the reference set of instruments.

1.1.2 Details of Instrument Components

Several critical types of instrument components common to many of the instruments are discussed in detail in Section V.3. Neutron chopper systems, neutron guides, beamline shielding, and detectors are included. Specific requirements in each of these areas are analyzed for the reference set of instruments.

1.1.3 Utilization of the Remaining 12 Beam Ports

Twelve beam ports remain available for future construction of instruments, by participating research teams and by IPNS Upgrade personnel, to support evolving needs of the user community.

1.2 OVERVIEW OF OTHER EXPERIMENTAL FACILITIES

The primary mission of IPNS Upgrade is neutron scattering. However, the various components of the facility provide capabilities that are extremely useful for other areas of science. Instrumentation to provide capabilities in radiation damage studies, neutron isotope production, and neutron activation analysis is included as part of this project. The facilities for these three areas are discussed in detail in Section V.4, and are included in the project cost and schedule.

IPNS Upgrade has potential capabilities in a number of other areas, including muon spin rotation. Some of these possibilities are discussed briefly in Appendix C.

2.1 POWDER DIFFRACTOMETERS

2.1.1 Transfer of Existing IPNS Instruments

2.1.1.1 SEPD — High-Intensity Powder Diffractometer

The Special Environment Powder Diffractometer (SEPD) and the General Purpose Powder Diffractometer (GPPD) at IPNS have identical scattering flight paths,[1] shown in Figure V.2.1-1. With minimal modification, the SEPD can be used as a high-intensity and special-environment powder diffractometer at IPNS Upgrade. The incident flight path is shortened from 14 m to 12 m to achieve a gain in intensity and an extension of the available d-spacing range at fixed scattering angle. This instrument provides high count rates while maintaining sufficient resolution in backscattering (150°) to obtain Rietveld-refinement-quality data. Added detectors approximately double the area of the original SEPD detector arrays to ~0.2 sr at both backscattering and 90°. This allows real-time studies with data-collection times on the order of 1-10 min for large samples. This instrument is also effective for the study of small samples. Rietveld-quality data for samples of 10-100 mg are obtained in a few hours. The moderator is designed to give essentially the same resolution on the somewhat shorter flight path. The repetition rate of 30 Hz allows this instrument to provide a large d-spacing range for experiments done at a single scattering angle, although a bandpass-limiting/frame-overlap chopper may be required. Table V.2.1-1 summarizes the parameters of this upgraded SEPD.

2.1.1.2 GPPD — Medium-Resolution Powder Diffractometer

The incident flight path of the GPPD is lengthened from 20 m to 25 m to obtain higher resolution in backscattering. The 90° detector arrays are moved to provide a much longer scattered flight path, as shown in Figure V.2.1-2, to maintain high resolution at 90° for experiments in such special environments as pressure cells and controlled-atmosphere furnaces. The resolution $\Delta d/d$ at 90° is 2×10^{-3} full width at half maximum (fwhm), an improvement of 2.5 over the IPNS version. This resolution is achieved by lengthening the scattered flight path at 90° to ~4 m and by using a Soller collimator (approximately $\Delta\phi = 0.08°$) in the incident flight path to reduce the incident angular divergence. The desired resolution is achieved while still maintaining the ability to use samples as large as 1-cm diameter $\times$ 5-cm long. Removing the incident Soller collimator increases the count rate by a factor of 3 for experiments where high resolution at 90° is not required, without degrading the resolution in backscattering. The 30-Hz source repetition rate permits the collection of full data sets with the desired d-spacing range at a single scattering angle, although a bandpass-limiting chopper is required to eliminate frame-overlap neutrons. The backscattering detectors of this instrument provide a resolution of 2×10^{-3}, giving Rietveld-quality data with data-collection times of a few minutes when the Soller collimators are removed. Table V.2.1-1 summarizes the parameters of this upgraded GPPD.
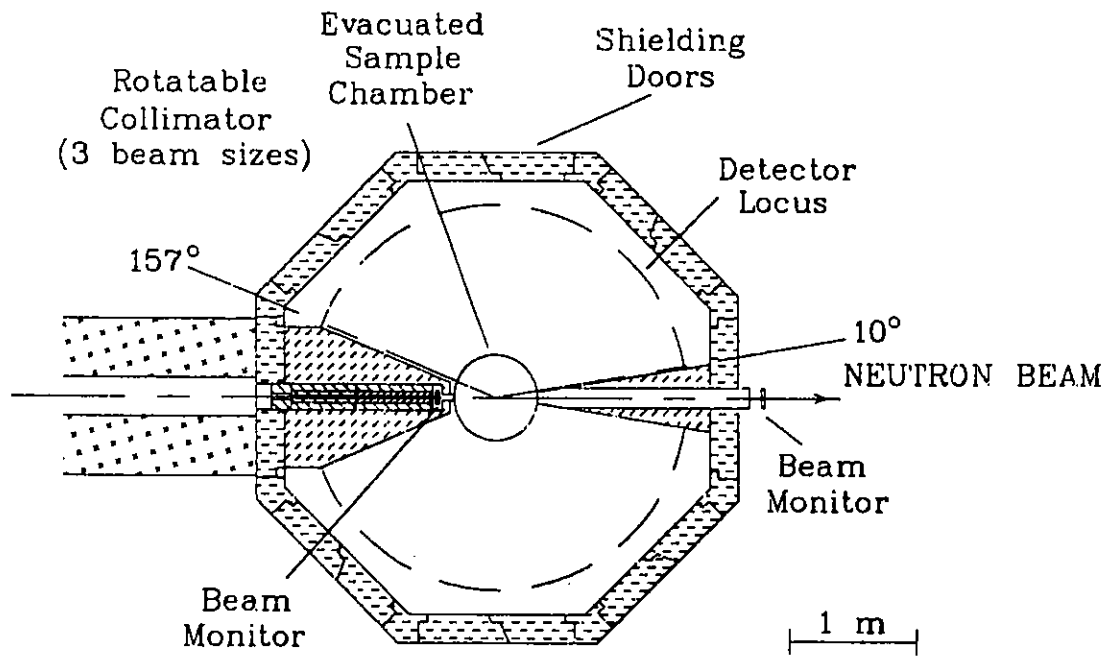
Figure V.2.1-1 Plan View of the SEPD Scattering Flight Path at IPNS Upgrade.

Table V.2.1-1 SEPD and GPPD Parameters at IPNS Upgrade

Parameter	SEPD	GPPD
Source-sample distance (m)	12	25
Source repetition rate (Hz)	30	30
Moderator material	liquid CH_4[a]	liquid CH_4[a]
Neutron guide	no	no
Sample volume (cm^3)	5	5
Wavelength range (Å)	0.4-9.1	0.4-4.6

	Scattering Angle (°)				Scattering Angle (°)			
	150	90	60	30	150	90	60	30
Sample-detector distance (m)	1.5	1.5	1.5	1.5	1.5	4.0	1.5	1.5
Detector solid angle (sr)	0.2	0.2	0.1	0.1	0.2	0.1	0.1	0.1
Minimum accessible d (Å)	0.2	0.3	0.4	0.8	0.2	0.3	0.4	0.8
Maximum accessible d (Å)	4.7	6.4	9.1	17.5	2.4	3.0	4.6	8.9
Resolution $\Delta d/d$, fwhm (10^{-3})	3.5	5	8	16	2[b]	2[b]	6[b]	12[b]
Flux at sample $(10^6$ n/cm^2-sec)	33	33	33	33	3[b]	3[b]	3[b]	3[b]
Experiment time for Rietveld-quality statistics (min)	3	3	3	3	30[b]	60[b]	30[b]	30ʲ

[a] Or room-temperature H_2O.

[b] With incident-beam Soller collimators.
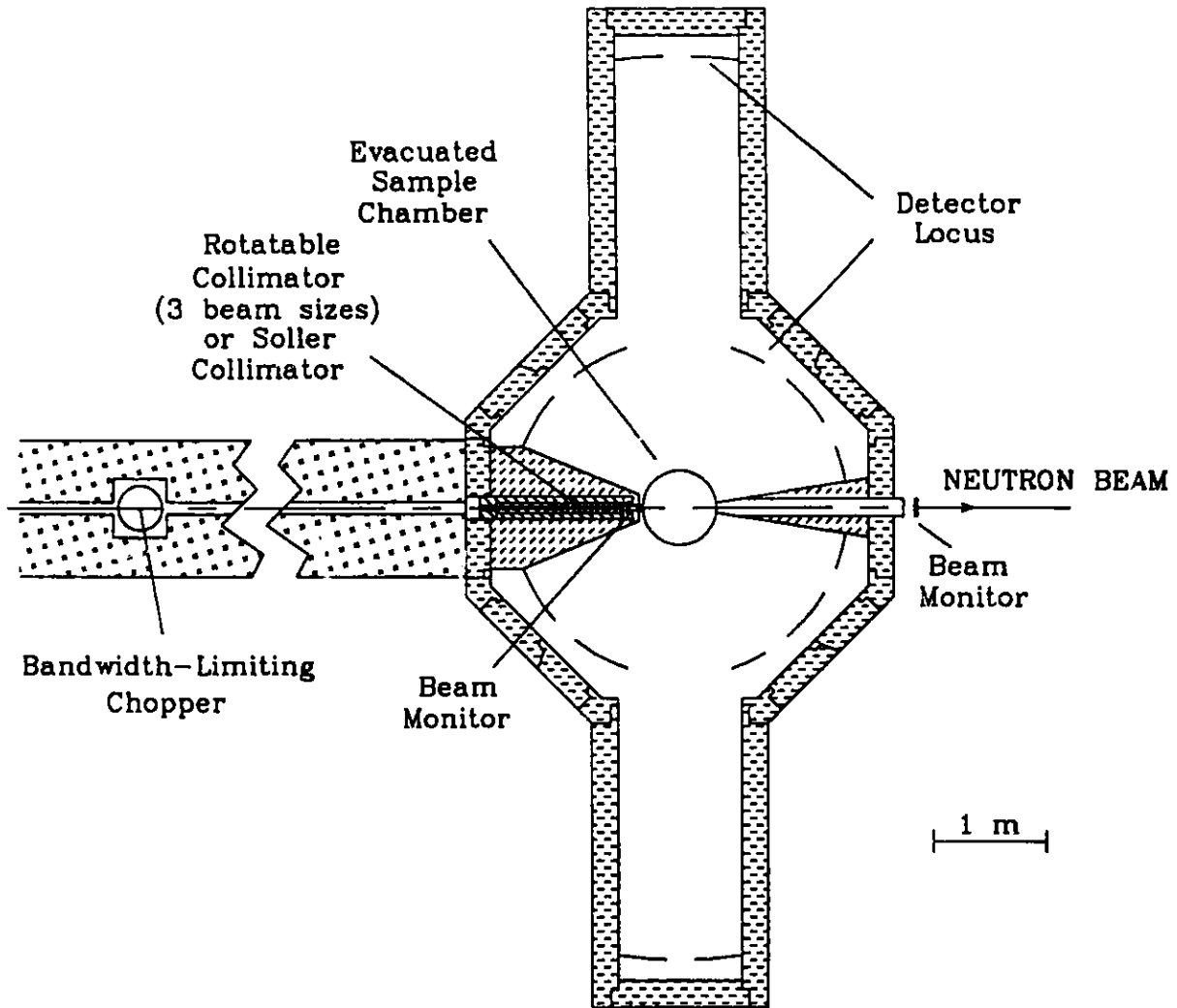
Figure V.2.1-2 GPPD Configuration at IPNS Upgrade, Showing Increased 90° Scattering Path Length.

2.1.2 New Reference Set Instruments

2.1.2.1 HRPD — High-Resolution Powder Diffractometer

The HRPD has an incident flight path of 50 m and is designed for state-of-the-art high-resolution powder diffraction for Rietveld refinement. Instruments optimized for such work can be used for other purposes, such as the solution of unknown structures from powder data. The HRPD employs multiple detector arrays covering a wide range of scattering angles,[2] so the sample-detector flight path looks like a somewhat larger version of the SEPD flight path shown in Figure V.2.1-1. The detectors are on a 2-m radius rather than 1.5 m. The positions of the detectors around this 2-m radius are shown schematically in Figure V.2.1-3. Parameters for the instrument are given in Table V.2.1-2. The instrument is intended to be operated at a repetition rate of 30 Hz, with choppers to select an appropriate band of wavelengths at the highest-intensity part of the spectrum. A room-temperature moderator is advantageous because it gives a higher neutron flux over the relatively narrow wavelength range of interest.

Data from detector arrays at several different scattering angles are combined to provide full diffraction data. The resolution at each angle is adequate to resolve Bragg peaks for typical structures. The chopper phasing can be varied to access the desired d-spacings in backscattering, or at a larger scattering angle than for normal operation, if higher resolution at long d-spacing is required for a particular experiment. A guide tube is used to significantly increase the flux on the sample. It is important not to increase the horizontal angular divergence beyond certain limits, to maintain a reasonable resolution at lower scattering angles. Two approaches can be used to satisfy this criterion. A guide tube with only top and bottom surfaces can be employed. Alternatively, a four-sided guide tube can be used with Soller collimators before the sample. The latter approach has the advantage that the collimators can be removed for experiments where high flux is desired at the expense of resolution.

2.1.2.2 RSD — Residual Stress Diffractometer

A powder diffractometer dedicated to residual stress measurements satisfies strict design criteria directly related to the three main types of experiments: (1) bulk material measurements such as reactor-vessel weldments or sections of airplane wings, (2) temperature- or pressure-dependent residual stress changes in small samples of composites, metal alloys, etc., and (3) triaxial stress-tensor measurements in complex mixed-phase materials.
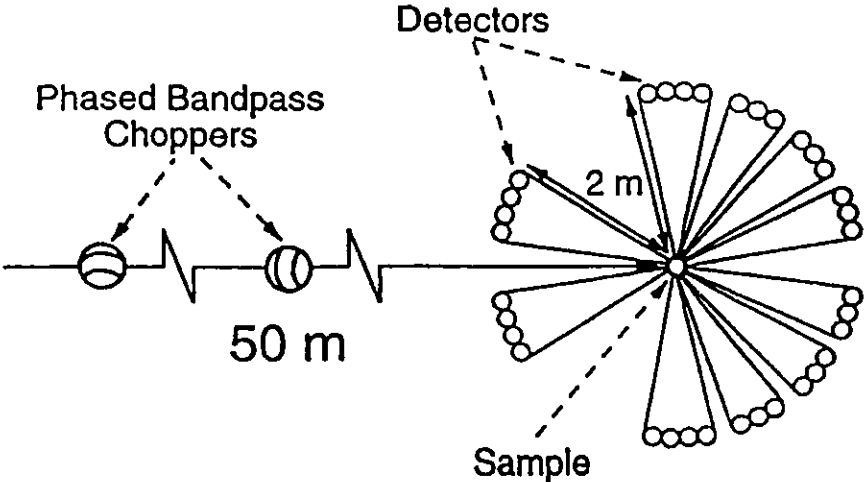
Figure V.2.1-3 Schematic Representation of the Detector
Positioning for the HRPD.

Table V.2.1-2 HRPD Parameters at IPNS Upgrade

Parameter	Value				
Source-sample distance (m)	50				
Source repetition rate (Hz)	30				
Moderator material	liquid CH_4[a]				
Neutron guide	yes[b]				
Sample volume (cm^3)	3				
Wavelength range (Å)	0.4-2.4				
	Scattering Angle (°)				
	160	90	60	45	30
Sample-detector distance (m)	2	2	2	2	2
Detector solid angle (sr)	0.1	0.1	0.1	0.1	0.1
Minimum accessible d (Å)	0.2	0.3	0.4	0.5	0.8
Maximum accessible d (Å)	1.2	1.7	2.4	3.1	4.6
Resolution $\Delta d/d$, fwhm (10^{-3})	0.8	4	7	9	14
Flux at sample (10^6 n/cm^2-sec)	3	3	3	3	3
Experiment time for Rietveld-quality statistics (min)	50	50	50	50	50

[a] Or room-temperature H_2O.

[b] With Soller collimators.

Bulk material measurements involve sending large samples stepwise through the beam with accurate determination of lattice spacings at each step. Ideal sampling volumes are on the order of $2 \times 2 \times 2$ mm^3 for typical stress gradients. This requires a 2×2-mm^2 incident beam, with a 2-mm defining slit in the scattered beam, or other comparable means of defining the sampling volumes. Neutron fluxes at the present pulsed sources are insufficient for this. For instance, residual stress measurements on the GPPD at IPNS require a $50.8 \times 2 \times 2$-mm^3 volume, with the long axis in the direction of minimal gradient. The RSD has a 12-m source-sample distance and concentrates on $90°$ scattering using a large, two-dimensional (2D) position-sensitive detector and Soller collimators in the scattered beam. This arrangement, shown schematically in Figure V.2.1-4, permits the detector to simultaneously sample a number of regularly shaped sampling volumes for all crystallographic reflections, thus giving a much more complete map of the stress distribution.

As is indicated in Table V.2.1-3, this instrument has the capability of collecting data sets from a number of $2 \times 2 \times 2$-mm^3 sampling volumes in ~15% of the time it now takes to collect data from a single sampling volume 25 times as large. The $\Delta d/d$ resolution is somewhat degraded relative to the current GPPD because of the shorter source-sample distance, but this resolution can be recovered by using incident-beam Soller collimators. If the incident-beam Soller collimators are used, data of comparable quality can be collected from a set of slightly larger sampling volumes ($3 \times 3 \times 3$ mm^3) in roughly the same time.

The residual stress measurements on high-tech composites are quite different from those in bulk materials, and require the highest possible resolution at $\pm 150°$ and $\pm 90°$, without significant loss in turn-around time. The current reference standard is a $50.8 \times 6.4 \times 6.4$-mm^3 metal-ceramic composite, for which 30 min is required on the GPPD at IPNS for good statistics. The RSD includes a second sample position at 25 m from the source, in order to provide the necessary $\pm 90°$ resolution. Incident- and scattered-beam ($\pm 90°$) Soller collimators and banks of detectors at $\pm 150°$ and $\pm 90°$ are also required, as shown schematically in Figure V.2.1-4. This gives dramatically improved resolution of 3×10^{-3} at $\pm 90°$, while also decreasing the turn-around time to less than 10 min.

Composites or other materials that are strongly textured or have stress states that are highly anisotropic require simultaneous measurement of the stresses in multiple, mutually orthogonal directions. Three 2D position-sensitive detectors are placed around the 25-m sample position at scattering angles of $70.5°$, such that the sampled scattering vectors are mutually perpendicular (see Figure V.2.1-4). The performance characteristics are essentially the same as those indicated in Table V.2.1-3 for the conventional-detector configuration at the 25-m position.

This instrument is constructed to provide ready access for large industrial-component samples.

12 m Position   **25 m Position**
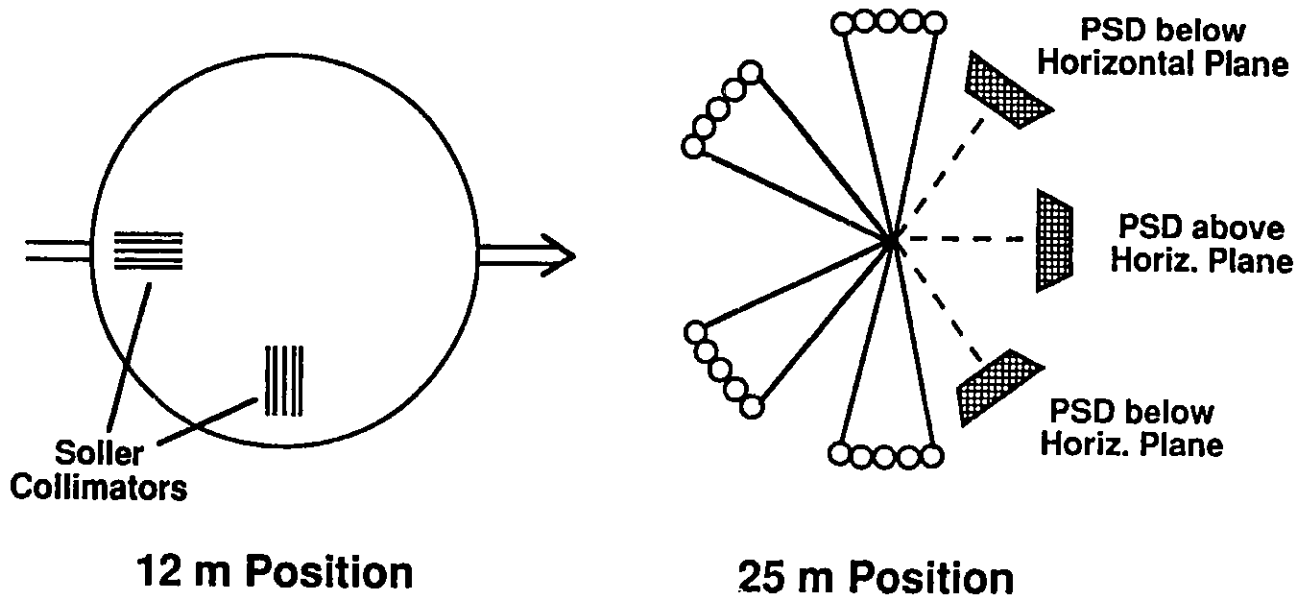
Figure V.2.1-4 Schematic Representation of the RSD, Showing the 12-m and 25-m Sample Positions.

Table V.2.1-3 Parameters for the RSD

Parameter	Source-Sample Distance (m)	
	12	25
Source repetition rate (Hz)	30	30
Moderator material	liquid CH_4[a]	liquid CH_4[a]
Sampling volume (mm^3)	2 x 2 x 2	2 x 2 x 2
Wavelength range (Å)	0.4-9	0.4-4.5
Scattering angle (°)	90	70.5, ±90, and ±150
Sample-detector distance (m)	1.5	1.5-3
Resolution $\Delta d/d$, fwhm (10^{-3})	5.5	3
Experiment time (min)	50	9

[a] Or room-temperature H_2O.

2.1.2.3 VSPD — Very-Small-Sample Powder Diffractometer

The solid-state science community has been hampered by sample-size limitations. Typically, chemists produce materials in 10-100 mg quantities, which are too small for neutron scattering measurements at most facilities. The very-small-sample powder diffractometer addresses this situation. This instrument is located 12 m from the source, and has a 0.75-m sample-to-detector distance and 0.635-cm-diameter detectors. The secondary flight path is similar to a reduced-size version of the SEPD flight path shown in Figure V.2.1-1. The detectors are placed at 0.75 m to increase the solid angle by a factor of four compared to the current SEPD for the same area coverage of detectors. Some of the detectors are placed above and below the scattering plane on Debye-Scherrer cones in order to cover this solid angle. Focusing techniques in the incident beam provide further increases in data rate. The 0.635-cm-diameter detectors match the 0.635-cm-diameter sample size. Monte Carlo simulations for this configuration indicate that the resolution at $\pm 150°$ and $\pm 90°$ is degraded less than 10% relative to that of the SEPD at IPNS Upgrade (see Table V.2.1-1). This combination of resolution and data rate allow Rietveld-quality data sets from 100-mg samples in ~70 min. Larger-diameter samples can also be used in this instrument, but the resolution is noticeably degraded, as much as 20-30% for 1.27-cm-diameter samples.

2.1.3 Other Possibilities

These instruments are not in the reference set and will probably not be among the initial complement at IPNS Upgrade. It is expected that instruments of these types will evolve and might be added at a later date.

2.1.3.1 LFHRPD — Low-Frequency High-Resolution Powder Diffractometer

A diffractometer having the same parameters as the HRPD can be located at the 10-Hz target station rather than the 30-Hz station. In this case, time-averaged incident fluxes are a factor of two lower than those indicated in Table V.2.1-2, but the maximum wavelength is tripled to ~7 Å. Requirements for bandwidth-limiting choppers are considerably relaxed. This instrument can be considered either as an alternative to the HRPD or as a supplement to the HRPD if the demand is sufficiently great to support two instruments in this resolution range.

2.1.3.2 LWPD — Long-Wavelength Powder Diffractometer

This diffractometer is optimized to use cold neutrons with $\lambda > 2$ Å to study magnetic structures and crystal structures with large unit cells over the range $2 \text{ Å} < d < 10 \text{ Å}$ while benefiting from the high resolution afforded by backscattering. This instrument views a liquid hydrogen moderator. It is designed for high count rates, fast enough for real-time studies in favorable cases such as real-time studies of absorption in zeolites.

2.1.3.3 PNPD — Polarized-Neutron Powder Diffractometer

This diffractometer has parameters similar to the SEPD. It has a source-sample distance of 12 m and a sample-detector distance of 1.5 m. It is outfitted with detectors at a number of scattering angles ($\pm150°$, $\pm90°$, $\pm60°$, etc.), thus allowing access to similar ranges of d-spacing. In addition, either nickel guides with a critical angle of 0.1° per Å or supermirrors with a critical angle of 0.3° per Å are used to polarize the incident beam. If full polarization analysis is desired, supermirrors can be placed in the scattered beams as well. Soller collimators can be used to enhance resolution. Polarized neutrons and polarization analysis are useful in the study of magnetic structures. They can also be used to discriminate against incoherent scattering backgrounds from hydrogenous samples, considerably extending the types of samples that can be studied.

2.1.3.4 UHPD — Ultra-High-Pressure Diffractometer

This instrument utilizes a press to apply pressures in excess of 250 kbar to sample sizes of a few cubic millimeters. Carefully designed gaskets between the press anvils allow neutrons in and out of the sample. Scattered neutrons can be detected at only a few discrete angles because of the collimation provided by the anvils, so this technique only works on a TOF instrument. Although the UHPD extends neutron powder diffraction capability to a previously inaccessible pressure regime, the small beams and limited solid angle for detection make this a low-data-rate instrument.

2.1.3.5 UHRPD — Ultra-High-Resolution Powder Diffractometer

This instrument is designed to achieve a backscattering resolution of $1\text{-}3 \times 10^{-4}$ and requires an incident flight path of ~100 m. Experience with the HRPD at ISIS has shown that such high resolution is advantageous for the investigation of many systems.[3] During the initial stages of operation of that instrument many samples were not of sufficient quality to make use of its resolution. Scientists have now improved the quality of their samples so that many samples have intrinsic peak widths comparable with the ISIS-HRPD instrumental resolution. In such cases, structure refinements of an unmatched quality can be achieved, and signal-to-noise ratios are improved enough to allow the study of hydrogenous samples by powder techniques. Strains, particle-size distributions, stacking faults, and twin boundaries in samples can be studied by using such an instrument.

2.1.4 Powder Diffractometer Summary

The diffractometers described in Sections V.2.1.1 and V.2.1.2 are taken as a reference set that spans the range of capabilities required for most anticipated powder diffraction experiments. These are the "workhorse" instruments, and are almost certain to be included among the initial 24 instruments. Their capabilities are summarized in Table V.2.1-4. Particularly exciting are the

Table V.2.1-4 Reference Set of TOF Powder Diffractometers at IPNS Upgrade

Instrument	Application/Special Feature	Range for d (Å)	Best Δd/d (%)	Measurement Time (min)
VSPD	Very small samples (10-100 mg)	0.2-17	0.35	70
SEPD[a]	High intensity	0.2-17	0.35	3
GPPD[b]	Medium resolution (excellent at 90°)	0.2-9	0.2	10-60
HRPD	High resolution	0.2-5	0.08	50
RSD	Residual stress			
	12-m position	0.3-6	0.55	50
	25-m position	0.2-3	0.30	10

[a] Transferred from IPNS with little change.

[b] Transferred from IPNS with flight-path modified.

small-sample capabilities, the very high resolution available at 90° which is essential for much of the work in specialized sample environments, and the short data-collection times, which make possible real-time studies of many types of systems.

A number of additional, more specialized, diffractometers are outlined in Section V.2.1.3. These instruments will probably not be among the initial complement at IPNS Upgrade, but might be added at a later date.

2.2 SMALL-ANGLE DIFFRACTOMETERS

2.2.1 Transfer of Existing IPNS Instruments

2.2.1.1 SAND — General-Purpose Small-Angle Neutron Diffractometer

The SAND is a new small-angle diffractometer at IPNS, shown in plan view in Figure V.2.2-1. As can be seen in the figure, the sample chamber is large, making it possible to accommodate a wide variety of ancillary equipment. Table V.2.2-1 lists parameters of the SAND at IPNS and IPNS Upgrade. The SAND has two automatically interchangeable sets of converging multiple-aperture collimators, so it can operate in either a low-resolution mode or a high-resolution mode to allow optimal trade-off between Q-range and intensity for a given experiment. It also has a cooled MgO filter to remove fast neutrons from the incident beam. This filter can be removed if a t_0 chopper, as described in Section V.3.1, is to be used. A chopper is also provided to eliminate most of the background caused by delayed neutrons. A 40×40-cm^2 area detector and a bank of 65 linear-position-sensitive detectors (LPSDs) with a total active area $\sim\!60 \times 70$ cm^2 are used.

An important feature of the SAND is the extremely wide Q-range it covers, even when restricted to wavelengths above the Bragg cutoff for crystalline samples. This entire Q-range can be measured with only one instrument setting. This is particularly important for the study of anisotropic scatterers and for kinetic or other time-dependent studies. The bank of LPSDs extends the maximum scattering angle up to 36°, making a huge improvement in the counting statistics in the higher-Q portion of the data. The SAND is exceptionally good for studies that can benefit from the wide Q-range.

Cooled
MgO Filter

Beam
Monitor

Mask and Window
(optional)

Automated
Beam Stop
Positioner

Sample
Chamber

Insertable
Transmission
Monitor

^{3}He Area PSD

NEUTRON BEAM

Background
Chopper

Converging
Soller
Collimators

Side-Access
Track for
Massive Sample
Environments

Evacuated
Flight Path

Bank of LPSDs

1 m
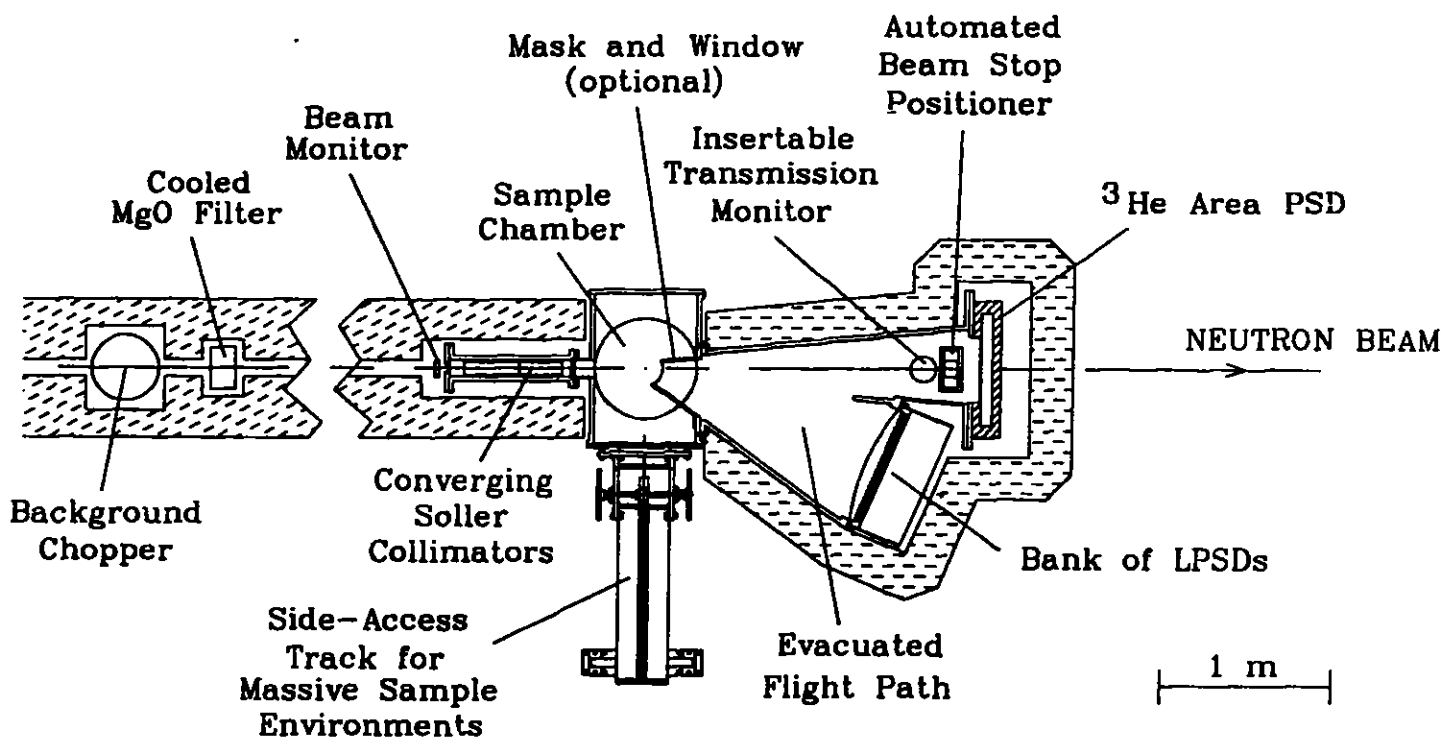
Figure V.2.2-1 Plan View of the SAND at IPNS Upgrade.

Table V.2.2-1 Parameters for the SAND

Parameter	IPNS	IPNS Upgrade
Moderator	decoupled liquid H_2	coupled liquid H_2
Source-to-sample distance	9.0 m	12 m
Sample-to-area-detector distance	2.0 m	
Sample-to-LPSD distance	1.524 m	
Beam size at sample	2.0-cm diameter	$\leq$ 2-cm diameter
Area detector		
active area	40×40 cm^2	a
active thickness	2.5 cm	a
resolution	4-6 mm	a
fill	2.6 atm ^{3}He plus	a
	1.4 atm CF_4	a
encoding	rise time, 256×256	a
LPSDs		
active volume per detector	1.1 cm diameter $\times$ 60 cm long	
number of detectors	65	
resolution	1-2 cm along detector	
fill	~10 atm ^{3}He	
encoding	charge division, 64 segments/ detector	
max. scattering angle	36°	
Focusing collimators, converging on area detector		
coarse	0.0034 rad fwhm	
fine	0.0014 rad fwhm	
Wavelength range	1-14 Å (5-14 Å for crystalline samples)	~1-20 Å (~5-20 Å for crystalline samples)
Q_{max}		
λ_{min} = 1.0 Å (noncrystalline)	>2.0 Å^{-1}	
λ_{min} = 5.0 Å (crystalline)	~0.6 Å^{-1}	
Q_{min}		
coarse collimation	~0.004 Å^{-1}	~0.0028 Å^{-1}
fine collimation	~0.002 Å^{-1}	~0.0014 Å^{-1}
Measurement time		
coarse collimation	0.5-17 h	0.01-0.3 h
fine collimation	3-100 h	0.06-2 h

a New detector with much faster encoding is required for the low-resolution mode.

The SAND views a coupled liquid H_2 moderator on the 10-Hz target. The moderator-to-detector distance is ~12 m. The useful wavelength is ~1-20 Å, limited on the short-wavelength end by the incident-beam filter and on the long-wavelength end by the low neutron flux. Frame overlap occurs for wavelengths >30 Å, so frame-overlap is not a significant background problem. Table V.2.2-1 indicates which instrument parameters are changed at IPNS Upgrade. The 300-400-μs pulse-width of coupled H_2 moderators gives $\Delta\lambda/\lambda \leq 10\%$ for the wavelength range of this instrument and so does not have a significant effect on the instrument resolution.

At IPNS Upgrade, the SAND count rate is increased by a factor of $\simeq$ 56 due to a factor of 25 from the improvement in source current and a factor of 4 from the improved moderator, reduced by $(9/12)^2$ due to the increased flight path. It is possible to operate SAND with an even higher resolution and still obtain reasonable data rates at IPNS Upgrade.

Instantaneous count rates on the SAND area detector in the low-resolution mode are estimated to be as high as $\simeq$ 150,000 counts/sec at IPNS Upgrade. The present SAND detector is not suitable at such high data rates. In the high-resolution mode, data rates are reduced by a factor of ~6, so this detector is adequate for use at IPNS Upgrade for most samples in this mode.

A higher-speed area detector will result in enhanced operation in the high-resolution mode in some cases and will permit operation in the low-resolution mode to obtain the higher data rates required for some kinetic studies. The development of a higher-resolution area detector with the same effective area coupled with the development of a tighter collimation system is necessary to allow the low-Q limit of the instrument to be significantly improved, so that larger structures can be studied.

2.2.2 New Reference Set Instruments

2.2.2.1 HRSAND — High-Resolution Small-Angle Neutron Diffractometer

This small-angle diffractometer provides a lower Q_{min} and better resolution than that given by the SAND. Based on an analysis of intensities, a Q_{min} of ~0.0005 Å^{-1} provides acceptable data rates, but this is essentially the limit to which the multiple-converging-aperture TOF small-angle-diffractometer concept can be pushed at IPNS Upgrade. A schematic layout of an instrument designed to achieve this Q_{min} is shown in Figure V.2.2-2, and Table V.2.2-2 gives some of the parameters of this instrument. The sample chamber is identical to that on the SAND to provide easy interchange of ancillary equipment.

A gas-proportional-counter area detector is used because of the excellent background characteristics of such detectors. The sizes of gas detectors with high position resolution are limited by technology. Current developments in microstrip gas detector technology[4,5] show promise of being able to provide the desired performance, but if they cannot, the detector size may have to be reduced in order to achieve the desired resolution.
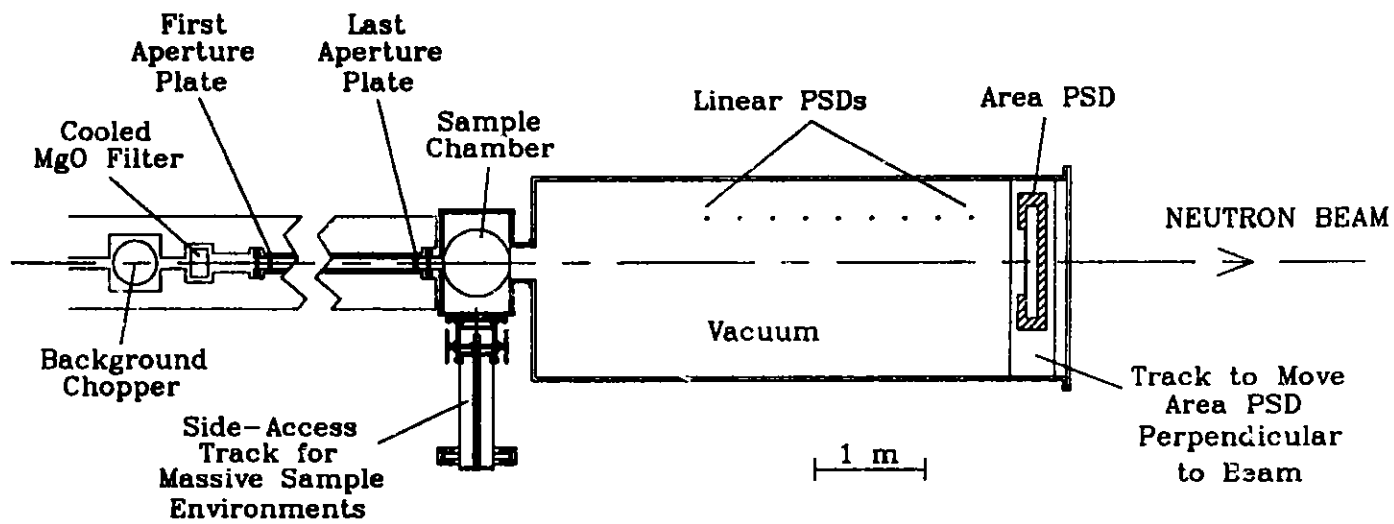
Figure V.2.2-2 Schematic Representation of the HRSAND.

Table V.2.2-2 Parameters for the HRSAND

Parameter	Value
Moderator	coupled liquid H_2
Source repetition rate (Hz)	10
Source-to-sample distance (m)	20
Collimation	converging multiple-aperture
Source-to-first-collimator-aperture distance (m)	6
Diameter of first apertures (cm)	0.784
Source-to-last-collimator-aperture distance (m)	19.5
Diameter of last apertures (cm)	0.227
Number of converging aperture channels	20-40
Sample-to-area-detector distance (m)	5
Beamstop diameter (cm)	0.84
Wavelength range (Å)	1-15[a]
Beam diameter at sample (cm)	2.0
Required resolution of area detector (mm)	~2 near beam[b]
Approximate size of area detector (cm)	60
Maximum scattering angle on area detector (°)	
on-axis	3.4
off-axis	6.8
Scattering angles for LPSDs (°)	~5-15
Q_{min} (Å⁻¹)	~0.0005
Q_{max} (Å⁻¹)	
area detector on-axis	~0.07-0.2
area detector off-axis	~0.15-0.4
Data rate	roughly like present SAD

[a] 5-15 Å for crystalline samples.

[b] Can be worse elsewhere.

The incident multiple-aperture converging collimation system is designed to account for the gravitational drop of the longer-wavelength neutrons. The sample-detector distance is sufficiently short that the gravitational drop of the scattered neutrons is not a significant problem. A coarser collimator can be substituted when the full Q resolution is not required. A background-suppression chopper is provided. The maximum wavelength is 15.8 Å before frame-overlap occurs for the 25-m total distance on the 10-Hz source. Wavelengths longer than this are removed by the background-suppression chopper. Because this instrument is intended to complement the SAND, no attempt is made to duplicate the extensive high-Q coverage obtainable with the latter instrument. However, many experiments focusing on the low-Q region can benefit from some coverage at higher Q, so a series of LPSDs is placed along one or both sides of the flight path to supplement the high-scattering-angle data, as shown schematically in Figure V.2.2-2.

2.2.2.2 SPSAND — Special-Purpose Small-Angle Neutron Diffractometer

One beamline viewing the coupled H_2 moderator on the 10-Hz source is reserved for special projects in small-angle diffraction. These can be either special experiments requiring specific instrument configurations not found on the other small-angle diffractometers or projects aimed at developing new small-angle scattering techniques. Among the possibilities are experiments using polarized neutrons, resonance small-angle scattering,[6] the study of inelasticity effects in small-angle scattering, and the development of techniques for reaching even lower Q_{min}.

This instrument is typically configured for one type of study for one or more months at a time, then reconfigured for a different study. It is not part of the user program in the usual sense but is open to proposals for extended use in specific configurations. Short experiments with a special configuration can be accommodated whenever that configuration is set up for other purposes.

The instrument is modular and very flexible. It includes shielded areas for choppers, a prompt-pulse-suppression chopper and other specialized choppers, a modular beamline and shielding, easily changeable collimation, one or more area detectors, and a large reserved section of floor space extending to ~40 m from the source. Development of some components are deferred until the need arises.

2.2.3 Other Possibilities

These instruments are not in the reference set and will probably not be among the initial complement at IPNS Upgrade. It is expected that instruments of these types will evolve and might be added at a later date.

2.2.3.1 QSSAND — Quasi-Steady-State Small-Angle Neutron Diffractometer

The high time-averaged cold-neutron flux available from the large coupled liquid H_2 moderator on the 30-Hz target station makes it practical to treat this as a QSS source of cold neutrons. A traditional reactor-type small-angle diffractometer can be placed on a beamline viewing this moderator. The 30-m small-angle diffractometers[7] operating at the National Institute of Standards and Technology (NIST) are state-of-the-art models for such an instrument. A velocity selector is used to define a variable wavelength band of 7-30% $\Delta\lambda/\lambda$ that is centered at the desired wavelength. Removable sections of the incident-beam guide tube are used to vary the incident-beam divergence, and a large, movable area detector on a track is used to detect the scattered neutrons with the desired resolution. An ILL-type area-position-sensitive detector capable of ~20,000 counts/sec and having a resolution of ~1 cm and an overall size of ~65 × 65 cm^2 is used. The expected Q-range is 0.001 to 0.6 $Å^{-1}$. The pulses from this moderator are ~1 ms long. In normal operation the counting electronics are gated on only during the time neutrons of the desired wavelength that are elastically scattered from the sample reach the detector. This provides discrimination against background and against most of the neutrons inelastically scattered from the sample. The electronics can also be set to count in broad time-slices over a much larger time window, to allow detailed concurrent measurement of both the elastically and inelastically scattered neutrons. This latter capability is useful in the study of samples containing hydrogen or deuterium, where inelastic scattering effects are known to be substantial. This energy-discrimination ability comes at essentially no cost in intensity, unlike the case of steady-state small-angle neutron scattering instruments. The pulsed nature of the source also makes possible measurements using pulsed sample environments synchronized to the data collection, with little or no loss in intensity.

2.2.3.2 DCSAND — Double-Perfect-Crystal Bonse-Hart Small-Angle Neutron Diffractometer

This instrument extends the minimum Q that can be accessed in small-angle-scattering experiments down to ~10^{-5} $Å^{-1}$ in some cases. It is constructed on one of the quasi-steady-state (QSS) beamlines, looking at a fully-coupled liquid H_2 moderator on the 30-Hz source. It can be easily placed upstream from the Cold-Neutron Quasi-Steady-State Triple-Axis Spectrometer (QSTAXC) (Section V.2.6.2.3) by using a premonochromator crystal to select a band of wavelengths from the guide serving the triple-axis spectrometer. The DCSAND is modeled after similar instruments at reactor sources,[8] and is shown schematically in Figure V.2.2-3. The perfect-crystal monochromator and analyzer select not only a very precise wavelength, but also a precise direction of the neutron beam. The intensity scattered at different angles is scanned by rotating the analyzer crystal through very small angles of typically less than one minute of arc.

Such instruments have been operated successfully at low-flux reactors, so there is no doubt that such an instrument can be successfully operated at IPNS Upgrade. The time-structure of this QSS source allows the detection electronics to be gated to minimize backgrounds (duty
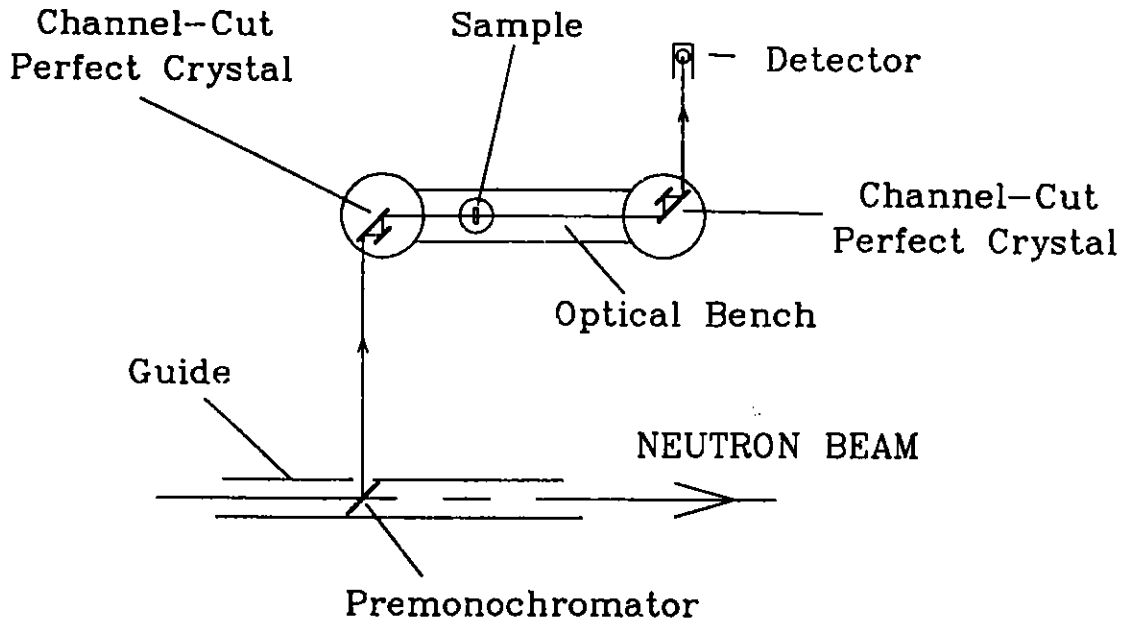
Figure V.2.2-3 Schematic Representation of the DCSAND.

cycle of less than 1:30) and allows the separation of concurrently collected spectra from the different orders of the monochromator and analyzer crystals. Although the time-averaged flux obtained with the DCSAND is considerably below that of a similar instrument at a high-flux reactor, this instrument is a useful complement to the other small-angle diffractometers discussed here.

2.2.4 Small-Angle Diffractometer Summary

The very high data rates and broad Q-range of the SAND offer new opportunities in the study of small samples and in real-time studies of kinetic or other time-dependent effects in many types of materials. The HRSAND is a state-of-the-art instrument for the study of larger structures using lower Q_{min} than can be accessed on any other general-purpose small-angle neutron diffractometer in the United States. The flexibility offered by the SPSAND to be reconfigured for different types of experiments permits the exploration of totally new scientific areas, such as resonance small-angle scattering and the use of polarized neutrons in small-angle scattering experiments. The three small-angle neutron scattering instruments described in Sections V.2.2.1 and V.2.2.2 and summarized in Table V.2.2-3 form a reference set that covers a broad range of capabilities. They satisfy the requirements for virtually all types of current small-angle scattering experiments, and they also provide opportunities for many new types of experiments.

The two quasi-steady-state small-angle diffractometers provide the capability for extending to even smaller Q_{min} for some types of experiments. They might be better optimized for some other types of experiments, such as the study of inelastic effects in small-angle scattering, than are the three TOF small-angle diffractometers in the reference set. Instruments of these types, although probably not among the initial complement of instruments at IPNS Upgrade, will be considered in greater detail for possible inclusion at a later date.

2.3 OTHER DIFFRACTOMETERS

2.3.1 Transfer of Existing IPNS Instruments

2.3.1.1 GLAD — Glasses, Liquids, and Amorphous Materials Diffractometer

The GLAD is designed to study diffraction from liquids, glasses, and amorphous materials.[9] It covers the Q-range of ~0.05 Å^{-1} to ~50 Å^{-1} using wavelengths from 0.1 to 4 Å. Measurements at each Q value are made using the smallest scattering angles and shortest wavelengths practical, in order to minimize the inelasticity corrections required. Considerable attention has been paid to the shielding in the GLAD, so that the backgrounds are low even at wavelengths below 0.1 Å. Converging Soller collimators focused on the detector locus allow the

Table V.2.2-3 Reference Set of TOF Small-Angle Diffractometers at IPNS Upgrade

Instrument	Application/Special Feature	Q_{min} (Å^{-1})	Q_{max} (Å^{-1})	Measurement Time (min)
SAND[a]	General purpose (wide Q-range)	0.002	2	1-90
HRSAND	High resolution	0.0005	0.4	60-1800
SPSAND	Reconfigurable for special purposes	-----------	variable	-----------

[a] Transferred from IPNS with little change.

use of relatively large samples with negligible sample-size contribution to the resolution. A large scattering solid angle is covered with LPSDs in order to achieve high data rates while maintaining good Q resolution. The GLAD is designed to utilize 408 such LPSDs, but only 235 are installed at present. Figure V.2.3-1 shows the GLAD design, and Table V.2.3-1 lists some of the performance parameters expected at IPNS Upgrade.

The GLAD can be moved to the 30-Hz target station with essentially no changes, although it is desirable to increase the detector complement to the full 408 LPSDs and to develop faster position encoding for these detectors. The source-sample distance to the high-resolution sample position is ~22 m at IPNS Upgrade. This provides greater time-of-flight separation between the prompt pulse and the 0.1-Å neutrons and allows more room for background-suppression choppers. This increased distance also provide much easier access at the sides of the instrument. A cold moderator is selected because this helps to minimize the inelasticity corrections. The data-rate gain is a factor of ~11 relative to IPNS. Frame-overlap is not a problem, but a bandwidth-limiting chopper can be inserted if necessary. The GLAD is designed to allow the use of an energy-selecting Fermi chopper in the incident beamline in special cases where it is desired to perform a detailed separation of the elastic and inelastic scattering.

Maximum instantaneous data rates on the GLAD occur at the shortest wavelength used. For an intensely-scattering sample at $\lambda = 0.1$ Å maximum instantaneous rates are ~1,000 counts/sec per LPSD at scattering angles above ~10°. The 1,000-counts/sec rate with the present encoding time of 8 μsec leads to dead-time losses of 0.8% at IPNS, which is acceptable. However, instantaneous rates at the IPNS Upgrade 30-Hz target station are a factor of 6 higher, so maximum dead-time losses reach ~5% or more at the shortest wavelengths for intensely-scattering samples at IPNS Upgrade. Until faster encoding systems can be developed, the variable-aperture device available on the GLAD can be used to reduce the beam size for intensely-scattering samples if necessary.

2.3.1.2 SCD — General-Purpose Single-Crystal Diffractometer

The SCD,[10] shown schematically in Figure V.2.3-2, is 10 m from the target at the 30-Hz target station. A new area detector is required to cope with the data rates at IPNS Upgrade. The instrument is upgraded to permit sample-to-detector distances in the range of 30 to 60 cm and detector angles of 60°, 90°, and 120°. A variable upstream collimator reduces the viewed portion of the moderator from 10-cm diameter to 5-cm diameter to improve the incident-beam collimation when desired. New shielding is required around the sample area. Some possible instrument configurations are described in Table V.2.3-2.

Configuration A is identical to the configuration of the SCD at IPNS. This configuration is used for small samples. The resolution required for background-to-background peak integration is five times $\Delta Q/Q$, or 0.045, which permits measurement to $d_{min} = 1$ Å for a 22-Å

Upstream
Sample
Position

Evacuated
Flight Path

Access
Flange

Detector Bank
(one of ten)

Downstream
Sample
Position

Preamps

Variable
Aperture

LPSDs

NEUTRON BEAM

Beam
Monitor

Soller
Collimators

Removable
Detector
Shielding

1 m
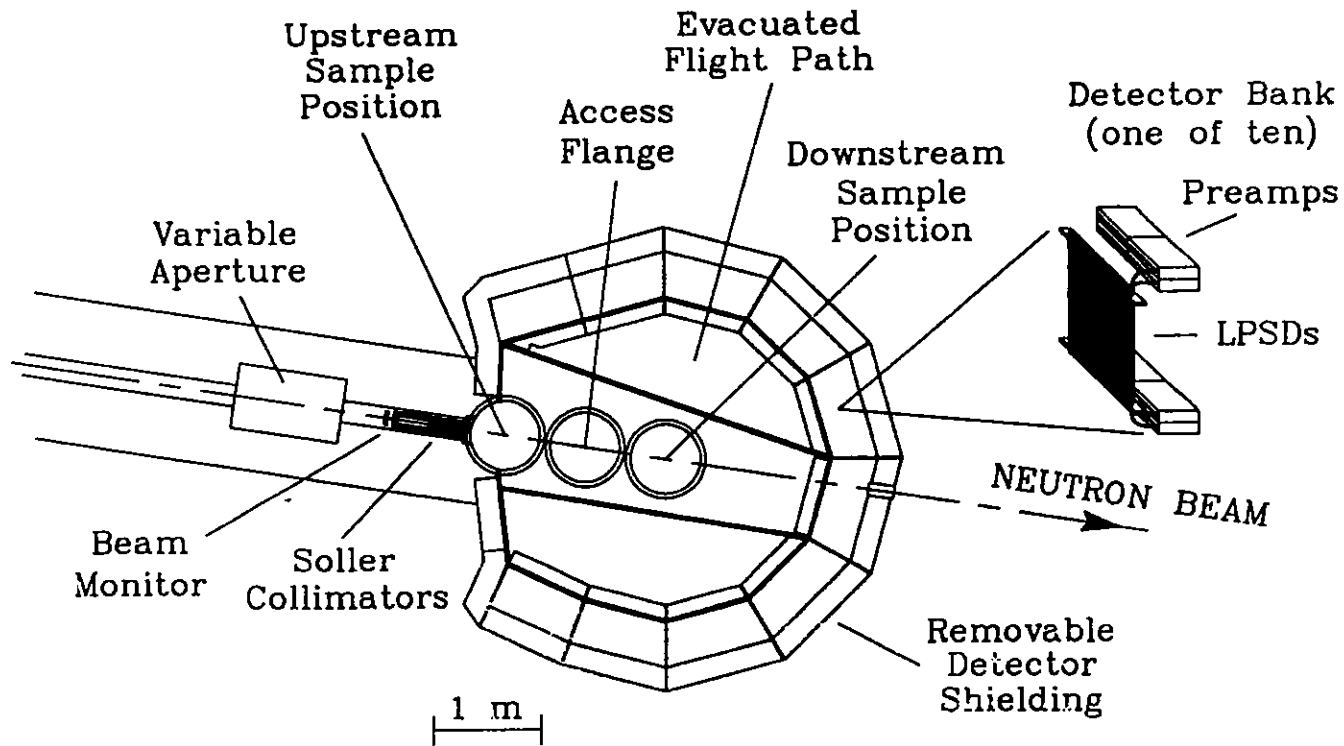
Figure V.2.3-1 Plan View of the GLAD.

Table V.2.3-1 GLAD Parameters at IPNS Upgrade

	Sample Position	
Parameter	High Resolution	High Intensity
Source-sample distance (m)	22	23.5
Source repetition rate (Hz)	30	30
Moderator material	liquid CH_4	liquid CH_4
Sample volume (cm^3)	3	3
Wavelength range (Å)	0.1-4.0	0.1-4.0
Scattering angles (°)	~2.5-95	~5-150
Sample-detector distance (m)	~3.0-1.0	~1.5 for all LPSDs
LPSD diameter (cm)	1.1	1.1
LPSD length (cm)	60	60
LPSD ^{3}He fill pressure (atm)	10	10
Collimation	converging Soller	converging Soller
Beam size at sample (cm^2)	1.2 × 1.2	0.6 × 0.6
Minimum accessible Q ($Å^{-1}$)	0.07	0.14
Maximum accessible Q ($Å^{-1}$)	92	120
Resolution $\Delta Q/Q$ (fwhm)	~0.1 at Q = 0.07	
	<0.012 for Q > 5	
Typical time to measure one data set (min)	20-50	10-30
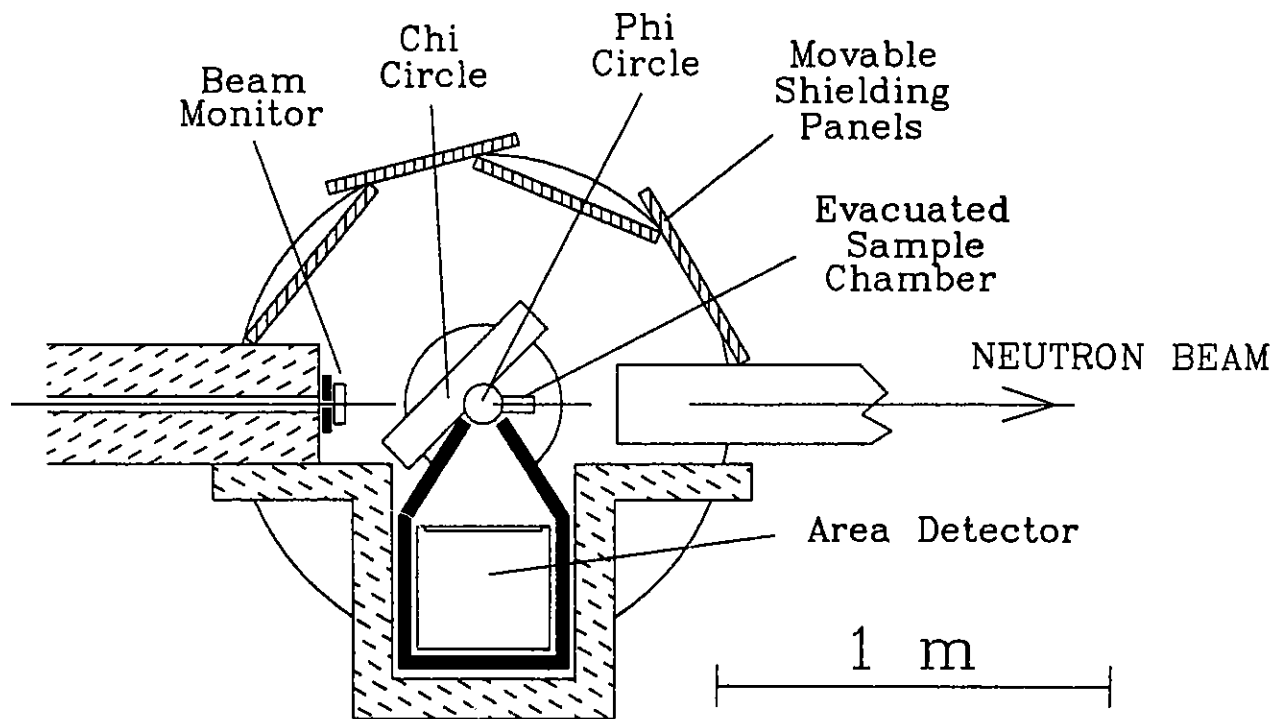
Figure V.2.3-2 Schematic Representation of the SCD.

Table V.2.3-2 SCD Parameters at IPNS Upgrade

Parameter	Configuration	
	A	B
Source-sample distance (m)	10	10
Sample-detector distance (cm)	32	60
Moderator size (cm)	10	5
Detector size (cm^2)	30 × 30	30 × 30
Detector type	Anger	Anger
Detector resolution (mm)	3	3
Detector dead time (μsec)	~3	~3
Wavelength range (Å)	~0.7-10	~0.5-10
Sample size (mm^3)	1 × 1 × 1	1 × 1 × 1
Crystal mosaic (°)	0.1	0.1
Total Δ2θ (°)	0.8	0.5
Nominal detector angle (°)	90	120
Δt/t	0.005	0.005
ΔQ/Q	0.009	0.0055
Data-rate gain over IPNS	40	3

lattice repetition. Texture measurements, which currently require 1-2 days for each sample, can be obtained on 20 samples per day. This permits a much more precise analysis of the effects of small, systematic changes in processing parameters on the texture of samples, such as high-T_c superconducting wires. For magnetic studies of single crystals, the detector can be rotated to the 60° angle to obtain low-Q data.

Configuration B is optimized for high resolution and high Q. It permits background-to-background peak integration of a 26-Å lattice for $d_{min} = 1$ Å. Alternatively, for a 10-Å lattice, a minimum d-spacing of 0.3 Å can be achieved with neutron wavelengths of 0.5 Å.

Frame-overlap occurs at ~12 Å for 30-Hz operation at the ~11-m source-detector distance. Thus, there are no significant frame-overlap problems for this instrument.

At IPNS maximum dead-time losses are $\leq 1\%$ for most samples on the SCD, with a few samples approaching 5%. Scaling to IPNS Upgrade implies that detector dead-time is a problem in configuration A for many samples if the present Anger detector is retained for this instrument. Development of a much faster area detector having dead-time of 0.5 μsec or less is necessary for full utilization of the capabilities of this instrument.

2.3.2 New Reference Set Instruments

2.3.2.1 HQSCD — High-Q Single-Crystal Diffractometer

This instrument is a higher-resolution, higher-Q-range complement to the SCD. Improving the resolution and extending the range to higher Q is important for many types of studies. Some examples are magnetostriction in MnF_2 with a shift of 0.002 Å; conformational disorder in organic superconductors, such as β-$(BETD-TTF)_2I_3$; analysis of anharmonic motion; resolution of the twin components of the low-temperature phase of high-T_c superconductors; deformation density mapping in combination with high-Q x-ray data; resolving satellite peaks near fundamental Bragg peaks; and Huang scattering. The improved resolution is also advantageous for diffuse scattering studies. Table V.2.3-3 gives some of the parameters for this instrument. The HQSCD has a geometry similar to the SCD shown in Figure V.2.3-2. The detector technology to be used is at present uncertain, since it is desirable to have a detector similar to the present SCD Anger detector but with a factor of two better resolution. If this is not possible, a larger detector placed farther from the sample can also be used. Data rates are down by at least a factor of 10 from those on SCD, so dead-time problems are not severe.

Table V.2.3-3 Parameters for the HQSCD

Parameter	Value
Moderator	liquid CH_4 or liquid H_2O
Source frequency (Hz)	30
Source-sample distance (m)	30
Sample-detector distance (cm)	30 (70)[a]
Moderator size (cm)	10
Detector size (cm^2)	30 × 30 (or 4 dets, each 30 × 30)[a]
Detector type	to be determined
Detector resolution (mm)	1.5 (3)[a]
Detector dead time (μsec)	~3
Wavelength range (Å)	~0.3-4
Sample size (mm^3)	1 × 1 × 1
Crystal mosaic (°)	0.1
Total $\Delta 2\theta$ (°)	0.8
Nominal detector angle (°)	centered at ~90 (or ~120)
$\Delta Q/Q$	0.004 (or 0.003)

[a] Depends on detector capabilities. One 30 × 30 cm^2 detector with 1.5-mm resolution is desirable, but four 30 × 30 cm^2 detectors with 3-mm resolution placed twice as far from the sample are roughly equivalent in data rate and resolution (but not in signal/background).

2.3.3 Other Possibilities

This instrument is not in the reference set and will probably not be among the initial complement at IPNS Upgrade. It is expected that such an instrument might be added at a later date.

2.3.3.1 PCSCD — Single-Crystal Diffractometer for Protein Crystallography

Neutron diffraction from single crystals of proteins plays an important complementary role in structural biology with respect to x-ray diffraction and NMR. Neutron sources are inherently less intense than the newer synchrotron x-ray sources, but neutron diffraction permits accurate location of a protein structure's hydrogen atoms, which is difficult with x-ray methods.[11,12] The chemistry of hydrogen dominates much of enzyme kinetics. Hydrogen structure is also crucial because such highly specific intermolecular recognition phenomena as DNA base pairing, genetic regulation, and expression require hydrogen bonding.

Calculations indicate that suitable data down to $d_{min} = 1.5$ Å on small proteins can be measured in a few weeks. The neutron data are complementary to the x-ray structural data. In virtually all cases, high resolution ($d_{min} = 1.2$ Å) x-ray data will exist, and this reduces the precision required of the neutron data to obtain suitable hydrogen structural results. This estimate assumes a crystal that is 50% deuterated, with unit cell axes of about 50 Å. It also assumes nearly 4π detector coverage about the crystal. We propose to perform feasibility experiments on one or both of the single-crystal diffractometers (SCD or HQSCD) when IPNS Upgrade is operating. If the experiments confirm the calculations, the design and construction of an instrument optimized for protein crystallography can be initiated.

2.3.4 Summary of Other Diffractometers

The three instruments GLAD, SCD, and HQSCD form a reference set of instruments for the study of neutron diffraction from noncrystalline materials and from single crystals. These three instruments are summarized in Table V.2.3-4.

Table V.2.3-4 Reference Set of Additional TOF Diffractometers at IPNS Upgrade

Instrument	Application/ Special Feature	Range for Q (Å^{-1})	ΔQ/Q (%)	Measurement Time (min)
GLAD[a]	Glass, liquids, amorphous materials	0.07-120	1.2-10	10-50
SCD[a]	Single crystals, general purpose	0.9-17	0.6-0.9	20-200
HQSCD	Single crystals, high real-space resolution	2-30	0.4	~200

[a] Transferred from IPNS with little change.

2.4 REFLECTOMETERS

2.4.1 Transfer of Existing IPNS

2.4.1.1 POSY-I — Polarized-Neutron Reflectometer

At IPNS, the POSY-I and POSY-II reflectometers are located on separate beams brought out of the same beam port. A diagram of the present configuration is shown in Figure V.2.4-1. Since reflectometers use relatively small beams, one beam port at IPNS Upgrade also has separate beams supporting two separate reflectometers. At IPNS Upgrade these reflectometers are placed at a source-sample distance of ~18 m at the 10-Hz target station, so the two beams have much greater separation at the sample position than is the case at IPNS. The mounting table supporting the optical components of the two reflectometers must be redesigned. Because of the increased spatial separation between the instruments, a separate optical table is used for each of the two reflectometers in this case. One of these reflectometers is configured as the present POSY-I, the polarized neutron instrument, and uses the components from this instrument.[13] It has a vertical sample surface fed by a vertical-slit collimation system, includes a high-resolution Drabkin resonant spin flipper, and is equipped with complete polarization analysis. A background-suppression chopper can be used to remove the prompt pulse and frame-overlap neutrons or delayed neutrons if necessary. For typical samples, this instrument can measure polarization-dependent reflectivities down to $R = 10^{-6}$ in 1-2 h.

The second reflectometer sharing this beam port is a new high-data-rate reflectometer, which is discussed in Section V.2.4.2.1.

2.4.1.2 POSY-II — General-Purpose Reflectometer

A second beam port for reflectometers at the 10-Hz target station provides three separate beams. One of these beams is configured essentially as the present POSY-II instrument,[14] but it has a horizontal sample surface and horizontal-slit collimation so it can be used to study liquid surfaces as well. Although it uses many of the components of the present POSY-II, this instrument requires a new design. It is also located at a source-sample distance of ~18 m. A background-suppression chopper can be used to remove the prompt pulse and frame-overlap neutrons or delayed neutrons if necessary. This instrument is able to measure reflectivities down to $R = 10^{-7}$ in 1-2 h from a wide variety of liquid and solid samples.

One of the other two beams sharing this beam port is devoted to a new reflectometer that is designed to study scattering at grazing incidence, as discussed below. The third beam is fed to an optical bench for experimentation to develop components and techniques. This is also discussed below.
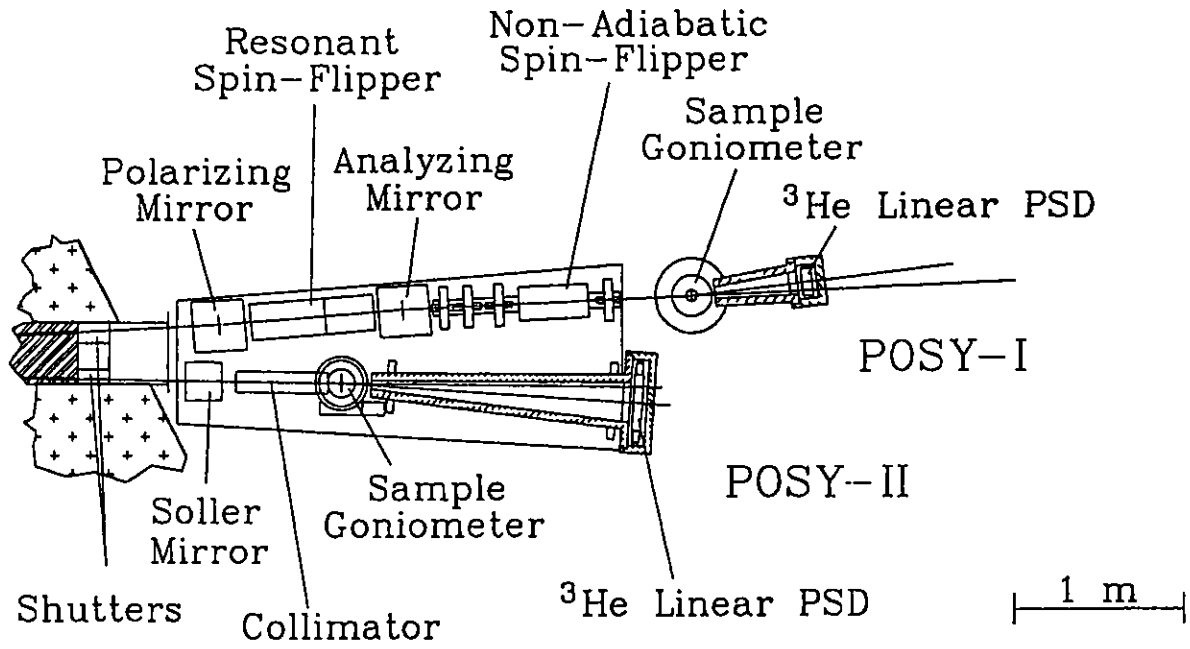
Figure V.2.4-1 Configurations of the POSY-I and POSY-II at IPNS.

2.4.2 New Reference Set Instruments

2.4.2.1 HIREF — High-Intensity Reflectometer

This reflectometer is on a separate beam coming from the same beam port that supports the upgraded POSY-I reflectometer. It is located at a source-sample distance of ~18 m and has a wide vertical slit, collimated horizontally so that beams of neutrons hit a horizontal sample surface at different angles, as shown schematically in Figure V.2.4-2. Table V.2.4-1 gives some of the parameters for this instrument. The higher-angle beams use curved guides in order to keep the total beam footprint small (~50 mm). The maximum wavelength necessary varies from $3\lambda_{min}$ to λ_{min} over the incident-angle range $\theta \sim 0.5°$ to $5.0°$, in order for each of these reflections to overlap the k-space range covered by the next-lowest-angle beam. This assumes that the minimum wavelength λ_{min} is the same for all beams. In the reflectivity mode with no scattering, this instrument is very fast. If ~20 beams illuminate the sample, with angles ranging from $0.5°$ to $5°$ and with a relative divergence of 0.03, a full reflectivity spectrum can be obtained in less than one minute. A background-suppression chopper can be used to remove the prompt pulse and frame-overlap neutrons or delayed neutrons if necessary. This instrument has the widest possible array of sample environments, including low and high temperature, vacuum, vapor-saturated or inert atmosphere, in order to study *in situ* the interfacial aspects of materials processing in real time.

2.4.2.2 GREF — Reflectometer for Grazing-Incidence Scattering

This instrument is located on one of the beams from the beam port shared by the rebuilt POSY-II, again at a source-sample distance of ~18 m. The GREF has a horizontal sample surface and horizontal-slit collimation. The collimation is variable in both directions. A 2D position-sensitive detector is used. A background-suppression chopper can be used to remove the prompt pulse and frame-overlap neutrons or delayed neutrons if necessary.

This instrument is able to measure specular reflectivity, forward small-angle off-specular scattering in the reflection plane, and small-angle off-specular scattering out of the reflection plane, as is shown schematically in Figure V.2.4-3. Table V.2.4-2 lists some parameters of this instrument.

2.4.2.3 REFD — Reflectometry Development

The beam for this instrument is round and comes from the same beam port that supports the rebuilt POSY-II. An optical bench permits a wide variety of configurations to be easily assembled and tested. This facility can be used, for example, for testing new optical components such as supermirrors and multilayers, or for assembly and testing of prototype instruments.

Focusing Microguides

Position–Sensitive
Detector
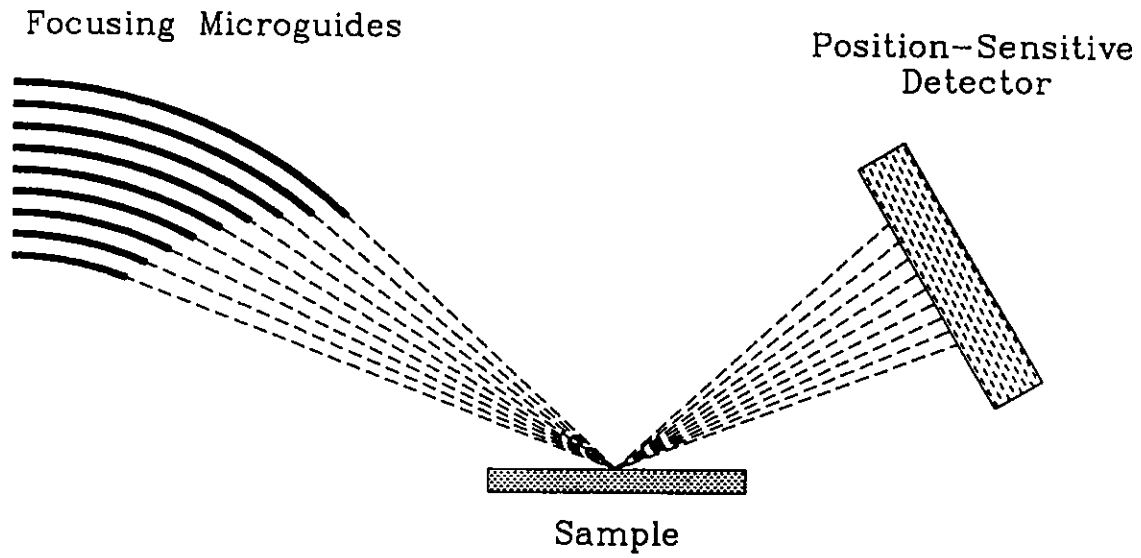
Sample

Figure V.2.4-2 Schematic Representation of the Multiple-Beam Geometry Used for the HIREF.

Table V.2.4-1 Parameters for the HIREF

Parameter	Value
Moderator	decoupled liquid H_2
Source repetition rate (Hz)	10
Source-to-sample distance (m)	18
Number of incident beams	~20
Footprint of beam (sample size) (mm)	50
Range of reflection angles (°)	2θ ~ 1-10
Wavelength range for 50% overlap of spectrum for adjacent beams (Å)	
1°	2.0 - 4.7
2°	2.0 - 4.0
5°	2.0 - 3.7
Nominal range of reflectivity	$1 \geq R \geq 10^{-4}$
Time per measurement (min)	≤ 1
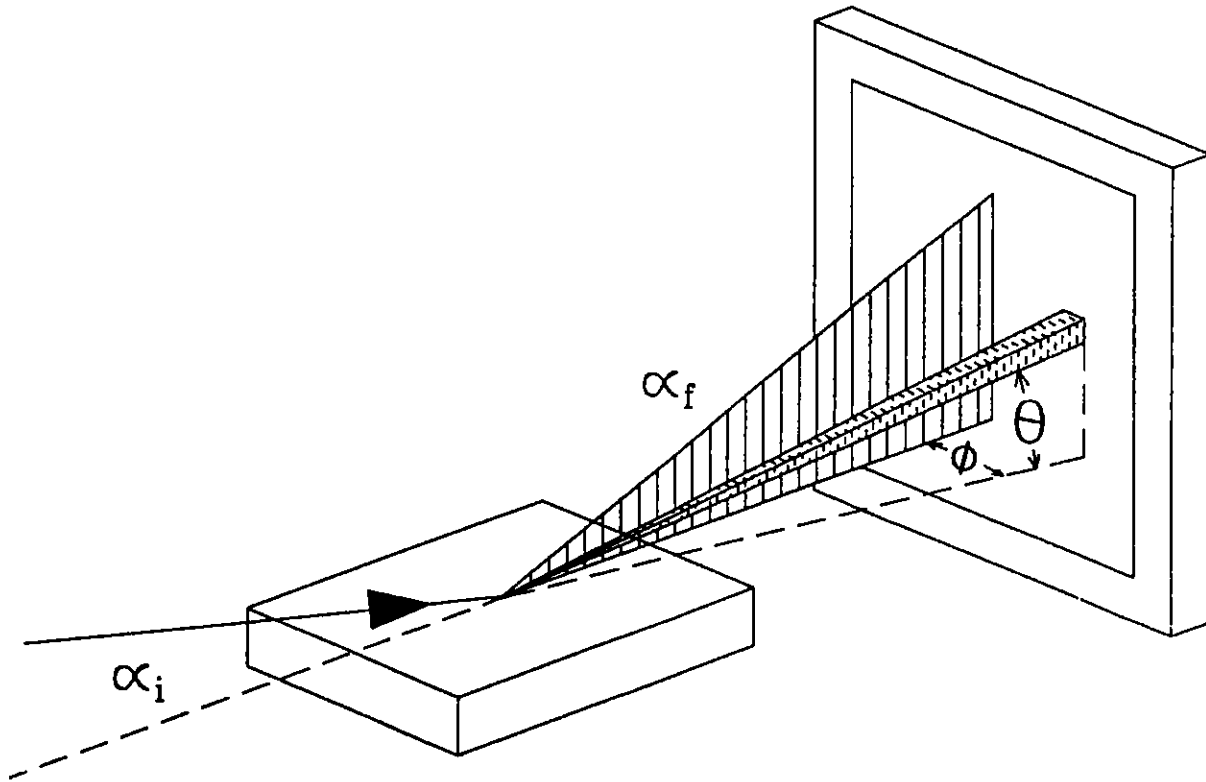
Figure V.2.4-3 Schematic Indication of the Geometry Used in the GREF Reflectometer. (α_i and α_f are the incident and outgoing angles for neutrons in the plane defined by the incoming beam and the specular reflection. An out-of-plane scattered beam is shown with angles θ with respect to the sample surface and ϕ with respect to the reflection plane.)

Table V.2.4-2 Parameters for the GREF

Parameter	Value
Moderator	decoupled liquid H_2
Source repetition rate (Hz)	10
Source-to-sample distance (m)	18
Sample-to-detector distance (m)	5
Maximum scattering or reflection angle (°)	6
Range in Q for scattering (Å^{-1})	$0.005 \leq Q \leq 1$
Nominal range of reflectivity	$1 \geq R \geq 10^{-7}$
Time per measurement (h)	1 - 2

2.4.3 Reflectometer Summary

The four reflectometers, POSY-I, POSY-II, HIREF, and GREF, discussed above form a set that provides a broad range of capabilities in this rapidly expanding field, and the associated development instrument REFD permits development of new or improved neutron optical components that can be used to enhance or expand these capabilities. Together, these five instruments are a reference set of reflectometers, and are summarized in Table V.2.4-3. These five instruments occupy only two beam ports.

2.5 CHOPPER INELASTIC-SCATTERING INSTRUMENTS

2.5.1 Transfer of Existing IPNS Instruments

2.5.1.1 HRMECS — High-Resolution Chopper Spectrometer

The HRMECS can be transferred from IPNS virtually unchanged to the 30-Hz target station at IPNS Upgrade. It views a liquid CH_4 moderator and has a source-sample distance of ~18 m.   Figure V.2.5-1 shows the present HRMECS, and Table V.2.5-1 lists some of its parameters.[15-17] At this distance, the HRMECS has a somewhat better resolution than at IPNS, particularly at low incident energies, and has a factor of ~30 increase in the data rate. This means that an experiment requiring a week at IPNS can be performed in a matter of hours at IPNS Upgrade. It also makes possible experiments on much smaller samples than are practical at present. With this higher flux, it is also practical to use tighter collimators and faster choppers to improve the resolution while still providing acceptable data rates.

The HRMECS is a very powerful and versatile instrument. However, some modifications make the HRMECS even more useful at IPNS Upgrade. One such modification is to change the forward-scattering portion of the vacuum flight path to allow a longer scattering flight path. This permits the use of position-sensitive detectors or an azimuthal array of short detectors to achieve much greater solid-angle coverage and better angular resolution at small scattering angles. A variable-aperture collimation system in the incident beam is required to optimize the use of these small scattering angles. Figure V.2.5-2 indicates this flight-path extension. Sufficient detectors are added to fill out the allowed detector complement on the HRMECS.

Table V.2.4-3 Reference Set of TOF Reflectometers at IPNS Upgrade

Instrument	Application/ Special Feature	Sample	Minimum Reflectivity	Measurement Time (min)
POSY-I[a]	Polarized neutrons	vertical	10^{-6}	60 - 120
POSY-II[a]	General purpose	horizontal	10^{-7}	60 - 120
HI REF	High intensity	horizontal	10^{-4}	≤ 1
GREF	Grazing incidence	horizontal	10^{-7}	60 - 120
REFD	Development	-	-	-

[a] Rebuilt from components of IPNS instruments.

Figure V.2.5-1 Plan View of the HRMECS at IPNS.

Table V.2.5-1 HRMECS and LRMECS Parameters at IPNS Upgrade

Parameter	HRMECS	LRMECS
Source-sample distance (m)	18	12
Source-chopper distance (m)	17	11
Background-suppression chopper	yes ~6 m from source	yes ~6 m from source
Source repetition rate (Hz)	30	30
Moderator material	liquid CH_4	liquid CH_4
Max. beam size at sample (cm^2)	7.5 × 10	5 × 10
Incident energy range (meV)	2-2000	2-2000
Scattering angles (°)	(-20)-(-2.5),2.5-140	(-10)-(-2.5),2.5-120
Sample-detector distance (m)	~4.0 (8.0 for low angle extension)	~2.5
Detector diameter (cm)	2.5	2.5
Detector length (cm)	42 (except at low angle)	42 (except at low angle)
Detector ^{3}He fill pressure (atm)	6	6
Present number of detectors	~240	160
Max. possible number of detectors[a]	~800	200
Available Fermi choppers[b]	Mechanical bearing, Be body, max. rotational speed of 270 Hz, interchangeable between the two instruments. Six choppers, optimized for different energies and resolutions.	
Energy resolution $\Delta E/E_{inc}$	2-4%	4-7%
Typical time to measure one data set (h)	2	<1

[a] Without desired modifications to flight paths.

[b] Faster, magnetic-bearing choppers are planned to provide higher resolutions than currently available.
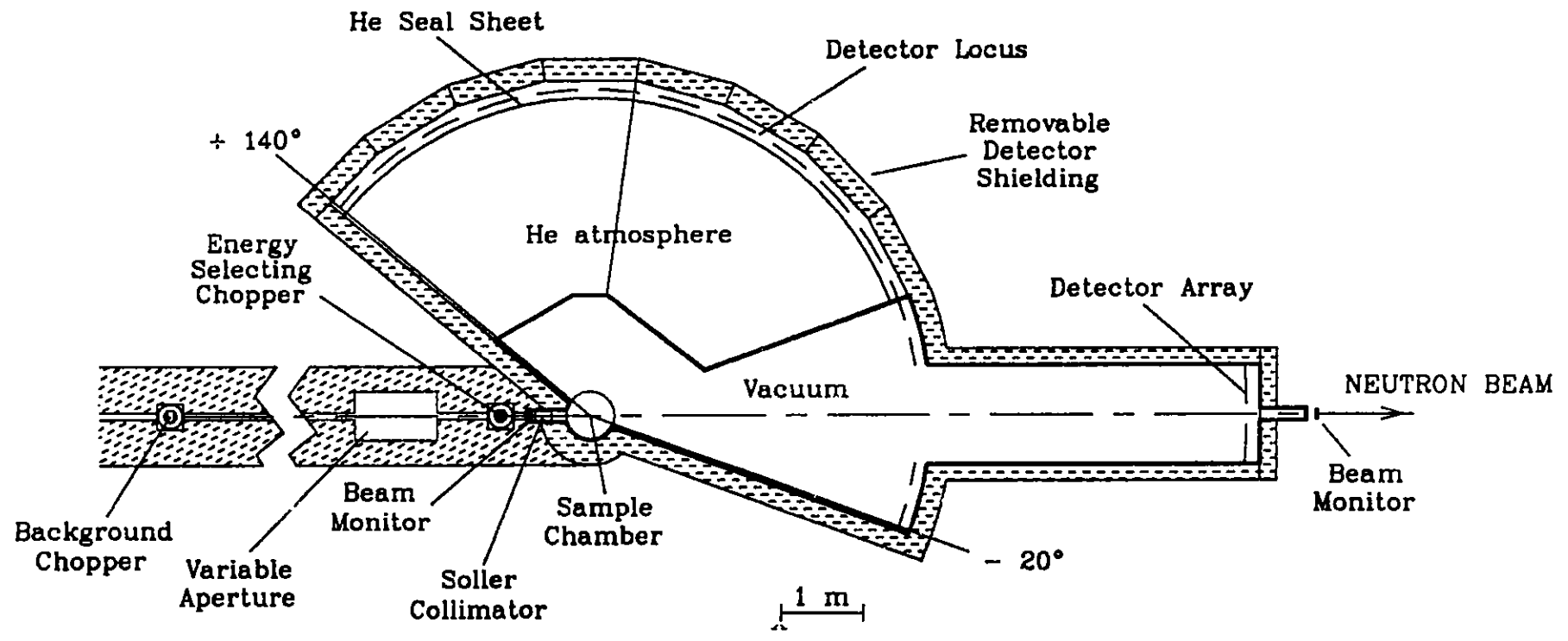
Figure V.2.5-2 Plan View of the HRMECS at IPNS Upgrade.

2.5.1.2 LRMECS — High-Intensity General-Purpose Chopper Spectrometer

The present LRMECS can also be transferred with virtually no changes to the 30-Hz target station at IPNS Upgrade, where it views a liquid CH_4 moderator with a source-sample distance of ~12 m. Figure V.2.5-3 shows the present LRMECS, and Table V.2.5-1 lists some of its parameters.[15-17] At IPNS Upgrade, the LRMECS has a resolution similar to that at IPNS, with a nearly 20-fold increase in data rates, so it is capable of performing modest-resolution experiments over a very wide region of Q-E space in a short time. Alternatively, similar experiments can be performed using small samples in a somewhat longer time.

Some improvements in LRMECS are also highly desirable. One improvement is modification of the entrance portion of the scattering flight path to accommodate larger sample apparatus. It is also desirable to modify the beam-exit portion of the scattering flight path to allow the installation of a detector or array of detectors providing azimuthal symmetry about the beam at small scattering angles.

2.5.2 New Reference Set Instruments

2.5.2.1 CNCS — Cold-Neutron Chopper Spectrometer

This spectrometer views a decoupled liquid H_2 moderator on the 10-Hz target station. The source-sample distance is 20 m and the sample-detector distance is 4 m, so neutron wavelengths up to ~16 Å, corresponding to incident energies down to ~0.32 meV, can be used without frame-overlap. Fermi choppers provide the highest resolutions near the short-wavelength end of the wavelength range, while disk choppers provide the desired resolution, with somewhat higher intensities, at other wavelengths. Both types are available and interchangeable. A background-suppression chopper at ~6 m from the source is required, and an additional chopper between this position and the E_0 chopper may be required in order to suppress frame-overlap from successive E_0 chopper pulses. A neutron guide is used to enhance the intensity at the sample. The secondary flight path accommodates a row of detectors centered on the scattering plane and additional rows of detectors above and below that plane, for a total of ~1000 detectors. An area-position-sensitive detector or an array of linear-position-sensitive detectors is used in the forward scattering direction in order to provide better momentum resolution at small momentum transfers.

This set of instrument parameters are shown in Table V.2.5-2 and roughly duplicate the wavelength and resolution capabilities of the IN5 instrument[18] at the ILL. With this choice of parameters, the resolution is at least as good as that of IN5 over the entire wavelength range (2-16 Å) and is much better than that of IN5 over most of this range. The resolution and flux on sample for IN5 for an incident wavelength of 6 Å, corresponding to an incident energy E_i of 2.3 meV, are $\Delta E/E_i \sim 3.8\%$ and flux ~6×10^4 n/cm^2-sec. The CNCS at this energy with the
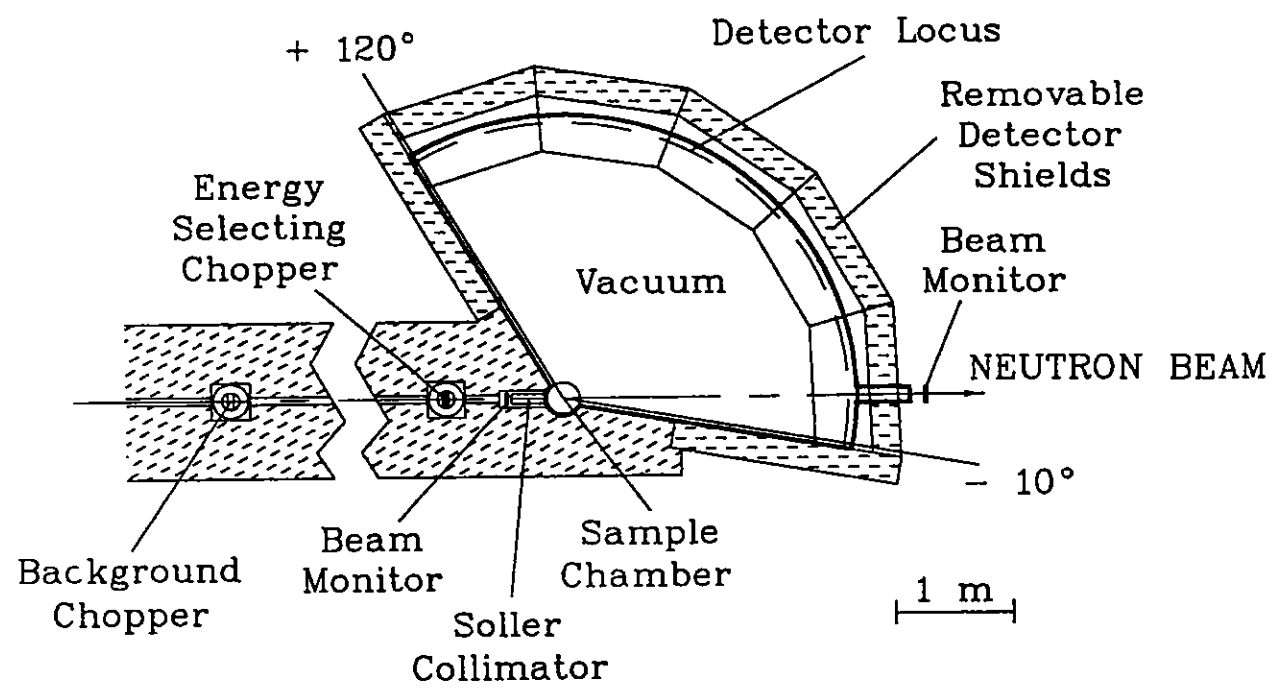
Figure V.2.5-3 Plan View of the LRMECS.

Table V.2.5-2 CNCS Parameters at IPNS Upgrade

Parameter	Value
Source-sample distance (m)	20
Source-chopper distance (m)	19
Background-suppression chopper	yes, ~6 m from source
Source repetition rate (Hz)	10
Moderator material	liquid H_2
Max. beam size at sample (cm^2)	2 × 10
Incident energy range (meV)	0.3-20
Incident wavelength range (Å)	2-16
Scattering angles (°)	~5-140, plus area detector or LPSD array at lower angles
Sample-detector distance (m)	~4.0
Detector diameter (cm)	1 × 3.5[a]
Detector length (cm)	25
Detector ^{3}He fill pressure (atm)	4
Maximum possible number of detectors	~1000, plus area detector or ~60 LPSDs
E_0 chopper	Fermi or disk — interchangeable, depending on desired energy and resolution
Energy resolution $\Delta E/E_{inc}$	≤ 1% over entire energy range
Typical time to measure one data set (h)	~12-24

[a] Uses flattened 2.54-cm-diameter cylindrical detectors to get good timing resolution.

parameters given here has $\Delta E/E_i \sim 1.0\%$ and flux $\sim 1 \times 10^4$ n/cm²-sec, making it comparable to or somewhat better than IN5, which is an instrument much in demand for a broad range of scientific investigations. A more detailed optimization of this instrument, with careful attention to the interaction of guide and chopper parameters,[19] may yield further improvements in performance.

2.5.2.2 SCCS — Chopper Spectrometer for Excitations in Single Crystals and Low-Dimensional Systems

Triple-axis spectrometers have long been used for the study of excitations in single crystals. However, the performance of triple-axis spectrometers begins to degrade rapidly as the neutron energy is increased, and only in special cases can they be used to study excitations with energies above 100 meV. Early work at IPNS[20] showed that chopper spectrometers at a pulsed neutron source can be used for the study of high-energy excitations in single crystals, and since then a number of experiments at ISIS[21,22] have shown that chopper spectrometers can perform extremely well for many such experiments. A new chopper spectrometer, the Multi-Angle Position-Sensitive Spectrometer (MAPS), optimized for and dedicated to the study of high-energy excitations such as magnetic excitations in single crystals, is being constructed[23] at ISIS. This spectrometer is designed to provide a continuous detector array covering the scattering angles -30° to +30° at a distance of 4 m from the sample, with the necessary gap for the unscattered beam near 0° made as small as possible. This detector array is made up of linear-position-sensitive gas proportional counters, each 2.5 cm in diameter × 1 m long and having position-encoding resolution of ~2 cm. A similar detector array covers scattering angles from -20° to +20° in the out-of-plane dimension. In all, ~256 LPSDs are required.

The SCCS instrument planned for IPNS Upgrade is similar to this MAPS instrument. However, since it will be constructed later than MAPS, its design will benefit from experience gained with MAPS. Figure V.2.5-4 shows schematically what this instrument might look like. The sample is located ~16 m from a room-temperature H_2O moderator on the 30-Hz source. A high-speed Fermi chopper near the sample is used for incident-beam energy selection, with energy resolution $\Delta E/E_i \sim 1\%$. One or more additional choppers closer to the moderator provide background suppression. The continuous detector coverage ensures that all likely Q vectors of interest can be covered for energy transfers greater than ~100 meV. The use of position-sensitive detectors permits the recording of neutrons in a fine-enough grid in terms of the Q vector and energy transfer to allow construction of scans in any Q direction and with good resolution in Q and energy transfer.

2.5.3 Other Possibilities

This instrument is not in the reference set and will probably not be among the initial complement at IPNS Upgrade. It is expected that instruments of this type will evolve and might be added at a later date.
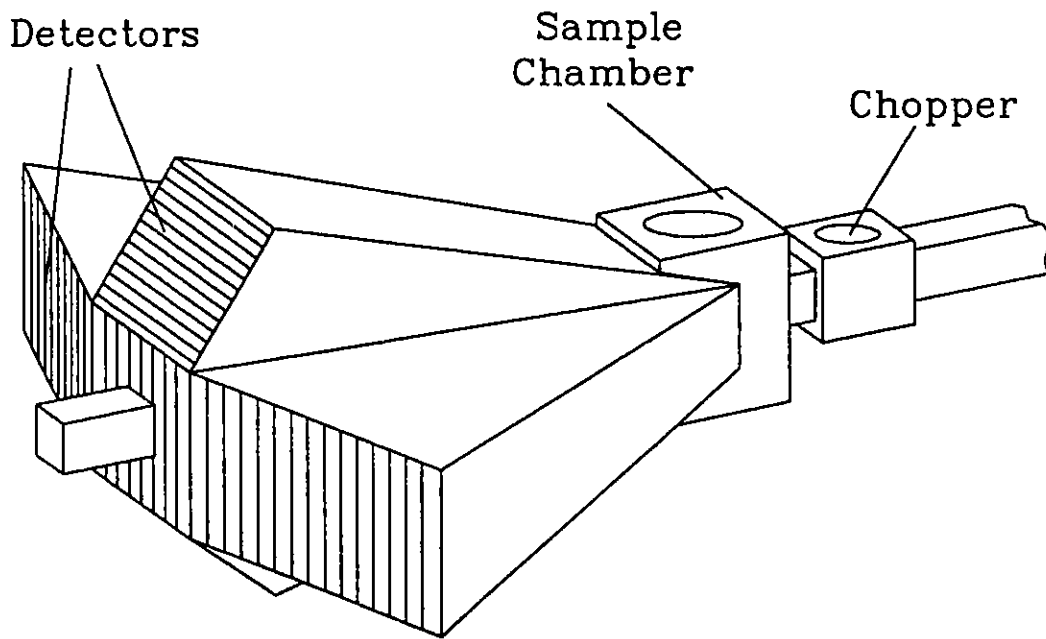
Figure V.2.5-4 Schematic Representation of the SCCS.

2.5.3.1 BSCS — Brillouin Scattering Chopper Spectrometer

Neutron Brillouin scattering involves the measurement of excitations at small Q values and moderate energy transfers. These are the requirements for the study of many of the collective excitations in liquids and glasses. Kinematic considerations require that such scattering is done with relatively high incident energies and small scattering angles. Robinson[24] has analyzed these kinematic requirements, along with the resolution requirements for such an instrument. He found that an instrument having an incident flight path of ~20 m and a scattering path of ~10 m in the forward direction, with a minimum scattering angle of ~0.4° and an energy resolution $\Delta E/E_i \sim 0.5\%$, is adequate for many such measurements. These flight-path lengths are not too different from those already specified for the modified version of the HRMECS, and the HRMECS can provide nearly this energy resolution if high-speed choppers are used. Therefore, the HRMECS instrument will be used for the initial Brillouin scattering experiments at IPNS Upgrade. An instrument optimized for Brillouin scattering can be designed and constructed if demand warrants, after experience with such experiments is gained on the HRMECS.

2.5.4 Chopper Spectrometer Summary

The chopper spectrometers HRMECS and LRMECS are very versatile, general-purpose inelastic-scattering instruments. These two instruments offer considerably different tradeoffs between resolution and intensity, permitting the conditions to be optimized for a wide range of experiments. The cold-neutron spectrometer CNCS provides high-resolution spectroscopy in the very important low-energy range, and the single-crystal chopper spectrometer SCCS provides capabilities optimized for the study of high-energy excitations in single crystals. These four spectrometers are taken as a reference set of chopper spectrometers. Their capabilities are summarized in Table V.2.5-3.

2.6 CRYSTAL-ANALYZER INELASTIC-SCATTERING INSTRUMENTS

2.6.1 Transfer of Existing IPNS Instruments

2.6.1.1 QENS — Medium-Resolution Crystal-Analyzer Spectrometer

The QENS is a crystal-analyzer spectrometer optimized to provide ~70-μeV resolution for quasielastic scattering, but it also has very good resolution for chemical spectroscopy at excitation energies up to ~150 meV. The polychromatic or white beam directly from the source is incident on the sample, so a separate detector can monitor diffraction from the sample. This allows a careful following of phase changes and *in situ* sample growth or modification, concurrently with the quasielastic- and inelastic-scattering measurements. The QENS has three

Table V.2.5-3 Reference Set of TOF Chopper Spectrometers at IPNS Upgrade

Instrument	Application/Special Feature	Range for E_{inc} (meV)	$\Delta E/E_i$ (%)	Measurement Time (h)
HRMECS[a]	High resolution, general purpose	4-2000	2-4	2
LRMECS[b]	Low resolution, general purpose	3-2000	4-7	≤1
CNCS	High resolution, low energy	0.3-20	≤1	12
SCCS	Excitations in single crystals	50-2000	~1	~12

[a] Transferred from IPNS with forward scattering path increased.

[b] Transferred from IPNS with little change.

focused-crystal-analyzer arms mounted on a rotating table so that a wide range of scattering angles can be covered. Figure V.2.6-1 shows the schematic layout of the QENS, and Table V.2.6-1 lists some of its parameters.[25] At IPNS Upgrade, the QENS spectrometer is placed on a beamline at the 30-Hz target station, where it views either a liquid CH_4 or a decoupled liquid H_2 moderator. A liquid H_2 moderator has a 3-5 times greater intensity at the long wavelengths used for most of the QENS experiments, but it also has a broader pulse so the total flight-path length must be increased in order to maintain the same resolution. Poisoning of the liquid H_2 moderator might decrease the pulse-width, and guides can be used to minimize flux losses due to the greater source-sample distance. Until a detailed instrument design is considered and more information concerning the performance of poisoned liquid H_2 moderators is available, it is not clear which moderator gives the better performance for QENS. If the liquid CH_4 moderator is used, QENS is placed at a source-sample distance of ~9 m. In this location, count rates are increased by a factor of ~40 over those at the present IPNS, where it currently takes between 1/2 day and 2 days to make a measurement on the QENS.

The QENS could be moved to IPNS Upgrade with essentially no changes, but it is considerably improved by incorporating a much greater solid angle of analyzer crystals and using a focusing guide system in the incident beam. A background-suppression chopper in the incident beam is also used. These changes result in an additional factor of 5 increase in instrument throughput. Such a redesign of the QENS is already in its initial stages at IPNS.

Neutron lenses made of capillary bundles or of silicon microguides are being developed at NIST and elsewhere. These offer the ability to focus a relatively large beam onto a sample of a few square millimeters or less in area.[26,27] These lenses look very promising for providing a very-small-sample capability for QENS, where the increased angular divergence of the incident beam caused by such focusing is not a problem. Once such lenses are somewhat more developed, one can be designed to match the requirements of QENS and installed on the instrument. This will allow the use of very small samples, down to a few square millimeters in area, with only a small reduction in data rates, making this spectrometer very attractive for chemical spectroscopy in a much broader class of materials.

2.6.2 New Reference Set Instruments

2.6.2.1 HRBS — High-Resolution Backscattering Spectrometer (5 μeV)

This spectrometer has a resolution of ~5 μeV and is optimized for the study of quasielastic scattering and low-lying excitations. It views a poisoned, decoupled liquid H_2 moderator at the 10-Hz target station. This crystal-analyzer backscattering spectrometer is similar in concept to the IRIS spectrometer[28] at ISIS, but with some significant differences. The spectrometer optimization is based on the use of near-back-reflection from the 004 planes of mica crystal analyzers. The 004 d-spacing of mica is ~5 Å, so ~10-Å (0.8-meV) neutrons are
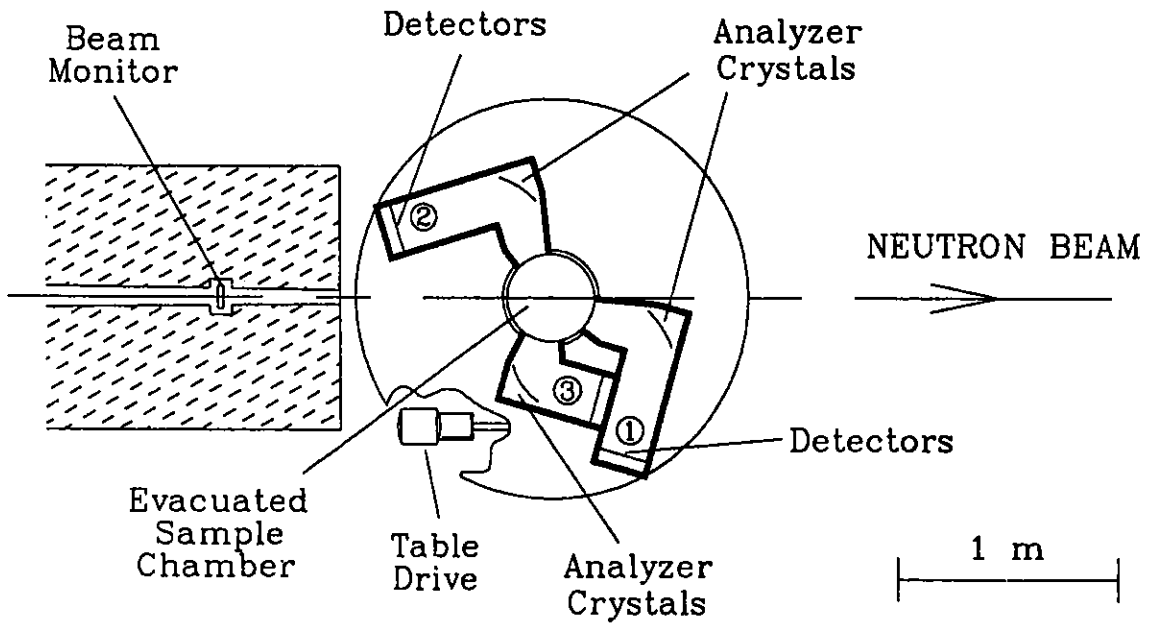
Figure V.2.6-1 Unmodified Configuration of the QENS. (Circled numbers identify the three analyzer arms.)

Table V.2.6-1 QENS (unmodified) Parameters at IPNS Upgrade

Parameter	Arm 1	Arm 2	Arm 3
Source-sample distance (m)	9[a]	9[a]	9[a]
Source repetition rate (Hz)	30	30	30
Moderator material	liquid CH_4[a]	liquid CH_4[a]	liquid CH_4[a]
Max. beam size at sample (cm^2)	1.27 × 10	1.27 × 10	1.27 × 10
Angular acceptance (°)	7	14	14
Range of scattering angles (°)	25-55	75-105	115-155
Analyzer crystals	graphite	graphite	graphite
Analyzer energy (meV)	~3.6[b]	~3.6[b]	~3.6[b]
Sample-crystal-detector distance (m)	1.117	1.117	0.800
Detector diameter (cm)	0.64	0.64	0.64
Detector length (cm)	10	10	10
Detector ^{3}He fill pressure (atm)	10	10	10
Number of detectors	13	13	9
Energy resolution ΔE (meV)			
energy transfer = 0 meV	0.07	0.07	0.08
energy transfer = 50 meV	1.57	1.57	1.57
Typical time to measure one data set (min)	-	20-80	-

[a] Might use a poisoned, decoupled liquid H_2 moderator, in which case the source-sample distance might have to be increased.

[b] Mosaic crystals are used, so there are a range of analyzer energies about this value. Each energy is focused on a different detector.

back-reflected from the 004 planes. A resolution of 5 µeV at this energy for elastic scattering means $\Delta E/E_i$ ~0.6%, which is evenly distributed in quadrature among the contributions from source pulse-width, path-length variations, and analyzer bandwidth. The pulse-width Δt_s from the moderator is ~150 µsec at this wavelength, so a source-sample distance of ~35 m is required to give $\Delta t_s/t_i$ ~ 0.17%. The analyzer crystals are operated off backscattering by an amount that gives an analyzer wavelength band of $\Delta\lambda/\lambda$ ~ 0.17%. The analyzer Bragg angle used depends on the mosaic spread of the particular mica. On the basis of reported values, a Bragg angle of ~82° is required for the analyzer crystal arrays. The analyzer and detector arrays are designed to minimize path-length uncertainties so that sample sizes can be as large as practical within the constraint $\Delta L/L_i$ ~0.17%.

The path lengths are chosen so that the portion of the TOF spectrum of interest is not obscured by the next prompt pulse from the source. Source-sample distance is reduced to 30 m to prevent this overlap. The resolution is still ~5 µeV for quasielastic scattering if the $\Delta L/L_i$ is reduced to ~0.14%. The spectrometer is also designed to prevent overlap of inelastic spectra. Within a given pulse at the sample, neutrons that are up-scattered to an energy corresponding to a high-order analyzer reflection can arrive at the detectors after neutrons down-scattered to low-order planes. For example, at some point the neutron-energy-gain spectrum of the 004 analyzers overlaps the neutron-energy-loss spectrum of the 002 analyzer planes. This sets an ultimate limit on the incident bandwidth that can be allowed to reach the sample. It is desirable to maximize this bandwidth, and this requires maximizing the ratio of sample-analyzer-detector distance to source-sample distance. A practical limit for the sample-analyzer distance is ~3 m, or ~6 m sample-analyzer-detector distance, so this ratio becomes 6:30. For this choice of flight paths, the separation in time of the 004 spectra from the 002 spectra requires that the incident bandwidth be restricted to $\Delta\lambda$ = 1.9 Å. Separation of the 004 spectra from the 006 spectra requires $\Delta\lambda$ = 0.6 Å. Larger-wavelength bands can be used if it is known that there is no neutron-energy-gain spectrum from the higher-order plane, as is the case if the sample is sufficiently cold. This bandpass can be centered at any wavelength simply by adjusting the phase of the bandpass chopper(s). In the most restrictive case with $\Delta\lambda$ = 0.6 Å, this corresponds to an energy range of ~100 µeV centered on elastic scattering using the 004 plane. The same bandpass corresponds to an energy range of ~375 µeV when centered at 2 meV and ~4200 µeV when centered at 10 meV.

Figure V.2.6-2 shows a schematic layout of this instrument, and Table V.2.6-2 summarizes some of its parameters. The instrument size is largely dictated by the moderator pulse width, so the final instrument configuration will not be fixed until the moderator performance has been optimized. The instrument uses a neutron guide over the incident flight path, with a converging supermirror section to focus the neutrons onto the sample. One or two choppers provide an adjustable bandpass. Either small ^{3}He detectors or an array of scintillation detectors based on the ZnS-LiF scintillator can be used.

A major difference between this spectrometer and the related spectrometers IRIS[28] at ISIS or LAM-80ET[29] at KENS is the large ratio of secondary to primary flight-path lengths. This permits a clean separation of the spectra from the various analyzer plane orders while
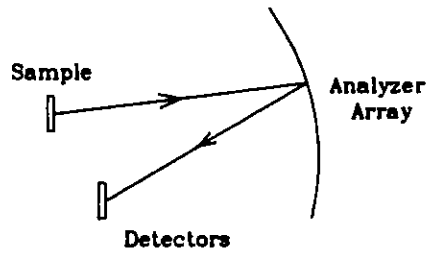
Section A—A

typical
sample–analyzer–detector
arrangement —— not to scale
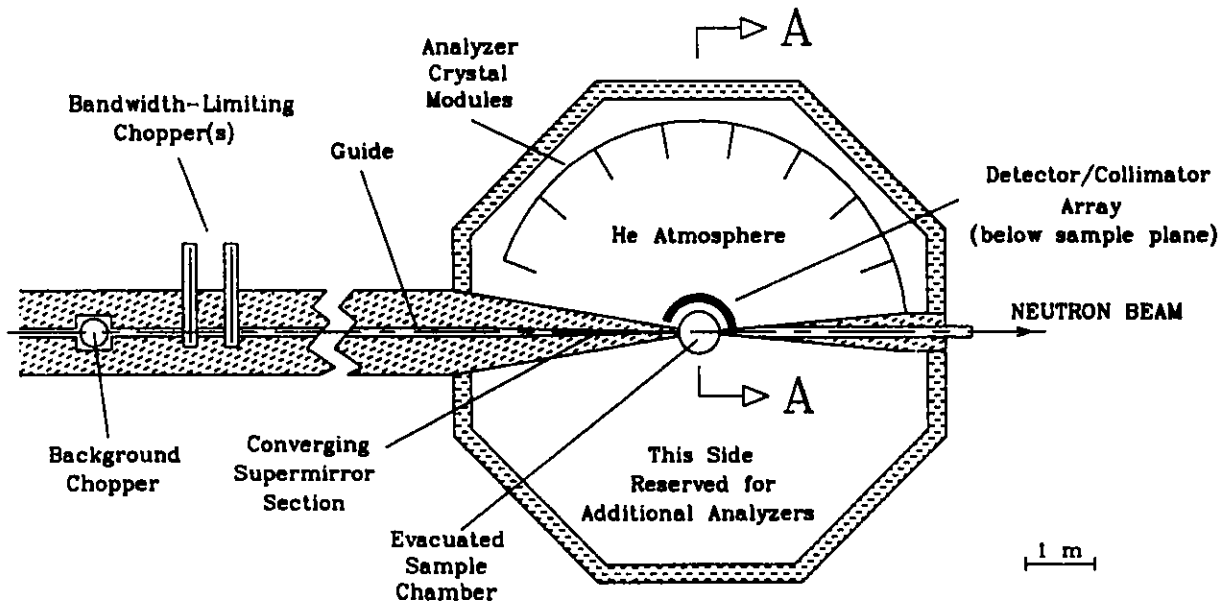
Figure V.2.6-2 Schematic Representation of the HRBS.

Table V.2.6-2 Parameters for the HRBS

Parameter	Value
Source-sample distance (m)	30
Source repetition rate (Hz)	10
Moderator material	poisoned, decoupled liquid H_2
Neutron guide	yes, with converging supermirror
Bandwidth-limiting choppers	one or two
Background-suppression chopper	if needed
Max. beam size at sample (cm^2)	~ 2 × 5
Range of scattering angles (°)	~ 5-165
Analyzer crystals	mica
Analyzer solid angle (sr)	~0.4
Analyzer area (m^2)	~4
Sample-crystal-detector distance (m)	~6
Detector type	to be determined
Number of detectors = number of scattering angles	~150

	Analyzer Crystal Planes		
	002	004	006
Analyzer energy (meV)	0.21	0.84	1.90
Energy resolution ΔE (meV)			
energy transfer = 0 meV	0.0012	0.0050	0.011
energy transfer = 2 meV	0.013	0.017	0.023
energy transfer = 10 meV	0.061	0.064	0.071
Typical time to measure one data set (min)		~80	

maintaining a relatively large energy range. This very large secondary flight path requires a large area of analyzer crystals in order to cover sufficient solid angle. Fortunately, mica is relatively inexpensive, so such a large-area analyzer array is feasible. The analyzer crystal array is made in modular sections to facilitate alignment. Initially, only one side of the flight path is filled with the mica analyzer array. The other side is left open for subsequent installation of a similar mica array to double the count rate, or of an array of other suitable analyzer crystals.

Although this instrument is optimized for the 004 planes of mica, cleanly separated spectra from the other planes (002, 006, etc.) are also obtained just by changing the chopper phasing. In order to aid the *in situ* study of the time-evolution of samples, the spectrometer is also equipped with an array of detectors located to measure the diffraction pattern from the sample concurrently with the inelastic-scattering spectra. These features, coupled with the ability to easily and independently select both the incident energy and incident-energy bandwidth, make this an extremely powerful and flexible instrument for high-resolution spectroscopy.

2.6.2.2 TFCA — Time-Focused Crystal-Analyzer Spectrometer for Chemical Spectroscopy

The TFCA is a time-focused crystal-analyzer spectrometer similar in principle to the Time-Focused Crystal Analyser Spectrometer (TFXA)[30] at ISIS. It provides a relatively high resolution for spectroscopy at energy transfers up to 1 eV or more, considerably extending the range for spectroscopy provided by the QENS. For energy transfers within the range covered by the QENS, this spectrometer offers somewhat poorer resolution but significantly increased data rates, and so it is complementary to the QENS over this range as well. Figure V.2.6-3 shows a schematic representation of this instrument, and Table V.2.6-3 indicates some of its parameters.

A neutron lens similar to that discussed above for the QENS can also be installed on the TFCA to allow measurements on much smaller samples with little or no loss in data rate.

2.6.2.3 QSTAXC — Cold-Neutron Quasi-Steady-State Triple-Axis Spectrometer

The QSTAXC is a conventional triple-axis spectrometer located ~17 m from a large, coupled liquid H_2 moderator on the 30-Hz target. A guide increases the cold neutron flux at the monochromator, and a focusing crystal monochromator is used. The spectrometer is modeled after successful reactor cold-neutron triple-axis spectrometers such as IN12 or IN14 at ILL.[31] The main difference is that the data acquisition is gated synchronously with the arrival of neutrons that have the desired energy. No order-removal filters are required. Some evolution of the instrument is expected as experience is gained with its use in the pulsed-source environment. The design incorporates features that enhance the flexibility and future adaptability of this instrument.
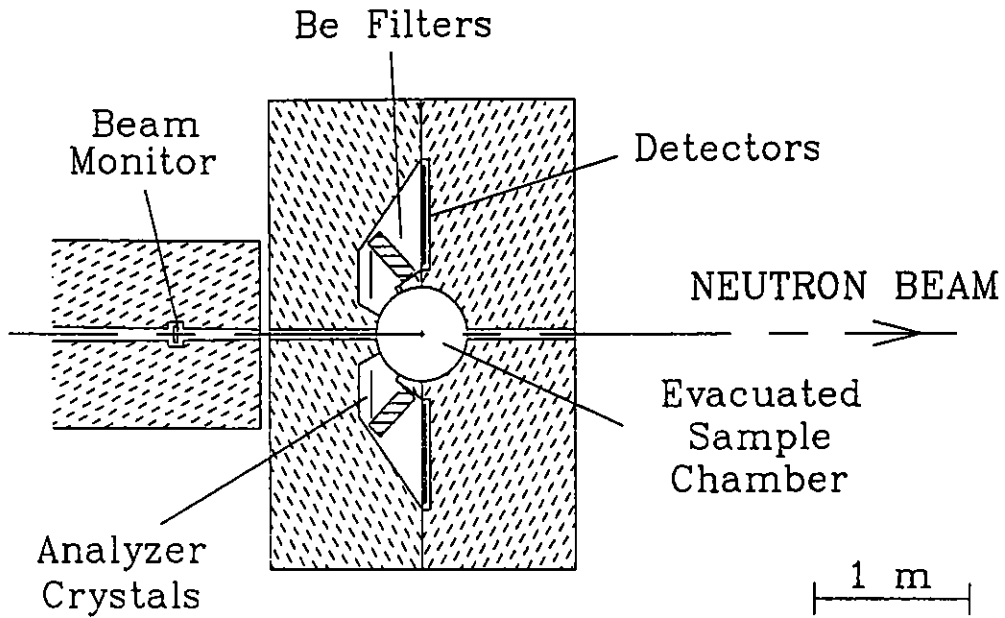
Figure V.2.6-3 Schematic Representation of the TFCA.

Table V.2.6-3 Parameters for the TFCA

Parameter	Value
Source-sample distance (m)	16
Source repetition rate (Hz)	30
Moderator material	poisoned liquid CH_4
Neutron guide	probably
Background-suppression chopper	if needed
Max. beam size at sample ($cm^{2)}$	~2 × 5
Analyzer crystals	pyrolytic graphite
Analyzer solid angle (sr)	~0.1-0.5
Detector type	^3He
Number of detectors	~200
Analyzer energy (meV)	~4
Energy resolution $\Delta E/E$	1-3%
Typical time to measure one data set (min)	20-80

Section IV.3.2.5 shows that the time-averaged flux of cold neutrons on a sample is roughly the same as that expected from a cold source at a medium-flux reactor. This is sufficient to make the QSTAXC a very good instrument. The background-rejection capabilities of the QSTAXC make it unique for some types of experiments. It also forms a natural complement to other instruments at IPNS Upgrade.

2.6.2.4 MICAS — Multiple-Independent-Crystal-Analyzer Spectrometer for Coherent Excitations

The multiple-crystal-analyzer instruments MAX[32] at KENS and PRISMA[33] at ISIS allow (Q,E) scans along high symmetry directions in reciprocal space for mapping the coherent excitations in single-crystal samples. The sample is exposed to a polychromatic beam in these instruments, and the final energies of the scattered neutrons are determined by an array of analyzers and detectors. Incident energies are determined by time-of-flight. In typical operation, a high symmetry direction in the crystal is aligned parallel to the incident wavevector k_{inc}. Each analyzer selects a particular k_{scatt}, and $|\,k_{inc}\,|$ is scanned by time-of-flight. All the analyzer-detector systems measure along the same line in reciprocal space if the Bragg angle θ_B of each analyzer is related to the scattering angle ϕ for that analyzer by the equation

$$Q_\perp = \pi \sin \theta_B / d_B \sin\phi \,. \qquad\qquad (V.2.6-1)$$

Here d_B is the spacing of the analyzer planes, and $Q_{||}$ and $Q_\perp$ are the wavevector transfer components parallel and perpendicular to the incident beam, respectively. The scattering angle ϕ is different for each of the analyzer arms, so each arm measures a different energy transfer and wavevector transfer. The spectrometer performs a net of scans in the $(Q_{||}, E)$ plane. Some lines in reciprocal space are not accessible to such a spectrometer.

A large amount of development work has gone into PRISMA and MAX, and there is now considerable operating experience on both instruments. In favorable cases, PRISMA can collect a set of dispersion curves in a few hours. A major difficulty is mechanical interference between the independent analyzer arms, which limits the ranges of θ_B that are accessible for some analyzers. In an effort to minimize this interference, shielding of the individual arms is kept to a minimum, and this leads to significant background problems in these instruments. Both of these problems can be significantly alleviated by the use of double analyzer crystals in each analyzer arm, so that the detector no longer needs to move about the analyzer position. Figure V.2.6-4 shows a schematic layout of a possible instrument configuration having 20 double-analyzer-crystal arms, each separated by 2° in ϕ. The entire bank of 20 analyzers can be rotated about the sample position, allowing coverage of ϕ roughly over the range -120° to +120°. Graphite or germanium analyzer crystals, or a combination of the two, are used. The desirable moderator is liquid CH_4 on the 30-Hz source, and the incident flight path is on the order of 12 m.
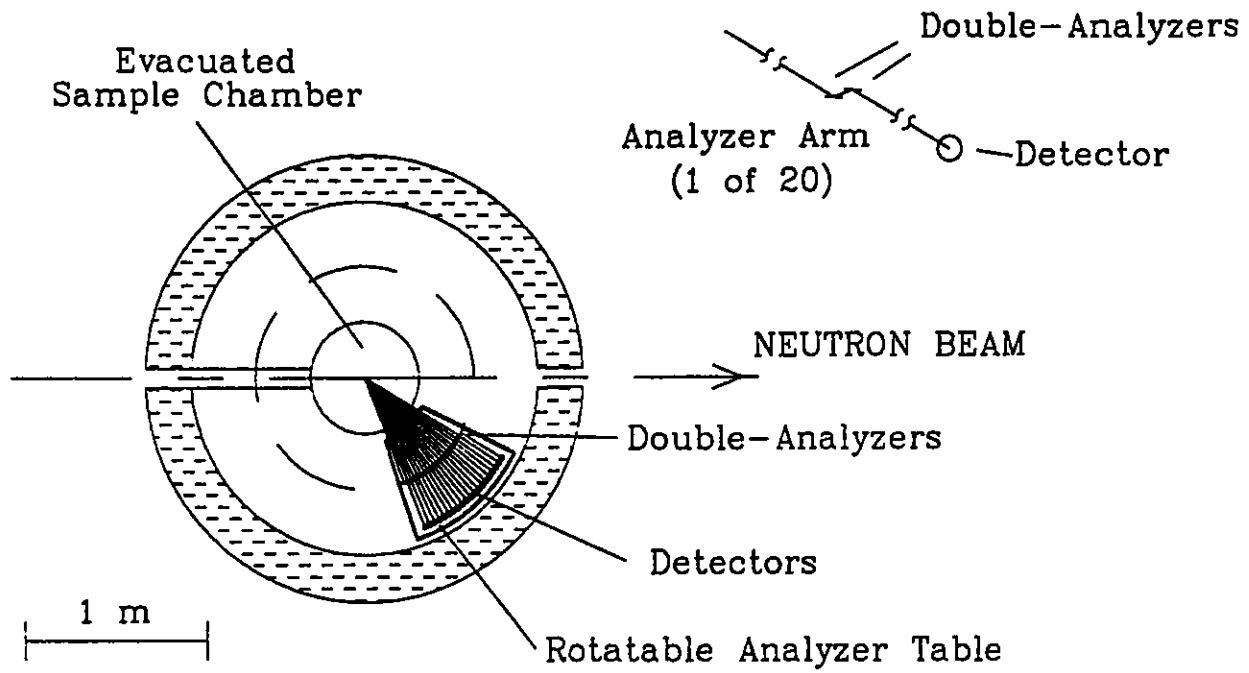
Figure V.2.6–4 Schematic Representation of the MICAS.

A detailed analysis of the kinematic constraints and the resolution ellipsoids as functions of the different geometrical parameters is essential before final design parameters are fixed. It is desirable to provide analyzer arms capable of giving a finer angular coverage, down to 1° separation between analyzers, if this can be done while still including adequate shielding for each analyzer. Such an instrument, optimized in light of the operating experience at MAX and PRISMA, can be a very useful survey instrument for mapping out coherent excitations in single crystals. In some cases, this might be followed by a detailed study of a more restricted region in reciprocal space using a triple-axis spectrometer, such as the QSTAXC or the QSTAXT (Section V.2.6.3.1).

2.6.3 Other Possibilities

This instrument is not in the reference set and will probably not be among the initial complement at IPNS Upgrade. It is expected that instruments of this type will evolve and might be added at a later date.

2.6.3.1 QSTAXT — Thermal-Neutron Quasi-Steady-State Triple-Axis Spectrometer

This is a complementary instrument to the cold-neutron triple-axis spectrometer QSTAXC. The QSTAXT is located ~17 m from a large, room-temperature, coupled liquid H_2O moderator on the 30-Hz target. A guide provides some increase in the thermal neutron flux at the monochromator, and a focusing crystal monochromator is used. This instrument is physically similar to the QSTAXC, except for the changes in monochromator and analyzer crystals to optimize them for the thermal neutron range. As is the case for the QSTAXC, this instrument has very good background characteristics and rejects spurious peaks. Construction of the QSTAXT will be deferred until some experience is gained with the QSTAXC.

2.6.4 Summary of Crystal-Analyzer Spectrometers

The three instruments TFCA, QENS, and HRBS are optimized for chemical spectroscopy, and this group spans the full range of resolution and energy transfers practical for crystal-analyzer spectrometers at IPNS Upgrade. The high data rates on these instruments and their ability to work with small samples allows neutron chemical spectroscopy to be used for a broad range of samples for which it has previously been impractical. The two instruments QSTAXC and MICAS, optimized for the study of excitations along high-symmetry directions in single-crystals, cover the medium- and low-energy-transfer ranges much more efficiently than does the SCCS chopper spectrometer discussed above. The TFCA, QENS, HRBS, MICAS, and QSTAXC are taken as a reference set of crystal-analyzer spectrometers, and their performances are summarized in Table V.2.6-4.

Table V.2.6-4 Reference Set of Crystal-Analyzer Spectrometers at IPNS Upgrade

Instrument	Application/Special Feature	Range for E (meV)	ΔE (meV)	Measurement Time (min)
TFCA	General purpose (TOF)	0-1000	0.5-30	20-80
QENS[a]	Quasielastic, medium resolution (TOF)	0-150	0.05-3	20-80
HRBS	Microvolt resolution (TOF)	0-10	0.005-0.06	~80
MICAS	Survey of single-crystal excitations (TOF)	0-20	-------- varies	--------
QSTAXC	Cold-neutron triple axis (QSS)	-	-	-

[a] Transferred from IPNS with little change.

2.7 OTHER INELASTIC-SCATTERING INSTRUMENTS

2.7.1 New Reference Set Instruments

2.7.1.1 TOFNSE — Time-of-Flight Neutron Spin-Echo Spectrometer

The spin-echo technique was first developed by Mezei and implemented on the IN11 spectrometer at ILL.[34-37] In this technique, a neutron polarized perpendicular to the magnetic-field direction travels through a precession field. The neutron rotates through an angle α during its traverse of the precession field region. The neutron spin is then flipped through an angle of π, before entering another precession field. There it rotates through an angle of α' in the opposite sense to the first precession. The sample is placed before the π spin flipper. If the fields are adjusted so that $\alpha' = \alpha$ when there is no sample, then the phase shift $\alpha - \alpha'$ is a measure of the energy change of the neutron upon scattering by the sample.

Mezei and Richter[38] have analyzed the adaptation of this technique to a pulsed spallation neutron source instrument and have shown that the neutron spin-echo technique is particularly well-suited to time-of-flight applications. There is a gain of a factor of ~8 or more in useful data rate and a significant improvement in Q-resolution relative to a comparable instrument at a steady-state source having the same time-averaged flux. At the IN11 or the more recently constructed IN15 spin-echo spectrometers at ILL, only a single scattering angle is utilized at any given time, and the magnetic field is scanned to provide the intermediate scattering function S(Q,t) for the sample. The TOFNSE instrument at IPNS Upgrade is based on the best features of IN11 and IN15, with time-of-flight electronics replacing the velocity selector for the wavelength determination. In this time-of-flight instrument, the wavelengths are scanned automatically to give concurrent data for a range of Q values, but it is still necessary to perform the magnetic-field scan to determine S(Q,t). The wavelength resolution, and hence Q resolution, of the TOF measurement is inherently much better than the ~20% wavelength resolution used on IN11. The accessible wavelength range, and hence Q range, is also much greater than on IN11. Also, as shown by Mezei and Richter, this scan over a broad wavelength range leads to a much larger range for the t variable in S(Q,t) than on IN11.

Penfold and Williams[39] proposed an instrument with multiple scattering angles. In this case the intermediate scattering function S(Q,t) is directly determined by measurement of the phase shift as a function of scattering angle and TOF . The magnetic-field scan is unnecessary. However, such an instrument requires magnetic fields with a plane of symmetry. As a consequence, the field inhomogeneities are larger and are not correctable as are the inhomogeneities in the solenoidal fields. The resolution in the variable t is considerably worse on such an instrument.[38] For this reason, and because the technology is further developed, the TOFNSE instrument is designed to use solenoidal fields, with components similar to those already developed for IN11 or IN15. The many magnetic fields used in this instrument require that there be no magnetic materials located within a few meters. Thus, it is placed on a relatively long beamline to provide the maximum separation from other instruments. A total moderator-to-

detector distance of 25 m on the 10-Hz source allows the use of wavelengths up to 15 Å without frame-overlap. The intensity at wavelengths longer than this is not adequate for most experiments. A coupled liquid H_2 moderator and a neutron guide provide the maximum flux of cold neutrons on the sample. Operation of this instrument is very similar to the operation of IN11. On the assumption that the gain in the effective use of neutrons is ~8, data rates are expected to be within a factor of ~2 of those on IN11, while resolution and dynamical range are at least a factor of 10 better[38] than on IN11. Table V.2.7-1 summarizes the expected performance of this instrument and makes comparisons with IN11 where appropriate. Figure V.2.7-1 shows a schematic representation of the TOFNSE instrument.

2.8 OTHER NEUTRON BEAM FACILITIES

2.8.1 New Reference Set Instrument

2.8.1.1 DEVEL — Instrument and Component Development

Many of the instruments contemplated for IPNS Upgrade require development of one or more components in order to optimize performance. To assist in such development, one beamline is provided for general development work on neutron instrument components such as crystal analyzers and monochromators, detectors, collimators, and polarization devices. Such a development beamline requires appropriate collimation and shielding, a suitable work area, one or more detectors, and a data-acquisition system. This instrument is at the 10-Hz target station.

2.8.2 Other Possible Beamline Facilities

These facilities are not included as part of the reference set, and will probably not be among the initial complement at IPNS Upgrade. They might be installed at a later date if demand warrants.

2.8.2.1 RADIO — Neutron Radiography/Tomography

The integrated thermal neutron beam current at the surface of a 10×10-cm^2 coupled liquid H_2 moderator on the 10-Hz target is $\sim 2 \times 10^{14}$ n/sr-sec. Cold neutrons make up 1/6 of this flux. The total thermal flux at the end of a 25-m beamline that views this moderator directly is $\sim 3 \times 10^7$ n/cm^2-sec, and the corresponding cold neutron flux is $\sim 5 \times 10^6$ n/cm^2-sec. These time-averaged fluxes are adequate for a wide range of neutron radiography.[41] A direct view of this moderator with no further collimation provides a length-to-diameter (L/D) ratio of 250, which

Table V.2.7-1 TOFNSE Parameters at IPNS Upgrade (comparison with IN11)

Parameter	IN11	TOFNSE
Source-sample distance (m)		~20
Sample-detector distance (m)		~5
Source repetition rate (Hz)		10
Moderator material		coupled liquid H_2
Neutron guide		yes
Bandwidth-limiting choppers		one or two
Background-suppression chopper		if needed
Max. beam size at sample (cm^2)	3 × 3	3 × 3
Wavelength range (Å)	~4-8	~4-15
Range of scattering angles (°)	1.5-140	1.5-140
Spectral resolution[a] (meV)		
at 4 Å	$6 \times 10^{-5} - 6 \times 10^{-1}$	$6 \times 10^{-5} - 6 \times 10^{-1}$
at 8 Å	$8 \times 10^{-6} - 8 \times 10^{-2}$	$8 \times 10^{-6} - 8 \times 10^{-2}$
at 15 Å	-	$1 \times 10^{-6} - 1 \times 10^{-2}$
Dynamical range t_{max}/t_{min}	~1000	~50,000
Q-resolution (%)	~20	<1.5
Typical time to measure one data set (h)	1-24	2-48

[a] The definition of "spectral resolution" differs from the definition of energy resolution on conventional spectrometers (see Reference 40).
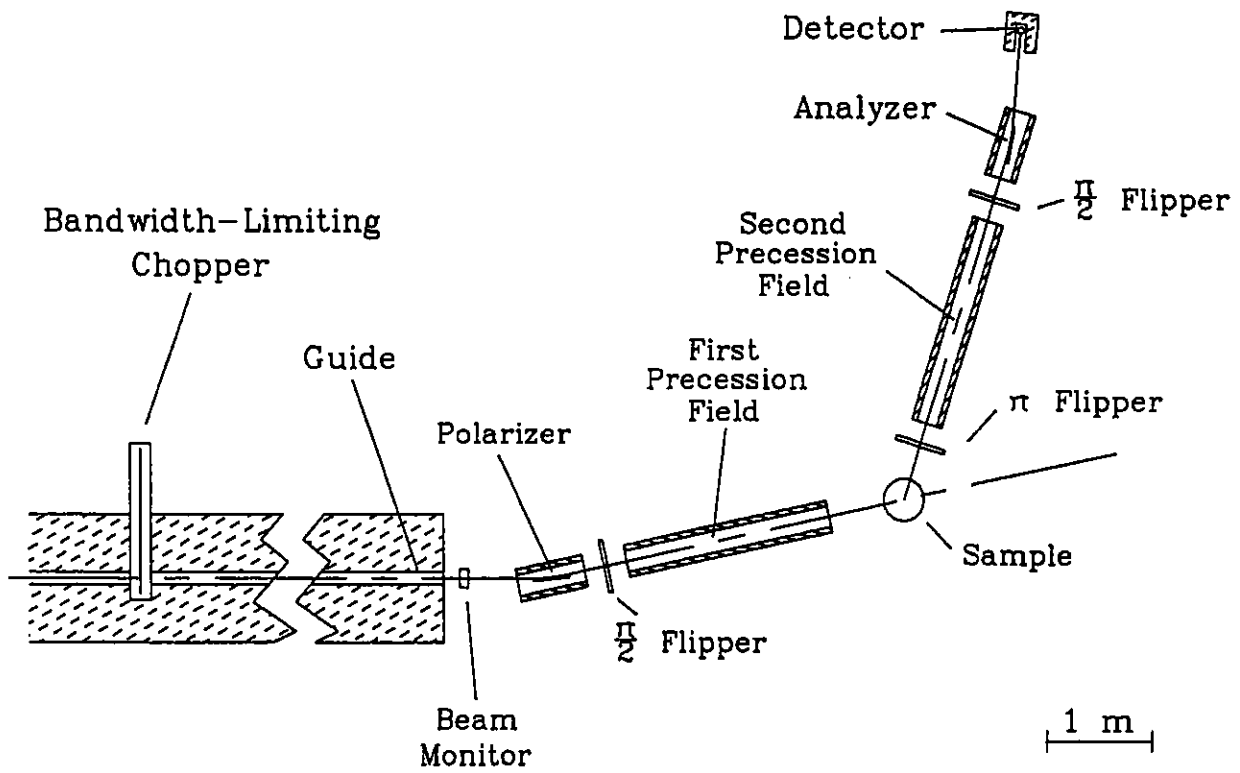
Figure V.2.7-1 Schematic Representation of the TOFNSE.

gives a resolution of 1 mm for an object 25 cm from the detector plane. This resolution is adequate for viewing many large objects, but additional collimation can be inserted when necessary.

The RADIO can perform high-resolution time-integrated radiography using standard film or transfer-foil techniques and inserting various filters in the beam. Insertion of a Be filter into the beam allows cold-neutron radiography, while an MgO or sapphire filter limits the beam to thermal neutrons. A Cd or Gd filter can be used to remove the thermal neutrons, so fast-neutron radiography can also be performed on the same beamline.

A detector with timing capabilities can be used to collect the fast, thermal, and cold neutron radiographs concurrently. Resonance radiography and time-dependent radiography can be done on the same beamline. This facility can also be used for neutron tomography to provide a three-dimensional image of the specimen when desired.

2.8.2.2 NDP/NAA — Neutron Depth Profiling and Neutron Activation Analysis

The relatively high time-averaged flux of cold neutrons available at IPNS Upgrade make it possible to perform NDP and NAA, as well as they can be done at a $\sim 10^{14}$-n/cm^2-sec reactor. The time structure of the pulsed source appears to offer no pronounced advantages for these techniques.

2.8.2.3 UCN — Ultra-Cold Neutron Facility

The relatively high time-averaged flux of cold neutrons available at IPNS Upgrade make it possible to construct an ultra-cold neutron facility that functions as well as at a $\sim 10^{14}$-n/cm^2-sec reactor. The time structure of the pulsed source may offer some advantages for the production of ultra-cold neutrons.

2.8.2.4 NINT — Neutron Interferometer

The relatively high time-averaged flux of cold neutrons available at IPNS Upgrade make it possible to build a neutron interferometer that performs as well as a comparable interferometer at a $\sim 10^{14}$-n/cm^2-sec reactor. The time structure of the pulsed source appears to offer no pronounced advantage for most types of interferometry experiments.

2.9 REFERENCE BEAM PORT ASSIGNMENTS

Table V.2.9-1 lists the reference set of neutron scattering instruments identified in this chapter, separated according to 30-Hz and 10-Hz target stations. Also listed in the table are the

flight-path lengths and moderator types required for these instruments. On the basis of these requirements, the instruments are assigned to beam ports on the two target stations, as indicated in the table. Table V.2.9-2 clearly indicates the types of moderators used in each of the six moderator locations on each target station and shows which instruments share each moderator.

Figure V.2.9-1 shows the locations of the instruments on their respective beamlines in the experiment halls. Buildings 369 and 370 accommodate all of the instruments in this reference set, with only the projected path that might be used for some configurations of the special-purpose small-angle neutron diffractometer SPSAND extending outside the buildings. If necessary, most of the remaining unused beamlines can be extended outside the buildings if some longer-flight-path instruments are desired in the future.

Table V.2.9-1 Beamline Requirements for Instruments

Instrument	Section	L_i (m)	L_f (m)	Moderator	Coupling[a]	Beam Port[b]
30-Hz Target						
*SEPD	2.1.1.1	12	1.5	CH_4[c]		H-B-3
*GPPD	2.1.1.2	25	1.5-4	CH_4[c]		H-B-2
HRPD	2.1.2.1	50	2	CH_4[c]		H-E-1
RSD	2.1.2.2	25	1.5-3	CH_4[c]		H-E-2
VSPD	2.1.2.3	12	0.75	CH_4[c]		H-F-3
*GLAD	2.3.1.1	23.5[d]	1.5	CH_4		H-A-1
*SCD	2.3.1.2	10	0.6	CH_4[c]		H-C-3
HQSCD	2.3.2.1	30	0.7	CH_4[c]		H-B-1
*HRMECS	2.5.1.1	18	4	CH_4		H-A-3
*LRMECS	2.5.1.2	12	2.5	CH_4		H-F-2
SCCS	2.5.2.2	16	4	H_2O		H-E-3
*QENS	2.6.1.1	9	≤1	CH_4[e]		H-F-1
TFCA	2.6.2.2	16	≤1.5	CH_4		H-C-1
QSTAXC	2.6.2.3	17	≤2	H_2	coupled	H-D-3
MICAS	2.6.2.4	12	1.5	CH_4		H-A-2
10-Hz Target						
*SAND	2.2.1.1	12	2	H_2	coupled	L-A-2
HRSAND	2.2.2.1	20	5	H_2	coupled	L-A-1
SPSAND	2.2.2.2	≤40		H_2	coupled	L-A-3
*POSY-I	2.4.1.1	18	≤2	H_2		L-F-2
HIREF	2.4.2.1	18	≤2	H_2		L-F-2
*POSY-II	2.4.1.2	18	≤2	H_2		L-F-3
GREF	2.4.2.2	18	5	H_2		L-F-3
REFD	2.4.2.3	18		H_2		L-F-3
CNCS	2.5.2.1	20	4	H_2		L-D-1
HRBS	2.6.2.1	30	3	H_2		L-D-2
TOFNSE	2.7.1.1	16	4	H_2	coupled	L-E-1
DEVEL	2.8.1.1					L-F-1

* Instruments transferred from IPNS. All other instruments are new construction.

[a] All moderators are decoupled unless otherwise noted.

[b] Beam ports are numbered clockwise from the proton beam, as viewed from above, for each target station. Numbering scheme is target station (L or H) - moderator (A thru F) and beam port on that moderator (1 thru 3). See Figure IV.4.1-2.

[c] Could be H_2O.

[d] To low-resolution sample position.

[e] Could be poisoned H_2.

Table V.2.9-2 Moderator Types

Beam Port[a]	Material	Instruments	Beam Port[a]	Material	Instruments
30-Hz target station			10-Hz target station		
H-A-1	liquid CH_4	GLAD	L-A-1	coupled liq. H_2	HRSAND
H-A-2		MICAS	L-A-2		SAND
H-A-3		HRMECS	L-A-3		SPSAND
H-B-1	room temp. H_2O	HQSCD	L-B-1	-[b]	-
H-B-2		GPPD	L-B-2		-
H-B-3		SEPD	L-B-3		-
H-C-1	liquid CH_4	TFCA	L-C-1	-	-
H-C-2		-	L-C-2		-
H-C-3		SCD	L-C-3		-
H-D-1	coupled liq. H_2	-	L-D-1	poisoned liq. H_2	CNCS
H-D-2		-	L-D-2		HRBS
H-D-3		QSTAXC	L-D-3		-
H-E-1	room temp. H_2O	HRPD	L-E-1	coupled liq. H_2	TOFNSE
H-E-2		RSD	L-E-2		-
H-E-3		SCCS	L-E-3		-
H-F-1	liquid CH_4	QENS	L-F-1	liquid H_2	DEVEL
H-F-2		LRMECS	L-F-2		POSY-I/HIREF
H-F-3		VSPD	L-F-3		POSY-II/GREF/ REFD

[a] Beam ports are numbered clockwise from the proton beam, as viewed from above, for each target station. Numbering scheme is target station (L or H) moderator (A thru F) and beam port on that moderator (1 thru 3). See Figure IV.4.1-2.

[b] - = not used for initial instrument complement.
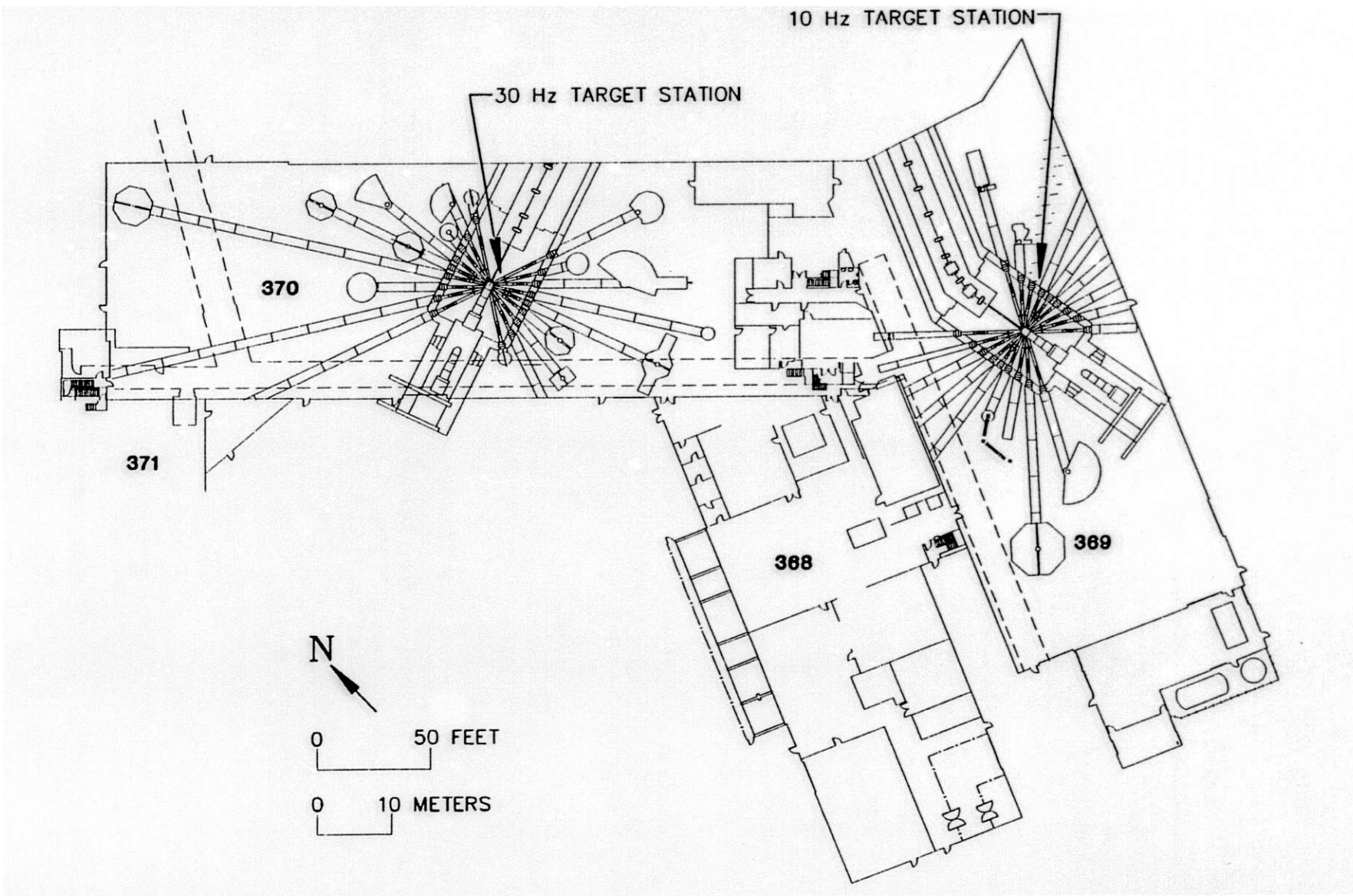
Figure V.2.9-1 Location of the Reference Set of Instruments on the Neutron Beamlines. (The 30-Hz target station is in Building 370, and the 10-Hz target station is in Building 369.)

2.10 REFERENCES

1. J.D. Jorgensen et al., "Electronically focused time-of-flight powder diffractometers at the Intense Pulsed Neutron Source," J. Appl. Cryst. **22**, 321-333 (1989).

2. J.D. Jorgensen, "Multiple-angle time-of-flight design concepts: Are we overlooking an order of magnitude in instrument performance for general structural studies?," in *Proceedings of the 1986 Workshop on Advanced Time-of-Flight Neutron Powder Diffraction* (Los Alamos, N.M., May 19-21, 1986), Los Alamos National Laboratory Report No. LA-10824-C, pp. 43-45 (1986).

3. W.I.F. David, "Powder diffraction at ISIS," in *Proceedings of the 11th Meeting of the International Collaboration on Advanced Neutron Sources (ICANS-XI)* (Tsukuba, Japan, Oct. 22-26, 1990), National Laboratory for High Energy Physics (KEK) Report No. 90-25, pp. 1114-1121 (1991).

4. A. Oed, "Position-sensitive detector with microstrip anode for electron multiplication with gases," Nucl. Instrum. Methods **A263**, 351-359 (1988).

5. P. Geltenbort and A. Oed, "Features of microstrip proportional counters," in *Proceedings of SPIE's 1992 International Symposium on Optical Applied Science and Engineering* (San Diego, Calif., July 19-24, 1992), vol. 1737, pp. 289-293 (1992).

6. J.E. Epperson and P. Thiyagarajan, "Anomalous and resonance small angle scattering," J. Appl. Cryst. **21**, 652-662 (1988).

7. B. Hammouda, S. Krueger, and C. Glinka, "Small angle neutron scattering at National Institute of Standards and Technology," NIST J. Res. (1991).

8. D. Schwahn et al., "Test of channel-cut perfect crystals for neutron small angle scattering experiments," Nucl. Instrum. Methods **A239**, 229-234 (1985).

9. R.K. Crawford et al., "Status of the new GLAD instrument at IPNS," in *Proceedings of the 11th Meeting of the International Collaboration on Advanced Neutron Sources (ICANS-XI)* (Tsukuba, Japan, Oct. 22-26, 1990), National Laboratory for High Energy Physics (KEK) Report No. 90-25, pp. 820-829 (1991).

10. A.J. Schultz, R.G. Teller, and J.M. Williams, "The IPNS time-of-flight single crystal diffractometer," in *Proceedings of the 6th Meeting of the International Collaboration on Advanced Neutron Sources (ICANS-VI)* (Argonne, Ill., June 28-July 2, 1982), Argonne National Laboratory Report No. ANL-82-80, pp. 116-124 (1982).

11. B.P. Schoenborn and R. Diamond, "Neutron diffraction analysis of metmyoglobin," in *Neutron Scattering for the Analysis of Biological Structures*, Report of Symposium (June 2-6, 1975), edited by B.P. Schoenborn, Brookhaven Symposia in Biology No. 27, Brookhaven National Laboratory Report No. BNL 50453, pp. II-3-II-11 (1976).

12. B.P. Schoenborn, "A protein structure is only as good as the data," in *Neutrons in Biology*, edited by B.P. Schoenborn, pp. 261-279 (Plenum, New York, 1984).

13. G.P. Felcher et al., "Polarized neutron reflectometer: A new instrument to measure magnetic depth profiles," Rev. Sci. Instrum. **58**, 609-619 (1987).

14. A. Karim et al., "An automated neutron reflectometer (POSY II) at the Intense Pulsed Neutron Source," Physica B **173**, 17-24 (1991).

15. D.L. Price et al., "The IPNS-I chopper spectrometers," in *Proceedings of the 6th Meeting of the International Collaboration on Advanced Neutron Sources (ICANS-VI)* (Argonne, Ill., June 28-July 2, 1982), Argonne National Laboratory Report No. ANL-82-80, pp. 207-215 (1982).

16. C.-K. Loong, S. Ikeda, and J.M. Carpenter, "The resolution function of a pulsed-source neutron chopper spectrometer," Nucl. Instrum. Methods **A260**, 381-402 (1987).

17. J.M. Carpenter and C.-K. Loong, "IPNS chopper spectrometer improvements," in *Proceedings of the 11th Meeting of the International Collaboration on Advanced Neutron Sources (ICANS-XI)* (Tsukuba, Japan, Oct. 22-26, 1990), National Laboratory for High Energy Physics (KEK) Report No. 90-25, pp. 711-716 (1991).

18. *Neutron Research Facilities at the ILL High Flux Reactor* (Institut Laue-Langevin, Grenoble, France, 1983).

19. R.E. Lechner, "Optimization of a multi-disk chopper spectrometer for cold neutron scattering experiments," in *Proceedings of the 11th Meeting of the International Collaboration on Advanced Neutron Sources (ICANS-XI)* (Tsukuba, Japan, Oct. 22-26, 1990), National Laboratory for High Energy Physics (KEK) Report No. 90-25, pp. 717-732 (1991).

20. C.-K. Loong et al., "Neutron scattering study of the magnetic excitations in ferromagnetic iron at high energy transfers," J. Appl. Phys. **55**, 1895-1897 (1984).

21. S. Hayden et al., "High energy spin waves in La_2CuO_4," Phys. Rev. Lett. **67**, 3622 (1991).

22. R.T. Heap et al., "High energy magnetic excitations in chromium," Physica B **174**, 22 (1991).

23. D.McK. Paul and A. Boothroyd, "MAPS: A Multi-Angle Position Sensitive Spectrometer," Rutherford Appleton Laboratory, 1992 (unpublished).

24. R.A Robinson, "On the kinematics and resolution of spectrometers for neutron Brillouin scattering," in *Advanced Neutron Sources 1988*, Proceedings of the 10th Meeting of the International Collaboration on Advanced Neutron Sources (ICANS-X) (Los Alamos, N.M., Oct. 3-7, 1988), Institute of Physics Conference Series No. 97, pp. 311-325 (Institute of Physics, New York, 1989).

25. K.F. Bradley et al., "The design and performance of QENS, a medium resolution, inverted geometry, TOF quasielastic and inelastic spectrometer at IPNS," Nucl. Instrum. Methods **A270**, 78-89 (1988).

26. H. Chen et al., "Cold neutron focusing using capillary optics," in *Proceedings of SPIE's 1992 International Symposium on Optical Applied Science and Engineering* (San Diego, Calif., July 19-24, 1992), Vol. 1738 (1992).

27. D.F.R. Mildner, A. Magerl, and U. Grüning, "Promise of thin silicon wafer microguides for future optical elements," in *Proceedings of SPIE's 1992 International Symposium on Optical Applied Science and Engineering* (San Diego, Calif., July 19-24, 1992), Vol. 1738 (1992).

28. C.J. Carlile et al., "Advances in crystal analyser spectroscopy at ISIS," in *Proceedings of the 11th Meeting of the International Collaboration on Advanced Neutron Sources (ICANS-XI)* (Tsukuba, Japan, Oct. 22-26, 1990), National Laboratory for High Energy Physics (KEK) Report No. 90-25, pp. 752-773 (1991).

29. S. Ikeda et al., "High resolution neutron spectrometer LAM-80ET and rotational tunnelling in 4-methylpyridine N-oxide," J. Phys. Soc. Japan **60**, 3340-3350 (1991).

30. J. Penfold and J. Tomkinson, *The ISIS Time Focused Crystal Analyser Spectrometer, TFXA*, Rutherford Appleton Laboratory Report No. RAL-86-019 (1986).

31. W.G. Stirling and W. Kaiser, *Preliminary Technical Specifications for Triple-Axis Spectrometer IN-14*, Institut Laue-Langevin Technical Report No. 83ST24T (Grenoble, France, 1984).

32. Y. Todate et al., "Recent progress on MAX," in *Proceedings of the 11th Meeting of the International Collaboration on Advanced Neutron Sources (ICANS-XI)* (Tsukuba, Japan, Oct. 22-26, 1990), National Laboratory for High Energy Physics (KEK) Report No. 90-25, pp. 739-742 (1991).

33. U. Steigenberger et al., "Progress with the PRISMA spectrometer," in *Proceedings of the 11th Meeting of the International Collaboration on Advanced Neutron Sources (ICANS-XI)* (Tsukuba, Japan, Oct. 22-26, 1990), National Laboratory for High Energy Physics (KEK) Report No. 90-25, pp. 743-751 (1991).

34. F. Mezei, "The principles of neutron spin echo," in *Neutron Spin Echo*, edited by F. Mezei Lecture Notes in Physics, vol. 128, pp. 3-26 (Springer-Verlag, New York, 1980).

35. O. Schärpf, "The polarized neutron technique of neutron spin echo," in *Neutron Spin Echo*, edited by F. Mezei, Lecture Notes in Physics, vol. 128, pp. 27-52 (Springer-Verlag, New York, 1980).

36. J. Hayter, "Theory of neutron spin-echo spectroscopy," in *Neutron Spin Echo*, edited by F. Mezei, Lecture Notes in Physics, vol. 128, pp. 53-65 (Springer-Verlag, New York, 1980).

37. P.A. Dagleish, J.B. Hayter, and F. Mezei, "The IN11 neutron spin echo spectrometer," in *Neutron Spin Echo*, edited by F. Mezei, Lecture Notes in Physics, vol. 128, pp. 66-71 (Springer-Verlag, New York, 1980).

38. F. Mezei and D. Richter, "Time-of-flight spin echo," in *Proceedings of the Workshop on Neutron Scattering Instrumentation for SNQ* (Maria Laach, Germany, Sept. 3-5, 1984), KFA Jülich Report No. 1954, pp. 368-377 (1984).

39. J. Penfold and W.G. Williams, *Neutron Spin Echo Spectroscopy on the Spallation Neutron Source*, Rutherford Appleton Laboratory Report No. RL-81-019 (1981).

40. A. Heidemann, W.S. Howells, and G. Jenkin, "Comparison of the performance of the backscattering spectrometer IN10 and the neutron spin echo spectrometer IN11 on the basis of experimental results," in *Neutron Spin Echo*, edited by F. Mezei, Lecture Notes in Physics, vol. 128, pp. 122-135 (Springer-Verlag, New York, 1980).

41. J.P. Barton and P. Von Der Hardt (editors), *Neutron Radiography*, proceedings of the First World Conference (San Diego, Calif., Dec. 7-10, 1981) (D. Reidel Publishing, Dordrecht, Holland, 1983).

3.1 CHOPPERS

3.1.1 Chopper Fundamentals

Neutron choppers are devices that interrupt a neutron beam in a controlled fashion. Most neutron choppers are rotating mechanical devices. The basic equations for estimating the performance of such devices are summarized below; a much more detailed discussion of performance and optimization of rotating mechanical choppers is available in the book by Windsor.[1] Alternatives to rotating mechanical choppers of the types discussed here have been used in some specialized applications. These alternatives include velocity selectors, statistical choppers, magnetic field choppers for polarized neutrons, oscillating or rotating Bragg-reflecting crystals, and nonrotating mechanical devices (linear motion, such as in piezoelectric, magnetic, or mechanical drives). However, since none of these alternative methods is required for use on the initial complement of instruments at IPNS Upgrade, the discussion here is restricted to the Fermi, drum, and disk types of rotating mechanical choppers.

The Fermi chopper is opaque to neutrons but contains a package of slits, usually curved, which transmit neutrons of certain speeds when the slits are lined up with the neutron beam. Such a chopper is shown schematically in Figure V.3.1-1a. Fermi choppers are rotated, usually at high rotational speeds, about an axis that is perpendicular to the neutron beam. Such choppers are capable of transmitting bursts of neutrons that have very narrow time-widths and hence are suitable for precise TOF measurements.

The time-width Δt of the pulse of optimal-energy neutrons from such a Fermi chopper is given by

$$\Delta t = \left[\left(\frac{d}{2\omega r} \right)^2 + \left(\frac{\Delta\alpha}{\omega} \right)^2 \right]^{1/2} , \qquad (V.3.1-1)$$

where the first term inside the square brackets is the square of the chopper pulse-width for a perfectly collimated beam and the second term gives the lighthouse effect resulting from the finite divergence $\Delta\alpha$ in the incident beam. Here ω is the angular frequency of the chopper, d is the chopper slit-width, and r is the chopper radius. The transmission of such a chopper is a maximum for neutrons of velocity

$$v_o = 2\omega R , \qquad (V.3.1-2)$$

where R is the radius of curvature of the chopper slits. For neutron velocities v not too different in value from v_o, the transmission T is given by

$$T = X \left[1 - \frac{8\omega^2 r^4}{3d^2} \left(\frac{1}{v} - \frac{1}{v_o} \right)^2 \right] , \qquad (V.3.1-3)$$
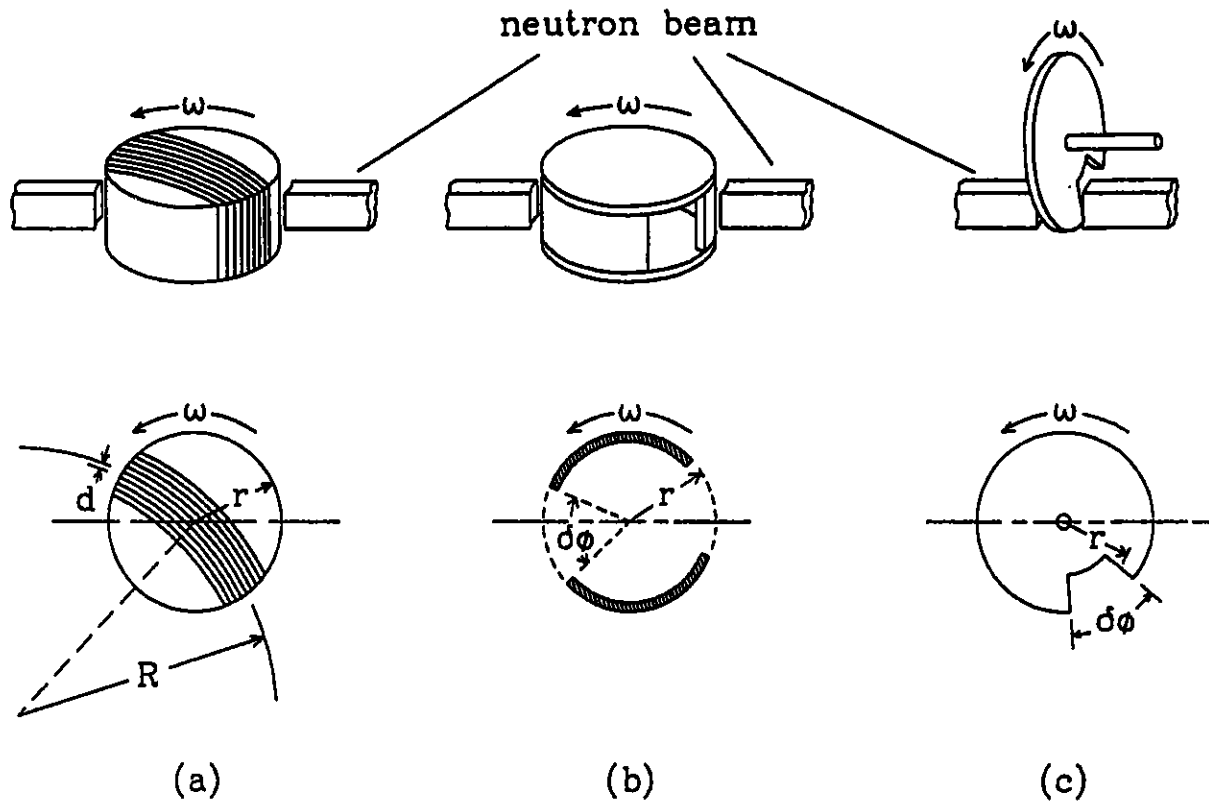
Figure V.3.1-1 Schematic Representations of (a) Fermi, (b) Drum, and (c) Disk Choppers. (Symbols used in the text are defined here.)

where X is the fraction of the cross-sectional area of the slit package that is transparent to neutrons.

Drum and disk choppers are shown schematically in Figures V.3.1-1b and V.3.1-1c, respectively. A drum chopper is rotated about an axis that is perpendicular to the neutron beam, while a disk chopper is rotated about an axis that is parallel to the neutron beam. These choppers are used to block the neutron beam for selected time intervals, such as when it is desired to limit the range of wavelengths that reach the sample or to prevent fast neutrons from the prompt t_0 pulse from reaching the sample. These types of choppers are generally not capable of producing sharp pulses of neutrons for precise TOF measurements except when very narrow beams of neutrons are being chopped.

The effective width W of the neutron beam at the chopper is

$$W = [W_s L_c + W_m(L_s - L_c)]/L_s , \qquad (V.3.1-4)$$

where W_m and W_s are the widths of the moderator and sample (or corresponding beam-defining apertures), respectively, and L_c and L_s are the moderator-to-chopper and moderator-to-sample distances, respectively. In order to go from fully open to fully closed, a disk chopper must rotate neutron absorber through the effective beam-width W, while each side of a drum chopper only has to rotate absorber through half the beam. The required angular rotation $\delta\phi_c$ in the two cases is given by

$$\delta\phi_c = 2 \sin^{-1} (W/2r) \qquad\qquad \text{disk}$$

$$\qquad\qquad\qquad\qquad\qquad\qquad\qquad\qquad (V.3.1-5)$$

$$\delta\phi_c = \sin^{-1} (W/2r) \qquad\qquad \text{drum} ,$$

where r is the chopper radius. This definition of $\delta\phi_c$ allows the following equations to apply to both types of choppers.

The time δt_c required for this rotation is

$$\delta t_c = \delta\phi_c/\omega . \qquad\qquad (V.3.1-6)$$

During this rotation, neutrons having a range of wavelengths $\delta\lambda_c$ are incident on, and partially transmitted by, the chopper:

$$\delta\lambda_c = (h/m) \, \delta\phi_c/\omega L_c , \qquad\qquad (V.3.1.-7)$$

where h/m = 3955.4 Å-m/sec is Planck's constant divided by the neutron mass.

If it is desired that a disk or drum chopper be fully open for neutrons with wavelengths between λ_{min} and λ_{max}, then the chopper must be fully open between times t_{min} and t_{max}. During this time interval, the chopper rotates through an angle $\delta\phi_r$ given by

$$\delta\phi_r = \omega\left(t_{max} - t_{min}\right) \tag{V.3.1-8}$$

$$= (m/h)\,\omega L_c\,\delta\lambda \; ,$$

where

$$\delta\lambda = \lambda_{max} - \lambda_{min} \; . \tag{V.3.1-9}$$

The total chopper open angle $\delta\phi$ required in order to give the desired bandpass is

$$\delta\phi = \delta\phi_r + \delta\phi_c \qquad\qquad\qquad \text{disk}$$
$$\tag{V.3.1-10}$$
$$\delta\phi = \delta\phi_r + 2\,\delta\phi_c \qquad\qquad\qquad \text{drum} \; .$$

Drum choppers have the advantage that they open and close uniformly across the beam, while disk choppers open and close less rapidly for the portions of the beam nearer the disk axis. Thus, disk choppers are less satisfactory for large beams. Drum choppers can also incorporate large amounts of neutron absorber more easily than can disk choppers. However, on instruments with neutron guides, a disk chopper requires only one cut in the guide, while a drum chopper requires two. Furthermore, a pair of synchronized counter-rotating disk choppers can be made to open and close twice as fast as a single disk chopper of the same size and speed. In practice, the spatial constraints imposed by adjacent equipment may dictate which type of chopper is to be used.

If the moderator-sample-detector distance is L_d and the source repetition rate is f, then the maximum wavelength of neutrons that can reach the detector before the next pulse occurs is λ_{frame}, given by

$$\lambda_{frame} = (h/m)\,/\,fL_d \; . \tag{V.3.1-11}$$

The maximum wavelength that is transmitted before the chopper is fully closed is λ_{cl}, given by

$$\lambda_{cl} = \lambda_{max} + \delta\lambda_c \; . \tag{V.3.1-12}$$

Neutrons of this wavelength arrive at the detector at the same time as neutrons having the wavelength λ_{fo} originating from the following pulse, where

$$\lambda_{fo} = \lambda_{cl} - \lambda_{frame} \; . \tag{V.3.1-13}$$

If λ_{fo} is negative, then none of the neutrons transmitted by the chopper arrive at the detectors during the following frame. However, if λ_{fo} is positive, the portion of the spectrum at wavelengths up to λ_{fo} is contaminated with such frame-overlap neutrons. If λ_{fo} is less than λ_{min}, this is still not a problem; if λ_{fo} is greater than λ_{min}, a frame-overlap condition exists, and the quality of the data may be degraded.

3.1.2 Survey of Chopper Requirements

Table V.3.1-1 lists the instruments that form the reference set and summarizes the requirements for choppers of various types. The sections of Chapter V where each of these instruments is discussed above are also indicated. Specific choppers to satisfy each of these requirements are discussed below.

3.1.3 Specific Chopper Designs

3.1.3.1 Fermi E_0 Choppers

The E_0 choppers are used to select the energy of the neutrons incident on the sample in chopper spectrometers and in specialized uses of some other instruments. At IPNS, several different choppers with transmissions optimized for different energies are available for use on the HRMECS and LRMECS.[2] These mechanical-bearing choppers, with relatively massive Be bodies and B/Al composite slit packages, are reliable and are very effective in stopping fast neutrons. They are designed to transmit relatively large beams, 5×10 cm^2 for the LRMECS and 7.5×10 cm^2 for the HRMECS, making it possible to take advantage of large samples. These choppers are used at IPNS Upgrade as well.

Additional choppers of this type are required in order to extend the energies for which optimized choppers are available and to avoid conflicts in scheduling the use of specific choppers for several instruments. These IPNS choppers are limited to a maximum rotational frequency of 270 Hz. Figure V.3.1-2 shows such a chopper schematically. Figure V.3.1-3 shows the transmissions of the IPNS choppers at 270 Hz as functions of neutron energy, calculated using the full expression for the transmission function.[3] This figure indicates that at least four, and perhaps five, different choppers are required to span the full range of incident energies useful on such instruments as the HRMECS and LRMECS.

Equation V.3.1-1 shows that the chopper pulse-width can be decreased, and hence the resolution improved, either by decreasing d or by increasing the rotational speed ω. There are practical limits to how small d can be made, so to provide better time resolution than that available from the IPNS choppers, ω must be increased. ISIS instruments operate with somewhat smaller choppers having Al bodies and B/Al composite slit packages. These choppers

Table V.3.1-1 Required Chopper Types

Instrument	Section	E_o	t_o Broad	t_o Narrow	Pulse-Eliminating	Background/Bandwidth[a]
SEPD	2.1.1.1					bkgnd
GPPD	2.1.1.2					<0.4 - 4.6>
HRPD	2.1.2.1		yes ?		<yes>	<0.4 - 2.4>
RSD	2.1.2.2					bkgnd
VSPD	2.1.2.3					bkgnd
SAND	2.2.1.1	yes ?	yes ?		?	<bkgnd>
HRSAND	2.2.2.1					<bkgnd>
SPSAND	2.2.2.2	yes ?	yes			bkgnd
GLAD	2.3.1.1	yes	?	yes		bkgnd
SCD	2.3.1.2					bkgnd ?
HQSCD	2.3.2.1					bkgnd ?
POSY-I	2.4.1.1		yes			?
POSY-II	2.4.1.2		yes			?
HIREF	2.4.2.1		yes			?
GREF	2.4.2.2		yes			?
REFD	2.4.2.3		yes			?
HRMECS	2.5.1.1	<yes>		<yes>		
LRMECS	2.5.1.2	<yes>		<yes>		
CNCS	2.5.2.1	<yes>		<yes>		
SCCS	2.5.2.2	<yes>		<yes>		
QENS	2.6.1.1					bkgnd ?
HRBS	2.6.2.1					<band>
TFCA	2.6.2.2					bkgnd ?
QSTAXC	2.6.2.3					
MICAS	2.6.2.4					bkgnd ?
TOFNSE	2.7.1.1					band?
Total Essential		4	0	4	1	5
Total Potential		7	8	5	1	16

<> Essential

[a] Abbreviated as "bkgnd" and "band" here.
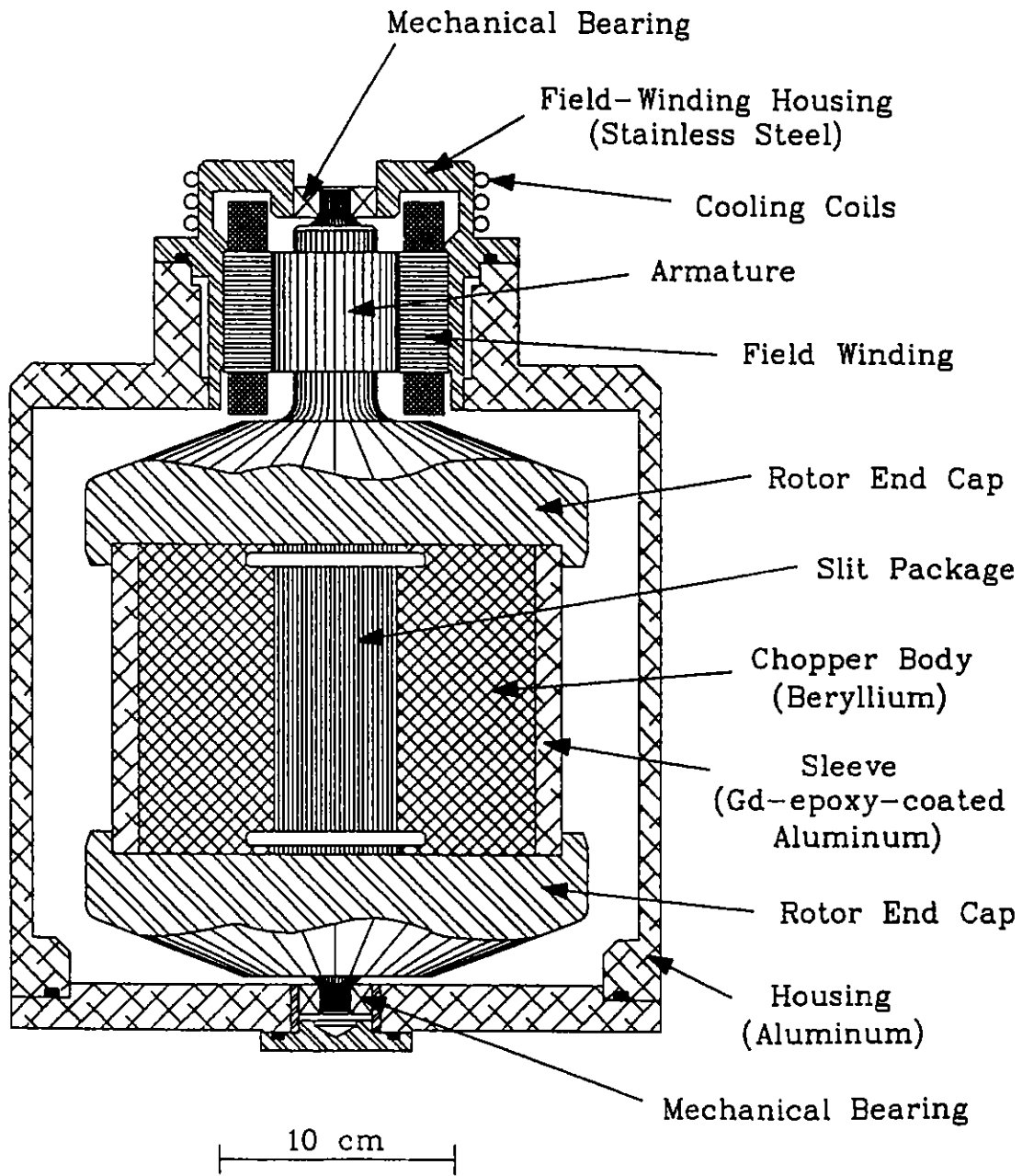
Figure V.3.1-2 The IPNS Fermi E_0 Chopper Design.
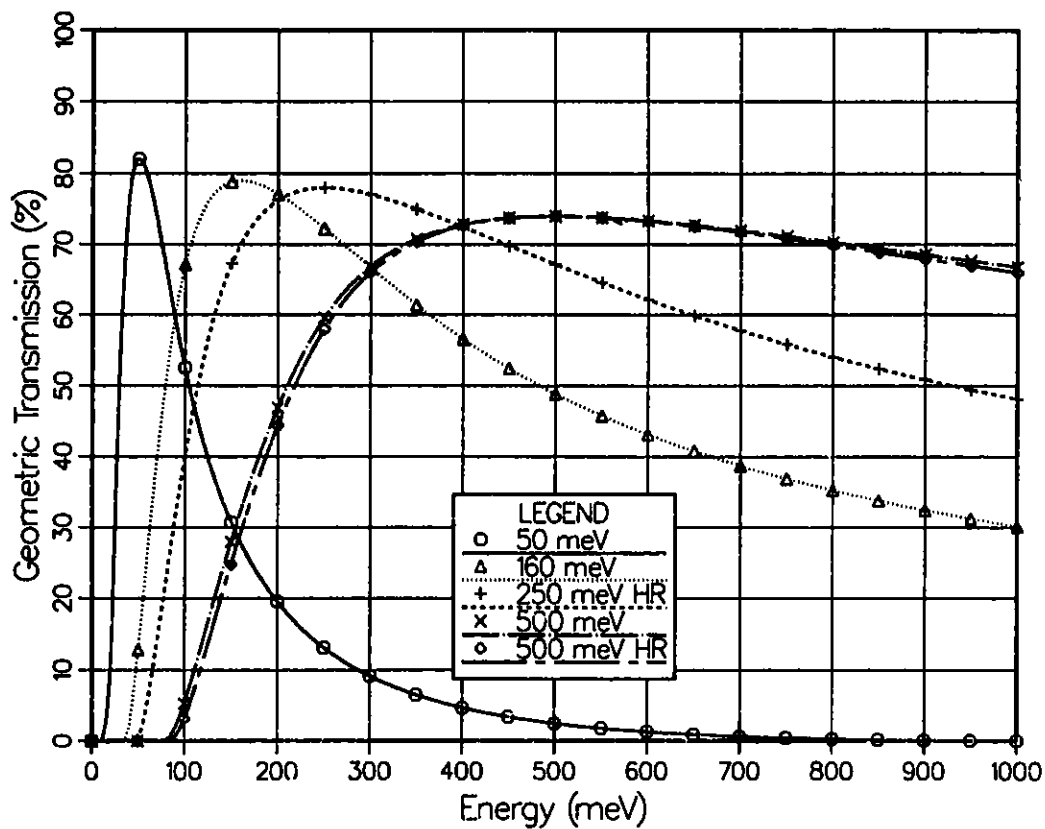
Figure V.3.1-3 Transmissions of the IPNS Fermi E_0 Choppers at 270 Hz.
HR indicates a high-resolution slit package.

have magnetic bearings and can rotate at frequencies up to 600 Hz.[4] However, because the choppers are smaller, they cannot transmit beams of such large cross section as can the IPNS choppers, and because they are made of Al, they have little stopping power for fast neutrons. Thus, a narrow-band t_0 chopper must be used upstream from such an E_0 chopper in order to reduce the fast-neutron background. Although it is not essential to have such fast choppers, the flexibility of the instruments and the extremes in resolution will be enhanced if several such choppers, optimized for different energy ranges, are available to complement the IPNS-type E_0 choppers. The technology developed at ISIS can be used for any such choppers designed for IPNS Upgrade instruments. This design can incorporate the same mounting fixtures used for the IPNS choppers, in order to facilitate the interchange of choppers on a given instrument and among instruments at IPNS Upgrade.

Table V.3.1-1 shows four instruments that require E_0 choppers and three other instruments for which they are useful in some applications. Each of the four chopper instruments needs to have access to a full set of ~ 5-7 E_0 choppers, optimized for different energies and resolutions. However, these choppers are interchangeable between instruments, so that somewhat fewer than 20-28 such choppers are required in total.

3.1.3.2 Narrow-Band t_0 Choppers

Narrow-band t_0 choppers are used for background suppression on chopper instruments, where the E_0 chopper passes only a narrow wavelength band $\Delta\lambda/\lambda$ of a few percent. In this case, the wavelength bandwidth passed by the t_0 chopper need be only slightly larger than the bandwidth passed by the E_0 chopper at this energy. The designation as a t_0 chopper implies that the chopper is neutronically opaque so that it significantly attenuates the fast neutrons in the prompt pulse at time t_0 when the chopper is closed. At IPNS, mechanical-bearing choppers made with Be bodies are used for this purpose.[5] These choppers, shown schematically in Figure V.3.1-4, are similar in size and design to the IPNS E_0 choppers but contain no slit package. The apertures in these choppers are sufficiently large to pass the full beam over the maximum bandwidth required by any of the E_0 choppers. These t_0 choppers can rotate at frequencies up to 150 Hz. Such a chopper makes many revolutions, and hence is open many times, during one time frame. Its rotational speed and phasing must be carefully chosen so that openings of the t_0 chopper only coincide with openings of the E_0 chopper for neutrons having the desired wavelength.[5] The t_0 choppers at IPNS are very effective. At least one such chopper is required for each chopper instrument at IPNS Upgrade, so 2-3 additional choppers must be fabricated in order to supply all the IPNS Upgrade instruments.

These choppers satisfy the drum chopper equations. Representative numbers for a t_0 chopper rotating at 150 Hz with $W = 6.5$ cm, $\delta\phi = 41°$, $r = 10$ cm, and $L_c = 5.5$ m, which are the conditions on the present LRMECS, are $\delta_{tc} = 351$ μsec, $\delta\lambda_c = 0.25$ Å, and $\delta\lambda_t = 0.04$ Å. If the chopper is phased to begin opening immediately after the prompt pulse, then it is fully open for neutron wavelengths of 0.25 - 0.29 Å (1309-972 MeV). If it is necessary to have a chopper fully
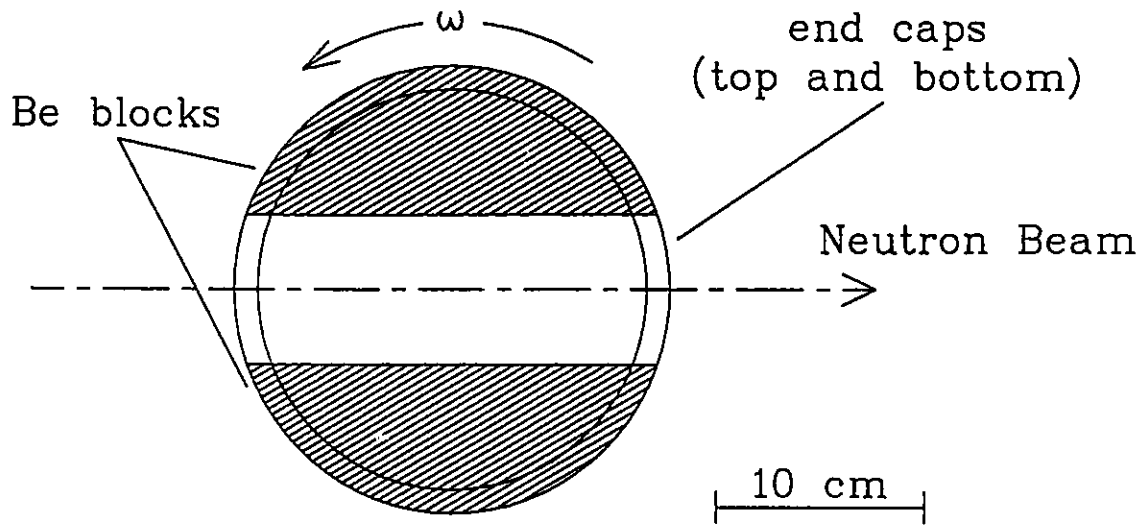
Figure V.3.1-4 The IPNS Narrow-Band t_0 Choppers.

closed at time t_0, that is fully open for shorter wavelengths, then either the beam-width at the chopper must be decreased, the distance of the chopper from the source must be increased, or the chopper radius or rotational frequency must be increased. The material properties determine the maximum peripheral velocity allowed for a particular chopper. For the IPNS t_0 chopper design, the combination of 150 Hz and 10-cm radius gives close to the allowed peripheral velocity. The only options remaining for operating such a chopper at shorter wavelengths are to increase L_c or decrease W.

3.1.3.3 Broad-Band t_0 Choppers

With the exception of the chopper instruments and a few crystal-monochromator instruments, all other TOF instruments rely on the use of a broad wavelength band of incident neutrons. However, in many of these instruments, backgrounds are improved if the fast neutrons from the prompt pulse are removed from the beam at a point far upstream from the sample. The narrow-band t_0 choppers discussed above cannot be used for this purpose, since they rotate through many revolutions in one time frame and transmit only a narrow bandwidth in each revolution. What is required is a slowly rotating chopper that places a neutronically opaque block in the beam for the duration of the prompt pulse and then moves this block out of the beam quickly and keeps it out for the remainder of the time frame of interest. Devices of this type are in operation at ISIS[6] and the Los Alamos Neutron Scattering Center (LANSCE). The ISIS t_0 chopper is shown schematically in Figure V.3.1-5. Choppers of this type satisfy all the requirements for broad-band t_0 choppers indicated in Table V.3.1-1.

The equations for a disk chopper apply to a chopper of this type. If such a chopper of radius 25 cm is operated at a frequency of 90 Hz in a 7-cm-wide beam at a distance of 5.5 m from the source, then $\delta t_c = 497$ μs and $\delta\lambda_c = 0.36$ Å. A symmetrical chopper, such as that shown in Figure V.3.1-5, places neutron absorber in the beam twice per revolution. Such a chopper rotating at 90 Hz blocks the neutron beam every 5,556 μsec, and if the chopper is located 5.5 m from the source, this occurs at intervals of 4.00 Å in the neutron spectrum. A chopper with the parameters given here operating at 90 Hz and having neutron absorber blocks as wide as the beam is fully open over the wavelength ranges 0.36-3.64 Å, 4.36-7.64 Å, etc. If the same chopper instead operates at 15 Hz so that it blocks the beam at a 30-Hz rate, then the corresponding open ranges are 2.16-21.84 Å, 26.16-45.84 Å, etc.

3.1.3.4 Pulse-Eliminating t_0 Choppers

For some of the instruments considered, the path-length and wavelength-band requirements are such that a second prompt pulse from the source occurs before the neutrons of interest reach the sample. The background at the sample is significantly reduced if this second prompt pulse is effectively blocked. It is desirable to block the fast neutrons from this second
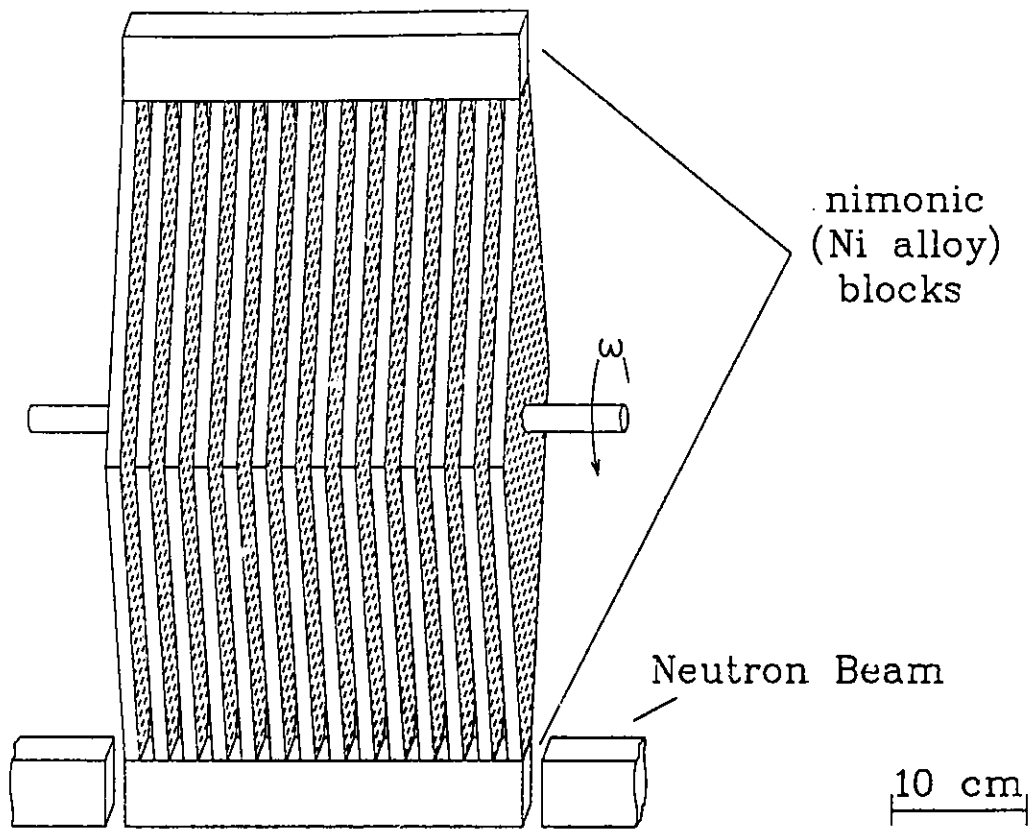
Figure V.3.1-5 The ISIS Broad-Band t_0 Chopper.

prompt pulse and also to cut out somewhat slower neutrons. These requirements can be met by operating an ISIS-style broad-band t_0 chopper to eliminate the fast neutrons from every pulse, in conjunction with one of the bandwidth-limiting choppers.

3.1.3.5 Bandwidth-Selecting Choppers

Several instruments at IPNS (SEPD, GPPD, and SAND) use slowly rotating drum choppers. These are closed for more than half of the time frame but are open for all of the neutron wavelengths used by the instrument, typically up to the maximum wavelength allowed by frame-overlap. Such choppers are very effective in eliminating much of the background due to delayed neutrons from the moderator, but they are not sufficiently opaque to stop significant numbers of fast neutrons.[7] Choppers of this type can also eliminate any background problems due to frame-overlap from longer-wavelength neutrons associated with the previous pulse.[8] The choppers in use at IPNS are 20-40 cm in diameter, with a 1-cm-thick annulus of B_4C as the stopping material and rotate at 15 Hz. This type of chopper is designed for use at a specific distance from the source on an instrument having a specific flight-path length, so these instrument-specific choppers are not usable at IPNS Upgrade. However, choppers of this type are relatively inexpensive to fabricate and can easily be installed on any of the IPNS Upgrade instruments. Since the tungsten targets at IPNS Upgrade produce only very small numbers of delayed neutrons, choppers of this type may not provide significant benefits except where frame-overlap is a problem. Therefore, such choppers are not included in most of the initial instrument configurations at IPNS Upgrade. Instrument beamlines are designed to provide for possible later inclusion of such choppers.

A few of the instruments considered (GPPD, HRPD, and HRBS) require the selection of a specific and sometimes adjustable bandwidth from the incident beam. For this purpose either disk choppers or drum choppers can be used.[7] If adjustability is required, properly phased pairs of such choppers can be used. Table V.3.1-2 indicates parameters appropriate for bandwidth-limiting choppers of either the drum or disk type on these instruments.

The data presented in the table indicate that serious frame-overlap problems occur for the GPPD and HRPD with the chopper parameters specified. In order to eliminate these problems, the choppers must be moved far enough from the source to reduce $\delta\lambda_c$ to the required value. For the 25-cm-radius disk choppers, this requires $L_c = 19.3$ m for the GPPD and $L_c = 7.75$ m for the HRPD. In both cases, it is desirable to have an additional chopper installed in the chopper cavity position described in Section IV.8 to remove most of the undesired neutrons, reducing the background generated by the downstream chopper.

For the HRBS, λ_{min} and λ_{max} are intended to be independently variable. This can be achieved by using two choppers and independently varying their phases relative to the source. If

TABLE V.3.1-2 Parameters for Bandwidth-Limiting Choppers

Instrument, by Chopper	L_s (m)	L_d (m)	W (cm)	λ_{min} (Å)	λ_{max} (Å)	λ_{frame} (Å)	$\omega/2\pi$ (Hz)	$\delta\phi_r$ (°)	$\delta\phi_c$ (°)	δt_c (μs)	$\delta\lambda_c$ (Å)	λ_{fo} (Å)
25-cm-radius disk chopper, $L_c = 5.5$ m												
GPPD	25	26.5	8	0.4	4.6	4.98	30	63.1	18.4	1705	1.23	0.85
		29				4.55						1.28
HRPD	50	52	5	0.4	2.4	2.54	30	30.0	11.5	1063	0.76	0.62
HRBS	30	36	5	2	10	10.99	10	40.1	11.5	3189	2.29	1.30
20-cm-radius drum chopper, $L_c = 5.5$ m												
GPPD	25	26.5	8	0.4	4.6	4.98	15	31.5	11.5	2137	1.54	1.16
		29				4.55						1.59
HRPD	50	52	5	0.4	2.4	2.54	15	15.0	7.2	1330	0.96	0.82
HRBS	30	36	5	2	10	10.99	5	20.0	7.2	3989	2.87	1.88

a sharper wavelength cutoff or smaller $\delta\lambda_c$ is desired, then one of these choppers can be placed farther from the source. Dual choppers can also be used on the GPPD and HRPD to permit independent variation of λ_{min} and λ_{max} for these instruments, to increase flexibility.

3.1.4 Chopper Control

Neutron choppers operating at a pulsed neutron source require a system to drive the chopper motor and maintain a constant phase with respect to the pulsed proton beam. The drive system runs the chopper at the chosen speed, monitors chopper parameters, and shuts off chopper power in the event of a potentially damaging condition. Choppers at a pulsed source typically operate at a harmonic frequency of the source. Experience has shown that a wide range of energies can be achieved with a particular chopper by operating the chopper at different harmonic frequencies. This flexibility allows optimization of the transmission efficiency for a particular chopper at a particular energy. The drive system also provides a method of damping oscillations in the line frequency. A control system must monitor and adjust the chopper-accelerator phase difference to keep the difference constant even when the accelerator pulsing frequency varies slowly with time. A tolerance of 10-20% of the source burst time of a few microseconds is required.

The control system must provide a sufficiently user-friendly interface that even the novice user can select the desired energy and operating harmonic. The system must also allow for control and monitoring of all functions from a remote terminal. Provision must also be made for saving data on chopper parameters so that a time analysis of chopper problems can be performed.

The design of the chopper control systems for IPNS Upgrade draws on more than 10 years of experience[3,9,10] in controlling a number of neutron choppers phased to the accelerator at IPNS. The IPNS Upgrade chopper control systems are based on closely coupled control modules that can be computer-controlled and monitored over a network, such as Ethernet. Each such system is located close to the chopper and instrument to which it belongs and is included as part of the data-acquisition system electronics. It is assumed that monitoring can be performed from any workstation on the network. The advantages of such a distributed chopper control system are minimized cabling, automated controls, similar configurations for all instruments and choppers, commercial availability of most modules, and remote monitoring capability.

The chopper control system is based on a standard instrumentation bus, such as the VXI bus. This structure combines the advantages of a large number of vendors supplying a wide variety of instruments, all of which are controlled by either their own on-board computer or a central crate computer. The central crate computer has the capability of communicating with and controlling each module in its crate. This computer is also the communication interface to the network for remote monitoring and control. A system can be configured with both commercial and custom modules that have the needed instrumentation to control and monitor the performance of one or more choppers on an instrument.

3.2 NEUTRON GUIDES

3.2.1 Important Considerations

Neutron guides utilize the phenomenon of total reflection to transport thermal and cold neutrons over extended distances with minimum loss in beam intensity. Carlile, Johnson, and Williams[11] provide an excellent review of the theories pertaining to the use of neutron guides at pulsed sources, as well as calculations and practical considerations related to the design of some of the guides for ISIS. The discussion presented here is based in part on their review.

The critical angle γ_c for reflection of neutrons from a surface is directly proportional to the neutron wavelength. Among the readily available mirror materials, natural Ni has the largest value of γ_c, given by

$$\gamma_c = 0.0017 \, \lambda \qquad \text{(V.3.2-1)}$$

for γ_c in radians and λ in Å.

If losses are ignored, a guide can transmit all neutrons falling within a solid angle of $\sim 4\gamma_c^2$ on the guide's entrance cross section. Full illumination of the guide by the moderator occurs when the projection of this maximum guide solid angle, from any point on the guide entrance to the plane of the moderator, is completely covered by the moderator area. For a fully illuminated guide, the differential flux Φ per unit solid angle at the guide entrance is uniform across this entrance and is equal to the differential flux Φ_m per unit solid angle leaving the moderator in the direction of the guide. For a perfect, straight guide, the differential flux at the guide exit is also equal to Φ_m and is uniform across the exit. Under conditions of full sample illumination by the guide, the differential flux at the sample is Φ_m as well. Full illumination in the horizontal and vertical directions occurs under the conditions

$$L_i \gamma_c \leq \frac{(M_h - g_h)}{2} \qquad \text{horizontal}$$

$$\text{(V.3.2-2)}$$

$$L_i \gamma_c \leq \frac{(M_v - g_v)}{2} \qquad \text{vertical .}$$

Here M_h and M_v are the moderator's horizontal and vertical dimensions, the corresponding guide dimensions are g_h and g_v, and the distance from the moderator to the guide entrance is L_i.

The practical gain G of a guide at a pulsed source with small moderators is defined as the ratio of the total neutron flux, integrated over solid angle at the sample, to the total flux at the same source-sample distance L with no guide but viewing the entire moderator face. This gain is the product of the one-dimensional gains R_h and R_v:

$$G = R_h R_v \qquad \text{(V.3.2-3)}$$

With full illumination of guide and sample, the one-dimensional gains (indicated with the subscript f) are given by

$$R_f = \frac{g}{M} + \frac{(L\gamma_c)^2}{gM} \qquad\qquad L\gamma_c < g$$

$$(V.3.2\text{-}4)$$

$$R_f = \frac{2L\gamma_c}{M} \qquad\qquad L\gamma_c > g,$$

where the subscript h or v is implied for R_f, M, and g. Gains of less than unity are possible at small values of $L\gamma_c$ if the guide is smaller than the moderator, because the guide can actually obscure the view of some of the moderator from the sample.

If the guide is not fully illuminated by the moderator in either the horizontal or vertical direction, then this gain must be multiplied by a factor F_{mh} or F_{mv}, respectively.   Under the conditions of uniform emission from the moderator face, the factors F are given approximately as

$$F_m = 1 \qquad\qquad L_i\gamma_c < \frac{(M - g)}{2}$$

$$F_m = \frac{g + M - L_i\gamma_c}{2g} - \frac{(M - g)^2}{8L_i\gamma_c g} \qquad \frac{(M - g)}{2} < L_i\gamma_c < \frac{(M + g)}{2} \qquad (V.3.2\text{-}5)$$

$$F_m = \frac{M}{2L_i\gamma_c} \qquad\qquad \frac{(M + g)}{2} < L_i\gamma_c ,$$

where the subscript h or v is implied. The corrected one-dimensional gain is then

$$R = R_f F_m . \qquad\qquad (V.3.2\text{-}6)$$

At sufficiently long wavelength, the corrected gain saturates at the value

$$R_{max} = \frac{L}{L_i} \qquad\qquad L_i\gamma_c > \frac{(M + g)}{2} . \qquad\qquad (V.3.2\text{-}7)$$

Similar conditions apply to the illumination of the sample by the guide. Full sample illumination occurs under the conditions

$$L_e\gamma_c \le \frac{(g_h - S_h)}{2} \qquad\qquad \text{horizontal}$$

$$(V.3.2\text{-}8)$$

$$L_e\gamma_c \le \frac{(g_v - S_v)}{2} \qquad\qquad \text{vertical} ,$$

where L_e is the distance from the guide exit to the sample and S_h and S_v are the horizontal and vertical sample dimensions.

If the sample is not fully illuminated, then the one-dimensional gains must be multiplied by the additional factor F_{sh} or F_{sv}, given by

$$F_s = 1 \qquad\qquad\qquad L_e\gamma_c < \frac{(g-S)}{2}$$

$$F_s = \frac{g + S - L_e\gamma_c}{2S} - \frac{(g-S)^2}{8L_e\gamma_c S} \qquad\qquad \frac{(g-S)}{2} < L_e\gamma_c < \frac{(g+S)}{2} \qquad (\text{V.3.2-9})$$

$$F_s = \frac{g}{2L_e\gamma_c} \qquad\qquad\qquad \frac{(g+S)}{2} < L_e\gamma_c \ ,$$

where again the subscript h or v is implied.

The gain in flux at the sample due to the use of a guide is accomplished by increasing the angular divergence of the beam incident on the sample. This divergence of the incident beam can affect the energy or momentum resolution of the instrument, which is inappropriate for some instruments. If the maximum incident-beam divergence $2\gamma_c(\lambda_{max})$ from the guide is greater than the maximum divergence $\Delta\alpha_{max}$ appropriate to the instrument, then the instrument resolution is compromised. One solution is to increase L_e or decrease g beyond the value that gives full sample illumination. The maximum beam divergence $\Delta\alpha$ at the sample is then given by

$$\Delta\alpha = 2(g + S)/L_e \qquad\qquad g + S < L_e\gamma_c \qquad\qquad (\text{V.3.2-10})$$

$$\Delta\alpha = 2\gamma_c \qquad\qquad\qquad g + S > L_e\gamma_c \ , \qquad\qquad (\text{V.3.2-11})$$

and the guide gain is reduced by the factor F_s, given by Equation V.3.2-9. In some cases, this solves the beam divergence problem while still leaving an appreciable gain from the guide. In other cases, however, the required increase in L_e or decrease in g is so large that the guide is of little or no benefit and can be omitted.

Equations V.3.2-5 and V.3.2-9 place some constraints on the dimensions g_h and g_v of the guide, but they do not fully determine these quantities. Usually, physical constraints set lower allowable limits on L_i and L_e. A practical approach is to use the minimum guide dimensions that allow full sample illumination with this value for L_e. Minimizing the guide cross-sectional area under these conditions minimizes the total number of neutrons brought to the instrument but does not affect the total number incident on the sample. This gives the best signal-to-background ratio possible. This approach must be modified if focusing is applied at the guide exit.

The neutron intensity on the sample can be increased by the use of a focusing guide section between the normal guide exit and the sample. If supermirror coatings are used on this

focusing guide, the critical angle in this section can be made twice that of natural Ni, or even higher. This allows the guide to focus most of the beam penumbra back into the umbra that strikes the sample. A twofold or greater increase in intensity on the sample results, at the price of still further increase in the angular divergence. It is of greatest benefit when small sample sizes must be used to minimize path-length differences for TOF measurements, or because of difficulties in sample preparation.

The guide tube gains determined from the above equations are based on perfect guides. Many factors can lower the actual gains observed.[11] If good-quality, state-of-the-art fabrication techniques are used in producing the guide sections, then the most important sources of losses are due to imperfections in the mechanical installation of the guide sections. These can include the following:

1. *Imperfect spatial alignment.* If individual sections are misaligned by an amount Δg, then the fractional loss $\Delta I/I$ per section in intensity is

$$\Delta I/I \sim \left(\Delta g_h/g_h\right)\left(\Delta g_v/g_v\right) .$$

<div align="right">(V.3.2-17)</div>

2. *Gaps between sections.* These losses are proportional to the ratio of the gap length ΔL to the distance between reflections,

$$\Delta I/I \sim \gamma_c \, \Delta L/g .$$

<div align="right">(V.3.2-18)</div>

3. *Imperfect angular alignment.* Imperfections in alignment must be kept within the expected variation in surface waviness, which is $\sim 10^{-4}$ radians. There is no simple formula for predicting these effects, but they can be easily simulated in Monte Carlo calculations.

Guides can be fabricated and installed to meet these stringent requirements and give good performance. At ISIS, guides have been used for HRPD, a high-resolution powder diffractometer, and IRIS, a high-resolution crystal-analyzer spectrometer. The HRPD guide is a combination of curved and straight sections, ~96 m total length, optimized for thermal neutrons. Measured transmissions[12] of this guide, defined as the fraction of neutrons accepted by the guide that reach the guide exit, level off at ~70% for wavelengths greater than ~3 Å. The IRIS guide is also a combination of curved and straight sections, ~28 m total length, but optimized for cold neutrons. Measured transmissions[12] of this guide level off at ~70% for wavelengths greater than ~5 Å.

3.2.2 Survey of Guide Requirements

Table V.3.2-1 lists the instruments that form the reference set and presents a preliminary assessment of the benefits of a guide on each instrument. Cases for which $\Delta\alpha_{max} \gtrsim \gamma_{c\text{-max}}$ and

Table V.3.2-1 Neutron Guide Assessment

Instrument	Section	L (m)	λ_{max} (Å)	$\Delta\alpha_{max}$[a] (rad)	$2\gamma_{c-max}$ (rad)	R_{f-max}[b]	Guide[c]	Focus[d]
SEPD	2.1.1.1	12	9.1	0.012	0.031	3.7	no	
GPPD	2.1.1.2	25	4.6	0.005	0.016	4	no	
HRPD	2.1.2.1	50	2.4	0.009	0.008	4	?	
RSD	2.1.2.2	25	4.5	0.004	0.015	3.8	no	
		12	9	0.012	0.031	3.7	no	
VSPD	2.1.2.3	12	9.1	0.012	0.031	3.7	no	
SAND	2.2.1.1	12	20	special[e]	0.068	8.2	?	
HRSAND	2.2.2.1	20	14		0.048	9.6	no	
SPSAND	2.2.2.2	?					no	
GLAD	2.3.1.1	22	4	0.007	0.014	3.1	?	
SCD	2.3.1.2	10	10	0.009	0.034	3.4	no	
HQSCD	2.3.2.1	30	4	0.005	0.014	4.2	no	
POSY-I	2.4.1.1	18	18	0.003	0.061	11	no	
POSY-II	2.4.1.2	18	18	0.004	0.061	11	no	
HIREF	2.4.2.1	18	4.7	special[e]	0.016	2.9	?	
GREF	2.4.2.2	18	18	0.004	0.061	11	no	
REFD	2.4.2.3	18	18	0.004	0.061	11	no	
HRMECS	2.5.1.1	18	6.0	0.012	0.020	3.6	?	
LRMECS	2.5.1.2	12	9.1	0.012	0.031	3.7	no	
CNCS	2.5.2.1	20	16	0.013	0.054	11	yes	
SCCS	2.5.2.2	16	~1	0.013	0.003	<1	no	
QENS	2.6.1.1	9	6.5	0.2	0.022	2	yes	yes
HRBS	2.6.2.1	30	20	0.08	0.068	20	yes	yes
TFCA	2.6.2.2	16	5	0.2	0.017	2.7	yes	yes
QSTAXC	2.6.2.3	17					yes	
MICAS	2.6.2.4	12					no	
TOFNSE	2.7.1.1	16	15	0.017	0.051	8	yes	

[a] Based on detector and sample sizes and separation, or on incident-beam collimators.

[b] Assumes 10-cm moderator.

[c] This column indicates whether a guide is potentially useful on a particular instrument. In most cases, this is determined from the requirements $\Delta\alpha_{max} \gtrsim \gamma_{c-max}$ and $R_{f-max} \gg 1$.

[d] This column indicates whether a focusing guide section would be useful.

[e] Used in conjunction with converging Soller collimator or microguide.

TABLE V.3.2-2 Neutron Guide Requirements

Instrument	$M_v{}^a$ (cm)	L (m)	λ_{min} (Å)	λ_{max} (Å)	S_h (cm)	S_v (cm)	g_h (cm)	g_v (cm)	$L_{e\text{-}max}{}^b$ (m)	$R_h (\lambda_{max})$ $L_i=1^c$	$L_i=2$	$L_i=5$	$R_v (\lambda_{max})$ $L_i=1$	$L_i=2$	$L_i=5$
HRPD	20	50	0.4	2.4	1.27	2.5	3	4.3	2.12	4.1	4.1	4.1	2.0	2.0	2.0
SAND	10	12	1	20	Note d										
GLAD	10	22	0.1	4	2	2	5	5	2.14	3.1	3.1	3.0	3.1	3.1	3.0
HIREF	10	18	2	4.7	Note e										
HRMECS	10	18	0.2	6.0	7.5	10	10	10	1.23^f	3.5	3.3	2.7	3.4	3.1	2.6
CNCS	10	20	2	16	2	10	8	10	0.92^f	10.1	8.4	4.0	8.1	6.9	3.5
QENS	10	9	0.7	6.5	0.65	10	5	10	1.97^f	2.0	2.0	1.7	1.7	1.6	1.3
HRBS	10	30	2	20	2	5	5	8	0.44	19.9	14.9	6.0	18.2	14.1	6.0
TFCA	10	16	0.3	5	2	5	5	8	1.76	2.7	2.7	2.5	2.7	2.7	2.3
QSTAXC	10	17			Note g										
TOFNSE	20	16	4	15	3	3	5	5	0.39	8.2	7.1	3.2	4.1	4.1	3.2

a M_h is assumed to be 10 cm in all cases.

b $L_{e\text{-}max}$ is the maximum value of L_e for full sample illumination at λ_{max} with the specified guide and sample dimensions. Guide dimensions are chosen to be no larger than the moderator and to produce reseasonable values for L_e.

c L_i is specified in meters.

d Guide is used to illuminate converging Soller collimators. Gain must be assessed and parameters optimized using Monte Carlo codes.

e Guide is used to illuminate entrance to converging Soller collimator or converging microguide assembly. Gain must be assessed and parameters optimized using Monte Carlo codes.

f Based on horizontal dimension only.

g Guide sized to accommodate several quasi-steady-state instruments.

$R_{f\text{-max}} \gg 1$ are indicated as possibly benefiting from guides. A few other instruments that violate these conditions but for which guides may still have some benefit are also indicated. Those instruments for which guides offer some advantage are analyzed in greater detail in Table V.3.2-2.

On the basis of this analysis, it appears that significant gains are provided by guides on the HRPD, GLAD, HRMECS, CNCS, QENS, HRBS, TFCA, and TOFNSE. In addition, a guide is used to transport the neutrons to the quasi-steady-state instrument QSTAXC so that it can be located in a region of low background some distance from the source. The use of guides on the SAND and HIREF, although not essential, might provide enough gain to be justified, but these specialized uses of the guides would have to be assessed by detailed Monte Carlo calculations.

The inner ends of the HRPD, GLAD, and TFCA guides can be terminated ~5 m from the moderator without appreciable reduction in gain, but the HRMECS, CNCS, QENS, HRBS, and TOFNSE guides need to extend to within ~2 m of the moderator. The CNCS, HRBS, and TOFNSE guides benefit even more if the end of the guide is ~1 m from the moderator .

3.3 BEAMLINE SHIELDING AND BEAMSTOPS

3.3.1 Beamline Shielding — Neutrons from Moderator

The neutron beamlines transport the neutrons from the moderators through the beam ports to the face of the biological shield, and then on to the sample positions for their respective instruments. The biological shield provides the shielding for the inner portions of the beamlines, typically ~6 m long. Separate shielding must be provided for the portion of each beamline external to the biological shield. These external portions range in length from ~1 m to ~42 m. The shielding thickness required around these external beamlines is assessed here. The shielding near the interface between the external beamlines and the biological shield has some additional requirements, which are addressed in Section V.3.3.2.

Each beamline is designed with apertures that remove small portions from the edges of the beam continuously along the beamline. These distributed-loss conditions are modeled as a line of isotropic point sources of neutrons within the beamline. This source produces S(E) neutrons per unit beamline length per unit energy per second at energy E. This source term is estimated by assuming that all of the beam intercepted by the defining apertures is elastically scattered, isotropically, at the source points. The dose rate D at distance r from a beamline with cylindrical shield of radius R is then

$$D = \frac{1}{2\pi r} \int [S(E)/F(E)] \, e^{-R/\Lambda(E)} \, dE \ , \tag{V.3.3-1}$$

where F(E) is the conversion factor between dose rate and neutron flux and $\Lambda(E)$ is the neutron mean-free-path in the shielding material. Figure V.3.3-1 shows the values for F(E) used here. The most difficult to stop are the high-energy (E > 50 MeV) and fast (1 < E < 50 MeV) neutrons, so these energy ranges dominate the shielding considerations. Table V.3.3-1 lists mean-free-paths associated with these energy ranges for several common shielding materials.

At IPNS Upgrade, the neutron beamlines view moderators operated in wing geometry or in flux-trap geometry, as shown in Figure V.3.3-2, so the beamlines have no direct view of the target. Representative spectra for the neutron beams have been calculated in Chapter IV. A typical spectrum is shown in Figure V.3.3-3 in the form of EI(E), normalized to EI(E) = 1 at 1 eV. Here I(E) is the time-averaged neutron beam current per unit solid angle per unit energy leaving the moderator face. Also shown in the figure is the dashed line $[EI(E)]_w$, which is an interpolated and extrapolated version of the calculated spectrum used for the shielding calculations here.

We assume a straight beam tube of internal cross-sectional area A. The fraction of the beam intercepted by the beam tube walls per unit length is

$$\frac{d\Omega}{dL} = \frac{2\,A}{L^3} \tag{V.3.3-2}$$

The source term S(E) to be used in Equation V.3.3-1 is then given by

$$S(E) = S_0 \frac{2A}{L^3} \frac{[EI(E)]_w}{E}, \tag{V.3.3-3}$$

where S_0 is the value of EI(E) at 1 eV for the moderator in question. Equation V.3.3-1 then becomes

$$D = S_0 \frac{2A}{L^3} \frac{1}{2\pi r} \sum_{E_1} e^{-R/\Lambda(E_1,E_2)} \Delta I(E_1,E_2), \tag{V.3.3-4}$$

where $\Lambda(E_1,E_2)$ is assumed to be constant over the range E_1 to E_2, as indicated in Table V.3.3-1, and

$$\Delta I(E_1,E_2) = \int_{E_1}^{E_2} \frac{[EI(E)]_w}{EF(E)}\, dE \tag{V.3.3-5}$$

$$= 0.66 \quad \text{for slow neutrons} \qquad (E_1=0,\ E_2=1\ \text{MeV})$$

$$= 1.01 \quad \text{for fast neutrons} \qquad (E_1=1,\ E_2=50\ \text{MeV})$$

$$= 0.0015 \quad \text{for high-energy neutrons} \qquad (E_1=50,\ E_2=2200\ \text{MeV}).$$
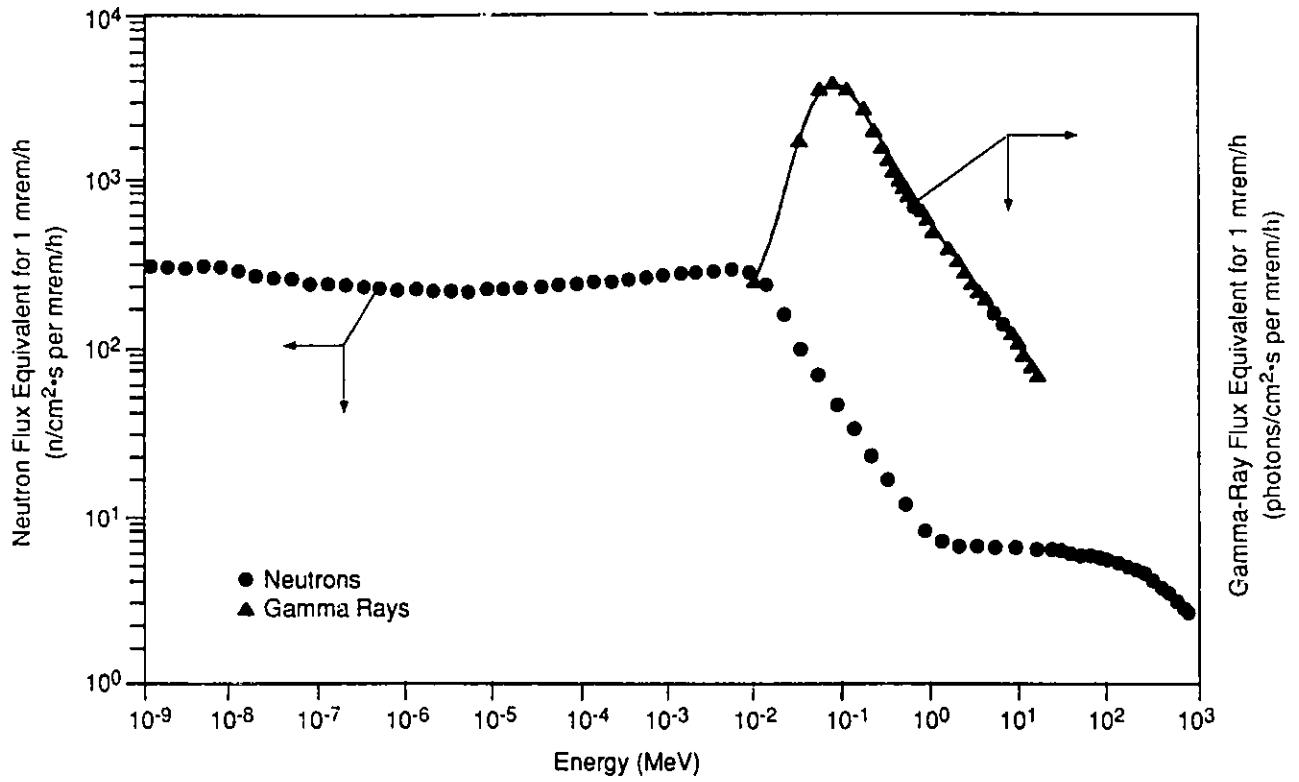
Figure V.3.3-1 Neutron and Gamma-Ray Dose-Rate-to-Flux Conversions (Source: Reference 13).

Table V.3.3-1 Neutron Mean-Free-Paths in
Shielding Materials (cm)

Material	Λ, 1<E<50 MeV	Λ, E>50 MeV
Beryllium	8.34	50.
Iron	6.25	17.34
Tungsten	5.08	10.1
Lead	8.5[a]	17.8
Uranium	5.97	11.1
Concrete	10.4	46.1
H_2O	9.62	90.25

[a] Using 3.5-barn removal cross section
instead of Barbier[14] value.

Source: Reference 14.
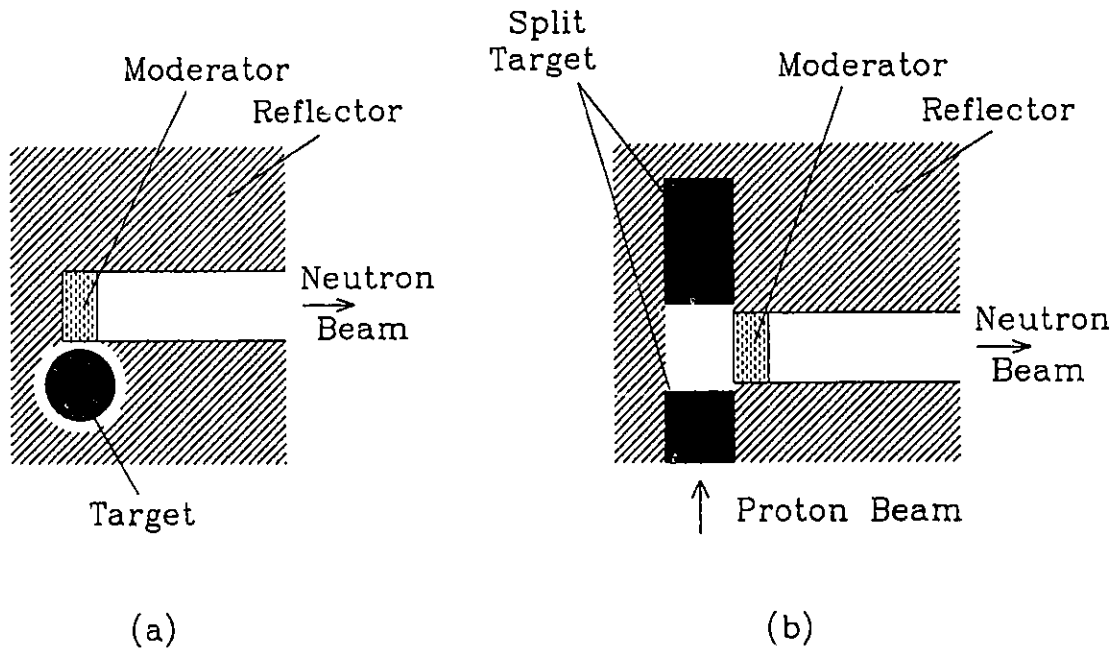
Figure V.3.3-2 Target-Moderator-Beamline Geometries: (a) Wing Geometry
with Proton Beam Direction Normal to the Page and (b) Flux-Trap
Geometry with Proton Beam Direction as Shown.
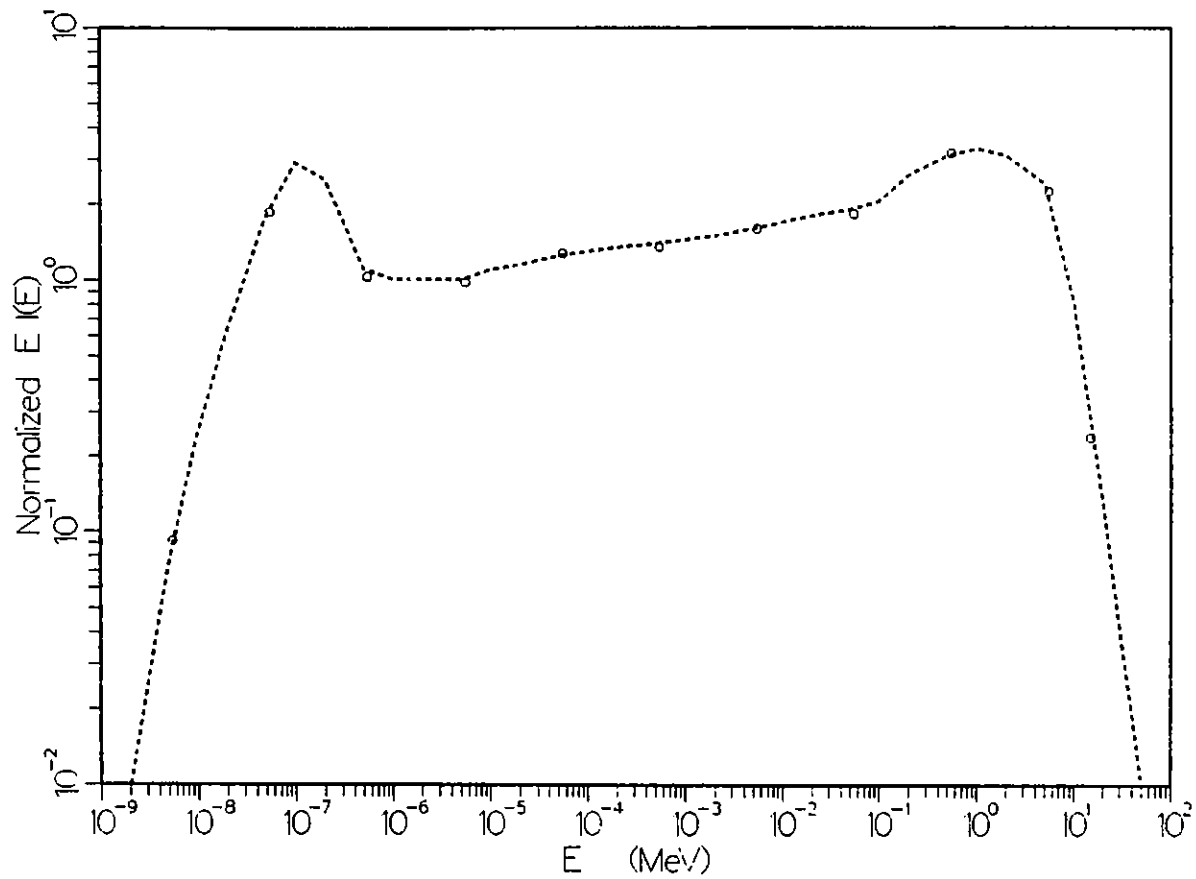
Figure V.3.3-3 Neutron-Beam Spectra from the IPNS Upgrade Moderators. (Circles indicate calculated values from Chapter IV for a representative moderator. The dashed line is the interpolated and extrapolated spectrum $[EI(E)]_W$ used for shielding calculations.)

For IPNS Upgrade, we assume $S_0 = 4 \times 10^{13}$ n/sr-sec on the basis of calculations in Chapter IV. This assumption is also consistent with scaling from measured IPNS values.[15] The dose rate D at radius R+30 cm is calculated as a function of R for beamline shielding made of different materials. Figure V.3.3-4 shows some of the calculated values for iron shielding, which is the most effective practical material. These calculations assume a 10×10 cm^2 beam, and so it is assumed that the remaining portions of the beam port are filled with iron shielding. These calculations indicate that at 6 m from the moderator, ~108 cm of iron is required to reduce the neutron dose rate to 0.125 mrem/h at 30 cm from the beamline shield surface. At this shield thickness the remaining dose rate is almost entirely due to the high-energy neutrons (> 50 MeV), even though there are very few in the original source term. Since scattering of high-energy neutrons is predominantly in the forward direction, this source term overestimates the required transverse shield thickness. An alternative is to base the shield thickness only on the fast neutrons. In that case only ~81 cm of iron is required to reduce the dose rate to 0.125 mrem/h. These two different calculations bracket the required shield thickness. Similar calculations show that the required iron-shielding thickness at L = 20 m from the moderator is between ~86 cm and ~73 cm. An average thickness of 80 cm of iron shielding on all sides is used for the IPNS Upgrade neutron beamlines.

These shielding estimates are based on the use of iron shielding. The primary mechanisms for removal of high-energy and fast neutrons by the shielding involve (1) the scattering of the neutron to a lower energy and different direction or (2) an inelastic nuclear reaction, resulting in the production of one or more lower-energy neutrons proceeding in different directions. Some additional shielding material is required to slow down and absorb these remaining neutrons. This additional shielding material is also needed to absorb the 25 keV and 125 keV neutrons transmitted through the iron with little attenuation. The best material for slowing down neutrons is hydrogen, and the absorptions are best done by ^{10}B, because this reaction produces no high-energy gamma rays. Slow-neutron mean-free-paths in borated hydrogenous material such as borated polyethylene or wax are of the order of 1 cm. Only a few centimeters of such material is required to slow the remaining neutrons down to an energy where the absorption cross-section of the boron becomes large. All of the beamline shielding needs to incorporate several centimeters of such material, in addition to the 80-cm thickness of iron shielding. This borated hydrogenous shielding can be replaced with a larger thickness of concrete where space permits.

3.3.2 Beamline Shielding — "Direct" Neutrons from the Target

Some of the high-energy and fast neutrons directly from the target surface are also present in the beamline near the biological shield because of the relatively weak shielding between the target and beamline. Figure V.3.3-5a shows a sketch of the relevant geometry. Here it is again assumed that shielding apertures define the beam to a cross section of 10×10 cm^2.
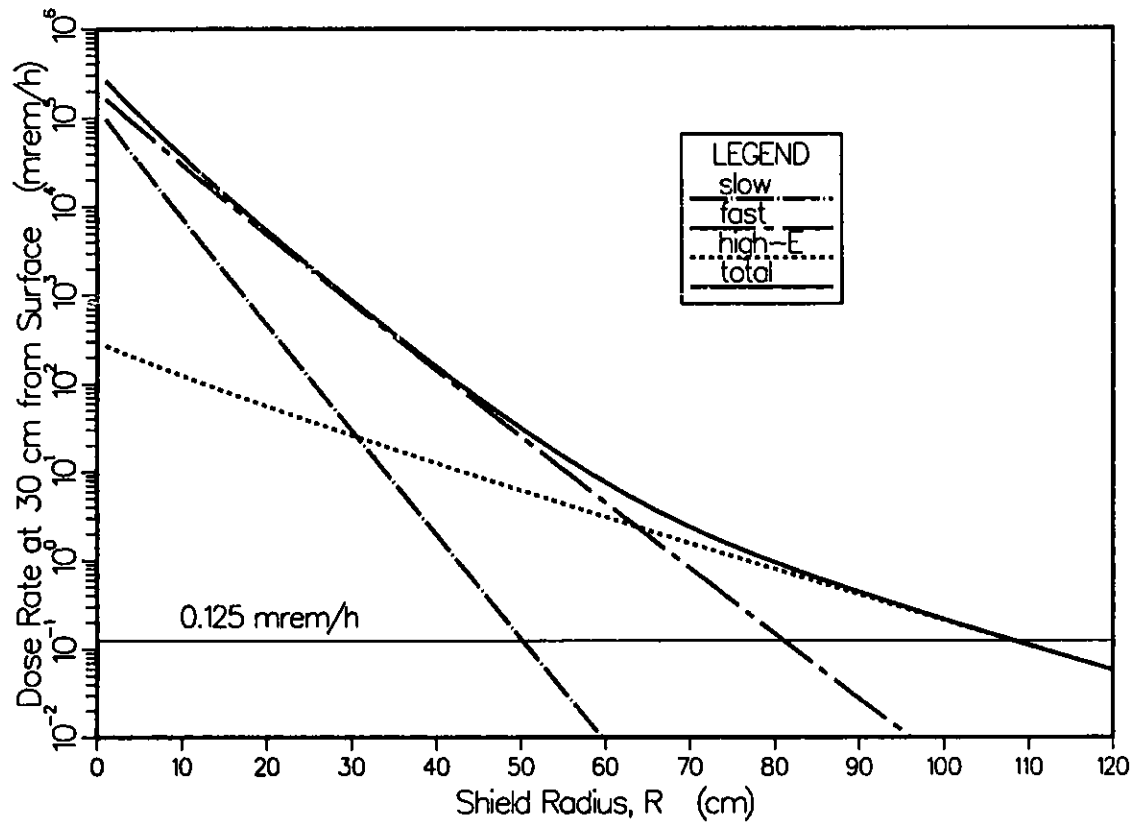
Figure V.3.3-4 Dose Rate 30 cm from the Surface of a Cylindrical Iron Beamline Shield of Radius R, Calculated for a Distance of 6 m from the Moderator.

The neutron path shown in the figure passes through lengths L_i and L_c of iron and concrete shielding. From the figure

$$L_i = (500 + d) \sec \alpha - 10 \csc \alpha \qquad \text{(IV.3.3-6)}$$

$$L_c = 100 \sec \alpha \qquad \text{(IV.3.3-7)}$$

$$\tan \alpha = \frac{R + 10}{600 + d} \qquad \text{(IV.3.3-8)}$$

We consider the dose at a distance 30 cm from the point the path exits the shielding. This is at a total path distance r given by

$$r = (600 + d) \sec \alpha + 30 \qquad \text{(V.3.3-9)}$$

In Section IV.4.3 it was shown that the dose rate under these conditions is

$$D = \frac{2.364 \times 10^{15}}{r^2} e^{-0.0437L_i - 0.0220L_c} \qquad \text{(V.3.3-10)}$$

for L_i, L_c, and r in cm.

The radius of the external beamline iron shielding is R = 80 cm. At this radius the dose rate due to neutrons directly from the target is reduced to 0.125 mrem/h at d = 77 cm. At the face of the biological shield where d = 0, a beamline shield radius of R = 216 cm is required to reduce the dose rate to 0.125 mrem/h. A transition shield at the interface with the biological shield provides this additional shielding. This transition shield is shown schematically in Figure V.3.3-5b. Alternatively, access to regions near the biological shield can be administratively limited to less than 40 hours per week.

3.3.3 Beamstops

Each neutron beamline must have a beamstop beyond the scattering flight path to stop all the remaining beam. The dose rate at the sides of this beamstop is estimated by assuming a point source which isotropically scatters all the neutrons within the beamstop. The calculation then proceeds similarly to that for the beamline shielding radius.

$$D = S_o \frac{A}{L^2} \frac{1}{4\pi r^2} \sum_{E_i} e^{-R/\Lambda(E_1 E_2)} \Delta I(E_1 E_2) \qquad \text{(V.3.3-11)}$$

The shortest beamline has its beamstop at least 12 m from the moderator. For this maximum dose rate condition an 80 cm thickness of iron reduces the dose rate to below 0.125 mrem/h at 30 cm from the beamstop sides.
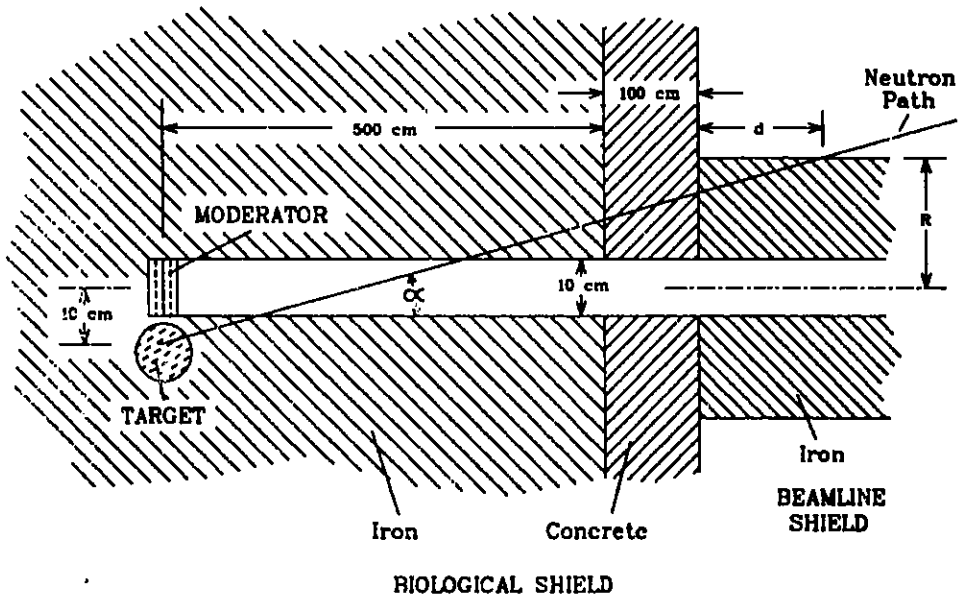
(a)
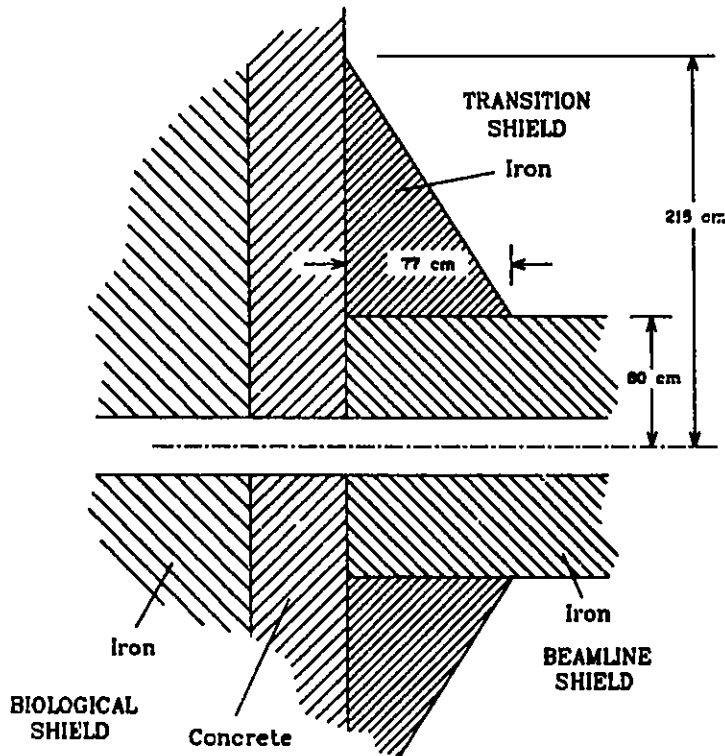
(b)

Figure V.3.3-5 (a) Geometry for Shielding against High-Energy Neutrons from the Target; (b) Transition Shield at the Beamline Interface with the Biological Shield.

The high-energy neutrons in the beam proceed in the forward direction through the beamstop, so the dose rate at the end of the beamstop is given approximately by

$$D \simeq S_0 \frac{A}{L^2} \frac{1}{4\pi R_f^2} \left[e^{-R_f/\Lambda(\text{slow})} \Delta I(\text{slow}) + e^{-R_f/\Lambda(\text{fast})} \Delta I(\text{fast}) \right]$$

$$+ S_0 \frac{1}{L^2} \left[e^{-R_f/\Lambda(\text{high-energy})} \Delta I(\text{high-energy}) \right] , \qquad \text{(V.3.3-12)}$$

where R_f is the thickness of the beamstop shielding in the forward direction. The beamstop thickness required by the last term in Equation V.3.3-12 for a 0.125-mrem/h dose rate in the forward direction from a beamstop 12 m from the moderator is

$$R_f' = -\Lambda \ln \left(L^2 D / S_0 \Delta I \right)$$

$$= 220 \text{ cm} . \qquad \text{(V.3.3-13)}$$

This value is much greater than the thickness required to shield against the slow and fast neutrons, so this high-energy-neutron term governs the beamstop shielding thickness in the forward direction.

As noted above for beamline shielding, the beamstops must also incorporate some borated hydrogenous material to perform the final slowing down and absorption of the neutrons.

3.3.4 Shielding Interlocks

The neutron dose rate in one of the neutron beams is estimated to be

$$D \simeq S_0 \frac{1}{L^2} \sum_{E_1} \Delta I(E_1, E_2)$$

$$\simeq 7 \times 10^{13}/L^2 \qquad \text{(V.3.3-14)}$$

for L in cm and D in mrem/h. At a distance of 20 m from the moderator, this dose rate is 17,000 rem/h. All movable shielding pieces, access to the sample area, and access to any other place in the beam are interlocked to the beam gate and to the accelerator. The interlocks prevent access to the beam while the beam gate is open and the accelerator is operating.

3.3.5 Summary of Neutron Beamline Shielding Requirements

Each neutron beamline is shielded on all sides by 80 cm of iron together with some hydrogenous and neutron absorbing materials. A larger-radius transition shield is used at the interface of each beamline with the biological shield. Each beamline has a beamstop that provides

80 cm of iron shielding on the sides and 220 cm of iron in the forward direction, and includes the necessary additional hydrogenous and neutron-absorbing materials.

3.4 NEUTRON POLARIZATION

Only two of the instruments in the reference set, the POSY-I and TOFNSE, are designed to operate with polarized neutrons. Both of these instruments work with cold neutrons and utilize limited angular ranges, so the neutron polarization can be done very well by reflection from polarizing supermirrors using current technology.

Other instruments that might be desired at IPNS Upgrade in the future require broad-band polarizers and analyzers that work at short wavelengths and over wide angular ranges. The technology to make satisfactory polarizers and analyzers of the type needed does not yet exist. Thus, although satisfactory solutions exist for the polarization requirements of the initial instrumentation of IPNS Upgrade, it is important to continue development of other types of polarization devices and techniques to provide for future expansion of the capabilities of IPNS Upgrade.

3.5 DETECTORS

3.5.1 Discrete Detectors

Table V.3.5-1 lists instruments from the reference set that use discrete detectors. The number and sizes of these detectors are also listed, and an estimate is made of the maximum instantaneous and time-averaged data rates per detector. All of these detectors are specified as ^{3}He gas proportional counters, but where background and geometrical considerations permit, scintillation counters can be used equally well.

Commercial cylindrical ^{3}He proportional counters and associated counting electronics typically have dead-times of ~2 μsec. Excluding for the moment the chopper spectrometers, the maximum instantaneous count rate listed in Table V.3.5-1 is 5×10^4 counts/sec per detector for the SEPD. With 2-μsec dead-time per detector, this gives dead-time losses of nearly 10% in the peaks of the spectrum. In the majority of cases instantaneous rates are significantly lower than those in Table V.3.5-1. Thus, it appears that ^{3}He proportional counters have adequate speed for all of the instruments in the table, excluding the chopper spectrometers operating in diffractometer mode, although dead-time corrections are needed in some cases.

The count-rate estimates for the chopper spectrometers listed in Table V.3.5-1 are made for the diffractometer mode, in which the choppers are removed from the beam and the instrument functions as a powder diffractometer. This mode is used only for instrument calibration and for rare cases when the growth or modification of samples *in situ* needs to be

Table V.3.5-1 Discrete Detector Requirements[a]

Instrument[b]	Section	Number of Detectors	Detector Dimensions		Max. Rate per Detector (counts/sec)[c]	
			Dia. (cm)	Length (cm)	Instantaneous	Time-Avg.
SEPD	2.1.1.1	~280	1.2	38	~5×10^4	~5×10^3
GPPD	2.1.1.2	~520	1.2	38	~5×10^3	~1×10^3
HRPD	2.1.2.1	~410	1.2	38	~9×10^2	~2×10^2
RSD	2.1.2.2	~250	1.2	38	~4×10^3	~7×10^2
VSPD	2.1.2.3	~560	0.6	19	~2×10^3	~3×10^2
HRMECS	2.5.1.1	~800	2.5	46	~$2 \times 10^{5\,d}$	~$3 \times 10^{4\,d}$
LRMECS	2.5.1.2	~160	2.5	46	~$7 \times 10^{5\,d}$	~$5 \times 10^{4\,d}$
CNCS	2.5.2.1	~1000	2.5[e]	25	~$4 \times 10^{4\,d}$	~$3 \times 10^{3\,d}$
QENS	2.6.1.1	~100	0.6	10	~2×10^3	~9×10^1
HRBS	2.6.2.1	~150	0.6	10	~9×10^1	~9×10^0
TFCA	2.6.2.2	~300	0.6	25	~2×10^3	~9×10^1
QSTAXC	2.6.2.3	~12	0.6	10	~5×10^4	~7×10^2
MICAS	2.6.2.4	~20	0.6	10	~5×10^4	~9×10^3
TOFNSE	2.7.1.1	~10	0.6	10	~2×10^2	~2×10^1

[a] Detectors are specified as cylindrical ^{3}He gas proportional counters, but in some cases scintillation detectors such as those used on some instruments at ISIS can be substituted.

[b] Instruments not listed do not use any discrete detectors.

[c] Scaled from IPNS rates where possible; otherwise, estimated on the assumption that the sample scatters 20% of the beam isotropically into a 4π solid angle.

[d] Maximum rates are for diffractometer mode (choppers removed). Rates in normal operation are much lower.

[e] This instrument uses flattened detectors with thickness ~1 cm and width ~3.5 cm.

monitored. In the normal operating mode with choppers in place, data rates are significantly lower than those given in the table and pose no problem for the detectors. If necessary, an attenuator can be placed in the incident beam on the few occasions when the instrument is operated in diffractometer mode. Since this mode is used only rarely and data rates are high in this mode, the use of an attenuator in such cases will not appreciably affect the overall performance of the instrument.

All of the instruments listed in Table V.3.5-1 can utilize ^{3}He proportional counters without serious problems. The ZnS-LiF scintillation detectors developed at ISIS[16] have very good intrinsic backgrounds and discrimination against gamma radiation, but they are no faster than the ^{3}He counters and so offer no advantage in this respect. Other types of scintillation detectors, such as Li-glass, can be significantly faster but suffer from intrinsic background problems.[17] These intrinsic background-contribution levels are not a problem for some of the instruments, and in these cases Li-glass scintillators can be used to achieve higher counting speeds than are feasible with the gas detectors.

3.5.2   Position-Sensitive Detectors

Table V.3.5-2 lists those instruments from the reference set that use position-sensitive detectors. The table indicates whether the required position encoding is one-dimensional (1D) or two-dimensional (2D). Some instruments use both 1D and 2D detectors, and some use a combination of position-sensitive and discrete detectors. The number of detectors required and the required sizes and position resolutions are also listed, and an estimate is made of the maximum instantaneous and time-averaged data rates per detector.

Most commercial 1D or 2D ^{3}He position-sensitive proportional counters require several microseconds for the position encoding. A neutron arriving anywhere on the same detector during encoding either will not be counted or, worse, will cause position misencoding for one or both neutrons.[18]   Multi-electrode position-sensitive gas proportional counters available commercially work reliably at instantaneous rates up to ~5×10^4, and such detectors are available at resolutions down to 1.5 mm. Other types of encoding can be used for those instruments in the table for which instantaneous rates per detector are not expected to reach or exceed ~10^4 counts/sec an appreciable fraction of the time. This criterion implies that 1D gas proportional counters of the types currently in use at IPNS are satisfactory for use on the SAND, HRSAND, GLAD, POSY-I, and POSY-II at IPNS Upgrade. These detectors already provide the required position resolutions for these instruments. As discussed in Section V.2.2.1.1, the 2D position-sensitive detector in use on the SAND at IPNS is fast enough for use in the high-resolution mode on the SAND at IPNS Upgrade. It is clear from Table V.3.5-2, however, that it cannot be used in the low-resolution mode. One of the multi-electrode proportional counters may be fast enough for this purpose. The multi-electrode detectors can also satisfy the requirements of the RSD and HIREF. A micro-channel-plate detector of the type used earlier on the POSY-I at IPNS[19] is satisfactory for use on the REFD.

The data rates estimated in the table for the chopper spectrometers are based on operation in the diffractometer mode. As noted in the previous section, this mode is used only a small fraction of the time, and the beam can be attenuated during this period. Thus, commercial ^{3}He gas proportional counters are appropriate for use as the 1D position-sensitive detectors on the chopper spectrometers HRMECS, LRMECS, CNCS, and SCCS.

Table V.3.5-3 summarizes the remaining position-sensitive detector requirements at IPNS Upgrade, for which no commercial solution currently exists. These detectors require development because of the data-rate limitations or because the required resolution is better than that usually found in a detector of the specified size, or both. The detector on the HQSCD is located close to the sample and needs to have high efficiency for short-wavelength neutrons, so gas-detector technology is inappropriate. All of these instruments operate in the TOF mode. Therefore, integrating detectors, which can provide good spatial resolution and are relatively unaffected by data rate, cannot be used. All of the instruments listed in this table can, if required, function using detectors at the limits of today's technology and still be extremely good instruments. For example, data-rate limitations can be overcome by using smaller samples or by partially attenuating the beam, and resolution limitations can be overcome by moving the detector farther from the sample or by using a smaller detector. However, these instruments will not reach their full potential at IPNS Upgrade without advances in detector technology. Emerging detector technologies[20] show promise of solving one or more of these requirements, so it is likely that all of these detectors will be technologically possible by the time they are required at IPNS Upgrade.

3.5.3 Beam Monitors

Nearly all the instruments at IPNS use BF_3 or ^{3}He pulsed ionization chambers as low-efficiency beam monitors[19] to monitor the spectral shape and overall intensity of the incident neutron beams. This type of detector is stable and reliable, is relatively insensitive to gamma rays and fast neutrons, and samples the entire beam uniformly. The detection efficiency is inversely proportional to the neutron velocity over several orders of magnitude in velocity. The overall efficiency level can be varied by several orders of magnitude by changing the partial pressure of BF_3 or ^{3}He in the fill gas. This technology is readily adaptable for use at IPNS Upgrade. At least one of these beam monitors is required for each instrument.

3.6 DATA ACQUISITION

The data-acquisition systems (DASs) for the instruments at IPNS Upgrade all use the same software and are based on a small number of standardized hardware modules. This philosophy has been followed at IPNS and has resulted in a large reduction in the effort required to maintain the data-acquisition systems and in minimal training requirements for users who utilize more than one instrument. The IPNS Upgrade system design draws on more than 10 years experience in operating TOF data acquisition systems at IPNS.[21]

TABLE V.3.5-2 Position-Sensitive Detector Requirements

Instrument[a]	Section	Dim.	Number of Detectors	Dimensions at Active Area Width (cm)	Length (cm)	Resolution (mm)	Max. Rate per Detector (counts/sec)[b] Instantaneous	Time-Avg.
RSD	2.1.2.2	2D	4	30	30	2	$\sim 1 \times 10^5$	$\sim 2 \times 10^4$
SAND	2.2.1.1	2D	1	40	40	4	$\sim 2 \times 10^5$	$\sim 7 \times 10^4$
		1D	65	1.2	60	10	$\sim 9 \times 10^3$	$\sim 3 \times 10^3$
HRSAND	2.2.2.1	2D	1	60	60	2	$\sim 5 \times 10^3$	$\sim 2 \times 10^3$
		1D	~ 20	1.2	60	10	$\sim 5 \times 10^2$	$\sim 2 \times 10^2$
SPSAND	2.2.2.2	2D	1	40	40	4	$\sim 5 \times 10^4$	$\sim 2 \times 10^4$
GLAD	2.3.1.1	1D	~ 410	1.2	60	10	$\sim 7 \times 10^3$	$\sim 3 \times 10^3$
SCD	2.3.1.2	2D	3	30	30	3	$\sim 1 \times 10^6$	$\sim 1 \times 10^5$
HQSCD	2.3.2.1	2D	1	30	30	1.5	$\sim 1 \times 10^5$	$\sim 1 \times 10^4$
POSY-I	2.4.1.1	1D	1	5	10	2	$\sim 1 \times 10^3$	$\sim 4 \times 10^2$
POSY-II	2.4.1.2	1D	1	5	20	2	$\sim 6 \times 10^3$	$\sim 2 \times 10^3$
HIREF	2.4.2.1	1D	1	5	10	2	$\sim 1 \times 10^5$	$\sim 3 \times 10^4$
GREF	2.4.2.2	2D	1	60	60	2	$\sim 1 \times 10^4$	$\sim 3 \times 10^3$
REFD	2.4.2.3	2D	1	3	3	0.5	$\sim 1 \times 10^3$	$\sim 4 \times 10^2$
HRMECS	2.5.1.1	1D	~ 40	2.5	100	20	$\sim 1 \times 10^{5\,c}$	$\sim 2 \times 10^{4\,c}$
LRMECS	2.5.1.2	1D	~ 30	2.5	46	20	$\sim 8 \times 10^{5\,c}$	$\sim 6 \times 10^{4\,c}$
CNCS	2.5.2.1	1D	~ 30	2.0[d]	60	20	$\sim 4 \times 10^{4\,c}$	$\sim 3 \times 10^{3\,c}$
SCCS	2.5.2.2	1D	~ 256	2.5	100	20	$\sim 4 \times 10^{4\,c}$	$\sim 8 \times 10^{3\,c}$

[a] Instruments not listed do not use any position-sensitive detectors.

[b] Scaled from IPNS rates where possible; otherwise, estimated on the assumption that the sample scatters 20% of the beam isotropically into a 4π solid angle.

[c] Maximum rates are for diffractometer mode (choppers removed). Rates in normal operation are much lower.

[d] This instrument uses flattened cylindrical linear-position-sensitive detectors with thickness ~ 0.8 cm and width ~ 2 cm.

TABLE V.3.5-3 Position-Sensitive Detectors Requiring Development

				Dimensions at Active Area			Max. Rate per Detector (counts/sec)	
Instrument	Section	Dim.	Number of Detectors	Width (cm)	Length (cm)	Resolution (mm)	Instantaneous	Time-Avg.
HRSAND	2.2.2.1	2D	1	60	60	2	$\sim 5 \times 10^3$	$\sim 2 \times 10^3$
SCD	2.3.1.2	2D	3	30	30	3	$\sim 1 \times 10^6$	$\sim 1 \times 10^5$
HQSCD	2.3.2.1	2D	1	30	30	1.5	$\sim 1 \times 10^5$	$\sim 1 \times 10^4$
GREF	2.4.2.2	2D	1	60	60	2	$\sim 1 \times 10^4$	$\sim 3 \times 10^3$

The DAS for IPNS Upgrade is based on a distributed processor system using a computer back-plane, such as VME, VXI, or Future Bus. Each crate in the system contains a local processor module, a crate control module, and as many digitizer modules as the crate accommodates. The detectors are located within 15 m of the digitizer modules and the preamps are within a few centimeters of the detectors. All connections to the digitizer modules are through the backplane to allow easy module removal and replacement. Each DAS has a workstation to serve as the user interface. Communications to the local processors and histogram memory are via fiber-optic local area networks, as indicated in Figure V.3.6-1.

Electronics capabilities change rapidly, so it is premature to choose a specific hardware implementation at this time. The following functionality must be provided:

1. *Local processor module.* The local processor module must provide for connection to a local area network (LAN), operate under a real-time kernel, and have a means of connection to a large, shared memory for accumulating histograms. The processor must also have a large local memory for execution software, as well as storage of large look-up tables. The software and look-up tables can be generated on a networked workstation and down-loaded to the processor at run time.

2. *Crate control module.* The crate control module contains the TOF clock generator, data gating circuitry, and data collection and buffer storage of raw data from within the crate. This module is custom-designed.

3. *Digitizer modules.* The digitizer modules are custom-designed and depend on the type of detector system. The number of detectors interfaced per module depends on the type of detector.

4. *Workstation.* The workstation serves as the main point of interaction between the user and the DAS. Each workstation communicates via network with the local processor in the data histograming system. A separate network connection provides the workstation with direct reading access to the live data accumulating in the histogram memory, as shown in Figure V.3.6-1. The choice of the type of workstation and operating system is based on an evaluation made at the time of detailed DAS design.

Each instrument has its own data-acquisition cabin to house all the data-acquisition and chopper-control electronics and local computers. Each cabin is a temperature-controlled modular room at least 3×4 m^2 in size and accommodates several electronics racks, a workstation, and a small desk. These cabins are located as close to their respective instruments as practical.
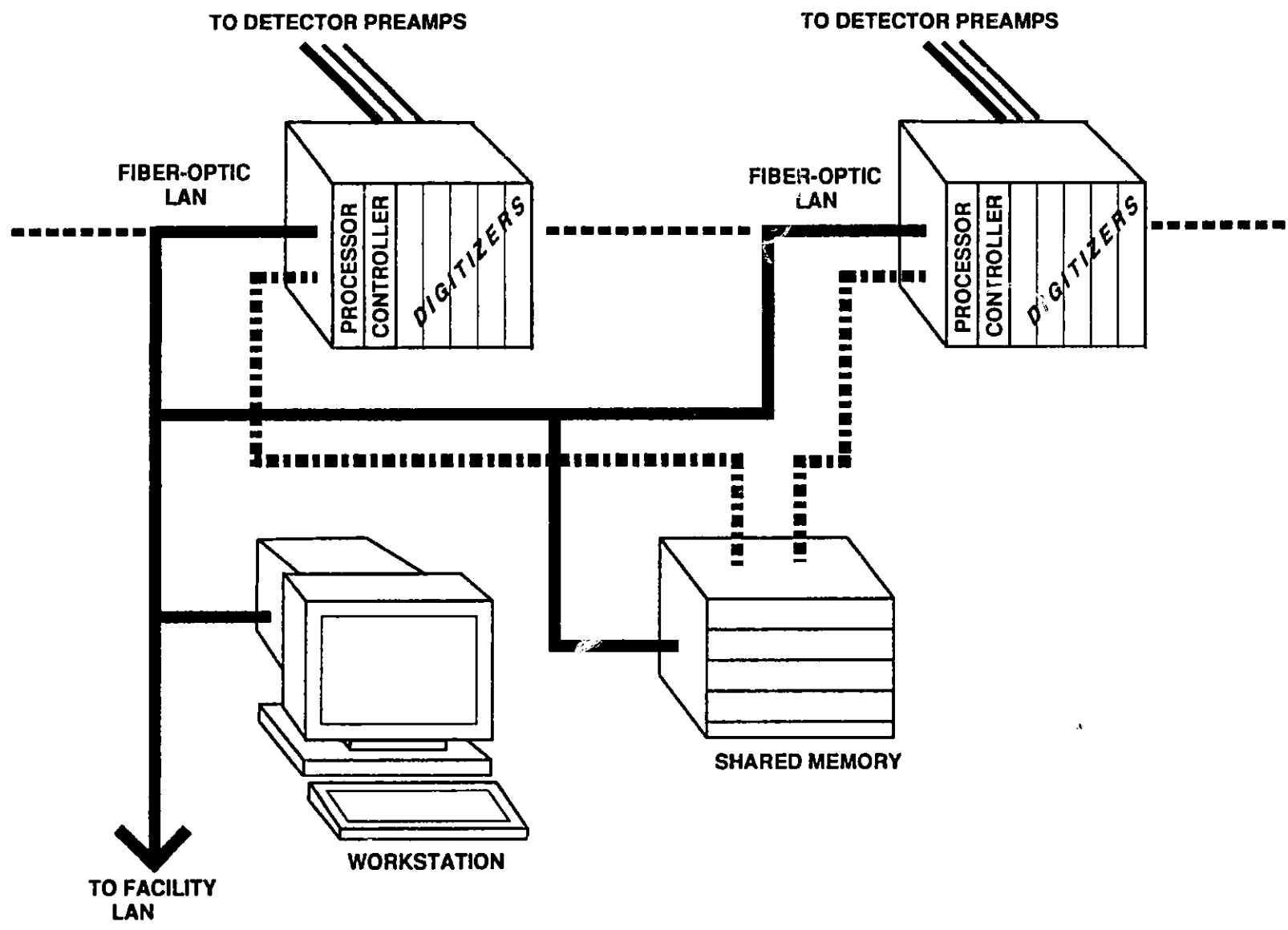
FIGURE V.3.6-1 Schematic Configuration of a Typical Instrument DAS.

3.7 DATA ANALYSIS

Rapid preliminary analysis is required to make informed decisions regarding experiments in progress. Data display, manipulation, and scientific visualization software are required.

The central computing facility handles at least 80 users, has at least 20 gigabytes of on-line storage, and 200 gigabyte of near-line storage. Archiving and restoring of files are achieved with a minimum of human intervention through automation of the loading of the archival media. The archiving software makes the process transparent to the user. A high-speed fiber-optic network handles transfer of large quantities of data and graphic images. The central computing facility also provides backup capability for the individual workstations and provides data bases for tracking facility maintenance, proposal and experiment status, user proposals, and safety concerns.

3.8 ANCILLARY EQUIPMENT

3.8.1 General-Use Items

Standard equipment and standard components are used wherever possible. Most sample-environment equipment is under computer control, so that experiments can be set up in sequence and the sample-environment variable changed automatically between measurements. This automation includes both cryogenic and furnace temperature control, sample position and orientation, choice of sample, and magnetic field. Interfaces for such automation are standardized to facilitate the automation of additional devices.

Closed-cycle refrigerators, cryostats, or furnaces are required for most experiments. Data rates on some of the IPNS Upgrade instruments are sufficiently high that more time is spent changing and equilibrating the sample temperature than is spent on collecting the data. It is important to initiate a program to develop designs for cryogenic and furnace environments that permit much more rapid change and equilibration of sample temperature. It is desirable to provide automated sample changers or other means of rapid change of samples within the controlled-temperature environment. The results of this development program will be incorporated into any new furnaces, displexes, and cryostats procured for IPNS Upgrade.

3.8.2 Specialized Items

3.8.2.1 Rotating-Crystal Insert for Diffractometers

Two ways are used to obtain structural information on disordered crystals by diffraction experiments. One method is to perform a single-crystal-diffraction experiment, and the other method is to carry out a powder-diffraction experiment. Both types of experiment measure the

diffuse scattering intensities, but both of these have drawbacks. The two-dimensional pair density function (2D-PDF) approach is a method in-between the single-crystal and powder-diffraction methods. In this approach, a single crystal is rotated around an axis while the scattering is recorded, providing a cylindrically averaged $S(Q_z,Q_r)$. A Q_z-resolved 2D-PDF is obtained by a Bessel transformation. With this method, all the diffuse scattering intensities are collected, resolved by Q_z. By changing the rotating axis it is possible to reconstruct the 3D picture. This method has already been used in the study of quasicrystals by x-ray diffraction,[22] but it has not yet been applied to neutron diffraction.

At IPNS Upgrade, both the GLAD and SEPD are suitable for such measurements. An insert for these instruments is required to rotate the sample at low temperatures. Such an insert will be developed.

3.8.2.2 Control of Sample Atmosphere

An increasing number of experiments are designed to study the behavior of a sample in contact with a controlled atmosphere (e.g., controlled oxidizing or reducing atmosphere, vapor-saturated gases, gas mixture, etc.). The study may involve following the time-evolution of the sample as it interacts with this atmosphere, or the presence of the atmosphere may be required to stabilize the sample. Standardized gas-handling systems are provided for such experiments. These systems have the capability for computer control and monitoring of the gas parameters such as pressure, concentration, etc.

3.8.2.3 Pulsed Sample Environments

The detection electronics in the QSS instruments are gated on for only a small fraction of the total time frame. A sample environment variable such as pressure, uniaxial-stress, magnetic field, laser heating, electric field, etc. can be pulsed in phase with the time gating of the data acquisition, so that the peak pulsed environment is present for the full time that the neutrons of interest are at the sample. This makes more effective use of the neutrons than is the case on a true steady-state beam. This argument applies equally well to the chopper TOF instruments, but not to most of the white-beam TOF instruments. Some techniques and equipment for pulsing sample variables exist, and others will be developed.

3.9 UTILITIES

3.9.1 Electrical Power

Each instrument at IPNS Upgrade has an installed capacity of 30 kW utility power and 10 kW clean power. Most of the clean power is installed in the data-acquisition cabins for the instruments, and the remaining power is installed in easily accessible distribution panels located on each of the instruments. Table V.3.9-1 summarizes expected utility usage by the instruments at IPNS Upgrade.

3.9.2 Other Utilities

Manifolds for N_2 gas, He gas, experiment water (32°C), lab chilled water (7°C), and compressed air (620 kPa) are available at easily accessible manifolds located on each of the instruments. For the IPNS instruments, monthly usage of N_2 gas and He gas are ~9×10^4 L and 6×10^4 L per instrument, respectively, and for compressed air, usage is 9×10^4 L at standard conditions per instrument. About 2×10^6 L of water, half of it chilled, is used per instrument per month. At IPNS Upgrade, these capacities per instrument are doubled, leading to the values given in Table V.3.9-1.

3.10 EXPERIMENTAL SUPPORT FACILITIES

A number of support facilities are required to maintain the instruments and to service the day-to-day needs of the experimental program. These include:

1. A small machine shop with a minimum of ~1,000 ft^2 (90 m^2).

2. An electronics shop with a minimum of ~1,000 ft^2 (90 m^2).

3. Laboratory space for development and testing of ancillary equipment and instrument components, having a minimum of ~2,000 ft^2 (180 m^2).

4. Laboratory space for development and testing of detectors, having a minimum of ~1,000 ft^2 (90 m^2).

5. Several well-equipped laboratories for sample preparation and handling. These must include hoods, chemical handling and storage facilities, and normal laboratory services and equipment. At least one of these must be a controlled area for handling of samples that have been activated. A minimum of ~3,000 ft^2 (270 m^2) is required for these laboratories.

Table V.3.9-1 Utility Requirements for the Instruments at IPNS Upgrade

Utility	Required Capacity per Instrument	Monthly Usage per Instrument
Electricity (normal)	~30 kW	~15 MWh
Electricity (clean)	~10 kW	~5 MWh
N_2 gas (low pressure)		~2 × 10^5 L
He gas (low pressure)		~1.5 × 10^5 L
Compressed air (at ~90 psig)		~2 × 10^5 L
Water (~80° F)	45 L/min	~2 × 10^6 L
Water (~45° F)	45 L/min	~2 × 10^6 L

6. Data-handling room, to contain a number of hard-copy devices, workstations, and terminals, as well as desks and tables for temporary use by the users, having a minimum of ~2,000 ft^2 (180 m^2).

Most of these spaces are in Building 368, between the 10-Hz and 30-Hz target buildings, to facilitate transport of equipment and samples back and forth to the instruments and for ease of access by the users. Additional facilities that are required, such as a site for the remainder of the shared computer facilities and laboratories for sample synthesis need not be contiguous to the experiment halls.

3.11 REFERENCES

1. C.G. Windsor, *Pulsed Neutron Scattering*, pp. 172-188 and 296-302 (Halsted Press, New York, 1981).

2. C.-K. Loong, S. Ikeda, and J.M. Carpenter, "The resolution function of a pulsed-source neutron chopper spectrometer," Nucl. Instrum. Methods **A260**:381-402 (1987).

3. G.E. Ostrowski et al., "The IPNS chopper control and accelerator interface system," in *Proceedings of the 8th Meeting of the International Collaboration on Advanced Neutron Sources (ICANS VIII)* (Oxford, U.K., July 8-12, 1985), Rutherford Appleton Laboratory Report No. RAL-85-110, pp. 676-688 (1985).

4. T.L.J. Jones et al., "Experience with the KFA/IGV (Jülich) magnetic bearing systems on an SNS neutron chopper," in *Proceedings of the 8th Meeting of the International Collaboration on Advanced Neutron Sources (ICANS VIII)* (Oxford, U.K., July 8-12, 1985), Rutherford Appleton Laboratory Report No. RAL-85-110, pp. 707-716 (1985).

5. J.M. Carpenter and C.-K. Loong, "IPNS chopper spectrometer improvements," in *Proceedings of the 11th Meeting of the International Collaboration on Advanced Neutron Sources (ICANS XI)* (Tsukuba, Japan, Oct. 22-26, 1990), National Laboratory for High Energy Physics (KEK) Report No. 90-25, pp. 711-716 (1991).

6. T.L.J. Jones et al., "The HET background suppressing chopper," in *Proceedings of the 9th Meeting of the International Collaboration on Advanced Neutron Sources (ICANS IX)* (Villigen, Switzerland, Sept. 22-26, 1986), Swiss Institute for Nuclear Research, ISBN 3-907998-01-4, pp. 529-533 (1987).

7. R.K. Crawford, Argonne National Laboratory, 1986 (unpublished information).

8. R.K. Crawford, Argonne National Laboratory, 1990 (unpublished information).

9. A.V. Rauchas et al., "IPNS accelerator system and neutron chopper synchronization," in *Proceedings of the 7th Meeting of the International Collaboration on Advanced Neutron Sources (ICANS VII)* (Chalk River, Canada, Sept. 13-16, 1983), Atomic Energy of Canada Limited Report No. AECL-8488, pp. 157-161 (1984).

10. L. Donley, "Phase locking the IPNS neutron chopper to the 60-Hz power line," in *Proceedings of the 8th Meeting of the International Collaboration on Advanced Neutron Sources (ICANS VIII)* (Oxford, U.K., July 8-12, 1985), Rutherford Appleton Laboratory Report No. RAL-85-110, pp. 689-696 (1985).

11. C.J. Carlile, M.W. Johnson, and W.G. Williams, *Neutron Guides on Pulsed Sources*, Rutherford Appleton Laboratory Report No. RL-79-084 (1979).

12. J.C. Sutherland et al., "The performance of the IRIS and HRPD guides on the SNS," in *Proceedings of the 8th Meeting of the International Collaboration on Advanced Neutron Sources (ICANS VIII)* (Oxford, U.K., July 8-12, 1985), Rutherford Appleton Laboratory Report No. RAL-85-110, pp. 771-776 (1985).

13. G.J. Russell et al., "Shielding concerns at a spallation source," *Advanced Neutron Sources 1988*, Proceedings of the 10th Meeting of the International Collaboration on Advanced Neutron Sources (ICANS X) (Los Alamos, N.M., Oct. 3-7, 1988), Institute of Physics Conference Series Number 97, Institute of Physics, New York, pp. 123-132 (1989).

14. M. Barbier, *Shielding and Activation Study for the Intense Pulsed Neutron Source at Argonne National Laboratory*, MITRE Technical Report No. MTR-6998 (MITRE Corp., McLean, Va., 1975).

15. J.M. Carpenter, C.W. Potts, and G.H. Lander, "Intense Pulsed Neutron Source (IPNS) at Argonne National Laboratory (ANL): A status report as of June, 1982," in *Proceedings of the 6th Meeting of the International Collaboration on Advanced Neutron Sources (ICANS VI)* (Argonne, Ill., June 28-July 2, 1982), Argonne National Laboratory Report No. ANL-82-80, pp. 77-101 (1983).

16. P.L. Davidson, M.W. Johnson, and N.J. Rhodes, "An Update on ISIS detectors," in *Proceedings of the 11th Meeting of the International Collaboration on Advanced Neutron Sources (ICANS XI)* (Tsukuba, Japan, Oct. 22-26, 1990), National Laboratory for High Energy Physics (KEK) Report No. 90-25, pp. 957-970 (1991).

17. P.L. Davidson et al., "Detector development at the ISIS facility," in *Advanced Neutron Sources 1988*, Proceedings of the 10th Meeting of the International Collaboration on Advanced Neutron Sources (ICANS X) (Los Alamos, N.M., Oct. 3-7, 1988), Institute of Physics Conference Series Number 97, Institute of Physics, New York, pp. 523-528 (1989).

18. D.G. Montague et al., "Use of a semi-opaque beamstop for monitoring sample transmissions at GLAD," in *Proceedings of the 11th Meeting of the International Collaboration on Advanced Neutron Sources (ICANS XI)* (Tsukuba, Japan, Oct. 22-26, 1990), National Laboratory for High Energy Physics (KEK) Report No. 90-25, pp. 830-839 (1991).

19. R.K. Crawford, J.R. Haumann, and G.E. Ostrowski, "Neutron detectors at IPNS," in *Proceedings of the 11th Meeting of the International Collaboration on Advanced Neutron Sources (ICANS XI)* (Tsukuba, Japan, Oct. 22-26, 1990), National Laboratory for High Energy Physics (KEK) Report No. 90-25, pp. 943-956 (1991).

20. P. Geltenbort and A. Oed, "Features of microstrip proportional counters," in *Proceedings of SPIE's International Symposium on Optical Applied Science and Engineering* (San Diego, Calif., July 19-24, 1992), vol. 1737, pp. 289-293 (1992).

21. R.K. Crawford et al., "The data acquisition system for the neutron scattering instruments at the Intense Pulsed Neutron Source," IEEE Trans. Nucl. Sci. **NS-28**, 3692-3700 (1981).

22. T. Egami, University of Pennsylvania, Philadelphia, 1992 (private communication).

4.1 INTRODUCTION

IPNS Upgrade includes neutron-irradiation facilities for the purpose of radiation damage studies, production of isotopes, and activation analysis. The anticipated uses of these facilities are discussed in Section 4.2, the details of the irradiation facilities are described in Section 4.3, and the external facilities to be used in support of these activities are described in Section 4.4.

The IPNS Upgrade neutron-irradiation facilities include four irradiation tubes for each of the two target stations. These tubes are designed to be used either for fast-neutron radiation damage measurements or for slow-neutron activation and isotope production. The tubes are located at different positions within the volumes surrounding each target. The integrated proton currents to these target stations differ by a factor of two, so the integrated neutron dose rate differs by a factor of two at the two stations. Irradiation positions at different distances from the target and at different angles with respect to the proton beam provide different neutron energy spectra, flux levels, and sample heat loads. These differences provide the opportunity to optimize the irradiation conditions for different purposes. The hot cells used to service target-system components, also serve as sample-handling facilities supporting these irradiation facilities. Radioactive samples and materials are transferred from the irradiation positions to in-house experimental facilities or to containers for shipment off-site.

4.2 ANTICIPATED USES OF THE FACILITIES

4.2.1 Radiation Effects

Samples are irradiated in the irradiation tubes to produce atomic defects that alter the structure and properties of the irradiated material. Investigation of these defects and their properties is an aspect of materials science research. Basic research in neutron radiation effects requires well-controlled and well-instrumented experimental facilities. A spallation neutron source has the advantages of ease of control, access, and instrumentation; low gamma flux; and constancy of neutron energy spectrum. The pulsed nature of the neutron flux offers additional scientific opportunities.

4.2.2 Isotope Production

The irradiation tubes provide available space in the neutron flux to produce various isotopes. Numerous isotopes can be produced, including iodine 125, molybdenum 99, xenon 133, dysprosium 165, tungsten 188, rhenium 186, samarium 153, and lutetium 177. These isotopes serve such fields as medicine, geology, biology, agriculture, manufacturing, and industrial calibration.

4.2.3 Activation Analysis

In activation analysis, traces of various elements can be identified and measured by analyzing the gamma rays they emit after neutron irradiation. Pneumatic capsules quickly transfer the irradiated activated samples to an automatic counting chamber. A computerized neutron cross-section and gamma-energy library provides accurate information on isotope quantities. Activation analysis is widely used in such fields as chemistry, biology, geology, forensics, and medicine.

4.3 OVERVIEW OF THE IRRADIATION FACILITIES

The irradiation tubes are located in the reflector material between the neutron beamlines in each station, allowing operation of the neutron scattering instruments and experiments on activation and radiation effects to proceed simultaneously. Figure V.4.3-1 shows a horizontal cutaway view through the midplane of the target and reflector assembly, indicating the locations of these tubes. Two irradiation tubes, labeled IT-1 and IT-2, are symmetrically placed on either side of and parallel to the long axis of the downstream section of the target in each target assembly. These tubes are located in the highest neutron flux and provide access to positions with intense fluxes of neutrons with energies up to 2 GeV. The highest-energy neutrons are found in the downstream direction, as illustrated in Figure IV.2.2-13. One irradiation tube, labeled IT-3, is also located in the beryllium reflector region, but is somewhat farther from the second target section than are IT-1 and IT-2. This tube provides a high neutron flux and low sample heating, with low fluxes of high-energy neutrons and scattered or secondary protons. These three tubes all have diameters of 5 cm and are designed for rapid insertion and removal of specimen capsules through use of a pneumatic system. Alternatively, the tube can be used for irradiation of an instrumented *in situ* experimental assembly. Figure IV.1.2-6 shows the arrangement of the pneumatic access tubes. A fourth, 10-cm diameter, vertically accessed tube (IT-4) is located between neutron beamlines in the iron shielding adjacent to the beryllium reflector, upstream from the target. The upstream position reduces the flux of very-high-energy neutrons and scattered protons. The thermal neutron flux is also lower in this tube.

Neutron fluxes and heat loads have been estimated at several positions in the IPNS Upgrade target assembly through the use of the High Energy Transport Code (HETC) and the low-energy Monte Carlo code for neutron and photon transport (MCNP). The computer model of the target is described in Section IV.2.2.1. Heat deposition was calculated for iron samples in the irradiation tubes. The neutron fluxes calculated for tubes IT-1 through IT-4 are given in Table V.4.3-1. The time-averaged available neutron flux, integrated over energies above 0.1 MeV, in thimble IT-1 or IT-2 is about 2×10^{13} n/cm^2-sec for 1 MW beam power.

The heat loads estimated for all tubes are sufficiently small that accurate temperature control can be maintained independent of variations in the proton current. Since experimental control is decoupled from neutron production, a spallation neutron source allows control of irradiation conditions superior to that available at any other neutron source.
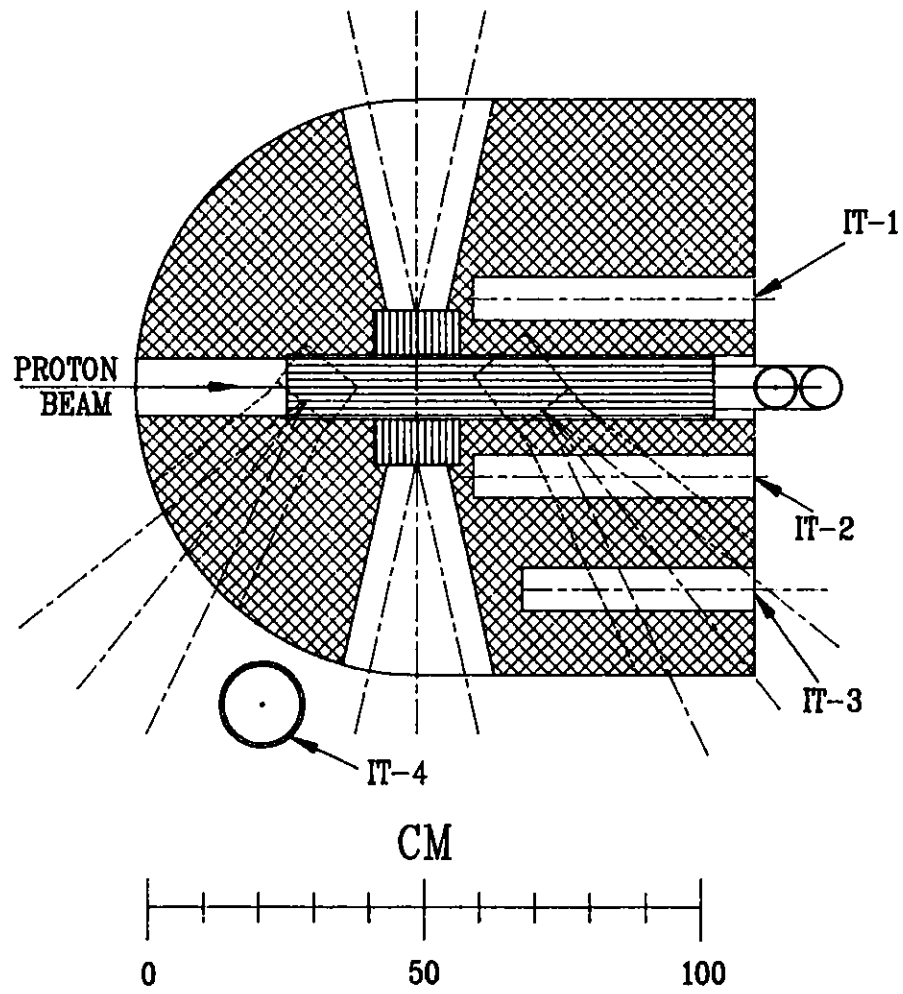
Figure V.4.3-1 Locations of the Irradiation Tubes.

Table V.4.3-1 Characteristics of IPNS Upgrade Neutron Irradiation
Tubes at 1-MW Proton Beam Power

Item	IT-1 or IT-2	IT-3	IT-4
Total neutron flux (10^{12} n/cm^2-sec)	60.6	14.1	3.8
Neutron flux > 0.1 MeV (10^{12} n/cm^2-sec)	17.8	2.8	1.5
% neutrons with energy > 20 MeV	3	1.5	<1
Heat load (W/g of Fe)	0.33	0.087	0.007
Diameter (cm)	5	5	10

All irradiation tubes in IPNS Upgrade permit penetration of electrical leads into the irradiation volumes for continuous specimen monitoring or experimental control during *in situ* experiments. The tubes are vacuum-tight, both for containment of radioactive gases or materials that will be produced during irradiation and for establishment of the desired controlled irradiation conditions. Each irradiation tube has an independent gas-handling system to allow purging before irradiation and removal of radioactive gases after irradiation. Because of the thermal heat load, each tube has an independent flowing-helium-gas cooling system that uses a coaxial piping design. Elevated irradiation temperatures are achieved by resistive-heater inserts and regulation of internal tube pressure.

For uninstrumented irradiations, such as for isotope production or activation analysis, the pneumatic tubes are accessed by pneumatic capsules, which have various sending and receiving stations. One receiving station is inside the hot cell. Radioactive specimens can be unloaded from the capsules and repackaged within the cell. Other unloading stations permit direct transfer of the capsule to small transfer shields or to other appropriate facilities for specialized handling. These other sending and receiving stations provide containment to preclude releases of airborne activity.

The vertical tube (IT-4) is accessed via stepped concrete and steel shield plugs that are slotted to accommodate instrumentation and control conduits. These shield plugs are lifted and set aside by a crane located in the roof-truss region of the building. A shielding cask is available to accommodate the removal of experiments.

4.4 IRRADIATION SUPPORT FACILITIES

4.4.1 Radiation Effects

In-house facilities external to the irradiation tubes include neutron scattering for atomic structure determination, transmission and scanning electron microscopy (TEM and SEM) for microstructure characterization, and gamma spectroscopy for isotope identification. Mechanical testing of irradiated specimens is performed within the hot cell facility. Local characterization facilities at Argonne include x-ray scattering at the Advanced Photon Source (APS) for study of atomic structure and microstructure. In addition, the radiation effects produced by the neutron irradiations at IPNS Upgrade will be studied at the Argonne electron microscopy/ion accelerator facility.

4.4.2 Isotope Production

Irradiated samples are loaded into shielded casks within the hot cell. These casks are ready for transport to the site at which the isotopes are to be used. The IPNS Upgrade facility has no additional facilities for preparation, characterization, or certification of the isotopes produced in such samples.

4.4.3 Activation Analysis

The samples irradiated for activation analysis are quickly transported to a shielded room equipped for gamma spectroscopy, where the gamma spectra produced by the induced activation is measured. This transport is by pneumatic capsule or by shielded cask. If a shielded cask is used, the samples are loaded into this cask within the hot cell. The shielded counting room is located nearby in one of the laboratory areas at IPNS Upgrade.

VI

Conventional Facilities

1.1 OVERVIEW

Argonne National Laboratory (ANL) is sited on 688 hectares (ha) in southern DuPage County, Illinois. The site is 43 km southwest of downtown Chicago and 38 km west of Lake Michigan. It is just north of the Des Plaines River valley, immediately south of Interstate Highway I-55, and west of Illinois Highway 83. Argonne's existing campus, as shown in Figure VI.1.1-1, houses several major research facilities, including the existing Intense Pulsed Neutron Source (IPNS) in the 360 area. Buildings associated with the existing IPNS are listed in Figure VI.1.1-2.

The IPNS Upgrade strategy is to reuse existing structures in the 360 area. There are 61,785 m^2 of existing facilities in this area that were completed in the early 1960s to house the 12.5-GeV Zero Gradient Synchrotron (ZGS). The ZGS site accommodates the IPNS Upgrade and has potential for adaptability and future expansion. The IPNS Upgrade reuses 51,370 m^2 of the existing space in its operation phase. An additional 3,700 m^2 of space is needed for the new linac facility, other buildings, and mechanical system modifications for a total of 55,200 m^2. The 360 area contains approximately 26.2 hectares of land with significant existing infrastructure, including 4.26 km of paved roads and a comparable amount of buried site utilities. The site utility study projects only minor amounts of new utilities and roads needed for the IPNS Upgrade.

The IPNS Upgrade consists of a 400-MeV linac and a 2-GeV Rapid Cycling Synchrotron (RCS), producing a 1-MW neutron source at 30 Hz. There are two target stations. One operates at 30 Hz, and the other operates at 10 Hz. The linac is housed in a new facility that is connected by the Low-Energy Transport (LET) tunnel to the existing ZGS Ring Building (Building 365) where the new RCS is installed. The existing ZGS Ring Building is an annular concrete tunnel with an inner diameter of 22.6 m, an outer diameter of 32.9 m, and an overall height of 12.8 m. Building 369 houses the 10-Hz target, and target support facilities are located in Building 367. Building 370 houses the 30-Hz target, and its support facilities are housed in Building 371. The two targets can accommodate 36 instrument lines. Sample preparation laboratories are located in Building 368 adjacent to the target facilities. The existing control room and office areas in Building 360 are used. Building 362 serves as a central laboratory and office facility for staff and users.

The Center Building (Building 364) and Power Supply Building (Building 376) both house mechanical and power systems for the RCS, High-Energy Transport (HET), and the LET. Site Facility 377 contains cooling towers and associated support facilities. Target coolant retention tanks are located in new buried vaults adjacent to the target cooling buildings. The site includes roads, parking, docks, facility support, and staging areas. Available utilities in the 360 area include water systems, cooling towers, power mains, transformer systems, sewers, special scientific services, general infrastructure, and miscellaneous amenities. Existing utility tunnels in the ZGS area are retained. An existing tunnel in Building 370 is relocated to allow construction of the pile foundation for the target biological shield.

WATERFALL GLEN
NATURE PRESERVE

WATERFALL GLEN
NATURE PRESERVE

WATERFALL GLEN
NATURE PRESERVE

LAND FILL
AREA

WATERFALL GLEN
NATURE PRESERVE

WATERFALL GLEN
NATURE PRESERVE

IPNS-UPGRADE
360 AREA

North

West — East

South
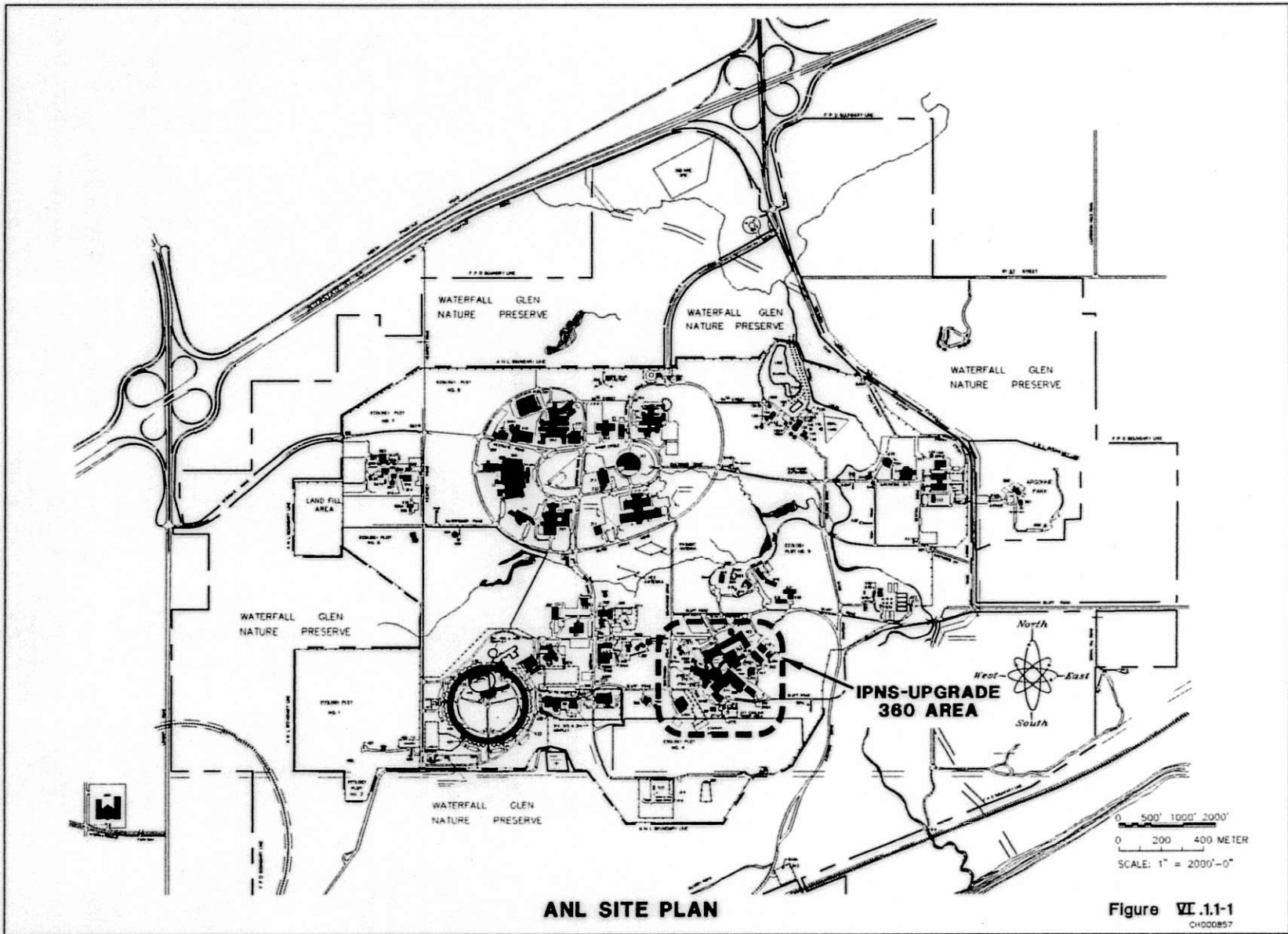
ANL SITE PLAN

Figure VI.1.1-1

CH000857

SCALE: 1" = 2000'-0"

LEGEND:

- - - - - - UTILITY TUNNEL SYSTEM
- · - · - · - STORAGE VAULTS
▢ IPNS-UPGRADE BUILDINGS
▨ NEW CONSTRUCTION

EXISTING IPNS BUILDINGS

360	389B
361	390
375	391
375A	399

IPNS-UPGRADE BUILDINGS/FACILITIES

360 - LAB/OFFICE
362 - LAB/OFFICES
364 - CENTER BUILDING
365 - RING BUILDING
367 - 10Hz TARGET SUPPORT
368 - LAB/PREP/SUPPORT
369 - 10Hz TARGET
370 - 30Hz TARGET
371 - 30HZ SUPPORT
376 - POWER SUPPLY
377 - COOLING TOWERS
394 - LINAC
394A - LINAC-LET. TUNNEL
549A - SWITCHGEAR FACILITY
549B - TRANSFORMER STATION

360/ZGS AREA SITE PLAN

0   50   100   150   200 FEET
0 10 20 30 40 50 60 70 80 90 100 METERS

Figure VI .1.1-2

The above-mentioned buildings are shown as hatched areas in Figure VI.1.1-2. The new linac building, Building 394, is also shown in crosshatch in Figure VI.1.1-2. Figure VI.1.1-3 is a photograph of the existing site with an overlay of the new linac and LET tunnel. The IPNS Upgrade conventional facilities are illustrated in Figure VI.1.1-4, the IPNS Upgrade Area Plan.

The adaptive reuse of these existing facilities addresses the usability and operational efficiency of the overall project. Engineering design provisions follow U.S. Department of Energy (DOE) Order 6430.1A, dated April 6, 1989, entitled "General Design Criteria Manual." The following significant criteria are considered in developing the siting, configuration, and building systems selections:

- Existing buildings are large enough to house the proposed technical facility.

- New technical components can be constructed within the existing buildings at reasonable cost.

Building rehabilitation, as described in this report, meets the above two criteria.

369 - 10-Hz TARGET

364/365 RCS →

370 - 30-Hz TARGET

← 367

POWER SUPPLY 376 →

368

LET

371

394A

377

LINAC 394
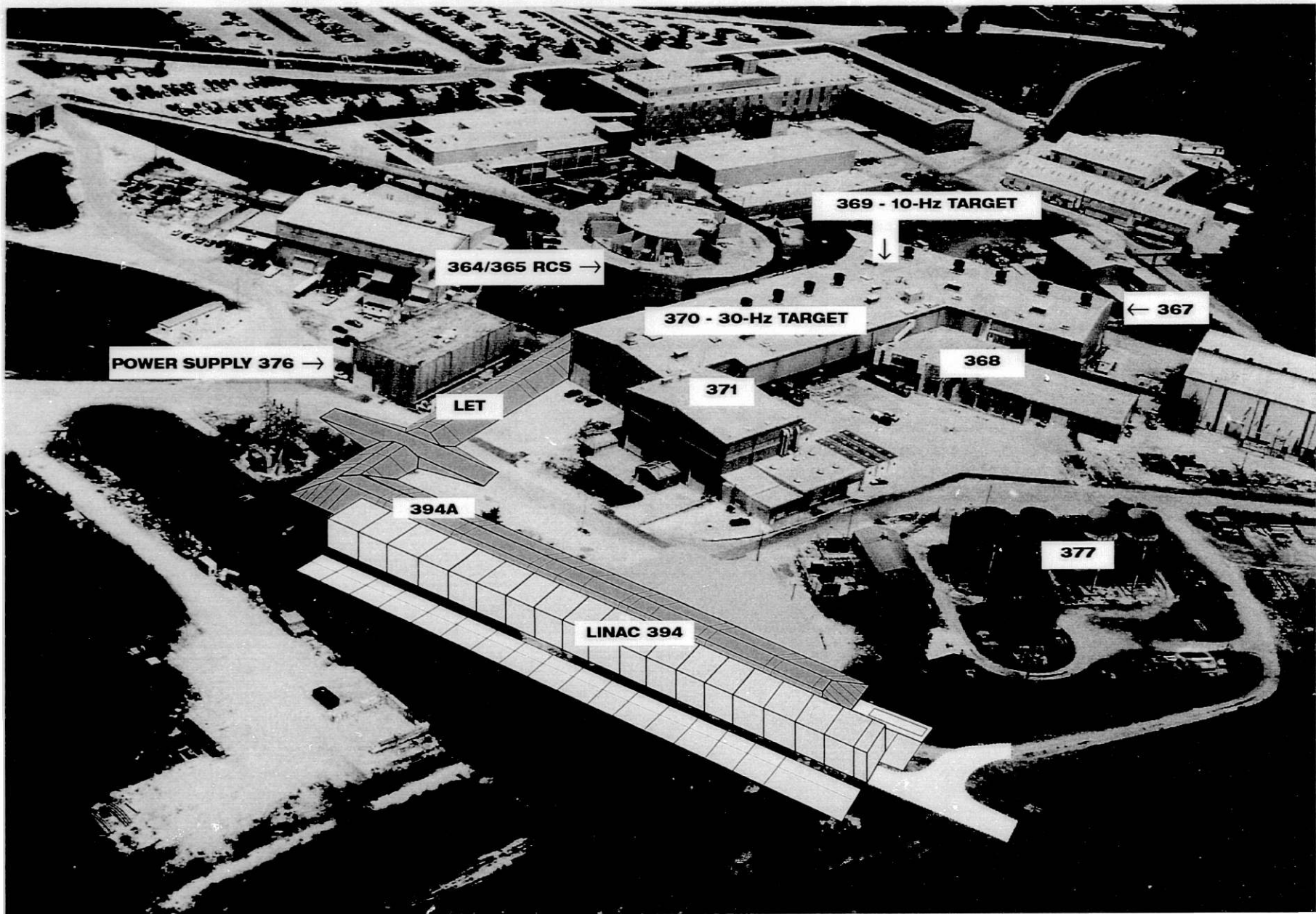
FIGURE VI.1.1-3 IPNS Upgrade Site Photo

IPNS UPGRADE
AREA PLAN
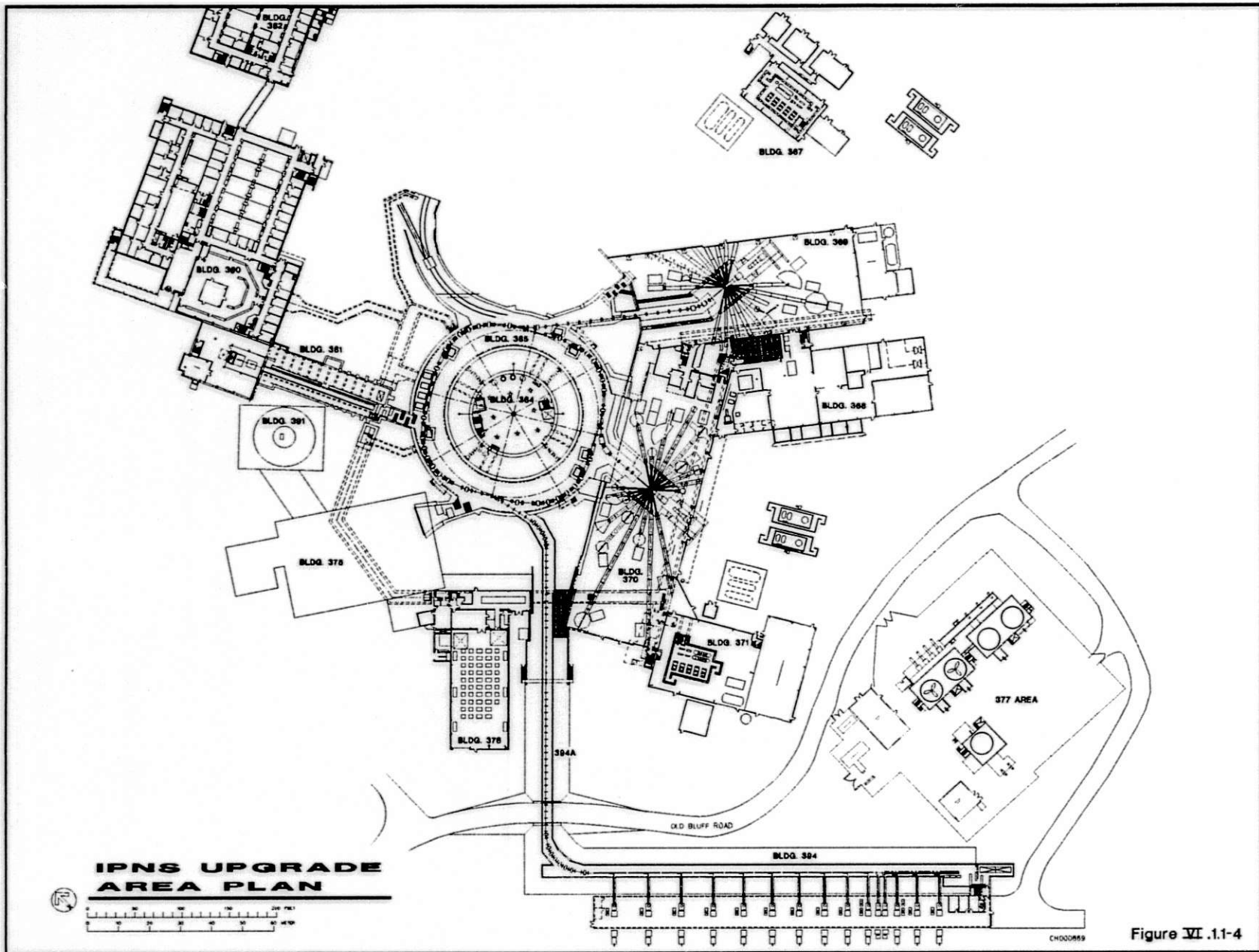
Figure VI.1.1-4

1.2 APPLICABLE CODES AND STANDARDS

All systems will be designed to meet the latest editions of the applicable codes, standards, and guides published by the organizations as listed below at the time the Title-II Design is begun. The design described in this report meets current codes, standards, and guides.

1.2.1 Architectural/Structural Codes and Standards

- U.S. Department of Energy, DOE 6430.1A, "General Design Criteria Manual"

- International Conference of Building Officials, "Uniform Building Code" (UBC)

- American Concrete Institute (ACI), ACI 318, "Building Code Requirements for Reinforced Concrete"

- American National Standards Institute (ANSI)/American Concrete Institute (ACI) standards:

  ANSI/ACI 302, "Practice for Concrete Floor and Slab Construction"

  ANSI/ACI 531, "Building Code Requirements for Concrete Masonry Structures"

- Prestressed Concrete Institute Standards

- American National Standards Institute (ANSI)/National Bureau of Standards (NBS)

  ANSI/NBS 211, "Building Code Requirements for Masonry"

  ANSI/NBS Handbook H74, "Building Code Requirements for Reinforced Masonry"

- Structural Clay Products Institute, "Recommended Building Code Requirements for Engineered Brick Masonry"

- National Concrete Masonry Association, "Specifications for the Design and Construction of Load Bearing Concrete Masonry"

- American Institute of Steel Construction, "Specification for Design, Fabrication, and Erection of Structural Steel for Buildings"

- Steel Joist Institute, "Standard Specifications, Load Tables and Weight Tables for Steel Joists and Joist Girders"

- Steel Deck Institute, "Steel Deck Design Manual for Composite Decks, Form Decks and Roof Decks"

- Steel Deck Institute, "Steel Deck Institute Diaphragm Design Manual"

- American Iron and Steel Institute, "Specifications for the Design of Light Gauge Cold-Formed Steel Structural Members"

- American Welding Society (AWS), AWS D1.1, "Structural Welding Code"

- American National Standards Institute (ANSI), ANSI A58.1, "Building Code Requirements for Minimum Design Loads in Buildings and Other Structures"

- Metal Building Manufacturers Association, "Metal Building Systems Manual"

- U.S. Department of the Army, TM-5-809-10, "Seismic Design for Buildings" (lateral force design methodologies in this technical manual can be used effectively for wind design as well as seismic design)

- Building Officials and Code Administrators, International, Inc. (BOCA), "National Building Code"

- National Fire Protection Association (NFPA), NFPA-101, "Life Safety Code"

1.2.2 Heating, Ventilation, and Air Conditioning (HVAC) Codes and Standards

- U.S. Department of Energy, DOE 6430.1A, "General Design Criteria Manual," Chapter 5

- American National Standards Institute (ANSI), "Code Requirements"

- American Society of Mechanical Engineers (ASME), "Boiler and Pressure Vessel Code Requirements"

- National Fire Protection Association (NFPA), "National Fire Codes" and Standard 90A, "Air Conditioning and Ventilation Systems"

- International Association of Plumbing and Mechanical Officials, "Uniform Mechanical Code"

- Associated Air Balance Council (AABC)

- Air Moving and Conditioning Association (AMCA)

- American National Standards Institute (ANSI)

- Air-Conditioning and Refrigeration Institute (ARI)

- American Society of Heating, Refrigerating and Air Conditioning Engineers, Inc. (ASHRAE), "Handbook of Fundamentals" and standards:

  90A, "Energy Conservation in New Building Design"

  15-1994, "Safety Code for Mechanical Refrigeration"

  62-1989, "Ventilation for Acceptable Air Quality"

- Construction Specifications Institute (CSI)

- Cooling Tower Institute (CTI)

- Hydronics Institute (HI)

- National Environmental Balancing Bureau (NEBB)

- National Electric Manufacturers Association (NEMA)

- Sheet Metal and Air Conditioning Contractors National Association, Inc. (SMACNA)

- Underwriters' Laboratories, Inc. (UL)

- American Conference of Government Industrial Hygienists, "Industrial Ventilation Manual"

- General Services Administration/Public Buildings Service (GSA/PBS) Publication, "Energy Conservation Design Guidelines for New Office Buildings"

- Federal Construction Council (FCC), "Federal Construction Guide Specifications"

1.2.3 Plumbing Codes and Standards

- U.S. Department of Energy, DOE 6430.1A, "General Design Criteria Manual" and DOE 5480.4, "Environmental Protection, Safety, and Health Protection Standards"

- "National Standard Plumbing Code"

- "Illinois State Plumbing Code"

1.2.4 Fire Protection Codes and Standards

- U.S. Department of Energy, DOE 6430.1A, "General Design Criteria Manual" and DOE 5480.4, "Environmental Protection, Safety, and Health Protection Standards"

- National Fire Protection Association

    NFPA 10, "Portable Fire Extinguishers"

    NFPA 13, "Installation of Sprinkler Systems"

    NFPA 24, "Installation of Private Fire Service Mains and their Appurtenances"

    NFPA 101, "Life Safety Code"

1.2.5 Electrical

- American National Standards Institute (ANSI)

- American Society for Testing Materials (ASTM)

- Certified Ballast Manufacturer (CBM)

- Electrical Testing Laboratories (ETL)

- Institute of Electrical and Electronics Engineers (IEEE)

- Insulated Power Cable Engineers Association (IPCEA)

- National Electric Code (NEC)

- National Electrical Manufacturers Association (NEMA)

- National Electrical Safety Code (NESC)

- National Fire Protection Association (NFPA)

- Occupational Safety and Health Act (OSHA)

- Underwriters Laboratories, Inc. (UL)

- Joint Industrial Council (JIC)

1.3 UTILITIES

Argonne National Laboratory owns and operates the following systems at the ANL-East site:

- Steam generation and distribution

- Natural gas distribution

- Domestic, laboratory, and canal water treatment and distribution

- Collection and treatment of sanitary waste

- Generation and distribution of chilled water

- Electric power distribution

- Telecommunications system.

Vendors and public utilities supply natural gas, oil, coal, electric power, and telephone service to ANL-East.

1.3.1 Steam

Most of the steam required by the Laboratory is generated in the Central Heating Plant (CHP) and distributed by an extensive piping network to most of the buildings. Steam is used primarily for central heating.

1.3.2 Natural Gas

Natural gas is purchased from the Defense Fuel Supply Center (operated by the Defense Logistics Administration). Northern Illinois Gas Co. delivers gas through its distribution grid to the Laboratory. The Central Heating Plant is the major user of natural gas.

1.3.3 General Water Supply

The general water supply of ANL-East is pumped from municipal water systems of adjacent communities and from four ANL wells to the Water Treatment Plant. After softening, the water is pumped into the storage tanks then into the general distribution system, which provides for domestic and laboratory process use and for fire protection.

1.3.4 Canal Water

The canal water system consists of a water-treatment facility, storage tanks, and a distribution system. Nonpotable canal water is used on-site, primarily in cooling towers and, to a lesser degree, for a variety of other cooling needs.

1.3.5 Storm Sewers

Roof drains, downspouts, and certain noncontact cooling water discharges are connected to storm sewers at most permanent buildings. Storm sewers are discharged into the nearest suitable outfall point, usually a creek or a well-drained low area.

1.3.6 Sanitary Sewers

Sanitary sewage from various buildings is conveyed by underground sewers to the Sanitary Wastewater Treatment Plant (SWTP).

1.3.7 Chilled Water Systems

Chilled water for process and comfort cooling is provided by three separate chilled water systems, serving many of the major buildings on-site: (1) the 360-Area Chilled Water System serving the IPNS Upgrade, (2) the APS Chilled Water System, and (3) the Central Chilled Water System.

1.3.8 Electric Power Distribution

Electric power for the ANL-East site is purchased from the Commonwealth Edison Company (CECo) at 138 kV. The CECo transmission consists of two lines, fed by the Joliet and McCook generating stations and routed along the Atchison, Topeka, and Santa Fe Railroad in the Des Plaines River valley south of the site.

1.3.9 Telecommunication Systems

An InteCom IBX S/80 digital private branch exchange (PBX) serves the ANL-East site. The PBX supports standard analog telephones, InteCom-manufactured digital stations for voice, data, or simultaneous voice and data service, and LANmark local area networking.

This section describes the buildings and facilities that support the various technical components of the IPNS Upgrade, including the linac, RCS, 10-Hz and 30-Hz targets, and experiment instrument lines. Each target station supports 18 neutron beam lines and scattering experiments. The existing structures in the 360 area are all surveyed and verified against existing as-built construction documents. Machine design and component layout are optimized to fit into the existing structures.

The existing buildings in the 360 area are at least 30-years old, but they have been included in ANL ongoing maintenance programs and have undergone various upgrades. All roofs in the 360 area were replaced in 1990 with new Inverted Roof Membrane Assembly (IRMA) systems. Electrical systems were upgraded on a building-by-building basis. Mechanical systems were also refurbished and updated on a per-building basis. Life-safety surveys were completed in 1992. Fire suppression systems and emergency exits were reviewed, and upgrades are in progress. Air conditioning refurbishing and replacement is on a per-building basis. Existing utility/control tunnels are in satisfactory condition.

Radiation-safe entrances to the linac tunnel, transfer line tunnel, and to the RCS are provided by shielded mazes. Access to the RCS is provided through a curved tunnel in Building 363 and through labyrinths in Buildings 361, 364, 369, 375, and 394A.

2.1 LINAC BUILDING (BUILDINGS 394 AND 394A)

The Linac Building is the only new building for the IPNS Upgrade. All other facilities are the adapted reuse of existing ZGS area buildings and facilities with minor modifications.

The new Linac Building, Building 394, is located in the southwest sector of the ZGS campus, southwest of existing Building 376 and parallel to Old Bluff Road, as shown in Figure VI.2.1-1.

Linac tunnel construction utilizes a "cut and cover" method that was successfully used at Fermilab. The top of the linac tunnel enclosure is at grade (Elevation 711.0 ft), with the tunnel floor 3.04 m below grade (Elevation 701.0 ft). Earth shielding is added to the grade above the tunnel, creating a tapered berm 3.20 m high. The linac tunnel cross section is 3.66 m wide × 2.74 m high and the LET tunnel is 3.04 m wide × 2.74 m high, as shown in Figures VI.2.1-2 and VI.2.1-3. The linac tunnel is 154.8 m long, and the transfer tunnel to the RCS is 118.9 m long. Tunnel segments are precast-concrete, inverted-U-shaped elements 2.44 m in length with 0.3-m-thick walls and roof, which are erected on a cast-in-place 0.6-m-thick concrete slab that has perimeter drains.

Linac construction generates minimal conflicts with existing site utilities. The two 475-mm-diameter main chiller lines are lowered by 1 m to pass under the LET tunnel (394A) and avoid interference, as shown in Figure VI.2.1-2, Section A. Existing Old Bluff Road crosses over

BLDG. 385

B-4

B-4

B-3

B-3

BLDG. 370

BLDG. 371

B-2

B-2

TUNNEL 394A

BLDG. 376

377 AREA

B-1

B-1

OLD BLUFF ROAD

A

A

BLDG. 394

LINAC
BUILDING 394
OPERATING FLOOR

0   10   25   50 FEET

0   10 METERS

Figure VI.2.1-1

CH030873

Linac

Low Energy Transport (LET) Tunnel

Existing Buildings 364-365

Old Bluff Road

Existing ZGS
Utility tunnel

Building 376 Beyond

365

364

365

B-1

B-2

B-3 B-4

See Fig. VI 2.1-3 for Sections B-1 thru B-4

See Section -A Below

SECTION Through Linac Facility & Low Energy Transport (LET) Tunnel into Ring Building (365)

Linac Building 394

Linac
Tunnel
394-A

Earth
Berm
Shielding

Old Bluff Road- Beyond
Ramp up and over tunnel

Klystron
Gallery

9.14 m

0.3m

B-1

Exterior
Power
Supplies

3.20m

Low Energy
Transport Tunnel

0.3m

2.74m

10.97m

6.09m

3.66m

0.6m

Existing 475 mm Dia. Chilled
Water Pipes lowered 1.0m

SECTION -A   Through Linac Building showing Klystron Gallery, Linac Tunnel (394A)

Figure VI.2.1-2 Sections

Earth Shield Berm
rises-up beyond

Building 376
Beyond

Earth
Shield
Berm

Building 370
Beyond

20m

2.74m

Grade

5.48m   3.04m   5.48m

SECTION B-2 Personnel Stairs and Bridge Over LET berm

Top of 364/365 Hill Beyond

Earth
Shield
Berm

3.96m   3.64m   5.48m

Concrete
Retaining
Wall -Typ

Building 370
100% Occupancy

Grade

3.04m   6.08m

SECTION B-4 LET at wide area next to Bldg 370

2.5m

Old Bluff Rd

Concrete Shield
9.15m

Earth
Shield
Berm
Beyond

20m

Grade

2.74m

5.48m   3.04m   5.48m

SECTION B-1 Old Bluff Rd Crossing Over LET

3.96m   3.04m   4.26m

Earth
Shield
Berm

Bldg 376

10% Occup

20m

Building 370
100% Occupancy

Grade

ZGS
Utility Tunnel
0% Occup

3.04m   3.64m

Concrete
Shielding

SECTION B-3 LET crossing utility tunnel at Bldg's 376 & 370

Figure VI. 2.1-3

the top of the LET tunnel southwest of Building 376. The LET tunnel roof is thickened and reinforced to carry vehicle loads and to provide the required shielding at the roadway, as shown in Figure VI.2.1-3, Section B-1.

The klystron gallery in the Linac Building (Building 394) is 10.97 m wide × 9.14 m high × 129.5 m long and has a gross floor area of 2,509 m^2. It houses the 15 klystrons and their pulse modulators. Other associated electrical equipment and power supplies are located on 15 concrete slabs outside of, but next to, the exterior west wall. There are three 3.04 m × 4.88 m rooms, two 2.0 m × 2.0 m handicapped-accessible toilets, and a janitor room, located inside the building at the south end. Space over this area has a floor for mechanical equipment and is accessed by adjacent stairs. These stairs also allow access to the linac tunnel (394A), which is below grade. The end of the linac tunnel has a 2 m × 12 m access hatch to allow installation of linac components.

2.1.1 Architecture (Buildings 394 and 394A)

The interior of the Linac Building is a single open space to house technical components along the length of the linac. The building can be entered through personnel doors at either the north or the south end. The south end has vehicle access for movement of major components into klystron and tunnel areas. Conduit, piping, duct-work and the exposed underside of the roof deck are unpainted. The floors are exposed, surface-hardened concrete.

Partitions are gypsum drywall on metal studs with painted finish. The south end contains office, shop, toilets, and technical-support rooms. The area above these rooms has a floor for mechanical equipment and is accessible by means of a stairway. Only these rooms have suspended acoustical tile ceilings, with recessed lighting and HVAC diffusers, concealing the electrical and mechanical distribution systems.

The Linac Building has 9.14-m-high, windowless facades with minimal architectural elements and is clad with 0.1-m-thick insulated metal building panels having a rating of R-19+. The vertical insulated metal panels are coated with a durable epoxy-type finish. Louvers and other accessories match the finish of the wall-panel system.

The roof has a side slope with roof scuppers and downspouts discharging at grade. The IRMA roof system meets existing Argonne standards. Insulated metal exterior doors are used for personnel access. Vehicle access is provided by a sectional overhead door of insulated metal panels.

2.1.2 Structure (Buildings 394 and 394A)

The structural system for the Linac Building consists of a steel beam-and-girder roof system supporting a welded-steel deck with wide-flange columns on spread footings. The frame has horizontal steel girts, which support vertical insulated-metal wall panels. A 0.2-m-thick

reinforced-concrete floor slab rests on 0.15-m-thick compacted granular backfill. The roof has a steel deck with an IRMA system, which consists of a single-ply roof membrane, protection board, and 7-cm-thick rigid foam insulation bonded to 1-cm-thick cement exterior board.

There are 273.7 m of tunnel associated with the linac and the LET. Basic tunnel construction is of precast concrete elements erected on a concrete base slab. The base slab is 0.6 m thick and runs the continuous length of the tunnel. Perimeter drains are located at the bottom edge of each side. There are weld plates embedded in the bottom exterior edge of the precast elements and cast-in-place base slab. The precast elements are joined every 2.44 m. The tunnel is covered with a multicomponent waterproofing system that consists of a 25-mm-diameter backer rod with bentonite sealant, multi-ply exterior sheet overlaid with a 3-mm-thick protection board. The tunnel is provided with a 0.3-m-thick layer of gravel backfill to allow water to flow around it to the continuous perimeter drains, which are connected to ejector pumps.

Unistrut channels are cast into the tunnel segments for mounting mechanical and technical components. The west wall of the linac tunnel has 15 openings for waveguide connections, as shown in Figures VI.2.1-1 and VI.2.1-2, Section A.

The top of the LET tunnel under the roadway is thickened and reinforced for shielding and vehicle support. The LET tunnel rises vertically and crosses over the existing main utility tunnel between Buildings 376 and 370, as shown in Figure VI.2.1-2. Shielding configurations in this area allow maximum exterior access to the existing facilities and provide for proper shielding performance. Concrete is used in the constricted locations between Buildings 376 and 370, as shown in Figures VI.2.1-1 and VI.2.1-3, Section B-3.

2.1.3 Mechanical Systems (Buildings 394 and 394A)

Heating, Ventilating, and Air Conditioning (HVAC). The klystron gallery is provided with one 30,000-cfm (cubic feet per minute) air-handling unit (AHU), with chilled-water cooling and steam-heating coils and return/exhaust fans. The temperature during summer does not exceed 32°C. In winter, 12 steam unit heaters with integral thermostats maintain the building to at least 16°C.

The linac and LET tunnels are furnished with 100% outside air. The AHU is located in the enclosure at ground level, near the intersection of the linac and LET tunnels. Capacity of the unit is approximately 20,000 cfm, and it contains chilled-water cooling and steam-heating coils. The tunnel conditions are maintained such that temperatures do not exceed 32°C in summer and do not fall below 16°C in winter. There are two exhaust fans located at the northernmost end of the LET tunnel and the southernmost end of the linac.

The Linac Building has fully automated direct digital controls (DDCs) for control of HVAC equipment. Winter humidification is provided; however, no summer dehumidification is provided.

Plumbing, Process Piping, and Fire Protection. Plumbing systems for the Linac Building and the LET consist of floor drains, domestic cold water, and sanitary waste and vent systems. Process piping systems supply compressed air and process water at 32°C as required for specific equipment and functions. Fire protection consists of a wet-pipe automatic-sprinkler system. Hand-operated fire extinguishers are located as required near electronic components. Two chilled-water pipes are routed from the utility tunnel through the LET tunnel, to the service floor of Building 365, as shown in Figure VI.2.1-3, Section B4.

2.1.4 Electrical Systems (Buildings 394 and 394A)

Electrical power is distributed at 480 V from substations west of the Linac Building. Electrical power to injector system components is supplied from three 480-V substations, as shown in Figure VI.2.1-4. These substations are located outside the Linac Building. Each substation consists of a 13.2-kV dual-primary-switch, 2000-kVA transformer, and associated 480-V switchgear. The 480-V switchgear feeds power distribution panels located inside the Linac Building. Power at 13.2 kV is supplied from Site Electrical Facility 549.

The linac and LET tunnels are lighted with two-lamp, surface-mounted fluorescent fixtures. Illuminated emergency exit signs are installed. Emergency lighting is provided by 1.5-h battery-powered units with built-in chargers. The klystron gallery is lighted with high-bay, metal-halide fixtures to an average of 30 foot-candles of illumination. Convenience receptacles and power and welding receptacles are provided at various locations.

A motor control center is provided to feed power to building mechanical equipment and other installed motors rated at 0.5 hp and above.

An equipment grounding system is provided. Each piece of equipment is connected to grounding conductors that run together with all power feeders. Lightning protection is provided by copper rods mounted around the roof perimeter. These rods are connected by copper cables Cadwelded to the building structural steel. The building ground system uses bare copper Cadwelded to the building structural steel, which is connected to ground rods spaced around the building. In addition, all computer and related equipment is provided with a separate quiet grounding system that is isolated from the other grounding systems and is connected to a separate counterpoise and ground rod system.

13.2kV

FACILITY 549
SWITCHGEAR

2000kVA
2400A

2000kVA
2400A

2000kVA
2400A

2000kVA
2400A

BACKUP
POWER SOURCE

480/277V
SWITCHGEAR

480/277V
SWITCHGEAR

480/277V
SWITCHGEAR

TO EQUIPMENT

BUILDING 394 SERVICE LAYOUT
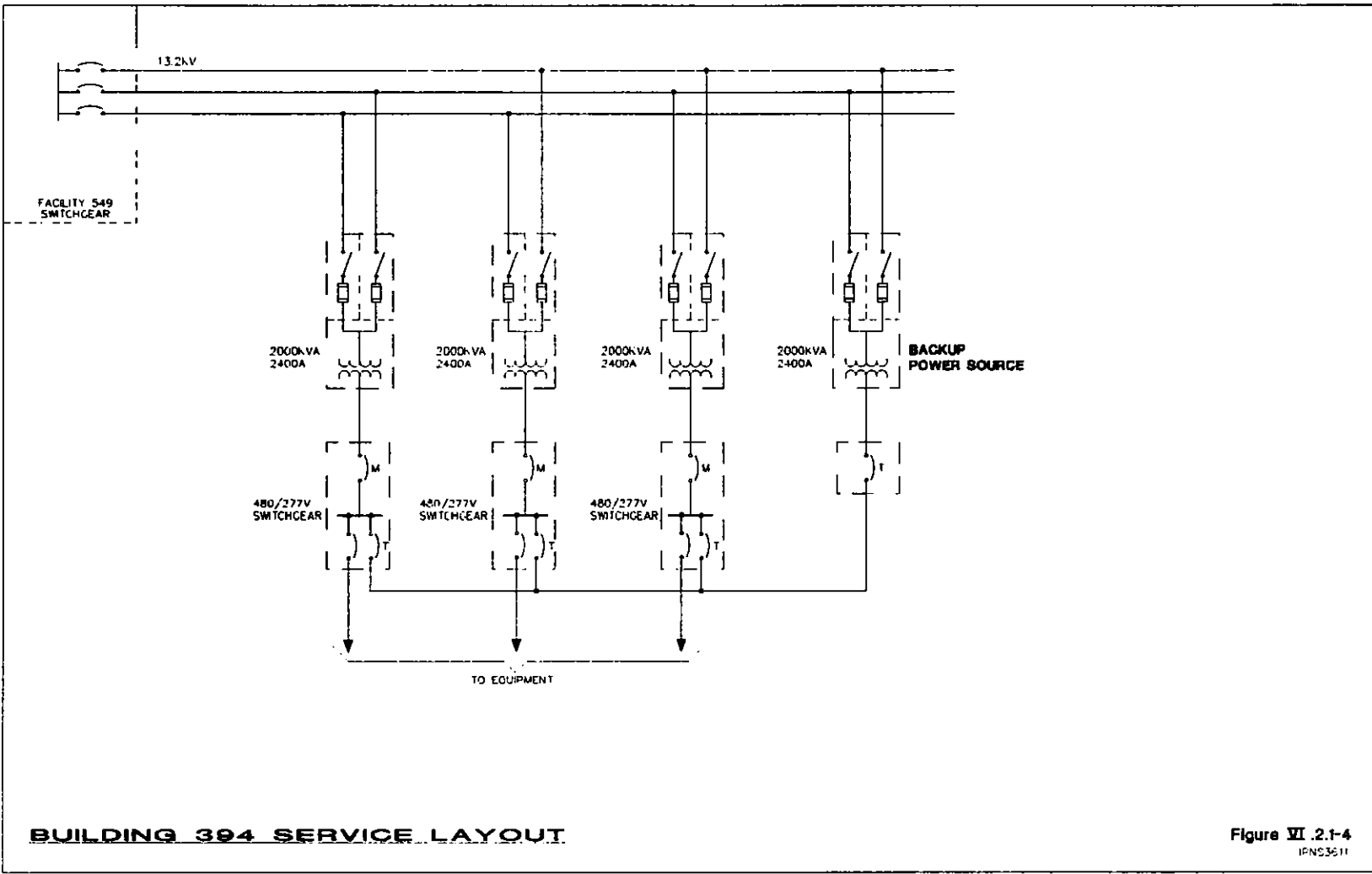
Figure VI.2.1-4

IPNS3611

The fire alarm system consists of manual pull stations located at building exits and flow and tamper switches in the sprinkler system. Smoke and heat detectors are installed throughout the building and in the HVAC system. The alarm system is annunciated at the Argonne Fire Station and in the IPNS Upgrade main control room.

Telecommunications are from a branch from the PBX in Building 360, with a telephone terminal in the Linac Building. Telephone communications equipment includes a new terminal cabinet, telephone outlets, and telephone cables. The paging system has new speakers, conduit, and wires and is tied to the existing system.

Clean power requirements are met by the use of 480-V/480-V isolation transformers. Emergency power is provided from an existing diesel generator rated at 250 kVA located near Building 376.

2.2 RING BUILDING (EXISTING BUILDING 365)

Building 365 was completed in 1962 to house the 12.5-GeV Zero Gradient Synchrotron. It has two floor levels and a gross floor area of 7,014 m^2. The upper level is the operating floor for the RCS, and there is a service floor below.

This building houses the IPNS Upgrade RCS, and it is totally surrounded by an existing earth berm. The Ring Building is donut-shaped, with an interior radius of 22.6 m and an outer radius of 32.9 m, and with an overall height of 12.8 m. It encircles the cylindrical-shaped Center Building 364. There are 7 m of earth shielding between these buildings. Building 365 is connected to Buildings 361, 363, 364, 369, 370, 375, and 394A. Figure VI.2.2-1 is a vertical cross section of the Ring Building and Center Building showing the original ZGS. Figure VI.2.2-2 is a plan view of the Ring Building operating floor and includes the RCS layout.

2.2.1 Architecture (Building 365)

This building is a two-level reinforced-concrete circular tunnel, with a clear floor width of 10.3 m, a floor-to-ceiling height of 9.9 m for the upper level, a floor-to-ceiling height of 2.9 m in the lower level, and a typical concrete wall thickness of 1.07 m. Personnel access to the Ring Building is provided through shielded labyrinths from Buildings 361, 364, 369, 375, 394A, and the utility tunnel system. Equipment access is provided through a tunnel from Building 363 having a rail-mounted, movable shield assembly. The lower-level service floor of Building 365 houses support equipment for the RCS. Four access stairways connect the operating floor and service floor.

Building modifications include new floor construction at the operating level, and stairway and life-safety exit relocation.
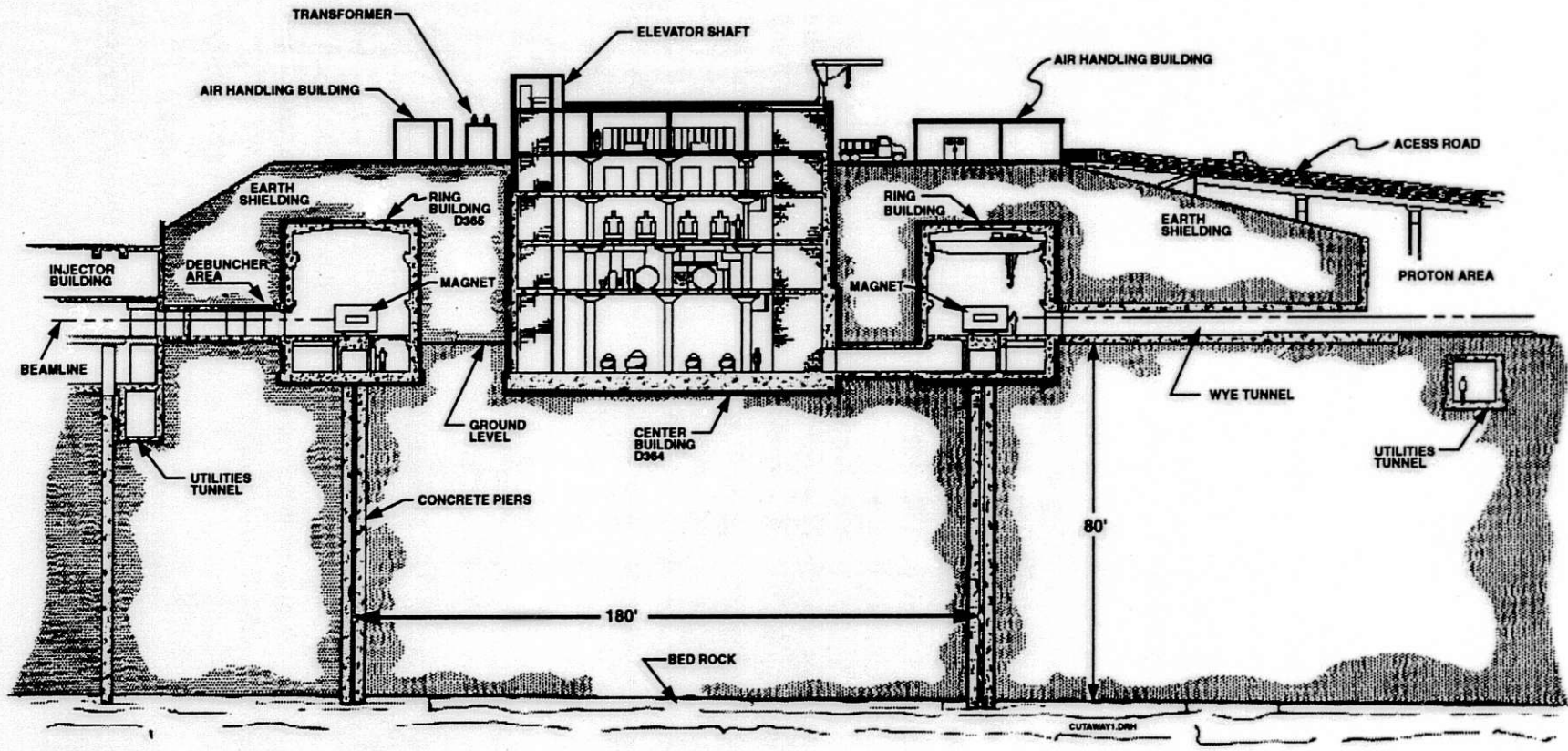
Figure VI.2.2-1 Vertical Cross Section of the Ring Building and Center Building Showing the Original ZGS.

MOVABLE SHIELDING SYSTEM
ON TRAIN RAILS

A

BLDG.
365

BLDG.
364

BLDG.
361

BLDG.
369

BLDG.
370

BLDG.
375

0   10   25   50 FEET

0   10 METERS

A

**OPERATING FLOOR
BUILDING 365**

CH000868

Figure VI.2.2-2
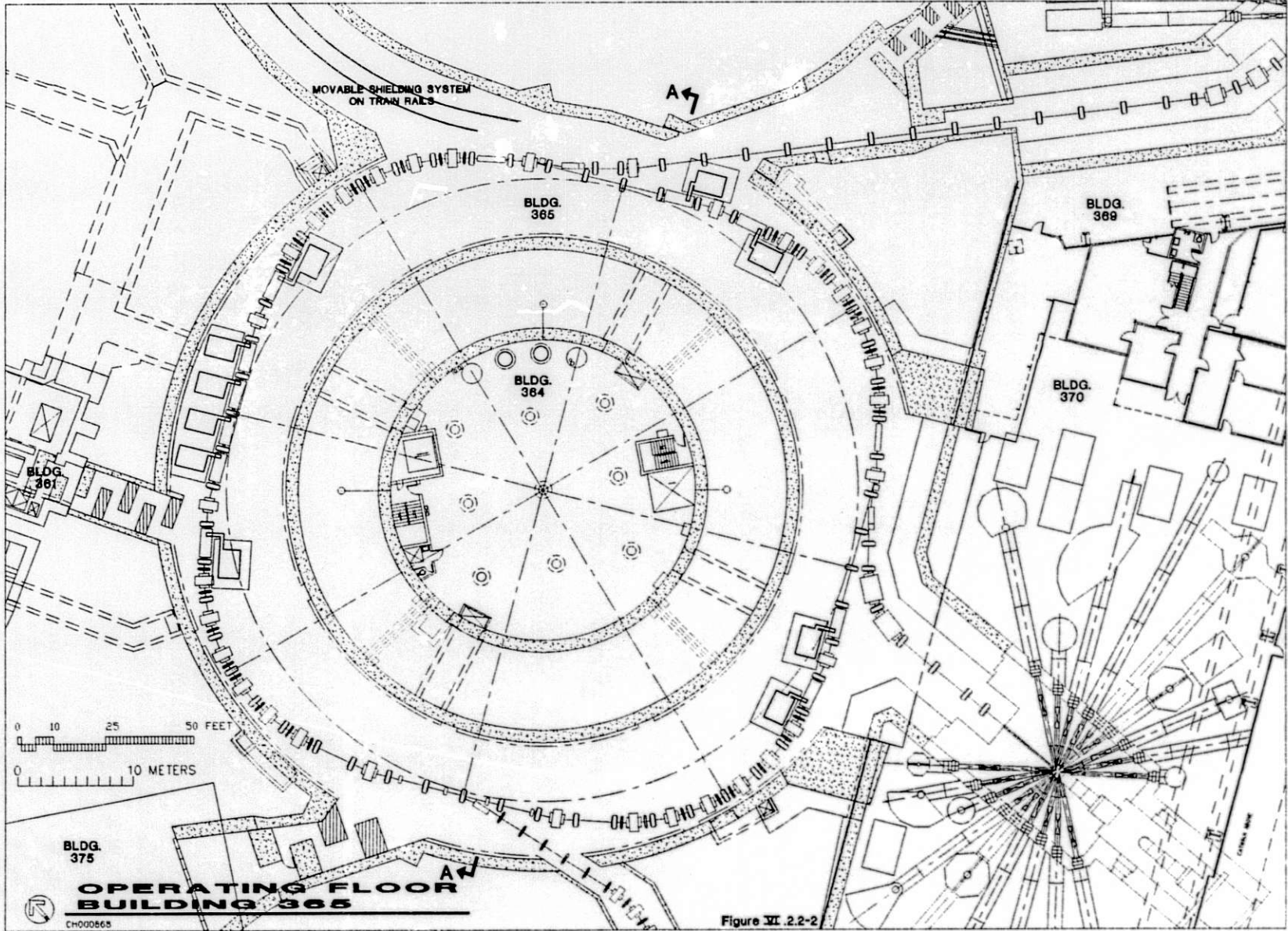
2.2.2 Structure (Building 365)

The building has eight 1-m-thick equipment piers supported on 24 concrete caissons that extend 24 m down to bedrock. The operating floor structural system ties into these pier supports, concrete columns, and outer walls. A new 0.3-m-thick concrete floor is constructed on a steel and girder subframe connected to the existing concrete substructure. The floor load capacity is 1000 lb/ft^2.

The outer and inner walls are poured-in-place reinforced concrete and are 1.07 m thick. The service level has a 1.07-m-thick reinforced concrete floor, with a floor load capacity of 2000 lb/ft^2.

Cranes and Hoists. Three overhead bridge cranes span the 10.3-m width and are capable of circling the tunnel in either direction. All three bridge cranes have a 20-ton capacity, and one crane also has a 2-ton auxiliary hoist. These cranes run on continuous circular rails that are supported by cast-in-place concrete wall brackets 7.5 m above the floor.

2.2.3 Mechanical Systems (Building 365)

Central Plant and Piping. No central cooling plant equipment, such as chillers, and no deionized water (DIW) plant equipment is located in the building. Chilled water and steam to the exterior perimeter AHUs are piped from Building 364. Deteriorated underground chilled-water and steam supply-and-return piping to exterior AHUs is replaced as required.

Air Distribution. Three existing, exterior 25,000-cfm AHUs are refurbished. Coils, motors, bearings, filters, and controls are replaced. New variable frequency drives (VFDs) are installed. Housing and fans are reused. A new fourth unit of similar capacity and configuration is installed on an available pad. The pad supports are also refurbished. The final total capacity is approximately 100,000 cfm.

Three of the AHUs serve the circular duct that runs at the underside of the ceiling slab. The fourth unit supplies air to the two HET tunnels, one of which connects Building 365 to 370 and the other of which connects Building 365 to 369. This double-wall ductwork runs outside and is insulated. The air is returned from Building 365 at the lower floor through the four existing return registers and air shafts as shown in Figure VI.2.2-3.

Existing circular ductwork is cleaned and utilized. Drainage traps are installed at points of main-duct tie-ins into the circular ductwork. Supply duct circular nozzles are modified to provide proper air distribution within the ring.

Existing unit heaters at the building entrance remain.

AIR SUPPLY SHAFT

AIR HANDLING EQUIPMENT

RETURN AIR SHAFT

OPERATING FLOOR

SERVICE FLOOR

RCS

ROADWAY

EARTH SHIELDING

TUNNEL

RF POWER SUPPLY AND ELECTRICAL SWITCHGEAR PAD

AIR HANDLING UNIT NO. 5

ROOF

FOURTH

THIRD

SECOND

FIRST

SERVICE

480 VOLT SWITCHGEAR

RF CONTROLS & EQUIPMENT RACKS

DIPOLE MAGNET POWER SUPPLIES

QUADRUPOLE MAGNET POWER SUPPLIES

MECHANICAL EQUIPMENT

AIR HANDLING UNIT NO. 1

ROADWAY

EARTH SHIELDING

EARTH SHIELDING

RCS

1.4 Meter

TUNNEL

SERVICE TUNNEL TO BUILDING 363

RING BUILDING BLDG. 365

CENTER BUILDING BLDG. 364

RING BUILDING BLDG. 365

CENTER BUILDING and RING BUILDING SECTION BUILDINGS 364/365

0 1 4 10   25   50 FEET

0 1 2 3 4 5 6 7 8 9 10
METERS

Figure VI.2.2-3

CH000871

Plumbing and Fire Protection. Existing building facilities and plumbing systems are used. Floor drains are provided at each of the concrete return-air shafts. New piping connects these floor drains to the existing building sewers.

Existing fire protection systems are upgraded as necessary to provide coverage for new equipment.

2.2.4 Electrical Systems (Building 365)

Electrical power to the RCS is supplied from Site Facility 549 by five 13.2-kV lines. Four of these lines feed 2,500-kVA, 480-V transformers and switchgear. Each of the 480-V switchgear units can be energized from either of two different 13.2-kV lines by using separate 15-kV switches. The secondary of the transformer is connected via bus duct to indoor 480-V switchgear located on the fourth floor. A one-line diagram is shown in Figure VI.2.2-4. A sixth 2,500-kVA, 480-V transformer provides backup power service. The backup power source is brought into service by disconnecting the 15-kV switchgear of the damaged transformer and toggling the 480-V switch from M to T, as shown in Figure VI.2.2-4. Power to the rf equipment is supplied by a fifth 13.2-kV line. This is done to minimize interactions between the rf amplifiers and the rest of the equipment.

The RCS components in Building 365 receive their ac power from 480-V switchgear located on the fourth floor of the Center Building 364. There are 480-V power-distribution panel boards located near the equipment.

Cleaned, repaired, and relamped existing lighting fixtures provide adequate lighting. Lighting fixture circuit wiring is new to improve reliability. New breakers are provided for existing power and lighting panel board interiors.

Telephone, paging, and fire alarm systems are used with only minor modifications.

New illuminated emergency exit signs are installed. Additional emergency lighting is provided by 1.5-h battery-powered units with built-in chargers.

EMERGENCY STANDBY
SUBSTATION FOR
TECH. EQUIPMENT

13.2KV(500 MCM) 133% EPR TYPE MV-90

FACILITY 549
SWITCHGEAR

OUTDOOR
EQUIPMENT
15KV
(TYP. ON 6
ASS'Y)

2500KVA
13.2KV/
450V

2500KVA
13.2KV/
480V

RF
D 1-2 F

RF
D 3-4 F

RF
D 5-6 F

RF
D 7-8 F

RF
D 9-10 F

RF EQUIPMENT

EXTERIOR
INTERIOR
BLDG. 364
(4TH FLR.)

INDOOR
SWGR.
480/277V

M   M   M   M   M   M

T   T   T   T   T

BACKUP
POWER SOURCE

TO RCS EQUIPMENT

BUILDING 364 AND 365 SERVICE LAYOUT

Figure VI .2.2-4
IPNS3641

2.3 CENTER BUILDING (EXISTING BUILDING 364)

The Center Building (Building 364) is a five-story cylindrical building, located inside the Ring Building. The plan view of Buildings 364 and 365 is shown in Figure VI.2.2-2, and a cross section through them is shown in Figure VI.2.2-3. This building was completed in 1962 to house equipment for the ZGS located in Building 365. Building 364 has a gross floor area of 3,196 m^2. The main mechanical distribution center for the ZGS area is located in this facility.

The function of this facility is similar to its original use. The service floor continues to provide the ZGS area mechanical systems support, with water chillers and a deionized-water plant. The first floor houses quadrupole magnet power supplies, and the second floor houses the dipole magnet power supply system for the RCS. The third floor houses controls and equipment for the rf amplifiers located in the Ring Building. The fourth floor contains electrical switchgear supplying power to all floors and also to Building 365. The dc power supplies and transformers for the rf amplifiers are located on the fourth-floor roadway level of the Center Building. The ring road around the fourth floor provides access to rf power supplies and electrical switchgear. A new air-handling unit located on the roof of the Center Building supplies conditioned air to all floors.

2.3.1 Architecture (Building 364)

The lower four floors of this five-story, concrete, cylindrical building are surrounded by earth shielding. This shield consists of 7 m of earth and a 1.07-m-thick reinforced concrete wall between the Ring Building (Building 365) and the Center Building (Building 364). There is an access/ring road at the building's fourth-floor level, as shown in Figure VI.2.2-3. There is a toilet room on each of the five floors. Vertical transportation with access to all levels is provided by a 2-ton capacity service elevator and two stairways.

Service Floor. This floor plan is circularly shaped, with an inside diameter of 26.8 m and a ceiling height of 7 m. The service floor is below the Ring Building operating floor. Mechanical equipment and piping for the 360 area are located on this floor, including three existing chillers and a new water-deionization plant. Three mechanical service tunnels and one labyrinth pedestrian tunnel connect this floor to the Ring Building (365) service floor. Figure VI.2.3-1 shows the service tunnel access and locations of chillers and deionization equipment on the service floor.

First Floor. This floor plan is circularly shaped, with an inside diameter of 26.8 m and a ceiling height of 3.96 m. There are 14 power supplies for the RCS, seven each for the focusing and defocusing quadrupole magnets located on this floor, as shown in Figure VI.2.3-2.

Second Floor. This floor plan is circularly shaped, with an inside diameter of 26.8 m and a ceiling height of 3.96 m. The 16 power supplies for the RCS dipole magnet power supply system are located on this floor, as shown in Figure VI.2.3-3.
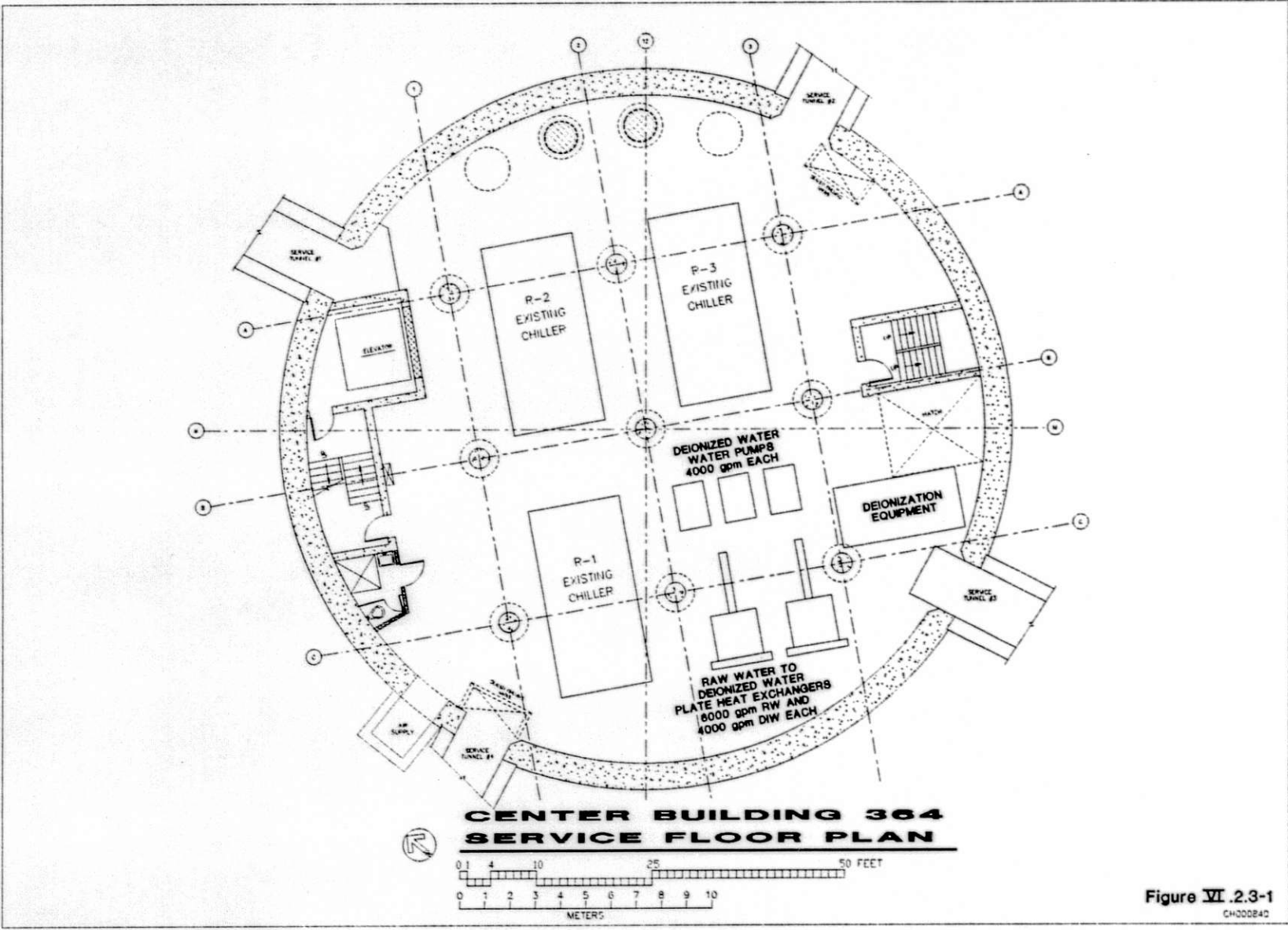
CENTER BUILDING 364
SERVICE FLOOR PLAN

Figure VI.2.3-1

CH000840

CENTER BUILDING 364
FIRST FLOOR PLAN

Figure VI.2.3-2

CH000839

**CENTER BUILDING 364
SECOND FLOOR PLAN**
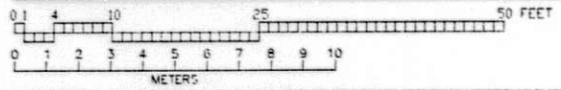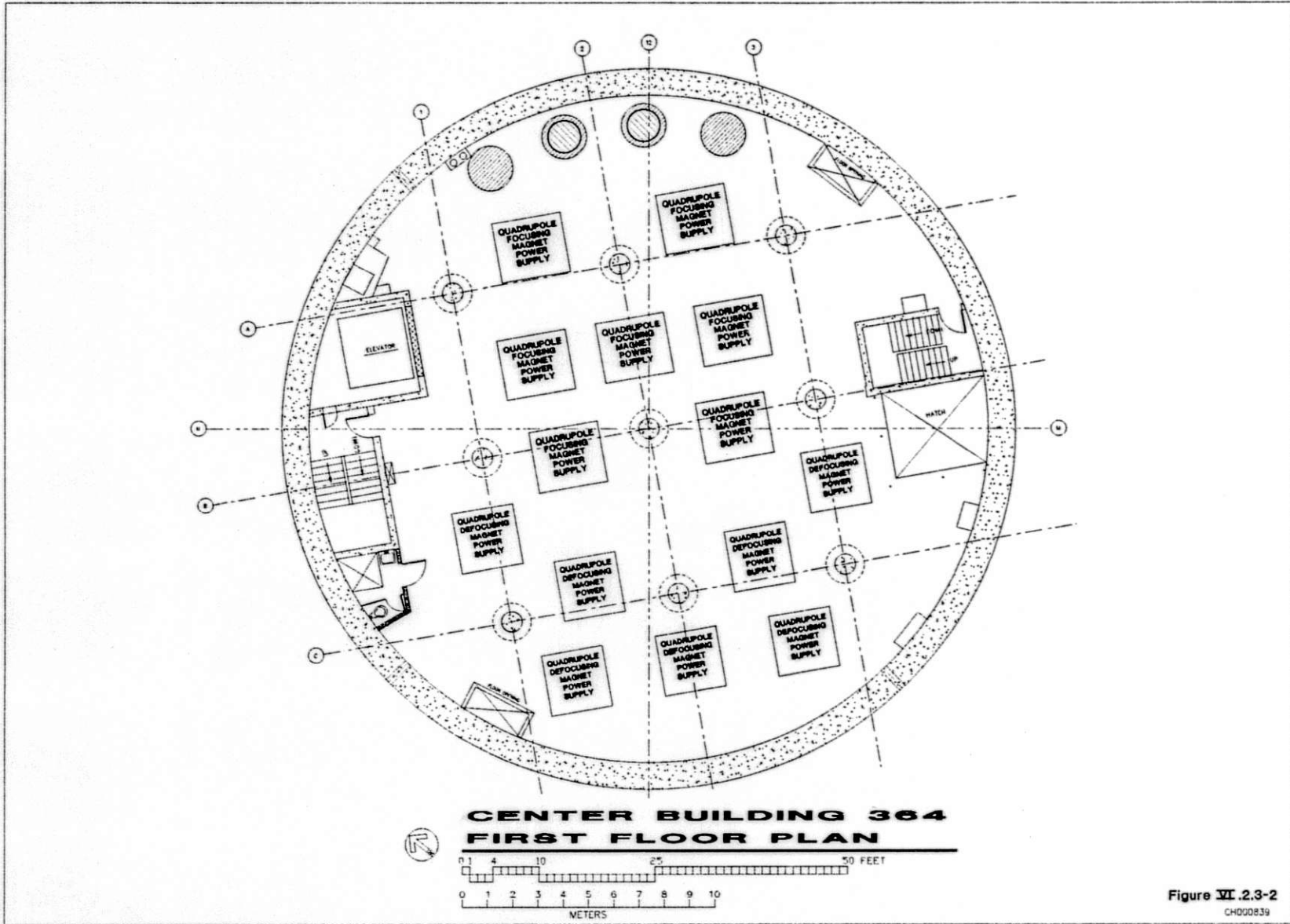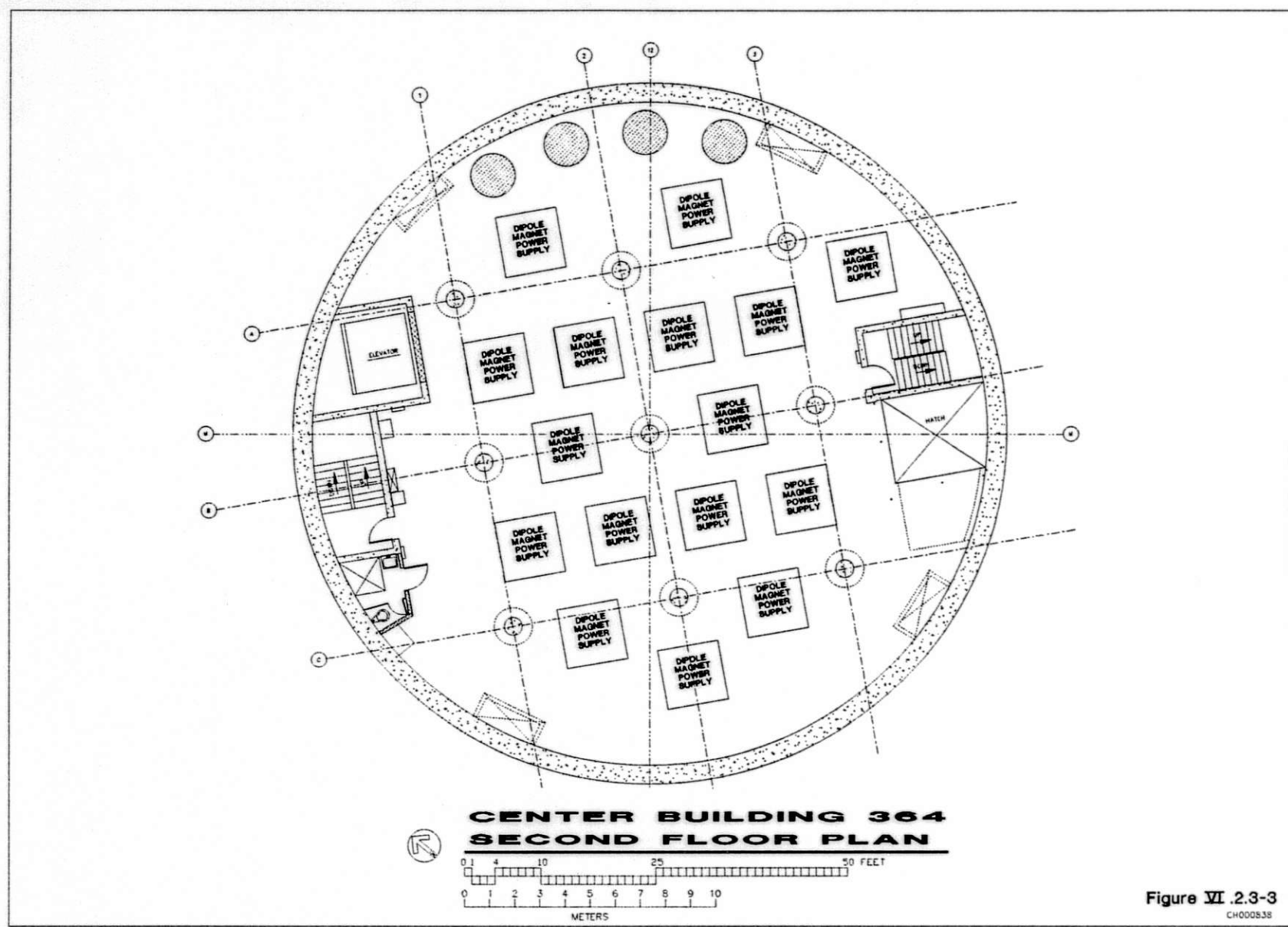
Figure VI .2.3-3

CH000838

Third Floor. This floor plan is circularly shaped, with an inside diameter of 26.8 m and a ceiling height of 3.65 m. The rf amplifier controls and equipment are located on this floor, as shown in Figure VI.2.3-4.

Fourth Floor. This floor plan is circularly shaped, with an inside diameter of 27.7 m and a ceiling height of 3.12 meters. On this floor there is a loading dock with direct access to the freight elevator. There is also a dock with a jib-crane to lower equipment to each floor through a hatch system. The fourth floor is 16.6 m above the Ring Building operating floor. This is the only floor without earth shielding surrounding it. The 480-V switchgear that provides power for the entire building is located on this floor, as shown in Figure VI.2.3-5.

Road Surrounding Fourth-Floor Level. A new road and new concrete transformer pads are located outside on the fourth-floor level, as shown in Figure VI.2.3-6. This road is accessed from a ramped roadway and bridge at the northwest side.

Roofing. In 1990, an IRMA roofing system with 5-cm insulation board and 1-cm cement topping was installed over the existing roof structure.

Building Modifications/Refurbishments. Minor modifications are made as necessary to bring the buildings into compliance with current life safety codes. Outdated areas, typically stairways and toilet rooms, are refurbished.

2.3.2 Structure (Building 364)

The cylinder-shaped Center Building is constructed of poured-in-place concrete with five floors and a roof. The floors below the fourth floor are all surrounded by the earth berm shield; their outer wall thicknesses vary from floor to floor. The outer concrete-wall thickness of the service and first floors is 1.07 m, that of the second and third floors is 0.8 m, and that of the fourth floor is 0.3 m.

The service floor is a 0.3-m-thick slab-on-grade, poured on a 1-m-thick concrete sub-base, and has a 1,000-lb/ft^2 floor load capacity.

The four floors above the service floor are all 0.3-m thick and are supported on nine round concrete columns with bell-shaped tops. The diameter of the columns varies from floor to floor. The first floor load capacity is 250 lb/ft^2; second floor, 200 lb/ft^2; third floor, 150 lb/ft^2; and fourth floor, 100 lb/ft^2.

The roof structure is a steel-beam and girder frame with metal deck and concrete topping, supported on nine steel columns. The roof deck slab is 0.15-m thick, and the roof load capacity is 50 lb/ft^2. There is a five-ton jib-crane at roof level with access to each floor through a roof hatch.
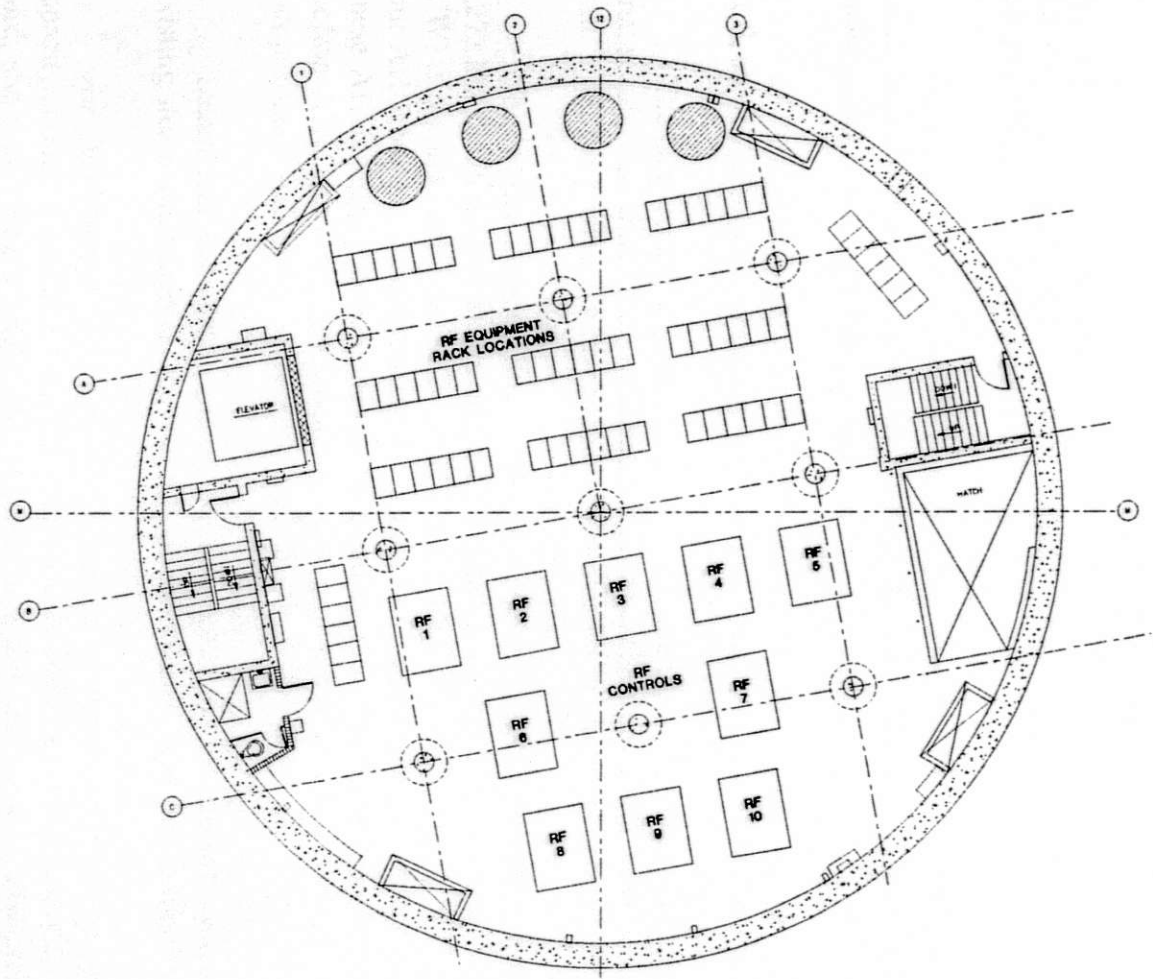
CENTER BUILDING 364
THIRD FLOOR PLAN

Figure VI .2.3-4

CH000951

RF POWER SUPPLIES

RF POWER SUPPLIES

RADIO TOWER EQUIPMENT AREA

ELEVATOR

DOWN

DOWN

HATCH

JIB CRANE

480 VOLT SWITCHGEAR

13.2 kV PRIMARY ELECTRICAL SWITCHGEAR

RF POWER SUPPLIES

CENTER BUILDING 364 FOURTH FLOOR PLAN

0 1 4   10   25   50 FEET

0 1 2 3 4 5 6 7 8 9 10
METERS

Figure VI.2.3-5

CH000641
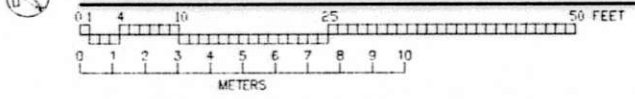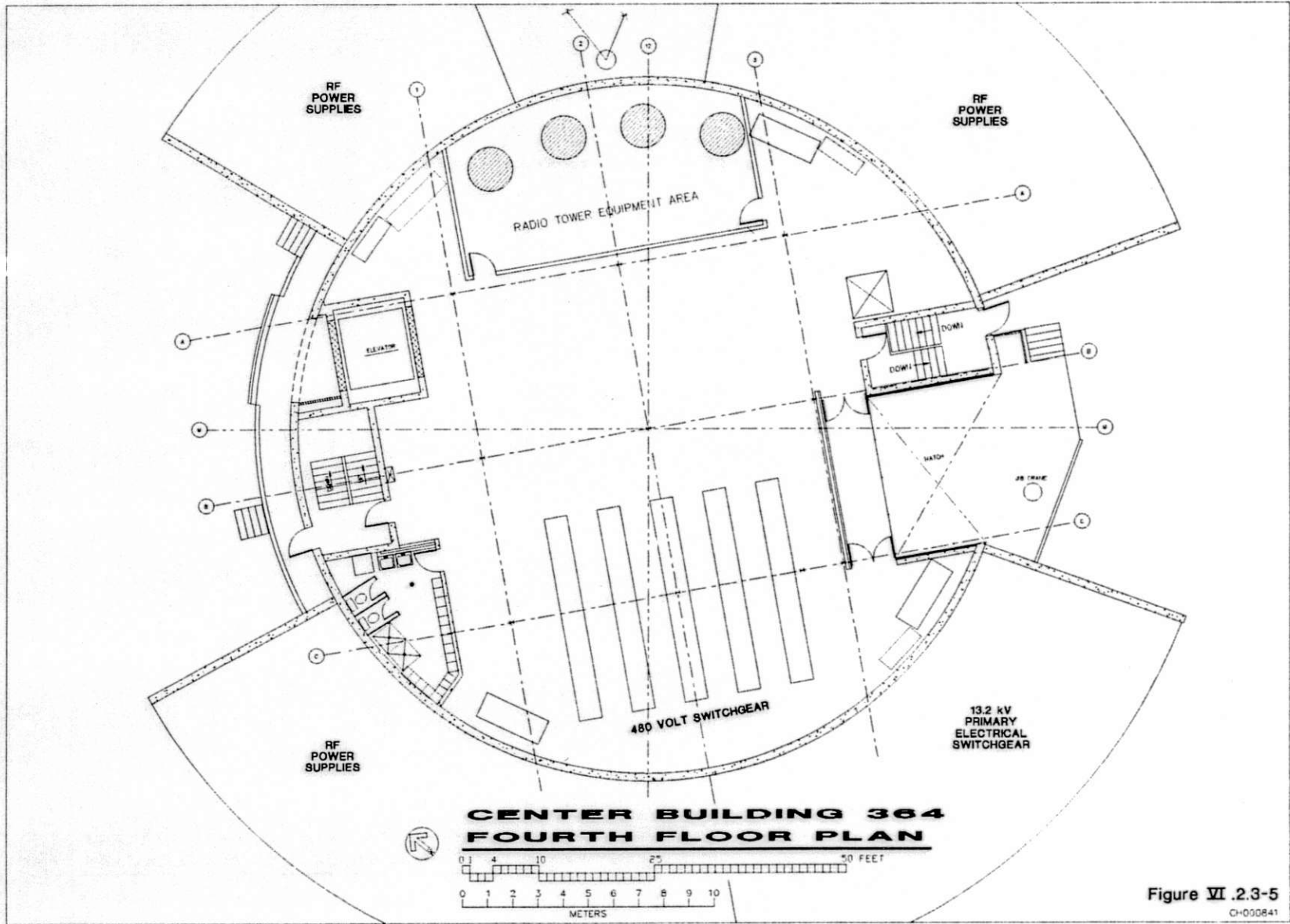
BUILDING 364 & 365
ROOF/ROADWAY PLAN
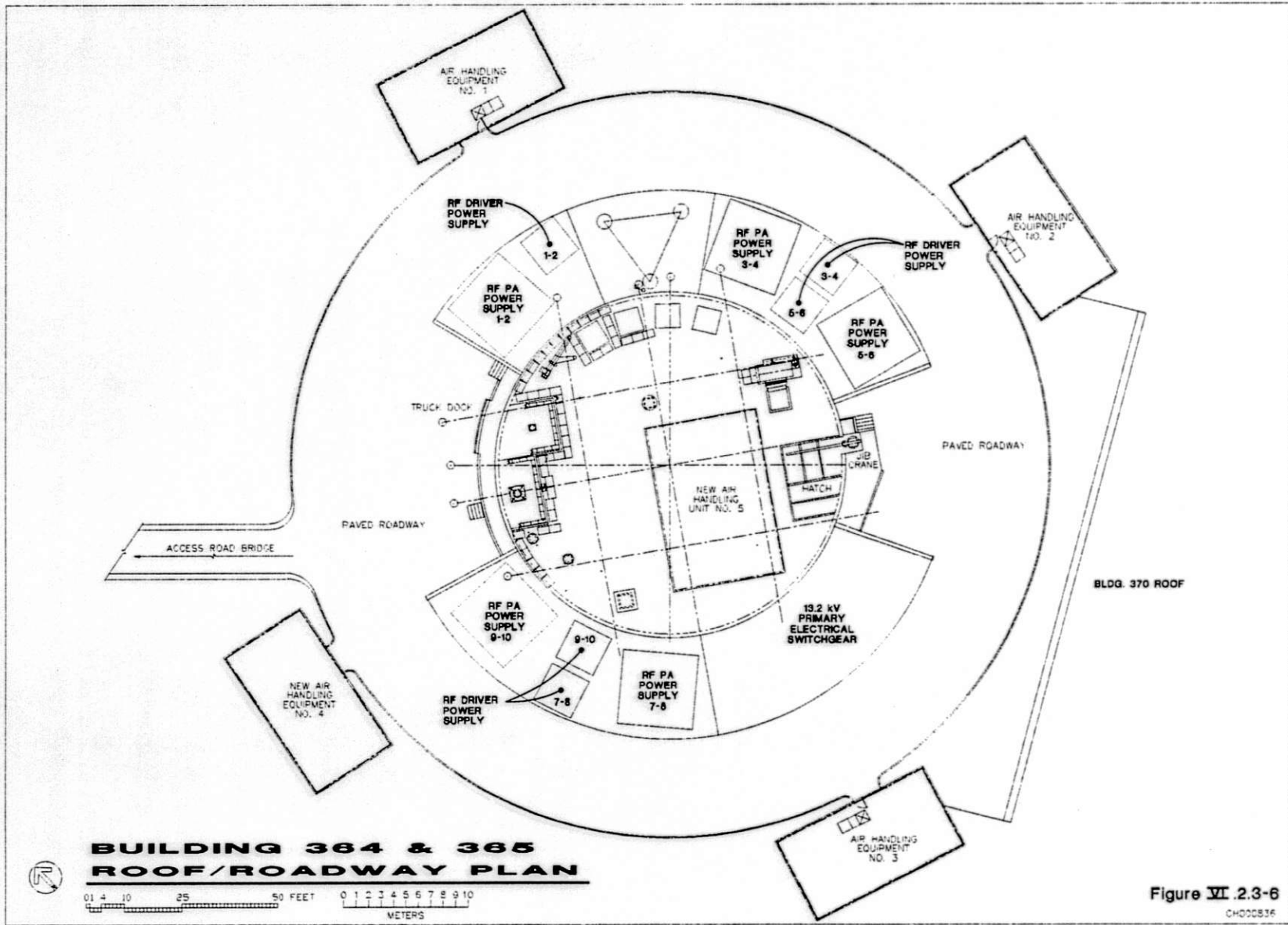
Figure VI.2.3-6

CH000836

2.3.3 Mechanical Systems (Building 364)

Demolition. The majority of existing mechanical systems and equipment in the service floor mechanical room remain, with minor demolition. Suspended fan-coil AHUs presently utilized for cooling of the first, second, and third floors are removed, along with the fourth floor AHU and associated piping. Miscellaneous piping at the service floor is relocated to permit installation and connection of new equipment.

Central Plant Equipment and Piping. A new deionized-water (DIW) plant for the IPNS Upgrade is located at the service floor of Building 364. The DIW plant incorporates two new, plate-type raw-water (RW) to DIW heat exchangers, each with an RW capacity of 6,000 gal/min and a DIW capacity of 4,000 gal/min.

Raw water to the new DIW plant is fed from the existing 750-mm-diameter RW main, which runs from the utility tunnel, through the LET tunnel, and across the service floor of Building 365 to this building.

DIW from the plant ties into the existing 350-mm-diameter piping in Building 365 for the RCS, as well as into a new piping loop that provides DIW to the linac facility.

The DIW supply (S) and return (R) risers are installed to serve equipment located on the first, second, and third floors of the building. At each of the floors, DIW S/R loops run along the wall. Piping is provided with capped valve-stubs for equipment connection.

The service floor of Building 364 houses three existing chillers, two with capacities of 5,275 kW (cooling output) and one with a capacity of 3,500 kW (cooling output). Chilled water (CW) is supplied to a new AHU located on the roof of this building (see Figure VI.2.2-3) and to four AHU buildings located along the access road, as shown in Figures VI.2.2-3 and VI.2.3-6. These AHUs supply conditioned air to Building 365. Piping and ductwork risers to the new rooftop AHU run through the building. CW piping branches out from the piping risers to the four perimeter AHUs that serve Building 365.

Steam and condensate piping are connected to the existing systems in the building. Existing steam unit heaters at the fourth floor are retained, with piping modifications.

Air Distribution. The new AHU located on the roof of Building 364 has 70,000-cfm capacity and has a return/exhaust fan with variable-speed drives to supply air to the first, second, third, and fourth floors. This unit consists of a CW cooling coil, low-pressure-steam heating coils, and two supply blowers.

Each of the equipment floors is served by cooling-only variable-air volume (VAV) boxes, ductwork, and diffusers. Air is returned to the return air duct risers through registers.

Plumbing and Fire Protection. Existing building toilet facilities and plumbing systems are used. Existing fire protection systems are modified to provide coverage for new equipment.

2.3.4 Electrical Systems (Building 364)

Electrical power to the RCS is supplied from Site Facility 549 by five 13.2-kV lines. Four of these lines feed 2,500-kVA, 480-V transformers and switchgear. Each of the 480-V switchgear units can be energized from either of two different 13.2-kV lines by using separate 15-kV switches. The secondary of the transformer is connected via bus duct to indoor 480-V switchgear located on the fourth floor. A one-line diagram is shown in Figure VI.2.2-4. A sixth 2,500-kVA, 480-V transformer provides backup power service.

Lighting fixture circuit wiring is new to improve reliability. Cleaned, repaired, and relamped existing fixtures provide adequate illumination. New breakers are provided for existing power and lighting panel board interiors.

New outdoor, high-pressure sodium fixtures are installed to provide perimeter lighting. New illuminated emergency exit signs are installed. Additional emergency lighting is provided by 1.5-h battery-powered units with built-in chargers.

The fire alarm system is upgraded as necessary to provide coverage for new equipment.

Additional telephone outlets are provided where required. A new amplifier is installed for the paging system, but existing speakers and wiring are retained.

2.4 POWER SUPPLY BUILDING (EXISTING BUILDING 376)

Building 376 is a one-story, high-bay building that was completed in 1961 and has a gross floor area of 1,978 m^2. The eight RCS sextupole supplies, 40 magnet power supplies for the transport lines, and a CW plant are located in this building. This building has access to the lower-level service floor and utility tunnel. Figure VI.2.4-1 shows the service floor with the CW processing plant, and Figure VI.2.4-2 shows the first floor with magnet power supplies.

2.4.1 Architecture (Building 376)

The existing building is approximately 18.9 m wide and 50.1 m long. The service level has utility tunnel connections to Building 370. The building exterior is constructed of insulated, corrugated-aluminum panels supported on a steel frame structure. The building facade has 2-m-high window bands on the long sides. The first floor has a 7.9-m high bay equipped with a 10-ton crane.

The existing building is in an ideal location to accept power from Site Electrical Facility 549 and water from Site Cooling Tower Facility 377. Utilities and magnet power supply cables from Building 376 are directly routed to the existing utility tunnels and LET tunnel.
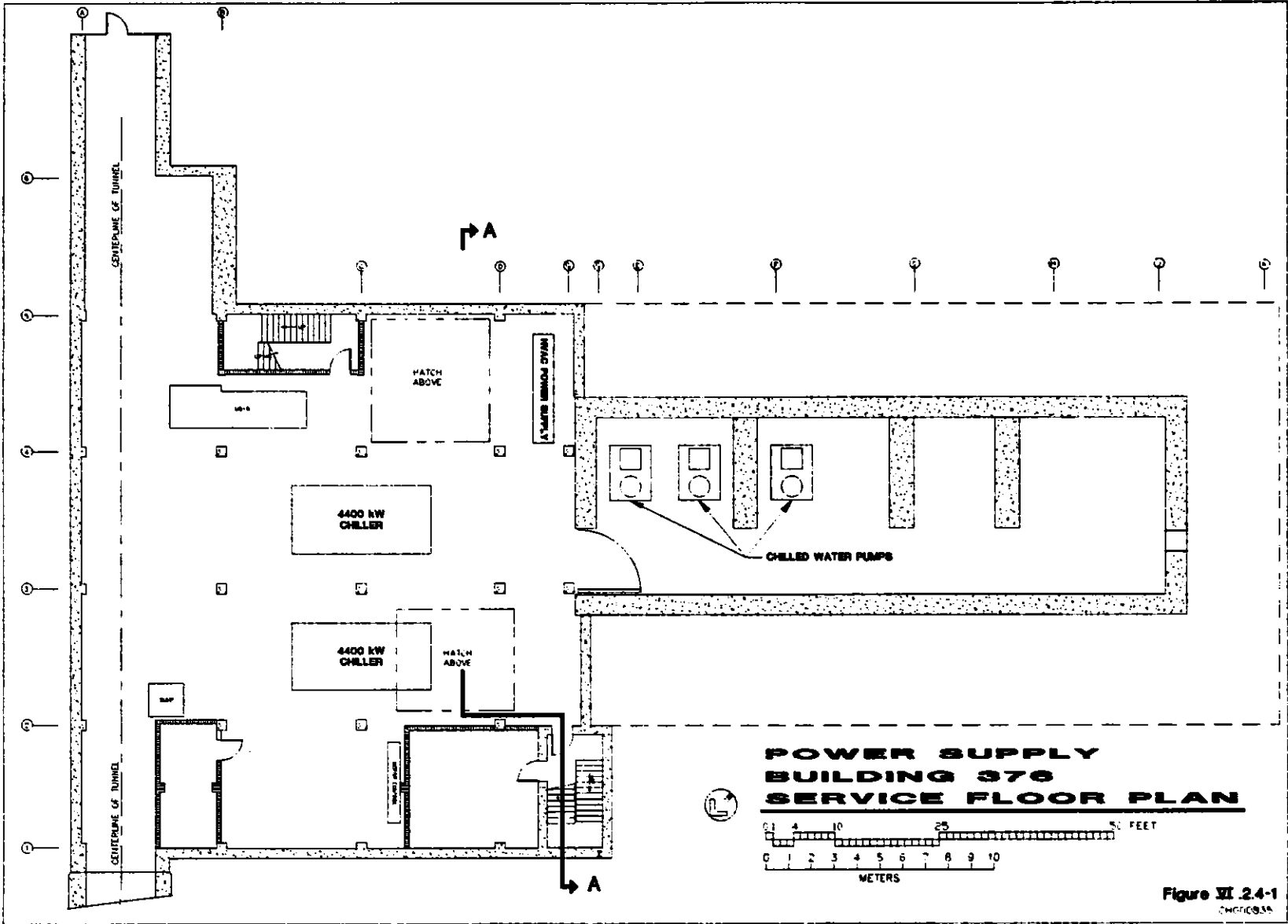
POWER SUPPLY
BUILDING 376
SERVICE FLOOR PLAN

Figure VI.2.4-1

A

ELECTRICAL
SWITCHGEAR

HVAC   HVAC   HVAC

8 RCS SEXTUPOLE MAGNET
POWER SUPPLIES
48"x48"

TRANSPORT LINES
20 DIPOLE MAGNET
POWER SUPPLIES
48"x70"

TRANSPORT LINES
20 QUADRUPOLE
MAGNET
POWER SUPPLIES
48"x51"

HATCH COVER

HATCH COVER

HVAC   HVAC   HVAC

A

**POWER SUPPLY
BUILDING 376
FIRST FLOOR PLAN**

0 1   4   10   25   50 FEET

0 1 2 3 4 5 6 7 8 9 10
METERS
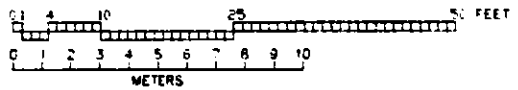
Figure VI.2.4-2
CH000834
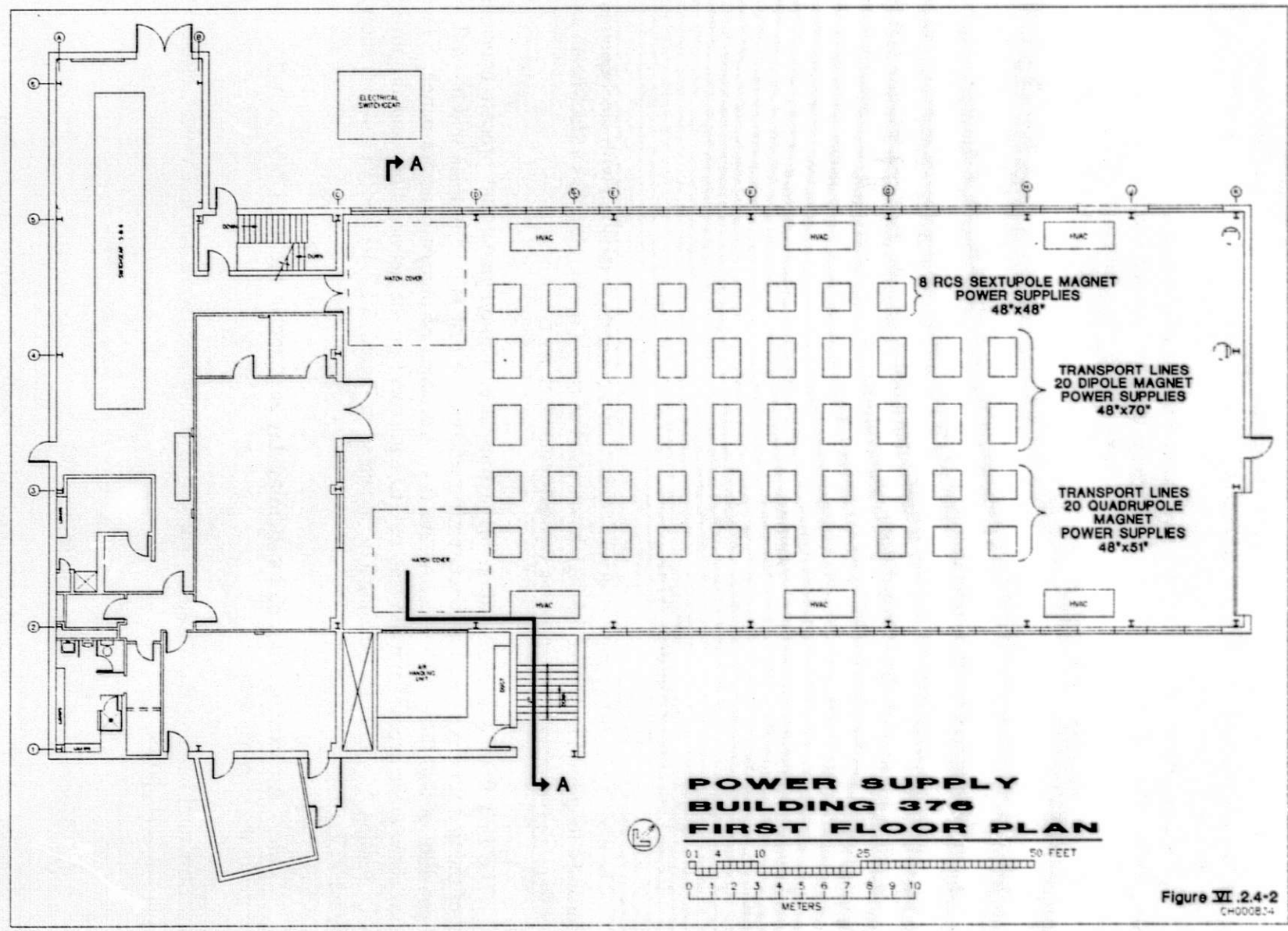
There are facility and support offices, toilet and locker facilities, and electrical rooms on the first floor. Existing walls and partitions are painted concrete-masonry units. Suspended acoustical tile ceilings with lay-in-type fluorescent lighting fixtures are used in office areas.

Access into the building is through five exterior personnel doors at the grade level. Access to the first floor is also possible by two stairwells from the service level, as well as through Building 375. A vehicle access door permits trucks to enter the building high bay. Vehicle unloading is accomplished with the 10-ton overhead crane. Vehicle parking areas are located adjacent to the building.

Roofing. In 1990, an IRMA roofing system with 5-cm-thick insulation board and 1-cm-thick cement topping was installed over the existing roof structure.

Utility Tunnel. The northeast section of the basement is part of the utility tunnel system. These tunnels are used for routing of utilities and controls. The average tunnel is 3.04 m wide and 4.26 m high.

Building refurbishing includes painting, minor exterior siding, and window, door, and partition repair work.

2.4.2 Structure (Building 376)

The existing high-bay superstructure consists of a concrete foundation with steel columns supporting a long-span truss over the high bay area. The rest of the building has a steel-beam and girder framing system, which supports a welded-metal deck roof.

The first floor is a combination of cast-in-place, slab-on-grade, and precast concrete. Most of the first floor is poured-in-place reinforced concrete that is 0.15 m thick and has a floor load capacity of 800 lb/ft^2. The rest of the floor has areas of precast-concrete panels. Two hatches allow crane access from the high bay to equipment on the service floor and the utility tunnel. Section A-A through Building 376, indicated in Figures VI.2.4-1 and VI.2.4-2, is shown in Figure VI.2.4-3.

Crane. An existing 10-ton, top-running bridge crane in the high bay provides full coverage for the high-bay area.

Structural building modifications consist of minor steel work for mechanical, electrical, and plumbing supports.

2.4.3 Mechanical Systems (Building 376)

Demolition. The existing, deteriorated AHU located in the mezzanine above the office area is removed, along with other unused mechanical equipment.

10-TON CRANE

MAGNET POWER SUPPLIES

AIR HANDLING UNIT

AIR HANDLING UNIT

FLOOR HATCH

FLOOR HATCH

HVAC POWER SUPPLY

SECTION A-A THROUGH BLDG. 376

0 1   4   10   25   50 FEET

0   1   2   3   4   5   6   7   8   9   10

METERS

Figure XI.2.4-3
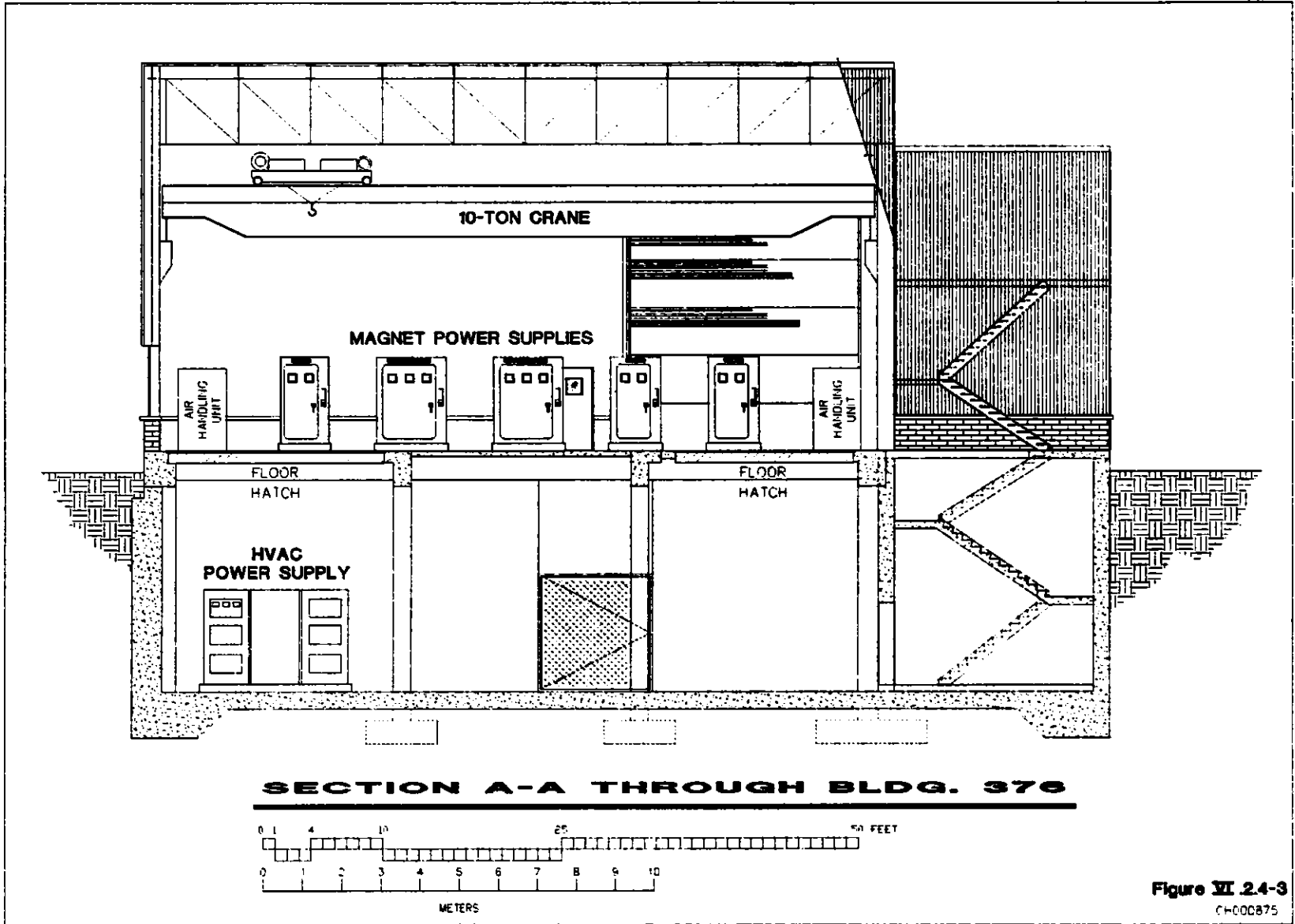
CH000875

Central Plant Equipment and Piping. A new chiller plant comprising two 4,400-kW chillers and three chilled-water pumps is housed on the service floor.

Chiller condensers are connected to existing RW piping in the tunnel. CWS and CWR piping from the chillers is routed through the utility tunnels to Buildings 364, 365, 369, and 370.

DIW for this building is supplied via the utility tunnel system. DIW S/R mains run along one wall of the high bay. The piping is equipped with capped valve-stubs to facilitate connection to user equipment. The following are routed through, and accessible in, the tunnels: Fire protection water, raw water, chilled water, domestic cold water, eight wall-mounted electric and communications cable trays, electric power, compressed air, and a mechanical service water piping system.

Existing unit heaters are retained and are relocated as required.

Air Distribution. Cooling for the high bay is provided by six new, self-contained packaged units, with a cooling capacity of 34 kW each. These units provide local air cooling of component equipment, distributed by integral overhead ductwork. Chilled water is piped to the six HVAC units in the high bay from the service floor, and coil condensate drains back down to the service floor. The location of the six HVAC units is indicated in Figure VI.2.4-2. Existing exhaust fans, unit heaters, and the switchgear room ventilation unit are refurbished.

A new AHU with ducts and diffusers serves offices on the first floor. The unit has CW cooling coil and steam preheat coils.

The service floor is furnished with a new ventilation system.

Plumbing and Fire Protection. Existing building toilet facilities and plumbing systems are used. Existing fire protection systems are used, with upgrades to provide coverage for new equipment. New sprinkler piping is provided on the service floor.

2.4.4 Electrical Systems (Building 376)

Electrical power to technical equipment is provided by two 13.2-kV to 480-V switchable feeds, as shown in Figure VI.2.4-4. The substation consists of two 13.2-kV incoming-line switches, two 2,000-kVA transformers, and a 480-V switchgear line-up. The 13.2-kV incoming switches and transformers are located outside the building and are supplied from switchgear located at Site Electrical Facility 549. Six 480-V power distribution panels are located inside the building on the service floor. These panel boards feed individual pieces of technical equipment.

A 250-kW diesel generator located near Building 376 provides part of the emergency backup power to the 360 area.

BUILDING 376 UTILITY SUBSTATION

Figure VI.2.4-4
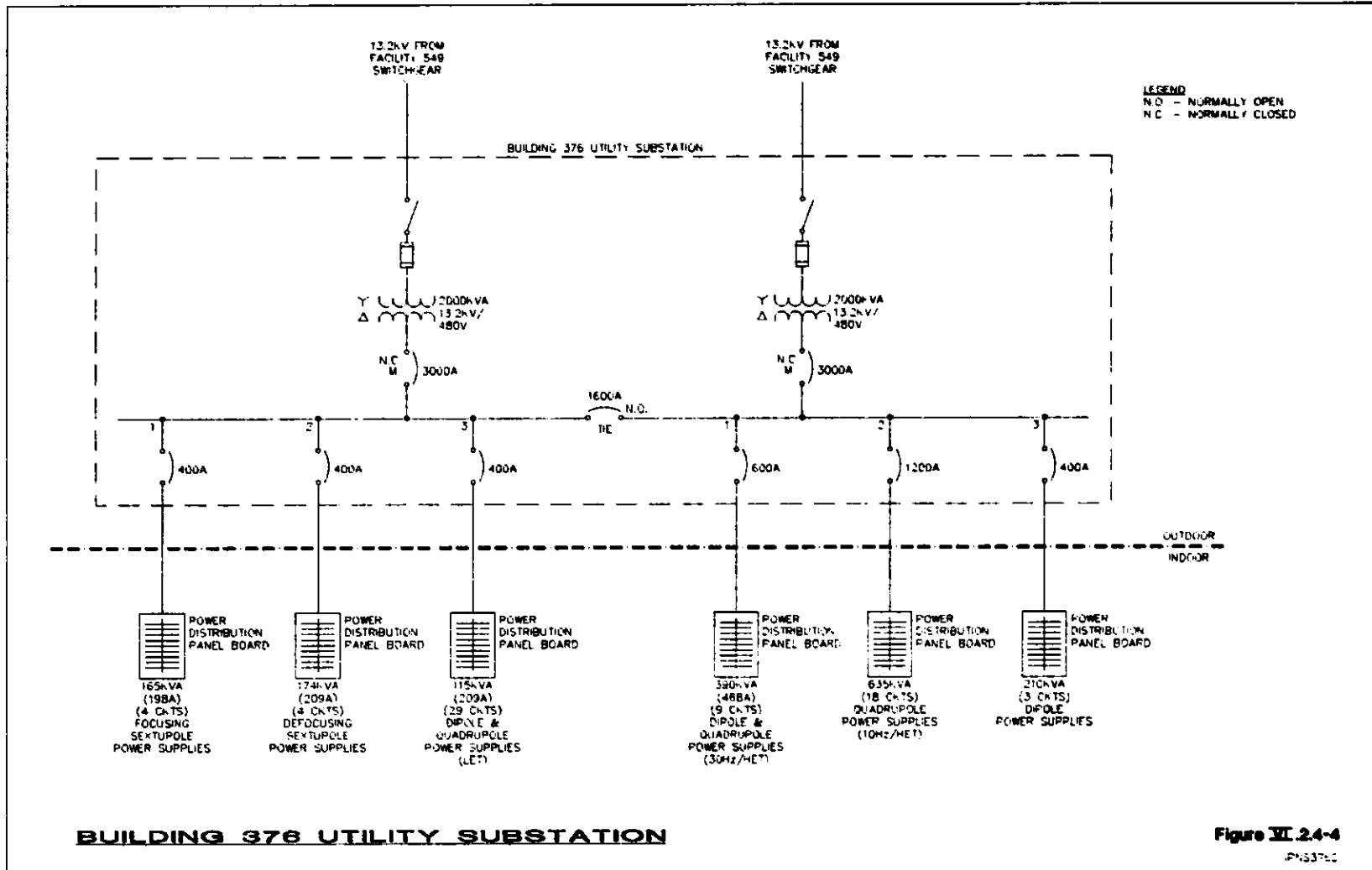
Cleaned, refurbished, and relamped lighting fixtures provide adequate lighting levels. Lighting fixture circuit wiring is new for improved reliability. New breakers are provided for existing power and lighting panel board interiors.

Special electrical systems, such as telephone, paging, and fire alarm, are satisfactory to meet requirements.

2.5 10-Hz TARGET BUILDING (EXISTING BUILDING 369)

Building 369, a one-story high-bay building, 32.4 m wide × 73.1 m long, houses the 10-Hz target and 18 instrument lines. An adjacent annex is 24.2 m long × 9.2 m wide. Completed in 1963, this high-bay building has a gross floor area of 2,471 m^2 and a clear height of 10.9 m to the bottom of the roof trusses. Building 369 adjoins Buildings 365, 368, and 370. Figure VI.2.5-1 shows the first-floor plan and 10-Hz target, and Figure VI.2.5-2 shows a section through the building.

2.5.1 Architecture (Building 369)

The exterior walls are insulated metal panels, supported on a steel-framed structure. The north wall is a cast-in-place concrete wall that is designed to hold in place the earth shielding separating the Target Building from the Ring Building. The earth shielding thickness varies from 6 m to 18 m.

2.5.2 Structure (Building 369)

The structural system, supported by a concrete foundation, is composed of steel columns and steel roof trusses with a welded-metal roof deck. The exterior walls, bridge crane, and roof are supported by steel structural system. The concrete floor is 0.15-m-thick slab-on-grade with 800-lb/ft^2 capacity. The welded-metal roof deck is protected by a PVC-IRMA roof system installed in 1990.

The targets, shields, and foundations are described in Chapter IV.

Existing first-floor trenches in Building 369 are eliminated.

Tunnel. The existing utility tunnel system covers the 360 area and carries utilities, power, and controls. Personnel access to these buildings is possible via the tunnels. An existing 60.95-m-long tunnel under Building 369 is 3.04-m wide × 2.62-m high and is used as a tornado shelter.

Cranes and Hoists. The high bay has a 35-ton, top-running bridge-crane with an auxiliary 10-ton hoist, which provides full high-bay coverage.
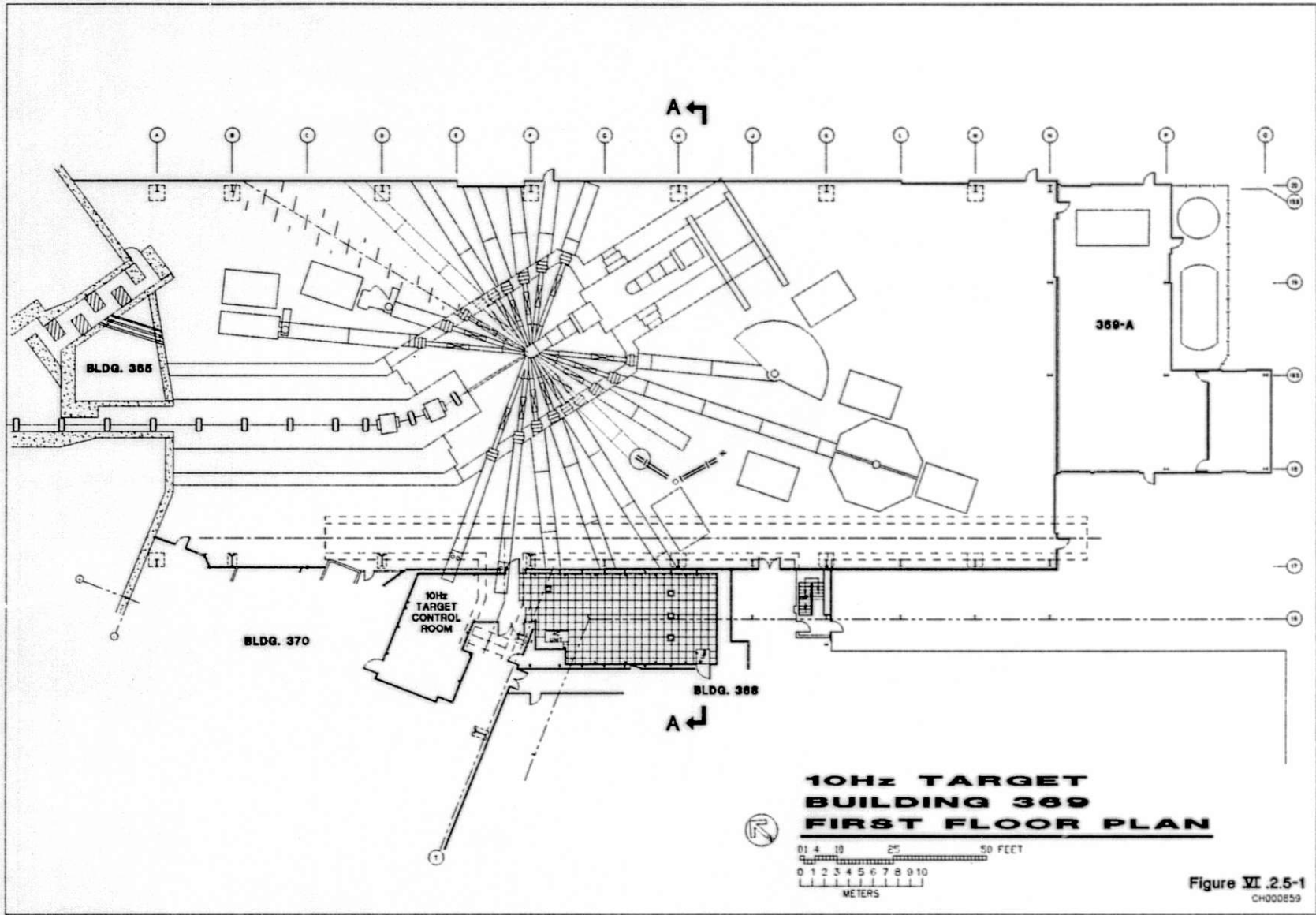
**10Hz TARGET
BUILDING 369
FIRST FLOOR PLAN**

Figure VI .2.5-1

CH000859

35-TON CRANE

BIOLOGICAL SHIELD

HOT CELL

INSTRUMENT LINES

UTILITY TUNNEL

SECTION A-A THROUGH BUILDING 369

0 1   4   10   25   50 FEET

0   1   2   3   4   5   6   7   8   9   10

METERS

Figure VI.2.5-2

CH000876
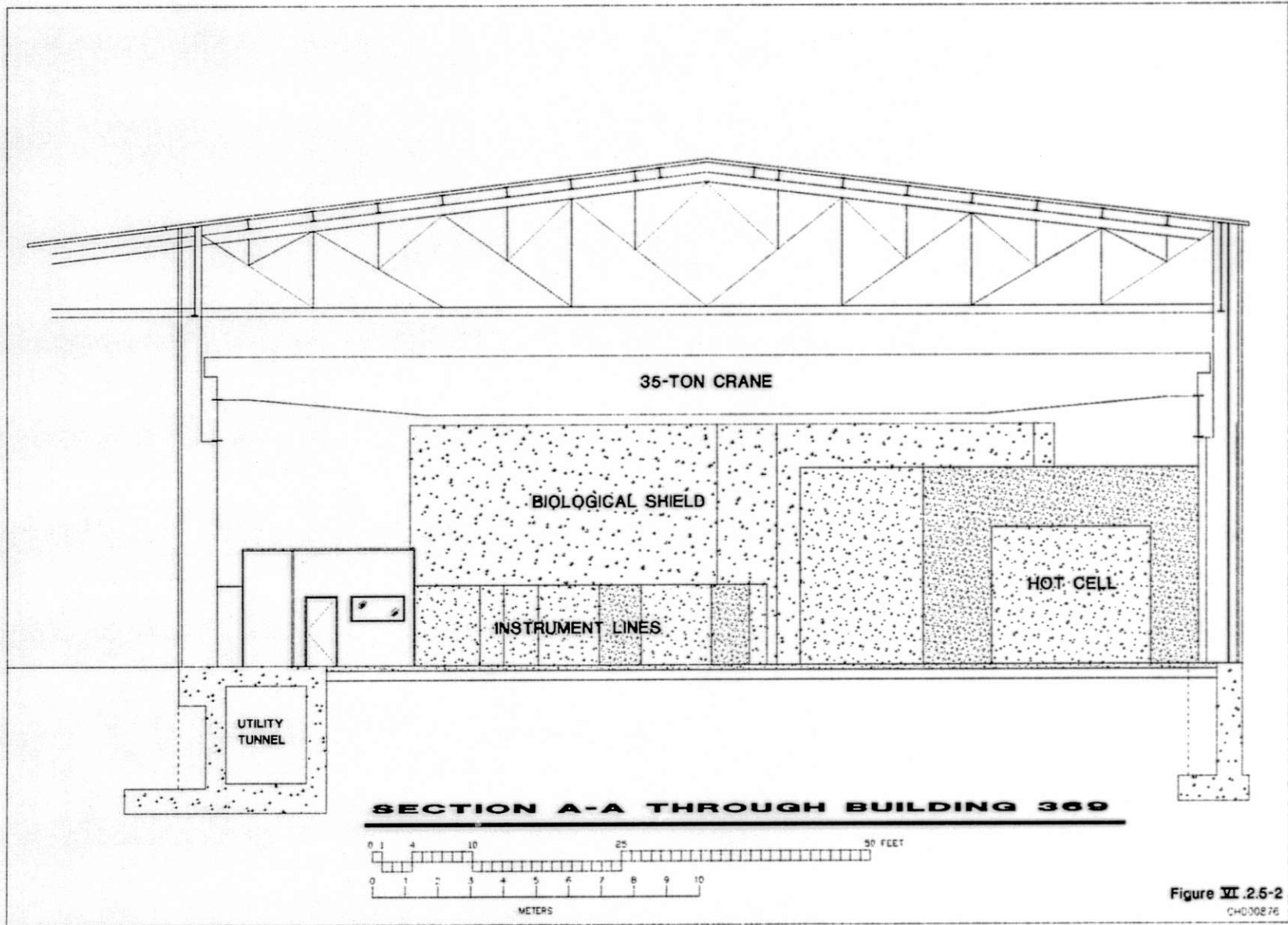
2.5.3 Mechanical Systems (Building 369)

Demolition. Miscellaneous mechanical systems and piping are relocated to facilitate construction of target biological shielding.

The existing tunnel under the southwest part of the building provides the following services: Fire protection water piping, high-pressure steam supply and condensate return piping, RW, CW, sanitary drain, wall-mounted electric cable trays, and electric power. This utility tunnel has an automatic sprinkler system, fire detection system, floor drains, and access panels to the building above; it also is used as a tornado shelter.

Central Plant Equipment and Piping. No DIW is required for the equipment in this building. Equipment utilizing DIW is located in Building 367. DIW piping runs from the utility tunnel through the building and feeds Building 367.

Existing CW piping presently utilized at the three existing AHU cooling coils is retained. New CW plant piping required for local cooling at the instrument lines is tied into the existing CW piping in the tunnel.

Existing unit heaters are retained. Heaters and piping are modified and moved as required to accommodate new equipment.

Air Distribution. The building is presently air-conditioned by three truss-mounted air handling units of 40,000-cfm capacity each. These units are refurbished and used, and new controls are provided. Existing diffusers and ductwork are retained.

The five existing 89,000-cfm hydrogen-evacuation exhaust fans on the roof are refurbished and used.

Plumbing and Fire Protection. Existing building plumbing systems are used. Existing fire protection systems are used, with upgrades to provide coverage for new equipment.

2.5.4 Electrical Systems (Building 369)

The existing 1,000-kVA transformer and 480-V switchboard are used to provide power for conventional facilities. The switchboard is modified to accommodate new equipment. A new motor control center provides power to building mechanical equipment and other installed motors that are rated at more than 0.5 hp.

The 10-Hz target equipment is fed from a 480-V double-ended substation, as shown in Figure VI.2.5-3. This substation has two 13.2-kV incoming line switches, two 2,000-kVA transformers, and associated 480-V switchgear. The 13.2-kV switchgear is located outdoors near Building 369, and power is supplied to it at 13.2 kV from switchgear located at Site Electrical

13.2KV FROM
FACILITY 549
SWITCHGEAR

13.2KV FROM
FACILITY 549
SWITCHGEAR

UTILITY
SUBSTATION

LEGEND
N.O. – NORMALLY OPEN
N.C. – NORMALLY CLOSED

2000kVA
13.2kV/480V

2000kVA
13.2kV/480V

N.C.
M   3000A

N.C.
M   3000A

1600A
N.O.
TIE

1   2   3   1   2   3

250A   400A   400A   400A   400A   250A

OUTDOOR
INDOOR

ISOLATION
XFMR
150kVA

400A
POWER
DISTRIBUTION
PANELBOARD

400A
POWER
DISTRIBUTION
PANELBOARD

400A
POWER
DISTRIBUTION
PANELBOARD

400A
POWER
DISTRIBUTION
PANELBOARD

ISOLATION
XFMR
150kVA

CLEAN
POWER
PANEL

CLEAN
POWER
PANEL

BUILDING 367 AND 369 UTILITY SUBSTATION

Figure VI.2.5-3
IPNS3691

Facility 549. The 480-V switchgear is located inside Building 369 and feeds power to distribution panel boards located near the technical equipment. Individual equipment is powered from these panels.

Clean power requirements are met by using 480-V to 480-V isolation transformers, as shown in Figure VI.2.5-3.

Cleaned, repaired, and relamped existing lighting fixtures provide adequate illumination. Lighting fixture circuit wiring is new to improve reliability. New breakers are provided for existing power and lighting panel board interiors.

Special systems, such as telephone, paging, and fire alarms, are satisfactory to meet requirements.

2.6 10-Hz TARGET SUPPORT BUILDING (EXISTING BUILDING 367)

Building 367 is a single-story high-bay building with three low-story areas connected by a common corridor, as shown in Figure VI.2.6-1. The high bay is 15.2 m long, 24.4 m wide, and 10.0 m high, with a 7-m-wide × 12-m-long annex to the south. This facility, completed in 1968, has a gross floor area of 677 m². The high-bay area is equipped with a 35-ton crane. A new shielded cooling system for the 10-Hz target in Building 369 is located in the high bay, as shown in Figure VI.2.6-2. Building 369 is approximately 27.4 m to the west of Building 367. The target cooling system is self-contained and the cooling system area is shielded, because the coolant is potentially radioactive. The building has monitored limited access. Target cooling water pipes are double-walled and are direct-buried between Buildings 367 and 369. Target cooling is discussed in detail in Chapter IV.

2.6.1 Architecture (Building 367)

The exterior walls consist of vertically corrugated, insulated metal panels on horizontal steel girts. Exterior access to the high bay is provided by three personnel doors and a vehicle door. Vehicle parking is available adjacent to the building.

The self-contained target cooling system housed in this building falls within the scope of technical components and is described in Chapter IV.

Roofing. In 1990, an IRMA roofing system with 5-cm-thick insulation board and 1-cm-thick cement topping was installed over the existing roof structure.

Building refurbishments include minor repairs to the wall-panel system, as well as general painting, sealing and caulking.

10Hz TARGET SUPPORT
BUILDING 367
FIRST FLOOR PLAN

0 1 4   10   25   50 FEET

0 1 2 3 4 5 6 7 8 9 10
METERS

Figure VI.2.6-1

CRANE

STACK

BUILDING 367

REMOVABLE REINFORCED
CONCRETE PANELS

SHIELDED TARGET COOLING
SYSTEM AREA

UNDERGROUND SHIELDED VAULT

SECTION A-A THROUGH BUILDING 367
with UNDERGROUND
ADJACENT VAULT

0 1 4   10   25   50 FEET

0   1   2   3   4   5   6   7   8   9   10
METERS
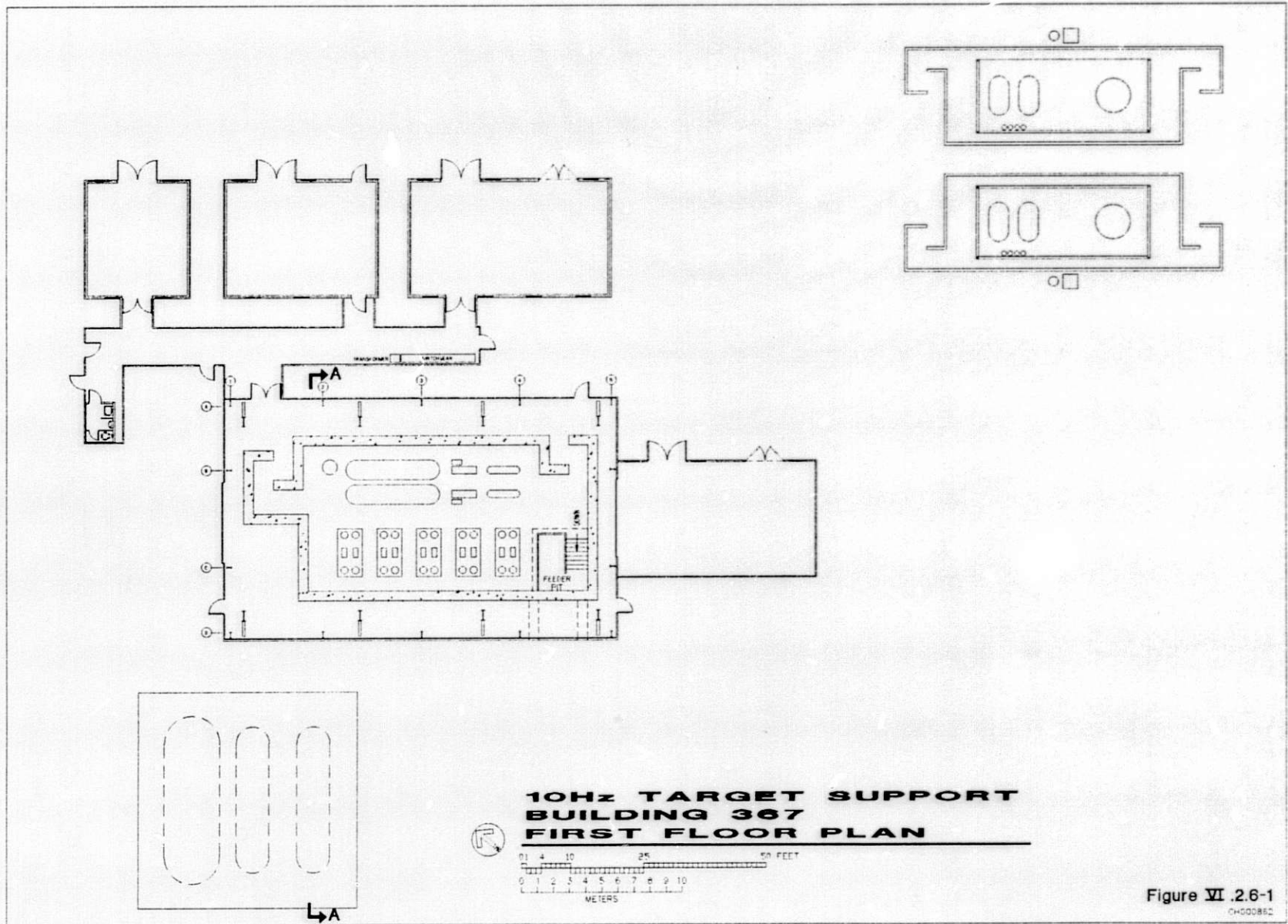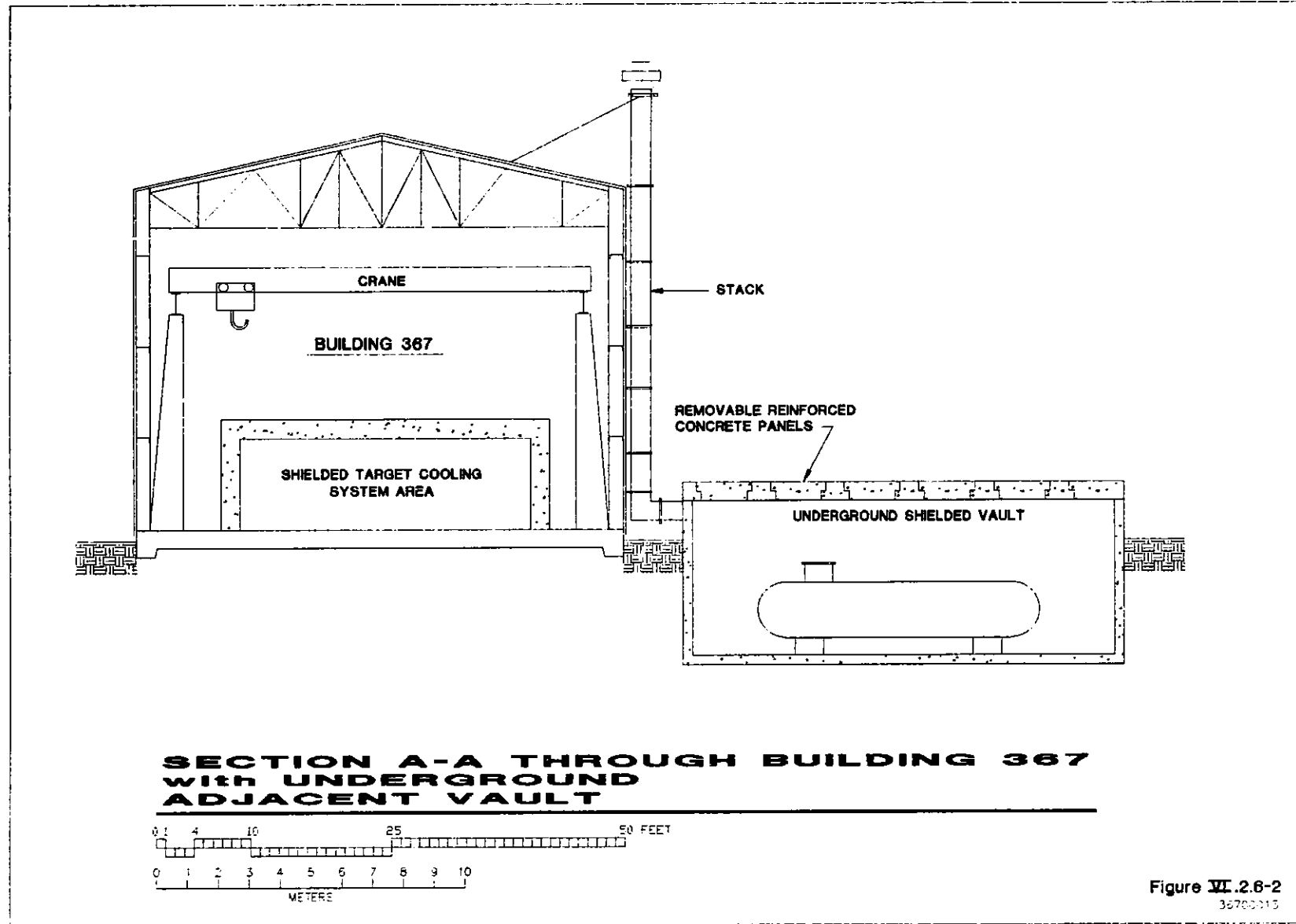
Figure VI.2.6-2

2.6.2 Structure (Building 367)

The existing building structural system consists of steel columns supporting a beam and girder framing system with a welded-metal deck roof. Structural steel bracing in the exterior wall provides resistance against lateral loads. Foundations are conventional reinforced-concrete spread footings. The floor is slab-on-grade reinforced concrete and is 0.45 m thick, with a floor load capacity of 3,000 lb/ft^2. The high bay is equipped with a top-running 35-ton crane, bridge-supported on an independent structure.

There are no structural modifications to Building 367 except for the addition of minor supports associated with the new technical, mechanical, and electrical equipment installations.

2.6.3 Mechanical Systems (Building 367)

Existing mechanical systems in the building are retained. Mechanical systems associated with the target cooling and coolant retention systems are described in Chapter IV.

Central Plant Equipment and Piping. There are no chillers, DIW plants, or other plant facilities cooling equipment located in the building.

DIW is provided from Building 369. DIW S/R runs along the high-bay wall. Piping is provided with capped valve-stubs to facilitate connection to user equipment.

Existing unit heaters are retained and relocated.

Air Distribution. The building uses existing, refurbished exhaust fans and louvers for ventilation. No air conditioning and no additional AHUs are provided.

Plumbing and Fire Protection. Existing building toilet facilities and plumbing systems are used. Existing fire protection systems are used, with upgrades to provide coverage for new equipment.
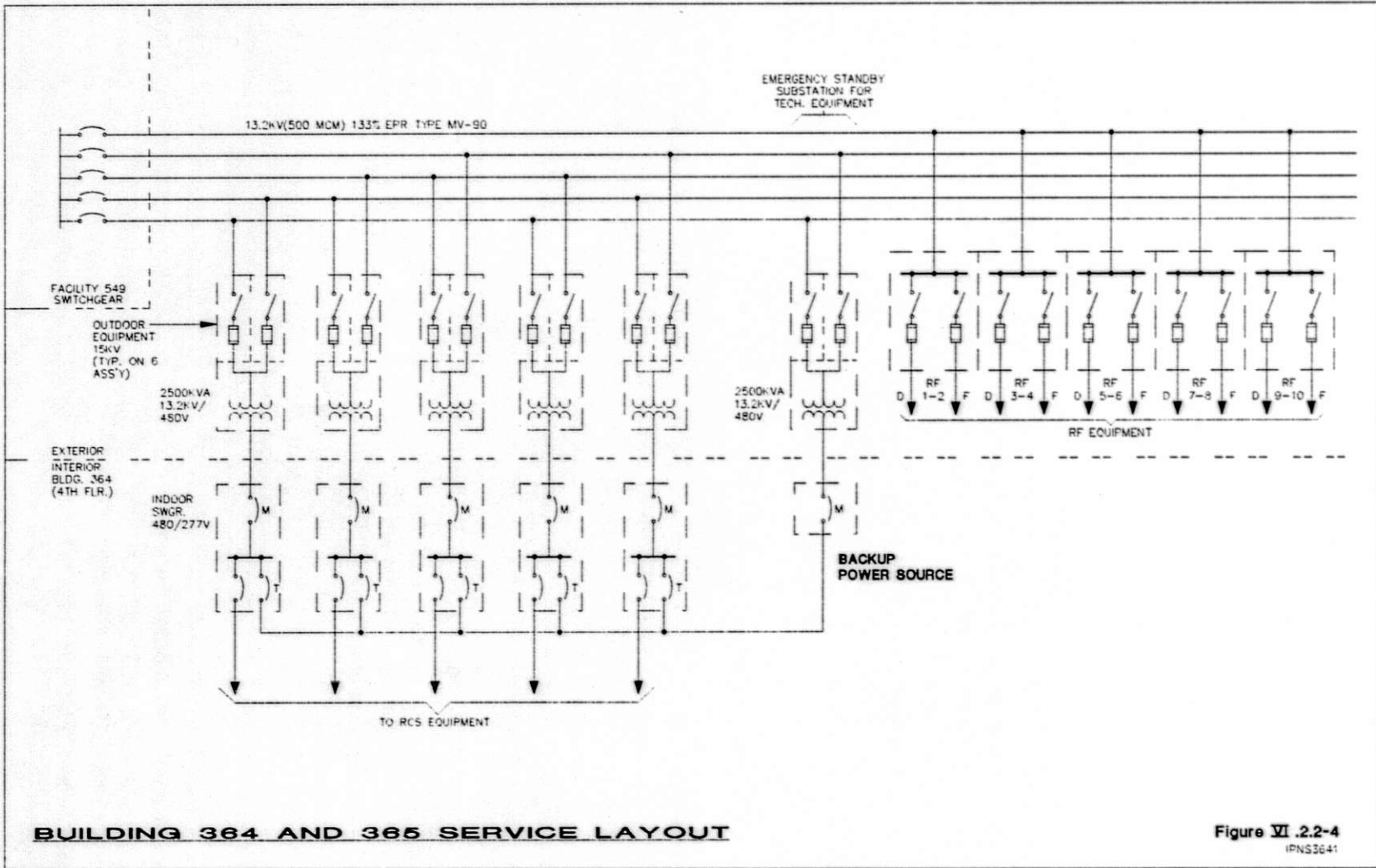
2.6.4 Electrical Systems (Building 367)

Electrical power to Building 367 is delivered from 480-V switchgear located in Building 369, as shown in Figure VI.2.5-3. This switchgear feeds new 480-V power distribution panel boards.

Lighting fixture circuit wiring is new to improve reliability. Cleaned, repaired, and relamped fixtures provide adequate illumination. New breakers are provided for existing power and lighting panel board interiors.

New outdoor, high-pressure sodium lighting fixtures are installed to provide perimeter lighting.

Emergency lighting is provided by 1.5-h battery-pack units. Special systems, such as telephone, paging, and fire alarms, are adequate to meet requirements.

2.7 30-Hz TARGET BUILDING (EXISTING BUILDING 370)

Building 370, a one-story high-bay building, 31.4 m wide × 97.5 m long, houses the 30-Hz target and 18 instrument lines. The high-bay building, completed in 1963, has a gross floor area of 3,679 m^2 and a clear height of 10.9 m to the bottom of the roof trusses. Building 370 adjoins Buildings 365, 368, 369, and 371. Figure VI.2.7-1 shows the first-floor plan and 30-Hz target, and Figure VI.2.7-2 shows a section through the building.

2.7.1 Architecture (Building 370)

The three exterior walls are insulated metal panels on horizontal girts. The north wall is the common concrete and earth shield wall between the Ring Building and the 30-Hz Target Building. It has a 3.6-m-wide × 4.6-m-high cast-in-place concrete girder that provides an opening 28.8 m wide × 2.9 m high between Buildings 365 and 370 for the high-energy transfer line to the 30-Hz target. A section through this area is shown in Figure VI.2.7-2.

The east wall is a common wall between the 10-Hz Target Building and the 30-Hz Target Building.

The existing control rooms at the east end of Building 370 are used.

Roofing. In 1990, an IRMA roofing system with 5-cm-thick insulation board and 1-cm-thick cement topping was installed over the existing roof structure.

2.7.2 Structure (Building 370)

The structural system is composed of steel columns on a concrete foundation supporting steel trusses and a welded-steel roof deck.

The slab-on-grade concrete floor is 0.15 m thick, with a floor load capacity of 800 lb/ft^2.

The targets, shields, and associated foundations are described in Chapter IV.

Existing floor trenches in Building 370 are eliminated.

30Hz TARGET BUILDING 370 FIRST FLOOR PLAN

Figure VI.2.7-1

CH000863

35-TON CRANE

HOT CELL

BIOLOGICAL SHIELD

BLDG 365

INSTRUMENT LINES

UTILITY TUNNEL

SECTION A-A THROUGH BUILDING 370

METERS
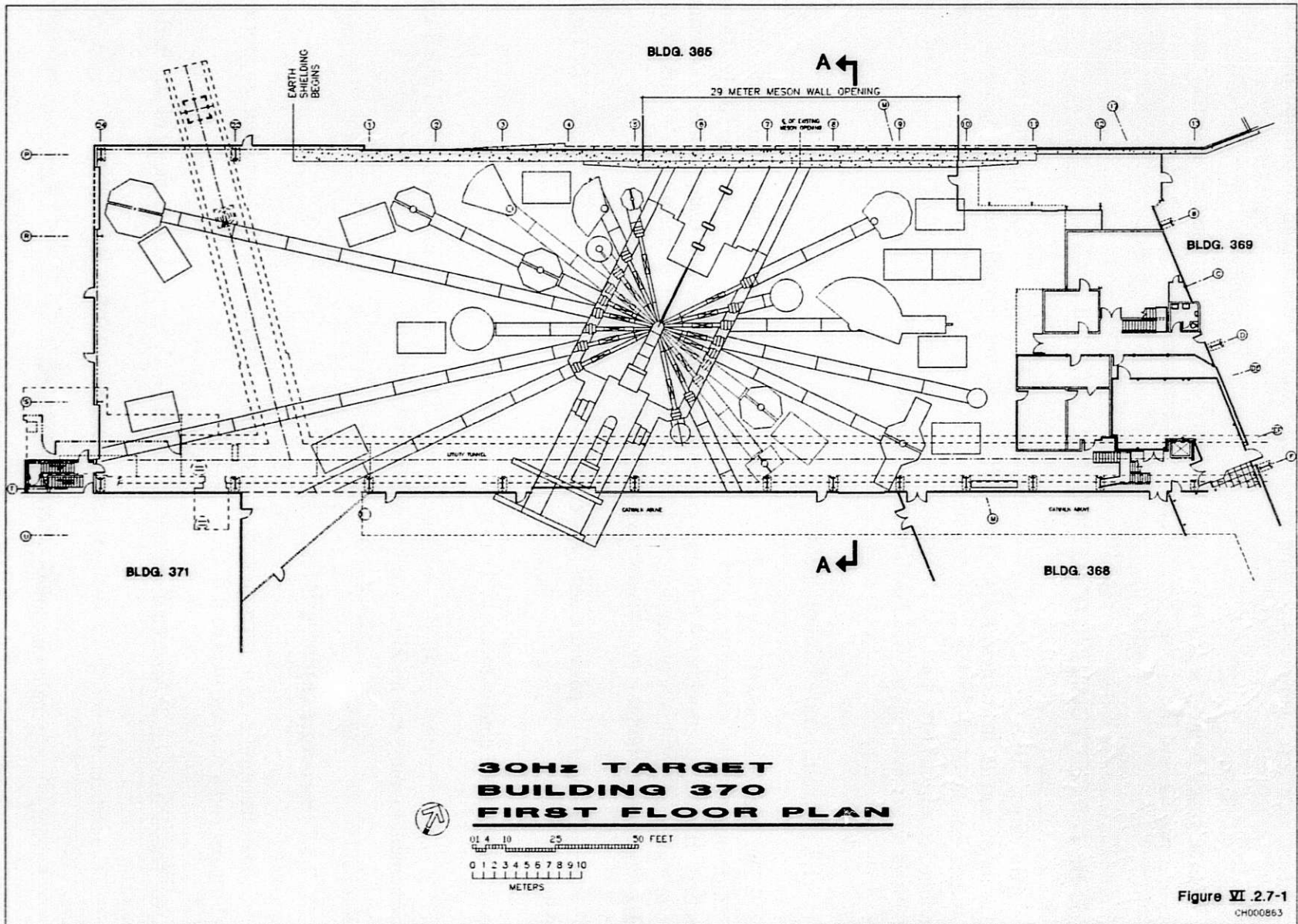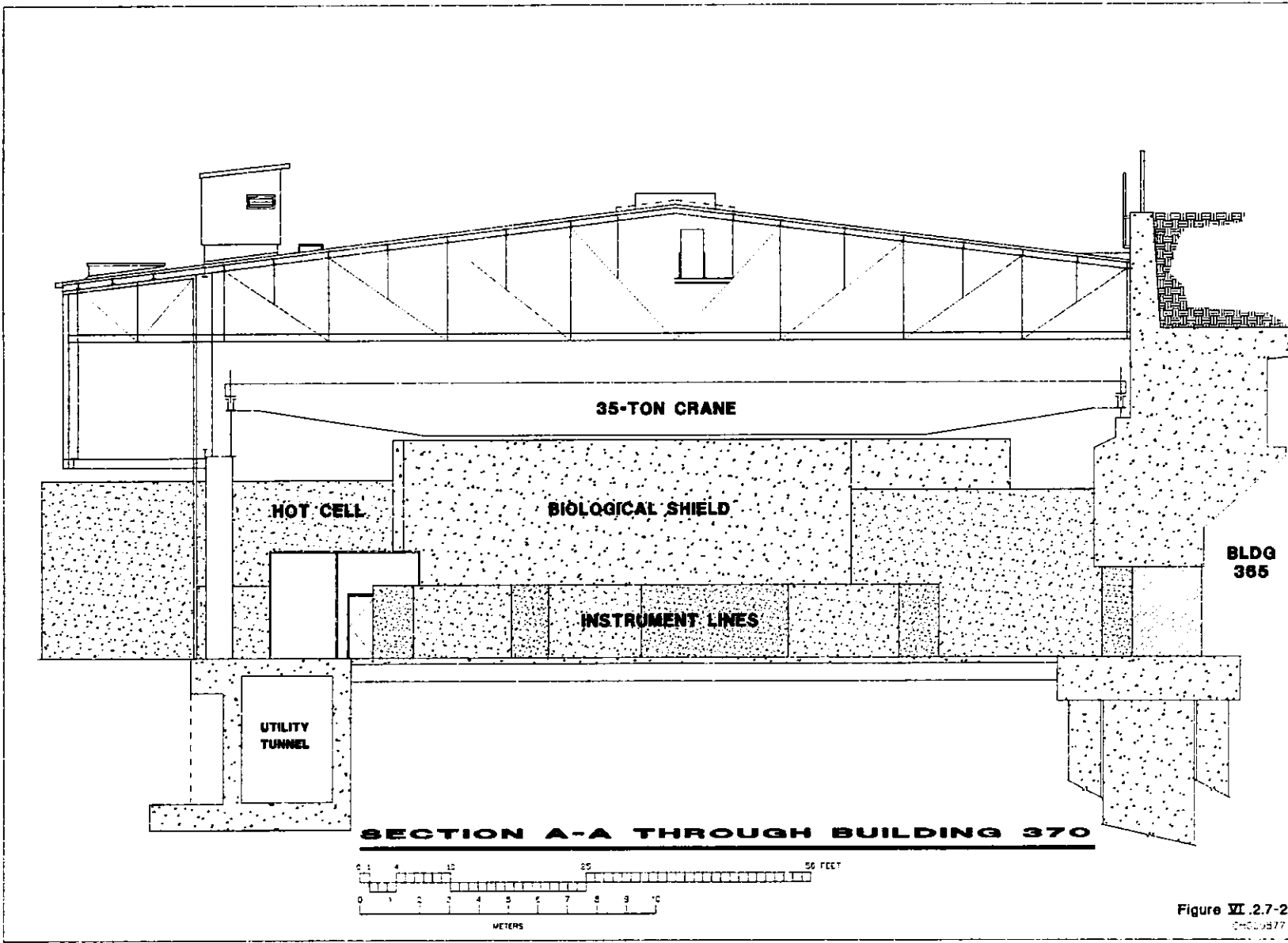
Figure VI.2.7-2

Tunnel. An existing tunnel system through the entire 360 area carries utilities, power, and controls and provides personnel access to these buildings. A 115.8-m-long utility tunnel runs under the south and west areas of the first floor of Building 370; this tunnel is 4.27-m high × 3.04-m wide.

Cranes and Hoists. The high bay is equipped with a 35-ton, top-running bridge crane with full high-bay coverage, plus an auxiliary 10-ton hoist.

2.7.3 Mechanical Systems (Building 370)

Demolition. Miscellaneous mechanical systems and piping are relocated as necessary to facilitate construction of target biological shielding. A section of the utility tunnel passing under this building is filled with concrete.

Mechanical systems associated with target cooling and coolant retention systems are described in Chapter IV.

Central Plant and Piping. No DIW is required for the equipment in this building. Equipment utilizing DIW is located in Building 371. Existing CW piping is used for local cooling. New CW plant piping for local cooling is tied into the existing CW piping in the tunnel. Existing unit heaters are used. Heaters and piping are modified or moved to accommodate new equipment.

The following services are provided in the utility tunnel: Fire protection water, steam, RW, hot water, CW, condensate return, domestic cold water, two mechanical water systems, sanitary drain, DIW, ten wall-mounted cable trays, and electric power. The tunnel system has an automatic sprinkler system, fire-detection system, floor drains, and access panels to the building above. It is also used as a tornado shelter.

Air Distribution. The building is presently ventilated by four refurbished, truss-mounted air-handling units of 40,000 cfm capacity each. Existing CW cooling coils that were not connected to CW piping are furnished with chilled water. New controls for all units are provided.

Existing diffusers and ductwork remain.

The six existing 89,000-cfm hydrogen-evacuation fans on the roof are refurbished and used.

Plumbing and Fire Protection. Existing building plumbing systems are used. Existing fire protection systems are used, with upgrades to provide coverage for new equipment.

2.7.4 Electrical Systems (Building 370)

The 30-Hz target equipment is fed from a 480-V double-ended substation, as shown in Figure VI.2.7-3. This substation has two 13.2-kV incoming line switches, two 2,000-kVA transformers, and associated 480-V switchgear. The 13.2-kV switchgear is located outdoors near Building 370, and power is supplied to it by switchgear located at Site Electrical Facility 549. The 480-V switchgear is located inside Building 370 and feeds power to distribution panel boards located near the technical equipment. Individual equipment is powered from these panels. Clean power requirements are met by using 480-V to 480-V isolation transformers.

A separate instrumentation grounding system for all computers and computer-related equipment is furnished.

Cleaned, repaired, and relamped existing lighting fixtures provide adequate illumination. Lighting fixture circuit wiring is new to improve reliability. New breakers are provided for existing power and lighting panel board interiors.

Special systems, such as telephone, paging, and fire alarms, are adequate to meet requirements.

LEGEND
N.O. – NORMALLY OPEN
N.C. – NORMALLY CLOSED

BUILDING 370 AND 371 UTILITY SUBSTATION

Figure VI.2.7-3

IPNS3701
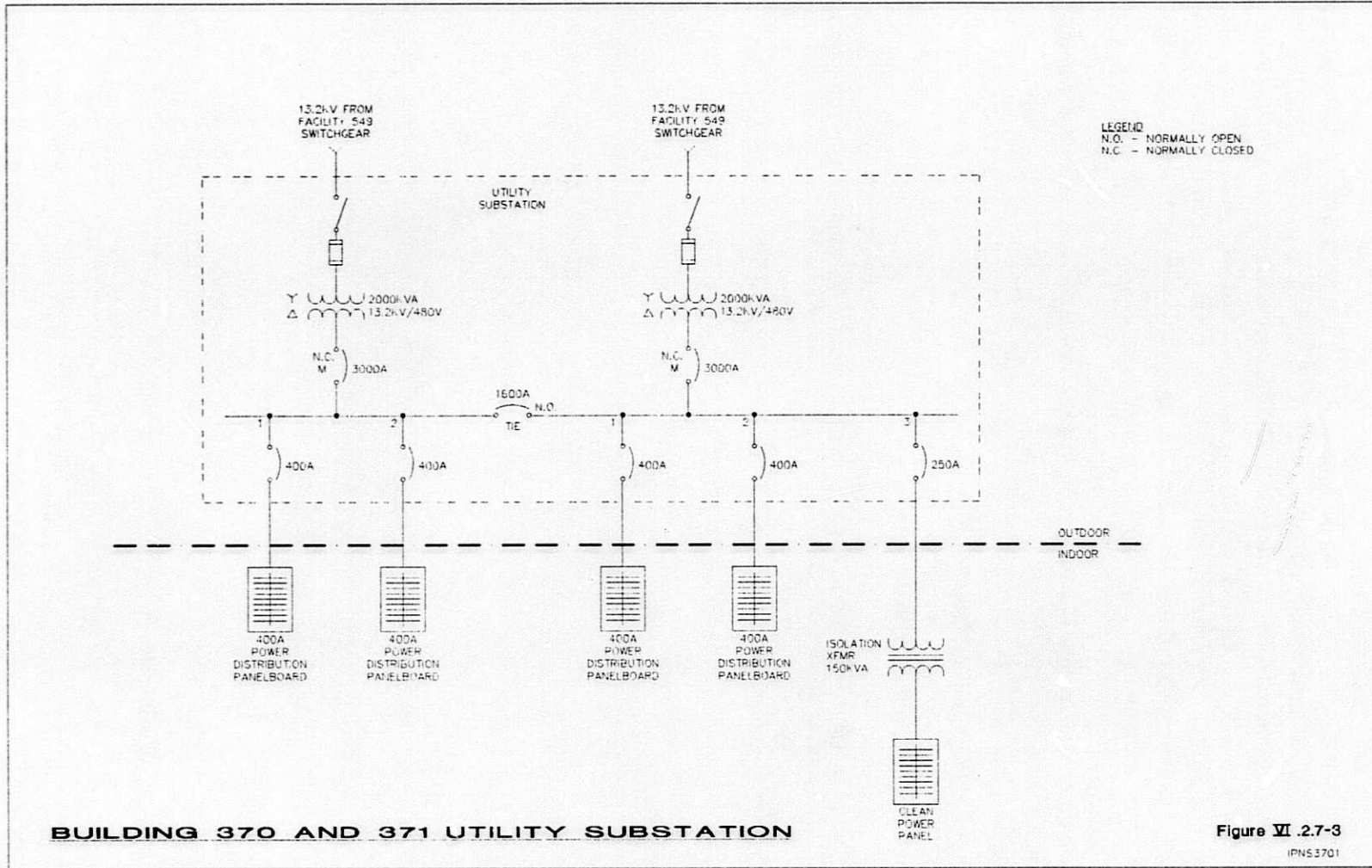
2.8 30-Hz TARGET SUPPORT BUILDING (EXISTING BUILDING 371)

Building 371 is a single-story high-bay building. It houses the cooling system for the 30-Hz target located in Building 370. The high bay is approximately 25 m wide × 31.7 m long, with a clear height of 12.4 m to the bottom of the roof trusses. An annex, Building 371A, adjacent to Building 371 is 32.7 m long × 16.0 m wide. A 35-ton crane serves the building. This building was completed in 1961 and, together with its annex, has a gross floor area of 1,361 m². A new shielded cooling system, shown in Figure VI.2.8-1, is located in the high bay for the 30-Hz target in Building 370. The target cooling system is self-contained and the cooling system area is shielded, because the coolant is potentially radioactive. Target cooling water pipes are double-walled construction and are direct-buried between Buildings 371 and 370. Cross sections of Building 371 and of the adjacent underground vault are shown in Figure VI.2.8-2. Target cooling is discussed in detail in Chapter IV.

2.8.1 Architecture (Building 371)

Exterior Facade and Entrances. The exterior walls are constructed of vertical corrugated insulated metal panels supported on a steel frame structure. Exterior access to the high-bay area is provided by three personnel doors and two vehicle access doors. Vehicle parking is available adjacent to the building.

The only direct connection to the underground utility tunnel system is through an access pit at the north corner of the building.

The self-contained target-cooling system housed in this building falls within the scope of technical components and is described in Chapter IV.

Building refurbishments include minor repairs to the wall-panel system, as well as general painting, sealing, and caulking.

2.8.2 Structure (Building 371)

The building structural system consists of concrete foundations and steel columns supporting a truss-and-girder roof. Building column framing has structural steel bracing for the exterior metal-panel walls, providing resistance against lateral wind loads. Foundation walls are supported by conventional, reinforced-concrete spread footings. The floor is reinforced-concrete slab-on-grade construction and is 0.3 m thick, with a floor load capacity of 3,000 lb/ft².

Cranes and Hoists. The high bay is equipped with a 35-ton, top-running bridge crane that provides high-bay coverage. A 10-ton auxiliary hoist is also available.

Building Modifications. There are no modifications to Building 371, except for the addition of minor structural supports associated with the new installations.

BLDG. 370

SUPPLY

DRAIN

FEEDER PIT

DOWN

A

A

BLDG. 371 ANNEX

**30Hz TARGET SUPPORT
BUILDING 371
FIRST FLOOR PLAN**

01 4   10   25   50 FEET

0 1 2 3 4 5 6 7 8 9 10
METERS

Figure VI.2.8-1

CH000864

SECTION A-A THROUGH BUILDING 371
WITH UNDERGROUND
ADJACENT VAULT
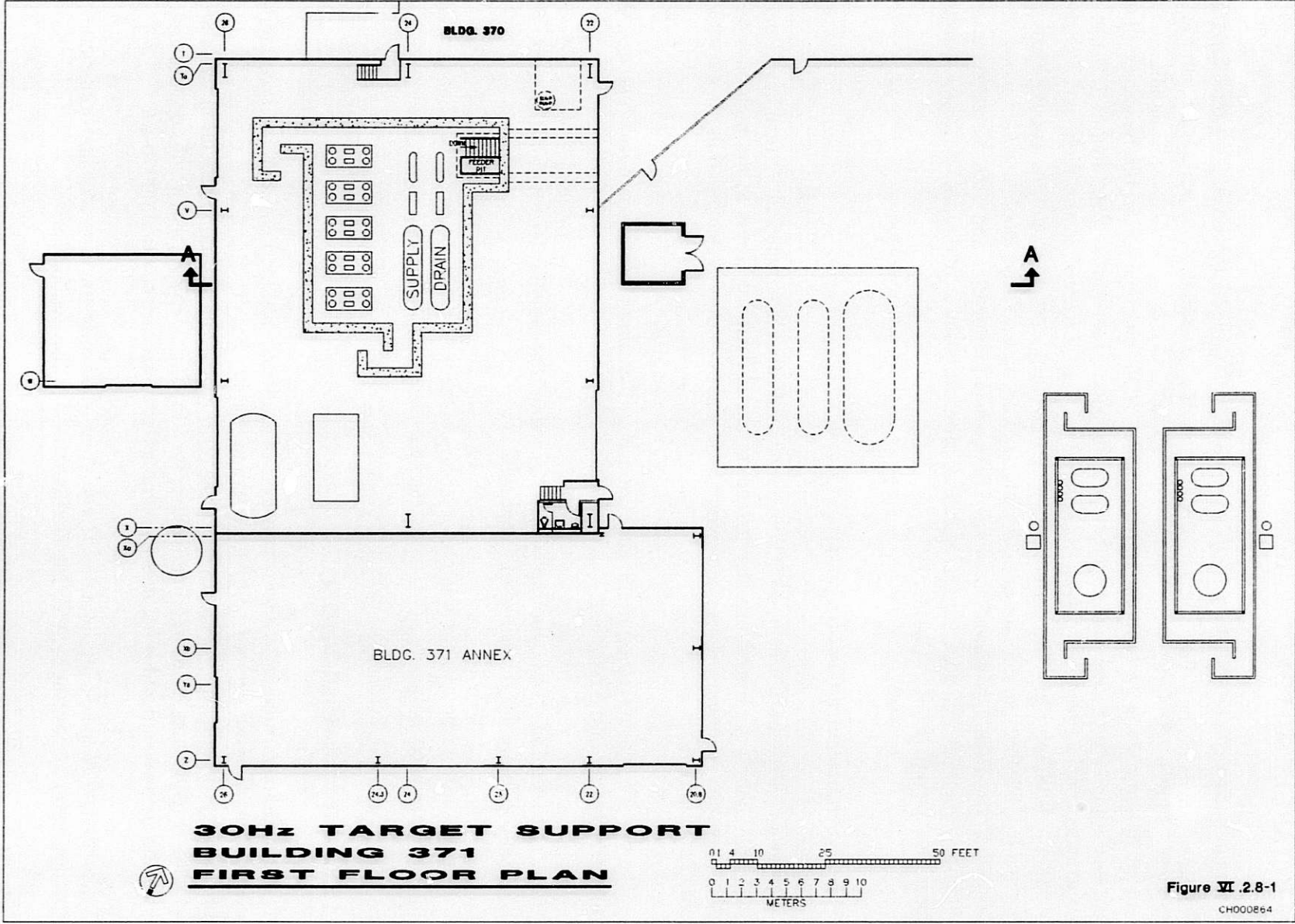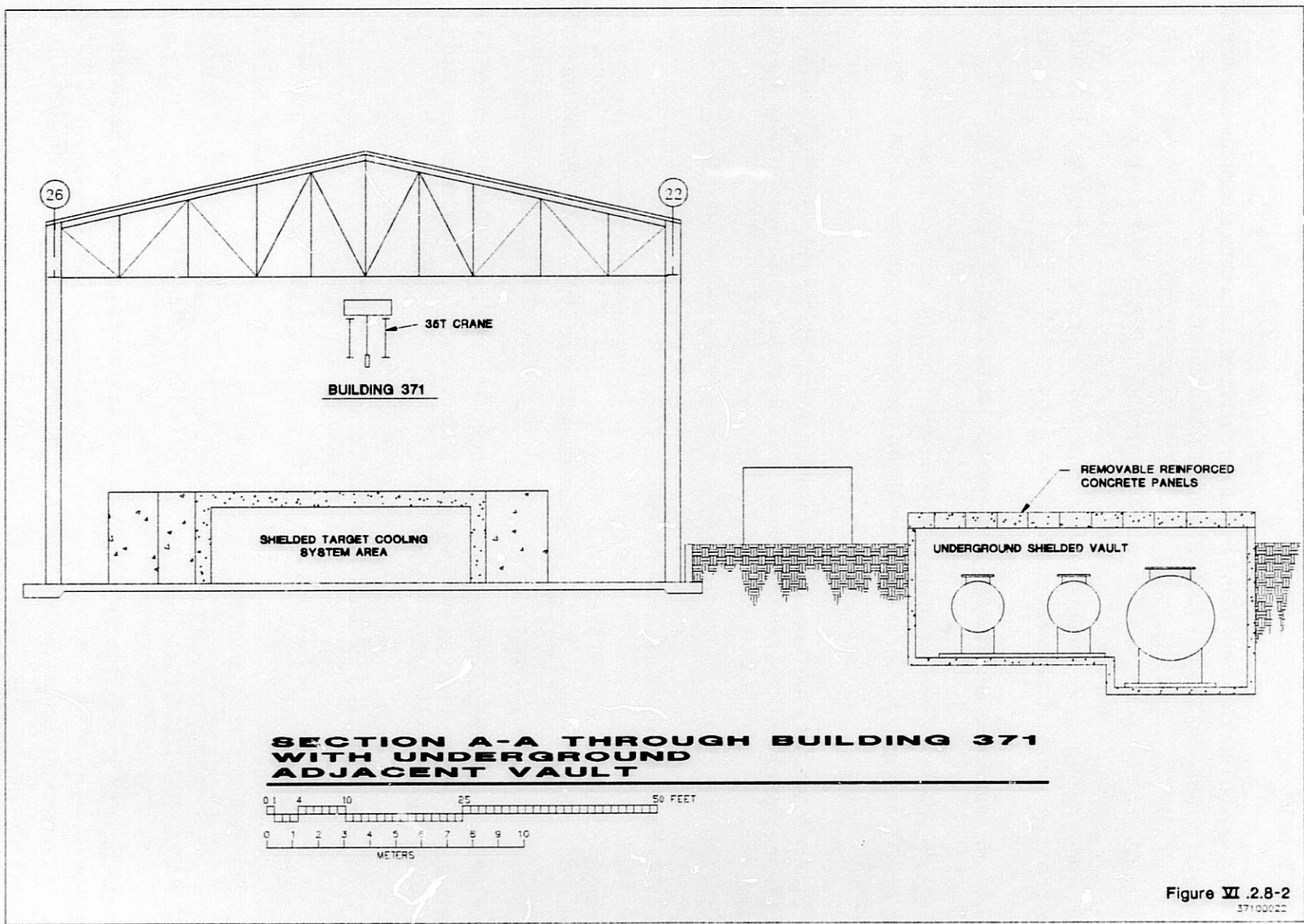
Figure VI.2.8-2

37100022

2.8.3 Mechanical Systems (Building 371)

Existing mechanical systems in the building are retained. Mechanical systems associated with the target cooling and coolant-retention systems are described in Chapter IV.

Central Plant Equipment and Piping. No central cooling plant equipment is located in the high bay. A previously inactive DIW plant in the adjacent Building 371A is restored to its original capacity to furnish the required pressure and flow. Piping in the high bay is provided with capped valve-stubs to facilitate connection to user equipment.

Existing unit heaters are retained and are relocated as necessary.

Air Distribution. Two refurbished, truss-mounted heating and ventilating AHUs each provide 20,000 cfm capacity. Six existing 89,000-cfm hydrogen-evacuation fans on the roof are refurbished.

Plumbing and Fire Protection. Existing building toilet facilities and plumbing systems are used. Existing fire protection systems are used, with upgrades to provide coverage for new equipment.

2.8.4 Electrical Systems (Building 371)

Electrical power to Building 371 is delivered from 480-V switchgear located in Building 370, as shown in Figure VI.2.7-3. This switchgear feeds 480-V power distribution panel boards.

Lighting fixture circuit wiring is new to improve reliability. Cleaned, repaired, and relamped existing lighting fixtures provide adequate illumination. New breakers are provided for existing power and lighting panel board interiors.

Outdoor, high-pressure sodium fixtures provide perimeter lighting.

Emergency lighting is provided by 1.5-h battery-powered units. Special systems, such as telephone, paging, and fire alarms, are adequate.

2.9 PREPARATION LABORATORIES (EXISTING BUILDING 368)

Building 368 houses preparation laboratories for the two target facilities. The building is 23 m wide × 67 m long × 4.6 m high. It was originally designed for heavy electrical distribution and has an experimental testing facility addition. This building, completed in 1963, has a gross floor area of 1,822 m².

A portion of the south wall of Building 370 forms the north wall of Building 368, and part of the Building 369 west wall forms Building 368's east wall. The layout of Building 368, with adjacent areas of 369 and 370, is shown in Figure VI.2.9-1. The control room for the 10-Hz target is located in the northeast corner of Building 368. The south half of this facility is used as a convenient laboratory and experiment preparation area. It has direct access to the two target buildings, as shown in Figure VI.2.9-1.

2.9.1 Architecture (Building 368)

The three exterior building walls are constructed of vertically corrugated, insulated metal panels on horizontal structural girts. Entrance to the building is provided by six personnel doors and two vehicle-access doors.

Roofing. In 1990, an IRMA roofing system with 5-cm-thick insulation board and 1-cm-thick cement topping was installed over the existing roof structure.

Building Modifications. There are no changes in the building function. Therefore, only minor modifications, refurbishing, and painting are required.

2.9.2 Structure (Building 368)

The existing building structural system consists of concrete foundations and steel columns supporting a beam-and-girder framing system. Foundation walls are supported by conventional spread footings. The floor is reinforced-concrete, 0.15-m-thick slab-on-grade with a floor load capacity of 800 lb/ft^2.

Structural Modifications. Building function is unchanged, so no structural modifications are required.

2.9.3 Mechanical Systems (Building 368)

Demolition. The existing DIW plant, which consists of a double-barrel shell-and-tube heat exchanger, two DIW pumps, and DIW equipment with tank, is removed.

Central Plant Equipment and Piping. A new 3,000-gpm-capacity DIW plant, which consists of a plate heat exchanger, two DIW pumps, DIW equipment, and tanks, is installed. The new DIW plant is connected to existing RW and DIW in the adjacent utility tunnel system under Building 370.

Existing unit heaters are reused and relocated as necessary.

BLDG. 369

BLDG. 370

DEIONIZATION EQUIPMENT

TARGET LABS/PREPARATION
BUILDING 368
FIRST FLOOR PLAN

0 1 4   10   25   50 FEET

0 1 2 3 4 5 6 7 8 9 10
METERS

Figure VI.2.9-1

CH000860

Air Distribution. The building uses existing, refurbished exhaust fans and louvers for ventilation. No additional air conditioning and no additional AHUs are provided. A refurbished AHU serves the transformer room.

Plumbing and Fire Protection. Existing building plumbing systems are used. Existing fire protection systems are used, with upgrades to provide coverage for new equipment.

2.9.4 Electrical Systems (Building 368)

Minor modifications are made to the electrical power system to feed mechanical equipment.

An existing 250-kW diesel-powered emergency generator is located in this building.

2.10 LABORATORY AND OFFICE BUILDING I (EXISTING BUILDING 360)

Building 360, a two-story laboratory and office building completed in 1961, houses the main accelerator control room, 22 laboratories, and 90 offices. The building is 56.4 m wide × 62.5 m long and has a gross floor area of 9,179 m². It has a roof fan room and a service floor. The layout of the first floor is shown in Figure VI.2.10-1.

2.10.1 Architecture (Building 360)

The building exterior is constructed of brick and insulated metal-sandwich panels supported on a structural-steel framing system.

The two main entrances are located on the north and west facades. The west entry has an L-shaped covered walkway. Other entrances make connections to Buildings 361, 362, and 363. The service floor of Building 360 is connected by a utility tunnel to the service floors of Buildings 362 and 365 and to the utility tunnel system.

Typical rooms and corridors in this building consist of tiled floor, dropped acoustical ceiling with fluorescent lighting, and either stud-and-panel or concrete-block walls.

Vehicle parking areas are located to the north of the building and across Rock Road.

Specialty Rooms. The existing IPNS accelerator control room is located on the first floor, between administrative offices and experimental facilities. The existing control room is equipped with floor-mounted control consoles, which have direct raceway connections to the cable trays at the service floor below and to the rest of the IPNS complex. These cable trays and raceways are used to route all signal, control, power, and fiber-optic cables for the IPNS Upgrade accelerators.

WEST ENTRY →

LOBBY

CONFERENCE ROOM

NORTH ENTRY

CONNECTING CORRIDOR

IPNS - UPGRADE CONTROL ROOM

BLDG. 361

LAB/OFFICE
BUILDING 360
FIRST FLOOR PLAN

01 4 10   25   50 FEET

0 1 2 3 4 5 6 7 8 9 10
METERS

Figure VI.2.10-1

CH000866
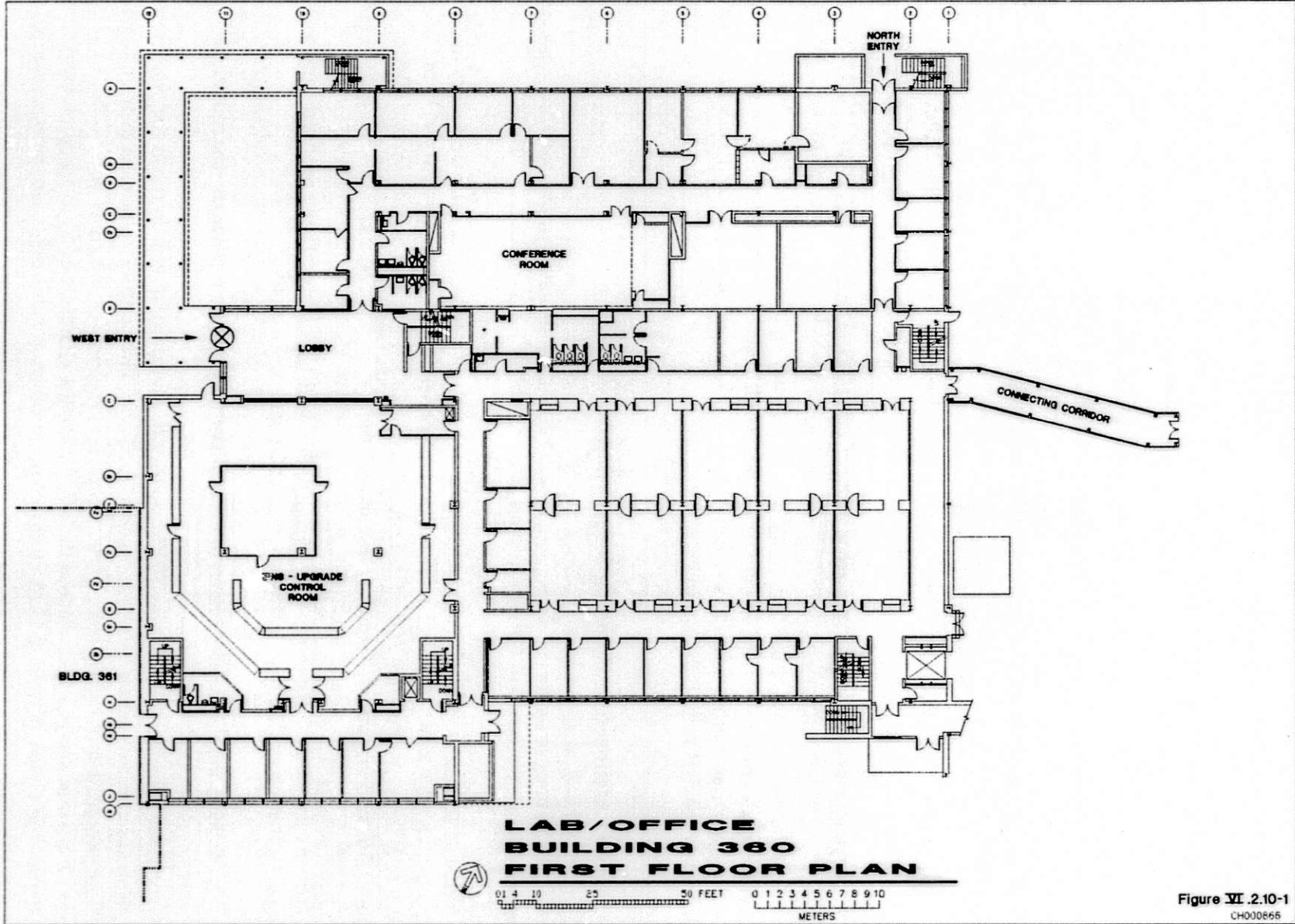
A 120-seat-capacity, theater-style conference room with a raised stage is located on the first floor. The 360 area main maintenance shop is located on the service floor. Building maintenance mechanics support all 360 area buildings from this shop.

Existing asbestos contamination, which is restricted to floor tiles and mechanical systems, is continually monitored by ANL Industrial Hygiene and PFS personnel.

Roofing. In 1990, an IRMA roofing system with 5-cm-thick insulation board and 1-cm-thick cement topping was installed over the existing roof structure.

2.10.2 Structure (Building 360)

The structural system for Building 360 consists of steel columns supporting a beam-and-girder framing system. Building framing is supported on a reinforced-concrete foundation. The steel framing system supports reinforced-concrete floor and roof slabs.

Elevators and Hoists. A five-ton hydraulic service elevator serves the basement, first floor, second floor, and roof. The first-floor stop also opens to an exterior loading-dock area. A 0.75-ton hydraulic elevator stops in the basement and on the first floor. The basement maintenance shop has a one-ton monorail electric hoist.

Modifications. No architectural, structural, mechanical, or electrical alterations are required in Building 360.

2.10.3 Mechanical Systems (Building 360)

Existing toilet facilities and plumbing systems are used. Existing fire protection systems are in satisfactory condition.

2.10.4 Electrical Systems (Building 360)

The existing electrical system is adequate to provide power to the required equipment. Lighting, telephone, paging, and fire alarm systems are adequate.

2.11 LABORATORY AND OFFICE BUILDING II (EXISTING BUILDING 362)

Building 362, a three-story laboratory and office building, houses a high-bay experimental assembly area, a 298-seat auditorium, library, 177 offices, and 84 laboratory spaces. This three-story building has a lower-level service floor. Completed in 1965, it has a gross floor area of 19,400 m². Figure VI.2.11-1 shows the first-floor plan.

AUDITORIUM

LIBRARY

CONF.   CONFERENCE

LIB.   LIB.

CONNECTING CORRIDOR

HIGH BAY

LAB/OFFICE
BUILDING 362
FIRST FLOOR PLAN

0 4 10   25   50 FEET

0 2 4 6 8 10
METERS

Figure VI .2.11-1

CH00087+
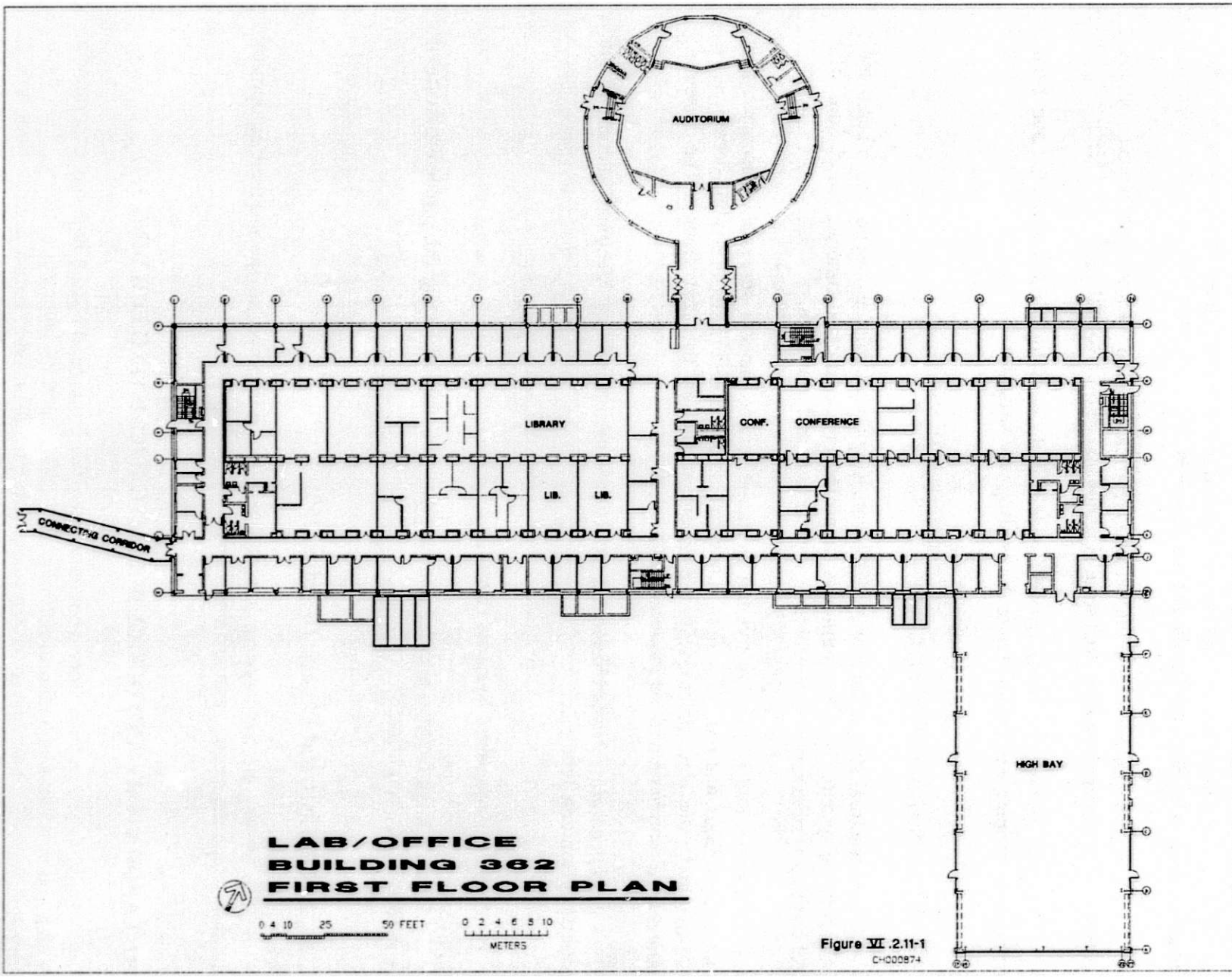
The building is 34.1 m wide × 112.8 m long and has a floor-to-floor height of 4.5 m. A 28.0-m-diameter circular brick building containing the 298-seat auditorium is connected to Building 362 by a common-entry vestibule. The 21.5-m × 44.0-m high-bay experimental and assembly area is located at the southeast corner of Building 362. It has a 20-ton overhead crane that provides full coverage of the high-bay area. Parking for 300 cars is provided in three lots to the north of the building.

2.11.1 Architecture (Building 362)

The building exterior is composed of brick and vertical metal wall panels. The first floor facade has large horizontal windows with low-height brick sill walls. The second and third floors are faced with vertical metal sandwich panels with vertical window elements. There is a service floor below and a fan room at the roof level.

Primary access to the building and auditorium is provided by two entrances at the connecting entry vestibule to the auditorium. A two-level corridor connects Building 362 to Building 360, with a tunnel below at the service floor level.

Typical rooms and corridors in this building consist of tiled floor, dropped acoustical ceiling with fluorescent lighting, and either stud-and-panel or concrete-block walls.

Specialty Rooms. A 298-seat auditorium adjacent to the central research laboratory and office area provides a facility for seminars, lecture activities, and other assemblies. Additional conference rooms are located within the building, providing facilities for 30, 40, and 70 people.

Roofing. In 1990, an IRMA roofing system with 5-cm-thick insulation board and 1-cm-thick cement topping was installed over the existing roof structure.

2.11.2 Structure (Building 362)

The Building 362 structural system consists of steel columns supporting a beam-and-girder framing system. Building framing is supported on a reinforced-concrete foundation. The steel framing system supports reinforced-concrete floor and roof slabs.

The spray-on fireproofing used to protect the structural-steel framing system contained asbestos. The original floor tile and mastic used in Building 362 also contain asbestos. A complete asbestos survey of the building was performed, and floor tiles in the first- and second-floor corridors were replaced. Remaining areas with asbestos-containing materials are monitored and maintained by Industrial Hygiene and PFS personnel. Existing asbestos is not considered a major problem.

Cranes and Elevators. A 20-ton, top-running bridge crane in the high bay provides full coverage for the experimental assembly area. Building 362 is equipped with four elevators, the

largest of which is a four-ton-capacity cable-hoist service elevator. The other three elevators are 1.25-ton-capacity cable-hoist elevators.

2.11.3 Mechanical Systems (Building 362)

No improvements or alterations to the existing mechanical systems are required. Existing toilet facilities and plumbing systems are in satisfactory condition. The existing fire protection system is in satisfactory condition.

2.11.4 Electrical Systems (Building 362)

Existing power distribution systems, lighting, telephone, PBX, paging, and fire alarm systems are adequate for IPNS Upgrade program requirements. Two 13.2-kV to 480-V electrical substations, one with a capacity of 2,500 kVA and the other with a capacity of 1,000 kVA, were installed during 1993.

2.12 UTILITIES AND SITE WORK

The existing ZGS/360 site is over 30 years old and has all of the required utilities to support the IPNS Upgrade. Only minor modifications are required to connect the existing mechanical utilities to new equipment. Site modifications for the 10- and 30-Hz target cooling systems, buried vaults, and cryogenic support facilities are described in Chapter IV.

2.12.1 Site Mechanical Systems

The existing site mechanical systems are refurbished and utilized wherever feasible. A new, modern chiller plant utilizing centrifugal chillers with CFC-free refrigerant is constructed at the service floor of Building 376. The plant includes new pumps, piping, and associated auxiliary equipment. The new chiller plant is connected to the existing Cooling Tower Facility 377, as shown in the Mechanical Site Plan in Figure VI.2.12-1. This cooling tower is completely rebuilt and is furnished with new condenser water pumps, as shown in the 377 Area Cooling Tower Plan in Figure VI.2.12-2. New cooling towers are not required for the IPNS Upgrade. The existing piping in the site utility tunnels, including steam and condensate along with CW, condenser, and DIW piping, is retained and modified as necessary to accommodate increased utility service demands associated with the IPNS Upgrade.

A new DIW plant is located in Building 364. The existing DIW plant in Building 371A is upgraded, and the existing DIW plant in Building 368 is replaced. The 360/ZGS Mechanical Site Plan is shown in Figure VI.2.12-1. New DIW piping and fittings are constructed of stainless steel. The existing shell-and-tube RW-to-DIW heat exchanger and associated pumps in Building 371A are reactivated.

360/ZGS MECHANICAL SITE PLAN

Figure VI.2.12-1

LEGEND

CW - CHILLED WATER (7.2C)
DIW - DEIONIZED WATER
    (ST. STL SCH 10) 32.2C
RW - RAW (COOLING TOWER) WATER 29.4C
AHU - AIR HANDLING UNIT
■ - PUMP
—— (HEAVY LINE) - NEW WORK
— (THIN LINE) - EXISTING WORK
☐ IPNS-UPGRADE BUILDINGS
▨ NEW CONSTRUCTION

NOTES:
1. EXISTING 24" RW IN TUNNEL FEEDING BLDG. 364 THROUGH BLDG. 370, WILL BE RELOCATED AND REPLACED WITH A 30" PIPE THROUGH THE LINAC LOW ENERGY TRANSPORT TUNNEL, BLDG. 394A.

2. ALL PIPING SHOWN IS NEW UNLESS NOTED OTHERWISE.
DEIONIZED WATER 32.2C
(ST. STL SCH 10)

3. EACH PIPE LINE SHOWN INDICATES 2 PIPES; SUPPLY AND RETURN.

RAW WATER PUMPS,
VERTICAL TURBINE TYPE
8000 gpm EACH CELL

TRANSFORMERS

TRANSFORMERS

TRANSFORMERS

BUILDING
377A

EXISTING TOWER

WOOD BRIDGE

1' PAD
(TYP.)

REBUILT (REFURBISHED) EXISTING
2-CELL COOLING TOWER

EXISTING
TOWER

BUILDING
377B

377 AREA
COOLING TOWER PLAN

0 1 4   10   25   50 FEET

0 1 2 3 4 5 6 7 8 9 10
METERS

Figure VI.2.12-2
CH000865

Existing site steam and condensate return piping systems furnished by the Argonne central boiler plant are utilized. The piping is modified and extended to accommodate a small number of new AHUs. Some of the underground steam piping is replaced.

Existing site plumbing systems are reused. No major modifications are anticipated. Existing site fire protection systems, including sprinkler piping, are used with minor modifications to accommodate new equipment in accordance with applicable standards.

2.12.2 Site Power Distribution System

The existing 360 site receives electrical power from site Electrical Facility 549A. A new 13.2-kV switchgear line-up in a prefabricated building at Facility 549 provides power to new technical equipment in various buildings, as shown on Figure VI.2.12-3, the 360/ZGS Electrical Site Plan. New 13.2-kV cable is routed to these buildings via underground duct banks and manholes. This switchgear line-up receives power from existing 138-kV to 13.2-kV transformers located at this facility. Building utility substations and diesel emergency power generators for the area are shown on Figure VI.2.12-3, the 360/ZGS Electrical Site Plan.

2.12.3 Site Work

The existing ZGS/360 area requires a minimum of site work to facilitate the installation of the IPNS Upgrade. The only major new site development is the construction of the new Linac Building and earth-bermed Linac and LET tunnel, as shown in Figure VI.1.1-2. Site work associated with additional concrete shielding over the LET tunnel results in the rebuilding of Old Bluff Road, as shown in section B-1 in Figure VI.2.1-3. Two existing, 475-mm chilled water pipes are lowered 1 m so they pass under the LET tunnel, to eliminate interference. This is shown in Figure VI.2.1-2, Section through Linac Facility.

The buried Linac and LET tunnels use earth berms for shielding. At the narrow area between Buildings 376 and 370, the LET changes elevation to cross over the existing ZGS utility tunnel, and the berm is contained with concrete retaining walls. A steel-grating stair allows pedestrian access over the LET berm, as shown in section B-2 in Figure VI.2.1-3.

Excavation and shoring of the existing earth berm at the RCS Ring Building 365 are required at the LET tunnel connection area. New buried piping between the target Buildings 369 and 370 and target cooling systems in Buildings 367 and 371 require minor trenching and replacement of pavement areas along piping lines shown in Figure VI.2.12-1, 360/ZGS Mechanical Site Area.

400 kW EMERGENCY
DIESEL GENERATOR

BUILDING 367 AND 369
UTILITY SUBSTATION

BUILDING 364 AND 365
UTILITY SUBSTATION

363
CENTRAL
SHOPS

250 kW EMERGENCY
DIESEL GENERATOR

BUILDING 370 AND 371
UTILITY SUBSTATION

250 kW EMERGENCY
DIESEL GENERATOR

BUILDING 376
UTILITY SUBSTATION

SUB.
549B

LINAC TUNNEL

STAGING
AREA

BUILDING 394
UTILITY SUBSTATION

SUB
549A

360/ZGS ELECTRICAL SITE PLAN

0   50   100   150   200 FEET
0 10 20 30 40 50 60 70 80 90 100 METERS

Figure VI.2.12-3

IPNSESP1

VII

Cost and Schedule

All costs for the IPNS Upgrade Project are developed from the work breakdown structure (WBS) by using the same method as that used for the Advanced Photon Source (APS) Project. The WBS encompasses all elements of the construction phase, from design to end of construction. The accelerator and neutron-generating target facilities' technical components and the initial set of beamlines and instrumentation were designed and cost-estimated by ANL personnel. The linac was designed and cost-estimated by AccSys Technology, Inc. The conventional facility designs associated with modifications to the existing buildings and with new construction were developed by personnel from ANL's Plant Facilities and Services Division (PFS) and by APS staff; these designs were cost-estimated by the construction consulting firm of Hanscomb Associates, Inc. This firm did the cost estimate for the APS project.

The WBS in Table VII.1-1 shows the project at Level 1. Level 2, the responsibility and functionality level, groups functionally identifiable items of the project. Also included in this level are project management, contingency, and miscellaneous costs, such as Laboratory overhead and materials and service expenses of the Laboratory staff. Level 3 in the WBS identifies major components of the facility, such as the linac, synchrotron, and target stations. The engineering, design, and inspection (ED&I) costs for each Level 2 item are shown in Level 3.

The cost estimates include all costs incurred after project approval. The project scope includes the accelerator facility, two neutron-generating target stations, an initial complement of 27 instruments, conventional facilities, and associated ED&I and project management. Preconstruction research and development (R&D) and preoperational activities required for commissioning of the facility and/or for the scientific research program are not included in the estimate.

The time estimates for engineering, design, and construction of the conventional facilities and the beneficial occupancy date of each building were generated by the APS and PFS staff. The beneficial occupancy dates are used to set schedules for activities related to the technical components. The schedule assumes availability of fiscal year (FY) 1996 preconstruction R&D funds.

Table VII.1-1 Complete Work Breakdown Structure

WBS Code	Element Description
1	IPNS UPGRADE (1 MW)
1.1	Project Management
1.1.1	Project Direction
1.1.2	Project Direction Support
1.2	Accelerator Systems
1.2.1	Injector System
1.2.1.1	Linac Injector System
1.2.1.2	DTL
1.2.1.3	Matching Section
1.2.1.4	SCL
1.2.1.5	DTL rf Systems
1.2.1.6	Matching Section rf Systems
1.2.1.7	SCL rf Systems
1.2.1.8	Beam Diagnostics
1.2.1.9	Control Systems
1.2.1.10	Documentation and Training
1.2.1.11	Installation
1.2.1.12	ANL Support
1.2.2	Main Accelerator System
1.2.2.1	Synchrotron
1.2.2.1.1	Magnets
1.2.2.1.1.1	Dipole Magnet
1.2.2.1.1.2	Quadrupole Magnet
1.2.2.1.1.3	Sextupole Magnet
1.2.2.1.1.4	Corrector Magnets
1.2.2.1.1.5	Injection (Inj.) Magnets
1.2.2.1.1.5.1	Inj. Septum A
1.2.2.1.1.5.2	Inj. Septum B
1.2.2.1.1.5.3	Inj. Bumper
1.2.2.1.1.6	Extraction (Extr.) Magnets
1.2.2.1.1.6.1	Extr. Kicker A
1.2.2.1.1.6.2	Extr. Kicker B
1.2.2.1.1.6.3	Extr. Kicker C
1.2.2.1.1.6.4	Extr. Septum C
1.2.2.1.1.6.5	Extr. Septum D
1.2.2.1.1.6.6	Extr. Septum E
1.2.2.1.1.7	Supports
1.2.2.1.1.8	Installation
1.2.2.1.1.9	Magnet ED&I[a]
1.2.2.1.2	Power Supplies
1.2.2.1.2.1	Power Supply Dipole
1.2.2.1.2.1.1	Power Supply Dipole
1.2.2.1.2.1.2	Installation and Wiring
1.2.2.1.2.2	Power Supply Quadrupole

Table VII.1-1 (Cont.)

WBS Code	Element Description
1.2.2.1.2.2.1	Power Supply Quadrupole
1.2.2.1.2.2.2	Installation and Wiring
1.2.2.1.2.3	Power Supply Sextupole
1.2.2.1.2.3.1	Power Supply Sextupole
1.2.2.1.2.3.2	Installation and Wiring
1.2.2.1.2.4	Injection Magnets
1.2.2.1.2.4.1	Power Supply Inj. Bumper
1.2.2.1.2.4.1.1	Power Supply Inj. Bumper
1.2.2.1.2.4.1.2	Installation and Wiring
1.2.2.1.2.4.2	Power Supply Inj. Septum
1.2.2.1.2.4.2.1	Power Supply Inj. Septum
1.2.2.1.2.4.2.2	Installation and Wiring
1.2.2.1.2.4.3	Power Supply Inj. Thick Septum
1.2.2.1.2.4.3.1	Power Supply Inj. Thick Septum
1.2.2.1.2.4.3.2	Installation and Wiring
1.2.2.1.2.5	Extraction Magnets
1.2.2.1.2.5.1	Power Supply Extr. Kicker
1.2.2.1.2.5.1.1	Power Supply Extr. Kicker
1.2.2.1.2.5.1.2	Installation and Wiring
1.2.2.1.2.5.2	Power Supply Extr. Thin Septum
1.2.2.1.2.5.2.1	Power Supply Extr. Thin Septum
1.2.2.1.2.5.2.2	Installation and Wiring
1.2.2.1.2.5.3	Power Supply Extr. Thick Septum
1.2.2.1.2.5.3.1	Power Supply Extr. Thick Septum
1.2.2.1.2.5.3.2	Installation and Wiring
1.2.2.1.2.6	Power Supply H/V Corrector
1.2.2.1.2.6.1	Power Supply H/V Corrector
1.2.2.1.2.6.2	Installation and Wiring
1.2.2.1.3	Vacuum
1.2.2.1.3.1	Vacuum Chambers
1.2.2.1.3.2	Pumping
1.2.2.1.3.3	Monitoring
1.2.2.1.3.4	Valves
1.2.2.1.3.5	Bellows
1.2.2.1.3.6	Misc. Vacuum Hardware
1.2.2.1.4	rf
1.2.2.1.4.1	rf Cavities
1.2.2.1.4.2	Power Amplifiers
1.2.2.1.4.3	Low-Level System
1.2.2.1.4.4	rf Effort
1.2.2.1.5	Diagnostics
1.2.2.1.5.1	Current Monitors
1.2.2.1.5.2	Position Monitors
1.2.2.1.5.3	Beam Loss System
1.2.2.1.5.4	Segmented Faraday Cups
1.2.2.1.5.5	Beam Scraper System

Table VII.1-1 (Cont.)

WBS Code	Element Description
1.2.2.1.5.6	Beam Excitation System
1.2.2.1.5.7	ED&I Effort
1.2.2.1.6	Controls/Interlocks
1.2.2.1.6.1	Network Infrastructure
1.2.2.1.6.2	Diagnostics Node
1.2.2.1.6.3	rf Node
1.2.2.1.6.4	Synchrotron Vacuum, Power Supply Node
1.2.2.1.6.5	Injector Systems Computer
1.2.2.1.6.6	Timing Node
1.2.2.1.6.7	Cable X-Bar Plant
1.2.2.1.6.8	Local Consoles
1.2.2.1.7	Personnel Access Control System
1.2.3	Beam Transports
1.2.3.1	Low-Energy Beam Transport
1.2.3.1.1	Magnets
1.2.3.1.1.1	Dipole Magnet
1.2.3.1.1.2	Quadrupole Magnet
1.2.3.1.1.3	Correction Magnet
1.2.3.1.1.4	Supports
1.2.3.1.1.5	Installation
1.2.3.1.1.6	Magnet ED&I
1.2.3.1.2	Power Supplies
1.2.3.1.2.1	Power Supply Dipole
1.2.3.1.2.1.1	Power Supply Dipole
1.2.3.1.2.1.2	Installation and Wiring
1.2.3.1.2.2	Power Supply Quadrupole
1.2.3.1.2.2.1	Power Supply Quadrupole
1.2.3.1.2.2.2	Installation and Wiring
1.2.3.1.2.3	Power Supply Horizontal/Vertical (HV) Corrector
1.2.3.1.2.3.1	Power Supply H/V Corrector
1.2.3.1.2.3.2	Installation and Wiring
1.2.3.1.3	Vacuum
1.2.3.1.3.1	Vacuum Chambers
1.2.3.1.3.2	Pumping
1.2.3.1.3.3	Monitoring
1.2.3.1.3.4	Valves
1.2.3.1.3.5	Bellows
1.2.3.1.3.6	Misc. Vacuum Hardware
1.2.3.1.5	Diagnostics
1.2.3.1.5.1	Current Monitors
1.2.3.1.5.2	Position Monitors
1.2.3.1.5.3	Beam Loss System
1.2.3.1.5.4	Profile Monitors
1.2.3.1.5.7	ED&I Effort
1.2.3.2	High-Energy Beam Transport

Table VII.1-1 (Cont.)

WBS Code	Element Description
1.2.3.2.1	Magnets
1.2.3.2.1.1	Dipole Magnet
1.2.3.2.1.2	Quadrupole Magnet
1.2.3.2.1.3	Correction Magnet
1.2.3.2.1.4	Supports
1.2.3.2.1.5	Installation
1.2.3.2.1.6	Magnet ED&I
1.2.3.2.2	Power Supplies
1.2.3.2.2.1	Power Supply Dipole (10-Hz transport)
1.2.3.2.2.1.1	Power Supply Dipole (10-Hz transport)
1.2.3.2.2.1.2	Installation and Wiring
1.2.3.2.2.2	Power Supply Quadrupole (10-Hz transport)
1.2.3.2.2.2.1	Power Supply Quadrupole (10-Hz transport)
1.2.3.2.2.2.2	Installation and Wiring
1.2.3.2.2.3	Power Supply H/V Corrector (10-Hz transport)
1.2.3.2.2.3.1	Power Supply H/V Corrector (10-Hz transport)
1.2.3.2.2.3.2	Installation and Wiring
1.2.3.3.2.4	Power Supply Dipole (30-Hz transport)
1.2.3.3.2.4.1	Power Supply Dipole (30-Hz transport)
1.2.3.3.2.4.2	Installation and Wiring
1.2.3.3.2.5	Power Supply Quadrupole (30-Hz transport)
1.2.3.3.2.5.1	Power Supply Quadrupole (30-Hz transport)
1.2.3.3.2.5.2	Installation and Wiring
1.2.3.3.2.6	Power Supply H/V Corrector (30-Hz transport)
1.2.3.3.2.6.1	Power Supply H/V Corrector (30-Hz transport)
1.2.3.3.2.6.2	Installation and Wiring
1.2.3.2.3	Vacuum
1.2.3.2.3.1	Vacuum Chambers
1.2.3.2.3.2	Pumping
1.2.3.2.3.3	Monitoring
1.2.3.2.3.4	Valves
1.2.3.2.3.5	Bellows
1.2.3.2.3.6	Misc. Vacuum Hardware
1.2.3.2.5	Diagnostics
1.2.3.2.5.1	Current Monitors
1.2.3.2.5.2	Position Monitors
1.2.3.2.5.3	Beam Loss System
1.2.3.2.5.4	Profile Monitors
1.2.3.2.5.5	Target Protection Monitor
1.2.3.2.5.7	ED&I Effort
1.2.4	Technical Support Systems
1.2.4.1	Central Control System
1.2.4.1.1	Central Control Computer System
1.2.4.1.1.1	File Server and Host Computer
1.2.4.1.1.2	Disk Drives
1.2.4.1.1.3	Printers

Table VII.1-1 (Cont.)

WBS Code	Element Description
1.2.4.1.1.4	Tape Drives
1.2.4.1.1.5	X Terminals
1.2.4.1.1.6	Central Network Equipment
1.2.4.1.1.7	Terminal Server Interface
1.2.4.1.1.8	Software Licenses
1.2.4.1.1.9	Operator Consoles
1.2.4.1.2	Control Consoles
1.2.4.1.2.1	Console Computers
1.2.4.1.2.2	Network Equipment
1.2.4.1.2.3	Engineering Development Computer
1.2.4.1.2.4	Software Licenses
1.2.4.1.2.5	Video Processors
1.2.4.1.2.6	Video Displays
1.2.4.1.2.7	Main Control Room Tables and Racks
1.2.4.1.2.8	Signal Display Systems
1.2.4.1.2.9	Cable Plant
1.2.4.1.3	Ancillary Control and Monitoring Equipment
1.2.4.1.3.1	Signal Analysis Instrumentation
1.2.4.1.3.2	Signal Oscilloscopes
1.2.4.1.3.3	Video Displays
1.2.4.1.3.4	Video Support Equipment
1.2.4.1.4	Networks
1.2.4.1.4.1	Network Infrastructure
1.2.4.1.4.2	Network Analysis Instrumentation
1.2.4.2	Survey and Alignment
1.2.4.2.1	Synchrotron Survey and Alignment
1.2.4.2.2	Injector and LET Survey and Alignment
1.2.4.2.3	HET Survey and Alignment
1.2.4.2.4	Survey and Alignment Hardware
1.2.4.3	Magnet Measurement
1.2.4.3.1	Magnet Measurement
1.3	Targets and Instruments
1.3.1	Target Stations
1.3.1.1	30-Hz Target Station
1.3.1.1.1	Target System
1.3.1.1.1.1	Target Assembly
1.3.1.1.1.2	Target Cooling System
1.3.1.1.1.3	Target Steel-Shield Plug
1.3.1.1.1.4	Target Sealed Tank
1.3.1.1.1.5	Target-Train Housing
1.3.1.1.1.6	Target Tank Cooling
1.3.1.1.1.7	Proton Beamline Vacuum Window Insert Cooling System
1.3.1.1.2	Moderators
1.3.1.1.2.1	Moderator Assemblies
1.3.1.1.2.1.1	Room Temperature Moderator Assembly

Table VII.1-1 (Cont.)

WBS Code	Element Description
1.3.1.1.2.1.2	Liquid H2 Moderator Assembly
1.3.1.1.2.1.3	Liquid H2 Premoderator Assembly
1.3.1.1.2.1.4	Liquid CH4 Moderator Assembly
1.3.1.1.2.1.5	Liquid CH4 Premoderator Assembly
1.3.1.1.2.2	Moderator Cooling
1.3.1.1.2.2.1	Premoderator and Room Temperature Moderator Cooling
1.3.1.1.2.2.2	Liquid H2 Moderator Cooling
1.3.1.1.2.2.3	Liquid CH4 Moderator Cooling
1.3.1.1.3	Reflector
1.3.1.1.3.1	Reflector Assembly
1.3.1.1.3.2	Reflector Cooling
1.3.1.1.4	Containment Systems
1.3.1.1.4.1	Bulk Shield Sealed Tank
1.3.1.1.4.2	Holdup System
1.3.1.1.4.3	He Supply System
1.3.1.1.4.4	HEPA Filter and Exhaust System
1.3.1.1.5	Remote Handling System
1.3.1.1.5.1	Hot Cell Accessories
1.3.1.1.5.2	Long-Term Storage Enclosures
1.3.1.1.6	Instrumentation and Control (I&C)
1.3.1.1.6.1	Target Monitoring System
1.3.1.1.6.1.1	Target Temperature Monitoring
1.3.1.1.6.1.2	Target Physical Parameter Monitoring
1.3.1.1.6.1.3	Target Cooling System Monitoring
1.3.1.1.6.2	Moderator Monitoring and Control
1.3.1.1.6.2.1	Moderator Temperature Monitoring
1.3.1.1.6.2.2	Moderator Coolant Flow Monitoring
1.3.1.1.6.2.3	Moderator Vacuum Monitoring
1.3.1.1.6.2.4	Moderator Composition Monitoring
1.3.1.1.6.3	Reflector Monitoring
1.3.1.1.6.4	Bulk Shield Monitoring
1.3.1.1.6.5	Radiation Monitoring
1.3.1.1.6.6	Accelerator I&C Interface
1.3.1.1.6.7	Accelerator Shutdown Interface
1.3.1.1.7	Beamlines (in bulk shield)
1.3.1.1.7.1	Beamline Assemblies
1.3.1.1.7.2	Beam Gates
1.3.1.1.8	Bulk Shielding
1.3.1.1.8.1	Biological Shield Assembly
1.3.1.1.8.2	Shield Cooling
1.3.1.1.8.3	Shield Structural Support
1.3.1.1.10	Piping Supports, Insulation, and Misc.
1.3.1.1.11	Liquid Nitrogen System
1.3.1.1.12	Pumproom Biological Shield
1.3.1.1.13	Relocate Existing 370 Tunnel Piping and Utilities

Table VII.1-1 (Cont.)

WBS Code	Element Description
1.3.1.1.14	Inside 370 Sub-Floor Piping Work
1.3.1.1.15	Outside 370 Below-Ground Piping
1.3.1.1.16	Target Group Management
1.3.1.2	10-Hz Target Station
1.3.1.2.1	Target System
1.3.1.2.1.1	Target Assembly
1.3.1.2.1.2	Target Cooling System
1.3.1.2.1.3	Target Steel-Shield Plug
1.3.1.1.1.4	Target Sealed Tank
1.3.1.2.1.5	Target-Train Housing
1.3.1.2.1.6	Target Tank Cooling
1.3.1.2.1.7	Proton Beamline Vacuum Window Insert Cooling System
1.3.1.2.2	Moderators
1.3.1.2.2.1	Moderator Assemblies
1.3.1.2.2.1.1	Room Temperature Moderator Assembly
1.3.1.2.2.1.2	Liquid H2 Moderator Assembly
1.3.1.2.2.1.3	Liquid H2 Premoderator Assembly
1.3.1.2.2.1.4	Liquid CH4 Moderator Assembly
1.3.1.2.2.1.5	Liquid CH4 Premoderator Assembly
1.3.1.2.2.2	Moderator Cooling
1.3.1.2.2.2.1	Premoderator and Room Temperature Moderator Cooling
1.3.1.2.2.2.2	Liquid H2 Moderator Cooling
1.3.1.2.2.2.3	Liquid CH4 Moderator Cooling
1.3.1.2.3	Reflector
1.3.1.2.3.1	Reflector Assembly
1.3.1.2.3.2	Reflector Cooling
1.3.1.2.4	Containment Systems
1.3.1.2.4.1	Bulk Shield Sealed Tank
1.3.1.2.4.2	Holdup System
1.3.1.2.4.3	He Supply System
1.3.1.2.4.4	HEPA Filter and Exhaust System
1.3.1.2.5	Remote Handling System
1.3.1.2.5.1	Hot Cell Accessories
1.3.1.2.5.2	Long-Term Storage Enclosures
1.3.1.2.6	Control and Instrumentation
1.3.1.2.6.1	Target Monitoring System
1.3.1.2.6.1.1	Target Temperature Monitoring
1.3.1.2.6.1.2	Target Physical Parameter Monitoring
1.3.1.2.6.1.3	Target Cooling System Monitoring
1.3.1.2.6.2	Moderator Monitoring and Control
1.3.1.2.6.2.1	Moderator Temperature Monitoring
1.3.1.2.6.2.2	Moderator Coolant Flow Monitoring
1.3.1.2.6.2.3	Moderator Vacuum Monitoring
1.3.1.2.6.2.4	Moderator Composition Monitoring
1.3.1.2.6.3	Reflector Monitoring
1.3.1.2.6.4	Bulk Shield Monitoring

Table VII.1-1 (Cont.)

WBS Code	Element Description
1.3.1.2.6.5	Radiation Monitoring
1.3.1.2.6.6	Accelerator I&C Interface
1.3.1.2.6.7	Accelerator Shutdown Interface
1.3.1.2.7	Beamlines (in bulk shield)
1.3.1.2.7.1	Beamline Assemblies
1.3.1.2.7.2	Beam Gates
1.3.1.2.8	Bulk Shielding
1.3.1.2.8.1	Biological Shield Assembly
1.3.1.2.8.2	Shield Cooling
1.3.1.2.8.3	Shield Structural Support
1.3.1.2.10	Piping Supports, Insulation, and Misc.
1.3.1.2.11	Liquid Nitrogen System
1.3.1.2.12	Pumproom Biological Shield
1.3.1.2.13	Inside 369 Methane Piping and Shielding
1.3.1.2.14	Outside 369 Below-Ground Piping
1.3.1.2.15	Target Group Management
1.3.2	Instruments and Support
1.3.2.1	Powder Diffractometers
1.3.2.1.1	SEPD - High Intensity Powder Diffractometer
1.3.2.1.2	GPPD - Medium-Resolution Powder Diffractometer
1.3.2.1.3	HRPD - High-Resolution Powder Diffractometer
1.3.2.1.4	RSD - Residual Stress Diffractometer
1.3.2.1.5	VSPD - Very-Small-Sample Powder Diffractometer
1.3.2.2	Small-Angle Diffractometers
1.3.2.2.1	SAND - General-Purpose Small-Angle Diffractometer
1.3.2.2.2	HRSAND - High-Resolution Small-Angle Diffractometer
1.3.2.2.3	SPSAND - Special-Purpose Small-Angle Diffractometer
1.3.2.3	Other Diffractometers
1.3.2.3.1	GLAD - Liquids and Amorphous Materials Diffractometer
1.3.2.3.2	SCD - General-Purpose Single-Crystal Diffractometer
1.3.2.3.3	HQSCD - High-Q Single-Crystal Diffractometer
1.3.2.4	Reflectometers
1.3.2.4.1	POSY-I - Polarized-Neutron Reflectometer
1.3.2.4.2	POSY-II - General-Purpose Reflectometer
1.3.2.4.3	HIREF - High-Intensity Reflectometer
1.3.2.4.4	GREF - Reflectometer for Grazing-Incidence Scattering
1.3.2.4.5	REFD - Reflectometry Development Beam
1.3.2.5	Inelastic Scattering Instruments
1.3.2.5.1	HRMECS - High-Resolution Chopper Spectrometer
1.3.2.5.2	LRMECS - General-Purpose Chopper Spectrometer
1.3.2.5.3	CNCS - Cold-Neutron Chopper Spectrometer
1.3.2.5.4	SCCS - Chopper Spectrometer for Single Crystals
1.3.2.6	Crystal-Analyzer Inelastic Scattering Instruments

Table VII.1-1 (Cont.)

WBS Code	Element Description
1.3.2.6.1	QENS - Medium-Resolution Crystal-Analyzer Spectrometer
1.3.2.6.2	HRBS - High-Resolution Backscattering Spectrometer
1.3.2.6.3	TFCA - Time-Focused Crystal Analyzer Spectrometer
1.3.2.6.4	QSTAXC - Cold-Neutron Quasi-Steady-State Triple-Axis Spectr.
1.3.2.6.5	MICAS - Multiple-Independent-Crystal-Analyzer Spectrometer
1.3.2.7	Other Inelastic Scattering Instruments
1.3.2.7.1	TOFNSE - Time-of-Flight Neutron Spin-Echo Spectrometer
1.3.2.8	Other Neutron Beam Facilities
1.3.2.8.1	DEVEL - Instrument/Component Development Beamline
1.3.2.9	Neutron Irradiation Facility
1.3.2.9.1	30-Hz Target Neutron Irradiation Facility
1.3.2.9.1.1	Irradiation Facility Sampling, Handling, and Preparation System
1.3.2.9.1.2	Irradiation Facility Sampling and Monitoring System
1.3.2.9.2	10-Hz Target Neutron Irradiation Facility
1.3.2.9.2.1	Irradiation Facility Sampling, Handling, and Preparation System
1.3.2.9.2.2	Irradiation Facility Sampling and Monitoring System
1.3.2.9.3	Activation Analysis Counting System
1.3.2.10	Data Analysis Systems
1.3.2.11	Ancillary Equipment
1.3.2.12	Sample Preparation Area
1.3.2.13	Hot Cell Handling Area
1.3.2.14	Instrumentation Group Management
1.4	Conventional Facilities
1.4.1	Existing Building Rehabilitation
1.4.1.1	Ring Building (365)
1.4.1.1.1	Architectural/Structural
1.4.1.1.1.1	General Demolition
1.4.1.1.1.2	Substructure
1.4.1.1.1.3	Superstructure
1.4.1.1.1.4	Exterior Closure
1.4.1.1.1.5	Roofing
1.4.1.1.1.6	Partitions and Doors
1.4.1.1.1.7	Finishes
1.4.1.1.1.8	Specialties
1.4.1.1.2	Mechanical
1.4.1.1.2.1	Mechanical Demolition
1.4.1.1.2.2	Plumbing
1.4.1.1.2.3	Heating, Ventilation, and Air Conditioning
1.4.1.1.2.4	Fire Protection
1.4.1.1.3	Electrical
1.4.1.1.3.1	Electrical Demolition
1.4.1.1.3.2	Service and Distribution

Table VII.1-1 (Cont.)

WBS Code	Element Description
1.4.1.1.3.3	Lighting and Power
1.4.1.1.3.4	Special Systems
1.4.1.1.4	Civil
1.4.1.1.4.1	Site Works
1.4.1.1.5	Shielding
1.4.1.2	Center Building (364)
1.4.1.2.1	Architectural/Structural
1.4.1.2.1.1	General Demolition
1.4.1.2.1.2	Substructure
1.4.1.2.1.3	Superstructure
1.4.1.2.1.4	Exterior Closure
1.4.1.2.1.5	Roofing
1.4.1.2.1.6	Partitions and Doors
1.4.1.2.1.7	Finishes
1.4.1.2.1.8	Specialties
1.4.1.2.2	Mechanical
1.4.1.2.2.1	Mechanical Demolition
1.4.1.2.2.2	Plumbing
1.4.1.2.2.3	Heating, Ventilation, and Air Conditioning
1.4.1.2.2.4	Fire Protection
1.4.1.2.3	Electrical
1.4.1.2.3.1	Electrical Demolition
1.4.1.2.3.2	Service and Distribution
1.4.1.2.3.3	Lighting and Power
1.4.1.2.3.4	Special Systems
1.4.1.2.4	Civil
1.4.1.2.4.1	Site Works
1.4.1.3	Power Supply Building (376)
1.4.1.3.1	Architectural/Structural
1.4.1.3.1.1	General Demolition
1.4.1.3.1.2	Substructure
1.4.1.3.1.3	Superstructure
1.4.1.3.1.4	Exterior Closure
1.4.1.3.1.5	Roofing
1.4.1.3.1.6	Partitions and Doors
1.4.1.3.1.7	Finishes
1.4.1.3.1.8	Specialties
1.4.1.3.2	Mechanical
1.4.1.3.2.1	Mechanical Demolition
1.4.1.3.2.2	Plumbing
1.4.1.3.2.3	Heating, Ventilation, and Air Conditioning
1.4.1.3.2.4	Fire Protection
1.4.1.3.3	Electrical
1.4.1.3.3.1	Electrical Demolition
1.4.1.3.3.2	Service and Distribution

Table VII.1-1 (Cont.)

WBS Code	Element Description
1.4.1.3.3.3	Lighting and Power
1.4.1.3.3.4	Special Systems
1.4.1.3.4	Civil
1.4.1.3.4.1	Site Works
1.4.1.4	10-Hz Target Building (369)
1.4.1.4.1	Architectural/Structural
1.4.1.4.1.1	General Demolition
1.4.1.4.1.2	Substructure
1.4.1.4.1.3	Superstructure
1.4.1.4.1.4	Exterior Closure
1.4.1.4.1.5	Roofing
1.4.1.4.1.6	Partitions and Doors
1.4.1.4.1.7	Finishes
1.4.1.4.1.8	Specialties
1.4.1.4.2	Mechanical
1.4.1.4.2.1	Mechanical Demolition
1.4.1.4.2.2	Plumbing
1.4.1.4.2.3	Heating, Ventilation, and Air Conditioning
1.4.1.4.2.4	Fire Protection
1.4.1.4.3	Electrical
1.4.1.4.3.1	Electrical Demolition
1.4.1.4.3.2	Service and Distribution
1.4.1.4.3.3	Lighting and Power
1.4.1.4.3.4	Special Systems
1.4.1.4.4	Civil
1.4.1.4.4.1	Site Works
1.4.1.4.5	Shielding
1.4.1.5	10-Hz Target Support Building (367)
1.4.1.5.1	Architectural/Structural
1.4.1.5.1.1	General Demolition
1.4.1.5.1.2	Substructure
1.4.1.5.1.3	Superstructure
1.4.1.5.1.4	Exterior Closure
1.4.1.5.1.5	Roofing
1.4.1.5.1.6	Partitions and Doors
1.4.1.5.1.7	Finishes
1.4.1.5.1.8	Specialties
1.4.1.5.2	Mechanical
1.4.1.5.2.1	Mechanical Demolition
1.4.1.5.2.2	Plumbing
1.4.1.5.2.3	Heating, Ventilation, and Air Conditioning
1.4.1.5.2.4	Fire Protection
1.4.1.5.3	Electrical
1.4.1.5.3.1	Electrical Demolition
1.4.1.5.3.2	Service and Distribution

Table VII.1-1 (Cont.)

WBS Code	Element Description
1.4.1.5.3.3	Lighting and Power
1.4.1.5.3.4	Special Systems
1.4.1.5.4	Civil
1.4.1.5.4.1	Site Works
1.4.1.5.5	Shielding
1.4.1.6	30-Hz Target Building (370)
1.4.1.6.1	Architectural/Structural
1.4.1.6.1.1	General Demolition
1.4.1.6.1.2	Substructure
1.4.1.6.1.3	Superstructure
1.4.1.6.1.4	Exterior Closure
1.4.1.6.1.5	Roofing
1.4.1.6.1.6	Partitions and Doors
1.4.1.6.1.7	Finishes
1.4.1.6.1.8	Specialties
1.4.1.6.2	Mechanical
1.4.1.6.2.1	Mechanical Demolition
1.4.1.6.2.2	Plumbing
1.4.1.6.2.3	Heating, Ventilation, and Air Conditioning
1.4.1.6.2.4	Fire Protection
1.4.1.6.3	Electrical
1.4.1.6.3.1	Electrical Demolition
1.4.1.6.3.2	Service and Distribution
1.4.1.6.3.3	Lighting and Power
1.4.1.6.3.4	Special Systems
1.4.1.6.4	Civil
1.4.1.6.4.1	Site Works
1.4.1.6.5	Shielding
1.4.1.7	30-Hz Target Support Building (371)
1.4.1.7.1	Architectural/Structural
1.4.1.7.1.1	General Demolition
1.4.1.7.1.2	Substructure
1.4.1.7.1.3	Superstructure
1.4.1.7.1.4	Exterior Closure
1.4.1.7.1.5	Roofing
1.4.1.7.1.6	Partitions and Doors
1.4.1.7.1.7	Finishes
1.4.1.7.1.8	Specialties
1.4.1.7.2	Mechanical
1.4.1.7.2.1	Mechanical Demolition
1.4.1.7.2.2	Plumbing
1.4.1.7.2.3	Heating, Ventilation, and Air Conditioning
1.4.1.7.2.4	Fire Protection
1.4.1.7.3	Electrical
1.4.1.7.3.1	Electrical Demolition

Table VII.1-1 (Cont.)

WBS Code	Element Description
1.4.1.7.3.2	Service and Distribution
1.4.1.7.3.3	Lighting and Power
1.4.1.7.3.4	Special Systems
1.4.1.7.4	Civil
1.4.1.7.4.1	Site Works
1.4.1.7.5	Shielding
1.4.1.8	Preparation Laboratories Building (368)
1.4.1.8.1	Architectural/Structural
1.4.1.8.1.1	General Demolition
1.4.1.8.1.2	Substructure
1.4.1.8.1.3	Superstructure
1.4.1.8.1.4	Exterior Closure
1.4.1.8.1.5	Roofing
1.4.1.8.1.6	Partitions and Doors
1.4.1.8.1.7	Finishes
1.4.1.8.1.8	Specialties
1.4.1.8.2	Mechanical
1.4.1.8.2.1	Mechanical Demolition
1.4.1.8.2.2	Plumbing
1.4.1.8.2.3	Heating, Ventilation, and Air Conditioning
1.4.1.8.2.4	Fire Protection
1.4.1.8.3	Electrical
1.4.1.8.3.1	Electrical Demolition
1.4.1.8.3.2	Service and Distribution
1.4.1.8.3.3	Lighting and Power
1.4.1.8.3.4	Special Systems
1.4.1.8.4	Civil
1.4.1.8.4.1	Site Works
1.4.1.8.5	Shielding
1.4.1.9	Laboratory and Office Building I (360)
1.4.1.9.1	Architectural/Structural
1.4.1.9.1.1	General Demolition
1.4.1.9.1.2	Substructure
1.4.1.9.1.3	Superstructure
1.4.1.9.1.4	Exterior Closure
1.4.1.9.1.5	Roofing
1.4.1.9.1.6	Partitions and Doors
1.4.1.9.1.7	Finishes
1.4.1.9.1.8	Specialties
1.4.1.9.2	Mechanical
1.4.1.9.2.1	Mechanical Demolition
1.4.1.9.2.2	Plumbing
1.4.1.9.2.3	Heating, Ventilation, and Air Conditioning
1.4.1.9.2.4	Fire Protection
1.4.1.9.3	Electrical

Table VII.1-1 (Cont.)

WBS Code	Element Description
1.4.1.9.3.1	Electrical Demolition
1.4.1.9.3.2	Service and Distribution
1.4.1.9.3.3	Lighting and Power
1.4.1.9.3.4	Special Systems
1.4.1.9.4	Civil
1.4.1.9.4.1	Site Works
1.4.1.10	Laboratory and Office Building II (362)
1.4.1.10.1	Architectural/Structural
1.4.1.10.1.1	General Demolition
1.4.1.10.1.2	Substructure
1.4.1.10.1.3	Superstructure
1.4.1.10.1.4	Exterior Closure
1.4.1.10.1.5	Roofing
1.4.1.10.1.6	Partitions and Doors
1.4.1.10.1.7	Finishes
1.4.1.10.1.8	Specialties
1.4.1.10.2	Mechanical
1.4.1.10.2.1	Mechanical Demolition
1.4.1.10.2.2	Plumbing
1.4.1.10.2.3	Heating, Ventilation, and Air Conditioning
1.4.1.10.2.4	Fire Protection
1.4.1.10.3	Electrical
1.4.1.10.3.1	Electrical Demolition
1.4.1.10.3.2	Service and Distribution
1.4.1.10.3.3	Lighting and Power
1.4.1.10.3.4	Special Systems
1.4.1.10.4	Civil
1.4.1.10.4.1	Site Works
1.4.2	New Construction
1.4.2.1	Injector - Linac Building, Tunnel, and LET (394 and 394-A)
1.4.2.1.1	Architectural/Structural
1.4.2.1.1.1	General Demolition
1.4.2.1.1.2	Substructure
1.4.2.1.1.3	Superstructure
1.4.2.1.1.4	Exterior Closure
1.4.2.1.1.5	Roofing
1.4.2.1.1.6	Partitions and Doors
1.4.2.1.1.7	Finishes
1.4.2.1.1.8	Specialties
1.4.2.1.2	Mechanical
1.4.2.1.2.1	Mechanical Demolition
1.4.2.1.2.2	Plumbing
1.4.2.1.2.3	Heating, Ventilation, and Air Conditioning
1.4.2.1.2.4	Fire Protection
1.4.2.1.3	Electrical

Table VII.1-1 (Cont.)

WBS Code	Element Description
1.4.2.1.3.1	Electrical Demolition
1.4.2.1.3.2	Service and Distribution
1.4.2.1.3.3	Lighting and Power
1.4.2.1.3.4	Special Systems
1.4.2.1.4	Civil
1.4.2.1.4.1	Site Works
1.4.2.1.5	Shielding
1.4.3	Utilities
1.4.3.1	Site Work
1.4.3.2	Mechanical Site Utilities
1.4.3.3	Electrical Site Utilities
1.4.4	Conventional Facilities EDI&A[b]
1.5	Shielding Structures
1.5.1	High-Energy Proton Transport Shielding
1.5.1.1	Low-Frequency PTS Shielding
1.5.1.2	High-Frequency PTS Shielding
1.5.2	30-Hz Target Shielding
1.5.2.1	Biological Shield Assembly
1.5.2.2	Biological Shield Structural Support
1.5.3	10-Hz Target Shielding
1.5.3.1	Biological Shield Assembly
1.5.3.2	Biological Shield Structural Support
1.8	Misc. Costs
1.8.1	Overheads
1.8.1.1	Materials and Subcontracts (@6.2%)
1.8.1.2	Common Support (@19.2%)
1.8.1.3	General and Adm. (@1.9%)
1.8.2	Unproductive Time
1.9	Contingency

[a] ED&I = engineering, design, and inspection.

[b] EDI&A = engineering, design, inspection, and administration.

All cost estimates include engineering, design, and inspection (ED&I) and hardware deliverables. Fiscal year 1995 dollars are used throughout. Crafts needed for construction are grouped into three categories, and details of the crafts used and their rates are shown in Table VII.2-1. Contingency is addressed at the estimating stage and is discussed later in this section. Escalation is added after the budget profile is applied. The escalation rates used for this purpose come from a collection of DOE rates provided annually by DOE-Chicago and accumulated by the APS project; these rates are shown in Table VII.2-2.

The project cost detail corresponding to each element of the WBS list shown in Table VII.1-1 is appended in two separate books, Supplement A for technical components and Supplement B for conventional facilities. The project cost summary, rolled up from these books, is shown in Table VII.2-3 in FY 1995 dollars. The costs are broken down into three categories: (a) ED&I cost, (b) construction cost, and (c) contingency. Each category is further subdivided to provide detail corresponding to Level 3 of the WBS. The costs for technical components, excluding the injector linac, are rolled up from detailed WBS sheets generated by the ANL staff that show all hardware and effort costs for each item, from design through installation and checkout. The costs for the injector linac and its associated technical components were estimated by the industrial firm AccSys Technology, Inc., of Pleasanton, California. One of the options under consideration is a turn-key procurement of the injector system from industry. The costs for conventional facilities are estimates generated by the construction consulting firm of Hanscomb Associates, Inc. (see Supplement B), and are based on designs by ANL staff from APS and PFS.

The project management costs shown in Table VII.2-3 consist of four parts:

1. *Project Management Costs.* These are the costs of personnel involved in project direction and coordination, together with the costs associated with compliance with environment, safety, and health (ES&H) requirements.

2. *Laboratory Overhead.* The Laboratory recovers its indirect expenses, which are the costs associated with administration (functions such as personnel, accounting, and procurement) and maintenance of physical facilities, by means of charges against the funds received for operations, which are commonly known as operating funds — in contrast to (1) capital equipment funds, which are used for equipment fabrication or purchase, and (2) plant funds, which are used for the construction project. Indirect Laboratory costs were previously recovered through a charge of 26.9% applied to all in-house direct operating costs. Construction projects, which usually add only incrementally to indirect expenses, contribute a smaller amount to cover indirect expenses. Under the old Laboratory policy, this cost recovery was achieved by a charge of 26.9% that was applied only to the in-house Laboratory project management and ED&I effort costs and not to other costs. The overhead for the APS Project under this rule was 22%, which was applied only to the in-house ED&I and

Table VII.2-1 Craft Code Rate for 1995

Item	Craft Code	Rate ($/hour)
Manufacturing/Fabrication/Assembly/Test[a]		
Technician (assembly, test, etc.), relatively unskilled	T1	25.00
Technician (assembly, test, etc.), experienced/skilled	T2	33.00
Shops (average capability machinists, fab, etc.)	S1	50.00
Shops (specialized, precision, high tech, etc.)	S2	55.00
Factory support (parts handling, inspections, QA, etc.)	F1	45.00
Factory support (superv., managers, prod. engineers, etc.)	F2	55.00
Installation ("Davis-Bacon")[a]		
Plumber, steam fitter, sheet metal worker, pipefitter	IP	56.00
Electrician	IE	54.00
Carpenter, painter, rigger, crane operator	IC	51.00
Laborer	IL	42.00
Technician	IT	54.00
Technical Engineering, Design, and Inspection (ED&I)[b]		
Physicist	PH	49.00
Engineer (mechanical and electrical)	EN	49.00
Computer software designer	SW	49.00
Designer/coordinator	DC	39.00
Drafter	DR	30.00
Management[b]		
Manager	MN	49.00
Secretary	SS	31.00

[a] The rate in this category includes hourly base pay, employee benefits and overhead, and profit for the outside vendor or contractor.

[b] The rate in this category includes hourly base pay and employee benefits, but it does not include laboratory overhead, which is included in a separate category.

Table VII.2-2 Escalation Rates

Fiscal Year	Inflation (%)	Scaling Factor
1995	–	1.000
1996	3.8	1.038
1997	3.9	1.078
1998	3.8	1.119
1999	3.6	1.159
2000	3.6	1.201
2001	3.6	1.244

Table VII.2-3 Project Cost Breakdown by Major Categories (FY 1995 k$)

A. Engineering, Design, and Inspection				43,158
1. Technical Components	16%		38,043	
a. Injector System	7%	3,965		
b. Synchrotron	22%	13,377		
c. Beam Transports	20%	2,744		
d. Technical Support Systems	34%	2,503		
e. Target Stations	31%	6,394		
f. Instrumentation and Support	14%	7,619		
g. Shielding Structures	5%	1,442		
2. Conventional Facilities (EDI&A)	13%		5,115	
B. Construction Costs				356,815
1. Technical Components			242,461	
a. Injector System		58,098		
b. Synchrotron		62,186		
c. Beam Transports		13,579		
d. Technical Support Systems		7,330		
e. Target Stations		20,616		
f. Instrumentation and Support		52,562		
g. Shielding Structures		28,090		
2. Conventional Facilities			40,921	
a. Existing Bldg. Rehabilitation		24,824		
b. New Construction		7,393		
c. Utilities		8,703		
3. Project Management			73,433	
a. Management Cost		10,102		
b. Laboratory Overhead Cost		44,527		
c. Unproductive Time		8,059		
d. M&S for Staff		10,745		
C. Contingency				78,066
1. ED&I	22%		9,559	
2. Technical Components	21%		51,950	
3. Conventional Facilities	21%		8,775	
4. Project Management	11%		7,782	
TOTAL PROJECT CONSTRUCTION COST				478,039

project-management effort costs. As of FY 1995, the new DOE policy is to collect indirect costs by using a graduated scale. The Laboratory now charges 6.2% for direct materials and subcontracts procurement and 19.2% for all other common support expenses. In addition to these charges of 6.2% and 19.2%, there is a charge of 1.9% of all costs for all general and administrative costs.

The indirect charge to be borne by this construction project under the new policy is $44.5 million in FY 1995 dollars. This number is to be compared with $14.2 million under the old policy.

3. *Materials and Services Costs*. These are the M&S costs of the Laboratory direct personnel in the project and are estimated to be 20% of the effort costs.

4. *Unproductive Time Costs for ANL Staff*. Under new DOE policy, vacation and holiday time accrued by the project personnel must be accounted for separately. The budgeted amount for this category is calculated by allocating 15.0% of the direct personnel effort costs.

It should be noted that inclusion of the last three items is necessitated by the fact that the craft code and craft rate shown in Table VII.2-1 for engineering, design, inspection, and administration (EDI&A) personnel only takes into account the hourly base pay and benefits.

The contingency costs are applied to the rate shown in Table VII.2-3. The rates shown for ED&I and technical components are averages for individual components and reflect the completeness of the design, uncertainties, and variability of market conditions. For example, a relatively high rate of 35% is assigned to some of the neutron-generating target components because the design of the target is somewhat uncertain at this time. The rate for conventional facilities is based on estimates by Hanscomb Associates, Inc.

The contents of Table VII.2-3 can be rearranged to show the project cost profile by the major cost components. This is shown in Table VII.2-4.

The cost schedule that takes into account escalation and budget time profile is discussed in Section VII.4.

Table VII.2-4 Project Cost Breakdown by WBS Code

WBS Code	Description	Cost in FY 1995 (k$)	Total Cost in FY 1995[a] (k$)
1	Total Estimated Construction Cost		478,039
1.1	Project Management	10,102	
1.2	Accelerator Systems		163,781
1.2.1	Injector System	58,098	
1.2.2	Synchrotron	62,186	
1.2.3	Beam Transports	13,579	
1.2.4	Support Systems	7,330	
1.2.5	Accelerator Systems ED&I	22,589	
1.3	Targets and Instrumentation		87,191
1.3.1	Target Stations	20,616	
1.3.2	Instrumentation and Support	52,562	
1.3.3	Targets and Instrumentation ED&I	14,012	
1.4	Conventional Facilities		46,036
1.4.1	Existing Building Rehabilitation	24,824	
1.4.2	New Construction	7,393	
1.4.3	Utilities	8,703	
1.4.4	Conventional Facilities EDI&A	5,115	
1.5	Shielding Structures		29,531
1.5.1	High Energy Proton Transfer Line Shielding	7,849	
1.5.2	10-Hz Target Shielding	10,120	
1.5.3	30-Hz Target Shielding	10,120	
1.5.4	Shielding ED&I	1,442	
1.8	Miscellaneous Costs		63,331
1.8.1	Laboratory Overheads	44,527	
1.8.2	Unproductive Time	8,059	
1.8.3	M&S for Staff	10,745	
1.9	Contingency		78,066

[a] Numbers are spreadsheet-generated, and costs may not exactly add up to totals because of rounding.

The schedule is based on the assumptions that (1) the construction project starts in FY 1997 and (2) there are sufficient funds to carry out preconstruction R&D and construction planning, including environmental assessment between FY 1996 and FY 1998. The preconstruction R&D activities are described in Appendix B. In addition, the following concepts have been incorporated in scheduling the construction:

- DOE Headquarters Key Decision (KD) milestones, KD 0 and KD 1, are met at the middle of fiscal years 1995 and 1996, respectively.

- With the KD 0 milestone, the environmental assessment process commences. National Environmental Protection Act (NEPA) and other permit requests are submitted soon after KD0.

- For optimal project efficiency, front loading of the project is exercised wherever possible.

- Design, construction, and installation periods for technical components used in the scheduling are based on experiences of accelerator personnel in this Laboratory, particularly at the APS; at other laboratories, such as the European Synchrotron Radiation Facility (ESRF); and on vendor quotations.

- All technical components of a subsystem to be installed in a building will be assembled and tested beforehand to maintain an optimal installation schedule with a relatively uniform level of effort.

- The existence of technical component assembly areas used to support the APS construction and of technical component support facilities, such as the magnet measuring facility and survey and alignment facility, has been taken into account in making the accelerator schedule.

- The conventional construction (rehabilitation) schedule of beneficial occupancy provided by PFS and APS conventional facilities personnel is used to determine the accelerator and target station schedules.

- Sequential commissioning of two major accelerators is planned. The first accelerator to be commissioned is the linac system. Six months after the linac is commissioned, the RCS is scheduled to be commissioned. Another six months after the synchrotron is commissioned, the commissioning of the neutron-generating target stations takes place.

Figure VII.3-1 shows the conventional facilities schedule, and Figures VII.3-2a through VII.3-2k show the technical component schedules. These figures also show the key technical component R&D schedules that are phased into the construction schedule. Figure VII.3-3 is the project critical path diagram for the major components of the project at Level 3 of the WBS. As the project design progresses, a more detailed critical path analysis at Level 4 and below will be

established and will be used to monitor the progress of the project. As shown in Figure VII.3-3, the commissioning of the synchrotron begins at the start of FY 2000, with neutron beam lines in routine operation beginning in the third quarter of FY 2001.

CONVENTIONAL FACILITIES SCHEDULE

Fiscal Year	FY95	FY96	FY97	FY98	FY99	FY00	FY01
KD 0 Milestone	❖						
KD 1 Milestone		❖					
E/A	▨	▨					
NEPA and Other Permits		▨	▨				
Construction Start Milestone			❖				
DESIGN							
Title I			▨				
Final Design			▨	▨			
CONSTRUCTION							
Linac, Klystron Gallery and LET Tunnel				▨	▨		
(New Construction for Linac)							
Center Building and Ring Building				▨	▨		
(Buildings 364 and 365)							
Magnet Power Supplies Building					▨		
(Building 376)							
Target Buildings			▨				
(Buildings 369 and 370)							
Target Support Buildings				▨			
(Buildings 367 and 371)							
Utilities				▨	▨		
All Other Buildings Rehab and Site						▨	
Commissioning Starts Milestone						❖	
Commissioning Ends Milestone							❖

Figure VII.3-1 Conventional Facilities Schedule.

LINAC SYSTEM SCHEDULE

Fiscal Year	FY95	FY96	FY97	FY98	FY99	FY00	FY01
KD 0 Milestone	❖						
KD 1 Milestone		❖					
Construction Start Milestone			❖				
R&D							
Ion Source R&D		▨					
RFQ R&D			▨				
CCL R&D			▨				
DESIGN / CONSTRUCTION							
Linac System Design			▨	▨			
DTL Procurement Milestone			❖				
CCL Procurement Milestone				❖			
Linac Building, Linac Tunnel & LET Tunnel					❖		
(Beneficial Occupancy Milestone)							
Linac Component Delivery					▨	▨	
Linac Component Testing					▨	▨	
Linac Installation/Check Out						▨	
Linac Commissioning Milestone						❖	
Commissioning Starts Milestone							❖
Commissioning Ends Milestone							❖

Figure VII.3-2a Linac System Schedule.

SYNCHROTRON MAGNET SCHEDULE

Fiscal Year	FY95	FY96	FY97	FY98	FY99	FY00	FY01
KD 0 Milestone	❖						
KD 1 Milestone		❖					
Construction Start Milestone			❖				
R&D							
Magnets Performance Design R&D	▨▨▨	▨▨▨					
DESIGN / CONSTRUCTION							
Magnets Engineering Design			▨▨▨				
Magnets Procurement Milestone				❖			
First Magnets Delivery Milestone					❖		
Magnets Production Starts Milestone					❖		
Magnets Delivery					▨▨▨		
Magnets Measurement					▨▨▨		
Ring Building (Beneficial Occupancy Milestone)						❖	
Magnets Installation						▨▨▨	
Commissioning Starts Milestone						❖	
Commissioning Ends Milestone							❖

Figure VII.3-2b Synchrotron Magnet Schedule.

SYNCHROTRON MAGNETS POWER SUPPLIES SCHEDULE

Fiscal Year	FY95	FY96	FY97	FY98	FY99	FY00	FY01
KD 0 Milestone	❖						
KD 1 Milestone		❖					
Construction Start Milestone			❖				
R&D							
Dual Frequency Model R&D		▨					
DESIGN / CONSTRUCTION							
Power Supplies Design			▨				
Power Supplies Procurement Milestone				◆			
First Supply Delivery Milestone					◆		
Power Supplies Delivery					▨		
Power Dummy Load Test					▨		
Power Supply Building (Beneficial Occupancy Milestone)					❖		
Power Supplies installation and Connection						▨	
Commissioning Starts Milestone						❖	
Commissioning Ends Milestone							❖

Figure VII.3-2c Synchrotron Magnets - Power Supplies Schedule.

SPECIAL MAGNETS AND POWER SUPPLIES SCHEDULE

Fiscal Year	FY95	FY96	FY97	FY98	FY99	FY00	FY01
KD 0 Milestone	❖						
KD 1 Milestone		❖					
Construction Start Milestone			❖				
R&D							
Kicker and Septum R&D			▨				
Kicker and Septum Prototype			▨				
Prototype Testing Milestone				❖			
DESIGN / CONSTRUCTION							
Kicker and Septum Engineering Design				▨			
Kicker/Septum Power Supplies Procurement				❖			
Kicker/Septum Power Supplies Delivery					▨		
Kicker/Septum Fabrication				▨			
Kicker/Septum Testing Milestone					❖		
Ring Building (Beneficial Occupancy Milestone)					❖		
INSTALLATION							
Injection Magnets Installation in Ring Building 365						▨	
Extraction Magnets Installation in Ring Building 365						▨	
Commissioning Starts Milestone							❖
Commissioning Ends Milestone							❖

Figure VII.3-2d Special Magnets and Power Supplies Schedule.

SYNCHROTRON rf SYSTEM SCHEDULE

Fiscal Year	FY95	FY96	FY97	FY98	FY99	FY00	FY01
KD 0 Milestone	❖						
KD 1 Milestone		❖					
Construction Start Milestone			❖				
R&D							
rf Amplifiers R&D (Cathode Follower)	▨	▨					
Decision on Amplifier Type Milestone			❖				
rf Cavities and Ferrite R&D			▨				
Low Level rf R&D				▨			
DESIGN / CONSTRUCTION							
rf Cavities and Amplifier Design			▨				
rf System Procurement				❖			
Cavities and Amplifiers Delivery					▨		
Cavities Measurement & Load Testing					▨		
Ring Building (Beneficial Occupancy Milestone)					❖		
rf Amplifier Power Supply Installation in Building 364					▨	▨	
rf Cavity & Amplifier Installation in Ring Building 365						▨	
Commissioning Starts Milestone						❖	
Commissioning Ends Milestone							❖

Figure VII.3-2e Synchrotron rf System Schedule.

SYNCHROTRON VACUUM SYSTEM SCHEDULE

Fiscal Year	FY95	FY96	FY97	FY98	FY99	FY00	FY01
KD 0 Milestone	❖						
KD 1 Milestone		❖					
Construction Start Milestone			❖				
R&D							
Ceramic Chamber Prototype R&D		▨					
Chamber Feed Through R&D			▨				
Chamber rf Shield R&D				▨			
DESIGN / CONSTRUCTION							
Chamber System Design			▨				
Chamber System Procurement				❖			
Pumping System Procurement				❖			
Chamber Delivery					▨		
rf Shield System Installation					▨		
Ring Building (Beneficial Occupancy Milestone)					❖		
Chamber Installation in Building 365						▨	
Pumping Down Sectors						▨	
Commissioning Starts Milestone						❖	
Commissioning Ends Milestone							❖

Figure VII.3-2f Synchrotron Vacuum System Schedule.

DIAGNOSTICS SYSTEM SCHEDULE

Fiscal Year	FY95	FY96	FY97	FY98	FY99	FY00	FY01
KD 0 Milestone	❖						
KD 1 Milestone		❖					
Construction Start Milestone			❖				
R&D							
Diagnostics and Feedback R&D		▨▨▨	▨▨▨	▨▨▨			
DESIGN/ CONSTRUCTION							
Diagnostics System Design			▨▨	▨			
BPM System Procurement				❖			
Diagnostics Electronics Procurement					❖		
BPM System Delivery					▨▨		
BPM Installation on Chambers					▨▨		
Ring Building (Beneficial Occupancy Milestone)					❖		
Chamber Installation in Building 365						▨▨	
Diagnostic Electronics Delivery						▨▨	
Installation of the System						▨▨	
Commissioning Starts Milestone						❖	
Commissioning Ends Milestone							❖

Figure VII.3-2g Diagnostics System Schedule.

CONTROLS AND COMPUTING SYSTEM SCHEDULE

Fiscal Year	FY95	FY96	FY97	FY98	FY99	FY00	FY01
KD 0 Milestone	❖						
KD 1 Milestone		❖					
Construction Start Milestone			❖				
R&D							
Control System R&D -Adapt from APS			▨▨▨				
Prototype Control Computer R&D Procurement				❖			
DESIGN							
Control System Design				▨▨			
Integration of Subsystems Control Design				▨▨▨			
CONSTRUCTION							
Write Control Software				▨▨▨	▨▨▨		
Control System Electronics Procurement				❖			
Control System Computers Procurement					❖		
Control System Electronics Delivery					▨▨		
Control Computers Delivery					▨▨	▨▨	
Ring Building (Benificial Occupancy Milestone)					❖		
Subsystem Testing					▨▨	▨▨	
Installation of the System						▨▨	
Data System Computer Procurement					❖		
Data System Computer Delivery						❖	
Commissioning Starts Milestone							❖
Commissioning Ends Milestone							❖

Figure VII.3-2h Controls and Computing System Schedule.

TRANSFER LINES SCHEDULE

Fiscal Year	FY95	FY96	FY97	FY98	FY99	FY00	FY01
KD 0 Milestone	❖						
KD 1 Milestone		❖					
Construction Start Milestone			❖				
R&D							
Performance Specifications			▨				
DESIGN / CONSTRUCTION							
Low Energy Transfer Line Procurement				❖			
Low Energy Transfer Line Delivery					▨		
Low Energy Transfer Line Measurements					▨		
Ring Building (Beneficial Occupancy Milestone)					❖		
Low Energy Transfer Line Installation					▨	▨	
Linac Commisioning Milestone						❖	
High Energy Transfer Line Procurement					❖		
High Energy Transfer Line Delivery					▨	▨	
High Energy Transfer Line Measurements					▨	▨	
High Energy Transfer Line Installation						▨	
Commissioning Starts Milestone						❖	
Commissioning Ends Milestone							❖

Figure VII.3-2i Transfer Lines Schedule.

NEUTRON TARGET STATIONS SCHEDULE

Fiscal Year	FY95	FY96	FY97	FY98	FY99	FY00	FY01
KD 0 Milestone	❖						
KD 1 Milestone		❖					
Construction Start Milestone			❖				
R&D							
Targets and Target Support R&D	▨	▨					
DESIGN / CONSTRUCTION							
Targets and Target Support Design			▨				
Targets Conventional Construction Procurement Milestone				❖			
Targets Technical Components Procurement Milestone				❖			
Target Buildings (369&370) Available Milestone				❖			
Targets Support (Shieldings) Construction				▨			
Transfer Enclosures at Ring Building Construction					▨		
Targets Installation					▨		
Ring Building (Beneficial Occupancy Milestone)					❖		
Targets Support Buildings Beneficial Occupancy				❖			
Targets Support Facilities Installation					▨	▨	
Target Control/Interlock Installation						▨	
Commissioning Starts Milestone						❖	
Commissioning Ends Milestone							❖

Figure VII.3-2j Neutron Target Stations Schedule.

INSTRUMENTATION SCHEDULE

Fiscal Year	FY95	FY96	FY97	FY98	FY99	FY00	FY01
KD 0 Milestone	❖						
KD 1 Milestone		❖					
Construction Start Milestone			❖				
R&D							
Instrumentation R&D	▨	▨	▨	▨			
DESIGN / CONSTRUCTION							
Instrumentation Design			▨	▨			
Instrument Early Procurement Milestone				❖			
Instrument Late Procurement Milestone					❖		
Instrument Delivery					▨	▨	
Instrument Installation						▨	▨
Instrument Control Check Out							▨
Commissioning Starts Milestone						❖	
Commissioning Ends Milestone							❖

Figure VII.3-2k Instrumentation Schedule.

PROJECT CRITICAL PATH

Fiscal Year	FY95	FY96	FY97	FY98	FY99	FY00	FY01
KD 0 Milestone							
KD 1 Milestone							
E/A							
NEPA and Other Permits							
Construction Start Milestone							
Conventional Facilities Design							
Title I							
Final Design							
Conventional Facilities Construction							
Linac Bldg, Tunnel, LET, Ring & Center Bldg)							
(New Construction for Linac, Refurbish 364 & 365)							
Target Buildings							
(Refurbish Buildings 369 and 370)							
Target Support Buildings							
(Refurbish Buildings 367 and 371)							
Technical Facilities Installation							
Linac Components Installation							
Synchrotron Magnet Delivery							
Magnets Installation							
Commissioning Starts Milestone							
Commissioning Ends Milestone							

Figure VII.3-3 Project Critical Path.

The cost schedule is obtained by adding the time-based person-power costs to the time-based materials costs. On the basis of the detailed WBS-based cost estimates (which contain the cost of materials and labor of various crafts for each of the components), together with the technical components construction schedule described in the previous section, technical component person-power needs per quarter year have been estimated as a function of time. The effort costs per year are shown in Figure VII.4-1. Materials costs based on the procurement schedule, and conventional facility construction costs based on the A/E schedule, are similarly projected for each quarter year.

The budget profile of the project is obtained from

- The manpower distribution (Figure VII.4-1),

- Materials costs distribution,

- Addition of contingency proportional to the part of the task or activities not completed, and

- Incorporation of the escalation shown in Table VII.2-2.

Table VII.4.1 shows the budget authority (BA) profile for high-level WBS elements. Integration of the schedule into the BA distribution can be seen in this table. Figure VII.4-2 shows the BA distribution, and Figure VII.4-3 shows the cumulative BA distribution that extends from FY 1997 to FY 2001.

This schedule projects that the total estimated cost (TEC) of the construction is $558.9 million. The schedule results in an escalation of $80.9 million, which is shown as the difference between the TEC of $558.9 million and the FY 1995 construction cost estimate of $478.0 million shown in Table VII.2-3. The TEC, broken down into (1) plant and capital equipment (PACE) construction costs and (2) ED&I costs, together with the escalation and contingency, is shown in Table VII.4-2. The breakdown follows the guidelines established by the Engineering, Design and Inspection Steering Committee of the U.S. Department of Energy (DOE) Committee for Cost Methods Development and described in a report dated August 23, 1985, and in DOE Order 4700.1.

The cash flow distribution, the budget outlay (BO), for high-level WBS elements is shown in Table VII.4-3. Figure VII.4-4 shows the comparison between the cumulative BA and the BO.

Effort Distribution
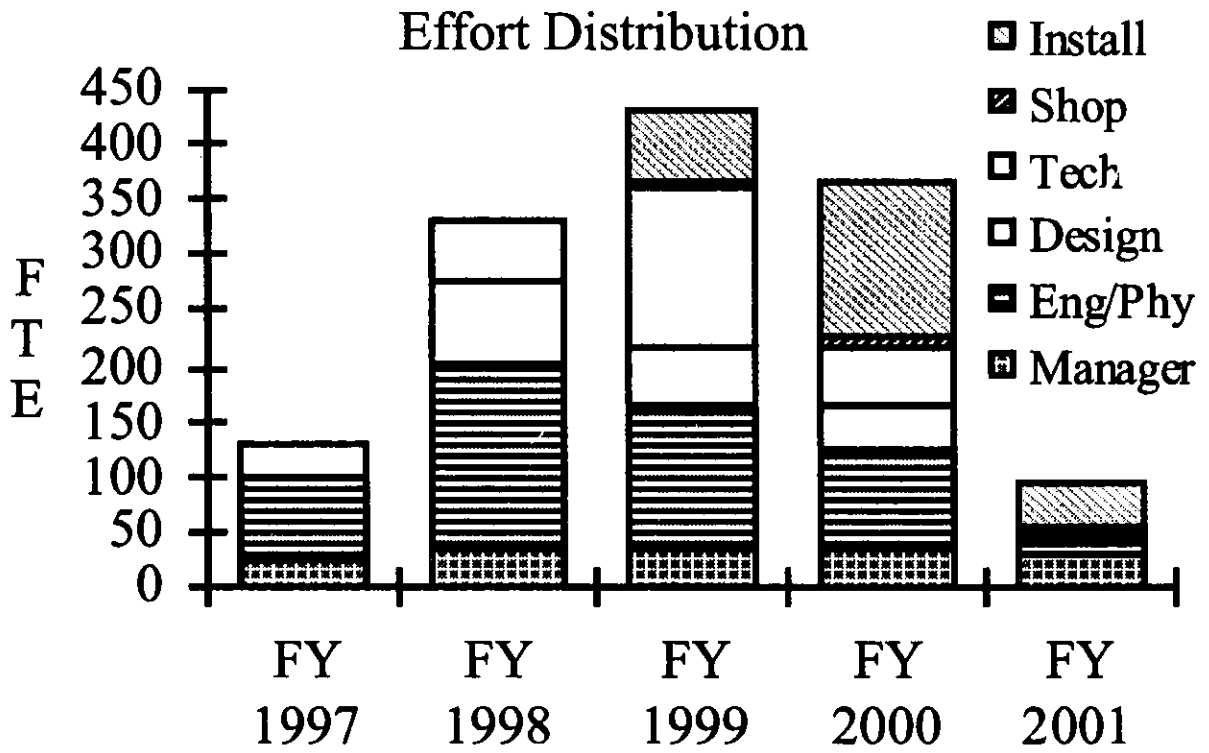
Figure VII.4-1 Construction Project Person-Effort Distribution.

Table VII.4-1 Budget Authority (BA) Distribution (Actual Year k$)[a]

WBS Code	Description	FY1997	FY1998	FY1999	FY2000	FY2001	Total
	Escalation % from FY 1995 $	7.8%	3.8%	3.6%	3.6%	3.6%	
	Escalation Factor	1.078	1.119	1.159	1.201	1.244	
1	IPNS UPGRADE (1 MW)	16839	95053	207294	205966	33786	558938
1.1	Project Management	2695	2238	2393	2283	2037	11645
1.2	Accelerator Systems	6145	41411	100223	41576	0	189354
1.2.1	Injector System	2911	17273	39994	11322	0	71500
1.2.2	Synchrotron	3234	19281	46821	17945	0	87281
1.2.3	Beam Transports	0	4353	9350	5243	0	18947
1.2.4	Technical Support Systems	0	504	4057	7065	0	11626
1.3	Targets and Instruments	1617	10686	14426	56717	20494	103940
1.3.1	Target Stations	1078	4867	6311	13439	6253	31949
1.3.2	Instruments and Support	539	5819	8115	43279	14241	71991
1.4	Conventional Facilities	1078	11749	19030	20957	834	53648
1.4.1	Existing Building Rehabilitation	0	5595	10707	12263	470	29034
1.4.2	New Construction	0	2238	3892	2445	0	8575
1.4.3	Utilities	0	1119	3478	5648	0	10245
1.4.4	Conventional Facilities EDI&A	1078	2797	953	600	365	5793
1.5	Shielding Structures	323	854	9908	23511	428	35024
1.5.1	HE Transport Shielding	108	182	2721	6608	0	9619
1.5.2	30-Hz Target Shielding	108	336	3594	8452	214	12703
1.5.3	10-Hz Target Shielding	108	336	3594	8452	214	12703
1.8	Misc. Costs	2231	12593	27462	27287	4476	74049
1.8.1	Overheads	1568	8854	19308	19185	3147	52062
1.8.2	Unproductive Time	284	1602	3495	3472	570	9423
1.8.3	M&S for Staff	378	2137	4659	4630	759	12563
1.9	Contingency	2750	15523	33852	33635	5518	91278

[a] Numbers are spreadsheet-generated, and costs may not exactly add up to totals because of rounding.

BA Distribution
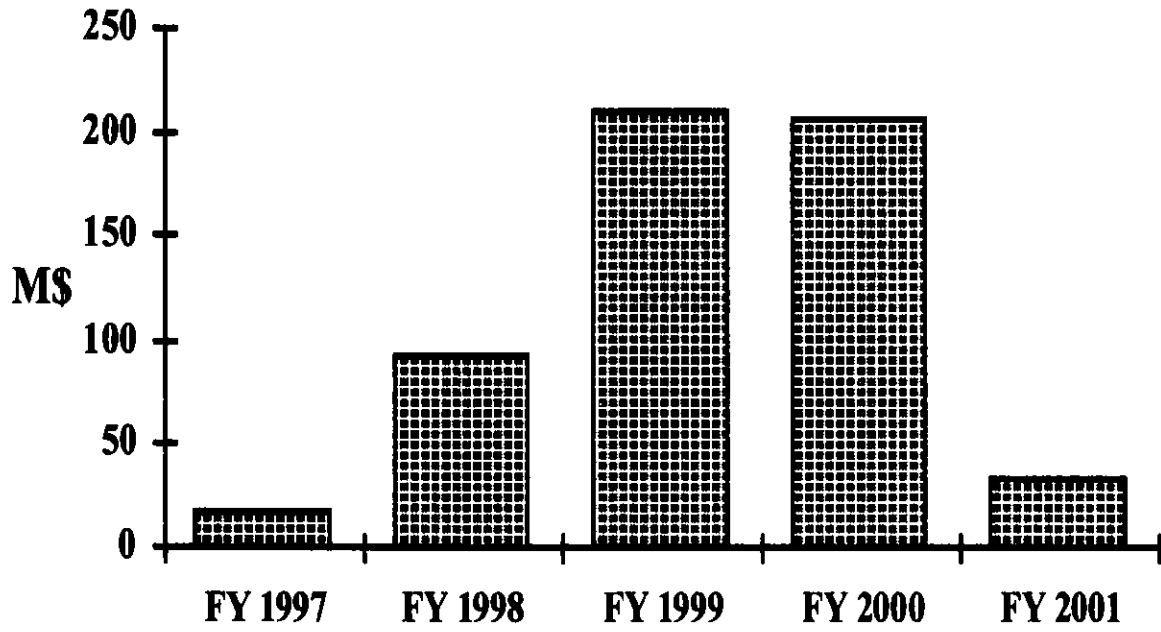
Figure VII.4-2 Budget Authority Distribution.
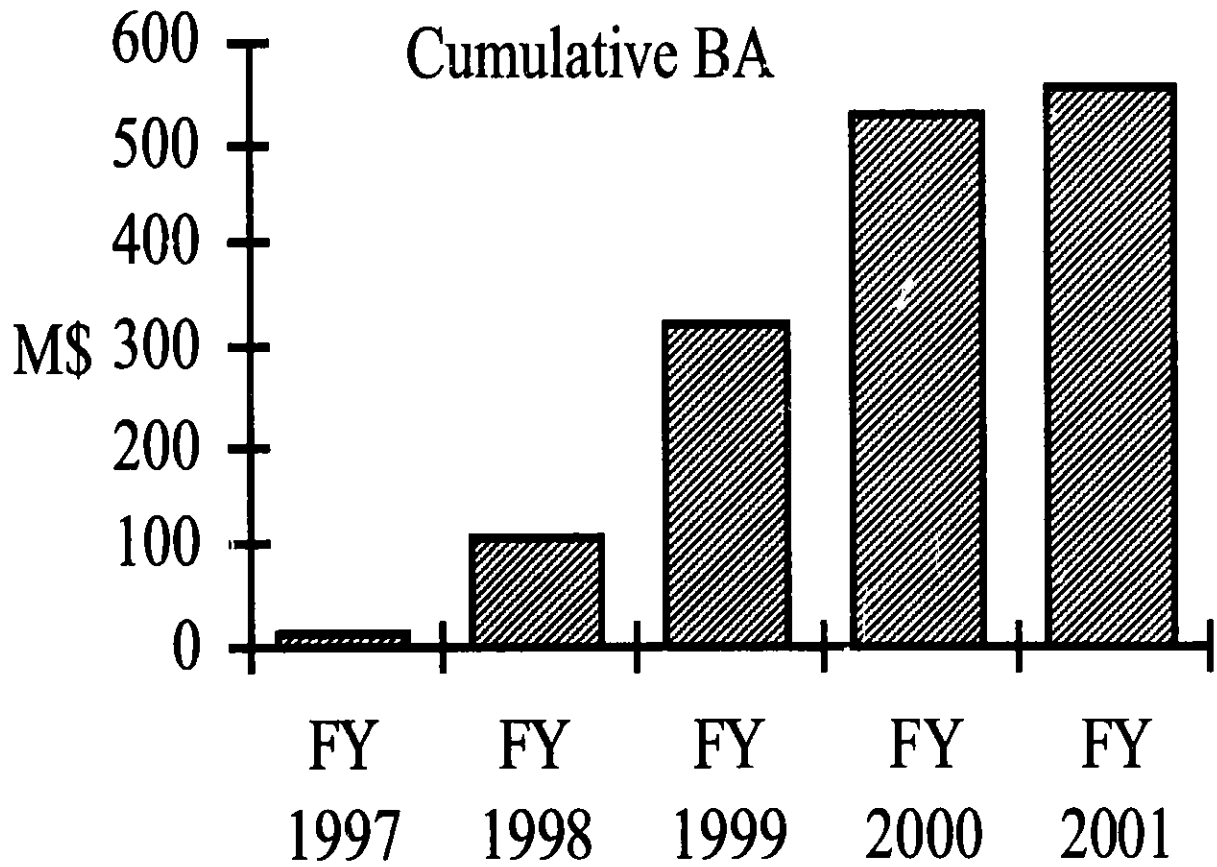
Figure VII.4-3 Cumulative BA Distribution.

Table VII.4-2 TEC Breakdown by Major Category
($ million estimated in FY 1995)

Engineering, Design, and Inspection	43.158
Construction	356.815
Contingency	78.066
Escalation	80.899
TEC	558.938

Table VII.4-3 Budget Outlay (BO) Distribution (Actual Fiscal Year k$)[a]

WBS Code	Description	FY1997	FY1998	FY1999	FY2000	FY2001	Total
1	IPNS UPGRADE (1 MW)	16838	69853	175759	228869	67620	558938
1.1	Project Management	2695	2238	2393	2283	2037	11645
1.2	Accelerator Systems	6145	23611	79023	80576	0	189354
1.2.1	Injector System	2911	9273	27994	31322	0	71500
1.2.2	Synchrotron	3234	11281	35821	36945	0	87281
1.2.3	Beam Transports	0	2553	11150	5243	0	18947
1.2.4	Technical Support Systems	0	504	4057	7065	0	11626
1.3	Targets and Instruments	1617	7686	12426	37717	44494	103940
1.3.1	Target Stations	1078	2867	6311	11439	10253	31949
1.3.2	Instruments and Support	539	4819	6115	26279	34241	71991
1.4	Conventional Facilities	1078	7349	14196	25359	5666	53648
1.4.1	Existing Building Rehabilitation	0	2994	8628	14611	2802	29034
1.4.2	New Construction	0	1238	3137	3700	500	8575
1.4.3	Utilities	0	319	1478	6448	2000	10245
1.4.4	Conventional Facilities EDI&A	1078	2797	953	600	365	5793
1.5	Shielding Structures	323	854	6408	22011	5428	35024
1.5.1	HE Transport Shielding	108	182	2221	7108	0	9619
1.5.2	30-Hz Target Shielding	108	336	2094	7452	2714	12703
1.5.3	10-Hz Target Shielding	108	336	2094	74F2	2714	12703
1.8	Misc. Costs	2230	12593	27462	27287	4477	74049
1.8.1	Overhead	1568	8854	19308	19185	3147	52062
1.8.2	Unproductive Time	284	1602	3495	3472	570	9423
1.8.3	M&S for Staff	378	2137	4659	4630	759	12563
1.9	Contingency	2750	15523	33852	33635	5518	91278

[a] Numbers are spreadsheet-generated, and costs may not exactly add up to totals because of rounding.

Cumulative BA and BO
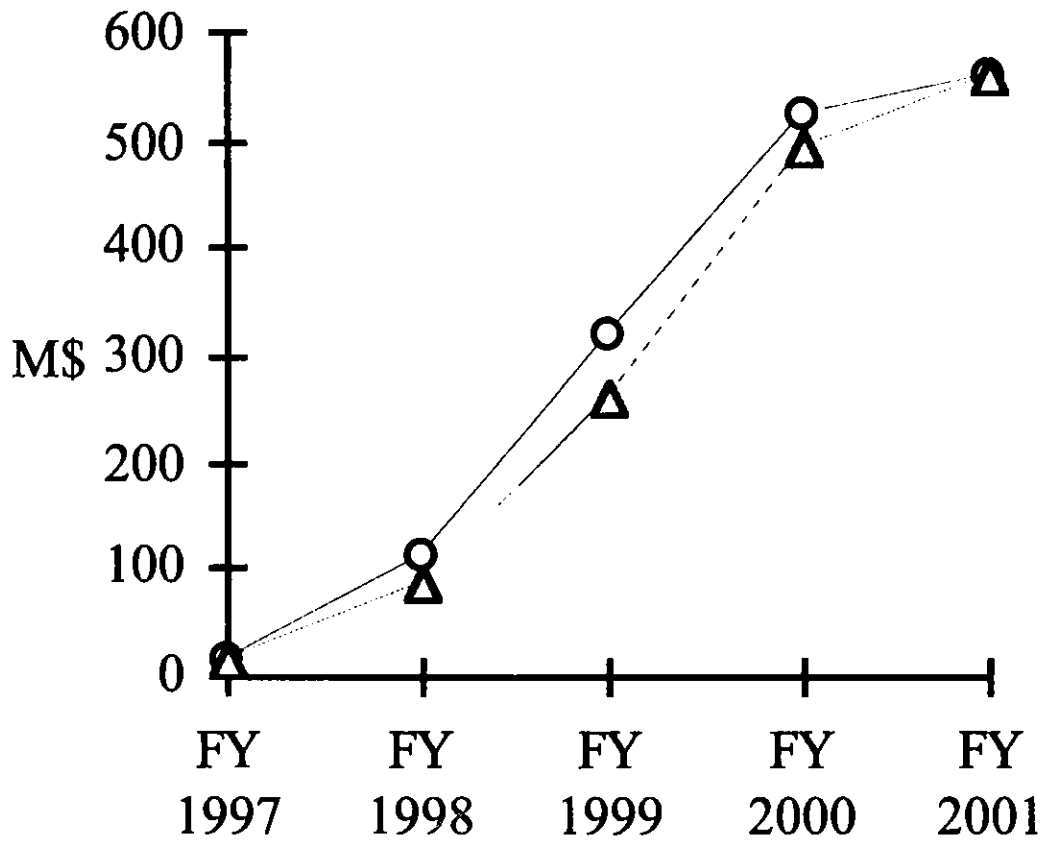
Figure VII.4-4 Comparison between Cumulative BA and BO.
(The top curve is BA, and the bottom curve is BO.)

Appendix A

Parameter List

All parameters are at nominal operating conditions, unless otherwise noted.

1. RCS Performance Parameters

Beam energy		
Injection	400	MeV
Extraction	2.0	GeV
Maximum design energy	2.2	GeV
Beam repetition rate	30	Hz
Beam average current	0.5	mA
Beam power	1.0	MW
Number of circulating protons	1.04×10^{14}	
Beam emittance		
Horizontal	375 π	mm-mrad
Vertical	375 π	mm-mrad
Longitudinal	7.3	eV sec
Momentum spread, $\Delta p/p$, fwhm		
Injection	1.0	%
Extraction	0.8	%
Kinetic energy spread, $\Delta T/T$, fwhm		
Injection	1.7	%
Extraction	1.1	%
Bunch length, baseline		
Injection	0.8×190.4	m
Extraction	0.3×190.4	m
Bunching factor, peak current/average current		
Injection	0.38	
Extraction	0.16	

2. RCS Lattice and Orbit Parameters

Circumference	190.4	m
Super-periodicity	4	
Revolution time		
Injection	890.1	nsec
Extraction	665.1	nsec
Harmonic number	1	
Radio frequency		
Injection	1.1235	MHz
Extraction	1.5035	MHz
Lattice structure		
Normal FODO cells per quadrant	3	
Missing magnet FODO cells per quadrant	2	
Empty FODO cells per quadrant	2	

Mean radius	30.3	m
Bending field		
Injection	0.48	T
Extraction	1.40	T
Maximum design value	1.51	T
Bending radius	6.62	m
Magnetic lengths in a normal FODO cell		
(D=drift, B=bend, Q=quad, S=sext)		
QD	0.25	m
D1	0.30	m
SD	0.20	m
D1	0.30	m
B	1.30	m
D2	0.80	m
QF	0.50	m
D1	0.30	m
SF	0.20	m
D1	0.30	m
B	1.30	m
D2	0.80	m
QD	0.25	m
Betatron tune		
Horizontal	6.821	
Vertical	5.731	
Synchrotron frequency		
Injection	3.0	kHz
Extraction	0.9	kHz
Natural chromaticity, $\xi = (\Delta v / v) / (\Delta p / p)$		
Horizontal	-1.06	
Vertical	-1.20	
Beta functions		
Maximum horizontal	10.59	m
Minimum horizontal	2.25	m
Maximum vertical	11.98	m
Minimum vertical	2.53	m
Dispersion function		
Maximum horizontal	2.16	m
Minimum horizontal	-0.06	m
Momentum compaction	3.42×10^{-2}	
Transition Gamma, γ_t	5.40	

3. RCS Tolerances, rms

Quadrupole placement	2.0×10^{-4}	m
Sextupole placement	2.0×10^{-4}	m
Random dipole roll-angle error	1.0×10^{-3}	rad
Dipole tracking error	1.0×10^{-3}	
Quadrupole tracking error	2.5×10^{-4}	

4. RCS Hardware

a. Magnets and power supplies
    Dipoles

Number	32	
Number of independent power supplies	24	
Magnetic length	1.3	m
Bending radius	6.62	m
Dipole field at 2 GeV	1.40	T
Beam-stay-clear		
Entrance, max		
Horizontal	136	mm
Vertical	156	mm
Center, max		
Horizontal	160	mm
Vertical	134	mm
Exit, max		
Horizontal	188	mm
Vertical	116	mm

Quadrupoles

Number, QF, QD	56	
QF family	28	
QD family	28	
Number of independent power supplies, QF, QD	42	
QF family	21	
QD family	21	
Magnetic length	0.50	m
Maximum gradient at 2 GeV	7.73	T/m
Beam-stay-clear		
QF family, max		
Horizontal	228	mm
Vertical	101	mm
QD family, max		
Horizontal	110	mm
Vertical	190	mm

Sextupoles

Number, SF, SD, S1	40	

SF family	16	
SD family	16	
S1 family	8	
Number of independent power supplies, SF, SD, S1	40	
SF family	16	
SD family	16	
S1 family	8	
Magnetic length	0.20	m
Maximum strength at 2 GeV	52	T/m^2
Beam-stay-clear		
SF family, max		
Horizontal	202	mm
Vertical	102	mm
SD family, max		
Horizontal	124	mm
Vertical	168	mm
S1 family, max		
Horizontal	100	mm
Vertical	174	mm
Correction dipoles		
Horizontal correctors		
Number	28	
Independent power supplies	28	
Magnetic length	0.15	m
Peak field at 2 GeV	0.07	T
Beam stay clear, max		
Horizontal	222	mm
Vertical	94	mm
Vertical correctors		
Number	28	
Independent power supplies	28	
Magnetic length	0.15	m
Peak field at 2 GeV	0.07	T
Beam stay clear, max		
Horizontal	114	mm
Vertical	182	mm

b. RF system

Frequency		
Injection	1.1235	MHz
Extraction	1.5035	MHz
Number of cavities	10	
Harmonic number	1	
Length (inside)	2.39	m

Peak voltage

Cavity	18	kV
Total rf system	180	kV

Cavity Q

Injection	33.2
Extraction	63.3

Cavity shunt impedance

Injection	5	kΩ
Extraction	8.1	kΩ
Total peak rf power	2.62	MW

c. Injection equipment

Injection Septa

Number	2	
Magnetic length		
Septum A	1.2	m
Septum B	0.3	m
Bending angle		
Septum A	228	mrad
Septum B	24	mrad
Maximum design field at 400 MeV		
Septum A	0.61	T
Septum B	0.52	T
Field index		
Septum A	-20	
Septum B	0	
Gap height		
Septum A	20	mm
Septum B	24	mm
Gap width		
Septum A	51	mm
Septum B	40	mm
Minimum septum thickness		
Septum A	33.4	mm
Septum B	3.0	mm

Bumper magnets

Number	4	
Magnetic length	0.3	m
Bending angle	20	mrad
Peak central field at 400 MeV	0.212	T
Gap height	241.5	mm
Gap width	300	mm

d. Extraction equipment
      Extraction septa
            Number   3
            Magnetic length
                  Septum C   0.5   m
                  Septum D   1.5   m
                  Septum E   0.9   m
            Bending angle
                  Septum C   55   mrad
                  Septum D   210   mrad
                  Septum E   126   mrad
            Peak central field at 2.0 GeV
                  Septum C   1.02   T
                  Septum D   1.3   T
                  Septum E   1.3   T
            Gap height
                  Septum C   70   mm
                  Septum D   90   mm
                  Septum E   110   mm
            Gap width
                  Septum C   122   mm
                  Septum D   102   mm
                  Septum E   70   mm
            Minimum septum thickness
                  Septum C   6.0   mm
                  Septum D   57.1   mm
                  Septum E   227.7   mm
      Kicker magnets
            Number   3
            Magnetic length
                  Kicker A   0.65   m
                  Kicker B   0.87   m
                  Kicker C   1.105   m
            Bending angle
                  Kicker A   4.37   mrad
                  Kicker B   4.79   mrad
                  Kicker C   4.84   mrad
            Peak central field at 2.0 GeV
                  Kicker A   0.0618   T
                  Kicker B   0.0512   T
                  Kicker C   0.0408   T
            Gap height
                  Kicker A   132.4   mm
                  Kicker B   159.2   mm
                  Kicker C   200.0   mm

Gap width

	Kicker A	220.0	mm
	Kicker B	195.0	mm
	Kicker C	170.0	mm

e. Beam diagnostics (number of each type)

2-Stripline BPMs	56	
Horizontal	28	
Vertical	28	
Current transformer	2	
Loss monitor	4	
Pingers	2	
Horizontal	1	
Vertical	1	
Segmented Faraday cup	6	
Horizontal	3	
Vertical	3	
Solid first-turn Faraday cup	1	

5. Injector Linacs

a. General

Accelerated ion	H⁻	
Output kinetic energy	400	MeV
Pulsed beam current	35	mA
Beam duty factor	1.5	%
Beam pulse length	500	μsec
Beam repetition rate	30	Hz
Time-averaged current	0.5	mA
Radio-frequency duty factor	3	%
Total rf power		
Peak	104	MW
Average	4.85	MW
Transverse emittance, normalized, rms		
Output from linac	0.2 π	mm - mrad
Input to RCS, required	1.0 π	mm - mrad
Output energy spread, fwhm	2.5	MeV
Length	120	m

b. Ion source

Output energy	35	keV
Output current	60	mA
Output transverse emittance, normalized, rms	0.1 π	mm - mrad
Length	0.5	m

c. RFQ

Input energy	35	keV
Output energy	2.0	MeV
Output current	35	mA
Output transverse emittance, normalized, rms	$0.12\,\pi$	mm - mrad
Operating frequency	425	MHz
Bore radius	2.4-3.0	mm
Synchronous phase	-30	deg
Peak structure power	0.22	MW
Number of tanks/modules	1	
Structure length	2.16	m
Peak beam power at 40 mA	0.08	MW

d. DTL

Input energy	2.0	MeV
Output energy	70.0	MeV
Output current	35	mA
Output transverse emittance, normalized, rms	$0.135\,\pi$	mm - mrad
Operating frequency	425	MHz
Accelerating gradient, $E_0 T$	2.4-4.6	MV/m
Bore radius	5.0-9.0	mm
Synchronous phase	-30	deg
Peak structure power	6.28	MW
Number of tanks/modules	4	
Structure length	20.54	m
Peak beam power at 40 mA	2.72	MW

e. MS

Input energy	70.0	MeV
Output energy	70.0	MeV
Output current	35	mA
Output transverse emittance, normalized, rms	$0.151\,\pi$	mm - mrad
Operating frequency	1,275	MHz
Accelerating gradient, $E_0 T$	—	MV/m
Bore radius	10.0	mm
Synchronous phase	—	deg
Peak structure power	1.2	MW
Number of tanks/modules	2	
Structure length	3.2	m
Peak beam power at 40 mA	—	MW

f. CCL

Input energy	70.0	MeV
Output energy	400.0	MeV
Output current	35	mA

Output transverse emittance, normalized, rms	0.194 π	mm - mrad
Operating frequency	1,275	MHz
Accelerating gradient, E_0T	5.9-5.5	MV/m
Bore radius	10.0-12.0	mm
Synchronous phase	-30 to -25	deg
Peak structure power	52.8	MW
Number of tanks/modules	6/10	
Structure length	92.1	m
Peak beam power at 40 mA	13.2	MW

6. Transport Line between Linac and RCS

a. Magnets

Dipoles, A

Number	15	
No. of independent power supplies	3	
Magnetic length	1.0	m
Peak field at 400 MeV	0.91	T
Bending angle at 400 MeV	286	mrad
Gap		
Height	40	mm
Width	140	mm

Quadrupoles, A

Number	62	
No. of independent power supplies	62	
Magnetic length	0.2	m
Peak strength at 400 MeV	14.0	T/m
Gap	53	mm

Quadrupoles, B

Number	3	
No. of independent power supplies	3	
Magnetic length	0.2	m
Peak strength at 400 MeV	12.0	T/m
Gap	72	mm

Correction dipoles

Number	16	
No. of independent power supplies	16	
Magnetic length	0.1	m
Peak field at 400 MeV	0.064	T
Bending angle at 400 MeV	2.0	mrad
Gap		
Height	53	mm
Width	135	mm

b. Beam diagnostics, number of each type

4-Stripline BPM	8	
Current transformer	3	
Profile detectors	16	
Loss monitor	1	

7. Transport Line between RCS and Target

a. Magnets, 10 Hz, 30 Hz

Dipoles, B

Number	1	
No. of independent power supplies	1	
Magnetic length	1.0	m
Peak field at 2.0 GeV	1.20	T
Bending angle at 2.0 GeV	129	mrad
Gap		
Height	182	mm
Width	450	mm

Dipoles, C

Number	2	
No. of independent power supplies	2	
Magnetic length	1.8	m
Peak field at 2.0 GeV	1.43	T
Bending angle at 2.0 GeV	277	mrad
Gap		
Height	182	mm
Width	450	mm

Dipoles, D

Number	2	
No. of independent power supplies	2	
Magnetic length	2.8	m
Peak field at 2.0 GeV	1.36	T
Bending angle at 2.0 GeV	410	mrad
Gap		
Height	182	mm
Width	450	mm

Quadrupoles, C

Number	17	
No. of independent power supplies	17	
Magnetic length	0.5	m
Peak strength at 2.0 GeV	9.1	T/m
Gap	170	mm

Quadrupoles, D

Number	8	
No. of independent power supplies	8	

Magnetic length	0.5	m
Peak strength at 2.0 GeV	7.3	T/m
Gap	264	mm
Correction dipoles		
Number	16	
No. of independent power supplies	16	
Magnetic length	0.15	m
Peak field at 2.0 GeV	0.127	T
Bending angle	2	mrad
Gap		
Height	300	mm
Width	300	mm

b. Beam diagnostics, number of each type

   10-Hz transport line

4-Stripline BPM	4
Current transformer	3
Profile detectors	4
Loss monitor	1
Target protection monitor	1

   30-Hz transport line

4-Stripline BPM	6
Current transformer	3
Profile detector	4
Loss monitor	1
Target protection monitor	1

Appendix B

Research and Development Plan

B.1 INTRODUCTION

Preconstruction research and development (R&D) work, when properly executed, can save construction costs and shorten the construction period. Therefore, a vigorous R&D program is planned as soon as funds for such activities are available. The R&D work in support of construction can be categorized in two parts. The first part is associated with support of hardware design activities to obtain the best possible level of performance, and the second part is associated with reliability of the hardware. Both categories of R&D will be pursued according to the plan described in this section. The assumption has been made that construction of the facility will start in FY 1997.

Accelerator-related R&D is described in Sections B.2 through B.10. R&D related to the target and instruments is discussed in Sections B.11 and B.12. Funding required to carry out this R&D program is described in Section B.13.

An accelerator with very high beam power, such as this rapid cycling synchrotron (RCS), must have beam losses less than about 0.1% in order to permit hands-on maintenance, as was discussed in Chapter II. Beam loss refers to those particles that are lost during the injection, capture, acceleration, and extraction processes. Understanding of the loss mechanisms and preventing the loss processes are the accelerator physics R&D topics.

The R&D plan covers the following:

- Accelerator physics - theoretical;

- Accelerator physics - experimental;

- H^- ion source reliability testing;

- Radio-frequency (rf) power source prototyping and testing;

- Ceramic vacuum chamber prototyping and testing; and

- Dual-harmonic ring magnet power supply prototyping and testing.

Preconstruction R&D is scheduled so that it blends in smoothly with the initiation of the construction phase in FY 1997. Decision-making milestones are scheduled for key R&D items and are phased appropriately with the construction schedule.

The schedule for R&D activities is presented in Figure B.1-1, a bar chart that indicates the duration of the activities and the associated milestones.

PRECONSTRUCTION R&D SCHEDULE

Fiscal Year	FY95	FY96	FY97	FY98	FY99	FY00	FY01
KD 0 Milestone	❖						
KD 1 Milestone		❖					
Construction Start Milestone			❖				
Commissioning Starts Milestone						❖	
Commissioning Ends Milestone							❖
Accelerator Physics							
rf Amplifiers R&D (Cathode Follower)							
Decision on Amplifier Type Milestone			❖				
rf Cavities and Ferrite R&D							
Low Level rf R&D							
Magnets Performance Design R&D							
Dual Frequency Model Power Supply R&D							
Ceramic Chamber Prototype R&D							
Chamber Feed Through R&D							
Chamber rf Shield R&D							
Ion Source R&D							
RFQ R&D							
CCL R&D							
Kicker and Septum R&D							
Kicker & Septum Prototype							
Prototype Testing Milestone				❖			
Diagnostics and Feedback R&D							
Control System R&D-Adapt from APS							
Prototype Control Computer R&D Procurement				❖			
Targets and Control Support R&D							
Instrumentation R&D							

Figure B.1-1 Preconstruction R&D Schedule.

B.2 ACCELERATOR PHYSICS

B.2.1 Theoretical — Beam Dynamics and Beam Loss

For the past several years, extensive beam dynamics studies have been carried out by personnel associated with this feasibility study. Beam loss conditions during the injection, capture, and acceleration processes have been simulated. The results are discussed in Chapter II. Work performed to date includes studies of longitudinal and transverse beam dynamics during the injection, capture, and acceleration processes. The effect of motion in the transverse plane on the dynamic aperture was studied. Magnet and beam position monitor placement tolerances and magnetic multipole components arising from fabrication tolerances were studied for synchrotron magnets under nonaccelerating conditions.

The results of these studies are incorporated into this feasibility report and cover (1) the need for chopping the linac beam to eliminate capture losses, (2) the specification of the linac beam momentum spread to eliminate acceleration losses and to meet Keil-Schnell longitudinal stability criteria, and (3) specifications for the alignment and multipole tolerances.

The plan for the coming years is to further refine the tracking study to include all relevant physical phenomena in the simulation, both individually and combined. After these detailed studies have been performed for the Intense Pulsed Neutron Source (IPNS) Upgrade lattice, particle tracking simulations will be performed with equal thoroughness for the existing IPNS accelerator. This procedure provides a way to experimentally check the calculations by using an actual accelerator.

B.2.2 Experimental — Measurements at Existing Synchrotrons

The longitudinal tracking studies performed to date have provided us with an understanding of many phenomena associated with beam losses. Many of these phenomena can be measured experimentally at existing fast cycling synchrotron facilities. Machine experiments will be performed at the existing IPNS accelerators. Planned studies are described below.

B.2.2.1 Chopped Beam Injection Studies

Chopped beam injection will be done to study the bunch to bucket beam transfer. A traveling wave chopper will be placed between the 750-kV preinjector and the drift tube linac (DTL) linac at IPNS. The injection and capture processes were already simulated by Monte Carlo tracking calculations, so experiments will be performed with the synchrotron to check the validity of the predictions.

B.2.2.2 rf Voltage Programming

The rf voltage programming affects various beam parameters and beam loss conditions. Several accelerator experiments are planned. One accelerator experiment verifies the rf voltage program in the later part of the acceleration cycle. At the end of acceleration, a high synchrotron frequency must be maintained to permit the bunches to follow rapid changes in the synchronous phase angle, as was discussed Chapter II.

It is foreseen that both theoretical and experimental accelerator physics activities will be carried out throughout the construction period in support of this facility. Personnel associated with those activities will participate in commissioning and operations-related work as the schedule progresses.

B.3 rf SYSTEM

The rf system is a key hardware element and requires early R&D work in three areas.

B.3.1 Cathode-Follower rf Amplifier

The cathode-follower rf amplifier system receives particular emphasis in the rf R&D studies. In theory, the system has a very small impedance, and it can automatically compensate for beam loading. That is an advantage of the cathode-follower when compared with the conventional amplifier system described in this report. A cathode-follower system would be built and tested as part of the proposed R&D in order to demonstrate its possible use in the IPNS Upgrade. Figure B.1-1 shows that the planned duration of this R&D activity is two years, after which the decision on amplifier type, shown as a milestone in the figure, must be made. Actual construction of the amplifier begins in the second quarter of FY 1997.

B.3.2 rf Cavities and Ferrite

There are 10 rf cavities in the design, for a total of 180 kV, and the resonance frequency varies from 1.1 to 1.5 MHz. The tuning is achieved by adjusting the biased magnetic field of ferrite rings. It is important to choose proper ferrite for this and to cool the ferrite to remove heat from rf losses. The duration of this R&D is about a year, and the effort is scheduled to be complete in FY 1997.

B.3.3 Low-Level rf System

Amplifier stability in the presence of the heavy beam loading in the RCS is achieved in part through low-level feedback loops. It is important to model and test as many of these systems in advance of construction as possible to ensure a successful design. The amplitude and

phase low-level feedback and feedforward loops are all studied in this R&D program. The planned duration of this activity is about a year.

B.4 MAGNET PERFORMANCE DESIGN

Synchrotron ring magnet procurement may take some time to accomplish. One way to expedite it is to select a vendor or vendors to produce the mechanical engineering designs on the basis of performance specifications provided by this facility. This method of procurement has been used at the APS and was used extensively at the European Synchrotron Radiation Facility (ESRF). This option for magnet procurement requires that a detailed performance specification be worked out. This activity is planned to start this year and be completed by next year so that the procurement can be initiated soon after the start of the project.

B.5 DUAL-HARMONIC POWER SUPPLY FOR THE RING MAGNETS

It is common practice to energize a rapid cycling synchrotron by using a resonant circuit composed of a capacitor bank and two inductive elements: a string of magnets and a choke. The stored energy in the circuit oscillates back and forth between the two inductive components. The oscillation frequency of the stored energy is the repetition rate of the synchrotron. One advanced feature of the IPNS Upgrade design is the use of a dual-frequency system to power the magnet system. The magnets are excited to the peak field with a 20-Hz sine wave, and are de-energized with a 60-Hz cosine wave, resulting in an average 30-Hz repetition rate. The R&D plan for this topic is to build and test a scale model of the power supply in FY 1996 so that power supply design engineering can commence in FY 1997.

B.6 VACUUM CHAMBER

B.6.1 Ceramic Chamber Prototype

Two types of vacuum chambers are commonly used for rapid cycling proton synchrotrons. In the first type, the magnet steel and the coils are encased inside vacuum-tight casings. That is used at the Fermilab booster and at the present IPNS 500-MeV machine. The other scheme is the ceramic chamber system, which is used at the ISIS facility. In recent years, TRIUMF personnel have constructed prototypes of these chambers for the proposed KAON facility. The R&D plan is to carry out a literature search and construct prototypes through FY 1997, as shown in Figure B.1-1.

B.6.2 Ceramic Chamber Feedthrough

The chamber system requires a large number of feedthroughs to extract diagnostic signals from the inside of the chamber. To design and construct a reliable chamber system, plans are to pursue an R&D program on feedthroughs in FY 1997. The vacuum chamber prototyping program started in FY 1996, and the resulting prototype chamber is used in the feedthrough study, as shown in Figure B.1-1.

B.6.3 Chamber rf Shields

The rf shield is a wire cage following the beam envelope. It shields the beam from induced rf signals and minimizes the coupling impedance between the beam and its surroundings. Such a shielding system has been operational at ISIS for many years. After chamber prototyping is complete, an R&D program for the shield will commence, as shown in Figure B.1-1. The shield must be mechanically rigid and have suitable rf properties.

B.7 LINAC SYSTEM

One procurement option is to obtain the linac from industry in a turn-key contract. The rationale for this is to directly use Superconducting Super Collider (SSC) industry-developed technology. In this case, the plan is to develop strong in-house capability in linac operations and improvements. The main emphasis is to be placed on operational reliability.

B.7.1 Ion Source

The source current and duty factor requirements for the IPNS Upgrade are satisfied by the existing Penning source of ISIS. In the Workshop on Ion Source Issues Relevant to a Pulsed Spallation Neutron Source held on October 24-26, 1994, at Lawrence Berkeley Laboratory, it was concluded that that extensive ion source R&D is required for all other pulsed source concepts. The IPNS Upgrade plan is to construct a test stand for reliability and serviceability testing of an ion source.

The plan is to obtain a Penning source and a volume source in FY 1996 and to construct a test stand on which a source can run 24 hours a day and 7 days a week for reliability testing. After this study, the source could be connected to the RFQ for further reliability testing. The linac-related schedules are shown in the bar charts in Figure B.1-1.

B.7.2 RFQ

The RFQ is added to the H^- ion source test stand after the H^- ion source has been studied for a year. The combined system of ion source and RFQ is tested starting in FY 1997.

The purpose of this program is to gain operational experience on serviceability and maintainability of the combined system.

The beam chopping requirement described in Chapter II is tested during this period by using a chopper that is placed between the ion source and the RFQ.

B.7.3 CCL

Argonne personnel must gain experience with the industrially produced linac, especially the CCL part. The plan is to participate in the early testing phase of the linac, develop operational expertise, and make operational and commissioning plans that will be ready when the linac is delivered to ANL. These activities are planned for FY 1997-1998.

B.8 KICKERS AND SEPTUM MAGNETS

These special magnets are pulsed at a 30-Hz repetition rate. They require prototyping at the earliest possible time to understand and implement a reliable system. Past experience shows that the time required to develop a reliable system is 1 to 2 years. This work is scheduled to start in the third quarter of 1997, as shown in Figure B.1-1.

B.9 DIAGNOSTICS

The Target Protection Monitor System monitors beam size and shape; its input is interpreted, along with focusing magnet setpoint and readback values, to provide a beam shutdown signal when required.

Research and development is required to choose suitable components and to ensure reliability, since this system functions in a very-high-radiation environment.

As fast electronics and digital technology improve, beam diagnostics and beam feedback technology improve accordingly. Therefore, diagnostics R&D is planned throughout the construction period to take advantage of these technology improvements, as shown in Figure B.1-1.

B.10 CONTROL SYSTEM

The APS project has developed the EPICS control system, as described in Chapter II. The IPNS Upgrade control system is adapted from the APS system. Minimal work is required for this task before the start of construction, as shown in Figure B.1-1. One notable requirement is that a control computer must be procured in FY 1998 before the control software is transferred from the APS.

B.11 RESEARCH AND DEVELOPMENT FOR TARGET STATIONS

The IPNS Upgrade has two target stations. The target stations include targets, moderators, and reflectors and their cooling and support systems, biological shields, hot cells, irradiation tubes, and other items. Both targets are identical and are able to accept the full 1-MW beam power. This power level lies considerably beyond current experience, although our studies indicate that systems for this performance are feasible. Some of the components can be designed on the basis of available information. Some components require design optimization, and some require hardware testing to provide a facility that is safe, effective, reliable, and efficient. This R&D program provides the needed information to support the IPNS Upgrade design.

B.11.1 Neutronic Calculations

Two categories of neutronic calculations are needed. The first and straightforward category is the calculation of power density distributions, radiation damage rates, isotope production, afterheat, high-energy neutron production, etc., to support the design of targets, moderators, reflectors, premoderators, and decouplers, and their respective cooling and support systems. The second is the optimization of these systems to provide optimal characteristics for the neutron beams. For both purposes, computer code packages such as HETC/NMTC, ORIHET, and ORIGEN suffice without significant modification. The tasks are substantial, however, since the codes and the geometrical models are complex and disparate. This work is planned for FY 1996-1997.

B.11.2 Metallurgy and Tests

Both targets consist of water-cooled tungsten alloy plates. Feasibility studies verify that such plates withstand temperatures and stresses that occur during normal operation and in some abnormal circumstances. Evidence is scant, however, to provide for understanding the likely mechanism of failure and to support estimates of lifetime against failure (targets will certainly have a short lifetime when compared with the facility lifetime) and estimates of corrosion and erosion rates. A program of research and testing is required to provide a basis for establishing a servicing strategy, designing against transport of radioactive materials in the coolant systems, and analyzing accident conditions. So far, feasibility studies have revealed that radiation-induced embrittlement due to hydrogen and helium accumulation in target material most likely represents the life-limiting effect. Materials surveys may identify candidate materials resistant to this embrittlement. Calculations of static and dynamic stresses will reveal methods to extend the lifetime of brittle-designed materials, possibly leading to specifications for proton beam spreading mechanisms in the high-energy proton transfer line upstream of the target. Bench-testing by using rapid-flowing coolant is performed to reveal the extent of cavitation and erosion in the real system. Testing in irradiated coolant provides corrosion rate data and identifies methods for controlling corrosion; in this effort, we expect close collaboration with British (ISIS), European Union (ESS), and Russian (Dubna, Troitsk) groups with shared interests. This work is planned for FY 1996-1997.

B.11.3 Thermal Hydraulics

Measurements in instrumented, electrically heated model target flow channels are intended to verify calculations of heat transfer and coolant pressure drops. This work is planned for FY 1996-1997.

B.11.4 Handling and Changing

Mockups of targets, moderators, reflectors, and shielding are constructed to test and refine methods for handling and changing these components. This work, which improves the reliability and availability of the target and moderator systems, is planned for FY 1996-1997.

B.11.5 Cryogenic Systems and Controls

Cryogenic moderators require attention on several fronts. The behavior of cryogenic moderator materials under irradiation presents numerous questions. Radiolysis in liquid methane produces heavy hydrocarbons that accumulate, restricting flow and diminishing neutronic performance. Methods need to be identified to extend the lifetime of liquid methane moderator systems, by reducing radiation damage through placement of premoderators, by removing hydrocarbon precursors of accumulating solids, or by removing accumulated solids. For example, ozone flushing may remove accumulated solids. Liquid hydrogen goes into the para phase at low temperatures but reverts to an ortho-para mixture under irradiation; the two phases have significantly different neutron thermalization properties, so some instability in the performance of liquid hydrogen moderators can be expected under intense irradiation, which is not understood. These effects — radiolysis of methane and para-to-normal conversion of hydrogen — are to be investigated experimentally in a reactor test being constructed for other, related purposes at the Penn State TRIGA reactor. If liquid methane cannot be made to perform satisfactorily, composite moderators of water or metal hydride and liquid hydrogen may provide the needed neutronic performance; development and neutronic measurements of these composite systems is occurring at the Hokkaido electron linac. Members of the R&D team are to participate in this program as part an already-existing collaboration. Mixed protonated/deuterated materials have the potential for better performance than pure protonated materials, and these are to be investigated both experimentally and theoretically. Neutronic measurements are coordinated with calculations. Big gains in performance and reliability are possible with further moderator system developments. Final moderator design depends on the outcome of these R&D efforts, which are planned for completion in FY 1998.

B.11.6 Shielding and Radiation Monitoring

Optimization of the shielding composition for the main biological shield, beamline shielding, beam stops, and special-purpose local shielding leads to more efficient shield design. This work, which is mostly confined to calculations of candidate material compositions, relies in

part on consulting others who have experience at existing spallation source installations. Some development and testing of radiation monitoring devices for area personnel are needed to assure efficient design and effective performance in pulsed radiation fields. The biological shield studies are planned for completion in FY 1996. The instrument shielding studies are planned for FY 1997-1998.

B.12 NEUTRON BEAM INSTRUMENTATION

The R&D required to provide the initial complement of neutron beam instrumentation at a pulsed neutron source falls naturally into two categories: R&D supporting the selection of instruments to be built, and R&D on instrument components. For the most part, the first category of R&D is done by the appropriate instrument scientists, with the involvement of the user community. The second category requires the heavy involvement of other types of specialists, including engineers, computer scientists and programmers, detector experts, or experts in neutron optics and surface deposition techniques. It may also include the considerable involvement of current or potential component vendors.

B.12.1 Selection of Neutron Beam Instruments

The suggested process is outlined in the following steps:

1. *Identification of Instrument Concepts.* Small workshops are convened to discuss concepts for instruments. The goal is to outline concepts for all instruments that could conceivably be among the initial set to be built. Such instruments amount to considerably more than would actually be built; they might add up to as many as 50 instruments. At these workshops, preliminary assessments of the appropriate mixes of instruments for various broad classes of science are made, such as structures at the atomic scale, large-scale structures, and inelastic scattering.

   Results from the workshop on scientific opportunities held at Argonne in May 1993, the instrumentation sections of the IPNS Upgrade feasibility study, and corresponding instrumentation considerations from LANSCE serve as input to this process. Reports from a number of earlier workshops (Shelter Island, Maria Laach, Rapallo, and the ESS instrumentation workshop at ISIS) are also relevant.

2. *Initial Assessment of Performance and Source Requirements for Each Instrument.* These instrument concepts are analyzed to determine instrument performance and source requirements for each of the potential instruments identified in step 1. This step 2 has already been accomplished for the 27 instruments considered as part of the IPNS Upgrade reference set; probably no more than 20-25 additional instrument concepts have to be

considered at this stage. Such analyses also include a moderately detailed sketch of the instrument concept, assessment of the usefulness of existing instruments versus new construction to fill the specified purpose, and indication of the component development required to optimize instrument performance.

3. *Selection of Prioritized Package of Instruments for Construction.* A steering committee or another group that represents the user community and includes a few technical experts uses the performance analyses of step 2 to recommend a selection of instruments to cover the types of science desired. This procedure may involve a redefinition of instrument concepts and a repetition of step 2 — to include some additional instruments to fill a gap or to combine the functions of two or more instruments, for example. The instrument selection is to be completed in FY 1997.

4. *Complete Conceptual Design of the Selected Set of Instruments.* This step represents a complete instrument conceptual design and optimization, involving extensive use of Monte Carlo design codes. Since staffing will not be adequate to carry out all these conceptual designs in parallel, the first step will be to establish an order of priority for the instruments in the selected set, based on the optimal timetable for beginning the detailed design for each of these instruments. This work is to begin in FY 1997 and continue through FY 1999.

B.12.2 Specific Beamline Instrument Components

A large number of instrument components that are improved in either performance or cost by R&D can be identified. The relative priorities of R&D in each of these areas depend in part on the ability of current state-of-the-art components to meet the requirements developed in the instrument analyses discussed above. Many of the instruments can be built with existing technology, but almost all benefit from improvements in one or more of these areas.

It is necessary to prioritize the component R&D. Criteria include the following: (1) one or more of the desired instruments cannot be built without improvement in the state-of-the-art for such components or (2) significant performance gains or savings in instrument cost result from improvements in such components. A further criterion in both cases is that an R&D program of reasonable scope and with a high probability of success can be defined. The workshop suggested in step 1 of the instrument selection process addressed the prioritization of these various component R&D programs, although these priorities may change as the process proceeds. The component R&D effort continues throughout the project.

For areas in which instrument component R&D is required or desired, several avenues are explored:

- Support of individual development efforts at universities or national laboratories. (For example, many of the data acquisition, visualization, and verification problems and the shielding questions can be handled in this manner.)

- Award of development contracts to current or potential component suppliers. (Development of detectors, some types of beamline optics, some aspects of choppers, and sample environment equipment can be handled in this manner.)

- Participation in European or Japanese development efforts. (The European Community is currently funding a two-year development program for some aspects of neutron beam instrumentation, and the Japanese have a very active program in the development of white-beam neutron polarizers.)

R&D programs for instrument components include the following:

1. *Detector Development.* Detectors represent a large portion (30-50%) of the cost of time-of-flight neutron scattering instruments. Several of the instruments at the IPNS Upgrade require position-sensitive detectors (PSDs) and the associated encoding electronics, which provide better resolution or higher speed than that available with current technology. We will work with the PSD manufacturers and detector development groups at various laboratories worldwide to extend existing technologies or develop new technologies to meet these requirements.

2. *Data Acquisition and Chopper Control Electronics.* This program involves the efforts of engineers and technicians to develop a complete set of prototype data acquisition and chopper control electronics and includes the design and testing of system components.

3. *Data Verification, Manipulation, and Visualization Software.* This effort involves software design engineering and programming, under the supervision of one or more of the neutron scattering scientists. The object is to develop general-purpose code packages for data verification, manipulation, and visualization at each step of the manipulation. Commercial software packages are used to the extent practical, and much of the additional work is done with the support of and in collaboration with faculty and students at university computer science departments. Coordination and collaboration with ongoing efforts in these areas at various centers are important.

4. *Collimator Development.* Multiple-aperture converging collimating systems must be developed to provide the maximum intensity on sample and provide

the tight, clean collimation required for some instruments. Development of these and other specialized collimators requires a combination of analysis, fabrication, and testing of prototypes. This work requires an available beam at an operating neutron source. The required effort involves overall technical direction by one or more scientists and some involvement of a mechanical designer or engineer, but other technical staff, technicians, and students do most of the fabrication and testing of prototypes.

5. *Beamline Optics.* Developments aimed at the improvement of neutron guides and other optical components that depend on the reflection of neutrons from mirrors or supermirrors are already underway at various laboratories and companies. Therefore, until specific device requirements are identified by the instrument analyses, all that is necessary is to maintain an awareness of the current status of and the performances achieved by these ongoing efforts.

6. *Polarization Devices.* Supermirror devices for the polarization and analysis of cold neutrons are readily available, and performances are continually being improved by some of the development efforts noted in program 5. However, suitable polarization devices for higher-energy neutrons and for wide-angle applications are not yet available. Despite recent progress in developing polarized ^{3}He filters for neutron polarization, continued long-term, large-scale development is required before any satisfactory devices are produced. We plan to participate in one of the ongoing development efforts, such as the program in Japan.

7. *Sample Environment Equipment.* The widest-possible range of modern automated sample environment equipment is essential for the effective utilization of IPNS Upgrade. Continuing development in this area is important. This involves efforts by engineers, designers, and technicians to develop and evaluate additional ancillary equipment such as furnaces, pressure cells, sample changers for furnaces, cryostats, displex refrigerators, and automated control systems. In some cases, scientific staff are also required to evaluate the performance of a given piece of ancillary equipment in a neutron instrument. A workshop is planned to assess and prioritize these needs.

B.13 COSTS FOR PRECONSTRUCTION RESEARCH AND DEVELOPMENT PROGRAM

The funds needed to accomplish the preconstruction R&D work are based on the R&D items identified in this Appendix B. The budget profile for this work takes into account the construction schedule described in Chapter VII of this report. One of the most important considerations in developing the schedule is the need for making a smooth transition from the R&D phase to the construction phase while maintaining the schedule for the key project milestones.

B-14

Adequate operating funds (not listed here) are needed to support the precommissioning activities necessary to make the transition to the commissioning phase as various subsystems of the facility are ready for trial operation. The precommissioning activities are scheduled to start in FY 1999. The costs for precommissioning activities are to be developed at a later date.

Costs for the preconstruction R&D effort, direct materials, and service are shown in Table B.13-1 in actual year's dollars.

Table B.13-1 Costs for Preconstruction R&D

Cost Item	Fiscal Year						
	FY95	FY96	FY97	FY98	FY99	FY00	FY01
KD 0 Milestone	○	-	-	-	-	-	-
KD 1 Milestone	-	○	-	-	-	-	-
Construction Start Milestone	-	-	○	-	-	-	-
Commissioning Start Milestone	-	-	-	-	-	-	○
Commissioning Ends Milestone	-	-	-	-	-	-	○
Accelerator R&D	6	21	35	27	8	3	-
Accelerator Physics	3	4	6	6	5	3	-
rf Amplifier R&D (Cathode Follower)	1	4	2	-	-	-	-
Decision on Amplifier Type Milestone	-	-	○	-	-	-	-
rf Cavity and Ferrite R&D	-	-	4	-	-	-	-
Low-Level rf R&D	-	-	-	4	-	-	-
Magnet Performance R&D	1	2	-	-	-	-	-
Dual Frequency Model Power Supply	-	3	-	-	-	-	-
Ceramic Chamber Prototype R&D	1	3	4	-	-	-	-
Chamber Feedthrough	-	-	3	-	-	-	-
Chamber rf Shield R&D	-	-	-	5	-	-	-
Ion Source R&D	-	3	3	-	-	-	-
RFQ R&D	-	-	3	3	-	-	-
CCL R&D	-	-	2	2	-	-	-
Kickers, Septum Magnets R&D	-	-	2	-	-	-	-
Prototype Kicker and Septum	-	-	3	4	-	-	-
Prototype Kicker Test Milestone	-	-	-	○	-	-	-
Diagnostics and Feedback R&D	-	2	2	3	3	-	-
Control System R&D - Import APS	-	-	1	-	-	-	-
Prototype Control Computer Procure	-	-	-	○	-	-	-
Target and Moderator R&D	1	12	16	7	3	-	-
Target Systems							
Neutronic Calculations	0.2	0.5	0.5	0.5	0.5	-	-
Metallurgy and Tests	0.2	2	5	2	-	-	-
Safety	-	0.5	0.5	-	-	-	-
Thermal-Hydraulics	0.1	0.5	1.5	-	-	-	-
Shielding	-	0.5	0.5	-	-	-	-
Monitoring	-	0.5	-	-	-	-	-
Handling/Changing	0.1	0.5	1.5	0.5	-	-	-
Moderator Systems							
Handling/Changing	0.1	0.5	0.5	0.5	-	-	-
Safety	-	0.5	-	-	-	-	-
Neutronic Calculations and Benchmarking	0.1	1.5	1.5	0.5	0.5	-	-
Tests	0.1	3	3	1	1	-	-
Cryogenic Systems and Control	0.1	1	1	2	1	-	-
Radiation Monitoring	-	0.5	0.5	-	-	-	-

Table B.13-1 (Cont.)

Cost Item	Fiscal Year						
	FY95	FY96	FY97	FY98	FY99	FY00	FY01
Instrumentation R&D	1	7	14	11	6	6	-
Instruments							
Conceptual Design Calculations	0.5	2.5	3	2	0.5	-	-
Crystals, Guides, Optics, Polarization, ^{3}He	0.1	1.5	2	1	0.5	0.5	-
Choppers, Controls, t_0, Magnetic Bearings	0.1	-	2	2	2	2	-
Data Acquistion							
Hardware	0.1	2	3	-	-	-	-
Software	0.1	0.5	2	2	0.5	1	-
Data Analysis							
Software Visualization	-	-	-	1	1	1	-
Detectors							
Area, LPSD	0.1	0.5	2	3	1.5	1.5	-
FTE[a]	8	40	65	45	17	9	-
Effort-Related Costs, million $	0.8	4.4	7.8	5.9	2.4	1.4	-
Accelerator Prototype Costs, million $	-	1.5	3	3	3	2.5	-
TOTAL, million $	0.8	5.9	10.8	8.9	5.4	3.9	-

[a] Full-time equivalent.

Appendix C

Possible Future Experimental Facilities

Although the primary mission of the Intense Pulsed Neutron Source (IPNS) Upgrade is neutron scattering, the various components of the facility provide capabilities that are extremely useful for other areas of science. Instrumentation to provide modest capabilities in three of these areas — radiation damage studies, neutron isotope production, and neutron activation analysis — is included as part of this project. The facilities for these three areas of investigation are discussed in detail in Section V.4. The project cost and schedule reflects commitment to build these facilities.

The IPNS Upgrade has potential capabilities in pulsed muon spin rotation and neutrino physics. These are discussed briefly in this appendix. The discussion of potential applications is not intended to be exhaustive, but rather to provide an indication of some of the possibilities. Costs of these potential future applications are not included within the scope of this project.

1 PULSED MUON SPIN ROTATION

Positive muons are an important probe for the study of condensed matter. They are used in the technique known as μSR, which stands for muon spin rotation, relaxation, or resonance, depending on the particular variation of the technique. This technique involves the implantation of initially spin-polarized muons into a sample and the monitoring of their subsequent decay. This is not a scattering technique; the muons are actually stopped in the sample. In most experiments, the muon behaves chemically as a light-weight proton, having a factor of ~9 smaller mass. It can bind an electron to form muonium, in analogy to hydrogen, and the subsequent decay is used to probe hydrogen chemistry in a wide variety of systems. The spin of the muon also serves as a very sensitive probe of local magnetic fields and electronic configurations. An extensive review of the types of science studied with μSR has been provided by Cox.[1] Timing of the decays of the muons is required in most of the muon spin relaxation techniques. A pulsed muon facility operating at a relatively low frequency provides this timing naturally, and so can deliver at least two orders of magnitude more useful muons on the sample than can steady-state sources. Relative advantages of pulsed muon sources for various types of μSR experiments have been discussed in great detail by Cox.[1]

Negative muons behave as very heavy electrons. These can be substituted for atomic electrons to form exotic atoms. Because of the muon's higher mass, its orbitals are much smaller in size, this being most pronounced for the exotic analogs of hydrogen, deuterium, and tritium. When a molecule is formed with a combination of exotic hydrogen analogs and normal hydrogen isotopes, the much smaller size of the exotic analogs allows close approaches of the nuclei, resulting in muon-catalyzed nuclear fusion. This is an area of active study.[2]

Fundamental experiments on the spectroscopy of free muonium are in progress at ISIS, where pulsed laser spectroscopy has been phased to the pulsing of the source to provide a significant advantage.[3] A relatively low-intensity pulsed muon facility is located at the KEK laboratory in Japan, and a high-intensity pulsed muon facility has been included from the beginning[4,5] as part of the ISIS pulsed neutron facility in the United Kingdom. This latter facility, which can be tuned to provide either positive or negative muons, is heavily

oversubscribed. Recently, this facility has been expanded and more muon beamlines have been added.[6]

Figure C.1-1 shows the configuration of the ISIS pulsed muon facility. An intermediate target is located in the proton beam upstream from the neutron production target. A few percent of the protons interact with this thin target, producing pions, which come to rest in the target. These pions decay with a 26-ns lifetime into muons and neutrinos, the muons being extracted at 90° to the proton beamline. For most experiments, the muon beamline optics are tuned to accept only surface muons (i.e., those produced by pions at rest near the surface of the target) that are fully polarized parallel to their flight direction. The muon optics are designed to eliminate muons of the wrong energy or charge and to eliminate other particles, such as positrons, that might interfere with the measurements. These optics also direct the muon beam onto the sample, where the muon is thermalized and then precesses about the local magnetic field. The muon decays with a 2.2-μs lifetime into a positron and two neutrinos, the positron being preferentially emitted along the muon spin direction. Fast positron detectors are used to detect the positrons, and the data-acquisition electronics forms a histogram of the number of detected positrons as a function of time after the proton pulse. This signal is then analyzed to determine the Larmor precession frequency and relaxation of the muon spin polarization with time.

Although few U.S. investigators make use of pulsed muon techniques at present, experience at ISIS suggests that demand for such a facility is likely to develop. No pulsed muon facility is included as part of the initial construction of the IPNS Upgrade, but such a facility, modeled on the one at ISIS, can easily be added after the IPNS Upgrade is operational. It is expected that any perturbation of the neutron scattering program resulting from such an addition would be minor, and losses in neutron production would be minimal.

Space has been reserved for a pulsed muon facility in one of the IPNS Upgrade experiment halls; Figure C.1-2 shows one possible location.
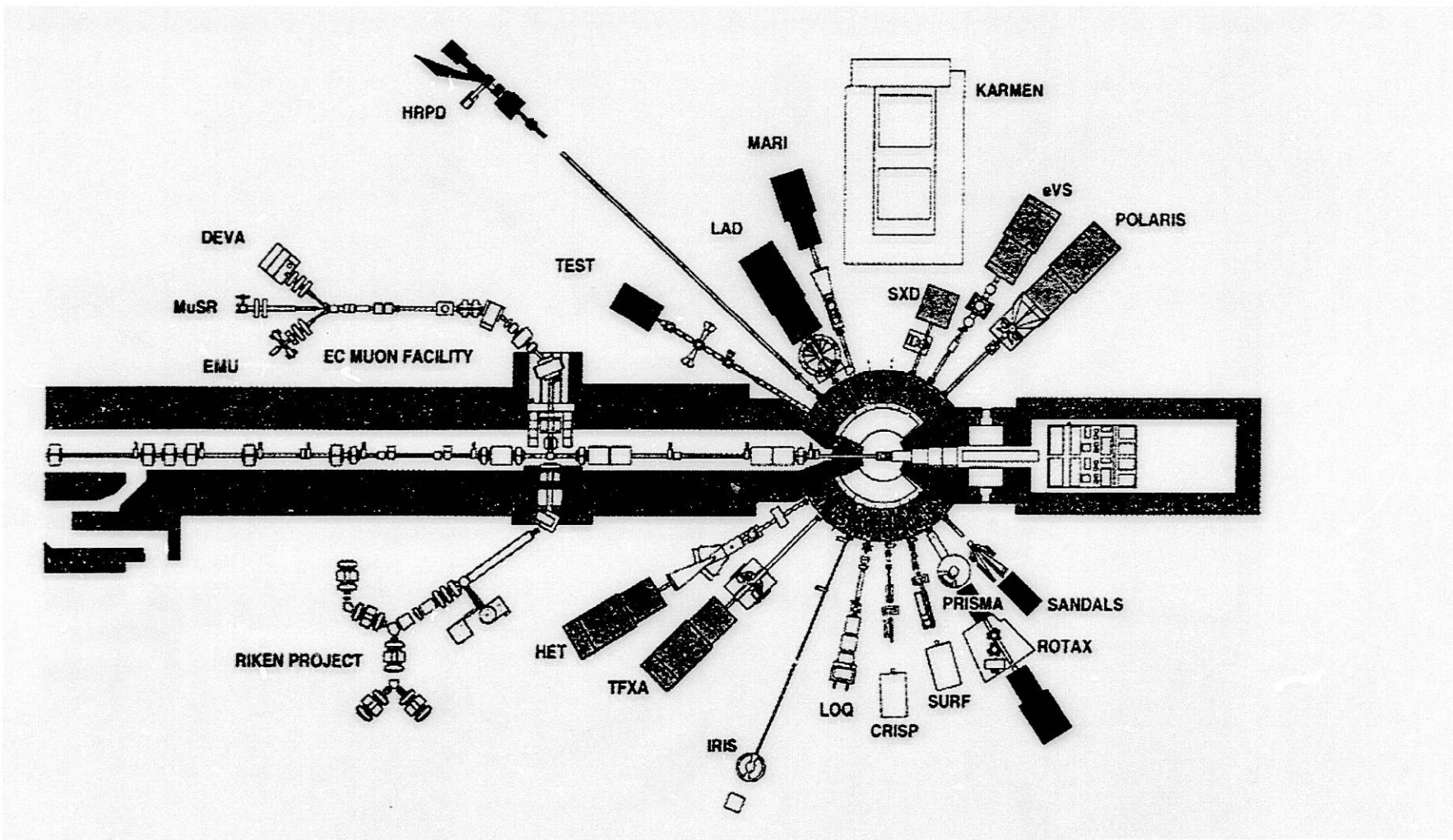
Figure C.1-1 Layout of the ISIS Pulsed Muon Facilities (Source: Reference 6)
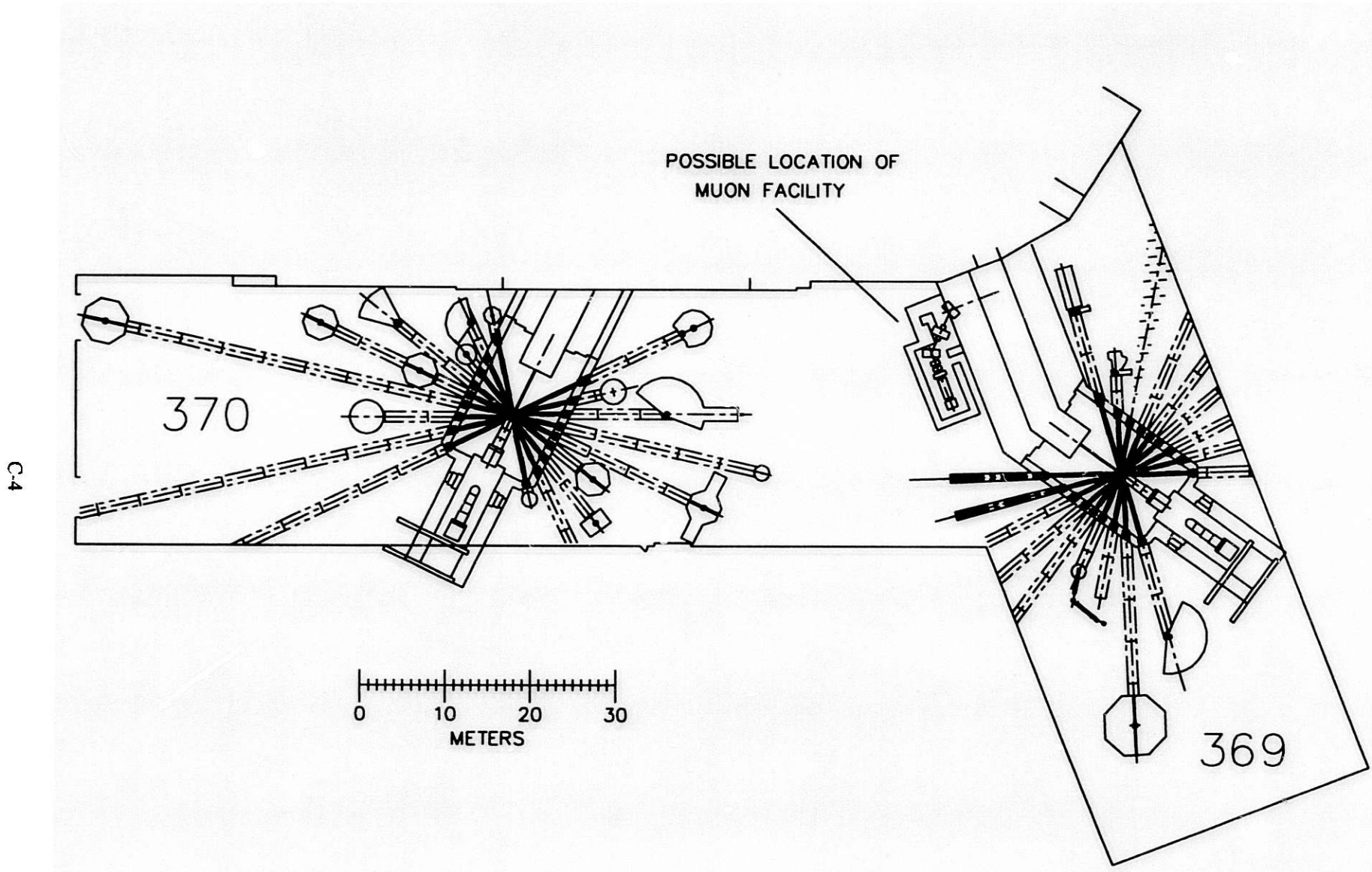
Figure C.1-2 IPNS Upgrade Experiment Halls, Showing a Muon Facility in One Possible Location.
(As shown, there is also adequate room for expansion.)

2 NEUTRINO PHYSICS

In addition to the neutrons produced in the IPNS Upgrade neutron scattering targets, the interactions of the 2-GeV proton beam with the targets also produce intense fluxes of pions. These pions decay according to

$$\pi^0 \rightarrow 2\,\gamma \qquad\qquad \text{(half life } \sim 10^{-16} \text{ s)}, \qquad\qquad \text{(C.2-1)}$$

$$\pi^+ \rightarrow \mu^+ + v_\mu \qquad\qquad \text{(half life } \sim 2.6 \times 10^{-8} \text{ s)}, \qquad\qquad \text{(C.2-2)}$$

and

$$\pi^- \rightarrow \mu^- + \bar{v}_\mu \qquad\qquad \text{(half life } \sim 2.6 \times 10^{-8} \text{ s)}, \qquad\qquad \text{(C.2-3)}$$

and the resulting muons decay according to

$$\mu^+ \rightarrow e^+ + v_e + \bar{v}_\mu \qquad\qquad \text{(half life } \sim 2.2 \times 10^{-6} \text{ s)} \qquad\qquad \text{(C.2-4)}$$

and

$$\mu^- \rightarrow e^- + \bar{v}_e + v_\mu \qquad\qquad \text{(half life } \sim 2.2 \times 10^{-6} \text{ s)}. \qquad\qquad \text{(C.2-5)}$$

However, most of the π^- are captured by the nuclei of the target material before they can decay according to this scheme (Equation C.2-3). Consequently, the neutrino production consists predominantly of v_μ, v_e, and $\bar{v}_\mu$ in equal numbers. The time-structure of the source and the fact that both electron and muon neutrinos are produced provide some unique advantages for neutrino studies with the IPNS Upgrade. Time separation can also be used to distinguish between the v_μ, which are produced promptly, and the v_e and $\bar{v}_\mu$, which are produced over the muon lifetime. These advantages have been recognized at the ISIS facility, where a major British-German collaboration has constructed the 300-ton KARMEN detector for neutrino interaction studies.[7] This detector has recently undergone commissioning and has begun its experimental program, which is expected to last at least five years.[8] The IPNS Upgrade will provide at least six times more neutrino flux than ISIS because of the higher energy and current at the IPNS Upgrade facility.

It is not clear at present whether there will be sufficient demand for a similar detector, or for a different type of detector, for neutrino studies at the IPNS Upgrade facility. It is not proposed at present to pursue this possibility, but merely to alert the physics community to the fact that it will be possible to carry out various types of fundamental physics studies using the neutrinos produced at the IPNS Upgrade facility.

3 REFERENCES

1. S.F.J. Cox, "Implanted muon studies in condensed matter science," J. Phys. C: Solid State Phys. **20**:3187-3319 (1987).

2. *ISIS Annual Report 1991, Vol. 1,* edited by C. Wilson, Rutherford Appleton Laboratory Report No. RAL-91-050, p. 42 (1991); see also Vol. 2, pages A300-A330, for experimental reports indicating the types of pulsed muon experiments recently performed at this facility.

3. *ISIS Annual Report 1989,* edited by A. Taylor and C. Wilson, Rutherford Appleton Laboratory Report No. RAL-89-050, p. 39 (1989).

4. G.H. Eaton et al., "A pulsed surface muon beam/pion beam for the Rutherford Appleton Laboratory Spallation Neutron Source," Nucl. Instrum. Methods **214**:151-167 (1983).

5. G.H. Eaton et al., "Commissioning of the Rutherford Appleton Laboratory Pulsed Muon Facility," Nucl. Instrum. Methods **A269**:483-491 (1988).

6. C.C. Wilson, "A guided tour of ISIS — the U.K. spallation neutron source," Neutron News **6**(2):27-34 (1995).

7. *ISIS Annual Report 1986,* edited by S. Biggin, Rutherford Appleton Laboratory Report No. RAL-86-061, pp. 67-69 (1986).

8. *ISIS Annual Report 1991, Vol. 1,* edited by C. Wilson, Rutherford Appleton Laboratory Report No. RAL-91-050, pp. 43-44 (1991).

Appendix D

Greenfield Option

D.1 INTRODUCTION

The IPNS Upgrade strategy to reuse the existing 360 area conventional facilities has a potential cost savings of approximately $150 million. For comparison, a design for a totally new facility on an alternate site (i.e., the "Greenfield Option") was also developed. Several existing sites that had prior Argonne National Laboratory (ANL) support facilities built on them were reviewed. The 800 area was selected as the IPNS Upgrade Greenfield site.

The 800 area is one of the oldest sites on the Argonne campus and has been used for a variety of functions since 1946. The 800 area buildings were constructed around 1950 and contain 3,950 m^2 of existing structures. Most of these buildings are World-War-II-era "quonset-hut" structures. Approximately one-third of the structures on the site have been demolished; the remaining buildings are scheduled for demolition as funding becomes available for replacement facilities. There are approximately 900 m of paved roads and buried site utilities in the 800 area.

The 800 area site is located on the west side of the ANL campus, as shown in Figure D.1.1-1. It is 650 m north of the Advanced Photon Source (APS) and approximately 620 m northwest of the APS User Residence Facility. The north side of the 800 area is defined by Westgate Road and the west entry to ANL. The west side of the 800 area is defined by the ANL site fence and the ANL landfill area. The east side of the 800 area is defined by Kearney Road. The south side is defined by an east-west line parallel to and approximately 600 m south of Westgate Road.

The land area of the 800 site is 23.4 ha, or about 10% smaller than the 360 site. The plot of land containing 11+ ha southwest of the 800 area was used for landfill disposal of ANL solid wastes. The landfill was closed in 1994; however, existing truck access to it through the 800 area will be maintained.

The design philosophy employed in the Greenfield study was to replicate the functionality of the 360 area buildings in the 800 area and to arrange the structures to suit the geography and the required building function. The total gross floor area of the 800 site buildings is the same as the 360 site buildings and is 55,200 m^2.

The cost estimators used the existing 360 area buildings' "as-built" construction documents for architectural, structural, mechanical, and electrical systems but assumed current construction techniques. Optimization of the Greenfield buildings requires detailed design development; however, use of the existing building documents enables the costs to be estimated to within 30% of the costs of a totally new design.

The new Linac Building (394) and tunnel (394A) conceptual design drawings were used to estimate this facility. The IPNS Upgrade 360 area site plan is shown in Figure VI.1.1-2. The 360 IPNS Upgrade buildings are shown in Figure VI.1.1-4. The Greenfield buildings are shown in Figure D.1.1-2.

IPNS-UPGRADE
GREENFIELD
800 AREA

360
AREA

WATERFALL GLEN
NATURE PRESERVE

WATERFALL GLEN
NATURE PRESERVE

WATERFALL GLEN
NATURE PRESERVE

WATERFALL
NATURE PRESERVE

WATERFALL GLEN
NATURE PRESERVE

North
West — East
South

0 500' 1000' 2000'
0 200 400 METER
SCALE: 1" = 2000'-0"

ANL SITE PLAN

Figure D .1.1-1

WESTGATE ROAD

LABORATORY
WEST GATE
ENTANCE

LAB. OFFICE I

LAB. OFFICE II

LINAC

BLDG.
894

BLDG.
860

BLDG.
862

BLDG.
894A

BLDG.
871A

BLDG.
888A

BLDG.
888B

BLDG.
871B

LET

885

BLDG.
870A

BLDG.
870B

864

30 Hz TARGET

10 Hz TARGET

RCS

HET

BLDG.
877

BLDG.
876

KEARNEY ROAD

IPNS-UPGRADE
GREENFIELD 800-SITE

0   50   100   150   200 FEET
0 10 20 30 40 50 60 METERS

Figure D.1.1-2

CHD00872

D.2 BUILDINGS

Costs of the buildings and facilities that support the various technical components of the IPNS Upgrade in the 800 area were estimated by using existing IPNS and APS facilities as models. Chapter VI includes complete building descriptions and plan details. Table D.2-1 lists the 360 site buildings and their counterparts in the 800 area. Except for two cases, the 300 number designation became the 800 site equivalent; for example, existing Building 364 became new Building 864.
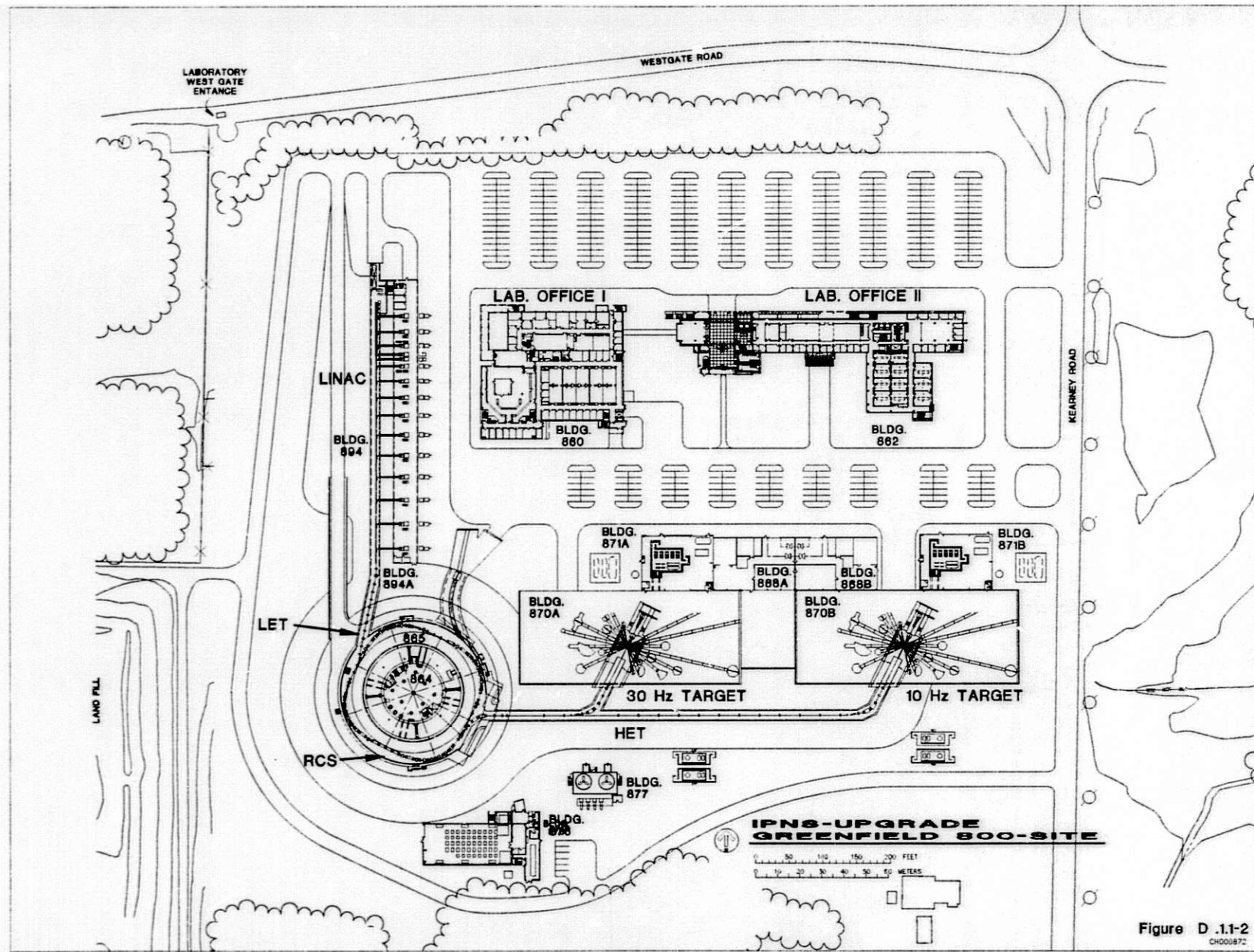
D.3 FACILITY DESCRIPTION

The Linac Building 894 and low-energy transport (LET) Tunnel 894A are placed on a north-to-south line parallel to the ANL west fence line, with the linac source at the north end. The operating floors of all 800 area buildings are at grade. The LET and high-energy transport (HET) tunnels are also at grade. The vehicle access ramp and bridge to the top of the Ring Building are 7 m west of the linac and parallel to it. The Ring and Center Buildings are at the south end of the linac tunnel, as shown in Figure D.1.1-2. The extraction point for the HET line is at the east side of the Ring Building. The HET tunnel and earth shielding run due east.

The 10-Hz and 30-Hz Target Buildings are identical in floor plan and cross section. Their south walls are constructed of cast-in-place concrete and function as retaining walls to hold in place the 8 m of HET tunnel earth shielding.

Preparation Laboratory Buildings 868A and 868B share the common wall of the Target Buildings at the northeast corner of Building 870A and the northwest corner of Building 870B. The two Target Support Buildings 871A and 871B also share the north wall of Buildings 870A and 870B and are located to the east and west of the Preparation Laboratory Building. Two vaults containing coolant retention tanks are buried to the east and west of Buildings 870A and 870B.

Located on an east-to-west line parallel and north of the Target Buildings are Laboratory Office Buildings I (860) and II (862). These two buildings are connected by a tunnel at the service level and a corridor at grade and second floors. A site utility tunnel system connects all of the buildings.

The area to the south of the Laboratory Office Buildings and north of the Target Buildings contains a staging area with truck access and parking for 100 automobiles. The area to the north of the Laboratory Office Buildings serves as a main building entrance and parking area for 300 automobiles, as shown in Figure D.1.1-2.

Table D.2-1 Relationships between 360 Area and 800 Area Buildings

Building Function	360 Area	800 Area	Comments
New Linac Building	394	894	-
New Linac and LET Tunnel	394A	894A	-
Ring Building	365	865	-
Center Building	364	864	-
Power Supply Building	376	876	-
10-Hz Target Building	369	870B	Building 370 was used as a typical design.
10-Hz Target Support Building	367	871B	Building 371 was used as a typical design.
30-Hz Target Building	370	870A	-
30-Hz Target Support Building	371	871A	-
Target Laboratories and Preparation Areas	368	868A and 868B	Half of Building 368 was used as a typical design for both.
Laboratory/Office I	360	860	-
Laboratory/Office II	401	862	See exception 1.[a]
Cooling Towers	377	877	-
Exterior HET Tunnel	None	Exterior HET Tunnel in earth-bermed shielding	See exception 2.[b]

[a] Exception 1. For Building 862, which is the 800 area Laboratory Office building II, data from the APS CLO and Building 401 were used for costing purposes. Building 401 is an office building with a laboratory wing and a gross floor area of 19,400 m^2 that is currently under construction. It is equal in size and function to Building 362 and meets the current DOE standards for office space planning and design. The structure is four stories high with a service floor.

[b] Exception 2. The 800 area option has a long exterior high-energy transport (HET) line that branches off to the 10-Hz and 30-Hz targets. The tunnel cross section is 3.04-m wide by 2.74-m high, the same as that of the linac low-energy transport (LET) tunnel, but the earth berm shield requirement increases from 3.2 m to 8 m. This structure has no counterpart in the 360 area.

D.4 SITE UTILITIES AT THE 800 AREA

New site utilities are included in the 800 area site development. A new steam line connects to the existing ANL central steam line 400 m to the east. Site electricity connects to existing ANL Site Electrical Facility 549A.

D.5 SUMMARY

The total estimated cost for the Greenfield Option conventional facilities and site development is summarized as $208.6 million in supplement C. This cost does not include EDI&A of $21.6 million that, added to the estimate, would make a grand total of $230.2 million.

The total estimated cost to refurbish and reuse the existing 360 area conventional facilities is listed in Supplement B as $49.5 million. This cost does not include EDI&A of $5.1 million, for a grand total of $54.6 million.

Therefore, refurbishing and reusing the existing 360 area for the IPNS Upgrade should save approximately $175.6 million with respect to the cost of constructing entirely new conventional facilities and associated site development.

It should be noted that an actual new IPNS design would not be the Greenfield Option illustrated in this appendix. No value engineering or trade-off studies were performed on the Greenfield Option. The basis of the Greenfield Option was only to ascertain the replacement value of the existing 360 area facility. A new IPNS design would not replicate the 360 area; instead, a specific design for a new facility would take into account current programming and planning guidelines and would incorporate the latest construction techniques. A specific design program would be developed first, which would define the many building components and functional relationships. Designs of various elements would be evaluated and optimized through value engineering studies. With a specific program and design, the new IPNS conventional facility could cost 20 to 25% less than the projected $230.2 million.

The detailed Greenfield estimate is described in Supplement C.

Appendix E

Notation

1D	one-dimensional
2D	two-dimensional
2D-PDF	two-dimensional pair diversity function
A/E	architect/engineer
AABC	Associated Air Balance Council
ac	alternating current
ACI	American Concrete Institute
ADC	analog-to-digital converter
AHU	air-handling unit
ai	analog input
ALARA	as low as reasonably achievable
AMCA	Air Moving and Conditioning Association
ANL	Argonne National Laboratory
ANS	Advanced Neutron Source
ANSI	American National Standards Institute
ao	analog output
APS	Advanced Photon Source
ARI	Air-Conditioning and Refrigeration Institute
ASHRAE	American Society of Heating, Refrigerating and Air Conditioning Engineers, Inc.
ASME	American Society of Mechanical Engineers
ASTM	American Society for Testing and Materials
ATM	asynchronous transfer mode
atm	atmosphere (pressure)
AWS	American Welding Society
BA	budget authority
BNL	Brookhaven National Laboratory
BO	budget outlay
BOCA	Building Officials and Code Administrators International, Inc.
BPM	Beam Position Monitor
BSC	beam-stay-clear
BSCS	Brillouin Scattering Chopper Spectrometer
BURT	backup and restore tool
CBM	Certified Ballast Manufacturer
cc	cubic centimeter(s)
CCL	coupled cavity linac
CEBAF	Continuous Electron Beam Accelerator Facility
CECo	Commonwealth Edison Company
cfm	cubic foot (feet) per minute
CHP	central heating plant
CNCS	Cold-Neutron Chopper Spectrometer
COD	closed-orbit distortion
CPU	central processing unit

CSI	Construction Specifications Institute
CTI	Cooling Tower Institute
CW	chilled water
cw	continuous wave
CWR	chilled-water return
CWS	chilled-water supply
DAC	digital-to-analog converter
DAS	data-acquisition system
dc	direct current
DCSAND	Double-Perfect-Crystal Bonse-Hart Small-Angle Neutron Diffractometer
DCT	database configuration tool
DDC	direct digital controls
DESY	Deutsches Electronen Synchrotron
DEVEL	Instrument and Component Development
DIW	deionized water
DOE	U.S. Department of Energy
DTL	drift tube linac
ED&I	engineering, design, and inspection
EDI&A	engineering, design, inspection, and administration
EDM	electronic distance measurement
EMI	electromagnetic interference
EPB1	Building 369
EPICS	Experimental Physics and Industrial Control System
ES&H	environment, safety, and health
ESRF	European Synchrotron Radiation Facility
ESS	European Spallation Source
ETL	Electrical Testing Laboratories
FCC	Federal Construction Council
FDDI	fiber-distributed data interface
FEL	Free Electron Laser
FET	field effect transistor
FFAG	fixed field alternating gradient
FODO	focus drift defocus drift; focusing/defocusing
fwhm	full width at half maximum
FY	fiscal year
GDCT	graphical database configuration tool
GIF	graphic interface format
GLAD	Glasses, Liquids, and Amorphous Materials Diffractometer
GPIB	general-purpose interface bus
gpm	gallon(s) per minute

GPPD	General Purpose Powder Diffractometer
GREF	Reflectometer for Grazing-Incidence Scattering
GSA/PBS	General Services Administration/Public Buildings Service
GUI	graphical user interface
HEPA	high-efficiency particulate air
HET	high-energy transport; high-energy transport line
HETC	High Energy Transport Code
HI	Hydronics Institute
HIREF	High-Intensity Reflectometer
HLRF	high-level radio-frequency
HQSCD	High-Q Single-Crystal Diffractometer
HRBS	High-Resolution Backscattering Spectrometer
HRMECS	High-Resolution Chopper Spectrometer
HRPD	High-Resolution Powder Diffractometer
HRSAND	High-Resolution Small-Angle Neutron Diffractometer
HVAC	heating, ventilating, and air conditioning
HVDC	high-voltage direct current
HVPS	high-voltage power supply
I/O	input/output
ICANS	International Collaboration on Advanced Neutron Sources
ID	inner diameter; inner dimension
IEEE	Institute of Electrical and Electronics Engineers
IGBT	insulated-gate bipolar transistor
ILL	Institut Laue-Langevin
IOC	input/output controller
IPCEA	Insulated Power Cable Engineers Association
IPNS	Intense Pulsed Neutron Source
IRMA	Inverted Roof Membrane Assembly
IT	irradiation tubes
JIC	Joint Industrial Council
K-V	Kapchinskij-Vladimirskij
KD	key decision
KM	knob manager
ksi	thousand pounds per square inch
L	liter(s)
L/D	length-to-diameter ratio
LAN	local area network
LANCSE	Los Alamos Neutron Scattering Center
LANL	Los Alamos National Laboratory

LBL	Lawrence Berkeley Laboratory
LEBT	low-energy beam transport
LET	low-energy transport; low-energy transport line
LFHRPD	Low-Frequency High-Resolution Powder Diffractometer
LIS	linac injector system
LLRF	low-level radio-frequency
LNPI	Leningrad Nuclear Physics Institute
LOCA	loss of coolant accident
LOTO	lockout/tagout
LPSD	linear-position-sensitive detector
LRMECS	High-Intensity General-Purpose Chopper Spectrometer
LWPD	Long-Wavelength Powder Diffractometer
MAPS	Multi-Angle Positron-Sensitive Spectrometer
MCNP	Monte Carlo code for neutron and photon transport
MCR	main control room
MEDM	Motif-based editor display/manager tool
MHD	magnetohydrodynamics
MICAS	Multiple-Independent-Crystal-Analyzer Spectrometer for Coherent Excitations
MIT	Massachusetts Institute of Technology
MS	matching section
mtbf	mean time before failure
NBS	National Bureau of Standards
NDP/NAA	Neutron Depth Profiling and Neutron Activation Analysis
NEBB	National Environmental Balancing Bureau
NEC	National Electric Code
NEMA	National Electric Manufacturers Association
NEPA	National Environmental Protection Act
NESC	National Electrical Safety Code
NFPA	National Fire Protection Association
NINT	Neutron Interferometer
NIST	National Institute of Standards and Technology
OD	outer diameter; outer dimension
OFHC	oxygen-free high-conductivity
OPI	operator interface
OSHA	Occupational Safety and Health Act
PACE	plant and capital equipment
PBS	private branch exchange
PCSCD	Single-Crystal Diffractometer for Protein Crystallography
PFN	pulse-forming network
PFS	Plant Facilities and Services Division (ANL)

PID	proportional integral derivative
PMQ	permanent magnet quadrupole
PNPD	Polarized-Neutron Powder Diffractometer
POSY-I	Polarized-Neutron Reflectometer
POSY-II	General-Purpose Reflectometer
ppm	part(s) per minute
PROM	programmable read-only memory
PRT	participating research team
PS	power supply
PSF	pound(s) per square foot
psi	pound(s) per square inch
PSI	Paul Scherrer Institut
PSS	pulsed spallation source
pv	process variable
PVC	polyvinyl chloride
PWM	pulse-width-modulated
QENS	Medium-Resolution Crystal-Analyzer Spectrometer
QSS	quasi-steady state
QSSAND	Quasi-Steady-State Small-Angle Neutron Diffractometer
QSTAXC	Cold-Neutron Quasi-Steady-State Triple-Axis Spectrometer
QSTAXT	Thermal-Neutron Quasi-Steady-State Triple-Axis Spectrometer
R	return
R&D	research and development
RADIO	Neutron Radiography/Tomography
RCS	Rapid Cycling Sychrotron
REFD	Reflectometry Development
rf	radio-frequency
RFQ	radio-frequency quadrupole
RGDTL	ramped-gradient drift tube linac
rms	root mean square
RSD	Residual Stress Diffractometer
RW	raw water
S	supply
SAND	General-Purpose Small-Angle Neutron Diffractometer
SCCS	Chopper Spectrometer for Excitations in Single Crystals and Low-Dimensional Systems
SCD	General-Purpose Single-Crystal Diffractometer
SCL	side-coupled linac
SD	defocusing sextupole
sec	second(s)
SEM	scanning electron microscopy; secondary emission monitor

SEPD	Special Environment Powder Diffractometer
SF	focusing sextupole
SLAC	Stanford Linear Accelerator Center
SMACNA	Sheet Metal and Air Conditioning Contractors National Association, Inc.
SNQ	Spallations Neutronenquelle
SPSAND	Special-Purpose Small-Angle Neutron Diffractometer
sr	steradian(s)
SSC	Superconducting Super Collider
Sv	Sievert(s)
SWTP	Sanitary Wastewater Treatment Plant

T	Tesla(s)
TCP/IP	transmission control protocol/Internet protocol
TCU	temperature control unit
TEC	total estimated cost
TEM	transmission electron microscopy
TFCA	Time-Focused Crystal-Analyzer Spectrometer for Chemical Spectroscopy
TFXA	Time-Focused Crystal Analyzer Spectrometer
TOF	time-of-flight
TOFNSE	Time-of-Flight Neutron Spin-Echo Spectrometer
TPM	target protection monitor

UBC	Uniform Building Code
UCN	Ultra-Cold Neutron Facility
UHPD	Ultra-High-Pressure Diffractometer
UHRPD	Ultra-High-Resolution Powder Diffractometer
UL	Underwriters' Laboratories, Inc.

VAV	variable air volume
VCO	voltage-controlled oscillator
VFD	variable frequency drives
VSPD	Very-Small-Sample Powder Diffractometer
VSWR	voltage standing wave ratio

W/G	waveguide
WBS	work breakdown structure

yr	year(s)

ZGS	Zero Gradient Synchrotron
ZING-P	ZGS Intense Neutron Generator Prototype